Transactions of the ASME®

Technical Editor, LEWIS T. WHEELER (1997)

Department of Mechanical Engineering,
University of Houston,
Houston, TX 77204-4792

APPLIED MECHANICS DIVISION

Chairman, WILLIAM S. SARIC
Secretary, THOMAS A. CRUSE
Associate Technical Editors,
R. ABEYARATNE (1994)
T. R. AKYLAS (1994)
S. A. BERGER (1994)
R. M. BOWEN (1993)
S. K. DATTA (1995)
G. J. DVORAK (1995)
M. E. FOURNEY (1993)
R. L. HUSTON (1993)
D. J. INMAN (1995)
S. LICHTER (1995)
X. MARKENSCOFF (1994)
R. M. McMEEKING (1993)
A. K. NOOR (1993)
D. M. PARKS (1995)
J. N. REDDY (1995)
J. W. RUDNICKI (1994)
W. N. SHARPE, JR. (1993)
C. F. SHIH (1995)
P. D. SPANOS (1994)
F. Y. M. WAN (1994)

BOARD ON COMMUNICATIONS

Chairman and Vice-President
R. D. ROCKE

Members-at-Large
T. BARLOW, W. BEGELL, T. F. CONRY
T. DEAR, J. KITTO, R. MATES
W. MORGAN, E. M. PATTON
S. PATULSKI, R. E. REDER
A. VAN DER SLUYS, F. M. WHITE

OFFICERS OF THE ASME
President, J. A. FALCON
Exec. Director
D. L. BELDEN
Treasurer
ROBERT A. BENNETT

PUBLISHING STAFF
Mng. Dir., Publ.,
CHARLES W. BEARDSLEY
Managing Editor,
CORNELIA MONAHAN
Production Editor,
JUDITH SIERANT
Production Assistant,
MARISOL ANDINO

Transactions of the ASME, Journal of Applied Mechanics (ISSN 0021-8936) is published quarterly (Mar., June, Sept., Dec.) for $165.00 per year by The American Society of Mechanical Engineers, 345 East 47th Street, New York, NY 10017. Second class postage paid at New York, NY and additional mailing office. POSTMASTER: Send address changes to Transactions of the ASME, Journal of Applied Mechanics, c/o THE AMERICAN SOCIETY OF MECHANICAL ENGINEERS, 22 Law Drive, Box 2300, Fairfield, NJ 07007-2300.

CHANGES OF ADDRESS must be received at Society headquarters seven weeks before they are to be effective. Please send old label and new address.

PRICES: To members, $40.00, annually: to nonmembers, $165.00. Add $24.00 for postage to countries outside the United States and Canada.

STATEMENT from By-Laws. The Society shall not be responsible for statements or opinions advanced in papers or . . . printed in its publications (B7.1, Par. 3).

COPYRIGHT © 1993 by The American Society of Mechanical Engineers. Authorization to photocopy material for internal or personal use under circumstances not falling within the fair use provisions of the Copyright Act is granted by ASME to libraries and other users registered with the Copyright Clearance Center (CCC) Transactional Reporting Service provided that the base fee of $3.00 per article is paid directly to CCC, 27 Congress St., Salem, MA 01970. Request for special permission or bulk copying should be addressed to Reprints/Permission Department.

INDEXED by Applied Mechanics Reviews and Engineering Information, Inc. Canadian Goods & Services Tax Registration #126148048

Journal of Applied Mechanics

Published Quarterly by The American Society of Mechanical Engineers

VOLUME 60 • NUMBER 2 • JUNE 1993

259 In Memoriam

TECHNICAL PAPERS

260 On the Dundurs Correspondence Between Cavities and Rigid Inclusions (93-APM-37)
X. Markenscoff

265 Universal Relations in Piezoelectric Composites With Eigenstress and Polarization Fields, Part I: Binary Media—Local Fields and Effective Behavior
Y. Benveniste

270 Universal Relations in Piezoelectric Composites With Eigenstress and Polarization Fields, Part II: Multiphase Media—Effective Behavior
Y. Benveniste

276 The Eigenvalues for a Self-Equilibrated, Semi-Infinite, Anisotropic Elastic Strip (93-APM-19)
E. C. Crafter, R. M. Heise, C. O. Horgan, and J. G. Simmonds

282 Antisymmetric Bifurcations in a Compressible Pressure-Sensitive Circular Cylinder Under Axisymmetric Tension and Compression (93-APM-29)
K. T. Chau

290 Buckling and Post-buckling Characteristics of Pressure-Loaded Cylinders (93-APM-27)
Seishi Yamada and J. G. A. Croll

300 On Axisymmetric Residual Stresses in Tubes With Longitudinally Nonuniform Stress Distribution (93-APM-24)
T. Nishimura

310 Stress Analysis for Rolling Contact Between Two Viscoelastic Cylinders
Guangqiu Wang and K. Knothe

318 A Study on Plastic Shakedown of Structures: Part I—Basic Properties
C. Polizzotto

324 A Study on Plastic Shakedown of Structures: Part II—Theorems
C. Polizzotto

331 Dynamics of Bipedal Gait: Part I—Objective Functions and the Contact Event of a Planar Five-Link Biped (93-APM-9)
Y. Hurmuzlu

337 Dynamics of Bipedal Gait: Part II—Stability Analysis of a Planar Five-Link Biped (93-APM-10)
Y. Hurmuzlu

344 Energy Considerations in the Flow Enhancement of Viscoelastic Liquids (93-APM-11)
A. Siginer and A. Valenzuela-Rendón

352 Scattering of Ultrasonic Wave by Cracks in a Plate (93-APM-7)
S. W. Liu and S. K. Datta

358 Power Spectral Density of Nonlinear System Response: The Recursion Method (93-APM-12)
R. Valéry Roy and P. D. Spanos

366 On the Stability of the Damped Hill's Equation With Arbitrary, Bounded Parametric Excitation (93-APM-30)
C. D. Rahn and C. D. Mote, Jr.

371 A Time Integration Algorithm for Structural Dynamics With Improved Numerical Dissipation: The Generalized-α Method (93-APM-20)
J. Chung and G. M. Hulbert

376 On Newton's and Poisson's Rules of Percussive Dynamics (93-APM-38)
J. A. Batlle

382 Vibration Absorbers for a Class of Self-Excited Mechanical Systems (93-APM-16)
S. Natsiavas

388 A Multiple Scales Analysis of Nonlinear, Localized Modes in a Cyclic Periodic System (93-APM-35)
A. Vakakis, T. Nayfeh, and M. King

398 Kinetic Energy and Complementary Kinetic Energy in Gyrodynamics (93-APM-8)
F. P. J. Rimrott, W. M. Szczygielski, and B. Tabarrok

406 The Axisymmetric Crack Problem in a Nonhomogeneous Medium (93-APM-4)
M. Ozturk and F. Erdogan

414 Vibration of Elastic Structures With Cracks (93-APM-15)
I. Y. Shen

422 Interfacial Fracture Mechanics for Anisotropic Bimaterials
J. Qu and J. L. Bassani

432 The $r^{-1/2}$ (ln r) Singularities at Interface Cracks in Monoclinic and Isotropic Bimaterials due to Heat Flow (93-APM-39)
G. Yan and T. C. T. Ting

438 Perturbation Eigensolutions of Elastic Structures With Cracks (93-APM-36)
I. Y. Shen

443 Separation of Strain Components in Composite Materials From Thermoelastic Temperature Measurements
S. A. Dunn

(Contents continued on Inside Back Cover)

Downloaded 04 May 2010 to 171.66.16.49. Redistribution subject to ASME license or copyright; see http://www.asme.org/terms/Terms_Use.cfm

CONTENTS (CONTINUED)

449 **On the Thermal Expansion Coefficient and Specific Heat at Constant Strain for Finite Plastic Deformation** (93-APM-17)
C. W. Bert and S. Huang

456 **On Uncoupling and Solving the Equations of Motion of Vibrating Linear Discrete Systems** (93-APM-13)
S. F. Felszeghy

463 **Thickness Expansions for Higher-Order Effects in Vibrating Cylindrical Shells** (93-APM-22)
J. G. McDaniel and J. H. Ginsberg

470 **Natural Frequencies and Stability of a Flexible Spinning Disk-Stationary Load System With Rigid-Body Tilting** (93-APM-32)
Jen-San Chen and D. B. Bogy

478 **Exact Analytical Solutions for the Vibrations of Sectorial Plates With Simply-Supported Radial Edges** (93-APM-31)
C. S. Huang, A. W. Leissa, and O. G. McGee

484 **On the Dynamic Response of Continuous Systems Including Model Uncertainty** (93-APM-25)
W. D. Iwan and H. Jensen

491 **Stability of Conventional Controller Design for Flexible Manipulators**
L. Tang and S. B. Skaar

498 **On the Flexural-Torsional Behavior of a Straight Elastic Beam Subject to Terminal Moments** (93-APM-3)
Z. Tan and J. A. Witz

506 **Stability Loss in Thick Transversely Isotropic Cylindrical Shells Under Axial Compression** (93-APM-33)
G. A. Kardomateas

514 **Buckling and Post-buckling of Composite Plates and Shells Subjected to Elevated Temperature**
V. Birman and C. W. Bert

520 **Elastic Wrinkling of a Tensioned Circular Plates Using von Kármán Plate Theory** (93-APM-21)
G. G. Adams

526 **Post-buckling of Geometrically Imperfect Shear-Deformable Flat Panels Under Combined Thermal and Compressive Edge Loadings** (93-APM-23)
L. Librescu and M. A. Souza

534 **Viscoelastic Response of a Strand** (93-APM-28)
T. A. Conway and G. A. Costello

541 **Multiply Loaded Timoshenko Beam on a Stressed Orthotropic Half-Plane via a Thin Elastic Layer** (93-APM-14)
H. Bjarnehed

548 **A Hardening Rule Between Stress Resultants and Generalized Plastic Strains for Thin Plates of Power-Law Hardening Material** (93-APM-34)
C. H. Chou, J. Pan, and S. C. Tang

BRIEF NOTES

Analytic Study of Linear and Nonlinear Mode Localization 555
A. F. Vakakis

The Elastic Field for a Sliding Conical Punch on an Isotropic Half-Space 557
M. T. Hanson

559 On the Peak Shear Stresses in Adhesive Joints With Voids
J. N. Rossettos and E. Zang

560 First-Order Perturbation Analysis of Transient Interlaminar Thermal Stress in Composites
Y. R. Wang and T.-W. Chou

DISCUSSIONS

564 **Equilibrium Configurations of Cantilever Beams Subjected to Inclined End Loads, by S. Navaee and R. E. Elling—Discussion by C. Y. Wang**

564 **Two-Dimensional Rigid-Body Collisions With Friction, by Y. Wang and M. T. Mason—Discussion by W. J. Stronge**

566 **The Complementary Potentials of Elasticity, Extremal Properties, and Associated Functionals, by G. Wempner—Discussion by R. T. Shield and S. J. Lee**

BOOK REVIEWS

567 ***Biomechanics: Motion, Flow, Stress, and Growth*, by Y. C. Fung . . .** Reviewed by **S. C. Cowin**

567 ***Stability of Structures: Elastic, Inelastic, Fracture, and Damage Theories*, by Z. P. Bazant and L. Cedolin . . .** Reviewed by **J. W. Hutchinson**

568 ***Elasticity: Mathematical Methods and Applications . . .*** Reviewed by **R. P. Srivastav**

ANNOUNCEMENTS AND SPECIAL NOTES

281 Change of Address Form

375 12th International Congress of Applied Mechanics

397 CSCE Engineering Mechanics Symposium—Announcement and Call for Papers

413 IUTAM Symposium—Call for Proposals

513 Symposium on Material Instabilities—Call for Papers

540 Symposium on Laser Anemometry—Call for Papers

570 Worldwide Mechanics Meetings List

572 Information for Authors

Downloaded 04 May 2010 to 171.66.16.49. Redistribution subject to ASME license or copyright; see http://www.asme.org/terms/Terms_Use.cfm

JOSEPH KESTIN
1913–1993

Joseph Kestin spent half of his nearly 80 years as a member of the mechanical engineering community in the United States, and he has left an enduring mark on the field through his contributions in teaching, research, and engineering practice. He was especially active within the American Society of Mechanical Engineers, and he served as Technical Editor of the *Journal of Applied Mechanics* from 1956 to 1971.

Born in Warsaw, Poland, in 1913, he earned his diploma in engineering at the University of Warsaw in 1937. His undergraduate thesis project was on the viscosity of steam, and a lifelong interest in the properties of steam and other transport media was launched. Joseph's subsequent travels brought him to London, where he began graduate studies at King's College. Returning to Warsaw for a visit late in the summer of 1939, he was enmeshed in the initial stage of World War II. Following his release from a prisoner-of-war camp in 1941, he served for a while on an Allied ship which ferried people back and forth across the Atlantic, and then returned to graduate study combined with duties on London rooftops as an air-raid warden.

Joseph resumed his graduate studies under Sir Owen Saunders, Head of Mechanical Engineering at Imperial College, and he completed a doctoral thesis on "High-speed flow of gases through channels." The University of London readily accommodated the Polish University College following the war as a unit to continue and complete the education of expatriate Poles, and Joseph became head of its Department of Mechanical Engineering. At the same time, Joseph was establishing a reputation as a dedicated experimentalist in transport properties and in transport processes. He built up an excellent teaching laboratory in an unused swimming pool in Putney, and a hobby of translating seminal texts in engineering and physics into English gradually evolved into an invaluable professional contribution. Joseph Kestin's interests in fluid mechanics were obvious from his translations of H. Schlichting's treatise on *Boundary Layer Theory*, edition by edition.

At the age of 39 years Joseph began his 40-year association with Brown University. With G. Newell he developed the theory of oscillating-body viscometers. With a succession of aspiring young students and post-doctoral associates from around the world he made extraordinary precise measurements of viscosity, and subsequently of thermal conductivity. The range and accuracy of these measurements led naturally to collaborations with physical chemists. Joseph found his own pattern of weaving research and teaching together, usually in an international context. His teaching of undergraduate and graduate courses in thermodynamics ran in parallel with his thermodynamics research, and his translations of the classic books by E. Schmidt and A. Sommerfeld were followed by the writing of his own two-volume *Course on Thermodynamics*. In his later years, he actively pursued an interest in the area of the thermodynamics of deformable solids.

Within the American Society of Mechanical Engineers, Joseph served on the Policy Board—Research, the National Nominating Committee, the Task Group on Energy, and the Basic Engineering Technical Group. He was also a member of the Executive Committee of the Applied Mechanics Division, serving as Division chair in 1972–73. For his contributions to the Society, he was awarded the ASME James Potter Gold Medal for Thermodynamics, and twice received the ASME Centennial Medallion for his contributions. His other awards include election to the National Academy of Engineering, election as a Foreign Member of the Polish Academy of Sciences, an honorary doctorate from the Claude Bernard University in Lyon, France, Fellowship of Imperial College, and a Humboldt Foundation Senior Scientist Prize.

Joseph Kestin died in Providence on March 16, 1993. He is survived by his wife Alicia and daughter Anita, a Providence physician. He was widely known for his uniformly high professional standards, attention to details, and cultivation of broad technical interests. He was appreciated by generations of undergraduate engineering students for his lucid and authoritative lectures on thermodynamics. After adoption of teaching evaluation procedures at Brown, a practice of which he never really approved, his courses received high praise from students year after year even though these courses were among the most challenging in the curriculum. He was fluent in several languages, and his precision and clarity in both written and spoken English were a marvel and delight to all who worked with him. He will be long remembered by his many friends and colleagues around the world.

Peter Richardson and Ben Freund
Providence, May 1993

Copyright © 1993 by ASME
Downloaded 03 May 2010 to 171.66.16.245. Redistribution subject to ASME license or copyright; see http://www.asme.org/terms/Terms_Use.cfm

On the Dundurs Correspondence Between Cavities and Rigid Inclusions[1]

X. Markenscoff
Professor of Applied Mechanics,
Department of Applied Mechanics
and Engineering Sciences,
University of California, San Diego,
La Jolla, CA 92093-0411

In plane elasticity the solutions of the stress field of rigid inclusion problems yield the solutions of cavity problems loaded by uniform shear tractions $\sigma = 2\mu(\Omega - \omega_0)|_{\kappa=-1}$, *where* Ω *is the rotation of the inclusion and* ω_0 *the rotation of the material (evaluated at* $\kappa = -1$, κ *being the Kolosov constant). It is proved that* if the limit of the stress field for the inclusion problem exists at $\kappa = -1$, then it corresponds to a constant rotation field.

Introduction

In a recent paper entitled "Cavities vis-à-vis rigid inclusions and some related results in plane elasticity," Dundurs (1989) showed that the stress field for cavity problems in plane elasticity may be obtained from that of rigid inclusions by setting in the solution of the inclusion problems the Kolosov constant $\kappa = -1$. However, the cavities in the corresponding problem may be either stress-free or stressed by a constant shear traction σ which is left undetermined in his analysis. Actually Dundurs claimed that the cavities are stress-free "most of the time" without specifying what "most of the time" means. He provided some specific examples in which σ is zero and some for which it is not. Here we prove for both plane strain and plane stress that, *if by setting* $\kappa = -1$ *in the solution for the stress of the rigid inclusion problem the limit of the solution exists*, then it corresponds to the solution of a cavity loaded by a constant shear traction σ of magnitude $2\mu(\Omega - \omega_0)$, where Ω is the value of the rotation of the inclusion (evaluated at $\kappa = -1$) and ω_0 the material rotation of the elastic field (at $\kappa = -1$), *which is proven to be a constant when evaluated at* $\kappa = -1$. Note at that $\kappa = -1$ or equivalently $\lambda + 2\mu = 0$, ellipticity fails and existence is not guaranteed. Several examples are provided that confirm the aforementioned result.

Proof

Consider a multiply connected body in plane elasticity. The traction boundary value problem consists of solving the equilibrium equations for the stress τ_{ij}.

$$\tau_{ij,j} = 0 \tag{1}$$

$$\text{with } \tau_{ij}n_j = T_i(s) \text{ on } C \tag{2}$$

where $T_i(s)$ is the specified traction vector and n_j the outward normal vector to the boundary $C(s)$. The solution to this problem is independent of the elastic constants of the material if no net forces are acting on the cavities C_i (Michell, 1899). Consequently, the solution to this traction boundary value problem could be possibly obtained from that of a displacement boundary value problem (which depends on the elastic constants) if the elastic constants are set to a certain numerical value.

The Kolosov constant (e.g., Sokolnikoff, p. 265) for plane strain is

$$\kappa = \frac{\lambda + 3\mu}{\lambda + \mu} = 3 - 4\nu$$

and for generalized plane stress,

$$\bar{\kappa} = \frac{\bar{\lambda} + 3\mu}{\bar{\lambda} + \mu} = \frac{3 - \nu}{1 + \nu}$$

where $\bar{\lambda} = 2\lambda\mu/\lambda + 2\mu$, ν is the Poisson's ratio and λ and μ are the Lamé constants of the constitutive equations for linear elastic material,

$$\begin{array}{ll} \text{(plane strain)} & \tau_{ij} = \lambda u_{k,k}\delta_{ij} + \mu(u_{i,j} + u_{j,i}) \\ \text{(plane stress)} & \tau_{ij} = \bar{\lambda} u_{k,k}\delta_{ij} + \mu(u_{i,j} + u_{j,i}) \end{array} \quad (i,j,k = 1,2) \tag{3}$$

with u_k being the displacement vector. The values $\kappa = -1$ and $\bar{\kappa} = -1$ correspond to $\lambda + 2\mu = 0$ and $\bar{\lambda} + 2\mu = 0$, respectively. In the sequel we omit the bar with the understanding that the sequel holds both for plane strain and generalized plane stress.

Equation (1) may be expressed in terms of the displacement by introducing (3) into (1). Let us specialize (3) for the case $\lambda + 2\mu = 0$ (or $\bar{\lambda} + 2\mu = 0$) which correspond to $\kappa = -1$ (or $\bar{\kappa} = -1$), and obtain

$$\tau_{11} = -2\mu u_{2,2}, \quad \tau_{22} = -2\mu u_{1,1}, \quad \tau_{12} = \mu(u_{1,2} + u_{2,1}) \tag{4}$$

Expressing (1) in terms of the displacement by means of (4), we obtain

[1]This paper is dedicated to Prof. John Dundurs on the occasion of his 70th birthday.

Contributed by the Applied Mechanics Division of THE AMERICAN SOCIETY OF MECHANICAL ENGINEERS for presentation at the First Joint ASCE-EMD, ASME-AMD, SES Meeting, Charlottesville, VA, June 6–9, 1993.

Discussion on this paper should be addressed to the Technical Editor, Professor Lewis T. Wheeler, Department of Mechanical Engineering, University of Houston, Houston TX 77204-4792, and will be accepted until four months after final publication of the paper itself in the ASME JOURNAL OF APPLIED MECHANICS.

Manuscript received by the ASME Applied Mechanics Division, Dec. 3, 1991; final revision, June 29, 1992. Associate Technical Editor: L. M. Keer.

Paper No. 93-APM-37.

 Copyright © 1993 by ASME

Downloaded 03 May 2010 to 171.66.16.245. Redistribution subject to ASME license or copyright; see http://www.asme.org/terms/Terms_Use.cfm

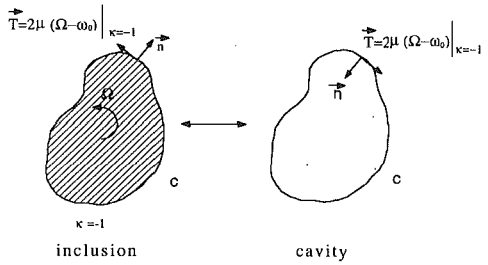


Fig. 1

$$\tau_{11,1}+\tau_{12,2}=0\rightarrow u_{1,22}-u_{2,21}=0\rightarrow[u_{1,2}-u_{2,1}]_{,2}=0$$
$$\tau_{21,1}+\tau_{22,2}=0\rightarrow u_{2,11}-u_{1,12}=0\rightarrow[u_{1,2}-u_{2,1}]_{,1}=0 \qquad (5)$$

which integrate to

$$u_{1,2}-u_{2,1}=2\omega_0. \qquad (6)$$

Equation (6) implies that for the case $\kappa = -1$ equilibrium is tantamount to a constant rotation field ω_0. An example of such a constant rotation field at $\kappa = -1$ is presented in the Appendix.

The expression for the traction (2) in terms of the displacement by substituting (4) into (2) becomes:

$$\tau_{1j}n_j=-2\mu u_{2,2}n_1+2\mu u_{2,1}n_2+2\mu\omega_0 n_2=-2\mu\frac{du_2}{ds}+2\mu\omega_0 n_2$$
$$\tau_{2j}n_j=+2\mu u_{1,2}n_1-2\mu\omega_0 n_1-2\mu u_{1,1}n_2=2\mu\frac{du_1}{ds}-2\mu\omega_0 n_1. \qquad (7)$$

The displacement corresponding to a rigid inclusion in C is

$$u_1=U_1-\Omega x_2,\quad u_2=U_2+\Omega x_1,\quad \text{on } C,$$

which, if introduced into (7), yields

$$T_1=\tau_{1j}n_j=-2\mu(\Omega-\omega_0)n_2$$
$$T_2=\tau_{2j}n_j=2\mu(\Omega-\omega_0)n_1 \qquad (8)$$

The traction vector with components given in (8) is tangent to the boundary of normal $\vec{n}$ and has magnitude $2\mu(\Omega - \omega_0)$ in the direction as shown in Fig. 1.

Thus, we proved that for $\lambda + 2\mu = 0$ the rigid-body displacement boundary conditions on C correspond to a tangential traction of magnitude $2\mu(\Omega - \omega_0)$, where $(\Omega - \omega_0)$ is the relative rotation of the inclusion with respect to the material. Equivalently *if the limit of the stress field for a rigid inclusion problem as* $\kappa \rightarrow -1$ *exists*, then it coincides with a cavity loaded by shear traction $\sigma = -2\mu(\Omega - \omega_0)|_{\kappa=-1}$ (see Fig. 1(*b*)). Obviously for n rigid inclusions, the same result holds for each of them with the corresponding Ω, and the body may be finite or infinite. The shape of the inclusions is arbitrary. The proof of the above result could also be obtained in the complex variable formulation of plane elasticity problems, but the one presented here was considered simpler.

Examples

Several examples are provided where the solution for rigid inclusions and cavities are known and the above results are confirmed. In all of these examples, except for example 4, the material rotation ω_0 of the inclusion problem evaluated at $\kappa = -1$ is zero.

(1) *Circular rigid inclusions in a field of uniform tension* $\xrightarrow{\kappa=-1}$ *. Circular cavity in a field of uniform tension* (*Fig. 2*).

Discussed in Dundurs (1989).

(2) *Rigid line inclusion* (*anticrack*) *in uniform tension* $\xrightarrow{\kappa=-1}$ *. Griffith crack in tension* (*Fig. 3*).

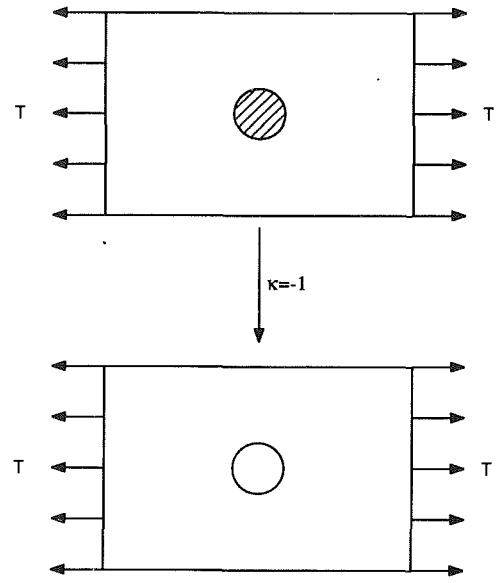


Fig. 2

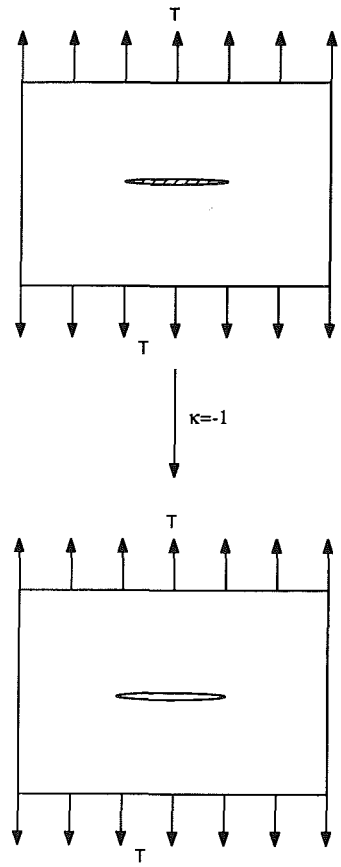


Fig. 3

Discussed in Dundurs (1989).

(3) *Rigid circular inclusion under a concentrated couple* $\xrightarrow{\kappa=-1}$ *. Circular cavity loaded with constant shear traction* (*Fig. 4*).

The Airy Stress function for a circular rigid inclusion loaded with a couple M is

$$U=-\frac{M}{2\pi}\theta$$

from which

Downloaded 03 May 2010 to 171.66.16.245. Redistribution subject to ASME license or copyright; see http://www.asme.org/terms/Terms_Use.cfm

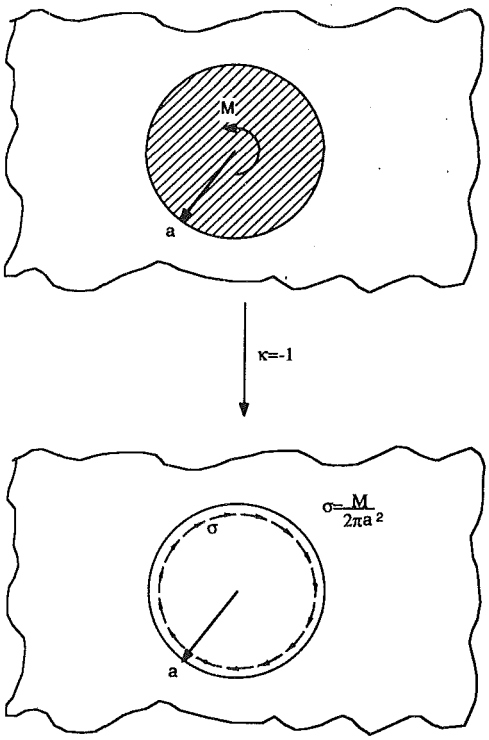


Fig. 4

$$\sigma_{r\theta} = -\frac{M}{2\pi}\frac{1}{r^2} \quad \text{and} \quad \sigma_{r\theta}|_{r=a} = -\frac{M}{2\pi a^2}. \tag{9}$$

Also, the rotation is (Muskhelishvili p. 366 op cit. (83.8a) for $m = 0$)

$$\Omega \equiv \epsilon = \frac{M}{4\pi\mu a^2} = \Omega|_{\kappa=-1}$$

so that

$$\sigma = -2\mu\Omega|_{\kappa=-1} = \frac{-M}{2\pi a^2}$$

which coincides with (9).

(4) *Rigid circular inclusion under a concentrated couple* M *in an annulus* $\xrightarrow{\kappa=-1}$ *. Circular annulus loaded by a constant shear traction at the inner boundary* (*Fig. 5*).

This problem is similar to the previous one except that the geometry is finite. The displacement of the inclusion problem is

$$u_\theta = \Omega\frac{a^2}{b^2-a^2}\left[\frac{b^2}{r^2} - r\right],$$

the stress

$$\sigma_{r\theta} = -2\mu\Omega\frac{a^2b^2}{b^2-a^2}\frac{1}{r^2}, \tag{10}$$

the moment applied on the inclusion

$$M = 4\pi\mu\Omega\frac{a^2b^2}{b^2-a^2},$$

and the rotation

$$\omega_z = \frac{1}{2}\frac{1}{r}\frac{\partial}{\partial r}\left(\frac{1}{r}u_\theta\right) = -\Omega\frac{a^2}{b^2-a^2} \equiv \omega_0 = \omega_0|_{\kappa=-1}.$$

Thus, the cavity will be loaded by a constant shear traction

$$\sigma = -2\mu(\Omega-\omega_0)|_{\kappa=-1} = -2\mu\Omega\frac{b^2}{b^2-a^2}$$

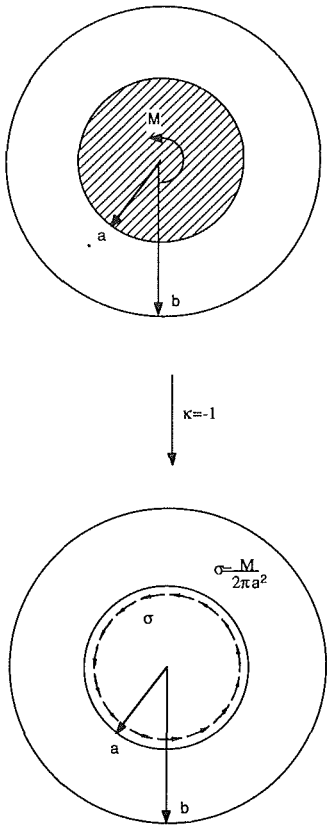


Fig. 5

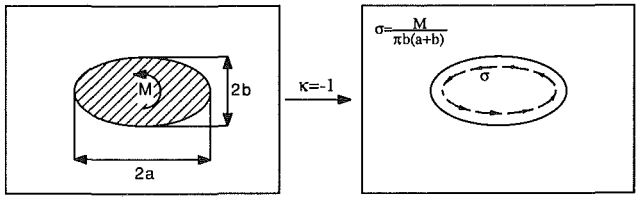


Fig. 6

so that (10) is retrieved at $r = a$.

(5) *Elliptic rigid inclusion with semi-axes* a, b, *under a concentrated couple* M $\xrightarrow{\kappa=-1}$ *elliptical cavity under constant traction* $\sigma = -2\mu\Omega|_{\kappa=-1} = -M/\pi b(a+b)$ (*Fig. 6*).

We will show that the limit of the inclusion problem for $\kappa = -1$ coincides with the solution of the cavity problem under a constant shear traction

$$\sigma = \frac{-M}{\pi b(a+b)}.$$

The solution for the inclusion problem is given by (Muskhelishvili, p. 366) in terms of the complex potentials (in the notation of Muskhelishvili)

$$\varphi(\zeta) = \frac{2\mu m\epsilon Ri}{\kappa\zeta}$$

$$\psi(\zeta) = \frac{2\mu\epsilon Ri}{\kappa\zeta}\left(\kappa + m\frac{1+m\zeta^2}{\zeta^2-m}\right) \tag{11}$$

$$R = \frac{a+b}{2}, \quad m = \frac{a-b}{a+b},$$

and the rotation ϵ is $\epsilon = \dfrac{M\kappa}{4\pi\mu R^2(m+\kappa)}$.

Downloaded 03 May 2010 to 171.66.16.245. Redistribution subject to ASME license or copyright; see http://www.asme.org/terms/Terms_Use.cfm

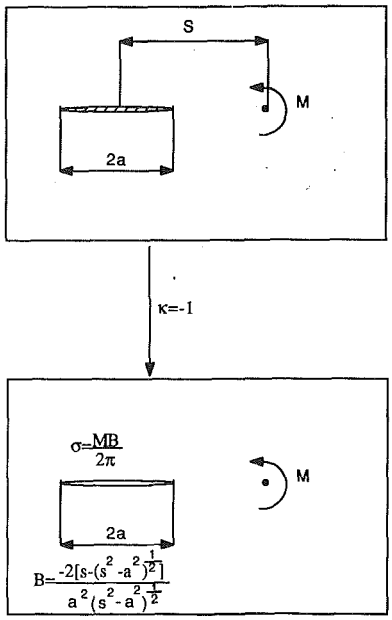


Fig. 7

For $\kappa = -1$, (11) yields

$$\varphi(\zeta) = \frac{-2\mu m \epsilon R i}{\zeta}$$

$$\psi(\zeta) = \frac{-2\mu\epsilon R i}{\zeta}\left(-1 + m\,\frac{1+m\zeta^2}{\zeta^2 - m}\right) \tag{13}$$

with

$$\epsilon|_{\kappa=-1} = \frac{-M}{4\pi\mu R^2(m-1)} = \frac{-M}{2\pi\mu b(a+b)}.$$

On the other hand, the solution for an ellipsoidal cavity under uniform shear T is given by Muskhelishvili (p. 354)

$$\varphi(\zeta) = \frac{TRmi}{\zeta}, \quad \psi(\zeta) = \frac{TRi}{\zeta}\left(-1 + m\,\frac{1+m\zeta^2}{\zeta^2 - m}\right). \tag{12}$$

If in the preceding expressions T has the value

$$T = -2\mu\Omega|_{\kappa=-1} \equiv -2\mu\epsilon|_{\kappa=-1},$$

then (13) becomes

$$\varphi(\zeta) = \frac{-2\mu\epsilon R m i}{\zeta}$$

$$\psi(\zeta) = \frac{-2\mu\epsilon R i}{\zeta}\left(-1 + m\,\frac{1+m\zeta^2}{\zeta^2 - m}\right)$$

which coincides with (11).

(6) *Rigid line inclusion and a moment away from the inclusion (Fig. 7).*

The stress field of a rigid line inclusion of length $2a$ (anticrack) and a concentrated couple M at a distance s from the center of the inclusion on its own plane was given by Dundurs and Markenscoff (1989).

$$\sigma_{xy}(x,0)) = \frac{-M(\kappa-1)}{4\pi\kappa}\left\{\frac{\kappa+1}{\kappa-1}\,\frac{1}{(x-s)^2} + B + j(x)\ \text{sgn}\ xH(|x|-a)\right\} \quad |x| < \infty \tag{14}$$

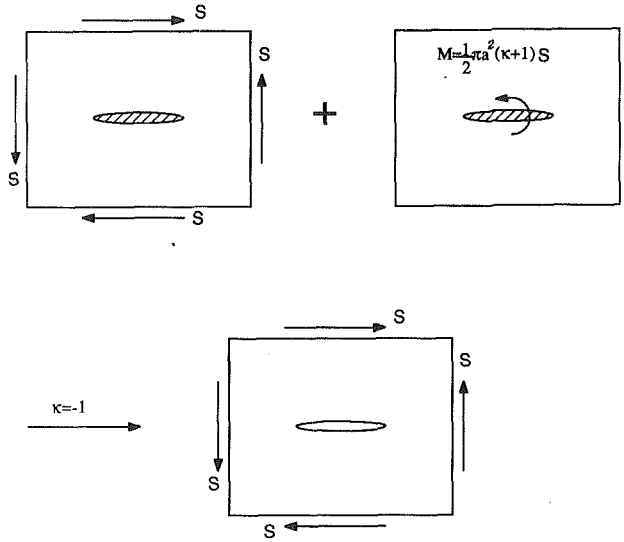


Fig. 8

with

$$B = -\frac{2[s-(s^2-a^2)^{1/2}]}{a^2(s^2-a^2)^{1/2}}$$

$$j(x) = \frac{1}{|x^2-a^2|^{1/2}}\left\{Bx + \frac{sx-a^2}{(s^2-a^2)^{1/2}(x-s)^2}\right\},$$

and the rotation

$$\Omega = \frac{\kappa}{2M(\kappa+1)}\,C \equiv \frac{1}{4\mu}\,\frac{M}{\pi}\,B. \tag{15}$$

Evaluation of (14) at $\kappa = -1$ yields

$$\sigma_{xy}(x,0) = \frac{-MB}{2\pi} \quad \text{for } |x| < a, \tag{16}$$

which would be a crack loaded by $\sigma_{xy} = -MB/2\pi$ on its faces. Obviously, (15) is also obtained by

$$\sigma = -2\mu\Omega|_{\kappa=-1} = -2\mu\,\frac{1}{4\mu}\,\frac{M}{\pi}\,B = -\frac{MB}{2\pi}.$$

(7) *Crack in a shear field from an anticrack in a shear field (Fig. 8).*

An anticrack does not disturb a shear field S; since it can rotate with it, it creates no stresses. Thus, it is not possible to obtain from it the solution of a crack in a shear field which is stressed. However, we can make the following observations. The anticrack in a shear field has rotation $\Omega = S/2\mu$. Thus the crack would be loaded by a constant shear of magnitude $\sigma = -2\mu\Omega$ which we can cancel by superposing an anticrack problem that has the opposite rotation at $\kappa = -1$. Indeed, the anticrack in a shear field S has rotation

$$\Omega = S/2\mu. \tag{17}$$

The anticrack loaded with a concentrated moment M (Fig. 1(*b*)) has rotation (Muskhelishvili, p. 366, for $m = 1$)

$$\Omega = \frac{M\kappa}{\pi\mu a^2(\kappa+1)}. \tag{18}$$

For $M = 1/2\ \pi a^2(\kappa+1)S$, (18) gives

$$\Omega = \frac{S\kappa}{2\mu}, \quad \text{and} \quad \Omega|_{\kappa=-1} = \frac{-S}{2\mu}. \tag{19}$$

The superposition of (17) and (19) gives zero rotation and the solution of the stress field for a crack in a shear field S is the superposition of the stress of pure shear S and that of an anticrack loaded with moment $M = 1/2\ \pi a^2(\kappa+1)S$ (evaluated at $\kappa = -1$).

Downloaded 03 May 2010 to 171.66.16.245. Redistribution subject to ASME license or copyright; see http://www.asme.org/terms/Terms_Use.cfm

Thus, the fact that the limit of the stress field of a rigid inclusion problem as $\kappa \to -1$, if it exists, is the solution for the corresponding cavity problem (loaded with uniform shear on the cavity boundary), can produce some useful solutions of cavity problems. The displacement of the cavity problem is obtained from the stress and involves the Lamé constants of the material.

Acknowledgment

This research was supported by the National Science Foundation grant #MSS-9002804.

References

Cherkaev, A., Lurie, K., and Milton, G. W., 1992, "Invariant Properties of the Stress in Plane Elasticity and Equivalence Classes of Composites," *Proc. Roy. Soc. London A* (in press).

Dundurs, J., 1989, "Cavities Vis-à-Vis Rigid Inclusions and Some Related Results in Plane Elasticity," ASME JOURNAL OF APPLIED MECHANICS, Vol. 56, pp. 786–790.

Dundurs, J., and Markenscoff, X., "A Green's Function Formulation of Anticracks and Their Interaction With Load-Induced Singularities," ASME JOURNAL OF APPLIED MECHANICS, Vol. 56, pp. 550–554.

Dundurs, J., and Markenscoff, X., "Invariance of Stresses Under a Change in Elastic Compliances," *Proc. Roy. Soc. London A* (in press).

Michell, J. H., 1899, "On the Direct Determination of Stress in an Elastic Solid, With Application to the Theory of Plates," *Proc. Lond. Math. Soc.*, Vol. 31, p. 100.

Muskhelishvili, N. I., 1953, *Some Basic Problems of the Mathematical Theory of Elasticity*, translated by J. R. M. Radok, P. Noordhoff.

Sokolnikoff, I. S., 1956, *Mathematical Theory of Elasticity*, McGraw-Hill, New York.

APPENDIX

An example of a constant rotation field is the one associated with invariance of stresses under a change in elastic constants (Cherkaev, Lurie, and Milton, 1992; Dundurs and Markenscoff, 1992). In terms of the shear and area compliances A and S, Hooke's law in plane elasticity is written

$$4\epsilon_{xx} = (A+S)(\tau_{xx}+\tau_{yy}) - 2S\tau_{yy}$$
$$4\epsilon_{xy} = 2S\tau_{xy}$$
$$4\epsilon_{yy} = (A+S)(\tau_{xx}+\tau_{yy}) - 2S\tau_{xx}. \quad \text{(A1)}$$

If the elastic compliances are changed so that (Dundurs and Markenscoff, 1992)

$$\overline{A} = A - a - bx - cy$$
$$\overline{S} = S + a + bx + cy \quad \text{(A2)}$$

where a, b, c are arbitrary constants, then the corresponding to the $\overline{A}$, $\overline{S}$, compliances stress field is

$$\overline{\tau}_{ij} = \tau_{ij}, \quad \text{(A3)}$$

while, of course, the corresponding strains and displacements are not equal.

If we look at the properties of the difference $\overline{u}_i^0(x, y) = u_i(x, y) - \overline{u}_i(x, y)$ of the displacement field then we can show that this displacement field is a constant rotation.

From (A2),

$$A + S = \overline{A} + \overline{S} \quad \text{(A4)}$$

so that

$$A^0 + S^0 \equiv (A+S) - (\overline{A}+\overline{S}) = 0. \quad \text{(A5)}$$

However,

$$A = \frac{\kappa - 1}{2\mu}, \quad S = \frac{1}{\mu}, \quad \text{so that for } A + S = 0\text{: } \kappa = -1.$$

Thus, $A^0 + S^0 = 0$ corresponds to $\kappa = -1$ and this problem is equivalent to the one treated here.

From (A1) we have for $A^0 + S^0 = 0$

$$2\epsilon_{xx}^0 = -S^0\tau_{yy}^0$$
$$2\epsilon_{yy}^0 = -S^0\tau_{xx}^0$$

which are equivalent to (4), so that everything follows as in the main text.

Downloaded 03 May 2010 to 171.66.16.245. Redistribution subject to ASME license or copyright; see http://www.asme.org/terms/Terms_Use.cfm

Universal Relations in Piezoelectric Composites With Eigenstress and Polarization Fields, Part I: Binary Media—Local Fields and Effective Behavior

Y. Benveniste
Department of Solid Mechanics, Materials and Structures, Faculty of Engineering, Tel-Aviv University, Ramat Aviv 69978, Israel

Binary composite media of arbitrary phase geometry are considered. The constituent phases have general anisotropic piezoelectric behavior and contain constant eigenstress and spontaneous polarization fields. An electromechanical loading of the composite aggregate is found which results in uniform strain and electric field intensity throughout the solid. The existence of these uniform fields is used to derive exact universal relations between the local fields as well as between the effective constants of the composite aggregate.

1 Introduction

The investigation of the effective behavior of composite materials in the domain of uncoupled phenomena is today well developed with most of the published work being concerned with uncoupled thermomechanical behavior and thermal conductivity of composites. The idea of using composite materials for optimizing the coupled field behavior of several technological devices is relatively recent. One such application is in the field of piezoelectricity. A piezoelectric material is one that becomes electrically polarized when it is strained, or conversely, one that becomes strained when exposed to an electric field. Since the late 1970s, piezoelectric composites have been used in the manufacture of ultrasonic transducers. A detailed exposition of the several advantages offered by such piezoelectric composites is given in a recent review article by Smith (1989). Many references can be found in that review which led the way to the technological application of such materials. Nevertheless, to the best knowledge of the author, theoretical work in *composites* concerning coupled field phenomena in general, and in piezoelectricity in particular, is rather scarce, especially in comparison with numerous results and micromechanics models which are established today on the uncoupled mechanical behavior of composite media. In recent works, Milgrom and Shtrikman (1989a, 1989b) were concerned with coupled field phenomena in which each driving field is derivable from a scalar function, and Schulgasser (1992) treated piezoelectric composites of a certain class which were effectively transversely isotropic. Turbé and Maugin (1991) have approached the effective dynamical properties of piezoelectric composites by considering Bloch expansions, and others have dealt with micromechanical modeling of such media (see, for example, Skinner et al. (1978), Furukawa et al. (1979), Grekov et al. (1989), Khoroshun and Maslov (1986), and Dunn and Taya (1992)). Somewhat related to heterogeneous media, there has also been interest in the past in dislocation and defects in homogeneous piezoelectric solids (see, for example, Barnett and Lothe (1975), Zhou et al. (1986), and Pak (1990)). For piezoelectric inclusion problems see Benveniste (1992) and the references therein. For a wide survey on coupled fields in general, the reader is referred to recent books by Maugin (1988) and Eringen and Maugin (1990).

The present paper is concerned with deriving exact results of universal nature for *binary* piezoelectric composites of arbitrary phase geometry in which there are eigenstress and polarization fields which are constant within the phases. Such a polarization which exists in addition to that due to the electric field is called "spontaneous polarization" in the literature (see Nye, 1957, p. 78). We will call it here simply "polarization." The derived exact results consist of relations between the *pointwise fields* as well as between *effective parameters* of the *binary* composite. The results are achieved by making use of the uniform fields concept in heterogeneous media recently established by Dvorak (1986, 1990) and Benveniste and Dvorak (1990a, 1990b) in the context of uncoupled mechanical behavior.

In the companion paper (Benveniste, 1993), *heterogeneous* piezoelectric media, in general, and *multiphase composites*, in particular, are considered. The methods of the present paper being exclusively applicable to two-phase systems, that second work makes recourse to virtual work theorems in order to

Contributed by the Applied Mechanics Division of THE AMERICAN SOCIETY OF MECHANICAL ENGINEERS for publication in the ASME JOURNAL OF APPLIED MECHANICS.

Discussion on this paper should be addressed to the Technical Editor, Professor Lewis T. Wheeler, Department of Mechanical Engineering, University of Houston, Houston, TX 77204-4792, and will be accepted until four months after final publication of the paper itself in the ASME JOURNAL OF APPLIED MECHANICS.

Manuscript received by the ASME Applied Mechanics Division, July 26, 1991; final revision, Apr. 24, 1992. Associate Technical Editor: G. J. Dvorak.

Copyright © 1993 by ASME
Downloaded 03 May 2010 to 171.66.16.245. Redistribution subject to ASME license or copyright; see http://www.asme.org/terms/Terms_Use.cfm

derive exact relations which are limited to the effective properties.

In the following two sections we consider a binary composite aggregate with constituents of general anisotropy. The solid has arbitrary phase geometry and does not need to possess statistical homogeneity. In Section 2, the constitutive relations of the phases are defined. Eigenstress and polarization fields which are constant within the phases are also admitted. Such a distribution of eigenstress and polarization fields would occur, for example, in piezoelectric constituents which exhibit pyroelectricity. We show that in these situations, it is possible to find a specific electromechanical loading on the external boundary which results in uniform strain and electric field intensity throughout the composite aggregate. In Section 3, the existence of such uniform fields is used to derive universal relations between the pointwise fields which are induced just by the eigenstresses and polarizations, and those resulting from an electromechanical loading of the external boundary. Section 4 is concerned with the effective behavior of the described composite which is now assumed to possess statistical homogeneity. Universal relations are derived between the effective eigenstress and polarization tensors and the effective elastic, piezoelectric and dielectric constants of the composite, the individual eigenstresses and polarizations, and constituent properties. These relations are shown to reduce to Levin's and Dvorak's result in the special case of uncoupled mechanical behavior, Levin (1967), Dvorak (1990).

2 Uniform Fields

Let us consider a two-phase composite with general anisotropic piezoelectric phases and arbitrary phase geometry. Let the constitutive relations of the phases be given by

$$\begin{aligned} \boldsymbol{\sigma}_r &= \mathbf{L}_r\boldsymbol{\epsilon}_r - \mathbf{e}_r^T\mathbf{E}_r + \boldsymbol{\lambda}_r, \\ \mathbf{D}_r &= \mathbf{e}_r\boldsymbol{\epsilon}_r + \boldsymbol{\kappa}_r\mathbf{E}_r + \mathbf{P}_r, \end{aligned} \qquad r=\alpha,\beta \tag{1}$$

where $r = \alpha, \beta$ denote the constituents, $\boldsymbol{\sigma}_r$, $\boldsymbol{\epsilon}_r$, $\mathbf{E}_r$, $\mathbf{D}_r$ are the stress, strain tensors, and the electric field intensity and displacement vectors, respectively. The elastic, piezoelectric and dielectric constants of the medium are represented by the fourth-order, third-order and second-order tensors $\mathbf{L}_r$, $\mathbf{e}_r$, $\boldsymbol{\kappa}_r$, respectively, and $(\mathbf{e}_r^T)_{ijk} = (\mathbf{e}_r)_{kij}$. Possible eigenstress and polarization fields are denoted by $\boldsymbol{\lambda}_r$ and $\mathbf{P}_r$. A common example of these quantities are stresses and electric displacement fields which are induced by a temperature field

$$\boldsymbol{\lambda}_r = \mathbf{l}_r\theta, \quad \mathbf{P}_r = \mathbf{p}_r\theta, \tag{2}$$

where θ is an increase in the temperature from a reference temperature, $\mathbf{l}_r$ denotes the thermal stress tensor, and $\mathbf{p}_r$ is the vector of pyroelectric coefficients (see, for example, Mindlin (1961).[1] Although such piezoelectric composites exhibiting pyroelectricity have been the main motivation behind the present study, the general formulation of (1) will be used throughout.

Since Eq. (1) involve second, third, and fourth-order tensors, it is useful to represent them by square and rectangular matrices. This can be achieved by using the following convention: replace ij or kl by p and q, where i, k, j, l take the values of 1, 2, 3 and p, q assume the values 1, 2, 3, 4, 5, 6 according to the following table (see, for example, Nye, 1957, p. 113):

Table 1

ij or kl	p or q
11	1
22	2
33	3
23 or 32	4
31 or 13	5
12 or 21	6

In accordance with this representation, it follows that

$$\begin{aligned} &\sigma_p = \sigma_{ij} && \text{for } p=1,2,3,4,5,6 \; i,j=1,2,3, \\ &\epsilon_p = \epsilon_{ij} && \text{for } i=j \; p=1,2,3, \\ &\epsilon_p = 2\epsilon_{ij} && \text{for } i\neq j \; p=4,5,6, \\ &L_{pq} = L_{ijkl} && \\ &e_{ip} = e_{ikl} && \text{for } i,j,k,l=1,2,3 \; p=1,2,3,4,5,6, \end{aligned} \tag{3}$$

and thus the tensors $\mathbf{L}$, $\mathbf{e}$, $\mathbf{e}^T$, and $\boldsymbol{\kappa}$ are represented by (6×6), (3×6), (6×3), and (3×3) matrices, respectively. The short notation used in Eq. (1) and in those which follow are to be interpreted simply as multiplication and addition of matrices.

We consider a state of static equilibrium of the composite aggregate in the presence of no body forces and free electric charges so that

$$\sigma_{ij,j}^{(r)} = 0, \quad D_{i,i}^{(r)} = 0 \quad r=\alpha,\beta. \tag{4}$$

Perfect bonding between the phases is assumed, and the following continuity conditions prevail at interphase boundaries

$$\begin{aligned} u_i^{(\alpha)} &= u_i^{(\beta)}, & \phi^{(\alpha)} &= \phi^{(\beta)}, \\ \sigma_{ij}^{(\alpha)} n_j &= \sigma_{ij}^{(\beta)} n_j, & D_i^{(\alpha)} n_i &= D_i^{(\beta)} n_i, \end{aligned} \tag{5}$$

where $u_i^{(r)}$ denote the mechanical displacement field, $\phi^{(r)}$ is the electric potential, and $\mathbf{n}$ is the normal at the interface between the constituents.

Let the composite aggregate be now subjected to external mechanical and electrical loading on its external surface S in the form of

$$u_i(S) = \epsilon_{ij}^o x_j, \quad \phi(S) = -E_i^o x_i, \tag{6}$$

where $\boldsymbol{\epsilon}^o$ and $\mathbf{E}^o$ denote a constant strain tensor and electric field vector, respectively. Together with (6), consider eigenstress and polarization fields $\boldsymbol{\lambda}_r$ and $\mathbf{P}_r$ which are constant in the phases. Such a distribution of these quantities would prevail, for example, if they were due to a temperature change as in (2).

In general, under boundary conditions (6) and the presence of $\boldsymbol{\lambda}_r$ and $\mathbf{P}_r$, the resulting strains $\boldsymbol{\epsilon}_r$, and electric fields $\mathbf{E}_r$ would be space-dependent throughout. We now ask whether, for *given* eigenstresses $\boldsymbol{\lambda}_r^o$ and polarizations $\mathbf{P}_r^o$ which are *constant* in the phases, it is possible to find a specific set of $\boldsymbol{\epsilon}^o$ and $\mathbf{E}^o$ in (6) so that the resulting $\boldsymbol{\epsilon}_r$ and $\mathbf{E}_r$ be uniform throughout the binary composite. Let these sought uniform fields be denoted by $\hat{\boldsymbol{\epsilon}}$ and $\hat{\mathbf{E}}$

$$\boldsymbol{\epsilon}_r(\mathbf{x}) = \hat{\boldsymbol{\epsilon}}, \quad \mathbf{E}_r(\mathbf{x}) = \hat{\mathbf{E}}. \tag{7}$$

The resulting stresses and electric displacements are obtained by substituting of (7) into (1). It follows therefore that the equilibrium Eqs. (4) are identically fulfilled, and the mechanical displacement field and electric potential pertaining to (7_1) and (7_2) would trivially satisfy (5_1) and (5_2). The unknown quantities $\hat{\boldsymbol{\epsilon}}$ and $\hat{\mathbf{E}}$ are now determined from the following conditions which are sufficient for the fulfillment of (5_3) and (5_4).

$$\boldsymbol{\sigma}_\alpha = \boldsymbol{\sigma}_\beta, \quad \mathbf{D}_\alpha = \mathbf{D}_\beta \tag{8}$$

Using (1) and (7) in (8) yields

$$\begin{aligned} \mathbf{L}_\alpha\hat{\boldsymbol{\epsilon}} - \mathbf{e}_\alpha^T\hat{\mathbf{E}} + \boldsymbol{\lambda}_\alpha^o &= \mathbf{L}_\beta\hat{\boldsymbol{\epsilon}} - \mathbf{e}_\beta^T\hat{\mathbf{E}} + \boldsymbol{\lambda}_\beta^o, \\ \mathbf{e}_\alpha\hat{\boldsymbol{\epsilon}} + \boldsymbol{\kappa}_\alpha\hat{\mathbf{E}} + \mathbf{P}_\alpha^o &= \mathbf{e}_\beta\hat{\boldsymbol{\epsilon}} + \boldsymbol{\kappa}_\beta\hat{\mathbf{E}} + \mathbf{P}_\beta^o, \end{aligned} \tag{9}$$

which are nine scalar equations for the nine unknowns $\hat{\boldsymbol{\epsilon}}$, $\hat{\mathbf{E}}$.

[1] Note that, as in Mindlin, the thermal stress tensor is usually defined in the literature as the negative of $\mathbf{l}_r$.

Downloaded 03 May 2010 to 171.66.16.245. Redistribution subject to ASME license or copyright; see http://www.asme.org/terms/Terms_Use.cfm

In order to represent conveniently the solution of (9), let us define the quantities

$$\Delta\mathbf{L}=\mathbf{L}_\alpha-\mathbf{L}_\beta,\quad \Delta\boldsymbol{\kappa}=\boldsymbol{\kappa}_\alpha-\boldsymbol{\kappa}_\beta,$$
$$\Delta\mathbf{e}=\mathbf{e}_\alpha-\mathbf{e}_\beta,\quad \Delta\mathbf{e}^T=\mathbf{e}_\alpha^T-\mathbf{e}_\beta^T,$$
$$\Delta\boldsymbol{\lambda}^o=\boldsymbol{\lambda}_\alpha^o-\boldsymbol{\lambda}_\beta^o,\quad \Delta\mathbf{P}^o=\mathbf{P}_\alpha^o-\mathbf{P}_\beta^o. \tag{10}$$

Solving for $\hat{\boldsymbol{\epsilon}}$, $\hat{\mathbf{E}}$ in (9) we obtain

$$\hat{\boldsymbol{\epsilon}}=\mathbf{R}\Delta\boldsymbol{\lambda}^o+\mathbf{S}\Delta\mathbf{P}^o,$$
$$\hat{\mathbf{E}}=\mathbf{Q}\Delta\boldsymbol{\lambda}^o+\mathbf{T}\Delta\mathbf{P}^o, \tag{11}$$

where $\mathbf{R}$, $\mathbf{S}$, $\mathbf{Q}$, and $\mathbf{T}$ are tensors represented by (6 × 6), (6 × 3), (3 × 6), and (3 × 3) matrices, respectively. They are given by

$$\mathbf{R}=-\mathbf{F}^{-1},\quad \mathbf{S}=-\mathbf{F}^{-1}\Delta\mathbf{e}^T\Delta\boldsymbol{\kappa}^{-1},$$
$$\mathbf{Q}=\Delta\boldsymbol{\kappa}^{-1}\Delta\mathbf{e}\mathbf{F}^{-1},\quad \mathbf{T}=\Delta\boldsymbol{\kappa}^{-1}(-\mathbf{i}-\Delta\mathbf{e}\mathbf{S}),$$
$$\mathbf{F}=\Delta\mathbf{L}+\Delta\mathbf{e}^T\Delta\boldsymbol{\kappa}^{-1}\Delta\mathbf{e}, \tag{12}$$[2]

where $\mathbf{i}$ is the second-order unit tensor.

We have therefore shown that it is indeed possible to find a set of $\boldsymbol{\epsilon}^o$, $\mathbf{E}^o$ in (6), which in conjunction with $\boldsymbol{\lambda}_r^o$, $\mathbf{P}_r^o$ result in uniform fields in the binary composite. The existence of such uniform fields will be shown to be of utmost importance in the derivation of *local* and *effective* universal relations for the binary piezoelectric composite in the following sections.

For binary systems with nonpiezoelectric constituents, $\mathbf{e}_r = \mathbf{0}$, so that (12) and (11) reduce to

$$\mathbf{R}=-\Delta\mathbf{L}^{-1},\ \mathbf{S}=\mathbf{0},$$
$$\mathbf{Q}=\mathbf{0},\quad \mathbf{T}=-\Delta\boldsymbol{\kappa}^{-1},\quad \mathbf{F}=\Delta\mathbf{L}, \tag{13}$$
$$\hat{\boldsymbol{\epsilon}}=-\Delta\mathbf{L}^{-1}\Delta\boldsymbol{\lambda}^o,$$
$$\hat{\mathbf{E}}=-\Delta\boldsymbol{\kappa}^{-1}\Delta\mathbf{P}^o. \tag{14}$$

In fact, Eqs. (13) and (14) remain valid for constituents which are piezoelectric but satisfy the special condition of $\Delta\mathbf{e} = \mathbf{e}_\alpha - \mathbf{e}_\beta = \mathbf{0}$. Equation ($14_1$) corresponds to Eq. (101) in Dvorak (1990), and for the case of $\Delta\boldsymbol{\lambda} = (\mathbf{l}_\alpha - \mathbf{l}_\beta)\theta$, it corresponds to Eq. (2.16) in Benveniste and Dvorak (1990a).

3 Influence Functions

Suppose now that the binary piezoelectric composite contains as before eigenstresses $\boldsymbol{\lambda}_r^o$ and polarization fields $\mathbf{P}_r^o$ which are constant in the phases. Furthermore, let the composite aggregate be subjected to general mechanical and electrical loads on its external surface $\mathbf{S}$ with arbitrary $\boldsymbol{\epsilon}^o$ and $\mathbf{E}^o$. The induced strain and electric field can then be formally represented as

$$\boldsymbol{\epsilon}_r=\mathbf{A}_r(\mathbf{x})\boldsymbol{\epsilon}^o+\mathbf{B}_r(\mathbf{x})\mathbf{E}^o+\sum_{s=\alpha,\beta}\mathbf{m}_{rs}(\mathbf{x})\boldsymbol{\lambda}_s^o+\sum_{s=\alpha,\beta}\mathbf{n}_{rs}(\mathbf{x})\mathbf{P}_s^o,$$
$$r=\alpha,\beta$$
$$\mathbf{E}_r=\mathbf{a}_r(\mathbf{x})\boldsymbol{\epsilon}^o+\mathbf{b}_r(\mathbf{x})\mathbf{E}^o+\sum_{s=\alpha,\beta}\mathbf{f}_{rs}(\mathbf{x})\boldsymbol{\lambda}_s^o+\sum_{s=\alpha,\beta}\mathbf{g}_{rs}(\mathbf{x})\mathbf{P}_s^o, \tag{15}$$

where we have defined the influence functions $\mathbf{A}_r(\mathbf{x})$, $\mathbf{B}_r(\mathbf{x})$, $\mathbf{a}_r(\mathbf{x})$, $\mathbf{b}_r(\mathbf{x})$, $\mathbf{m}_{rs}(\mathbf{x})$, $\mathbf{n}_{rs}(\mathbf{x})$, $\mathbf{f}_{rs}(\mathbf{x})$, and $\mathbf{g}_{rs}(\mathbf{x})$. In the framework of the notation introduced in Section 2, $\mathbf{A}_r(\mathbf{x})$, $\mathbf{m}_{rs}(\mathbf{x})$ are represented by (6 × 6) matrices, $\mathbf{b}_r(\mathbf{x})$, $\mathbf{g}_{rs}(\mathbf{x})$ by (3 × 3) matrices, $\mathbf{B}_r(\mathbf{x})$, $\mathbf{n}_{rs}(\mathbf{x})$ by (6 × 3) matrices, and finally $\mathbf{a}_r(\mathbf{x})$, $\mathbf{f}_{rs}(\mathbf{x})$ by (3 × 6) matrices.

Note that if the quantities $\boldsymbol{\lambda}_r^o$ and $\mathbf{P}_r^o$ were due to the same cause, like the temperature θ as in (2), then some simplification would have been possible in the representation of (15). Instead of the last two terms in (15_1) and (15_2), it would have been sufficient to have $\boldsymbol{\eta}_r(\mathbf{x})\theta$ and $\boldsymbol{\xi}_r(\mathbf{x})\theta$, respectively, where $\boldsymbol{\eta}_r(\mathbf{x})$ and $\boldsymbol{\xi}_r(\mathbf{x})$ would be the influence functions related to the temperature θ.

Since Eqs. (15) are completely general, they should also hold for the uniform field solutions described in (7) and (11). Substituting (11) in (15_1) and equating the coefficients of $\boldsymbol{\lambda}_\alpha^o$, $\boldsymbol{\lambda}_\beta^o$, $\mathbf{P}_\alpha^o$ and $\mathbf{P}_\beta^o$ gives, respectively,

$$\mathbf{m}_{r\alpha}(\mathbf{x})=-\mathbf{m}_{r\beta}(\mathbf{x})=(\mathbf{I}-\mathbf{A}_r(\mathbf{x}))\mathbf{R}-\mathbf{B}_r(\mathbf{x})\mathbf{Q},$$
$$r=\alpha,\beta$$
$$\mathbf{n}_{r\alpha}(\mathbf{x})=-\mathbf{n}_{r\beta}(\mathbf{x})=(\mathbf{I}-\mathbf{A}_r(\mathbf{x}))\mathbf{S}-\mathbf{B}_r(\mathbf{x})\mathbf{T}, \tag{16}$$

where $\mathbf{I}$ is the fourth-order unit tensor. Equation (16) shows, therefore, that the influence functions $\mathbf{m}_{rs}(\mathbf{x})$ and $\mathbf{n}_{rs}(\mathbf{x})$ related to the eigenstress and polarization fields can be expressed in terms of the influence functions $\mathbf{A}_r(\mathbf{x})$ and $\mathbf{B}_r(\mathbf{x})$. We emphasize that Eq. (16) are valid also for composites which are not statistically homogeneous.

For the special case of nonpiezoelectric constituents with no electromechanical coupling, demanding $\mathbf{B}_r(\mathbf{x}) = 0$ in (15) and using (13) reduces (16) to the form

$$\mathbf{m}_{r\alpha}(\mathbf{x})=-\mathbf{m}_{r\beta}(\mathbf{x})=-(\mathbf{I}-\mathbf{A}_r(\mathbf{x}))\Delta\mathbf{L}^{-1},$$
$$r=\alpha,\beta$$
$$\mathbf{n}_{r\alpha}(\mathbf{x})=\mathbf{n}_{r\beta}(\mathbf{x})=0. \tag{17}$$

It can be shown that Eq. (17_1) corresponds to Eqs. (123)–(124) in Dvorak (1990). To this end, let us reproduce here Eq. (103) in that paper:

$$\boldsymbol{\epsilon}_r(\mathbf{x})=\mathbf{A}_r(\mathbf{x})\boldsymbol{\epsilon}^0+\mathbf{D}_{r\alpha}(\mathbf{x})\boldsymbol{\mu}_\alpha+\mathbf{D}_{r\beta}(\mathbf{x})\boldsymbol{\mu}_\beta, \tag{18}$$

where $\mathbf{D}_{rs}(\mathbf{x})$ are the influence functions defined there for the eigenstrains $\boldsymbol{\mu}_r = -\mathbf{L}_r^{-1}\boldsymbol{\lambda}_r$. Therefore, in the notation of the present work

$$\mathbf{m}_{rs}(\mathbf{x})=-\mathbf{D}_{rs}(\mathbf{x})\mathbf{L}_s^{-1}\quad r,s=\alpha,\beta \text{ (no sum on } s). \tag{19}$$

To proceed further, note that in his Eqs. (123) and (124), Dvorak finds

$$\mathbf{D}_{r\alpha}(\mathbf{x})=(\mathbf{I}-\mathbf{A}_r(\mathbf{x}))(\mathbf{L}_\alpha-\mathbf{L}_\beta)^{-1}\mathbf{L}_\alpha,$$
$$r-\alpha,\beta$$
$$\mathbf{D}_{r\beta}(\mathbf{x})=(\mathbf{I}-\mathbf{A}_r(\mathbf{x}))(\mathbf{L}_\alpha-\mathbf{L}_\beta)^{-1}\mathbf{L}_\alpha. \tag{20}$$

It is therefore seen that the $\mathbf{m}_{r\alpha}(\mathbf{x})$, $\mathbf{m}_{r\beta}(\mathbf{x})$ resulting from (19) and (20) are in agreement with those given in (17_1).

In order to obtain similar relations between the influence functions $\mathbf{f}_{rs}(\mathbf{x})$, $\mathbf{g}_{rs}(\mathbf{x})$ and $\mathbf{a}_r(\mathbf{x})$, $\mathbf{b}_r(\mathbf{x})$, substitute (11) in (15_2) and equate the coefficients of $\boldsymbol{\lambda}_\alpha^o$, $\boldsymbol{\lambda}_\beta^o$, $\mathbf{P}_\alpha^o$, $\mathbf{P}_\beta^o$. This provides

$$\mathbf{f}_{r\alpha}(\mathbf{x})=-\mathbf{f}_{r\beta}(\mathbf{x})=(\mathbf{i}-\mathbf{b}_r(\mathbf{x}))\mathbf{Q}-\mathbf{a}_r(\mathbf{x})\mathbf{R}, \tag{21}$$
$$r=\alpha,\beta$$
$$\mathbf{g}_{r\alpha}(\mathbf{x})=-\mathbf{g}_{r\beta}(\mathbf{x})=(\mathbf{i}-\mathbf{b}_r(\mathbf{x}))\mathbf{T}-\mathbf{a}_r(\mathbf{x})\mathbf{S}. \tag{22}$$

4 Effective Properties

Let us now consider the binary piezoelectric composite which has general anisotropic constituents and arbitrary phase geometry, but now possesses statistical homogeneity. Constant eigenstresses $\boldsymbol{\lambda}_r^o$, and polarization fields $\mathbf{P}_r^o$, $r = \alpha, \beta$, are admitted in the phases. We seek a representation for the effective behavior in the form

$$\bar{\boldsymbol{\sigma}}=\mathbf{L}\bar{\boldsymbol{\epsilon}}-\mathbf{e}^T\mathbf{E}+\boldsymbol{\lambda},$$
$$\overline{\mathbf{D}}=\mathbf{e}\bar{\boldsymbol{\epsilon}}+\boldsymbol{\kappa}\overline{\mathbf{E}}+\mathbf{P}, \tag{23}$$

where $\bar{\boldsymbol{\sigma}}$, $\bar{\boldsymbol{\epsilon}}$, $\overline{\mathbf{D}}$, $\overline{\mathbf{E}}$ denote the average field variables in a representative volume element. Any such quantity denoted by $\bar{\chi}$ is given by

[2]Note that these expressions for $\mathbf{R}$, $\mathbf{S}$, $\mathbf{Q}$, and $\mathbf{T}$ require that $\Delta\boldsymbol{\kappa} \neq \mathbf{o}$. Alternative but equivalent expressions requiring $\Delta\mathbf{L} \neq 0$ are given in Eqs. (B3) of the companion paper. If both $\Delta\mathbf{L} = 0$ and $\Delta\boldsymbol{\kappa} = \mathbf{0}$, then no uniform fields solution is possible.

Downloaded 03 May 2010 to 171.66.16.245. Redistribution subject to ASME license or copyright; see http://www.asme.org/terms/Terms_Use.cfm

$$\overline{\chi} = c_\alpha \overline{\chi}_\alpha + c_\beta \overline{\chi}_\beta, \tag{24}$$

where $\overline{\chi}_r$ with $r = \alpha, \beta$ is the average of the corresponding quantity inphase r, and c_r are the volume fractions of the phases. In (23), $\mathbf{L}$, $\mathbf{e}$, $\boldsymbol{\kappa}$, $\boldsymbol{\lambda}$, and $\mathbf{P}$ denote the effective parameters.

Subject now the composite aggregate to the boundary conditions (6) with arbitrary ϵ^0 and $\mathbf{E}^0$ under which, due to statistical homogeneity, body volume averages $\overline{\epsilon}_{ij}^V$, $\overline{E}_i^V$ are equal to representative volume averages, and there exists

$$\overline{\boldsymbol{\epsilon}}^V = \overline{\boldsymbol{\epsilon}} = \boldsymbol{\epsilon}^o, \quad \overline{\mathbf{E}}^V = \overline{\mathbf{E}} = \mathbf{E}^o. \tag{25}$$

Use of (1), (23), (24), and (25) gives the following equations which provide a basis for the determination of the sought effective quantities:

$$\begin{aligned}
\mathbf{L} &= \mathbf{L}_\alpha + c_\beta(\mathbf{L}_\beta - \mathbf{L}_\alpha)\mathbf{A}_\beta - c_\beta(\mathbf{e}_\beta^T - \mathbf{e}_\alpha^T)\mathbf{a}_\beta,\\
\mathbf{e}^T &= \mathbf{e}_\alpha^T + c_\beta(\mathbf{e}_\beta^T - \mathbf{e}_\alpha^T)\mathbf{b}_\beta - c_\beta(\mathbf{L}_\beta - \mathbf{L}_\alpha)\mathbf{B}_\beta,\\
\mathbf{e} &= \mathbf{e}_\alpha + c_\beta(\mathbf{e}_\beta - \mathbf{e}_\alpha)\mathbf{A}_\beta + c_\beta(\boldsymbol{\kappa}_\beta - \boldsymbol{\kappa}_\alpha)\mathbf{a}_\beta,\\
\boldsymbol{\kappa} &= \boldsymbol{\kappa}_\alpha + c_\beta(\mathbf{e}_\beta - \mathbf{e}_\alpha)\mathbf{B}_\beta + c_\beta(\boldsymbol{\kappa}_\beta - \boldsymbol{\kappa}_\alpha)\mathbf{b}_\beta,
\end{aligned} \tag{26}$$

$$\begin{aligned}
\boldsymbol{\lambda} = \boldsymbol{\lambda}_\alpha^o + c_\beta(\boldsymbol{\lambda}_\beta^o - \boldsymbol{\lambda}_\alpha^o) + c_\beta(\mathbf{L}_\beta - \mathbf{L}_\alpha)\left[\sum_{s=\alpha,\beta}\mathbf{m}_{\beta s}\boldsymbol{\lambda}_s^o + \sum_{s=\alpha,\beta}\mathbf{n}_{\beta s}\mathbf{P}_s^o\right]\\
- c_\beta(\mathbf{e}_\beta^T - \mathbf{e}_\alpha^T)\left[\sum_{s=\alpha,\beta}\mathbf{f}_{\beta s}\boldsymbol{\lambda}_s^o + \sum_{s=\alpha,\beta}\mathbf{g}_{\beta s}\mathbf{P}_s^o\right],
\end{aligned}$$

$$\begin{aligned}
\mathbf{P} = \mathbf{P}_\alpha^o + c_\beta(\mathbf{P}_\beta^o - \mathbf{P}_\alpha^o) + c_\beta(\mathbf{e}_\beta - \mathbf{e}_\alpha)\left[\sum_{s=\alpha,\beta}\mathbf{m}_{\beta s}\boldsymbol{\lambda}_s^o + \sum_{s=\alpha,\beta}\mathbf{n}_{\beta s}\mathbf{P}_s^o\right]\\
+ c_\beta(\boldsymbol{\kappa}_\beta - \boldsymbol{\kappa}_\alpha)\left[\sum_{s=\alpha,\beta}\mathbf{f}_{\beta s}\boldsymbol{\lambda}_s^o + \sum_{s=\alpha,\beta}\mathbf{g}_{\beta s}\mathbf{P}_s^o\right],
\end{aligned}$$

where $\mathbf{A}_r$, $\mathbf{a}_r$, $\mathbf{b}_r$, $\mathbf{B}_r$, $\mathbf{m}_{rs}$, $\mathbf{n}_{rs}$, $\mathbf{f}_{rs}$, $\mathbf{g}_{rs}$, appearing now without the argument $\mathbf{x}$, are simply the averages of the influence functions defined in (15) over V_r of the representative volume element and are called concentration factors. Equating (26_2) and (26_3) provides a consistency condition between the first four concentration factors:

$$(\mathbf{e}_\beta - \mathbf{e}_\alpha)\mathbf{A}_\beta + (\boldsymbol{\kappa}_\beta - \boldsymbol{\kappa}_\alpha)\mathbf{a}_\beta = \mathbf{b}_\beta^T(\mathbf{e}_\beta - \mathbf{e}_\alpha) - \mathbf{B}_\beta^T(\mathbf{L}_\beta - \mathbf{L}_\alpha). \tag{27}$$

A rigorous proof of this consistency condition can be given by making use of the virtual work theorems and appears in the Appendix of the companion paper (Benveniste, 1993).

The concentration factors appearing in (26) can be approximated in the framework of micromechanics models to provide approximate expressions for the effective tensors. We will not pursue this line of inquiry in this paper but will be concerned instead with deriving exact universal relations that the effective tensors need to satisfy among themselves. To achieve that goal, recall first that the concentration factors $\mathbf{m}_{\beta r}$, $\mathbf{n}_{\beta r}$, $\mathbf{f}_{\beta r}$, $\mathbf{g}_{\beta r}$, $r = \alpha, \beta$ can be expressed in terms of $\mathbf{A}_\beta$, $\mathbf{B}_\beta$, $\mathbf{a}_\beta$, $\mathbf{b}_\beta$ through the relations (16) and (21). Next, note that Eqs. $(26_1$-$26_4)$ can be used to express these four tensors in terms of the effective quantities $\mathbf{L}$, $\mathbf{e}$, $\boldsymbol{\kappa}$. It turns out therefore that for binary piezoelectric composites, the effective eigenstress and polarization tensors $\boldsymbol{\lambda}$ and $\mathbf{P}$ can be expressed in terms of the effective piezoelectric tensors $\mathbf{L}$, $\mathbf{e}$, and $\boldsymbol{\kappa}$, and the individual eigenstresses and polarizations.

Solving $(26_1$-$26_4)$ for $\mathbf{A}_\beta$, $\mathbf{a}_\beta$, $\mathbf{B}_\beta$, and $\mathbf{b}_\beta$ provides

$$\begin{aligned}
c_\beta\mathbf{A}_\beta &= (\Delta\mathbf{L} + \Delta\mathbf{w})^{-1}[(\mathbf{L}_\alpha - \mathbf{L}) + \Delta\mathbf{e}^T\Delta\boldsymbol{\kappa}^{-1}(\mathbf{e}_\alpha - \mathbf{e})],\\
c_\beta\mathbf{b}_\beta &= (\Delta\boldsymbol{\kappa} + \Delta\mathbf{v})^{-1}[(\boldsymbol{\kappa}_\alpha - \boldsymbol{\kappa}) + \Delta\mathbf{e}\Delta\mathbf{L}^{-1}(\mathbf{e}_\alpha^T - \mathbf{e}^T)],\\
c_\beta\mathbf{B}_\beta &= \Delta\mathbf{L}^{-1}(\mathbf{e}^T - \mathbf{e}_\alpha^T) + \Delta\mathbf{L}^{-1}\Delta\mathbf{e}^T(\Delta\boldsymbol{\kappa} + \Delta\mathbf{v})^{-1}[(\boldsymbol{\kappa}_\alpha - \boldsymbol{\kappa})\\
&\qquad + \Delta\mathbf{e}\Delta\mathbf{L}^{-1}(\mathbf{e}_\alpha^T - \mathbf{e}^T)],\\
c_\beta\mathbf{a}_\beta &= \Delta\boldsymbol{\kappa}^{-1}(\mathbf{e}_\alpha - \mathbf{e}) - \Delta\boldsymbol{\kappa}^{-1}\Delta\mathbf{e}(\Delta\mathbf{L} + \Delta\mathbf{w})^{-1}[(\mathbf{L}_\alpha - \mathbf{L})\\
&\qquad + \Delta\mathbf{e}^T\Delta\boldsymbol{\kappa}^{-1}(\mathbf{e}_\alpha - \mathbf{e})],
\end{aligned} \tag{28}$$

where

$$\Delta\mathbf{w} = \Delta\mathbf{e}^T\Delta\boldsymbol{\kappa}^{-1}\Delta\mathbf{e}, \quad \Delta\mathbf{v} = \Delta\mathbf{e}\Delta\mathbf{L}^{-1}\Delta\mathbf{e}^T. \tag{29}$$

Use of (28) in (16) and (21) with $r = \beta$ and their subsequent substitution in (26_5) and (26_6) yield the desired universal relations. These equations as obtained by the described procedure are long and will not be given here. In the companion paper (Benveniste, 1993) a completely different approach will be shown to provide equivalent results which can be succinctly summarized as Eqs. (39) in that paper. The effective tensors $\boldsymbol{\lambda}$ and $\mathbf{P}$ can therefore be expressed in terms of the effective tensors $\mathbf{L}$, $\mathbf{e}$, and $\boldsymbol{\kappa}$, the constituent properties, and the individual eigenstresses and polarizations. This result is a generalization of the well-known Levin's Eqs. (1967) to the case of piezoelectricity and in the *general context* of eigenstress and polarization fields.

Let us now verify that the above described analysis does yield the existing universal relations in the special case of the nonpiezoelectric composite. Note that with $\mathbf{e}_r = \mathbf{0}$, we have from (29)

$$\Delta\mathbf{w} = \Delta\mathbf{v} = \mathbf{0}, \tag{30}$$

so that when combined with (28), this provides the simple relations

$$\begin{aligned}
c_\beta\mathbf{A}_\beta &= \Delta\mathbf{L}^{-1}(\mathbf{L}_\alpha - \mathbf{L}),\\
c_\beta\mathbf{b}_\beta &= \Delta\boldsymbol{\kappa}^{-1}(\boldsymbol{\kappa}_\alpha - \boldsymbol{\kappa}),\\
c_\beta\mathbf{a}_\beta &= c_\beta\mathbf{B}_\beta = 0.
\end{aligned} \tag{31}$$

Use of (31) in (17) and (22) yields

$$c_\beta\mathbf{m}_{\beta\alpha} = -c_\beta\mathbf{m}_{\beta\beta} = -[c_\beta\mathbf{I} - \Delta\mathbf{L}^{-1}(\mathbf{L}_\alpha - \mathbf{L})]\Delta\mathbf{L}^{-1},$$

$$\mathbf{n}_{r\alpha} = \mathbf{n}_{r\beta} = 0, \tag{32}$$

$$c_\beta\mathbf{g}_{\beta\alpha} = -c_\beta\mathbf{g}_{\beta\beta} = -[c_\beta\mathbf{i} - \Delta\boldsymbol{\kappa}^{-1}(\boldsymbol{\kappa}_\alpha - \boldsymbol{\kappa})]\Delta\boldsymbol{\kappa}^{-1},$$

$$\mathbf{f}_{r\alpha} = \mathbf{f}_{r\beta} = 0, \tag{33}$$

Finally, substitution of (32) and (33) in (26_5) and (26_6), respectively, yields

$$\boldsymbol{\lambda} = \boldsymbol{\lambda}_\alpha^o + (\mathbf{L}_\alpha - \mathbf{L})(\mathbf{L}_\beta - \mathbf{L}_\alpha)^{-1}(\boldsymbol{\lambda}_\alpha^o - \boldsymbol{\lambda}_\beta^o), \tag{34}$$

$$\mathbf{P} = \mathbf{P}_\alpha^o + (\boldsymbol{\kappa}_\alpha - \boldsymbol{\kappa})(\boldsymbol{\kappa}_\beta - \boldsymbol{\kappa}_\alpha)^{-1}(\mathbf{P}_\alpha^o - \mathbf{P}_\beta^o). \tag{35}$$

Equation (34) coincides with the effective eigenstress given in Eq. (131) of Dvorak (1990), which is

$$\boldsymbol{\lambda} = (\mathbf{L} - \mathbf{L}_\alpha)(\mathbf{L}_\alpha - \mathbf{L}_\beta)^{-1}\mathbf{L}_\beta\boldsymbol{\mu}_\beta - (\mathbf{L} - \mathbf{L}_\beta)(\mathbf{L}_\alpha - \mathbf{L}_\beta)^{-1}\mathbf{L}_\alpha\boldsymbol{\mu}_\alpha. \tag{36}$$

Noting that $\boldsymbol{\lambda}_\beta^0 = -\mathbf{L}_\beta\boldsymbol{\mu}_\beta$, $\boldsymbol{\lambda}_\alpha^o = -\mathbf{L}_\alpha\boldsymbol{\mu}_\alpha$ it can be shown indeed after some manipulation that (34) and (36) are equivalent. If the eigenstress are due to a change in temperature as in (2_1) then (34) reduces to Levin's result (1967), see also Benveniste and Dvorak (1990a). Finally, it should be mentioned here that in the case of pyroelectricity, the corresponding equation (35) loses any physical relevance since all pyroelectric materials are piezoelectric.

Conclusions

We have shown in this paper how the existence of uniform fields in heterogeneous media established by Dvorak (1986, 1990), and Benveniste and Dvorak (1990a, 1990b) in the context of uncoupled mechanical behavior, can be extended to binary composite piezoelectric media. These uniform fields have been used to determine exactly the *local fields* induced in a binary piezoelectric medium due to a distribution of constant eigenstresses and polarizations in the phases, in terms of the *local fields* produced in the same medium which has no eigenstresses and polarizations but is instead subjected on its external boundary to an electromechanical loading. An outcome of these *local relations* is that the effective eigenstresses and polarizations

Downloaded 03 May 2010 to 171.66.16.245. Redistribution subject to ASME license or copyright; see http://www.asme.org/terms/Terms_Use.cfm

can be determined in terms of the effective elastic, dielectric and piezoelectric constants of the *binary* composite, its constituent properties, and the individual eigenstresses and polarizations. These results would simplify considerably the analysis of specific problems because only part of that analysis needs in fact to be performed. Furthermore, they can be useful in verifying a certain internal consistency of various approximate micromechanical models. In the adopted form of the constitutive equations in the present paper the stress and electric displacement are expressed in terms of the strains and electric fields. The chosen electromechanical loading on the external boundary is such that the mechanical displacements and electric potential are prescribed. A similar analysis to that given in the present paper can be readily performed for alternative versions of the constitutive laws and electromechanical loading of the composite aggregate.

The extension of the uniform fields concept to multiphase media has been recently studied by Dvorak and Benveniste (1992) in the case of uncoupled mechanical behavior. Although certain results concerning the local fields can indeed be obtained, connections relating *fully* the eigenstress-induced fields to those produced by an external loading are not forthcoming. In the absence of such a result in the uncoupled mechanical case, it follows that it is also nonexistent in the multiphase piezoelectric composite. This leads the way to the companion paper (Benveniste, 1993) which is concerned with multiphase piezoelectric media but limits itself to produce results only on the effective properties by means of virtual work theorems.

Acknowledgment

Helpful conversions with K. Schulgasser and S. Shtrikman are acknowledged.

References

Barnett, D. M., and Lothe, J., 1975, "Dislocation and Line Charges in Anisotropic Piezoelectric Insulators," *Phys. Stat. Sol.* (*b*), Vol. 67, pp. 105–111.

Benveniste, Y., 1992, "The Determination of the Elastic and Elastic Fields in a Piezoelectric Inhomogeneity," *J. of Applied Physics*, Vol. 72, pp. 1082–1095.

Benveniste, Y., 1993, "Universal Relations in Piezoelectric Composites with Eigenstress and Polarization Fields,, Part II: Multiphase Media—Effective Behavior," Vol. 60, pp. 270–275.

Benveniste, Y., and Dvorak, G. J., 1990a, "On a Correspondence Between Mechanical and Thermal Effects in Two-Phase Composites," *Micromechanics and Inhomogeneity*, (Toshio Mura Anniversary Volume) G. J. Weng, M. Taya, and H. Abé, eds., Springer-Verlag, New York, pp. 65–81.

Benveniste, Y., and Dvorak, G. J., 1990b, "On a Correspondence Between Mechanical and Thermal Fields with Slipping Interfaces," *Inelastic Deformation of Composite Materials*, George J. Dvorak, ed., IUTAM Symposium, Troy, NY, May 29–June 1, Springer-Verlag, New York, pp. 77–98.

Benveniste, Y., and Dvorak, G. J., 1992, "On Uniform Fields and Universal Relations in Piezoelectric Composites," *J. Mech. and Phys. of Solids*, Vol. 40, pp. 1295–1312.

Dunn, M. L., and Taya, M., 1993, "Micromechanics Predictions of the Effective Electro-Elastic Moduli of Piezoelectric Composites, *Int. J. Solid Structures*, Vol. 30, pp. 161–175.

Dvorak, G. J., 1986, "Thermal Expansion of Elastic-Plastic Composite Materials," ASME JOURNAL OF APPLIED MECHANICS, Vol. 53, pp. 737–743.

Dvorak, G. J., 1990, "On Uniform Fields in Heterogeneous Media, *Proceedings of the Royal Society, London*, Vol. A431, pp. 89–110.

Dvorak, G. J., and Benveniste, Y., 1992, "On Transformation Strains and Uniform Fields in Multiphase Elastic Media," *Proc. Roy. Soc. Lond.*, Vol. A437, pp. 291–310.

Eringen, C., and Maugin, G. A., 1990, *Electrodynamics of Continua (I), Foundations and Solid Media*, Springer-Verlag, New York.

Furukawa, T., Ishida, K., and Fukuda, E., 1979, "Piezoelectric Properties in the Composite Systems of Polymers and PZT Ceramics," *J. Appl. Phys.*, Vol. 50, pp. 4904–4912.

Grekov, A. A., Kramarov, S. O., and Kuprienko, A. A., 1989, "Effective Properties of a Transversely Piezoelectric Composite with Cylindrical Inclusions," *Mech. of Composite Mats.*, Vol. 25, pp. 54–60.

Khoroshun, L. P., and Maslov, B. P., 1979, "Prediction of Electromechanical Properties of Inhomogeneous Piezoelectrics," *Prikl. Mekh.*, Vol. 15, p. 37.

Levin, V. M., 1967, "Thermal Expansion Coefficients of Heterogeneous Materials," *Mekhanika Tverdogo Tela*, Vol. 2, pp. 88–94 (English translation: *Mechanics of Solids*, Vol. 11, pp. 58–61).

Maugin, G. A., 1988, *Continuum Mechanics of Electromagnetic Solids*, North-Holland, Amsterdam.

Milgrom, M., and Shtrikman, S., 1989a, "Linear Response of Two-Phase Composites with Cross-Moduli: Exact Universal Relations," *Physical Review A*, Vol. 40, pp. 1568–1575.

Milgrom, M., and Shtrikman, S., 1989a, "Linear Response of Polycrystals to Coupled Fields: Exact Relations Among Coefficients," *Physical Review B*, Vol. 40, pp. 5991–5994.

Mindlin, R. D., 1961, "On the Equations of Motion of Piezoelectric Crystals," *Problems in Continuum Mechanics*, SIAM, pp. 282–290.

Nye, J. F., 1957, *Physical Properties of Crystals: Their Representation by Tensors and Matrices*, Clarendon Press, Oxford, U.K.

Pak, Y. E., 1990, "Force on a Piezoelectric Screw Dislocation," ASME JOURNAL OF APPLIED MECHANICS, Vol. 57, pp. 863–869.

Schulgasser, K., 1992, "Relationships Between the Effective Properties of Transversely Isotropic Piezoelectric Composites," *J. Mech. and Phys. of Solids*, Vol. 40, pp. 473–479.

Skinner, D. P., Newnham, R. E., and Cross, L. E., 1978, "Flexible Composite Transducers," *Mat. Res. Bull.*, Vol. 13, pp. 599–607.

Smith, W. A., 1989, "The Role of Piezocomposites in Ultrasonic Transducers," *1989 Ultrasonics Symposium IEEE*, pp. 755–766.

Turbé, N., and Maugin, G. A., 1991, "On the Linear Piezoelectricity of Composite Materials," *Mathematical Methods in Applied Science*, Vol. 14, pp. 403–412.

Zhou, S. A., Hsieh, R. K. T., and Maugin, G. A., 1986, "Electric and Elastic Multipole Defects in Finite Piezoelectric Media," *Int. J. Solids Structures*, Vol. 22, pp. 1411–1422.

Downloaded 03 May 2010 to 171.66.16.245. Redistribution subject to ASME license or copyright; see http://www.asme.org/terms/Terms_Use.cfm

Universal Relations in Piezoelectric Composites With Eigenstress and Polarization Fields, Part II: Multiphase Media—Effective Behavior

Y. Benveniste
Department of Solid Mechanics, Materials and Structures, Faculty of Engineering, Tel-Aviv University, Ramat Aviv 69978, Israel

We consider heterogeneous piezoelectric media in general and multiphase piezoelectric composites in particular. A distribution of statistically homogeneous eigenstress and spontaneous polarization fields is admitted in the solid which is itself statistically homogeneous, and the effective eigenstress and spontaneous polarization is sought. The method here is based on the use of virtual work theorems in piezoelectric media and therefore differs from the approach used in the companion paper (Benveniste, 1993). We show that the effective eigenstress and polarization follow from a knowledge of the influence functions related to an electromechanical loading of the composite aggregate in which no eigenstresses and polarizations are present. When applied to the special case of binary systems with constant eigenstress and polarization fields in the phases, the above result implies that the effective eigenstress and polarization can be determined in terms of the effective elastic, piezoelectric, dielectric tensors of the medium, the constituent properties, and the individual eigenstresses and polarizations.

1 Introduction

The present paper is the third in a series of recent works by the author which are concerned with deriving exact results of universal nature in piezoelectric composites. For a background and relevant references on composites exhibiting coupled behavior in general and piezoelectricity in particular, the reader is referred to Benveniste (1993). In that companion paper, *binary* composite media of *arbitrary phase geometry* with constituent phases of general anisotropic behavior and containing *constant* eigenstress and polarization fields are considered. Exact universal relations are derived there between the *pointwise* fields as well as between the *effective tensors* of the composite aggregate.

In Benveniste and Dvorak (1992), *binary* composites with transversely isotropic constituents and *no* eigenstress and polarization fields are treated. The phase boundaries are *cylindrical* and parallel to the axis of transverse isotropy, but otherwise the microgeometry is totally arbitrary. Exact relations are derived in that work between the pointwise fields generated in this composite by purely mechanical and purely electrical loading. The effective behavior of the composite aggregate is also studied, and exact connections are found between the effective moduli.

The methodology and findings of the above works relies on the creation of uniform fields in piezoelectric composites. Although this concept can be extended to multiphase media of arbitrary phase geometry, it is less powerful and provides weaker results in that context (see Dvorak and Benveniste (1992) for a treatment in the case of uncoupled mechanical behavior). Therefore, in the present paper, which is concerned with *heterogeneous* piezoelectric media in general, and *multiphase composites* in particular, we use virtual work theorems in piezoelectricity. This limits us, however, to obtain universal results on the effective properties only and not on the local fields. A distribution of statistically homogeneous eigenstress and spontaneous polarization fields is admitted in the medium which is itself statistically homogeneous and the effective eigenstress and polarization is sought. The second section of the paper deals with heterogeneous media in general and shows that the effective eigenstress and polarization follow from a knowledge of the influence functions related to an electromechanical loading of the composite aggregate in which no eigenstresses and polarizations are present. The obtained result is an extended generalization of Levin's idea in thermoelastic composites (Levin, 1967), to heterogeneous piezoelectricity. As in that last paper use is made of virtual work theorems, this time, however, which are two in number. The first is related to the mechanical variables and the other to the dielectric ones.

Contributed by the Applied Mechanics Division of THE AMERICAN SOCIETY OF MECHANICAL ENGINEERS for presentation in the ASME JOURNAL OF APPLIED MECHANICS.

Discussion on this paper should be addressed to the Technical Editor, Professor Lewis T. Wheeler, Department of Mechanical Engineering, University of Houston, Houston, TX 77204-4792, and will be accepted until four months after final publication of the paper itself in the ASME JOURNAL OF APPLIED MECHANICS.

Manuscript received by the ASME Applied Mechanics Division, Aug. 29, 1991; final revision, Apr. 24, 1992. Associate Technical Editor: G. J. Dvorak.

Copyright © 1993 by ASME
Downloaded 03 May 2010 to 171.66.16.245. Redistribution subject to ASME license or copyright; see http://www.asme.org/terms/Terms_Use.cfm

The third section of the paper specializes the results of the previous section to multiphase composites. Finally, reduction is made to binary systems and it is shown that in this case the effective eigenstress and polarization can be determined from a knowledge of the effective elastic, piezoelectric, dielectric tensors of the medium, the constituent properties, and the individual eigenstresses and polarizations. This is in agreement with some of the findings in Benveniste (1993) where stronger results for the *local fields* are also obtained for binary media and have been reached in that work by means of the uniform fields concept.

2 Heterogeneous Piezoelectric Media

Let us consider a heterogeneous piezoelectric medium defined by the constitutive laws

$$\sigma(\mathbf{x}) = \mathbf{L}(\mathbf{x})\epsilon(\mathbf{x}) - \mathbf{e}^T(\mathbf{x})\mathbf{E}(\mathbf{x}) + \lambda(\mathbf{x}),$$
$$\mathbf{D}(\mathbf{x}) = \mathbf{e}(\mathbf{x})\epsilon(\mathbf{x}) + \kappa(\mathbf{x})\mathbf{E}(\mathbf{x}) + \mathbf{P}(\mathbf{x}), \tag{1}$$

where σ, ϵ, $\mathbf{E}$, $\mathbf{D}$ are the stress, strain tensors, and the electric field intensity and displacement vectors, respectively. The elastic, piezoelectric, and dielectric constants of the medium are represented by the space-dependent fourth-order, third-order, and second-order tensors $\mathbf{L}(\mathbf{x})$, $\mathbf{e}(\mathbf{x})$, $\kappa(\mathbf{x})$, respectively, and $(\mathbf{e}^T)_{ijk} = (\mathbf{e})_{kij}$. Possible eigenstress and spontaneous polarization fields are denoted by $\lambda(\mathbf{x})$ and $\mathbf{P}(\mathbf{x})$.[1] The heterogeneous medium described in (1) may represent, for example, a multiphase composite in which case the tensors $\mathbf{L}(\mathbf{x})$, $\mathbf{e}(\mathbf{x})$, $\kappa(\mathbf{x})$ are piecewise constant quantities in $\mathbf{x}$. In the case of pyroelectricity, the eigenstresses and polarizations are given by

$$\lambda(\mathbf{x}) = \mathbf{l}(\mathbf{x})\theta, \quad \mathbf{P}(\mathbf{x}) = \mathbf{p}(\mathbf{x})\theta \tag{2}$$

where θ is an increase in the temperature from a reference temperature, $\mathbf{l}(\mathbf{x})$ denotes the thermal stress tensor, and $\mathbf{p}(\mathbf{x})$ is the vector of pyroelectric coefficients (see for example, Mindlin, 1961). For the case of multiphase composites, clearly, $\mathbf{l}(\mathbf{x})$ and $\mathbf{p}(\mathbf{x})$ are piecewise constant functions in $\mathbf{x}$.

Since Eq. (1) involve second, third, and fourth-order tensors, it is useful to represent them by square and rectangular matrices as explained in Nye (1957, p. 113) and also recapitulated in the companion paper (Benveniste, 1993). Accordingly, the short notation used in Eq. (1) and in those which will appear in several places in the paper are to be interpreted simply as multiplication and addition of matrices.

Let now the heterogeneous piezoelectric medium be statistically homogeneous, and assume that the prescribed eigenstresses and polarizations possess also this property. We are interested in the representation of this medium by a homogenized law of the form

$$\bar{\sigma} = \mathbf{L}\bar{\epsilon} - \mathbf{e}^T\bar{\mathbf{E}} + \lambda,$$
$$\bar{\mathbf{D}} = \mathbf{e}\bar{\epsilon} + \kappa\bar{\mathbf{E}} + \mathbf{P}, \tag{3}$$

where $\bar{\sigma}$, $\bar{\epsilon}$, $\bar{\mathbf{D}}$, $\bar{\mathbf{E}}$ denote the average field variables in a representative volume element, and $\mathbf{L}$, $\mathbf{e}$, κ, λ, and $\mathbf{P}$ are the effective parameters.

The effective elastic, piezoelectric, and dielectric constants $\mathbf{L}$, ϵ, κ can be obtained by considering vanishing eigenstress and polarization fields,

$$\lambda(\mathbf{x}) = \mathbf{P}(\mathbf{x}) = \lambda = \mathbf{P} = \mathbf{0} \tag{4}$$

and then subjecting the external surface of the body to an electromechanical loading of the form

$$u_i(S) = \epsilon^o_{ij}x_j, \quad \phi(S) = -E^o_i x_i, \tag{5}$$

for which there exists

$$\bar{\epsilon}_{ij} = \epsilon^o_{ij}, \quad \bar{E}_i = E^o_i. \tag{6}$$

Under (4) and (5), the solution for the strain and electric field can formally be written as

$$\epsilon(\mathbf{x}) = \mathbf{A}(\mathbf{x})\epsilon^o + \mathbf{B}(\mathbf{x})\mathbf{E}^o,$$
$$\mathbf{E}(\mathbf{x}) = \mathbf{a}(\mathbf{x})\epsilon^o + \mathbf{b}(\mathbf{x})\mathbf{E}^o, \tag{7}$$

where we have defined the influence functions $\mathbf{A}(\mathbf{x})$, $\mathbf{B}(\mathbf{x})$, $\mathbf{a}(\mathbf{x})$, $\mathbf{b}(\mathbf{x})$ which are represented by (6×6), (6×3), (3×6) and (3×3), matrices, respectively. Note that in view of (6), these functions need to satisfy

$$\frac{1}{V}\int_V \mathbf{A}(\mathbf{x})dV = \mathbf{I}, \qquad \frac{1}{V}\int_V \mathbf{B}(\mathbf{x})dV = \mathbf{0}, \tag{8}$$

$$\frac{1}{V}\int_V \mathbf{a}(\mathbf{x})dV = \mathbf{0}, \qquad \frac{1}{V}\int_V \mathbf{b}(\mathbf{x})dV = \mathbf{i}, \tag{9}$$

with V standing either for the total volume or for a representative volume. In the above equation, $\mathbf{I}$ and $\mathbf{i}$ are the fourth and second-order unit tensors, respectively.

Use of (1), (3), (4), (6), and (7), provide

$$\mathbf{L} = \frac{1}{V}\int_V \mathbf{L}(\mathbf{x})\mathbf{A}(\mathbf{x})dV - \frac{1}{V}\int_V \mathbf{e}^T(\mathbf{x})\mathbf{a}(\mathbf{x})dV,$$
$$\mathbf{e}^T = \frac{1}{V}\int_V \mathbf{e}^T(\mathbf{x})\mathbf{b}(\mathbf{x})dV - \frac{1}{V}\int_V \mathbf{L}(\mathbf{x})\mathbf{B}(\mathbf{x})dV,$$
$$\mathbf{e} = \frac{1}{V}\int_V \mathbf{e}(\mathbf{x})\mathbf{A}(\mathbf{x})dV + \frac{1}{V}\int_V \kappa(\mathbf{x})\mathbf{a}(\mathbf{x})dV,$$
$$\kappa = \frac{1}{V}\int_V \mathbf{e}(\mathbf{x})\mathbf{B}(\mathbf{x})dV + \frac{1}{V}\int_V \kappa(\mathbf{x})\mathbf{b}(\mathbf{x})dV. \tag{10}$$

Note that, for consistency of (10_2) and (10_3), the influence functions should comply with

$$\frac{1}{V}\int_V \mathbf{e}(\mathbf{x})\mathbf{A}(\mathbf{x})dV + \frac{1}{V}\int_V \kappa(\mathbf{x})\mathbf{a}(\mathbf{x})dV = \frac{1}{V}\int_V \mathbf{b}^T(\mathbf{x})\mathbf{e}(\mathbf{x})dV - \frac{1}{V}\int_V \mathbf{B}^T(\mathbf{x})\mathbf{L}(\mathbf{x})dV, \tag{11}$$

where we have invoked the diagonal symmetry of the $\mathbf{L}$ and κ tensors, $(L_{ijkl}(\mathbf{x}) = L_{klij}(\mathbf{x}), \kappa_{ij}(\mathbf{x}) = \kappa_{ji}(\mathbf{x}))$. An independent proof of Eq. (11) can be given by making use of the virtual work theorems for the mechanical and dielectric variables. These theorems, which will also be needed in deriving the main result of this paper, are briefly reviewed in Appendix A, which is devoted mainly to the proof of (11). The theorems state that

$$\int_V \sigma_{ij}(\mathbf{x})\epsilon'_{ij}(\mathbf{x})dV = \int_S t_i(\mathbf{x})u'_i(\mathbf{x})dS,$$
$$\int_V D_i(\mathbf{x})E'_i(\mathbf{x})dV = -\int_S D_n(\mathbf{x})\phi'(\mathbf{x})dS, \tag{12}$$

where $\sigma_{ij}(\mathbf{x})$ is a divergenceless stress field in V, in equilibrium with the tractions t_i on S, and $\epsilon'_{ij}(\mathbf{x})$ is an unrelated strain field derivable from the displacement field $u'_i(\mathbf{x})$; similarly, $D_i(\mathbf{x})$ is a divergenceless electric displacement field in V, compatible with the normal component $D_n(\mathbf{x})$ on S, and $E'_i(\mathbf{x})$ is an unrelated electric field derivable from an electric potential $\phi'(\mathbf{x})$.

We now proceed with the main result of this paper: state it first and then prove it. For the statistically homogeneous piezoelectric media with prescribed eigenstresses and polarization fields which are also statistically homogeneous, we claim that the effective eigenstress λ and polarization $\mathbf{P}$ are given by

$$\lambda = \frac{1}{V}\int_V \mathbf{A}^T(\mathbf{x})\lambda(\mathbf{x})dV - \frac{1}{V}\int_V \mathbf{a}^T(\mathbf{x})\mathbf{P}(\mathbf{x})dV,$$
$$\mathbf{P} = \frac{1}{V}\int_V \mathbf{b}^T(\mathbf{x})\mathbf{P}(\mathbf{x})dV - \frac{1}{V}\int_V \mathbf{B}^T(\mathbf{x})\lambda(\mathbf{x})dV. \tag{13}$$

In order to derive Eq. (13), consider first the piezoelectric medium with vanishing eigenstress $\lambda(\mathbf{x}) = \mathbf{0}$ and polarization

[1] As in Benveniste (1993), the spontaneous polarization $\mathbf{P}$ will be called here simply as "polarization."

Downloaded 03 May 2010 to 171.66.16.245. Redistribution subject to ASME license or copyright; see http://www.asme.org/terms/Terms_Use.cfm

fields $\mathbf{P}(\mathbf{x}) = \mathbf{0}$, and subject it to an electromechanical loading in the form (see Fig. 1(*a*))

$$u_i(S) = \epsilon_{ij}^{o\prime}\, x_j, \quad \phi'(S) = -E_i^{o\prime} x_i. \tag{14}$$

Let the local fields induced by this loading be denoted by "primed" quantities.

On the other hand, consider the same piezoelectric medium with

$$u_i(S) = 0, \quad \phi(S) = 0, \tag{15}$$

but this time under the presence of eigenstresses $\boldsymbol{\lambda}(\mathbf{x})$ and polarizations $\mathbf{P}(\mathbf{x})$ (Fig. 1(*b*)). The local fields induced by this distribution of $\boldsymbol{\lambda}(\mathbf{x})$ and $\mathbf{P}(\mathbf{x})$ will be denoted by "unprimed" quantities. Use of the virtual work theorem (12_1) provides

$$\int_V (L_{ijkl}(\mathbf{x})\epsilon_{kl}(\mathbf{x}) - e_{kij}(\mathbf{x})E_k(\mathbf{x}) + \lambda_{ij}(\mathbf{x}))\epsilon'_{ij}(\mathbf{x})dV =$$

$$= \int_S t_i(\mathbf{x})\epsilon_{ij}^{o\prime}\, x_j dS = V\,\epsilon_{ij}^{o\prime}\,\frac{1}{V}\int_S t_i(\mathbf{x})x_j dS = V\,\epsilon_{ij}^{o\prime}\,\bar{\sigma}_{ij}. \tag{16}$$

Note that since for the "unprimed" fields Eq. (15) prevails, then in accordance to (6)

$$\bar{\epsilon}_{ij} = 0, \quad \bar{E}_i = 0, \tag{17}$$

so that using (3_1), the right-hand side of (16) can be written as

$$V\,\epsilon_{ij}^{o\prime}\,\bar{\sigma}_{ij} = V\,\epsilon_{ij}^{o\prime}\,\lambda_{ij}. \tag{18}$$

Let us now use again the theorem of virtual work (12_1), this time in the form of

$$\int_V \sigma'_{ij}(\mathbf{x})\epsilon_{ij}(\mathbf{x})dV = \int_S t'_i(\mathbf{x})u_i(\mathbf{x})dS, \tag{19}$$

while adhering, however, to the same definition of the primed and unprimed fields in Fig. 1. Equation (19) then provides

$$\int_V (L_{ijkl}(\mathbf{x})\epsilon'_{kl}(\mathbf{x}) - e_{kij}(\mathbf{x})E'_k(\mathbf{x}))\epsilon_{ij}(\mathbf{x})dV = 0. \tag{20}$$

Using this last equation in (16), invoking the diagonal symmetry of the $\mathbf{L}$ tensor, and recalling (18) gives

$$\int_V e_{kij}(\mathbf{x})\,(E'_k(\mathbf{x})\epsilon_{ij}(\mathbf{x}) - E_k(\mathbf{x})\epsilon'_{ij}(\mathbf{x}))dV$$

$$+ \int_V \lambda_{ij}(\mathbf{x})\epsilon'_{ij}(\mathbf{x})dV = V\epsilon_{ij}^{o\prime}\lambda_{ij}. \tag{21}$$

Equation (21) is an intermediate result towards the desired proof.

At this stage we make use of the virtual work theorem (12_2) to obtain

$$\int_V (e_{ikl}(\mathbf{x})\epsilon_{kl}(\mathbf{x}) + \kappa_{ik}(\mathbf{x})E_k(\mathbf{x}) + P_i(\mathbf{x}))E'_i(\mathbf{x})dV$$

$$= E_i^o \int_S D_n(\mathbf{x})x_i dS = VE_i^o\,\frac{1}{V}\int_S D_n(\mathbf{x})x_i dS = VE_i^{o\prime}\bar{D}_i, \tag{22}$$

where, in similarity to (18), we now have

$$VE_i^{o\prime}\bar{D}_i = VE_i^{o\prime}P_i. \tag{23}$$

A repeated use of the virtual work theorem (12_2) in the form

$$\int_V D'_i(\mathbf{x})E_i(\mathbf{x})dV = -\int_S D'_n(\mathbf{x})\phi(\mathbf{x})dS, \tag{24}$$

yields

$$\int_V (e_{ikl}(\mathbf{x})\epsilon'_{kl}(\mathbf{x}) + \kappa_{ik}(\mathbf{x})E'_k(\mathbf{x}))E_i(\mathbf{x})dV = 0. \tag{25}$$

Combine now Eq. (25) with (22), and use the property $\kappa_{ik}(\mathbf{x}) = \kappa_{ki}(\mathbf{x})$ to yield

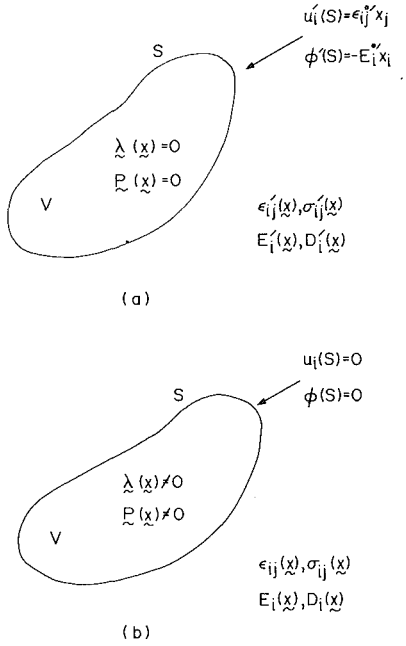


Fig. 1 An electromechanical loading of the heterogeneous piezoelectric medium

$$\int_V e_{ikl}(\mathbf{x})\,(\epsilon_{kl}(\mathbf{x})E'_i(\mathbf{x}) - \epsilon'_{kl}(\mathbf{x})E_i(\mathbf{x}))dV$$

$$+ \int_V P_i(\mathbf{x})E'_i(\mathbf{x})dV = VE_i^{o\prime}P_i. \tag{26}$$

With appropriate change in the indexes, it is seen that the first integrals in Eqs. (21) and (26) are identical to each other. Therefore, these equations provide

$$\frac{1}{V}\int_V \lambda_{ij}(\mathbf{x})\epsilon'_{ij}(\mathbf{x})dV - \frac{1}{V}\int_V P_i(\mathbf{x})E'_i(\mathbf{x})dV$$

$$= \epsilon_{ij}^{o\prime}\lambda_{ij} - E_i^{o\prime}P_i. \tag{27}$$

Next, introducing the definitions (7) in (27) gives

$$\left[\frac{1}{V}\int_V \lambda_{ij}(\mathbf{x})A_{ijkl}(\mathbf{x})dV - \frac{1}{V}\int_V P_i(\mathbf{x})a_{ikl}(\mathbf{x})dV\right]\epsilon_{kl}^{o\prime} +$$

$$+\left[\frac{1}{V}\int_V \lambda_{ij}(\mathbf{x})B_{ijk}(\mathbf{x})dV - \frac{1}{V}\int_V P_i(\mathbf{x})b_{ik}(\mathbf{x})dV\right]E_k^{o\prime}$$

$$= \lambda_{kl}\epsilon_{kl}^{o\prime} - P_k E_k^{o\prime}. \tag{28}$$

Finally, equating the coefficients of $\epsilon_{kl}^{o\prime}$ and $E_k^{o\prime}$ in (28) provides the desired result

$$\lambda_{kl} = \frac{1}{V}\int_V A_{ijkl}(\mathbf{x})\lambda_{ij}(\mathbf{x})dV - \frac{1}{V}\int_V a_{ikl}(\mathbf{x})P_i(\mathbf{x})dV,$$

$$P_k = \frac{1}{V}\int_V b_{ik}(\mathbf{x})P_i(\mathbf{x})dV - \frac{1}{V}\int_V B_{ijk}(\mathbf{x})\lambda_{ij}(\mathbf{x})dV, \tag{29}$$

whose form in the indexless notation is in fact Eq. (13).

3 Piezoelectric Composites

Consider now multiphase composite media of N distinct phases with constitutive laws

$$\boldsymbol{\sigma}_r(x) = \mathbf{L}_r\boldsymbol{\epsilon}_r(\mathbf{x}) - \mathbf{e}_r^T\mathbf{E}_r(\mathbf{x}) + \boldsymbol{\lambda}_r^o,$$

$$r = 1,2,\ldots N$$

$$\mathbf{D}_r(\mathbf{x}) = \mathbf{e}_r\boldsymbol{\epsilon}_r(\mathbf{x}) + \boldsymbol{\kappa}_r\mathbf{E}_r(\mathbf{x}) + \mathbf{P}_r^o, \tag{30}$$

Downloaded 03 May 2010 to 171.66.16.245. Redistribution subject to ASME license or copyright; see http://www.asme.org/terms/Terms_Use.cfm

where λ_r^o and $\mathbf{P}_r^o$ are prescribed eigenstresses and polarizations which are *constant* in the phases.

In this special case of N-distinct phases, Eqs. (8) and (9) reduce to:

$$\sum_{r=1}^{N} c_r \mathbf{A}_r = \mathbf{I}, \quad \sum_{r=1}^{N} c_r \mathbf{B}_r = \mathbf{0}, \tag{31}$$

$$\sum_{r=1}^{N} c_r \mathbf{a}_r = \mathbf{I}, \quad \sum_{r=1}^{N} c_r \mathbf{b}_r = \mathbf{i}, \tag{32}$$

where the quantities $\mathbf{A}_r$, $\mathbf{B}_r$, $\mathbf{a}_r$, $\mathbf{b}_r$, without the argument $\mathbf{x}$, denote simply the average of the respective influence functions over phase r, in the representative volume element—they are called concentration factors. The volume fractions of the phases are denoted by c_r in (31).

Equations (10), (11), and (13), in their turn, become

$$\mathbf{L} = \sum_{r=1}^{N} c_r \mathbf{L}_r \mathbf{A}_r - \sum_{r=1}^{N} c_r \mathbf{e}_r^T \mathbf{a}_r,$$

$$\mathbf{e}^T = \sum_{r=1}^{N} c_r \mathbf{e}_r^T \mathbf{b}_r - \sum_{r=1}^{N} c_r \mathbf{L}_r \mathbf{B}_a, \tag{33}$$

$$\mathbf{e} = \sum_{r=1}^{N} c_r \mathbf{e}_r \mathbf{A}_r + \sum_{r=1}^{N} c_r \kappa_r \mathbf{a}_r,$$

$$\kappa = \sum_{r=1}^{N} c_r \mathbf{e}_r \mathbf{B}_r + \sum_{r=1}^{N} c_r \kappa_r \mathbf{b}_r,$$

$$\sum_{r=1}^{N} c_r \mathbf{e}_r \mathbf{A}_r + \sum_{r=1}^{N} c_r \kappa_r \mathbf{a}_r = \sum_{r=1}^{N} c_r \mathbf{b}_r^T \mathbf{e}_r - \sum_{r=1}^{N} c_r \mathbf{B}_r^T \mathbf{L}_r, \tag{34}$$

$$\lambda = \sum_{r=1}^{N} c_r \mathbf{A}_r^T \lambda_r^o - \sum_{r=1}^{N} c_r \mathbf{a}_r^T \mathbf{P}_r^o,$$

$$\mathbf{P} = \sum_{r=1}^{N} c_r \mathbf{b}_r^T \mathbf{P}_r^o - \sum_{r=1}^{N} c_r \mathbf{B}_r^T \lambda_r^o. \tag{35}$$

With *piecewise constant* eigenstresses and polarizations, there is of course an alternative way to write expressions for the effective quantities λ and $\mathbf{P}$. This can be achieved, as in Benveniste (1993), by defining directly influence functions related to λ_r^o, $\mathbf{P}_r^o$, $r = 1, 2, \ldots N$. With prescribed λ_r^o and $\mathbf{P}_r^o$, constant in the phases, and boundary conditions (5), the local fields can then be written as

$$\epsilon_r(\mathbf{x}) = \mathbf{A}_r(\mathbf{x})\epsilon^o + \mathbf{B}_r(\mathbf{x})\mathbf{E}^o + \sum_{s=1}^{N} \mathbf{m}_{rs}(\mathbf{x})\lambda_s^o + \sum_{s=1}^{n} \mathbf{n}_{rs}(\mathbf{x})\mathbf{P}_s^o,$$

$$\mathbf{E}_r(\mathbf{x}) = \mathbf{a}_r(\mathbf{x})\epsilon^o + \mathbf{b}_r(\mathbf{x})\mathbf{E}^o + \sum_{s=1}^{N} \mathbf{f}_{rs}(\mathbf{x})\lambda_s^o + \sum_{s=1}^{N} \mathbf{g}_{rs}(\mathbf{x})\mathbf{P}_s^o, \tag{36}$$

where $\mathbf{m}_{rs}(\mathbf{x})$, $\mathbf{n}_{rs}(\mathbf{x})$, $\mathbf{f}_{rs}(\mathbf{x})$, $\mathbf{g}_{rs}(\mathbf{x})$ are influence functions related to λ_r^o and $\mathbf{P}_r^o$. Taking averages of $\epsilon_r(\mathbf{x})$ and $\mathbf{E}_r(\mathbf{x})$ over the phase r in a representative volume element, and using (30), (3), and (6) provide now, in addition to (33), the following equations:

$$\lambda = \sum_{r=1}^{N} c_r \lambda_r^o + \sum_{r=1}^{N}\sum_{s=1}^{N} c_r \mathbf{L}_r \mathbf{m}_{rs} \lambda_s^o + \sum_{r=1}^{N}\sum_{s=1}^{N} c_r \mathbf{L}_r \mathbf{n}_{rs} \mathbf{P}_s^o$$
$$- \sum_{r=1}^{N}\sum_{s=1}^{N} c_r \mathbf{e}_r^T \mathbf{f}_{rs} \lambda_s^o - \sum_{r=1}^{N}\sum_{s=1}^{N} c_r \mathbf{e}_r^T \mathbf{g}_{rs} \mathbf{P}_s^o,$$

$$\mathbf{P} = \sum_{r=1}^{N} c_r \mathbf{P}_r^o + \sum_{r=1}^{N}\sum_{s=1}^{N} c_r \mathbf{e}_r \mathbf{m}_{rs} \lambda_s^o + \sum_{r=1}^{N}\sum_{s=1}^{N} c_r \mathbf{e}_r \mathbf{n}_{rs} \mathbf{P}_s^o$$
$$+ \sum_{r=1}^{N}\sum_{s=1}^{N} c_r \kappa_r \mathbf{f}_{rs} \lambda_s^o + \sum_{r=1}^{N}\sum_{s=1}^{N} c_r \kappa_r \mathbf{g}_{rs} \mathbf{P}_s^o, \tag{37}$$

where $\mathbf{m}_{rs}$, $\mathbf{n}_{rs}$, $\mathbf{f}_{rs}$, and $\mathbf{g}_{rs}$, now without an argument, denote the averages of the respective influence functions over phase r and are again called concentration factors. In the process of deriving Eq. (37) it can also be shown that, in addition to (32), there is

$$\sum_{r=1}^{N} c_r \mathbf{m}_{rs} = \mathbf{0}, \quad \sum_{r=1}^{N} c_r \mathbf{n}_{rs} = \mathbf{0},$$

$$\sum_{r=1}^{N} c_r \mathbf{f}_{rs} = \mathbf{0}, \quad \sum_{r=1}^{N} c_r \mathbf{g}_{rs} = \mathbf{0}. \tag{38}$$

Two-phase media deserve special attention. In this case there are eight concentration factors $\mathbf{A}_r$, $\mathbf{B}_r$, $\mathbf{a}_r$, $\mathbf{b}_r$ $r = \alpha, \beta$ entering in (35). The eight tensorial Eqs. (31)–(33) provide a means to express these concentration factors in terms of the effective tensors $\mathbf{L}$, $\mathbf{e}$, and κ and the phase variables. After some straightforward algebra, which consists basically of using Eq. (28) of the companion paper in the two-phase versions of (35) herein, we obtain the following equations:

$$\lambda = \lambda_\alpha^o + \{(\Delta\mathbf{L} + \Delta\mathbf{w})^{-1}[(\mathbf{L}_\alpha - \mathbf{L}) + \Delta\mathbf{e}^T \Delta\kappa^{-1}(\mathbf{e}_\alpha - \mathbf{e})]\}^T (\lambda_\beta^o - \lambda_\alpha^o) +$$
$$+ \{\Delta\kappa^{-1}(\mathbf{e}_\alpha - \mathbf{e}) - \Delta\kappa^{-1}\Delta\mathbf{e}(\Delta\mathbf{L} + \Delta\mathbf{w})^{-1}[(\mathbf{L}_\alpha - \mathbf{L}) + \Delta\mathbf{e}^T \Delta\kappa^{-1}(\mathbf{e}_\alpha - \mathbf{e})]\}^T (\mathbf{P}_\alpha^o - \mathbf{P}_\beta^o), \tag{39}$$

$$\mathbf{P} = \mathbf{P}_\alpha^o + \{(\Delta\kappa + \Delta\mathbf{v})^{-1}[(\kappa_\alpha - \kappa) + \Delta\mathbf{e}\Delta\mathbf{L}^{-1}(\mathbf{e}_\alpha^T - \mathbf{e}^T)]\}^T (\mathbf{P}_\beta^o - \mathbf{P}_\alpha^o) +$$
$$+ \{\Delta\mathbf{L}^{-1}(\mathbf{e}^T - \mathbf{e}_\alpha^T) + \Delta\mathbf{L}^{-1}\Delta\mathbf{e}^T(\Delta\kappa + \Delta\mathbf{v})^{-1}[(\kappa_\alpha - \kappa) + \Delta\mathbf{e}\Delta\mathbf{L}^{-1}(\mathbf{e}_\alpha^T - \mathbf{e}^T)]\}^T (\lambda_\alpha^o - \lambda_\beta^o).$$

where

$$\Delta\mathbf{w} = = \Delta\mathbf{e}^T \Delta\kappa^{-1} \Delta\mathbf{e}, \quad \Delta\mathbf{v} = \Delta\mathbf{e}\Delta\mathbf{L}^{-1}\Delta\mathbf{e}^T, \tag{40}$$

with

$$\Delta\mathbf{L} = \mathbf{L}_\alpha - \mathbf{L}_\beta, \ \Delta\kappa = \kappa_\alpha - \kappa_\beta, \ \Delta\mathbf{e} = \mathbf{e}_\alpha - \mathbf{e}_\beta,$$
$$\Delta\mathbf{e}^T = \mathbf{e}_\alpha^T - \mathbf{e}_\beta^T, \ \Delta\lambda = \lambda_\alpha^o - \lambda_\beta^o, \ \Delta\mathbf{P} = \mathbf{P}_\alpha^o - \mathbf{P}_\beta^o. \tag{41}$$

The conclusion that in *binary systems* the effective eigenstress λ and polarization $\mathbf{P}$ can be expressed in terms of the effective tensors $\mathbf{L}$, $\mathbf{e}$, κ, and constituent properties was reached by an alternative means in the companion paper (Benveniste, 1993). As mentioned in the Introduction, in that work, which dealt specifically with binary systems, stronger results concerning the pointwise local fields were derived. The conclusion concerning the effective λ and $\mathbf{P}$ was an outcome of these more general local relations. It is therefore important now to make contact with that paper and establish consistency with the present findings. In that last work it was shown that, for binary systems, the local influence functions $\mathbf{m}_{\alpha\beta}(\mathbf{x})$, $\mathbf{n}_{\alpha\beta}(\mathbf{x})$, $\mathbf{f}_{\alpha\beta}(\mathbf{x})$, $\mathbf{g}_{\alpha\beta}(\mathbf{x})$ can be expressed in terms of $\mathbf{A}_r(\mathbf{x})$, $\mathbf{B}_r(\mathbf{x})$, $\mathbf{b}_r(\mathbf{x})$, $\mathbf{a}_r(\mathbf{x})$ with $r = \alpha, \beta$. For convenience, we reproduce here these relations:

$$\mathbf{m}_{r\alpha}(\mathbf{x}) = -\mathbf{m}_{r\beta}(\mathbf{x}) = (\mathbf{I} - \mathbf{A}_r(\mathbf{x}))\mathbf{R} - \mathbf{B}_r(\mathbf{x})\mathbf{Q},$$
$$\mathbf{n}_{r\alpha}(\mathbf{x}) = -\mathbf{n}_{r\beta}(\mathbf{x}) = (\mathbf{I} - \mathbf{A}_r(\mathbf{x}))\mathbf{S} - \mathbf{B}_r(\mathbf{x})\mathbf{T},$$
$$r = \alpha, \beta$$
$$\mathbf{f}_{r\alpha}(\mathbf{x}) = -\mathbf{f}_{r\beta}(\mathbf{x}) = (\mathbf{i} - \mathbf{b}_r(\mathbf{x}))\mathbf{Q} - \mathbf{a}_r(\mathbf{x})\mathbf{R},$$
$$\mathbf{g}_{r\alpha}(\mathbf{x}) = -\mathbf{g}_{r\beta}(\mathbf{x}) = (\mathbf{i} - \mathbf{b}_r(\mathbf{x}))\mathbf{T} - \mathbf{a}_r(\mathbf{x})\mathbf{S}, \tag{42}$$

where $\mathbf{R}$, $\mathbf{Q}$, $\mathbf{S}$, $\mathbf{T}$ are given by

$$\mathbf{R} = -\mathbf{F}^{-1}, \ \mathbf{Q} = \Delta\kappa^{-1}\Delta\mathbf{e}\mathbf{F}^{-1}, \ \mathbf{S} = -\mathbf{F}^{-1}\Delta\mathbf{e}^T\Delta\kappa^{-1},$$
$$\mathbf{T} = \Delta\kappa^{-1}(-\mathbf{i} - \Delta\mathbf{e}\mathbf{S}), \ \mathbf{F} = \Delta\mathbf{L} + \Delta\mathbf{e}^T\Delta\kappa^{-1}\Delta\mathbf{e}. \tag{43}$$

Local correspondence relations of the type (42) do not exist for multiphase media of arbitrary phase geometry.

Downloaded 03 May 2010 to 171.66.16.245. Redistribution subject to ASME license or copyright; see http://www.asme.org/terms/Terms_Use.cfm

Based on (42), the effective λ and $\mathbf{P}$ can be now obtained in the following manner. First, take the average of (42) over phase r. This gives relations between the concentration factors exactly in the same form as in (42), simply by omitting the argument $\mathbf{x}$. Next, solve for $\mathbf{A}_r$, $\mathbf{B}_r$, $\mathbf{a}_r$, $\mathbf{b}_r$ in (31)–(33) in terms of $\mathbf{L}$, $\mathbf{e}$, and κ as in Eq. (28) of the companion paper, and introduce them into (42). Finally, substitute the resulting $\mathbf{m}_{\alpha\beta}$, $\mathbf{n}_{\alpha\beta}$, $\mathbf{g}_{\alpha\beta}$, and $\mathbf{f}_{\alpha\beta}$ in (37) to get the desired λ and $\mathbf{P}$. This procedure is longer than the one which led to Eqs. (39), and the resulting equivalent equations were not explicitly given in Benveniste (1992). To establish consistency, it is sufficient, however, to prove that substitution of the phase averaged versions of (42) into (37) with $r = \alpha, \beta$, identically provides (35), with $r = \alpha, \beta$. Due to the involved algebra, the proof is given in Appendix B. Having established consistency, we can refer to Eqs. (39) as the final result of the two equivalent schemes.

We finally mention that for the case of pyroelectric composites

$$\lambda_r = \mathbf{l}_r\theta \quad \text{and} \quad \mathbf{P}_r = \mathbf{p}_r\theta, \tag{44}$$

the expressions for the effective thermal tensor $\mathbf{l}$ and pyroelectric vector $\mathbf{p}$ are immediately recovered from (35) and (39). For nonpiezoelectric composites, Eqs. (35_1) and (39_1) reduce to the well-known Levin's equation (Levin, 1967).

Conclusion

The effective eigenstress and polarization is sought in arbitrary heterogeneous piezoelectric media containing a distribution of statistically homogeneous eigenstress and polarization fields. It is shown that these effective quantities are determined in terms of the influence functions related to electromechanical loading of the piezoelectric composite in which no eigenstresses and polarizations are present. Since the idea of uniform fields employed in Benveniste (1993) cannot be implemented in multiphase media to the same extent as it does in binary systems, the present paper makes use of the virtual work theorems in piezoelectric solids. The obtained universal relations concern therefore only the *effective properties* and not the *pointwise local fields*.

References

Benveniste, Y., 1993, "Universal Relations in Piezoelectric Composites with Eigenstress and Polarization Fields, Part I: Binary Media—Local Fields and Effective Behavior," ASME JOURNAL OF APPLIED MECHANICS, Vol. 60, pp. 265–269.

Benveniste, Y., and Dvorak, G. J., 1992, "On Uniform Fields and Universal Relations in Piezoelectric Composites," *J. Mech. and Phys. of Solids*, Vol. 40, pp. 1295-1312.

Dvorak, G. J., and Benveniste, Y., 1992, "On Transformation Strains and Uniform Fields in Multiphase Elastic Media," *Proc. Roy. Soc. London*, Vol. A437, pp. 291-310.

Hashin, Z., 1972, "Theory of Fiber Reinforced Materials," NASA, CR-1974.

Levin, V. M., 1967, "Thermal Expansion Coefficients of Heterogeneous Materials," *Mekhanika Tverdogo Tela*, Vol. 2, pp. 88-94. (English Translation: *Mechanics of Solids*, Vol. 11, pp. 58-61.)

Mindlin, R. D., 1961, "On the Equations of Motion of Piezoelectric Crystals," *Problems in Continuum Mechanics*, pp. 282-290.

Nye, J. F., 1957, *Physical Properties of Crystals: Their Representation by Tensors and Matrices*, Clarendon Press, Oxford, U.K.

APPENDIX A

Virtual Work Theorems and Proof of the Constraint Condition (11)

In this Appendix, we briefly review the virtual theorems (12) and, then give and independent proof of Eq. (11).

(a) Virtual Work Theorems. Consider a stress field $\sigma_{ij}(\mathbf{x})$ which is in equilibrium in V

$$\sigma_{ij,j} = 0, \tag{A1}$$

and let the corresponding tractions on S be given by $\mathbf{t}$. Next, define an unrelated strain field $\epsilon'_{ij}(\mathbf{x})$ derivable from a displacement field $u'_i(\mathbf{x})$

$$\epsilon'_{ij}(\mathbf{x}) = \frac{1}{2}\,(u'_{i,j} + u'_{j,i}). \tag{A2}$$

The virtual work theorem states that

$$\int_V \sigma_{ij}(\mathbf{x})\epsilon'_{ij}(\mathbf{x})dV = \int_S t_i(\mathbf{x})u'_i(\mathbf{x})dS. \tag{A3}$$

The proof of (A3) is readily achieved through (A1), (A2), and use of the Gauss Divergence Theorem. It is noted that since no constitutive laws are invoked in the proof, the statement (A3) is completely general and thus applies to piezoelectric materials as well.

A dual theorem exists for the dielectric variables. Let $D_i(\mathbf{x})$ be an electric displacement field satisfying

$$D_{i,i} = 0, \tag{A4}$$

with the corresponding normal component on S being denoted by D_n. Next, consider an unrelated electric intensity field E'_i derivable from an electric potential ϕ' by

$$E'_i = -\frac{\partial \phi'}{\partial x_i}. \tag{A5}$$

The virtual work theorem now states

$$\int_V D_i(\mathbf{x})E'_i(\mathbf{x})dV = -\int_S D_n(\mathbf{x})\phi'(\mathbf{x})dS. \tag{A6}$$

The proof of (A6) is based on (A4), (A5), and the Gauss Divergence Theorem. Again, no constitutive laws are invoked and thus the statement (A6) applies to piezoelectric materials.

The theorems (A3) and (A6) are valid for heterogeneous media in general. For their statement, in the context of uncoupled mechanical and heat conduction phenomena in composites with distinct phases which are perfectly bonded to each other, see Hashin (1972).

(b) Proof of the Constraint Condition (11). Let us consider the following two sets of boundary conditions on the piezoelectric composite in which no eigenstresses and polarizations are present, $\lambda(\mathbf{x}) = \mathbf{P}(\mathbf{x}) = \mathbf{0}$.

$$u_i(S) = \epsilon^o_{ij}x_j, \quad \phi(S) = 0, \tag{A7}$$

$$u'_i(S) = 0, \quad \phi'(S) = -E^{o\prime}_i x_i. \tag{A8}$$

The fields induced by (A7) will be denoted by "unprimed" quantities, and those due to (A8) by "primed" ones.

Application of the theorem (A3) to these variables yields

$$\int_V (L_{ijkl}(\mathbf{x})\epsilon_{kl}(\mathbf{x}) - e_{kij}(\mathbf{x})E_k(\mathbf{x}))\epsilon'_{ij}(\mathbf{x})dV = 0. \tag{A9}$$

Next, use again (A3), this time in the form

$$\int_V \sigma'_{ij}(\mathbf{x})\epsilon_{ij}(\mathbf{x})dV = \int_S t'_i(\mathbf{x})u_i(\mathbf{x})dS, \tag{A10}$$

which provides

$$\int_V (L_{ijkl}(\mathbf{x})\epsilon'_{kl}(\mathbf{x}) - e_{kij}(\mathbf{x})E'_k(\mathbf{x}))\epsilon_{ij}(\mathbf{x})dV$$

$$= \int_S t'_i(\mathbf{x})\epsilon^o_{ij}x_j dS = \epsilon^o_{ij}\bar{\sigma}'_{ij}V, \tag{A11}$$

where $\bar{\sigma}'_{ij}$ is the average of $\sigma'_{ij}(\mathbf{x})$ in V. After invoking the diagonal symmetry of the $\mathbf{L}$ tensor, (A9) and (A11) give

$$\int_V e_{kij}(\mathbf{x})\,(E_k(\mathbf{x})\epsilon'_{ij}(\mathbf{x}) - E'_k(\mathbf{x})\epsilon_{ij}(\mathbf{x}))dV = \epsilon^o_{ij}\bar{\sigma}'_{ij}V. \tag{A12}$$

On the other hand, a similar repeated use of the virtual work theorem (A6) to the "primed" and "unprimed" fields yields

Downloaded 03 May 2010 to 171.66.16.245. Redistribution subject to ASME license or copyright; see http://www.asme.org/terms/Terms_Use.cfm

$$\int_V e_{ijk}(\mathbf{x})\,(\epsilon_{jk}(\mathbf{x})E_i' - \epsilon_{jk}'(\mathbf{x})E_i)dV = E_i^{o\prime}\overline{D}_i V, \quad \text{(A13)}$$

with $\overline{D}_i$ being the average of $D_i(\mathbf{x})$ in V. After an appropriate change of indexes on the left-hand side of (A13), it is seen that the left-hand sides of (A12) and (A13) are equal and opposite in sign to each other. Equations (A12) and (A13) provide, therefore, the following principal result of this Appendix:

$$\epsilon_{ij}^o\overline{\sigma}_{ij}' = -E_i^{o\prime}\overline{D}_i, \quad \text{(A14)}$$

on which is based the proof of Eq. (11).

Equation (A14) can be further written as

$$\left[\frac{1}{V}\int_V (L_{ijkl}(\mathbf{x})\epsilon_{kl}'(\mathbf{x}) - e_{kij}(\mathbf{x})E_k'(\mathbf{x}))dV\right]\epsilon_{ij}^o =$$

$$= \left[-\frac{1}{V}\int_V (e_{ijk}(\mathbf{x})\epsilon_{jk}(\mathbf{x}) + \kappa_{ij}(\mathbf{x})E_j(\mathbf{x}))dV\right]E_i^{o\prime}, \quad \text{(A15)}$$

where, in accordance to the boundary conditions (A7) and (A8) and the definitions in (7), there is

$$\epsilon_{jk}(\mathbf{x}) = A_{jkmn}(\mathbf{x})\epsilon_{mn}^o, \quad E_j(\mathbf{x}) = a_{jmn}(\mathbf{x})\epsilon_{mn}^o,$$
$$\epsilon_{kl}'(\mathbf{x}) = B_{klm}(\mathbf{x})E_m^{o\prime}, \quad E_k'(\mathbf{x}) = b_{km}(\mathbf{x})E_m^{o\prime}. \quad \text{(A16)}$$

Substitution of (A16) in (A15) and an appropriate change of indexes provides

$$\frac{1}{V}\int_V ((e_{mrs}(\mathbf{x})A_{rsij}(\mathbf{x}) + \kappa_{mr}(\mathbf{x})a_{rij}(\mathbf{x}))dV$$

$$= \frac{1}{V}\int_V b_{km}(\mathbf{x})e_{kij}(\mathbf{x})dV - \frac{1}{V}\int_V B_{klm}(\mathbf{x})L_{klij}(\mathbf{x})dV, \quad \text{(A17)}$$

whose indexless form is identical to Eq. (11). Clearly, this proof applies also to Eq. (27) in the companion paper.

APPENDIX B

Binary Piezoelectric Media: A Proof of Consistency

In this Appendix we will show that substitution of the phase averages of (42) into (37), for the case of two-phase media, gives results which are in agreement with (35).

We start by writing the special forms of (35) and (37) for binary composites. In view of (32), Eq. (35) reads

$$\boldsymbol{\lambda} = \boldsymbol{\lambda}_\alpha^o + c_\beta\mathbf{A}_\beta^T(\boldsymbol{\lambda}_\beta^o - \boldsymbol{\lambda}_\alpha^o) - c_\beta\mathbf{a}_\beta^T(\mathbf{P}_\beta^o - \mathbf{P}_\alpha^o),$$
$$\mathbf{P} = \mathbf{P}_\alpha^o + c_\beta\mathbf{b}_\beta^T(\mathbf{P}_\beta^o - \mathbf{P}_\alpha^o) - c_\beta\mathbf{B}_\beta^T(\boldsymbol{\lambda}_\beta^o - \boldsymbol{\lambda}_\alpha^o), \quad \text{(B1)}$$

whereas (37) and (38) reduce to

$$\boldsymbol{\lambda} = \boldsymbol{\lambda}_\alpha^o + c_\beta(\boldsymbol{\lambda}_\beta^o - \boldsymbol{\lambda}_\alpha^o) + c_\beta(\mathbf{L}_\beta - \mathbf{L}_\alpha)[\mathbf{m}_{\beta\alpha}\boldsymbol{\lambda}_\alpha^o$$
$$+ \mathbf{m}_{\beta\beta}\boldsymbol{\lambda}_\beta^o + \mathbf{n}_{\beta\alpha}\mathbf{P}_\alpha^o + \mathbf{n}_{\beta\beta}\mathbf{P}_\beta^o] -$$
$$- c_\beta(\mathbf{e}_\beta^T - \mathbf{e}_\alpha^T)[\mathbf{f}_{\beta\alpha}\boldsymbol{\lambda}_\alpha^o + \mathbf{f}_{\beta\beta}\boldsymbol{\lambda}_\beta^o + \mathbf{g}_{\beta\alpha}\mathbf{P}_\alpha + \mathbf{g}_{\beta\beta}\mathbf{P}_\beta],$$
$$\mathbf{P} = \mathbf{P}_\alpha^o + c_\beta(\mathbf{P}_\beta^o - \mathbf{P}_\alpha^o) + c_\beta(\mathbf{e}_\beta - \mathbf{e}_\alpha)[\mathbf{m}_{\beta\alpha}\boldsymbol{\lambda}_\alpha^o$$
$$+ \mathbf{m}_{\beta\beta}\boldsymbol{\lambda}_\beta^o + \mathbf{n}_{\beta\alpha}\mathbf{P}_\alpha^o + \mathbf{n}_{\beta\beta}\mathbf{P}_\beta^o] +$$
$$+ c_\beta(\boldsymbol{\kappa}_\beta - \boldsymbol{\kappa}_\alpha)[\mathbf{f}_{\beta\alpha}\boldsymbol{\lambda}_\alpha^o + \mathbf{f}_{\beta\beta}\boldsymbol{\lambda}_\beta^o + \mathbf{g}_{\beta\alpha}\mathbf{P}_\alpha^o + \mathbf{g}_{\beta\beta}\mathbf{P}_\beta^o], \quad \text{(B2)}$$

where, as in the main text, α and β denote the phases of the binary composite.

We need to show in this Appendix that substitution of the phase averaged version of (42) into (B2) yields identically (B1). Before proceeding further, it is necessary to exhibit here alternative, but equivalent forms to **R**, **Q**, **S**, and **T** in (43). These are

$$\mathbf{R} = \Delta\mathbf{L}^{-1}(-\mathbf{I} + \Delta\mathbf{e}^T\mathbf{Q}),\ \mathbf{Q} = \mathbf{H}^{-1}\Delta\mathbf{e}\Delta\mathbf{L}^{-1},$$
$$\mathbf{S} = -\Delta\mathbf{L}^{-1}\Delta\mathbf{e}^T\mathbf{H}^{-1},\ \mathbf{T} = -\mathbf{H}^{-1},\ \mathbf{H} = \Delta\boldsymbol{\kappa} + \Delta\mathbf{e}\Delta\mathbf{L}^{-1}\Delta\mathbf{e}^T. \quad \text{(B3)}$$

Some algebra shows the equivalency between (43) and (B3).

Let us now first show that substitution of (42) into ($B2_1$) yields ($B1_1$). Carrying out the substitution shows that ($B1_1$) is recovered if the following two relations are fulfilled:

$$(\mathbf{L}_\alpha - \mathbf{L}_\beta)[(\mathbf{I} - \mathbf{A}_\beta)\mathbf{R} - \mathbf{B}_\beta\mathbf{Q}]$$
$$- (\mathbf{e}_\alpha^T - \mathbf{e}_\beta^T)[(\mathbf{i} - \mathbf{b}_\beta)\mathbf{Q} - \mathbf{a}_\beta\mathbf{R}] + \mathbf{I} = \mathbf{A}_\beta^T, \quad \text{(B4)}$$

and

$$-\mathbf{a}_\beta^T = (\mathbf{L}_\alpha - \mathbf{L}_\beta)[(\mathbf{I} - \mathbf{A}_\beta)\mathbf{S} - \mathbf{B}_\beta\mathbf{T}]$$
$$- (\mathbf{e}_\alpha^T - \mathbf{e}_\beta^T)[(\mathbf{i} - \mathbf{b}_\beta)\mathbf{T} - \mathbf{a}_\beta\mathbf{S}]. \quad \text{(B5)}$$

To show the validity of (B4), we make use of the expressions for **F**, **Q**, **R** in (43). These reduce (B4) to

$$\Delta\mathbf{L}(\mathbf{A}_\beta - \mathbf{B}_\beta\Delta\boldsymbol{\kappa}^{-1}\Delta\mathbf{e}) + \Delta\mathbf{e}^T(-\mathbf{a}_\beta + \mathbf{b}_\beta\Delta\boldsymbol{\kappa}^{-1}\Delta\mathbf{e})$$
$$= \mathbf{A}_\beta^T(\Delta\mathbf{L} + \Delta\mathbf{e}^T\Delta\boldsymbol{\kappa}^{-1}\Delta\mathbf{e}), \quad \text{(B6)}$$

where the definitions in (41) have been used.

We now invoke the diagonal symmetry of **L** in (33_1), and also recall the condition (34). Note that for binary systems, making use of (32), the effective tensor **L** and the condition (34) can be written as

$$\mathbf{L} = \mathbf{L}_\alpha + c_\beta(\mathbf{L}_\beta - \mathbf{L}_\alpha)\mathbf{A}_\beta - c_\beta(\mathbf{e}_\beta^T - \mathbf{e}_\alpha^T)\mathbf{a}_\beta,$$
$$\Delta\mathbf{e}\mathbf{A}_\beta + \Delta\boldsymbol{\kappa}\mathbf{a}_\beta = \mathbf{b}_\beta^T\Delta\mathbf{e} - \mathbf{B}_\beta^T\Delta\mathbf{L}. \quad \text{(B7)}$$

The diagonal symmetry of **L** implies in ($B7_1$)

$$-\Delta\mathbf{L}\mathbf{A}_\beta + \Delta\mathbf{e}^T\mathbf{a}_\beta = -\mathbf{A}_\beta^T\Delta\mathbf{L} - \mathbf{a}_\beta^T\Delta\mathbf{e}. \quad \text{(B8)}$$

Finally, making use of ($B7_2$) and (B8) in (B6), show that (B6) and therefore (B4) are fulfilled.

To show the validity of (B5), we proceed in a similar manner, but use this time **S** and **T** from (B3). Invoking ($B7_2$) and (B8) shows after some algebra that (B5) is fulfilled. This completes the proof that substitution of (42) into ($B2_1$) yields ($B1_1$).

The proof that (42) and ($B2_2$) yields ($B1_2$) is carried out along the same lines. Substitution of (42) into ($B2_2$) shows first that ($B1_2$) is recovered if

$$\Delta\boldsymbol{\kappa}[\mathbf{a}_\beta\mathbf{S} - (\mathbf{i} - \mathbf{b}_\beta)\mathbf{T}] + \Delta\mathbf{e}[\mathbf{B}_\beta\mathbf{T} - (\mathbf{I} - \mathbf{A}_\beta)\mathbf{S}] - \mathbf{I} = -\mathbf{b}_\beta^T, \quad \text{(B9)}$$

and

$$\mathbf{B}_\beta^T = \Delta\boldsymbol{\kappa}[\mathbf{a}_\beta\mathbf{R} - (\mathbf{i} - \mathbf{b}_\beta)\mathbf{Q}] + \Delta\mathbf{e}[\mathbf{B}_\beta\mathbf{Q} - (\mathbf{I} - \mathbf{A}_\beta)\mathbf{R}]. \quad \text{(B10)}$$

To show the validity of (B9), we make use of **S**, **T**, and **H** in (B3), and also invoke the consistency condition (B7) together with the symmetry of $\boldsymbol{\kappa}$. Note here that the effective tensor $\boldsymbol{\kappa}$ for binary systems is given by

$$\boldsymbol{\kappa} = \boldsymbol{\kappa}_\alpha + c_\beta(\mathbf{e}_\beta - \mathbf{e}_\alpha)\mathbf{B}_\beta + c_\beta(\boldsymbol{\kappa}_\beta - \boldsymbol{\kappa}_\alpha)\mathbf{b}_\beta, \quad \text{(B11)}$$

whereas its symmetry implies

$$\Delta\mathbf{e}\mathbf{B}_\beta + \Delta\boldsymbol{\kappa}\mathbf{b}_\beta = \mathbf{B}_\beta^T\Delta\mathbf{e}^T + \mathbf{b}_\beta^T\Delta\boldsymbol{\kappa}. \quad \text{(B12)}$$

The validity of (B10) is provided by using **Q**, **R**, and **F** from (43) and also invoking (B7) and (B12). This concludes the proof that (42) and ($B2_2$) yields ($B1_2$).

Downloaded 03 May 2010 to 171.66.16.245. Redistribution subject to ASME license or copyright; see http://www.asme.org/terms/Terms_Use.cfm

The Eigenvalues for a Self-Equilibrated, Semi-Infinite, Anisotropic Elastic Strip[1]

E. C. Crafter

R. M. Heise

C. O. Horgan
Fellow ASME

J. G. Simmonds
Fellow ASME

Department of Applied Mathematics,
University of Virginia,
Charlottesville, VA 22903

The linear theory of elasticity is used to study an homogeneous anisotropic semi-infinite strip, free of tractions on its long sides and subject to edge loads or displacements that produce stresses that decay in the axial direction. If one seeks solutions for the (dimensionless) Airy stress function of the form $\phi = e^{-\gamma x}F(y)$, γ *constant, then one is led to a fourth-order eigenvalue problem for* F(y) *with complex eigenvalues* γ. *This problem, considered previously by Choi and Horgan (1977), is the anisotropic analog of the eigenvalue problem for the Fadle-Papkovich eigenfunctions arising in the isotropic case. The decay rate for Saint-Venant end effects is given by the eigenvalue with smallest positive real part. For an isotropic strip, where the material is described by two elastic constants (Young's modulus and Poisson's ratio), the associated eigencondition is* independent *of these constants. For transversely isotropic (or specially orthotropic) materials, described by* four *elastic constants, the eigencondition depends only on* one *elastic parameter. Here, we treat the fully anisotropic strip described by* six *elastic constants and show that the eigencondition depends on only* two *elastic parameters. Tables and graphs for a scaled complex-valued eigenvalue are presented. These data allow one to determine the Saint-Venant decay length for the* fully anisotropic *strip, as we illustrate by a numerical example for an end-loaded off-axis graphite-epoxy strip.*

1 Introduction

Let *OXYZ* denote a fixed, right-handed Cartesian reference frame. We consider an homogeneous elastic body which, if undeformed, occupies the region $0 \le X$, $|Y| \le H$, $|Z| \le T$. We shall regard the thickness, T, of the body as either infinitesimal or infinite and we shall assume that the deformation of the body is governed by the equations of static linear elasticity. All faces of the body are traction-free except $X = 0$ on which any combination of stress and/or displacement may be prescribed which induce stresses in the body that decay as $X \to \infty$. (Thus, the stresses on the end $X = 0$, whether known or not, must, necessarily, be self-equilibrating.) We shall assume that the infinitesimally thin body is in a state of plane stress with the Cartesian components τ_{xz}, τ_{yz}, and τ_{zz} of the stress tensor all zero; we shall assume that the infinitely thick body is in a state of plane strain with the Cartesian components ϵ_{xz}, ϵ_{yz}, and ϵ_{zz} of the strain tensor all zero. Except for different values of the elastic constants, the governing equations are identical mathematically. In both cases, we assume that the body is fully anisotropic in the xy-plane in the sense that ϵ_{xx}, ϵ_{yy}, and $2\epsilon_{xy}$, regarded as the components of a column vector $e \equiv [e_1, e_2, e_3]^T$ are related to τ_{xx}, τ_{yy}, and τ_{xy}, regarded as a column vector $s \equiv [s_1, s_2, s_3]^T$, by the relation

$$e = Bs, \text{ that is, } \begin{bmatrix} e_1 \\ e_2 \\ e_3 \end{bmatrix} = \begin{bmatrix} \beta_{11} & \beta_{12} & \beta_{16} \\ \beta_{12} & \beta_{22} & \beta_{26} \\ \beta_{16} & \beta_{26} & \beta_{66} \end{bmatrix} \begin{bmatrix} s_1 \\ s_2 \\ s_3 \end{bmatrix}, \tag{1}$$

where B is the (symmetric) compliance matrix and where we have followed the subscript notation of Lekhnitskii (1981). We henceforth refer to the problem of computing the stresses in either case (plane stress or plane strain) as the *anisotropic strip problem*.

This problem has been studied by Choi and Horgan (1977) who have emphasized that Saint-Venant's Principle—that article of faith of the structural engineer—must be used with extreme caution if an elastic material is strongly anisotropic. (See also Horgan, 1982 and 1989.) Their conclusion rests on the fact that if one assumes solutions for the (dimensionless) Airy stress function of the form

$$\phi = e^{-\gamma x}F(y), \tag{2}$$

where

$$x = X/H, \quad y = Y/H, \tag{3}$$

and $\gamma = \kappa + i\lambda$ is a complex *eigenvalue* with $\kappa > 0$, then for cer-

[1] This research was supported by the National Science Foundation under Grants MSS-8903130-01 (J. G. S.) and MSS-9102155 (C. O. H. and J. G. S.), and by the U.S. Army Research Office under Grant DAAL 03-91-G-0022 (C. O. H. and J. G. S.).

Contributed by the Applied Mechanics Division of THE AMERICAN SOCIETY OF MECHANICAL ENGINEERS for presentation at the First Joint ASCE-EMD, ASME-AMD, SES Meeting, Charlottesville, VA, June 6-9, 1993.

Discussion on this paper should be addressed to the Technical Editor, Professor Lewis T. Wheeler, Department of Mechanical Engineering, University of Houston, Houston, TX 77204-4792, and will be accepted until four months after final publication of the paper itself in the ASME JOURNAL OF APPLIED MECHANICS.

Manuscript received by the ASME Applied Mechanics Division, Nov. 26, 1991; final revision, Aug. 14, 1992. Associate Technical Editor: F. Y. M. Wan. Paper No. 93-APM-19.

Copyright © 1993 by ASME

Downloaded 03 May 2010 to 171.66.16.245. Redistribution subject to ASME license or copyright; see http://www.asme.org/terms/Terms_Use.cfm

tain transversely isotropic or specially orthotropic materials (e.g., graphite epoxy), the smallest value of κ (i.e, the decay rate for end effects) may be considerably smaller than that for an isotropic material. Our aim herein is to present tables and graphs so that one may readily compute $\kappa_1 \equiv \min \kappa$ for *any* anisotropic strip. We show how to do this with a numerical example in Section 7.

For an isotropic strip, the material is described by two elastic constants only, E and ν, Young's modulus and Poisson's ratio. Thus, $\beta_{11}=\beta_{22}=(1-\nu^2)/E$, $\beta_{12}=-\nu(1+\nu)/E$, $\beta_{66}=2(1+\nu)/E$, with $\beta_{16}=\beta_{26}=0$. However, the associated eigencondition, sin $2\gamma=\pm 2\gamma$, is *independent* of E and ν. Likewise, although an orthotropic (or transversely isotropic) strip ($\beta_{16}=\beta_{26}=0$) depends on *four* elastic constants, Horgan and Simmonds (1991) have shown that the eigencondition depends only on *one* combined elastic parameter,[2]

$$\epsilon=\frac{\sqrt{\beta_{11}\beta_{22}}}{2\beta_{12}+\beta_{66}}. \tag{4}$$

Herein, we show that, although the general anisotropic strip depends on *six* elastic constants, the associated eigencondition depends on *two* elastic parameters only, θ and ψ, where $0\le\theta<\pi/4$ and $0\le\psi<\pi/2$. If a certain combination of the β_{ij}'s vanish—a condition we call *generalized orthotropy* because it includes ordinary orthotropy (or transverse isotropy) ($\beta_{16}=\beta_{26}=0$) as a special case—then *either* ψ *or* θ vanishes. If, additionally, $\psi=\theta=0$, we have what we may call *generalized isotropy* because it includes ordinary isotropy as a special case. Finally, we present tables and graphs of the real and imaginary parts of a scaled, complex-valued eigenvalue, $\rho\gamma_1=\zeta_1=\xi_1+i\eta_1$, with smallest positive real part. Here, ρ is an amplitude factor depending on the elastic constants. In conjunction with (2) these results allow one to estimate the (Saint-Venant) decay length for self-equilibrating end data. (Similar results using parameters other than θ and ψ have been computed independently by Wang et al., 1992). We present a numerical example for an end-loaded, off-axis, graphite-epoxy strip to illustrate the results.

We remark here that, while there are points of similarity between the present paper and the recent work of Wang et al. (1992), the emphases in the two papers are quite different. The first seven sections of Wang et al. (1992) are devoted to showing how the elegant Stroh formalism can be used to examine the elastic strip problem, for general anisotropy, with a wide variety of boundary conditions on the sides and on the ends. Only in Section 8 of Wang et al. (1992) is the material restricted to one allowing plane deformations (i.e., monoclinic materials). The eigencondition (15) of the present paper (first obtained by Choi and Horgan, 1977) is independently derived (in a different notation) in Wang et al. (1992). They do show that the eigencondition depends only on *two* elastic parameters which, as remarked above, are different from θ and ψ used in the present paper. We will remark in the sequel on other points of contact between the work presented here and that of Wang et al. (1992).

2 Analysis

If U_x and U_y denote components of the displacement vector in the xy-plane, then the strain displacement relations are

$$\epsilon_{xx}=U_{x,x},\quad \epsilon_{yy}=U_{y,y},\quad 2\epsilon_{xy}=U_{x,y}+U_{y,x}, \tag{5}$$

where a subscript preceded by a comma denotes differentiation with respect to that subscript. Differential elimination of the displacement components from the above equation leads to the well-known compatibility condition

$$\epsilon_{yy,xx}-2\epsilon_{xy,xy}+\epsilon_{xx,yy}=0. \tag{6}$$

[2]We remark that while the parameter ϵ was assumed positive in Horgan and Simmonds (1991), we make no such assumption here.

Setting

$$\tau_{xx}=\phi_{,yy},\quad \tau_{yy}=\phi_{,xx},\quad \tau_{xy}=-\phi_{,xy} \tag{7}$$

to satisfy the in-plane equilibrium equations identically, substituting (2) into (7), (7) into (1), and (1) into (6), we obtain the fourth-order linear ordinary differential equation for $F(y)$:

$$\beta_{11}\gamma^4\mathcal{P}(\gamma^{-1}d/dy)F=0,\quad -1<y<1. \tag{8}$$

Here,

$$\mathcal{P}(\mu)=\mu^4+2\alpha_{16}\mu^3+\bar{\alpha}\mu^2+2\alpha_{26}\mu+\alpha_{22}, \tag{9}$$

where

$$\alpha_{ij}=\beta_{ij}/\beta_{11},\quad i,j=1,2,6,\quad \text{and}\quad \bar{\alpha}\equiv 2\alpha_{12}+\alpha_{66}. \tag{10}$$

Following Choi and Horgan (1977), we seek solutions to (8) of the form $F=e^{\mu\gamma y}$ which leads to the characteristic polynomial $\mathcal{P}(\mu)=0$. As Lekhnitskii (1981) notes, the roots of $\mathcal{P}(\mu)$ cannot be real, because the special choice of the stress vector, $s_\mu=[\mu^2, 1, \mu]^T$ and the positive definiteness of the stress-energy density (which we assume here) imply

$$\beta_{11}\mathcal{P}(\mu)=s_\mu^T B s_\mu>0\quad \text{for all real } \mu. \tag{11}$$

Furthermore, as the coefficients of the polynomial $\mathcal{P}(\mu)$ are real, its roots must occur in conjugate pairs; thus $\mathcal{P}(\mu)$ has the factored form

$$\mathcal{P}(\mu)=(\mu-\mu_1)(\mu-\bar{\mu}_1)(\mu-\mu_2)(\mu-\bar{\mu}_2), \tag{12}$$

where

$$\mu_k=p_k+iq_k,\quad k=1,2,\quad q_k\neq 0,\quad p_k, q_k \text{ real}. \tag{13}$$

Because the loads on the end of the strip (whether known or not) are self-equilibrating, it may be shown that the stress-free conditions on the sides of the strip, $\tau_{yy}(x, \pm 1)=\tau_{xy}(x, \pm 1)=0$, may be replaced by the integrated conditions

$$F(\pm 1)=F'(\pm 1)=0. \tag{14}$$

The solutions of (8) are of the form

$$F=\sum_{k=1}^{2}(A_k e^{\mu_k\gamma y}+B_k e^{\bar{\mu}_k\gamma y}),$$

where the A_k and B_k are unknown constants. If we substitute this solution into (14) and write the roots of $\mathcal{P}(\mu)=0$ in the form (13), we obtain the *eigencondition* of Choi and Horgan (1977):

$$\begin{aligned}[(p_1-p_2)^2+(q_1+q_2)^2]\cos 2(q_1-q_2)\gamma \\ -[(p_1-p_2)^2+(q_1-q_2)^2]\cos 2(q_1+q_2)\gamma \\ =4q_1q_2\,\mathrm{ch}\,2(p_1-p_2)\gamma,\end{aligned} \tag{15}$$

where here and elsewhere we denote the hyperbolic sine and cosine by sh and ch. An equivalent condition has been obtained by Wang et al. (1992).

3 Simplification of the Eigencondition

Introducing into (15) the spherical representation

$$p_1-p_2=\rho\sin\psi,\quad q_1-q_2=\rho\cos\psi\cos\theta,\quad q_1+q_2=\rho\cos\psi\sin\theta$$
$$\rho>0,\quad -\pi/2\le\psi\le\pi/2,\quad 0\le\theta<2\pi, \tag{16}$$

the *modified* eigenvalue

$$\zeta=\rho\gamma, \tag{17}$$

and the identities $\cos 2w=1-2\sin^2 w$, $\mathrm{ch}\,2w=1+2\,\mathrm{sh}^2 w$, we obtain the *reduced eigencondition*

$$\begin{aligned}f(\zeta,\psi,\theta)\equiv\cos^2\psi\cos 2\theta\,\mathrm{sh}^2(\zeta\sin\psi) \\ +(\sin^2\psi+\cos^2\psi\cos^2\theta)\sin^2(\zeta\cos\psi\sin\theta) \\ -(\sin^2\psi+\cos^2\psi\sin^2\theta)\sin^2(\zeta\cos\psi\cos\theta)=0.\end{aligned} \tag{18}$$

Observe that $f(\zeta, \psi, \theta)$ is even in ψ and θ. Moreover,

$$f(\zeta,\psi,\theta+\pi/2)=-f(\zeta,\psi,\theta)\quad \text{and}$$
$$f(\zeta,\psi,\pi/2-\theta)=f(\zeta,\psi,\theta). \tag{19}$$

Downloaded 03 May 2010 to 171.66.16.245. Redistribution subject to ASME license or copyright; see http://www.asme.org/terms/Terms_Use.cfm

Table 1 $\xi_1(\psi, \theta)$ real part of the first eigenvalue

ψ \ θ	0	5	10	15	20	25	30	35	40	45
0	4.2122	4.2584	4.4041	4.6763	5.1402	6.0182	5.1096	4.6744	4.4952	4.4429
10	4.1598	4.2016	4.3325	4.5694	4.9388	5.4026	5.5762	5.4977	5.0645	4.9363
20	4.0110	4.0434	4.1424	4.3122	4.5497	4.8153	5.0172	5.1140	5.1460	5.1524
30	3.7850	3.8073	3.8743	3.9848	4.1321	4.2972	4.4486	4.5596	4.6232	4.6434
40	3.5015	3.5153	3.5559	3.6214	3.7066	3.8021	3.8945	3.9700	4.0185	4.0351
50	3.1816	3.1889	3.2100	3.2435	3.2863	3.3337	3.3798	3.4183	3.4438	3.4527
60	2.8524	2.8554	2.8639	2.8773	2.8940	2.9122	2.9297	2.9443	2.9539	2.9573
70	2.5521	2.5528	2.5549	2.5582	2.5623	2.5667	2.5708	2.5742	2.5764	2.5772
80	2.3328	2.3328	2.3330	2.3332	2.3335	2.3338	2.3341	2.3344	2.3346	2.3346
90	2.2507	2.2507	2.2507	2.2507	2.2507	2.2507	2.2507	2.2507	2.2507	2.2507

Table 2 $\eta_1(\psi, \theta)$ imaginary part of first eigenvalue

ψ \ θ	0	5	10	15	20	25	30	35	40	45
0	0.2508	2.2463	2.2275	2.1724	2.0121	1.4138	0.0000	0.0000	0.0000	0.0000
10	2.3328	2.3293	2.3136	2.2649	2.1221	1.7122	1.0144	0.4288	0.0000	0.0000
20	2.5521	2.5509	2.5434	2.5152	2.4355	2.2615	2.0036	1.7597	1.6010	1.5472
30	2.8524	2.8535	2.8545	2.8479	2.8213	2.7623	2.6731	2.5779	2.5074	2.4818
40	3.1816	3.1839	3.1897	3.1955	3.1964	3.1878	3.1692	3.1458	3.1265	3.1191
50	3.5015	3.5038	3.5100	3.5187	3.5277	3.5350	3.5395	3.5411	3.5411	3.5409
60	3.7850	3.7864	3.7903	3.7962	3.8031	3.8101	3.8164	3.8212	3.8242	3.8253
70	4.0110	4.0144	4.0128	4.0148	4.0173	4.0199	4.0223	4.0242	4.0255	4.0259
80	4.1598	4.1598	4.1599	4.1601	4.1603	4.1606	4.1608	4.1610	4.1611	4.1612
90	4.2124	4.2124	4.2124	4.2124	4.2124	4.2124	4.2124	4.2124	4.2124	4.2124

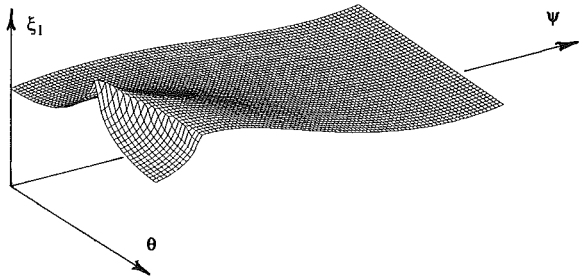


Fig. 1 Graph of $\xi_1(\psi, \theta)$, the real part of the first modified eigenvalue

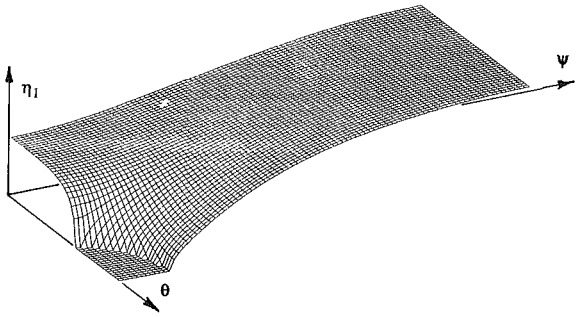


Fig. 2 Graph of $\eta_1(\psi, \theta)$, the imaginary part of the first modified eigenvalue

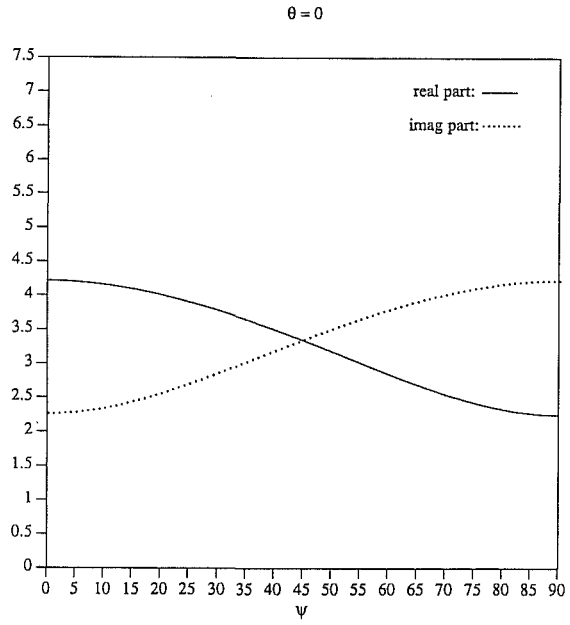


Fig. 3 Graphs of the real and imaginary parts of $\zeta_1(\psi, 0)$, the first modified eigenvalue for $\theta = 0$

Thus, in solving (18) for ζ, it is sufficient to restrict the domains of ψ and θ to $0 \le \psi \le \pi/2$ and $0 \le \theta \le \pi/4$. In fact, $\psi = \pi/2$ would imply by (16) that $q_1 = q_2 = 0$, which violates the stipulations in (13). Similarly, from (16), $\theta = \pi/4$ would imply that $q_2 = 0$, which again violates (13). Thus, the domains for ψ and θ may be further restricted to

$$0 \le \psi < \pi/2 \quad \text{and} \quad 0 \le \theta < \pi/4. \tag{20}$$

Finally, we note that $f(\zeta, \psi, \theta) = 0$ implies that $f(\bar{\zeta}, \psi, \theta) = 0$.

For various angles ψ and θ, Tables 1 and 2 list, respectively, the real and imaginary parts, $\xi_1(\psi, \theta)$ and $\eta_1(\psi, \theta)$ of the modified eigenvalue $\zeta_1(\psi, \theta)$ of smallest positive real part. Figures 1 and 2 are graphs of ξ_1 and η_1 as functions of ψ and θ. We conjecture (and prove in Section 5 in the special case $\psi = 0$) that there is a multiple eigenvalue along the ridge line in Fig. 1. Figure 3 is a graph of $\xi_1(\psi, 0)$ and $\eta_1(\psi, 0)$; Fig. 4 is a graph of $\xi_1(0, \theta)$ and $\eta_1(0, \theta)$.

We assured ourselves that the values of ζ_1 that we computed numerically were actually the eigenvalues of smallest positive real part by using Newton's method and proceeding in small increments of θ and ψ from the known value of $\zeta_1(0, 0)$—that is, from the known isotropic value—listed on p. 62 of Timoshenko and Goodier (1970).

4 Limiting Cases of the Eigencondition

Even though $\theta < \pi/4$ and $\psi < \pi/2$, it is useful for the sake

Downloaded 03 May 2010 to 171.66.16.245. Redistribution subject to ASME license or copyright; see http://www.asme.org/terms/Terms_Use.cfm

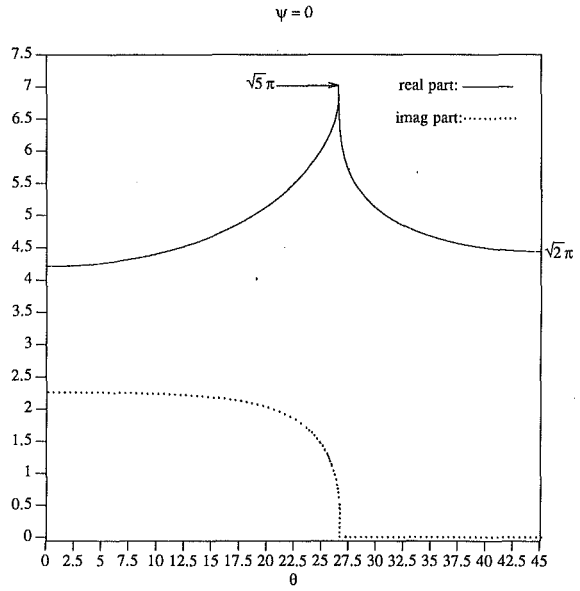


Fig. 4 Graphs of the real and imaginary parts of $\zeta_1(0, \theta)$, the first modified eigenvalue for $\psi = 0$

of completeness and as a check on the numerical work to consider the following limiting forms of the eigencondition (18).

(i) $\theta \to \pi/4$. Setting $\theta = \pi/4 - \phi$, expanding (18) in a Taylor series about $\phi = 0$, and letting $\phi \to 0$, we obtain the limiting eigencondition

$$f_{,\theta}(\zeta, \psi, \pi/4) = -2\cos^2\psi[\mathrm{sh}^2(\zeta\sin\psi) + \sin^2(\zeta\cos\psi/\sqrt{2})] + \sqrt{2}\,\zeta\cos\psi[\sin^2\psi + (1/2)\cos^2\psi]\sin(\sqrt{2}\,\zeta\cos\psi) = 0, \quad (21)$$

where $f_{,\theta} = \partial f/\partial\theta$. The last column in both tables was found by solving (21) numerically for the value of ζ with smallest positive real part. In particular,

$$f_{,\theta}(\zeta, 0, \pi/4) = 2\sin(\zeta/\sqrt{2})[(\zeta/\sqrt{2})\cos(\zeta/\sqrt{2}) - \sin(\zeta/\sqrt{2})] = 0 \quad (22)$$

which yields

$$\zeta_1(0, \pi/4) = \xi_1(0, \pi/4) = \sqrt{2}\,\pi = 4.4428\cdots. \quad (23)$$

(ii) $\psi \to \pi/2$. Setting $\psi = \pi/2 - \phi$ so that $\cos\psi = \phi + O(\phi^3)$ and $\sin\psi = 1 + O(\phi^2)$, we obtain from (18)

$$f(\zeta, \pi/2 - \phi, \theta) = \phi^2\cos 2\theta(\mathrm{sh}^2\zeta - \zeta^2) + O(\phi^4), \quad (24)$$

from which follows the limiting eigencondition

$$\mathrm{sh}\,\zeta = \pm\zeta. \quad (25)$$

The value of ζ with smallest positive real part corresponds to taking the negative sign in (25), and we find, numerically, that

$$\zeta_1(\pi/2, \theta) = 2.2507\cdots + i4.2123\cdots, \quad (26)$$

which determines the last row in both tables.

5 Determining ρ, ψ, and θ From the Elastic Constants

Multiplying out the right side of (12), the factored form of $\mathcal{P}(\mu)$, comparing the resulting expression with (9), expressing μ_1, μ_2 and their conjugates in terms of p_1, p_2, q_1, and q_2 via (13), and finally, using the spherical representation (16), we find that

$$\alpha_{16} = -(p_1 + p_2) \quad (27)$$

$$\overline{\alpha} = p_1^2 + q_1^2 + p_2^2 + q_2^2 + 4p_1p_2 = (3/2)\alpha_{16}^2 + (1/2)\rho^2\cos 2\psi \quad (28)$$

$$\alpha_{26} = -[p_1(p_2^2 + q_2^2) + p_2(p_1^2 + q_1^2)] = (1/4)(\alpha_{16}^3 + \alpha_{16}\rho^2\cos 2\psi + \rho^3\sin\psi\cos^2\psi\sin 2\theta) \quad (29)$$

$$\alpha_{22} = (p_1^2 + q_1^2)(p_2^2 + q_2^2) = (1/16)[(\alpha_{16}^2 + \rho^2)^2 - (\rho^2\cos^2\psi\sin 2\theta - 2\alpha_{16}\rho\sin\psi)^2]. \quad (30)$$

To use the tables and to compute the eigenvalue, γ_1, with smallest positive real part for a specific material, we need to solve (27)–(30) for ρ, ψ, and θ in terms of the α_{ij}. From (28) follows

$$\rho^2\cos 2\psi = 2\overline{\alpha} - 3\alpha_{16}^2 \equiv a. \quad (31)$$

Inserting this result into (29) and rearranging, we obtain

$$\rho^3\sin\psi\cos^2\psi\sin 2\theta = 2[2\alpha_{26} + \alpha_{16}(\alpha_{16}^2 - \overline{\alpha})] \equiv b. \quad (32)$$

Finally, if we let

$$(\overline{\alpha} - \alpha_{16}^2)^2 - 4\alpha_{22} \equiv c, \quad (33)$$

and note (31) and (32), we may rearrange (30) to read

$$\rho^4 + 4c - a^2 + 4\alpha_{16}b = (\rho^2\cos^2\psi\sin 2\theta)^2. \quad (34)$$

5.1 The case $b = 0$. A major simplification occurs if $b = 0$. Because $\rho > 0$ and $0 \le \psi < \pi/2$, $0 \le \theta < \pi/4$, (32) implies that $b = 0$ if either (i) $\psi = 0$ or (ii) $\theta = 0$ or (iii) $\psi = \theta = 0$. In terms of the material constants α_{ij}, the condition $b = 0$ can be written, on using (10) and (32), as

$$2\alpha_{26} = \alpha_{16}(2\alpha_{12} + \alpha_{66} - \alpha_{16}^2). \quad (35)$$

(i) $\psi = 0$. From (31) and (34) follows

$$\rho^2 = a, \quad \theta = 1/2\,\mathrm{Sin}^{-1}(2\sqrt{c}/a), \quad (36)$$

where Sin^{-1} denotes the principal branch of the inverse sine. Note from $(36)_2$ that $c \ge 0$ in this case. The eigencondition (18) reduces to

$$\cos\theta\sin(\zeta\sin\theta) = \pm\sin\theta\sin(\zeta\cos\theta). \quad (37)$$

The minus sign should be used in (37) to obtain the smallest positive ξ_1.

Figure 4 shows (as does Fig. 4 of Wang et al., 1992) that the graph of $\zeta_1(0, \theta)$ has a cusp at $\theta^* = \tan^{-1}(1/2) = 26.56\cdots$deg. At such a cusp there is a *multiple* eigenvalue:

$$\zeta_1(0, \theta^*) = \bar{\zeta}_1(0, \theta^*) = \zeta_2(0, \theta^*) = \bar{\zeta}_2(0, \theta^*) = \zeta_3(0, \theta^*) = \bar{\zeta}_3(0, \theta^*) = \sqrt{5}\pi. \quad (38)$$

To see why, let

$$\tan\theta = 1/2 + t, \quad \zeta\cos\theta = 2\pi + \epsilon. \quad (39)$$

Then (37) takes the form

$$\sin(1/2\,\epsilon + 2\pi t + \epsilon t) = \pm(1/2 + t)\sin\epsilon. \quad (40)$$

Taking the minus $(-)$ sign on the right and setting $\sin\phi = \phi + O(\phi^3)$, we obtain

$$\epsilon = -2\pi t + O(t^2). \quad (41)$$

Taking the plus $(+)$ sign on the right and setting $\sin\phi = \phi - (1/6)\phi^3 + O(\phi^5)$, we obtain

$$\epsilon^3 = -32\pi t + O(t^{5/3}). \quad (42)$$

Substituting (41) or solutions of (42) into $(39)_2$ and noting that $\cos\theta = (2/\sqrt{5})[1 - (2t/5) + O(t^2)]$, we obtain

$$\zeta_1/\sqrt{5} = \pi - \begin{cases} (4\pi t)^{1/3} + O(t), & t \ge 0 \\ (1/2)(-4\pi t)^{1/3}(1 + i\sqrt{3}) + O(t), & t < 0 \end{cases}$$

$$\zeta_1/\sqrt{5} = \pi(1 - 3t/5) + O(t^2)$$

$$\zeta_3/\sqrt{5} = \pi + \begin{cases} (1/2)(4\pi t)^{1/3}(1 + i\sqrt{3}) + O(t), & t \ge 0 \\ (-4\pi t)^{1/3} + O(t), & t < 0 \end{cases} \quad (43)$$

together with their complex conjugates, $\bar{\zeta}_1$, $\bar{\zeta}_2$, and $\bar{\zeta}_3$.

(ii) $\theta = 0$. From (34) and (31) (in that order) follows

$$\rho^2 = \sqrt{a^2 - 4c}, \quad \psi = 1/2\,\mathrm{Cos}^{-1}(a/\sqrt{a^2 - 4c}), \quad (44)$$

Downloaded 03 May 2010 to 171.66.16.245. Redistribution subject to ASME license or copyright; see http://www.asme.org/terms/Terms_Use.cfm

where Cos^{-1} denotes the principal branch of the inverse cosine. Note from $(44)_2$ that $c \le 0$ in this case. The eigencondition (18) reduces to

$$g_{\pm}(\zeta, \psi) \equiv \cos\psi \,\mathrm{sh}(\zeta \sin\psi) \pm \sin\psi \sin(\zeta\cos\psi) = 0. \quad (45)$$

The minus sign should be used in (45) to obtain $\zeta_1(\psi, 0)$, the complex eigenvalue with smallest positive real part. Note that

$$ig_{\pm}(\zeta, \pi/2-\psi) = g_{\pm}(\pm i\zeta, \psi) \quad (46)$$

which, because $\bar{g}_{\pm}(\zeta, \psi) = g_{\pm}(\bar{\zeta}, \psi)$, implies that $\zeta_1(\pi/2-\psi, 0) = i\bar{\zeta}_1(\psi, 0)$, as is evident from Fig. 3. This *conjugate symmetry* of $\zeta_1(\psi, 0)$ about $\psi = \pi/4$ is not manifest in Fig. 3 of Wang et al. (1992) because their parameter $\hat{\alpha}$ is different from our parameter ψ.

(iii) $\psi = \theta = 0$. Here, (36) and (44) hold simultaneously which means that

$$\rho^2 = a \quad \text{and} \quad c = 0. \quad (47)$$

As $\psi, \theta \to 0$, the eigencondition (18) reduces to

$$\sin\zeta = \pm\zeta. \quad (48)$$

In case *(i)* or *(ii)* we say that the material has *generalized orthotropy* because the transcendental eigenconditions (37) or (45) are identical in form to those governing a *specially orthotropic (or transversely isotropic)* material. (See Section 6.) In case *(iii)*, we say that the material has *generalized isotropy* because the eigencondition (48) is identical in form to that for an *isotropic material*. (See Section 6.)

5.2 The case $b \neq 0$. Here it is useful to define the auxiliary variable

$$\delta \equiv \rho^2 - a \ge |a| - a \quad (49)$$

and use (31) to get

$$\rho \sin\psi = \rho\sqrt{(1-\cos 2\psi)/2} = \sqrt{\delta/2}. \quad (50)$$

Note from (32) that if $b \neq 0$ then $\psi \neq 0$ and $\theta \neq 0$ and thus, by (31) and (49), $\delta \neq 0$. With the aid of (32), (49), and (50), Eq. (34) may be rewritten as the cubic

$$\mathcal{Q}(\delta) \equiv \delta^2 + 2a\delta^2 + 4(c + b\alpha_{16})\delta - 2b^2 = (\delta-\delta_1)(\delta-\delta_2)(\delta-\delta_3) = 0. \quad (51)$$

Because all the coefficients of $\mathcal{Q}(\delta)$ are real and $\mathcal{Q}(0) < 0$, $\mathcal{Q}(\delta)$ always has one positive root. We claim that there is one and only one positive root of (51), call it δ_1, satisfying (49). For suppose there were a second root, δ_2, satisfying (49). Then, because $\mathcal{Q}(\delta) \to \infty$ as $\delta \to \infty$ and $\mathcal{Q}(0) < 0$, continuity would imply the existence of a third positive root, δ_3. But from (51),

$$2a = -(\delta_1 + \delta_2 + \delta_3) \quad (52)$$

and

$$4(c + b\alpha_{16}) = \delta_1\delta_2 + \delta_2\delta_3 + \delta_3\delta_1, \quad (53)$$

so that a would then be negative and $4(c + b\alpha_{16})$ positive. By Rolle's Theorem, there exists a $\hat{\delta}$ between δ_1 and δ_2 such that

$$\mathcal{Q}'(\hat{\delta}) = 3\hat{\delta}^2 + 4a\hat{\delta} + 4(c + b\alpha_{16}) = 0 \quad (54)$$

which yields

$$\hat{\delta} = 2\left(\frac{|a| \pm \sqrt{a^2 - 3(c + b\alpha_{16})}}{3}\right) \le 4|a|/3. \quad (55)$$

This is a contradiction because, by (49) and (52), $\delta_1, \delta_2 \ge 2|a|$. Thus, we have shown that (51) has one and only one positive root δ_1 satisfying (49).

With δ_1 in hand, we have from (49), (31), (50), and (32) (in this order),

$$\rho = \sqrt{\delta_1 + a}, \quad \psi = \frac{1}{2}\mathrm{Cos}^{-1}\left(\frac{a}{\delta_1 + a}\right), \quad \theta = \frac{1}{2}\mathrm{Sin}^{-1}\left(\frac{2\sqrt{2}\,b}{(\delta_1 + 2a)\sqrt{\delta_1}}\right). \quad (56)$$

6 Transversely Isotropic and Isotropic Materials

A material is *transversely isotropic* (or *specially orthotropic*) if $\alpha_{16} = \alpha_{26} = 0$ in which case, in view of (31)–(33), *either* (36) holds in the simplified form

$$\rho^2 = 2\bar{\alpha}, \quad \psi = 0, \quad \theta = 1/2\,\mathrm{Sin}^{-1}(\sqrt{1-4\epsilon^2}), \quad (57)$$

or else (44) holds in the simplified form

$$\rho^2 = 4\sqrt{\alpha_{22}}, \quad \psi = 1/2\,\mathrm{Cos}^{-1}(1/2\,\epsilon), \quad \theta = 0, \quad (58)$$

where $\epsilon = \sqrt{\alpha_{22}}/\bar{\alpha}$ is the parameter introduced in (4). The respective eigenconditions are (37) or (45) as in the more general case when the only relation among the elastic constants α_{16}, α_{26}, α_{12}, and α_{66} is (35). Choi and Horgan (1977), Horgan and Simmonds (1991), and Wang et al. (1992) have also obtained equivalent versions of (37) and (45).

A material is *isotropic* if $\alpha_{16} = \alpha_{26} = 0$, $\alpha_{22} = 1$, and $\bar{\alpha} = 2$ in which case $\epsilon = 1/2$ and both (57) and (58) reduce to

$$\rho = 2, \quad \psi = \theta = 0. \quad (59)$$

Because $\zeta = 2\gamma$ in this case—see (17)—the eigencondition (48) reduces to the well-known Fadle-Papkovich eigencondition

$$\sin 2\gamma = \pm 2\gamma. \quad (60)$$

(See, e.g., Timoshenko and Goodier, 1970, p. 62.) The eigenvalue with smallest positive real part comes from taking the minus sign in (60) and is $\gamma_1 = 2.1061\cdots + i1.1254\cdots$.

7 Numerical Example

Consider a sheet of transversely isotropic material with a compliance matrix $B \equiv B(0)$ from which we cut a (very long) strip whose x-axis makes an angle ϕ with the principal (x_1-) axis of the sheet. The compliance matrix $B(\phi)$ of the strip is then given by

$$B(\phi) = T^T(\phi)B(0)T(\phi), \quad (61)$$

where, from Jones (1975, p. 49),

$$T(\phi) = \begin{bmatrix} \cos^2\phi & \sin^2\phi & \sin 2\phi \\ \sin^2\phi & \cos^2\phi & -\sin 2\phi \\ -1/2\sin 2\phi & 1/2\sin 2\phi & \cos 2\phi \end{bmatrix}. \quad (62)$$

To be specific, we take our sheet to be graphite/epoxy and $\phi = 15$ deg. Then, from (10), (61), (62), and Table 1 of Choi and Horgan (1977) (where a minus sign should be placed in front of the value of β_{12}), we obtain the following dimensionless *reduced* compliance coefficients:

$$\alpha_{16} = -2.4179, \quad \bar{\alpha} = 9.2944, \quad \alpha_{26} = -0.5447, \quad \alpha_{22} = 6.1314. \quad (63)$$

From (31)–(33) follows

$$a = 1.0500, \quad b = 14.4956, \quad c = -12.6360. \quad (64)$$

Inserting these values along with that for α_{16} into the cubic (51) and solving for its one positive root, we obtain

$$\delta_1 = 13.8555 \quad (65)$$

and thence, from (56),

$$\rho = 3.8608, \quad \psi = 42.9803, \quad \theta = 21.8284 \text{ deg}. \quad (66)$$

Interpolating from the tables, we find that the first reduced eigenvalue is

$$\zeta_1 = 3.6083 + i3.3009 \quad (67)$$

and hence, by (17) and (66), that the actual first eigenvalue is

$$\gamma_1 = 0.9346 + i0.8550. \quad (68)$$

Thus, for the off-axis graphite epoxy specimen, the decay rate for the end effects, $\Re\gamma_1$, is less than one half that for the isotropic strip. (For the $\phi = 0$ deg strip, the decay rate is given by Choi and Horgan, 1977, as 0.5640 which is almost one

Downloaded 03 May 2010 to 171.66.16.245. Redistribution subject to ASME license or copyright; see http://www.asme.org/terms/Terms_Use.cfm

fourth of that for the isotropic case.) The results of the present work allow us to determine the decay rate for an arbitrary off-axis orientation.

8 Concluding Remarks

We have examined the plane stress (or plane strain) problem for an homogeneous anisotropic semi-infinite strip, free of tractions on its long sides and subject to self-equilibrating end loads. Seeking solutions which decay exponentially in the axial direction leads to a fourth-order eigenvalue problem with complex-valued eigenvalues. The decay rate for Saint-Venant end effects is given by the eigenvalue with smallest positive real part. We have simplified the transcendental Eq. (15) governing the eigenvalues and showed that, while the fully anisotropic strip is described by *six* elastic constants, the eigencondition depends on only *two* elastic parameters. Further, we have presented tables and graphs for the real and imaginary parts of a scaled, complex-valued eigenvalue (the one of smallest positive real part) which allow one to determine the Saint-Venant decay length for the *fully anisotropic* strip.

Acknowledgments

We are grateful to Prof. T. C. T. Ting for his comments on an earlier version of the manuscript. We are also grateful to the referees for their constructive comments.

References

Choi, I., and Horgan, C. O., 1977, "Saint-Venant's Principle and End Effects in Anisotropic Elasticity," ASME JOURNAL OF APPLIED MECHANICS, Vol. 44, pp. 424–430.

Horgan, C. O., 1982, "Saint-Venant End Effects in Composites," *J. Composite Materials*, Vol. 16, pp. 411–422.

Horgan, C. O., 1989, "Recent Developments Concerning Saint-Venant's Principle: An Update," ASME *Appl. Mech. Rev.*, Vol. 42, pp. 295–303.

Horgan, C. O., and Simmonds, J. G., 1991, "Asymptotic Analysis of an End-Loaded, Transversely Isotropic, Elastic, Semi-Infinite Strip Weak in Shear," *Int. J. Solids Structures*, Vol. 27, pp. 1895–1914.

Jones, R. M., 1975, *Mechanics of Composite Materials*, Hemisphere Publ. Co., New York.

Lekhnitskii, S. G., 1981, Theory of Elasticity of an Anisotropic Body, MIR Publishers, Moscow.

Timoshenko, S. P., and Goodier, J. N., 1970, *Theory of Elasticity*, 3rd ed., McGraw-Hill, New York.

Wang, M. Z., Ting, T. C. T., and Yan, G., 1992, "The Anisotropic Elastic Semi-Infinite Strip," *Quart. Appl. Math.*, in press.

Downloaded 03 May 2010 to 171.66.16.245. Redistribution subject to ASME license or copyright; see http://www.asme.org/terms/Terms_Use.cfm

Antisymmetric Bifurcations in a Compressible Pressure-Sensitive Circular Cylinder Under Axisymmetric Tension and Compression

K. T. Chau
Department of Civil and Structural Engineering, Hong Kong Polytechnic, Hung Hom, Hong Kong
Mem. ASME

This paper examines antisymmetric bifurcations of geometric diffuse modes, including buckling and surface rumpling modes, for a compressible pressure-sensitive circular cylinder of finite length under axisymmetric loadings. The analysis includes the effects of nonnormality, transverse isotropy, and confining stress on the appearance of antisymmetric geometric diffuse modes and their relationship to the onset of localization. The long wavelength limit of the eigenvalue equation is found corresponding to the Euler's buckling load; the short wavelength limit corresponds to the eigenstress for the surface rumpling mode if the cylinder is incompressible and satisfies plastic normality. If the lateral stress is nonzero, a finite solution exists for the antisymmetric long wavelength limit; for the cases that the in-plane bulk modulus becomes unbounded, this finite eigenstress equals to the plane-strain results obtained by Chau and Rudnicki (1990). The lowest possible bifurcation stresses are plotted for various constitutive parameters by combining the results of the bifurcation analyses for both the axisymmetric (Chau, 1992) and the antisymmetric modes. This eigenvalue surface also provides a condition that determines whether buckling (antisymmetric) or bulging (axisymmetric) appears first for a fixed specimen geometry under compression. For typical specimen size (length/radius ratio from 4 to 6), the numerical results suggest that the first possible bifurcation is always the antisymmetric buckling mode under compression; however, for specimen sizes with length/radius ratio approximately less than $\pi/2$, bulging mode becomes the first possible bifurcation. The hypothesis that the prepeak and antisymmetric bifurcation triggers the subsequent localization of deformation is further discussed.

1 Introduction

Localization of shear deformation in a narrow zone is a remarkably common phenomenon which appears in many materials, such as metals, concrete, clay, sand, polymers, but is particularly widespread in brittle rocks. When these materials deform sufficiently into the inelastic range, smooth and continuously varying deformation pattern often yields to intensely concentrated deformation in a planar form.

For axisymmetric compression of rock cylinders, Chau (1992) suggested that the axisymmetric diffuse modes, such as bulging, necking and surface rumpling, may trigger nonhomogeneous deformation and, eventually, lead to pre-peak localization of deformation. The bifurcation analysis given by Chau (1992) was a continuation of the works by Cheng et al. (1971), Hutchinson and Miles (1974), Rudnicki (1977), Vardoulakis (1983), and Miles and Nuwayhid (1985) and provided an analogous study of the plane-strain counterpart by Chau and Rudnicki (1990). However, the possibility of the antisymmetric diffuse modes for circular cylinders is not included in the above studies.

To further investigate the conjecture by Chau (1992) that pre-peak diffuse modes trigger subsequent localization of deformation, all possible pre-peak diffuse mode bifurcations, including antisymmetric one, should be examined. Therefore, we extend, in this study, the bifurcation analysis by Chau (1992) to include the antisymmetric diffuse modes for a circular cylinder, characterized by Rudnicki's (1977) constitutive relation, deforming under axisymmetric tension or compression. In ad-

Contributed by the Applied Mechanics Division of THE AMERICAN SOCIETY OF MECHANICAL ENGINEERS for presentation at the First Joint ASCE-EMD, ASME-AMD, SES Meeting, Charlottesville, VA, June 6-9, 1993.

Discussion on this paper should be addressed to the Technical Editor, Professor Lewis T. Wheeler, Department of Mechanical Engineering, University of Houston, Houston, TX 77204-4792, and will be accepted until four months after final publication of the paper itself in the ASME JOURNAL OF APPLIED MECHANICS.

Manuscript received by the ASME Applied Mechanics Division, Aug. 2, 1991; final revision, Aug. 4, 1992. Associate Technical Editor: R. M. McMeeking.

Paper No. 93-APM-29.

Copyright © 1993 by ASME
Downloaded 03 May 2010 to 171.66.16.245. Redistribution subject to ASME license or copyright; see http://www.asme.org/terms/Terms_Use.cfm

dition, the combined results of the axisymmetric (Chau, 1992) and the antisymmetric (present study) bifurcations can also provide an answer to whether buckling or bulging appears first in circular cylinders under compression. In particular, it is possible to obtain a fixed slenderness ratio that separates the bulging (or barreling) phenomenon from the buckling one if all material parameters are known.

More specifically, we consider the problem that: the ends of the cylinder are loaded by a prescribed velocity with no shear traction; and a constant lateral stress is applied with zero shear traction on the sides of the cylinder. An initial state of homogeneous deformation is always a solution to the governing equations and we investigate the conditions for which an antisymmetric bifurcated state of nonuniform deformation is also possible under the same boundary conditions.

The buckling problem of a compressible isotropic elastic circular cylinder of finite length has been considered by Sensenig (1964). However, Senenig's (1964) analysis is restricted to hyperelastic materials, that is strain energy function must exist; furthermore, the effects of non-normality, transverse isotropy, and confining stress are not included. The method of solution considered here for the antisymmetric diffuse mode bifurcation is a continuation of the line of works by Love (1927), Elliott (1948), Hu (1954), and Pan and Chou (1976) for linear elastic transversely isotropic solids. Hu (1954) considered a general theory to solve the problems for a three-dimensional transversely isotropic solid. Elaborating upon the work of Love (1927) and Elliott (1948), Pan and Chou (1976) also proposed a general method of solving three-dimensional problems for transversely isotropic solids by introducing three potentials but, as pointed out by Hu (1954), one of these potentials is redundant. Furthermore, Pan and Chou (1976) considered the analysis only in the Cartesian coordinates. In this study, we extend the method of displacement potentials (Hu, 1954; Pan and Chou, 1976) to the bifurcation analysis of Rudnicki's (1977) incrementally linear constitutive model in cylindrical polar coordinates.

The combined results for the antisymmetric diffuse bifurcation modes considered here and the axisymmetric modes obtained by Chau (1992) should provide a complete picture of all the possible geometric bifurcation before strain localization occurs; and these combined results also provide an analogous study of the plane-strain counterpart by Chau and Rudnicki (1990).

2 Constitutive Relation

We consider a circular cylinder of radius a and length L under initial axisymmetric deformations. The current configuration is adopted as reference and the subsequent deformation of the material is characterized by the following time and rate-independent constitutive relation (Rudnicki, 1977):

$$\overset{\nabla}{\sigma}_{zz}=\left(\frac{E+9Kr^*\nu}{2}\right)D_{zz}+\frac{9Kr^*}{4}(D_{rr}+D_{\theta\theta}),$$

$$\overset{\nabla}{\sigma}_{z\alpha}=2G_1D_{z\alpha}(\alpha,\ \beta=r,\ \theta),$$

$$\overset{\nabla}{\sigma}_{\alpha\beta}=2G_t\left[D_{\alpha\beta}-\frac{1}{2}\delta_{\alpha\beta}(D_{rr}+D_{\theta\theta})\right]+\delta_{\alpha\beta}\frac{9K}{2}\left[\nu D_{zz}+\frac{1}{2}(D_{rr}+D_{\theta\theta})\right], \quad (2.1)$$

where (r, θ, z) are the cylindrical polar coordinates, $\boldsymbol{\sigma}$ is the Cauchy stress, the superposed ∇ denotes the Jaumann or co-rotational rate (Prager, 1961), and $\mathbf{D}$ is the rate of deformation tensor. As discussed by Rudnicki (1977), E is the instantaneous tangent modulus which is the slope of the axial stress-strain curve at fixed confining stress; therefore, E decreases with deformation, equals zero at peak applied stress, and becomes negative for post-peak regime. The axial straining is inhibited by the lateral stress rate by a factor of r^*. The effective Poisson's ratio ν is the slope of the lateral strain versus axial strain curve at constant lateral confining stress. The incremental transverse and longitudinal shear moduli, and the in-plane bulk modulus is denoted by G_t, G_1, and K respectively. For further details of (2.1), such as the normality limit ($r^*=2\nu$), interpretations of r^* and ν in terms of Rudnicki-Rice (1975) model, etc., one should refer to Rudnicki (1977) and Chau (1992).

For antisymmetric deformations, velocity components, v_r, v_θ, v_z, are, in general, functions of (r, z, θ); and the rate of deformation tensor becomes

$$D_{zz}=\frac{\partial v_z}{\partial z},\quad D_{rr}=\frac{\partial v_r}{\partial r},\quad D_{\theta\theta}=\frac{v_r}{r}+\frac{1}{r}\frac{\partial v_\theta}{\partial\theta},$$

$$D_{r\theta}=\frac{1}{2}\left(\frac{\partial v_\theta}{\partial r}+\frac{1}{r}\frac{\partial v_r}{\partial\theta}-\frac{v_\theta}{r}\right),$$

$$D_{\theta z}=\frac{1}{2}\left(\frac{1}{r}\frac{\partial v_z}{\partial\theta}+\frac{\partial v_\theta}{\partial z}\right),\quad D_{rz}=\frac{1}{2}\left(\frac{\partial v_r}{\partial z}+\frac{\partial v_z}{\partial r}\right). \quad (2.2)$$

In addition, using relations between the material time rate and the Jaumann rate of the Cauchy stress ((9) of Chau, 1992) and between the nominal and the Cauchy stress rates ((11) of Chau, 1992), the following nominal stress rate components are obtained:

$$\dot{t}_{zr}=\dot{\sigma}_{zr}-\sigma_{rr}\frac{\partial v_z}{\partial r},\quad \dot{t}_{rz}=\dot{\sigma}_{rz}-\sigma_{zz}\frac{\partial v_r}{\partial z},\quad \dot{t}_{\theta r}=\dot{\sigma}_{\theta r}-\sigma_{rr}\frac{\partial v_\theta}{\partial r},$$

$$\dot{t}_{z\theta}=\dot{\sigma}_{z\theta}-\sigma_{rr}\frac{1}{r}\frac{\partial v_z}{\partial\theta},\quad \dot{t}_{\theta z}=\dot{\sigma}_{\theta z}-\sigma_{zz}\frac{\partial v_\theta}{\partial z},$$

$$\dot{t}_{r\theta}=\dot{\sigma}_{r\theta}-\sigma_{rr}\left(\frac{1}{r}\frac{\partial v_r}{\partial\theta}-\frac{v_\theta}{r}\right),\quad \dot{t}_{zz}=\dot{\sigma}_{zz}+\sigma_{zz}\frac{1}{r}\left[\frac{\partial(rv_z)}{\partial r}+\frac{\partial v_\theta}{\partial\theta}\right],$$

$$\dot{t}_{\theta\theta}=\dot{\sigma}_{\theta\theta}+\sigma_{rr}\left(\frac{\partial v_r}{\partial r}+\frac{\partial v_z}{\partial z}\right),\quad \dot{t}_{rr}=\dot{\sigma}_{rr}+\sigma_{rr}\left(\frac{\partial v_z}{\partial z}+\frac{v_r}{r}+\frac{1}{r}\frac{\partial v_\theta}{\partial\theta}\right) \quad (2.3)$$

and we have assumed an initial axisymmetric stress state (that is, $\sigma_{rr}=\sigma_{\theta\theta}$) in obtaining (2.3).

3 Governing Equations

Following Chau (1992), we choose a cylindrical polar coordinate system (r, θ, z) such that the origin rests on the bottom of the cylinder and the z-axis coincides with the axis of symmetry. The ends $(z=0, L)$ are loaded by a prescribed velocity in the z-direction in such a way that shear traction vanishes; and a constant lateral stress is applied in the r-direction with zero shear traction on the curved boundary $r=a$. The circular cylinder deforms homogeneously up to the current state and a further homogeneous deformation is always a possible solution for the next increment of deformation; bifurcation occurs if there exists an alternative solution for the next increment of deformation.

The boundary conditions governing the difference in incremental solutions are then

$$v_z^*=0,\quad \dot{t}_{zr}^*=0,\quad \dot{t}_{z\theta}^*=0,\quad \text{on } z=0, L, \quad (3.1)$$

$$\dot{t}_{rr}^*=0,\quad \dot{t}_{rz}^*=0,\quad \dot{t}_{r\theta}^*=0,\quad \text{on } r=a, \quad (3.2)$$

where the superscript * denotes the difference between the bifurcation and the homogeneous solution. Note that under axisymmetric deformations $\dot{t}_{z\theta}^*$ and $\dot{t}_{r\theta}^*$ are identically zero; and, for this special case, (14) and (15) of Chau (1992) are recovered. Continued equilibrium of both incremental solutions, $\nabla\cdot\dot{\mathbf{t}}=0$, can be written in terms of the Cauchy stress rate as follows:

$$\frac{\partial\dot{\sigma}_{rr}^*}{\partial r}+\frac{\partial\dot{\sigma}_{zr}^*}{\partial z}+\frac{1}{r}\frac{\partial\dot{\sigma}_{r\theta}^*}{\partial\theta}+\frac{\dot{\sigma}_{rr}^*-\dot{\sigma}_{\theta\theta}^*}{r}=0,$$

Downloaded 03 May 2010 to 171.66.16.245. Redistribution subject to ASME license or copyright; see http://www.asme.org/terms/Terms_Use.cfm

$$\frac{1}{r}\frac{\partial}{\partial r}(r\dot{\sigma}^*_{rz})+\frac{\partial \dot{\sigma}^*_{zz}}{\partial r}+\frac{1}{r}\frac{\partial \dot{\sigma}^*_{z\theta}}{\partial \theta}=0,$$

$$\frac{1}{r}\frac{\partial \dot{\sigma}^*_{\theta\theta}}{\partial \theta}+\frac{\partial \dot{\sigma}^*_{r\theta}}{\partial r}+\frac{\partial \dot{\sigma}^*_{z\theta}}{\partial z}+2\frac{\dot{\sigma}^*_{r\theta}}{r}=0, \tag{3.3}$$

and, again, we have used the condition $\sigma_{rr}=\sigma_{\theta\theta}$ at the homogeneous axisymmetric state. For axisymmetric deformations ($\dot{\sigma}^*_{r\theta}=\dot{\sigma}^*_{z\theta}=0$ and $\dot{\boldsymbol{\sigma}}^*$ is independent of θ), (16) of Chau (1992) is recovered as a special case. Substitution of (2.1) and (2.2) into (3.3), the equilibrium equations, in terms of $\mathbf{v}$, become

$$\left(G_t+\frac{9K}{4}\right)\frac{\partial e}{\partial r}+2G_t\frac{1}{r}\frac{\partial \Omega_{r\theta}}{\partial \theta}+G_1(1+s)\frac{\partial^2 v_r}{\partial z^2}+\left[G_1(1-s)+\frac{9K\nu}{2}-\left(G_t+\frac{9K}{4}\right)\right]\frac{\partial^2 v_z}{\partial r\partial z}=0,$$

$$\left(G_t+\frac{9K}{4}\right)\frac{1}{r}\frac{\partial e}{\partial \theta}+2G_t\frac{\partial \Omega_{\theta r}}{\partial r}+G_1(1+s)\frac{\partial^2 v_\theta}{\partial z^2}+\left[G_1(1-s)+\frac{9K\nu}{2}-\left(G_t+\frac{9K}{4}\right)\right]\frac{1}{r}\frac{\partial^2 v_z}{\partial \theta\partial z}=0,$$

$$\left(\frac{9Kr^*}{4}+2G_1\right)\frac{\partial e}{\partial z}+\left[E-2G_1-\frac{9Kr^*}{4}(1-2\nu)\right]\frac{\partial^2 v_z}{\partial z^2}+2G_1(1-s)\left[\frac{1}{r}\frac{\partial \Omega_{z\theta}}{\partial \theta}+\frac{1}{r}\frac{\partial}{\partial r}(r\Omega_{zr})\right]=0, \tag{3.4}$$

where

$$s=(\sigma_{zz}-\sigma_{rr})/2G_1,\quad e=\frac{1}{r}\frac{\partial (rv_r)}{\partial r}+\frac{1}{r}\frac{\partial v_\theta}{\partial \theta}+\frac{\partial v_z}{\partial z}, \tag{3.5}$$

and $\boldsymbol{\Omega}=(\mathbf{L}-\mathbf{L}^T)/2$ is the anti-symmetric part of the velocity gradient tensor. Equation (3.4) is more convenient than (3.3) to work with if the method of velocity potentials is employed instead of the method of stress rate potentials. Because of the intimate resemblance between the characteristics equation for the normal to the shear band and the equilibrium equations for stress or velocity potentials (for example, see Needleman, 1979; Chau and Rudnicki, 1990; Chau, 1992), the localization analysis will be summarized in the next section before the method of solution is discussed. In particular, the result of the shear band analysis should provide a check for the validity of the method of solution for the equilibrium Eqs. (3.4); and it will be shown that the type of the differential equations for the velocity potentials, to be introduced, depends on how many real roots exist for the shear band mode.

4 Localization and Classification of Regimes

The condition of the onset of strain localization in a planar narrow band is summarized briefly in this section. For more details about the shear band analysis, one should refer to Rudnicki (1977) and Chau (1992). In general, two conditions have to be satisfied: the geometrical compatibility, which requires the velocity increment to be continuous but permits a jump in the velocity gradient across the band; and the incremental equilibrium across the shear band. In tensor notation, these conditions are (Hill, 1961; Rice, 1976)

$$(\nabla \mathbf{v}^*)^T=\mathbf{c}\,\mathbf{g},\quad \mathbf{g}\cdot\dot{\mathbf{t}}^*=\mathbf{0}, \tag{4.1}$$

where $\mathbf{c}$ is the vector of the jump of the velocity gradient and $\mathbf{g}$ is the normal to the incipient band. Substitution of (2.1), (2.2), and (2.3) into (4.1) yields three simultaneous equations for c_r, c_θ, and c_z. A nontrivial solution for the velocity gradient jumps requires the determinant of the coefficients for c_r, c_θ, and c_z to vanish. This condition gives the following characteristic equation for $\mathbf{g}$:

$$(g^2+\nu_3^2 g_z^2)(A g^2+B g^2 g_z^2+C g_z^4)=0 \tag{4.2}$$

where $g^2=g_\theta^2+g_r^2$ and A, B, and C are defined as

$$A=(1-s)(4G_t+9K),$$
$$B=E(4G_t+9K)/G_1+9K[2r^*\nu G_t/G_1-(2\nu+r^*)+s(r^*-2\nu)]$$
$$C=2(1+s)(9Kr^*\nu+2E), \tag{4.3}$$

and ν_3 is defined as

$$\nu_3=[G_1(1+s)/G_t]^{1/2}. \tag{4.4}$$

As expected, g_r and g_θ only appear in the combination g and is consistent with the result by Rudnicki (1977). Note that A, B, and C have been obtained previously by Chau (1992). Therefore, the second bracket term in (4.2) is same as (25) of Chau (1992) if g is replaced by g_r.

Shear band bifurcation is possible only if a real value for the ratio g/g_z exists. Similar to the discussion by Hill and Hutchinson (1975) and by Hill (1979), the parameter regimes can be defined as elliptic, parabolic or hyperbolic if there are zero, two or four real roots for (4.2), respectively. More specifically, if $(g^2+\nu_3^2 g_z^2)\neq 0$, the regimes for different behavior have been discussed in details by Chau (1992), and will not be repeated here. Note, however, that except for the compressive parabolic regime ($s<-1$) ν_3^2 is always positive; that is, there is no real root of g/g_z for $(g^2+\nu_3^2 g_z^2)=0$.

5 Method of Solution

In this section, we extend the method of the displacement potentials (Hu, 1954; Pan and Chou, 1976) to the bifurcation analysis of solids characterized by (2.1). Since the procedure is similar to the works by Hu (1954) and by Pan and Chou (1976), the details are omitted and only the results are summarized. In particular, two velocity potentials can be introduced such that

$$v_r=\frac{\partial^2\Phi}{\partial r\partial z}+\frac{1}{r}\frac{\partial \Psi}{\partial \theta},\quad v_\theta=\frac{1}{r}\frac{\partial^2\Phi}{\partial\theta\partial z}-\frac{\partial\Psi}{\partial r},$$
$$v_z=-\left[\frac{9K/4+G_t}{9K\nu/2+G_1(1-s)}\right]\nabla_1\Phi-\left[\frac{G_1(1+s)}{9K\nu/2+G_1(1-s)}\right]\frac{\partial^2\Phi}{\partial z^2}, \tag{5.1}$$

where

$$\nabla_1=\frac{1}{r}\frac{\partial}{\partial r}\left(r\frac{\partial}{\partial r}\right)+\frac{1}{r^2}\frac{\partial^2}{\partial\theta^2}. \tag{5.2}$$

Substitution of (5.1) into (3.4), the following governing equation for Φ and Ψ are obtained:

$$\left(\nabla_1-\nu_1^2\frac{\partial^2}{\partial z^2}\right)\left(\nabla_1-\nu_2^2\frac{\partial^2}{\partial z^2}\right)\Phi=0,\quad \left(\nabla_1+\nu_3^2\frac{\partial^2}{\partial z^2}\right)\Psi=0, \tag{5.3}$$

and ν_1 and ν_2 satisfy

$$A\nu_\alpha^4+B\nu_\alpha^2+C=0,\quad (\alpha=1,\,2), \tag{5.4}$$

where A, B, and C have been defined in (4.3) and ν_3 is given in (4.4). If $\Psi=0$ and Φ is independent of θ, (5.3) reduces to the equilibrium equation for axisymmetric deformation (Chau, 1992). As expected, there exists a close resemblance between (5.4) and the characteristic equation for shear band (4.2). For $\nu_3^2>0$, the real root of ν_α implies that the bifurcation of the shear band mode is possible because ν_α satisfies the same characteristic equation, (4.2), for g/g_z. Therefore, if ν_1 and ν_2 are complex and ν_3 is real, the current state is in the elliptic regime; or equivalently, there is no shear band bifurcation for such combination of parameters. However, if ν_1 and ν_2 are real or ν_3 is imaginary, shear band mode occurs prior to the solutions obtained by solving (5.3) with appropriate the boundary conditions.

The Cauchy stress rates can be obtained by substituting (5.1) into (2.1) and the results are

Downloaded 03 May 2010 to 171.66.16.245. Redistribution subject to ASME license or copyright; see http://www.asme.org/terms/Terms_Use.cfm

$$\dot{\sigma}_{rr}=\left\{\left[\frac{9K}{4}-G_t-\frac{(9K/4+G_t)9K\nu/2}{9K\nu/2+G_1(1-s)}\right]\nabla_1 - \frac{9K\nu}{2}\left[\frac{G_1(1+s)}{9K\nu/2+G_1(1-s)}\right]\frac{\partial^2}{\partial z^2}\right\}\frac{\partial\Phi}{\partial z} + 2G_t\left[\frac{\partial^3\Phi}{\partial z\partial r^2}+\frac{\partial}{\partial r}\left(\frac{1}{r}\frac{\partial\Psi}{\partial\theta}\right)\right], \quad (5.5)$$

$$\dot{\sigma}_{\theta\theta}=\left\{\left[\frac{9K}{4}-G_t-\frac{(9K/4+G_t)9K\nu/2}{9K\nu/2+G_1(1-s)}\right]\nabla_1 - \frac{9K\nu}{2}\left[\frac{G_1(1+s)}{9K\nu/2+G_1(1-s)}\right]\frac{\partial^2}{\partial z^2}\right\}\frac{\partial\Phi}{\partial z} - 2G_t\left[\frac{\partial^3\Phi}{\partial z\partial r^2}+\frac{\partial}{\partial r}\left(\frac{1}{r}\frac{\partial\Psi}{\partial\theta}\right)\right], \quad (5.6)$$

$$\dot{\sigma}_{zz}=\left\{\left[\frac{9Kr^*}{4}-\frac{(9K/4+G_t)(E+9Kr^*\nu/2)}{9K\nu/2+G_1(1-s)}\right]\nabla_1 - \left[\frac{G_1(1+s)(E+9Kr^*\nu/2)}{9K\nu/2+G_1(1-s)}\right]\frac{\partial^2}{\partial z^2}\right\}\frac{\partial\Phi}{\partial z} \quad (5.7)$$

$$\dot{\sigma}_{rz}=\left\{-\left[\frac{G_1(1-s)(9K/4+G_t)}{9K\nu/2+G_1(1-s)}\right]\frac{\partial}{\partial r}\nabla_1 + \left[\frac{G_1(1+s)9K\nu/2}{9K\nu/2+G_1(1-s)}\right]\frac{\partial^3}{\partial r\partial z^2}\right\}\Phi + G_1(1+s)\frac{1}{r}\frac{\partial^2\Psi}{\partial\theta\partial z}, \quad (5.8)$$

$$\dot{\sigma}_{z\theta}=\left\{-\left[\frac{G_1(1-s)(9K/4+G_t)}{9K\nu/2+G_1(1-s)}\right]\frac{1}{r}\frac{\partial}{\partial\theta}\nabla_1 + \left[\frac{G_1(1+s)9K\nu/2}{9K\nu/2+G_1(1-s)}\right]\frac{1}{r}\frac{\partial^3}{\partial\theta\partial z^2}\right\}\Phi - G_1(1+s)\frac{\partial^2\Psi}{\partial r\partial z}, \quad (5.9)$$

$$\dot{\sigma}_{r\theta}=2G_t\frac{\partial}{\partial r}\left(\frac{1}{r}\frac{\partial^2\Phi}{\partial\theta\partial z}\right)+G_t\left(\frac{1}{r}\frac{\partial\Psi}{\partial r}+\frac{1}{r^2}\frac{\partial^2\Psi}{\partial\theta^2}-\frac{\partial^2\Psi}{\partial r^2}\right). \quad (5.10)$$

The method of solution for the equilibrium equations given in this section is independent of the geometry and the boundary conditions of the solids; therefore, it is not restricted to the analysis of a circular cylinder with boundary conditions given by (3.1) and (3.2).

6 Diffuse Bifurcation Modes

For a finite cylinder of radius a and length L, the ends ($z=0$, L) are loaded by a prescribed velocity in the z-direction in such a way that shear traction vanishes. This boundary condition, described mathematically by (3.1), is satisfied exactly if the following diffuse modes are considered

$$\Phi=C_1\psi_1(r)\sin(\eta z)\cos(n\theta),\qquad \Psi=C_2\psi_2(r)\cos(\eta z)\sin(n\theta), \quad (6.1)$$

where $\eta=m\pi/L$, with m, $n=0, 1, 2, \ldots$, and C_1 and C_2 are constants.

Substitution of (6.1) into (5.3) gives

$$(\nabla_2+\eta^2\nu_1^2)(\nabla_2+\eta^2\nu_2^2)\psi_1=0,\quad (\nabla_2-\eta^2\nu_3^2)\psi_2=0, \quad (6.2)$$

where

$$\nabla_2=\frac{1}{r}\frac{d}{dr}\left(r\frac{d}{dr}\right)-\frac{n^2}{r^2}. \quad (6.3)$$

Note that if we set $n=0$ and $\psi_2=0$ in (6.2), (38) of Chau (1992) is recovered. In addition, we restrict our attention here to flexural modes, that is, (6.1) has to satisfy the following conditions (pp. 292, Love, 1927):

$$\lim_{r\to 0}(v_r\sin\theta+v_\theta\cos\theta)=0 \text{ and } \lim_{r\to 0}v_z=0, \quad (6.4)$$

which imply that the center of the circular cylinder only translates in r-direction along $\theta=0$. The general solutions for ψ_1 and ψ_2 are the Bessel function and the modified Bessel function of order n, respectively. It can be shown that (6.4) is satisfied if we set $n=1$ in (6.1). Thus, with $n=1$, the general solutions for ψ_1 are

$$\psi_1=A_1J_1(\eta\nu_1 r)+A_2J_1(\eta\nu_2 r), \quad (6.5)$$

where J_1 is the Bessel function of first order, and the constants A_1 and A_2 are; in general, complex. Substitution of (6.5) into the first of (6.2) leads to (5.4), that is, ν_α, where $\alpha=1, 2$, also satisfies the characteristic equation for shear band. For ν_3^2 greater than zero, the general solution form for ψ_2 is

$$\psi_2=A_3I_1(\eta\nu_3 r) \quad (6.6)$$

where I_1 is the modified Bessel function of first order and A_3 is a real constant. As expected, substitution of (6.6) into the second of (6.2) gives (4.4) again.

The boundary conditions, (3.2), can be expressed in terms of Φ and Ψ, by using (2.3), (5.1), (5.5), (5.8), and (5.10), as

$$\left(Y_1\nabla_1+Y_1\frac{\partial^2}{\partial z^2}\right)\frac{\partial\Phi}{\partial z}+Y_3\left[\frac{\partial^3\Phi}{\partial z\partial r^2}+\frac{\partial}{\partial r}\left(\frac{1}{r}\frac{\partial\Psi}{\partial\theta}\right)\right]=0,$$
$$\left(Y_4\frac{\partial}{\partial r}\nabla_1+Y_5\frac{\partial^3}{\partial r\partial z^2}\right)\Phi+Y_6\frac{1}{r}\frac{\partial^2\Psi}{\partial\theta\partial z}=0,$$
$$Y_3\frac{\partial}{\partial r}\left(\frac{1}{r}\frac{\partial^2\Phi}{\partial\theta\partial z}\right)+Y_7\left(\frac{1}{r}\frac{\partial\Psi}{\partial r}+\frac{1}{r^2}\frac{\partial^2\Psi}{\partial\theta^2}\right)-Y_8\frac{\partial^2\Psi}{\partial r^2}=0, \quad (6.7)$$

where

$$Y_1=\frac{9K}{4}-G_t+\sigma_{rr}-\frac{(9K/4+G_t)(9K\nu/2+\sigma_{rr})}{9K\nu/2+G_1(1-s)},$$
$$Y_2=-\frac{G_1(1+s)(9K\nu/2+\sigma_{rr})}{9K\nu/2+G_1(1-s)},\quad Y_3=2G_t-\sigma_{rr},$$
$$Y_4=-\frac{G_1(1-s)(9K/4+G_t)}{9K\nu/2+G_1(1-s)},$$
$$Y_5=\frac{G_1(1-s)(9K\nu/2-2G_1s)}{9K\nu/2+G_1(1-s)}-\sigma_{rr},$$
$$Y_6=G_1(1-s)-\sigma_{rr},\quad Y_7=G_t-\sigma_{rr},\quad Y_8=G_t. \quad (6.8)$$

Since the calculation for the eigenvalue equations is similar to that for the axisymmetric diffuse modes considered by Chau (1992), only the results are summarized briefly. Furthermore, both the long wavelength buckling mode and the short wavelength surface rumpling mode are considered as special cases.

6.1 Elliptic Regime. As mentioned by Chau (1992), the elliptic regime can further be subdivided into the ellipic complex (EC) subregime, where the roots for (5.4) are complex conjugates, and the elliptic imaginary (EI) subregime, where the roots for (5.4) are pure imaginary. In the elliptic complex subregime, the solution form for (6.2) are (with $n=1$)

$$\psi_1=A_1J_1(\eta\rho r)+\overline{A}_1J_1(\eta\bar{\rho}r),\quad \psi_2=A_3I_1(\eta\nu_3 r), \quad (6.9)$$

where $\overline{A}_1$ denotes the complex conjugate of A_1. The complex conjugate pairs of ν_α are $\rho=p+iq$ and $\bar{\rho}=p-iq$; p and q are defined as

$$p^2-q^2=-B/2A,\quad p^2+q^2=(C/A)^{1/2}, \quad (6.10)$$

where A, B, and C are given in (4.3). The eigenvalue equation, obtained by satisfying (6.7), is

$$W_1\,\mathrm{Im}[\overline{Y}(\rho)Z(\rho)]+W_2\,\mathrm{Im}[\overline{Z}(\rho)X(\rho)]+W_3\,\mathrm{Im}[\overline{X}(\rho)Y(\rho)]=0, \quad (6.11)$$

where Im[...] is the imaginary part of [...]. The definitions for W_1, W_2, and W_3 are as follows:

$$W_1=-4\nu_3^2Y_3\frac{I_2(\nu_3\gamma)}{(\nu_3\gamma)},\quad W_2=\nu_3Y_6\frac{I_1(\nu_3\gamma)}{(\nu_3\gamma)}$$

Downloaded 03 May 2010 to 171.66.16.245. Redistribution subject to ASME license or copyright; see http://www.asme.org/terms/Terms_Use.cfm

$$W_3=\frac{\nu_3^2}{4}\left\{\frac{2Y_7}{\nu_3\gamma}\left[I_0(\nu_3\gamma)+I_2(\nu_3\gamma)-2\frac{I_1(\nu_3\gamma)}{(\nu_3\gamma)}\right]\right.$$
$$\left.-Y_8[3I_1(\nu_3\gamma)+I_3(\nu_3\gamma)]\right\} \quad (6.12)$$

with $\gamma=\eta a$; and the complex functions $X(\xi)$, $Y(\xi)$, and $Z(\xi)$ are defined as:

$$X(\xi)=[(4Y_1+3Y_3)\xi^2+4Y_2]J_1(\xi\gamma)-\xi^2Y_3J_3(\xi\gamma),$$
$$Y(\xi)=\frac{\xi}{2}(\xi^2Y_4+Y_5)[J_0(\xi\gamma)-J_2(\xi\gamma)],$$
$$Z(\xi)=\xi^2Y_3\frac{J_2(\xi\gamma)}{(\xi\gamma)}, \quad (6.13)$$

where Y_1, Y_2, Y_3, Y_4, and Y_5 are given in (6.8).

For the elliptic imaginary subregime, the roots of ν_α are $\pm ip$ and $\pm iq$ and the solution form for (6.2) are

$$\psi_1=A_1I_1(\eta pr)+A_2I_1(\eta qr),\quad \psi_2=A_3I_1(\eta\nu_3 r), \quad (6.14)$$

where p and q are defined as

$$p^2-q^2=(B^2-4AC)^{1/2}/A,\quad p^2+q^2=B/A. \quad (6.15)$$

The parameters A, B, and C are, again, given in (4.3). The eigenvalue equation for the EI subregime is

$$W_1[Q(p)R(q)-Q(q)R(p)]+W_2[P(q)R(p)-P(p)R(q)]$$
$$+W_3[P(p)Q(q)-P(q)Q(p)]=0, \quad (6.16)$$

where W_1, W_2, and W_3 have been defined in (6.12); and $P(\xi)$, $Q(\xi)$, and $R(\xi)$ are

$$P(\xi)=[(4Y_1+3Y_3)\xi^2-4Y_2]I_1(\xi\gamma)+\xi^2Y_3I_3(\xi\gamma),$$
$$Q(\xi)=\frac{\xi}{2}(Y_4\xi^2-Y_5)[I_0(\xi\gamma)+I_2(\xi\gamma)],$$
$$R(\xi)=\xi^2Y_3\frac{I_2(\xi\gamma)}{(\xi\gamma)}. \quad (6.17)$$

The long wavelength limit ($\gamma\to 0$) and the short wavelength limit ($\gamma\to\infty$) of the eigenvalues of both the elliptic complex and the elliptic imaginary subregimes are considered here. For small argument, both the Bessel and the modified Bessel functions are expanded in series form (Abramowitz and Stegun, 1964). The fairly lengthy expansion of the eigenvalue Eq. (6.11) for small γ gives the antisymmetric long wavelength limit for the EC subregime:

$$AL_1+\frac{\gamma^2}{24}L_2+0(\gamma^4)=0, \quad (6.18)$$

where

$$L_1=\nu_3^2Y_3^2Y_5+4Y_2Y_3Y_6$$
$$+\nu_3^2(Y_7-3Y_8)[Y_5(4Y_1+3Y_3)-4Y_2Y_4], \quad (6.19)$$

$$L_2=4Y_3Y_6[C(Y_1+Y_3)+2Y_2B+3\nu_3^2AY_2]$$
$$+\nu_3^2Y_3^2[7Y_4C+2Y_5B+2\nu_3^2Y_5A]$$
$$+\nu_3^2\{2\nu_3^2A(Y_7-5Y_8)[Y_5(4Y_1+3Y_3)-4Y_2Y_4]$$
$$+(Y_7-3Y_8)(Y_4C(24Y_1+17Y_3)$$
$$+2B[Y_5(6Y_1+5Y_3)-18Y_2Y_4]+24Y_2Y_5A)\}. \quad (6.20)$$

This complicated form of (6.18) can be simplified considerably by setting $\sigma_{rr}=0$ in (6.19) and (6.20). In particular, in this case the only root for $L_1=0$ in the elliptic regime is $s=0$, indicating that σ_{zz} is of the order γ^2. Using this information and reconsidering L_1 and L_2 for small γ, the rather delicate and lengthy simplification gives

$$\sigma_{zz}=-\frac{1}{4}E\left(\frac{m\pi a}{L}\right)^2+0(\gamma^4). \quad (6.21)$$

Note that the first term on the right side of (6.21) is independent of ν, r^*, K, G_1, and G_t; as expected, this term corresponds to the Euler's buckling formula if $m=1$ (pp. 49, Timoshenko and Gere, 1961). This result shows that Euler's buckling formula is indifferent to the details of the constitutive model used.

When $\sigma_{rr}\neq 0$, the solutions for (6.18) is rather complicated. In particular, as observed in the analysis by Chau and Rudnicki (1990) for plane-strain deformation, there exists an antisymmetric long wavelength bifurcation that is independent of the geometric term γ. Due to the complexity of L_1, we are not able to find an explicit expression for this finite solution. It is, however, not difficult to show that this finite solution is independent of the instantaneous tangent modulus E. Furthermore, for the special case that $K\to\infty$, setting $L_1=0$ yields the following finite solution for σ_{zz} in the elliptic regime:

$$\sigma_{zz}/G_1=1\pm[1+2(\sigma_{rr}/G_1)-(\sigma_{rr}/G_1)^2]^{1/2} \quad (6.22)$$

where $1-2^{1/2}\le\sigma_{rr}/G_1\le 1+2^{1/2}$ for a real solution. This finite solution for antisymmetric long wavelength limit has been obtained previously for rectangular specimens under plane-strain deformation (Chau and Rudnicki, 1990). In particular, if σ_{zz} and σ_{rr} are replaced by σ_{11} and σ_{22} respectively, (5.24) of Chau and Rudnicki (1990) is recovered. The reason for this coincidence is that if the cylinder is incompressible in the r-θ plane ($K\to\infty$), any rectangular section formed by cutting the cylinder through the axis can be viewed as a specimen under plane strain deformation. If the configuration of testing is such that the confining stress are of the "follower type," which acts always normal to the deforming boundary, σ_{rr} should be set to zero in (6.8) (except for σ_{rr} in s). In this case, the antisymmetric long wavelength solution is given by (6.21) if σ_{zz} is replaced by $\sigma_{zz}-\sigma_{rr}$.

A similar expansion for (6.16) gives (6.18) again; therefore, the long wavelength buckling mode continues in the EI subregime.

To consider the short wavelength limit ($\gamma\to\infty$), the asymptotic forms for J_n and I_n (Abramowitz and Stegun, 1964) are used; and the short wavelength limit of (6.11) becomes

$$(AC)^{1/2}[Y_5(Y_1+Y_3)-Y_2Y_4]+Y_2Y_5A$$
$$+Y_4[C(Y_1+Y_3)-Y_2B]=0. \quad (6.23)$$

We are not able to show analytically that (6.23) is equivalent to the short wavelength limit for the axisymmetric geometric diffuse modes obtained by Chau (1992). However, the numerical results for (6.23) and (46) of Chau (1992) are the same for all the parameters that we have tried; therefore, we suspect that these two short wavelength limits of the eigenvalue equations for the axisymmetric and the antisymmetric modes are indeed the same. For an incompressible solid ($2\nu=1$ and $K\to\infty$) obeying normality ($r^*=2\nu$) subjected to zero σ_{rr}, (6.23) can be simplified to

$$\frac{\sigma_{zz}}{(E+G_t)}=1+\frac{\sigma_{zz}}{(E+G_t)}\left[\frac{2G_1-\sigma_{zz}}{2G_1+\sigma_{zz}}\right]^{1/2}. \quad (6.24)$$

This short wavelength eigenvalue equation has been obtained previously by Chau (1992) for the axisymmetric diffuse mode bifurcations. As mentioned by Chau (1992), (6.24) also corresponds to the bifurcation stress for an incompressible half-space satisfying normality (Biot, 1965; Bassani et al., 1980). The same form of this bifurcation condition was also obtained by Hill and Hutchinson (1975) and by Young (1976) for the short wavelength diffuse mode under plane-strain conditions. Similarly, appropriate specializations of the short wavelength diffuse mode by Needleman (1979) and by Chau and Rudnicki (1990) lead again to the form of (6.24).

The short wavelength limit of (6.16) also leads to (6.23) for the EI subregime; hence, the short wavelength surface rumpling modes continue across the EI/EC boundary.

6.2 Parabolic Regime. In the parabolic regime, the general solution for (6.2) becomes

Downloaded 03 May 2010 to 171.66.16.245. Redistribution subject to ASME license or copyright; see http://www.asme.org/terms/Terms_Use.cfm

$$\psi_1 = A_1 J_1(\eta p r) + A_2 I_1(\eta q r), \tag{6.25}$$

and

$$\psi_2 = A_3 I_1(\eta \nu_3 r) \quad \text{for } s>1,$$
$$= A_3 J_1(\eta \nu_3 r) \quad \text{for } s<-1, \tag{6.26}$$

where ν_3^2 is defined by (4.4) for $s>1$ and equals to $G_1|1+s|/G_t$ for $s<-1$. The roots for (5.4) are $\nu_1 = \pm p$ and $\nu_2 = \pm iq$, where p and q are related to A, B, and C by

$$p^2+q^2 = (B^2-4AC)^{1/2}/|A|, \quad p^2-q^2 = -B/A. \tag{6.27}$$

Substitution of (6.1), (6.25), and (6.26) into (6.7) leads to

$$W_1[Y(p)R(q)-Q(q)Z(p)] + W_2[P(q)Z(p) - X(p)R(q)] + W_3[X(p)Q(q)-P(q)Y(p)] = 0, \tag{6.28}$$

for $s>1$. For $s<-1$, the eigenvalue equation is given by (6.28) if W_1, W_2, and W_3 are replaced by

$$W_4 = 4\nu_3^2 Y_3 \frac{J_2(\nu_3\gamma)}{(\nu_3\gamma)}, \quad W_5 = \nu_3 Y_6 \frac{J_1(\nu_3\gamma)}{(\nu_3\gamma)},$$

$$W_6 = \frac{\nu_3^2}{4}\left\{\frac{2Y_7}{\nu_3\gamma}\left[J_0(\nu_3\gamma) - J_2(\nu_3\gamma) - 2\frac{J_1(\nu_3\gamma)}{(\nu_3\gamma)}\right] + Y_8[3J_1(\nu_3\gamma) - J_3(\nu_3\gamma)]\right\}, \tag{6.29}$$

respectively.

The short wavelength limit ($\gamma \to \infty$) of (6.28) yields

$$\tan(\gamma p) = [g_1(p,q)+g_2(p,q)]/[g_1(p,q)-g_2(p,q)], \tag{6.30}$$

where $g_1(p, q)$ and $g_2(p, q)$ are polynominals of p and q. A similar form of the short wavelength limit for the parabolic regime has been obtained previously for the axisymmetric diffuse mode by Chau (1992). Consequently, the argument by Chau (1992) shows that there is an infinite sequence of eigenvalues available in the vicinities of both the tensile and the compressive E/P boundaries for some sufficiently large m (since $\gamma = m\pi a/L$). Therefore, both the shear band modes and the short wavelength diffuse modes are available simultaneously in the parabolic regime.

6.3 Hyperbolic Regime. The roots for (5.4) are $\nu_1 = \pm p$ and $\nu_2 = \pm q$ in the hyperbolic regime. The solutions for ψ_1 and ψ_2 are given by

$$\psi_1 = A_1 J_1(\eta p r) + A_2 J_1(\eta q r), \quad \psi_2 = A_3 I_1(\eta \nu_3 r), \tag{6.31}$$

where p and q satisfy the following relation:

$$p^2+q^2 = -B/A, \quad p^2-q^2 = (B^2-4AC)^{1/2}/A. \tag{6.32}$$

The eigenvalue equation for the hyperbolic regime is

$$W_1[Y(p)Z(q)-Y(q)Z(p)] + W_2[X(q)Z(p)-X(p)Z(q)] + W_3[X(p)Y(q)-X(q)Y(p)] = 0, \tag{6.33}$$

again W_1, W_2, W_3, $X(\xi)$, $Y(\xi)$, and $Z(\xi)$ are defined previously in (6.12) and (6.13).

The expansion of (6.33) for small γ, corresponding to the long wavelength limit, again leads to (6.18); therefore, the antisymmetric long wavelength limit also continues across the elliptic-hyperbolic boundary. The short wavelength limit ($\gamma \to \infty$) of (6.33) is found in the form:

$$\tan(\gamma p) = [f_2(p,q) + f_1(p,q)\tan(\gamma q)]/[f_1(p,q) - f_2(p,q)\tan(\gamma q)], \tag{6.34}$$

where $f_1(p, q)$ and $f_2(p, q)$ are polynomials of p and q. The short wavelength limit (6.34) is, again, of the same form as the short wavelength limit for the axisymmetric diffuse modes in the hyperbolic regime (Chau, 1992). The same argument discussed by Chau (1992) shows that bifurcation into some sufficiently short wavelength modes is possible as soon as the hyperbolic regime is encountered.

7 Numerical Results for Elliptic Diffuse Mode

As remarked by Chau (1992), the diffuse bifurcation modes available in the hyperbolic and the parabolic regimes are of less interest because the shear band modes are expected to be the dominant modes of failure. But the diffuse modes in elliptic regimes may be crucial to the subsequent deformation pattern of the localized deformations (Chau, 1992); therefore, only the numerical results for the eigenvalue equations of the elliptic complex regime (EC) is considered in this section. A numerical search used by Chau (1992) was employed to calculate the eigenvalue surfaces for (6.11). Eigenvalue surfaces for (6.11) given in Fig. 1 are evaluated by holding all parameters, except one, constant. In general, it is, of course, not the case since the material parameters in (2.1) may evolute in a complex way under external loads.

The eigenvalue surfaces, obtained by combining the axisymmetric modes (Fig. 3 of Chau, 1992) and the antisymmetric modes (solutions for (6.11)), are given in Fig. 1. Figure 1(a) shows typical eigenvalue surfaces with changing E/G_1 for a solid that does not obey normality ($\mu \neq \beta$ or $r^* \neq 2\nu$); while Fig. 1(b) shows similar plots for solid obeying normality ($\mu = \beta$ or $r^* = 2\nu$). The effects of transverse isotropy and compressive lateral stress on the eigenvalue surfaces are illustrated in Figs. 1(c) and 1(d), respectively. Only the lowest possible bifurcation stress for any fixed value of γ is shown. The dotted portions of the eigenvalue surfaces are obtained from the antisymmetric modes; while the solid portions correspond to the axisymmetric modes by Chau (1992). Similar to the numerical plots by Hill and Hutchinson (1975) and Young (1976) for plane-strain analysis, the lowest possible bifurcations are of axisymmetric types under tension and antisymmetric types under compression provided that $\sigma_{rr} = 0$ (see Fig. 1(a) to 1(c)). This observation is consistent with the antisymmetric long wavelength limit, (6.21), because the negative sign on the right of (6.21) suggests that the antisymmetric diffuse mode for vanishing small γ is not available under tension ($\sigma_{zz} > 0$) but readily available under compression ($\sigma_{zz} < 0$). The festooned-shaped curve for $\sigma_{zz} > 0$ in Fig. 1(a) alternates with the axisymmetric and the antisymmetric modes as γ increases. The segments of the axisymmetric modes are, however, suppressed by the increase of E/G_1. Similar results are also observed in Fig. 1(b). Under compression ($\sigma_{zz} < 0$), the eigenvalue surfaces, shown in Fig. 1(a-b), simply consist of two segments, with the first and the second ones corresponding to the antisymmetric and the axisymmetric modes, respectively. However, Fig. 1(c) shows that if G_t/G_1 decreases, segments of antisymmetric modes begin to appear in eigenvalue surfaces under compression as γ increases. For $\sigma_{rr} \neq 0$, Fig. 1(d) shows that the first possible bifurcation for $s>0$ is of antisymmetric type; and the first possible bifurcation is no longer occurring at $\gamma = 0$ for $s<0$ but at some finite γ.

Figure 1 also suggests that there exists a transition value γ_0, which corresponds to the first intersecting point between the antisymmetric and the axisymmetric eigenvalue surfaces as γ increases from zero, such that for specimen ratio $\pi a/L$ greater than γ_0 the axisymmetric bulging becomes the first possible bifurcation otherwise the antisymmetric buckling will appear first under compression ($s<0$). Similar transition value of γ also exists under tension; however, it is of less practical interest. The experimental observations summarized by Beatty (1977) for rubber bodies under compression seem to support the existence of such a transition value of γ. More generally, (6.11) and (41) of Chau (1992) should be solved simultaneously for s and γ for any known combination of material parameters in order to obtain such transition slenderness ratio a/L that separates buckling from bulging. Figure 1(a)-(d) suggests that if $\pi a/L$ is smaller than 1.8 to 2.3 (approximately), the first possible diffuse mode is the buckling mode under compression. Therefore, for typical dimensions of specimens used in ex-

Downloaded 03 May 2010 to 171.66.16.245. Redistribution subject to ASME license or copyright; see http://www.asme.org/terms/Terms_Use.cfm

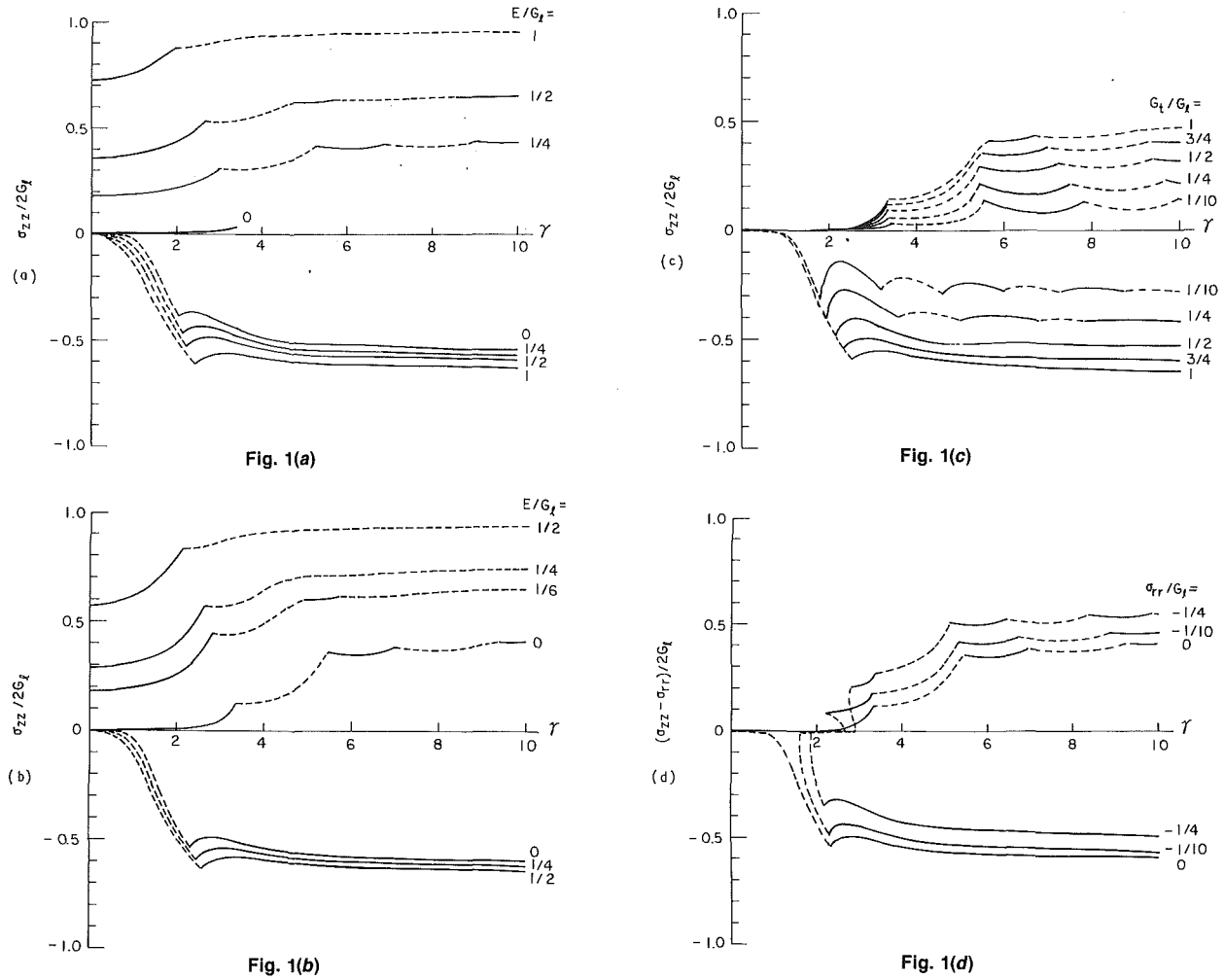


Fig. 1(a) Fig. 1(c) Fig. 1(b) Fig. 1(d)

Fig. 1 The lowest bifurcation stresses by combining the axisymmetric (obtained from Chau, 1992) and the antisymmetric modes in the EC subregime at finite γ ($=m\pi a/L$): (*a*) changing E/G_1 with $\mu=0.6$, $\beta=0.2$, $G_t/G_1=0.75$, $G_1/K=0.2$, and $\sigma_{rr}/G_1=0$; (*b*) changing E/G_1 with $\mu=\beta=0.4$, $G_t/G_1=0.75$, $G_1/K=0.2$, and $\sigma_{rr}/G_1=0$; (*c*) changing G_t/G_1 with $\mu=\beta=0.4$, $E/G_1=0$, $G_1/K=0.2$, and $\sigma_{rr}/G_1=0$; and (*d*) changing σ_{rr}/G_1 with $\mu=\beta=0.4$, $E/G_1=0$, $G_1/K=0.2$, and $G_t/G_1=0.75$. Note that r^* and ν are related to β and μ by (3) of Chau (1992).

periments (a/L ranging from 1/4 to 1/6, Chau, 1992), the first possible bifurcation is the antisymmetric buckling. For nonzero σ_{rr}, Fig. 1(*d*) shows that the earliest possible mode may not correspond to $m=1$; the first bifurcation may become $m=2$ depending on the values of σ_{rr}/G_1 and a/L.

Furthermore, for the short wavelength surface undulation ($\gamma\to\infty$) the numerical results for (6.23), as mentioned previously, have been found identical to the results for the axisymmetric short wavelength limit obtained by Chau (1992); consequently, Figs. 5–7 of Chau (1992) are equally applied to the antisymmetric bifurcations considered here.

8 Discussion

By assuming all parameters, except E/G_1, to vary slowly with s, Chau (1992) discussed the possible bifurcation picture in the (s, E/G_1) space. These bifurcation pictures for axisymmetric modes can be extended to include antisymmetric modes by simply adding (6.18) to Figs. 8–10 of Chau (1992). Besides the addition of (6.18), the discussion for the possible bifurcations is exactly the same as those given by Chau (1992); therefore, the details for the possible bifurcations will not be repeated here.

More specifically, if tensile σ_{rr} is applied ($\sigma_{rr}/G_1<1+2^{1/2}$), as discussed in Section 6, a finite solution of negative s exists for the antisymmetric long wavelength bifurcation. As suggested by (6.22), another solution of (6.18) is also available near the parabolic boundary at $s=1.0$. For compressive $\sigma_{rr}/G_1>1-2^{1/2}$, a finite solution of positive s exists for the antisymmetric long wavelength mode. Another finite solution for (6.18) is also available in the vicinity of the parabolic boundary at $s=1.0$.

Chau (1992) suggested that the diffuse mode bifurcation available in the pre-peak regime of the stress-strain curve may change the subsequent nonuniform deformation and leads, eventually, to the localization of deformation. However, as mentioned earlier, the axisymmetric diffuse mode with finite wave number is no longer the first possible bifurcation for typical specimen size if antisymmetric diffuse mode is allowed. For small σ_{rr}/G_1, the possible localizations that may be triggered by the antisymmetric modes under compression are shown in Fig. 2. If the amplitude of the diffuse modes shown in Fig. 2 is negligible, the bifurcation angle ranges from 45 deg to 56.3 deg for specimen with a/L ranging from 1/4 to 1/6. Although these values are within the ranges of the bifurcation angle for shear band mode predicted by Section 4 of Chau (1992), they are relatively small compared to the experimentally observed fracture angles for various rocks, which range from

Downloaded 03 May 2010 to 171.66.16.245. Redistribution subject to ASME license or copyright; see http://www.asme.org/terms/Terms_Use.cfm

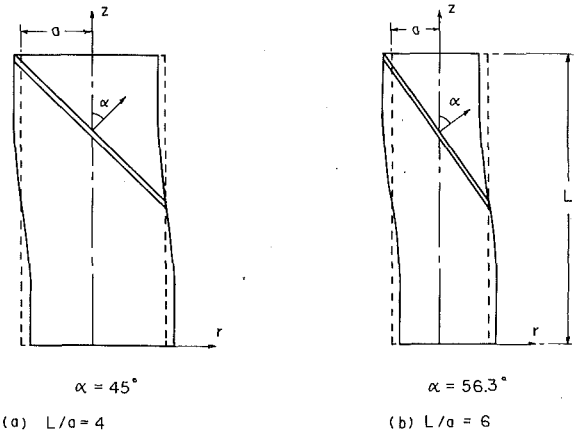


Fig. 2 Sketches illustrate the earliest possible pre-peak antisymmetric diffuse mode under compression. Possible shear band localization triggered by these diffuse modes is also shown. The sketches are for: (*a*) *a*/*L* = 1/4; and (*b*) *a*/*L* = 1/6.

58 deg to 77 deg (Chau, 1992). One possible explanation is that the end surfaces are not perfectly lubricated for most experimental configurations; therefore, frictional shear traction may inhibit the occurrence of the antisymmetric buckling modes shown in Fig. 2. Nevertheless, as suggested by Chau (1992), the nonuniform deformations that occur before the formation of shear band deserve more extensive studies.

9 Conclusion

A bifurcation analysis of the antisymmetric geometric diffuse modes for circular cylinders is given. In particular, both the Euler's buckling formula and the bifurcation stress for the surface rumpling mode are recovered as the long and the short wavelength limits respectively. A finite solution for the antisymmetric long wavelength limit exists if the confining stress is not zero. This finite solution corresponds to the plane-strain result obtained by Chau and Rudnicki (1990) if the in-plane bulk modulus becomes unbounded.

More importantly, the effect of the constitutive parameters on the EC antisymmetric diffuse modes is studied numerically and the results are combined with the axisymmetric results by Chau (1992). The lowest possible bifurcation stresses, including both the axisymmetric and antisymmetric modes, are given in Fig. 1 for various combinations of material parameters. Consequently, a complete picture of all possible geometric diffuse modes before the formation of shear bands is obtained. Furthermore, this combined results provide a transition value of a/L that separates buckling from bulging. More specifically, the first possible bifurcation becomes bulging modes if a/L larger than approximately $2/\pi$ under compression otherwise buckling is always the first bifurcation to occur.

Under compression, numerical results in Fig. 1 suggest that the antisymmetric buckling mode is always the first available bifurcation for typical specimens with a/L ranging from 1/4 to 1/6. It is because both 1/4 and 1/6 are much smaller than the transition value of a/L ($\approx 2/\pi$) obtained in Fig. 1. Therefore, in contrast to the conclusion by Chau (1992), the earliest possible bifurcation mode becomes the antisymmetric buckling mode but not the axisymmetric diffuse mode with finite wave number. The angle of shear band promoted by these buckling modes falls within the range of bifurcation angles predicted by the shear band analysis, but it appears too small compared to the experimental observation of the fracture angles for rocks. However, such antisymmetric buckling mode may be inhibited by the end friction that appears in real experimental testing; and, consequently, it is possible that the first bifurcation is indeed the axisymmetric modes discussed by Chau (1992) under compression.

We have outlined a framework for the antisymmetric bifurcation analysis for compressible pressure-sensitive circular cylinders under compression and tension. However, the possible link between diffuse and localized modes, suggested by Chau (1992), requires further study.

Acknowledgments

The research in this paper was carried out while the author held a post-doctoral fellowship at Northwestern University. The author is grateful to Prof. John Rudnicki who reviewed the first draft and gave suggestions that substantially improve the manuscript. This work was supported by National Science Foundation Grants No. MSM-8612876 and No. MSS-8915607 to Northwestern University.

References

Abramowitz, M., and Stegun, I. A., eds., 1964, *Handbook of Mathematical Functions*, (Appl. Math. Ser. 55) National Bureau of Standards, Washington, DC (reprinted by Dover, 1965).

Bassani, J. L., Durban, D., and Hutchinson, J. W., 1980, "Bifurcations at a Spherical Hole in an Infinite Elastoplastic Medium," *Math. Proc. Camb. Phil. Soc.*, Vol. 87, pp. 339–356.

Beatty, M. F., 1977, "Elastic Stability of Rubber Bodies in Compression," *Finite Elasticity*, R. S. Rivlin, ed., ASME, AMD-Vol. 27, pp. 125–150.

Biot, M. A., 1965, *Mechanics of Incremental Deformations*, John Wiley and Sons, New York, pp. 201–213.

Chau, K. T., 1992, "Non-normality and Bifurcation in a Compressible Pressure-Sensitive Circular Cylinder under Tension and Compression," *Int. J. Solids Struct.*, Vol. 29, pp.801–824.

Chau, K. T., and Rudnicki, J. W., 1990, "Bifurcations of Compressible Pressure-Sensitive Materials in Plane Strain Tension and Compression," *J. Mech. Phys. Solids*, Vol. 38, pp. 875–898.

Cheng, S. Y., Ariaratnam, S. T., and Dubey, R. N., 1971, "Axisymmetric Bifurcation in an Elastic-Plastic Cylinder under Axial Load and Lateral Hydrostatic Pressure," *Quart. Appl. Math.*, Vol. 29, p. 41–51.

Elliott, H. A., 1948, "Three-Dimensional Stress Distributions in Hexagonal Aeolotropic Crystals," *Math. Proc. Camb. Phil. Soc.*, Vol. 44, pp. 522–533.

Hill, R., 1961, "Discontinuity Relations in Mechanics of Solids," *Progress in Solid Mechanics*, I. N. Sneddon and R. Hill, eds., Vol. 2, pp. 246–276.

Hill, R., 1979, "On the Theory of Plane Strain in Finitely Deformed Compressible Materials," *Math. Proc. Camb. Phil. Soc.*, Vol. 86, pp. 161–178.

Hill, R., and Hutchinson, J. W., 1975, "Bifurcation Phenomena in the Plane Tension Test," *J. Mech. Phys. Solids*, Vol. 23, pp. 239–264.

Hu, H.-C., 1954, "On the Three-Dimensional Problems of the Theory of Elasticity of a Transversely Isotropic Body," *Acta Scientia Sinica*, Vol. 2, pp. 145–151.

Hutchinson, J. W., and Miles, J. P., 1974, "Bifurcation Analysis of the Onset of Necking in an Elastic/Plastic Cylinder under Uniaxial Tension," *J. Mech. Phy. Solids*, Vol. 22, pp. 67–71.

Love, A. E. H., 1927, *A Treatise on the Mathematical Theory of Elasticity*, 4th ed., Cambridge University Press (reprinted by Dover, 1944).

Miles, J. P., and Nuwayhid, U. A., 1985, "Bifurcation in Compressible Elastic/Plastic Cylinders under Uniaxial Tension," *Appl. Sci. Res.*, Vol. 42, pp. 33–54.

Needleman, A., 1979, "Non-Normality and Bifurcation in Plane Strain Tension and Compression," *J. Mech. Phys. Solids*, Vol. 27, pp. 231–254.

Pan, Y.-C., and Chou, T.-W., 1976, "Point Force Solution for an Infinite Transversely Isotropic Solid," ASME JOURNAL OF APPLIED MECHANICS, Vol. 43, pp. 608–612.

Prager, W., 1961, *Introduction to the Mechanics of Continua*, Ginn and Company, Boston (reprinted by Dover, 1973).

Rice, J. R., 1976, "The Localization of Plastic Deformation," *Proc. 14th Int. Cong. Theoretical and Appl. Mech.*, Vol. 1, T. W. Koiter, ed., Delft, North-Holland, Amsterdam, pp. 207–220.

Rudnicki, J. W., 1977, "The Effect of Stress-Induced Anisotropy on a Model of Brittle Rock Failure as Localization of Deformation," *Energy Resources and Excavation Technology, Proc. 18th U.S. Symposium on Rock Mechanics*, Keystone, CO, June 22–24, 1977, pp. 3B4-1–3B4-8.

Rudnicki, J. W., and Rice, J. R., 1975, "Conditions for the Localization of Deformation in Pressure-Sensitive Dilatant Materials," *J. Mech. Phys. Solids*, Vol. 23, pp. 371–394.

Sensenig, C. B., 1964, "Instability of Thick Elastic Solids," *Comm. Pure Appl. Math.*, Vol. 17, pp. 451–491.

Timoshenko, S. P., and Gere, J. M., 1961, *Theory of Elastic Stability*, 2nd ed., McGraw-Hill, New York.

Vardoulāski, I., 1983, "Rigid Granular Plasticity Model and Bifurcation in the Triaxial Test," *Acta Mechanica*, Vol. 49, pp. 57–79.

Young, N. J. B., 1976, "Bifurcation Phenomena in the Plane Compression Test," *J. Mech. Phys. Solids*, Vol. 24, pp.77–91.

Downloaded 03 May 2010 to 171.66.16.245. Redistribution subject to ASME license or copyright; see http://www.asme.org/terms/Terms_Use.cfm

Seishi Yamada
Assoc. Professor,
Toyohashi University of Technology,
Toyohashi 441, Japan

J. G. A. Croll
Professor,
Department of Civil and
Environmental Engineering,
University College London,
London WC1E 6BT, U.K.

Buckling and Post-buckling Characteristics of Pressure-Loaded Cylinders

Nonlinear Ritz analysis is used to investigate the elastic buckling behavior of pressure loaded cylinders. Careful analysis of the energy changes during the buckling process allows definition of a reduced stiffness theoretical model. This reduced stiffness model provides a convenient means for estimating lower bounds to the imperfection sensitive elastic buckling behavior.

1 Introduction

In providing structural efficiency in such diverse applications as pressure vessels, subsea and aerospace hulls, pipelines, and many other important components, where loading is of an essentially axisymmetric form, the circular cylinder has long been recognized as providing an almost optimal form. It has also been appreciated for some time that a consequence of this near optimality is that small changes, or imperfections, in the loading, geometry and material can have disproportionately large consequences in reducing the buckling load carrying capacity. That is, the corollary of a shell displaying a "strong optimality" is that it is likely to exhibit severe imperfection sensitivity (Thompson and Hunt, 1973).

For structural components such as cylinders that display these buckling characteristics, the designer is faced with something of a dilemma. To avoid the consequences of uncertainty associated with imperfection sensitivity, it is often recommended that optimal buckling design be avoided. For example, in the design of stiffened cylinders most design procedures recommend that stiffener properties should be chosen so as to avoid simultaneity in the local stiffener or inter stiffener buckling loads and the general orthotropic shell buckling loads. However, in doing so, the designer is denied the chance of taking full advantage of "optimal design" conditions. To be able to take advantage of the possibilities offered by optimization the designer needs analytical tools which, while remaining safe under uncertain conditions, are sufficiently simple that they can be routinely incorporated into the design process.

Classical eigenvalue analysis provides unsafe upper bounds of the buckling of even unstiffened cylinders. The complexities of the nonlinear post-buckling analysis required to account for the effects of even small imperfections have so far not provided sufficiently simple or compact analyses that they can be incorporated into the design process. When imperfections become large, as they so often are in Civil Engineering Structures, the even more formidable analytical difficulties make the likelihood of classical analysis providing a basis for design even more remote. Consequently, many have turned to nonlinear numerical analysis to provide a complete theoretical modelling of buckling response. Like the alternative practice of relying upon physical tests, this approach without considerable additional effort fails to provide an indication of what might happen when one or more of the many design parameters are changed. Furthermore, almost by definition, numerical or physical tests are essentially checks on "what is" rather than "what might be." Just how they can be converted into truly conceptual design tools is only beginning to be addressed.

An alternative approach is that of the reduced stiffness method (Croll, 1975). It is based upon the simple idea that a structures loss of stiffness during post-buckling, and consequently the stiffness that is eroded due to presence of initial imperfections, should be able to be understood by an examination of the stiffness components that provide the initial resistance to buckling in a classical analysis. As has been highlighted in numerous previous publications (see, for example, Croll, 1987), it is the membrane contributions to this initial resistance that are most likely to be lost in the buckling of highly optimized structures, like shells. So that while a shell derives much advantage from the presence of membrane stiffness (or energy) it is its loss during buckling that accounts for the at times highly nonlinear and imperfection sensitive behavior. The reduced stiffness method is based upon a classical analysis from which these at risk membrane stiffness components have been eliminated. By comparing with accumulated physical test data it has been shown that the reduced stiffness method provides realistically safe lower bounds to the scatter of imperfection sensitive elastic buckling loads for a variety of shell form (Zintilis and Croll, 1986) subjected to a range of loadings (Croll and Ellinas, 1983). What has only recently begun to be undertaken is a validation through carefully controlled numerical tests (Yamada and Croll, 1989).

Contributed by the Applied Mechanics Division of THE AMERICAN SOCIETY OF MECHANICAL ENGINEERS for presentation at the First Joint ASCE-EMD, ASME-AMD, SES Meeting, Charlottesville, VA, June 6-9, 1993.

Discussion on this paper should be addressed to the Technical Editor, Professor Lewis T. Wheeler, Department of Mechanical Engineering, University of Houston, Houston, TX 77204-4792, and will be accepted until four months after final publication of the paper itself in the ASME JOURNAL OF APPLIED MECHANICS.

Manuscript received by the ASME Applied Mechanics Division, Oct. 15, 1991; final revision, Apr. 28, 1992. Associate Technical Editor: A. K. Noor.

Paper No. 93-APM-27.

Copyright © 1993 by ASME
Downloaded 03 May 2010 to 171.66.16.245. Redistribution subject to ASME license or copyright; see http://www.asme.org/terms/Terms_Use.cfm

The present work summarizes aspects of a cooperative program of research initiated by the first author's sabbatical year spent in London 1985/1986[1]. It aims to show that controlled numerical studies allow systematic confirmation of the conceptual ideas underpinning the reduced stiffness method. It also demonstrates for cylinders under pressure loading how the use of numerical studies within the interpretive framework of classical buckling analysis, and its extension to the reduced stiffness method, allow a sharpening of our understanding of the buckling process; as a consequence future design methods have the potential for considerable improvement. Although concentrating upon elastic buckling, similar procedures can be employed to extend our understanding of and ability to design for, the effects of elastic-plastic behavior on the buckling of pressure loaded cylinders.

A brief description is first given of the nonlinear modeling used for the present analysis. This is based upon a total potential energy expression, made discrete using a suitably truncated set of harmonic functions, the stationarity of which generates sets of nonlinear equilibrium paths. Of particular concern is the nature of the incremental energy of resistance at various stages along the nonlinear imperfect paths; examination of the energy demonstrates how it approaches an incremental bending energy of resistance in a certain mode at loads which reaches its minimum at levels closely predicted by the reduced stiffness analysis. While the approach to the reduced stiffness behavior occurs for fairly large imperfections for the load cases considered in the present paper, it is suggested that numerical experiments of the type described could be used to study this phenomenon for shell buckling problems in which the loss of stiffness is of even greater design significance. In these cases numerical studies like those reported could be used to calibrate the simpler reduced stiffness predictions of lower bounds to imperfection sensitivity of buckling loads.

2 Theoretical Background

Because it provides a systematic framework for the interpretation of behavior, and also represents a convenient and compact basis for analytical modeling, the principle of stationary total potential energy will be used to formulate the equations of equilibrium.

2.1 Total Potential Energy. For an imperfect thin-walled circular cylinder of longitudinal length L, wall thickness t, and radius R shown in Fig. 1, the change in the total potential energy, consequent upon the application of a radial pressure load of q, may be written as

$$V_T = U_B + U_M + V_Q \tag{1}$$

where the bending and membrane strain energies (U_B, U_M) and the increase in load potential V_Q for a radial pressure of q, are given as

$$U_B = \frac{1}{2}\int_0^{2\pi R}\int_0^L (m_x\kappa_x + m_y\kappa_y + 2m_{xy}\kappa_{xy})\,dxdy \tag{2a}$$

$$U_M = \frac{1}{2}\int_0^{2\pi R}\int_0^L (n_x\epsilon_x + n_y\epsilon_y + 2n_{xy}\epsilon_{xy})\,dxdy \tag{2b}$$

$$V_Q = -\int_0^{2\pi R}\int_0^L \left(qw - \sigma t\frac{\partial u}{\partial x}\right)dxdy \tag{2c}$$

In these expressions, (m_x, m_y, m_{xy}) and (n_x, n_y, n_{xy}) are the total bending and membrane stress resultants, and (κ_x, κ_y, κ_{xy}) and (ϵ_x, ϵ_y, ϵ_{xy}) are the corresponding strains associated with total displacements (u, v, w) from an imperfect but stress-free unloaded state. The axial compressive stress may be written in terms of the external pressure q as

$$\sigma = cqR/t > 0 \tag{3}$$

where c may be chosen to cover a number of different cases of practical significance, for example, $c = 1/2$ would correspond with the case of hydrostatic loading usually associated with the behavior of a pressure hull, while $c = \mu$ (Poisson's ratio) would represent the behavior of say a subsea pipeline for which the plane-strain condition would be appropriate.

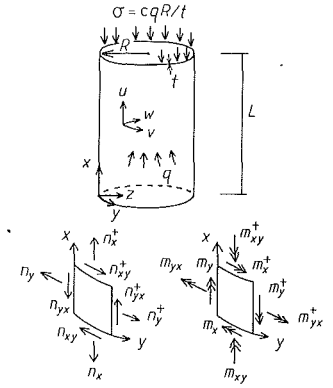


Fig. 1 Notation and convention adopted for geometry and internal stress and moment resultants

The bending and membrane stress resultants are related to strains through the constitutive equations

$$m_x = D(\kappa_x + \mu\kappa_y), \quad m_y = D(\mu\kappa_x + \kappa_y), \quad m_{xy} = D(1-\mu)\kappa_{xy} \tag{4a}$$

$$n_x = K(\epsilon_x + \mu\epsilon_y), \quad n_y = K(\mu\epsilon_x + \epsilon_y), \quad n_{xy} = K(1-\mu)\epsilon_{xy} \tag{4b}$$

where $D = Et^3/12(1-\mu^2)$, $K = Et/(1-\mu^2)$, E = modulus of elasticity, and μ = Poisson's ratio.

The strain-displacement relations associated with deformation from an initial imperfection w^0, are taken as

$$\kappa_x = -\frac{\partial^2 w}{\partial x^2}, \quad \kappa_y = -\frac{\partial^2 w}{\partial y^2}, \quad \kappa_{xy} = -\frac{\partial^2 w}{\partial x\partial y} \tag{5a}$$

$$\epsilon_x = \frac{\partial u}{\partial x} + \frac{\partial w^0}{\partial x}\frac{\partial w}{\partial x} + \frac{1}{2}\left(\frac{\partial w}{\partial x}\right)^2 \tag{5b}$$

$$\epsilon_y = \frac{\partial v}{\partial y} - \frac{w}{R} + \frac{\partial w^0}{\partial y}\frac{\partial w}{\partial y} + \frac{1}{2}\left(\frac{\partial w}{\partial y}\right)^2 \tag{5c}$$

$$\epsilon_{xy} = \frac{1}{2}\left(\frac{\partial u}{\partial y} + \frac{\partial v}{\partial x} + \frac{\partial w^0}{\partial x}\frac{\partial w}{\partial y} + \frac{\partial w^0}{\partial y}\frac{\partial w}{\partial x} + \frac{\partial w}{\partial x}\frac{\partial w}{\partial y}\right). \tag{5d}$$

2.2 Boundary Conditions and Modal Approximation. The end boundary is assumed to be supported in such a way as to conform with the classical simple support, corresponding with the conditions

$$w = \frac{\partial^2 w}{\partial x^2} = \frac{\partial u}{\partial x} = v = 0, \quad \text{at } x = 0, L. \tag{6}$$

By taking displacement functions u, v and w as linear combinations of the harmonic expressions,

$$u = \frac{Lt}{R}\sum_{i=0,1,2,\ldots}\ \sum_{j=1,3,5,\ldots}^{J_i^u} \tilde{u}_{ij}\cos(iy/R)\cos(j\pi x/L) \tag{7a}$$

$$v = \frac{Lt}{R}\sum_{i=1,2,\ldots}\ \sum_{j=1,3,5,\ldots}^{J_i^v} \tilde{v}_{ij}\sin(iy/R)\sin(j\pi x/L) \tag{7b}$$

$$w = t\sum_{i=0,1,2,\ldots}\ \sum_{j=1,3,5,\ldots}^{J_i^w} \tilde{w}_{ij}\cos(iy/R)\sin(j\pi x/L). \tag{7c}$$

[1]The authors are grateful to Ministry of Eduction, Science and Culture of Japanese Government for providing financial support which made this sabbatical year possible.

Downloaded 03 May 2010 to 171.66.16.245. Redistribution subject to ASME license or copyright; see http://www.asme.org/terms/Terms_Use.cfm

These boundary conditions will be exactly satisfied since each separate component satisfies the boundary conditions of Eq. (6). In these expressions, i and j are the circumferential full-wave and the longitudinal half-wave numbers; $\tilde{u}_{ij}$, $\tilde{v}_{ij}$ and $\tilde{w}_{ij}$ are the non-dimensional amplitudes of each harmonic function.

The initial geometric imperfection is expressed as

$$w^0 = t \sum_{i=0,1,2,\ldots} \sum_{j=1,3,5,\ldots}^{J_i^0} W_{ij}^0 \cos(iy/R)\sin(j\pi x/L). \quad (8)$$

2.3 Equilibrium Equation by Ritz Method. By substituting Eqs. (4), (5), (7), and (8) into Eq. (2), the energy components associated with the unknown coefficients $\tilde{u}_{ij}$, $\tilde{v}_{ij}$, and $\tilde{w}_{ij}$ are obtained using nondimensional pressure $Q = qRL^2/(\pi^2 D)$ as

$$U_B = (24\pi DL/R) \sum_{r'}^{N^w} \sum_{m'}^{N^w} \tilde{w}_{r'} \tilde{w}_{m'} \alpha_{m'r'}^{B33} \quad (9a)$$

$$\begin{aligned} U_M = (24\pi DL/R) \Bigg\{ & \sum_{r'}^{N^u} \tilde{u}_{r'} \left(\sum_{m'}^{N^u} \tilde{u}_{m'} \alpha_{m'r'}^{11} + \sum_{m'}^{N^v} \tilde{v}_{m'} \alpha_{m'r'}^{21} + \sum_{m'}^{N^w} \tilde{w}_{m'} \alpha_{m'r'}^{31} \right) \\ & + \sum_{r'}^{N^v} \tilde{v}_{r'} \left(\sum_{m'}^{N^v} \tilde{v}_{m'} \alpha_{m'r'}^{22} + \sum_{m'}^{N^w} \tilde{w}_{m'} \alpha_{m'r'}^{32} \right) \\ & + \sum_{r'}^{N^w} \sum_{m'}^{N^w} \tilde{w}_{r'} \tilde{w}_{m'} \alpha_{m'r'}^{33} + \sum_{r'}^{N^u} \sum_{m'}^{N^w} \sum_{k'}^{N^w} \tilde{u}_{r'} \tilde{w}_{m'} \tilde{w}_{k'} \alpha_{k'm'r'}^{331} \\ & + \sum_{r'}^{N^v} \sum_{m'}^{N^w} \sum_{k'}^{N^w} \tilde{v}_{r'} \tilde{w}_{m'} \tilde{w}_{k'} \alpha_{k'm'r'}^{332} \\ & + \sum_{r'}^{N^w} \sum_{m'}^{N^w} \sum_{k'}^{N^w} \tilde{w}_{r'} \tilde{w}_{m'} \tilde{w}_{k'} \alpha_{k'm'r'}^{333} \\ & + \sum_{r'}^{N^w} \sum_{m'}^{N^w} \sum_{k'}^{N^w} \sum_{i'}^{N^w} \tilde{w}_{r'} \tilde{w}_{m'} \tilde{w}_{k'} \tilde{w}_{i'} \alpha_{i'k'm'r'}^{3333} \Bigg\} \end{aligned} \quad (9b)$$

$$V_Q = (24\pi DL/R) Q \left(\sum_{r'}^{N^u} \tilde{u}_{r'} \alpha_{r'}^{1} + \sum_{r'}^{N^w} \tilde{w}_{r'} \alpha_{r'}^{3} \right) \quad (9c)$$

where $(\tilde{u}_{r'}, \tilde{v}_{r'}, \tilde{w}_{r'})$ is a set of generalized coordinates equivalent to $(\tilde{u}_{ij}, \tilde{v}_{ij}, \tilde{w}_{ij})$ and $\alpha_{m'r'}^{B33}$, $\alpha_{m'r'}^{11}$, $\alpha_{m'r'}^{21}$, ... are constants obtained from the integrations of Eq. (2); for completeness these are listed in the Appendix.

The Ritz method is used to obtain approximate solutions, by requiring the total potential energy to be stationary with respect to all the independent degrees-of-freedom, so that

$$\frac{\partial V_T}{\partial \tilde{u}_{r'}} = \frac{\partial V_T}{\partial \tilde{v}_{r'}} = \frac{\partial V_T}{\partial \tilde{w}_{r'}} = 0. \quad (10)$$

A total of $(N^u + N^v + N^w)$ nonlinear algebraic equations expressing the unknown coefficients $\tilde{u}_{r'}$, $\tilde{v}_{r'}$, and $\tilde{w}_{r'}$, in terms of the load parameter Q are obtained; these nondimensionalized forms can be represented as

$$\begin{aligned} & Q\alpha_{r'}^1 + \sum_{m'}^{N^u} \tilde{u}_{m'} 2\alpha_{m'r'}^{11} + \sum_{m'}^{N^v} \tilde{v}_{m'} \alpha_{m'r'}^{21} + \sum_{m'}^{N^w} \tilde{w}_{m'} \alpha_{m'r'}^{31} \\ & \quad + \sum_{m'}^{N^w} \sum_{k'}^{N^w} \tilde{w}_{m'} \tilde{w}_{k'} \alpha_{k'm'r'}^{331} = 0, \quad r' = 1, 2, 3, \ldots, N^u \end{aligned} \quad (11a)$$

$$\begin{aligned} & \sum_{m'}^{N^u} \tilde{u}_{m'} \alpha_{r'm'}^{21} + \sum_{m'}^{N^v} \tilde{v}_{m'} 2\alpha_{m'r'}^{22} + \sum_{m'}^{N^w} \tilde{w}_{m'} \alpha_{m'r'}^{32} \\ & \quad + \sum_{m'}^{N^w} \sum_{k'}^{N^w} \tilde{w}_{m'} \tilde{w}_{k'} \alpha_{k'm'r'}^{332} = 0, \quad r' = 1, 2, 3, \ldots, N^v \end{aligned} \quad (11b)$$

$$\begin{aligned} & Q\alpha_{r'}^3 + \sum_{m'}^{N^u} \tilde{u}_{m'} \alpha_{r'm'}^{31} + \sum_{m'}^{N^v} \tilde{v}_{m'} \alpha_{r'm'}^{32} \\ & \quad + \sum_{m'}^{N^w} \tilde{w}_{m'} 2(\alpha_{m'r'}^{B33} + \alpha_{m'r'}^{33}) \\ & \quad + \sum_{m'}^{N^w} \sum_{k'}^{N^u} \tilde{w}_{m'} \tilde{u}_{k'} (\alpha_{r'm'k'}^{331} + \alpha_{m'r'k'}^{331}) \\ & \quad + \sum_{m'}^{N^w} \sum_{k'}^{N^v} \tilde{w}_{m'} \tilde{v}_{k'} (\alpha_{r'm'k'}^{332} + \alpha_{m'r'k'}^{332}) \\ & \quad + \sum_{m'}^{N^w} \sum_{k'}^{N^w} \tilde{w}_{m'} \tilde{w}_{k'} (\alpha_{k'm'r'}^{333} + \alpha_{m'r'k'}^{333} + \alpha_{r'k'm'}^{333}) \\ & \quad + \sum_{m'}^{N^w} \sum_{k'}^{N^w} \sum_{i'}^{N^w} \tilde{w}_{m'} \tilde{w}_{k'} \tilde{w}_{i'} (\alpha_{i'k'm'r'}^{3333} \\ & \quad + \alpha_{k'm'r'i'}^{3333} + \alpha_{m'r'i'k'}^{3333} + \alpha_{r'i'k'm'}^{3333}) = 0, \\ & \quad r' = 1, 2, 3, \ldots, N^w \end{aligned} \quad (11c)$$

2.4 Incremental Strain Energy Analysis. The sets of nonlinear equations (Eq. (11)) can be solved using a step-by-step process in which either load or displacement are used as a control parameter. At each step a Newton-Raphson iteration is used to provide convergence to an acceptable level of precision. This incremental analytical procedure makes it convenient to compute at any stage along the equilibrium path the nature of the incremental strain energy components. A sufficiently small amplitude ($0.001t$ in the present study) of a displacement control parameter, provides a very close approximation to the tangent vectors $(\Delta^u, \Delta^v, \Delta^w)$ in the form of differences between the two close equilibrium states (u^E, v^E, w^E) and $(u^E + \Delta^u, v^E + \Delta^v, w^E + \Delta^w)$. The total strain components at a point (x, y) after the small incremental deformations about the equilibrium state may be written

$$\kappa_x \equiv \kappa_x^E + \kappa_x', \quad \kappa_y \equiv \kappa_y^E + \kappa_y', \quad \kappa_{xy} \equiv \kappa_{xy}^E + \kappa_{xy}' \quad (12)$$

$$\epsilon_x \equiv \epsilon_x^E + \epsilon_x' + \epsilon_x'^E + \epsilon_x'', \quad \epsilon_y \equiv \epsilon_y^E + \epsilon_y' + \epsilon_y'^E + \epsilon_y'',$$
$$\epsilon_{xy} \equiv \epsilon_{xy}^E + \epsilon_{xy}' + \epsilon_{xy}'^E + \epsilon_{xy}'' \quad (13)$$

where

$$\kappa_x^E = -\frac{\partial^2 w^E}{\partial x^2}, \quad \kappa_y^E = -\frac{\partial^2 w^E}{\partial y^2}, \quad \kappa_{xy}^E = -\frac{\partial^2 w^E}{\partial x \partial y} \quad (14a)$$

$$\kappa_x' = -\frac{\partial^2 \Delta^w}{\partial x^2}, \quad \kappa_y' = -\frac{\partial^2 \Delta^w}{\partial y^2}, \quad \kappa_{xy}' = -\frac{\partial^2 \Delta^w}{\partial x \partial y} \quad (14b)$$

$$\epsilon_x^E = \frac{\partial u^E}{\partial x} + \frac{\partial w^0}{\partial x}\frac{\partial w^E}{\partial x} + \frac{1}{2}\left(\frac{\partial w^E}{\partial x}\right)^2 \quad (15a)$$

$$\epsilon_y^E = \frac{\partial v^E}{\partial y} - \frac{w^E}{R} + \frac{\partial w^0}{\partial y}\frac{\partial w^E}{\partial y} + \frac{1}{2}\left(\frac{\partial w^E}{\partial y}\right)^2 \quad (15b)$$

Downloaded 03 May 2010 to 171.66.16.245. Redistribution subject to ASME license or copyright; see http://www.asme.org/terms/Terms_Use.cfm

$$\epsilon^E_{xy}=\frac{1}{2}\left(\frac{\partial u^E}{\partial y}+\frac{\partial v^E}{\partial x}+\frac{\partial w^0}{\partial x}\frac{\partial w^E}{\partial y}+\frac{\partial w^0}{\partial y}\frac{\partial w^E}{\partial x}+\frac{\partial w^E}{\partial x}\frac{\partial w^E}{\partial y}\right) \quad (15c)$$

$$\epsilon'_w=\frac{\partial \Delta^u}{\partial x},\quad \epsilon'_y=\frac{\partial \Delta^v}{\partial y}-\frac{\Delta^w}{R},\quad \epsilon'_{xy}=\frac{1}{2}\left(\frac{\partial \Delta^u}{\partial y}+\frac{\partial \Delta^v}{\partial x}\right) \quad (16)$$

$$\epsilon_x'^E=\frac{\partial(w^0+w^E)}{\partial x}\frac{\partial \Delta^w}{\partial x} \quad (17a)$$

$$\epsilon_y'^E=\frac{\partial(w^0+w^E)}{\partial y}\frac{\partial \Delta^w}{\partial y} \quad (17b)$$

$$\epsilon_{xy}'^E=\frac{1}{2}\left\{\frac{\partial(w^0+w^E)}{\partial x}\frac{\partial \Delta^w}{\partial y}+\frac{\partial(w^0+w^E)}{\partial y}\frac{\partial \Delta^w}{\partial x}\right\} \quad (17c)$$

$$\epsilon''_x=\frac{1}{2}\left(\frac{\partial \Delta^w}{\partial x}\right)^2,\quad \epsilon''_y=\frac{1}{2}\left(\frac{\partial \Delta^w}{\partial y}\right)^2,\quad \epsilon''_{xy}=\frac{1}{2}\frac{\partial \Delta^w}{\partial x}\frac{\partial \Delta^w}{\partial y}. \quad (18)$$

The corresponding stress components are

$$m'_x=D(\kappa'_x+\mu\kappa'_y),\quad m'_y=D(\mu\kappa'_x+\kappa'_y),$$
$$m'_{xy}=D(1-\mu)\kappa'_{xy} \quad (19a)$$

$$n^E_x=K(\epsilon^E_x+\mu\epsilon^E_y),\quad n^E_y=K(\mu\epsilon^E_x+\epsilon^E_y),$$
$$n^E_{xy}=K(1-\mu)\epsilon^E_{xy} \quad (19b)$$

$$n'_x=K(\epsilon'_x+\mu\epsilon'_y),\quad n'_y=K(\mu\epsilon'_x+\epsilon'_y),$$
$$n'_{xy}=K(1-\mu)\epsilon'_{xy} \quad (19c)$$

$$n_x'^E=K(\epsilon_x'^E+\mu\epsilon_y'^E),\quad n_y'^E=K(\mu\epsilon_x'^E+\epsilon_y'^E),$$
$$n_{xy}'^E=K(1-\mu)\epsilon_{xy}'^E \quad (19d)$$

$$n''_x=K(\epsilon''_x+\mu\epsilon''_y),\quad n''_y=K(\mu\epsilon''_x+\epsilon''_y),$$
$$n''_{xy}=K(1-\mu)\epsilon''_{xy}. \quad (19e)$$

To fully understand the changing nature of the resistance to incremental deformations as buckling progresses, it is necessary to break the quadratic form for the incremental energy into its component parts. These component parts of the quadratic form for incremental energy may be written as

$$V_{2T}=U_{2B}+U_{2M}+V_{2M}, \quad (20)$$

where the contributions U_{2B} and U_{2M} would represent the usual bending and membrane strain energy terms expressed as

$$U_{2B}=\frac{1}{2}\int_0^{2\pi R}\int_0^L (m'_x\kappa'_x+m'_y\kappa'_y+2m'_{xy}\kappa'_{xy})\,dxdy \quad (21)$$

$$U_{2M}=U^x_{2M}+U^y_{2M}+U^{xy}_{2M} \quad (22)$$

$$U^x_{2M}=\frac{1}{2}\int_0^{2\pi R}\int_0^L n'_x\epsilon'_x\,dxdy,\quad U^y_{2M}=\frac{1}{2}\int_0^{2\pi R}\int_0^L n'_y\epsilon'_y\,dxdy,$$
$$U^{xy}_{2M}=\int_0^{2\pi R}\int_0^L n'_{xy}\epsilon'_{xy}\,dxdy. \quad (23)$$

For convenience, U_{2B} and U_{2M} will be referred to as the linear bending and membrane strain energies to reflect their origins in the linear strain displacement components. Since it is the membrane resistance that is undergoing the most significant change as buckling progresses, the linear membrane strain energy, U_{2M}, has been broken down into its component parts associated with axial, hoop and in-plane shear action. Changes in membrane energy are also generated by the term V_{2M} which represents the interaction between the current total equilibrium state (including imperfections) and the nonlinear incremental membrane action. The various contributions to this so called "linearized" membrane energy term may be represented as

$$V_{2M}=V'_{2M}+V''_{2M} \quad (24a)$$

where

$$V'_{2M}=\overline{V}'^x_{2M}+\overline{V}'^y_{2M}+\overline{V}'^{xy}_{2M}+\overline{\overline{V}}'^x_{2M}+\overline{\overline{V}}'^y_{2M}+\overline{\overline{V}}'^{xy}_{2M}$$
$$+\overline{\overline{\overline{V}}}'^x_{2M}+\overline{\overline{\overline{V}}}'^y_{2M}+\overline{\overline{\overline{V}}}'^{xy}_{2M} \quad (24b)$$

$$V''_{2M}=\overline{V}''^x_{2M}+\overline{V}''^y_{2M}+\overline{V}''^{xy}_{2M}+\overline{\overline{V}}''^x_{2M}+\overline{\overline{V}}''^y_{2M}+\overline{\overline{V}}^{xy}_{2M}, \quad (24c)$$

and the individual contributions would be given by

$$\overline{V}'^x_{2M}=\frac{1}{2}\int_0^{2\pi R}\int_0^L n_x'^E\epsilon'_x\,dxdy,\quad \overline{V}'^y_{2M}=\frac{1}{2}\int_0^{2\pi R}\int_0^L n_y'^E\epsilon'_y\,dxdy,$$
$$\overline{V}'^{xy}_{2M}=\int_0^{2\pi R}\int_0^L n_{xy}'^E\epsilon'_{xy}\,dxdy \quad (25a)$$

$$\overline{\overline{V}}'^x_{2M}=\frac{1}{2}\int_0^{2\pi R}\int_0^L n'_x\epsilon_x'^E\,dxdy,\quad \overline{\overline{V}}'^y_{2M}=\frac{1}{2}\int_0^{2\pi R}\int_0^L n'_y\epsilon_y'^E\,dxdy,$$
$$\overline{\overline{V}}'^{xy}_{2M}=\int_0^{2\pi R}\int_0^L n'_{xy}\epsilon_{xy}'^E\,dxdy \quad (25b)$$

$$\overline{\overline{\overline{V}}}'^x_{2M}=\frac{1}{2}\int_0^{2\pi R}\int_0^L n_x'^E\epsilon_x'^E\,dxdy,\quad \overline{\overline{\overline{V}}}'^y_{2m}=\frac{1}{2}\int_0^{2\pi R}\int_0^L n_y'^E\epsilon_y'^E\,dxdy,$$
$$\overline{\overline{\overline{V}}}'^{xy}_{2M}=\int_0^{2\pi R}\int_0^L n_{xy}'^E\epsilon_{xy}'^E\,dxdy \quad (25c)$$

$$\overline{V}''^x_{2M}=\frac{1}{2}\int_0^{2\pi R}\int_0^L n^E_x\epsilon''_x\,dxdy,\quad \overline{V}''^y_{2M}=\frac{1}{2}\int_0^{2\pi R}\int_0^L n^E_y\epsilon''_y\,dxdy,$$
$$\overline{V}''^{xy}_{2M}=\int_0^{2\pi R}\int_0^L n^E_{xy}\epsilon''_{xy}\,dxdy \quad (26a)$$

$$\overline{\overline{V}}''^x_{2M}=\frac{1}{2}\int_0^{2\pi R}\int_0^L n''_x\epsilon^E_x\,dxdy,\quad \overline{\overline{V}}''^y_{2M}=\frac{1}{2}\int_0^{2\pi R}\int_0^L n''_y\epsilon^E_y\,dxdy,$$
$$\overline{\overline{V}}''^{xy}_{2M}=\int_0^{2\pi R}\int_0^L n''_{xy}\epsilon^E_{xy}\,dxdy. \quad (26b)$$

3 Nature of Buckling

To illustrate the behavior of a typical cylinder under hydrostatic loading, $c = 0.5$, and to use this behavior to exemplify the mechanics of postbuckling, a sample of the shells tested by Yamaki (1984) is considered. This is one of a number of shells that in the past have been the subject of extensive numerical studies and against which the present solutions have been validated. The geometry is defined by R = 100 mm, t = 0.247 mm, L = 51 mm; R/t = 405, L/R = 0.51, $Z=\sqrt{1-\mu^2L^2/(Rt)}$ = 100, where for this and all subsequent examples the material is taken to have μ = 0.3.

3.1 Classical Bifurcation Analysis. An "idealized" classical bifurcation analysis (Yamada and Croll, 1989) can easily allow derivation of the nondimensional classical load spectrum

$$Q^C=Q^B+Q^M, \quad (27)$$

where

$$Q^B=(\beta_i^2+j^2)^2/(\beta_i^2+cj^2) \quad (28)$$

$$Q^M=12Z^2j^4/\{\pi^4(\beta_i^2+j^2)^2(\beta_i^2+cj^2)\} \quad (29)$$

$\beta_i=iL/(\pi R)$; normalized circumferential wave number. (30)

Then, as illustrated in Fig. 2 this shell has a minimum classical pressure occurring at Q^C_{min} = 11.1 in a mode closely approximated by $i = b = 16$.

Through nonlinear post-buckling analysis, solution convergence has been found to reach acceptable limits by using in Eq. (7)

Downloaded 03 May 2010 to 171.66.16.245. Redistribution subject to ASME license or copyright; see http://www.asme.org/terms/Terms_Use.cfm

$$J_i^u = (15, 11, 7, 3) \quad \text{for } i = (0, b, 2b, 3b)$$

$$J_i^v = (11, 7, 3) \quad \text{for } i = (b, 2b, 3b)$$

$$J_i^w = (9, 7, 5) \quad \text{for } i = (0, b, 2b)$$

implying the total numbers of displacement degrees-of-freedom in Eqs. (9) and (11) as $(N^u, N^v, N^w) = (20, 12, 12)$.

Post-buckling from this classical critical bifurcation state is illustrated in Fig. 3. Two cases of perfect shell bifurcation are shown. An "idealized" bifurcation model, shown dotted, is based upon the assumption that prior to buckling the effects of bending are ignored and the internal shell stress takes the form of a uniform membrane state, for which

$$n_x^F = -cqR, \quad n_y^F = -qR, \quad n_{xy}^F = 0. \tag{31}$$

It is this idealized model that has also been used to determine the critical pressure spectrum of Fig. 2. The curve marked "exact perfect" in Fig. 3(*a*) corresponds with an analysis which includes the effects of bending deflections in the pre-buckled configuration. Since the effects of bending are confined to a very localized region near the ends of the shell, and because most of the buckling energy is concentrated over the central portion of the shell where the stress approaches that of the idealized membrane state, the two analyses are very close. For values of $Z < 10$, the differences between the two analyses will be considerably greater.

3.2 Imperfect Shell Response. Also included in Fig. 3(*a*) are representative imperfect curves, where the horizontal axis

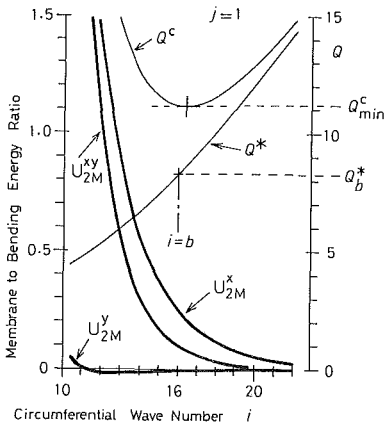


Fig. 2 Membrane energy spectra normalized by U_{2B}, and nondimensional classical buckling and inextentional reduced stiffness loads, for an idealized model having $c = 0.5$, $R/t = 405$, $L/R = 0.51$ and $Z = 100$

W_b represents the nondimensional total displacement component which has circumferential full-wave number $i = b$ and a single half-wave in the axial direction, $j = 1$. In order to concentrate upon buckling into a critical mode $b = 16$, the initial imperfection function Eq. (8) is taken to be a single mode having the form of this classical critical mode; that is the imperfection takes the form

$$w^0 = tW_b^0 \cos(by/R)\sin(\pi x/L). \tag{32}$$

Recalling that the imperfection amplitude W_b^0 has been nondimensionalized with respect to the shells thickness, it can be seen that the sensitivity of buckling to changes in imperfection is most severe when the imperfection has a very small amplitude. An imperfection in the critical mode of just 2 percent the shells thickness will reduce the buckling load by around 8 percent of the classical bifurcation load. With an imperfection of around 20 percent the shells thickness the maximum load has all but disappeared with the behavior approaching that which is more reminiscent of column buckling; the buckling load in this case has been reduced by some 35 percent. This imperfection sensitivity is more clearly illustrated in Fig. 3(*b*). All of the above behavior is well documented, but what has not been so well documented are the reasons why this loss of load carrying capacity occurs. In particular it would be helpful to know which components of the shells stiffness are lost as a result of the nonlinear mode couplings responsible for this loss of capacity.

3.3 Energy Analysis of Post-buckling. As has been pointed out in many previous studies, that it is the membrane behavior which gives the shell its advantage in terms of weight for weight load carrying capacity over an equivalent width of flat plating. However, it is the changes in membrane behavior occurring in the nonlinear mode couplings that also give rise to the post-buckling nonlinearities, such as the initial loss of stiffness in the present shell in addition to the eventual restiffening which occurs in the advanced post-buckled region of behavior. This consideration is implicitly taken into account in virtually all nonlinear shell analysis, which like that described in Eq. (5) include nonlinearities in only the membrane strain-displacement relations. In contrast, the incremental bending resistance in a particular mode U_{2B} remains practically invariant and consequently provides a useful reference against which all the remaining incremental energy contributions for buckling into that mode may be measured.

Figure 4(*a*) illustrates the variations in incremental quadratic total potential energy, normalized with respect to U_{2B}, for the perfect shell behavior of Fig. 3(*a*) by the continuous lines and for the imperfect shell responses of Fig. 3(*a*) by the broken

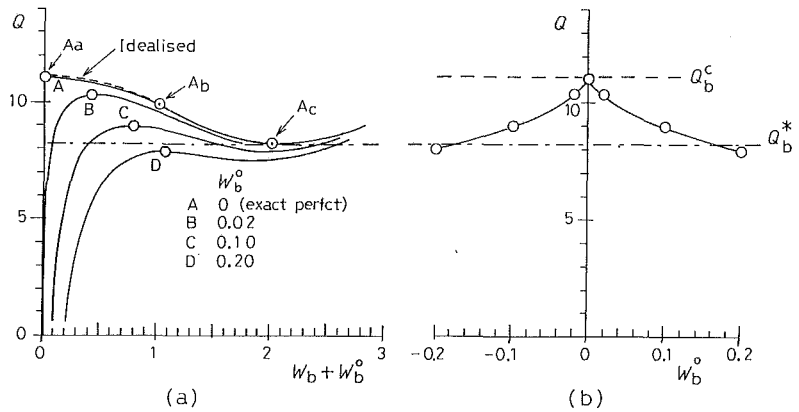


Fig. 3 Effects of initial imperfection for hydrostatic pressurized cylindrical shells ($R/t = 405$, $L/R = 0.51$, $Z = 100$, $b = 16$); (*a*) nondimensional pressure versus total deflection in harmonic $i = b = 16$ and $j = 1$; (*b*) imperfection sensitivity

Downloaded 03 May 2010 to 171.66.16.245. Redistribution subject to ASME license or copyright; see http://www.asme.org/terms/Terms_Use.cfm

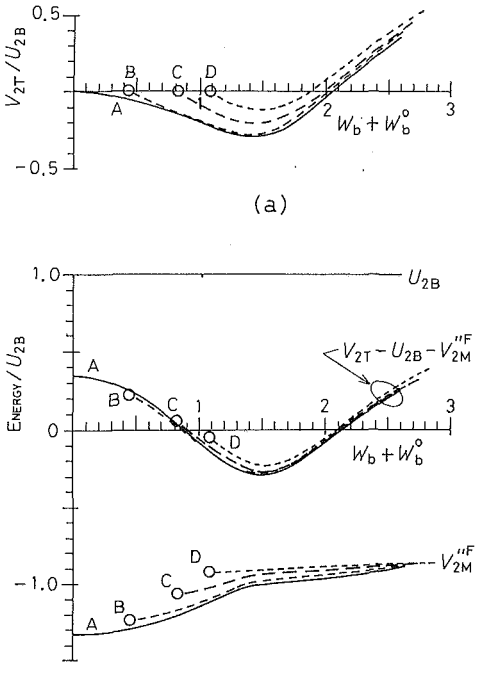


Fig. 4(*a*)-(*b*)

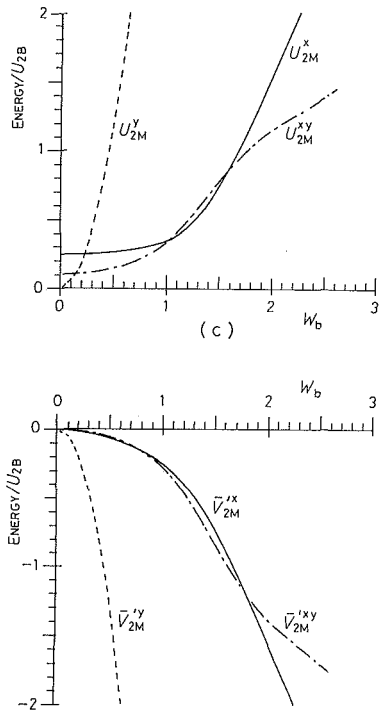


Fig. 4(*c*)-(*d*)

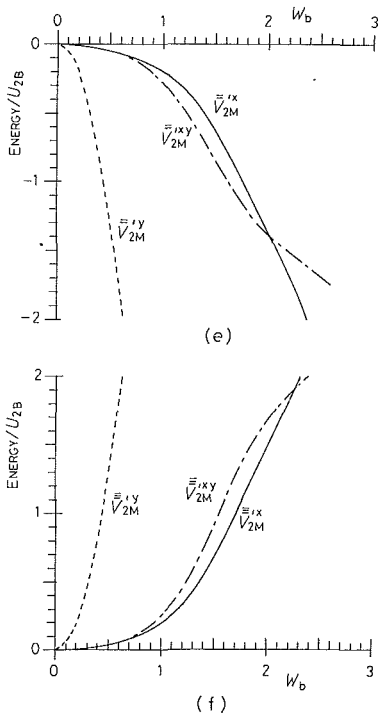


Fig. 4(*e*)-(*f*)

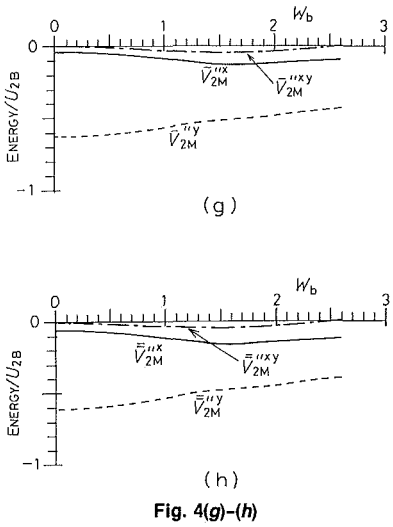


Fig. 4(*g*)-(*h*)

Fig. 4 Various incremental energy components variations in post-buckling paths (c = 0.5, R/t = 405, L/R = 0.51, Z = 100, b = 16); see also Fig. 3(*a*)

lines. As would be expected, the quadratic form is identically zero at the bifurcation pressure, point "Aa", and at the post-buckled minimum, point "Ac", where the stability of equilibrium is at a critical state; stability at these critical states would of course be determined by the higher order components of incremental total potential energy. The negative incremental energy for deformations over the falling branch of the perfect path indicates of course, unstable equilibrium. For $W_b > 2.0$ the positive incremental V_{2T} means that equilibrium is once again stable on the rising path of the curve. The membrane contributions to the incremental energy approximated using Eq. (31) are summarized in Fig. 4(*b*).

The linear membrane energy contribution to the stability of the shell at the classical bifurcation load, shown for curve "A" as $W_b \to 0$, can be seen to be approximately 0.35 that from the linear bending energy. Most of this initial linear membrane resistance derives from the axial component U^x_{2M} with a smaller contribution from in-plane shear U^{xy}_{2M}; this is illustrated in Fig. 4(*c*). As the classical bifurcation state the linear bending and membrane energies provide the total resistance to buckling which is destabilized by the linearized term V_{2M}, consisting of the circumferential component V''^y_{2M} ($= \bar{V}''^y_{2M} + \bar{\bar{V}}''^y_{2M}$) with a relatively minor contribution from V''^x_{2M} ($= \bar{V}''^x_{2M} + \bar{\bar{V}}''^x_{2M}$).

As deformation progresses into the post-buckled region, it is incremental membrane energy associated with the buckling mode that undergoes change. This is illustrated by the aggregated positive and negative contributions shown in Fig. 4(*b*),

Downloaded 03 May 2010 to 171.66.16.245. Redistribution subject to ASME license or copyright; see http://www.asme.org/terms/Terms_Use.cfm

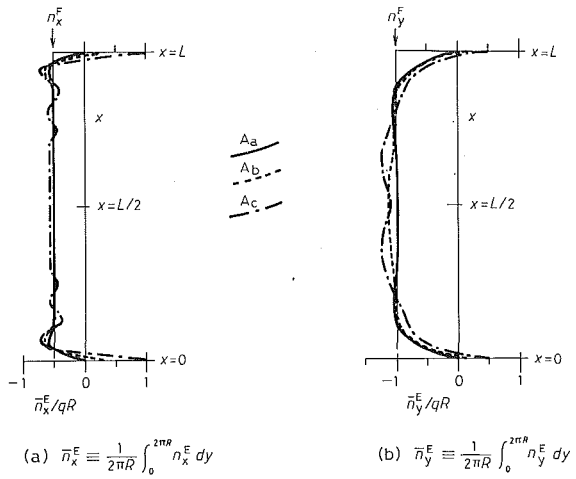


Fig. 5 Axial distributions of the average of total stress components (c = 0.5, R/t = 405, L/R = 0.51, Z = 100, b = 16); Aa, Ab, and Ac are post-buckling equilibrium states as shown in Fig. 3(*a*)

and by the more detailed breakdowns, according to Eq. (24), summarized in Fig. 4(*c*) to (*h*). Incremental bending strain energy is virtually unchanged throughout the post-buckling response. The role of geometric imperfection in eroding the membrane energy is also apparent in Fig. 4(*b*). At the snap buckling loads associated with the three imperfect paths of Fig. 3 the quadratic form of the total potential energy is seen in Fig. 4(*a*) to be zero, as would be expected for these states of critical stability. Figure 4(*b*) shows that the contribution to stabilization from membrane energy at these snap buckling loads is reduced as the imperfection is increased. Again, the total potential energy is shown in Fig. 4(*a*) to be zero at the post-buckled minimum, which, as is apparent in Fig. 4(*b*), correspond with an incremental resistance in which the contributions from membrane energy (the upper sets of curves in Fig. 4(*b*)) are effectively zero.

For the perfect post-buckling response the all important linearized terms $\overline{V}''^{y}_{2M}$ and $\overline{\overline{V}}''^{y}_{2M}$ are seen in Fig. 4(*g*) and (*h*) to vary almost in direct proportion to the pressure level Q on the post-buckled path. This is a consequence of the incremental nonlinear stresses and strains, (n_x'', n_y'', n_{xy}'') and $(\epsilon_x'', \epsilon_y'', \epsilon_{xy}'')$, being dependent upon just the incremental out-of-plane buckling deformation which remains effectively invariant. It is the average components of these nonlinear stresses and strains that combine with the average membrane stresses and strains, (n_x^E, n_y^E, n_{xy}^E) and $(\epsilon_x^E, \epsilon_y^E, \epsilon_{xy}^E)$, associated with the current equilibrium state "E" to give the linearized membrane contribution V''_{2M}. Since the average membrane stresses and strains on the nonlinear path will for the same pressure Q be essentially the same as those of the idealized membrane state given by Eq. (31), as is shown in Fig. 5, the terms V''_{2M} in Eq. (24*c*) will be closely approximated by

$$V''^{F}_{2M} = \frac{1}{2}\int_0^{2\pi R}\int_0^{L}(n_x^F\epsilon_x'' + n_y^F\epsilon_y'')\,dxdy + \frac{1}{2}\int_0^{2\pi R}\int_0^{L}(n_x''\epsilon_x^F + n_y''\epsilon_y^F)\,dxdy = \int_0^{2\pi R}\int_0^{L}(n_x^F\epsilon_x'' + n_y^F\epsilon_y'')\,dxdy \simeq V''_{2M}. \quad (33)$$

Figure 4(*b*) demonstrates that V''^{F}_{2M} is effectively proportional to the current level of pressure Q. Associated with this decline in the destabilizing terms V''^{F}_{2M}, the remaining membrane strain energy term $(V_{2T} - U_{2B} - V''^{F}_{2M})$ which provide part of the other contributions to stabilization from the linear and linearized membrane energy, are seen to undergo a decrease. Figure 4(*b*) shows that the term $(V_{2T} - U_{2B} - V''^{F}_{2M})$ is effectively lost at the point "Ac" where the post-buckled path has reached the minimum load carrying capacity, having become negative on account of the effects of terms $\overline{V}'_{2M}$ and $\overline{\overline{V}}'_{2M}$ over the falling branch of the post-buckling path. The role of the coupled stresses and strains $n_x'^{E}, \ldots, \epsilon_x'^{E} \ldots$ in eroding the membrane energy is evident in Figs. 4(*d*) and 4(*e*) in these energy contributions $\overline{V}'_{2M}$ and $\overline{\overline{V}}'_{2M}$. Beyond the minimum post-buckling load carrying capacity the combined stabilization from the linear membrane energy, U_{2M} (shown in Fig. 4(*c*)), and the nonlinear components, $\overline{\overline{V}}'_{2M}$ (shown in Fig. 4(*f*)), again give the membrane energy positive overall contribution to the buckling resistance. This restabilization in advanced post-buckled region, and its concomitant increases in overall stiffness are well documented in relation to physical tests (Batista, 1979). The importance of membrane energy in controlling this restabilization is clear from the energy breakdown shown in Figs. 4(*c*)–(*h*).

At the post-buckled minimum pressure the major contribution to the shells resistance to incremental bending deformations is derived from the bending energy U_{2B}. Destabilization is provided by the linearized terms V''_{2M} given in Eq. (26). This suggests a simple way of representing the load levels associated with the post-buckled minimum pressure.

3.4 Reduced Stiffness Post-buckled Behavior. Each of the integrals of Eq. (26) involves the products of the nonlinear incremental stresses or strains and the current total stresses or strains. Nonlinear incremental stresses and strains, $n_x'', \ldots, \epsilon_x'', \ldots$, arising from the development of a buckling mode having "b" circumferential full-waves, will consist, as shown in Figs. 6(*d*) and 7(*d*), of average components and components having a periodicity of "$2b$". The total stresses and strains $n_x^E, \ldots, \epsilon_x^E, \ldots$ by which these are multiplied will also consist of an average component and periodic components. Only two components in the quadratures of Eq. (26) will give rise to a net energy contribution: the products of the average total stresses and strains (which will be the same as those existing at this pressure level in the idealized unbuckled shell as given by Eq. (31)) and average incremental stresses and strains; and, the products of the components in each at the total and incremental stresses and strains that have periodicity of "$2b$". Of these two components it is the components associated with the average stresses and strains that dominate. Hence as the post-buckled equilibrium path approaches the minimum load carrying capacity, the only two significant energy contributions are U_{2B} and V''_{2M}. It has already been observed that V''_{2M} may be approximated by V''^{F}_{2M} as given by Eq. (33). With V''^{F}_{2M} involving ϵ_x'' and ϵ_y'' this means that both U_{2B} and V''^{F}_{2M} are dependent only upon the out-of-plane buckling mode "b". A critical condition corresponding with post-buckling minimum could therefore be written as

$$U_{2B} + Q^*(\partial V''^{F}_{2M}/\partial Q) = 0. \quad (34)$$

Comparing this with the equivalent critical energy expressions at the initial bifurcation,

$$U_{2B} + U_{2M} + Q^c(\partial V''^{F}_{2M}/\partial Q) = 0. \quad (35)$$

Then it follows from energy consideration that

$$Q^* = Q^c U_{2B}/(U_{2B} + U_{2M}) = Q^B \text{ (see Eq. (28))}. \quad (36)$$

This condition has already been described as representing the reduced stiffness critical analysis.

The explanation for the reduction in membrane strain energy in post-buckling behavior is indicated in Fig. 5, 6, and 7. While the asymmetric stress component n_x' is significant at $W_b = 0$, it can be observed that as W_b increases there is a positive component $n_x'^{E}$ which tends to counterbalance n_x'. When buck-

Downloaded 03 May 2010 to 171.66.16.245. Redistribution subject to ASME license or copyright; see http://www.asme.org/terms/Terms_Use.cfm

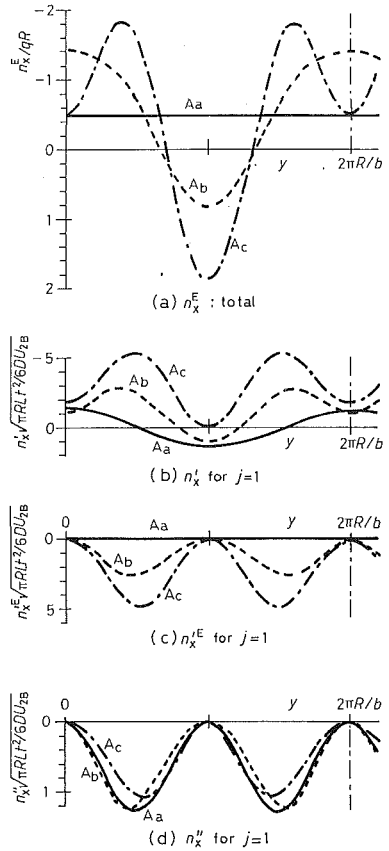


Fig. 6 Circumferential distributions of the axial stress components (c = 0.5, R/t = 405, L/R = 0.51, Z = 100, b = 16); Aa, Ab, and Ac are post-buckling equilibrium states as shown in Fig. 3(a)

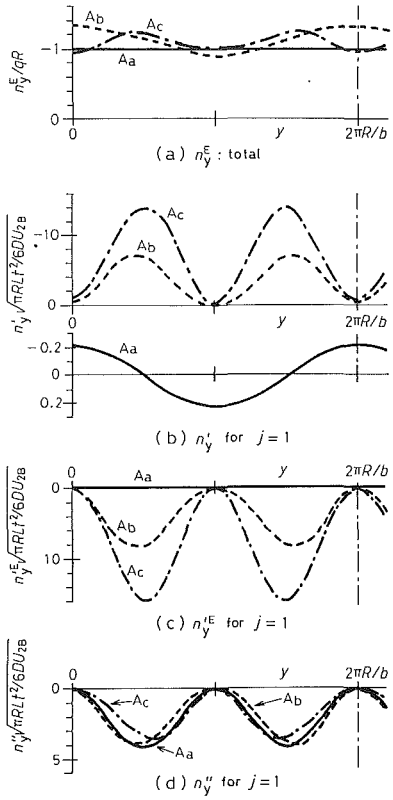


Fig. 7 Circumferential distributions of the hoop stress components (c = 0.5, R/t = 405, L/R = 0.51, Z = 100, b = 16); Aa, Ab and Ac are post-buckling equilibrium state as shown in Fig. 3(a)

ling has reached the point "Ac" corresponding with the post-buckled minimum the combined periodic stress in the $j = 1$ has all but been annihilated. Only the higher mode $j = 3, 5, \ldots$, components are found to have any significance. As deformation increases the stiffening contributions from membrane energy arises as the result of the development of the higher mode $j = 3, 5, \ldots$ components of n_x' and n_y'.

3.5 Effect of Coupled Imperfection Modes. It may be observed that the possibility of a buckling load lower than Q_b^* could occur if the imperfection in a longer wavelength mode was sufficiently large. However, the magnitude of the imperfection in this noncritical buckling mode would need to be considerably larger than that in the critical mode if this noncritical buckling is to occur.

This dominance of the lowest, or classical, critical mode is made clear in the following addition imperfection study. An imperfection is taken in the form

$$W^0 = t[W_b^0\cos(by/R) + W_{b-1}^0\cos\{(b-1)y/R\}]\sin(\pi x/L)$$
$$= tW_c^0[S\cos(by/R) + (1-S)\cos\{(b-1)y/R\}]\sin(\pi x/L). \quad (37)$$

To provide convergence the mode ranges taken in Eq. (7) are for this case adopted as

$$J_i^u = (15, 11, 11, 7, 7, 3, 3)$$
$$\text{for } i = \{0, b-1, b, 2(b-1), 2b, 3(b-1), 3b\}$$
$$J_i^v = (11, 11, 7, 7, 3, 3)$$
$$\text{for } i = \{b-1, b, 2(b-1), 2b, 3(b-1), 3b\}$$
$$J_i^w = (9, 7, 7, 5, 5)$$
$$\text{for } i = \{0, b-1, b, 2(b-1), 2b\}.$$

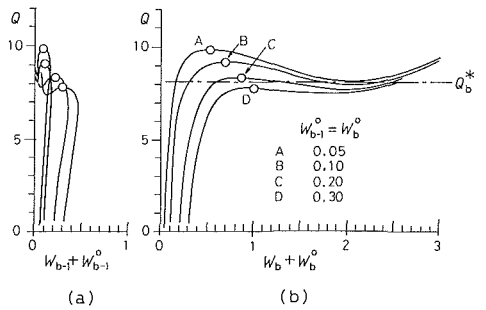


Fig. 8 Effects of coupled imperfection mode in the case of S = 0.5; c = 0.5, R/t = 405, L/R = 0.51, Z = 100, b = 16

Figure 8 shows the behavior for an imperfection having equal components from modes $i = b - 1$ and $i = b$ (i.e., S = 0.5 in Eq. (37)). In this case it is the classical mode $i = b$ which dominates. Furthermore, the lower bound for this coupled imperfection mode is effectively the same as that for uncoupled $i = b$ imperfection shown in Fig. 3. In the case of S = 0.1 where the imperfection component with $i = b - 1$ mode dominates, Fig. 9 shows that it is new deflection into mode $i = b - 1$ that controls buckling. The lower bound in this case is approximated by the reduced stiffness critical pressure for ($i = b - 1, j = 1$) mode, Q_{b-1}^*, as illustrated in Fig. 9. Unless the dominant imperfection in a noncritical mode is considerably larger than that of the classical critical mode, it can be concluded that buckling will tend to be controlled by that occurring in the classical critical mode. However, the fact that a noncritical imperfection can force buckling into a noncritical

Downloaded 03 May 2010 to 171.66.16.245. Redistribution subject to ASME license or copyright; see http://www.asme.org/terms/Terms_Use.cfm

mode suggests that this is an area worthy of further investigation.

3.6 Parameter Study. To illustrate the behavior desired above over a range of shell geometric parameters, Fig. 10 shows the effects of varying R/t for a shell having fixed $L/R = 0.51$ and $\mu = 0.3$. Classical critical loads are shown by the upper spectrum of curves, with the associated reduced stiffness critical loads shown by the lower bound set of continuous curves. Adopting the reduced stiffness lower bound as that in the mode "b" associated with the minimum classical critical load results in the theoretical lower bounds by the broken line.

Superimposed upon Fig. 10 are the results of nonlinear analyses for a range of shell with imperfections corresponding with the integer mode closest to the classical critical mode "b". In each case the classical critical loads Q^c_{min} are seen to provide upper bounds to observed snap buckling loads; even very small critical imperfections are observed to result in considerable reductions in buckling load from that predicted by classical theory. As imperfections are increased the reduced stiffness critical loads are seen to provide close approximations to the snap buckling loads experienced by the shell. That buckling loads can occur at loads slightly lower than Q^*_b can be explained by the negative incremental membrane energy that exists between the maximum "snap" buckling loads and the post-buckling minimum. This is evident for the shell having $Z = 100$ in Fig. 4(b), where for case "D" the membrane energy contribution ($V_{2T} - U_{2B} - V''^F_{2M}$) reaches approximately -0.05 of the incremental bending energy between the snap buckling load and the eventual minimum post-buckling.

The result over all the numerical experiments undertaken is that the lower bound of the imperfect buckling loads is 8 percent to 10 percent below the reduced stiffness buckling load Q^*_b. The reason for this would be relate to the slight increase of the mid-shell current stress level at the snap buckling load. Actually, the average hoop stress at the central portion is found to increase around 10 percent by comparison to idealized membrane stress condition, just similar to case "Ab" in Fig. 5(b), in the case of $Z = 100$ and $W^0_b = 0.20$. However, Q^*_b can be seen to predict the trend of the lower bounds to buckling loads.

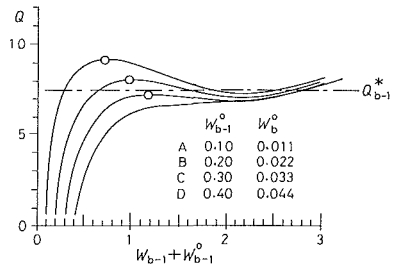


Fig. 9 Effects of coupled imperfection mode in the case of $S = 0.1$; $c = 0.5$, $R/t = 405$, $L/R = 0.51$, $Z = 100$, $b = 16$

4 Conclusions

For the case of pressure loaded circular cylindrical shells, a nonlinear Ritz analysis of elastic buckling has shown that classical bifurcation theory results in unreliable upper bounds to observed imperfection sensitive buckling pressures. Post-buckling changes in stiffness have been shown to result from changes in the incremental membrane energy. Over the initial post-buckling phase the initially stabilizing membrane energy components are lost, resulting in an overall loss of load carrying capacity. In the more advanced post-buckling region other components of membrane energy are developed, which lead to a recovery of load carrying capacity. At the post-buckled minimum load carrying capacity the incremental stabilizing energy is dominated by the invariant bending energy. This observation allows the development of reduced stiffness buckling model from which the initially stabilizing incremental membrane energy has been eliminated. Reduced stiffness buckling loads are shown to provide close lower bounds to the imperfection sensitive buckling loads observed in extensive numerical studies. This suggests that the reduced stiffness method provides a simple but safe extension to classical analysis for the design of pressure loaded cylinders.

References

Batista, R. C., 1979, "Lower Bound Estimates for Cylindrical Shell Buckling," Ph.D. Dissertation, University of London.

Croll, J. G. A., 1975, "Towards Simple Estimates of Shell Buckling Loads," *Der Stahlbau*, Vol. 8, pp. 243-248.

Croll, J. G. A., and Ellinas, C. P., 1983, "Reduced Stiffness Axial Load Buckling of Cylinders," *Int. J. Solids Structures*, Vol. 19, pp. 461-477.

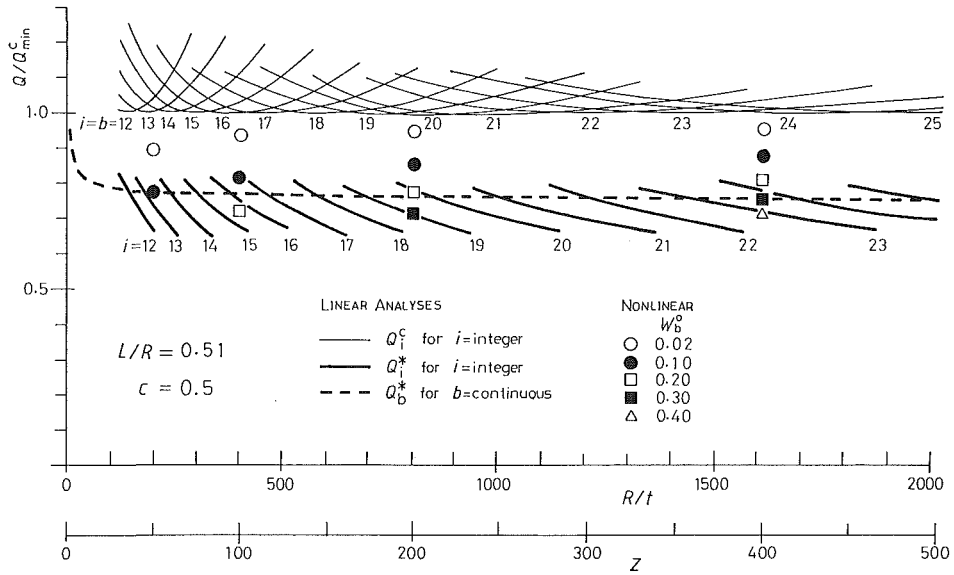


Fig. 10 Summary of buckling loads from nonlinear analysis for imperfect shells, and comparison with linear classical and reduced stiffness analyses

Downloaded 03 May 2010 to 171.66.16.245. Redistribution subject to ASME license or copyright; see http://www.asme.org/terms/Terms_Use.cfm

Croll, J. G. A., 1987, "Lower Bound Methods in Shell Buckling," *Developments of Thin-Walled Structures 3*, Elsevier, London, pp. 117–163.

Thompson, J. M. T., and Hunt, G. W., 1973, *General Theory of Elastic Stability*, John Wiley and Sons, London.

Yamada, S., and Croll, J. G. A., 1989, "Buckling Behavior of Pressure Loaded Cylindrical Panel," *J. Engrg. Mech., ASCE*, Vol. 115, pp. 327–344.

Yamaki, N., 1984, *Elastic Stability of Circular Cylindrical Shells*, North-Holland, Amsterdam.

Zintilis, G. M., and Croll, J. G. A., 1986, "Pressure Buckling of Cantilevered Shells of Revolution," *Int. J. Thin-Walled Structures*, Vol. 4, pp. 381–408.

APPENDIX

Coefficients of Energy Expression Eq. (9)

Subscripts r', m', k' and i' in Eq. (9) are defined as (circumferential fullwave number, longitudinal half-wave number) = (r, g), (m, n), (k, l), and (i, j), respectively. Using nondimensional geometric parameter Z and normalized circumferential wave number β_i (see Eq. (30)), the coefficients of Eq. (9) are

$$\alpha^{1}_{r'} = -\frac{c\pi^2\sqrt{1-\mu^2}}{6Z}; \quad \text{for } r=0 \text{ and } g=\text{odd} \tag{A1a}$$

$$\alpha^{1}_{r'} = 0; \quad \text{for } r\neq 0 \text{ or } g=\text{even} \tag{A1b}$$

$$\alpha^{3}_{r'} = -\frac{\pi\sqrt{1-\mu^2}}{6Zg}; \quad \text{for } r=0 \text{ and } g=\text{odd} \tag{A2a}$$

$$\alpha^{3}_{r'} = 0; \quad \text{for } r\neq 0 \text{ or } g=\text{even} \tag{A2b}$$

$$\alpha^{B33}_{m'r'} = \frac{\pi^4(1-\mu^2)}{96Z^2}\left[\{g^2n^2 + 2\mu g^2\beta_m^2 + \beta_r^2\beta_m^2\}F_1^{rm}F_2^{gn} + 2(1-\mu)\beta_r g\beta_m n F_2^{rm}F_1^{gn}\right] \tag{A3}$$

$$\alpha^{11}_{m'r'} = \frac{\pi^2}{8}\left\{gnF_1^{rm}F_2^{gn} + \frac{1-\mu}{2}\beta_r\beta_m F_2^{rm}F_1^{gn}\right\} \tag{A4}$$

$$\alpha^{21}_{m'r'} = \frac{\pi^2}{8}\left\{-2\mu g\beta_m F_1^{rm}F_2^{gn} - (1-\mu)\beta_r n F_2^{rm}F_1^{gn}\right\} \tag{A5}$$

$$\alpha^{31}_{m'r'} = \frac{\pi}{4}\mu g F_1^{rm}F_2^{gn} + \frac{\pi^2\sqrt{1-\mu^2}}{8Z}\sum_{k'}^{N^0} W_{k'}^0\left\{-gnlF_3^{rmk}F_5^{gnl} - \mu g\beta_m\beta_k F_4^{mkr}F_6^{gnl} + \frac{1-\mu}{2}\beta_r\beta_m l F_4^{rmk}F_5^{nlg} + \frac{1-\mu}{2}\beta_r n\beta_k F_4^{krm}F_5^{lgn}\right\} \tag{A6}$$

$$\alpha^{22}_{m'r'} = \frac{\pi^2}{8}\left\{\beta_r\beta_m F_1^{rm}F_2^{gn} + \frac{1-\mu}{2}gnF_2^{rm}F_1^{gn}\right\} \tag{A7}$$

$$\alpha^{32}_{m'r'} = -\frac{\pi}{4}\beta_r F_1^{rm}F_2^{gn} + \frac{\pi^2\sqrt{1-\mu^2}}{8Z}\sum_{k'}^{N^0} W_{k'}^0\left\{\beta_r\beta_m\beta_k F_4^{mkr}F_6^{gnl} + \mu\beta_r nlF_3^{rmk}F_5^{gnl} - \frac{1-\mu}{2}g\beta_m l F_4^{rmk}F_5^{nlg} - \frac{1-\mu}{2}gn\beta_k F_4^{krm}F_5^{lgn}\right\} \tag{A8}$$

$$\alpha^{33}_{m'r'} = \frac{1}{8}F_1^{rm}F_2^{gn} - \frac{\pi\sqrt{1-\mu^2}}{8Z}\sum_{k'}^{N^0} W_{k'}^0\{\beta_m\beta_k F_4^{mkr}F_6^{gnl} + \mu nlF_3^{rmk}F_5^{gnl}\} + \frac{\pi^4(1-\mu^2)}{128Z^2}\sum_{k'}^{N^0}\sum_{i'}^{N^0} W_{k'}^0 W_{i'}^0\left\{gnljF_7^{rmki}F_7^{nglj} + \beta_r\beta_m\beta_k\beta_i F_9^{rmki}F_9^{gnlj} + \frac{1-\mu}{2}\beta_r\beta_m l j F_8^{rmki}F_8^{gnlj} + \frac{1-\mu}{2}gn\beta_k\beta_i F_8^{kirm}F_8^{ljgn} + (1+\mu)g\beta_m\beta_k j F_8^{mkir}F_8^{nljg}\right\} \tag{A9}$$

$$\alpha^{331}_{k'm'r'} = \frac{\pi^2\sqrt{1-\mu^2}}{16Z}\{-gnlF_3^{rmk}F_5^{gnl} - \mu g\beta_m\beta_k F_4^{mkr}F_6^{gnl} + (1-\mu)\beta_r\beta_m l F_4^{rmk}F_5^{nlg}\} \tag{A10}$$

$$\alpha^{332}_{k'm'r'} = \frac{\pi^2\sqrt{1-\mu^2}}{16Z}\{\mu\beta_r nlF_3^{rmk}F_5^{gnl} + \beta_r\beta_m\beta_k F_4^{mkr}F_6^{gnl} - (1-\mu)g\beta_m l F_4^{rmk}F_5^{nlg}\} \tag{A11}$$

$$\alpha^{333}_{k'm'r'} = -\frac{\pi\sqrt{1-\mu^2}}{16Z}\{\mu nlF_3^{rmk}F_5^{gnl} + \beta_m\beta_k F_4^{mkr}F_6^{ngl}\} + \frac{\pi^4(1-\mu^2)}{128Z^2}\sum_{i'}^{N^0} W_{i'}^0\{gnljF_7^{rmki}F_7^{gnlj} + \beta_r\beta_m\beta_k\beta_i F_9^{rmki}F_9^{gnlj} + \beta_r\beta_m l j F_8^{rmki}F_8^{gnlj} + \beta_r nl\beta_i F_8^{irmk}F_8^{jgnl}\} \tag{A12}$$

$$\alpha^{3333}_{i'k'm'r'} = \frac{\pi^4(1-\mu^2)}{512Z^2}\{gnljF_7^{rmki}F_7^{gnlj} + \beta_r\beta_m\beta_k\beta_i F_9^{rmki}F_9^{gnlj} + 2\beta_r\beta_m l j F_8^{rmki}F_8^{gnlj}\} \tag{A13}$$

where

$$F_1^{ij} \equiv 2\int_0^1 \cos i\pi s \cos j\pi s ds \tag{A14}$$

$$F_2^{ij} \equiv 2\int_0^1 \sin i\pi s \sin j\pi s ds \tag{A15}$$

$$F_3^{ijk} \equiv 4\int_0^1 \cos i\pi s \cos j\pi s \cos k\pi s ds \tag{A16}$$

$$F_4^{ijk} \equiv 4\int_0^1 \sin i\pi s \sin j\pi s \cos k\pi s ds \tag{A17}$$

$$F_5^{ijk} \equiv 2\pi\int_0^1 \sin i\pi s \cos j\pi s \cos k\pi s ds \tag{A18}$$

$$F_6^{ijk} \equiv 2\pi\int_0^1 \sin i\pi s \sin j\pi s \sin k\pi s ds \tag{A19}$$

$$F_7^{ijkl} \equiv 8\int_0^1 \cos i\pi s \cos j\pi s \cos k\pi s \cos l\pi s ds \tag{A20}$$

$$F_8^{ijkl} \equiv 8\int_0^1 \sin i\pi s \sin j\pi s \cos k\pi s \cos l\pi s ds \tag{A21}$$

$$F_9^{ijkl} \equiv 8\int_0^1 \sin i\pi s \sin j\pi s \sin k\pi s \sin l\pi s ds. \tag{A22}$$

Downloaded 03 May 2010 to 171.66.16.245. Redistribution subject to ASME license or copyright; see http://www.asme.org/terms/Terms_Use.cfm

On Axisymmetric Residual Stresses in Tubes With Longitudinally Nonuniform Stress Distribution

T. Nishimura
Professor,
Department of Mechanical Engineering,
Tokyo Metropolitan College,
Higashiohi 1-10-40, Shinagawa-ku,
Tokyo 140, Japan

New equations for calculating residual stress distribution are derived from the theory of elasticity for tubes. The initial distribution of the stresses including the shearing stress is computed from longitudinal distributions of residual stresses measured by the X-ray methods at the surface after removal of successive concentric layers of material. For example, the residual stresses of a steel tube quenched in water were measured by the X-ray diffraction method. The new method was also applied to a short tube with hypothetical residual stress distribution. An alternative finite element analysis was made for a verification. The residual stresses computed by finite element modeling agreed well with the hypothetical residual stresses measured. This shows that good results can be expected from the new method. The equations can also be used for bars by simple modification.

Introduction

Determination of subsurface residual stresses requires removal of material in the present state of practical techniques. This removal of stressed layers induces changes in the stresses and strains in the remaining parts. The total changes depend on all the stresses that were contained in the volume which has been removed up to the radius of interest. A main problem in residual stress analysis is the development of equations relating the true stresses that had existed before the layers were removed to the stresses or strains measured. The equations for calculating residual stresses can be derived from the theory of elasticity. The Sachs method (Sachs, 1927) and the X-ray diffraction techniques developed by Moore and Evans (1958) have been used to determine axisymmetric residual stresses in a solid and a hollow long cylinder. All these methods have a common assumption that the stress distributions in cylinders are uniform in the longitudinal direction. However, in practice, stress distributions are not always uniform and special methods have to be adopted if these are to be defined.

A determination of nonuniform residual stress distribution in girth welded pipes has been given by Rybicki and Shadley (1986). Ueda and Fukuda (1989) have proposed a method for measurement of three-dimensional residual stresses using inherent strains in welded thick plate. Cheng and Finnie (1986, 1987) have proposed a compliance method based on fracture mechanics for measurement of the hoop or longitudinal residual stresses in cylinders as functions of radius. This simple method may be applied for longitudinally nonuniform residual stresses in the case of the gradient of stress is not too large. These methods involve splitting or cutting steps into small pieces. The repetitive process of separating material makes the chance of introducing new residual stresses (Masubuchi, 1980). The use of chemical etching seems to be justified as a way of eliminating one further possible source of error.

The finite element method can be applied to measurement of residual stress (Ueda et al., 1975). An application of finite element method has been proposed and applied to the measurement of residual stress in the hole drilling method by Schajer (1981, 1988), Rybicki and Shadley, referred to previously, have also applied this method. However, it seems that there have been few papers on determination of residual stress by using the finite element method from stresses measured by the X-ray methods. The numerical method has recently become the subject of interest for predictions of the residual stresses in welded or metal-forming parts (Mok and Pick, 1990; Sawamiphakdi et al., 1990). Tomishima and Yada (1990) have reported an application of an inverse analysis boundary element method to estimate residual stresses in a plate. Comparisons with numerical method are described in the following discussion.

This investigation was carried out to develop a new method for the calculations of the axially symmetric and longitudinally nonuniform residual stresses in tubes. The original residual stresses are related to the stresses measured at a surface after

Contributed by the Applied Mechanics Division of THE AMERICAN SOCIETY OF MECHANICAL ENGINEERS for presentation at the First Joint ASCE-EMD, ASME-AMD, SES Meeting, Charlottesville, VA, June 6-9, 1993.

Discussion on this paper should be addressed to the Technical Editor, Professor Lewis T. Wheeler, Department of Mechanical Engineering, University of Houston, Houston, TX 77204-4792, and will be accepted until four months after final publication of the paper itself in the ASME JOURNAL OF APPLIED MECHANICS.

Manuscript received by the ASME Applied Mechanics Division, July 26, 1990; final revision, May 19, 1992. Associate Technical Editor: M. E. Fourney.

Paper No. 93-APM-24.

Copyright © 1993 by ASME
Downloaded 03 May 2010 to 171.66.16.245. Redistribution subject to ASME license or copyright; see http://www.asme.org/terms/Terms_Use.cfm

removing some layers of material in these equations. The X-ray diffraction techniques can be used to measure the residual stresses at a surface. There are certain well-known fundamental limitations, such as excessively large grain size and the effects of sever plastic deformation, that detract from universal acceptance of the technique. Major sources of experimental error in X-ray diffraction residual stress measurement, both random and systematic, have been discussed by Prevey (1981). Random error in the X-ray stress measurement has been analyzed statistically by Kurita (1988). Mainly because of elastic anisotropy of crystals in a textured material, the application of this technique on severely cold-rolled metals can increase the error. Hauk (1986) and Hanabusa et al. (1991) have described calibration procedures on textured materials. The stress determined by X-ray diffraction is the arithmetic average stress in the volume of material defined by the area irradiated on the surface and the depth of penetration. The mean X-ray penetration depth is not constant with the angle (ψ) of inclination of the sample, so that a problem may be found when there are large stress gradient with depth. This difficulty has been overcome by Christenson (1960). It is known that the error remains small in general engineering practice (Maeder et al., 1981). In a majority of manufacturing processes, such as machining, grinding, welding, heat treating and shot peening, the X-ray is accurate. A brief evaluation is made to the effect of random measurement errors on the calculated stresses.

Examples are shown for longitudinally nonuniform residual stress distributions in tubes. The residual stresses at a surface were measured by the X-ray diffraction techniques. The original distribution of residual stresses were numerically calculated by a computer, based on the longitudinal distribution of residual stresses at the surfaces after removal of each layer. The results were discussed and compared with the distribution obtained by the conventional method which assumes a longitudinally uniform residual stress distribution.

Theoretical Development

Consider an isotropic and homogeneous hollow cylinder with an outer radius b, inner radius a and length $2h$. Let the z-axis in a $r\theta z$-coordinate system be the axis of the tube. Under condition of axial symmetry and in the absence of body forces, the following equations of equilibrium in a cylindrical coordinates hold for stresses including residual stresses.

$$\frac{\partial \sigma_r}{\partial r}+\frac{\partial \tau_{rz}}{\partial z}+\frac{\sigma_r-\sigma_\theta}{r}=0 \tag{1}$$

$$\frac{\partial \tau_{rz}}{\partial r}+\frac{\tau_{rz}}{r}+\frac{\partial \sigma_z}{\partial z}=0 \tag{2}$$

At the surface of a cylinder, the residual stress $\sigma_r = \tau_{rz} = 0$ and $\partial\tau_{rz}/\partial z = 0$, therefore the Eqs. (1) and (2) reduces to as follows:

$$\frac{\partial \sigma_r}{\partial r}=\frac{\sigma_\theta}{r} \qquad \frac{\partial \tau_{rz}}{\partial r}=-\frac{\partial \sigma_z}{\partial z}.$$

During the removing process, the radius and stresses are changing continuously and these are measured step by step after removing thin layers. Consider the mth step in which the outer radius of the specimen reduces to ρ from b. On removing the surface layer of small thickness $\Delta\rho$, the force, which has been removed from each square unit of surface of remaining cylinder, is the small outward force

$$-\Delta\sigma_r=-\Delta\rho\,\frac{\sigma_{\theta m}}{\rho} \tag{3}$$

$$-\Delta\tau_{rz}=\Delta\rho\,\frac{\partial \sigma_{zm}}{\partial z} \tag{4}$$

where $\sigma_{\theta m}$ and σ_{zm} are circumferential and longitudinal measured stresses at the side surface of radius ρ.

Consider a cylinder with an outer radius ρ and inner radius a and length $2h$. Suitable boundary conditions in this residual stress analysis are expressed as follows:

$$\left.\begin{aligned}
&\bar\sigma_r=\bar\tau_{rz}=0 && \text{for } r=a\\
&\bar\sigma_r=p_0+\sum_{n=1}^{\infty}p_n\cos\beta_n z+\sum_{n=1}^{\infty}p_n'\sin\beta_n z && \text{for } r=\rho\\
&\bar\tau_{rz}=\sum_{n=1}^{\infty}s_n\cos\beta_n z+\sum_{n=1}^{\infty}s_n'\sin\beta_n z && \text{for } r=\rho\\
&\bar\sigma_z=\bar\tau_{rz}=0 && \text{for } z=\pm h
\end{aligned}\right\} \tag{5}$$

where, $\beta_n = n\pi/h$ ($n = 1, 2, 3, \ldots$), p_0, p_n, p_n', s_n and s_n' are coefficients of Fourier series. Symbols $\bar\sigma$ and $\bar\tau$ represent the stresses induced by external forces, in this analysis. The stress distribution of a hollow cylinder of finite length subjected to arbitrary axisymmetric external forces has been derived by Shibahara and Oda (1968). Their stress function satisfying the boundary conditions (5) is

$$\begin{aligned}
\phi=&A_0\frac{Z^3}{6}+B_0 z\ln r+C_0\frac{zr^2}{2}+\sum_{n=1}^{\infty}\frac{1}{\beta_n^3}\\
&\times(A_nI_{0r}+B_n\beta_n rI_{1r}+C_nK_{0r}+D_n\beta_n rK_{1r})\sin\beta_n z\\
&-\sum_{n=1}^{\infty}\frac{1}{\beta_n^3}(A_n'I_{0r}+B_n'\beta_n rI_{1r}+C_n'K_{0r}+D_n'\beta_n rK_{1r})\cos\beta_n z\\
&+\sum_{s=1}^{\infty}\frac{1}{\gamma_s^3}(E_s\sinh\gamma_s z+F_s\gamma_s z\cosh\gamma_s z+G_s\cosh\gamma_s z\\
&+H_s\gamma_s z\sinh\gamma_s z)Z_0(\gamma_s r)
\end{aligned} \tag{6}$$

where, A_0, B_0, C_0, A_n, B_n, C_n, D_n, A_n', B_n', C_n', D_n', E_s, F_s, G_s, and H_s are arbitrary constants. I_{0r}, I_{1r}, K_{0r} and K_{1r} are $I_0(\beta_n r)$, $I_1(\beta_n r)$, $K_0(\beta_n r)$ and $K_1(\beta_n r)$, respectively. I_0 and I_1 are modified Bessel functions of first kind, zeroth, and first orders, respectively. J_0 and J_1 are Bessel functions of first kind, zeroth and first orders, respectively. K_0, K_1 are modified Bessel functions of second kind, zeroth, and first orders, respectively. Y_0 and Y_1 are Bessel functions of second kind, zeroth, and first orders, respectively. $Z_i(\gamma_s r)$ is defined by the following equation:

$$Z_i(\gamma_s r)=J_i(\gamma_s r)-J_1(\gamma_s\rho)\,\frac{Y_i(\gamma_s r)}{Y_1(\gamma_s\rho)} \quad (i=0,1).$$

Symbol $\gamma_s = \lambda_s/a$ and λ_s is the sth real root satisfying $Z_1(\lambda_s a) = 0$.

The stress components in terms of the stress function are

$$\left.\begin{aligned}
&\sigma_r=\frac{\partial}{\partial z}\left[\nu\nabla^2\phi-\frac{\partial^2\phi}{\partial r^2}\right] && \sigma_\theta=\frac{\partial}{\partial z}\left[\nu\nabla^2\phi-\frac{1}{r}\frac{\partial\phi}{\partial r}\right]\\
&\sigma_z=\frac{\partial}{\partial z}\left[(2-\nu)\nabla^2\phi-\frac{\partial^2\phi}{\partial z^2}\right] && \tau_{rz}=\frac{\partial}{\partial r}\left[(1-\nu)\nabla^2\phi-\frac{\partial^2\phi}{\partial z^2}\right]
\end{aligned}\right\} \tag{7}$$

The symbol ∇^2 is Laplace's operator in cylindrical coordinates, and ν is Poisson's ratio. Arbitrary constants A_0, B_0, C_0, A_n, B_n, C_n, D_n, . . , E_s, etc. of Eq. (6) are determined from the boundary conditions (5) as follows:

$$A_0\nu+\frac{B_0}{a^2}-C_0(1-2\nu)=0, \quad \nu A_0+\frac{B_0}{\rho^2}-C_0(1-2\nu)=p_0,$$

$$A_0(1-\nu)+C_0 2(2-\nu)=\sum_{n=1}^{\infty}\frac{2(-1)^{n+1}}{(\rho^2-a^2)\beta_n}\rho s_n',$$

$$E_s\sinh\gamma_s h=-F_s(2\nu\sinh\gamma_s h+\gamma_s h\cosh\gamma_s h),$$

$$G_s\sinh\gamma_s h=H_s\{(1-2\nu)\sinh\gamma_s h-\gamma_s h\cosh\gamma_s h\},$$

Downloaded 03 May 2010 to 171.66.16.245. Redistribution subject to ASME license or copyright; see http://www.asme.org/terms/Terms_Use.cfm

$$A_nI_{1a}+B_n[2(1-\nu)I_{1a}+\beta_naI_{0a}]$$
$$-C_nK_{1a}+D_n[2(1-\nu)K_{1a}-\beta_naK_{0a}]=0,$$
$$A_n'I_{1a}+B_n'[2(1-\nu)I_{1a}+\beta_naI_{0a}]$$
$$-C_n'K_{1a}+D_n'[2(1-\nu)K_{1a}-\beta_naK_{0a}]=0,$$
$$A_nI_{1\rho}+B_n[2(1-\nu)I_{1\rho}+\beta_n\rho I_{0\rho}]$$
$$-C_nK_{1\rho}+D_n[2(1-\nu)K_{1\rho}-\beta_n\rho K_{0\rho}]=s_n',$$
$$A_n'I_{1\rho}+B_n'[2(1-\nu)I_{1\rho}+\beta_n\rho I_{0\rho}]$$
$$-C_n'K_{1\rho}+D_n'[2(1-\nu)K_{1\rho}-\beta_n\rho K_{0\rho}]=-s_n,$$
$$A_n\left(I_{0a}-\frac{I_{1a}}{\beta_na}\right)+B_n[(1-2\nu)I_{0a}+\beta_naI_{1a}]$$
$$+C_n\left(K_{0a}+\frac{K_{1a}}{\beta_na}\right)-D_n[(1-2\nu)K_{0a}-\beta_naK_{1a}]$$
$$=\sum_{s=1}^{\infty}F_s\frac{(-1)^n4\beta_n^2\gamma_sZ_0(\gamma_sa)}{(\beta_n^2+\gamma_s^2)^2}\cdot\frac{\sinh\gamma_sh}{h},$$
$$A_n'\left(I_{0a}-\frac{I_{1a}}{\beta_na}\right)+B_n'[(1-2\nu)I_{0a}+\beta_naI_{1a}]$$
$$+C_n'\left(K_{0a}+\frac{K_{1a}}{\beta_na}\right)-D_n'[(1-2\nu)K_{0a}-\beta_naK_{1a}]$$
$$=\sum_{s=1}^{\infty}H_s\frac{(-1)^{n+1}4\beta_n^3Z_0(\gamma_sa)}{(\beta_n^2+\gamma_s^2)^2}\cdot\frac{\sinh\gamma_sh}{h},$$
$$A_n\left(I_{0\rho}-\frac{I_{1\rho}}{\beta_n\rho}\right)+B_n[(1-2\nu)I_{0\rho}+\beta_n\rho I_{1\rho}]$$
$$+C_n\left(K_{0\rho}+\frac{K_{1\rho}}{\beta_n\rho}\right)-D_n[(1-2\nu)K_{0\rho}-\beta_n\rho K_{1\rho}]$$
$$=-p_n+\sum_{s=1}^{\infty}F_s\frac{(-1)^n4\beta_n^2\gamma_sZ_0(\gamma_s\rho)}{(\beta_n^2+\gamma_s^2)^2}\cdot\frac{\sinh\gamma_sh}{h},$$
$$A_n'\left(I_{0\rho}-\frac{I_{1\rho}}{\beta_n\rho}\right)+B_n'[(1-2\nu)I_{0\rho}+\beta_n\rho I_{1\rho}]$$
$$+C_n'\left(K_{0\rho}+\frac{K_{1\rho}}{\beta_n\rho}\right)-D_n'[(1-2\nu)K_{0\rho}-\beta_n\rho K_{1\rho}]$$
$$=-p_n'+\sum_{s=1}^{\infty}H_s\frac{(-1)^{n+1}4\beta_n^3Z_0(\gamma_s\rho)}{(\beta_n^2+\gamma_s^2)^2}\cdot\frac{\sinh\gamma_sh}{h},$$
$$\sum_{n=1}^{\infty}\frac{(-1)^n2\beta_n\gamma_s^2}{(\beta_n^2+\gamma_s^2)^2}\left\{s_n'\frac{\beta_n^2+\gamma_s^2}{2\gamma_s^2}\rho Z_0(\gamma_s\rho)\right.$$
$$+B_n[\rho I_{1\rho}Z_0(\gamma_s\rho)-\alpha I_{1a}Z_0(\gamma_sa)]$$
$$\left.+D_n[\rho K_{1\rho}Z_0(\gamma_s\rho)-\alpha K_{1a}Z_0(\gamma_sa)]\right\}$$
$$=-F_s\frac{\Omega_s}{2\sinh\gamma_sh}[\rho^2Z_0^2(\gamma_s\rho)-\alpha^2Z_0^2(\gamma_sa)],$$
$$\sum_{n=1}^{\infty}\frac{(-1)^n2\beta_n^2\gamma_s}{(\beta_n^2+\gamma_s^2)^2}\left\{s_n\frac{\beta_n^2+\gamma_s^2}{2\gamma_s^2}\rho Z_0(\gamma_s\rho)\right.$$
$$+B_n'[\rho I_{1\rho}Z_0(\gamma_s\rho)-aI_{1a}Z_0(\gamma_sa)]$$
$$\left.+D_n'[\rho K_{1\rho}Z_0(\gamma_s\rho)-aK_{1a}Z_0(\gamma_sa)]\right\}$$
$$=H_s\frac{\Omega_s'}{2\sinh\gamma_sh}[\rho^2Z_0^2(\gamma_s\rho)-\alpha^2Z_0^2(\gamma_sa)] \quad (8)$$

where $\Omega_s=\sinh\gamma_sh\cosh\gamma_sh+\gamma_sh$, $\Omega_s'=\sinh\gamma_sh\cosh\gamma_sh-\gamma_sh$.

Now imagine removing the mth layer of thickness $\Delta\rho$ with stresses $\sigma_{\theta m}$ and σ_{zm}. The remaining cylinder subject to the external forces $-\Delta\sigma_r$ and $\Delta\tau_{rz}$. The boundary conditions (5) can be related to the measured stresses by Eqs. (3) and (4).

$$\left.\begin{aligned}\Delta p_0+\sum_{n=1}^{\infty}\Delta p_n\cos\beta_nz+\sum_{n=1}^{\infty}\Delta p_n'\sin\beta_nz&=-\frac{\sigma_{\theta m}}{\rho}\Delta\rho,\\ \sum_{n=1}^{\infty}\Delta s_n\cos\beta_nz+\sum_{n=1}^{\infty}\Delta s_n'\sin\beta_nz&=\frac{\partial\sigma_{zm}}{\partial z}\Delta\rho\end{aligned}\right\} \quad (9)$$

The coefficients of these Fourier series can be obtained in the usual manner.

$$\left.\begin{aligned}\Delta p_0=-\frac{\Delta\rho}{2h\rho}\int_{-h}^{h}\sigma_{\theta m}dz,\quad \Delta p_n=-\frac{\Delta\rho}{h\rho}\int_{-h}^{h}\sigma_{\theta m}\cos\beta_nzdz,\\ \Delta p_n'=-\frac{\Delta\rho}{h\rho}\int_{-h}^{h}\sigma_{\theta m}\sin\beta_nzdz,\\ \Delta s_n=\frac{\Delta\rho\beta_n}{h}\int_{-h}^{h}\sigma_{zm}\sin\beta_nzdz,\\ \Delta s_n'=-\frac{\Delta\rho\beta_n}{h}\int_{-h}^{h}\sigma_{zm}\cos\beta_nzdz\end{aligned}\right\} \quad (10)$$

Substituting the coefficients of the series into simultaneous Eqs. (8), the arbitrary constants A_0, B_0, C_0, . . , and H_s can be expressed in terms of the measured stresses. The small stress changes caused by the removal of the thin layers can be derived from Eq. (7). The total stress changes which are caused by the removal of outer-surface layers from radius b to radius ρ, can be obtained by summing the small stress changes, as functions of r, z, and ρ. Supposing the thickness $\Delta\rho$ tends to zero, these can be expressed by integrating the stress changes. In this integration, it is required that the arbitrary constants and the real roots satisfying $Z_1(\lambda_sa)=0$ mentioned previously are defined as functions of the integral variable. In this analysis, it is assumed that the deformation due to removal of layers of material is elastic. If $\sigma_{\theta m}$ and σ_{zm} are the stresses measured by the X-ray diffraction techniques at a surface of a tube after removal with an outer radius $\rho(a<\rho<b)$. We find the following final expressions:

$$\sigma_r=\int d\bar{\sigma}_r=\left(1-\frac{a^2}{\rho^2}\right)\int_{\rho}^{b}\frac{\rho^2}{\rho^2-a^2}dp_0-\sum_{n=1}^{\infty}\int_{\rho}^{b}d\{A_n\left(I_{0\rho}-\frac{I_{1\rho}}{\beta_n\rho}\right)$$
$$+B_n[(1-2\nu)I_{0\rho}+\beta_n\rho I_{1\rho}]$$
$$+C_n\left(K_{0\rho}+\frac{K_{1\rho}}{\beta_n\rho}\right)-D_n[(1-2\nu)K_{0\rho}-\beta_n\rho K_{1\rho}]\}\cos\beta_nz$$
$$-\sum_{n=1}^{\infty}\int_{\rho}^{b}d\{A_n'\left(I_{0\rho}-\frac{I_{1\rho}}{\beta_n\rho}\right)+B_n'[(1-2\nu)I_{0\rho}$$
$$+\beta_n\rho I_{1\rho}]+C_n'\left(K_{0\rho}+\frac{K_{1r}}{\beta_n\rho}\right)$$
$$-D_n'[(1-2\nu)K_{0\rho}-\beta_n\rho K_{1\rho}]\}\sin\beta_nz$$
$$+\sum_{s=1}^{\infty}\int_{\rho}^{b}d\{E_s\cosh\gamma_sz+F_s[(1+2\nu)\cosh\gamma_sz$$
$$+\gamma_sz\sinh\gamma_sz]+G_s\sinh\gamma_sz+H_s[(1+2\nu)\sinh\gamma_sz$$
$$+\gamma_sz\cosh\gamma_sz]\}Z_0(\gamma_s\rho)$$
$$-\sum_{s=1}^{\infty}\int_{\rho}^{b}d\{E_s\cosh\gamma_sz+F_s(\cosh\gamma_sz+\gamma_sz\sinh\gamma_sz)$$
$$+G_s\sinh\gamma_sz+H_s(\sinh\gamma_sz+\gamma_sz\cosh\gamma_sz)\}\frac{Z_1(\gamma_z\rho)}{\gamma_s\rho} \quad (11)$$

Downloaded 03 May 2010 to 171.66.16.245. Redistribution subject to ASME license or copyright; see http://www.asme.org/terms/Terms_Use.cfm

$$\sigma_\theta = \sigma_{\theta m} + \int d\bar{\sigma}_\theta = \sigma_{\theta m} + \left(1+\frac{a^2}{\rho^2}\right)\int_\rho^b \frac{\rho^2}{\rho^2-a^2}\,dp_0$$
$$-\sum_{n=1}^{\infty}\int_\rho^b d\Big[A_n\frac{I_{1\rho}}{\beta_n\rho}+B_n(1-2\nu)I_{0\rho}-C_n\frac{K_{1\rho}}{\beta_n\rho}$$
$$-D_n(1-2\nu)K_{0\rho}\Big]\cos\beta_n z$$
$$-\sum_{n=1}^{\infty}\int_\rho^b d\Big[A_n'\frac{I_{1\rho}}{\beta_n\rho}+B_n'(1-2\nu)I_{0\rho}-C_n'\frac{K_{1\rho}}{\beta_n\rho}$$
$$-D_n'(1-2\nu)K_{0\rho}\Big]\sin\beta_n z+2\nu\sum_{s=1}^{\infty}\int_\rho^b d(F_s\cosh\gamma_s z$$
$$+H_s\sinh\gamma_s z)Z_0(\gamma_s\rho)+\sum_{s=1}^{\infty}\int_\rho^b\{E_s\cosh\gamma_s z+F_s(\cosh\gamma_s z$$
$$+\gamma_s z\sinh\gamma_s z)+G_s\sinh\gamma_s z$$
$$+H_s(\sinh\gamma_s z+\gamma_s z\cosh\gamma_s z)\}\frac{Z_1(\gamma_s\rho)}{\gamma_s\rho} \quad (12)$$

$$\sigma_z = \sigma_{zm} + \int d\bar{\sigma}_z = \sigma_{zm} + 2\sum_{n=1}^{\infty}\int_\rho^b \frac{(-1)^{n+1}\rho}{(\rho^2-a^2)\beta_n}\,ds_n'$$
$$+\sum_{n=1}^{\infty}\int_\rho^b d\{A_nI_{0\rho}+B_n[2(2-\nu)I_{0\rho}+\beta_n\rho I_{1\rho}]$$
$$+C_nK_{0\rho}-D_n[2(2-\nu)K_{0\rho}-\beta_n\rho K_{1\rho}]\}\cos\beta_n z$$
$$+\sum_{n=1}^{\infty}\int_\rho^b d\{A_n'I_{0\rho}+B_n'[2(2-\nu)I_{0\rho}+\beta_n\rho I_{1\rho}]+C_n'K_{0\rho}$$
$$-D_n'[2(2-\nu)K_{0\rho}-\beta_n\rho K_{1\rho}]\}\sin\beta_n z-\sum_{s=1}^{\infty}\int_\rho^b d\{E_s\cosh\gamma_s z$$
$$-F_s[(1-2\nu)\cosh\gamma_s z-\gamma_s z\sinh\gamma_s z]+G_s\sinh\gamma_s z$$
$$-H_s[(1-2\nu)\sinh\gamma_s z-\gamma_s z\cosh\gamma_s z]\}Z_0(\gamma_s\rho) \quad (13)$$

$$\tau_{rz} = \int d\bar{\tau}_{rz} = \sum_{n=1}^{\infty}\int_\rho^b d\{A_nI_{1\rho}+B_n[2(1-\nu)I_{1\rho}+\beta_n\rho I_{0\rho}]$$
$$-C_nK_{1\rho}+D_n[2(1-\nu)K_{1\rho}-\beta_n\rho K_{0\rho}]\}\sin\beta_n z$$
$$-\sum_{n=1}^{\infty}\int_\rho^b d\{A_n'I_{1\rho}+B_n'[2(1-\nu)I_{1\rho}+\beta_n\rho I_{0\rho}]-C_n'K_{1\rho}$$
$$+D_n'[2(1-\nu)K_{1\rho}-\beta_n\rho K_{0\rho}]\}\cos\beta_n z+\sum_{s=1}^{\infty}\int_\rho^b d[E_s\sinh\gamma_s z$$
$$+F_s(2\nu\sinh\gamma_s z+\gamma_s z\cosh\gamma_s z)+G_s\cosh\gamma_s z$$
$$+H_s(2\nu\cosh\gamma_s z+\gamma_s z\sinh\gamma_s z)]Z_1(\gamma_s\rho). \quad (14)$$

In long hollow cylinders with longitudinally uniform stress distribution, the above equations can be rearranged as follows. For this stress field, it can be assumed that the residual stresses σ_r, σ_θ and σ_z are functions of r (or ρ) alone in most of the tube except in the vicinity of ends. If $\sigma_{\theta m}$ and σ_{zm} are represented by a Fourier cosine series, $\Delta p_n' = \Delta s_n' = 0$ holds. The stress components are independent of z in most of the tube. Therefore, the arbitrary constants of Eqs. (8) can be negligible except A_0, B_0 and C_0. The above formulas can be simplified by using $\Delta p_0 = -(\sigma_{\theta m}/\rho)\Delta\rho$ which comes from the first of Eq. (10). The Eqs. (11) and (12) reduce to

$$\sigma_r = -\left(1-\frac{a^2}{\rho^2}\right)\int_\rho^b \frac{\rho\sigma_{\theta m}}{\rho^2-a^2}\,d\rho \quad (15)$$

$$\sigma_\theta = \sigma_{\theta m} - \left(1+\frac{a^2}{\rho^2}\right)\int_\rho^b \frac{\rho\sigma_{\theta m}}{\rho^2-a^2}\,d\rho. \quad (16)$$

By using the final equation of Eq. (10), and by applying the formula for the basic Fourier sine series corresponding to the function $f(x) = x\ (-\pi < x < \pi)$, Eq. (12) becomes as follows:

$$\sigma_z = \sigma_{zm} - 2\int_\rho^b \frac{\rho}{\rho^2-a^2}\frac{1}{h}\sum_{n=1}^{\infty}2(-1)^{n-1}\left(\int_0^{h'}\sigma_{zm}\cos\beta_n z\,dz\right.$$
$$\left.+\int_{h'}^{h}\sigma_{zm}\cos\beta_n z\,dz\right)d\rho = \sigma_{zm} - 2\int_\rho^b \frac{\rho}{\rho^2-a^2}\frac{2}{h}$$
$$\times\sum_{n=1}^{\infty}(-1)^{n-1}\left[\sigma_{zm}\frac{\sin(n\pi h'/h)}{n\pi/h}\right.$$
$$\left.+\int_{h'}^{h}\sigma_{zm}\cos\beta_n z\,dz\right]d\rho \simeq \sigma_{zm} - 2\int_\rho^b \frac{\rho\sigma_{zm}}{\rho^2-a^2}\,d\rho \quad (17)$$

where, h' ($\simeq h$) is length in which the stresses have uniform distribution in the longitudinal direction. Equations (15), (16), and (17) are equal to the conventional equations developed by Moore and Evans.

By putting $a = B_0 = C_n = D_n = C_n' = D_n' = 0$ and $Z_i(\gamma_s r) = J_i(\gamma_s r)$ into the above equations, we obtain the formulas for a solid cylinder.

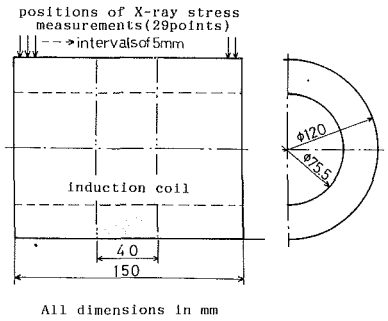


Fig. 1 Shape of the specimen and locations measured by the X-rays

Experiments and Results

Example 1. An experiment was carried out with a tube which had longitudinally nonuniform residual stress distribution. The material used was a JIS S45C (AISI 1045) steel. A tube with an outer diameter 120 mm, inner diameter 75.5 mm and length 150 mm was machined from a commercial steel tube. After machining, the tube was annealed in air at 973 K for 2 hours. This tube was heated to 973 K by an induction coil and quenched in water, and the quenched scale was chemically removed.

The longitudinal distribution of residual stresses was measured by the X-ray diffraction technique at each surface after removing thin concentric layers from the tube. The layers were removed 25 times and total depth of removal was 6.3 mm. The longitudinal and circumferential residual stresses were measured at 29 positions, by equal intervals of 5 mm in the longitudinal direction. The etching solution was commercial chemical polishing liquid and the inner and end surfaces of the specimen were protected by vinyl tape. The shape of the specimen and locations measured by the X-ray diffraction method are shown in Fig. 1.

Residual stress was measured by a parallel beam X-ray diffractometer with a scintillation counter. The conditions of the X-ray stress measurements are shown in Table 1.

The distributions of the longitudinal and circumferential stresses measured are shown in Figs. 2 and 3, respectively. Each figure shows a plot of the residual stress as a function of radius and longitudinal position. The measured stresses at shown every four removals in these figures for simplicity. In

Downloaded 03 May 2010 to 171.66.16.245. Redistribution subject to ASME license or copyright; see http://www.asme.org/terms/Terms_Use.cfm

Table 1 Conditions for X-ray stress measurements

Characteristic X-rays	Cr-kα
Diffraction plane	α-Fe(211)
Fillter	Vanadium foil
Stress determination	$\sin^2\psi$ method
Irradiated area	2×4mm²
Tube voltage and current	30Kv, 8mA
Scan condition of 2θ	Step scanning
Divergence angle of slit	1.0°
Peak determination	Half value width method

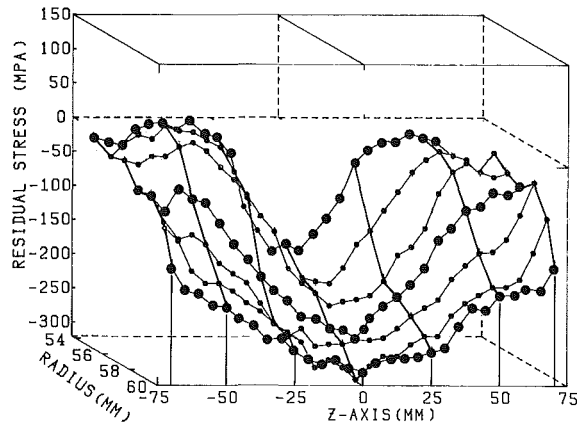


Fig. 2 Axial distributions of longitudinal residual stress at surfaces after removal of some layers of induction quenched tube. Values shown by symbols are measured using X-ray methods. Stress data at the three radii 60, 57.3, and 54 mm are shown solid circles.

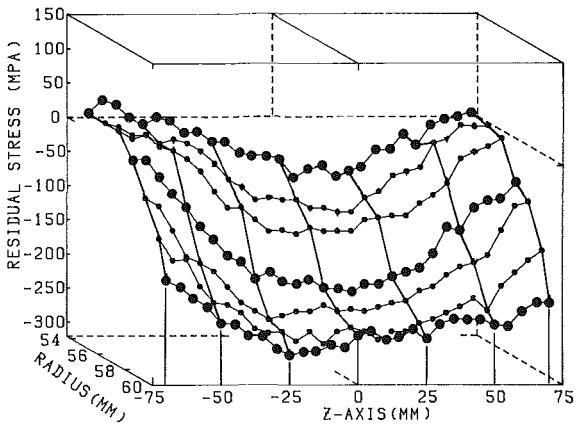


Fig. 3 Axial distributions of circumferential residual stress at surfaces after removal of some layers of the tube. Values shown by symbols are measured using X-ray methods. Stress data at the three radii 60, 57.3, and 54 mm are shown solid circles.

these figures, the 68.3 percent confidence intervals of the measured stresses were within ±10 MPa. The difference of measured stresses at four positions, circumferentially 90 deg apart were within the range of ±10 MPa. The measured stresses at radii 60 mm, 57.3 mm and 54 mm are denoted by the solid circles to which special attention should be paid. Figures 2 and 3 show clearly that longitudinal distributions are not uniform, and the true residual stress distribution cannot be obtained by using the conventional method.

By using the proposed equations, the original distributions of the residual stresses were calculated. The calculations of residual stresses from the observed longitudinal distributions

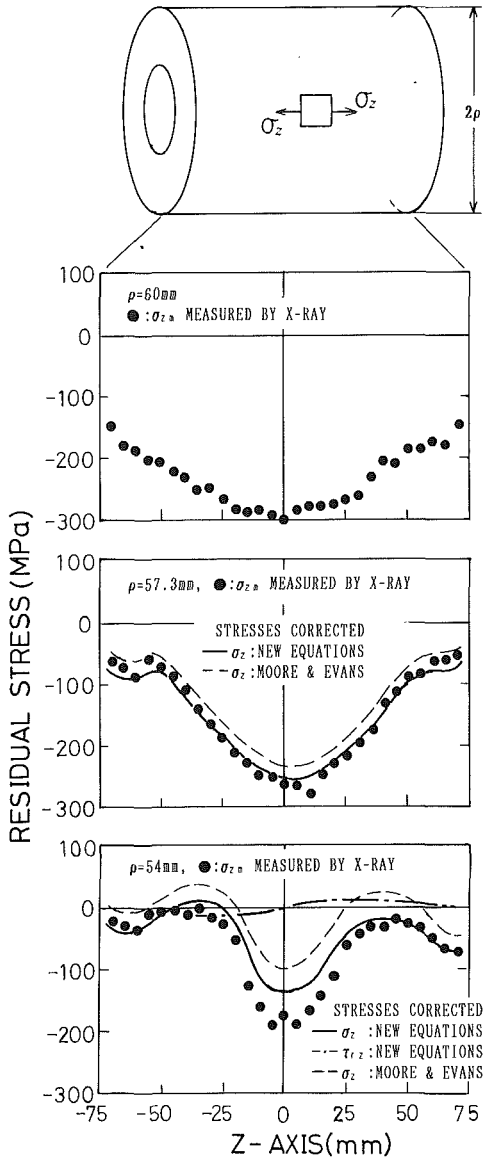


Fig. 4 Axial distributions of longitudinal and shearing residual stresses at the corresponding radii 60, 57.3, and 54 mm. Values shown by solid circles are longitudinal stresses measured using X-ray methods. Solid lines and dashed-and-dotted line represent the corrected longitudinal and shearing stresses, respectively, by the new method. Dashed lines represent the corrected longitudinal stresses by the conventional method.

were made by a computer. Its input data consisted of the observed stresses σ_{zm}, $\sigma_{\theta m}$ and the corresponding radial and the longitudinal positions. The integration for the coefficients of Fourier series expressed by Eq. (10) was computed by using Simpson's rule. Poisson's ratio $\nu = 0.3$ and the number of terms of the series $n = 10, s = 10$ were used in the calculations. The number of terms used in the calculation might affect the results, but the changes were slight, with n or s chosen between 6 to 12. The variation was smaller than 1.0 percent in this case.

When stress distributions are not uniform, new method must be adopted if these are to be determined. Such methods may involve the modification of a standard technique. Figure 4 shows measured longitudinal stresses and corrected results obtained by using the proposed and the conventional equations (Moore and Evans') at the corresponding radii. The measured stresses are marked by the solid circles. The shearing residual distribution at the radius 57.3 mm was less than ±19 MPa. Therefore, the curve was neglected in the figure. Figure 5 shows circumferential stresses and radial stresses in the same manner

Downloaded 03 May 2010 to 171.66.16.245. Redistribution subject to ASME license or copyright; see http://www.asme.org/terms/Terms_Use.cfm

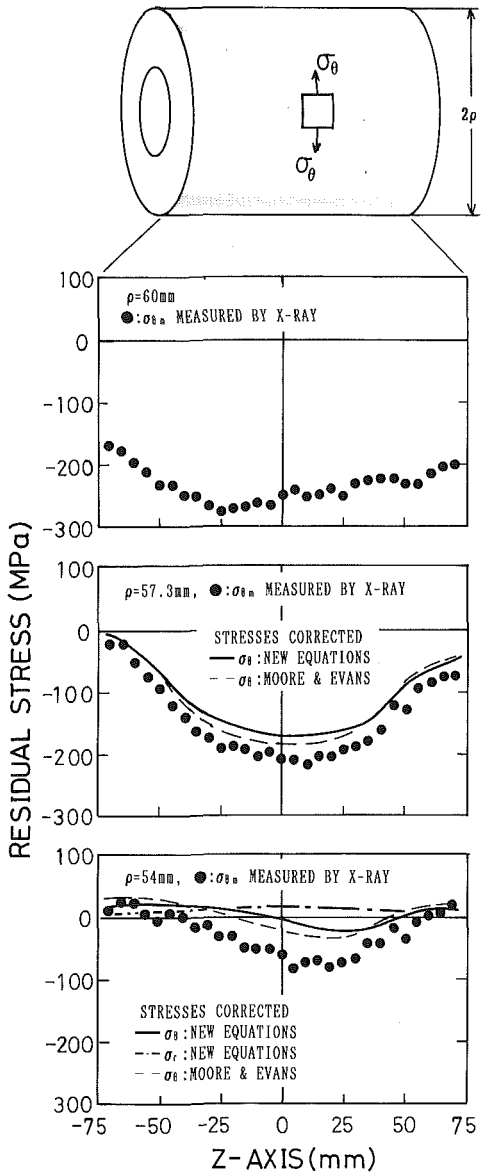


Fig. 5 Axial distribution of circumferential and radial residual stresses at the corresponding radii 60, 57.3, and 54 mm. Values shown by solid circles are circumferential stresses measured using X-ray methods. Solid lines and dashed-and-dotted line represent the corrected circumferential and radial stresses, respectively, by the new method. Dashed lines represent the corrected circumferential stresses by the conventional method.

as mentioned previously. The magnitude of radial stress at radius 57.3 mm is on the order of 3 to 10 MPa.

Figures 4 and 5 show that the values obtained from the new equations are not so different from the ones obtained from the conventional method, in the range of gentle longitudinal gradient of residual stresses or in the little depth.

Example 2. The correction is directly related to the magnitude of the stresses removed and to the depth. In shallow depth, the correction might be neglected, but in greater depth, it becomes increasingly significant. The conventional method can only be applied when it is reasonable to assume that the stress varies through the thickness of a tube but is uniform along the length, while in practice, stress distributions are not always uniform. The following simulation will clarify the effect of longitudinal nonuniformity on the difference in the corrected results. Stresses are assumed to be measured from the outer surface decreasing quadratically to zero at the inner

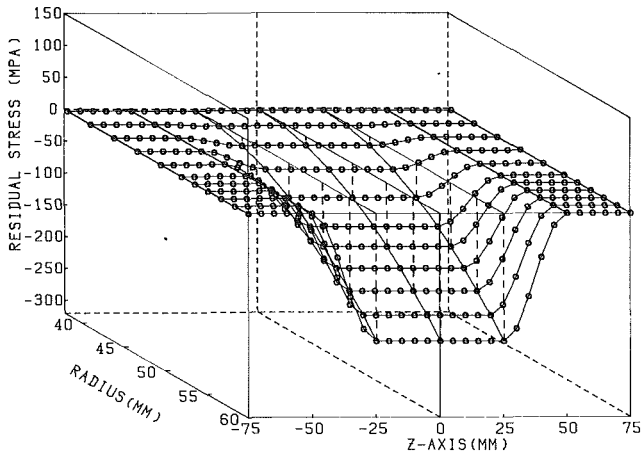


Fig. 6 Hypothetical plots of measured longitudinal residual stress distribution of a tube

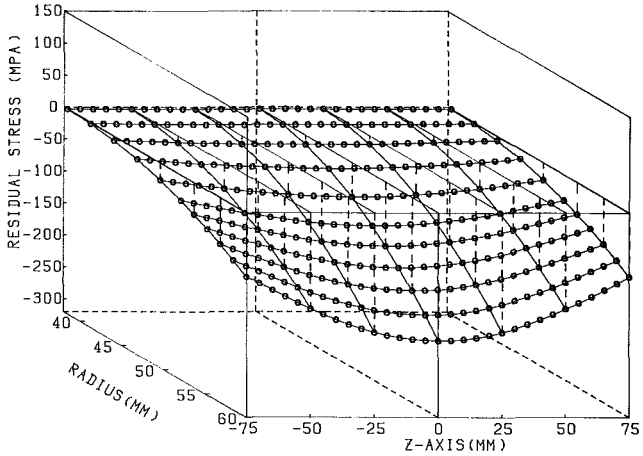


Fig. 7 Hypothetical plots of measured circumferential residual stress distribution of a tube

surface. Residual stress distributions measured at each cylindrical surface of radius ρ are made from hypothetical data which are defined by the following equations:

$$\sigma_{\theta m}(\rho, z) = -\frac{\sigma_{\theta 0}}{2}\left(1+\cos\frac{\pi z}{2h}\right)\left(\frac{\rho-a}{b-a}\right)^2 \quad |z| \leqq h$$

$$\sigma_{zm}(\rho, z) = \begin{cases} -\sigma_{z0}\left(\dfrac{\rho-a}{b-a}\right)^2 & |z| \leqq \dfrac{h}{3} \\ -\dfrac{\sigma_{z0}}{2}\left(1+\cos\dfrac{3\pi z}{h}\right)\left(\dfrac{\rho-a}{b-a}\right)^2 & \dfrac{h}{3} \leqq |z| \leqq \dfrac{2h}{3} \\ 0 & 2h/3 \leqq |z| \leqq h \end{cases}$$

where $\sigma_{\theta 0}$ and σ_{z0} are constants; $\sigma_{\theta 0} = \sigma_{z0} = 200$ MPa was used in this example.

The dimensions of the specimen are the same as the previous experiment. It was assumed that the concentric layers were completely removed from outer radius b to inner radius a, and the thickness of layer $\Delta\rho$ was about $(b - a)/160$. Figure 6 shows hypothetical plots of measured longitudinal residual stress at 31 positions in the longitudinal direction and at 12 positions in the radial direction. Figure 7 shows the measured circumferential residual stress in the same manner as Fig. 6.

The calculations of residual stresses from the hypothetical data were made by a computer in the same manner as the previous example. Poisson's ratio $\nu = 0.3$, $n = s = 15$ were

Downloaded 03 May 2010 to 171.66.16.245. Redistribution subject to ASME license or copyright; see http://www.asme.org/terms/Terms_Use.cfm

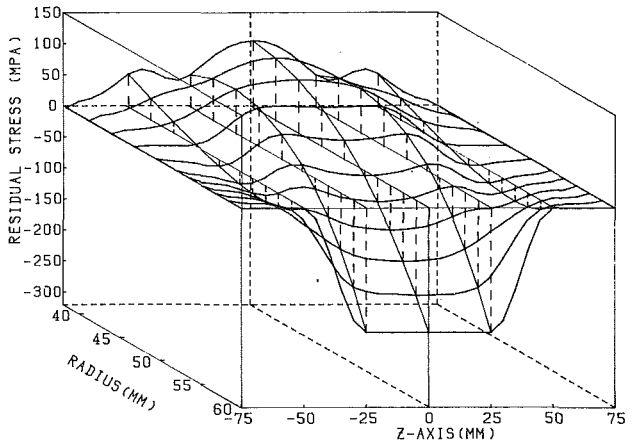


Fig. 8 Original distribution of longitudinal residual stress calculated from the hypothetical data in a tube

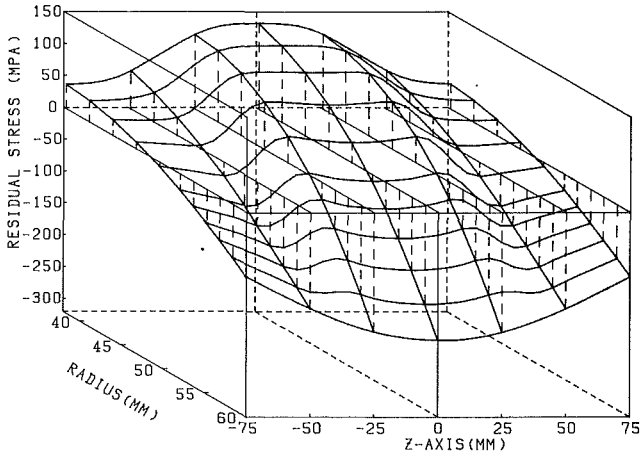


Fig. 10 Original distribution of circumferential residual stress calculated from the hypothetical data in a tube

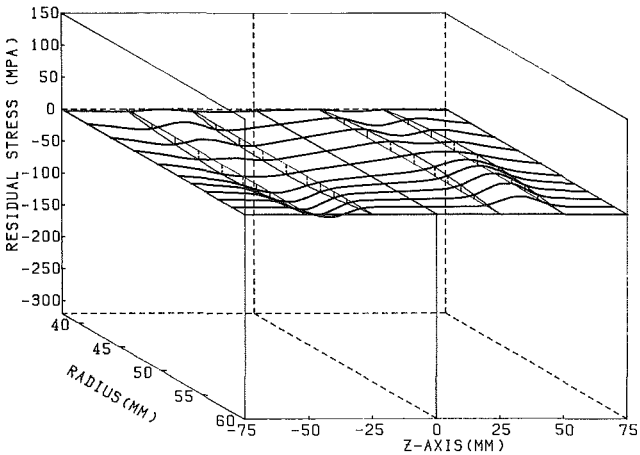


Fig. 9 Original distribution of shearing residual stress calculated from the hypothetical data in a tube

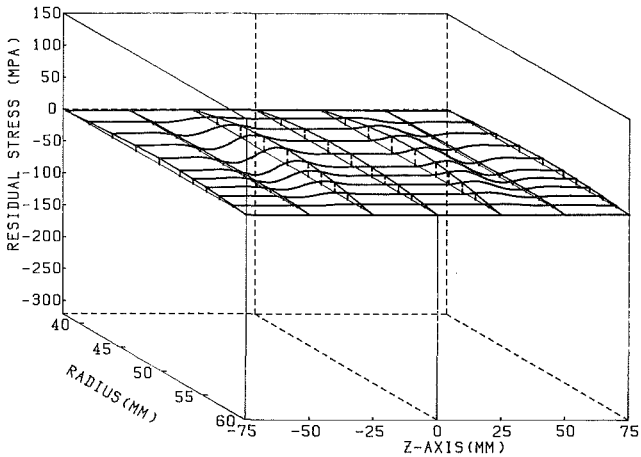


Fig. 11 Original distribution of radial residual stress calculated from the hypothetical data in a tube

used. Figures 8 and 9 show the original longitudinal distributions of the longitudinal and shearing residual stresses, respectively, calculated by using the proposed equations at the corresponding radius. Figure 9 shows the residual shearing stress that exists as a result of the nonuniformity of the longitudinal stresses. The original longitudinal distributions of the circumferential and radial residual stresses obtained from the new method are shown in Figs. 10 and 11.

The longitudinal residual stress corrected by the conventional method is shown in Fig. 12. Figures 13 and 14 show the circumferential and radial residual stresses obtained from the same method.

It is apparent from Figs. 8 through 14 that considerable variance exists in the corrected results regarding the stress patterns. As the radius of the specimen after removal of material decreases, the difference between these two values becomes larger. It should be noted that the shearing and radial residual stresses at the parts where the stress gradients change sharply are greater than those at others.

The Finite Element Model

Verification of any residual stress measurement method is difficult because residual stress distributions in an actual test piece are not known. It is considered that there are two different ways to evaluate the accuracy of a residual stress measurement method. One is an experimental and the other is a numerical. There are no other experimental method that can be applied to the case of this study. A practical way to evaluate a residual stress measurement method is to use a finite element model of the piece. An alternative method was used to verify the results in Figs. 6–11. An axisymmetric finite element analysis of the layer removal process described in Example 2 was carried out. In the present study, the EPIC-4 general-purpose finite element program developed by Yamada and Yokouchi (1980) was employed to simulate the hypothetical measured stress data. On removing up the layers from outer radius b to a radius interest the forces, which have been removed from each square unit of surface of remaining tube, are the original radial and shearing residual stresses that existed in the tube before removing any layer. The removing step was represented by unloading the radial and shearing force distributions from corresponding nodes on the model. The finite element model was selected to represent an outer diameter of 120 mm, inner diameter of 75.5 mm, and length of 150 mm steel tube with the same residual stress distributions and other characteristics. Because of symmetry of residual stress distribution, it is sufficient to consider only one half of axial length. The finite element model of the surface layer removed tube consists of 18 three-node elements in the radial direction and 30 columns of elements in the longitudinal direction. The total number of elements and longitudinal element density were constant in the procedure of all layer removal. The distributions of the longitudinal and circumferential stresses computed from the finite element models at the surface of the remaining tube are shown in Figs. 15 and

Downloaded 03 May 2010 to 171.66.16.245. Redistribution subject to ASME license or copyright; see http://www.asme.org/terms/Terms_Use.cfm

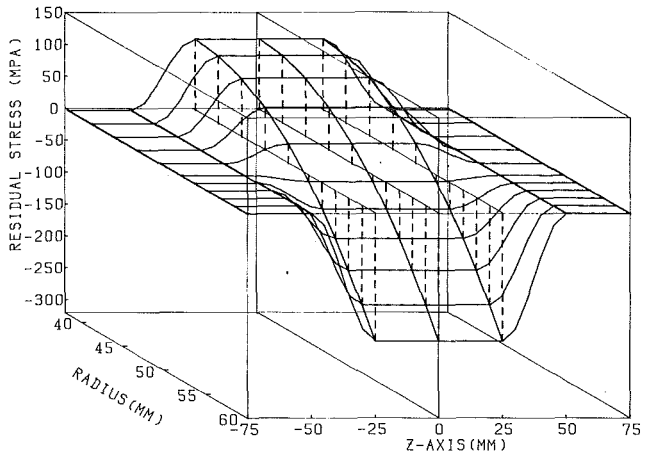


Fig. 12 Corrected longitudinal residual stress distribution by the conventional method in a tube

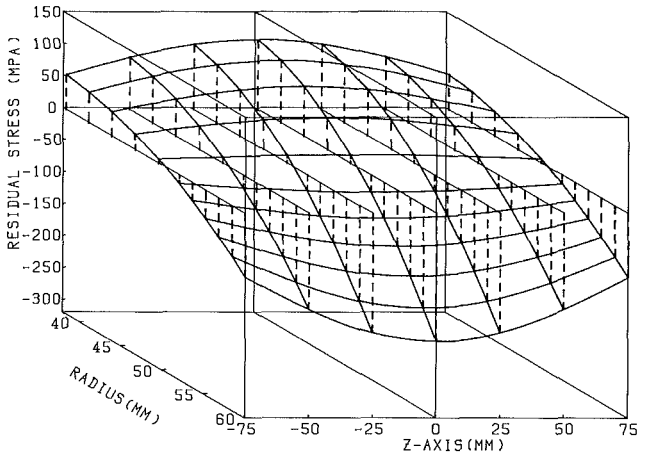


Fig. 13 Corrected circumferential residual stress distribution by the conventional method in a tube

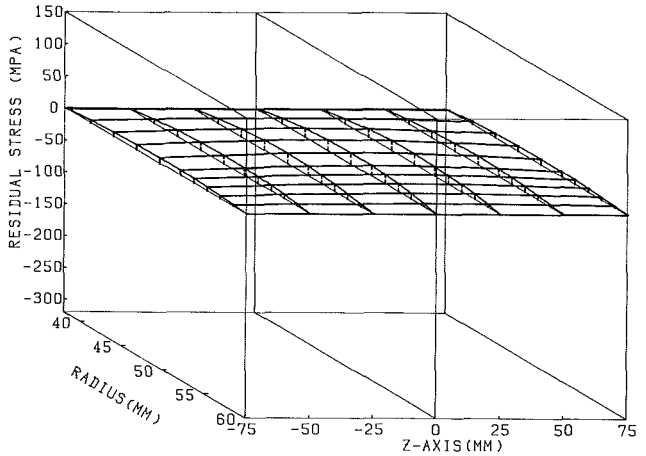


Fig. 14 Corrected radial residual stress distribution by the conventional method in a tube

16, respectively. The residual stress distributions computed by finite element modeling are in good agreement with the hypothetical residual stress distributions measured, as is obvious from Figs. 6 and 7 and Figs. 15 and 16. The difference of the two distributions were within 10 MPa. The comparisons show good agreement and indicate that good results can be expected from the new method.

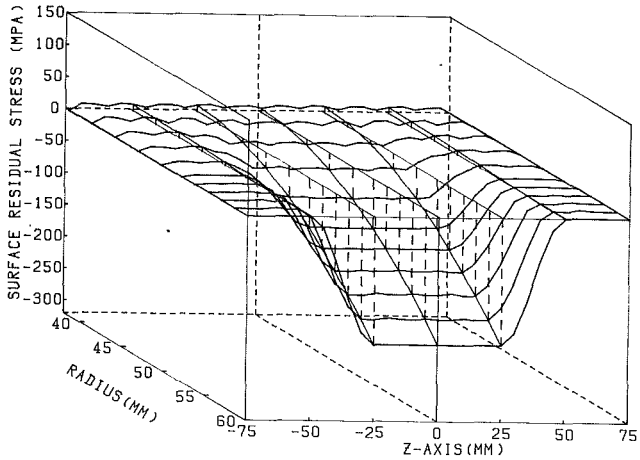


Fig. 15 Distribution of longitudinal surface residual stresses computed from the finite element modeling after each layer removal. This distribution agrees well with plots of longitudinal hypothetical stresses measured (Fig. 6).

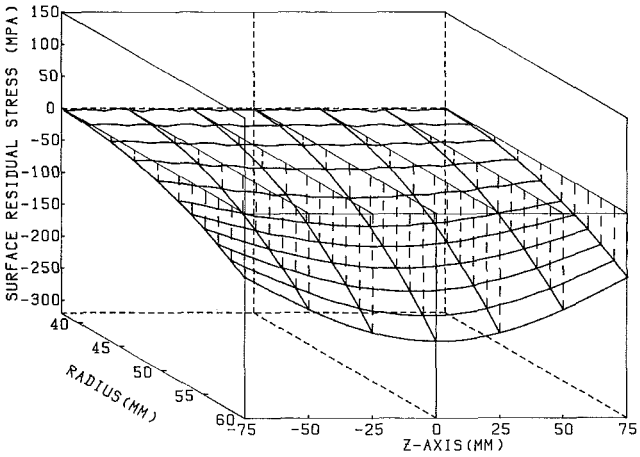


Fig. 16 Circumferential residual stress distribution computed from the finite element models at the exposed surfaces of the remaining tube. This figure is also in good agreement with Fig. 7.

Our next step is to compare the stress changes obtained from the theoretical calculations with the finite element results. The equations for calculating these stresses can be provided by differentiating both sides of Eqs. (11), (12), (13), and (14) by ρ. That is, $\bar{\sigma}_r$, $\bar{\sigma}_\theta$, $\bar{\sigma}_z$ and $\bar{\tau}_{rz}$ were used, where the outer radius is ρ. Then, stresses were compared at two locations corresponding to zero and 37 mm axially from the center. One location was selected in the region ($z = 0$) of no gradient in the stress distribution and the other was selected in the region ($z = 37$ mm) of maximum gradient. A comparison of the stresses at the surface of the remaining tube induced by removal of stressed layers are given in Table 2; the applied forces per unit area are printed in italics. The theoretical results for the location $z = 0$ agree with the finite element results within 2.5 MPa. At the location $z = 37$ mm, the theoretical stress distribution and the finite element results differ by less than 11.5 MPa. This larger difference may be due to too few elements, because the accuracy generally increases with the number of elements used.

Discussion

The X-ray stress measurement technique is based on the fact that the shift in the peak position of a diffraction line changes in proportion to the strain and thereby to the stress. Scatter

Downloaded 03 May 2010 to 171.66.16.245. Redistribution subject to ASME license or copyright; see http://www.asme.org/terms/Terms_Use.cfm

Table 2 Comparison of theoretical and numerical results for changes in stresses induced by removal of some layers

Radius after Removal	Method	*Forces* loaded to square unit of remaining tube, Stresses(MPa) and Axial Locations(mm)			
		τ_{rz}	σ_z	σ_θ	σ_r
		z=0, z=37	z=0, z=37	z=0, z=37	z=0, z=37
ρ=58.4mm		*Shearing Force 0.0, 15.2*			*Normal Force 4.8, 4.8*
at beneath outer wall	Theory	0.0, 14.1	17.6, 29.8	16.0, 14.7	4.9, 4.9
	FEM	0.0, 10.4	18.8, 18.3	16.7, 14.8	4.6, 5.4
ρ=49.5mm		*Shearing Force 0.0, 19.3*			*Normal Force 17.2 20.6*
at middle part of thickness	Theory	0.0, 19.4	80.3, 53.4	85.7, 66.2	18.2, 19.5
	FEM	0.2, 16.2	80.1, 53.4	85.4, 67.6	17.4, 19.7
ρ=41.1mm		*Shearing Force 0.0, -1.6*			*Normal Force 9,7, 8.8*
at beneath inner wall	Theory	0.0, -0.7	98.3, 44.5	125.4, 90.2	9.9, 8.5
	FEM	0.4, -2.6	95.8, 46.5	125.2, 90.7	8.7, 7.5

in the peak position and in the stress is fundamentally dependent on the inherent statistical variability in X-ray intensities. Assuming that the random errors generated by uniform random numbers have hypothetical values less than ±10 MPa, a simulation was made to calculate the magnitude of their influence on the results of Example 2. This simulation shows that the scatter of computed residual stress is also less than ±10 MPa. Therefore, it is considered that the propagation of random measurement errors does not occur in the calculation.

The stress determined by X-ray diffraction is the arithmetic average stress in the volume of material defined by the area irradiated on the surface and the depth of penetration. It is necessary to select the X-ray beam size which would give the desired degree of resolution of the stress distribution on the surface of the sample. If a sample has significant stress gradient along the surface, it is required a smaller irradiated area to the stress distribution. Because X-rays are diffracted from the surface layer only, a determination of stress distribution with depth requires removal of material to the depth desired. The 'soft' X-rays used penetrate the surface of the material only to a very shallow depth. For steels, that of chromium $K\alpha$ radiation is normally on the order of about 20 microns or less. Stress measurements made in the presence of steep stress gradient through depths of this magnitude will result in significant error if corrections are not made. It has been found that a ground surface sometimes shows this phenomena. For the stress gradient of heat treated tube such as the Example 1, the distribution of the stress will not differ to a results obtained with a smaller beam and corrected for the influence of the penetration.

Furthermore, from the conditions that the outer, inner, and end boundaries of the tube are free from external forces, the measured stresses must satisfy equilibrium conditions in the radial and longitudinal directions. If the stresses are rotationally symmetric, the equilibrium condition in the radial direction is evidently satisfied. The following equations are required for the conditions of equilibrium in the longitudinal direction, i.e.,

$$|\sigma_{zm}|_{z=\pm h}=0, \quad \int_{-h}^{h}\Delta\tau_{rz}dz=0, \quad |\Delta\tau_{rz}|_{z=\pm h}=0 \qquad (18)$$

It may be impossible to measure the exact stress values at the ends of a tube, but it can be considered that the first equation of Eq. (18) holds. By substituting Eqs. (4), (9) and (10) into the above conditions (18), we find that the second equation of (18) is always satisfied, and the final condition becomes the following equation:

$$\frac{\Delta\rho\pi}{h^2}\sum_{n=1}^{\infty}n(-1)^n\int_{-h}^{h}\sigma_{zm}\sin\beta_n\, zdz=0. \qquad (19)$$

In the previous experimental results, this condition (19) is satisfied by the measured stresses.

Let us now turn to the method of calculation. It may be seem that the new equations are so complicated that the usual advantage of an analytical approach is giving insights into the nature of the solution is completely lost. However, the equations show that corrected stresses σ_r, σ_θ, and σ_z can be regarded as consisting of two parts. The first part is due to the components of residual stresses which are independent of z. The remaining parts consisting of sums of trigonometric, hyperbolic, and Bessel functions represent stresses in a long or a short circular cylinder submitted to actions of shearing forces and normal pressures (Timoshenko and Goodier, 1951; Shibahara and Oda, 1970). The component τ_{rz} also gives a shearing stress in the same cylinder mentioned above. These equations can be evaluated numerical means; a mainframe computer, an engineering work station or a 32-bit PC machine would be applicable for the entire work. It may be possible to choose a finite element approach before the previous equations. However, accurate analysis of σ_r and τ_{rz} require skill and experience, since these component of stress results in elements with applied nodal forces will not yield the best results (Steele, 1989).

An application of numerical method such as finite element method has been proposed and applied to measurement of residual stress (Ueda et al., 1975 and Schajer, 1981, 1988). This application has a great flexibility of choice of specimen shape and experimental procedure. But it seems that there are very few reports which have described the finite element application using X-ray techniques for determination of residual stresses; several papers deal with an application of finite element calculation for a cutting or a hole-drilling method.

Because the finite element method is a numerical approximation, there is no absolutely correct answer; the accuracy generally increases with the number of elements used. When this method is applied for a residual stress analysis, sources

Downloaded 03 May 2010 to 171.66.16.245. Redistribution subject to ASME license or copyright; see http://www.asme.org/terms/Terms_Use.cfm

of the finite element uncertainty can be divided into three main factors; (1) model geometry, (2) boundary constraint conditions, and (3) applied forces. While these parameters must be satisfied in the continuum mechanics, the applied forces have a particularly strong influence on finite element results. Because forces are applied only at the node points, it is impossible to achieve a perfectly distributed or continuously variable forces. The general rule of thumb is to use a radius of three elements away from the element with the applied force to find good stress results (Steele, 1989). It also appears for the type of elements and the mesh condition in this study that the finite element results for σ_r and τ_{rz} are generally not quite in agreement with the radial and the tangential applied forces per unit area.

In order to test and bound the effects of model geometry and mesh density, the rate of convergence of a particular model may be established by running several cases with mesh densities comparing the results as a function of density. It is known that all models should converge to the best result with increasing mesh density. Probably the most difficult part of any finite element analysis is making an estimate or the absolute accuracy of the results. This part of an analysis requires skill and experience both in the finite element method and with understanding the actual residual stress distribution under analysis.

Conclusions

Longitudinally nonuniform stress distributions would frequently occur in tubes, particularly in ones which have been machined, ground, or received other partial heat or mechanical treatments. Determination of subsurface residual stresses by the X-ray diffraction techniques must be corrected in order to obtain the true stress distribution that had existed before the layers were removed. New equations for correction of longitudinally nonuniform residual stress distributions are derived for tubes, including short ones. The equations can be applied for bars by simple modification.

The new method was applied to a short steel tube that had been quenched in water and to a hypothetical residual stress distribution. An alternative method was used to verify the results. A finite element analysis was made in this verification. The residual stresses computed by finite element modeling agreed well with the hypothetical residual stresses measured by using the X-ray method. This indicates that good results can be expected from the new method.

Stress gradient governs the depth of any one removed layer. Obviously, a minimum number of layers removed is desired, but the number should be great enough to ascertain changes in stress distribution involved.

Acknowledgment

The author is grateful to Prof. Syotaro Kodama of Tokyo Metropolitan University for careful reading of the manuscript and to the members of the Puro seminar for their many discussions.

References

Cheng, W., and Finnie, I., 1986, "Examination of the Computational Model for the Layer-Removal Method for Residual Stress Measurement," *Experimental Mechanics*, Vol. 26, pp. 150–153.

Christenson, A. L., et al., 1960, "The Measurement of Stress by X-Ray," SAE TR-182, pp. 23–24.

Hanabusa, T., Tani, M., and Fujiwara, H., 1991, "X-Ray Stress Measurement of Coled-Rolled Steels Using CrKα and MoKα Characteristic Radiation," *Journal of the Society of Materials Science, Japan*, Vol. 40, pp. 2–8 (in Japanese).

Hauk, V. M., 1986, "Evaluation of Macro- and Micro-Residual Stresses on Textured Materials by X-Ray, Neutron Diffraction and Deflection Measurements," *Advances in X-Ray Analysis*, Vol. 29, pp. 1–15.

Kurita, M., Kano, T., and Sato, T., 1991, "Residual Stress Analysis of Brazed Ceramic Metal Joint," *Trans. Japan Soc. Mech. Engrs.*, Vol. 57, pp. 215–222 (in Japanese).

Kurita, M., 1988, "A New Method for Evaluating X-ray Diffraction Peak Broadening with Engineering Applications," *Advances in X-Ray Analysis*, Vol. 31, pp. 277–285.

Maeder, G., Lebrun, J. L., and Sprauel, J. M., 1981, "Present Possibilities for the X-ray Diffraction Method of Stress Measurement," *NDT International*, Vol. 45-5, pp. 235–247.

Moore, M. G., and Evans, W. P., 1958, "Mathematical Correction for Stress in Removed Layers in X-ray Diffraction Residual Stress Analysis," *SAE Trans.*, Vol. 66, pp. 340–345.

Prevey, P. S., 1981, "The Accuracy of X-Ray Diffraction Residual Stress Measurement," US DOE. Rep., EPRI-WS-80-136, pp. 10.1–10.20.

Sachs, G. "Der Nachweis Innerer Spannungen in Stangen und Rohren," *Zeischrift für Metallkunde*, Vol. 19, 1927, pp. 352–357.

Sawamiphakdi, K., Kropp, P. K., and Lahoti, G. D., 1990, "Investigation of Residual Stresses in Drawn Wire by the Finite Element Method," ASME *Journal of Engineering Materials and Technology*, Vol. 110, pp. 231–235.

Schajer, G. S., 1988, "Measurement of Non-uniform Residual Stresses Using the Hole-Drilling Method. Part II—Practical Application of the Integral Method," ASME *Journal of Engineering Materials and Technology*, Vol. 110, pp. 344–349.

Shibahara, M., and Oda, J., 1968, "Axisymmetric Deformation of Hollow Cylinders of Finite Length," *Trans. Japan Soc. Mech. Engrs.*, Vol. 34, pp. 388–402 (in Japanese).

Shibahara, M., and Oda, J., 1970, "Axisymmetric Deformation of Hollow Cylinders of Finite Length, Part-2," *Trans. Japan Soc. Mech. Engrs.*, Vol. 36, pp. 168–176 (in Japanese).

Steele, J. M., 1989, "Applied Finite Element Modeling," Marcel Dekker, New York, pp. 50.

Timoshenko, S. P., and Goodier, J. N., 1951, "Theory of Elasticity," 2nd ed., International Student Edition, McGraw-Hill, Tokyo, pp. 384–390.

Ueda, Y., and Fukuda, K., 1989, "New Measuring Method of Three-Dimensional Residual Stresses in Long Welded Joints Using Inherent Strains as Parameters—Lz Method," ASME *Journal of Engineering Materials and Technology*, Vol. 111, pp. 1–8.

Downloaded 03 May 2010 to 171.66.16.245. Redistribution subject to ASME license or copyright; see http://www.asme.org/terms/Terms_Use.cfm

Guangqiu Wang
Dr.-Ing.
BMW & Rolls Royce Aero Engines GmbH,
D-8044 Lohhof,
München, Germany

K. Knothe
Professor,
Aerospace Institute,
Technical University of Berlin,
D-1000 Berlin 10, Germany

Stress Analysis for Rolling Contact Between Two Viscoelastic Cylinders

The two-dimensional viscoelastic rolling contact with Coulomb's dry friction is considered for steady-state rolling. A so-called standard linear solid (three parameter model) is used to characterize the viscoelastic material behavior. Rolling contact stresses between two rolling cylinders are investigated by a boundary element method, based on the half-space theory. Numerical results are presented including the stress distribution at the contact surfaces and in viscoelastic bodies as well as rolling resistance.

1 Introduction

During the development of material sciences and technology more and more cylinders or rotating bodies composed of viscoelastic materials have been used in recent years, e.g., for transportation systems and printing machines. Special advantages of this type of roller include better damping properties, less rolling noise generation, and less weight. A stress analysis for the rolling contact problem is of great importance for engineers constructing and designing such rollers. Researchers in other fields have also been interested in the rolling contact problem between viscoelastic cylinders. The present paper is concerned with a theoretical study on viscoelastic rolling contact. There has been much theoretical work in this field and some important contributions are summarized here, which can be divided into the boundary element method (BEM) and the finite element method (FEM).

In the field of BEM the viscoelastic contact problem was first studied by Hunter (1961) and Morland (1967) for a rigid cylinder rolling over a viscoelastic half-space. Both analyses are restricted to the normal contact problem without considering friction. Panek and Kalker (1980) have considered the three-dimensional viscoelastic normal contact problem. The viscoelastic tangential contact problem was first solved by Goriacheva (1973). The solution is only valid for cylinders of the same material and even in this case the numerical solution is not complete.

Papat and Batra (1982) probably have been the first who investigated numerically a viscoelastic rubber-covered roller using FEM. Once again, the analysis was restricted to the normal contact problem without friction. In a relatively recent paper, Oden and Lin (1986) have used FEM to study the general geometrically nonlinear rolling contact of hyperelastic and viscoelastic cylinders. Friction and inertial forces were considered. An interesting aspect of the paper is that already for a free-spinning cylinder, bifurcation phenomena have been observed for angular velocities higher than a critical value. As the numerical effort of the analysis is enormous it has to be asked whether for technically relevant viscoelastic rolling contact phenomena, other methods are available.

The aim of the work presented here is to develop a numerical method for the analysis of rolling contact problems of viscoelastic cylinders. The method should be applicable for engineering problems at practical rolling speeds. The following additional assumptions have been introduced:

1 Coulomb's frictional law, with a constant coefficient of friction, and no difference between the adhesion and the sliding coefficient of friction, is used. Therefore, stick-slip phenomena are excluded.

2 The length of the cylinder is infinite and the contact width is small compared with the radius of the cylinder. Thus, a two-dimensional half-space theory can be used.

3 The rolling speed of the cylinder is assumed to be small compared with the wave propagation speed v_{cr} of Rayleigh's surface waves. This assumption is valid for many elastic and viscoelastic materials (for example: v_{cr} is approximately 3000 m/s for steel, 158 m/s for PUR (polyurethane), 940 m/s for PA6 (polyamide), and only for rubber $v_{cr} = 26$ m/s).

Therefore, except for rubber tires at higher vehicle speeds, inertia effects can be neglected within the contact mechanical analysis (Wang and Knothe, 1989) and bifurcation phenomena as observed by Oden and Lin (1986) and discussed by Rabier and Oden (1989) can be disregarded.

4 The analysis is carried out within the usual framework of the linear theory of viscoelasticity.

Under these assumptions, the simplest method to solve the viscoelastic rolling contact problem is a boundary element method. With this classical approach we are on a level with, e.g., Hertz (1887), Carter (1926), and Kalker (1983, 1986). The basic algorithm of our method has been developed by Kalker

Contributed by the Applied Mechanics Division of THE AMERICAN SOCIETY OF MECHANICAL ENGINEERS for publication in the ASME JOURNAL OF APPLIED MECHANICS.

Discussion on this paper should be addressed to the Technical Editor, Professor Lewis T. Wheeler, Department of Mechanical Engineering, University of Houston, Houston, TX 77204-4792, and will be accepted until four months after publication of the paper itself in the ASME JOURNAL OF APPLIED MECHANICS.

Manuscript received by the ASME Applied Mechanics Division, June 4, 1990; final revision, Nov. 19, 1991. Associate Technical Editor: L. M. Keer.

Copyright © 1993 by ASME
Downloaded 03 May 2010 to 171.66.16.245. Redistribution subject to ASME license or copyright; see http://www.asme.org/terms/Terms_Use.cfm

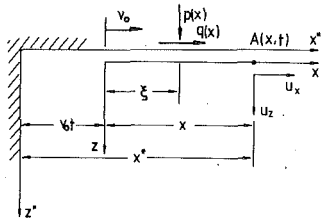


Fig. 1 Coordinate systems and distributed line loads

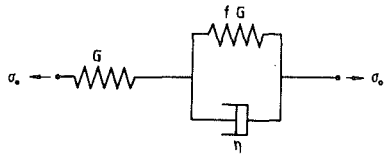


Fig. 2 Three-parameter model (standard linear solid)

(1983, 1986) and has been used to solve three-dimensional elastic contact problems. The reader is referred to the articles by Knothe and Wang (1988), Wang and Knothe (1989), and Wang (1991) for details of the algorithm in the case of two-dimensional viscoelastic rolling contact and for further numerical results. It should be mentioned that similar approaches can be used for layered viscoelastic cylinders (see Kalker, 1991; and Hiss et al., 1992).

2 Constitutive Equations

The constitutive equations of contact mechanics are defined as the relationships between the surface displacements of a half-space and the normal and tangential line-force acting on the surface of the half-space. Figure 1 shows a basic system of coordinates x^*, z^* and a moving system of coordinates x, z. The line-load vector $\mathbf{p}(x) = \{q(x), p(x)\}^T$ is moving with a constant velocity in the x^*-direction.

To derive the viscoelastic constitutive equations we assume that Poisson's ratio ν of the viscoelastic solid is constant, and that the behavior of the solid can be described by a so-called standard linear solid or three-parameter model (Fig. 2). For this model, the creep function in shear, $J(t)$, is given by

$$J(t) = \frac{1}{G}\,[1 + f(1 - e^{-t/\tau})]H(t) \tag{1}$$

where G is the dynamic shear modulus, η the damper constant, τ ($\tau = \eta/(fG)$) the retardation time, f the strength of the single-line retardation spectrum, and $H(t)$ Heaviside's step function.

The viscoelastic constitutive relation for a normal moving load problem has been given by Hunter (1961). His solution is derived from the associated elastic solution by the use of Laplace Transforms. Following this correspondence principle in the present problem leads to constitutive relations between the surface displacement vector $\mathbf{u}(x) = \{u_x(x), u_z(x)\}^T$ and the distributed line-load vector $\mathbf{p}(x) = \{q(x), p(x)\}^T$. It can be shown (Wang and Knothe, 1988) that the constitutive equations in a coordinate system traveling with v_o, as shown in Fig. 3, are given by

$$\mathbf{u} = \frac{1}{2\pi G}\left[\int_{-\infty}^{\infty} \mathbf{H}(x-\xi)\mathbf{p}(\xi)\,d\xi + f\int_0^{\infty}\int_{-\infty}^{\infty} e^{-s}\mathbf{H}(x-\xi+v_o\tau s)\mathbf{p}(\xi)\,d\xi\,ds\right] \tag{2}$$

where the elastic influence functions are defined as

$$\mathbf{H}(x) = \begin{bmatrix} -2(1-\nu)\ln|x| & -\pi/2(1-2\nu)\,\mathrm{sign}(x) \\ \pi/2(1-2\nu)\,\mathrm{sign}(x) & -2(1-\nu)\ln|x| \end{bmatrix}. \tag{3}$$

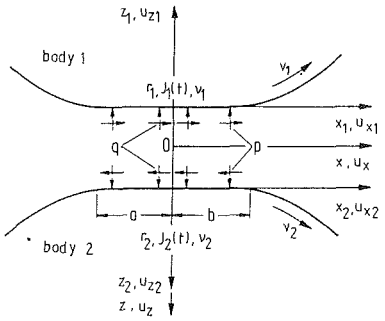


Fig. 3 Coordinate systems and stresses in the contact area

3 Integral Equations

We consider two cylinders rolling at tangential velocities v_1 and v_2. The cylinders are pressed together under a constant normal load N. Let $\mathbf{u}_i$ be the surface displacement vector of body (i) (i = 1, 2). The deformed distance between two cylinders at point x can be defined as

$$d_r(x) = [u_{z1}(x) + u_{z2}(x)] - [u_{z1}(x_o) + u_{z1}(x_o)] + \frac{1}{2}(x^2 - x_o^2)\left[\frac{1}{r_1} + \frac{1}{r_2}\right]. \tag{4}$$

The contact condition can then be written as

$$d_r(x) = 0, \quad \text{for } x \in \Omega \tag{4a}$$

$$d_r(x) > 0, \quad \text{for } x \notin \Omega \tag{4b}$$

where x_o is an arbitrary point in the contact area Ω and r_i is the radius of body (i). The expression for local slip $w(x)$ is given by

$$w(x) = s - \frac{d}{dx}\,[u_{x1}(x) - u_{x2}(x)] \tag{5}$$

where the average rolling velocity v_o and the creep s are defined as

$$s = \frac{v_1 - v_2}{v_o}, \quad v_o = -\frac{1}{2}\,[v_1 + v_2]. \tag{6}$$

The normal pressure $p(x)$ is always compressive and vanishes outside the contact area Ω,

$$p(x) > 0, \quad x \in \Omega \tag{7a}$$

$$p(x) = 0, \quad x \notin \Omega. \tag{7b}$$

The tangential traction $q(x)$ is assumed to obey Coulomb's frictional law. $q(x)$ cannot exceed its limiting value given by the product of coefficient of friction

$$|q(x)| < \mu p(x), \quad w(x) = 0, \quad x \in \Omega_a, \text{ (adhesion zone)} \tag{8a}$$

$$|q(x)| = \mathrm{sgn}(w)\mu p(x), \quad x \in \Omega_s, \text{ (sliding zone)} \tag{8b}$$

where μ is constant coefficient of friction. In addition, the global equilibrium condition must be satisfied

$$N = \int_{-a}^{b} p(x)\,dx \tag{9}$$

where a and b are the values of x at the trailing edge and leading edge (see Fig. 3).

The constitutive relation (Eq. (2)) can be substituted into Eqs. (4) and (5). Thus, we finally get the following integral equations for the contact condition (4a):

Downloaded 03 May 2010 to 171.66.16.245. Redistribution subject to ASME license or copyright; see http://www.asme.org/terms/Terms_Use.cfm

$$\frac{C}{2}\int_{-a}^{b}\{\operatorname{sgn}(x-\xi)-\operatorname{sgn}(x_o-\xi)\}q(\xi)d\xi$$
$$+\frac{1}{2}\sum_{k=1}^{2}D_k(-1)^{(k+1)}\int_{-\infty}^{\infty}\int_{-a}^{b}e^{-s}q(\xi)\{\operatorname{sgn}(x+\lambda_k s-\xi)$$
$$-\operatorname{sgn}(x_o+\lambda_k s-\xi)\}d\xi ds$$
$$-\sum_{k=1}^{2}F_k\int_{o}^{\infty}\int_{-a}^{b}e^{-s/\lambda_k}p(\xi)\ln\left|\frac{x-\xi+s}{x_o-\xi+s}\right|d\xi ds$$
$$-\int_{-a}^{b}p(\xi)\ln\left|\frac{x-\xi}{x_o-\xi}\right|d\xi=-\frac{B}{2R}\{x^2+x_o^2\} \quad (10)$$

and for the sliding condition (5)

$$Bw(x)=Bs+Cp(x)+\sum_{k=1}^{2}(-1)^{k+1}D_k\int_{o}^{\infty}e^{-s}p(x+\lambda_k s)ds$$
$$+\int_{-a}^{b}q(\xi)\frac{d\xi}{x-\xi}+\sum_{k=1}^{2}F_k\int_{o}^{\infty}\int_{-a}^{b}e^{-s/\lambda_k}\frac{q(\xi)}{x-\xi+s}d\xi, \quad (11)$$

where

$$B=\frac{\pi G_1G_2}{G_1(1-\nu_2)+G_2(1-\nu_1)},\qquad C=\frac{\pi}{2}\frac{G_2(1-2\nu_1)-G_1(1-2\nu_2)}{G_1(1-\nu_2)+G_2(1-\nu_1)} \quad (12a, b)$$

$$D_k=B\frac{f_k(1-2\nu_k)}{2G_k},\qquad F_k=B\frac{f_k(1-\nu_k)}{\lambda_k\pi G_k} \quad (12c, d)$$

$$\frac{1}{R}=\frac{1}{r_1}+\frac{1}{r_2},\qquad \lambda_k=\nu_k\tau_k, \quad (12e, f)$$

where the index $k = 1, 2$ is for body 1 or 2, respectively.

Equations (10) and (11) are two simultaneous integral equations for the unknown normal pressure $p(x)$, tangential traction $q(x)$ at the contact zone, and length of the contact area $(a + b)$. These equations, together with Eqs. (7) to (9), describe a complicated nonlinear boundary value problem. In the sense of contact mechanics, Eq. (10) describes normal contact and Eq. (11) tangential contact, but they are usually dependent. The independent normal and tangential contact problem can only be obtained for $C = 0$. This condition is exactly satisfied if the two contacting bodies are of the same material.

4 Solutions

Introducing the piecewise linear approximation for $p(x)$ and $q(x)$ (see the Appendix, Eqs. (A1)) into Eqs. (10) and (11), the integral equations are transformed into algebraic equations for $2(n - 1)$ unknown stress amplitudes p_i and q_i, respectively.

First we consider the normal contact problem determined by (10), (4*b*) and (7), assuming that the tangential stress amplitudes q_i are known. Using the expressions for influence coefficients derived in the Appendix, the normal contact condition is satisfied at $(n - 2)$ points $(j = 1, 2, \ldots, i - 1, i + 1, \ldots, n - 1)$:

$$(1+F_1\lambda_1+F_2\lambda_2)\sum_{i=1}^{n-1}[g_i(x_j,x_i)-g_i(x_o,x_i)]p_i$$
$$-\sum_{k=1}^{2}F_k\lambda_k\left\{\sum_{i=1}^{n-1}[d_i(x_j,x_i,\lambda_k)-d_i(x_o,x_i,\lambda_k)]p_i\right\}$$
$$=-\frac{C^*\Delta x}{2}\sum_{i=1}^{n-1}\{\operatorname{sgn}(x_j-x_i)-\operatorname{sgn}(x_o-x_i)\}q_i-\sum_{k=1}^{2}D_k(-1)^{k+1}$$
$$\times\left\{\sum_{i=n_x}^{n-1}[h_i(x_j,x_i,\lambda_k)-h_i(x_o,x_i,\lambda_k)]q_i\right\}+\frac{B}{2}(x_j^2-x_o^2),$$
$$(j=1,2,\ldots,i-1,i+1,\ldots,n-1) \quad (13)$$

where

$$C^*=C+D_1-D_2. \quad (13a)$$

In addition to these $(n - 2)$ equations, the equilibrium condition (9) has to be fulfilled, resulting in

$$N=\Delta x\sum_{i=1}^{n-1}p_i. \quad (14)$$

These $(n - 1)$ linear equations for $(n - 1)$ unknown pressure amplitudes p_i, together with the boundary conditions (4*b*) and (7), which can also be expressed in a discrete form, have been solved by an iteration method (see Kalker, 1983, 1986). The solution of the normal contact problem not only includes the normal pressure p_i but also the half-width a_o of the contact area $(a_o = [a + b]/2)$.

In a similar manner, we consider Eqs. (11) and (8) defining the tangential contact problem in which the normal pressure p_i and the contact area a_o are now known. In order to simplify numerical treatment of Eq. (11), the kinematic relation for tangential contact (5) can be approximately written as a finite difference coefficient

$$w(x)=s-\frac{u_{x1}(x+\Delta x)-u_{x2}(x+\Delta x)-u_{x1}(x)+u_{x2}(x)}{\Delta x}. \quad (15)$$

Changing Eq. (11) accordingly, and introducing the influence coefficients derived in the Appendix, we finally obtain the following linear equations for the tangential traction q_i and the slip w_i at $x = x_i$:

$$(1+F_1\lambda_1+F_2\lambda_2)\sum_{i=1}^{n-1}[g_i(x_j+\Delta x,x_i)-g_i(x,x_i)]q_i$$
$$-\sum_{k=1}^{2}F_k\lambda_k\left\{\sum_{i=1}^{n-1}[d_i(x_j+\Delta x,x_i,\lambda_k)-d_i(x_j,x_i,\lambda_k)]q_i\right\}$$
$$=-\Delta x\sum_{k=1}^{2}D_k(-1)^{k+1}\left\{\sum_{i=n_x}^{n-1}h_i(x_j,x_i,\lambda_k)p_i\right\}$$
$$-\Delta x[Bs+C^*p_j]+\Delta xBw_j \quad (j=1,2,\ldots,n-1). \quad (16)$$

Under consideration of the nonlinear slip adhesion condition (8) at $x = x_i$, the linear Eqs. (16) have been solved by Kalker's algorithm.

Until now we have only discussed the uncoupled normal and tangential contact problem, assuming that tangential traction does not influence normal contact process. However, this assumption is only valid for two cylinders of the same material. In general, normal and tangential contact are always coupled. From (10) it can be seen that $q(x)$ influences $p(x)$, and hence normal contact, and vice verse.

In solving these simultaneous integral equations, a so-called Panagiotopoulos process has been used. The normal contact problem (noted here by "*N*") has to be solved first, since the tangential contact problem ("*T*"), depends on $\mathbf{p}$. We solve "*N*" by giving a start value for $\mathbf{q}_o = \{q_1, q_2, \ldots, q_{n-1}\}_o$, such as $\mathbf{q}_o = \mathbf{0}$, then we solve "*T*". In next iteration, we replace the start $\mathbf{q}_o$ by $\mathbf{q}_1$ obtained from the solution of "*T*", and then solve "*N*" again. We continue solving "*N*" and "*T*" until convergence occurs.

Downloaded 03 May 2010 to 171.66.16.245. Redistribution subject to ASME license or copyright; see http://www.asme.org/terms/Terms_Use.cfm

5 Stress Distribution

We next consider the stress distribution in a viscoelastic body. It should be mentioned that evaluating stress distributions from given normal pressure p_i and tangential traction q_i is independent of material parameters. Once the stress distribution is assumed to be known, there is no difference between elastic and viscoelastic cylinders in the calculation.

Following the formula given by Johnson (1985), it can be shown that the expressions for stresses σ_x, σ_z, and τ_{xz} in a body, assuming a piecewise linear distribution of p_i and q_i are given by

$$\sigma_x(x)=\frac{1}{\pi\Delta x}\sum_{i=1}^{n-1}\{[\beta_i+2z\ln(r_1r_2/r^2)]p_i-[2(x-x_i)\ln(r_1r_2/r^2)+2\Delta x\ln(r_2/r_1)-3z\theta_i^*]q_i\} \quad (17a)$$

$$\sigma_z(x)=\frac{1}{\pi\Delta x}\sum_{i=1}^{n-1}\{[\beta_i]p_i-[z\theta_i^*]q_i\} \quad (17b)$$

$$\tau_{xz}(x)=\frac{1}{\pi\Delta x}\sum_{i=1}^{n-1}\{[-z\theta_i^*]p_i+[\beta_i+2z\ln(r_1r_2/r^2)]q_i\} \quad (17c)$$

where

$$\beta_i=(x-x_i-\Delta x)\theta_1+(x-x_i+\Delta x)\theta_2-2(x-x_i)\theta \quad (18a)$$

$$\theta_i^*=\theta_1+\theta_2-2\theta \quad (18b)$$

$$r_1^2=(x-x_i-\Delta x)^2+z^2,\ r_2^2=(x-x_i+\Delta x)^2+z^2,\ r^2=(x-x_i)^2+z^2 \quad (18c)$$

$$\tan\theta_1=z/(x-x_i-\Delta x),\ \tan\theta_2=z/(x-x_i+\Delta x),\ \tan\theta=z/(x-x_i). \quad (18d)$$

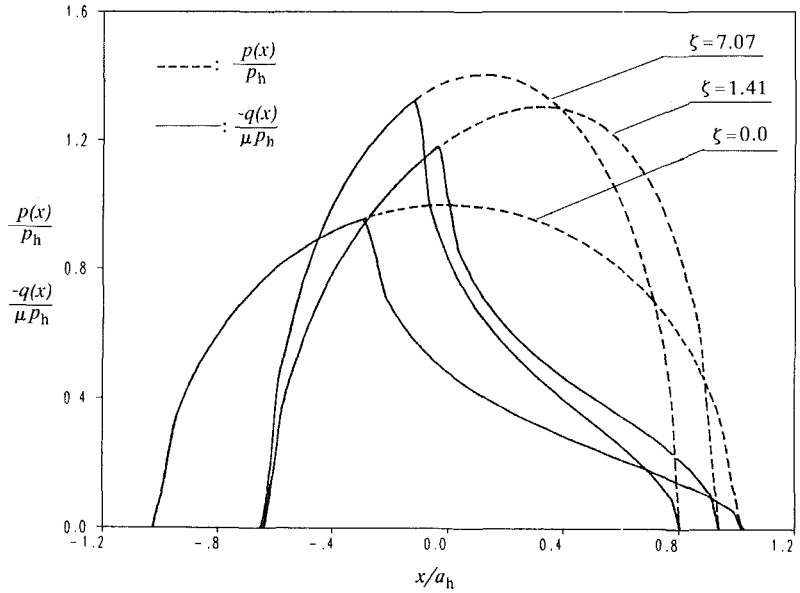


Fig. 4 Normal pressure $p(x)$ and tangential traction $q(x)$ in the contact area for $Tl(\mu N) = -0.6$

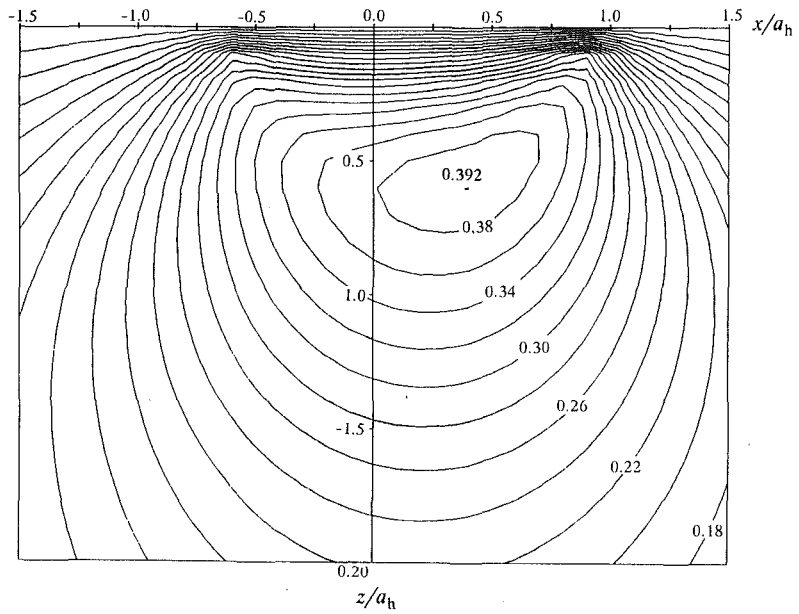


Fig. 5 Contours of τ_1/p_h only the viscoelastic pressure $p(x)$ for $\zeta = 1.41$

Downloaded 03 May 2010 to 171.66.16.245. Redistribution subject to ASME license or copyright; see http://www.asme.org/terms/Terms_Use.cfm

It can be seen from the above equations that no material parameters appear in these expressions. Using Eqs. (17), the stresses in a cylinder are easily evaluated. From σ_x, σ_z and τ_{xz} the principal stresses σ_j ($i = 1, 2, 3$) may be found, and hence, e.g., the principal shear stress τ_1 can be obtained

$$\tau_1 = \left| \frac{\sigma_1 - \sigma_3}{2} \right|. \tag{19}$$

6 Numerical Results

Two kinds of numerical results will be given. At first, stress distributions at the contacting surface and in the interior of viscoelastic bodies are presented. Secondly, integrated relations like creepforce/creep relations or rolling resistance depending on the rolling velocity parameter, are shown.

The numerical calculations to get stress distributions have been carried out for two examples. First, we consider two cylinders of the same material ($C = 0$), i.e., the uncoupled contact problem, in which the viscoelastic material is polymer PA6. Then, we consider the contact of dissimilar materials ($C \neq 0$), i.e., the coupled contact problem. In the presentation of the results, the stress distribution in the contact area and the body are always given for the lower cylinder. In both cases, the contact area is divided into 49 elements, the normal force, and the average radius are $N = 300$ N/mm and $R = 100$ mm, respectively.

From the known stress distributions at the contacting surface, the tangential force T_c transmitted in the contact area due to Coulomb's friction can be obtained by integrating the tangential traction $q(x)$ over the contact area. The tangential

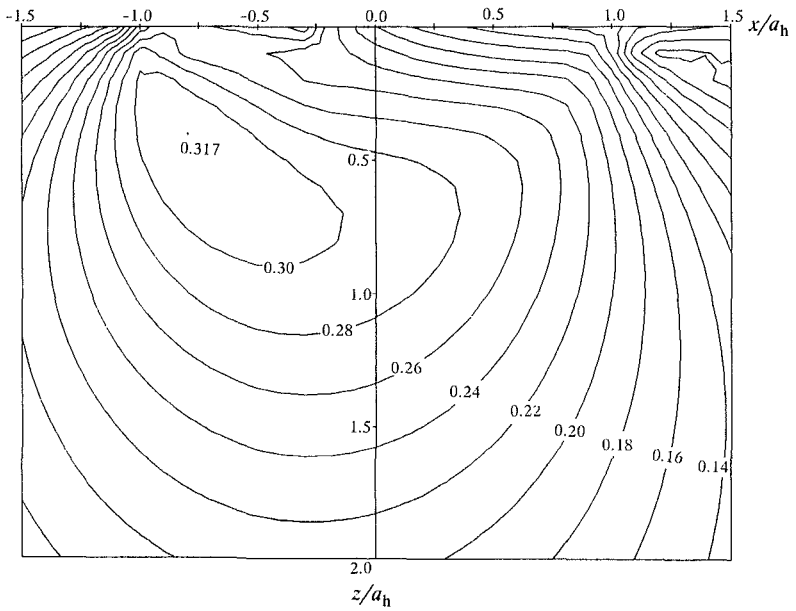


Fig. 6(*a*) Contours of τ_1/p_h due to the elastic pressure $p(x)$ and the tangential traction $q(x)$

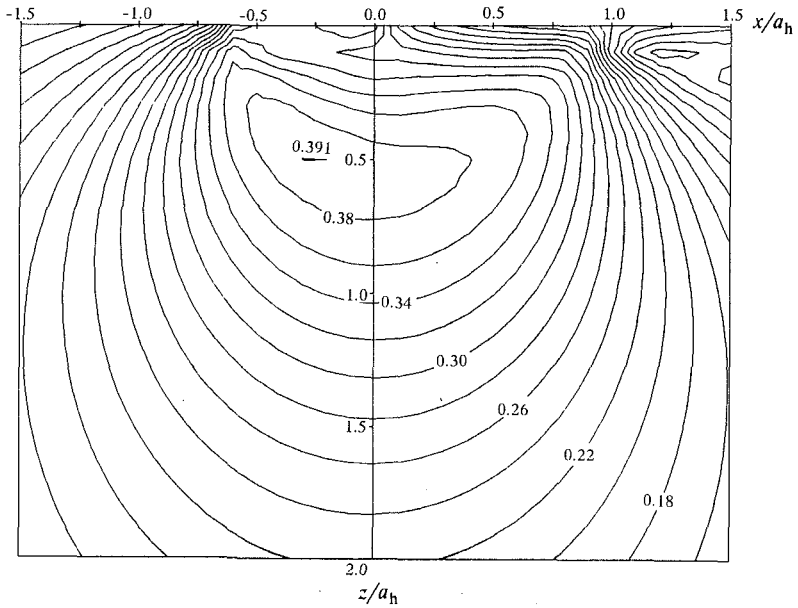


Fig. 6(*b*) Contours of τ_1/p_h due to the viscoelastic pressure $p(x)$ and the tangential traction $q(x)$ for $\zeta = 1.41$

Downloaded 03 May 2010 to 171.66.16.245. Redistribution subject to ASME license or copyright; see http://www.asme.org/terms/Terms_Use.cfm

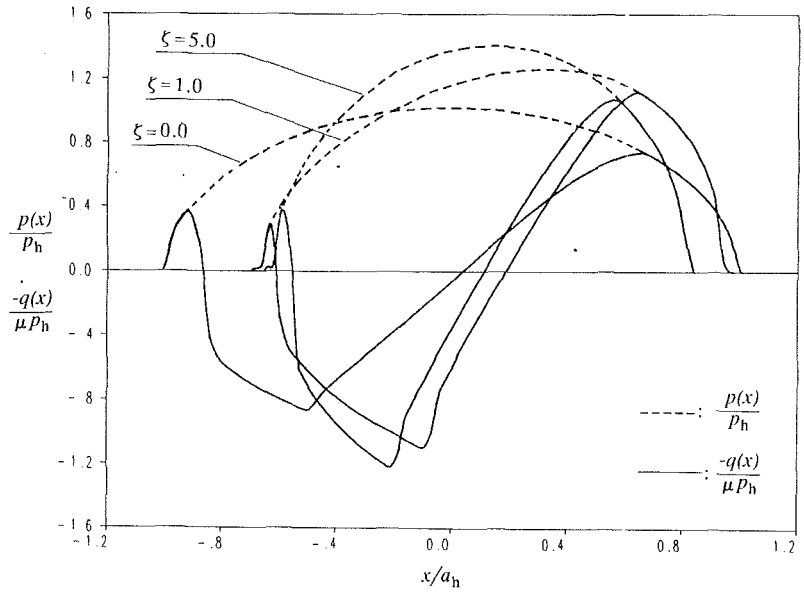


Fig. 7 Normal pressure $p(x)$ and tangential traction $q(x)$ in the contact area for $T/(\mu N) = 0$

force T_c then not only depends on the creepage but also on the rolling velocity. The rolling resistance T_r, which is caused mainly by taking into account the viscoelastic material properties, can be calculated by considering the normal pressure distribution $p(x)$ and the deformed contacting surfaces (Wang, 1991).

6.1 Stresses for Cylinders of Similar Materials. The values of the parameters used in this case are listed as follows:

Elasticity modulus: $E = 3200$ MPa; Poisson's ratio: $\nu = 0.4$

viscoelastic material parameter: $f = 1$; coefficient of friction: $\mu = 0.3$.

Figure 4 depicts the normal pressure and tangential traction distribution in the contact area depending on the rolling speed v_o, which is represented by the parameter $\zeta = v_o\tau/a_h$. Here, τ is the retardation time, a_h and p_h are the half-width of the contact area and the maximal pressure of Hertzian solution, respectively. In the special case $\zeta = 0$, the elastic solutions of Hertz and Carter (1926) are obtained. It can be seen that the rolling velocity has a considerable influence on the viscoelastic rolling contact, in particular on the normal contact. As expected, the normal pressure has an asymmetric distribution. With increasing rolling velocity, i.e., with increasing parameter ζ, the maximum value of $p(x)$ increases and the half-width of the contact area decreases. The maximum asymmetric pressure distribution occurs near $\zeta = 1$. Compared to Carter's solution the principle form of the tangential traction $q(x)$ has not been changed qualitatively by taking viscoelastic effects into account. As the parameter ζ tends to infinity, the distributions of $p(x)$ and $q(x)$ qualitatively have the same form as the elastic solution for $\zeta = 0$. The viscoelastic contact problem in this case corresponds with an elastic contact problem, in which the elasticity modulus E is replaced by $\sqrt{1+f}\,E$.

Corresponding contours of the principle shear stress τ_1 are shown in Fig. 5 ($T = 0$) and in Fig. 6 ($T \neq 0$). In Fig. 5, isolines of τ_1 for the viscoelastic case in the absence of friction are plotted. The maximal value of approximately $0.39p_h$ is shifted to the leading edge, whereas in the elastic case (see Johnson, 1985), the maximum value $0.3\ p_h$ is situated on the z-axis. In Fig. 6, the contours of τ_1, due to combined normal force and tangential traction ($T/(\mu N) = -0.6$), are shown for different parameters ζ. Because of the viscoelastic effects, the maximum value of τ_1 for $\zeta = 1.41$ (Fig. 6*b*) is closer to the z-axis than for $\zeta = 0$ (elastic case) in Fig. 6(*a*).

6.2 Stresses for Cylinders of Dissimilar Materials. For this example, it is assumed that the first cylinder is elastic and the second one viscoelastic. We have taken the values of the parameters as far as possible according to Bentall and Johnson (1967): Elasticity moduli: $E_1 = 200000$ MPa, $E_2 = 10{,}500$ MPa; Poisson's ratios: $\nu_1 = 0.22$, $\nu_2 = 0.28$ viscoelastic material parameters: $f_1 = 0$, $\eta_1 = 0$, $f_2 = 1$; coefficient of friction: $\mu = 0.1$.

Here a special contact case is investigated with a total tangential force $T = 0$. The normal pressure and tangential traction at the contact area are shown in Fig. 7, in which the elastic solution of Bentall and Johnson (1967) is obtained by putting $\zeta = 0$. The elastic solution has nearly a symmetric pressure distribution, whereas the viscoelastic curve for $\zeta = 1$ presents a distinct asymmetric form. In marked contrast to the curves in Fig. 4, more than one slip and adhesion region may appear at the contact area in both the elastic and the viscoelastic case. For dissimilar materials the variation of the rolling speed shows similar influence as for cylinders of the same material.

The contours for the elastic case, which are plotted in Fig. 8(*a*), are almost symmetric with respect to the z-axis, although this principle shear stress is caused by combined normal and tangential stresses $p(x)$ and $q(x)$. The asymmetric contours for the viscoelastic case in Fig. 8(*b*) show that the maximum value of τ_1 again is shifted to the leading edge. This corresponds to the contours in Fig. 5, indicating that the asymmetric property of the internal stress distributions is mainly caused by the asymmetric normal pressure distribution in the contact area due to viscoelastic effects. It is clear that the influence of the tangential traction $q(x)$ on the stress fields is insignificant, at least in the present case of $T = 0$. The position of the maximal value of τ_1 moves toward the z-axis, when the parameter ζ increases.

6.3 Rolling Resistance and Contact Width. For simplicity, the investigation of global contact parameters is restricted to cylinders of similar materials. The variation of the half-width $a_o(\zeta)$ of the contact area and the rolling resistance $T_r(\zeta)$ with the velocity parameter ζ are shown in Fig. 9. $a_o(\zeta)$ decreases with increasing rolling velocity ζ. The asymptotic value of $a_o(\zeta)$ for $\zeta \to \infty$ is given by $a_h/\sqrt{1+f}$. The maximum creepage creepage $s_m(\zeta)$ of Fig. 9 can be used to normalize the creep force/creep relations in such a way that all curves nearly

Downloaded 03 May 2010 to 171.66.16.245. Redistribution subject to ASME license or copyright; see http://www.asme.org/terms/Terms_Use.cfm

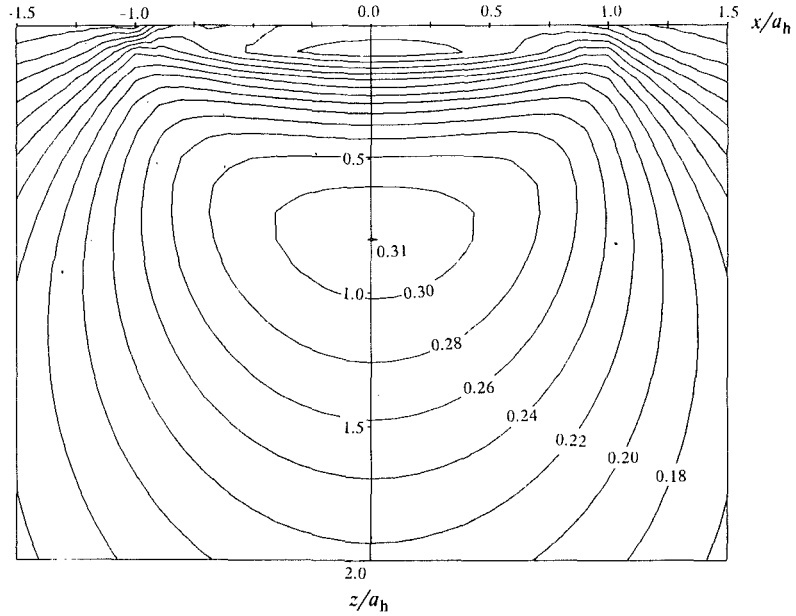


Fig. 8(*a*) Contours of τ_1/p_h due to the elastic pressure $p(x)$ and the tangential traction $q(x)$

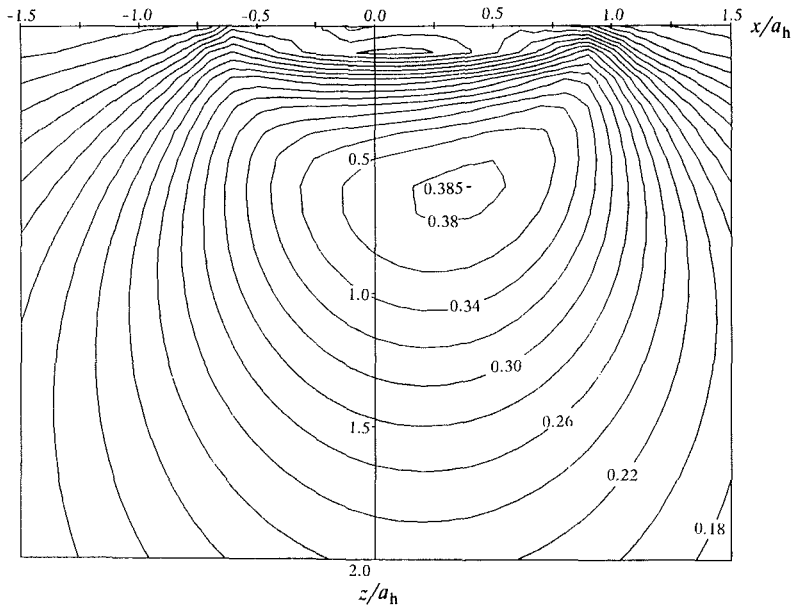


Fig. 8(*b*) Contours of τ_1/p_h due to the viscoelastic pressure $p(x)$ and the tangential traction $q(x)$ for $\zeta = 1$

coincide with the purely elastic solution of Carter (see Hiss, 1992). The rolling resistance $T_r(\zeta)$ reaches its maximum value between $\zeta = 1$ and 2. In general, the ratio $T_r(\zeta)/N$ is rather small compared with the coefficient of friction μ. For our example ($r_1 = 200$ mm and $a_h = 8.96$ mm) this ratio is about 0.0045, which can evidently be neglected in comparison with Coulomb's friction coefficient in the usual case of dry contact ($\mu > 0.1$). However, the tangential force may be dominated by the rolling resistance T_r in the case that the contact procedure occurs in the region of very small creepages or in the case of lubricated contact with a very small frictional coefficient. Inspite of this, investigating the energy losses for viscoelastic rolling contact the rolling resistance is of great importance. It determines the energy dissipation in the interior of viscoelastic bodies.

7 Conclusions

A stress analysis for viscoelastic rolling contact with Coulomb's friction has been performed. The numerical method presented in the paper can be used for solving contact problems of cylinders composed of similar and dissimilar viscoelastic materials. In the present analysis, the influence of the rolling velocity on the stress distribution, on the rolling resistance and the width of the contact area especially for cylinders of similar materials has been investigated.

To simplify our investigations, we have assumed that the rolling contact process is steady state and isothermal. For further investigations considering the energy dissipation and the heat transfer created by viscoelastic rolling, the results obtained here may be used as the initial condition for the calculation.

Downloaded 03 May 2010 to 171.66.16.245. Redistribution subject to ASME license or copyright; see http://www.asme.org/terms/Terms_Use.cfm

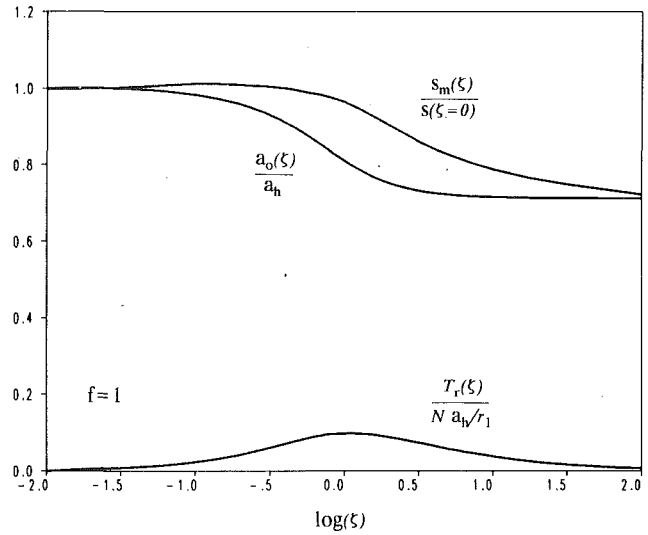


Fig. 9 Variation of the half-width of the contact area $a(\zeta)$, the rolling resistance $T_r(\zeta)$ and the maximal creepage $s_m(\zeta)$ with the rolling velocity parameter ζ

References

Carter, F. W., 1926, "On the Action of Locomotive Driving Wheel," *Pro. Roy. Soc., London*, Vol. A112, pp. 151–157.

Bentall, R. H., and Johnson, K. L., 1967, "Slip in the Rolling Contact of Two Dissimilar Elastic Rollers," *Int. J. Mech. Sci.*, Vol. 9, pp. 389–404.

Gradsteyn, I. S., and Ryzhik, I. M., 1980, *Tables of Integrals, Series and Products*, Academic Press, New York.

Goriacheva, I. G., 1973, "Contact Problem of Rolling of a Viscoelastic Cylinder on a Base of the Same Material," *PMM 37*, No. 5, pp. 925–933.

Hiss, F., Knothe, K., and Wang, G., 1992, "Stationärer Rollkontakt für Walzen mit viskoelastischen Bandagen," *Konstruktion 44*, (3), pp. 105–122.

Hunter, S. C., 1961, "The Rolling Contact of a Rigid Cylinder with a Viscoelastic Half Space," ASME JOURNAL OF APPLIED MECHANICS, Vol. 28, No. 4, pp. 611–617.

Johnson, K. L., 1985, *Contact Mechanics*, Cambridge University Press, Cambridge, England.

Kalker, J. J., 1983, "Two Algorithms for the Contact Problem in Elastostatics," *Proc. Int. Symp. Contact Mechanics and Wear of Rail/Wheel Systems*, Kalousek, Dukkipati, Gladwell, eds., University of Waterloo Press, Vancouver, Canada.

Kalker, J. J., 1986, "User's Manual of the Fortran Program CONTACT Version 1 and 3," Delft University of Technology.

Kalker, J. J., 1991, "Multilayered Viscoelastic Cylinder," ASME JOURNAL OF APPLIED MECHANICS, Vol. 58, pp. 666–680.

Knothe, K., and Wang, G., 1989, "Zur Theorie der Rollreibung Zylindrischer Kunststofflaufräder," *Konstruktion*, Vol. 41, pp. 193–200.

Morland, L. W., 1967, "Exact Solutions for Rolling Contact Between Viscoelastic Cylinders," *Q. J. Mech. Appl. Math.*, Vol. 20, Part 1, pp. 73–106.

Oden, J. T., and Lin, T. L., 1986, "On the General Rolling Contact Problem for Finite Deformations of a Viscoelastic Cylinder," *Comput. Math. Appl. Mech. Engrg.*, Vol. 57, No. 3, pp. 297–367.

Panek, C., and Kalker, J. J., 1980, "Three-dimensional Contact of a Rigid Roller Traversing a Viscoelastic Half Space," *J. Inst. Math. Applies.*, Vol. 26, pp. 299–313.

Papat, C., and Batra, R. C., 1982, "Identification of a Viscoelastic Rubber Covered Roll by a Rigid Plane Surface," *Mechanics Research Communications*, Vol. 9, No. 4, pp. 265–278.

Rabier, P. J., Oden, J. T., 1989, *Bifurcation in Rotating Bodies*, Springer-Verlag, New York.

Wang, G., and Knothe, K., 1989, "The Influence of Inertial Forces on Steady-State Rolling Contact," *Acta Mechanica*, Vol. 79, pp. 221–232.

Wang, G., and Knothe, K., 1988, "Theorie und numerische Behandlung des allgemeinen rollenden Kontaktes zweier viskoelastischer Walzen," *VDI Fortschr.*—Ber. Reihe 1, Nr. 165, Düsseldorf, VDI—Verlag.

Wang, G., 1991, "Rollkontakt zweier viskoelastischer Walzen mit Coulombscher Reibung," Doctoral Thesis, Technical University of Berlin, Berlin.

APPENDIX

Derivation of the Influence Coefficients

The contact area is first divided into N elements of length Δx, in which the surface stress distributions are approximated by a linear function defined at the interval $[x_i - \Delta x, x_i + \Delta_x]$. The expression for $p(x)$ and $q(x)$ in an element is given by

$$p(x) = \sum_{i=1}^{n-1} \phi_i(x) p_i \tag{A1a}$$

$$q(x) = \sum_{i=1}^{n-1} \phi_i(x) q_i \tag{A1b}$$

$$\phi_i(x) = \frac{1}{\Delta x} \begin{cases} x - x_i + \Delta x, & x_i - \Delta x \le x \le x_i \\ x_i + \Delta x - x, & x_i \le x \le x_i + \Delta x. \end{cases} \tag{A1c}$$

p_i and q_i are the amplitudes of the stress distributions at x_i. Introducing (A1) into the integrals in (10) and (11), the integrals can be expressed in terms of p_i and q_i at the points x_i. Integrating the first integral in the left side of (10) by part and then carrying out some calculations, one finds

$$I(x) = \int_0^\infty \int_{-a}^{b} e^{-s/\lambda} p(\xi) \ln|x + s - \xi| \, d\xi ds \approx \lambda \left\{ \sum_{i=1}^{n-1} g_i(x, x_i) p_i + \sum_{i=1}^{n-1} d_i(x, x_i, \lambda) p_i \right\}. \tag{A2}$$

The elastic influence coefficient $g_i(x, x_i)$ is given by

$$g_i(x, x_i) = \frac{1}{2\Delta x} \{ (x - x_i - \Delta x)^2 \ln|x - x_i - \Delta x| - 2(x - x_i)^2 \ln|x - x_i| + (x - x_i + \Delta x)^2 \ln|x - x_i + \Delta x| \} \tag{A3}$$

and the viscoelastic influence coefficient d_i has the following form:

$$d_i(x, x_i, \lambda) = -\frac{\lambda^2}{\Delta x} \{ F_i(\eta_1) + F(\eta_3) - 2F(\eta_2) \} \tag{A4}$$

where

$$F(u) = -e^u E_i(-u) + u \ln|u| + \ln|u|, \tag{A5a}$$

$$\eta_1 = (x - x_i + \Delta x)/\lambda, \quad \eta_2 = (x - x_i)/\lambda, \quad \eta_3 = (x - x_i - \Delta x)/\lambda \tag{A5b}$$

In the above equation, the exponential integral function $E_i(x)$ is introduced (Gradsteyn and Ryzhik, 1980). Using their asymptotic expansion for this function, (A5a) can be formulated as

$$F(u) = \ln|u| [u + 1 - e^u] - Ce^u - e^u \sum_{n+1}^{\infty} \frac{(-u)^n}{n!n}. \tag{A6}$$

In the above equation, Euler's constant $C = 0.57721566$. The limit value of $F(u)$ tends to $-C$ as $u \to 0$.

Next, the integrals connecting the normal and tangential stresses in (10) and (11) are calculated. Integrating the second integral on the left side of Eq. (10) by part, then inserting Eq. (A1) into the integrals yields the following expression:

$$J(x) = \int_0^\infty \int_{-a}^{b} e^{-s} q(\xi) \operatorname{sgn}(x + \lambda s - \xi) \, d\xi ds = \Delta x \sum_{i=1}^{n-1} \operatorname{sgn}(x - x_i) q_i + 2 \sum_{i=n_x}^{n-1} h_i(x, x_i, \lambda) q_i \tag{A7}$$

where the influence coefficient in the second part is related to viscoelastic effects, and takes the form

$$h_i(x, x_i, \lambda) = \frac{\lambda^2}{\Delta x} e^{(x - x_j)/\lambda} [e^{-\Delta x/\lambda} + e^{-\Delta x/\lambda} - 2]. \tag{A8}$$

Here, n_x is the number of elements involved in the interval from x to b.

Downloaded 03 May 2010 to 171.66.16.245. Redistribution subject to ASME license or copyright; see http://www.asme.org/terms/Terms_Use.cfm

A Study on Plastic Shakedown of Structures: Part I—Basic Properties

C. Polizzotto
Dipartimento di Ingegneria Strutturale & Geotecnica, DISEG, Università di Palermo, I-90128 Palermo, Italy

For a continuous elastic-perfectly plastic solid body subjected to a combination of cyclic (mechanical and/or kinematical) load and of a steady (mechanical) load such as to produce plastic shakedown (i.e., alternating plasticity), a number of characterizing properties are established and discussed. The conditions for the body's transition from plastic shakedown to ratchetting are also addressed.

Introduction

According to classical results of plasticity theory, a solid body (or structure) of elastic-perfectly plastic material subjected to cyclic loads shows a transient (short-term) response first, then a steady-state (long-term) response; see e.g., Frederich and Armstrong (1966), Martin (1975), Halphen (1979), Zarka and Casier (1979), and Gokhfeld and Cherniavsky (1980). The steady-state response, characterized by stresses σ and plastic strain rates $\dot{\epsilon}^p$ both periodic with the same period of the loads, may be either an elastic response whenever *elastic shakedown* occurs (in which case $\dot{\epsilon}^p$ vanishes identically and the only plastic strains present in the body are those occurred in the transient phase), or an elastic-plastic response with actual plastic flow whenever *inadaptation* (i.e., lack of elastic shakedown) occurs and thus plastic strain production continues even beyond the transient phase. In case of inadaptation, the structure is exposed to a form of collapse, either *incremental collapse* (or *ratchetting*) when the ratchet strain $\Delta\epsilon^p$, i.e., the compatible cycle net increment of plastic strains, is nonvanishing at least somewhere in the volume V of the body, or *alternating plasticity collapse* (or *plastic shakedown*) when $\Delta\epsilon^p$ vanishes everywhere in V.

It must be noticed that, in accordance with a tendency of the more recent literature concerned with elastic-plastic analysis under cyclic loads; see, e.g., Gokhfeld and Cherniavsky (1980), Ponter (1983), Ponter and Karadeniz (1985a, b), and Zarka and Casier (1979), the term "shakedown" is here understood as the long-term structural behavior characterized by *absence of plastic strain growth in a complete cycle*, i.e., zero ratchet strain in the whole V. Thus, "shakedown" has her a meaning wider than the usual one (absence of any plastic flow manifestation in the long-term response), the latter being here referred as "elastic shakedown" instead of simply "shakedown." There is at least one reason justifying such terminology: namely, the (elastic) shakedown and the alternating plasticity can be viewed as cases of a more general phenomenon, object of an extended shakedown theory, as in Ponter and Karadeniz (1985a, b).

Structural design based on elastic shakedown can be achieved by the classical shakedown theorems, which enable one to recognize whether elastic shakedown occurs or not under a specified loading; see, e.g., Symonds and Neal (1951), Koiter (1960), Martin (1975), Gokhfeld and Cherniavsky (1980), König and Maier (1981), Polizzotto (1982), Ponter (1983), and König (1987). Such design criterion is most appropriate because it enables structures to escape from the different forms of failure which are possible in case of inadaptation, namely, either rupture due to excessive deformation in condition of incremental collapse, or low-cycle fatigue associated with alternating plasticity. However, often in practice (for instance within the framework of nuclear power plants applications), structures are required to operate in condition of plastic shakedown and unfortunately related theorems as clear as those of elastic shakedown are not available, to the author's knowledge. Ponter (1983) and Ponter and Karadeniz (1985a, b) provided such theorems which, however, are based upon heuristic arguments and are applicable only within particular structural and loading configurations.

The main purpose of the present work is the formulation of plastic shakedown theorems of general applicability, to be used as criteria to recognize whether plastic shakedown occurs or not under a specific loading. Truly, the elastic-perfectly plastic material model herein considered is perhaps too poor in comparison with other more realistic materials models more suitable to cyclic plasticity. But one has to remark that many design rules are inspired by perfect plasticity phenomenology and, anyway, the solid mechanics problem to address is still open.

The entire work is divided into two companion papers, the first of which is intended to establish a number of properties which characterize plastic shakedown as well as the transition from plastic shakedown to ratchetting, whereas the second one is devoted to the formulation of plastic shakedown theorems

Contributed by the Applied Mechanics Division of THE AMERICAN SOCIETY OF MECHANICAL ENGINEERS for publication in the ASME JOURNAL OF APPLIED MECHANICS.

Discussion on this paper should be addressed to the Technical Editor, Professor Lewis T. Wheeler, Department of Mechanical Engineering, University of Houston, Houston, TX 77204-4792, and will be accepted until four months after final publication of the paper itself in the ASME JOURNAL OF APPLIED MECHANICS.

Manuscript received by the ASME Applied Mechanics Division, June 11, 1991; final revision, Jan. 24, 1992. Associate Technical Editor: C. F. Shih.

Copyright © 1993 by ASME
Downloaded 03 May 2010 to 171.66.16.245. Redistribution subject to ASME license or copyright; see http://www.asme.org/terms/Terms_Use.cfm

and of a related method for the direct determination of the plastic shakedown boundary.

A compact notation will be used throughout, with vectors and tensors denoted by boldface symbols and their scalar products denoted by a dot or a colon, for instance, using the summation rule for repeated indices: $\mathbf{u} \cdot \mathbf{v} = u_i v_i$, $\boldsymbol{\sigma} : \boldsymbol{\epsilon} = \sigma_{ji}\epsilon_{ji}$, $\boldsymbol{\sigma} : \mathbf{A} : \boldsymbol{\sigma} = A_{ijhk}\sigma_{ij}\sigma_{jk}$, $(\mathbf{n} \cdot \boldsymbol{\sigma})_i = (\boldsymbol{\sigma} \cdot \mathbf{n})_i = \sigma_{ji}n_j$, $(\mathbf{A} : \boldsymbol{\sigma})_{ij} = A_{ijhk}\sigma_{hk}$. Other symbols will be defined where they first appear.

The Steady-State Response and Preliminary Remarks

Let a solid body (or structure) of elastic-perfectly plastic material occupy the (open) domain V of boundary surface ∂V and let it be referred to a Cartesian orthogonal coordinate system $\mathbf{x} = (x_1, x_2, x_3)$. The body is subjected to external actions like body forces in V, tractions on the free boundary $\partial_t V \subset \partial V$, imposed (e.g., thermal) strains in V, and imposed displacements on the constrained boundary $\partial_u V \subset \partial V$, $\partial_t V \cup \partial_u V = \partial V$. All these actions are here collectively denoted by the symbol P and represented as

$$P(t) = P^c(t) + P^0,\ 0 \le t \le \Delta t,\ P^0 \in \mathcal{P}^0 \tag{1}$$

to point out that the loading is a combination of a cyclically variable load $P^c(t)$ and of a time-independent (or steady) load P^0. By hypothesis $P^c(t)$ includes mechanical and/or kinematical loads like those mentioned here above, whereas P^0 includes only mechanical loads; additionally, the set $\mathcal{P}^0$ collects all the loads below the plastic collapse limit values (but on occasion may be a narrower one). Further hypotheses are: the inertia and the viscous forces are negligible, the material data is independent of temperature variations, and the classical infinitesimal displacement theory is applicable.

Let $\boldsymbol{\sigma}^E(\mathbf{x}, t)$ denote the elastic stress response of the body to $P(t)$, that is, the actual stress response when the existence of a yield surface is ignored. Obviously, one can write

$$\boldsymbol{\sigma}^E(\mathbf{x},t) = \boldsymbol{\sigma}^c(\mathbf{x},t) + \boldsymbol{\sigma}^0(\mathbf{x}) \tag{2}$$

where $\boldsymbol{\sigma}^c(\mathbf{x},t)$ and $\boldsymbol{\sigma}^0(\mathbf{x})$ are the elastic stress responses to $P^c(t)$ and P^0, respectively. Let $\boldsymbol{\sigma}$ and $\dot{\boldsymbol{\epsilon}}^p$ be the actual stresses and plastic strain rates in the steady cycle, showing periodicity features with the same period Δt of the loads, that is $\boldsymbol{\sigma}(\mathbf{x}, t) = \boldsymbol{\sigma}(\mathbf{x}, t + \Delta t)$ and $\dot{\boldsymbol{\epsilon}}^p(\mathbf{x}, t) = \dot{\boldsymbol{\epsilon}}^p(\mathbf{x}, t + \Delta t)$ everywhere in V and for all $t \in (0, \Delta t)$. The existence of such a steady cycle, or steady-state response, in perfect plasticity has been proven by many authors; see, e.g., Frederich and Armstrong (1966), Martin (1975), Halphen (1979), and Gokhfeld and Cherniavsky (1980). The equations which govern this steady-state response can be written as

$$\phi(\boldsymbol{\sigma}) \le 0,\ \dot{\lambda} \ge 0,\ \dot{\lambda}\phi(\boldsymbol{\sigma}) = 0 \text{ all in } V \times (0, \Delta t) \tag{3}$$

$$\boldsymbol{\sigma} = \boldsymbol{\sigma}^E + \boldsymbol{\sigma}^R,\ \dot{\boldsymbol{\epsilon}}^p = \frac{\partial \phi}{\partial \boldsymbol{\sigma}}\dot{\lambda} \text{ all in } V \times (0, \Delta t) \tag{4}$$

$$C^T\boldsymbol{\sigma}^R = \mathbf{0} \text{ in } V \times (0, \Delta t),\ \boldsymbol{\sigma}^R \cdot \mathbf{n} = \mathbf{0} \text{ on } \partial_t V \times (0, \Delta t) \tag{5a}$$

$$C\dot{\mathbf{u}}^R = \mathbf{A} : \dot{\boldsymbol{\sigma}}^R + \dot{\boldsymbol{\epsilon}}^p \text{ in } V \times (0, \Delta t),\ \dot{\mathbf{u}}^R = \mathbf{0} \text{ on } \partial_t V \times (0, \Delta t) \tag{5b}$$

$$\Delta\boldsymbol{\epsilon}^p = \int_0^{\Delta t} \dot{\boldsymbol{\epsilon}}^p dt,\ \Delta\mathbf{u}^R = \int_0^{\Delta t} \dot{\mathbf{u}}^R dt \text{ all in } V \tag{6a}$$

$$C\Delta\mathbf{u}^R = \Delta\boldsymbol{\epsilon}^p \text{ in } V,\ \Delta\mathbf{u}^R = \mathbf{0} \text{ on } \partial_u V. \tag{6b}$$

Here above, $\boldsymbol{\sigma}^R$ denotes the actual residual stresses, $\Delta\boldsymbol{\epsilon}^p$ the ratchet (plastic) strain compatible with the cycle net residual displacement $\Delta\mathbf{u}^R$; moreover, C denotes the compatibility differential operator, whereas C^T is the adjoint of C, that is

$$C\mathbf{u} = \frac{1}{2}[\text{grad } \mathbf{u} + (\text{grad } \mathbf{u})^T],\ C^T\boldsymbol{\sigma} = \text{div}\boldsymbol{\sigma}. \tag{7}$$

Finally, $\mathbf{A}$ is the elastic compliance fourth-order tensor with its usual symmetry properties, $\mathbf{n}$ denotes the unit external normal to the boundary surface, and $\phi(\boldsymbol{\sigma})$ is the yield function, by hypothesis convex and smooth, playing also the role of plastic potential (associated plasticity). Equations (3)–(6) look like a standard elastic-plastic evolutive problem, but instead of the usual initial conditions one has time-integral conditions expressing that the net plastic strains produced, $\Delta\boldsymbol{\epsilon}^p$, be a compatible strain field.

For a specified load as (1), Eqs. (3)–(6) admit a solution that describes the body's steady-state response. This solution, referred to as the "steady-state solution" in the following, enjoys the following properties; see, e.g., Martin (1975) and Polizzotto et al. (1990):

(i) The plastic strain rates $\dot{\boldsymbol{\epsilon}}^p$ are uniquely determined at all instants in $(0, \Delta t)$ and at all points in V—including the "elastic" region $V_e \subset V$ (if any) where $\dot{\boldsymbol{\epsilon}}^p$ turns out to vanish identically.

(ii) The residual stresses $\boldsymbol{\sigma}^R$ are uniquely determined only within the "plastic" region V_p, where $\dot{\boldsymbol{\epsilon}}^p$ is not identically vanishing, $V_p \cup V_e = V$.

(iii) The steady-state solution is independent of any initial plastic strains as well as of the load cycle origin.

The residual stresses $\boldsymbol{\sigma}^R$ can be written as

$$\boldsymbol{\sigma}^R(\mathbf{x}, t) = \boldsymbol{\rho}(\mathbf{x}) + \tau(\mathbf{x}, t) \tag{8}$$

where, by definition, $\boldsymbol{\rho}$ denotes the *post-transient* (PT) self-stresses, that is the residual stresses at the instant of stabilization, i.e., the instant at which the transient phase terminates and the steady-state one begins. The latter instant coincides with some $t_0 \in (0, \Delta t)$ within some subsequent load cycle, such that $\boldsymbol{\rho}(\mathbf{x}) = \boldsymbol{\sigma}^R(\mathbf{x}, t_0)$. Thus, in virtue of property (iii), possibly through superposition of a suitable initial plastic strain and a change of the load cycle origin, t_0 can be thought to vanish (i.e., stabilization occurs at the start of some subsequent cycle), such that $\tau(\mathbf{x}, t)$ is expressed as

$$\tau(\mathbf{x}, t) = \int_0^t \dot{\boldsymbol{\sigma}}^R(\mathbf{x}, \bar{t})\, d\bar{t}. \tag{9}$$

Since $\dot{\boldsymbol{\sigma}}^R \equiv \dot{\tau}$ is uniquely determined in $V \times (0, \Delta t)$ like the corresponding $\dot{\boldsymbol{\epsilon}}^p$, from property (ii) above stems that $\boldsymbol{\rho}$ in Eq. (8) is uniquely determined only within V_p. It is worth noting that, on applying the body the given cyclic load together with initial stresses identifying with the above $\boldsymbol{\rho}$, no transient phase is displayed by the body's response.

The plastic strain rates $\dot{\boldsymbol{\epsilon}}^p$ pertaining to the steady-state solution constitute a Plastic Accumulation Mechanism (PAM), meaning that they result in compatible plastic strains, $\Delta\boldsymbol{\epsilon}^p$, at every cycle. Three types of steady-state solutions can be distinguished on the basis of the related PAM, namely

—*elastic shakedown*, when $\dot{\boldsymbol{\epsilon}}^p = \mathbf{0}$ in $V \times (0, \Delta t)$;

—*plastic shakedown*, when $\dot{\boldsymbol{\epsilon}}^p$ is not identically vanishing, but $\Delta\boldsymbol{\epsilon}^p = \mathbf{0}$ in V; and

—*ratchetting*, when $\Delta\boldsymbol{\epsilon}^p \neq \mathbf{0}$ at least somewhere in V.

Let $P^c(t)$ belong to a one-parameter load family, i.e., $P^c(t) = \beta\bar{P}^c(t)$, with β being a scalar variable and $\bar{P}^c(t)$ some specified cyclic load, hence $\boldsymbol{\sigma}^c = \beta\bar{\boldsymbol{\sigma}}^c$, where $\bar{\boldsymbol{\sigma}}^c$ is the elastic stress response to $\bar{P}^c(t)$. The steady-state response as the solution to Eqs. (3)–(6) turns out to depend on the load parameters (P^0, β); thus on the basis of the related PAM, the domain B of the load set (P^0, β) not exceeding the plastic collapse limit values can be divided into three zones, i.e., $B = B_S \cup B_F \cup B_R$, where B_S is the elastic shakedown zone, B_F the plastic shakedown zone, and B_R the ratchetting zone, so obtaining an interaction diagram (or generalized Bree diagram); see Fig. 1(*a*, *b*) relative to the one-dimensional case $P^0 = \alpha\bar{P}^0$, hence $\mathcal{P}^0 = \{\alpha\}$. The boundary ∂B identifies with the plastic collapse limit surface of the structure.

As pointed out by Polizzotto (1993a, b), for a given structure-cyclic load system, a value $\beta = \beta^*$ can be determined called the "plastic shakedown limit load," such that for $\beta \le$

Downloaded 03 May 2010 to 171.66.16.245. Redistribution subject to ASME license or copyright; see http://www.asme.org/terms/Terms_Use.cfm

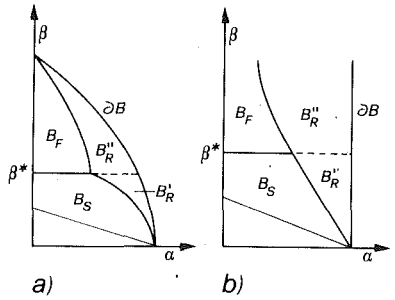


Fig. 1 Sketches of the interaction diagram for a cyclic load $P^c(t)$ and a steady mechanical load $P^0 = \alpha\bar{P}^0$: (a) mechanical cyclic load; (b) thermal cyclic load

β^* plastic shakedown cannot occur, whatever the steady load $P^0 \in \mathcal{P}^0$ acting with $\beta\bar{P}^c(t)$, (but the structure is in a limit state with an impending alternating plasticity collapse for $\beta = \beta^*$, provided P^0 is within some range). Also, the following can be stated:

—The plane $\beta = \beta^*$ leaves the B_S and B_F zones in opposite sides and cuts the B_R zone into two parts, $B_R = B_R' \cup B_R''$ (with B_R' for $\beta \le \beta^*$, see Fig. 1(a, b)).

—For $\beta \le \beta^*$ the only forms of steady-state response are either elastic shakedown (B_S), or ratchetting (B_R''), and the classical shakedown theorems enable one to specify the boundary between the B_S and the B_R'' zones; this may be useful for design purposes in order to prevent the structure from plastic strain growth.

—For $\beta > \beta^*$ the only forms of steady-state response are either plastic shakedown or ratchetting, but theorems like those of elastic shakedown theory to locate the boundary between the B_F and the B_R'' zones are not available, as already explained in the Introduction.

Sensitivity of the Steady-State Response to Load Changes

As pointed out in the preceding section, the steady-state response as the solution to Eqs. (3)–(6) turns out to depend on the load parameter (P^0, β). It is crucial for the purposes of this paper to investigate the sensitivity of the above solution to changes of these parameters. Such an investigation was previously achieved by Polizzotto et al. (1990), but a one-parameter steady load $P^0 = \alpha\bar{P}^0$ was considered there. Here, P^0 is allowed to change freely within some specified set $\mathcal{P}^0$, hereafter assumed to collect all loads below the plastic collapse limit values.

The plastic dissipation density $D(\dot{\epsilon}^p)$ in the steady cycle corresponding to a specified set (P^0, β) is

$$D(\dot{\epsilon}^p) = \sigma : \dot{\epsilon}^p = (\beta\bar{\sigma}^c + \sigma^0 + \rho + \tau) : \dot{\epsilon}^p \ge 0 \text{ in } V \times (0, \Delta t) \tag{10}$$

and the total plastic work dissipated in the body in a complete cycle is

$$W = \int_0^{\Delta t} \int_V D(\dot{\epsilon}^p) dV\, dt$$

$$= A_0 + \beta A_c + \int_V \rho : \Delta\epsilon^p dV + \int_0^{\Delta t} \int_V \tau : \dot{\epsilon}^p dV\, dt \tag{11}$$

where, by definition,

$$A_0 = \int_V \sigma^0 : \Delta\epsilon^p\, dV \quad \text{(primary accumulation parameter)} \tag{12}$$

$$A_c = \int_0^{\Delta t} \int_V \bar{\sigma}^c : \dot{\epsilon}^p dV\, dt$$

(secondary net accumulation parameter). (13)

Since in virtue of Eqs. (5) and (6) the two integrals on the r.h.s. of Eq. (11) can be shown to vanish, Eq. (11) simplifies to

$$W = A_0 + \beta A_c. \tag{14}$$

Obviously, W is a non-negative function of P^0 and β, i.e., $W = W(P^0, \beta) \ge 0$, and it vanishes only within the B_S zone, including ∂B_S. W equals the total work performed by the loads in a complete cycle, as it can be easily shown.

Let $(P^0 + dP^0, \beta + d\beta)$ be another load set with the increments dP^0 and $d\beta$ arbitrary but sufficiently small. The new steady-state response will slightly differ—on assumption of structural stability conditions—from the previous one, and let $d\sigma, d\dot{\epsilon}^p, \ldots$ be the relevant response increments. By Drucker's local stability postulate one can write

$$d^2D(\dot{\epsilon}^p) = d\sigma : d\dot{\epsilon}^p \ge 0 \text{ in } V \times (0, \Delta t) \tag{15}$$

where d^2D is the second variation of D consequent to the load change. The integration of (15) over $V \times (0, \Delta t)$ yields

$$d^2W = \int_0^{\Delta t} \int_V d^2D\, dV\, dt = \int_0^{\Delta t} \int_V d\sigma : d\dot{\epsilon}^p dV\, dt \ge 0 \tag{16}$$

where d^2W is the second variation of W. Since

$$d\sigma(\mathbf{x}, t) = d\beta\bar{\sigma}^c(\mathbf{x}, t) + d\sigma^0(\mathbf{x}) + d\rho(\mathbf{x}) + d\tau(\mathbf{x}, t), \tag{17}$$

Eq. (16) becomes

$$d^2W = d^2A_0 + d\beta dA_c + \int_V d\rho : d(\Delta\epsilon^p) dV + \int_0^{\Delta t} \int_V d\tau : d\dot{\epsilon}^p dV\, dt \tag{18}$$

where

$$d^2A_0 = \int_V d\sigma^0 : d(\Delta\epsilon^p) dV = \int_V d\sigma^0 : \Delta(d\epsilon^p) dV \tag{19}$$

$$dA_c = \int_0^{\Delta t} \int_V \bar{\sigma}^c : d\dot{\epsilon}^p dV\, dt. \tag{20}$$

As the two integrals on the r.h.s. of (18) vanish like the analogous integrals on the r.h.s. of (11), Eq. (16) becomes

$$d^2W = d^2A_0 + d\beta dA_c \ge 0. \tag{21}$$

This inequality generalizes to a multidimensional P^0 that given by Polizzotto et al. (1990) for $P^0 = \alpha\bar{P}^0$ and $\mathcal{P}^0 = \{\alpha\}$, but its meaning remains unaltered. It constitutes a *Stability Principle* for the steady-state solution, in the sense that:

—If $d^2W > 0$ at a point (P^0, β) and for all $(dP^0, d\beta)$ the steady-state solution is there *strongly stable*, namely the PAM at (P^0, β) is fully sensitive to the load increments. This is the typical behavior of the B_R zone.

—If $d^2W = 0$ at some (P^0, β) and for load increments in some subset $dB = \{dP^0, d\beta\}$, but $d^2W > 0$ for any other load increments, the steady-state solution is *weakly stable*, namely it is stable for all load increments $(dP^0, d\beta)$, except those in dB for which it shows indifference, that is, the PAM pertaining to (P^0, β) is insensitive to load increments in dB. This is the typical behavior of the B_F zone, with $dB = \{dP^0, 0\}$.

—If $d^2W = 0$ at a point (P^0, β) and for all load increments $(dP^0, d\beta)$, the steady-state solution is indifferent, namely the PAM at (P^0, β) is fully insensitive to the load increments. This is the typical behavior of the B_S zone.

From what precedes, it transpires that the second variation of the through-cycle total plastic dissipation, d^2W, provides a scalar quantity measuring the sensitivity of the steady-state response to the load changes, able to characterize the different zones of the interaction diagram with their different structural behaviors (Polizzotto et al., 1990). This will be discussed in more detail in the next section for the B_F zone.

Downloaded 03 May 2010 to 171.66.16.245. Redistribution subject to ASME license or copyright; see http://www.asme.org/terms/Terms_Use.cfm

Plastic Shakedown and Insensitivity of the PAM to Steady Load Changes

Let at a load point (P^0, β) where $W(P^0, \beta) > 0$ the equality

$$d^2W = d^2A_0 + d\beta dA_c = 0 \tag{22}$$

be satisfied for all steady load increments dP^0 and some $d\beta$. As a consequence of (15) and (16), it is

$$d^2D(\dot{\epsilon}^p) = d\sigma : d\dot{\epsilon}^p = 0 \text{ in } V \times (0, \Delta t). \tag{23}$$

In consideration of the smoothness of ϕ, Eq. (23) implies that $d\dot{\epsilon}^p = \mathbf{0}$ and $d\sigma = \mathbf{0}$ in $V_p \times (0, \Delta t)_p$ where $\dot{\epsilon}^p \neq \mathbf{0}$, with $(0, \Delta t)_p$ being the set of times in $(0, \Delta t)$ at which $\dot{\epsilon}^p$ is not vanishing, whereas in the complementary space-time domain one has $d\dot{\epsilon}^p \equiv \mathbf{0}$ but $d\sigma$ may be not vanishing. Therefore, the PAM related to the considered load point does not change in consequence of the above load increments. In addition, in virtue of Eq. (17) and remarking that $d\tau = \int_0^t d\dot{\tau}(\mathbf{x}, \bar{t})\, d\bar{t}$ must vanish identically as a consequence of the vanishing of $d\dot{\epsilon}^p$ everywhere in $V \times (0, \Delta t)$, one can write

$$d\sigma = d\beta\bar{\sigma}^c(\mathbf{x}, t) + d\sigma^0(\mathbf{x}) + d\rho(\mathbf{x}) = \mathbf{0} \tag{24}$$

to hold within $V_p \times (0, \Delta t)_p$. Since $(0, \Delta t)_p$ cannot reduce to an isolated time instant (otherwise the PAM would be a plastic collapse mechanism, what is impossible), Eq. (24) is satisfied only if

$$d\beta = 0,\ d\sigma = d\sigma^0(\mathbf{x}) + d\rho(\mathbf{x}) = \mathbf{0} \text{ in } V_p. \tag{25}$$

In other words, one can state the following:

(a) The only load increments for which $d^2W = 0$, hence $d^2D = 0$ identically, are increments of the steady loads alone ($d\beta = 0$).

(b) The region V_p cannot include points of application of dP^0, for in V_p—where $\sigma(\mathbf{x}, t)$ remains unaltered—the elastic stress response $d\sigma^0$ to dP^0 must constitute a self-stress field.

(c) A complementary nonempty elastic region, V_e, must exist where the stress increment $d\sigma = d\sigma^0 + d\rho$ is in equilibrium with dP^0, without attaining the yield condition, i.e., $\phi(\sigma + d\sigma) < 0$ for all $t \in (0, \Delta t)$.

(d) The PAM pertaining to (P^0, β) is insensitive to any dP^0 as indicated above.

The above picture may change somewhat in case of a nonsmooth yield function, but here points (a) to (d) are assumed to hold in any case.

The integral

$$\int_0^{\Delta t}\int_V d\sigma : \dot{\epsilon}^p dV\, dt = \int_V d\sigma^0 : \Delta\epsilon^p dV + \int_V d\rho : \Delta\epsilon^p dV = 0 \tag{26}$$

is vanishing because $d\sigma = d\sigma^0 + d\rho$ vanishes in V_p (where $\dot{\epsilon}^p \not\equiv \mathbf{0}$) and $\dot{\epsilon}^p = \mathbf{0}$ in $V_e \times (0, \Delta t)$ (where $d\sigma \not\equiv \mathbf{0}$). Considering that the last integral on the r.h.s. of (26) is zero ($d\rho$ is a self-stress field, $\Delta\epsilon^p$ is a compatible strain field with zero displacements on $\partial_u V$), one has

$$\int_V d\sigma^0 : \Delta\epsilon^p dV = 0. \tag{27}$$

The latter equality, being satisfied for arbitrary dP^0, hence for arbitrary fields $d\sigma^0$, yields

$$\Delta\epsilon^p(\mathbf{x}) = \mathbf{0} \text{ in } V, \tag{28}$$

that is, plastic shakedown occurs under the considered load (P^0, β). Due to the insensitivity of the PAM to dP^0, plastic shakedown occurs also under the augmented loads $(P^0 + dP^0, \beta)$ with the alternating plastic strains taking place always within the same region $V_p = V_F$.

Conversely, let plastic shakedown occurs under the load (P^0, β), as well as under the augmented load $(P^0 + dP^0, \beta)$, for arbitrary small dP^0. Since, then, $\Delta\epsilon^p = \mathbf{0}$ in V and $d(\Delta\epsilon^p) = \mathbf{0}$ in V for arbitrary small dP^0, it follows that $d^2W = d^2A_0 = 0$ for arbitrary steady load increments and thus properties (b) to (d) above are met.

The results of this section can be summarized by the following propositions:

Proposition 1. Plastic shakedown is characterized by the vanishing of the second variation of the through-cycle total plastic dissipation of the body as a result of small changes of the steady (mechanical) load, as well as by the insensitivity of the related PAM to the said load changes.

Proposition 2. In conditions of plastic shakedown, the body is divided into two regions, $V = V_F \cup V_e$, with V_F being the region where alternating plastic strains take place and V_e that where no plastic strains occur (within the steady cycle); furthermore, any small increments of steady mechanical loads dP^0 applied upon V_e leave unaltered the region V_F together with the cyclic stress and plastic strain rate histories therein occurring, but cause equilibrium stress increments in the region V_e without yield violations.

It is worth remarking that whenever the load point (P^0, β) is one of the set $\partial B_F \cap \partial B_R$, i.e., the boundary between the B_F zone and the B_R zone, the load increments dP^0 considered in the above propositions cannot be completely arbitrary, for $(P^0 + dP^0, \beta)$ must still be in B_F.

Existence of an Elastic Region V_e

Proposition 2 states that the body suffering plastic shakedown contains a nonempty region V_e where the material responds elastically to the loads in the cycle. It can be proven that, for loads above the elastic shakedown limit, such an elastic region can exist only if plastic shakedown occurs.

To this purpose, let the body be loaded by some load (P^0, β) such that $W(P^0, \beta) > 0$ and let, by hypothesis, there correspondingly exist a region $V_e \subset V$ where $\dot{\epsilon}^p(\mathbf{x}, t)$ vanishes identically in the cycle. Reminding Eqs. (3)–(6), one can write

$$\phi(\sigma) \leq 0,\ \dot{\lambda} \geq 0,\ \dot{\lambda}\phi(\sigma) = 0 \text{ in } V_p \times (0, \Delta t) \tag{29a}$$

$$\phi(\sigma) < 0,\ \dot{\lambda} = 0 \text{ in } V_e \times (0, \Delta t) \tag{29b}$$

$$\sigma = \sigma^E + \sigma^R = \sigma^E + \rho + \tau \text{ in } V \times (0, \Delta t) \tag{29c}$$

where V_p is the region of V where some nonvanishing plastic flow must take place ($V_p \cup V_e = V$), and σ^R is the actual residual stress history, Eq. (8).

Let $d\sigma^0$ denote the elastic stress response of the body to an arbitrary dP^0, but having application points in V_e, and let $d\rho$ be some time-independent self-stress field in V. dP^0 is assumed sufficiently small and $d\rho$ is so chosen that the stress field $d\sigma = d\rho + d\sigma^0$ satisfies the conditions

$$d\sigma = \mathbf{0} \text{ in } V_p \text{ and } \phi(\sigma + d\sigma) < 0 \text{ in } V_e \times (0, \Delta t), \tag{30}$$

such that Eqs. (29*a*, *b*) are still satisfied if σ is replaced by $\sigma + d\sigma$, but $\dot{\lambda}$ left unchanged. This implies that Eqs. (3)–(6) are all satisfied by the same kinematical variables $\dot{\epsilon}^p(\mathbf{x}, t)$, $\dot{\lambda}(\mathbf{x}, t)$, $\dot{\mathbf{u}}^R(\mathbf{x}, t)$ pertaining to (P^0, β), but the statical variables replaced by the following starred ones (except τ which is left unaltered), i.e.,

$$\sigma^* = \sigma + d\sigma = \sigma^{E*} + \sigma^{R*}, \text{ where} \tag{31a}$$

$$\sigma^{E*} = \sigma^E + d\sigma^0,\ \sigma^{R*} = \rho + d\rho + \tau = \rho^* + \tau, \tag{31b}$$

where $d\sigma = d\rho + d\sigma^0$ is the same stress field of (30). Since Eqs. (3)–(6), so rewritten, provide the steady-state response to the load $(P^0 + dP^0, \beta)$, and in view of the solution uniqueness features, one can state that the PAM related to (P^0, β) does not change, thus $d^2W = 0$ as a consequence of arbitrary (sufficiently small) dP^0 applied upon V_e, and therefore the load (P^0, β) produces plastic shakedown. Obviously, for loads

Downloaded 03 May 2010 to 171.66.16.245. Redistribution subject to ASME license or copyright; see http://www.asme.org/terms/Terms_Use.cfm

not exceeding the elastic shakedown limit, one has $V_e = V$. As a conclusion, one can state the following:

Proposition 3. The existence within the body of a nonempty region $V_e \subset V$ where the material responds to the loads in a purely elastic manner in the steady cycle is possible if and only if the given load (by hypothesis exceeding the elastic shakedown limit) produces plastic shakedown.

Partial Elastic Shakedown

Let the body be subjected to a load (P^0, β) producing plastic shakedown, and let $V_p = V_F$ be the region of V where alternating plastic strains take place and V_e the complementary elastic region, the two regions being separated by the interface Γ. Within V_e, the actual stresses σ do not attain the yield condition, i.e.,

$$\phi(\sigma) < 0 \text{ in } V_e \times (0, \Delta t), \text{ where} \tag{32a}$$

$$\sigma = \sigma(\mathbf{x}, t) = \sigma^E(\mathbf{x}, t) + \rho(\mathbf{x}) + \tau(\mathbf{x}, t). \tag{32b}$$

Since the field $\rho(\mathbf{x})$ is uniquely determined in V_F but not in V_e, one can write

$$\rho(\mathbf{x}) = \hat{\rho}(\mathbf{x}) + \mathbf{r}(\mathbf{x}) \text{ in } V_e \tag{33}$$

where $\hat{\rho}$ is some particular choice for ρ within V_e and $\mathbf{r}(\mathbf{x})$ is an arbitrary time-independent self-stress field of V_e, that is, of V_e considered isolated after removal of V_F (Fig. 2). Thus, the actual stress field σ in V_e can be given the expression

$$\sigma(\mathbf{x}, t) = \hat{\sigma}^E(\mathbf{x}, t) + \mathbf{r}(\mathbf{x}) \text{ in } V_e \times (0, \Delta t), \text{ where} \tag{34a}$$

$$\hat{\sigma}^E(\mathbf{x}, t) = \sigma^E(\mathbf{x}, t) + \hat{\rho}(\mathbf{x}) + \tau(\mathbf{x}, t) \text{ in } V_e \times (0, \Delta t). \tag{34b}$$

The stress field $\hat{\sigma}^E(\mathbf{x}, t)$ can be viewed as the elastic stress response of V_e to external actions applied upon it, namely (Fig. 2):

—$\sigma^E(\mathbf{x}, t)$ is the elastic stress response to the given loads directly applied upon V_e and to the tractions $\mathbf{t}^E_{(\nu)} = \sigma^E \cdot \nu$ on Γ, with ν = unit external normal of Γ (oriented towards V_F).

—$\hat{\rho}(\mathbf{x})$ can always be identified with the elastic stress response of V_e to the tractions $\mathbf{t}^{\{\rho\}}_{(\nu)} = \rho \cdot \nu$ on Γ, the latter being uniquely determined as so is ρ all over Γ.

—$\tau(\mathbf{x}, t)$ is the elastic stress response of V_e to the tractions $\mathbf{t}^{\{\tau\}}_{(\nu)} = \tau \cdot \nu$ on Γ, due to the fact that no plastic strains occur in V_e during the steady cycle.

Since the stress field (34*a*) does not violate the yield condition throughout V_e and for all the load conditions, in virtue of the Bleich-Melan theorem one can state that elastic shakedown occurs in V_e. This statement was firstly given without proof by Ponter (1983) (see also Ponter and Karadeniz (1985a, b)). The symbols V_F and V_S for V_p and V_e were used by Ponter to emphasize the above phenomena. The above result is also in agreement with that given by Polizzotto (1993a, b) for a body in the plastic shakedown limit state, that is, under a cyclic load $\beta^* \overline{P}^c(t)$. Thus, one can state the following:

Proposition 4. Plastic shakedown implies that the body finds itself in a condition of partial elastic shakedown, that is, the given load history causes a nonempty region $V_S \subset V$ to shake down to the elastic state, whereas the complementary region V_F suffers alternating plastic strains.

Transition From Plastic Shakedown to Ratchetting

Let the body of the previous section still be considered and let $P^0_a = \alpha \overline{P}^0_a$ be an additional steady mechanical load, with $\overline{P}^0_a$ specified and α a scalar variable, and let its application points belong to the V_S region of the body. Since, by hypothesis, the body is in condition of plastic shakedown, the related PAM is insensitive to the additional load P^0_a, and thus plastic shakedown continues to occur with increasing α, provided α is not too large to make the isolated body V_S lose its capacity to shake down to the elastic state. Thus, a limit value α_R can

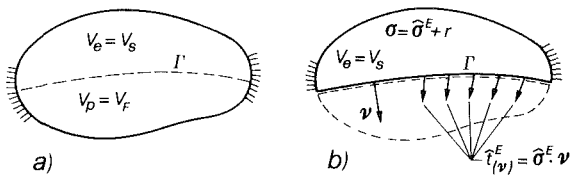


Fig. 2 Solid body subjected to a combined load $P^c(t) + P^0$ producing plastic shakedown: (*a*) subdivision of the body into V_F = region of alternating plastic strains, and V_S = elastic region; (*b*) isolated body V_S (after removal of V_F) in conditions of (partial) elastic shakedown

be envisaged, which corresponds to the body's transition from plastic shakedown to ratchetting, such that the load point $(P^0 + \alpha_R \overline{P}^0_a, \beta)$ belongs to the boundary $\partial B_F \cap \partial B_R$.

Obviously, α_R can be determined as the elastic shakedown limit load for the isolated body V_S, namely, on replacing the self-stresses $\mathbf{r}$ of Eq. (34*a*) with the stresses $\mathbf{s}_a$ equilibrating $\alpha \overline{P}^0_a$, one has to solve the problem:

$$\alpha_R = \max_{(\alpha, \mathbf{s}_a)} \alpha \text{ s.t. } \begin{cases} \phi(\hat{\sigma}^E(\mathbf{x}, t) + \mathbf{s}_a(\mathbf{x})) \le 0 \text{ in } V_S \times (0, \Delta t) \\ \text{equilibrium conditions on } \mathbf{s}_a \text{ with } \alpha \overline{P}^0_a \end{cases} \tag{35}$$

where "s.t." stands for "subject to." However, two difficulties must be overcome before problem (35) may be actually solved, one of which is the a priori determination of the V_S region, and another is the presence of the actual cyclic self-stresses τ as part of $\hat{\sigma}^E$. Obviously, if the V_S body turns out to be unconstrained upon its boundary surface, i.e., if $\partial_u V \cap \partial V_S = 0$, one has $\alpha_R = 0$. The topic of this section will be addressed in the Part II of this paper. It will be shown that (35) appeals to Ponter's method for the approximate determination of the plastic shakedown boundary for cyclically hardening materials (see Ponter (1983), Ponter and Karadeniz (1985a, b), Ponter et al. (1990), and Polizzotto (1989)). In the meanwhile, one can state the following:

Proposition 5. The occurrence of plastic shakedown under a given load (P^0, β) acting alone, or also together with an arbitrary additional steady (mechanical) load P^0_a applied upon the V_S region, will persist as long as V_S, viewed as an isolated body, has the capacity to shake down to the elastic state. Exhaustion of this capacity marks the transition of the body from plastic shakedown to ratchetting.

It is worth noting that, for the loads (P^0, β^*) at the plastic shakedown limit, problem (35) coincides with one envisaged by Polizzotto (1993a, b) for the determination of the boundary line of the upper plateau (the flat portion in general present at the top of the B_S zone in Fig. 1(*a*, *b*)). The upper plateau reduces to a single point if problem (35) gives $\alpha_R = 0$.

Conclusions

Plastic shakedown of an elastic-perfectly plastic solid body may be caused by the action of a combination of a cyclic (mechanical and/or kinematical) load and a steady (mechanical) load. Whenever this is the case, some peculiar phenomena and properties can be recognized to characterize plastic shakedown. They are:

(a) The body is divided into two regions, $V = V_F \cup V_S$, V_F being the region where alternating plastic strains take place and V_S is the region of (partial) elastic shakedown, that is no plastic strains occur there in the steady cycle.

(b) This plastic shakedown state is insensitive to any additional (small) steady (mechanical) load with application points in V_S, which causes only a change of the stress field in V_S such as to equilibrate the additional load.

(c) A transition of the body from plastic shakedown to ratchetting occurs whenever the augmented load of point (b)

Downloaded 03 May 2010 to 171.66.16.245. Redistribution subject to ASME license or copyright; see http://www.asme.org/terms/Terms_Use.cfm

above is an elastic shakedown limit load for V_S viewed as an isolated body after removal of V_F.

The above picture generalizes, to a wider context, a similar picture previously envisaged by Ponter (1983) and Ponter and Karadeniz (1985a, b) with reference to thermal cyclic loads, mainly on the basis of heuristic, but strongly effective, arguments. Here, a more rational basis is provided together with some new concepts and results: as the concept of insensitivity to steady mechanical loads, the conditions for the existence of an elastic region, and the precise specification of the transition at point (c) above.

The above characterization of plastic shakedown will be utilized in Part II of this paper, which is devoted to the formulation of theorems of plastic shakedown.

Acknowledgment

This paper has been completed with the financial support of the Consiglio Nazionale delle Richerche, CNR, of Italy.

References

Frederich, C. O., and Armstrong, P. J., 1966, "Convergent Internal Stresses and Steady Cyclic States of Stress," *J. Strain Analysis*, Vol. 1, p. 154.

Gokhfeld, D. A., and Cherniavsky, D. F., 1980, *Limit Analysis of Structures at Thermal Cycling*, Sijthoff and Noordhoff, Alphen aan der Rijn, The Netherlands.

Halphen, B., 1979, "Steady Cycles and Shakedown in Elastic-Viscoplastic and Plastic Structures," *Matériaux et Structures sous Chargement Cyclique*, Association Amicale des Ingenieurs Anciens Elèves de l'Ecole National des Ponts et Chaussées, pp. 203–229.

Koiter, W. T., 1960, "General Theorems for Elastic-Plastic Solids," *Progress in Solid Mechanics*, Vol. 1, J. N. Sneddon, and R. Hill, eds., North Holland, Amsterdam, pp. 167–221.

König, J. A., 1987, *Shakedown of Elastic-Plastic Structures*, PWN—Polish Scientific Publishers, Warsaw, and Elsevir, Amsterdam.

König, J. A., and Maier, G., 1981, "Shakedown Analysis of Elastoplastic Structures: A Review of Recent Developments," *J. Nuclear Engng. Design*, Vol. 66, pp. 81–95.

Martin, J. B., 1975, *Plasticity: Fundamentals and General Results*, The MIT Press, Cambridge, MA.

Polizzotto, C., 1982, "A Unified Treatment of Shakedown Theory and Related Bounding Techniques," *S. M. Archives*, Vol. 7, pp. 19–75.

Polizzotto, C., 1989, *Simplified Methods of Structural Analysis for Cyclic Plasticity*, Final Report RA1-0116(I), Commission of European Communities, Brussels, and Dipartimento di Ingegneria Strutturale & Geotecnica, Università di Palermo, Palermo.

Polizzotto, C., 1993a, "On the Condition to Prevent Plastic Shakedown of Structures, Part 1: Theory," ASME JOURNAL OF APPLIED MECHANICS, Vol. 60, pp. 15–19.

Polizzotto, C., 1993b, "On the Condition to Prevent Plastic Shakedown of Structures, Part 2: The Plastic Shakedown Limit Load," ASME JOURNAL OF APPLIED MECHANICS, Vol. 60, pp. 20–25.

Polizzotto, C., Borino, G., and Fuschi, P., 1990, "On the Steady-State Response of Elastic Perfectly Plastic Solids to Cyclic Loads," *Inelastic Solids and Structures*, M. Kleiber and J. A. König, eds., Pineridge Press, Swansea, U.K., pp. 473–488.

Ponter, A. R. S., 1983, *Shakedown and Ratchetting Below the Creep Range*, Report EUR 8702 EN, Commission of European Communities, Brussels.

Ponter, A. R. S., and Karadeniz, S., 1985a, "An Extended Shakedown Theory for Structures that Suffer Cyclic Thermal Loadings, Part 1: Theory," ASME JOURNAL OF APPLIED MECHANICS, Vol. 60, pp. 877–882.

Ponter, A. R. S., and Karadeniz, S., 1985b, "An Extended Shakedown Theory for Structures that Suffer Cyclic Thermal Loadings, Part 2: Applications," ASME JOURNAL OF APPLIED MECHANICS, Vol. 60, pp. 883–889.

Ponter, A. R. S., Karadeniz, S., and Carter, K. F., 1990, "Extended Upper Bound Shakedown Theory and Finite Element Method for Axisymmetric Thin Shells," *Inelastic Solids and Structures*, M. Kleiber and J. A. König, eds., Pineridge Press, Swansea, U.K., pp. 433–449.

Symonds, P. S., and Neal, B. G., 1951, "Recent Progress in the Plastic Methods of Structural Analysis," *J. of the Franklin Institute*, Vol. 252, pp. 383–492.

Zarka, J., and Casier, J., 1979, "Cyclic Loading on Elastic-Plastic Structures," *Mechanics Today*, S. Nemat-Nasser, ed., Pergamon Press, Oxford, pp. 93–198.

Downloaded 03 May 2010 to 171.66.16.245. Redistribution subject to ASME license or copyright; see http://www.asme.org/terms/Terms_Use.cfm

Castrenze Polizzotto
Dipartimento di Ingegneria
Strutturale & Geotecnica, DISEG,
Università di Palermo,
I-90128 Palermo, Italy

A Study on Plastic Shakedown of Structures: Part II—Theorems

For a continuous elastic-perfectly plastic solid body subjected to a combination of cyclic (mechanical and/or kinematical) load and of a steady (mechanical) load, two theorems of plastic shakedown are presented, one stating a necessary condition, another stating a sufficient condition. The problem of the direct determination of the plastic shakedown boundary is also briefly addressed.

Introduction

In Part I of this paper, an elastic-perfectly plastic structure has been considered subjected to cyclic loads producing plastic shakedown, that is a long-term, or steady-state, response characterized by alternating plasticity. A number of peculiar properties of plastic shakedown have been there established. These properties, some of which had been previously envisaged by Ponter (1983) and Ponter and Karadeniz (1985a,b), with reference to a narrower context, (see also Polizzotto, 1989), can be summarized as follows:

(a) The volume V of the body is divided into two parts, $V = V_F \cup V_S$, where V_F is the region where alternating plastic strains take place, and V_S is the elastic region, namely where no plastic strains occur in the steady cycle.

(b) The V_S region—considered as an isolated body after removal of V_F and solicited by the loads directly applied upon it, including tractions transmitted by V_F through the interface Γ—finds itself in a condition of elastic shakedown.

(c) The body's state of plastic shakedown is insensitive to any additional steady mechanical load with application points in V_S, but a change of the stress field in V_S is produced such as to equilibrate the additional load, as far as the body's ability for partial elastic shakedown as described at point (b) above is not yet exhausted.

(d) A transition of the body from plastic shakedown to ratchetting occurs when the augmented load resulting from point (c) above is an elastic shakedown limit load for the isolated body V_S.

(e) No elastic region $V_e \subset V$ can exist in the state of ratchetting (i.e., incremental collapse).

The purpose of the present paper is the formulation of theorems of plastic shakedown, that is, theorems to recognize whether plastic shakedown occurs under a given cyclic load. Two theorems will be provided, one stating a necessary condition, another a sufficient condition for plastic shakedown. Also, a method for the direct determination of the plastic shakedown boundary will be discussed. The knowledge of such a boundary is paramount for design purposes in order to prevent plastic strain growth whenever a structure or structural component is required to operate, even in condition of plastic shakedown, as it may occur in the engineering practice, for instance within the framework of nuclear power plant applications.

A compact notation will be used throughout, with vectors and tensors denoted by boldface symbols and their scalar products denoted by a dot or a colon, for instance, using the summation rule for repeated indices: $\mathbf{u} \cdot \mathbf{v} = u_i v_i$, $\boldsymbol{\sigma} : \boldsymbol{\epsilon} = \sigma_{ji}\epsilon_{ji}$, $\boldsymbol{\sigma} : \mathbf{A} : \boldsymbol{\sigma} = A_{ijhk}\sigma_{ij}\sigma_{hk}$, $(\mathbf{n} \cdot \boldsymbol{\sigma})_i = (\boldsymbol{\sigma} \cdot \mathbf{n})_i = \sigma_{ji}n_j$, $(\mathbf{A} : \boldsymbol{\sigma})_{ij} = A_{ijhk}\sigma_{hk}$. Other symbols will be defined where they first appear.

Positions and Preliminary Considerations

A solid body (or structure) of elastic-perfectly plastic material, occupying the (open) domain V with boundary surface $\partial V = \partial_u V \cup \partial_t V$, is referred to a Cartesian orthogonal coordinate system $\mathbf{x} = (x_1, x_2, x_3)$. The external actions may be mechanical actions (as body forces in V, tractions on $\partial_t V$), or kinematical actions (as imposed strains in V and imposed displacements on $\partial_u V$), or both. All these actions are hereafter collectively represented as

$$P(t) = P^c(t) + P^0, \quad 0 \le t \le \Delta t, \quad P^0 \in \mathcal{P}^0 \tag{1}$$

to mean that the loading is a combination of a cyclic load $P^c(t)$ and of a time-independent (or steady) load P^0. By assumption, $P^c(t)$ may include any type of mechanical and/or kinematical loads among those aforementioned and constitutes a one-parameter load family, i.e., $P^c(t) = \beta \bar{P}^c(t)$, where $\bar{P}^c(t)$ is some reference cyclic loading and β is a non-negative scalar; furthermore, P^0 includes only mechanical loads and the set $\mathcal{P}^0$ collects all the loads below the plastic collapse limit values—but on occasion may be narrower. Further hypotheses are: temperature-independent material data, negligible inertia and viscous forces, and applicability of the classical infinitesimal displacement theory.

The elastic stress response (i.e., the actual response if the existence of a yield surface is ignored) of the body to a load as (1) with specified parameters (P^0, β) is denoted as

$$\boldsymbol{\sigma}^E(\mathbf{x}, t) = \boldsymbol{\sigma}^c(\mathbf{x}, t) + \boldsymbol{\sigma}^0(\mathbf{x}) \tag{2}$$

Contributed by the Applied Mechanics Division of THE AMERICAN SOCIETY OF MECHANICAL ENGINEERS for publication in the ASME JOURNAL OF APPLIED MECHANICS.

Discussion on this paper should be addressed to the Technical Editor, Professor Lewis T. Wheeler, Department of Mechanical Engineering, University of Houston, Houston, TX 77204-4792, and will be accepted until four months after final publication of the paper itself in the ASME JOURNAL OF APPLIED MECHANICS.

Manuscript received by the ASME Applied Mechanics Division, June 11, 1991; final revision, Jan. 24, 1992. Associate Technical Editor: C. F. Shih.

Copyright © 1993 by ASME
Downloaded 03 May 2010 to 171.66.16.245. Redistribution subject to ASME license or copyright; see http://www.asme.org/terms/Terms_Use.cfm

where $\sigma^c(\mathbf{x}, t)$ and $\sigma^0(\mathbf{x})$ are the elastic stress response to $P^c(t)$ and P^0, respectively. The actual elastic-plastic response includes a transient (short-term) response—which shows no periodicity features—and a steady-state (long-term) response, showing some periodicity features, namely the stresses σ and plastic strain rates $\dot{\epsilon}^p$ are periodic with the same period Δt of the loads (see, e.g., Frederich and Armstrong, 1966; Martin, 1975; Halphen, 1979; Zarka and Casier, 1979; Gokhfeld and Cherniavsky, 1980). The steady-state response is governed by a set of equations (see Polizzotto, 1991) which, assuming a smooth yield function $\phi(\sigma)$, enable one to state a number of properties which are worth being noticed here for greater clarity:

—The plastic strain rates $\dot{\epsilon}^p(\mathbf{x}, t)$ are uniquely determined in $V \times (0, \Delta t)$.

—The residual stresses $\sigma^R(\mathbf{x}, t)$ are uniquely determined everywhere, except within the "elastic" region V_e (if any) where no plastic strains occur in the steady cycle.

—The steady-state response is independent of any initial plastic strains, as well as of the load cycle origin.

On the basis of the above properties, the residual stresses can be represented as (see Polizzotto, 1991)

$$\sigma^R(\mathbf{x}, t) = \rho(\mathbf{x}) + \tau(\mathbf{x}, t) \tag{3}$$

where ρ denotes the post-transient (PT) self-stresses—that is the residual stresses corresponding to the plastic strains existing in the body at the stabilization time (i.e., the time at which the transient phase terminates and the steady-state one begins), whereas τ denotes the residual stresses corresponding to the net plastic strains occurring in the steady cycle. As pointed out in the companion paper, it is always possible—to within some initial plastic strains and a change of the load cycle origin—to make the stabilization to occur at the start of some subsequent cycle, such that τ reads

$$\tau(\mathbf{x}, t) = \int_0^t \dot{\sigma}^R(\mathbf{x}, \bar{t}) d\bar{t} \text{ in } V \times (0, \Delta t). \tag{4}$$

Since $\dot{\sigma}^R(\mathbf{x}, t) \equiv \dot{\tau}(\mathbf{x}, t)$ is uniquely determined everywhere in $V \times (0, \Delta t)$, hence so is $\tau(\mathbf{x}, t)$, and as a consequence of the second property mentioned above, $\rho(\mathbf{x})$ turns out to be uniquely determined everywhere, except in the elastic region V_e (if any).

Post-Transient Stresses and Plastic Overpotential (POP)

Combining Eqs. (2) and (3), the actual stress response can be written as

$$\sigma(\mathbf{x}, t) = \sigma^E(\mathbf{x}, t) + \sigma^R(\mathbf{x}, t) = \hat{\sigma}(\mathbf{x}, t) + \tau(\mathbf{x}, t) \tag{5}$$

where $\hat{\sigma}$, referred to as the post-transient (PT) stress field, is defined as

$$\hat{\sigma}(\mathbf{x}, t) = \sigma^E(\mathbf{x}, t) + \rho(\mathbf{x}) = \sigma^c(\mathbf{x}, t) + \sigma^0(\mathbf{x}) + \rho(\mathbf{x}). \tag{6}$$

In the stress space, the stress history $\sigma^c = \beta\bar{\sigma}^c$ defines—for every $\mathbf{x} \in V$—a stress path $S^c = \{\sigma^c(\mathbf{x}, t), 0 \le t \le \Delta t\}$, a closed line cyclically travelled by the stress point σ^c. In principle, S^c may be arbitrarily shaped, but in practice is a (plane, convex) polygonal line with a few vertices, quite often a straight segment. Analogously, the PT stress history $\hat{\sigma}(\mathbf{x}, t)$ defines, at every $\mathbf{x}$, the PT stress path $\hat{S}$ which, as shown by Fig. 1, can be thought of as being derived either from $S^c = \beta\bar{S}^c$ through the translation $\mathbf{s} = \sigma^0 + \rho$; i.e., $\hat{S} = S^c + \mathbf{s}$, or from $S^E = S^c + \sigma^0$, the stress path associated with σ^E, through the translation ρ; i.e., $\hat{S} = S^E + \rho$. Obviously, the PT stress path $\hat{S}$ is response dependent and its configuration depends on the load parameters (P^0, β).

In case of elastic shakedown, $\hat{S}$ is inside the yield surface $\phi(\sigma) = 0$ everywhere in V; otherwise, $\hat{S}$ exceeds the yield surface at least somewhere in V. A suitable measure of the yield violations of $\hat{S}$ at $\mathbf{x}$ is provided by a non-negative scalar, y,

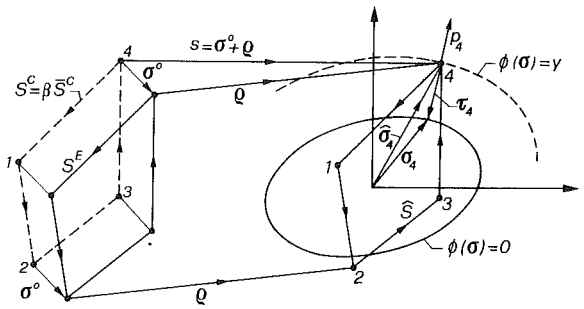


Fig. 1 Sketch illustrating the post-transient (PT) stress path $\hat{S} = \{\sigma^E(x, t) + \rho(x), 0 \le t \le \Delta t\}$ at a point $x \in V$, and related fictitious yield surface $\phi(\sigma) = y$

expressed in terms of the peak value of the plastic potential all along $\hat{S}$. In consideration of the polygonal shape of $\hat{S}$, characterized by the corner stresses $\hat{\sigma}_m = \hat{\sigma}(\mathbf{x}, t_m)$, all $m \in I(e) = \{1, 2, \ldots, e\}$, y can be defined as

$$y = \max\{0, \max_{m \in I(e)} \phi(\hat{\sigma}_m)\}. \tag{7}$$

The scalar y will be referred to as the PT *plastic overpotential* (POP) at $\mathbf{x}$ in the following, and the integral

$$Y = \int_V y dV \tag{8}$$

as the *total* PT-POP. The simplifying, but reasonable, hypothesis is here made that the instants t_m are independent of $\mathbf{x}$.

Let y_0 be the POP of S^E at $\mathbf{x}$, that is a quantity defined like y by (7), but with $\hat{\sigma}_m$ replaced by σ^E_m, and let $Y_0 = \int_V y_0 dV$. The transient response phase can be viewed as a process making the transfer of S^E to $\hat{S}$ through the translation ρ be accompanied by a global reduction of the stress path yield violations throughout V in the sense that $Y \le Y_0$. More precisely, let $\epsilon^p_{(i)}$ be the plastic strains in V at the end of the ith cycle and let $\rho_{(i)}$ be the corresponding residual stresses. At every $\mathbf{x} \in V$, a sequence of stress paths $S_{(i)} = S^E + \rho_{(i)}$ and of related POP's, $y_{(i)}$, are determined. The field $\epsilon^p_{(1)}$ is likely incompatible, so the field $\rho_{(1)}$ is nonvanishing, hence $y_{(1)} \ne y_0$ at least somewhere in V, but $Y_{(1)} \le Y_0$; then, if $\epsilon^p_{(2)} - \epsilon^p_{(1)}$ is incompatible too, one has $\rho_{(2)} \ne \rho_{(1)}$, hence $y_{(2)} \ne y_{(1)}$ at least somewhere in V, but $Y_{(2)} \le Y_{(1)}$; and so on until the nth cycle, at which $\epsilon^p_{(n)} - \epsilon^p_{(n-1)}$ is compatible, thus $\rho_{(n)} = \rho_{(n-1)}$ and $y_{(n)} = y_{(n-1)}$ in V. The nth cycle coincides with the steady cycle, $\rho_{(n)}$ is the PT stress field ρ and $y_{(n)}$ is the related PT-POP field y. The above picture is quite reasonable and enables one to state the following.

Principle of Nonincreasing Total POP. The total plastic overpotenital cannot increase through the transient response phase.

The Fictitious Plastic Yielding Laws for the PT Stresses

The y value given by (7) is also provided by the following minimization problem:

$$y = \min_{(z)} z \quad \text{s.t. } \phi(\hat{\sigma}_m) \le z,\ z \ge 0, \text{ all } m \in I(e) \tag{9}$$

where "s.t." stands for "subject to" and $\hat{\sigma}_m = \sigma^c_m + \sigma^0 + \rho$ with $\sigma^0 + \rho$ fixed. Introducing the augmented function

$$L = L(z, l_m) \equiv z + \sum_{m=1}^{e} l_m[\phi(\hat{\sigma}_m) - z)] \tag{10}$$

where the $l_m \ge 0$ are a set of unknown Lagrangian multipliers, the Kuhn-Tucker conditions related to (9) read

$$\phi(\hat{\sigma}_m) \le y,\ l_m \ge 0,\ l_m[\phi(\hat{\sigma}_m) - y] = 0, \text{ all } m \in I(e) \tag{11a}$$

Downloaded 03 May 2010 to 171.66.16.245. Redistribution subject to ASME license or copyright; see http://www.asme.org/terms/Terms_Use.cfm

$$\Delta l \equiv \sum_{m=1}^{e} l_m \leq 1,\ y \geq 0,\ y(\Delta l - 1) = 0. \tag{11b}$$

Due to the convexity of problem (9), Eqs. (11) are not only necessary, but also sufficient conditions for the latter problem.

Equations (11*a*) read as the plastic yielding laws obeyed by the PT stresses $\hat{\boldsymbol{\sigma}}$, with a (fictitious) yield surface $\phi(\boldsymbol{\sigma}) = y$ homothetic to $\phi(\boldsymbol{\sigma}) = 0$, as if a (fictitious) isotropic hardening had transformed the actual yield surface into the expanded one, with the POP y playing the role of (fictitious) internal variable, see Fig. 1. The Lagrangian multipliers l_m take the meaning of plastic activation coefficients such that the fictitious plastic strain increments, $\mathbf{p}_m$, at a touching stress point $\hat{\boldsymbol{\sigma}}_m$ is given by

$$\mathbf{p}_m = l_m \left. \frac{\partial \phi(\hat{\boldsymbol{\sigma}})}{\partial \hat{\boldsymbol{\sigma}}} \right|_{\hat{\boldsymbol{\sigma}} = \hat{\boldsymbol{\sigma}}_m}. \tag{12}$$

As a consequence of (11*b*), a nonvanishing y implies that $\Delta l = 1$, that is the set of touching points (*critical stress points*) between $\hat{S}$ and the fictitious yield surface contains at least one corner point. It is to be noticed that the discrete form of (11) is only due to the hypothesis that $\hat{S}$ is polygonal; otherwise Eqs. (11*a*) would have taken the usual rate form enforced at all times in $(0, \Delta t)$, and Δl the expression of an integral instead of a sum.

The PT-POP y at $\mathbf{x}$ turns out to be a function of the *transfer stress* $\mathbf{s} = \boldsymbol{\sigma}^0 + \boldsymbol{\rho}$. The sensitivity of y to changes of $\mathbf{s}$ at $\mathbf{x}$ can be derived from (10) written at the optimal solution (at which $L = y$). Thus, since $\hat{\boldsymbol{\sigma}}_m = \beta \bar{\boldsymbol{\sigma}}_m^c + \mathbf{s}$, one has for $\beta = \text{const.}$

$$\frac{\partial y}{\partial \mathbf{s}} = \frac{\partial L}{\partial \mathbf{s}} \bigg|_{z=y} = \Delta \mathbf{p} \equiv \sum_{m=1}^{e} \mathbf{p}_m \tag{13}$$

where $\Delta \mathbf{p}$ is the fictitious ratchet strain at $\mathbf{x}$.

The *absolute minimum* POP, k say, is the minimum value of y as a function of $\mathbf{s}$ at every $\mathbf{x}$ in V, that is

$$k = \min_{(z,s)} z \quad \text{s.t. } \phi(\beta \bar{\boldsymbol{\sigma}}_m^c + \mathbf{s}) \leq z,\ z \geq 0, \text{ all } m \in I(e). \tag{14}$$

The Kuhn–Tucker conditions of the latter problem are easily found to be Eqs. (11) together with the condition $\Delta \mathbf{p} = \mathbf{0}$, that is, the absolute minimum POP is characterized by the vanishing of the fictitious ratchet strain. The latter condition makes the PT stress path $\hat{S}$ find itself in a balanced position with respect to the fictitious yield surface, Fig. 2. This position, called *neutral configuration*, is characterized by a set of (at least two) critical stress points $\hat{\boldsymbol{\sigma}}_r$, all $r \in I(\bar{e})$, $2 \leq \bar{e} \leq e$, such that the vectors $\mathbf{q}_r = \partial \phi(\hat{\boldsymbol{\sigma}}) / \partial \hat{\boldsymbol{\sigma}}|_{\hat{\sigma}_r}$, if drawn from the stress origin, span a convex hypercone whose halves contain each at least one of these $\mathbf{q}_r$. In other words, the $\mathbf{q}_m$, all $m \in I(e)$, are a set of linearly and positively dependent set such that there exists a related set of scalars, $l_m \geq 0$, not all vanishing, satisfying the condition $\Delta \mathbf{p} = \Sigma_{m=1}^{e} \mathbf{q}_m l_m = \Sigma_{r=1}^{\bar{e}} \mathbf{q}_r l_r = \mathbf{0}$. The concept of neutral configuration was previously utilized by Polizzotto (1993a,b) to study the steady response of the body to cyclic loads at the plastic shakedown limit, that is at the elastic shakedown limit with an impending alternating plasticity collapse.

A Central Inequality for the Fictitious Plastic Yielding Laws

Let $(\hat{\boldsymbol{\sigma}}', \mathbf{p}', l')$ and $(\hat{\boldsymbol{\sigma}}'', \mathbf{p}'', l'')$ be two sets of variables satisfying Eqs. (11*a*) and (12), with the lowerscript m dropped for simplicity. Due to the convexity of ϕ, one can write

$$\phi(\hat{\boldsymbol{\sigma}}') - \phi(\hat{\boldsymbol{\sigma}}'') \geq (\hat{\boldsymbol{\sigma}}' - \hat{\boldsymbol{\sigma}}'') \frac{\partial \phi}{\partial \hat{\boldsymbol{\sigma}}''};$$

$$\phi(\hat{\boldsymbol{\sigma}}'') - \phi(\hat{\boldsymbol{\sigma}}') \geq (\hat{\boldsymbol{\sigma}}'' - \hat{\boldsymbol{\sigma}}') \frac{\partial \phi}{\partial \hat{\boldsymbol{\sigma}}'} \tag{15}$$

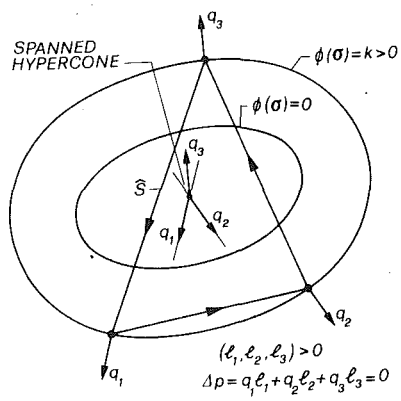


Fig. 2 Sketch illustrating the post-transient (PT) stress path $\hat{S}$ in a neutral configuration and related hypercone spanned by the gradient vectors $\mathbf{q}_r = \partial \phi / \partial \hat{\sigma}_r$ evaluated at the critical stress points $\hat{\sigma}_r$

where—provided ϕ is smooth as assumed—the equality sign holds if and only if $\hat{\boldsymbol{\sigma}}' = \hat{\boldsymbol{\sigma}}''$. Then, multiplication of the first of (15) by $l'' > 0$ and of the second of (15) by $l' > 0$ and using the first of Eqs. (11*a*) gives, respectively,

$$-(\hat{\boldsymbol{\sigma}}' - \hat{\boldsymbol{\sigma}}''): \mathbf{p}'' \geq y'' l'' - l'' \phi(\hat{\boldsymbol{\sigma}}') \geq -(y' - y'') l''$$
$$(\hat{\boldsymbol{\sigma}}' - \hat{\boldsymbol{\sigma}}''): \mathbf{p}' \geq y' l' - l' \phi(\hat{\boldsymbol{\sigma}}'') \geq (y' - y'') l' \tag{16}$$

that is, summing the latter inequalities with each other,

$$(\hat{\boldsymbol{\sigma}}' - \hat{\boldsymbol{\sigma}}''):(\mathbf{p}' - \mathbf{p}'') \geq (y' - y'')(l' - l''). \tag{17}$$

The latter inequality is the equivalent of Drucker's stability postulate for the fictitious plastic yielding laws. It holds for any pair of PT stress points $\hat{\boldsymbol{\sigma}}'$, $\hat{\boldsymbol{\sigma}}''$ with associated fictitious plastic strain increments $\mathbf{p}'$, $\mathbf{p}''$ and fictitious yield surfaces $\phi(\hat{\boldsymbol{\sigma}}') = y'$, $\phi(\hat{\boldsymbol{\sigma}}'') = y''$, respectively. If the equality sign holds in (17), then either $\hat{\boldsymbol{\sigma}}' = \hat{\boldsymbol{\sigma}}''$, $\mathbf{p}' = \mathbf{p}'' \neq \mathbf{0}$ and $y' = y''$, or $\mathbf{p}' = \mathbf{p}'' = \mathbf{0}$ and thus $l' = l'' = 0$, whereas the stress $\hat{\boldsymbol{\sigma}}'$ may differ from $\hat{\boldsymbol{\sigma}}''$, just as y' may differ from y''. The above picture changes somewhat in case of nonsmooth yield function, but here it is assumed to be always true for simplicity.

The Minimum Total Plastic Overpotential

Let the total POP in (8) be minimized with respect to $\boldsymbol{\rho}$, treated as a free self-stress field. Thus, one has the problem

$$Y_{\min} = \min_{(y,\rho)} \int_V y dV \text{ s.t. } \begin{cases} \phi(\sigma_m^E + \boldsymbol{\rho}) \leq y,\ y \geq 0, \text{ in } V, \text{ all } m \in I(e) \\ \mathbf{C}^T \boldsymbol{\rho} = \mathbf{0} \text{ in } V,\ \boldsymbol{\rho} \cdot \mathbf{n} = \mathbf{0} \text{ on } \partial_t V \end{cases} \tag{18}$$

where C^T is the differential operator adjoint of C, the compatibility differential operator; i.e., $C(\bullet) = 1/2[\text{grad}(\bullet) + \text{grad}(\bullet)^T]$, $C^T(:) = \text{div}(:)$. In order to derive the Euler-Lagrange equations of (18), let one consider the augmented functional

$$\tilde{Y} = \int_V y dV + \sum_{m=1}^{e} \int_V l_m [\phi(\sigma_m^E + \boldsymbol{\rho}) - y] dV + \int_V \mathbf{v} \cdot C^T \boldsymbol{\rho} dV - \int_{\partial_t V} \mathbf{v} \cdot \boldsymbol{\rho} \cdot \mathbf{n} d\partial_t V \tag{19}$$

where $l_m(\mathbf{x}) \geq 0$ and $\mathbf{v}(\mathbf{x})$ are unknown scalar- and vector-valued Lagrange multipliers. The first variation of $\tilde{Y}$, bearing in mind the identity

$$\int_V \mathbf{v} \cdot C^T \delta \boldsymbol{\rho} dV = \int_{\partial V} \mathbf{v} \cdot \delta \boldsymbol{\rho} \cdot \mathbf{n} d\partial V - \int_V \delta \boldsymbol{\rho} : C \mathbf{v} dV \tag{20}$$

and making use of the definitions in (11*b*) and (13), reads

Downloaded 03 May 2010 to 171.66.16.245. Redistribution subject to ASME license or copyright; see http://www.asme.org/terms/Terms_Use.cfm

$$\delta\tilde{Y}=\int_V \delta y(1-\Delta l)dV+\int_V \delta\rho\colon(\Delta\mathbf{p}-C\mathbf{v})dV$$
$$+\int_{\partial_u V}\mathbf{n}\cdot\delta\rho\cdot\mathbf{v}d\partial_u V+\sum_{m=1}^{e}\int_V \delta l_m[\phi(\hat{\sigma}_m)-y]dV$$
$$+\int_V \delta\mathbf{v}\cdot C^T\rho dV-\int_{\partial_t V}\delta\mathbf{v}\cdot\rho\cdot\mathbf{n}d\partial_t V \quad (21)$$

such that the desired Euler-Lagrange equations turn out to be

$$\phi(\hat{\sigma}_m)\le y,\ l_m\ge 0,\ l_m[\phi(\hat{\sigma}_m)-y]=0,\ \text{all } m\in I(e),\ \text{in } V \quad (22a)$$

$$\hat{\sigma}_m=\sigma_m^E+\rho,\ \mathbf{p}_m=l_m\left.\frac{\partial\phi}{\partial\hat{\sigma}}\right|_{\hat{\sigma}=\hat{\sigma}_m},\ \text{all } m\in I(e),\ \text{in } V \quad (22b)$$

$$\Delta l\equiv\sum_{m=1}^{e} l_m\le 1,\ y\ge 0,\ y(\Delta l-1)=0,\ \text{in } V \quad (23)$$

$$\Delta\mathbf{p}\equiv\sum_{m=1}^{e}\mathbf{p}_m=C\mathbf{v}\ \text{in } V,\ \mathbf{v}=\mathbf{0}\ \text{on } \partial_u V \quad (24)$$

$$C^T\rho=\mathbf{0}\ \text{in } V,\ \rho\cdot\mathbf{n}=\mathbf{0}\ \text{on } \partial_t V. \quad (25)$$

From here above, it transpires that the l_m take on the meaning of plastic activation coefficients and $\mathbf{v}$ of displacement field. Additionally, Eqs. (22)–(23) state that y is the POP of the stress path related to $\hat{\sigma}=\sigma^E+\rho$ at $\mathbf{x}$, whereas Eqs. (24) state that the fictitious ratchet strain field is compatible with displacements $\mathbf{v}$ vanishing on $\partial_u V$; Eqs. (25) are a restatement of self-equilibrium for ρ. Due to the convexity of problem (18), the latter equations are not only necessary, but also sufficient conditions for the above problem. If $Y_{\min}=0$, hence $y=0$ in the whole V in Eqs. (22*a*) and (23), by the first of Eqs. (22*a*) follows that elastic shakedown occurs.

Assuming $Y_{\min}>0$, let $(\rho',\ l_m',\ y')$ and $(\rho'',\ l_m'',\ y'')$ be two possible solutions to Eqs. (22)–(25). Making use of (17), one can write

$$(\rho'-\rho'')\colon(\mathbf{p}_m'-\mathbf{p}_m'')\ge(y'-y'')(l_m'-l_m'')\ \text{all } m\in I(e),\ \text{in } V. \quad (26)$$

The sum with respect to $m\in I(e)$ and an integration over V then yields

$$\int_V(\rho'-\rho'')\colon(\Delta\mathbf{p}'-\Delta\mathbf{p}'')dV\ge\int_V(y'-y'')(\Delta l'-\Delta l'')dV. \quad (27)$$

Since the l.h.s. of (27) vanishes by the virtual work principle and since, by (23) and (27)

$$0\ge\int_V(y'-y'')(\Delta l'-\Delta l'')dV$$
$$=\int_V(y'+y''-y'\Delta l''-y''\Delta l')dV\ge 0, \quad (28)$$

it follows that both sides of (27) vanish and thus (26) applies as an equality. As a consequence one has $\rho'=\rho''=\rho$, $\mathbf{p}_m'=\mathbf{p}_m''=\mathbf{p}_m$, $l_m'=l_m''=l_m$ and $y'=y''=y$ in the (by hypothesis nonempty) region $V_Y\subseteq V$ where $y>0$, whereas in the complementary region (if any), one has $\mathbf{p}_m'=\mathbf{p}_m''=\mathbf{0}$, $l_m'=l_m''=0$, $y'=y''=0$, but ρ' and ρ'' may be different from each other. The conclusion is that the solution to Eqs. (22)–(25), or to (18), is unique for all, except the *minimizing* self-stresses ρ, which turn out to be uniquely determined only within the region V_Y.

The above minimizing self-stresses can be shown to coincide with the PT self-stresses within the region $V_p\subseteq V_Y$, where plastic strains occur in the steady cycle. To this aim, let one remark that:

(i) on applying upon the body the given load $(P^0,\ \beta)$ together with initial stresses identifying with the PT self-stresses, say ρ^*, no transient phase is displayed, such that the related elastic stress path $S^{E*}=S^E+\rho^*$ coincides with the corresponding PT stress path; i.e., $\hat{S}^*=S^{E*}$, the PT-POP being y^*, say.

(ii) on applying upon the body the same loads, but initial stresses identifying with the minimizing self-stresses, say ρ, a transient phase is in general displayed with production of non-compatible plastic strains and additional self-stresses, say ρ'. Due to the fact that the steady-state response is independent of any initial strains, one can state

$$\rho+\rho'=\rho^*\ \text{in } V_p; \quad (29)$$

additionally, since both ρ^* and ρ' are uniquely determined in V_p and ρ is uniquely determined in V_Y, it follows that V_Y must contain V_p; i.e., $V_p\subseteq V_Y$.

(iii) the transient phase mentioned at point (ii) above causes a change of the total initial POP, $Y_{\min}=\int_V y_{\min}dV$, into the corresponding total PT-POP, say $Y'=\int_V y'dV$, with $Y'\le Y_{\min}$ and thus $Y'=Y_{\min}$, such that both ρ and $\rho+\rho'$ are minimizing self-stresses; then, in view of the uniqueness of the latter stresses in V_Y, ρ' must vanish in V_Y and therefore $\rho=\rho^*$, hence $y_{\min}=y^*$, in V_p.

From what precedes it transpires that the minimum total POP problem (18) represents a means to determine the PT self-stresses within the region V_p (where they are uniquely determined) and thus to assess the essential features of the structure's state at the end of the transient phase, upon which the subsequent structural behavior depends. In case of elastic shakedown V_p is empty and problem (18) loses its effectiveness.

The minimum total POP given by (18) turns out to be a function of the load parameters $(P^0,\ \beta)$. The increment of $Y_{\min}$ produced by an arbitrary (small) dP^0 (with $\beta=$ const.) is

$$dY_{\min}=\int_V dy_{\min}dV=\int_V\Delta\mathbf{p}\colon d\sigma^0 dV \quad (30)$$

such that the sensitivity of $Y_{\min}$ to dP^0 is locally expressed by

$$\frac{\partial y_{\min}}{\partial\sigma^0}=\Delta\mathbf{p}. \quad (31)$$

A Necessary Condition of Plastic Shakedown

Let the load $(P^0,\ \beta)$ be inside the zone B_F of plastic shakedown of the interaction diagram (or generalized Bree diagram; Polizzotto, 1991), such that plastic shakedown occurs under the above load, as well as under the augmented load $(P^0+dP^0,\ \beta)$, with arbitrary small dP^0 applied upon the elastic region V_S. As shown in the companion paper, this dP^0 causes only a stress field change $d\sigma=d\sigma^0+d\rho$ such as to equilibrate dP^0 within V_S, but vanishing everywhere in V_F, i.e.,

$$d\sigma=d\sigma^0+d\rho=\mathbf{0}\ \text{in } V_F. \quad (32)$$

Under the same augmented load, the PT stress path $\hat{S}$ at $\mathbf{x}$ undergoes a small change of position described by $d\hat{\sigma}=d\sigma^0+d\rho$, and a small change of the POP, dy. On comparing the sets $(\hat{\sigma}_m,\ \mathbf{p}_m,\ l_m)$ and $(\hat{\sigma}_m+d\hat{\sigma}_m,\ \mathbf{p}_m+d\mathbf{p}_m,\ l_m+dl_m)$, in virtue of (17) one can write, for arbitrary dP^0 applied upon V_S,

$$d\hat{\sigma}_m\colon d\mathbf{p}_m\ge dydl_m\ \text{in } V,\ \text{all } m\in I(e) \quad (33)$$

that is, since $d\hat{\sigma}_m=d\sigma^0+d\rho$,

$$(d\sigma^0+d\rho)\colon d\mathbf{p}_m\ge dydl_m\ \text{in } V,\ \text{all } m\in I(e). \quad (34)$$

Summing with respect to $m\in I(e)$, one has

$$(d\sigma^0+d\rho)\colon d(\Delta\mathbf{p})\ge dyd(\Delta l)\ \text{in } V. \quad (35)$$

As the r.h.s. of the latter inequality vanishes (because it is the second variation of the identically vanishing product $y(\Delta l-1)$), and as the l.h.s. vanishes everywhere in V_F because of (32), it follows that Eq. (33) applies as an equality for all $m\in I(e)$ and in V_F and this implies, besides (32),

Downloaded 03 May 2010 to 171.66.16.245. Redistribution subject to ASME license or copyright; see http://www.asme.org/terms/Terms_Use.cfm

$$d\mathbf{p}_m = \mathbf{0} \text{ for all } m \in I(e) \text{ in } V_F,\ dy = 0 \text{ in } V_F \tag{36}$$

that is, within the region V_F the POP and hence the PT stress path $\hat{S}$ turns out to be insensitive to arbitrary (small) load increments dP^0 applied upon V_S. Furthermore, bearing in mind Eq. (31), one can write

$$dy = \frac{\partial y}{\partial \sigma^0} : d\sigma^0 = \Delta\mathbf{p} : d\sigma^0 = 0 \text{ in } V_F \tag{37}$$

for arbitrary $d\sigma^0$, such that

$$\Delta\mathbf{p} = \mathbf{0} \text{ in } V_F, \tag{38}$$

that is, in V_F the PT stress path $\hat{S}$ finds itself in a neutral configuration, hence there $y_{\min} = k =$ absolute minimum. Thus, one can state the following:

First Theorem of Plastic Shakedown—A Necessary Condition. For a given elastic-perfectly plastic body under a combined cyclic/steady load producing plastic shakedown, a necessary condition is that there exists some time-independent self-stress field, $\boldsymbol{\rho}$, such as on superposing it to the elastic stress field $\boldsymbol{\sigma}^E$, the stress path $\hat{S}$ associated with the resulting stress history, $\hat{\boldsymbol{\sigma}} = \boldsymbol{\sigma}^E + \boldsymbol{\rho}$, finds itself in a neutral configuration everywhere within some region $V_K \subseteq V$ containing the region V_F of alternating plastic strains, and inside the yield surface within the remaining part.

A Sufficient Condition of Plastic Shakedown.

The assumption is here made, that under the given load (P^0, β) there exists a minimizing self-stress field $\boldsymbol{\rho}(\mathbf{x})$ such that $y_{\min} = k =$ absolute minimum, $V_Y = V_K \subseteq V$ being the body's region where $k > 0$. Thus, the stress path $\hat{S}$ corresponding to the stress history $\hat{\boldsymbol{\sigma}} = \boldsymbol{\sigma}^E + \boldsymbol{\rho}$ finds itself in a neutral configuration at all points in V_K. Since $\boldsymbol{\rho}$ coincides with the PT self-stress field in $V_p \subseteq V_K$, the actual stresses at the critical instants t_r; i.e., the instants corresponding to the critical stress points, turn out to be expressed as $\boldsymbol{\sigma}_r = \hat{\boldsymbol{\sigma}}_r + \boldsymbol{\tau}_r$ and satisfy the conditions

$$\begin{aligned} &\phi(\hat{\boldsymbol{\sigma}}_r + \boldsymbol{\tau}_r) = 0 \text{ in } V_p, \text{ all } r \in I(\bar{e}) \\ &\phi(\hat{\boldsymbol{\sigma}}_r + \boldsymbol{\tau}_r) < 0 \text{ in } V_e = V - V_p, \text{ all } r \in I(\bar{e}) \end{aligned} \tag{39}$$

where V_e is the elastic region. This elastic region V_e is not empty not only in the obvious most general case $V_K \subset V$, but also when $V_K = V$ due to the reason that the first of Eqs. (39) can hardly be satisfied in the whole V (except perhaps in very special cases not considered here). Therefore, as a consequence of the existence of an elastic region $V_e = V_S$, plastic shakedown must occur, with $V_F = V_p \subseteq V_K$ identified as the region for which a set of self-stress fields $\boldsymbol{\tau}_r$, $r \in I(\bar{e})$, can be found such as to satisfy Eqs. (39). Thus, one can state the following.

Second Theorem of Plastic Shakedown—A Sufficient Condition. For a given elastic-perfectly plastic body under a combined cyclic/steady load exceeding the elastic shakedown limit value, a sufficient condition of plastic shakedown is that there exists some time-independent self-stress field, $\boldsymbol{\rho}$, such as on superposing it to the elastic stress field $\boldsymbol{\sigma}^E$, the stress path $\hat{S}$ associated with the resulting stress history, $\hat{\boldsymbol{\sigma}} = \boldsymbol{\sigma}^E + \boldsymbol{\rho}$, finds itself in a neutral configuration everywhere $\hat{S}$ exceeds the yield surface and inside the yield surface in the remaining part.

Remark. In order to obtain a stress path $\hat{S}$ as required by the theorem here above, instead of (18) one can solve the problem

$$K = \min_{(y,s)} \int_V y dV \text{ s.t.} \phi(\beta\bar{\boldsymbol{\sigma}}_m^c + \mathbf{s}) \le y, \quad y \ge 0 \text{ in } V, \text{ all } m \in I(e) \tag{40}$$

with no restrictions on the transfer stresses $\mathbf{s}$. This is equivalent to solving the problem (14) independently at every $\mathbf{x} \in V$.

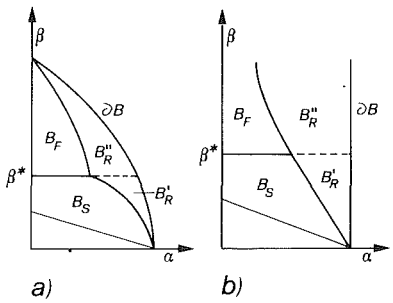


Fig. 3 Interaction diagram for a cyclic load $P^c(t) = \beta\bar{P}^c(t)$ and a steady mechanical load $P^0 = \alpha\bar{P}^0$: (a) mechanical cyclic load; (b) thermal cyclic load

Obviously, if the minimizing transfer stresses turn out to be expressed as $\mathbf{s} = \boldsymbol{\sigma}^0 + \boldsymbol{\rho}$, with $\boldsymbol{\sigma}^0$ being related to the given P^0, $\boldsymbol{\rho}$ is the minimizing self-stress field. Otherwise, one can write $\mathbf{s} = \boldsymbol{\sigma}^0 + \boldsymbol{\sigma}_a^0 + \boldsymbol{\rho}$ where $\boldsymbol{\sigma}_a^0$ is the elastic stress response to some additional steady load, P_a^0, such that the neutral configuration condition of the theorem above applies to the load $(P^0 + P_a^0, \beta)$.

The Boundary of the Plastic Shakedown Zone

In the interaction diagram of the (P^0, β)-space, Fig. 3(*a*, *b*), the boundary of the B_F region can be divided into two portions; i.e., the "upper plateau" $\partial B_F \cap \partial B_S$, which is the flat region $\beta = \beta^* =$ plastic shakedown limit load, and the portion $\partial B_F \cap \partial B_R''$, constituted by load points (P^0, β) marking the transition from plastic shakedown to ratchetting. The methods given by Polizzotto (1993a, b) are devoted to the evaluation of β^* and of the boundary of the upper plateau. The determination of the above transition points can be achieved by the method shown in the companion paper. According to this method, the body being in a plastic shakedown condition, the V_F region is removed and an elastic shakedown limit load problem is solved for V_S loaded by the given load, plus some additional steady load $\alpha\bar{P}_a^0$. The problem to solve is (see Polizzotto, 1989, 1993c),

$$\alpha_R = \max_{(\alpha, s a)} \alpha \text{ s.t.} \begin{cases} \phi(\hat{\boldsymbol{\sigma}}_r + \boldsymbol{\tau}_r + \mathbf{s}_a) \le 0 \text{ in } V_S, \text{ all } r \in I(\bar{e}) \\ C^T \mathbf{s}_a = \mathbf{0} \text{ in } V_S,\ \mathbf{s}_a \cdot \mathbf{n} = \alpha\bar{\mathbf{T}}^0 \text{ on } \partial_t V_S \end{cases} \tag{41}$$

where $\mathbf{s}_a$ denotes a stress field of V_S in equilibrium with $\alpha\bar{P}_a^0$, $\bar{P}_a^0$ being here taken as a traction $\bar{\mathbf{T}}^0$ upon the free boundary of V_S (but vanishing on Γ, the interface between V_S and V_F); also, the $\hat{\boldsymbol{\sigma}}_r$ denote the PT critical stress fields and the $\boldsymbol{\tau}_r$ are self-stress fields in V satisfying Eqs. (39) with $V_p = V_F$. The stress path $\hat{S}$, specified by the critical stress points $\hat{\boldsymbol{\sigma}}_r$, finds itself in a neutral configuration condition as required by the second theorem above, such that plastic shakedown occurs under the given load.

It is worth noticing that, with the assumptions $V_F = V_K$, hence $V_S = V - V_K$, and $\boldsymbol{\tau}_r = \mathbf{0}$ for all $r \in I(\bar{e})$, the above method coincides with Ponter's method, devised to obtain approximate conservative values of the plastic shakedown boundary loads for both cyclically hardening and nonhardening materials in case of thermal loadings (see Ponter, 1983; Ponter and Karadeniz, 1985a,b; Ponter et al. 1990). Thus Ponter's method gives exact answers for perfect plasticity in cases where the foregoing assumptions correspond to the truth. Solving (41) for $\beta > \beta^*$ requires the preliminary determination of $V_K \subseteq V$ with the related minimizing self-stresses $\boldsymbol{\rho}$, as well as the region $V_F \subseteq V_K$ together with the self-stress fields $\boldsymbol{\tau}_r$ satisfying Eqs. (39) with $V_p = V_F$. Due to lack of space, the topic of this section will be discussed in a future paper, together with related computational methods. Two simple numerical examples are reported hereafter with the aim to illustrate the new concepts within a known solution context.

Downloaded 03 May 2010 to 171.66.16.245. Redistribution subject to ASME license or copyright; see http://www.asme.org/terms/Terms_Use.cfm

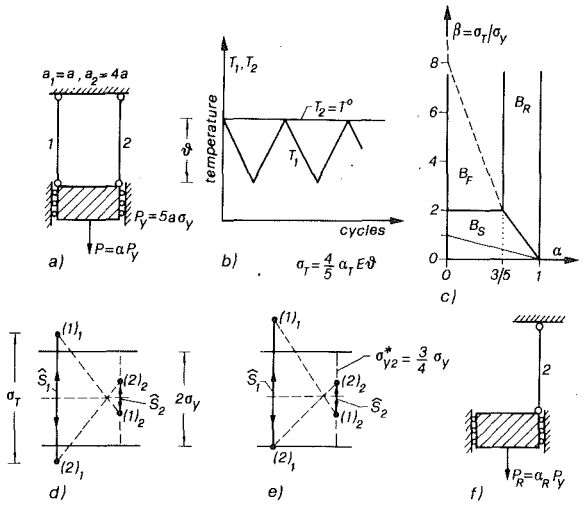


Fig. 4 Nonsymmetric two-bar structure under cyclic thermal loading and steady mechanical load: (*a*) geometrical and loading scheme; (*b*) thermal loading history; (*c*) interaction diagram; (*d*) PT stress paths in bars 1 and 2 for $2 < \beta < 8$; (*e*) modified positions of the PT stress paths at a critical instant; (*f*) V_S body

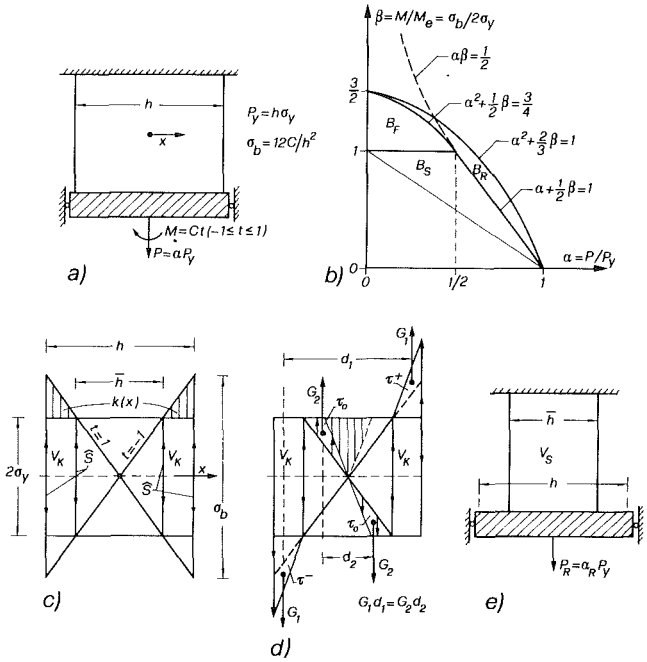


Fig. 5 Beam segment under alternating bending moment and steady axial force: (*a*) geometrical and loading scheme; (*b*) interaction diagram; (*c*) distribution of PT stress paths in the beam depth; (*d*) modified positions of the PT stress paths at a critical instant; (*e*) V_s body

Numerical Examples

(a) Nonsymmetric Two-Bar Structure. Figure 4(*a–f*). The two bars have equal lengths and cross-sections $a_1 = a$, $a_2 = 4a$, and are connected with a rigid block as shown in Fig. 4(*a*). Bar 2 is taken at a fixed temperature T^0, whereas bar 1 undergoes a cyclic temperature variation as shown in Fig. 4(*b*); a steady load $\alpha\bar{P}^0$, with $\alpha \geq 0$ and $\bar{P}^0 = 5a\sigma_y = P_y$ (plastic collapse limit load), is applied upon the rigid block. The thermoelastic stresses are $\sigma_1^c = \beta\sigma_y t$, $\sigma_2^c = -\sigma_1^c/4$, where t is a timelike parameter, $0 \leq t \leq 1$, $\beta = \sigma_T/\sigma_y$, σ_y = yield stress, $\sigma_T = 4\alpha_T E\theta/5$ = max thermoelastic stress, α_T = thermal expansion coefficient and E = Young modulus. In the (α, β)-plane, the interaction diagram is as shown in Fig. 4(*c*). For $\beta > 2$, the elastic stress path at bar 1, S_1^c—segment of length σ_T—exceeds $2\sigma_y$, whereas that at bar 2, S_2^c, exceeds $2\sigma_y$ for $\beta > 8$. For a given $\beta > 2$ and $\alpha = 0$ the minimizing self-stresses are $\rho_1 = -\beta\sigma_y/2$, $\rho_2 = \beta\sigma_y/8$, $(\rho_1 + 4\rho_2 = 0)$, such that the PT stresses $\hat{\sigma}_1 = (t - 1/2)\beta\sigma_y$ and $\hat{\sigma}_2 = -\hat{\sigma}_1/4$ admit stress paths $\hat{S}_1$ and $\hat{S}_2$ each in a neutral configuration, with $k_1 = \sigma_T/2 - \sigma_y > 0$ and $k_2 = 0$ for $\beta < 8$, but $k_2 = \sigma_T/8 - \sigma_y > 0$ for $\beta > 8$, Fig. 4(*d*). Therefore, V_K includes only bar 1 for $\beta < 8$, but both bars for $\beta > 8$.

According with the second theorem, plastic shakedown occurs for all $\beta \geq 2$ and $\alpha = 0$, with V_F always including only bar 1 because the self-stresses $\tau_1|_{t=1} \equiv \tau_1^{(2)} = -k_1 = -\sigma_y(\beta/2 - 1)$ and $\tau_2^{(2)} = k_1/4$ make the PT stress paths move such as the extreme point $(2)_1$ of $\hat{S}_1$ is at the yield limit and $(2)_2$ of $\hat{S}_2$ below the yield limit, as depicted in Fig. 4(*e*); analogously for the extreme points $(1)_1$ and $(1)_2$ as a result of $\tau_1|_{t=0} \equiv \tau_1^{(1)} = k_1$ and $\tau_2^{(1)} = -k_1/4$. Thus, the V_S body to consider is as depicted in Fig. 4(*f*) and the elastic shakedown limit load of it is

$$P_R = \alpha_R P_y = 4a\sigma_{y2}^*$$

where

$$\sigma_{y2}^* = \sigma_y - \|\hat{\sigma}_2|_{t=1} + \tau_2^{(2)}\| = 3\sigma_y/4,$$

that is $\alpha_R = 3/5$, in agreement with the diagram of Fig. 4(*c*). Ponter's method gives $\alpha_R = 4/5 - \beta/10$ for $2 \leq \beta \leq 8$ and $\alpha_R = 0$ for $\beta > 8$ (dashed line in Fig. 4(*c*)). See Ponter (1983) and Ponter and Karadeniz (1985a,b).

(b) Beam Segment. Figure 5(*a–e*). A beam segment of rectangular cross-section $1 \times h$ is subjected to a cyclic bending moment $M = Ct$ with $C > 0$ and $-1 \leq t \leq 1$, as well as a steady axial force $P^0 = \alpha\bar{P}^0$, $\bar{P}^0 = h\sigma_y = P_y$ (axial yield force), Fig. 5(*a*). The elastic stress response to M is $\sigma^c = tx\sigma_b/h$, where $\sigma_b = 12C/h^2$ = max elastic stress variation. The interaction diagram is reported in Fig. 5(*b*), where $\beta = M/M_e = \sigma_b/2\sigma_y$ and $M_e = h^2\sigma_y/6$ = elastic limit bending moment. For $1 < \beta < 3/2$, the elastic stress path S^c exceeds $2\sigma_y$ within two outer layers of the beam, Fig. 5(*c*). For $\alpha = 0$, S^c is already in a neutral configuration at all x in the outer beam layers, so that the minimizing self-stresses are vanishing. The V_K region includes these two outer layers, the POP distribution is $k(x) = \sigma_y(2\|x\|/h - 1)$, $\bar{h}/2 < \|x\| \leq h/2$, (dashed triangles in Fig. 5(*c*)), where $\bar{h} = h/\beta$. According to the second theorem, plastic shakedown occurs for all β, $1 \leq \beta < 3/2$, with $V_F = V_K$, as in fact it is possible to find a self-stress field $\tau(x)$ such as to make the PT stress paths $\hat{S} = S^c$ have the synchronous extremes at the yield limit in V_K and inside the yield limit in the remaining core region. For $t = 1$, this field τ is, Fig. 5(*d*),

$$\tau = \begin{cases} \tau^- = k(x), & -h/2 \leq x \leq -\bar{h}/2 \\ \tau_0(x), & -\bar{h}/2 \leq x \leq \bar{h}/2 \\ \tau^+ = -k(x), & \bar{h}/2 \leq x \leq h/2 \end{cases}$$

where $\tau_0(x)$ must only satisfy the condition $\|\sigma^c(x) + \tau_0(x)\| \leq \sigma_y$ and restate the cross-section's equilibrium violated by the τ in the outer layers, as shown in Fig. 5(*d*). Thus, V_S identifies with the core region $-\bar{h}/2 \leq x \leq \bar{h}/2$; i.e., $V_S = V - V_K$, Fig. 5(*e*). The plastic shakedown limit load can be found with the aid of some geometrical considerations, explained by Fig. 5(*d*), where G_1 denotes the resultant of the stresses $\tau^-(x)$ (and of τ^+ either) and G_2 denotes the resultant of the stresses $\tau_0(x)$ in a half-core section. Thus, one can write

$$M_1 = G_1 d_1 = G_2 d_2$$

$$G_2 = (P_y\bar{h}/4h)\{1 - \sqrt{(1 - 3M_1h^2/M_y\bar{h}^2)}\}$$

$$M_1 = M - M_y + \bar{M}_y + \bar{M}_e$$

where $M_y = h\sigma_y/4$ = yield bending moment of the beam cross-section (V); $\bar{M}_y = \bar{h}\sigma_y/4$ = yield bending moment of the core cross-section (V_S), $\bar{M}_e = \bar{h}\sigma_y/6$ = elastic limit bending moment of the core cross-section (V_S). The elastic shakedown limit load

Downloaded 03 May 2010 to 171.66.16.245. Redistribution subject to ASME license or copyright; see http://www.asme.org/terms/Terms_Use.cfm

of V_S is $P_R = \alpha_R P_y = \bar{h}\bar{\sigma}_y/2 - 2G_2$, (dashed triangle in Fig. 5(*d*)), that is $\alpha_R = \sqrt{(3/4 - \beta/2)}$, in agreement with the diagram of Fig. 5(*b*). Ponter's method instead gives $\alpha_R = (2\beta)^{-1}$ (dashed line in Fig. 5(*b*)).

Conclusions

For an elastic-perfectly plastic solid body subjected to cyclic/steady loads, two theorems have here been established, one stating a necessary condition, the other a sufficient condition for plastic shakedown. A number of novel concepts have played a crucial role in deriving these two theorems, like the concept of "plastic overpotential" (POP) as a suitable measure of the yield violations of the elastic stress history at a point in the body, or the concept of "minimum total POP" as a tool for determining the so-called "post-transient" (PT) self-stresses, that is the residual stresses at the instant of stabilization of the body's actual response. Also, the transient response phase has been envisaged as a process in which the elastic stress path is translated to the PT stress path at every point in the body and is accompanied by a reduction of the total POP. This is the "Principle of nonincreasing total POP," whose validity has been accepted just as quite reasonable, but not rigorously proven. The theory so builded generalizes previous results of Ponter (1983), Ponter and Karadeniz (1985a,b), and Polizzotto (1989). The problem of the direct determination of the plastic shakedown boundary has been also briefly addressed pointing out a method which strongly appeals to Ponter's method devised for a similar purpose. Two simple numerical examples have been presented to illustrate the present theory. The approach to cyclic plasticity employed in these two companion papers has proven to be effective, in the author's opinion, in providing a clear understanding of many aspects of the cyclic plasticity problem. Further developments and questions more strictly related to computational methods will be treated in a future paper.

Acknowledgment

This paper has been completed with the financial support of the Consiglio Nazionale delle Ricerche, CNR, of Italy.

References

Frederich, C. O., and Armstrong, P. J., 1966, "Convergent Internal Stresses and Steady Cyclic States of Stress," *J. Strain Analysis*, Vol. 1, p. 154.

Gokhfeld, D. A., and Cherniavsky, D. F., 1980, *Limit Analysis of Structures at Thermal Cycling*, Sijthoff & Noordhoff, Alphen aan der Rijn, The Netherlands.

Halphen, B., 1979, "Steady Cycles and Shakedown in Elastic-Viscoplastic and Plastic Structures," *Matériaux et Structures sous Chargement Cyclique*, Association Amicale des Ingenieurs Anciens Eléves de l'Ecole Nationale des Ponts et Chaussèes, pp. 203–229.

Martin, J. B., 1975, *Plasticity: Fundamentals and General Results*, The M.I.T. Press, Cambridge, MA.

Polizzotto, C., 1989, "Simplified Methods of Structural Analysis for Cyclic Plasticity," Final Report RA1-0116(I), Commission of European Communities, Brussels, and Dipartimento di Ingegneria Strutturale & Geotecnica, Università di Palermo, Palermo.

Polizzotto, C., 1993a, "On the Conditions to Prevent Plastic Shakedown of Structures: Part 1—Theory," ASME JOURNAL OF APPLIED MECHANICS, Vol. 60, pp. 15–19.

Polizzotto, C., 1993b, "On the Conditions to Prevent Plastic Shakedown of Structures: Part 2—The Plastic Shakedown Limit Load," ASME JOURNAL OF APPLIED MECHANICS, Vol. 60, pp. 20–25.

Polizzotto, C., 1993c, "A Study on Plastic Shakedown of Structures: Part 1—Basic Properties," ASME JOURNAL OF APPLIED MECHANICS, Vol. 60, pp. 318–323.

Ponter, A. R. S., 1983, "Shakedown and Ratchetting Below the Creep Range," Report EUR 8702 EN, Commission of European Communities, Brussels.

Ponter, A. R. S., and Karadeniz, S., 1985a, "An Extended Shakedown Theory for Structures that Suffer Cyclic Thermal Loadings: Part 1—Theory," ASME JOURNAL OF APPLIED MECHANICS, Vol. 52, pp. 877–882.

Ponter, A. R. S., and Karadeniz, S., 1985b, "An Extended Shakedown Theory for Structures that Suffer Cyclic Thermal Loadings: Part 2—Applications," ASME JOURNAL OF APPLIED MECHANICS, Vol. 52, pp. 883–889.

Ponter, A. R. S., and Karadeniz, S., and Carter, K. F., 1990, "Extended Upper Bound Shakedown Theory and Finite Element Method for Axisymmetric Thin Shells," *Inelastic Solids and Structures*, ed. by M. Kleiber, and J. A. König, eds., Pineridge Press, Swansea, U.K., pp. 443–449.

Downloaded 03 May 2010 to 171.66.16.245. Redistribution subject to ASME license or copyright; see http://www.asme.org/terms/Terms_Use.cfm

Dynamics of Bipedal Gait: Part I—Objective Functions and the Contact Event of a Planar Five-Link Biped

Y. Hurmuzlu
Mechanical Engineering Department,
Southern Methodist University,
Dallas, TX 75275
Assoc. Mem. ASME

Previous approaches to the problem of prescribing the motion of bipedal machines do not completely characterize the desired walking patterns in terms of coherent parameters. A well-structured parametric formulation that ties the objective functions to the resulting gait patterns has never been established. This article presents an approach that can be followed to formulate objective functions which can be used to prescribe the gait of a planar, five-element, bipedal automaton during single support phase. The motion of the biped is completely characterized in terms of progression speed, step length, maximum step height, and stance knee bias. Kinematic relations have been derived and the inverse problem has been solved to perform a parametric study that correlates the regions of the four-dimensional parameter space with the respective gait patterns. Major limitations include the assumptions of rigid elements and point contact between the lower limbs and the walking surface. Most importantly, the motion of the biped is assumed to perfectly conform with the objective functions at the instant of contact. The control and stability issues are presented in Part II of this paper.

1 Introduction

A sound understanding of the dynamic principles governing legged locomotion is an essential requirement in developing high-performance all-terrain vehicles and in the diagnosis and treatment of gait problems. Mathematical modeling of gait is a complex task which requires knowledge of the dynamics of multilink mechanisms, control theory, nonlinear dynamics, and stability theory.

Several studies addressing the postural stability of standing bipeds have been published by Hemami et al. To name only a few, the stability of a three-link biped in the vicinity of vertical stance has been considered in Hemami et al. (1979). Hemami and Zheng (1984) have considered a five-link, three-dimensional biped. A methodology was developed to formulate the equations of motion in an embedded large dimensional state space and to obtain projection transforms to represent some basic motions such as one or two-foot stance, and jumping in the air. A nonlinear control strategy with computational delays and predictive algorithms is applied to simulate the resulting motions. Zheng and Hemami (1984) have addressed the effect of impacts of biped impact with the environment. They have demonstrated that impulsive contact forces lead to sudden velocity jumps that cause disturbances that should be eliminated by the underlying control mechanisms. The main thrust of Hemami's work has been directed toward developing proper methods to represent the equations of motion. A particular emphasis was placed on the incorporation of holonomic and nonholonomic constraints that arise from the interconnection of members and interaction with the environment. Several control strategies have been presented to realize nonwalking motions such as swaying in the frontal plane, jumping in the air, etc. Coordination of the overall locomotion has never been considered.

On the other hand, Vukobratovic et al. (1980 and 1990) have considered locomotion directly. The fundamental aspect of their approach is the adaptation of human walking data to prescribe the motion of the lower limbs and the application point of the resultant of the reaction forces among the lower limbs and the walking surface. Furthermore, repeatability conditions are added to impose further symmetry conditions on the motion.

Vukobratovic's approach is novel in several aspects such as development very complicated models having upper body components such as head, shank, and upper limbs and foot structures, yet it possesses several important shortcomings. If the mathematical modeling is to be performed to design a bipedal robot, prescription of the motion is based on the data obtained from human locomotion. Normally, a practical walking ma-

Contributed by the Applied Mechanics Division of THE AMERICAN SOCIETY OF MECHANICAL ENGINEERS for presentation at the First Joint ASCE-EMD, ASME-AMD, SES Meeting, Charlottesville, VA, June 6-9, 1993.

Discussion on this paper should be addressed to the Technical Editor, Professor Lewis T. Wheeler, Department of Mechanical Engineering, University of Houston, Houston, TX 77204-4792, and will be accepted until four months after final publication of the paper itself in the ASME JOURNAL OF APPLIED MECHANICS.

Manuscript received by the ASME Applied Mechanics Division, Aug. 12, 1991; final revision, June 3, 1992. Associate Technical Editor: D. J. Inman.

Paper No. 93-APM-9.

Copyright © 1993 by ASME
Downloaded 03 May 2010 to 171.66.16.245. Redistribution subject to ASME license or copyright; see http://www.asme.org/terms/Terms_Use.cfm

chine would be considerably simpler than the human biped. Therefore, the validity of mimicking the dynamics of a system without a good knowledge of its internal structure and its strategies is questionable. A second problem arises when the design problem is considered. A designer should be able to make decisions based on some tangible characteristics of gait such as walking speeds, step lengths, step elevations, etc. Then, if the robot in question is expected to perform a wide range of gait patterns, numerous synergies should be obtained, stored, and implemented on-line. Formulating the objective functions as kinematic relations seems to be the more natural approach to the design of bipedal robots. Whereas, if the modeling is performed to understand the dynamics of human gait by using simplified models, the approach fails to address nonsymmetric classes of gait. Such gait patterns are frequently observed in amputees, post-polio syndrome patients, etc.

Beletskii (1984) has considered several bipedal locomotion models that possess massless lower limbs. He has formulated closed-form solutions for bipedal systems and identified initial conditions that satisfy periodicity conditions. He neglects the masses of legs and the locomotion system is represented by a two-dimensional mass which possesses a moving pivot. Since the lower limbs and their interaction with the ground surface play a major role in bipedal locomotion, applicability of these results to the general area of bipedal gait is questionable. Yet, Beletskii's work is based on completely synthesized bipeds, therefore, he defines two parameters to characterize the gait, the velocity of the pivot point and its height. But, since the lower limbs are neglected, his parametric formulation does not address limb coordination at all.

Furusho and Masubuchi (1987, 1988) have developed numerical and experimental models to synthesize five-element bipeds. The approach is based on linearizing the equations of motion around the vertical equilibrium and applying proportional plus derivative feedbacks at individual joints to track prescribed angular displacement profiles. The results are verified experimentally by using a walking machine and periodicity is demonstrated for several walking patterns. Trajectory tracking is carried out in the joint space only, and a coherent method to specify the joint profiles was never presented.

Katoh and Mori (1984), have also developed numerical and experimental models with telescopic legs to simulate bipedal gait. They have used coupled van der Pol's equations to prescribe the motion. Yet, no direct ties were established between the parameters in the equations and the resulting walking patterns.

In the light of the prevailing locomotion literature, it seems that there is a gap in the design of walking machines regarding the specification of objective functions. How should these objective functions and their associated parameters be set so that the biped generates a specific gait pattern? Can we cast these objective functions in terms of physically coherent parameters such as step length, progression speed, and equip the biped with the ability of walking on nonsmooth surfaces?

The first goal of the present article is to develop objective functions that can be used to synthesize a five-element, nonhuman, bipedal automaton. These functions are cast in terms of four parameters that completely characterize the motion of the biped during the single support phase. Although this article considers walking on level surfaces, other actions such as stair climbing and walking on sloped surfaces can be implemented by appropriate selection of the parameters.

The second objective is to establish a correlation among the parameters that characterize the motion and the outcome of the contact of the limbs with the walking surface. This correlation is important because the double support phase arises as a direct consequence of the contact event. In addition, slippage of the lower limbs as a result of contact is considered and parameter choices that violate specific friction conditions are identified.

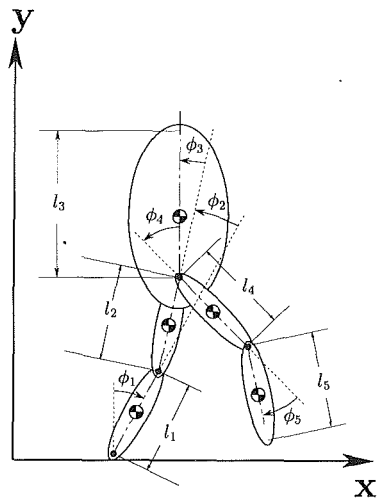


Fig. 1 Planar, five-link biped

Several assumptions are made here. The impact is taken to be perfectly plastic and the links are assumed to be rigid. Point contact is taken between the lower limbs and the walking surface. Most importantly, the motion of the system is assumed to perfectly conform with the prescribed gait at the end of the step cycle (constrained contact). This is not an overly restricting assumption since the perturbed system response should be close to the desired one by the end of the step cycle whenever the control action is successful.

First we present a brief description of the system and summarize the methods that are used in solving the impact problem. Next, kinematic relations that represent the objective functions are derived. Subsequently, the inverse kinematic problem is solved, and the values of the generalized coordinates immediately before contact are computed in closed form. Finally, a parametric study of the contact event is performed. The results are presented in graphical form to facilitate the correlation between the locomotion parameters and the constrained contact.

2 The Bipedal System, Equations of Motion, and the Dynamic Constraints

In the present study, we consider a planar bipedal model that has five rigid members connected to one another by purely rotational joints. There is an actuator located at each joint. Figure 1 depicts a schematic representation of this system. We assume massless feet to simplify our analysis. Although we neglect the dynamics of the feet, we assume that the biped can apply torques at the ankles.

Equations of motion during the single support phase can be written in the following general form

$$\mathbf{M}_s(\Phi)\ddot{\Phi} + \mathbf{H}_s(\Phi, \dot{\Phi}) + \mathbf{G}_s(\Phi) = \mathbf{T}_s \tag{1}$$

where $\mathbf{M}_s$ is the 5 × 5 positive definite and symmetric mass matrix, $\mathbf{H}_s$ is the 5 × 1 matrix of centrifugal and Coriolis terms, $\mathbf{G}_s$ is the 5 × 1 matrix of gravity terms, and Φ, $\dot{\Phi}$, $\ddot{\Phi}$, and $\mathbf{T}_s$ are the 5 × 1 vectors of generalized coordinates, velocities, accelerations, and actuator torques, respectively.

We present the equations of motion in their general forms only. The specific forms and the actual derivation is straight forward and can be found in previously published articles (Furusho and Masubuchi, 1987).

During locomotion, when the swing limb (i.e., the limb that is not on the ground) contacts the ground surface (heel strike), the generalized velocities will be subject to jump discontinuities resulting from the impact event. Also, the roles of the swing and the stance limbs will be exchanged, resulting in additional discontinuities in the generalized coordinates and velocities

Downloaded 03 May 2010 to 171.66.16.245. Redistribution subject to ASME license or copyright; see http://www.asme.org/terms/Terms_Use.cfm

(Hurmuzlu and Moskowitz, 1986). The individual joint rotations and velocities do not actually change as the result of switching. Yet, from biped's point of view, there is a sudden exchange in the role of the swing and stance side members. This leads to a discontinuity in the mathematical model. We incorporate the switching in the model by relabeling the members corresponding to the lower extremities (i.e., members 1, 2, 4, and 5). The overall effect of the impact and switching can be written as the following transformation matrix between the generalized coordinates immediately before and after these events

$$\Phi^+ = \begin{pmatrix} 1 & 1 & 1 & -1 & -1 \\ 0 & 0 & 0 & 0 & 1 \\ 0 & 0 & 0 & 1 & 0 \\ 0 & 0 & 1 & 0 & 0 \\ 0 & 1 & 0 & 0 & 0 \end{pmatrix} \Phi^- \tag{2}$$

where the superscripts $-$ and $+$ denote quantities immediately before and after impact and switching, respectively.

Impact equations are derived using the principles of linear and angular impulse and momentum. However, applying these principles require some prior assumptions about the impulsive forces acting on the system during the instant of impact. The solution is subject to two conditions. The impact at the contact point is perfectly plastic (i.e., the tip of the swing limb does not leave the ground surface after impact) and the impulsive moments at the joints are negligible. We identify the proper solution as follows:

2.1 Single Impact. There are no impulses at the contact point of the trailing limb, and it is lifted off the ground surface immediately after the contact. The equation representing this case is

$$\begin{bmatrix} \mathbf{K}(\Phi^+) & \mathbf{0} \\ \mathbf{C}(\Phi^+) & \begin{bmatrix} -1 & 0 \\ 0 & -1 \end{bmatrix} \end{bmatrix} \begin{bmatrix} \dot{\Phi}^+ \\ \hat{\mathbf{F}}_r \end{bmatrix} = \begin{bmatrix} \mathbf{R}_1(\Phi^-, \dot{\Phi}^-) \\ \mathbf{R}_2(\Phi^-, \dot{\Phi}^-) \end{bmatrix} \tag{3}$$

where $\mathbf{K}$ is a 5×5, $\mathbf{C}$ is a 2×5, $\mathbf{R}_1$ is a 5×1, and $\mathbf{R}_2$ is a 2×1 matrix function, and $\hat{\mathbf{F}}_r = [\hat{F}_{rx}, \hat{F}_{ry}]^T$ is the impulse at the contact point of the swing (leading) limb with the ground. Here, $\mathbf{K}(\Phi^+)\,\dot{\Phi}^+$ represents the angular momentum of the system about the pivot after impact. Whereas, $\mathbf{R}_1(\Phi^-, \dot{\Phi}^-)$ represents the angular momentum of the mechanism about the same point before impact. Also, $\mathbf{C}(\Phi^+)\dot{\Phi}^+$ represents the linear momentum after impact and $\mathbf{R}_2(\Phi^-, \dot{\Phi}^-)$ represents the linear momentum before impact. The superscripts $-$ and $+$ denote quantities immediately before and after impact and switching, respectively. We use Eqs. (2) and (3) to calculate the quantities immediately after impact in terms of the quantities immediately before impact. This solution is valid when

(i)

$$\left|\frac{\hat{F}_{rx}}{\hat{F}_{ry}}\right| < \mu. \tag{4}$$

(ii)

$$\dot{y}_T^+ \geq 0 \tag{5}$$

where, $\dot{y}_T^+$ is the velocity of the tip of the trailing limb immediately after impact and μ is the coefficient of friction between the feet and the ground. Inequality (4) is the no slip condition at the contact point. Inequality (5) has to be satisfied because of the assumption that the tip of the trailing limb does not experience any impulsive forces during impact.

2.2 Double Impact. There are impulsive forces between the contact points of the stance and swing limbs and the ground. The velocities of these contact points immediately after impact are zero. The corresponding equations can be written as

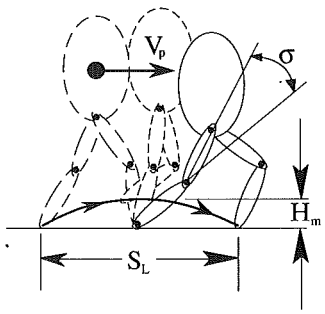


Fig. 2 Locomotion parameters

$$\begin{bmatrix} \mathbf{H}(\Phi^+) \\ \mathbf{Q}(\Phi^+) \begin{bmatrix} 0 & 0 \\ 0 & 0 \end{bmatrix} \end{bmatrix} \begin{bmatrix} \dot{\Phi}^+ \\ \hat{\mathbf{F}}_l \end{bmatrix} = \begin{bmatrix} \mathbf{R}_1(\Phi^-, \dot{\Phi}^-) \\ 0 \\ 0 \end{bmatrix} \tag{6}$$

where $\mathbf{H}$ is a 5×7, $\mathbf{Q}$ is a 2×5, $\mathbf{R}_1$ is a 5×1, and $\hat{\mathbf{F}}_l = [\hat{F}_{lx}, \hat{F}_{ly}]^T$ is the impulse at the contact point of the stance (trailing) limb with the ground. Here, $\mathbf{H}(\Phi^+)\,[\dot{\Phi}^+, \hat{\mathbf{F}}_l]^T$ represents the angular momentum of the system about the pivot after impact. Whereas, $\mathbf{R}_1(\Phi^-, \dot{\Phi}^-)$ represents the angular momentum of the mechanism about the same point before impact. Also, $\mathbf{Q}(\Phi^+)\,\dot{\Phi}^+$ represents the velocity constraint due to the double impact. The validity of this solution, however, is dependent on three conditions:

(i)
$$\hat{F}_{ly} > 0 \tag{7}$$

(ii)
$$\left|\frac{\hat{F}_{lx}}{\hat{F}_{ly}}\right| < \mu \tag{8}$$

(iii)
$$\left|\frac{\hat{F}_{rx}}{\hat{F}_{ry}}\right| < \mu \tag{9}$$

Inequality (7) should be met if the trailing limb is expected to remain on the ground after impact. Inequalities (8) and (9) represent the no-slip conditions at the points of contacts of the limbs with the ground.

3 Objective Functions

In this section we develop five dynamic constraint functions that can be used as objective functions by a controller. Using these relations, we cast the locomotion of the system in terms of four basic quantities: step length S_L, overall locomotion speed V_p, maximum clearance of the swing limb H_m, and the stance knee bias σ (see Fig. 2). Our aim in this part of the article is to correlate the parameter space with the outcomes of the impact event. The impact event is one of the main determinants of the overall motion of the biped. We analyze the contact phenomenon assuming that the objective functions relations are fully satisfied when the system encounters this event. We drop this requirement in Part II. Numerical values of the geometrical dimensions, masses, and moments of inertia that are used in the numerical simulation are presented in Table 1.

The constraint relations can be described as follows:

(1) Erect Body Posture: One of the basic aspects of bipedal locomotion is that the biped should maintain an erect posture during locomotion. We will enforce this condition by the following relation

$$S_1 = \phi_1 + \phi_2 + \phi_3 = 0. \tag{10}$$

(2) Overall Progression Velocity. We define the "overall progression velocity" as the speed of the center of mass of the upper body in the positive x-direction. Using kinematic relations, we obtain the corresponding constraint equation as

Downloaded 03 May 2010 to 171.66.16.245. Redistribution subject to ASME license or copyright; see http://www.asme.org/terms/Terms_Use.cfm

Table 1 Dimensions, masses, and moments of inertia

Member	Mass m_i (kg)	Length l_i (m)	Moment of Inertia J_i (kg.m^2)
1	5	0.5	0.5
2	5	0.5	0.5
3	20	1.0	4.0
4	5	0.5	0.5
5	5	0.5	0.5

$$S_2 = -\frac{1}{2}\left[\cos[\phi_1]\dot{\phi}_1 + \cos[\phi_1+\phi_2](\dot{\phi}_1+\dot{\phi}_2) + \cos[\phi_1+\phi_2+\phi_3](\dot{\phi}_1+\dot{\phi}_2+\dot{\phi}_3)\right] - V_p = 0 \quad (11)$$

where V_p is the desired progression velocity.

(3) Trajectory of the Swing Limb During the Single Support Phase: The trajectory of the tip of the swing limb during the single-support phase is a significant factor in bipedal locomotion. This aspect of the locomotion is similar to the end effector problem in robotic manipulators. The swing limb has to be lifted off the ground surface at the beginning of the step cycle and has to be landed back at the end of it. During the cycle, the tip has to stay clear off the surface to avoid accidental contact. We achieve this goal by invoking the following quadratic relation between the x and y-coordinates of the tip:

$$y_T = c_1 x_T^2 + c_2 x_T + c_3, \quad (12)$$

where x_T and y_T are the x and y-coordinates of the tip, respectively, and the constants c_1, c_2, and c_3 are parameters that are yet to be determined in terms of step length and the maximum tip clearance. We chose a quadratic relation, because it is the simplest form that allows us to prescribe the desired step length and the tip maximum clearance independently. The advantage of this strategy is the ability of varying the parameters c_i to adjust the locomotion according to the walking surface. Gaits such as climbing stairs (walking on inclined surfaces) can be easily implemented by the appropriate selection of these parameters. For walking on a smooth horizontal surface, the constants in Eq. (12) become

$$c_1 = -\frac{4H_m}{S_L^2} \quad (13)$$

$$c_2 = 0 \text{ and} \quad (14)$$

$$c_3 = H_m \quad (15)$$

where S_L is the step length, and H_m is the maximum tip clearance. The final form of the constraint relation corresponding to the trajectory of the swing limb is obtained from Eqs. (12) through (15) as

$$S_3 = \frac{1}{2}\left\{\cos[\phi_1] + \cos[\phi_1+\phi_2] - \cos[\phi_1+\phi_2+\phi_3-\phi_4] - \cos[\phi_1+\phi_2+\phi_3-\phi_4-\phi_5]\right\} - H_m + \frac{H_m}{S_L^2}\left\{\sin[\phi_1] + \sin[\phi_1+\phi_2] - \sin[\phi_1+\phi_2+\phi_3-\phi_4] - \sin[\phi_1+\phi_2+\phi_3-\phi_4-\phi_5]\right\}^2 = 0. \quad (16)$$

(4) Bias of the Stance Knee: Unlike the knee joints of a human being, the "knee joints" of our system do not lock at certain positions. During the preliminary stages of modeling, we have observed that the stance knee has the tendency to collapse because of the lack of a locking mechanism. We overcome this difficulty by forcing the system to fix the stance knee at a certain angular position during the single support phase. The constraint relation that corresponds to this task is

$$S_4 = \phi_2 - \sigma \quad (17)$$

where σ is the bias angle.

(5) Coordination of the Motion of the Limbs: Although Eq. (16) prescribes the trajectory of the tip of the swing limb, it does not specify the direction of its motion. The direction can be specified by setting

$$x_T = 2x_3 \quad (18)$$

where x_3 is the x-coordinate of the center of mass of the upper body. This relation also implies that the tip moves twice as fast as the center of mass of the upper body in the positive x-direction. Thus, we also assure that the swing limb arrives at the contact point when the upper body is properly centered with respect to the two lower limbs. The dynamic constraint derived from Eq. (18) and the kinematic relations is

$$S_5 = \frac{1}{2}\left\{\sin[\phi_1] + \sin[\phi_1+\phi_2] + 2\sin[\phi_1+\phi_2+\phi_3] + \sin[\phi_1+\phi_2+\phi_3-\phi_4] + \sin[\phi_1+\phi_2+\phi_3-\phi_4-\phi_5]\right\} = 0. \quad (19)$$

4 Constrained Contact

The term *constrained contact* is used to imply that the five constraint relationships presented above are satisfied at the onset of the contact event. As we have mentioned previously, this assumption will be relaxed in the Part II of this study.

We use Eqs. (10), (16), (17), and (19) to obtain

$$\phi_1^- = -\arcsin\left\{\frac{S_L}{4\cos\left[\frac{\sigma}{2}\right]}\right\} - \frac{\sigma}{2} \quad (20)$$

$$\phi_2^- = \phi_5^- = \sigma \quad (21)$$

$$\phi_3^- = -\phi_1^- - \phi_2^- \quad (22)$$

$$\phi_4^- = -\arcsin\left\{\frac{S_L}{4\cos\left[\frac{\sigma}{2}\right]}\right\} - \frac{\sigma}{2}. \quad (23)$$

The angular velocities immediately before contact are found from the time derivatives of Eqs. (10), (16), (17), and (19) and Eq. (11) as

$$\dot{\phi}_2^- = 0 \quad (24)$$

$$\dot{\phi}_1^- = -\dot{\phi}_3^- = -\frac{V_p}{h} \quad (25)$$

$$\dot{\phi}_4^- = \left\{\frac{1}{h} + \frac{16H_m\left\{\frac{h}{2} + \frac{1}{8}S_L\frac{1-\cos\sigma}{\sin\sigma}\right\}}{S_L\sin\sigma}\right\} - V_p \quad (26)$$

$$\dot{\phi}_5^- = -\frac{16H_m h}{S_L\sin\sigma}V_p \quad (27)$$

where

$$h = \sqrt{\cos^2\left[\frac{\sigma}{2}\right] - \frac{1}{16}S_L^2}. \quad (28)$$

Equations (20) through (27) represent the values of the joint coordinates and velocities in terms of the four basic locomotion parameters S_L, V_p, σ, and H_m. There are two singular positions

Downloaded 03 May 2010 to 171.66.16.245. Redistribution subject to ASME license or copyright; see http://www.asme.org/terms/Terms_Use.cfm

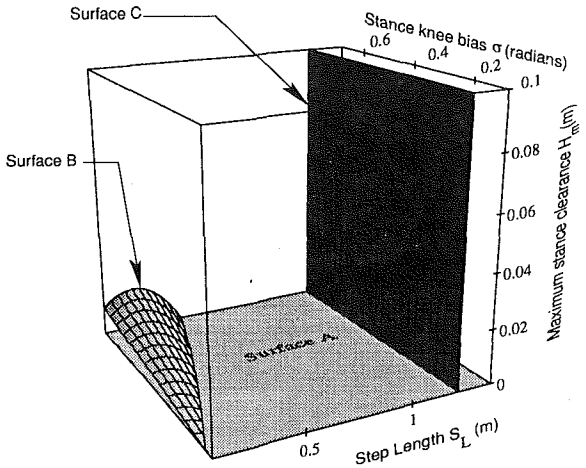


Fig. 3 Single and double-impact regions

that correspond to the values of $\sigma = 0$ and $\sigma = \pm\pi$. The former singularity corresponds to the fully extended knees and the latter to the fully collapsed knees.

5 Parametric Study of the Constrained Contact

After specifying the contact event, we now identify the range of the four locomotion parameters that yield a particular type of contact. We substitute Eqs. (20) through (28) into Eqs. (3) and (6) to obtain the post impact velocities and the impulsive forces. This yields

$$\begin{bmatrix} \dot{\boldsymbol{\Phi}}^+ \\ \hat{\mathbf{F}}_r \end{bmatrix} = V_p[\mathbf{N}_1(S_L,\sigma)H_m + \mathbf{N}_2(S_L,\sigma)] \tag{29}$$

where $\mathbf{N}_1$ and $\mathbf{N}_2$ are 7×1 vector functions of the parameters S_L and σ. The exact form of $\mathbf{N}_1$ and $\mathbf{N}_2$ depends on whether single or double impact occurs. This solution exists everywhere except for the singular positions of the biped where the coefficient matrix does not have an inverse. The exact form of this relation and some of the relations that are presented below were obtained by the symbolic manipulation algorithms of Mathematica™. These are excessively long relations. Presenting them in their full forms does not add to the understanding of the material presented here and makes the article unnecessarily lengthy. Therefore, we prefer to present some of the equations in their general forms only.

We observe from Eq. (29) that the solution depends linearly on the locomotion speed, V_p, and maximum stance limb clearance, H_m. The required friction force for no-slip impact does not depend on V_p. Varying V_p causes proportional changes in the x and y-components of the impulse forces. Thus, the ratio of the x and y-components remains unchanged. The general form of the impulse ratio for single impact is

$$\frac{\hat{F}_{rx}}{\hat{F}_{ry}} = \mu_s = \frac{\mathbf{N}_1^{[6]}(S_L,\sigma) + \mathbf{N}_2^{[6]}(S_L,\sigma)}{\mathbf{N}_1^{[7]}(S_L,\sigma)H_m + \mathbf{N}_2^{[7]}(S_L,\sigma)} \tag{30}$$

where the bracketed superscripts denote the nth element of the corresponding vectors.

For the double impact case, the slip conditions must be checked for the two contact points between the ground and the limbs. The corresponding impulse ratios are

$$\frac{\hat{F}_{rx}}{\hat{F}_{ry}} = \mu_{dL} = \frac{\mathbf{G}_{11}^{[L]}(S_L,\sigma) + \mathbf{G}_{12}^{[L]}(S_L,\sigma)}{\mathbf{H}_{11}^{[L]}(S_L,\sigma)H_m + \mathbf{H}_{12}^{[L]}(S_L,\sigma)} \tag{31}$$

$$\frac{\hat{F}_{rx}}{\hat{F}_{ry}} = \mu_{dT} = \frac{\mathbf{G}_{11}^{[T]}(S_L,\sigma) + \mathbf{G}_{12}^{[T]}(S_L,\sigma)}{\mathbf{H}_{11}^{[T]}(S_L,\sigma)H_m + \mathbf{H}_{12}^{[T]}(S_L,\sigma)} \tag{32}$$

where μ_{dL} and μ_{dT} are the no-slip impulse ratios for the leading and trailing limbs, respectively. Also, $\mathbf{G}_{ij}^{[L]}$, $\mathbf{G}_{ij}^{[T]}$, $\mathbf{H}_{ij}^{[L]}$, and $\mathbf{H}_{ij}^{[T]}$ are functions of the parameters S_L and σ. The vertical velocity of the trailing limb immediately after impact for the single impact case is

$$\dot{y}_T^+ = [Y_1(S_L,\sigma)H_m + Y_2(S_L,\sigma)]V_p \tag{33}$$

If $\dot{y}_T^+$ is positive, the single impact solution is used. When $\dot{y}_T^+$ is negative, the double impact solution is used. Equation (33) reveals that V_p does not affect this transition process. Therefore, considering Eqs. (30) through (33), we observe that the no-slip conditions and the transition from single to double impact depend only on the three parameters, S_L, σ, and H_m. We now identify the regions of the three-dimensional parameter space that correspond to the single or the double impact cases. Then, for each region we find the subregions where the corresponding parameter values lead to no-slip impact.

5.1 Single and Double Impact Regions. Figure 3 depicts the three surfaces that divide the parameter space into four adjacent volumes. We obtain the surfaces by setting the left-hand side of Eq. (34) to zero and solving the resulting relation for H_m.

Surface A represents the zero H_m plane; the portion of the parameter space below this plane contains negative H_m values and is not acceptable (the swing limb should stay above the ground for all times). Surfaces B and C contain the parameter values where $\dot{y}_T^+$ is zero for short and long step lengths, respectively. The volume bounded by A, B, and C is the single impact region.

There are two double impact regions, one bounded by A and B, and the other falling to the right of C. For small values of S_L, the biped is more likely to encounter double impact with larger values of σ and smaller values of H_m. Increasing H_m causes the swing limb to strike the ground with higher vertical velocities, eventually leading to the lifting off the trailing limb without an impact at the contact point. When σ is increased, the angular momentum of the system about the contact point before impact varies such that the forward roll of the biped decreases, eventually leading to double impact.

As the parameter S_L is increased we encounter C. This surface is almost insensitive to variations in H_m and σ. There is a transition that does not depend on σ or H_m at the step length of approximately 1.23 m. The equation that represents this surface is obtained from Eq. (33) as

$$H_m = -\frac{Y_1(S_L,\sigma)}{Y_2(S_L,\sigma)}. \tag{34}$$

5.2 The No-Slip Impact Regions. Having identified the double and single impact regions in the parameter space, we now use Eqs. (30) through (32) to find the no-slip subregions in each impact region. We solve for H_m in terms of the other two parameters and the friction coefficients. A critical coefficient of friction, μ, of 1.2 between the feet and the ground is used to obtain the surfaces depicted in Figs. (4), (5), and (6). Higher coefficients cause the respective friction surfaces to translate in the positive H_m direction, whereas lower values lead to translate in the negative direction. Figure 4 shows the no-slip surface corresponding to the single impact case. Parameter values that lie above F_s produce contact with no slipping. We observe that F_s lies above B and that F_s replaces B as the bounding surface of the single impact, no-slip region. Therefore, F_s, A, and C bound the volume in which the biped undergoes single impact without slipping.

We use Eqs. (31) and (32) to find the no-slip regions for double impact case. Figure 5 displays the region for short step lengths. Again, a critical friction coefficient, μ, of 1.2 is used for both sides. The no-slip region for the leading and the trailing limbs are the volumes that lie above F_{sL} and below F_{sT}, respectively. Since both F_{sL} and F_{sT} lie above B, the double impact case cannot exist for short step lengths without the slippage of the leading limb during impact for $\mu = 1.2$.

Downloaded 03 May 2010 to 171.66.16.245. Redistribution subject to ASME license or copyright; see http://www.asme.org/terms/Terms_Use.cfm

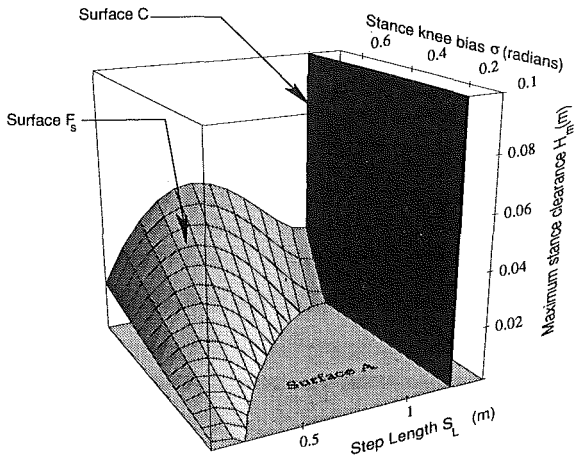


Fig. 4 Single impact, no-slip region

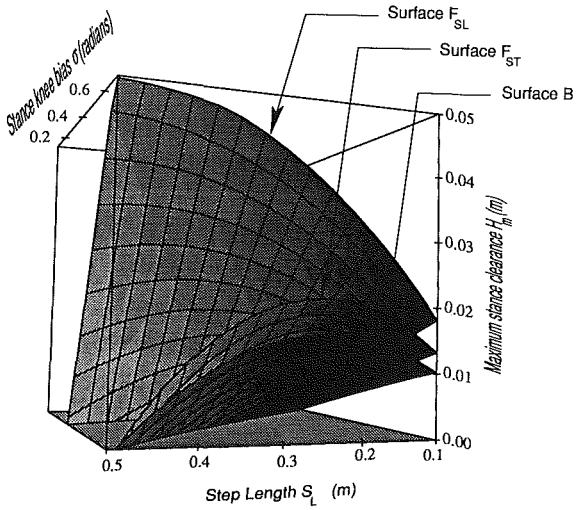


Fig. 5 Double impact, no-slip region for short step lengths

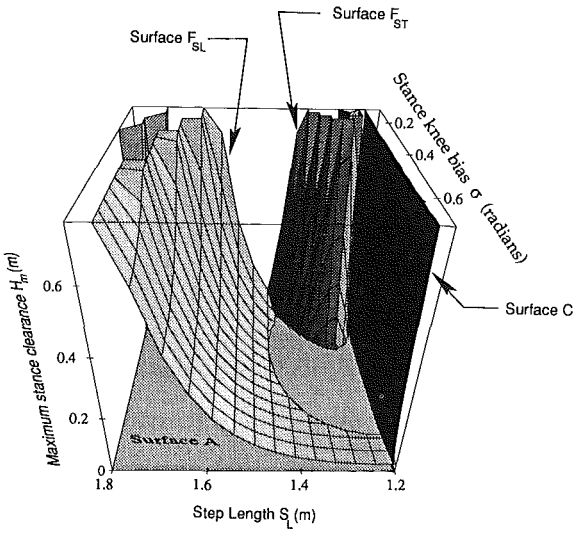


Fig. 6 Double impact, no-slip region for short long lengths

Figure 6 represents the double impact case for long step lengths. The no-slip regions for the leading and trailing limb lie above F_{sL} and inside F_{sT}, respectively. Therefore, the no-slip subspace for the double impact at longer step lengths, i.e., the intersection of F_{sL} and F_{sT}, effectively becomes the volume enclosed by F_{sT} and A. Increasing σ increases the likelihood of the slippage of the trailing limb without a significant effect on the leading limb, and increasing S_L makes both limbs more likely to slip.

6 Conclusions

Previous approaches to the problem of prescribing the motion of bipedal machines seem to fall short in terms of possessing a well-defined structure to address the design process. An approach has been presented to develop objective functions that can be used in conjunction with a controller to regulate the gait of a planar, five-element bipedal automaton. These functions are cast in terms of the progression speed, step length, maximum step height, and the stance knee bias. The transition process between successive steps is a crucial factor that should be considered in the modeling of gait. The contact event which initiates this transition may lead to locomotion with single and/or double-support phases, or slippage of the feet at contact.

A parametric study in the four-dimensional space is performed to correlate the locomotion parameters with the outcome of the contact event. The results for a fixed friction coefficient are presented in graphical form to directly observe this correlation and facilitate the choice of a parameter set that produces a specific type of contact.

Simplifying assumptions include rigid elements and point contact between the lower limbs and the walking surface. Most importantly, the motion of the biped is assumed to perfectly conform with the objective functions at the instant of contact. We did not elaborate on a control algorithm that will be responsible for the trajectory tracking. The relation between the trajectory tracking and the dynamics and stability of the overall gait has also been left uncovered. The conformity condition is dropped in Part II of this article. Also, Part II will address the control and stability issues for the overall motion and present a thorough analysis of the dynamics.

References

Beletskii, V. V., 1984, *Biped Walk*, Nauka, Moscow, (in Russian).

Furusho, J., and Masubichi, M., 1987, "A Theoretically Reduced Order Model for the Control of Dynamic Biped Locomotion," *ASME Journal of Dynamic Systems, Measurement, and Control*, Vol. 109, pp. 155–163.

Furusho, J., and Masubichi, M., 1986, "Control of a Dynamical Biped Locomotion System for Steady Walking," *ASME Journal of Dynamic Systems, Measurement, and Control*, Vol. 108, pp. 111–118.

Hemami, H., and Zheng, Y. F., 1984, "Dynamics and Control of Motion on the Ground and in the Air with Application to Bipied Robots," *Journal of Robotic Systems*, Vol. 1, No. 1, pp. 101–116.

Hemami, H., and Wyman, B. F., 1979, "Modeling and Control of Constrained Dynamic Systems with Application to Biped Locomotion in the Frontal Plane," *IEEE Trans. Aut. Control*, Vol. 24, pp. 526.

Hurmuzlu, Y., and Moskowitz, G., 1986, "The Role of Impact in the Stability of Bipedal Locomotion," *Int. J. Dynamics and Stability of Systems*, Vol. 1, No. 3, pp. 217–234.

Katoh, R., and Mori, M., 1984, "Control Method of Biped Locomotion Giving Asymptotic Stability of Trajectory," *Automatica*, Vol. 20, No. 4, pp. 405–414.

Vukobratovic, M., Borovac, B., Surla, D., and Stokic, D., 1990, *Scientific Fundamentals of Robotics 7. Biped Locomotion: Dynamics Stability, Control and Application*, Springer-Verlag, New York.

Vukobratovic, M., and Stokic, D., 1980, "Significance of Force-Feedback in Controlling Artificial Locomotion-Manipulation Systems," *IEEE Trans. on Biomedical Engineering*, Vol. BME-27, No. 12, pp. 705–713.

Zheng, Y. F., and Hemami, H., 1984, "Impact Effects of Biped Contact with the Environment," *IEEE Trans. Syst. Man Cyber.*, Vol. SMC-14, No. 3, pp. 437–443.

Downloaded 03 May 2010 to 171.66.16.245. Redistribution subject to ASME license or copyright; see http://www.asme.org/terms/Terms_Use.cfm

Dynamics of Bipedal Gait: Part II—Stability Analysis of a Planar Five-Link Biped

Y. Hurmuzlu
Mechanical Engineering Department,
Southern Methodist University,
Dallas, TX 75275
Assoc. Mem. ASME

A general approach based on discrete mapping techniques is presented to study stability of bipedal locomotion. The approach overcomes difficulties encountered by others on the treatment of discontinuities and nonlinearities associated with bipedal gait. A five-element bipedal locomotion model with proper parametric formulation is considered to demonstrate the utility of the proposed approach. Changes in the stability of the biped as a result of bifurcations in the four-dimensional parameter space are investigated. The structural stability analysis uncovered stable gait patterns that conform to the prescribed motion. Stable nonsymmetric locomotion with multiple periodicity was also observed, a phenomenon that has never been considered before. Graphical representation of the bifurcations are presented for direct correlation of the parameter space with the resulting walking patterns.

The bipedal model includes some idealizations such as neglecting the dynamics of the feet and assuming rigid bodies. Some additional simplifications were performed in the development of the controller that regulates the motion of the biped.

1 Introduction

Analysis of dynamics and stability of bipedal gait and development of control algorithms to regulate the motion of bipedal automata is a challenging problem which has prompted ongoing research efforts by many investigators.

Furusho and Matsubuchi (1986) considered a five-element biped. The equations of motion were linearized about the upright position of the biped and proportional plus derivative feedback are used at the individual joints. The system behavior was analyzed on a two-dimensional subspace of the phase space that represents the dominant poles of the linear system. The stability was tested by establishing a recursive relation among successive velocities at foot contact. Although this method was never characterized in the article as discrete mapping, it was the first attempt in studying the stability of bipedal gait by some type of a discrete map. But, the system was simplified to an extent that the resulting dynamics represented a very restricted subset of the actual behavior.

Katoh and Mori (1984) have considered a simple biped with telescopic legs. The equations of motion were partially linearized about vertical stance, and coupled van der Pol equations were used to prescribe the locomotion. The model has also included the impact of the lower limbs with the walking surface, and the article stressed the unavoidability of the impact problem in bipedal walk. Stability of the walking motion was established by proving convergence to the dynamics prescribed by the van der Pol equations and few numerical examples that demonstrate limit cycles on the phase plane.

Hemami et al. authored several articles studying the upright stability of inverted pendulums using Lyapunov's second method. In Hemami and Chen (1984), a two-link inverted pendulum model complete with ligament and muscle structures was constructed. Stability of the system about operating points was guaranteed by constructing feedback strategies based on Lyapunov functions. Zheng and Hemami (1984) have considered impact effects of the biped with its environment. Disturbances resulting from the velocity jumps as a result of impact were eliminated by using appropriate feedback functions. The general focus of Hemami et al. is feedback stabilization of inverted pendulum models that are correlated mostly with nonlocomotive actions (jumping, side sway, frontal sway, etc.) of man-made bipedal systems. Lyapunov's method has been proved to be an effective tool in developing robust controllers to regulate such actions. Its applicability to study the stability of the overall gait still remains to be an open question.

One of the latest work addressing stability of gait has appeared in Vukobratovic et al. (1990). The analysis is based on the concept of *practical stability* which is introduced by the authors. The definition identifies three regions in the state space. The system is said to be stable if for all state trajectories starting from a subspace X^I reach a subspace X^F within a time interval τ_s while remaining in a subspace X^I. As implied by the term *practical*, this is not a formal definition that conforms to the general notion of stability as it understood in the area of nonlinear dynamics. In general, one can identify invariant

Contributed by the Applied Mechanics Division of THE AMERICAN SOCIETY OF MECHANICAL ENGINEERS for presentation at the First Joint ASCE-EMD, ASME-AMD, SES Meeting, Charlottesville, VA, June 6–9, 1993.

Discussion on this paper should be addressed to the Technical Editor, Professor Lewis T. Wheeler, Department of Mechanical Engineering, University of Houston, Houston, TX 77204-4792, and will be accepted until four months after final publication of the paper itself in the ASME JOURNAL OF APPLIED MECHANICS.

Manuscript received by the ASME Applied Mechanics Division, Aug. 12, 1991; final revision, Mar. 20, 1992. Associate Technical Editor: D. J. Inman.

Paper No. 93-APM-10.

Copyright © 1993 by ASME
Downloaded 03 May 2010 to 171.66.16.245. Redistribution subject to ASME license or copyright; see http://www.asme.org/terms/Terms_Use.cfm

solutions where the state is trapped in a periodic orbit but deviates from it when perturbed along the unstable manifold. Yet, according to the practical stability definition, these solutions should be identified as stable. Based on the definition of *practical stability* a two-stage control methodology is developed. In the first stage, the control algorithm guarantees the realization of the nominal motion in the absence of disturbances. Then a decentralized control scheme is built assuming no dynamic coupling between the joints and is incorporated into the existing controller. Finally, additional control loops are applied to take into account the nonlinear coupling effects among various joints. The control strategy is applied to a nine d.o.f. bipedal model, and numerical simulation is performed to demonstrate the effectiveness of the proposed schemes. The approach is novel since the equations of motion are kept in nonlinear forms, actuator models are included, and a complicated example is worked out. Yet, the question arises whether such sophistication in control strategy is needed at all. Furthermore, the stability analysis is convoluted with the proposed control scheme, the method serves as a development tool rather than testing tool that can be used to study the stability of bipedal systems in general.

Bipedal locomotion systems are highly nonlinear; thus, a thorough stability analysis necessitates the inclusion of nonlinear effects. Such analysis should bring a formal definition to the stability of gait and provide mechanisms that can be used to capture the complicated facets of the nonlinear behavior. Stability analyses based on Lyapunov's second method are ad hoc, primarily because of the difficulties associated with constructing Lyapunov functions that are applicable to a general class of systems.

In the present article we adopt a different approach to the study and control of bipedal systems. First, we introduce a methodology to define and analyze the stability of bipedal locomotion in general. Then we will synthesize a five-element bipedal system based on the objective functions of Part I. The system includes a controller that tracks desired trajectories during the continuous phases of the step cycle (between successive ground contacts). Finally, we perform a parametric analysis to correlate the four-dimensional parameter space with the stability and dynamics of the overall gait. Graphical representation of a subset of possible motions in the four-dimensional parameter space are presented to evaluate the performance of the controller and determine its limitations.

2 Stability Analysis

In this article, the approach to the stability analysis takes into account two generally excepted facts about bipedal locomotion. The motion is discontinuous because of the impact of the limbs with the walking surface, Hurmuzlu and Moskowitz (1986), Katoh and Mori (1984), and Zheng (1989). The dynamics is highly nonlinear and linearization about vertical stance should be avoided (Hurmuzlu and Moskowitz, 1987; Vukobratovic, 1990).

Given the two facts that have been presented above we propose to apply discrete mapping techniques to study the stability of bipedal locomotion. This approach has been applied previously to study of the dynamics of bouncing ball (Guckenheimer and Holmes, 1985) and to the study of vibration dampers (Holmes and Shaw, 1983; Shaw and Shaw, 1989). The approach eliminates the discontinuity problems, allows the application of the analytical tools developed to study nonlinear dynamical systems, and brings a formal definition to the stability of bipedal locomotion.

The method is based on the construction of a first return map by considering the intersection of periodic orbits with an n-1 dimensional cross-section in the n-dimensional state space. There is one complication that will arise in the application of this method to bipedal locomotion. Namely, different set of kinematic constraints govern the dynamics of various modes of motion. Removal and addition of constraints in locomotion systems has been studied before by Hemami and Wyman (1979). They describe the problem as a two-point boundary value problem where such changes may lead to changes in the dimensions of the state space required to describe the dynamics. Due to the basic nature of discrete maps, the events that occur outside the cross-section are ignored. The situation can be resolved by taking two alternative actions. In the first case a mapping can be constructed in the highest dimensional state space that represents all possible motions of the biped. When the biped exhibits a mode of motion which occurs in a lower dimensional subspace, extra dimensions will be automatically included in the invariant subspace. Yet, his approach will complicate the analysis and it may not be always possible to characterize the exact nature of the motion. An alternate approach will be to construct several maps that represent different types of motion, and attach various conditions that reflect the particular type of motion. We will adopt the second approach in this article. Accordingly, for no slip walking, without the double-support phase, a mapping $\mathbf{P}_{nsls}$ is obtained as a relation between the state $\mathbf{x}$ immediately after the contact event of a locomotion step and a similar state ensuing the next contact. This map describes the behavior of the intersections of phase trajectories with a Poincaré section Σ_{nsls} that can be defined as

$$\Sigma_{nsls}=\left\{(\mathbf{x},\ \dot{\mathbf{x}})\in\mathcal{R}^n \mid x_T(\mathbf{x})>0,\ y_T(\mathbf{x})=0 \mid \dot{y}_T^+(\mathbf{x})>0,\ \left|\frac{\hat{F}_{rx}}{\hat{F}_{ry}}\right|>\mu,\ \left|\frac{F_{rx}}{F_{ry}}\right|>\mu,\ F_{ry}>0\right\}, \quad (1)$$

where x_T and y_T are the x and y-coordinates of the tip of the swing limb, respectively. The first two conditions in Eq. (1) establish the Poincaré section (the cross-section is taken immediately after foot contact during forward walking). Whereas, the attached four conditions denote no double support phase, no slip impact, no slippage of pivot during the single-support phase, and no detachment of pivot during the single-support phase, respectively. For example, to construct a map representing no slip running, the last condition will be removed to allow pivot detachments as they normally occur during running. We will not elaborate on all possible maps that may exist for bipedal locomotion, but we note that the approach can address a variety of possible motions by construction of maps with the appropriate set of attached conditions.

The discrete map obtained by the procedure described above can be written in the following general form:

$$\xi_i=\mathbf{P}(\xi_{i-1}) \quad (2)$$

where ξ is the n-1 dimensional state vector, and the subscripts denote the ith and $i-1$st return values, respectively.

Periodic motions of the biped correspond to the fixed points of $\mathbf{P}$ where

$$\xi^*=\mathbf{P}^k(\xi^*) \quad (3)$$

where $\mathbf{P}^k$ is the kth iterate. Stability of $\mathbf{P}^k$ reflects the stability of the corresponding flow. The fixed point ξ^* is said to be stable when the eigenvalues ν_i, of the linearized map,

$$\delta\xi_i=\mathbf{DP}^k(\xi^*)\delta\xi_{i-1}, \quad (4)$$

have moduli less that one.

This method has several advantages. First, the stability of gait now agrees with the formal stability definition accepted in nonlinear mechanics. Eigenvalues of the linearized map (Floquet Multipliers) provide quantitative measures of the stability of bipedal gait. Finally, to apply the analysis to locomotion one only requires the kinematic data that represent all the relevant degrees-of-freedom. No specific knowledge of the internal structure of the system is needed.

Downloaded 03 May 2010 to 171.66.16.245. Redistribution subject to ASME license or copyright; see http://www.asme.org/terms/Terms_Use.cfm

In general, the exact form of $\mathbf{P}$ cannot be obtained in closed form. For example, if the system under investigation is a numerical model of a man-made machine, the equations of motion will be solved numerically to compute the fixed points of the map from kinematic data. Then stability of each fixed point will be investigated by computing the Jacobian using numerical techniques. This procedure will be demonstrated for the five-element bipedal model in the ensuing sections. Whereas, if the system in consideration is an experimental prototype, kinematic data will be obtained by measurement and various types of perturbations will be used to investigate the stability. The method can also be applied to the human system. Yet, the complexity of the human locomotor brings about many challenging questions. The number measurements required to capture the dynamic behavior and the external perturbation methods that have to be employed to measure stability are important open questions that are beyond the scope of the present article.

3 Application to the Five-Element Bipedal System

During its motion the biped is subject to repeated disturbances caused by the contact of the lower limbs with the ground surface. Perturbations resulting from the contact event are not directly controllable because the actuators cannot generate impulsive moments to compensate for the effect of contact forces that arise during impact. All the previous work addressing the control of gait are based on some type of trajectory tracking during the continuous phases of locomotion. In some cases, the effect of impulsive forces are neglected altogether to avoid the complications that may arise due to repeated disturbances. In others, specific results are presented that correspond to a very limited choice of parameter values where superior convergence rates can be readily achieved. Yet, the question of the effect of increasing tracking errors on the overall locomotion picture is a rarely addressed issue: Does the motion loosen its stability altogether, or does some other type of anomalous gait emerge during which stability is still conserved? For example, the locomotion of an amputee may be stable, yet it may not conform to any accepted notion of normal locomotion. Study of anomalous motions is important, and may lead to better understanding of human gait abnormalities. One may create simplified biped models and attempt to induce specific types of abnormalities to better understand the dynamics of the more realistic cases. This study does not address the human gait in any sense. But it demonstrates the complexity of the motion of a system which is substantially simpler than the human being.

The control strategy in the present work is based on trajectory tracking during the forward swing motion only. The controller proposed below is a computed torque algorithm that is based on full-state feedback and assumes perfect knowledge of the system parameters. Controllers of this form are practically limited because of the latter requirement. Yet, the subsequent analysis demonstrates the dynamic behavior for a "best scenario controller." With this added advantage, we will demonstrate that the biped exhibits very complicated dynamic behavior. The system may generate stable gait patterns that are entirely different than the ones prescribed by the objective functions.

3.1 Control law. Equations of motion of the biped during the forward swing phase can be written as

$$\dot{\mathbf{x}} = \mathbf{f}(\mathbf{x}) + \mathbf{b}(\mathbf{x})\mathbf{u}. \tag{5}$$

Here, $\mathbf{x} = \{x_1, \ldots, x_{10}\}^T$, is the ten-dimensional state vector, $\mathbf{u} = \{u_1, \ldots, u_5\}^T$ is the five-dimensional control, $\mathbf{f}$ and $\mathbf{b}$ are vector fields. Also, the dot indicates differentiation with respect to time. The constraint relations that we seek to prescribe during the motion can be written as

$$\mathbf{S}_\omega(\mathbf{x}) = 0,\ \omega \in \mathcal{R}^4 \tag{6}$$

where $\mathbf{S}_\omega = \{S_1, \ldots, S_5\}^T$ is the constraint function and depends on $\omega = \{V_p, H_m, S_L, \sigma\}$, the vector of locomotion parameters as described in Part I. We drop ω from our notation for simplicity and let

$$\ddot{\tilde{\mathbf{S}}} := \mathbf{C}_1\ddot{\mathbf{S}} + \mathbf{C}_2\dot{\mathbf{S}} + \mathbf{C}_3 = 0, \tag{7}$$

where $\mathbf{C}_1$, $\mathbf{C}_2$ and $\mathbf{C}_3$ are 5×5 matrices containing the design parameters that will be explained below. If S_i is a holonomic constraint (ex. S_1), then the ith row of $\mathbf{C}_1$ is set to $\mathbf{e}_i$, whereas if the constraint is nonholonomic (ex. S_2), the ith row of $\mathbf{C}_1$ is set to $\mathbf{0}$ and the ith row of $\mathbf{C}_2$ is set to $\mathbf{e}_i$ where $\mathbf{e}_1 = \{1, 0, \ldots, 0\}$, $\mathbf{e}_2 = \{0, 1, \ldots, 0\}$, etc. The matrices $\mathbf{C}_2$ and $\mathbf{C}_3$ are diagonal and contain parameters that can be chosen such that the solution set of $\tilde{\mathbf{S}}$ is asymptotically stable about the origin (i.e., $S_i \to 0$ as $t \to 0$).

We use Eqs. (10), (11), (16), (17), and (19) of Part I to write $\tilde{\mathbf{S}}$ in the form

$$\tilde{\mathbf{S}} = \mathbf{G}(\mathbf{x})\dot{\mathbf{x}} + \mathbf{H}(\mathbf{x}) \tag{8}$$

where $\mathbf{G}$ and $\mathbf{H}$ are 5×5 vector valued functions. Using Eq. (5) to eliminate $\dot{\mathbf{x}}$ from Eq. (8), solving for the control vector $\tilde{\mathbf{u}}$ and dropping $\mathbf{x}$ to simplify the notation yields

$$\tilde{\mathbf{u}} = -(\mathbf{G}\mathbf{b})^{-1}(\mathbf{G}\mathbf{f} + \mathbf{H}). \tag{9}$$

Equation (9) represents a nonlinear feedback law which expresses the controls in terms of the ten state variables.

3.2 Symbolic derivation of $\mathbf{P}_{nsls}$. The control algorithm presented above allows us to prescribe a hierarchical approach to the constraint space by appropriate selection of the approach parameters in the matrices $\mathbf{C}_2$ and $\mathbf{C}_3$ of Eq. (7). However, in the present study we adopt a uniform approach and choose the matrices $\mathbf{C}_1$, $\mathbf{C}_2$ and $\mathbf{C}_3$ as follows:

$$\mathbf{C}_1 = \mathrm{diag}\{1, 0, 1, 1, 1\} \tag{10}$$

$$\mathbf{C}_2 = \mathrm{diag}\{\alpha, 1, \alpha, \alpha, \alpha\} \tag{11}$$

$$\mathbf{C}_3 = \mathrm{diag}\{\beta, \lambda_1, \beta, \beta, \beta\} \tag{12}$$

where

$$\lambda_{1,2} = -\frac{\alpha}{2} \pm \sqrt{\frac{\beta^2}{4} - \alpha\beta} \text{ and } \beta > 4\alpha > 0. \tag{13}$$

Now Eq. (7) can be solved for $\mathbf{S}$.

First we obtain the expressions of the angular displacements and velocities at $t > t_0$ in terms of the locomotion parameters, initial time t_0, and initial values of the angular displacements and velocities. We use Eqs. (10), (11), (16), (17), and (19) of Part I and their time derivatives to obtain

$$\phi_2(t) = \sigma + S_4(t) \tag{14}$$

$$\phi_1(t) = -\frac{\phi_2(t)}{2} + \arcsin\left[\frac{\int_{t_0}^{t} S_2(t)\,dt + \eta_1(t)}{\cos\dfrac{\phi_2(t)}{2}}\right] \tag{15}$$

$$\phi_3(t) = S_1(t) - \phi_1(t) - \phi_2(t) \tag{16}$$

$$\phi_5(t) = \begin{cases} 2\arccos\sqrt{\dfrac{\eta_2^2(t) + \eta_3^2(t)}{4}} & \text{for } \phi_5(t_0) > 0 \\ -2\arccos\sqrt{\dfrac{\eta_2^2(t) + \eta_3^2(t)}{4}} & \text{for } \phi_5(t_0) < 0 \end{cases} \tag{17}$$

$$\phi_4(t) = S_1(t) - \frac{\phi_5(t)}{2} - \arctan\left[\frac{\eta_2(t)}{\eta_3(t)}\right] \tag{18}$$

where

Downloaded 03 May 2010 to 171.66.16.245. Redistribution subject to ASME license or copyright; see http://www.asme.org/terms/Terms_Use.cfm

$$\eta_1(t) = -V_p(t-t_0) - \frac{\sin S_1(t) - \sin S_1(t_0) - \sin\phi_1(t_0) - \sin[\phi_1(t_0)+\phi_2(t_0)]}{2} \quad (19)$$

$$\eta_2(t) = 2S_5(t) - \sin\phi_1(t) - \sin[\phi_1(t)+\phi_2(t)] - 2\sin S_1(t) \quad (20)$$

$$\eta_3(t) = 2S_3(t) + 8\frac{H_m}{S_L^2} + H_m + \{S_5(t) - \sin\phi_1(t) - \sin[\phi_1(t)-\phi_2(t)] - \sin S_1(t)\}^2 \quad (21)$$

$$\dot{\phi}_1(t) = -\frac{S_1(t) + V_p + \dot{S}_1(t)\cos S_1(t) + \dot{S}_4(t)\cos[\phi_1(t)+\phi_2(t)]}{\cos\phi_1(t) + \cos[\phi_1(t)+\phi_2(t)]} \quad (22)$$

$$\dot{\phi}_2(t) = \dot{S}_4(t) \quad (23)$$

$$\dot{\phi}_3(t) = \dot{S}_1(t) - \dot{\phi}_2(t) \quad (24)$$

$$\dot{\phi}_4(t) = \frac{-2\gamma_1(t)}{\sin\left[\frac{\phi_5(t)}{2}\right]} \quad (25)$$

$$\dot{\phi}_5(t) = \frac{-2\gamma_2(t)}{\sin\left[\frac{\phi_5(t)}{2}\right]} \quad (26)$$

We simplified the notation by leaving the terms $S_i(t)$, $\dot{S}_i(t)$, and $\int_{t_0}^{t} S_2(t)$ unevaluated in the above equations. We also did not present the expressions for $\gamma_1(t)$ and $\gamma_2(t)$. These expressions are excessively long and the calculations to derive these velocities are relatively straightforward. We used kinematic relations and $\dot{S}_i(t)$, which linearly depend on these velocities to obtain the final expressions.

Equations (25) and (26) reflect singular positions at $\phi_5 = 0, \pm\pi$. These singularities correspond to the fully collapsed and extended swing knee configurations, respectively.

The y-coordinate of the swing limb can be written as

$$y_T(t) = S_3(t) + \frac{1}{2}\{\cos\phi_1(t) + \cos[\phi_1(t)+\phi_2(t)] - \cos[-S_1(t)+\phi_4(t)] - \cos[-S_1(t)+\phi_4(t)+\phi_5(t)]\}. \quad (27)$$

Equation (27) depends on the values of the angular positions at $t = t_0$ and the time t. At contact,

$$y_T(t_c) = 0. \quad (28)$$

Equation (28) depends on t_c only, yet the exact solution requires the usage of numerical techniques. Once calculated, t_c can be substituted into Eqs. (14) through (26) to compute the remainder of the unknown quantities. Finally, we substitute the angular positions and velocities at the instant of contact in Eqs. (2) and (3) of Part I to incorporate the impact and switching to obtain the mapping from the initial state to the state immediately after contact.

4 Numerical Simulation and Analysis of P_{nsls}

The overall behavior is governed by the union of two solution sets (equation of motion during the single-support phase and the impact and switching equations). We now focus on the interaction of these solution sets and the possible outcomes of this interaction. Numerical analysis is carried out by selecting the control parameters such that $\lambda_1 = -6$ and $\lambda_2 = -7$ to assure higher rates of convergence for trajectory tracking.

4.1 Fixed Points of P_{nsls}. The constrained motion possesses a singular point at $\phi_5 = 0$. This singularity forms a hyperplane which bisects the state space into two disjoint subspaces; the positive subspace where $\phi_5 > 0$ and the negative subspace where $\phi_5 < 0$. Trajectories that start from either subspace do not cross to the other. Solution curves of the prescribed motion $\mathfrak{M}_c$ also include two portions $\mathfrak{M}_c^+$ and $\mathfrak{M}_c^-$

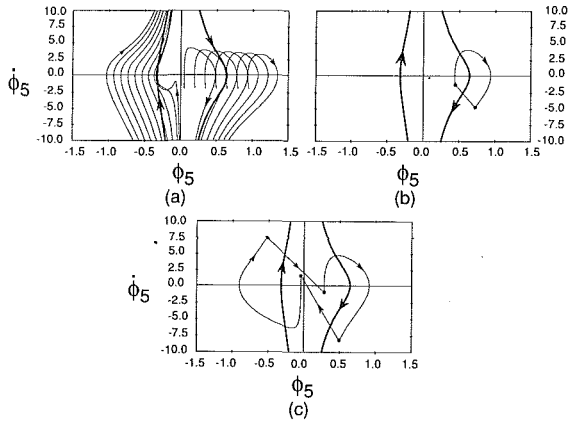


Fig. 1 Type I and Type II attractors for V_p = 1.4 m/s, H_m = 0.05 m, S_L = 0.82 m, and σ = 0.1 radians

located on either side of hyperplane representing $\phi_5 = 0$. The swing limb is bent forwards during the forward motion when the solution conforms with $\mathfrak{M}_c^+$, or it is bent backwards when it conforms with $\mathfrak{M}_c^-$. The condition of the swing knee during each step depends on the direction of the knee flexion at the onset of the particular step (ϕ_5^+). When the system encounters the contact, the switching causes the exchange of the stance and swing knee angles. Accordingly, the state of the stance knee at the end of a particular step (ϕ_2^-) also affects the condition of the swing knee during the ensuing step. Yet, the kinematic constraints fix the stance knee at a bias of σ, which is chosen as a positive constant. Therefore, the motion that conforms to the kinematic constraints corresponds to $\mathfrak{M}_c^+$. However, when the motion deviates from the constraints for various reasons, we may expect the trajectories to crisscross from one subspace to the other as a result of switching. As we will see below, a special class of periodic motions which exhibit crisscrossing of state trajectories are indeed observed in certain parameter regimes. Here, solutions ξ^* of Eq. (3) are classified under two general categories.

(1) Type I Cycles. *TYPE 1* cycles are periodic solutions that include one contact per cycle. Figure 1(*a*) represents the cross-section of the phase space taken at $\omega = \{1.4, 0.05, 0.82, 0.1\}$. Trajectories that start from an initial ϕ_5 in the right-hand plane where $\phi_5 > 0$, tend to negative infinity as they approach the singularity ($\phi_5 = 0$) along $\mathfrak{M}_c^+$. Whereas trajectories in the left-hand plane tend to positive infinity as they approach the singularity along $\mathfrak{M}_c^-$. The phase trajectories converge exponentially to $\mathfrak{M}_c^+$ and $\mathfrak{M}_c^-$ for $t > t_0$. The tendency of state trajectories approaching the singular position is actually a natural consequence of the motion in $\mathfrak{M}_c$. We have prescribed a quadratic tip trajectory accompanied by forward motion. In the absence of the walking surface, tip of the swing limb tracks the quadratic trajectory even for negative y_T values. This action forces the swing knee to extend further so that the tip is kept on the quadratic path, eventually leading to the singular configuration. Figure 1(*b*) depicts the phase plane picture of the steady-state behavior when we incorporate the contact. The configuration depicted in the figure reveals a closed orbit that includes a portion of a state trajectory accompanied by a sudden transfer. Subsequent calculation of the characteristic multipliers at this limit cycle yields max[mod(ν_i)] = 0.08, which denotes a strongly stable attractor. The numerical study for the present system produces *Type I* cycles that are located in the positive subspace. Cycles of this class have not been encountered in the negative subspace.

(2) TYPE II$^{(n)}$ Cycles. We define the *TYPE II*$^{(n)}$ cycles as periodic solutions that include n contacts per period. Figure 1(*c*) depicts the second cycle, which appears when contact is

Downloaded 03 May 2010 to 171.66.16.245. Redistribution subject to ASME license or copyright; see http://www.asme.org/terms/Terms_Use.cfm

incorporated. This closed orbit is formed by portions of dynamic trajectories that are located on opposite sides of the singular point. During the motion that corresponds to this solution, the biped takes one step during which the swing knee is bent backwards, followed by a step during which the knee is bent forwards.

The numerical search for this class of cycles produced closed orbits that always include state trajectories that cross over at least once per period. We did not encounter any *TYPE II*$^{(n)}$ that lie entirely in either the positive or the negative subspaces.

4.2 Structural Stability of the Fixed Points of $\mathbf{P}_{nsls}$. The focus of this section is to investigate the structural stability of the limit cycles subject to variations in the components of the parameter vector ω.

Figure 2 depicts bifurcations of *Type I* cycles that take place at $\sigma = 0.1$ radians and $H_m = 0.05$ m when progression velocity and step length are varied. We obtain the bifurcation diagram by plotting c_1 versus ϕ_5^+. We use c_1 instead of S_L as one of the variables. This choice stretches the bifurcation diagram for very small step lengths and provides better visualization of the diagrams. Solid lines in the figure represent stable cycles while dashed lines represent unstable cycles. For progression velocities $V_p < 1.2$ m/s, loci of stable limit cycles are given by a single branch. This branch ends when it reaches the horizontal axis where $\phi_5^+ = 0$. At this point a very complex set of bifurcations are encountered. We will return to these bifurcations later in this section. When the velocity is increased, a codimension two bifurcation occurs and the three-limit cycles emerge as this branch folds creating two saddle node (SN) bifurcations (point *D*). A third SN bifurcation enters the picture from the left, revealing existence of two more cycles for short step lengths. As the velocity is further increased (1.21 m/s $< V_p <$ 1.22 m/s), a second codimension two bifurcation occurs when two of the SN bifurcations collide and disappear, leading to a stable and an unstable branch (*A*). When progression velocity is further increased, the third SN bifurcation reaches zero at $V_p = 1.43$ m/s (*C*). Furthermore, at this velocity a similar set of events take place in reverse order for long step lengths. We observe the birth of two SN bifurcations for 1.43 m/s $< V_p <$ 1.44 m/s (*B*). Then, one of the SN bifurcations gradually moves to the right and disappears for higher velocity values ($V_p = 1.55$ m/s).

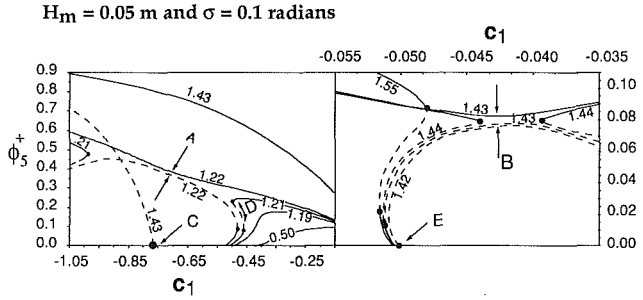


Fig. 2 Bifurcation diagrams at σ = 0.1 radians and H_m = 0.05 m

The overall picture is depicted in Fig. 3. Solid curves in the figure represent SN bifurcations, whereas dashed curves represent crossings to negative ϕ_5^+ values. We highlighted the two regions that correspond to the events described in Fig. 2 and marked the five transition points of the figure accordingly. As Fig. 3 denotes, *TYPE I* cycles are less likely to occur for shorter step lengths, faster velocities, higher clearances, and smaller stance knee biases. Shortening the step length causes the biped to take a larger number of forward steps to keep up with the prescribed progression velocity, decreasing the duration of each locomotion step. This diminishes the time available to the control algorithm for restoring the prescribed motion. Increasing the progression velocity has the same effect on the duration of steps. Increasing the clearance increases the vertical velocity of the tip at contact. Higher vertical tip velocities lead to increased perturbations and may lead to the disappearance of *TYPE I* cycles.

The dashed curves that are present for low clearance values indicate that the zero crossings occur for low clearances and short-to-moderate step lengths.

Zero crossings trigger a very complex pattern of bifurcations. Figure 4(*a*) depicts the bifurcation diagram for the parameter values shown. A variety of complex of bifurcations are apparent from the diagram. Periodic windows exist where the steady-state limit cycles lock into subharmonics, there are also regions of accumulation of bifurcations.

The *TYPE II*$^{(n)}$ cycles are detected in open parameter intervals. End points of the intervals correspond to parameter values when a certain iterate of a cycle is located on the singularity plane. Therefore, the cycles cease to exist at the exact end points. Furthermore, when a particular iterate of a cycle approaches the singularity plane, a secondary cycle emerges and coexists with first cycle until the iterate moves on the

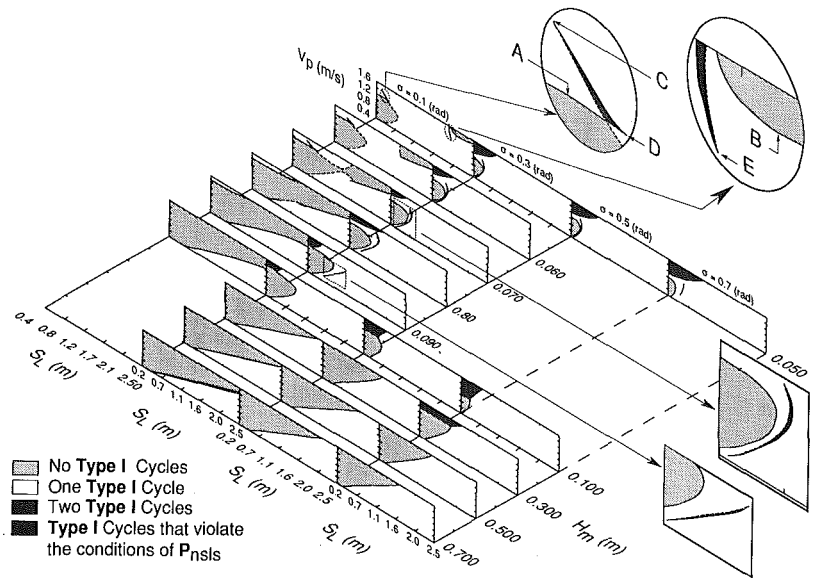


Fig. 3 Bifurcation of *TYPE I* cycles

Downloaded 03 May 2010 to 171.66.16.245. Redistribution subject to ASME license or copyright; see http://www.asme.org/terms/Terms_Use.cfm

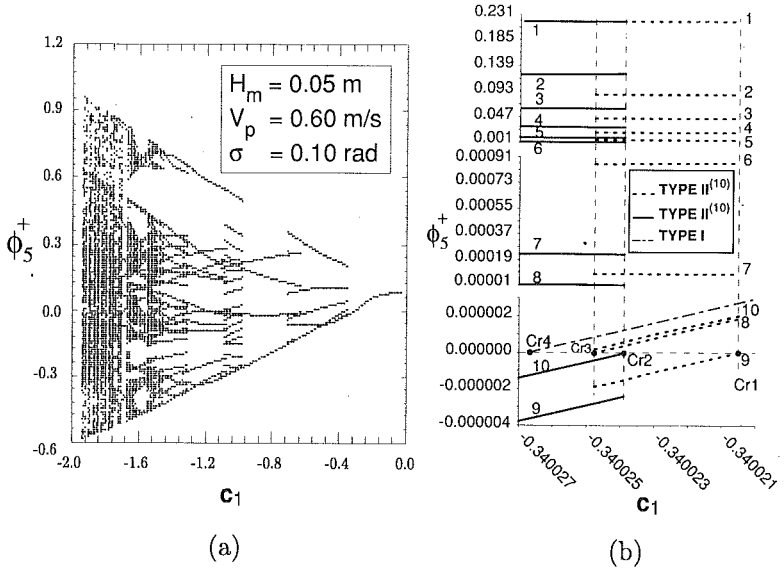


Fig. 4 Zero-crossing bifurcations

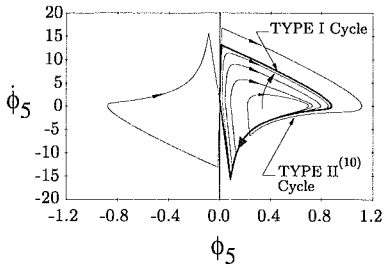


Fig. 5 The Cr1 transition on the phase-plane portrait

singularity plane. The mapping exhibits this hysteretic behavior at every bifurcation point. Accordingly, the parameter range consists of open subintervals of *TYPE II*$^{(n)}$ cycles with overlapping portions.

The details of the first crossing is depicted in Fig. 4(*b*). As the *TYPE I* branch approaches the crossing point, we observe the birth of a *TYPE II*$^{(10)}$ cycle at Cr1. The two cycles coexist between Cr1 and Cr2. When the eighth iterate of the period-ten cycle approaches the crossing point a second period-ten cycle emerges at Cr2. The former cycle disappears when its eighth iterate becomes singular at Cr3. Finally, the period-one cycle disappears at Cr4.

Figure 5 depicts the phase plane picture in the Cr1-Cr2 interval. The darker state trajectory in the figure corresponds to the period-one cycle. When a trajectory starts from an initial condition sufficiently close to the *TYPE I* cycle, it is captured by this cycle. Yet, if an initial condition is not located in the vicinity of the *TYPE I* cycle, impact and switching transfers the trajectory to the negative half-plane. Following a single loop in the negative half-plane the trajectory crosses back. Then it starts to descend toward the *TYPE I* cycle. But, the trajectory crosses to the negative half-plane again before it is completely captured by the period-one cycle. This leads to the first period-ten cycle shown if Fig. 4(*b*). In the parameter interval (Cr2-Cr3) three cycles coexist. A new *TYPE II*$^{(10)}$ cycle with two loops in the negative half-plane emerges. This bifurcation takes place when the destination of the loop in the negative half-plane does not cross back to the positive half-plane, leading to two successive iterates in the negative half-plane (see Fig. 4(*b*)).

The complexity of the motion for other parameter values are apparent from the bifurcation diagram. We will not elaborate on all of the aspects of the dynamic structure in this article for the sake of brevity.

5 Discussion and Conclusions

The first objective of the present article is to develop a general methodology to study the stability of bipedal locomotion without any specific assumptions about the internal structure of the biped. The second goal is to demonstrate the utility of the proposed methodology by using it to study the structural stability of a bipedal locomotion model with a proper parametric formulation.

We have proposed a discrete mapping technique that addresses the nonlinear and discontinuous nature of bipedal gait. The proposed approach brings a formal definition to the stability of gait and enables the utilization of the analytical tools of nonlinear dynamics to analyze the motion of a general class of bipedal locomotion systems.

The method was applied to perform a study of the bifurcations of a five-element bipedal locomotion model in the four-dimensional parameter space. The model was constructed by using the objective functions of Part I in conjunction with a computed torque control algorithm. The analysis demonstrated the existence of variety of gait patterns that can be radically different from the ones intended by the objective functions. The discrete mapping technique was successfully used in capturing many aspects of the motion that would have been impossible with the previous approaches that have been followed by other researchers in the bipedal locomotion area.

The bipedal model used in this study includes some idealizations such as neglecting the dynamics of the feet and assuming rigid bodies. Furthermore, the computed torque algorithm assumes perfect knowledge of system parameters and some practical issues such as the actuator dynamics and limitations of actuator torques were not considered. We believe, however, that the model has successfully served to establish the main results intended by the article. More practical models equipped with realistic controllers are currently under study and will be the subject of forthcoming publications.

References

Furusho, J., and Masubichi, M., 1986, "Control of a Dynamical Biped Locomotion System for Steady Walking," *ASME Journal of Dynamic Systems, Measurement, and Control*, Vol. 108, pp. 111–118.

Guckenheimer, J., and Holmes, P., 1985, *Nonlinear Oscillations, Dynamical*

Downloaded 03 May 2010 to 171.66.16.245. Redistribution subject to ASME license or copyright; see http://www.asme.org/terms/Terms_Use.cfm

Systems, and Bifurcations of Vector Fields, Springer-Verlag, New York.

Hemami, H., and Wyman, B. F., 1979, "Modelling and Control of Constrained Dynamic Systems with Application to Biped Locomotion in the Frontal Plane," *IEEE Trans. Aut. Control*, Vol. 24, pp. 526.

Hemami, H., and Chen, B. R., 1984, "Stability Analysis and Input Design of a Two-Link Planar Biped," *The International Journal of Robotics Research*, Vol. 3, No. 2, pp. 93–100.

Hurmuzlu, Y., and Moskowitz, G., 1987, "Bipedal Locomotion Stabilized by Impact and Switching: I. Two and Three Dimensional, Three Element Models," *Int. J. Dynamics and Stability of Systems*, Vol. 2, No. 2, pp. 73–96.

Katoh, R., and Mori, M., 1984, "Control Method of Biped Locomotion Giving Asymptotic Stability of Trajectory," *Automatica*, Vol. 20, No. 4, pp. 405–414.

Shaw, J., and Shaw, S. W., 1989, "The Onset of Chaos in a Two-Degree-of-Freedom Impacting System," ASME JOURNAL OF APPLIED MECHANICS, Vol. 56, pp. 168–174.

Shaw, S. W., and Holmes, P. J., 1983, "A Periodically Forced Piecewise Linear Oscillator," *Journal of Sound and Vibration*, Vol. 90, No. 1, pp. 129–155.

Vucobratovic, M., Borovac, B., Surla, D., and Stokic, D., 1990, *Scientific Fundamentals of Robotics 7. Biped Locomotion: Dynamics Stability, Control and Application*, Springer-Verlag, New York.

Zheng, Y. F., 1989, "Acceleration Compensation for Biped Robots to Reject External Disturbances," *IEEE Trans. Syst. Man Cyber.*, Vol. 19, No. 1, pp. 74–84.

Zheng, Y. F., and Hemami, H., 1984, "Impact Effects of Biped Contact with the Environment," *IEEE Trans. Syst. Man Cyber.*, Vol. SMC-14, No. 3, pp. 437–443.

Downloaded 03 May 2010 to 171.66.16.245. Redistribution subject to ASME license or copyright; see http://www.asme.org/terms/Terms_Use.cfm

Energy Considerations in the Flow Enhancement of Viscoelastic Liquids

A. Siginer
Mem. ASME.

A. Valenzuela-Rendón

Department of Mechanical Engineering,
Auburn University,
Auburn, AL 36849

Flow enhancement effects due to different waveforms in the tube flow of rheologically complex fluids driven by a pulsating pressure gradient are investigated. It is found that the squarer the waveform the larger the enhancement. In each case the enhancement is strongly dependent on the viscosity function, but the elastic properties also play an important role. We determine that considerable energy savings may be obtained in the transport of viscoelastic liquids if an oscillatory gradient is superposed on a mean gradient. The closer the oscillation to the square wave the larger the energy savings.

1 Introduction

In a previous paper one of us investigated the behavior of the integral fluid of order three in the pulsating pressure gradient-driven flows (Siginer, 1991a) hereafter referred to as (I). In that paper a perturbation method, in terms of the amplitude of the oscillation in the pressure gradient, has been applied to analyze pulsating flows driven by a pressure gradient pulsating about a nonzero mean. The analysis was good for small strains, i.e., small mean gradients and small amplitudes, but there were no restrictions on the strain rates, that is, on the frequency of the oscillation. The investigation was focused on the mean properties of the flow. In particular, the mean flow field and the mean flow rate have been determined. It was found that at the third order of the analysis a change in the mean volumetric flow rate occurred. This change depends on the frequency, the mean gradient, and the material properties of the liquid, but is independent of the explicit form of the material functions, that is, it would occur no matter the explicit form of the material functions. The explicit forms adopted for those functions would only change the magnitudes involved, keeping, very possibly, the qualitative behavior the same. Explicit forms for the shear dependent viscosity and other material functions, rapidly decaying in time, have been introduced by Siginer (1991b) and a parametric study of the enhancement has been conducted. An extensive literature survey is also given in that paper.

In this paper we continue the work of (I) and investigate the effect on the enhancement of different waveforms. We start with the saw-tooth waveform and investigate successively the triangular, sinusoidal, and square waves. For each we conduct a parametric study for a particular fluid. We determine that no matter the parameters adopted, a larger enhancement is obtained for squarer waves although the qualitative behavior of the enhancement corresponding to different waveforms remain very similar to that of the sinusoidal wave. Next we investigate the mean energy requirement to transport the enhanced flow rate with and without a pulsating gradient. The enhanced flow, if driven by a constant pressure gradient, necessarily requires a higher energy input. We compute the energy savings in percentages for different waveforms. The variation of energy savings with frequency shows patterns similar to the variation of enhancement with frequency, that is, the squarer the waveform the larger the energy savings at any given frequency. With the parameters adopted in the parametric study, we show that considerable energy savings may result in the pumping of viscoelastic liquids if controlled pulsations may be introduced in the pressure gradient.

The enhancement and the resulting energy savings are very sensitive to the form of the shear dependent viscosity function and to the elastic properties of the liquid. The parametric enhancement study conducted in (Siginer, 1991b) clearly demonstrates this point. Consequently, to determine the energy savings for a particular fluid at a given frequency, the experimentally fitted shear dependent viscosity curve should be used together with relaxation properties. The possible energy savings presented in this paper are only tentative for the fluid studied and may change considerably if the true values were known. Nevertheless, the present authors are convinced, in view of the results presented in this paper, that further investigation of the energy savings, when the flow is driven by a pulsating gradient, is amply justified. In particular, the analysis used does not allow the determination of the trends for large mean pressure gradients. The enhancement and the corresponding energy savings depend on the mean gradient and will show variations with it. Although the analysis presented in this paper clearly demonstrates that at a given mean gradient (albeit small),

Contributed by the Applied Mechanics Division of THE AMERICAN SOCIETY OF MECHANICAL ENGINEERS for presentation at the First Joint ASCE-EMD, ASME-AMD, SES Meeting, Charlottesville, VA, June 6–9, 1993.

Discussion on this paper should be addressed to the Technical Editor, Professor Lewis T. Wheeler, Department of Mechanical Engineering, University of Houston, Houston, TX 77204-4792, and will be accepted until four months after final publication of the paper itself in the ASME JOURNAL OF APPLIED MECHANICS.

Manuscript received by the ASME Applied Mechanics Division, Aug. 20, 1991; final revision, June 3, 1992. Associate Technical Editor: S. A. Berger.

Paper No. 93-APM-11.

Copyright © 1993 by ASME
Downloaded 03 May 2010 to 171.66.16.245. Redistribution subject to ASME license or copyright; see http://www.asme.org/terms/Terms_Use.cfm

imposing a controlled pulsation on the mean gradient leads to savings at any frequency, it is by no means clear that the same trend would prevail at a fixed frequency with varying mean gradient. There is some evidence in the literature that for a certain range of relatively high mean gradients, the mean energy input required with the pulsations is higher than the energy necessary to transport the same enhanced flow rate with a steady pressure gradient (Barnes et al., 1971). It may be that the ratio of the energies is larger than one and consequently more energy may be expended to transport a given flow rate with pulsations for a range of relatively large mean gradients.

2 Mathematical Analysis

We consider flow in a cylindrical tube of radius R:

$$\rho \frac{D\mathbf{u}}{Dt} = -\nabla\phi + \nabla\cdot\mathbf{S}, \quad \nabla\cdot\mathbf{u} = 0 \text{ in } D_\epsilon, \tag{1}$$

$$D_\epsilon = \{(r, \theta, z) \mid 0 \le r \le R,\ 0 \le \theta < 2\pi, \quad -\infty < z < +\infty\},$$

$$\mathbf{u}(R, \theta, z) = 0, \quad \mathbf{u}(0, \theta, z) < \infty, \tag{2}$$

$$\phi_{,z} = -\epsilon[P + f(\lambda, \omega, t)]. \tag{3}$$

The extra stress in $(1)_1$ is given in the form of a series of nested integrals with the nth term containing n nested integrals with tensor polynomial integrands. The extra stress has been expanded in a Fréchet series in (I) in terms of the small parameter ϵ in the pressure gradient (3),

$$\mathbf{S}[\mathbf{G}(\mathbf{X};\ \epsilon)] = \epsilon\mathbf{S}^{(1)} + \epsilon^2\mathbf{S}^{(2)} + \epsilon^3\mathbf{S}^{(3)} + O(\epsilon^4), \tag{4}$$

where the expansion of the history $\mathbf{G}$ of the strain on a particle $\mathbf{X}$ in a series in terms of ϵ has been used,

$$\mathbf{G}(\mathbf{X}, s;\ \epsilon) = \epsilon\mathbf{G}_1(\mathbf{X}, s) + \epsilon^2\mathbf{G}_2(\mathbf{X}, s) + O(\epsilon^3). \tag{5}$$

The notation $\mathbf{S}^{(i)}$ in (4) indicates $n!$ times the ith functional derivative of the extra stress functional with respect to ϵ evaluated at $\epsilon = 0$ and s in (5) represents the difference between the present time t and a given past time τ. The expansion (5) of the strain history which implies small strains allows, together with incompressibility, the explicit expression of the Fréchet stresses $\mathbf{S}^{(i)}$ in (4) to be written down as

$$\mathbf{S}^{(1)} = \int_0^\infty \zeta(s)\mathbf{G}_1(s)\,ds, \tag{6}$$

$$\mathbf{S}^{(2)} = \int_0^\infty \zeta(s)\mathbf{G}_2(s)\,ds + \int_0^\infty\int_0^\infty \beta_1(s_1, s_2)\mathbf{G}_1(s_1)\mathbf{G}_2(s_2)\,ds_1 ds_2, \tag{7}$$

$$\begin{aligned}\mathbf{S}^{(3)} = {} & \int_0^\infty \zeta(s)\mathbf{G}_3(s)\,ds + \int_0^\infty\int_0^\infty \beta_2(s_1, s_2)[\mathrm{tr}\mathbf{G}_2(s_1)]\mathbf{G}_1(s_2)\,ds_1 ds_2 \\ & + \int_0^\infty\int_0^\infty \beta_1(s_1, s_2)[\mathbf{G}_1(s_1)\mathbf{G}_2(s_2) + \mathbf{G}_2(s_1)\mathbf{G}_1(s_2)]\,ds_1 ds_2 \\ & + \int_0^\infty\int_0^\infty\int_0^\infty \psi_1(s_1, s_2, s_3)\mathbf{G}_1(s_1)\mathbf{G}_1(s_2)\mathbf{G}_1(s_3)\,ds_1 ds_2 ds_3 \\ & + \int_0^\infty\int_0^\infty\int_0^\infty \psi_4(s_1, s_2, s_3)\mathrm{tr}[\mathbf{G}_1(s_1)\mathbf{G}_1(s_2)]\mathbf{G}_1(s_3)\,ds_1 ds_2 ds_3.\end{aligned} \tag{8}$$

These Fréchet derivatives can be further expressed in more workable form in terms of the first Rivlin-Ericksen kinematic tensor $\mathbf{A}_1$, particle trajectories ξ, and new material functions G, γ, α, σ_1 and σ_4 defined by,

$$\zeta(s) = \frac{dG}{ds}, \quad \beta_1 = \frac{\partial^2\gamma}{\partial s_1 \partial s_2}, \quad \beta_2 = \frac{\partial^2\alpha}{\partial s_1 \partial s_2},$$

$$\psi_1 = \frac{\partial^3\sigma_1}{\partial s_1 \partial s_2 \partial s_3}, \quad \psi_4 = \frac{\partial^3\sigma_4}{\partial s_1 \partial s_2 \partial s_3}.$$

The computation ready expressions for $\mathbf{S}^{(i)}$ are quite long and given in (I) and will not be repeated here.

When the forcing $f(\lambda, \omega, t)$ in (3) is a single sinusoidal wave,

$$f(\lambda, \omega, t) = \lambda\sin\omega t,$$

the problem defined by (1), (2), and (3) has been solved in (I) by expanding the remaining flow variables into power series

$$\mathbf{u}(\mathbf{X}, t;\ \epsilon) = \sum_{n=1}^{\infty} \epsilon^n \mathbf{u}^{(n)}(\mathbf{X}, t),$$

$$\phi(\mathbf{X}, t;\ \epsilon) = \sum_{n=1}^{\infty} \epsilon^n \phi^{(n)}(\mathbf{X}, t),$$

and also by using (4) together with (6), (7), and (8). It is determined there that the flow rate up to and including the third order is given by,

$$Q = \epsilon Q^{(1)} + \epsilon^3 Q^{(3)} + O(\epsilon^5), \tag{9}$$

where $Q^{(1)}$ is the Newtonian Poiseuille flow rate and $Q^{(3)}$ is the additional flow rate due to the non-Newtonian nature of the fluid. It is shown in (I) that the latter is given by,

$$Q^{(3)} = Q_0^{(3)} + Q_1^{(3)}, \tag{10}$$

$$Q_0^{(3)} = \frac{4\pi}{3}\left(\frac{P}{4}\right)^3 \frac{R^6}{\mu^4}\Psi_0, \tag{11}$$

$$Q_1^{(3)} = \frac{\pi P}{2}\left(\frac{\lambda}{\rho\mu\omega}\right)^2 \left|\frac{\Lambda}{I_0(\Lambda R)}\right|^2 \Psi_1 \int_0^R r \int^r \xi |A_{,\xi}|^2 d\xi dr. \tag{12}$$

The non-Newtonian flow rate $Q^{(3)}$ has two components $Q_0^{(3)}$ and $Q_1^{(3)}$; the former due to shear dependent viscosity under the steady component P of the pressure gradient (3) and the latter to the periodic component of (3) superposed on the steady mean gradient P. The entity A in (12) comes from the oscillatory part of the first-order velocity field,

$$\mathbf{u}^{(1)}(r, z, t) = (w_1(r) + w_2(r, t))\mathbf{e}_z,$$

$$w_2(r, t) = 2\mathrm{Re}[A(r)e^{i\omega t}], \tag{13}$$

$$A(r) = \frac{\lambda}{2\rho\omega}\left[\frac{I_0(\Lambda r)}{I_0(\Lambda R)} - 1\right]. \tag{14}$$

The integration of (12) subject to (14) gives

$$Q_1^{(3)} = \frac{\pi P}{2}\left(\frac{\lambda}{\rho\mu\omega}\right)^2 \left|\frac{\Lambda}{I_0(\Lambda R)}\right|^2 \Psi_1 F(\Lambda R). \tag{15}$$

The entities Ψ_0, Ψ_1, and F which appear in (11), (12), and (15) are defined as follows:

$$\Psi_0 = \int_0^\infty\int_0^\infty \left[2(\gamma + \alpha)s_1 - \int_0^\infty (\sigma_1 + 2\sigma_4)ds_3\right] ds_1 ds_2, \tag{16}$$

$$\Psi_1 = \int_0^\infty\int_0^\infty \left[2(\gamma + \alpha)\psi_1 - \int_0^\infty (\sigma_1 + 2\sigma_4)\psi_1^* ds_3\right] ds_1 ds_2, \tag{17}$$

$$\psi_1 = \omega^{-1}[\sin\omega s_1 + \sin\omega s_2 + \omega s_1\cos\omega(s_1 - s_2) + \sin\omega(s_1 - s_2)], \tag{18}$$

$$\psi_1^* = \cos\omega(s_1 - s_2) + \cos\omega(s_1 - s_3) + \cos\omega(s_2 - s_3), \tag{19}$$

$$F(\Lambda R) = \frac{R^3}{2(\Lambda^2 - \bar{\Lambda}^2)}[\Lambda I_0\bar{I}_1 - \bar{\Lambda}I_1\bar{I}_0] - \frac{(\Lambda^2 + \bar{\Lambda}^2)}{(\Lambda^2 - \bar{\Lambda}^2)^2} R^2|I_1|^2 + \frac{2|\Lambda|^2}{(\Lambda^2 - \bar{\Lambda}^2)^2} R^2|I_0|^2 + \frac{4|\Lambda|^2}{(\Lambda^2 - \bar{\Lambda}^2)^3} R[\bar{\Lambda}\bar{I}_1 I_0 - \Lambda\bar{I}_0 I_1]. \tag{20}$$

Λ, which appears in (14), (15), and (20), is a first-order quantity and is given by

$$\Lambda^2 = \frac{i\rho\omega}{\int_0^\infty G(s)e^{-i\omega s}ds} = \frac{i\rho\omega}{\eta^*}, \tag{21}$$

where η^* is the complex viscosity. I_j, $j = 0, 1$ in (14), (15), and (20) represent modified Bessel functions of the first kind

Downloaded 03 May 2010 to 171.66.16.245. Redistribution subject to ASME license or copyright; see http://www.asme.org/terms/Terms_Use.cfm

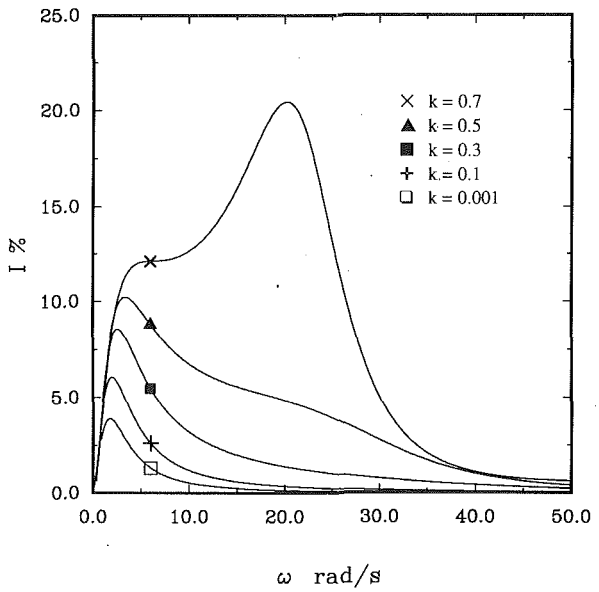


Fig. 1 Enhancement variation with frequency for different power indices with a single sinusoidal wave in the pressure gradient in a tube of radius R. Parameters used in the figure are: P = 100 dynes/cm^3, μ = 100 Poise, R = 2 cm, η_∞' = 0, λ = 50 dynes/cm^3, β_4 = −50 gr s/cm, β_5 = 40 gr s/cm, β_6 = 60 gr s/cm, ρ_1 = 3 s^{-1}, m_1 = 2 s^{-1}, n_1 = 1 s^{-1}, ϵ = 0.4.

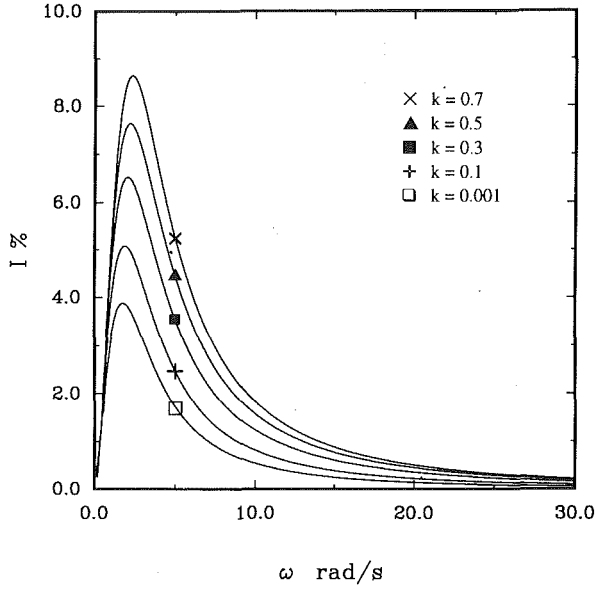


Fig. 2 Same as Fig. 1 except there is a second Newtonian viscosity at high shear rates: η_∞' = 50 Poise

with complex argument ΛR and overbar indicates complex conjugate.

We note that the results embodied in (11) and (15) are free of any explicit representations for the constitutive functions. But for quantitative results such representations are needed. Possible representations, by no means unique, have been introduced by Siginer (1991b).

$$G(s)=\frac{\mu-\eta_\infty'}{\theta^k\Gamma(k)}s^{k-1}e^{-s/\theta}+\delta(s)\eta_\infty', \tag{22}$$

$$\theta=\frac{\alpha_1}{k(\eta_\infty'-\mu)}>0,\quad \alpha_1<0,\quad 0<k\le 1,\quad \eta_\infty'<\mu, \tag{23}$$

$$\gamma=\alpha_2\sum_i^N C_{1i}k_i^2e^{-k_i(s_1+s_2)};\quad \sum_i^N C_{1i}=1, \tag{24}$$

$$\alpha=-\beta_4\sum_i^N C_{2i}\rho_i^3e^{-\rho_i(s_1+s_2)};\quad \sum_i^N C_{2i}=1, \tag{25}$$

$$\sigma_1=\beta_6\sum_i^N C_{3i}m_i^3e^{-m_i(s_1+s_2+s_3)};\quad \sum_i^N C_{3i}=1, \tag{26}$$

$$\sigma_4=\beta_5\sum_i^N C_{4i}n_i^3e^{-n_i(s_1+s_2+s_3)};\quad \sum_i^N C_{4i}=1. \tag{27}$$

Γ, δ, μ, η_∞', and k in (22) are the gamma and dirac functions, zero shear viscosity, a second Newtonian viscosity at high shear rates, and power index, respectively. The remaining parameters appearing in (23)–(27) are the first two Rivlin-Ericksen constants α_1 and α_2, the shear thinning parameters in oscillatory shear β_4, β_5, β_6 and the relaxation times k_i^{-1}, ρ_i^{-1}, m_i^{-1}, n_i^{-1}. It is shown (Siginer, 1991b) that working with the lowest orders in (24)–(27) is enough to quantitatively describe nearly viscometric flows of the type investigated in this paper. Then with the lowest order terms in (24)–(27) and expressions (16)–(19), we compute

$$\Psi_0=-2\left(-\frac{\alpha_2}{k_1}+\beta_4+\beta_5+\frac{\beta_6}{2}\right), \tag{28}$$

$$\Psi_1=2\left[2\alpha_2k_1\frac{(3k_1^2+2\omega^2)}{(k_1^2+\omega^2)^2}-2\beta_4\rho_1^2\frac{(3\rho_1^2+2\omega^2)}{(\rho_1^2+\omega^2)^2}-\frac{3m_1^2\beta_6}{m_1^2+\omega^2}-\frac{6n_1^2\beta_5}{n_1^2+\omega^2}\right]. \tag{29}$$

An algorithm involving several experiments of rheometry is described by Siginer (1991b) which allows the determination of α_1, α_2, k_1 and the sum of β_4, β_5, $\beta_6/2$. It is hoped that the remaining parameters may be determined from nearly viscometric flow experiments of the type investigated in this paper.

3 Enhancement Considerations

Enhancement is defined as

$$I(\omega)=\frac{\epsilon^3Q_1^{(3)}}{\epsilon Q^{(1)}+\epsilon^3Q_0^{(3)}}, \tag{30}$$

and is positive and negative for shear thinning and thickening liquids, respectively (Siginer, 1991b). To conduct a parametric study we choose a liquid, TLA-227, for which α_1, α_2, k_1 and the sum of β_4, β_5, $\beta_6/2$ have been determined based on the algorithm outlined by Siginer (1991b).

$$\alpha_1=-50\ \text{gr/cm},\quad \alpha_2=83.9\ \text{gr/cm},$$

$$k_1^2=15.43\ \text{s}^{-2},\quad \beta_4+\beta_5+\frac{\beta_6}{2}=20.26\ \text{gr s/cm},$$

$$\rho=0.896\ \text{gr/cm}^3,\quad \Psi_0=2.2\ \text{gr s/cm}. \tag{31}$$

We present plots of the enhancement in Figs. 1 and 2 for a single sinusoidal wave in the pressure gradient without and with a second Newtonian viscosity η_∞', respectively, with the remaining parameter values in (29) chosen to satisfy the requirements of the moment theory

$$\beta_4<0,\quad (\beta_5,\ \beta_6)>0, \tag{32}$$

and the relaxation times in (24)–(27) in ascending order,

$$k_1>\rho_1>m_1>n_1. \tag{33}$$

Expressions (11), (15), (20)–(23), (28)–(29) have been used in (30), together with ϵ = 0.4, to obtain Figs. 1 and 2.

The figures show that the existence of a second Newtonian plateau for the viscosity at high shear rates reduces the en-

Downloaded 03 May 2010 to 171.66.16.245. Redistribution subject to ASME license or copyright; see http://www.asme.org/terms/Terms_Use.cfm

hancement at any frequency, and more so for high than for low power indices at a given frequency. The structure of (15) plays an important role in defining the enhancement. Ψ_1 in (15) defines the influence of the nonlinear elastic and shear thinning effects on the change in the volumetric flow rate. A parametric study of Ψ_1 defined by (29) shows that it displays a resonancelike behavior with varying frequency, with a rather sharp peak located around $\omega \sim 5$ rad/s. Increasing the values assigned to β_4, β_5, β_6 and observing (31) and (32) increases the shear thinning capability of the fluid in oscillatory shear. As a consequence, enhancement is increased at any frequency keeping the location of the maximum the same. On the other hand if k_1, ρ_1, m_1, n_1 are changed, (keeping β_4, β_5, β_6 the same) that is if the shear thinning capability is kept the same and the elastic properties are changed, the curve translates to the left or to the right depending on whether the relaxation times are being increased (translation to the left, peak comes closer to $\omega \sim 0$, curve is compressed horizontally) or decreased (translation to the right, peak goes away from $\omega \sim 0$, curve is further spread over the frequency range). The remaining terms in (15) contain only the effect of linear viscoelastic quantities embedded in (21) and consequently in (20) and (15) through the complex modulus η^*. We denote, by ψ,

$$\psi = \left| \frac{\Lambda}{\omega I_0(\Lambda R)} \right|^2 F(\Lambda R), \tag{34}$$

the remaining terms in $Q_1^{(3)}$ which depend on the frequency and show the influence of the linear viscoelastic properties. ψ also embodies the effect of the flow geometry and shows a resonancelike behavior for power indices larger than 0.5. That this is indeed the case is clear from Fig. 1 where the peak around $\omega \sim 20$ rad/s at $k = 0.7$ is entirely due to the effect of the geometry and the linearly viscoelastic properties. The larger the radius of the pipe the closer is the peak to the origin with varying frequency and the same linear properties. This, of course, necessarily implies that the enhancement rises more and more sharply in the neighborhood of $\omega \sim 0$ as the geometry gets larger. But more importantly for relatively large radii and high power indices, the two resonancelike effects may come very close to each other and even coincide, thereby increasing the enhancement considerably for a frequency window at relatively small frequencies. The existence of a second Newtonian viscosity η_∞' completely smoothes out the resonancelike effect due to the coupling of the linear viscous and elastic properties as is clear from Fig. 2. In addition, the overall enhancement at any frequency is reduced due to the reduced effect of the linear properties as represented by ψ defined by (34).

Next we try to answer the question as to which waveform is optimal in producing the maximum enhancement. To this end we investigate the enhancement produced by three types of waves oscillating around the same mean gradient P with the same amplitude λ, the saw-tooth, triangular, and square waves. For these waves, the time-periodic forcing $f(\lambda, \omega, t)$ in the pressure gradient (3) is given by

$$f(\lambda, \omega, t) = \frac{2\lambda}{\pi} \sum_1^\infty (-1)^{k+1} \frac{\sin k\omega t}{k}, \tag{35}$$

$$f(\lambda, \omega, t) = \frac{8\lambda}{\pi^2} \sum_1^\infty (-1)^{k+1} \frac{\sin(2k-1)\omega t}{(2k-1)^2}, \tag{36}$$

$$f(\lambda, \omega, t) = \frac{4\lambda}{\pi} \sum_1^\infty \frac{\sin(2k-1)\omega t}{(2k-1)}, \tag{37}$$

respectively. In general, the pressure gradient may be conceived of as

$$\phi_{,z} = -\epsilon \left[P + \sum_1^\infty C_k \sin k\omega t \right], \tag{38}$$

which would lead to the modification of the first-order oscillatory solution (13) for the flow field for a single sinusoidal wave, which now becomes

$$w_2(r, t) = 2\mathrm{Re}\left[\sum_1^\infty A_k(r) e^{ik\omega t} \right],$$

$$A_k = \frac{C_k}{2\rho k\omega} \left[\frac{I_0(\Lambda_k r)}{I_0(\Lambda_k R)} - 1 \right].$$

The change in the volumetric flow rate can now be shown, after some algebra, to be defined by an extension of (12)

$$Q_1^{(3)} = \frac{\pi P}{2} \sum_1^\infty \left\{ \left(\frac{C_k}{\rho\mu k\omega} \right)^2 \left| \frac{\Lambda_k}{I_0(\Lambda_k R)} \right|^2 \Psi_{1k} \times \int_0^R r \int^r \xi |A_{k,\xi}|^2 d\xi dr \right\},$$

yielding

$$Q_1^{(3)} = \frac{\pi P}{2} \sum_1^\infty \left\{ \left(\frac{C_k}{\rho\mu k\omega} \right)^2 \left| \frac{\Lambda_k}{I_0(\Lambda_k R)} \right|^2 \Psi_{1k} F_k(\Lambda_k R) \right\}, \tag{39}$$

where Λ_k, Ψ_{1k}, and F_k are given by (21), (29), and (20), respectively, with ω replaced with $k\omega$. Now if C_k is appropriately chosen to correspond to any one of the series (35)–(37) we would obtain the total volumetric flow rate change corresponding to the series in question in view of (38). The results are presented in Figs. 3, 4, and 5 in the absence of a second Newtonian plateau.

All the figures are drawn with $8 \sim 10$ terms in the series (33)–(37) but except for the saw-tooth waveform represented by (35) there is not much difference in the successive enhancement curves after the fourth term using either (36) or (37). Figs. 1, 3, 4, and 5 show that the squarer the waveform the larger the enhancement at any given frequency with the saw-tooth yielding the smallest and the square wave the largest enhancement. The enhancement increase from saw-tooth to the triangular wave, from triangular to the sine and from sine to the square wave is smaller for small power indices and gets gradually larger as the power index assumes larger values with the largest jump occurring, for both small and large power

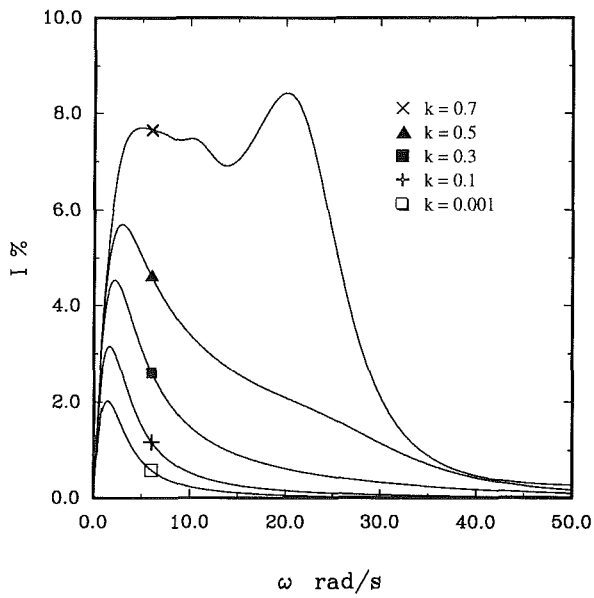


Fig. 3 Enhancement variation with frequency for different power indices for the saw-tooth waveform with eight terms in the expansion in the absence of a second Newtonian plateau. The parameters used are the same as those in Fig. 1.

Downloaded 03 May 2010 to 171.66.16.245. Redistribution subject to ASME license or copyright; see http://www.asme.org/terms/Terms_Use.cfm

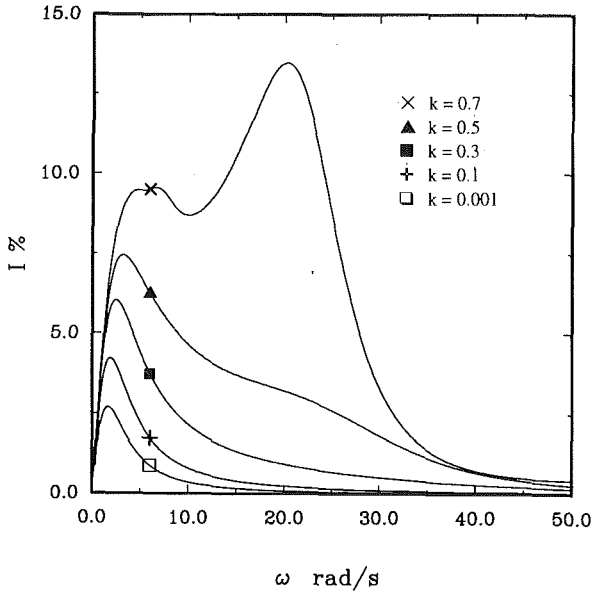


Fig. 4 Same as Fig. 3 except the waveform is triangular

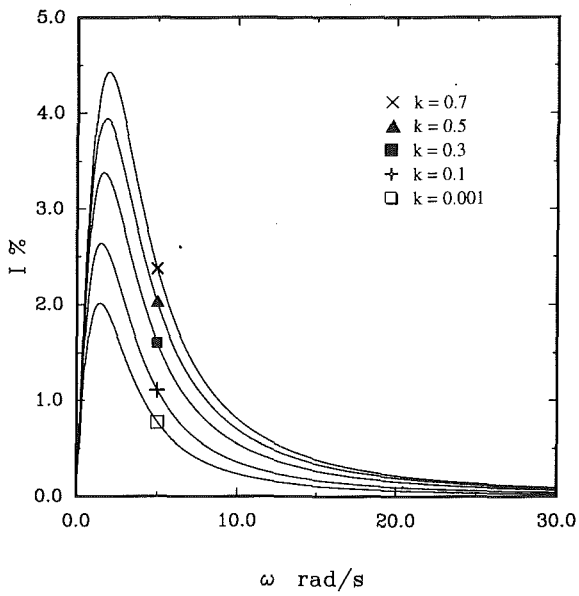


Fig. 6 Same as Fig. 3 except for the existence of a second Newtonian viscosity $\eta_\infty' = 50$ Poise

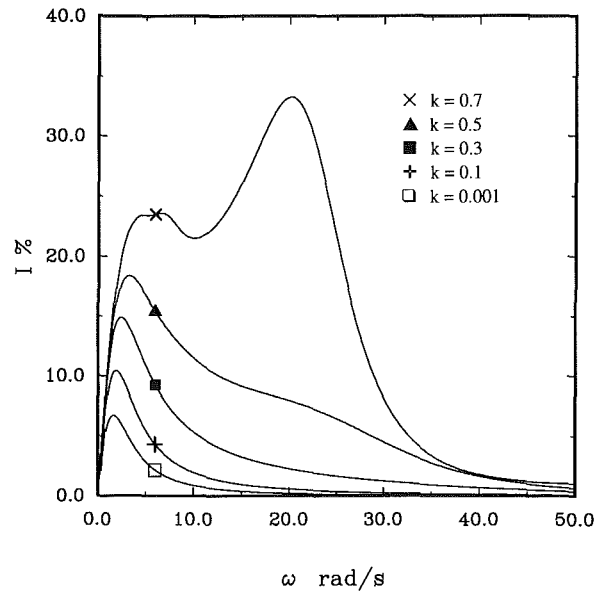


Fig. 5 Same as Fig. 3 except the waveform is square

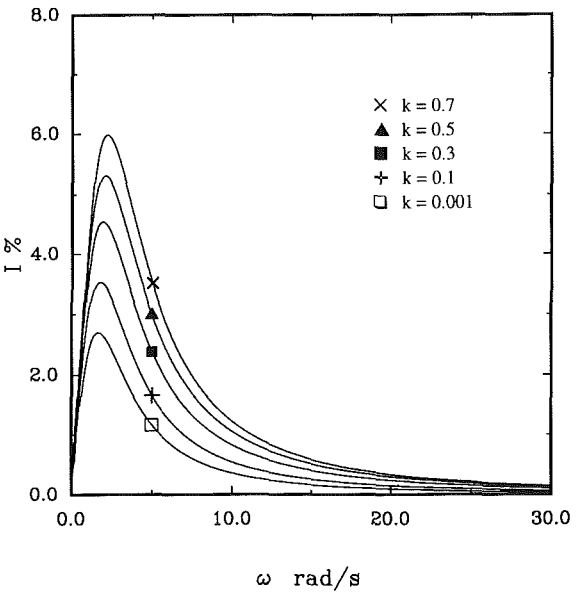


Fig. 7 Same as Fig. 3 except the waveform is triangular and there is a second Newtonian viscosity $\eta_\infty' = 50$ Poise

indices, from the sine to the square wave. But interestingly enough, if the percent increase in the I percent from one wave to another is computed at a given frequency, one finds almost a constant, although the constant is different for different pairs of waves. There is also a plateau of sorts which appears for rather high power indices, for a frequency window between 5 and 10 rad/s. This plateau is very pronounced for the saw-tooth wave and for $k = 0.7$ starts at about $\omega \sim 4$ rad/s and extends up to $\omega \sim 12$ rad/s, Fig. 3. For the sine wave the plateau is not there, and it is almost the same size for the triangular and square waves (Figs. 1, 4, and 5).

The effect of the presence of a second Newtonian viscosity η_∞' at high shear rates is shown in Figs. 6, 7, and 8 for the saw-tooth, triangular, and square waves, respectively. The observation may be made that for any waveform, enhancement curves are almost the same regardless $\eta_\infty' \geq 0$ when the power index $k \leq 0.001$. For larger power indices, the enhancement at any frequency for any waveform is smaller when $\eta_\infty' \neq 0$. Numerical experimentation shows that the smaller the difference $(\mu - \eta_\infty')$, the more reduced the enhancement is as compared to the case $\eta_\infty' = 0$ for any given wave. As the difference $(\mu - \eta_\infty')$ gets smaller the whole process of enhancement becomes entirely dominated by the nonlinear shear thinning and elastic effects as represented by Ψ_1 given by (29); and the effect of the linear properties and of the geometry, as represented by ψ, defined by (34), gets smaller and smaller. The reduced influence of the linear viscous and elastic effects manifests itself in the smoothing of the resonancelike effect due to the strong coupling of the linear viscous and elastic properties at high power indices.

Again it is computed that the percent change in I percent for a given pair of waveforms is a constant at a given frequency and for any power index k. For instance, for the saw-tooth/triangular wave pair it is around 35 percent and for triangular/sinusoidal and sinusoidal/square wave pairs it is around 45 percent and 68 percent, respectively.

Downloaded 03 May 2010 to 171.66.16.245. Redistribution subject to ASME license or copyright; see http://www.asme.org/terms/Terms_Use.cfm

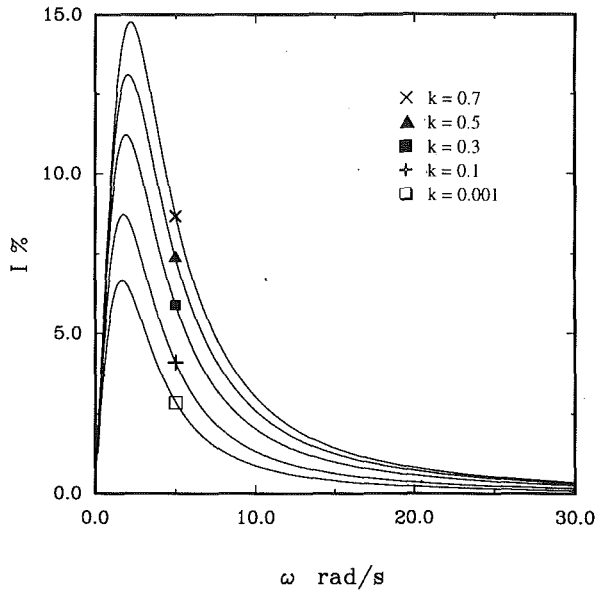


Fig. 8 Same as Fig. 3 except the waveform is square and there is a second Newtonian plateau $\eta'_\infty = 50$ Poise

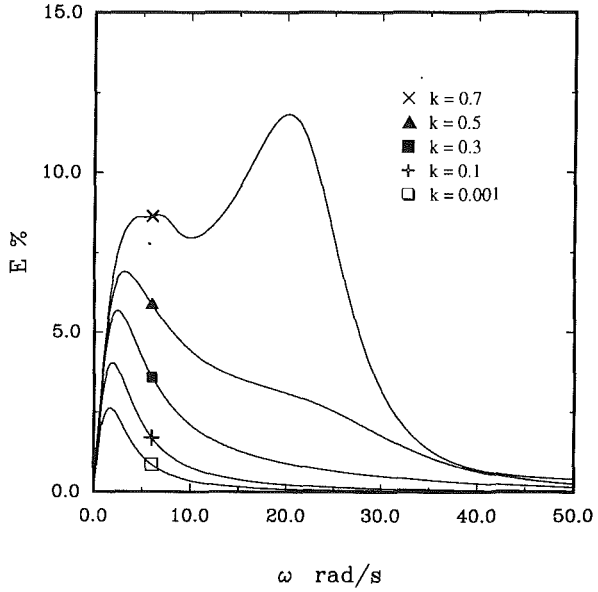


Fig. 10 Same as Fig. 9 except the wave is triangular

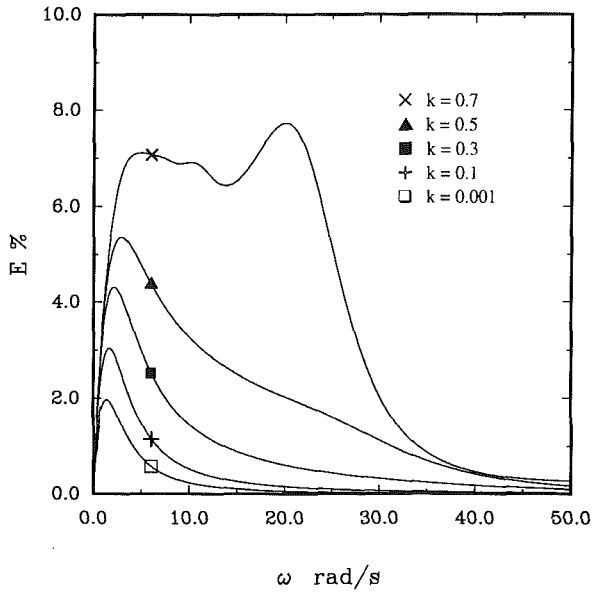


Fig. 9 Variation of the energy savings with frequency for different power indices for the saw-tooth wave. The parameters used are the same as those in Fig. 1.

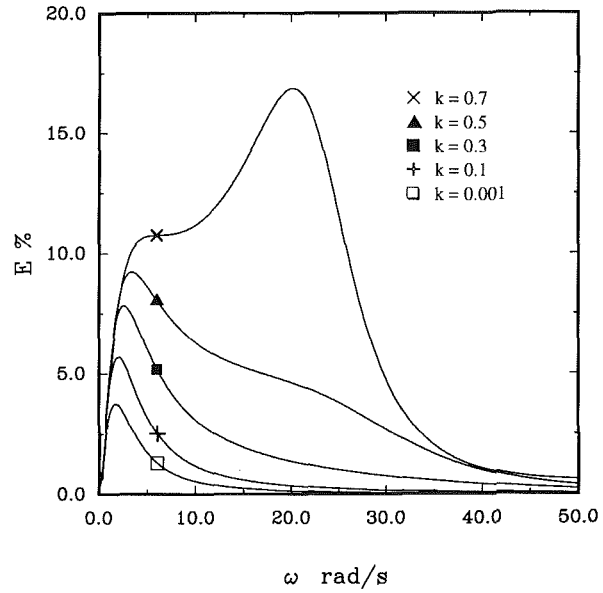


Fig. 11 Same as Fig. 9 except the wave is sinusoidal

4 Energy Considerations

We ask the following question: How much energy would it take to transport the enhanced flow rate (9) with and without the pulsations? The mean energy required with the pulsations, that is the energy required averaged over a period, is given by

$$E_p = P(\epsilon Q^{(1)} + \epsilon^3 Q^{(3)}). \tag{40}$$

On the other hand, the energy required without the pulsations is defined by

$$E_s = P_s(\epsilon Q^{(1)} + \epsilon^3 Q^{(3)}). \tag{41}$$

P_s in (41) is computed from

$$Q(\omega) = \epsilon Q^{(1)} + \epsilon^3 Q^{(3)} = \epsilon \frac{\pi P_s R^4}{8\mu} + \epsilon^3 \frac{4\pi}{3}\left(\frac{P_s}{4}\right)^3 \frac{R^6}{\mu^4}\Psi_0, \tag{42}$$

where $Q(\omega)$ is the enhanced flow rate due to the pulsations and Ψ_0 is given by (28). The RHS of (42) defines the same enhanced flow rate, but this time due to a steady gradient P_s. (42) is applicable to any waveform and requires the solution of a cubic equation, with one real root, for P_s for each and every frequency ω. We define the energy ratio,

$$E = \frac{E_s - E_p}{E_s} = 1 - \frac{P}{P_s}, \tag{43}$$

where the numerator is the difference of the energies required to transport the enhanced flow rate $Q(\omega)$ without and with the pulsations. It turns out that $P_s > P$ for all frequencies. Consequently depending on the frequency, substantial energy savings may result if a controlled pulsation is introduced in the pressure gradient. We determine that energy savings follow a pattern closely related to enhancement. That is, the squarer the waveform in the pressure gradient, the larger the energy savings. The energy savings in percent are given in Figs. 9, 10, 11, 12 in the absence of a second Newtonian viscosity. These

Downloaded 03 May 2010 to 171.66.16.245. Redistribution subject to ASME license or copyright; see http://www.asme.org/terms/Terms_Use.cfm

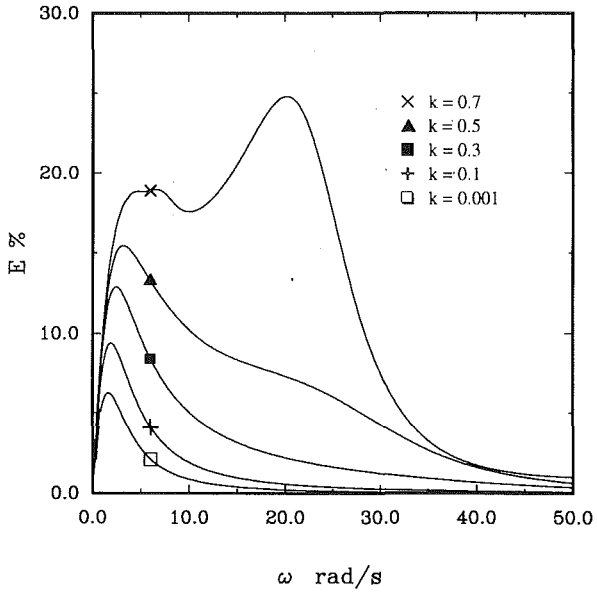


Fig. 12 Same as Fig. 9 except the wave is square

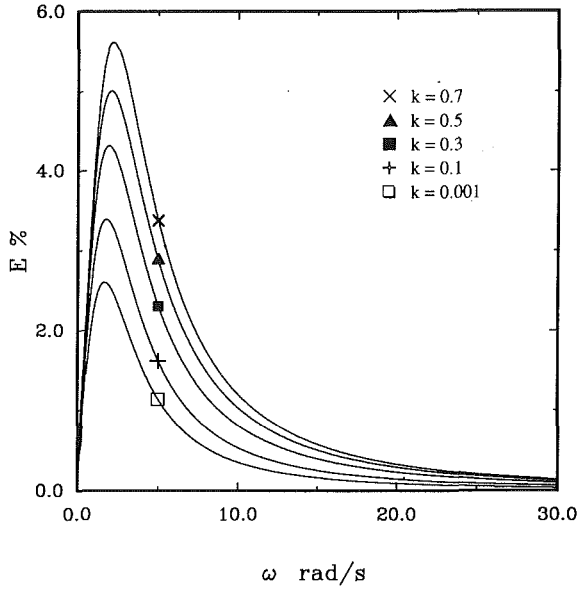


Fig. 14 Same as Fig. 9 except the wave is triangular and $\eta_\infty' = 50$ Poise

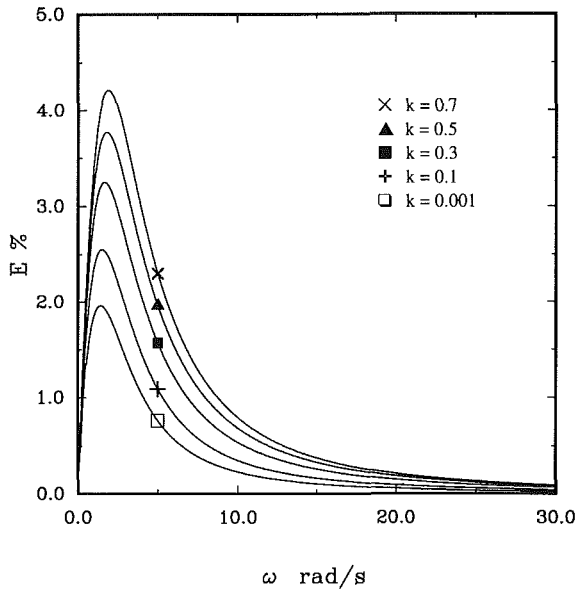


Fig. 13 Same as Fig. 9 except there is a second Newtonian plateau at high shear rates: $\eta_\infty' = 50$ Poise

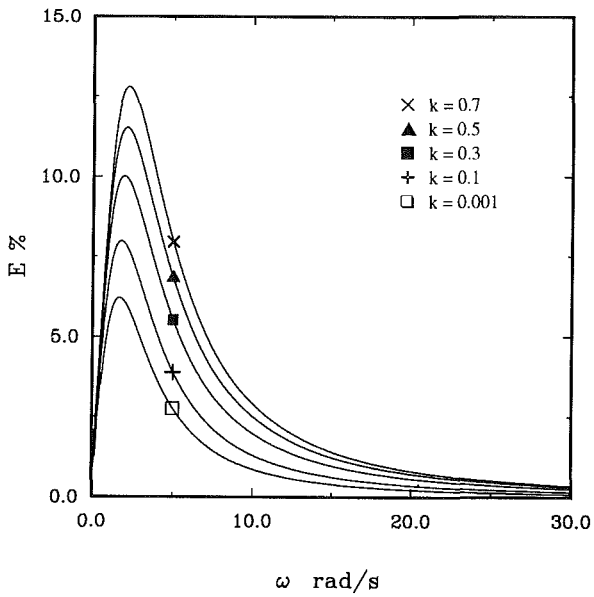


Fig. 15 Same as Fig. 9 except the wave is sinusoidal and $\eta_\infty' = 50$ Poise

figures correspond to the enhancement Figs. 3, 4, 1, and 5, respectively.

Comparison with Figs. 3, 4, 1, and 5 shows that corresponding figures in the sets are qualitatively the same, but the enhancement is always larger at any frequency than the corresponding energy savings for any power index. The difference is large for large power indices and gets smaller as the power index becomes smaller. Also, the window of frequency over which substantial savings of energy would be obtained by superposing any one of the four types of waves investigated in this paper onto a mean gradient becomes smaller as the power index gets smaller. Energy savings show a dramatic jump from the saw-tooth waveform to the square waveform, the two extremes studied here, for instance from 7 percent to 20 percent, for $k = 0.7$.

We present in Figs. 13, 14, 15, and 16 the energy savings corresponding to the saw-tooth, triangular, sinusoidal, and square waves, respectively, in the presence of a second Newtonian viscosity.

Several observations are in order. Energy savings are considerably reduced for any one given waveform if $\eta_\infty' \neq 0$ as compared to when $\eta_\infty' = 0$ and more so for higher power indices. For instance, savings are about 35 percent less when $k = 0.7$ for the saw-tooth wave. Savings are further reduced as $(\mu - \eta_\infty')$ becomes smaller. They are again less than the corresponding enhancement, and the difference grows larger as the power index gets larger in keeping with the trends shown in the enhancement.

5 Conclusions

The integral fluid of order three shows enhancement variations with frequency. The enhancement is governed by the coupling of the nonlinear shear thinning and elastic properties and the coupling of the linear viscous and elastic properties.

Downloaded 03 May 2010 to 171.66.16.245. Redistribution subject to ASME license or copyright; see http://www.asme.org/terms/Terms_Use.cfm

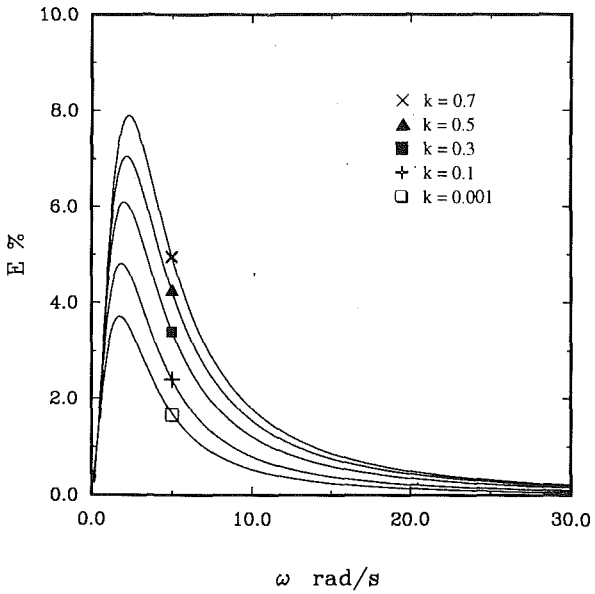


Fig. 16 Same as Fig. 9 except the wave is square and η'_∞ = 50 Poise

For certain values of the parameters the couplings become stronger and show resonancelike characteristics. Optimum enhancement is dependent on the shape of the waveform defining the pulsation in the pressure gradient. The squarer the waveform the larger the enhancement, and the flatter the waveform the smaller the enhancement. At any frequency and for any waveform the mean energy required to transport the enhanced flow rate is less than the energy required to transport the same enhanced flow rate with a steady gradient without any superposed oscillations. Energy savings follow a pattern quite similar to enhancement behavior. For square waves which give the largest enhancement, energy savings could be quite substantial, as much as 25 percent with the constitutive parameters used in this study.

References

Barnes, H. A., Townsend, P., and Walters, K., 1971, "On Pulsatile Flow of Non-Newtonian Liquids," *Rheologica Acta*, Vol. 10, pp. 517–527.

Siginer, A., 1991a, "Oscillating Flow of a Simple Fluid in a Pipe," *International Journal of Engineering Science*, Vol. 29, 12, pp. 1557–1567.

Siginer, A., 1991b, "On Some Nearly Viscometric Flows of Viscoelastic Liquids," *Rheologica Acta*, Vol. 30, 5, pp. 447–475.

Downloaded 03 May 2010 to 171.66.16.245. Redistribution subject to ASME license or copyright; see http://www.asme.org/terms/Terms_Use.cfm

S. W. Liu[1]

S. K. Datta

Department of Mechanical Engineering,
CIRES and Center for Space Construction,
University of Colorado,
Boulder, CO 80309-0427

Scattering of Ultrasonic Wave by Cracks in a Plate

A hybrid numerical method combining finite elements and the boundary integral representation is used to investigate the transient scattering of ultrasonic waves by a crack in a plate. The incident wave models the guided waves generated by a steel ball impact on the plate. Two surface-breaking cracks and one subsurface crack are studied here. The results show that the location and depth of cracks have measurable effects on the surface responses in time and frequency domains. Also, the scattered fields have distinct differences in the three cases.

1 Introduction

A crack in the interior of a plate can often be detected nondestructively by observation of its effect on an externally applied ultrasonic field. The solution to this direct scattering problem is a necessary prerequisite to the solution of the inverse problem, which is the problem of inferring the characteristics of an unknown flaw from the scattered field. The scattered field generated by the interaction of incident waves with a crack is expected to carry a substantial amount of information on the geometry of the crack. Cracks can cause significant changes in the mechanical behavior of materials, the most remarkable change being the possibility of fracture. Thus, in the field of quantitative nondestructive evaluation (QNDE), there is considerable interest in understanding the scattering by surface-breaking and subsurface cracks in an elastic plate.

Several numerical studies of scattering by a crack in an infinite or semi-infinite medium have been reported. By using the boundary integral equation, the scattering of incident surface waves and incident body waves by a surface-breaking crack in an elastic half-space was investigated by Mendelsohn et al. (1980). The case of a subsurface crack was studied by Achenbach and Brind (1981) for scattering of Rayleigh waves. An approximate solution that is valid at low frequencies was presented by Datta (1979) for SH wave diffraction by a canted surface-breaking planar crack. A hybrid finite element and eigenfunction technique was used by Datta et al. (1982) to study SH wave scattering by a planar surface-breaking crack in a plate. Subsequently, Shah et al. (1987) used the same hybrid technique as in Datta et al. (1982) to investigate the scattering of in-plane body and surface waves by canted planar and normal surface-breaking branched cracks. The interaction of Love waves with a surface-breaking crack normal to the free surface of a layered half-space has been investigated by Angel (1986). The scattering of body waves by an inclined surface-breaking crack in a half-space has also been studied by Zhang and Achenbach (1988) by using boundary integral equations. Using finite difference methods, the scattering due to incident body and surface waves by a step and a slot has been investigated by Saffari and Bond (1987) in the time domain.

For most studies cited above, the scattering is assumed to occur in a semi-infinite medium. However, the scattering of waves in a plate is far more complicated because of multiple reflections. Only few papers consider transient scattering from defects in plates. The scattering of elastic waves by a normal surface-breaking crack in a plate has been investigated in time domain by Harker (1984), and Scandrett and Achenbach (1987) by using a finite difference method.

In this paper, a hybrid method combining the finite element discretization of the near field with the boundary integral representation of the far field is used to study the scattering of ultrasound by cracks in a glass plate. The incident wave used here models the response generated by a steel ball impact on the glass plate. This hybrid numerical method has been used by Liu et al. (1991) to simulate the experimental results presented by Paffenholz et al. (1990). Good agreement has been obtained between the experiment and numerical simulations. Here, in order to further understand the characteristics of different cracks in a plate, we apply the same hybrid method to investigate two surface-breaking cracks of different lengths and one subsurface crack. The numerical results show that the locations and the depths of different cracks can be easily distinguished from the surface responses in time as well as frequency domains.

2 Formulation

Figure 1 shows the two-dimensional configuration of a surface-breaking crack in a plate. Two artificial boundaries (*B*

[1]Current address: Department of Mechanical Engineering, Chinese Air Force Academy, Taiwan, Republic of China.

Contributed by the Applied Mechanics Division of THE AMERICAN SOCIETY OF MECHANICAL ENGINEERS for presentation at the First Joint ASCE-EMD, ASME-AMD, SES Meeting, Charlottesville, VA, June 6–9, 1993.

Discussion on this paper should be addressed to the Technical Editor, Professor Lewis T. Wheeler, Department of Mechanical Engineering, University of Houston, Houston, TX 77204-4792, and will be accepted until four months after final publication of the paper itself in the ASME JOURNAL OF APPLIED MECHANICS.

Manuscript received by the ASME Applied Mechanics Division, May 14, 1991; final revision, Apr. 27, 1992. Associate Technical Editor: L. M. Keer.

Paper No. 93-APM-7.

Copyright © 1993 by ASME

Downloaded 03 May 2010 to 171.66.16.245. Redistribution subject to ASME license or copyright; see http://www.asme.org/terms/Terms_Use.cfm

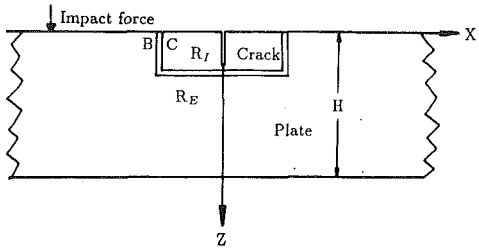


Fig. 1 Configuration of the problem

and C) are introduced here. Waves propagating in this plate are scattered by the crack, which is completely enclosed by the boundary C. Then we define the interior region R_I to be bounded by the boundary B. The exterior region R_E is bounded inside by the contour C. So the area between the contour C and boundary B is shared by both regions. The interior region R_I is discretized with finite elements and an integral representation over C for the displacements on the boundary B is introduced to solve for the scattered field.

Let u_i be the displacement component in the ith direction in the Cartesian frame and σ_{ij} the second-order Cauchy stress tensor $(i,j = 1, 3)$ having time-harmonic behavior of the form $e^{-i\omega t}$, where ω is the circular frequency. u_i and σ_{ij} satisfy the equation of motion

$$\sigma_{ij,j} + \rho\omega^2 u_i = -f_i \quad (i,j=1,3) \tag{1}$$

where ρ is the mass density, f_i the force per unit volume, and the factor $e^{-i\omega t}$ has been dropped.

2.1 Boundary Integral Representation. Boundary integral representation of the exterior field is used for the exterior region R_E. The total displacement u_i is composed of two parts:

$$u_i = u_i^{(f)} + u_i^{(s)}, \tag{2}$$

where $u_i^{(f)}$ is the free-field displacement and $u_i^{(s)}$ is the scattered field. The free-field displacement can be expressed in an analytical form and easily evaluated numerically. The scattered displacement field is represented by a surface integral as discussed below.

In order to derive the boundary integral representation on B, we apply the following elastodynamic reciprocity theorem over boundary C,

$$\int\int_A (\mathbf{f}\cdot\mathbf{v} - \mathbf{g}\cdot\mathbf{u})\,dA = \oint_C (\mathbf{u}\cdot\mathbf{s} - \mathbf{v}\cdot\mathbf{t})\,dC. \tag{3}$$

This theorem presents a relation between two elastodynamic states in the same problem domain, **(u, t, f)** and **(v, s, g)**, which are a pair of solutions to Eq. (1). Here, **u**, **t** represent the displacement and surface traction caused by body force **f** while **v**, **s** are the displacement and surface traction due to body force **g**.

First, this theorem is applied to the exterior region R_E. The scattered field is taken to be the first state and the second state is the Green's displacement field. The scattered field has no sources inside R_E, hence $\mathbf{f} = 0$. For the Green's displacement field the source is chosen to be on boundary B and represented by

$$\mathbf{g} = \delta(x-x')\delta(z-z')e^{-i\omega t}\mathbf{e}_i \tag{4}$$

where $\mathbf{e}_i$ is the unit vector in the ith direction. The Green's displacement function and the scattered fields are the solutions to the following equations:

$$\Sigma_{ijk,k} + \rho\omega^2 G_{ij} = -\delta_{ij}\delta(x-x')\delta(z-z') \tag{5}$$

and

$$\sigma_{jk,k}^{(s)} + \rho\omega^2 u_j^{(s)} = 0, \tag{6}$$

respectively. In the above equations, j stands for the displacement direction and i stands for the force direction. G_{ij} and Σ_{ijk} are the Green's displacement tensor and the corresponding stresses. $\sigma_{jk}^{(s)}$ denotes the stress tensor corresponding to the scattered field. Substituting **g**, **f** and the corresponding tractions and displacements into Eq. (3), we have

$$-u_i^{(s)}(x',z') = \oint_C (u_j^{(s)}\Sigma_{ijk} - G_{ij}\sigma_{jk}^{(s)})(-n_k)\,dC. \tag{7}$$

The contour integration is carried out in clockwise direction and n_k are the components of the outward unit normal vector to C.

Secondly, we apply Eq. (3) to the part of region R_I, which includes the scatterer and bounded by contour C. Two states considered here are the Green's field with its source outside this region, and the free field. Thus, both fields have no sources here. This yields

$$0 = \oint_C (u_j^{(f)}\Sigma_{ijk} - G_{ij}\sigma_{jk}^{(f)})n_k\,dC. \tag{8}$$

The integration along C is calculated in counterclockwise direction. $\sigma_{jk}^{(f)}$ denotes the stress tensor associated with the free field. Reversing the direction of integration in Eq. (7) and adding it to Eq. (8), using Eq. (2), we have

$$u_i(x',z') = \oint_C (u_j\Sigma_{ijk} - G_{ij}\sigma_{jk})n_k\,dC + u_i^{(f)}(x',z'). \tag{9}$$

Equation (9) is the integral representation of the total field at any point in the exterior region R_E.

2.2 Finite Element Method. The interior region R_I encloses all the inhomogeneities. In order to get the solution in this region, we use the finite element technique to discretize this region into N elements. The equation of motion for each element can be written in the following form:

$$\mathbf{K}_e\mathbf{u}_e - \omega^2\mathbf{M}_e\mathbf{u}_e = \mathbf{r}_e, \tag{10}$$

where $\mathbf{K}_e$ and $\mathbf{M}_e$ are the stiffness and mass matrices, respectively, $\mathbf{r}_e$ is the nodal force vector, and $\mathbf{u}_e$ the nodal displacement vector. Equation (10) can be written in another form:

$$\mathbf{S}_e\mathbf{u}_e = \mathbf{r}_e, \tag{11}$$

where the matrix $\mathbf{S}_e$ is defined as

$$\mathbf{S}_e = \mathbf{K}_e - \omega^2\mathbf{M}_e. \tag{12}$$

Then the equations of motion for all elements can be assembled into a global equation of motion,

$$\mathbf{S}\mathbf{u} = \mathbf{r}, \tag{13}$$

where **u** and **r** represent all the nodal displacements and forces, respectively. The nodal displacement $\mathbf{u}_B$ at boundary B can be separated from the interior nodal displacement $\mathbf{u}_I$. Noting that there are no forces on the interior nodes, Eq. (13) is partitioned into the following form:

$$\begin{bmatrix} \mathbf{S}_{BB} & \mathbf{S}_{BI} \\ \mathbf{S}_{IB} & \mathbf{S}_{II} \end{bmatrix} \begin{Bmatrix} \mathbf{u}_B \\ \mathbf{u}_I \end{Bmatrix} = \begin{Bmatrix} \mathbf{r}_B \\ \mathbf{0} \end{Bmatrix} \tag{14}$$

where $\mathbf{r}_B$ represents the nodal force at the boundary B.

2.3 Numerical Solution. Now, evaluating the integrals at all the nodes N_B on the boundary B and separating $\mathbf{u}_B$ from $\mathbf{u}_I$, Eq. (9) gives

$$\mathbf{u}_B = \mathbf{u}_B^{(f)} + \mathbf{A}_{BI}\mathbf{u}_I + \mathbf{A}_{BB}\mathbf{u}_B \tag{15}$$

where $\mathbf{A}_{BI}$ and $\mathbf{A}_{BB}$ are complex matrices and $\mathbf{u}_B^{(f)}$ is the free-field displacement solution at the boundary B. Combining Eq. (15) and the second of Eq. (14), we obtain

$$\begin{bmatrix} \mathbf{I} - \mathbf{A}_{BB} & -\mathbf{A}_{BI} \\ \mathbf{S}_{IB} & \mathbf{S}_{II} \end{bmatrix} \begin{Bmatrix} \mathbf{u}_B \\ \mathbf{u}_I \end{Bmatrix} = \begin{Bmatrix} \mathbf{u}_B^{(f)} \\ \mathbf{0} \end{Bmatrix}. \tag{16}$$

The total field solutions at a certain frequency can be obtained by solving Eq. (16). Once the nodal displacements are solved,

Downloaded 03 May 2010 to 171.66.16.245. Redistribution subject to ASME license or copyright; see http://www.asme.org/terms/Terms_Use.cfm

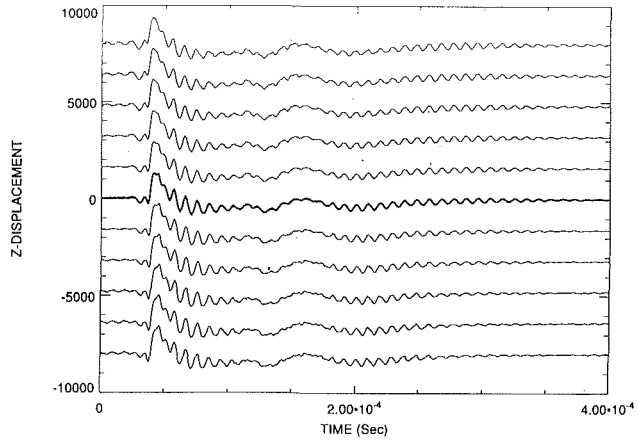


Fig. 2(*a*)

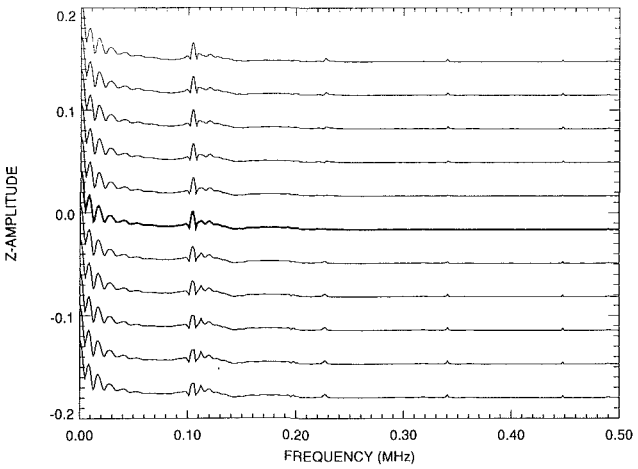


Fig. 2(*b*)

Fig. 2 Vertical displacements in (*a*) time and (*b*) frequency domains for the case without a crack

the displacement at any point in the exterior region can be easily calculated by using Eq. (9). The time-domain solution is then obtained from the frequency-domain solution by using an FFT.

In order to obtain the frequency spectrum, Eq. (16) has to be solved for many frequencies. To alleviate the need for large storage space, the sparse matrix elements involved in Eq. (16) are stored in a column list data scheme. An iterative method (biconjugate gradient method) is then used to solve the sparse unsymmetric complex equations. Both computation time and memory required are reduced considerably this way. The time-domain response is then easily obtained.

3 Description of the Problem

For the numerical simulation a long glass plate 25.4 mm high (H) and of small thickness is considered. Thus, the problem is two-dimensional (plane stress). The material properties of the glass are: compressional wave velocity, 5.64 mm/μs, shear wave velocity, 3.35 mm/μs, and density, 2.61 g/cm^3. These correspond to a Young's modulus of 72 GPa and a Poisson's ratio of 0.228.

Three different vertical cracks are considered here. They are: two surface-breaking cracks of different lengths (defined as crack I and II for convenience) and one subsurface crack. Crack I is a vertical cut 6 mm deep and 0.5 mm wide. Crack II is 3 mm deeper than crack I. The subsurface crack has the same dimension as crack I but it is embedded 3 mm underneath the top surface of the glass plate.

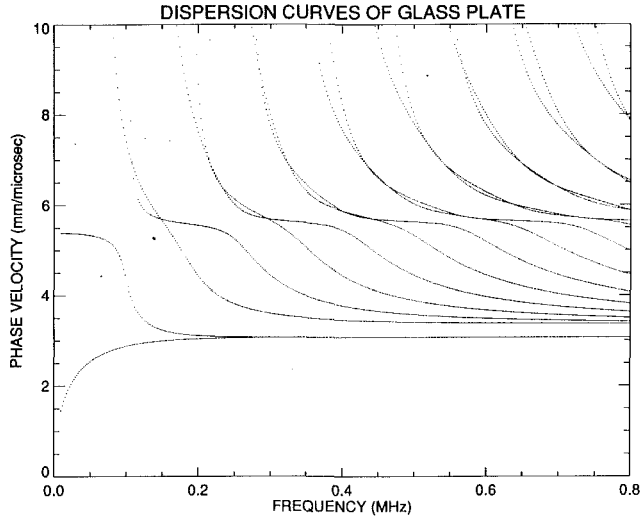


Fig. 3 Dispersion of Rayleigh-Lamb waves in a glass plate

The incident wave considered here is the same as generated experimentally and described in Paffenholz et al. (1990). It was extracted from the response generated by the impact of a steel ball on the glass plate. Most of the contribution of the incident wave was found to be confined within 0.5 MHz (see Spetzler and Datta, 1990). So 0.625 MHz is chosen here as the maximum frequency and 256 frequency responses are used of our numerical modeling. The finite element mesh size is then determined according to the desired numerical accuracy at the maximum frequency. Note that the wavelengths of the incident wave train are much longer than the thickness (5.6 mm) of the plate. Thus, a plane stress state can be assumed.

4 Numerical Results

As shown in our previous study (Liu et al., 1991), the effect of crack I was found to be quite noticeable in the normal surface displacement. Generally, it was found that the effect of the crack was most pronounced in the near field. The far-field response was found to be not affected appreciably by the presence of the crack. So we focus our attention here on the near field response. The source is located on the top surface at a distance $5H$ ($x = -5H$) from the crack. The receiver array is positioned at $x = -5$ mm to $x = 5$ mm in 1 mm intervals around the crack. Therefore, the total number of receivers is ten, five on the left of the crack and the other five on the right. Both vertical and horizontal components of the surface displacements are shown.

In order to understand the effect due to the presence of the crack the vertical surface displacements for the case without a crack are shown in Fig. 2. Note, as a reference, Fig. 2 also shows the response at $x = 0$ mm when there is no crack by thick solid lines. This is the experimentally measured signal (Paffenholz et al., 1990) which is used to extract the source function. Thus, the amplitude scale of the numerical simulations shown in this paper is based on this signal. Note that the peak displacement is about 10 nm in magnitude. The sharp peaks in Fig. 2(b) occur at about 0.1 MHz, which corresponds to the cutoff frequency of the first symmetric thickness stretch mode. In this figure, peaks (weak) are also observed at the cutoff frequencies of the thickness stretch modes (see the dispersion curves in Fig. 3).

Figures 4–6 show, respectively, the vertical surface responses for the cases with crack I, crack II, and subsurface crack. Comparing the time-domain responses due to crack I and crack II shown, respectively, in Figs. 4(a) and 5(a), it is found that the amplitudes in the presence of crack II have larger magnitudes in the back-scattered region. So there is more reflected

Downloaded 03 May 2010 to 171.66.16.245. Redistribution subject to ASME license or copyright; see http://www.asme.org/terms/Terms_Use.cfm

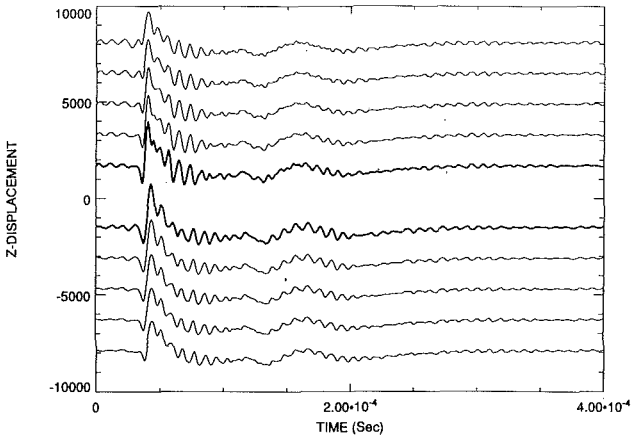


Fig. 4(*a*)

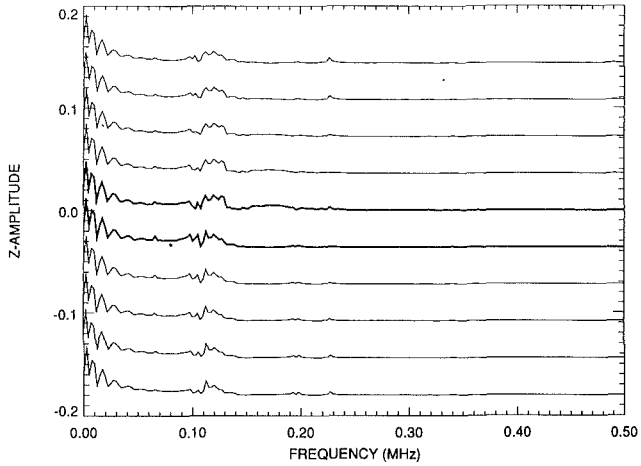


Fig. 4(*b*)

Fig. 4 Vertical displacements in (*a*) time and (*b*) frequency domains for the case with surface-breaking crack I

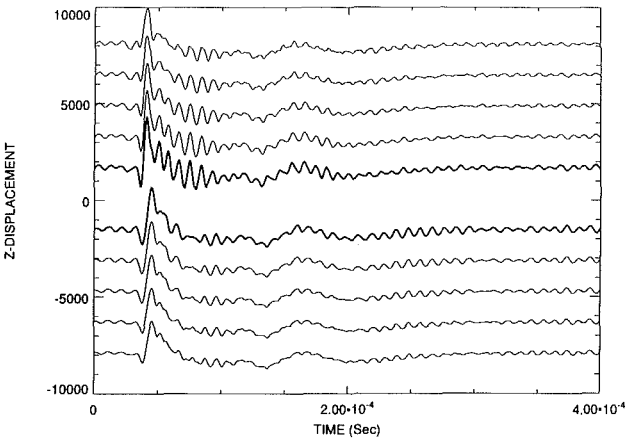


Fig. 5(*a*)

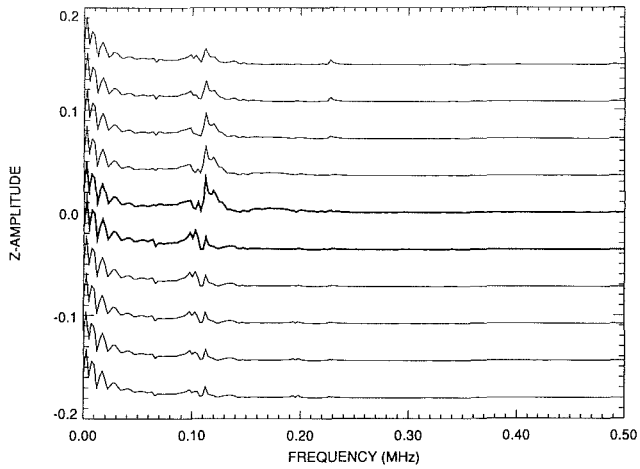


Fig. 5(*b*)

Fig. 5 Vertical displacements in (*a*) time and (*b*) frequency domains for the case with surface-breaking crack II

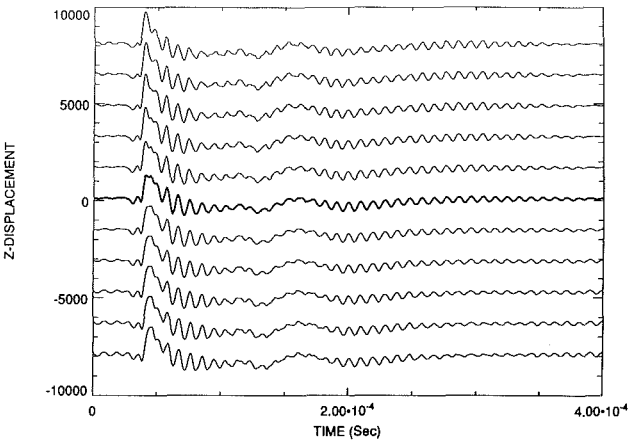


Fig. 6(*a*)

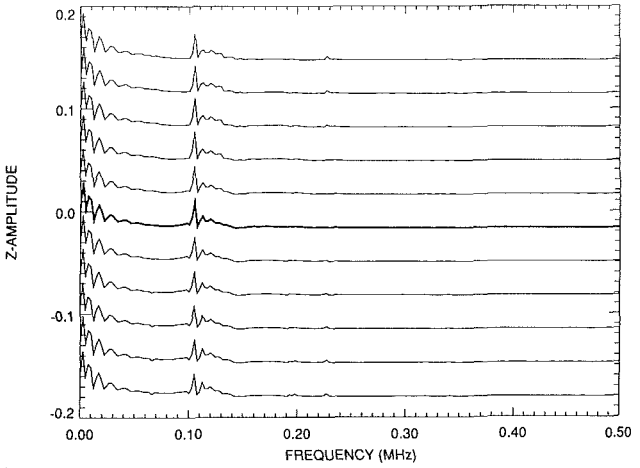


Fig. 6(*b*)

Fig. 6 Vertical displacements in (*a*) time and (*b*) frequency domains for the case with a subsurface crack

energy from the deeper crack. It is further seen from the forward scattered responses in Fig. 5 that the delay in the arrival time of the peak amplitude is approximately 4.81 μs. Taking the Rayleigh wave speed of 3.0 mm/μs this corresponds to distance of travel of about 15 mm. From Fig. 4 it is found that the delay is about 2.89 μs, which corresponds to travel distance of 9 mm. Thus, the difference between the two crack depths is estimated to be 3 mm (1/2(15 − 9)). Figures 4(*b*) and 5(*b*) show significant differences at 0.11 MHz. For the subsurface crack, the transient response shown in Fig. 6(*a*) is similar to the case without crack shown in Fig. 2(*a*). However, the effect of the crack still can be seen from the larger am-

Downloaded 03 May 2010 to 171.66.16.245. Redistribution subject to ASME license or copyright; see http://www.asme.org/terms/Terms_Use.cfm

plitudes of the scattered field. Figure 6(*b*) shows the corresponding spectrum, which has noticeable difference from the case without crack shown in Fig. 2(*b*) at frequencies around 0.105 MHz. A comparison of spectra for all three cases with cracks and the case without crack shows that the main difference is in the frequency responses at around 0.11 MHz, which is the first symmetric mode cutoff, and 0.066 MHz, which is the first antisymmetric mode cutoff. Also the response at higher frequency ($f > 0.3$ MHz) is diminished in the presence of the cracks.

The discussion above was confined to the vertical surface displacement. In the following figures the horizontal displacements are shown. Figures 7–10 show the horizontal displacements for the cases without and with cracks. A comparison between the time-domain responses in the cases without a crack as shown in Fig. 7(*a*) and with crack I as shown in Fig. 8(*a*) shows noticeable effects of the crack: (i) the scattered field in the vicinity of the crack is larger; (ii) the back-scattered field has larger amplitude than the forward-scattered field; this effect is more striking than seen in the vertical components; (iii) the arrival time of the dominant peak in the forward-scattered field is delayed due to the crack; (iv) there are persistent oscillations in the displacement for a long time; this phenomenon was not observed in the vertical component. Figure 7(*b*) shows a small dip at 0.066 MHz, whereas Figs. 8(*b*) and 9(*b*) show pronounced peaks at this frequency. This is the cutoff frequency of the first antisymmetric thickness shear mode. There are large differences in the response at this frequency for the three cases as well as in the response due to the buried crack. Figures 8(*a*) and 9(*a*) show the delays in the arrival times of the peak amplitudes. For crack I the delay is shorter than the crack II, the difference is about 2 μs as was found in Figs. 4(*a*) and 5(*a*). A comparison between Fig. 8(*a*) and Fig. 9(*a*) shows that the deeper crack causes larger amplitudes in the back-scattered field, but smaller in the forward-scattered field. Figure 10(*a*) shows the transient response due to the subsurface crack. Unlike surface-breaking cracks I and II studied above, the response is similar to the case without a crack, but the effect due to the presence of the subsurface crack is very different in the frequency response than in the case of surface-breaking cracks. The difference is particularly striking between 0.05 MHz and 0.11 MHz.

5 Conclusions

Three different cracks, including two surface-breaking cracks with different depths and one subsurface crack, are studied here. It is found that the effects of these three cracks cause significantly different responses in time and frequency domains. It is found that different depths of surface-breaking cause different delays in arrivals of the peaks in the displacements. The difference can be used to estimate the difference in crack depths. Generally, the deeper crack is found to cause larger amplitude of the back-scattered field. In addition, there

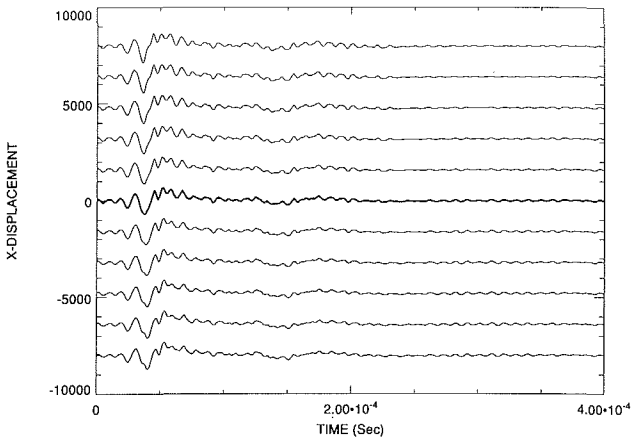


Fig. 7(*a*)

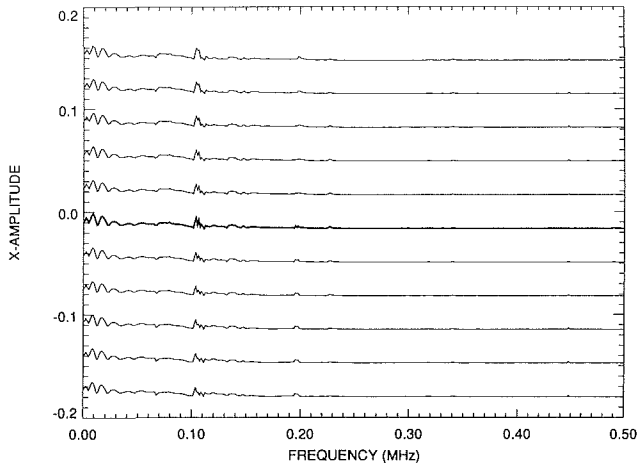


Fig. 7(*b*)

Fig. 7 Horizontal displacements in (*a*) time and (*b*) frequency domains for the case without a crack

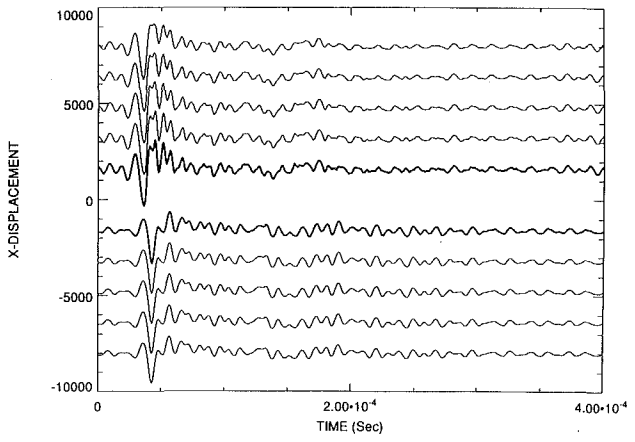


Fig. 8(*a*)

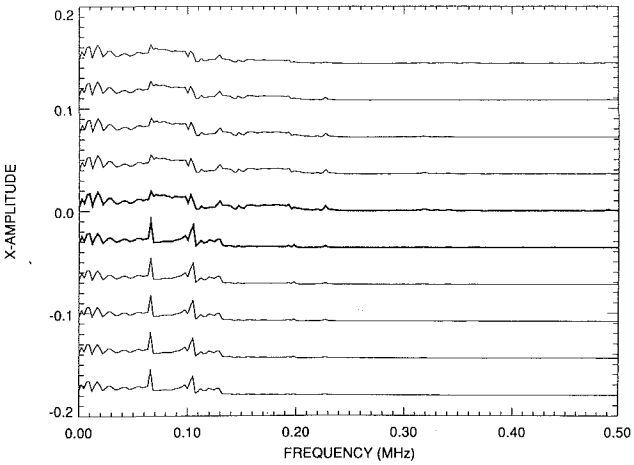


Fig. 8(*b*)

Fig. 8 Horizontal displacements in (a) time and (b) frequency domains for the case with surface-breaking crack I

Downloaded 03 May 2010 to 171.66.16.245. Redistribution subject to ASME license or copyright; see http://www.asme.org/terms/Terms_Use.cfm

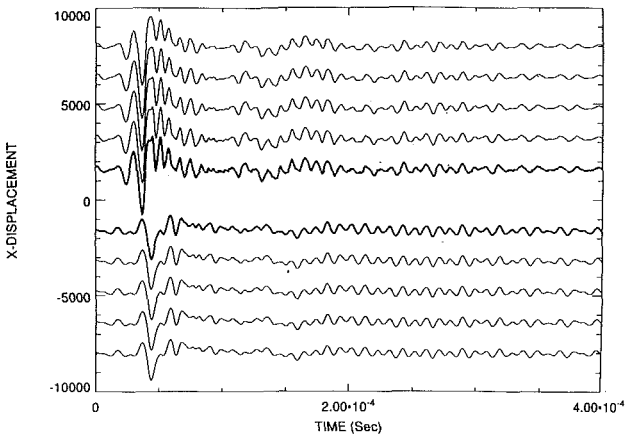


Fig. 9(*a*)

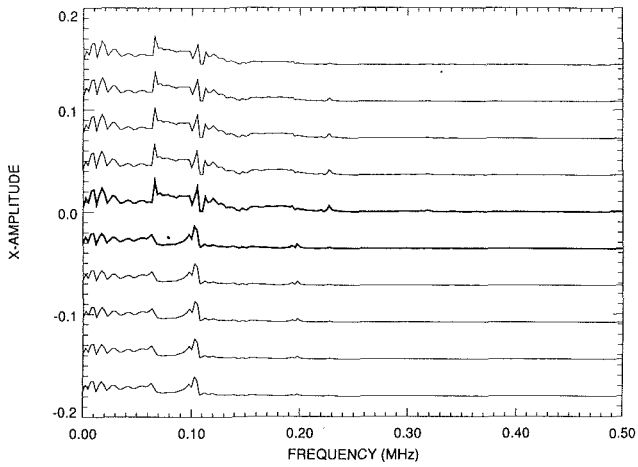


Fig. 9(*b*)

Fig. 9 Horizontal displacements in (*a*) time and (*b*) frequency domains for the case with surface-breaking crack II

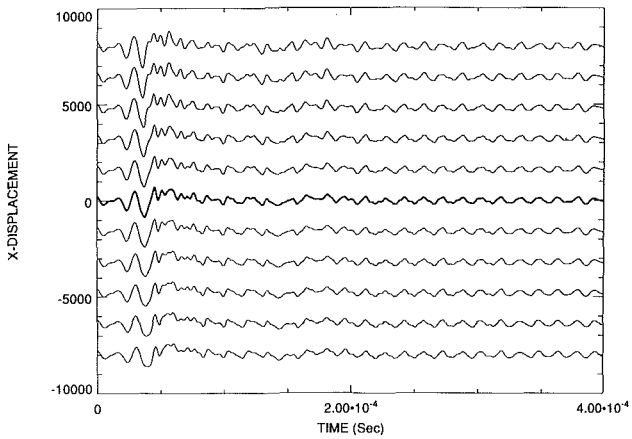


Fig. 10(*a*)

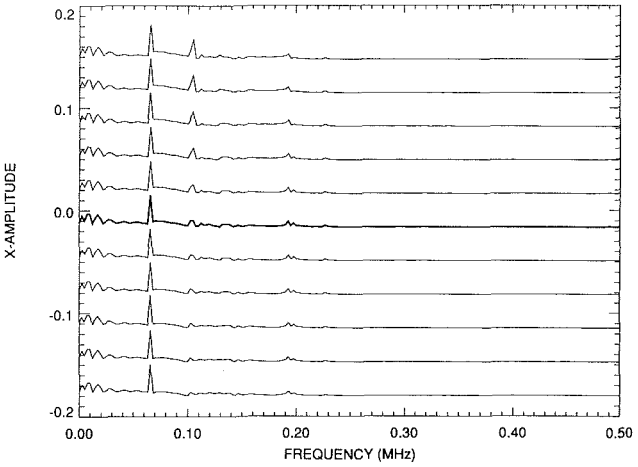


Fig. 10(*b*)

Fig. 10 Horizontal displacements in (*a*) time and (*b*) frequency domains for the case with subsurface crack

are distinct differences in the responses due to surface-breaking and subsurface cracks, particularly around the cutoff frequencies of the first thickness stretch and thickness shear modes.

The numerical results presented here are confined to the surface displacements, but the displacement at any location in the plate can be easily obtained by the hybrid method. The crack-opening displacements can also be calculated and used to obtain the dynamic stress intensity factors for fracture mechanics studies.

Acknowledgments

The work reported here was supported in part by grants from the National Science Foundation (MSM-8609813), the Office of Naval Research (# N00014-86-K-0280) and NASA (# NAGW-1388).

References

Achenbach, J. D., and Brind, R. J., 1981, "Scattering of Surface Waves by a Sub-Surface Crack," *Journal of Sound and Vibration*, Vol. 76, pp. 43–56.

Angel, Y. C., 1986, "Scattering of Love Waves by a Surface-Breaking Crack," ASME Journal of Applied Mechanics, Vol. 53, pp. 587–592.

Datta, S. K., 1979, "Diffraction of SH-Waves by Edge Cracks," ASME Journal of Applied Mechanics, Vol. 46, pp. 101–106.

Datta, S. K., Shah, A. H., and Fortunko, C. M., 1982, "Diffraction of Medium and Long Wavelength Horizontally Polarized Shear Waves by Edge Cracks," *J. Appl. Phys.*, Vol. 53, pp. 2895–2903.

Harker, A. H., 1984, "Numerical Modelling of the Scattering of Elastic Waves in Plates," *Journal of Nondestructive Evaluation*, Vol. 4, pp. 89–106.

Liu, S. W., Datta, S. K., and Ju, T. H., 1991, "Transient Scattering of Rayleigh-Lamb Waves by a Surface-Breaking Crack: Comparison of Numerical Simulation and Experiment," *Journal of Nondestructive Evaluation*, Vol. 10, pp. 111–126.

Mendelsohn, D. A., Achenbach, J. D., and Keer, L. M., 1980, "Scattering of Elastic Waves by a Surface-Breaking Crack," *Wave Motion*, Vol. 2, pp. 277–292.

Paffenholz, J., Fox, J. W., Gu, X., Jewett, G. S., Datta, S. K., and Spetzler, H. A., 1990, "Experimental and Theoretical Study of Rayleigh-Lamb Waves in a Plate Containing a Surface-Breaking Crack," *Res. Nondestr. Eval.*, Vol. 1, pp. 197–217.

Saffari, N., and Bond, L. J., 1987, "Body to Rayleigh Wave Mode-Conversion at Steps and Slots," *Journal of Nondestructive Evaluation*, Vol. 6, pp. 1–22.

Scandrett, C. L., and Achenbach, J. D., 1987, "Time-Domain Finite Difference Calculations for Interaction of an Ultrasonic Wave With a Surface-Breaking Crack," *Wave Motion*, Vol. 9, pp. 171–190.

Shah, A. H., Chin, Y. F., and Datta, S. K., 1987, "Elastic Wave Scattering by Surface-Breaking Planar and Nonplanar Cracks," ASME Journal of Applied Mechanics, Vol. 54, pp. 761–767.

Spetzler, H., and Datta, S. K., 1990, "Experimental Flaw Detection by Scattering of Plate Waves," *Elastic Waves and Ultrasonic Nondestructive Evaluation*, S. K. Datta, J. D. Achenbach, and Y. S. Rajapakse, eds., Elsevier Science Publishers B. V., Amsterdam, pp. 135–141.

Zhang, Ch., and Achenbach, J. D., 1988, "Scattering of Body Waves by an Inclined Surface-Breaking Crack," *Ultrasonics*, Vol. 26, pp. 132–138.

Downloaded 03 May 2010 to 171.66.16.245. Redistribution subject to ASME license or copyright; see http://www.asme.org/terms/Terms_Use.cfm

Power Spectral Density of Nonlinear System Response: The Recursion Method

R. Valéry Roy
Department of Mechanical Engineering,
University of Delaware,
Newark, DE 19716
Mem. ASME

P. D. Spanos
L. B. Ryon Chair in Engineering,
Rice University,
Houston, TX 77251
Fellow ASME

Spectral densities of the response of nonlinear systems to white noise excitation are considered. By using a formal solution of the associated Fokker-Planck-Kolmogorov equation, response spectral densities are represented by formal power series expansion for large frequencies. The coefficients of the series, known as the spectral moments, are determined in terms of first-order response statistics. Alternatively, a J-fraction representation of spectral densities can be achieved by using a generalization of the Lanczos algorithm for matrix tridiagonalization, known as the "recursion method." Sequences of rational approximations of increasing order are obtained. They are used for numerical calculations regarding the single-well and double-well Duffing oscillators, and Van der Pol type oscillators. Digital simulations demonstrate that the proposed approach can be quite reliable over large variations of the system parameters. Further, it is quite versatile as it can be used for the determination of the spectrum of the response of a broad class of randomly excited nonlinear oscillators, with the sole prerequisite being the availability, in exact or approximate form, of the stationary probability density of the response.

Introduction

The prediction of first-order statistics of the response of nonlinear stochastic systems is often found insufficient for reliability analysis. Higher-order response statistics, such as correlation functions or their Fourier transform, power spectral densities, are necessary in making decisions concerning the safety and reliability of stochastic systems. Spectral densities provide important average amplitude information and frequency composition of the sample functions of random processes. Yet, little has been done in improving the existing approximate techniques for the computations of such statistics. The difficulty in the determination of correlation functions and spectra stems from the fact that knowledge of the second-order probability density function $p(\mathbf{X}_1, t_1; \mathbf{X}_2, t_2)$ of the response vector $\mathbf{X}(t)$ is required. For nonlinear systems, exact expressions for response correlations or spectra are almost nonexistent, and thus approximate techniques must be used; see Caughey and Dienes (1961) and Atkinson (1973) for closed-form solutions of simple first-order systems.

The simplest way to determine approximate expressions of correlations and spectra is by employing the method of statistical linearization (Roberts and Spanos, 1990). Once an equivalent linear and time-invariant system has been determined, simple input-output relationships can readily be written for spectral densities. The validity of such estimates has often been questioned, and the nonlinearity effects may not be adequately taken into account. Recently, Reinhall and Miles (1989) have shown that the method of equivalent linearization fails to predict the broadening of the resonant peak observed in the spectral response of nonlinear plates as the excitation level is increased.

Perturbation expansions, used by Crandall (1963) for stochastic systems, have yielded expressions of spectral densities, valid only for small nonlinearities. Only a few terms with limited range of application can be realistically determined. The technique for turbulent flow proposed by Kraichnan (1961) can also be used, with considerable effort, to obtain a summation of such perturbation series by regrouping the terms in "consolidated expansions." This approach was adopted by Morton and Corrsin (1970) for the Duffing oscillator, and the resulting approximation for the response spectral density, termed the "second Kraichnan-Wyld" approximation, involves three coupled, nonlinear integral equations.

Improved analytical methods can be devised by taking into account the Markov property of systems driven by white Gaussian noise. One of these methods relies on determining eigenfunction expansions of the transition probability density function (p.d.f.) solution of the Fokker-Planck-Kolmogorov (FPK) equation; see Caughey (1971), Atkinson (1973), and Gardiner (1983). Correlation functions and spectra can then readily be expressed in terms of the eigenfunctions and eigenvalues associated with the FPK equation. Unfortunately, exact

Contributed by the Applied Mechanics Division of THE AMERICAN SOCIETY OF MECHANICAL ENGINEERS for presentation at the First Joint ASCE-EMD, ASME-AMD, SES Meeting, Charlottesville, VA, June 6-9, 1993.

Discussion on this paper should be addressed to the Technical Editor, Professor Lewis T. Wheeler, Department of Mechanical Engineering, University of Houston, Houston, TX 77204-4792, and will be accepted until four months after final publication of the paper itself in the ASME JOURNAL OF APPLIED MECHANICS.

Manuscript received by the ASME Applied Mechanics Division, Jan. 27, 1992; final revision, June 4, 1992. Associate Technical Editor: L. M. Keer.

Paper No. 93-APM-12.

Copyright © 1993 by ASME
Downloaded 03 May 2010 to 171.66.16.245. Redistribution subject to ASME license or copyright; see http://www.asme.org/terms/Terms_Use.cfm

eigenfunction expansions cannot be found in general, and one must rely on numerical solutions based on a variational Rayleigh-Ritz formulation (Atkinson, 1973). Another way to exploit the Markov character of the system response is to derive differential equations governing correlation functions of the response vector, leading to infinite hierarchies. Hence, closure or truncation schemes are necessary; see Crandall (1973), and Bugdor, Lindenberg, and Schuler (1976). Closure schemes have been devised by using the "quasi-normal" assumption for the response, leading to nonlinear integral or differential equations. It is shown in particular, that the cumulant-discard closure method does not improve the results obtained by equivalent linearization (Budgor et al., 1976).

The method presented herein for the calculation of correlation functions and spectral densities has its origin on the theoretical work of Zwanzig (1961) and Mori (1965) in the field of statistical and quantum physics. The method is known as the "projection operator" technique and has been extensively used in statistical mechanics. By adopting a formal representation of the solution of the FPK equation, formal power series expansions of spectral densities are obtained. The coefficients of such expansions can be shown to be in the form of spectral moments. Analytical expressions are then obtained by transforming the power series into Padé approximants or continued fractions. These transformations amount to performing analytical continuations over the entire imaginary axis of the complex plane. The continued fraction representation of spectral densities is equivalent to that derived by Bixon and Zwanzig (1971) for the Duffing oscillator excited by white noise, or that derived by Mori (1965) for quantum mechanical oscillators. Matsuo (1978) also used the projection operator formalism to derive response spectral densities in the form of continued fractions for a general class of multi-degree-of-freedom (MDOF) systems and gave numerical results for a single-degree-of-freedom (SDOF) oscillator with a double-well potential.

Alternatively, the J-fraction representation of spectral densities can be obtained directly by employing the "Recursion Method" of computational solid state physics; see Pettifor and Weaire (1985). The recursion method applied to linear Hermitian operators is based on the Lanczos algorithm for the tridiagonalization of matrices. The generalization of this process to the adjoint Fokker-Planck operator yields a J-fraction whose truncation at increasing finite orders gives a sequence of approximations of spectral densities. The convergence of sequences of approximations obtained by the "recursion method" is tested on various SDOF oscillators by performing digital simulations. It is shown that the procedure yields quite reliable approximations with minimal programming and computing labor.

A Formal Power Series Representation of Correlations and Spectra

Consider the n-dimensional stationary response $\mathbf{X}(t) = (X_1, X_2, \ldots, X_n)$ of the following time-invariant system of Itô stochastic differential equations

$$d\mathbf{X}(t) = \mathbf{f}(\mathbf{X})dt + \mathbf{G}(\mathbf{X})d\mathbf{W}(t), \tag{1}$$

where $\mathbf{W}(t) = (w_1, w_2, \ldots, w_m)^T$ represents m uncorrelated unit Wiener processes. It is known that the response $\mathbf{X}(t)$ is Markovian and that its probabilistic state is entirely described by a transition probability density function $p(\mathbf{X}, \tau|\mathbf{X}_0)$ which satisfies an associated Fokker-Planck-Kolmogorov (FPK) equation ($\tau > 0$). That is,

$$\frac{\partial p}{\partial \tau} = \mathcal{L}_{FP}(\mathbf{X})p = -\frac{\partial}{\partial X_i}(f_i p) + \frac{1}{2}\frac{\partial^2}{\partial X_i X_j}((\mathbf{G}\mathbf{G}^T)_{ij}p), \tag{2}$$

where the usual summation convention is adopted. The transition probability density function satisfies the initial condition $p(\mathbf{X}, 0|\mathbf{X}_0) = \delta(\mathbf{X} - \mathbf{X}_0)$, where $\delta(\mathbf{X} - \mathbf{X}_0)$ is the Dirac delta function. The process $\mathbf{X}(t)$ is assumed to have an infinite region of definition, so that $\lim_{\mathbf{X}\to\infty} p(\mathbf{X}, \tau|\mathbf{X}_0) = 0$. The stationary first-order probability density function is denoted by $p_s(\mathbf{X}) = \lim_{\tau\to\infty} p(\mathbf{X}, \tau|\mathbf{X}_0)$. Further, the symbol $\langle .\,;\,. \rangle_o$ denotes the scalar product defined by the equation

$$\langle u; v\rangle_o = \int_{\mathbf{R}^n} u(\mathbf{X})v(\mathbf{X})p_s(\mathbf{X})d\mathbf{X}. \tag{3}$$

Taking into account the Markov property of the system, the stationary correlation function, denoted by $R_{A,B}(\tau) = \langle A(\mathbf{X})(t)B(\mathbf{X})(t+\tau)\rangle\rangle$, between the scalar processes $A(\mathbf{X})(t) = A(X_1(t), X_2(t), \ldots, X_n(t))$ and $B(\mathbf{X})(t+\tau) = B(X_1(t+\tau), X_2(t+\tau), \ldots, X_n(t+\tau))$ can be expressed, for $\tau > 0$, as

$$R_{A,B}(\tau) = \int_{\mathbf{R}^n}\int_{\mathbf{R}^n} A(\mathbf{X}_0)B(\mathbf{X})p(\mathbf{X}, t+\tau; \mathbf{X}_0, t)d\mathbf{X}_0 d\mathbf{X}$$

$$= \int_{\mathbf{R}^n}\int_{\mathbf{R}^n} A(\mathbf{X}_0)B(\mathbf{X})p(\mathbf{X}, \tau|\mathbf{X}_0)p_s(\mathbf{X}_0)d\mathbf{X}_0 d\mathbf{X}. \tag{4}$$

An explicit or approximate expression for the transition probability density function is not sought. Following Risken (1989), the solution of the Eq. (2) (that is $\partial_\tau p = \mathcal{L}_{FP}(\mathbf{X})p$) is expressed in the following formal way involving the operator $\mathcal{L}_{FP}(\mathbf{X})$

$$p(\mathbf{X}, \tau|\mathbf{X}_0) = \exp(\mathcal{L}_{FP}(\mathbf{X})\tau)\delta(\mathbf{X} - \mathbf{X}_0)$$

$$= \left(\mathcal{I} + \mathcal{L}_{FP}(\mathbf{X})\tau + \ldots + \mathcal{L}^k_{FP}(\mathbf{X})\frac{\tau^k}{k!} + \ldots\right)\delta(\mathbf{X} - \mathbf{X}_0), \tag{5}$$

where $\mathcal{I}$ the identity operator and the exponential has been replaced by its power series. A rigorous mathematical definition of the exponential of a differential operator such as $\mathcal{L}_{FP}(\mathbf{X})$ is not attempted. The correlation function $R_{A,B}(\tau)$ can then be expressed in the following power series expansion of the variable $\tau > 0$:

$$R_{A,B}(\tau) = \sum_{k=0}\frac{\tau^k}{k!}\int_{\mathbf{R}^n}\int_{\mathbf{R}^n} A(\mathbf{X}_0)B(\mathbf{X})p_s(\mathbf{X}_0) \times \{\mathcal{L}^k_{FP}(\mathbf{X})\delta(\mathbf{X} - \mathbf{X}_0)\}d\mathbf{X}_0 d\mathbf{X}$$

$$= \int_{\mathbf{R}^n}\int_{\mathbf{R}^n} A(\mathbf{X}_0)\delta(\mathbf{X} - \mathbf{X}_0)p_s(\mathbf{X}_0) \times \{(\mathcal{L}^*_{FP})^k(\mathbf{X})B(\mathbf{X})\}d\mathbf{X}_0 d\mathbf{X}$$

$$= \langle A; \exp(\mathcal{L}^*_{FP}\tau)B\rangle_o = \sum_{k=0}^{\infty} c_k\frac{\tau^k}{k!}, \tag{6}$$

where $c_k = \langle A; (\mathcal{L}^*_{FP})^k B\rangle_o$, and $\mathcal{L}^*_{FP}$ is the adjoint operator of $\mathcal{L}_{FP}$. That is,

$$\int_{\mathbf{R}^n} u(\mathbf{X})\mathcal{L}_{FP}v(\mathbf{X})d\mathbf{X} = \int_{\mathbf{R}^n} v(\mathbf{X})\mathcal{L}^*_{FP}u(\mathbf{X})d\mathbf{X}. \tag{7}$$

A similar power series expansion can be derived for $\tau < 0$ by using the fact that the stationarity of the system response implies the following property for correlation functions

$$R_{A,B}(-\tau) = R_{B,A}(\tau) = \langle B; \exp(\mathcal{L}^*_{FP}\tau)A\rangle_o. \tag{8}$$

In particular, auto-correlation functions $R_{A,A}(\tau)$ are even functions of τ. It is seen that the series coefficients c_k are defined as long as the powers of the operator $\mathcal{L}^*_{FP}$ can be determined; this is the case when the nonlinearities of the systems are all analytic functions of $\mathbf{X}$. The determination of $(\mathcal{L}^*_{FP})^k$ is especially straightforward for polynomial-type nonlinearities. If, in addition, the functions $A(\mathbf{X})$ and $B(\mathbf{X})$ are also of polynomial type, these coefficients are readily expressed as linear combinations of stationary response moments. It is assumed

Downloaded 03 May 2010 to 171.66.16.245. Redistribution subject to ASME license or copyright; see http://www.asme.org/terms/Terms_Use.cfm

that these statistics can be evaluated from a closed-form solution of $p_s(\mathbf{X})$ or from any approximate scheme available for stochastic dynamical systems. The following development is now restricted to the case $A(\mathbf{X}) = B(\mathbf{X})$ without loss of generality.

Response power auto-spectral densities can be determined from the Laplace transform $\bar{S}_{A,A}(z)$ of the restriction of $R_{A,A}(\tau)$ to positive values of τ. Specifically,

$$\bar{S}_{A,A}(z) = \int_0^\infty R_{A,A}(\tau)\exp(-z\tau)d\tau = \langle A;\ (z\mathcal{I} - \mathcal{L}_{FP}^*)^{-1}A\rangle_o = \sum_{k=0}^{\infty} \frac{c_k}{z^{k+1}}. \quad (9)$$

Using the evenness of auto-spectral densities, the following power series expansion is obtained:

$$S_{A,A}(\omega) = 2\Re\{\bar{S}_{A,A}(j\omega)\} = 2\Re\{\langle A;\ (j\omega\mathcal{I} - \mathcal{L}_{FP}^*)^{-1}A\rangle_o\} = 2\Re\left\{\sum_{k=0}^{\infty} \frac{c_k}{(j\omega)^{k+1}}\right\}, \quad (10)$$

where $j^2 = -1$, and $\Re$ denotes the real part of complex numbers. Note that the series coefficients $(c_k)_{k>0}$ represent the spectral moments associated with the spectral density $S_{A,A}(\omega)$. That is,

$$c_k = \frac{1}{2\pi}\int_{-\infty}^{\infty} (j\omega)^k \bar{S}_{A,A}(j\omega)d\omega. \quad (11)$$

The problem of reconstructing the spectral density from its spectral moments is an old problem dating back to the last century, and is known in mechanics, physics, and mathematics as the "Problem of Moments"; see Shohat and Tamarkin (1943).

The determination of the coefficients $c_k = \langle A;\ (\mathcal{L}_{FP}^*)^k A\rangle_o$ is illustrated for the spectral density $S_{X,X}(\omega)$, for $X(t)$ being the response of the one-dimensional system governed by the equation

$$dX(t) = -(X(t) + \epsilon X^3(t))dt + \sqrt{2D}dW(t). \quad (12)$$

The corresponding Fokker-Planck operator and its adjoint are given by

$$\mathcal{L}_{FP}(X) = \frac{\partial}{\partial X}(X + \epsilon X^3) + D\frac{\partial^2}{\partial X^2}$$

$$\mathcal{L}_{FP}^*(X) = -(X + \epsilon X^3)\frac{\partial}{\partial X} + D\frac{\partial^2}{\partial X^2} \quad (13)$$

The first powers $(\mathcal{L}_{FP}^*)^k$ applied to $A(X) = X$ yield the following expressions:

$$\begin{aligned}
(\mathcal{L}_{FP}^*)^0 X &= X\\
(\mathcal{L}_{FP}^*)^1 X &= -X - \epsilon X^3\\
(\mathcal{L}_{FP}^*)^2 X &= (1 - 6D\epsilon)X + 4\epsilon X^3 + 3\epsilon^2 X^5\\
(\mathcal{L}_{FP}^*)^3 X &= (-1 + 30D\epsilon)X + \epsilon(-13 + 66D\epsilon)X^3 - 27\epsilon^2 X^5 - 15\epsilon^3 X^7.\\
&\vdots
\end{aligned} \quad (14)$$

The expansion coefficients are then given by

$$\begin{aligned}
c_0 &= \langle X^2\rangle\\
c_1 &= -\langle X^2\rangle - \epsilon\langle X^4\rangle\\
c_2 &= (1 - 6D\epsilon)\langle X^2\rangle + 4\epsilon\langle X^4\rangle + 3\epsilon^2\langle X^6\rangle\\
c_3 &= (-1 + 30D\epsilon)\langle X^2\rangle + \epsilon(-13 + 66D\epsilon)\langle X^4\rangle - 27\epsilon^2\langle X^6\rangle - 15\epsilon^3\langle X^8\rangle\\
&\vdots
\end{aligned} \quad (15)$$

where $\langle X^i\rangle$ represents the ith stationary response moment.

Rational Approximation of Spectra by Padé Approximants or *J*-Fractions

The formal power series expansion of Eq. (9) cannot be used, as it stands, over the entire frequency interval $[0, \infty)$. In general, an analytic continuation is necessary and can be achieved by use of Padé approximants or by continued fractions. The fundamental idea is to build rational approximations $[L/M](1/j\omega)$ whose power series expansions match the formal power series $\Sigma_{k=0}^{\infty} c_k/(j\omega)^{k+1}$ as far as possible. More explicitly, the $[L/M]$ Padé approximant is the rational function

$$[L/M](1/j\omega) = \frac{P_L(1/j\omega)}{Q_M(1/j\omega)} = \frac{p_1/j\omega + \ldots + p_L/(j\omega)^L}{q_0 + q_1/j\omega + \ldots + q_M/(j\omega)^M} \quad (16)$$

such that

$$P_L(1/j\omega) - Q_M(1/j\omega)\sum_{k=0}^{\infty}\frac{c_k}{(j\omega)^{k+1}} = O(1/(j\omega)^{L+M+1}), \quad (17)$$

where "$O(1/z^n)$" means "of order $1/z^n$ as $1/z \to 0$." Upon matching the coefficients of equal powers of $1/j\omega$ in Eq. (17) up to order $L + M$, the denominator and numerator coefficients of $[L/M]$ are found from the first $L + M$ coefficients $(c_k)_{k\geq 0}$ by solving two linear algebraic systems. Alternatively, the formal power series of $\bar{S}_{A,A}(j\omega)$ can be recast in the form of continued fractions, also called *J*-fractions (Wall, 1948), expressed as

$$\sum_{k=0}^{\infty}\frac{c_k}{(j\omega)^{k+1}} = \cfrac{b_0}{j\omega - a_0 - \cfrac{b_1}{j\omega - a_1 - \cfrac{b_2}{\ddots - \cfrac{b_{N-1}}{j\omega - a_{N-1}}}}} + O(1/(j\omega)^{2N+1}), \quad (18)$$

where the expansion of the *J*-fraction in powers of $1/j\omega$ matches that of $\bar{S}_{A,A}(j\omega)$ up to order $2N$. Various algorithms can be used for the determination of the continued fraction coefficients $(a_k)_{k\geq 0}$ and $(b_k)_{k>0}$ from the series coefficients (see, for example, Wall, 1948). In fact, it can be shown that the sequence of approximants of *J*-fractions is nothing but the diagonal sequence of [1/1], [2/2], ..., $[L/L]$ Padé approximants in the variable $1/j\omega$ as shown by Eq. (16). Bixon and Zwanzig (1971) and Matsuo (1978) constructed *J*-fraction approximations from the high-frequency expansion $\Sigma_{k=0}^{\infty} K_k/(j\omega)^{k+1}$ of the memory kernel $K(t)$ obtained by operator projection.

Padé approximants or continued fractions are expected to converge far better to the exact function than the corresponding power series expansions. Unfortunately, the computation of Padé approximants or continued fractions is an ill-conditioned problem. That is, rounding errors in the coefficients $(c_k)_{k\geq 0}$ are amplified in the Padé approximant's numerator and denominator coefficients $(p_k)_{k\geq 1}$ and $(q_k)_{k>0}$, or in the coefficients $(a_k)_{k\geq 0}$ and $(b_k)_{k>0}$ of the continued fraction. Therefore, the higher the order of the approximation to be constructed, the more precision is required. Since numerical integration is in general necessary to compute the series coefficients, the required precision might not be sufficiently high to obtain high-order approximations. There is, however, a stable and efficient way to obtain continued fraction representation of spectral densities without having to generate the series coefficients. This technique is known in the field of solid state physics as the "Recursion Method" presented in the following section.

Downloaded 03 May 2010 to 171.66.16.245. Redistribution subject to ASME license or copyright; see http://www.asme.org/terms/Terms_Use.cfm

Continued Fraction Representation of Spectra by the Recursion Method

Continued fractions have emerged as a powerful tool in quantum mechanics for the determination of Greenian or resolvent $G(E) = \langle \psi; (E\mathcal{I} - \mathcal{H})^{-1}\psi \rangle$ of Hamiltonian operators $\mathcal{H}$. The recursion method (Pettifor and Weaire, 1985) gives a convergent sequence of J-fractions to the function $G(E)$ for any linear, Hermitian operator $\mathcal{H}$. It can also be used to obtain a continued fraction representation of spectral densities $S_{A,A}(\omega) = 2\Re\{\bar{S}(j\omega)\}$ in the context of nonlinear stochastic systems

$$\bar{S}(j\omega) = \langle A; (j\omega\mathcal{I} - \mathcal{L}^*_{FP})^{-1}A \rangle_o \tag{19}$$

where $\mathcal{L}^*_{FP}$ is the adjoint of the non-Hermitian, time-independent Fokker-Planck operator. The recursion method relies on constructing an orthogonal basis $(u_n)_{n\geq 0}$ in which the operator $\mathcal{L}^*_{FP}$ has a tridiagonal representation with respect to the scalar product $\langle . ; . \rangle_o$. Starting with the initial vector $u_0 = A(\mathbf{X})$, a sequence of vectors $(u_n)_{n\geq 1}$, also called "states," is defined from the following recursive relations

$$u_1 = (\mathcal{L}^*_{FP} - a_0\mathcal{I})u_0 \tag{20}$$

$$u_{n+1} = (\mathcal{L}^*_{FP} - a_n\mathcal{I})u_n - b_n u_{n-1}, \quad n \geq 1. \tag{21}$$

The sequences of scalar numbers $(a_n)_{n\geq 0}$ and $(b_n)_{n\geq 0}$ are determined such that the vectors u_n are mutually orthogonal with respect to the scalar product $\langle . ; . \rangle_o$. The orthogonality condition between u_{n+1} and u_n implies the following expression for a_n

$$a_n = \frac{\langle u_n; \mathcal{L}^*_{FP}u_n \rangle_o}{\langle u_n; u_n \rangle_o}. \tag{22}$$

Then, the coefficient b_n is determined by expressing the orthogonality condition between u_{n+1} and u_{n-1} $(n \geq 1)$. That is,

$$b_n = \frac{\langle u_{n-1}; \mathcal{L}^*_{FP}u_n \rangle_o}{\langle u_{n-1}; u_{n-1} \rangle_o}. \tag{23}$$

Equations (20), (21), (22), and (23) are the basis of the recursion algorithm for the determination of the sequences $(a_n)_{n\geq 0}$ and $(b_n)_{n\geq 0}$ and that of the orthogonal basis $(u_n)_{n\geq 1}$, starting with $u_0 = A(\mathbf{X})$. Then, the operator $(j\omega\mathcal{I} - \mathcal{L}^*_{FP})$ has the following infinite tridiagonal matrix representation on the basis $(u_n)_{n\geq 0}$

$$(j\omega\mathcal{I} - \mathcal{L}^*_{FP}) = \begin{bmatrix} j\omega - a_0 & -1 & & & \\ -b_1 & j\omega - a_1 & -1 & & \\ & \ddots & \ddots & \ddots & \\ & -b_n & j\omega - a_n & -1 & \\ & & \ddots & \ddots & \ddots \end{bmatrix}. \tag{24}$$

As explained by Haydock, see Pettifor et al. (1985), there exists a close relationship between the recursion method, the classical moment problem, and the Lanczos algorithm for tridiagonalizing matrices, all of which involve three-term recurrences.

It is now possible to find $\bar{S}(j\omega)$ by expressing $(j\omega\mathcal{I} - \mathcal{L}^*_{FP})^{-1}u_0$ on the basis $(u_n)_{n\geq 0}$. That is,

$$\bar{S}(j\omega) = \langle u_0; (j\omega\mathcal{I} - \mathcal{L}^*_{FP})^{-1}u_0 \rangle_o = \langle u_o; \alpha_0 u_0 + \alpha_1 u_1 + \alpha_2 u_2 + \ldots \rangle_o = \alpha_0 \langle u_0; u_0 \rangle_o, \tag{25}$$

where the orthogonality of the u_n's has been used. By denoting the determinant of the infinite size matrix of Eq. (24) by $D_0(j\omega)$ and by $D_n(j\omega)$, the determinant obtained by deleting the first n rows and n columns of this matrix, then, using Cramer's rule, one finds

$$\bar{S}(j\omega) = \alpha_0 \langle u_0; u_0 \rangle_o = \langle u_0; u_0 \rangle_o \frac{D_1(j\omega)}{D_0(j\omega)}. \tag{26}$$

Further, using the properties of determinants, it is found that the ratio $r_n(j\omega) = D_n(j\omega)/D_{n+1}(j\omega)$ $(n \geq 0)$ satisfies the following recurrence relationship

$$r_n(j\omega) = j\omega - a_n - \frac{b_{n+1}}{r_{n+1}(j\omega)}. \tag{27}$$

By applying Eq. (27) to $r_0(j\omega)$, the following J-fraction representation for the spectral density $S_{A,A}(\omega)$ is derived:

$$S_{A,A}(\omega) = 2\langle A^2(\mathbf{X}) \rangle \Re \left\{ \cfrac{1}{j\omega - a_0 - \cfrac{b_1}{j\omega - a_1 - \cfrac{b_2}{\ddots - \cfrac{b_n}{j\omega - a_n - t_{n+1}(j\omega)}}}} \right\} \tag{28}$$

where the termination function $t_{n+1}(j\omega) = b_{n+1}/r_{n+1}(j\omega)$ is usually taken to be zero. It is seen that the recursion method does not require the evaluation of the series coefficients $(c_n)_{n\geq 0}$. As the order of truncation is increased, a sequence of rational approximations for the spectral response of nonlinear systems is obtained without having to solve the corresponding FPK equation. The corresponding approximations to the auto-correlation function $R_{A,A}(\tau) = \langle A; \exp(\mathcal{L}^*_{FP}\tau)A \rangle_o$, being the inverse Laplace transform of a rational function, will be in the form of sums of exponentials of the type $\Sigma_{k\geq 0}\mu_k \exp(\lambda_k \tau)$.

If the asymptotic behavior of the continued fraction coefficients can be determined from physical or numerical considerations, an analytic expression for the tail $t_{n+1}(j\omega)$ of the continued fraction can often be given, which can considerably improve the convergence of the approximants. For example, if the coefficients $(a_n)_{n\geq 0}$ and $(b_n)_{n\geq 0}$ are known to reach asymptotic finite limits, then one can expect that $t_n(j\omega) \approx t_{n+1}(j\omega)$ for n sufficiently large. Since $t_n(j\omega)$ and $t_{n+1}(j\omega)$ satisfy the relation

$$t_n(j\omega) = \frac{b_n}{j\omega - a_n - t_{n+1}(j\omega)}, \tag{29}$$

the following square root terminating function is found

$$t_n(j\omega) = \frac{1}{2}\left(j\omega - a_n \pm \sqrt{(j\omega - a_n)^2 - 4b_n} \right), \tag{30}$$

where here, the negative sign is chosen, so that $t_n(j\omega)$ vanishes as $\omega \to \infty$, in accordance with the asymptotic behavior of the spectral density.

The recursion method is illustrated for the broad class of SDOF systems governed by the equation

$$\ddot{X} + g(X,\dot{X})\dot{X} + f(X) = F(t), \tag{31}$$

where $F(t)$ is a Gaussian white noise excitation such that $\langle F(t)F(t+\tau) \rangle = 2D\delta(\tau)$. In order to evaluate the displacement spectral density $S_{X,X}(\omega)$, the first elements of the orthogonal basis $(u_n)_{n\geq 0}$, and those of the sequences $(a_n)_{n\geq 0}$ and $(b_n)_{n\geq 0}$ are obtained by application of Eq. (20)–(23). Specifically set $Y = \dot{X}$. Then,

$$u_0(X,Y) = X, \quad a_0 = \frac{\langle XY \rangle}{\langle X^2 \rangle} = 0,$$

$$u_1(X,Y) = Y, \quad a_1 = -\frac{\langle g(X,Y)Y^2 \rangle}{\langle Y^2 \rangle},$$

$$b_1 = -\frac{\langle g(X,Y)XY - Xf(X) \rangle}{\langle X^2 \rangle} = -\frac{\langle Y^2 \rangle}{\langle X^2 \rangle},$$

$$u_2(X,Y) = -(g(X,Y) + a_1)Y - f(X) - b_1 X,$$

$$a_2 = -D\frac{\langle (u_{2,Y})^2 \rangle}{\langle u_2^2 \rangle}, \quad b_2 = \frac{\langle u_2(f(X) + (g(X,Y)Y^2)_{,Y}) \rangle}{\langle Y^2 \rangle} \tag{32}$$

Downloaded 03 May 2010 to 171.66.16.245. Redistribution subject to ASME license or copyright; see http://www.asme.org/terms/Terms_Use.cfm

where $h_{,Y}$ stands for the partial derivative of the function h with respect to Y. These expressions are obtained by using the adjoint Fokker-Planck operator

$$\mathcal{L}^*_{FP} = Y\frac{\partial}{\partial X} - (g(X,Y)Y + f(X))\frac{\partial}{\partial Y} + D\frac{\partial^2}{\partial Y^2}, \quad (33)$$

and they lead to the continued fraction representation

$$S_{X,X}(\omega) = 2\langle X^2\rangle \Re\left\{\frac{1}{j\omega + \dfrac{\langle Y^2\rangle/\langle X^2\rangle}{j\omega + \langle g(X,Y)Y^2\rangle/\langle Y^2\rangle - b_2 t_2(j\omega)}}\right\}. \quad (34)$$

Note that, in the case of $g(X, Y) = \alpha$ and $f(X) = X$, a harmonic oscillator with additive noise excitation, the parameter b_2 becomes zero. Hence, the continued fraction of Eq. (34) terminates exactly.

Without the use of the projection operator formalism, this expression is precisely the one obtained by Bixon and Zwanzig (1971). In the next section, the recursion method is applied to various SDOF oscillators. Numerical results regarding the computation of continued fraction of response spectral densities are shown. Special attention is given to the convergence of the sequence of approximations by relying on results obtained by Monte Carlo simulations. Note that no mathematical proof of the convergence of this sequence is available in the general case of a non self-adjoint Fokker-Planck operator $\mathcal{L}_{FP}(\mathbf{X})$.

Applications

A Linear Parametric Oscillator. The recursion method is first illustrated by considering the linear oscillator governed by the Stratonovich-type differential equation

$$\ddot{X}(t) + (2\eta + \xi_1(t))\dot{X}(t) + (1 + \xi_2(t))X(t) = \xi_3(t), \quad (35)$$

where the white Gaussian noise excitations $\xi_i(t)$ $(i = 1, 2, 3)$ are independent random processes such that $\langle \xi_i(t)\xi_i(t+\tau)\rangle = 2D_i\delta(\tau)$. The corresponding adjoint Fokker-Planck operator is given by the equation

$$\mathcal{L}^*_{FP} = Y\frac{\partial}{\partial X} - ((2\eta - D_1)Y + X)\frac{\partial}{\partial Y} + (D_1 Y^2 + D_2 X^2 + D_3)\frac{\partial^2}{\partial Y^2}, \quad (36)$$

where the variable Y stands for the velocity process $\dot{X}(t)$. It is found that the recursion method terminates the continued fraction representation of $S_{X,X}(\omega)$ and $S_{Y,Y}(\omega)$ exactly. That is, the constructed basis $(u_n)_{n\geq 0}$ is such that $u_n = 0$ for all $n \geq 2$ and

$$S_{X,X}(\omega) = 2\langle X^2\rangle \Re\left\{\frac{1}{j\omega + \dfrac{1}{j\omega + 2\eta - D_1}}\right\},$$

$$S_{Y,Y}(\omega) = 2\langle Y^2\rangle \Re\left\{\frac{1}{j\omega + 2\eta - D_1 + \dfrac{1}{j\omega}}\right\}. \quad (37)$$

The stationary moments are found by generating the moment equations

$$\langle X^2\rangle = \langle Y^2\rangle = \frac{D_3}{2(\eta - D_1) - D_2}. \quad (38)$$

Note that mean-square stability conditions can be determined from Eq. (38); see Ibrahim (1985). In general, spectral densities of linear, time-independent oscillators can be shown to be rational functions of the frequency ω and can therefore always be represented exactly by continued fractions as obtained by the recursion method.

The Single-Well Duffing Oscillator. The important merit of the recursion method involves its application to nonlinear systems. Thus, it is natural to first test its performance on the single-well Duffing oscillator governed by the equation

$$\ddot{X}(t) + 2\eta\dot{X}(t) + X(t) + \epsilon X^3(t) = F(t), \quad (39)$$

where $F(t)$ is a white Gaussian noise such that $\langle F(t)F(t+\tau)\rangle = 2D\delta(\tau)$. The method is applied to determine the displacement spectral density $S_{X,X}(\omega)$. Starting with $u_0(X, Y) = X$, each element of the orthogonal basis $(u_n)_{n\geq 1}$ is a multivariate polynomial in $(X, Y = \dot{X})$ and is readily determined numerically. The sets of coefficients $(a_n)_{n\geq 0}$ and $(b_n)_{n\geq 0}$ are determined from the knowledge of the response stationary moments $\langle X^{2i}Y^{2j}\rangle$ which are known to satisfy the following relationships derived from the exact first-order joint probability density function

$$\langle X^{2i}Y^{2j}\rangle = \langle X^{2i}\rangle\langle Y^{2j}\rangle$$

$$\langle X^{2i}\rangle = \left((2i-3)\frac{D}{2\eta}\langle X^{2i-4}\rangle - \langle X^{2i-2}\rangle\right)/\epsilon, \quad (i \geq 2)$$

$$\langle Y^{2j}\rangle = (2j-1)\frac{D}{2\eta}\langle Y^{2j-2}\rangle, \quad (j \geq 1). \quad (40)$$

The displacement mean square $\langle X^2\rangle = (D/\eta\epsilon)^{1/2}(\Gamma(3/2)/\Gamma(1/2))D_{-3/2}(1/\sqrt{\bar{\epsilon}})/D_{-1/2}(1/\sqrt{\bar{\epsilon}})$, where $\bar{\epsilon} = \epsilon D/\eta$ and $D_\nu(z)$ is the parabolic cylinder function, is evaluated by numerical quadrature. The recursion method as given by Eq. (20)–(23) yields the expressions

$$a_0 = 0,$$

$$a_1 = -2\eta, \quad b_1 = -1 - \epsilon\frac{\langle X^4\rangle}{\langle X^2\rangle},$$

$$a_2 = 0, \qquad b_2 = \epsilon\langle X^2\rangle\left(-3 + \frac{\langle X^4\rangle}{\langle X^2\rangle^2}\right),$$

$$a_3 = -2\eta, \quad b_3 = -3 + 3\epsilon\langle X^2\rangle\left(1 + \frac{\langle X^2\rangle\langle X^6\rangle - \langle X^8\rangle}{\langle X^2\rangle\langle X^6\rangle - \langle X^4\rangle^2}\right),$$

$$\vdots \qquad\qquad \vdots \quad (41)$$

obtained by using the operator $\mathcal{L}^*_{FP}$ of Eq. (33) with $g(X, Y) = 2\eta$ and $f(X) = X + \epsilon X^3$. The resulting continued fraction representation of Eq. (28) leads to sequences of approximations by adopting the termination functions

$$t_{n+1}(j\omega) = 0, \quad \text{or}$$

$$t_{n+1}(j\omega) = 1/2\left(j\omega - a_{n+1} - \sqrt{(j\omega - a_{n+1})^2 - 4b_{n+1}}\right). \quad (42)$$

First, the case $\epsilon = 1.0$, $\eta = D = 0.1$ is treated. Figure 1 shows the resulting approximations obtained by using the square root terminator and taking $n = 2, 4, 6, 8$; they are in excellent agreement with digital simulation data. The latter are obtained by fast Fourier transform of 4096 point records with sampling period of 1/60th of the natural period, and by subsequent averaging of 100 records. In general, numerical experiments show that the smaller the value of the "effective nonlinearity" parameter $\bar{\epsilon} = \epsilon D/\eta$, the faster the convergence. Figure 2 shows the resulting approximations for the value of $\eta = D = 0.1$, and for increasing nonlinearity $\epsilon = 0.1$, 1.0, and $\epsilon = 10.0$, by determining a maximum of 18 terms in the sequences $(a_n)_{n\geq 0}$ and $(b_n)_{n\geq 0}$. The shifting and broadening of the main resonant peak for increasing nonlinearity is in good agreement with

Downloaded 03 May 2010 to 171.66.16.245. Redistribution subject to ASME license or copyright; see http://www.asme.org/terms/Terms_Use.cfm

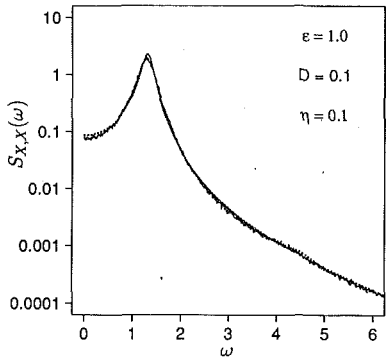


Fig. 1 Spectral response $S_{X,X}(\omega)$ of the single-well Duffing oscillator. Continued fractions approximations with square root terminant, as given by Eq. (28) with n = 2, 4, 6, 8 (dotted lines) and digital simulations (solid line). ϵ = 1.0, D = 0.1, η = 0.1.

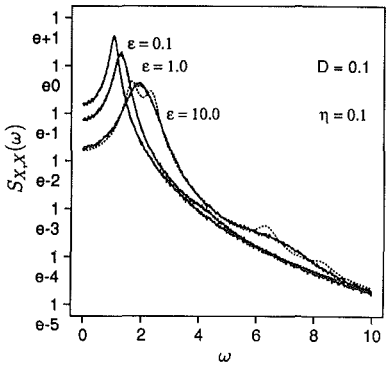


Fig. 2 Spectral response $S_{X,X}(\omega)$ of the single-well Duffing oscillator by continued fraction approximations as given by Eq. (28) (dotted lines). Comparison with digital simulations (solid lines). η = D = 0.1, ϵ = 0.1, 1.0, 10.0. Terminant $t_{n+1}(j\omega)$ = 0 with max n = 18.

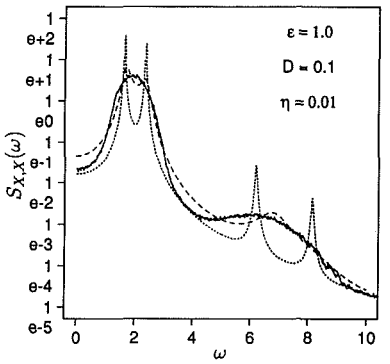


Fig. 3 Spectral response $S_{X,X}(\omega)$ of the single-well Duffing oscillator by continued fraction approximations and digital simulations (solid lines). η = 0.01, D = 0.1, ϵ = 1.0. Terminant $t_{n+1}(j\omega)$ = 0 (dotted lines) and $t_{n+1}(j\omega) = 1/2(j\omega - a_{n+1} - \sqrt{(j\omega - a_{n+1})^2 - 4b_{n+1}})$ (dashed lines) with max n = 18.

digital simulations. Note, however, for ϵ = 10.0, the appearance of a spurious splitting of the main peak, as well as of other small, spurious peaks. For lower values of the damping ratio η, the convergence becomes slower, and the observed spurious splitting phenomenon obtained by choosing $t_{n+1}(j\omega)$ = 0 is noticeably increasing, as shown by Fig. 3, for ϵ = 1.0, D = 0.1, and η = 0.01. The order of truncation in Eq. (28) is fixed to n = 18 and both terminating methods are displayed. The continued fraction approximation with the square root analytic tail yields far better results for spectral densities in comparison with digital simulations, predicting well the main resonant peak in both height and bandwidth, as well as the subsequent flattening of the spectrum for intermediate frequencies. Most methods are known to fail in the low damping limit. When choosing $t_{n+1}(j\omega)$ = 0, it was found numerically that the poles of the constructed rational fractions are located almost nearly on the imaginary axis of the complex plane, that is, located at points $z_i = \epsilon_i \pm j\omega_i$, where $\epsilon_i \approx 0$. The spurious spikes appearing on the approximate spectral density correspond exactly to those frequencies ω_i. The use of the square root termination has the effect of moving these poles away from the immediate vicinity of the imaginary axis, despite the fact the coefficients $(a_n)_{n\geq 0}$ and $(b_n)_{n\geq 0}$ do not seem to tend towards finite asymptotic values. The use of more sophisticated termination schemes taking into account the proper asymptotic behavior of these coefficients could greatly improve the convergence of the recursion method. Note that the tail of the spectral density exhibits in all cases the exact asymptotic shape, since the continued fraction approximation agrees with its $1/\omega$ expansion, as $\omega \to \infty$.

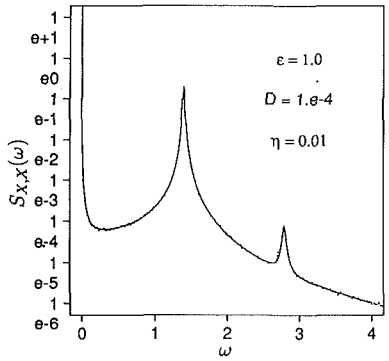


Fig. 4 Spectral response $S_{X,X}(\omega)$ of the double-well Duffing oscillator. ϵ = 1.0, η = 0.01, $D = 10^{-4}$. Results obtained by the recursion method, with $t_{n+1}(j\omega)$ = 0 (n = 10) in Eq. (28) (solid lines), and digital simulations (dotted lines).

The Double-Well Duffing Oscillator. The double-well Duffing oscillator driven by white Gaussian noise, and governed by the equation

$$\ddot{X}(t) + 2\eta\dot{X}(t) - X(t) + \epsilon X^3(t) = F(t), \qquad (43)$$

belongs to the class of systems with multiple positions of stable static equilibrium. The response spectral density $S_{X,X}(\omega)$ possesses some very distinct characteristics, which are now well documented; see, for example, Dykman et al. (1988). The noise-free oscillator response will settle at one or the other of the bottom of the two wells, depending on the initial conditions. The addition of noise to the system will always cause jumps between the two wells, however small the noise intensity is. The J-fraction representation of $S_{X,X}(\omega)$ is determined as in the case of the single-well Duffing oscillator with $\mathcal{L}^*_{FP}$ given by Eq. (33) with $g(X, Y) = 2\eta$ and $f(X) = -X + \epsilon X^3$. The value of the nonlinearity parameter is fixed to ϵ = 1, and the influence of the damping ratio η and the noise intensity D is examined.

The low damping case η = 0.01 is first studied. Figure 4 shows the spectral density $S_{X,X}(\omega)$ for the values of $D = 10^{-4}$. First observed is a peak at the frequency ω = 0. This peak corresponds to the trajectories of transitions between the two stable equilibrium states. The "snap-through" of the oscillator from one well to the other is produced by a constant force, thus creating a maximum at the zero frequency. The smaller the noise intensity, the narrower and higher this peak is. For $D = 10^{-4}$, it is shaped like the Dirac delta function, and could not be well observed by digital simulation. That is, the sample functions could not be generated sufficiently long to observe enough jumps from one potential well to the other, in the case of weak noise intensity. However, this zero-frequency peak was observed by Dykman et al. (1988) by analog simulations even for very small noise intensity. The spectral density also

Downloaded 03 May 2010 to 171.66.16.245. Redistribution subject to ASME license or copyright; see http://www.asme.org/terms/Terms_Use.cfm

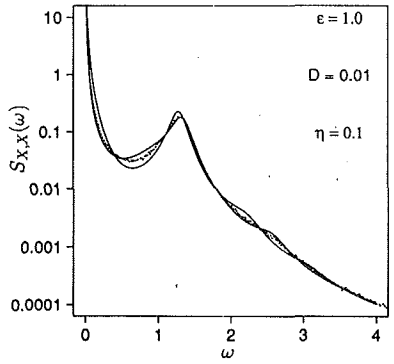


Fig. 5 Same as Fig. 4 for $\epsilon = 1.0$, $\eta = 0.10$, $D = 0.01$. Solid lines display odd and even truncation of J-fraction approximation with $t_{n+1}(j\omega) = 0$ ($n = 10, 11$).

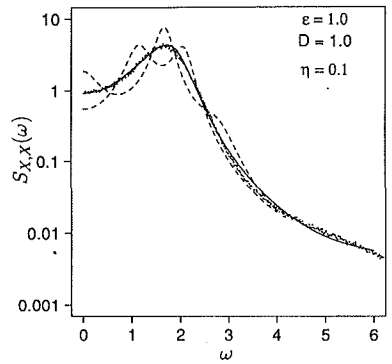


Fig. 6 Comparison between continued fraction approximations with square root terminant (solid line, $n = 10$), with vanishing terminant (dashed lines, $n = 10, 11$), and digital simulations (dotted line) for the double-well Duffing oscillator response, in the case $\epsilon = 1.0$, $\eta = 0.10$, $D = 1.0$

exhibits a peak at the frequency $\omega_1 \approx \sqrt{2}$ which corresponds to the small-amplitude trajectories about one of the equilibrium positions, that is to intra-well vibrations. Also note a peak of much smaller intensity at the frequency $\omega_2 \approx 2\sqrt{2}$.

For the larger value of $\eta = 0.1$, convergence of the J-fraction approximations is improved, as shown in Fig. 5 for the values of $D = 0.01$. Again, as D is increased, the zero-frequency peak broadens and decreases in intensity, while the peak due to intra-well trajectories gradually fuses with lower frequency spectral components due to trajectories in and out of the two wells. However, no distinctive peak is observed for these latter trajectories, as was the case for $\eta = 0.01$. Figure 5 suggests that two consecutive J-fraction approximations obtained with the truncation $t_{n+1}(j\omega) = 0$ seem to give an upper and lower bound for the exact function $S_{X,X}(\omega)$. Figure 6 shows that the use of a square root terminating function can greatly improve the convergence of the sequence of approximations for the case of $\eta = 0.1$ and $D = 1.0$.

The Van der Pol Oscillator. The recursion method is applied to the modified version of the Van der Pol oscillator

$$\ddot{X}(t) + 2\eta(-1 + \epsilon/2(X^2 + \dot{X}^2))\dot{X}(t) + X(t) = F(t), \quad (44)$$

where $F(t)$ is a white Gaussian noise such that $\langle F(t)F(t+\tau)\rangle = 2D\delta(\tau)$. Since the stationary response probability density function is known in a closed form, and is a function of the total energy variable $E = X^2/2 + \dot{X}^2/2$ only, it is advantageous to determine the first-order statistics $\langle \dot{X}^{2i}\dot{X}^{2j}\rangle$ by making the change of variables $X = A\cos\theta$, $\dot{X} = -A\sin\theta$. Specifically,

$$\langle X^{2i}\dot{X}^{2j}\rangle = \langle A^{2i+2j}\rangle \int_0^{2\pi} \cos^{2i}\theta \sin^{2j}\theta \frac{d\theta}{2\pi}$$

$$= \langle A^{2i+2j}\rangle \frac{1}{\pi}\Gamma\left(\frac{2i+1}{2}\right)\Gamma\left(\frac{2j+1}{2}\right)\Gamma(i+j+1) \quad (45)$$

where the amplitude moments can be found recursively from the equation

$$\langle A^{2i}\rangle = \frac{2}{\epsilon}\left[(2i-2)\frac{D}{2\eta}\langle A^{2i-4}\rangle + \langle A^{2i-2}\rangle\right], \quad (i \geq 2). \quad (46)$$

With the operator $\mathcal{L}^*_{FP} = Y\partial/\partial X - (2\eta(-1 + \epsilon(X^2/2 + Y^2/2))Y + X)\partial/\partial Y + D\partial^2/\partial Y^2$, and starting with $u_0(X, Y) = X$, the following coefficients are found for the J-fraction representation of $S_{X,X}(\omega)$ by the recursion method of Eq. (20)–(23)

$$a_0 = 0, \qquad b_1 = -1$$

$$a_1 = -2\eta\left(-1 + \frac{\epsilon}{2}\frac{\langle A^4\rangle}{\langle A^2\rangle}\right), \quad b_2 = -\eta\epsilon\left(6D + 3\eta\frac{\langle A^4\rangle}{\langle A^2\rangle} + \eta\epsilon\frac{\langle A^4\rangle^2}{\langle A^2\rangle^2} - \frac{5}{2}\eta\epsilon\frac{\langle A^6\rangle}{\langle A^2\rangle}\right),$$

$$\vdots \qquad \vdots \quad (47)$$

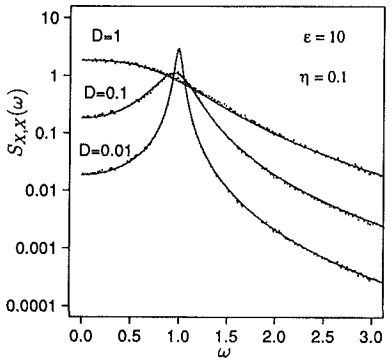


Fig. 7 Spectral response $S_{X,X}(\omega)$ of the modified Van der Pol oscillator governed by the Eq. (44). $\epsilon = 10$, $\eta = 0.10$, $D = 0.01, 0.1, 1.0$. Results obtained by the recursion method with $t_{n+1}(j\omega) = 0$, $n = 8$ (solid lines) and digital simulations (dotted lines).

The recursion method yields rapidly converging J-fractions approximations of $S_{X,X}(\omega)$ for all cases shown in Fig. 7 for the combination of parameters $\epsilon = 10$, $\eta = 0.10$, $D = 0.01, 0.1, 1.0$. A maximum of $n = 8$ stages in the J-fractions are evaluated, with $t_{n+1}(j\omega) = 0$. All cases agree very well with results obtained by digital simulations. For sufficiently small values of D, $S_{X,X}(\omega)$ is sharply peaked at $\omega = 1$ over a very narrow bandwidth. As D is increased, this resonant peak gradually broadens, yet remains centered at $\omega = 1$ for all cases shown in Fig. 7, as opposed to the systems with nonlinear stiffness previously analyzed. For D being sufficiently large, the spectrum flattens out and the resonant peak eventually vanishes.

When the Van der Pol oscillator is taken in the form

$$\ddot{X}(t) + 2\eta(-1 + \epsilon X^2)\dot{X}(t) + X(t) = F(t), \quad (48)$$

no closed-form expression is available for the stationary first-order response probability density function $p_s(X, \dot{X})$. If the parameters D and η are small, the technique of stochastic averaging can be used to derive an approximate expression for $p_s(X, \dot{X})$. Referring to the review article by Roberts and Spanos (1986), it can be shown that this expression is

$$p_s(X,\dot{X}) = N\exp\left(\frac{\eta}{D}(X^2 + \dot{X}^2) - \frac{\eta\epsilon}{8D}(X^2 + \dot{X}^2)^2\right). \quad (49)$$

Approximate values for the J-fraction representation of $S_{X,X}(\omega)$

Downloaded 03 May 2010 to 171.66.16.245. Redistribution subject to ASME license or copyright; see http://www.asme.org/terms/Terms_Use.cfm

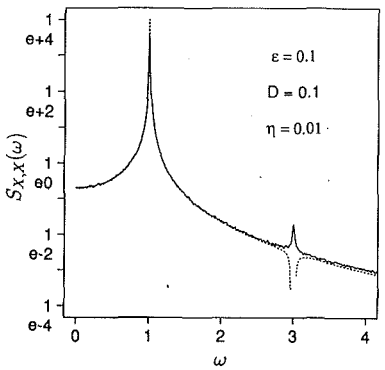


Fig. 8 Spectral response $S_{X,X}(\omega)$ of the Van der Pol oscillator governed by Eq. (48). $\epsilon = 0.1$, $D = 0.1$, $\eta = 0.01$. Results obtained by the recursion method with $t_{n+1}(j\omega) = 0$, $n = 8$, (solid lines) and digital simulations (dotted lines). The joint probability density function $p_s(X, \dot{X})$ used in the recursion method is obtained by the method of stochastic averaging.

can then be derived by using the operator $\mathcal{L}^*_{FP} = Y\partial/\partial X - (2\eta(-1 + \epsilon X^2)Y + X)\partial/\partial Y + D\partial^2/\partial Y^2$. Pertinent results are shown in Fig. 8 for $\epsilon = 0.1$, $\eta = 0.01$, and $D = 0.1$. The analytical solutions agree very well with digital simulation data. However, the approximations cannot reproduce the secondary peak at $\omega \approx 3$ and negative values of $S_{X,X}(\omega)$ appear around the vicinity of this frequency. This is due to the fact that the recursion method is used with the exact expression of the adjoint Fokker-Planck operator, but with an approximate expression of the corresponding scalar product. A smooth spectrum can be obtained by using an "averaged" adjoint operator corresponding to the "averaged" expression of $p_s(X, \dot{X})$ of Eq. (49). The peak at $\omega \approx 3$ corresponds to higher harmonics in the response of the noise-free Van der Pol oscillator, which are not taken account in the method of stochastic averaging.

Concluding Remarks

The recursion method gives sequences of J-fraction approximations of power spectral densities without requiring the determination of the response transition probability density function. It is easy to use and considerably faster than digital simulations. Most examples considered herein used a closed-form expression of the first-order stationary probability density function. Future work can be devoted to the use of approximate techniques, such as the aforementioned method of stochastic averaging, to evaluate J-fraction coefficients, when the stationary density is not known explicitly. Other truncating schemes taking into account the proper asymptotic behavior of these coefficients can also be investigated to improve the rate of convergence for systems with low damping.

Collectively, the proposed approach is quite appealing since it is applicable to a broad class of nonlinear systems subject to white noise excitation, and can be used to find the spectrum of the system response by requiring only the corresponding stationary probability density function of the response.

Acknowledgment

The partial support of this work by the grant DE-FG05-91ER14215 from the Department of Energy is gratefully acknowledged.

References

Atkinson, J. D., 1973, "Eigenfunction Expansion for Randomly Excited Non-Liner Systems," *Journal of Sound and Vibration*, Vol. 30 pp. 153–172.

Baker, G. A., and Graves-Morris, P., 1981, *Padé Approximants*, Addison-Wesley, Reading, PA.

Bixon, M., and Zwanzig, R., 1971, "Brownian Motion of a Nonlinear Oscillator," *Journal of Statistical Physics*, Vol. 3, pp. 245–260.

Budgor, A. B., Lindenberg, K., and Shuler, K. E., 1976, "Studies in Nonlinear Stochastic Processes. II. The Duffing Oscillator Revisited," *Journal of Statistical Physics*, Vol. 15, pp. 375–391.

Caughey, T. K., and Dienes, J. K., 1961, "Analysis of a Nonlinear First-Order System with a White Noise Input," *Journal of Applied Physics*, Vol. 11, pp. 2476–2479.

Crandall, S. H., 1963, "Perturbation Technique for Random Vibration of Non-linear System," *Journal of the Acoustical Society of America*, Vol. 35, pp.1700–1705.

Crandall, S. H., 1973, "Correlations and Spectra of Nonlinear System Response," *Nonlinear Vibration Problems (Zagadnienia Drgań Nielinowych)*, Vol. 14, pp. 39–53.

Dykman, M. I., Mannella, R., McClintock, P. V. E., Moss, F., and Soskin, S. M., 1988, "Spectral Density of Fluctuations of a Double-Well Duffing Oscillator Driven by White Noise," *Physical Review A*, Vol. 37, pp. 1303–1313.

Fronzoni, L., Grigolini, P., Mannella, R., and Zambon, B., 1985, "The Duffing Oscillator in the Low-Friction Limit: Theory and Analog Simulation," *Journal of Statistical Physics*, Vol. 41, pp. 553–579.

Gardiner, C. W., 1983, *Handbook of Stochastic Methods*, Springer-Verlag, New York.

Ibrahim, R. A., 1985, *Parametric Random Vibration*, John Wiley and Sons, New York.

Matsuo, K., 1978, "Brownian Motion of Nonlinear Oscillators: The Projection Operator Method and Its Application to a Double-Well-Potential Oscillator," *Journal of Statistical Physics*, Vol. 18, pp. 535–555.

Mori, H., 1965, "A Continued Fraction Representation of Time-Correlation Functions," *Progress of Theoretical Physics*, Vol. 34, pp. 399–416.

Morton, J. B., and Corrsin, S., 1970, "Consolidated Expansions for Estimating the Response of a Randomly Driven Nonlinear Oscillator," *Journal of Statistical Physics*, Vol. 2, pp. 153–194.

Pettifor, D. G., and Weaire, D. L., eds., 1985, *The Recursion Method and Its Applications*, Springer-Verlag, New York.

Reinhall, P. G., and Miles, R. N., 1989, "Effect of Damping and Stiffness on the Random Vibration of Non-Linear Periodic Plates," *Journal of Sound and Vibration*, Vol. 132, pp.33–43.

Risken, H., 1989, *The Fokker-Planck Equation*, Springer-Verlag, New York.

Roberts, J. B., and Spanos, P. D., 1986, "Stochastic Averaging: An Approximate Method of Solving Random Vibration Problems," *International Journal of Nonlinear Mechanics*, Vol. 21, pp. 111–134.

Roberts, J. B., and Spanos, P. D., 1990, *Random Vibration and Statistical Linearization*, John Wiley and Sons, New York.

Shohat, J. A., and Tamarkin, J. D., 1943, *The Problem of Moments* (Mathematical Surveys, No. 1), American Mathematical Society, New York.

Wall, H. S., 1948, *The Analytic Theory of Continued Fractions*, Von Nostrand, New York.

Zwanzig, R., 1961, "Statistical Mechanics of Irreversibility," *Lectures in Theoretical Physics (Boulder)*, Vol. 3, Interscience Publishers, New York.

Downloaded 03 May 2010 to 171.66.16.245. Redistribution subject to ASME license or copyright; see http://www.asme.org/terms/Terms_Use.cfm

C. D. Rahn
Assistant Professor,
Department of Mechanical Engineering,
Clemson University,
Clemson, SC 29634
Assoc. Mem. ASME

C. D. Mote, Jr.
FANUC Chair in Mechanical Systems.
Mem. ASME

Department of Mechanical Engineering,
University of California, Berkeley,
Berkeley, CA 94720

On the Stability of the Damped Hill's Equation With Arbitrary, Bounded Parametric Excitation

The minimum damping for asymptotic stability is predicted for Hill's equation with any bounded parametric excitation. It is shown that the response of Hill's equation with bounded parametric excitation is exponentially bounded. The parametric excitation maximizing the bounding exponent is identified by time optimal control theory. This maximal bounding exponent is balanced by viscous damping to ensure asymptotic stability. The minimum damping ratio is calculated as a function of the excitation bound. A closed form, more conservative estimate of the minimum damping ratio is also predicted. Thus, if the general (e.g., unknown, aperiodic, or random) parametric excitation of Hill's equation is bounded, a simple, conservative estimate of the damping required for asymptotic stability is given in this paper.

1 Introduction

Hill (1886) introduced a linear, time-varying, second-order, ordinary differential equation during his studies of motions of the moon. It became the fundamental equation of parametrically excited systems (Magnus and Winkler, 1966; Nayfeh and Mook, 1979). Under certain parametric excitations, continuing growth in the response gives unstable solutions. Introduction of viscous damping can asymptotically stabilize some of these solutions.

Different approaches have been taken to predict the stability of parametrically excited systems. Floquet (1883) showed that integrating the response over one period of the excitation for a set of independent initial conditions determines a fundamental matrix whose eigenvalues characterize the stability of the system. Hill (1886) estimated an infinite determinant to predict the stability of Hill's equation. Starzhinskii (1955) summarized work on functional constraints on the parametric excitation that guarantee stability of response. For Hill's equation, Liapunov (1949) showed that if the mean of positive parametric excitation is less than four times it frequency, the response is stable. Yakubovich and Starzhinskii (1975) determined a similar inequality for the viscously damped Hill's equation. Finally, perturbation methods have been used extensively in parametric excitation problems to predict stability and response (Nayfeh, 1981). None of these approaches, however, can predict the stability of the damped Hill's equation with bounded but unknown, aperiodic, or random parametric excitation.

In this paper, the maximum growth from bounded parametric excitation is balanced by damping to achieve asymptotic stability. Two theorems are presented that relate maximum growth state trajectories and minimum time state trajectories. Time optimal control theory generates the parametric excitation that causes maximum growth in minimum time. Following Yakubovich and Starzhinskii (1975), application of Pontryagin's Minimum Principle (Athans and Falb, 1966) with a time optimal functional yields the parametric excitation maximizing response. This excitation is bang-bang with a period equal to one-half the period of the response.

Due to the periodicity of the excitation, the maximum response is exponentially bounded and can be balanced as needed by the exponential decay provided by viscous damping. This balance condition gives the minimum damping for asymptotic stability, a sufficient condition for stability of Hill's equation with arbitrary, bounded parametric excitation. An upper bound on the maximal exponent provides an approximate, closed-form relation between the minimum damping to guarantee asymptotic stability and the bound on the parametric excitation.

2 Problem Statement

The viscously damped Hill's equation is

$$\frac{d^2z}{dt^2}+2\zeta\omega_0\frac{dz}{dt}+(\omega_0^2+Q(t))z=0 \tag{1}$$

where the damping coefficient $\zeta \geq 0$, the average of the stiffness term is ω_0^2, and the parametric excitation $Q(t)$ is bounded,

$$\left|\frac{Q(t)}{\omega_0^2}\right| \leq \Delta Q. \tag{2}$$

Substitution of

Contributed by the Applied Mechanics Division of THE AMERICAN SOCIETY OF MECHANICAL ENGINEERS for presentation at the First Joint ASCE-EMD, ASME-AMD, SES Meeting, Charlottesville, VA, June 6–9, 1993.

Discussion on this paper should be addressed to the Technical Editor, Professor Lewis T. Wheeler, Department of Mechanical Engineering, University of Houston, Houston, TX 77204-4792, and will be accepted until four months after final publication of the paper itself in the ASME JOURNAL OF APPLIED MECHANICS.

Manuscript received by the ASME Applied Mechanics Division, Sept. 18, 1991; final revision, July 10, 1992. Associate Technical Editor: D. J. Inman.

Paper No. 93-APM-30.

Copyright © 1993 by ASME
Downloaded 03 May 2010 to 171.66.16.245. Redistribution subject to ASME license or copyright; see http://www.asme.org/terms/Terms_Use.cfm

$$z(t) = y(t)e^{-\zeta\omega_0 t}, \tag{3}$$

$$\tau = \omega_0 t\sqrt{1-\zeta^2},\ u(\tau) = \frac{Q(\tau/\omega_0\sqrt{1-\zeta^2})}{\omega_0^2(1-\zeta^2)} \tag{4}$$

into (1) yields

$$\ddot{y} + (1+u(\tau))y = 0 \tag{5}$$

where $(\dot{}) = d(\ )/d\tau$. It further is assumed that

$$|u(\tau)| \le \Delta u = \frac{\Delta Q}{1-\zeta^2} < 1 \tag{6}$$

In state space form (5) becomes

$$\dot{x} = \begin{bmatrix} 0 & 1 \\ -(1+u(\tau)) & 0 \end{bmatrix} x, \tag{7}$$

where $\mathbf{x} = [y, \dot{y}]'$.

The first objective of this paper is to determine whether the maximum y is exponentially bounded and, if so, the value of the bound as a function of Δu. For the maximal bounding exponent, β^*, then

$$|y(\tau)| \le Ce^{\beta^*\tau}, \tag{8}$$

and (3) gives

$$|z(t)| = |y(\omega_0 t\sqrt{1-\zeta^2})|e^{-\zeta\omega_0 t} \le Ce^{(\beta^*\sqrt{1-\zeta^2}-\zeta)\omega_0 t}, \tag{9}$$

where C is a constant that depends on initial conditions. The absolute value of the response of z is bounded above by a decaying exponential if

$$\zeta > \zeta_{\min} = \frac{\beta^*}{\sqrt{1+\beta^{*2}}} \tag{10}$$

and, since $z \to 0$ implies that $dz/dt \to 0$, the response of (1) is asymptotically stable.

3 Maximum Growth Trajectories

Two theorems are presented relating maximum growth and minimum time state trajectories. The first proves existence of maximum growth functions for Hill's equation with bounded parametric excitation. The second shows the least minimum time state trajectories are maximum growth state trajectories.

Let $\varphi(\tau, \tau_0, \mathbf{x}_0, u(\tau))$ be any state trajectory starting from $\mathbf{x}_0$ at time τ_0. The φ satisfies (7) for a given $u(\tau)$ satisfying (6). A maximum growth function $g(\tau, \tau_0, \mathbf{x}_0)$ has the property that

$$|y(\tau)| \le \sqrt{y^2+\dot{y}^2} = \|\mathbf{x}(\tau)\| = \|\varphi(\tau,\tau_0,\mathbf{x}_0,u\| \le g(\tau,\tau_0,\mathbf{x}_0) \tag{11}$$

for all $u(\tau)$ satisfying (6).

Theorem 1. *If the parametric excitation of Hill's equation is bounded, then there exist maximum growth functions.*

Proof: The time rate of change of $\|\mathbf{x}\|$ is calculated, bounded, and integrated to give a $g(\tau, \tau_0, \mathbf{x}_0)$.

$$\frac{d}{dt}\|\mathbf{x}\| = \frac{y\dot{y}+\dot{y}\ddot{y}}{\sqrt{y^2+\dot{y}^2}} = \frac{-u(\tau)y\dot{y}}{\|\mathbf{x}\|}$$

$$\le \frac{\Delta u|y||\dot{y}|}{\|\mathbf{x}\|}$$

$$\le \frac{\Delta u\|\mathbf{x}\|^2}{\|\mathbf{x}\|}$$

$$= \Delta u\|\mathbf{x}\| \tag{12}$$

Integration of (12) gives

$$\|\mathbf{x}\| \le \|\mathbf{x}_0\|e^{\Delta u(\tau-\tau_0)} = g(\tau,\tau_0,\mathbf{x}_0), \tag{13}$$

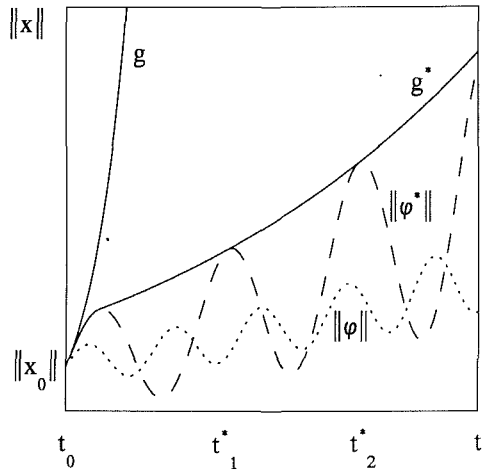


Fig. 1 History of the norm of the state $\|\mathbf{x}\|$. The norm of a state trajectory $\|\varphi\|$, the norm of a maximum growth state trajectory $\|\varphi^*\|$, and two maximum growth functions are plotted. The least maximum growth function, g^*, is tangent to the maximum growth state trajectories at several times t_i^*.

a maximum growth function for Hill's equation with bounded parametric excitation. □

The least $g(\tau, \tau_0, \mathbf{x}_0)$ that is strictly increasing is termed the least maximum growth function, $g^*(\tau, \tau_0, \mathbf{x}_0)$ (see Fig. 1). This g^* is at least tangent to one state trajectory at one point. The maximum growth state trajectories, $\varphi^*(\tau, \tau_0, \mathbf{x}_0, u^*)$, have the property

$$\|\varphi^*(\tau^*,\tau_0,\mathbf{x}_0,u^*)\| = g^*(\tau^*,\tau_0,\mathbf{x}_0) \tag{14}$$

for at least one $\tau^* \neq 0$.

Minimum time trajectories elapse the least time from a given $\mathbf{x}_0$ to a given $\mathbf{x}_f$. Of the many minimum time trajectories from $\|\mathbf{x}_0\|$ to $\|\mathbf{x}_f\|$, there is one least minimum time trajectory.

Theorem 2. *Maximum growth state trajectories are least minimum time state trajectories.*

Proof by Contradiction: Assume there exists a state trajectory, $\varphi(\tau, \tau_0, \mathbf{x}_0, u)$, whose norm equals $g^*(\tau^*, \tau_0, \mathbf{x}_0)$ at $\tau_1 < \tau^*$, or

$$\|\varphi(\tau_1<\tau^*,\tau_0,\mathbf{x}_0,u)\| = g^*(\tau^*,\tau_0,\mathbf{x}_0). \tag{15}$$

The least maximum growth function monotonically increases in time:

$$\|\varphi(\tau_1,\tau_0,\mathbf{x}_0,u(\tau))\| = g^*(\tau^*,\tau_0,\mathbf{x}_0) > g^*(\tau_1,\tau_0,\mathbf{x}_0). \tag{16}$$

At time τ_1, φ violates the definition of a maximum growth function (11) and therefore φ does not exist, contradicting the initial assumption. □

Therefore, an increasing function that upper bounds the norm of the least minimum time state trajectories is a maximum growth function for Hill's equation.

4 Minimum Time State Trajectories

Minimum time state trajectories minimize the cost functional

$$J(u) = \int_{\tau_0}^{\tau_f} p_0 d\tau = p_0(\tau_f - \tau_0) \tag{17}$$

where p_0 is a positive constant.

The Minimum Principle of Pontryagin (Athans and Falb (1966)) provides a necessary condition for optimality of $u(\tau)$. The Minimum Principle states that $u^*(\tau)$ minimizes J if

$$H(\mathbf{x},\mathbf{p},u^*) = \min_{\forall u\in U} H(\mathbf{x},\mathbf{p},u) = 0, \tag{18}$$

Downloaded 03 May 2010 to 171.66.16.245. Redistribution subject to ASME license or copyright; see http://www.asme.org/terms/Terms_Use.cfm

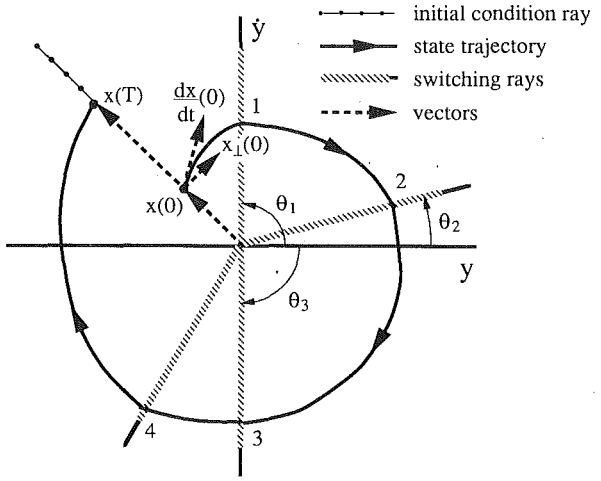


Fig. 2 Schematic of a phase plane trajectory of Hill's equation with bang-bang parametric excitation. The state trajectory starts on an initial condition ray, orbits the origin in a clockwise direction, and finishes on the same ray. Switches 1-4 occur on switching rays that emanate from the origin.

where H is the Hamiltonian and U is the set of all admissible $u(\tau)$.

For Hill's equation, the Hamiltonian is

$$H(\mathbf{x},\mathbf{p},u) = p_0 + p_1\dot{y} - (1-u(\tau))p_2 y, \tag{19}$$

where $\mathbf{p} = [p_1, p_2]'$ is the co-state vector with dynamics

$$\dot{\mathbf{p}} = \begin{bmatrix} 0 & (1+u(\tau)) \\ -1 & 0 \end{bmatrix} \mathbf{p} \tag{20}$$

The set U includes all functions satisfying the constraint (6). The optimal $u(\tau)$, satisfying the constraint and minimizing (19), is

$$u^*(\tau) = \Delta u \ \text{sign}(p_2 y). \tag{21}$$

It is a bang-bang function that switches between $\pm\Delta u$ when y or p_2 changes sign. No singular trajectories exist because $p_2 y$ cannot be identically zero without $\mathbf{p}$ or $\mathbf{x}$ identically zero.

The optimal excitation (21) is not an explicit function of the state. The p_2 switches cannot be calculated without the initial conditions on the costate. The ambiguity in $u^*(\tau)$ allows the time optimal solution to cover all possible initial and final states.

5 Observations

The following observations pertain to Hill's equation with the parametric excitation given in (21).

Observation 1. Starting from an initial condition on a ray emanating from the origin, the state trajectories of $\mathbf{x}$ *and* $\mathbf{p}$ *circle the phase plane clockwise and recross the ray after one cycle.*

For $\mathbf{x}_\perp = [\dot{y}, -y]'$, a vector pointing in the clockwise direction, Fig. 2 shows that the component of $d\mathbf{x}/dt$ in the $\mathbf{x}_\perp$ direction is always positive, or

$$\mathbf{x}_\perp' \frac{d\mathbf{x}}{dt} = \dot{y}^2 + (1+u(\tau))y^2 > 0 \tag{22}$$

This is similarly true for $\mathbf{p}$.

Observation 2. *The responses of* $\mathbf{x}$ *and* $\mathbf{p}$ *are scale invariant.* Let

$$\mathbf{x} = K_x \mathbf{x}^*, \ \mathbf{p} = K_p \mathbf{p}^* \tag{23}$$

where K_x and K_p are arbitrary, positive constants. Substitution into (21)

$$u^*(\tau) = \Delta u \ \text{sign}(K_x K_p p_2^* y^*) = \Delta u \ \text{sign}(p_2^* y^*) \tag{24}$$

shows the optimal excitation is unaffected by scale changes. Substitution of (24) and (23) into (7) and (20) gives (7) and (20) in the variables $\mathbf{x}^*$ and $\mathbf{p}^*$. Thus the dynamics of $\mathbf{x}$ and $\mathbf{p}$ are also scale invariant. As a result, the phase plane can be arbitrarily contracted (or dilated) without changing the shape of the $\mathbf{x}$ and $\mathbf{p}$ trajectories.

Observation 3.. *Switching points lie on rays that emanate from the origin.*

The optimal excitation is bang-bang, with regions in the phase plane of constant u and switching points where u changes sign. With u constant, $\mathbf{x}$ and $\mathbf{p}$ follow elliptical trajectories. The aspect ratios of the ellipses depend on u. For scale invariant phase plane trajectories, the switching points lie on straight lines or rays emanating from the origin.

Observation 4. *The optimal parametric excitation is periodic with four switches per cycle.*

In each phase plane sector of constant u the system response is that of a harmonic oscillator. The time required to cross a sector is amplitude independent, making $u^*(\tau)$ periodic. $\mathbf{x}$ and $\mathbf{p}$ oscillate at the same frequency between switches, giving four switches per cycle of $\mathbf{x}$: two when $y = 0$ and two more when $p_2 = 0$.

6 Locating the p_2 Switching Rays in the Phase Plane

By Floquet theory, the periodicity of $u^*(\tau)$ guarantees that the maximum response is exponentially bounded. The least minimum time trajectory has the largest bounding exponent. In this section we find the angles of the p_2 switching rays that give the maximal bounding exponent.

Define the energy norm

$$\|\mathbf{x}\|_e = \sqrt{(1+u(t))y^2 + \dot{y}^2}, \tag{25}$$

and the two natural frequencies

$$\omega_+ = \sqrt{1+\Delta u}, \ \omega_- = \sqrt{1+\Delta u}. \tag{26}$$

The energy norm is constant between switches, and it jumps by

$$\frac{\|\mathbf{x}(t_s^+)\|_e}{\|\mathbf{x}(t_s^-)\|_e} = \sqrt{\frac{\cos^2(\theta)u(t_s^+)+1}{\cos^2(\theta)u(t_s^-)+1}}, \tag{27}$$

at a switching time, t_s. θ is the angle of the switching ray in the phase plane. The gain per cycle is

$$\|\mathbf{x}((k+1)T)\|_e = \sqrt{\left\{\prod_{i=1}^{4} \frac{\cos^2(\theta_i)u(t_{si}^+)+1}{\cos^2(\theta_i)u(t_{si}^-)+1}\right\}} \|\mathbf{x}(kT)\|_e$$
$$= \sqrt{\lambda}\|\mathbf{x}(kT)\|_e \tag{28}$$

where k is the cycle number, T is the cycle time, and λ is the gain.

The bounding exponent is

$$\beta = \frac{1}{2T} \ln(\lambda) \tag{29}$$

with

$$T = \sum_{i=1}^{4} \frac{1}{\omega} \text{atan}\left(\frac{\tan(\theta_i) - \tan(\theta_{i+1})}{\omega + \tan(\theta_i)\tan(\theta_{i+1})/\omega}\right) \tag{30}$$

where ω is ω_- or ω_+ depending on the trajectory sector.

Two switches occur at $y = 0$ giving $\theta_1 = \pi/2$ and $\theta_3 = -\pi/2$. The switching line $y = 0$ divides the phase plane into antisymmetric halves. Locating θ_2 in the right half-phase plane simultaneously locates θ_4 in the left. Therefore, the two p_2 switching rays are colinear, forming one switching line at angle $\theta = \theta_2 = \theta_4 - \pi$. The period of $u^*(\tau)$ equals $T/2$.

Downloaded 03 May 2010 to 171.66.16.245. Redistribution subject to ASME license or copyright; see http://www.asme.org/terms/Terms_Use.cfm

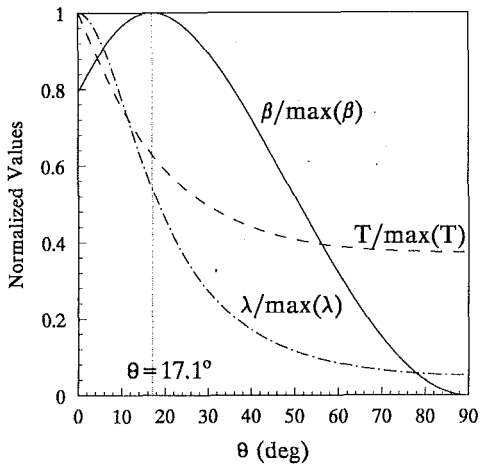


Fig. 3 The normalized values of β, λ, and T with $\Delta u = .9$. $\beta = \beta^*$ at $\theta = 17.1$ deg.

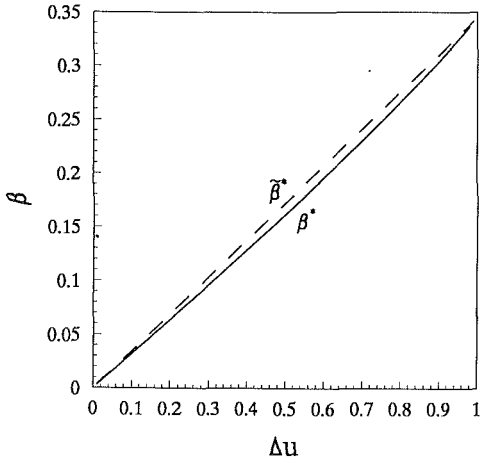


Fig. 4 The maximal bounding exponent, β^*, and the approximate maximal bounding exponent, $\tilde{\beta}^*$

Simplifying (28) and (30) for one-half a cycle of $\mathbf{x}$, with one switch at $\theta_1 = \pi/2$, and the other at $\theta_2 = \theta$ gives

$$\lambda(\theta,\Delta u) = \frac{1+\cos^2(\theta)\Delta u}{1-\cos^2(\theta)\Delta u}, \tag{31}$$

$$T(\theta,\Delta u) = \frac{1}{\omega_-}\operatorname{atan}\left(\frac{\omega_-}{\tan(\theta)}\right) + \frac{1}{\omega_+}\left\{\pi - \operatorname{atan}\left(\frac{\omega_+}{\tan(\theta)}\right)\right\} \tag{32}$$

The bounding exponent β in (29) is a function of λ and T which, by (31) and (32), are functions of θ and Δu. For given Δu, the $\theta = \theta^*$ maximizing $\beta = \beta^*$ can be found. The normalized λ, T, and β as functions of θ with $\Delta u = .9$ are shown in Fig. 3. T and λ are maximums at $\theta = 0$. β is maximum at approximately 17.1 deg. At $\theta = 90$ deg the two switching lines cancel, λ is unity, and β is zero.

Differentiation of (29) with respect to θ shows the maximal bounding exponent, β^*, occurs at

$$\frac{\lambda' T}{\lambda T'} - \ln(\lambda) = 0 \tag{33}$$

or, after simplification,

$$\beta^* = \frac{\lambda'}{2\lambda T'} = \tan(\theta^*) \tag{34}$$

where $(\,)' = \partial(\,)/\partial\theta$. Substitution of (34) into (33) gives

$$2\beta^*\left\{\frac{1}{\omega_-}\operatorname{atan}\left(\frac{\omega_-}{\beta^*}\right) + \frac{1}{\omega_+}\left(\pi - \operatorname{atan}\left(\frac{\omega_+}{\beta^*}\right)\right)\right\} - \ln\left(\frac{\beta^{*2}+\omega_+^2}{\beta^{*2}+\omega_-^2}\right) = 0. \tag{35}$$

From Fig. 3, β has only one maximum at $\theta = \theta^*$. Accordingly, (35) has only one solution β^*. This solution, found using a Newton-Raphson numerical method, is the solid curve in Fig. 4.

The two characteristic exponents associated with Hill's equation have opposite sign (Sanchez (1968)). The least minimum time trajectories are linear combinations of the two fundamental solutions

$$\mathbf{x}_1(\tau) = \mathbf{v}_1(\tau)e^{\beta^*\tau} \tag{36}$$

$$\mathbf{x}_2(\tau) = \mathbf{v}_2(\tau)e^{-\beta^*\tau} \tag{37}$$

or

$$\varphi^*(\tau,0,\mathbf{x}_0,u^*) = a_1\mathbf{v}_1(\tau)e^{\beta^*\tau} + a_2\mathbf{v}_2(\tau)e^{-\beta^*\tau} \tag{38}$$

where $\mathbf{v}_1$ and $\mathbf{v}_2$ have period $T/2$ and the a_i depend on initial conditions. The norm of φ^* is bounded by

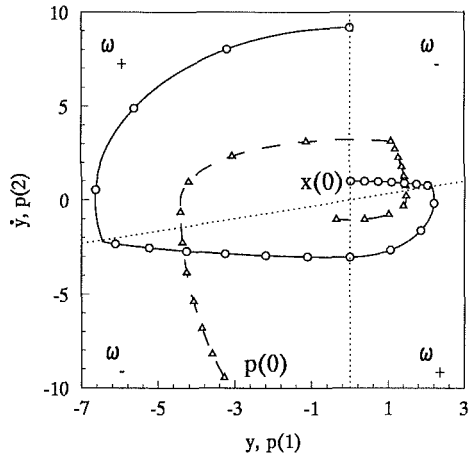


Fig. 5 The state ($\circ$) and costate (Δ) under optimal excitation. Switches occur when y or p_2 equal zero. The zero crossings occur on switching lines (dotted) for the state

$$\|\varphi^*(\tau,0,\mathbf{x}_0,u^*)\| \le \left(|a_1| \max_{\tau\in[0,T/2]}(\|\mathbf{v}_1(\tau)\|) + |a_2| \max_{\tau\in[0,T/2]}(\|\mathbf{v}_2(\tau)\|)\right)e^{\beta^*\tau} = Ce^{\beta^*\tau}. \tag{39}$$

By Theorem 2, an upper bound on the norm of the least minimum time trajectories is a maximum growth function. Thus, by (39) and (11), the bound in (8) is found.

The extreme cases of Δu are now examined. First, with $\Delta u = 0$, $\beta^* = 0$. Second, if $\Delta u \to 1$, (35) becomes

$$2 + \sqrt{2}\beta^*\left(\pi - \operatorname{atan}\left(\frac{\sqrt{2}}{\beta^*}\right)\right) - \ln\left(1 + \frac{2}{\beta^{*2}}\right) = 0 \tag{40}$$

whose solution is $\beta^*(1) = .34455 = M$.

The phase plane trajectories of the state and costate for one cycle of $\mathbf{x}$ under optimal excitation are shown in Fig. 5 for $\Delta u = .9$ and $\mathbf{x}(0) = [0, 1]'$. The co-state initial condition causes p_2 to vanish when $\mathbf{x}$ crosses the first switching line. The circles and triangles, demarking twenty equal time intervals, show that the switching lines compress the regions in the phase plane of low frequency (ω_-), reducing the cycle time. At the end of one cycle of $\mathbf{x}$ and $\mathbf{p}$, two periods of $u^*(\tau)$ have been completed. If p_0 is chosen to be 3.278, the Hamiltonian is zero throughout the cycle.

In Fig. 6, the characteristic exponents of three parametric excitations are compared to the maximal bounding exponent for given Δu. They include the maximum Mathieu excitation (Nayfeh and Mook (1979)),

Downloaded 03 May 2010 to 171.66.16.245. Redistribution subject to ASME license or copyright; see http://www.asme.org/terms/Terms_Use.cfm

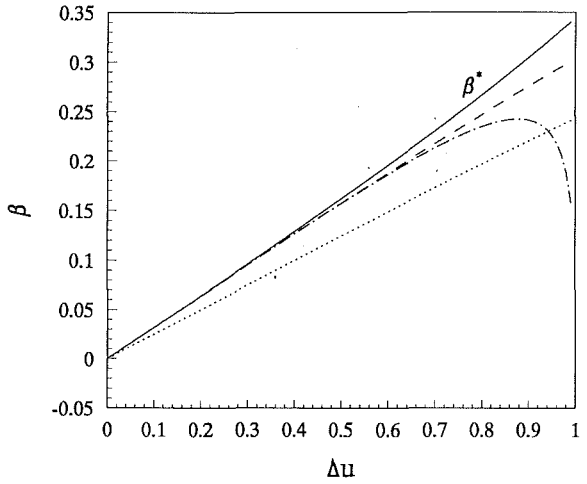


Fig. 6 β^* **(solid line) and the characteristic exponents of the maximum Miessner excitation (dashed line), maximum gain excitation (dash-dotted line), and maximum Mathieu excitation (dotted line)**

$$u(\tau) = \Delta u \sin(2\tau), \tag{41}$$

and two switching excitations

$$u(\tau) = \begin{cases} \Delta u & 0 < \tau < T_1 \\ -\Delta u & T_1 < \tau < T_1 + T_2 \\ \Delta u & T_1 + T_2 < \tau < 2T_1 + T_2 \\ \vdots & \end{cases} \tag{42}$$

the maximum Meissner excitation (Magnus and Winkler, 1966), when $T_1 = T_2 = \pi/2$, and the maximum gain ($\theta = 0$) excitation, when $T_1 = \pi/(2\omega_+)$ and $T_2 = \pi/(2\omega_-)$. For each excitation, the equations of motion are integrated over one period of the excitation for two independent initial conditions and the maximum eigenvalue of the computed fundamental matrix is calculated. β is calculated from the log of this eigenvalue divided by the period of the excitation.

The β of the maximum Meissner and maximum λ switching excitations are nearly equal to β^* for $\Delta u < .25$. For $\Delta u > .25$, β^* exceeds the other two. The Mathieu equation characteristic exponent is the smallest except for $\Delta u > .94$ where it exceeds the maximum λ case. As $\Delta u \to 1$, the period of the maximum λ excitation $\to \infty$ and its $\beta \to 0$.

7 Minimum Damping for Asymptotic Stability

The minimum damping for asymptotic stability is determined from the maximal bounding exponent. To find $\zeta_{\min}$ as a function of ΔQ we simultaneously satisfy (10) and (35):

$$\zeta_{\min} = \frac{\beta^*}{\sqrt{1+\beta^{*2}}} \tag{43}$$

$$\beta^* = \beta^*(\Delta u) = \beta^*\left(\frac{\Delta Q}{1-\zeta_{\min}^2}\right) \tag{44}$$

for β^* and $\zeta_{\min}$. The solution exists for all ΔQ satisfying (6):

$$\Delta Q < 1 - \zeta_{\min}^2 = \frac{1}{1+\beta^*(1)^2} = \frac{1}{1+M^2} = .89388. \tag{45}$$

The resulting $\zeta_{\min}$ is plotted versus ΔQ in Fig. 7.

Due to the concavity of $\beta^*(\Delta u)$ (Fig. 4), a conservative, approximate solution for $\zeta_{\min}(\Delta Q)$ is easily constructed. Let

$$\tilde{\beta}^* = M\Delta u \geq \beta^*. \tag{46}$$

$\tilde{\beta}^*$ upper bounds β^* (maximum 8.2 percent error) and $\tilde{\zeta}_{\min}$ calculated from $\tilde{\beta}^*$ satisfies $\tilde{\zeta}_{\min} \geq \zeta_{\min}$.

Substitution of (46) into (43) leads to

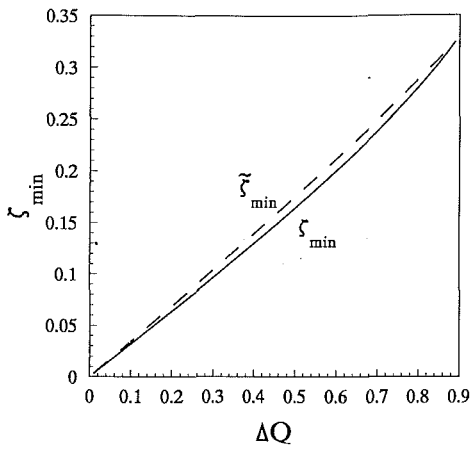


Fig. 7 The minimum damping for asymptotic stability, $\zeta_{\min}$**, and the approximate value,** $\tilde{\zeta}_{\min}$**.**

$$\tilde{\zeta}_{\min} = \sqrt{\frac{1}{2}\left(1 - \sqrt{1 - 4M^2\Delta Q^2}\right)}, \tag{47}$$

a conservative estimate of the minimum damping for asymptotic stability. In Fig. 7, $\tilde{\zeta}_{\min}$ bounds $\zeta_{\min}$ from above (maximum 8.2 percent error).

Conclusions

The response of Hill's equation with bounded parametric excitation is exponentially bounded. The parametric excitation causing maximum growth is periodic and bang-bang with four switches per cycle of the state. The switches occur on switching lines that are fixed in the phase plane and intersect the origin. One of the switching lines is $y = 0$, and the angle of the other switching line varies depending on Δu but always compresses the first and third quadrants where the frequency is low.

Damping in Hill's equation can be made large enough to overcome the destabilizing affect of any bounded parametric excitation with $\Delta Q \leq .89388$. The exact value of the minimum damping for asymptotic stability is calculated from (43) and (44) or read from Fig. 7. An approximate, more conservative value of the minimum damping is calculated from the closed-form (47). Thus, if only the bounds on the parametric excitation are given, whether the excitation is unknown, aperiodic, or random, the damping for asymptotic stability can be calculated.

References

Athans, M., and Falb, P., 1966, *Optimal Control: An Introduction to the Theory and Its Applications*, McGraw-Hill, New York.

Floquet, M. G., 1883, "Sur les Équation Différentielles Linéaires a Coefficients Périodiques," *Ann. Sci. L'École Norm. Sup.*, Ser. 2, Num. 2, pp. 1–36.

Hill, G. W., 1886, "On the Part of the Motion of the Lunear Perigee Which is a Function of the Mean Motions of the Sun and Moon," *Acta Math.*, Vol. 8, pp. 47–88.

Liapunov, M. A., 1949, *Problème Général de la Stabilité du Mouvement*, Princeton Univ. Press, Princeton, NJ, p. 406.

Magnus, W., and Winkler, S., 1966, *Hill's Equation*, John Wiley and Sons, New York.

Nayfeh, A. H., 1981, *An Introduction to Perturbation Techniques*, John Wiley and Sons, New York, pp. 234–256.

Nayfeh, A. H., and Mook, D. T., 1979, *Nonlinear Oscillations*, John Wiley and Sons, New York, pp. 258–301.

Sánchez, D. A., 1968, *Ordinary Differential Equations and Stability Theory: An Introduction*, W. H. Freeman and Company, San Francisco, CA, pp. 158–159.

Starzhinskii, V. M., 1955, "A Survey of Works on the Conditions of Stability of the Trivial Solution of Linear Differential Equations with Periodic Coefficients," *Amer. Math Translations*, Ser. 2, Vol. 1.

Yakubovich, V. A., and Starzhinskii, V. M., 1975, *Linear Differential Equations with Periodic Coefficients*, John Wiley and Sons, New York, pp. 595–596, 798–808.

Downloaded 03 May 2010 to 171.66.16.245. Redistribution subject to ASME license or copyright; see http://www.asme.org/terms/Terms_Use.cfm

J. Chung
Graduate Research Assistant.

G. M. Hulbert
Assistant Professor,
Assoc. Mem. ASME.

Department of Mechanical Engineering,
and Applied Mechanics,
The University of Michigan,
Ann Arbor, MI 48109-2125

A Time Integration Algorithm for Structural Dynamics With Improved Numerical Dissipation: The Generalized-α Method

A new family of time integration algorithms is presented for solving structural dynamics problems. The new method, denoted as the generalized-α method, possesses numerical dissipation that can be controlled by the user. In particular, it is shown that the generalized-α method achieves high-frequency dissipation while minimizing unwanted low-frequency dissipation. Comparisons are given of the generalized-α method with other numerically dissipative time integration methods; these results highlight the improved performance of the new algorithm. The new algorithm can be easily implemented into programs that already include the Newmark and Hilber-Hughes-Taylor-α time integration methods.

1 Introduction

The need has been long recognized for step-by-step time integration algorithms to possess algorithmic damping when solving structural dynamics problems. In particular, it is desirable to have controllable numerical dissipation in the higher frequency modes since, using standard finite elements to discretize the spatial domain, the spatial resolution of these high-frequency modes typically is poor. By using algorithms with high-frequency dissipation, spurious high-frequency response may be damped out. Also, when solving highly nonlinear problems, high-frequency numerical dissipation has been found to improve the convergence of iterative equation solvers. However, the addition of high-frequency dissipation should not incur a loss of accuracy nor introduce excessive algorithmic damping in the important low frequency modes. For example, the Newmark family of algorithms contains methods that possess high-frequency dissipation (Newmark, 1959); however, these methods are only first-order accurate and are too dissipative in the low-frequency domain. Numerous dissipative algorithms have been developed that attain high-frequency dissipation with little low-frequency damping while maintaining second-order accuracy; e.g., the θ method of Wilson (1968), the HHT-α method of Hilber, Hughes and Taylor (1977), the WBZ-α method of Wood, Bossak, and Zienkiewicz (1981), the ρ method of Bazzi and Anderheggen (1982) and the θ_1-method of Hoff and Pahl (1988a, 1988b) (also Hoff et al. (1989)).

The matrix equation of linear structural dynamics is

$$\mathbf{M}\ddot{\mathbf{X}} + \mathbf{C}\dot{\mathbf{V}} + \mathbf{K}\mathbf{X} = \mathbf{F} \tag{1}$$

where $\mathbf{M}$, $\mathbf{C}$, and $\mathbf{K}$ are the mass, damping, and stiffness matrices, respectively, $\mathbf{F}$ is the vector of applied loads (a given function of time), $\mathbf{X}$ is the vector of displacement unknowns, and superposed dots indicate differentiation with respect to time. The initial value problem consists of finding a function $\mathbf{X} = \mathbf{X}(t)$ which satisfies (1) for all $t \in [0, t_N]$, $t_N > 0$, and the initial conditions

$$\mathbf{X}(0) = \mathbf{d} \tag{2}$$

$$\dot{\mathbf{X}}(0) = \mathbf{v} \tag{3}$$

where $\mathbf{d}$ and $\mathbf{v}$ are given vectors of initial displacements and velocities, respectively. The numerically dissipative time integration algorithms listed above have the following common form: $\mathbf{d}_n$, $\mathbf{v}_n$ and $\mathbf{a}_n$ are given approximations to $\mathbf{X}(t_n)$, $\dot{\mathbf{X}}(t_n)$, and $\ddot{\mathbf{X}}(t_n)$, respectively. Expressions for $\mathbf{d}_{n+1}$ and $\mathbf{v}_{n+1}$ are specified as linear combinations of $\mathbf{d}_n$, $\mathbf{v}_n$, $\mathbf{a}_n$ and $\mathbf{a}_{n+1}$. An additional equation is needed to determine $\mathbf{a}_{n+1}$. This additional equation represents a modified version of Eq. (1). Each algorithm is defined by the specific form of the displacement and velocity update equations and the modified balance equation. Algorithms having this form may be classified as one-step, three-stage (or three-level) time integration methods. The algorithms are one-step methods because the solution at time t_{n+1} depends only on the solution history at time t_n. The three-stage designation refers to the solution being described by the three solution vectors: $\mathbf{d}_n$, $\mathbf{v}_n$, and $\mathbf{a}_n$.

In this paper, we present a new family of one-step, three-stage, numerically dissipative time integration algorithms. This family, which we call the generalized-α method, contains the HHT-α and WBZ-α algorithms; in addition, we identify a new

Contributed by the Applied Mechanics Division of THE AMERICAN SOCIETY OF MECHANICAL ENGINEERS for presentation at the First Joint ASCE-EMD, ASME-AMD, SES Meeting, Charlottesville, VA, June 6-9, 1993.

Discussion on this paper should be addressed to the Technical Editor, Professor Lewis T. Wheeler, Department of Mechanical Engineering, University of Houston, Houston, TX 77204-4792, and will be accepted until four months after final publication of the paper itself in the ASME JOURNAL OF APPLIED MECHANICS.

Manuscript received by the ASME Applied Mechanics Division, Dec. 2, 1991; final revision, Aug. 17, 1992. Associate Technical Editor: C. F. Shih.

Paper No. 93-APM-20.

Copyright © 1993 by ASME
Downloaded 03 May 2010 to 171.66.16.245. Redistribution subject to ASME license or copyright; see http://www.asme.org/terms/Terms_Use.cfm

algorithm that achieves an optimal combination of high-frequency and low-frequency dissipation. That is, for a given value of high-frequency dissipation, this optimal algorithm minimizes the low-frequency dissipation. From a practical viewpoint, the generalized-α method is particularly convenient since the algorithmic parameters are defined in terms of the desired amount of high-frequency dissipation. The design of the generalized-α method is discussed and comparisons with other numerically dissipative algorithms are provided that demonstrate the improved performance of the new time integration method.

2 The Generalized-α Algorithm

The basic form of the generalized-α method is given by

$$\mathbf{d}_{n+1} = \mathbf{d}_n + \Delta t \mathbf{v}_n + \Delta t^2 \left(\left(\frac{1}{2} - \beta \right) \mathbf{a}_n + \beta \mathbf{a}_{n+1} \right) \tag{4}$$

$$\mathbf{v}_{n+1} = \mathbf{v}_n + \Delta t ((1-\gamma)\mathbf{a}_n + \gamma \mathbf{a}_{n+1}) \tag{5}$$

$$\mathbf{M}\mathbf{a}_{n+1-\alpha_m} + \mathbf{C}\mathbf{v}_{n+1-\alpha_f} + \mathbf{K}\mathbf{d}_{n+1-\alpha_f} = \mathbf{F}(t_{n+1-\alpha_f}) \tag{6}$$

$$\mathbf{d}_0 = \mathbf{d} \tag{7}$$

$$\mathbf{v}_0 = \mathbf{v} \tag{8}$$

$$\mathbf{a}_0 = \mathbf{M}^{-1}(\mathbf{F}(0) - \mathbf{C}\mathbf{v} - \mathbf{K}\mathbf{d}) \tag{9}$$

where

$$\mathbf{d}_{n+1-\alpha_f} = (1-\alpha_f)\mathbf{d}_{n+1} + \alpha_f \mathbf{d}_n \tag{10}$$

$$\mathbf{v}_{n+1-\alpha_f} = (1-\alpha_f)\mathbf{v}_{n+1} + \alpha_f \mathbf{v}_n \tag{11}$$

$$\mathbf{a}_{n+1-\alpha_m} = (1-\alpha_m)\mathbf{a}_{n+1} + \alpha_m \mathbf{a}_n \tag{12}$$

$$t_{n+1-\alpha_f} = (1-\alpha_f)t_{n+1} + \alpha_f t_n \tag{13}$$

in which $n \in \{0,1,\ldots,N-1\}$, N is the number of time steps and Δt is the time step. The displacement and velocity update Eqs. (4) and (5) are identical to those of the Newmark algorithm. The structure of these update equations was obtained by restricting the sum of the coefficients of their acceleration terms to equal the coefficient of the acceleration term in a Taylor series expansion of $\mathbf{d}(t_{n+1})$ and $\mathbf{v}(t_{n+1})$ about t_n. Simple numerical experiments have shown that this update equation structure results in a monotone increase per period in the peak displacement and velocity errors. The modified balance equation, (6), is effectively a combination of the HHT-α and WBZ-α balance equations. The crucial task is to determine relationships between the algorithmic parameters, α_f, α_m, β, and γ. With appropriate expressions for γ and β, if $\alpha_m = 0$, the algorithm reduces to the HHT-α method; $\alpha_f = 0$ produces the WBZ-α method; $\alpha_m = \alpha_f = 0$ gives rise to the Newmark family. We shall show that other choices of the algorithmic parameters engender time integration algorithms with better numerical dissipation characteristics.

3 Analysis of the Generalized-α Algorithm

For purposes of analysis, it is advantageous to reduce the coupled equations of motion and the algorithmic equations to a series of uncoupled single-degree-of-freedom systems. This is accomplished by invoking the property of eigenvector orthogonality; see, e.g., (Hughes, 1987). The single-degree-of-freedom problem is given by

$$\ddot{u} + 2\xi\omega\dot{u} + \omega^2 u = f, \tag{14}$$

and $u(0) = d$, $\dot{u}(0) = v$. To study the accuracy and stability properties of an algorithm, it suffices to consider $f = 0$ for all $t \in [0, t_N]$. The generalized-α method, applied to (14) with $f = 0$, may be written in the compact form

$$\mathbf{X}_{n+1} = \mathbf{A}\mathbf{X}_n, \quad n \in \{0,1,\ldots,N-1\} \tag{15}$$

in which $\mathbf{X}_n = \{d_n, \Delta t v_n, \Delta t^2 a_n\}^T$; $\mathbf{A}$ is called the amplification matrix.

The accuracy of an algorithm may be determined from its local truncation error, τ, defined by

$$\tau = \Delta t^{-2} \sum_{i=0}^{3} (-1)^i A_i u(t_{n+1-i}) \tag{16}$$

where $A_0 = 1$, A_1 is the trace of $\mathbf{A}$, A_2 is the sum of the principal minors of $\mathbf{A}$ and A_3 is the determinant of $\mathbf{A}$. An algorithm is kth order accurate provided that $\tau = O(\Delta t^k)$. The generalized-α method is second-order accurate, provided

$$\gamma = \frac{1}{2} - \alpha_m + \alpha_f. \tag{17}$$

The stability, numerical dissipation and numerical dispersion of an algorithm depend upon the eigenvalues of its amplification matrix. The spectral radius, ρ, of an algorithm is defined by

$$\rho = \max(|\lambda_1|, |\lambda_2|, |\lambda_3|) \tag{18}$$

where λ_i is the ith eigenvalue of $\mathbf{A}$. Of particular interest is the variation in ρ as a function of $\Omega = \omega \Delta t$. An algorithm is unconditionally stable for linear problems if $\rho \le 1$ for all $\Omega \in [0,\infty)$ (strictly less than one for repeated real roots). The generalized-α method is unconditionally stable, provided

$$\alpha_m \le \alpha_f \le \frac{1}{2}, \quad \beta \ge \frac{1}{4} + \frac{1}{2}(\alpha_f - \alpha_m). \tag{19}$$

The spectral radius also is a measure of numerical dissipation; a smaller spectral radius value corresponds to greater numerical dissipation. Algorithmic damping in the high frequency regime is desired; it should be controllable and should be achieved without inducing excessive dissipation in the important low frequency region. In terms of its spectral radius, an algorithm with these desirable dissipation properties has spectral radius value close to unity in the low-frequency domain and the value smoothly decreases as Ω increases. This smoothness property imposes several restrictions on the values of the amplification matrix eigenvalues.

To discuss these restrictions, we shall order the eigenvalues of $\mathbf{A}$ so that for a convergent algorithm there exists a positive value, e.g., Ω_c, such that if $0 < \Omega < \Omega_c$, then two of the eigenvalues are complex conjugate. These two roots, λ_1 and λ_2, are the principal roots while λ_3 is the so-called spurious root. Typically, in the low-frequency domain, $|\lambda_3| < |\lambda_{1,2}|$. Thus, for the spectral radius to decrease smoothly as Ω increases, $|\lambda_3| \le |\lambda_{1,2}|$ for all $\Omega \in [0,\infty)$. Violation of this condition is manifested in the corresponding spectral radius plot as a "cusp" where, as Ω increases, the spectral radius also increases. Such an algorithm possesses more numerical dissipation for values of Ω near the cusp than in the high-frequency region and thus is of less practical interest.

The behavior of the principal roots as a function of Ω is also important. To maximize high-frequency dissipation, the principal roots should remain complex conjugate as Ω increases. If root bifurcation occurs (both principal roots become real), typically one root increases in magnitude with increasing Ω; this results in a increase in the spectral radius with increasing Ω which corresponds to a decrease in the high-frequency dissipation. High-frequency dissipation is maximized if the principal roots become real in the high-frequency limit. That is, if the principal roots are given by $\lambda_{1,2}(\Omega) = A(\Omega) \pm iB(\Omega)$, where A and B are real numbers and $i = \sqrt{-1}$, then high-frequency dissipation is maximized provided $\lim_{\Omega \to \infty} B(\Omega) = 0$. For the generalized-$\alpha$ method, this condition is satisfied when

$$\beta = \frac{1}{4}(1 - \alpha_m + \alpha_f)^2. \tag{20}$$

To summarize the smoothness design conditions, we require

Downloaded 03 May 2010 to 171.66.16.245. Redistribution subject to ASME license or copyright; see http://www.asme.org/terms/Terms_Use.cfm

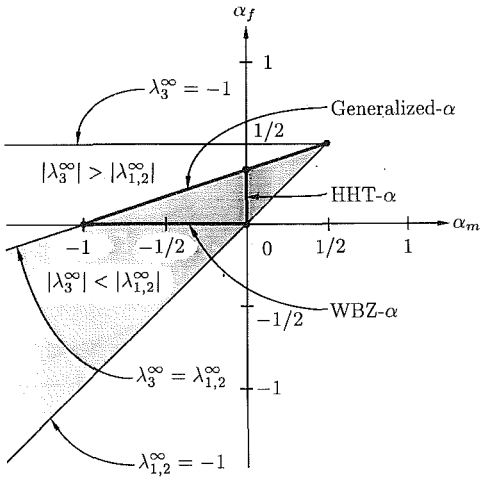


Fig. 1 Classification of generalized-α method in $\alpha_m - \alpha_f$ space

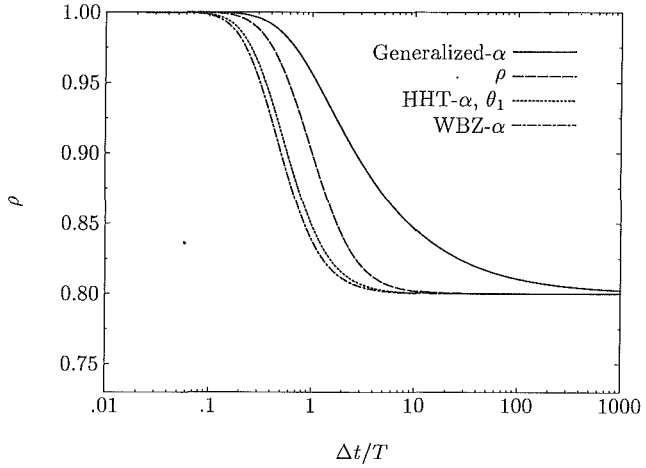


Fig. 2 Comparison of spectral radii of numerically dissipative algorithms

the magnitude of the spurious root to be less than or equal to the magnitude of the principal roots for all Ω and the principal roots to have real values only in the high-frequency limit.

Provided (17), (19), and (20) hold, the generalized-α method can be described in terms of the two remaining free parameters, α_m and α_f; this is depicted in Fig. 1. The stability region is denoted by the shaded areas; these areas are bounded by two lines: (1) $\lambda_{1,2}^\infty = -1$, which corresponds to $\alpha_m \leq \alpha_f$ in (19); (2) $\lambda_3^\infty = -1$, which corresponds to $\alpha_f \leq 1/2$ in (19); the ∞ superscript on λ_i denotes the high-frequency limit of the root.

Let ρ_∞ denote the user-specified value of the spectral radius in the high-frequency limit (user-specified high-frequency dissipation). Since, by design, we require that $|\lambda_3| \leq |\lambda_{1,2}|$ for all Ω, $\rho_\infty = |\lambda_{1,2}^\infty|$. The value of $\lambda_{1,2}^\infty$ can be obtained using

$$\lambda_{1,2}^\infty = \frac{\alpha_f - \alpha_m - 1}{\alpha_f - \alpha_m + 1}. \tag{21}$$

Thus, given ρ_∞, we can define α_m and α_f in terms of ρ_∞. For example, the HHT-α method is given by

$$\alpha_m = 0, \quad \alpha_f = \frac{1 - \rho_\infty}{1 + \rho_\infty} \tag{22}$$

where $\rho_\infty \in [1, 1/2]$. Similarly, using (21) and recalling that $\alpha_f = 0$, the WBZ-α method is given by

$$\alpha_f = 0, \quad \alpha_m = \frac{\rho_\infty - 1}{\rho_\infty + 1} \tag{23}$$

where $\rho_\infty \in [1, 0]$. These are more convenient expressions for the HHT-α and WBZ-α algorithmic parameters than exist in the literature as they directly relate the parameters to the desired value of high-frequency dissipation. We have found that for a given level of high-frequency dissipation, i.e., for fixed ρ_∞, low-frequency dissipation is minimized when $\lambda_3^\infty = \lambda_{1,2}^\infty$. Using (21) and

$$\lambda_3^\infty = \frac{\alpha_f}{\alpha_f - 1}, \tag{24}$$

low-frequency dissipation is minimized when $\alpha_f = (\alpha_m + 1)/3$. It is more convenient to describe this optimal case by defining α_m and α_f in terms of ρ_∞:

$$\alpha_m = \frac{2\rho_\infty - 1}{\rho_\infty + 1}, \quad \alpha_f = \frac{\rho_\infty}{\rho_\infty + 1} \tag{25}$$

The generalized-α method, with parametric values given in (17), (20), and (25), is an unconditionally stable, second-order accurate algorithm possessing an optimal combination of high-frequency and low-frequency dissipation.

Remarks.

(1) The optimal generalized-α method permits high-frequency dissipation to vary from the no dissipation case ($\rho_\infty = 1$) to the so-called asymptotic annihilation case ($\rho_\infty = 0$). In the latter case, high-frequency response is annihilated after one time step. It is advantageous, from the user viewpoint, to able to specify the algorithmic parameters in terms of the high-frequency dissipation, ρ_∞, since the degree of high-frequency dissipation desired is usually a known quantity.

(2) Hoff and Pahl (1988a) presented a generalized algorithm possessing six free parameters; a modified version of this algorithm was developed by Hoff et al. (1989) for consistent treatment of applied loads. The generalized-α method is a member of the modified Hoff-Pahl family (for linear problems) by setting $\hat{\theta}_1 = \hat{\theta}_2 = \hat{\theta}_3 = 1 - \alpha_f$, $\hat{\eta} = (1 - \alpha_m)/(1 - \alpha_f)$, and β and γ given by (20) and (17), respectively. However, we emphasize that the precise definitions of the algorithmic parameters for the optimal case are unique to the present work.

(3) For the optimal case, the spurious root value in the low-frequency limit ($\lambda_3^0 = \lim_{\Omega \to 0} \lambda_3$) is nonzero. While concern has been expressed in the literature regarding nonzero values of λ_3^0, we have shown that the impact on algorithmic accuracy is negligible (Hulbert, 1991).

(4) The problem of "overshoot" in displacements obtained by time integration algorithms was studied by Hilber and Hughes (1978). We note that the generalized-α method does not exhibit the overshoot phenomenon.

4 Comparison of Algorithms

In this section, we compare algorithms that possess numerical dissipation, in particular, the HHT-α, WBZ-α, ρ, θ_1, and generalized-α methods.

Spectral radii of the algorithms are plotted in Fig. 2. For all comparisons, the algorithmic parameters were chosen such that for each algorithm, the spectral radius in the high-frequency limit is 0.8; no physical damping is included in the model problem. It is clear that for the given value of ρ_∞, the generalized-α method with optimal parameters given by (25) (hereafter referred to as the generalized-α method) has a significantly better spectral radius than the other algorithms. Its improved performance can be seen more clearly when comparing the numerical dissipation and dispersion of the various algorithms.

Measures of numerical dissipation and dispersion are provided by the algorithmic damping ratio and relative period error. Provided the principal roots are complex, these roots may be expressed as

Downloaded 03 May 2010 to 171.66.16.245. Redistribution subject to ASME license or copyright; see http://www.asme.org/terms/Terms_Use.cfm

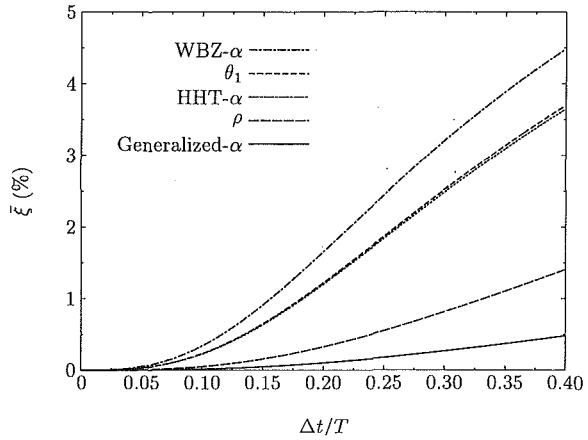


Fig. 3 Algorithmic damping ratios of numerically dissipative algorithms

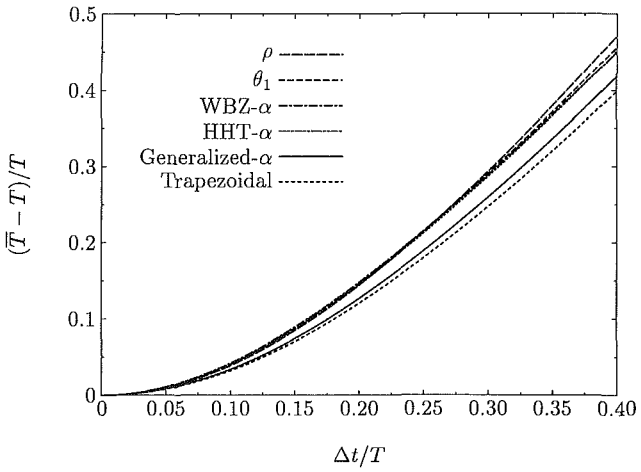


Fig. 4 Relative period errors of time integration algorithms

$$\lambda_{1,2} = \exp(\bar{\omega}\Delta t(-\bar{\xi} \pm i)) \tag{26}$$

where $\bar{\xi}$ and $\bar{\omega}$ are the algorithmic damping ratio and algorithmic frequency, respectively. The relative period error is given by $(\bar{T}-T)/T$, where $T=2\pi/\omega$ and $\bar{T}=2\pi/\bar{\omega}$.

Figure 3 shows algorithmic damping ratios for the dissipative algorithms. For the same value of high-frequency dissipation, it can be seen that the generalized-α method has substantially less low-frequency dissipation. Relative period errors are shown in Fig. 4; also included is the relative period error of the trapezoidal rule algorithm. The trapezoidal rule possesses the smallest period error of second-order accurate, unconditionally stable linear multistep methods and thus its period error may be used as a basis to compare the period errors of the numerically dissipative methods. From Fig. 4, it can be seen that the period error of the generalized-α method is closest to that of the trapezoidal rule algorithm.

As a final comparison, (14) was solved using different time integration algorithms with $\omega=\pi$, $\xi=0$, $d=1$ and $v=1$. The displacement error (difference between the exact and numerical displacement values) was computed at $t_N=0.4$. Figure 5 shows this error as a function of the number of time steps, N, for various algorithms. All algorithms shown achieve second-order accuracy; the ρ-method is not included as it is only first-order accurate. Dahlquist (1963) proved that the trapezoidal rule has the smallest error of unconditionally stable, second-order accurate methods; from Fig. 5 it may be seen that amongst the numerically dissipative algorithms investigated, the generalized-α method has the smallest error.

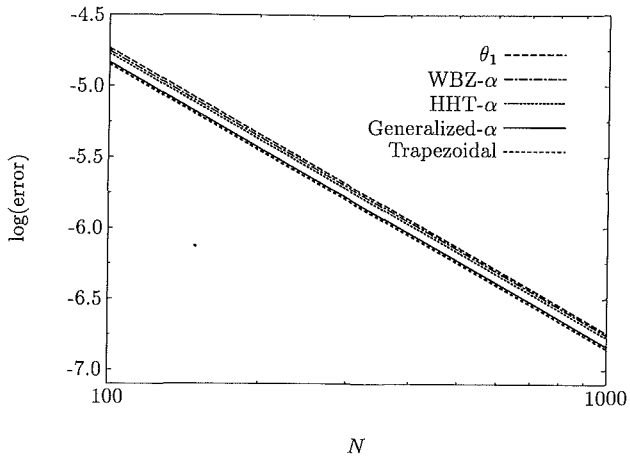


Fig. 5 Comparison of displacement errors of time integration algorithms. N is the number of time steps.

5 Conclusions

A new family of time integration methods has been presented for solving structural dynamics problems. The new scheme includes both the HHT-α and WBZ-α methods; indeed, the new generalized-α method may be considered as a synthesis or generalization of these two methods. An analysis of the generalized-α method was performed to define appropriate values of the algorithmic parameters. Expressions were provided that define the algorithmic parameters in terms of a user-specified value of high-frequency dissipation. The resultant time integration algorithm is unconditionally stable, second-order accurate and possesses an optimal combination of high-frequency and low-frequency dissipation. That is, for a desired level of high-frequency dissipation, the low-frequency dissipation is minimized. The generalized-α method was shown to have better numerical dissipation characteristics, and smaller period and displacement errors than other numerically dissipative schemes. We emphasize that the improved performance of the algorithm is not obtained by increasing the complexity of the algorithm beyond that associated with the HHT-α and WBZ-α methods. This is important from a practical viewpoint since the generalized-α method can be directly implemented with minimal additional coding into programs that already include the Newmark, HHT-α or WBZ-α methods.

The generalized-α method has been presented for structural dynamics. Of interest is extending the method to systems of first-order ordinary differential equations. Research efforts are underway in this area as well as developing improved implicit-explicit time integration methods using the generalized-α method as the parent implicit algorithm.

Acknowledgment

We would like to acknowledge support provided by a Korean Government Overseas Scholarship for the first author.

References

Bazzi, G., and Anderheggen, E., 1982, "The ρ-Family of Algorithms for Time-Step Integration with Improved Numerical Dissipation," *Earthquake Engineering and Structural Dynamics*, Vol. 10, pp. 537–550.

Dahlquist, G., 1963, "A Special Stability Problem for Linear Multistep Methods," *BIT*, Vol. 3, pp. 27–43.

Hilber, H. M., Hughes, T. J. R., and Taylor, R. L., 1977, "Improved Numerical Dissipation for Time Integration Algorithms in Structural Dynamics," *Earthquake Engineering and Structural Dynamics*, Vol. 5, pp. 283–292.

Hilber, H. M., and Hughes, T. J. R., 1978, "Collocation, Dissipation and 'Overshoot' for Time Integration Schemes in Structural Dynamics," *Earthquake Engineering and Structural Dynamics*, Vol. 6, pp. 99–118.

Hoff, C., and Pahl, P. J., 1988a, "Development of an Implicit Method with

Downloaded 03 May 2010 to 171.66.16.245. Redistribution subject to ASME license or copyright; see http://www.asme.org/terms/Terms_Use.cfm

Numerical Dissipation from a Generalized Single-Step Algorithm for Structural Dynamics," *Computer Methods in Applied Mechanics and Engineering*, Vol. 67, pp. 367–385.

Hoff, C., and Pahl, P. J., 1988b, "Practical Performance of the θ_1 Method and Comparison with Other Dissipative Algorithms in Structural Dynamics," *Computer Methods in Applied Mechanics and Engineering*, Vol. 67, pp. 87–110.

Hoff, C., Hughes, T. J. R., Hulbert, G., and Pahl, P. J., 1989, "Extended Comparison of the Hilbert-Hughes-Taylor α-Method and the θ_1-Method," *Computer Methods in Applied Mechanics and Engineering*, Vol. 76, pp. 87–93.

Hughes, T. J. R., 1987, *The Finite Element Method: Linear Static and Dynamic Finite Element Analysis*, Prentice-Hall, Englewood Cliffs, New Jersey.

Hulbert, G. M., and Chung, J., 1991, "On the (Non-)Importance of the Spurious Root of Time Integration Algorithms for Structural Dynamics," submitted for publication in *Communications in Applied Numerical Methods*.

Newmark, N. M., 1959, "A Method of Computation for Structural Dynamics," *Journal of the Engineering Mechanics Division ASCE*, Vol. 85, No. EM3, pp. 67–94.

Wilson, E. L., 1968, *A Computer Program for the Dynamic Stress Analysis of Underground Structures*, SESM Report No. 68-1, Division of Structural Engineering and Structural Mechanics, University of California, Berkeley, CA.

Wood, W. L., Bossak, M., and Zienkiewicz, O. C., 1981, "An Alpha Modification of Newmark's Method," *International Journal for Numerical Methods in Engineering*, Vol. 15, pp. 1562–1566.

Downloaded 03 May 2010 to 171.66.16.245. Redistribution subject to ASME license or copyright; see http://www.asme.org/terms/Terms_Use.cfm

On Newton's and Poisson's Rules of Percussive Dynamics

J. A. Batlle
Department of Mechanical Engineering,
Polytechnical University of Catalunya,
08028 Barcelona, Spain

Newton's and Poisson's rules are widely used in percussive dynamics because they lead to an "all linear" solution. However, they are in general energetically inconsistent in rough collisions. The equivalence between both rules and a broad condition for them to be energetically consistent is presented for single point collisions in multibody systems with perfect constraints. It is fulfilled in collisions described by equations of motion with constant coefficients—sliding in the same direction or no sliding—and in "balanced" collisions—sliding velocity would not change if friction were negligible—Coulomb's friction and infinite tangential stiffness are assumed at the collision point.

1 Introduction

Newton's rule of percussive dynamics, which assumes that the normal separating and approaching velocities v_s and v_a at the collision point are proportional through a restitution coefficient e_N, $0 \leq e_N \leq 1$, is widely used because it translates into a linear form an assumption of the work done by the normal percussive force. If described by means of the energy equation, it leads to a quadratic equation and prevents an otherwise "all linear" solution.

Poisson's rule leads also to an "all linear" solution as it assumes that the normal expansion and compression percussions $P_{n\,\mathrm{exp}}$ and $P_{n\,\mathrm{comp}}$ are proportional through a restitution coefficient e_P, $0 \leq e_P \leq 1$. Compression and expansion phases correspond, respectively, to the normal velocity v_n ranges $-v_a \leq v_n \leq 0$ and $0 \leq v_n \leq v_s$. Its use is favored by authors (Kilmister, 1966) that distrust Newton's rule but don't realize that both rules are equivalent when energetically consistent.

These rules are energetically inconsistent in the general case of rough collisions. Beghin (1967) was aware of this fact and developed a geometry-based method to solve three-dimensional rough collisions. Batlle and Barjau Condomines (1991) extended Beghin's approach to multibody systems by means of the Lagrangian formulation. However, erroneous applications of Newton's and Poisson's rules are frequently found in books on mechanics (Kilmister, 1966; Roy, 1964; Whittaker, 1965) and in articles (Brach, 1984, 1989; Keller, 1986; Wang and Mason, 1987). When not properly used, these rules can lead to different wrong solutions, as shown by Stronge (1990). Newton's and Poisson's rules can be generalized, as suggested by Smith (1991), by considering an energetically consistent upper bound $\neq 1$ for e_N and e_p. However, as this bound depends upon specific initial velocities, values e_N and e_P have no range of applicability in this case, as is pointed out by Stronge (1990). An alternative to this generalization could be the use of coefficients $0 \leq e'_N \leq 1$ and $0 \leq e'_P \leq 1$ relating v_s and P_{exp} to their maximum values (those for a perfectly elastic collision), respectively. However, these maximum values depend also upon the specific initial velocities.

In this article the equivalence between Newton's and Poisson's rules is presented and their energetical consistency is studied by means of the Lagrangian formulation for single-point rough collisions in multibody systems with perfect constraints. Coulomb's friction and infinite tangential stiffness are assumed at the collision point.

A broad sufficiency condition for energetical consistency is obtained which is fulfilled to two general cases: that of collisions by differential equations with constant coefficients (Section 5) and that of "balanced" collisions—a generalization of central or collinear collisions—(Section 7). Two classical illustrative cases are presented.

2 The Lagrangian Formulation of Rough Collisions in Multibody Systems

The equations of motion for rough collisions must be formulated in differential form instead of algebraic form in general, because the law relating tangential force to normal force (such as Coulomb's law) does not translate into a law relating tangential and normal percussions in the general case.

The differential Lagrangian equations of motion for single-point rough collisions in a multibody system with n-degrees-of-freedom, described by means of generalized velocities $\{u\}^T = \{u_1, u_2, \ldots u_n\}$, with perfect constraints, can be written in matrix form as:

$$[M]\{du\} = \{d\Pi_n\} + \{d\Pi_t\} \triangleq \{d\Pi\}, \qquad (1)$$

where $[M]$ is the $n \times n$ inertia matrix of the system for the impact configuration and $\{d\Pi_n\}$ and $\{d\Pi_t\}$ are the generalized

Contributed by the Applied Mechanics Division of THE AMERICAN SOCIETY OF MECHANICAL ENGINEERS for presentation at the First Joint ASCE-EMD, ASME-AMD, SES Meeting, Charlottesville, VA, June 6-9, 1993.

Discussion on this paper should be addressed to the Technical Editor, Professor Lewis T. Wheeler, Department of Mechanical Engineering, University of Houston, Houston, TX 77204-4792, and will be accepted until four months after final publication of the paper itself in the ASME JOURNAL OF APPLIED MECHANICS.

Manuscript received by the ASME Applied Mechanics Division, May 13, 1992; final revision, Sept. 14, 1992. Associate Technical Editor: R. L. Huston.

Paper No. 93-APM-38.

Copyright © 1993 by ASME
Downloaded 03 May 2010 to 171.66.16.245. Redistribution subject to ASME license or copyright; see http://www.asme.org/terms/Terms_Use.cfm

normal and tangential differential impulses, respectively. The n-vector $\{d\Pi\}$ is related to differential normal and tangential impulses dP_n and $d\mathbf{P}_t$ by means of the equation

$$\{d\Pi\} = [k]\begin{Bmatrix} dP_n \\ d\mathbf{P}_t \end{Bmatrix} \triangleq [k]\{dP_n\}, \tag{2}$$

where $[k]$ is a $n \times 3$ matrix of kinematical coefficients relating the normal velocity v_n and tangential velocity $\mathbf{v}_t$ at the collision point to the generalized velocities:

$$\{v\} \equiv \begin{Bmatrix} v_n \\ \mathbf{v}_t \end{Bmatrix} = [\{\alpha\}[\beta]]^T\{u\} \triangleq [k]^T\{u\}. \tag{3}$$

Equations (1), (2), and (3) lead to

$$\{du\} = [M]^{-1}[k]\{dP\}, \tag{4}$$

$$\{dv\} = [k]^T[M]^{-1}[k]\{dP\} \triangleq [N]\{dP\}, \tag{5}$$

where $[N]$ is a symmetrical positive definite matrix that is conveniently written in the form

$$[N] = \begin{bmatrix} \alpha^T M^{-1}\alpha & \alpha^T M^{-1}\beta \\ \beta^T M^{-1}\alpha & \beta^T M^{-1}\beta \end{bmatrix} \triangleq \begin{bmatrix} a & \mathbf{h}^T \\ \mathbf{h} & [b] \end{bmatrix}. \tag{6}$$

$\{dP\}$ can be expressed as a function of dP_n under the assumption of Coulomb's law for friction forces and infinite tangential stiffness at the collision point.

When sliding occurs, $\{dP\}$ can be expressed in terms of dP_n, the friction coefficient μ and the unit vector $\boldsymbol{\sigma} = \mathbf{v}_t/|\mathbf{v}_t|$ defining the sliding direction

$$\{dP\} = \begin{Bmatrix} 1 \\ -\mu\boldsymbol{\sigma} \end{Bmatrix} dP_n. \tag{7}$$

Substitution of Eq. (7) into Eqs. (4) and (5) leads to

$$\{du\} = [M]^{-1}[k]\begin{Bmatrix} 1 \\ -\mu\boldsymbol{\sigma} \end{Bmatrix} dP_n \triangleq \{C^s\}dP_n, \tag{8}$$

$$\begin{Bmatrix} dv_n^s \\ d\mathbf{v}_t \end{Bmatrix} = \begin{Bmatrix} a - \mu\mathbf{h}^T\boldsymbol{\sigma} \\ \mathbf{h} - \mu[b]\boldsymbol{\sigma} \end{Bmatrix} dP_n. \tag{9}$$

In the nonsliding case, the kinematical constraint $\mathbf{v}_t = 0$ leads to

$$\begin{Bmatrix} dv_n^{ns} \\ 0 \end{Bmatrix} = \begin{Bmatrix} adP_n + \mathbf{h}^T d\mathbf{P}_t \\ \mathbf{h}dP_n + [b]d\mathbf{P}_t \end{Bmatrix}, \tag{10}$$

from which

$$d\mathbf{P}_t = -[b]^{-1}\mathbf{h}dP_n. \tag{11}$$

Substitution of Eq. (11) into Eqs. (4) and (10) leads to

$$\{du\} = [M]^{-1}[k]\begin{Bmatrix} 1 \\ -[b]^{-1}\mathbf{h} \end{Bmatrix} dP_n \triangleq \{C^{ns}\}dP_n \tag{12}$$

$$dv_n^{ns} = \{\mathbf{a} - \mathbf{h}^T[b]^{-1}\mathbf{h}\}dP_n \tag{13}$$

Incidentally, in the case of planar movement, equations can be simplified by taking a tangential axis on the plane of movement. In such a case $\sigma = \pm 1$, an n-vector $\{\beta\}$ substitutes for $[\beta]$, and, accordingly, scalars $h = \{\beta\}^T[M]^{-1}\{\alpha\}$ and $b = \{\beta\}^T[M]^{-1}\{\beta\}$ substitute for $\mathbf{h}$ and $[b]$, respectively.

3 Newton's Rule Energetical Consistency

The work W_n done by the normal percussive force is a nonpositive quantity. In Newton's rule a perfectly elastic collision, in which $W_n = 0$, is associated with $v_s = v_a$. Partially or perfectly plastic collisions, in which W_n is negative, are associated with $v_s < v_a$. So Newton's rule will be energetically consistent if $W_n = 0$ implies $v_s = v_a$ and $W_n < 0$ implies $v_s < v_a$.

The work W_n done by the normal force F_n can be expressed as:

$$W_n = \int_0^T F_n v_n dt = \int_0^{P_n} v_n dP_n, \tag{14}$$

but dP_n, according to Eqs. (9) and (13), is proportional to dv_n

$$dP_n \triangleq \eta dv_n. \tag{15}$$

Substitution of Eq. (15) into Eq. (14) leads to:

$$W_n = \int_{-v_a}^{v_s} \eta v_n dv_n. \tag{16}$$

If η is constant over the full collision interval, then

$$W_n = \eta\int_{-v_a}^{v_s} v_n dv_n = \frac{1}{2}\eta(v_s^2 - v_a^2), \tag{17}$$

and integration of Eq. (15) leads to

$$P_n = \eta\int_{-v_a}^{v_s} dv_n = \eta(v_s + v_a). \tag{18}$$

This expression for P_n can be substituted into Eq. (29) to obtain

$$W_n = \frac{1}{2}P_n(v_s - v_a). \tag{19}$$

Equation (17) shows that $W_n = 0$ implies $v_s = v_a$ and Eq. (19) shows that $W_n < 0$ implies $v_s < v_a$, *so the ratio* η *of* dP_n *to* dv_n *to be constant over the collision interval is a sufficiency condition for Newton's rule to be energetically consistent.*

According to Eqs. (9) and (13), expressions for η in the sliding and in the nonsliding cases are, respectively:

$$\eta^s \equiv dP_n/v_n^s = 1/(a - \mu\mathbf{h}^T\boldsymbol{\sigma}). \tag{20}$$

$$\eta^{ns} \equiv dP_n/v_n^{ns} = 1/(a - \mathbf{h}^T[b]^{-1}\mathbf{h}), \tag{21}$$

where a, $\mathbf{h}$ and $[b]$ depend upon configuration only, which is kept constant during the collision, while $\boldsymbol{\sigma}$ is also velocity dependent. From Eqs. (20) and (21) it is clear that condition of η constant is verified in the following cases:

(a) non-frictional case,
(b) non-sliding case,
(c) permanently sliding case with constant sliding direction ($\boldsymbol{\sigma}$ constant), and
(d) $\mathbf{h} = 0$ case (regardless of sliding), which is presented in Section 7.

In cases (a), (b), and (c), the equations of motion have constant coefficients, as can be checked from Eqs. (8) and (12), and this leads, if Newton's rule is applied, to an all algebraic solution as shown in Section 5. Conclusions concerning cases (a), (b), and (c) can be extended to multibody systems with impulsive drivers as shown in the Appendix.

For $\mathbf{h} \neq 0$ there is also a case of η constant in spite of sliding stopping ($\eta^s = \eta^{ns}$), but it requires precise $\boldsymbol{\sigma}$ and μ ($\boldsymbol{\sigma}$ orthogonal to $[b]^{-1}\mathbf{h}$ and verifying $\mathbf{h}^T\boldsymbol{\sigma} > 0$, and $\mu = \mathbf{h}^T[b]^{-1}\mathbf{h}/\mathbf{h}^T\boldsymbol{\sigma}$), which makes it far more restrictive that case (d) and no detailed attention is given to it in this article.

4 Equivalence Between Newton's and Poisson's Rules

Under Poisson's rule, $P_{n\,\mathrm{exp}} = P_{n\,\mathrm{comp}}$ and $P_{n\,\mathrm{exp}} < P_{n\,\mathrm{comp}}$ are associated with $W_n = 0$ and $W_n < 0$, respectively. In the general case, Eq. (14) does not lead to an expression of W_n as a function of P_n because Eq. (15) cannot be integrated to relate v_n to P_n.

If η is constant during the collision interval, then, according to Eq. (15),

$$P_{n\,\mathrm{comp}} = \int_{-v_a}^{0} \eta dv_n = \eta v_a \tag{22}$$

$$P_{n\,\mathrm{exp}} = \int_0^{v_s} \eta dv_n = \eta v_s. \tag{23}$$

So, under the assumption of constant η, $P_{n\,\mathrm{comp}}$ and $P_{n\,\mathrm{exp}}$ are proportional to v_a and v_s, respectively. As Newton's rule is

Downloaded 03 May 2010 to 171.66.16.245. Redistribution subject to ASME license or copyright; see http://www.asme.org/terms/Terms_Use.cfm

energetically consistent in this case, the same happens to Poisson's rule and both restitution coefficients have the same value, $e_P = e_N$.

5 Collisions Described by Differential Equations of Motion With Constant Coefficients

If the equations of motion $\{du\} = \{C\}dP_n$ given by Eqs. (8) and (12) have constant coefficients and Newton's rule is applied, they can be analytically integrated over the collision interval:

$$\{\Delta u\} = \{C\}P_n, \tag{24}$$

but

$$P_n = (\{\alpha\}^T\{C\})^{-1}\Delta v_n, \tag{25}$$

and from Newton's rule,

$$\Delta v_n = -(1+e)v_n^{(0)} = -(1+e)\{\alpha\}^T\{u^{(0)}\}. \tag{26}$$

Substitution of Eqs. (25)-(26) into Eq. (24) leads to

$$\{\Delta u\} = [\mathcal{P}]\{u^{(0)}\} \tag{27}$$

with

$$[\mathcal{P}] \triangleq -(1+e)\{C\}(\{\alpha\}^T\{C\})^{-1}\{\alpha\}^T. \tag{28}$$

The final velocities can be expressed as

$$\{u\} = ([I] + [\mathcal{P}])\{u^{(0)}\}, \tag{29}$$

where matrix $[I] + \mathcal{P}]$ is the transfer matrix of the collision.

The work W_n dissipated by the normal force can be calculated by means of Eqs. (17) or (19). The work W_t dissipated by friction can also be analytically integrated in case of constant sliding direction,

$$W_t = \int_0^T \mathbf{v}_t^T\mathbf{F}_t dt = -\int_0^{P_t} v_t dP_t, \tag{30}$$

but, according to Eq. (9),

$$dv_t \triangleq \boldsymbol{\sigma}^T d\mathbf{v}_t = (\boldsymbol{\sigma}^T\mathbf{h} - \mu\boldsymbol{\sigma}^T[b]\boldsymbol{\sigma})dP_n. \tag{31}$$

Substitution of Eq. (31) into Eq. (30) through $dP_t = \mu dP_n$ leads to

$$W_t = -\frac{1}{2}\mu(\boldsymbol{\sigma}^T\mathbf{h} - \mu\boldsymbol{\sigma}^T[b]\boldsymbol{\sigma})^{-1}(v_t^{(e)2} - v_t^{(0)2}) = \tag{32a}$$

$$= -\frac{1}{2}\mu P_n|v_t^{(e)} + v_t^{(0)}| = \tag{32b}$$

$$= -\mu P_n|v_t^{(0)}| - \frac{1}{2}\mu(\boldsymbol{\sigma}^T\mathbf{h} - \mu\boldsymbol{\sigma}^T[b]\boldsymbol{\sigma})P_n^2, \tag{32c}$$

being $v_t^{(0)}$ and $v_t^{(e)}$ the initial and end tangential velocities, respectively.

6 Application Example 1: Tangential Collision

Tangential collisions are a paradigmatical example of collisions that do not fulfill Newton's rule because in them $v_a = 0$ while $v_s \neq 0$. They are also the most illustrative case of dynamic wedging or jam process (according to Stronge's (1990) terminology) which happens when $dv_n < 0$ during sliding. In this case, if Newton's or Poisson's rules are wrongly applied, they lead to different wrong solutions.

Lets consider the tangential collision of the rigid body depicted in Fig. 1 with the fixed rough plane. To make the study easier, it is considered that the axis 3 is an inertia eigendirection of inertia moment $I_G = m\rho^2$, and that initial movement is a translation tangential to the fixed plane. Notation defined in Fig. 1 will be used.

The three degrees-of-freedom $\{u\}$ and initial conditions $\{u^{(0)}\}$ of the body are described by

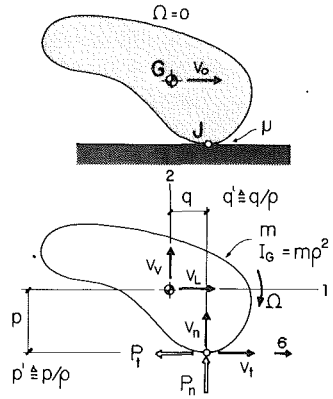


Fig. 1 Tangential collision; notation

$$\{u\} = \begin{Bmatrix} v_u \\ v_L \\ \Omega \end{Bmatrix}; \quad \{u^{(0)}\} = \begin{Bmatrix} 0 \\ v_0 \\ 0 \end{Bmatrix}. \tag{33}$$

It is assumed that the normal force is not perfectly elastic and that it gives back only a fraction e_w^2 of the compression work $W_{n\,\text{comp}}$.

Under conditions for dynamic wedging, as $dv_n < 0$ while sliding, the collision is composed by a first phase in which v_n evolves from zero to a negative value $v_n^{(1)}$ until sliding stops, and a second phase without sliding in which compression is completed as v_n evolves from $v_n^{(1)}$ to zero and then the expansion takes place until the end of the collision.

As it is always the case in plane movements, the differential equations of percussive dynamics can be integrated over collision subintervals of constant coefficients.

From Eqs. (8) and (12)—for the first and second phase, respectively— and Eqs. (3) and (19), it is obtained that

$$\{u^{(i)}\} = \{u^{(i-1)}\} + \{C\}\Delta P_n^{(i)}, \tag{34a}$$

$$\{v^{(i)}\} = \{v_n^{(i-1)}\} + [k]^T\{C\}\Delta P_n^{(i)}, \tag{34b}$$

$$W_n^{(i)} = W_n^{(i-1)} + \frac{1}{2}\Delta P_n^{(i)}(v_n^{(i)} + v_n^{(i-1)}). \tag{34c}$$

The energy dissipated by friction can be calculated by means of Eqs. (32) with $P_n^{(1)}$ (normal percussion for phase with sliding) substituting for P_n.

Basic matrices are:

$$[M] = m\begin{bmatrix} 1 & & \\ & 1 & \\ & & \rho^2 \end{bmatrix}; \quad [k] = \begin{bmatrix} 1 & 0 \\ 0 & 1 \\ -q & -p \end{bmatrix}, \tag{35}$$

For sliding conditions, with $\sigma = \pm 1$,

$$\{C^s\} = \frac{1}{m}\begin{Bmatrix} 1 \\ -\mu \\ (\mu p' - q')/\rho \end{Bmatrix}; \begin{matrix} p' \triangleq p/\rho, \\ q' \triangleq q/\rho, \end{matrix} \tag{36}$$

$$[k]^T\{C^s\} = -\frac{1}{m}\begin{Bmatrix} \mu p'q' - q'^2 - 1 \\ \mu + \mu p'^2 - p'q' \end{Bmatrix} \triangleq -\frac{1}{m}\begin{Bmatrix} \mu'' \\ \mu' \end{Bmatrix}. \tag{37}$$

For non-sliding conditions,

$$\{C^{ns}\} = \frac{1}{m(1+p'^2)}\begin{Bmatrix} 1+p'^2 \\ -p'q' \\ -q'/\rho \end{Bmatrix}, \tag{38}$$

$$[k]^T\{C^{ns}\} = -\frac{1}{m(1+p'^2)}\begin{Bmatrix} 1+p'^2-q'^2 \\ 0 \end{Bmatrix} \triangleq -\frac{1}{m(1+p'^2)}\begin{Bmatrix} \chi \\ 0 \end{Bmatrix}. \tag{39}$$

Downloaded 03 May 2010 to 171.66.16.245. Redistribution subject to ASME license or copyright; see http://www.asme.org/terms/Terms_Use.cfm

Condition for dynamic wedging, $dv_n^s < 0$, requires, according to Eqs. (34b) and (37),

$$\mu'' \triangleq \mu p' q' - q'^2 - 1 > 0 \rightarrow \mu > \frac{1+q'^2}{p'q'} \triangleq \mu_{DW}. \tag{40}$$

If this condition is verified then μ', defined in Eq. (37), is also > 0. Value μ_{DW} is identical to $\mu_\square$ used by Stronge (1990) and obviously is greater than the boundary value μ_c (μ_* in Stronge notation) over which sliding does not restart once it has stopped. From Eqs. (34b) and (37), condition $dv_t = 0$ leads to

$$\mu_c' \triangleq \mu_c + \mu_c p'^2 - p'q' = 0 \rightarrow \mu_c = \frac{p'q'}{1+p'^2} < \mu_{DW}. \tag{41}$$

Three steps must be taken into account:

Step 1 Compression with sliding; ends for $v_t^{(1)} = 0$,

Step 2 Compression without sliding; ends for $v_n^{(2)} = 0$. This step is necessary to calculate $W_{n\,\mathrm{comp}} = W_n^{(2)}$.

Step 3 Expansion with sliding; ends for $\Delta W_n^{(3)} = -e_w^2 W_{\mathrm{comp}}$.

Step 1. Condition $v_t^{(1)} = 0$ and Eqs. (34) and (32) lead to

$$\left.\begin{aligned} &\Delta P_n^{(1)} = mv_0/\mu' \\ &\{u^{(1)}\} = \frac{v_0}{\mu'}\begin{Bmatrix} 1 \\ b'(\mu p' - q') \\ (\mu p' - q')/\rho \end{Bmatrix} \\ &v_n^{(1)} = -v_0\mu''/\mu' \\ &W_n^{(1)} = -T_0\mu''/\mu'^2; \quad T_0 \triangleq (1/2)mv_0^2 \\ &W_t = -T_0\mu/\mu' \end{aligned}\right\}. \tag{42}$$

Step 2. Condition $v_n^{(2)} = 0$ and Eqs. (34) lead to

$$\left.\begin{aligned} &\Delta P_n^{(2)} = mv_0(1+p'^2)\mu''/(\mu'\chi); \\ &P_n^{(2)} = mv_0 p'q'/\chi \equiv P_{n\,\mathrm{comp}} \\ &\{u^{(2)}\} = \frac{v_0}{\lambda}\begin{Bmatrix} p'q' \\ p' \\ p'/\rho \end{Bmatrix} \\ &W_n^{(2)} = -T_0\mu'' p'q'/(\mu'\chi) \equiv W_{n\,\mathrm{comp}} \end{aligned}\right\}. \tag{43}$$

It is interesting to note that $\{u^{(2)}\}$ is independent from friction coefficient μ.

Step 3. Condition $\Delta W_n^{(3)} = -e_w^2 W_{n\,\mathrm{comp}}$ and Eqs. (34) lead to

$$\Delta P_n^{(3)} = mv_0 e_w \varphi p'q'/\chi = e_w \varphi P_{n\,\mathrm{comp}} = P_{n\,\mathrm{exp}}, \tag{44}$$

$$\{u^{(3)}\} = \begin{Bmatrix} v_v^{(2)}(1+e_w\varphi) \\ v_L^{(2)}(1-e_w\varphi q'^2/(1+p'^2)) \\ \Omega^{(2)}(1-e_w\varphi q'^2(1+p'^2)) \end{Bmatrix}, \tag{45}$$

$$v_n^{(3)} = v_0 e_w \sqrt{\frac{\mu'' p'q'}{\mu'(1+p'^2)}} \triangleq v_0 e_w \varphi \frac{p'q'}{1+p'^2} \equiv v_s, \tag{46}$$

where

$$\varphi \triangleq \sqrt{\frac{1+p'^2}{p'q'}\frac{\mu''}{\mu'}}. \tag{47}$$

Equations (44) and (46) show, respectively, that Poisson's and Newton's rules cannot be applied because, for a perfectly elastic collision ($e_w = 1$) $P_{n\,\mathrm{exp}} \neq P_{n\,\mathrm{comp}}$, as $\varphi \neq 1$, and $v_s \neq v_a = 0$ as $\varphi \neq 0$.

A generalization of the above rules based in the use of e_N and e_P upper bounds $\neq 1$, cannot be defined for Newton's rule as $v_0 = 0$ and $v_s \neq 0$, and leads to $e_P = e_w\varphi$ for Poisson's rule. Conversely, a generalization based on $0 \leq e_N' \leq 1$ and $0 \leq e_P' \leq 1$ applied, respectively, to $v_{s\,\max} = v_0\varphi p'q'/(1+p'^2)$ and $P_{n\,\mathrm{exp.max}} = mv_0\varphi p'q'/\chi$ leads to $e_N' = e_P' = e_w$ in this particular problem.

The energy dissipated in the collision can be calculated as $W_t + W_n^{(3)}$,

$$W_{\mathrm{dis}} = -T_0(\mu + (1-e_w^2)\mu'' p'q'/\chi)/\mu' \tag{48}$$

7 Balanced Collisions

As it has been shown in Section 3, condition $\mathbf{h} = 0$ makes Newton's rule energetically consistent—and Poisson's rule as well, according to the equivalence presented in Section 4—regardless of the kind of sliding.

According to the expression of $d\mathbf{v}_t$ given by Eq. (9), $\mathbf{h}dP_n$ describes that part of $d\mathbf{v}_t$ independent of friction. As a consequence with $\mathbf{h} = 0$, the collision would not affect the tangential velocity if friction were negligible. Collisions that verify $\mathbf{h} = 0$ are named "balanced collisions" in this article, and they generalize the more restrictive concept of central or colinear collisions.

In this case, according to Eq. (9) for $d\mathbf{v}_t$,

$$d\mathbf{v}_t = -\mu[b]\sigma dP_n. \tag{49}$$

As $[b]$ is a symmetrical and positive definite matrix, Eq. (49) implies

$$\sigma^T d\mathbf{v}_t = -\mu\sigma^T[b]\sigma dP_n < 0, \tag{50}$$

and, consequently, $\mathbf{v}_t$ tends to $\mathbf{v}_t = 0$. So sliding never restarts once it has stopped. Sliding with constant directions occurs only along the eigendirections of $[b]$, according to Eq. (49).

The constant ratio $\eta^s = \eta^{ns} = a^{-1}$, according to Eqs. (20)–(21), between dP_n and dv_n for sliding or non-sliding conditions, respectively, leads to

$$\left.\begin{aligned} &P_{n\,\mathrm{comp}} = a^{-1}v_a; \qquad P_n = a^{-1}(v_a + v_s), \\ &W_{n\,\mathrm{comp}} = -a^{-1}v_a^2/2; \quad W_n = a^{-1}(v_s^2 - v_a^2)/2. \end{aligned}\right\}. \tag{51}$$

If Newton's rule is applied, an "all linear solution" can always be obtained for a balanced collision provided sliding stops, regardless the sliding direction being constant or not.

In integrated form, the percussive Lagrangian equations and Eq. (5) are

$$\{\Delta u\} = [M]^{-1}[k]\{P\}, \tag{52}$$

$$\{dv\} = [N]\{P\} \rightarrow \{P\} = [N]^{-1}\{\Delta v\}, \tag{53}$$

but

$$\left.\begin{aligned} &[N]^{-1} = \begin{bmatrix} a^{-1} & 0 \\ 0 & [b]^{-1} \end{bmatrix}, \\ &\{\Delta v\} = \begin{Bmatrix} (1+e)v_a \\ -\mathbf{v}_t^{(0)} \end{Bmatrix} = -\begin{Bmatrix} (1+e)\{\alpha\}^T \\ [\beta] \end{Bmatrix}\{u^{(0)}\} \end{aligned}\right\}. \tag{54}$$

Substitution of Eqs. (53) and (54) into Eq. (52) leads to

$$\{\Delta u\} = [\mathcal{P}']\{u^{(0)}\}, \tag{55}$$

with

$$[\mathcal{P}'] \equiv -[M]^{-1}((1+e)a^{-1}\{\alpha\}\{\alpha\}^T + [\beta][b]^{-1}[\beta]^T). \tag{56}$$

The final velocities can be expressed as

$$\{u\} = ([I] + [\mathcal{P}'])\{u^{(0)}\}, \tag{57}$$

where matrix $[I] + [\mathcal{P}']$ is the transfer matrix of the collision.

The energy dissipated by the normal force is W_n defined by Eq. (51), and the one dissipated by friction can be calculated analytically if the sliding direction is constant. For balanced collisions with constant σ in which sliding stops, Eq. (32a) reduces to

$$W_t = -b_o^{-1}v_t^{(0)2} \tag{58}$$

where b_o is the eigenvalue of $[b]$ associated with the eigenvector

Downloaded 03 May 2010 to 171.66.16.245. Redistribution subject to ASME license or copyright; see http://www.asme.org/terms/Terms_Use.cfm

σ. In this case W_t is independent from μ (provided that μ is great enough to stop the sliding).

In case of sliding with constant direction, the condition for stopping sliding $|P_t| = \mu P_n^s \leq \mu P_n$, (where P_n^s is the normal percussion associated with the sliding interval) leads to

$$|v_t^{(0)}| \leq \mu \frac{b_\sigma}{a}(1+e)v_a. \tag{59}$$

If sliding does not stop, even though Newton's rule may be applied, an "all linear" solution is only possible if the sliding direction is constant (it must be one of the eigenvectors of $[b]$), and in such a case, if Newton's rule is applied Eq. (29) of Section 5 applies. Otherwise, even though Newton's rule were applied the two equations concerning $\mathbf{P}_t$ would be lacking.

8 Application Example: Bounding of a Sphere on a Fixed Surface

The bounding of a rough sphere on a fixed surface, Fig. 2, is an illustrative example of balanced collision in which an "all linear" solution is always possible.

It is always a balanced collision because P_n goes through the mass center, no matter the impact configuration, and consequently $\mathbf{v}_t$ is unchanged if friction is neglected. An all linear solution is always possible because all tangential directions are sliding eigendirections, so sliding direction does not change.

Lets assume the planar movement with the initial conditions depicted in Fig. 2. Notation defined in Fig. 2 will be used. The degrees-of-freedom and initial velocities are described by

$$\{u\} = \begin{Bmatrix} v_v \\ v_L \\ \Omega \end{Bmatrix}; \{u^{(0)}\} = \begin{Bmatrix} -u_0 \\ v_0 \\ \omega_0 \end{Bmatrix}. \tag{60}$$

Basic matrices and vectors are

$$[M] = m\begin{bmatrix} 1 & & \\ & 1 & \\ & & \rho^2 \end{bmatrix}; [k] = \begin{bmatrix} 1 & 1 \\ 0 & 1 \\ 0 & -r \end{bmatrix}. \tag{61}$$

It is assumed $v_t^{(0)} \triangleq v_0 - \omega r > 0$, and hence $\sigma = +1$.

If sliding does not stop and Newton's rule is applied, Eq. (28) leads to

$$[\mathcal{P}] = -(1+e)\begin{bmatrix} 1 & 0 & 0 \\ -\mu & 0 & 0 \\ \mu r'/\rho & 0 & 0 \end{bmatrix}; r' \triangleq r/\rho, \tag{62}$$

and from Eq. (29) for final velocities,

$$\{u\} = \begin{Bmatrix} eu_0 \\ v_0 - \mu(1+e)u_0 \\ \omega_0 - \mu(1+e)u_0 r'/\rho \end{Bmatrix}, \tag{63a}$$

$$\begin{Bmatrix} v_n \\ v_t \end{Bmatrix} = [k]^T\{u\} = \begin{Bmatrix} eu_0 \\ v_0 - \omega_0 r - \mu(1+e)u_0(1+r'^2) \end{Bmatrix}. \tag{63b}$$

The condition for not stopping sliding is

$$v_t^{(0)} \triangleq v_0 - \omega_0 r \geq \mu(1+e)u_0(1+r'^2). \tag{64}$$

The energy dissipated by the normal force and by friction can be calculated by means of Eq. (19) and by any of Eqs. (32), respectively, with $P_n = mu_0(1+e)$, $\mathbf{h} = 0$ and $\boldsymbol{\sigma}^T[b]\boldsymbol{\sigma} = (1+r'^2)/m$.

$$\left.\begin{aligned} W_n &= -mu_0^2(1-e^2)/2 \\ W_t &= -\mu(1+e)mu_0(v_t^{(0)} - u_0\mu(1+e)(1+r'^2)/2 \end{aligned}\right\}. \tag{65}$$

If sliding stops and Newton's rule is also applied, then Eq. (56) leads to

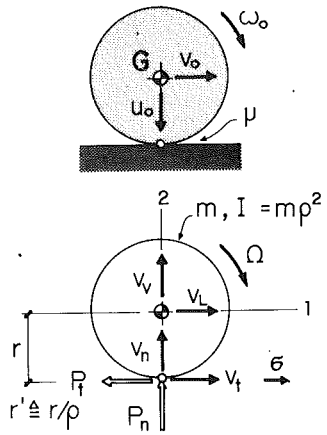


Fig. 2 Bounding of a rough sphere; notation

$$[\mathcal{P}'] = -\frac{1}{1+r'^2}\begin{bmatrix} (1+e)(1+r'^2) & 0 & 0 \\ 0 & 1 & -r \\ 0 & -r'/\rho & r'^2 \end{bmatrix}, \tag{66}$$

and from Eq. (57) for final velocities,

$$\{u\} = \begin{Bmatrix} eu_0 \\ v_0 - v_t^{(0)}/(1+r'^2) \\ \omega_0 + v_t^{(0)}r'/\rho(1+r'^2) \end{Bmatrix}; \begin{Bmatrix} v_n \\ v_t \end{Bmatrix} = \begin{Bmatrix} eu_0 \\ 0 \end{Bmatrix}. \tag{67}$$

The energy dissipated by the normal force and by friction can be calculated by means of Eq. (19) and Eq. (58), respectively, with $P_n = mu_0(1+e)$ and $b_\sigma = (1+r'^2)/m$,

$$\left.\begin{aligned} W_n &= -mu_0^2(1-e^2)/2 \\ W_t &= -mv_t^{(0)2}/(1+r'^2) \end{aligned}\right\}. \tag{68}$$

9 Conclusions

A broad sufficiency condition for Newton's or Poisson's, rules to be energetically consistent has been presented, and the equivalence between both rules in such a case has been demonstrated.

For single-point rough collisions in multibody systems with perfect constraints, in which Coulomb's friction and infinite tangential stiffness are assumed at the collision point, the broad condition requires a constant ratio of the differential normal percussion dP_n to the differential normal velocity dv_n during the collision interval.

This condition is fulfilled in two general cases:

- that of equations of motion with constant coefficients (which includes smooth collisions, rough collisions without sliding, and rough collisions with permanent sliding with constant direction) and
- that of "balanced" collisions: the sliding velocity would not change if there were no friction. In this case, sliding may change direction and stop during the collision interval.

In the first case Newton's or Poisson's rules allow always an "all linear" solution while in the second case if sliding direction varies such a possibility exists only if sliding stops.

The case of constant equations of motion has been extended to multibody systems with impulsive drivers that guarantee the continuity of a set of generalized velocities during the collision.

Acknowledgments

The author expresses his thanks to Ana Barjau Condomines for her useful comments and suggestions on this work, and to the referees, whose advice has been of great value to improve the final version of the article.

Downloaded 03 May 2010 to 171.66.16.245. Redistribution subject to ASME license or copyright; see http://www.asme.org/terms/Terms_Use.cfm

References

Batlle, J. A., and Barjau Condomines, A., 1991, "Rough Collisions in Multibody Systems," *Mech. Mach. Theory*, Vol. 26, No. 6, pp. 565–577.

Beghin, H., 1967, *Cours de Mécanique Théorique et Appliquée*, Gauthier-Villars, Paris, pp. 457–483.

Brach, R. M., 1989, Rigid Body Collisions," ASME JOURNAL OF APPLIED MECHANICS, Vol. 56, pp. 133–138.

Brach, R. M., 1984, "Friction, Restitution and Energy Loss in Planar Collisions," ASME JOURNAL OF APPLIED MECHANICS, Vol. 51, pp. 164–170.

Keller, J. B., 1986, "Impact With Friction," ASME JOURNAL OF APPLIED MECHANICS, Vol. 53, pp. 1–4.

Kilmister, C. W., and Reeve, J. E., 1966, *Rational Mechanics*, Longmans, London, Chapter 4, pp. 178–195.

Roy, M., 1964, *Méchanique, I. Corps Rigides*, Dunod, Paris, Chapter 4.

Smith, C. E., 1991, "Predicting Rebounds Using Rigid-Body Dynamics," ASME JOURNAL OF APPLIED MECHANICS, Vol. 58, pp. 755–758.

Stronge, W. J., 1990, "Rigid Body Collisions with Friction," *Proc. R. Soc. Lond.*, Vol. A431, pp. 169–181.

Wang, Y., and Mason, M. T., 1987, "Modelling Impact Dynamics for Robotic Operations," *Proc. of IEEE Int. Conf. on Robotics and Automation*, pp. 678–685.

Whittaker, E. T., 1965, *A Treatise on the Analytical Dynamics of Particles and Rigid Bodies*, Cambridge University Press, London, Section 95, pp. 234–235.

APPENDIX

Extension to Multibody Systems With Impulsive Drivers

As a first approach, high-impedance drivers found in certain multibody systems can be modeled as impulsive drivers able to guarantee the continuity of a set of generalized velocities $\{v_a\}^T = \{v_{a1}, v_{a2}, \ldots, v_{ap}\}$ during the impact interval (Batlle and Barjau Condomines, 1991).

If $\{dP_a\}$ is the p-column vector of the differential percussions associated with drivers, then the generalized differential impulse $\{d\Pi_a\}$ associated with them is

$$\{d\Pi_a\} = [A]^T\{dP_a\}, \tag{A1}$$

where $[A]$ is the $n \times p$ matrix relating $\{v_a\}$ to the generalized velocities

$$\{v_a\} = [A]^T\{u\}. \tag{A2}$$

Matrix $[A]$ depends only upon configuration.

The insertion of $\{d\Pi_a\}$ into the differential equation of motion following a process similar to that presented in Section 2 leads to the equations of motion $\{du\} = \{C\}dP_n$, with

$$\{C^s\} = [M]^{-1}([I] - [A][A'])(\{\alpha\} - \mu[\beta]\sigma), \tag{A3}$$

$$\{C^{ns}\} = [M]^{-1}([I] - [\beta][B'])\{\alpha\}, \tag{A4}$$

for sliding or not sliding conditions, respectively, where

$$[A'] \triangleq ([A]^T[M]^{-1}[A])^{-1}[A]^T[M]^{-1}, \tag{A5}$$

$$[B'] \triangleq ([\beta|A]^T[M]^T[\beta|A])^{-1}[\beta|A]^T[M]^{-1}. \tag{A6}$$

Similarly to $\{C^s\}$ and $\{C^{ns}\}$ defined by Eqs. (8) and (12), $\{C^{ns}\}$ defined by Eq. (A4) is only configuration dependent while $\{C^s\}$ defined by Eq. (A3) depends upon the configuration and the sliding direction σ. Values $\eta = dP_n/dv_n = (\{\alpha\}^T\{C\})^{-1}$ imply that the sufficiency condition (η constant) for Newton's rule to be energetically consistent is verified if the equations of motion have constant coefficients. So, according to Eqs. (A3) and (A4) conclusions (a), (b), and (c) of Section 3 can be extended to systems with impulsive drivers. Conclusion (d), however, cannot be extended, in general, to such systems.

For $\{C\}$ constant, if Newton's rule is applied, the final velocities $\{u\}$ can be calculated by means of Eq. (29) by using $\{C\}$ defined by Eq. (A3) or (A4), as appropriate.

Downloaded 03 May 2010 to 171.66.16.245. Redistribution subject to ASME license or copyright; see http://www.asme.org/terms/Terms_Use.cfm

Vibration Absorbers for a Class of Self-Excited Mechanical Systems

S. Natsiavas
Assoc. Professor,
Department of Mechanical and Aerospace Engineering,
Arizona State University,
Tempe, AZ 85287
Assoc. Mem. ASME

An averaging methodology is employed in studying dynamics of a two-degree-of-freedom nonlinear oscillator. The main system is modeled as a van der Pol oscillator under harmonic forcing. The objective is to reduce its amplitude of oscillation near resonance, by attaching to it a damped vibration absorber with a Duffing spring. It is first shown that substantial reduction in the response amplitude can be achieved in this way. However, for some combinations of the parameters, the low-amplitude periodic motion of the system in the original resonance regime becomes unstable through a Hopf bifurcation of the averaged equations. Direct numerical integration shows that this gives rise to amplitude modulated or chaotic response of the oscillator, with much higher vibration amplitudes than the unstable periodic response, which coexists with these complex motions. Finally, it is shown that the present analysis can be employed in selecting the parameters in ways that exploit the significant practical advantages arising from the presence of the absorber, by predicting and avoiding these instabilities.

Introduction

There are many examples of mechanical systems which possess technical characteristics leading to self-excited oscillations (e.g., Den Hartog, 1985; Nayfeh and Mook, 1979). In most of these systems, the resulting vibrations cause undesirable effects. As a result, ways to quench these vibrations are of large practical value (e.g., Tondl, 1975; Asfar, 1989). The present work investigates the effectiveness of a damped dynamic vibration absorber in reducing the vibration amplitude of a self-excited oscillator, harmonically forced near resonance. This method of controlling vibration has found extensive application in other mechanical systems with linear (e.g., Den Hartog, 1985) or nonlinear (e.g., Pipes, 1953; Rice, 1986; Shaw et al., 1989; Natsiavas, 1992) stiffness characteristics.

The objective of this study is to develop an analysis predicting the behavior of a two-degree-of-freedom dynamical system, consisting of a self-excited main component and of an auxiliary mass attached to it. The main component is modeled as a van der Pol oscillator under harmonic excitation. The absorber spring is chosen to be of Duffing type. First, the normalized equations of motion of the system are presented. Then, approximate solutions are determined by applying the method of averaging. The stability analysis of these solutions is also carried out. Next, numerical results are presented, verifying the effectiveness of the absorber for the system considered. However, it is also demonstrated that the nonlinearities may give rise to dangerous instabilities. Various complex motions associated with these instabilities—involving destruction and anagenesis of smooth attractors, torus doublings, etc.—are investigated with direct numerical integration. The study concludes by presenting a series of stability diagrams.

Normalized Equations of Motion

The system examined is shown in Fig. 1. The main component is modeled by a van der Pol oscillator with damping force: $-c_1\dot{x}_1 + \hat{c}_1\dot{x}_1^3$, while the spring of the absorber (mass m_2) results in restoring force: $k_2x_2 + \hat{k}_2x_2^3$. The main mass m_1 is subjected to a forcing $F_1(t) = F\cos(\Omega t)$.

In order to facilitate the analysis, the absolute displacement x_1 of m_1 and the relative displacement x_2 of the absorber with respect to m_1 are first normalized by $x_c = \sqrt{m_1c_1/(3k_1\hat{c}_1)}$, i.e., $y_i = x_i/x_c$, $(i = 1, 2)$, which requires that $c_1\hat{c}_1 > 0$. In addition, the following dimensionless parameters are introduced:

$$\omega_i = \sqrt{k_i/m_i}, \quad \zeta_i = c_i/(2\sqrt{k_im_i}), \quad (i = 1,2),$$

$$\omega = \Omega/\omega_1, \quad \rho = \omega_2/\omega_1,$$

$$\epsilon_1 = 2\zeta_1, \quad \epsilon_2 = (\hat{k}_2/k_2)x_c^2, \quad f = F/(k_1x_c), \quad \mu = m_2/m_1.$$

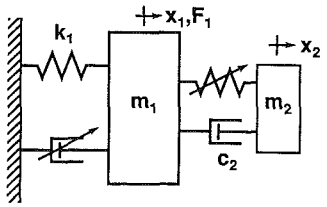


Fig. 1 Mechanical model of system

Contributed by the Applied Mechanics Division of THE AMERICAN SOCIETY OF MECHANICAL ENGINEERS for presentation at the First Joint ASCE-EMD, ASME-AMD, SES Meeting, Charlottesville, VA, June 6-9, 1993.

Discussion on this paper should be addressed to the Technical Editor, Professor Lewis T. Wheeler, Department of Mechanical Engineering, University of Houston, Houston, TX 77204-4792, and will be accepted until four months after final publication of the paper itself in the ASME JOURNAL OF APPLIED MECHANICS.

Manuscript received by the ASME Applied Mechanics Division, Aug. 20, 1991; final revision, Apr. 14, 1992. Associate Technical Editor: D. J. Inman.

Paper No. 93-APM-16.

Copyright © 1993 by ASME
Downloaded 03 May 2010 to 171.66.16.245. Redistribution subject to ASME license or copyright; see http://www.asme.org/terms/Terms_Use.cfm

Finally, if the normalized time is defined by $\tau \equiv \omega_1 t$, the equations of motion of the system can be cast in the following matrix form:

$$M\ddot{\mathbf{y}} + K\mathbf{y} = \mathbf{g}(\tau, \mathbf{y}, \dot{\mathbf{y}}) \equiv \begin{pmatrix} f\cos(\omega\tau) + \epsilon_1 \dot{y}_1(1 - \dot{y}_1^2/3) \\ -2\mu\rho\zeta_2\dot{y}_2 - \epsilon_2\mu\rho^2 y_2^3 \end{pmatrix}, \quad (1)$$

where the mass and stiffness matrices are expressed by

$$M = \begin{pmatrix} 1+\mu & \mu \\ \mu & \mu \end{pmatrix}, \quad K = \begin{pmatrix} 1 & 0 \\ 0 & \mu\rho^2 \end{pmatrix}, \quad \text{while } \mathbf{y} = \begin{pmatrix} y_1 \\ y_2 \end{pmatrix}.$$

Approximate Steady-State Solutions

Averaging is applied in seeking solutions of (1) in the vicinity of $\omega = 1$, with form

$$\mathbf{y}(\tau) = \mathbf{u}(\tau)\cos(\omega\tau) + \nu(\tau)\sin(\omega\tau), \quad (2)$$

and velocity expressed by

$$\dot{\mathbf{y}}(\tau) = -\omega[\mathbf{u}(\tau)\sin(\omega\tau) - \nu(\tau)\cos(\omega\tau)]. \quad (3)$$

These equations imply that

$$\dot{\mathbf{u}}(\tau)\cos(\omega\tau) + \dot{\nu}(\tau)\sin(\omega\tau) = \mathbf{0}, \quad (4)$$

$$\ddot{\mathbf{y}}(\tau) = -\omega^2\mathbf{y}(\tau) - \omega[\dot{\mathbf{u}}(\tau)\sin(\omega\tau) - \dot{\nu}(\tau)\cos(\omega\tau)]. \quad (5)$$

Substituting (2), (3), and (5) in (1) yields

$$\omega M[\dot{\nu}\cos(\omega\tau) - \dot{\mathbf{u}}\sin(\omega\tau)] + (K - \omega^2 M)[\mathbf{u}\cos(\omega\tau) + \nu\sin(\omega\tau)] = \mathbf{h}(\tau, \mathbf{u}, \nu),$$

with $\mathbf{h}(\tau, \mathbf{u}, \nu) \equiv \mathbf{g}(\tau, \mathbf{y}, \dot{\mathbf{y}})$.

In order to get the evolution equations for the amplitudes $\mathbf{u}$ and ν, first premultiply (4) by $\omega M\cos(\omega\tau)$, multiply (6) by $-\sin(\omega\tau)$ and add to obtain

$$\omega M\dot{\mathbf{u}} = (K - \omega^2 M)[\mathbf{u}\cos(\omega\tau) + \nu\sin(\omega\tau)]\sin(\omega\tau) - \mathbf{h}\sin(\omega\tau).$$

Then, integrate the last equation over a forcing period $T = 2\pi/\omega$, by assuming that $\mathbf{u}$ and ν are slowly varying functions of τ. This operation yields the following autonomous equations:

$$2\omega M\dot{\mathbf{u}} = (K - \omega^2 M)\nu + \begin{pmatrix} \omega\epsilon_1 u_1 - \omega^3 e_1 u_1 \\ \mu\rho(3\rho e_2\nu_2 - 2\zeta_2\omega u_2) \end{pmatrix}. \quad (7)$$

Similarly, premultiply (4) by $\omega M\sin(\omega\tau)$, multiply (6) by $\cos(\omega\tau)$, add and integrate the resulting equation over a forcing period to get

$$2\omega M\dot{\nu} = (\omega^2 M - K)\mathbf{u} + \begin{pmatrix} f + \omega\epsilon_1\nu_1 - \omega^3 e_1\nu_1 \\ -\mu\rho(3\rho e_2 u_2 + 2\zeta_2\omega\nu_2) \end{pmatrix}, \quad (8)$$

where

$$e_i \equiv \epsilon_i(u_i^2 + \nu_i^2)/4 \quad (i = 1,2). \quad (9)$$

Constant solutions of the averaged system (7) and (8), expressed by

$$\dot{\mathbf{u}} = \mathbf{0} = \dot{\nu}, \quad (10)$$

correspond to T-periodic motions of the original system (1). These solutions are determined by applying (10) in (7) and (8), which leads to the following:

$$(\omega\epsilon_1 - \omega^3 e_1)u_1 - a_1\nu_1 - \mu\omega^2\nu_2 = 0 \quad (11)$$

$$a_3 u_2 + \omega^2\nu_1 + (a_2 - a_4 e_2)\nu_2 = 0, \quad (12)$$

$$a_1 u_1 + \mu\omega^2 u_2 + (\omega\epsilon_1 - \omega^3 e_1)\nu_1 = -f \quad (13)$$

$$\omega^2 u_1 + (a_2 - a_4 e_2)u_2 - a_3\nu_2 = 0, \quad (14)$$

where $a_1 = (1 + \mu)\omega^2 - 1$, $a_2 = \omega^2 - \rho^2$, $a_3 = 2\omega\rho\zeta_2$ and $a_4 = 3\rho^2$.

Equations (11)–(14) represent a system of four coupled nonlinear algebraic equations for u_i and ν_i. However, this system is reduced to a system of two equations, involving the displacement amplitudes e_i only. This is accomplished by first solving (11)–(14) and obtaining u_i and ν_i in closed form in terms of e_i. This yields four equations of the form

$$u_i = u_i(e_1, e_2), \quad \nu_i = \nu_i(e_1, e_2) \quad (i = 1,2). \quad (15)$$

Then, simultaneous application of (9) and (15) results in two coupled polynomial equations of the form

$$\Phi_i(e_1, e_2) = e_i - \epsilon_i[u_i^2(e_1, e_2) + \nu_i^2(e_1, e_2)]/4 = 0 \quad (i = 1,2). \quad (16)$$

Equations (15) and (16) are obtained in terms of lengthy but closed-form polynomial expressions involving the e_i's. Numerical solution of the two polynomial equations represented by (16) determines the e_i's and therefore the periodic solutions sought, by back substitution in (15).

For the case of no damping (which needs redefinition of x_c), (11) and (12) imply that $\nu_1 = 0 = \nu_2$, as expected. Also, the present analysis is simplified when the absorber stiffness is constant (i.e., $\epsilon_2 = 0 = e_2$). Then, the equation to be solved is

$$\phi_1(e_1) = 4e_1 - \epsilon_1[u_1^2(e_1) + \nu_1^2(e_1)] = 0$$

which turns out to be a fifth-order polynomial in e_1.

Stability of Periodic Motions

First, let $\mathbf{w} \equiv (\mathbf{u}\ \nu)^T$ and cast the averaged Eqs. (7) and (8) in the compact form

$$\dot{\mathbf{w}}(\tau) = \mathbf{q}(\mathbf{w}(\tau)). \quad (17)$$

Next, let $\mathbf{w}_o$ be a steady-state solution of (17). To reveal its stability characteristics, $\mathbf{w}_o$ is perturbed by

$$\mathbf{w}(\tau) = \mathbf{w}_0 + \epsilon\mathbf{w}_1(\tau),$$

where $|\epsilon| \ll 1$. Substituting the last expression in (17), Taylor-expanding around $\mathbf{w}_o$ and keeping terms up to first order in ϵ results in the following linear system:

$$\dot{\mathbf{w}}_1 = \Pi\mathbf{w}_1 = \left(\frac{\partial\mathbf{q}}{\partial\mathbf{w}}(\mathbf{w}_o)\right)\mathbf{w}_1. \quad (18)$$

When $\mathbf{w}_o$ is a constant vector, the elements of the 4×4 Jacobian Π—obtained in closed form—are also constant. Therefore, $\mathbf{w}_o$ corresponds to an asymptotically stable periodic solution of (1) provided that the real part of all the eigenvalues of Π—which are found as solutions of quartic equations—is negative. In cases, where the real part of an eigenvalue of Π is positive, the solution is unstable. Finally, when the maximum real part of the eigenvalues of Π is zero bifurcations occur (e.g., Guckenheimer and Holmes, 1983). Two types of bifurcations were encountered in the present study. The first type is a saddle-node bifurcation and results in the classical jump phenomena. It occurs when a real eigenvalue of Π changes sign. The second type is Hopf bifurcation, it occurs when the real part of a pair of complex eigenvalues changes sign and results in quasi-periodic (amplitude modulated) oscillations of the original system (1).

A Note on Ordering of the Parameters

Let $\bar{\omega}_i$ ($i = 1, 2$) be the eigenvalues and Y be the modal matrix of the linearized undamped system with

$$Y^T M Y = I, \quad Y^T K Y = \Lambda, \quad (19)$$

where I is the 2×2 identity matrix and Λ is a diagonal matrix with elements $\lambda_i = \bar{\omega}_i^2$. Rescaling according to

$$\mathbf{u} = Y\alpha, \quad \nu = Y\beta, \quad (20)$$

using (19) and assuming that the parameters ϵ_1, ϵ_2, and ζ_2 are of order ϵ (with ϵ small), Eqs. (7) and (8) can be written in the form

$$2\omega\dot{\boldsymbol{\gamma}} = \begin{pmatrix} 0 & \Lambda - \omega^2 I \\ \omega^2 I - \Lambda & 0 \end{pmatrix}\boldsymbol{\gamma} + \epsilon\mathbf{s}(\boldsymbol{\gamma}) + \mathbf{f},$$

with $\boldsymbol{\gamma} = [\alpha\ \beta]^T$ and $\mathbf{f} = [0\ 0\ f\ 0]^T$. Therefore, if the parameters of the system are chosen so that $\bar{\omega}_i \to 1$—which means

Downloaded 03 May 2010 to 171.66.16.245. Redistribution subject to ASME license or copyright; see http://www.asme.org/terms/Terms_Use.cfm

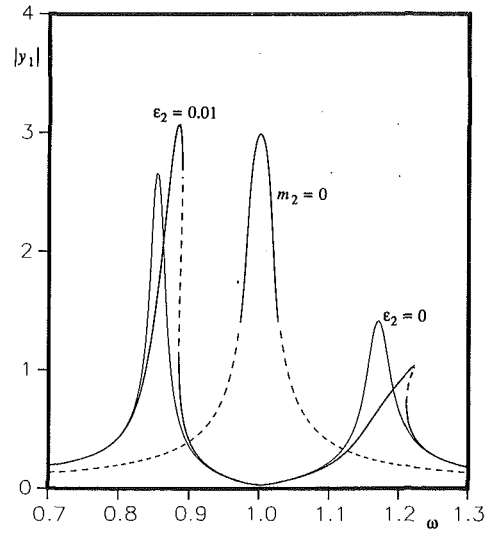


Fig. 2 Response diagram of main mass ($\zeta_2 = 0.02$)

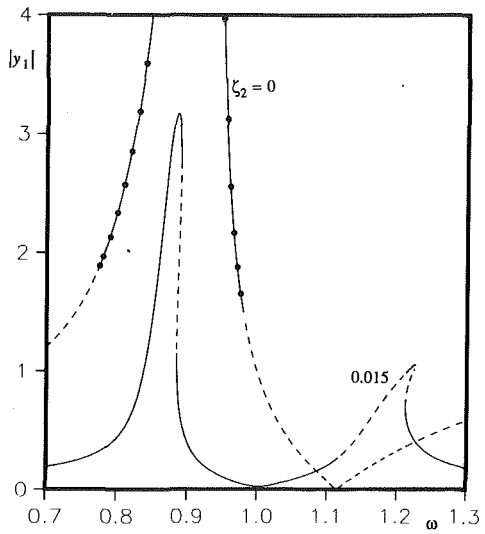


Fig. 3 Response diagram of main mass ($\zeta_2 = 0$ and 0.015)

that $\mu \to 0$ and $\rho \to 1$—the scaled averaged equations can be put in the standard form

$$\dot{\gamma} = \epsilon \mathbf{p}(\gamma),$$

provided that f and $\omega^2 - 1$ are of order ϵ. Therefore, the analysis developed is expected to give accurate results for parameter values satisfying the restrictions mentioned above.

Whenever $\bar{\omega}_i \to 1$, the system approaches 1:1 internal resonance conditions (see Nayfeh and Balachandran, 1989). It can be shown that 3:1 as well as nonresonant oscillations are also possible for the system examined. However, this happens for combinations of μ and ρ not fitting the purposes of this study.

Numerical Results

This section presents results confirming the analysis and investigating the effectiveness of the vibration absorber for the system examined.

Response Diagrams. The parameters of the system analyzed first are: $\zeta_1 = 0.01$, $\zeta_2 = 0.02$, $\mu = 0.1$, $\rho = 1$ and $f = 0.08$. Figure 2 shows the response diagram of the main mass for $\epsilon_2 = 0$ (linear absorber) and 0.01. The response diagram of the main mass alone—see section 4.3.1 of Nayfeh and Mook, 1979, with ω_o, ρ, k, and σ replaced by 1, $y_1^2/4$, $(\omega - 1)/\epsilon_1$ and f/ϵ_1—is also shown for comparison. Obviously, the presence of the absorber results in substantial reduction of the vibration amplitude of the main mass, near resonance. The effect of the absorber nonlinearity is to bend both solution branches to the right, resulting in better performance of the nonlinear absorber in the range $\omega > 1$. For an absorber with a softening spring, the response curves lean towards left, resulting in better performance in $\omega < 1$. These results demonstrate the practical importance of the absorber in quenching resonant vibrations of self-excited oscillators.

The unstable branches—broken lines—that appeared in Fig. 2 for $\epsilon_2 = 0.01$ were generated through saddle-node bifurcations and occurred away from the $\omega = 1$ range. However, varying the system parameters results in bifurcations which give rise to potentially dangerous instabilities, similar to those observed for systems with nonlinear stiffness (e.g., Rice, 1986; Shaw et al., 1989 and Natsiavas, 1992). This is illustrated by Fig. 3, for two such cases. First, the parameters of the previous example are utilized ($\epsilon_2 = 0.01$), with ζ_2 reduced to 0.015. Here, portion of a previously stable branch of solutions (from $\omega = 1.12$ to 1.20) becomes unstable. Next, the damping levels are reduced to $\zeta_1 = 0.001$, $\zeta_2 = 0$, while the level of the absorber nonlinearity is increased to $\epsilon_2 = 0.02$ and the forcing to $f = 0.5$. As can be seen, this results in even worse situations. The consequences of these instabilities on the effectiveness of the absorber are analyzed in the following subsection.

In the last example, the value of f is relatively high. To check the validity and accuracy of the developed analysis, results obtained by direct integration of (1) are also presented in Fig. 3 for that case. Namely, the steady-state response obtained by direct integration—represented by the thick dots—was periodic for ω between 0.775 and 0.975. The corresponding values predicted by the present analysis were 0.771 and 0.981, respectively.

Direct Integration of the Averaged and the Original Equations of Motion. In both the last examples, the unstable branches near $\omega = 1$ were generated through Hopf bifurcations of (17). A comprehensive study of the complex motions of the averaged system that are generated by similar bifurcations for a system with 3:1 internal resonance was performed by Tousi and Bajaj (1985). For the system considered here, the modes are close to 1:1 internal resonance. As a result, this system is shown to exhibit behavior with similar complex characteristics, following these bifurcations (see also Miles, 1984; Bajaj and Johnson, 1990).

First, performing direct integration of the averaged Eqs. (17), it is found that for the case with $\zeta_2 = 0.015$, the Hopf bifurcation at $\omega = 1.12$ is supercritical. The unstable constant solutions of the averaged system (17) for $\omega > 1.12$ are replaced by stable periodic solutions. For example, Fig. 4 shows the steady-state response of the solution amplitudes at $\omega = 1.15$. The normalized period of these solutions is 25.30. This value is almost identical to $2\pi/0.247$, where 0.247 is the imaginary part of the critical eigenvalues of Π at $\omega = 1.15$ (see Tousi and Bajaj, 1985).

Typically, the frequency of the periodic solutions of the averaged equations generated by a Hopf bifurcation is much smaller than the forcing frequency. As a result, the corresponding solutions of the original system (1) are amplitude modulated. To illustrate this, Fig. 5 shows the Poincare section at $\omega = 0.985$, obtained by direct integration of (1) and by sampling y_1 and $\dot{y}_2$ at every forcing period, for the system with $\zeta_2 = 0$. Note that in the present case, the resulting invariant dense circle was found to retain its topology throughout the frequency range examined. For example, the Poincare section at $\omega = 1.0426$ is also shown in Fig. 5. Clearly, the only change observed is a magnification of the original geometry. However, during this numerical search, another set of solutions was

Downloaded 03 May 2010 to 171.66.16.245. Redistribution subject to ASME license or copyright; see http://www.asme.org/terms/Terms_Use.cfm

found to coexist in that frequency range, with much richer dynamics. Figure 6 presents a few typical Poincare sections of these solutions, for different forcing frequencies. The axes ranges of Fig. 6 are the same as those of Fig. 5.

The first remarkable feature of the second set of solutions is that there is a consistent sequence of events in going from one smooth attractor to the next, as ω is varied. Namely, the changes in the shapes of the attractor are triggered by collisions

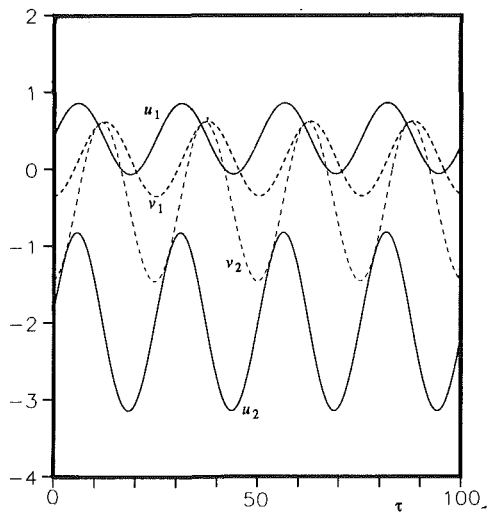


Fig. 4 Time histories of averaged amplitudes (ζ_2 = 0.015, ω = 1.15)

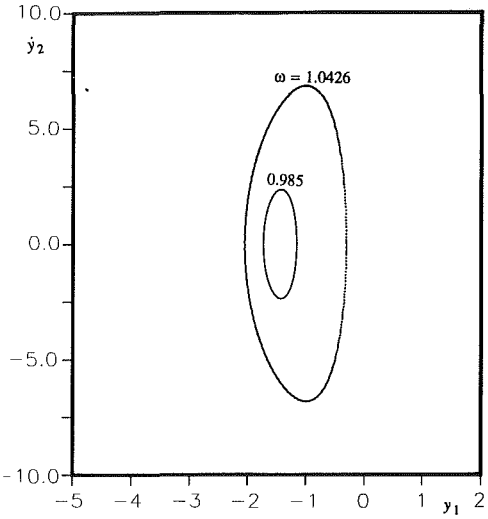


Fig. 5 Poincare sections at ω = 0.985 and 1.0426

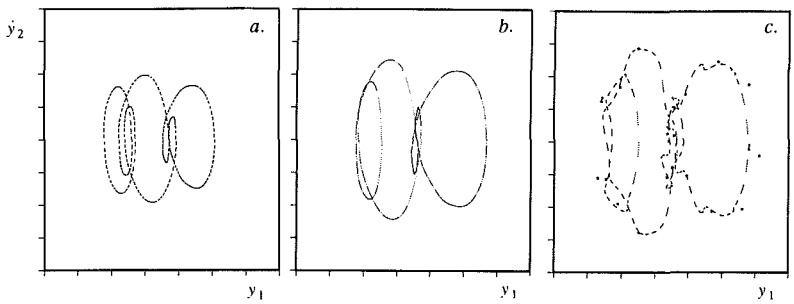


Fig. 6(*a*) Poincare section at ω = 0.985; (*b*) ω = 1; (*c*) ω = 1.004 and 1.005

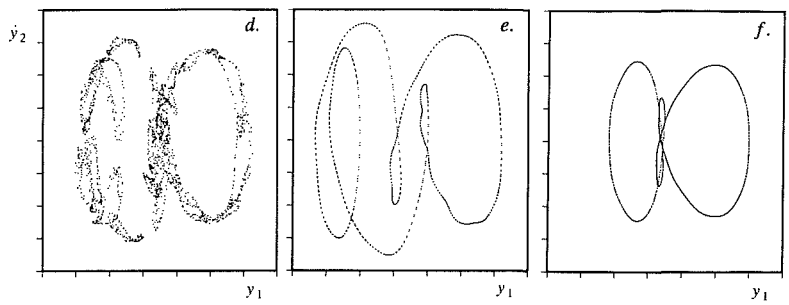


Fig. 6(*d*) Poincare section at ω = 1.008; (*e*) ω = 1.015; (*f*) ω = 1.020

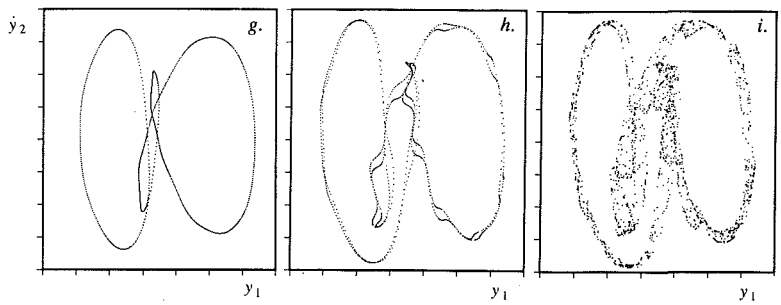


Fig. 6(*g*) Poincare section at ω = 1.035; (*h*) ω = 1.0416; (*i*) ω = 1.0426

Downloaded 03 May 2010 to 171.66.16.245. Redistribution subject to ASME license or copyright; see http://www.asme.org/terms/Terms_Use.cfm

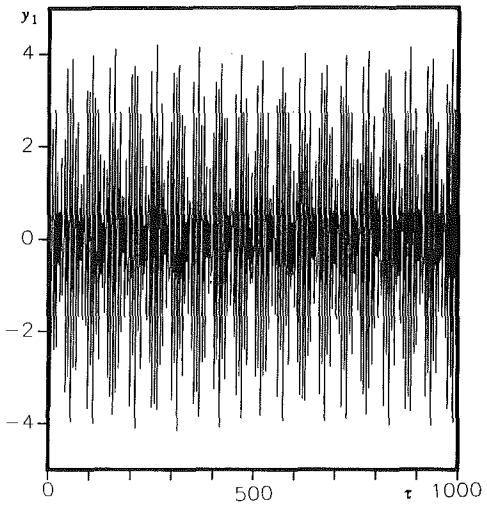


Fig. 7 Response history of m_1 at $\omega = 1.0426$

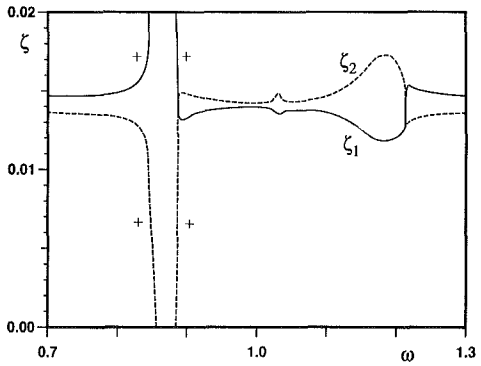


Fig. 8 Stability diagram (effect of damping)

and merging of their lobes. In the transition ranges, the attractors distort and split, before they become smooth again. During these transitions, a chaotic response (Fig. 6(*d*)) or a phase locked response may be obtained occasionally. For example, a subharmonic solution of order $n = 21$ (obtained at $\omega = 1.005$) is represented by the thick dots in Fig. 6(*c*). The quasiperiodic response obtained at $\omega = 1.004$ is also shown in the same figure, represented by the thinner dots. These changes are in agreement with Aronson's scenario (Aronson et al., 1982), according to which the generation and destruction of a smooth invariant circle may happen repeatedly, while moving away from the Hopf bifurcation value. Similar phenomena have also been observed for single-degree-of-freedom oscillators with nonlinear nonpositive damping (Natsiavas, 1991).

The second observation, referring to the same set of solutions, is that no cascades of torus doublings—corresponding to period doublings of the averaged equations—were observed here, in contrast to what was observed for other systems (e.g., Miles, 1984; Tousi and Bajaj, 1985; Bajaj and Johnson, 1990). The only torus doubling captured is shown in Fig. 6(*h*). After that doubling, the solution becomes chaotic, with no further doubling (see Arneodo et al., 1983; Kaneko, 1984 for explanations of cascade interruptions).

In closing, note that the numerical simulations indicated that the appearance of a complex sequence like that of Fig. 6 is more likely to occur for larger values of the forcing parameter but lower values of the damping nonlinearity and ζ_2. Such a sequence was not observed for the cases examined in a previous study (Natsiavas, 1992), where the nonlinearity of the main mass was of the Duffing type. Finally, for the second set of solutions the transition intervals are extremely small, while no

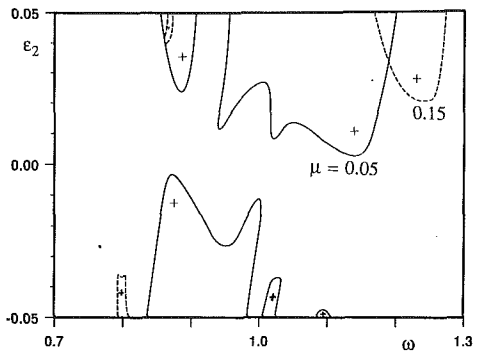


Fig. 9 Stability diagram (effect of absorber nonlinearity and mass ratio)

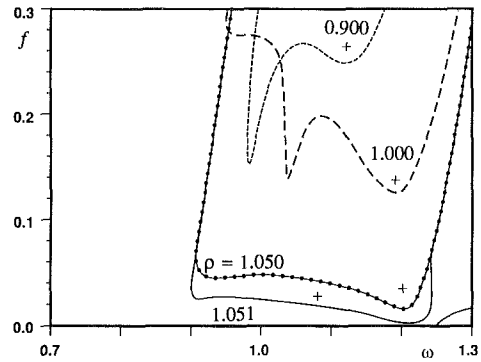


Fig. 10(*a*) Stability diagram (effect of forcing and tuning)

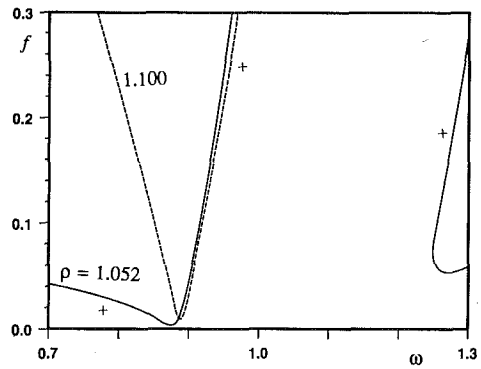


Fig. 10(*b*) Stability diagram (effect of forcing and tuning)

significant change occurs for the other coexisting sequence of amplitude modulated motions (Fig. 5), in the frequency range examined. In addition, the response amplitude of these solutions is much higher than the amplitude of the coexisting unstable periodic solution. For example, Fig. 7 shows the response history $y_1(\tau)$ at $\omega = 1.0426$, resulting in the section of Fig. 6(*i*). A chaotically modulated response is observed. The corresponding amplitude of the unstable periodic solution is only 0.45 (Fig. 3).

Stability Charts. The results that follow show that the analysis developed can help in first detecting and then eliminating the instabilities encountered in the previous subsections by adjusting the parameters. Namely, Figs. 8–10 present bifurcation diagrams, obtained by varying the system parameters from the reference combination: $\zeta_1 = 0.01$, $\zeta_2 = 0.02$, $\mu = 0.1$, $\rho = 1$, $f = 0.08$ and $\epsilon_2 = 0.01$. The lines in these diagrams represent parameter combinations giving birth to Hopf bifurcation. The sides of these curves marked by + represent ranges of parameters where the periodic motions of the system are unstable and should therefore be avoided, when designing the

Downloaded 03 May 2010 to 171.66.16.245. Redistribution subject to ASME license or copyright; see http://www.asme.org/terms/Terms_Use.cfm

absorber. Although the conclusions drawn are based on a limited number of cases, these diagrams provide an insight into the effects of these parameters on the stability of the periodic motions studied.

First, Fig. 8 shows the effect of the two damping parameters. Obviously, increasing ζ_1 results in enlargement of the unstable regime, while increasing ζ_2 has opposite effects, as expected. Note the rapid transition in the stability of the solutions near $\zeta = 0.014$ and some symmetry with respect to that line between the ζ_1 and ζ_2 curves.

Next, Fig. 9 illustrates the effect of the vibration absorber nonlinearity, for $\mu = 0.05$ and 0.15. Clearly, increasing the mass of the absorber results in stabilization of the periodic motions, but increasing the absolute value of ϵ_2 enlarges the unstable regimes. In some other cases with $\epsilon_2 < 0$, escape phenomena can occur (e.g., Nayfeh and Sanchez, 1989; Natsiavas, 1992).

Finally, Fig. 10 illustrates effects of the forcing and the tuning parameters. Increasing ρ enlarges the ranges of the unstable motions. Note the change of the stability boundary around $\rho = 1.051$, for small forcing levels. Also, the form of these diagrams—especially the one for $\rho = 1.1$—is reminiscent of bifurcation diagrams presented and analyzed for other coupled but unforced oscillators (e.g., Aronson et al., 1990; Taylor and Kevrekidis, 1991). In fact, the mathematical structure of the present problem is similar but more complex in the sense that it represents a *perturbed* resonant double Hopf bifurcation. Results of a similar problem but with a *single* resonant Hopf bifurcation (see Chapter 2 of Guckenheimer and Holmes, 1983) suggest that a complete analysis of this mathematical problem will reveal a lot of exotic dynamics.

Summary

Effects of a vibration absorber on a harmonically forced self-excited oscillator near resonance are investigated. First, an analytical procedure is developed for determining periodic response of the system. The method of averaging is applied and yields a set of four autonomous first-order differential equations governing the evolution of the amplitudes of oscillation. Determination of periodic solutions is then further reduced to solving a system of two algebraic equations. The analysis is completed by performing the stability of the located solutions. Then, the performance of the vibration absorber is studied by employing this analysis in conjunction with direct integration.

It is shown that the absorber causes a substantial reduction of the periodic vibration of the main mass. However, for some combinations of the parameters the constant solutions of the averaged equations loose stability in the range of the operating frequency, through a Hopf bifurcation. Direct integration verified that this gives rise to periodic solutions of the averaged equations, corresponding to amplitude modulated response of the original system. Moreover, as the forcing frequency is varied away from the bifurcation values, the system is shown to exhibit complex motions. Large order periodic motions as well as quasi-periodic and chaotic responses with much higher amplitudes than the predicted unstable periodic responses were found to coexist. A variety of phenomena, including rapid transitions between smooth invariant circles with changing topology and torus doubling were observed. Finally, the present analysis was employed in systematically predicting parameter ranges where dangerous instabilities are possible. These results provide insight into the effect of the system parameters and show that the analysis developed can help in choosing them so that the instabilities are eliminated, while preserving the technical advantages of the absorber.

References

Arneodo, A., Coullet, P. H., and Spiegel, E. A., 1983, "Cascade of Period Doublings of Tori," *Physics Letters*, Vol. 94A, pp. 1–6.

Aronson, D. G., Chory, M. A., Hall, G. R., and McGehee, R. P., 1982, "Bifurcations from an Invariant Circle for Two Parameter Families of Maps of the Plane: A Computer Assisted Study," *Comm. Math. Phys.*, Vol. 83, pp. 303–354.

Aronson, D. G., Ermentrout, G. B., and Kopell, N., 1990, "Amplitude Response of Coupled Oscillators," *Physica D*, Vol. 41, pp. 403–449.

Asfar, K. R., 1989, "Quenching of Self-Excited Vibrations," *ASME J. Vibrat. Acoustics*, Vol. 111, pp. 130–133.

Bajaj, A. K., and Johnson, J. M., 1990, "Asymptotic Techniques and Complex Dynamics in Weakly Nonlinear Forced Mechanical Systems," *Int. J. Nonlinear Mech.*, Vol. 25, pp. 211–226.

Den Hartog, J. P., 1984, *Mechanical Vibrations*, Dover, New York.

Guckenheimer, J., and Holmes, P., 1983, *Nonlinear Oscillations, Dynamical Systems and Bifurcations of Vector Fields*, Springer-Verlag, New York.

Kaneko, K., 1984, "Oscillation and Doubling of Torus," *Progress of Theoretical Physics*, Vol. 72, pp. 202–215.

Miles, J., 1984, "Resonant Motion of a Spherical Pendulum," *Physica D*, Vol. 11, pp. 309–323.

Natsiavas, S., 1991, "Dynamics of Piecewise Linear Oscillators with van der Pol Type Damping," *Int. J. Nonlinear Mech.*, Vol. 26, pp. 349–366.

Natsiavas, S., 1992, "Steady State Oscillations and Stability of Nonlinear Dynamic Vibration Absorbers," *J. Sound Vibrat.*, Vol. 156, pp. 227–245.

Nayfeh, A. H., and Mook, D. T., 1979, *Nonlinear Oscillations*, John Wiley and Sons, New York.

Nayfeh, A. H., and Sanchez, N. E., 1989, "Bifurcations in a Forced Softening Duffing Oscillator," *Int. J. Nonlinear Mech.*, Vol. 24, pp. 483–497.

Nayfeh, A. H., and Balachandran, B., 1989, "Modal Interactions in Dynamical and Structural Systems," ASME *Appl. Mech. Rev.*, Vol. 42, pp. S175–S201.

Pipes, L. A., 1953, "Analysis of a Nonlinear Dynamic Vibration Absorber," ASME JOURNAL OF APPLIED MECHANICS, Vol. 20, pp. 515–518.

Rice, H. J., 1986, "Combinational Instability of the Nonlinear Vibration Absorber," *J. Sound Vibrat.*, Vol. 108, pp. 526–532.

Shaw, J., Shaw, S. W., and Haddow, A. G., 1989, "On the Response of the Nonlinear Vibration Absorber," *Int. J. Nonlinear Mech.*, Vol. 24, pp. 281–293.

Taylor, M. A., and Kevrekidis, I. G., 1991, "Some Common Dynamic Features of Coupled Reacting Systems," *Physica D*, Vol. 51, pp. 274–292.

Tousi, S., and Bajaj, A. K., 1985, "Period-Doubling Bifurcations and Modulated Motions in Forced Mechanical Systems," ASME JOURNAL OF APPLIED MECHANICS, Vol. 52, pp. 446–452.

Tondl, A., 1975, "Quenching of Self-Excited Vibrations: Equilibrium Aspects," *J. Sound Vibrat.*, Vol. 42, pp. 251–260.

Downloaded 03 May 2010 to 171.66.16.245. Redistribution subject to ASME license or copyright; see http://www.asme.org/terms/Terms_Use.cfm

A Multiple-Scales Analysis of Nonlinear, Localized Modes in a Cyclic Periodic System

A. Vakakis
Assistant Professor,
Assoc. Mem. ASME.

T. Nayfeh
Graduate Student.

M. King
Graduate Student.

Department of Mechanical and Industrial Engineering, University of Illinois, Urbana, IL 61801

In this work the nonlinear localized modes of an n-degree-of-freedom (DOF) nonlinear cyclic system are examined by the averaging method of multiple scales. The set of nonlinear algebraic equations describing the localized modes is derived and is subsequently solved for systems with various numbers of DOF. It is shown that nonlinear localized modes exist only for small values of the ratio (k/μ), *where* k *is the linear coupling stiffness and* μ *is the coefficient of the grounding stiffness nonlinearity. As* (k/μ) *increases the branches of localized modes become nonlocalized and either bifurcate from "extended" antisymmetric modes in inverse, "multiple" Hamiltonian pitchfork bifurcations (for systems with even-DOF), or reach certain limiting values for large values of* (k/μ) *(for systems with odd-DOF). Motion confinement due to nonlinear mode localization is demonstrated by examining the responses of weakly coupled, perfectly periodic cyclic systems caused by external impulses. Finally, the implications of nonlinear mode localization on the active or passive vibration isolation of such structures are discussed.*

1 Introduction

In this work we present some new results on the dynamics of monocoupled, discrete, conservative, nonlinear periodic systems processing localized nonlinear modes. The concept of nonlinear normal mode in a discrete, conservative nonlinear system was first introduced by Rosenberg (1966), and was subsequently implemented to the study of the free (Rand, 1971, 1974; Month, 1979; Caughey et al., 1990) and forced responses of nonlinear oscillators (Manevich and Mikhlin, 1972), (Caughey and Vakakis, 1991a,b). A system vibrates in a nonlinear normal mode if all its coordinates oscillate equi-periodically, reaching their extremum values at the same instant of time. Depending on the representation of the motion in the configuration space, a nonlinear mode can be classified as similar (corresponding to straight modal lines), or nonsimilar (corresponding to modal curves) (Rosenberg, 1966).

In a number of recent works, the interesting phenomenon of mode localization in "perturbed" linear periodic systems was investigated (Hodges, 1982, Wei and Pierre, 1988a,b; Bendiksen, 1987; Kissel, 1987; Pierre and Cha, 1989). In these references it was shown that the (extended) normal modes of weakly coupled, symmetric linear systems become localized when weak perturbations of the periodicity are introduced. Linear mode localization was detected when the coupling between subsystems was of the order or smaller than the spread in natural frequencies of the component systems; moreover, it was shown that due to mode localization a motion confinement of external disturbances is possible (Cornwell and Bendiksen, 1989), a feature which can be beneficial for passive and/or active vibration isolation of large-scale period structures.

In Vakakis (1991), the localized modes of a nonlinear periodic system with two degrees-of-freedom (DOF) were examined by means of an asymptotic methodology. The modal curves were approximated by set of functional equations which were then solved by a power series expansion. In that reference the existence of the nonlinear localized modes was confirmed by numerical integrations of the equations of motion. A generalization of the theory was presented in Vakakis and Cetinkaya (1991), where it was proven that for *sufficiently weak substructure coupling*, "weak" and "strong" mode localization exists in a perfectly symmetric periodic system (i.e., a system with no perturbation of its symmetry). In (Vedenova et al., 1985) an analytical study of the localized nonsimilar modes in a weakly coupled, nonlinear two-DOF vibro-impact system was carried out. Some additional results on nonlinear normal modes were recently reported in (Shaw and Pierre 1991), were a new methodology for detecting nonlinear normal modes was described; this method is based on the computation of invariant manifolds for the motion, and is valid even for systems with damping. An application of this methodology in a two-degree-of-freedom asymmetric nonlinear system was made in (Pierre and Shaw 1991). In that work nonlinear mode

Contributed by the Applied Mechanics Division of THE AMERICAN SOCIETY OF MECHANICAL ENGINEERS for presentation at the First Joint ASCE-EMD, ASME-AMD, SES Meeting, Charlottesville, VA, June 6-9, 1993.

Discussion on this paper should be addressed to the Technical Editor, Professor Lewis T. Wheeler, Department of Mechanical Engineering, University of Houston, Houston, TX 77204-4792, and will be accepted until four months after final publication of the paper itself in the ASME JOURNAL OF APPLIED MECHANICS.

Manuscript received by the ASME Applied Mechanics Division, Oct. 7, 1991; final revision, Oct. 22, 1992. Associate Technical Editor: D. J. Inman.

Paper No. 93-APM-35.

Copyright © 1993 by ASME
Downloaded 03 May 2010 to 171.66.16.245. Redistribution subject to ASME license or copyright; see http://www.asme.org/terms/Terms_Use.cfm

localization was numerically detected, but was solely attributed to symmetry-breaking nonlinearities; *as shown in the present work, the basic mechanism for nonlinear mode localization is not nonlinear asymmetries, but the dependence of the frequency of oscillation on the amplitude.*

In what follows, the mode localization in a discrete, nonlinear periodic system will be investigated by means of a multiple-scales averaging methodology. The system is similar to the one examined in Vakakis and Cetinkaya (1991), but the scope of the analysis differs. In that previous reference the ratio, k/μ, of coupling stiffness between substructures, k, to substructure nonlinearity, μ, was assumed to be small, and asymptotic approximations to the nonlinear modal curves were constructed. In this work no such restriction on k/μ will be imposed and harmonic approximations to the localized nonsimilar modes will be developed even for finite values of k/μ. The "effective mistuning" introduced by the stiffness nonlinearity will be studied by the method of multiple scales and it will be shown that a perfectly periodic nonlinear system is equivalent to a "mistuned" linear one, due to the dependence of its frequency of oscillation on the amplitude. In addition, it will be shown that the localized modes first identified in Vakakis and Cetinkaya (1991) become nonlocalized as k/μ increases, in some cases bifurcating from "extended" antisymmetric modes. To the authors' knowledge, this is the first study where the transition from mode localization to mode nonlocalization in a nonlinear periodic system is analytically studied.

2 Localized Modes in the n-DOF Nonlinear System

The system under consideration is shown in Fig. 1. It is conservative (i.e., no damping is assumed), and consists of n discrete masses connected to each other by means of massless elements having linear stiffnesses. Each mass is connected to a rigid foundation by massless elements having a nonlinear stiffness of the third degree. This model can be considered as a first approximation of an antenna-type structure possessing n continuous beams coupled by linear stiffness elements. Assuming that the beams execute large-amplitude oscillations (and thus possess kinematic-geometric nonlinearities) and that their deflections correspond to their first linear flexural modes, a one-mode Galerkin analysis leads to a mathematical model similar to that of Fig. 1.

It is assumed that the nonlinearities of the grounding stiffnesses, $\epsilon\mu$, and the linear coupling stiffnesses, ϵk, are weak but that their ratio, $R=\epsilon\mu/\epsilon k$, can take finite values. The equations of motion are given by (see Fig. 1 for definitions of the various quantities).

$$\ddot{x}_i + x_i + \epsilon\mu x_i^3 + \epsilon k\ (x_i - x_{i+1}) + \epsilon k\ (x_i - x_{i-1}) = 0,\ i=1,\ \ldots,\ n \quad (1)$$

where $x_{n+1} \equiv x_1$, $x_0 \equiv x_n$, dots denote differentiation with respect to time, ϵ is a small dimensionless parameter of perturbation order (i.e., $|\epsilon| << 1$), and all other variables are assumed to be finite (i.e., of $O(1)$).

The method of multiple scales will now be applied to the problem in order to obtain a uniformly valid, first order approximation to the dynamic response of the system. For general expositions of this method the reader is referred to the books by Nayfeh and Mook (1979) and Rand and Armbruster (1987). "Fast" and "slow" independent variables ξ and η are introduced, defined as:

$$\eta = \epsilon\tau, \quad \xi = \tau. \quad (2)$$

The time derivatives of x_i in expressions (1) can then be expressed in terms of these new variables using the chain rule as follows:

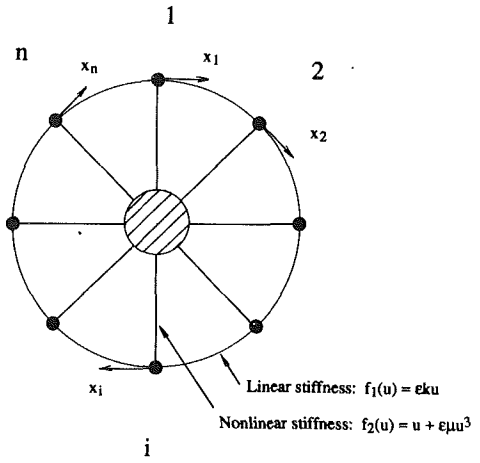


Fig. 1 The n-DOF nonlinear cyclic system

$$\dot{x}_i = x_{i_\xi} + \epsilon x_{i_\eta}, \quad \ddot{x}_i = x_{i_{\xi\xi}} + 2\epsilon x_{i_{\xi\eta}} + O(\epsilon^2). \quad (3)$$

Equations (1) are then expressed in terms of the new independent variables as:

$$x_{i_{\xi\xi}} + 2\epsilon x_{i_{\xi\eta}} + x_i + \epsilon\mu\ x_i^3 + \epsilon k\ (2x_i - x_{i-1} - x_{i+1}) + O(\epsilon^2) = 0,\ i=1,\ \ldots,\ n \quad (4)$$

where the dependent variables are now functions of the new independent variables, i.e., $x_i = x_i(\xi,\eta,\epsilon)$. Next, we seek expansions of the form

$$x_i(\xi,\ \eta,\ \epsilon) \sim \sum_{p=0}^{\infty} \epsilon^p x_{ip}(\xi,\ \eta), \quad i=1,\ \ldots,\ n. \quad (5)$$

Substituting (5) into (4) and setting the coefficients of respectively powers of ϵ equal to zero, we obtain successive approximations to the solutions of (1).

The equations of the $O(1)$ approximation are solved as follows:

$$x_{i0_{\xi\xi}} + x_{i0} = 0 \Rightarrow x_{i0} = A_i(\eta)\ \exp(j\xi) + cc,\ i=1,\ \ldots,\ n \quad (6)$$

where $j=(-1)^{1/2}$ and (cc) denotes the complex conjugate of the preceding term. The unknown (complex) amplitudes $A_i(\eta)$ are obtained by substituting (6) into the equations of the $O(\epsilon)$ approximation

$$x_{i1_{\xi\xi}} + x_{i1} = -2x_{i0_{\xi\eta}} - k\ (2x_{i0} - x_{(i-1)0} - x_{(i+1)0} - \mu\ x_{i0}^3),\quad i=1,\ \ldots,\ n \quad (7)$$

and eliminating "secular terms," i.e., terms containing $\exp(\pm j\xi)$ as a multiplicative factor (Nayfeh and Mook, 1979). The following equations for the amplitudes $A_i(\eta)$ are then derived:

$$-2jA_i' - 3\mu A_i^2\ A_i^* - k\ (2A_i - A_{i+1} - A_{i-1}) = 0,\quad i=1,\ \ldots,\ n \quad (8)$$

where $(\bullet)' \equiv (\bullet)_\eta$ and $(\bullet)^*$ denotes the complex conjugate.

Equations (8) constitute a set of n complex differential equations of first order, which can be transformed to a set of $2n$ real differential equations by introducing the polar transformation

$$A_i(\eta) = (1/2)\ a_i(\eta)\ \exp(j\beta_i(\eta)),\ i=1,\ \ldots,\ n \quad (9)$$

where $a_i(\eta)$ and $\beta_i(\eta)$, $i=1,\ \ldots,\ n$ are the (real) amplitudes and (real) phases of the complex amplitudes $A_i(\eta)$. Substituting relations (9) into (8) and separating real and imaginary parts, we obtain

$$a_i' = (k/2)\ a_{i+1}\ \sin\phi_{i+1} - (k/2)\ a_{i-1}\ \sin\phi_i \quad (10a)$$

Downloaded 03 May 2010 to 171.66.16.245. Redistribution subject to ASME license or copyright; see http://www.asme.org/terms/Terms_Use.cfm

$$a_i\beta_i' = (3\mu/8)\, a_i^3 + k\, a_i - (k/2)\, a_{i+1}\cos\phi_{i+1} - (k/2)\, a_{i-1}\cos\phi_i,\ i=1,\ \ldots,\ n. \quad (10b)$$

The angles ϕ_j in (10) are defined by the relation $\phi_j = \beta_j - \beta_{j-1}$.

Combining the first n Eqs. (10a) it can be shown that

$$a_1 a_1' + \ldots + a_n a_n' = 0 \Rightarrow a_1^2 + \ldots + a_n^2 = \rho^2. \quad (11)$$

Thus, it is proven that during free oscillations the sum of the squares of the amplitudes is conserved, a fact which (within this order of approximation) is equivalent to the statement that the total energy of the system during free oscillations is conserved. The quantity ρ^2 is an energy-like quantity, which can be directly related to the total energy of the system. Using relation (11) the number of independent amplitudes is reduced by one. In addition, using the definition of the angles ϕ_j we can combine Eqs. (10b) and develop the following autonomous set of $(2n-1)$ differential equations with dependent variables a_i, $i=1,\ \ldots,\ n$, and ϕ_i, $i=2,\ \ldots,\ n$:

$$a_i' = (k/2)a_{i+1}\sin\phi_{i+1} - (k/2)\, a_{i-1}\sin\phi_i \quad (12a)$$

$$\phi_i' = (3\mu/8)(a_i^2 - a_{i-1}^2) - (k/2)\,[(a_{i+1}/a_i)\cos\phi_{i+1} - (a_i/a_{i-1})\cos\phi_i] - (k/2)[(a_{i-1}/a_i)\cos\phi_i - (a_{i-2}/a_{i-1})\cos\phi_{i-1}]. \quad (12b)$$

The remaining phase angle ϕ_1 is determined by the compatibility relation $\phi_1 = -\sum_{k=2}^{\infty} \phi_k$.

Equations (12) together with relation (11) describe (correct to $O(\epsilon)$) the free oscillations on the isoenergetic manifold of the cyclic system. By imposing the stationary conditions $a_i' = 0$, $\phi_i' = 0$, $i=1,\ \ldots,\ n$, we determine the values of the amplitudes a_i and ϕ_i corresponding to periodic motions (the corresponding harmonic approximations to the motions of the physical coordinates are then derived by expressions (6)).

Before proceeding with a general discussion of the stationary values of (12), it is of interest to examine the motions of the *uncoupled* system corresponding to $\epsilon k = 0$. For the uncoupled system Eqs. (12) become

$$a_i' = 0 \Rightarrow a_i = a_{i0},\ i=1,\ \ldots,\ n \quad (13a)$$

$$\phi_i' = (3\mu/8)(a_{i0}^2 - a_{(i-1)0}^2) \Rightarrow \phi_i = (3\mu/8)(a_{i0}^2 - a_{(i-1)0}^2)\eta + \phi_{i0},\ i=2,\ \ldots,\ n. \quad (13b)$$

The corresponding expressions for the coordinates of the system are

$$x_1(t) = a_{10}\cos((1 + 3\epsilon\mu a_{10}^2/8)t + \beta_{10}) + O(\epsilon)$$

$$x_i(t) = a_{i0}\cos((1 + 3\epsilon\mu a_{10}^2/8 + \epsilon\Delta_i)t + \beta_{i0}) + O(\epsilon),\ i=2,\ \ldots,\ n \quad (14)$$

where β_{10} and β_{i0} are constant phase angles and the quantities Δ_i are given by

$$\Delta_i = \sum_{k=2}^{i} (3\mu/8)(a_{k0}^2 - a_{(k-1)0}^2),\ i=2,\ \ldots,\ n. \quad (15)$$

From equations (15) it is concluded that, for given amplitudes a_{i0}, and correct to $O(\epsilon)$, the uncoupled nonlinear system is equivalent to a system of n "mistuned" linear oscillators with frequency "mistunings" equal to $\epsilon\Delta_i$. As shown in the literature, such a system of "mistuned" oscillators, if coupled by sufficiently weak stiffnesses, gives rise to localized modes (Wei and Pierre, 1988a,b). Therefore, it is expected that *the introduction of weak substructure coupling will lead to mode localization in the perfectly periodic nonlinear system.* The aforementioned analysis shows that, because of the nonlinearities in the substructures, the uncoupled system reduces to a set of weakly perturbed oscillators, a consequence of the fact that the frequencies of oscillation of nonlinear systems generally depend on their amplitudes of motion. This property of nonlinear systems also explains why nonlinear mode localization takes place in the perfectly periodic system, i.e., in the absence of any substructure mistuning.

From Eqs. (14) it is concluded that synchronous periodic motions of all substructures of the uncoupled system take place when either one of the following conditions is satisfied:

(i) $\Delta_i = 0 \Rightarrow a_{i0}^2 = a_{(i-1)0}^2$ for all $i\epsilon\Sigma = [2,\ \ldots,\ n]$

(ii) $\Delta_i = 0$ for all $i\epsilon S$, and $a_{j0} = 0$ for all $j\notin S$, where S is a subset of Σ

(iii) $a_{i0} = 0$ for all $i\epsilon\Sigma$

Condition (i) corresponds to "extended" symmetric and antisymmetric degenerate modes of the uncoupled system, which after the addition of coupling give rise to extended modes of the oscillator. Condition (ii) corresponds to "weakly" localized degenerate modes of the uncoupled system; with weak coupling these modes give rise to "weakly" localized similar or nonsimilar modes, during which only a limited number of subsystems oscillates, the remaining system being virtually motionless. Condition (iii) is the most interesting case since it corresponds to a degenerate mode during which *only one of the coordinates (namely x_1) has nonzero amplitude*; with the addition of weak coupling it will be proven that this degenerate mode gives rise to a "strongly" localized mode, during which only one of the coordinates oscillates with an amplitude of $O(1)$, the remaining coordinates being of $O(\epsilon)$ or higher. Note that, since the system under consideration is nonlinear, there is a need for an additional stability analysis in order to determine if the resulting modes are physically realizable. It must also be pointed out that because of the cyclicity of the system under investigation, there exist n "strongly localized" modes, each corresponding to an $O(1)$ motion of only one of the coordinates of the system (in the above discussion the localized coordinate was assumed to be x_1 but this does not restrict the generality of the analysis).

As an example, consider a system with only two subsystems (i.e., $n=2$). In this case we have only one equivalent "frequency mistuning" $\Delta_2 = (3\mu/8)\,(a_{20}^2 - a_{10}^2)$, and only conditions (i) and (iii) are realizable. Introducing the polar transformation for the amplitudes $a_{20} = \rho\sin\psi$, $a_{10} = \rho\cos\psi$ (where ρ is the energy-like quantity defined by relation (11)), the quantity Δ_2 takes the form:

$$\Delta_2 = -(3\mu\rho^2/8)\cos 2\psi \text{ (2 DOF)} \quad (16)$$

A graph of $\Delta_2(3\mu\rho^2/8)^{-1}$ versus angle ψ is given in Fig. 2(a), and the values corresponding to degenerate symmetric ($a_{10} = -a_{20}$, $\phi_2 = \pi$), antisymmetric ($a_{10} = a_{20}$, $\phi_2 = \pi$), and strongly localized modes ($a_{10} = \rho$ and $a_{20} = 0$, or $a_{10} = 0$ and $a_{20} = \rho$) are indicated. *Note that the degenerate localized modes correspond to extremum values of the frequency "mistuning."* Each of the identified degenerate modes gives rise to (orbitally stable or unstable) extended or localized modes of the weakly coupled system.

Considering the systems with $n = 3$ and introducing the polar transformation $a_{10} = \rho\cos\psi_1$, $a_{20} = \rho\sin\psi_1\cos\psi_2$, $a_{30} = \rho\sin\psi_1\sin\psi_2$, the following two "equivalent mistunings" result:

$$\Delta_2 = (3\mu\rho^2/8)\,[\sin^2\psi_1\cos^2\psi_2 - \cos^2\psi_1]$$

$$\Delta_3 = \Delta_2 - (3\mu\rho^2/8)\sin^2\psi_1\cos 2\psi_2 \text{ (3 DOF)} \quad (17)$$

In this case all conditions (i – iii) can be realized, as seen for the plots of Fig. 2(b) where the quantities $\Delta_2(3\mu\rho^2/8)^{-1}$ and $\Delta_3(3\mu\rho^2/8)^{-1}$ are plotted versus angles ψ_1 and ψ_2. Again it is noted that strong mode localization occurs for extremum values of the "frequency mistunings."

After examining the degenerate uncoupled oscillator, we now return to the analysis of the stationary values of the autonomous system (12). In what follows we will be mainly

Downloaded 03 May 2010 to 171.66.16.245. Redistribution subject to ASME license or copyright; see http://www.asme.org/terms/Terms_Use.cfm

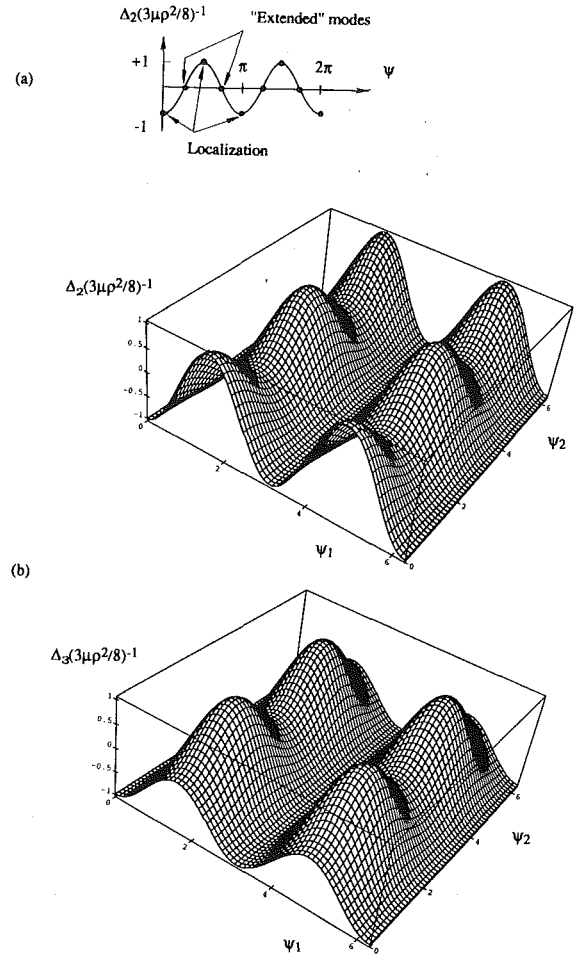


Fig. 2 Equivalent "mistunings" for a system with (*a*) two DOF (*b*) three DOF

interested in the "strongly localized" modes of the coupled system; that is, those corresponding to free motions during which only one of the coordinates of the system oscillates with $O(1)$ amplitude. Clearly, such modes result as perturbations of the degenerate "strongly localized" modes of the uncoupled system (corresponding to condition (iii), a fact which was fully utilized by Vakakis and Cetinkaya (1991) where asymptotic approximations for these modes were computed. However, the analysis presented in that work was only "local" since it was valid only for small values of the ratio $R=k/\mu$; that is, only for weak coupling and/or strong grounding stiffness nonlinearities. In what follows, we seek a "strongly localized" mode during which only coordinate x_1 oscillates with $O(1)$ amplitude. Motivated by the asymptotic results of Vakakis and Cetinkaya (1991) and the cyclic symmetry of the system under investigation, we impose the following relations for the amplitudes and phases during the normal mode oscillations:

For $n=(2p+1)$

$$a_2=a_n,\ a_3=a_{n-1},\ a_4=a_{n-2},\ \ldots,\ a_{p+1}=a_{p+2}$$
$$\phi_i=\pi,\ i=1,\ \ldots,\ n,\ i\neq p+2,\ \phi_{p+2}=-2p\pi \quad (18a)$$

For $n=(2p-1)$

$$a_2=a_n,\ a_3=a_{n-1},\ a_4=a_{n-2},\ \ldots,\ a_{p-1}=a_{p+1}$$
$$\phi_i=\pi,\ i=1,\ \ldots,\ n,\ i\neq p,\ \phi_p=-(2p-3)\pi \quad (18b)$$

Thus, antiphase motion is assumed between almost all adjacent coordinates of the system. Imposing the stationary conditions $a_i'=\phi_i'=0$ on the system of Eqs. (12), and taking into account conditions (18), we obtain the following set of algebraic equations describing the modes of the coupled system:

For $n=(2p+1)$

$$(3\mu/8k)\,(a_{k-1}{}^2-a_k^2)-(1/2)\,(a_{k-1}{}^2-a_k^2)/a_{k-1}a_k + (1/2)\,[(a_{k-2}/a_{k-1})-(a_{k+1}/a_k)]=0$$

for $k=2,\ \ldots,\ p$

$$(3\mu/8k)\,(a_p^2-a_{p+1}{}^2-(1/2)\,(a_p{}^2-a_{p+1}{}^2)/a_pa_{p+1} + (1/2)\,[(a_{p-1}/a_p)+1]=0 \quad (19a)$$

For $n=(2p-1)$

$$(3\mu/8k)\,(a_{k-1}{}^2-a_k^2)-(1/2)\,(a_{k-1}{}^2-a_k^2)/a_{k-1}a_k + (1/2)\,[(a_{k-2}/a_{k-1})-(a_{k+1}/a_k)]=0$$

for $k=2,\ \ldots,\ p$ (19*b*)

The solution of the nonlinear set of algebraic Eqs. (19) together with the imposed conditions (18) leads to the determination of the localized nonsimilar modes of the system. Since no analytic solutions for the general n-DOF are available, we resort to numerical computations. The following motions for the physical coordinates of the system then result:

For $n=(2p+1)$

$$x_1\ (t)=a_1\cos((1+\epsilon\alpha)\ t+\beta_{10})+O(\epsilon)$$
$$x_2\ (t)=x_{n-1}=-a_2\cos((1+\epsilon\alpha)\ t+\beta_{10})+O(\epsilon)$$
$$x_3\ (t)=x_{n-2}(t)=+a_3\cos((1+\epsilon\alpha)\ t+\beta_{10})+O(\epsilon)$$
$$\bullet\quad\bullet\quad\bullet$$
$$x_{p+1}\ (t)=x_{p+2}\ (t)=(-1)^p\ a_{p+1}\cos((1+\epsilon\alpha)t+\beta_{10})+O(\epsilon)$$

For $n=(2p-1)$

$$x_1\ (t)=a_1\cos((1+\epsilon\alpha)\ t+\beta_{10})+O(\epsilon)$$
$$x_2\ (t)=x_{n-1}(t)=-a_2\cos((1+\epsilon\alpha)\ t+\beta_{10})+O(\epsilon)$$
$$x_3\ (t)=x_{n-2}(t)=+a_3\cos((1+\epsilon\alpha)\ t+\beta_{10})+O(\epsilon)$$
$$\bullet\quad\bullet\quad\bullet$$
$$x_{p-1}\ (t)=x_{p+1}\ (t)=(-1)^p\ a_{p-1}\cos((1+\epsilon\alpha)t+\beta_{10})+O(\epsilon)$$
$$x_p\ (t)=(-1)^{p+1}\ a_p\cos((1+\epsilon\alpha)t+\beta_{10})+O(\epsilon)$$

where the constant angle β_{10} is determined by the initial conditions, and $\epsilon\alpha=\epsilon\alpha(a_1)$ is the small amplitude-depended nonlinear correction to the frequency of oscillation which is determined by integrating Eqs. (10*b*).

We remark that although Eqs. (19) cannot be solved analytically, nevertheless, *the existence of the localized modes in the general system can be predicted by means of a simple perturbation analysis*. To this end, we consider the set of Eqs. (19), we assume that $(k/\mu)=O(\epsilon_1)$, where ϵ_1 is a perturbation parameter such that $|\epsilon_1|\ll 1$, and we seek solutions such that $a_1=O(1)$, and $a_i=O(\epsilon_1{}^{i-1})$, $i=2,\ \ldots,P$ where $P=p+1$, if $n=2p+1$, and $P=p$, if $n=2(p-1)$. These assumptions correspond to a cyclic system which is weakly coupled and/or strongly nonlinear, oscillating in a nonlinear mode localized in coordinate x_1. Considering the orders of the various terms in Eqs. (19), taking into account that $a_1{}^2=\rho^2+O(\epsilon_1{}^2)$, and retaining only quantities of $O(1)$, we obtain the following perturbation results for the localized mode oscillation:

For $n=(2p+1)$

$$a_2/a_1=(4/3\rho^2)(k/\mu)+O(\epsilon_1{}^2)=O(\epsilon_1)$$
$$a_i/a_1=(4/3\rho^2)^{i-1}(k/\mu)^{i-1}+O(\epsilon_1{}^i) = O(\epsilon_1{}^{i-1}),\ i=3,\ \ldots,\ p+1 \quad (20a)$$

For $n=(2p-1)$

$$a_2/a_1=(4/3\rho^2)(k/\mu)+O(\epsilon_1{}^2)=O(\epsilon_1)$$
$$a_i/a_1=(4/3\rho^2)^{i-1}(k/\mu)^{i-1}+O(\epsilon_1{}^i) = O(\epsilon_1{}^{i-1}),\ i=3,\ \ldots,\ p-1$$
$$a_p/a_1=2(4/3\rho^2)^{p-1}(k/\mu)^{p-1}+O(\epsilon_1{}^p)=O(\epsilon_1{}^{p-1}) \quad (20b)$$

Downloaded 03 May 2010 to 171.66.16.245. Redistribution subject to ASME license or copyright; see http://www.asme.org/terms/Terms_Use.cfm

The perturbation solutions confirm the existence of "strongly" localized modes in the nonlinear system during which the energy of the motion is essentially confined in only one coordinate (x_1); moreover, it is shown that the amplitudes, of the coordinates adjacent to the $O(1)$ coordinate are oscillating with $O(\epsilon_1)$ amplitudes, while the rest of the coordinates have amplitudes which rapidly diminish as their distance from the $O(1)$ coordinate increases. These results are in full agreement with the asymptotic results reported for a slightly different system by Vakakis and Cetinkaya (1991); an interesting observation on the perturbation results (20) is that *the ratio a_2/a_1 during the localized mode is independent of the actual number of degrees of freedom of the system*, meaning that it is possible to predict the amplitudes of the $O(1)$ and $O(\epsilon_1)$ coordinates irrespective of how large is the system under examination. These last results will be shortly confirmed when numerical solutions of Eqs. (19) are carried out.

2 Applications of the Theory

In the following sections, the general theory will be applied to the study of the nonsimilar localized modes of cyclic systems with $n=2,3,4$ and five degrees-of-freedom (DOF). In addition, the results of the averaging analysis will be confirmed by examining the impulsive responses of systems with 12 and 50 DOF.

2.1 Localized Modes in a System with Two DOF. For $n=2$, relations (19a) degenerate to the following equation for a_1 and a_2:

$$(3\mu/8k)(a_1^2-a_2^2)-(a_1^2-a_2^2)/a_1a_2=0 \tag{21}$$

with solutions

$$a_1^2=a_2^2,\ a_1a_2=\pm 8k/3\mu. \tag{22}$$

Taking into account that $a_1^2+a_2^2$, we obtain the following relations for the normal modes:

(i) $a_1=a_2=\rho/2^{1/2}, \phi_2=\pi$(antisymmetric mode)

(ii) $a_1=-a_2=\rho^2/2^{1/2}, \phi_2=\pi$(symmetric mode)

(iii) $a_2=(2^{-1/2})\{\rho^2\pm\{\rho^4-(16k/3\mu)^2\}^{1/2}$

$$a_1=(2^{1/2})(8k/3\mu)\{\rho^2\pm\{\rho^4-(16k/3\mu)^2\}^{-1/2}$$

$$\phi_2=\pi,\ \text{for}\ (\mu/k)\geq(16/3\rho^2).$$

Modes (i) and (ii) are similar (since they correspond to straight modal lines), "extended" modes and their modal ratio $a_1/a_2=\pm 1$ does not depend on the the energy-like quantity ρ^2 (considering the expression for the total energy of the oscillator, E, it can be shown that $\rho^2=2E+O(\epsilon)$). Modes (iii) exist only for weak coupling and/or large substructure nonlinearities and they correspond to modal ratios that depend on the energy:

$$a_2/a_1=(3\mu/16k)\{\rho^2\pm\{\rho^4-(16k/3\mu)^2\}^{1/2}\},$$

$$\phi_2=\pi,\ \text{for}\ (k/\mu)\leq(3E/8). \tag{23}$$

Therefore, these modes are nonsimilar and bifurcate from the antisymmetric mode at $(k/\mu)=(3E/8)+O(\epsilon)$. The bifurcating nonsimilar modes give rise to mode localization since it can be proven that $\lim_{(k/\mu\to 0)}(a_2/a_1)=0$ or ∞ depending on the choice of sign in (23). In Fig. 3 we present the bifurcation of the nonsimilar modes for $\rho^2=1$. Note that nonlinear mode localization takes place only for small values of the ratio k/μ. As this ratio increases, the localized nonsimilar modes become nonlocalized and eventually coalesce with the antisymmetric mode in an inverse Hamiltonian pitchfork bifurcation. The stability analysis of the identified modes was carried out by introducing small unsteady perturbations to the normal mode solutions and considering the eigenvalues of the corresponding variational matrix resulting from Eqs. (12) for $n=2$ (Nayfeh and Mook, 1979). Using this procedure it is found that the bifurcating modes are orbitally stable.

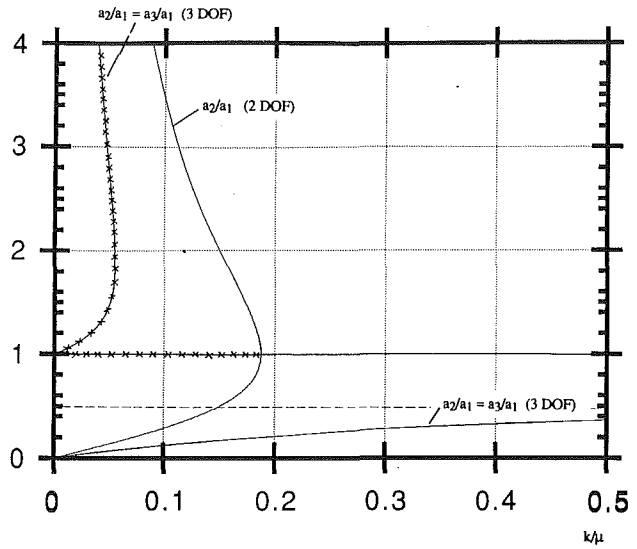


Fig. 3 Transition from mode localization to mode nonlocalization for cyclic systems with two and three DOF: ——— stable solutions ✶✶✶✶✶ unstable solutions

In order to investigate the transition from the localized nonsimilar modes of the coupled system to the degenerate modes of the uncoupled system we examined Poincare′ maps of the oscillator for the constant value of energy $E=0.3078$ and for nonlinearity coefficient $\epsilon\mu=1$. The Poincare' plots were constructed by numerically integrating the equations of motion with constant energy (thus creating a flow on the isoenergetic manifold), "cutting" the flow by the Poincare′ cut section $T:\{x_1=0\}$, and then sampling the dynamics on the section $\Sigma=\{x_1=0,\ \dot{x}_1>0\}\cap\{E=0.308\}$. By construction, a period-one orbit pierces the cut section only once, and thus, a nonlinear normal mode appears as a single point in the Poincare′ map. The stability of the nonlinear normal mode is then easily studied by considering the Poincare′ map of nearby orbits (i.e., the ones obtained by integrating the equations of motion with initial conditions close to those corresponding to the nonlinear mode): stable modes appears as centers in the Poincare′ (surrounded by closed curves), whereas unstable modes appear as saddle points. For more details on the construction of this Poincare′ map the reader is referred to Vakakis and Rand (1991) and Month and Rand (1980). In Fig. 4(a) the Poincare′ map of the system corresponding to $\epsilon k=0.05$ is presented. The symmetric and bifurcating modes appear as stable centers whereas the antisymmetric mode as an unstable saddle with two homoclinic orbits (saddle connections). For $\epsilon k=0.005$ (Fig. 4(b)) the homoclinic orbits expand in size and the two bifurcating modes become localized approaching the point $(x_2,\ \dot{x}_2)=(0,0)$ and the boundary of the plot corresponding to $(x_1,\ \dot{x}_1)=(0,0)$. *For $\epsilon k=0$,* (Fig. 4(c)) *the two homoclinic branches coalesce with the symmetric mode and form a closed line of equilibria connecting the former symmetric and antisymmetric modes*; this line of equilibrium positions represents synchronous periodic motions of the two subsystems of the uncoupled oscillator (with "equivalent mistuning" $\Delta_1=0$). In addition, the two bifurcating modes coalesce with the center $(x_2,\ \dot{x}_2)=(0,0)$ and the boundary $(x_1,\ \dot{x})=(0,0)$, respectively, (corresponding to extremum values of Δ_2, as shown in Fig. 2(a)). The plots of Fig. 4 demonstrate that Poincare′ maps can be an effective tool for a better understanding of the physics of mode localization in weakly coupled nonlinear periodic systems.

Downloaded 03 May 2010 to 171.66.16.245. Redistribution subject to ASME license or copyright; see http://www.asme.org/terms/Terms_Use.cfm

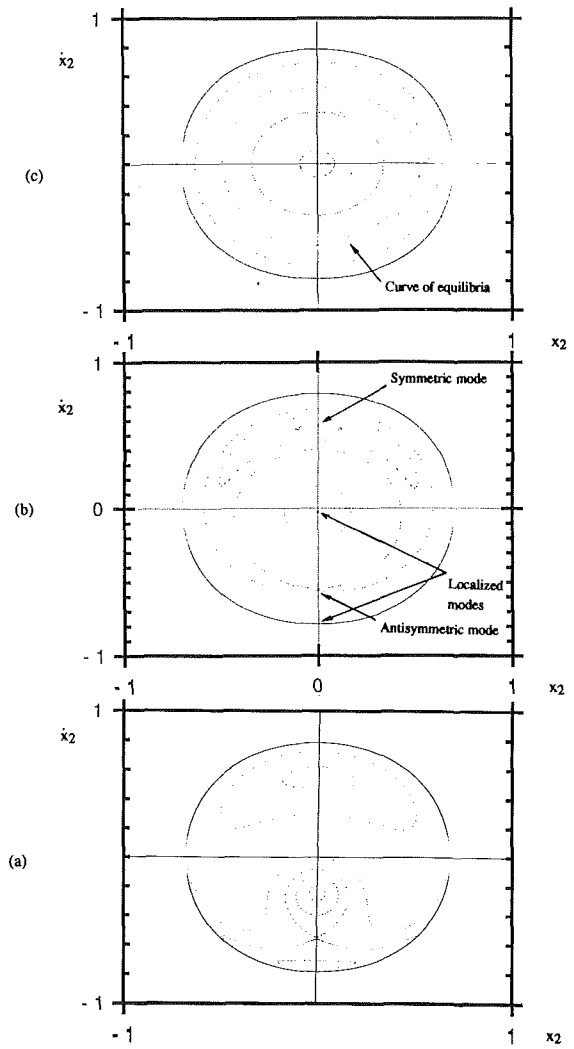


Fig. 4 Poincare′ maps for a two-DOF system corresponding to E = 0.3078, $\epsilon\mu = 1.0$ and (*a*) $\epsilon k = 0.05$, (*b*) $\epsilon k = 0.005$, (*c*) $\epsilon k = 0.0001 \cong 0$

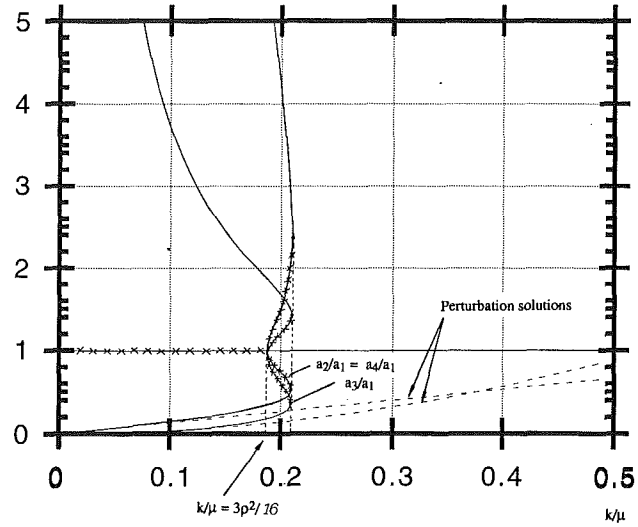


Fig. 5 Transition from mode localization to mode nonlocalization for a cyclic system with four DOF: ——— stable solutions ×-×-×-× unstable solutions

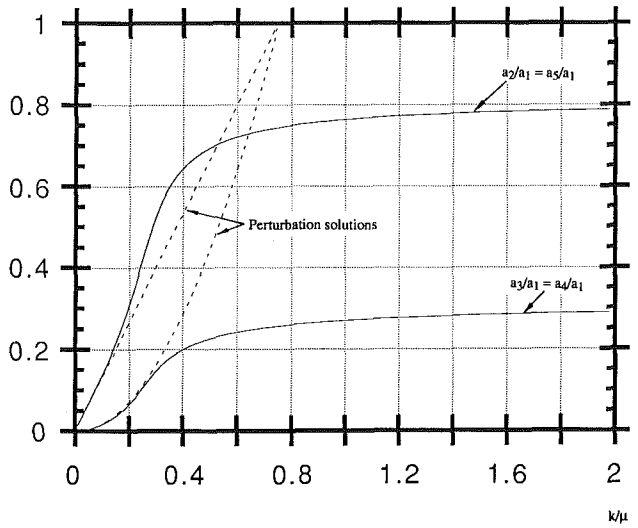


Fig. 6 Transition from mode localization to mode nonlocalization for a cyclic system with five DOF: ——— stable solutions ×-×-×-× stable solutions

2.2 Localized Modes in the System with Three DOF. For $n = 3$, Eqs. (19*a*) reduce to a single equation for a_1 and $a_2 = a_3$:

$$(3\mu/8k)(a_1^2 - a_2^2) - (1/2)(a_1^2 - a_2^2)/a_1 a_2 + (1/2)\,[a_2/a_1) + 1] = 0 \quad (24)$$

with the additional condition

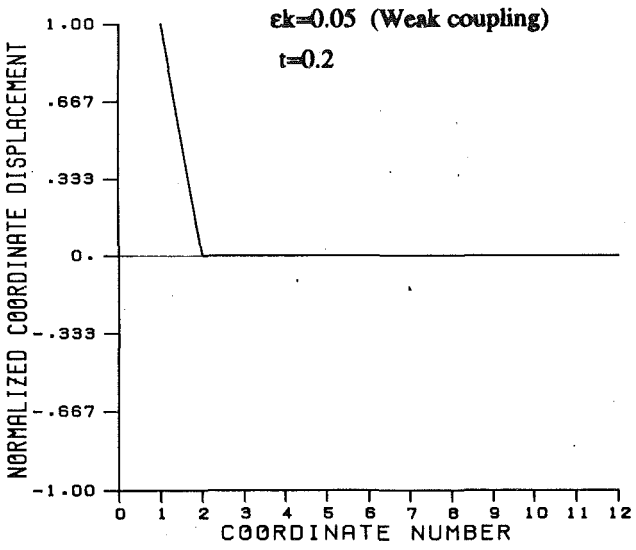
$$a_1^2 + 2a_2^2 = \rho^2. \quad (25)$$

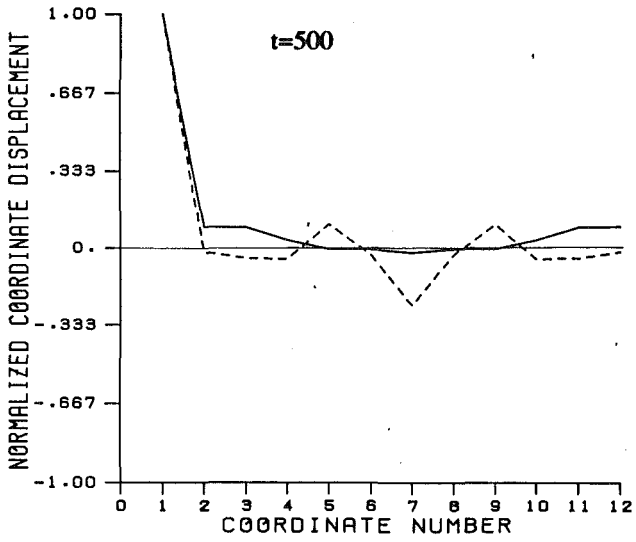
Equations (24) and (25) were numerically solved with a Newton-Raphson algorithm, and the identified modes corresponding to $\rho^2 = 1$ are presented in Fig. 3. Two branches of nonsimilar normal modes are identified. The first branch represents orbitally stable-free oscillations and for sufficiently small values of (k/μ) gives rise to localized motions during which the energy is essentially confined to coordinate x_1. The second branch represents orbitally unstable motions and thus is not physically realizable. *It is concluded that, for n = 3 the branch of solutions that gives rise to mode localization does not bifurcate from any other solution branch; instead, as the ratio* (k/μ) *increases, the localized nonlinear modes become nonlocalized, their modal ratios* $a_2/a_1 = a_3/a_1$ *approaching asymptotic values equal to (1/2).*

Thus, nonlinear mode localization for $n = 3$ is qualitatively different from the case $n = 2$. In addition to the modes shown in Fig. 3, a number of other modes exist in the system. However, these modes are not localized and thus are of no interest in the present discussion (for an evaluation of these additional modes the reader is referred to (Vakakis and Cetinkaya 1991)). Finally note, that because of the cyclic symmetry of the system under consideration, the localized mode presented in Fig. 3 can be also realized in any one of the remaining two coordinates of the system x_2 and x_3.

2.3 Localization in Systems with Four and Five DOF. The set of algebraic equations for determining the localized modes for systems with $n = 4$ and five DOF, are derived from Eqs. (19*b*) and (19*a*), respectively, and are listed in the Appendix. These sets of equations were solved numerically and the branches of solutions giving rise to nonlinear mode localization are presented in Fig. 5 (for $n = 4$) and 6 (for $n = 5$) for $\rho^2 = 1$. For low values of the ratio (k/μ) (≤ 0.1), nonlinear mode localization occurs and the numerical solutions are approximately equal to the perturbation results (20). As (k/μ) increases, the localized branches of the 4-DOF system become nonlocalized and eventually coalesce with the antisymmetric extended mode corresponding to $(a_1 = a_2 = a_3 = a_4$, $\phi_1 = \phi_2 = \phi_4 = \pi$, $\phi_3 = 3\pi)$ in a very degenerate inverse "double" hamiltonian pitchfork bifurcation.

Downloaded 03 May 2010 to 171.66.16.245. Redistribution subject to ASME license or copyright; see http://www.asme.org/terms/Terms_Use.cfm





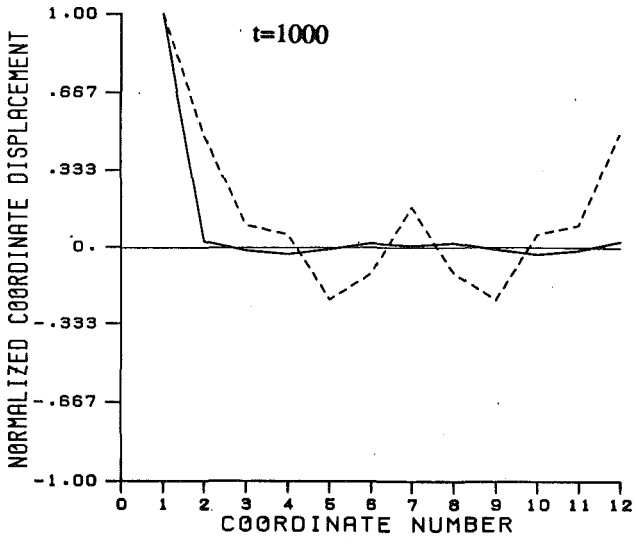
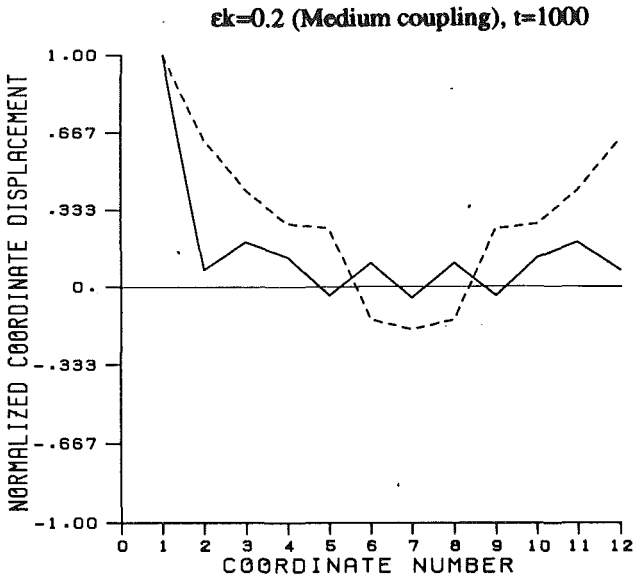


Fig. 7(*a*)



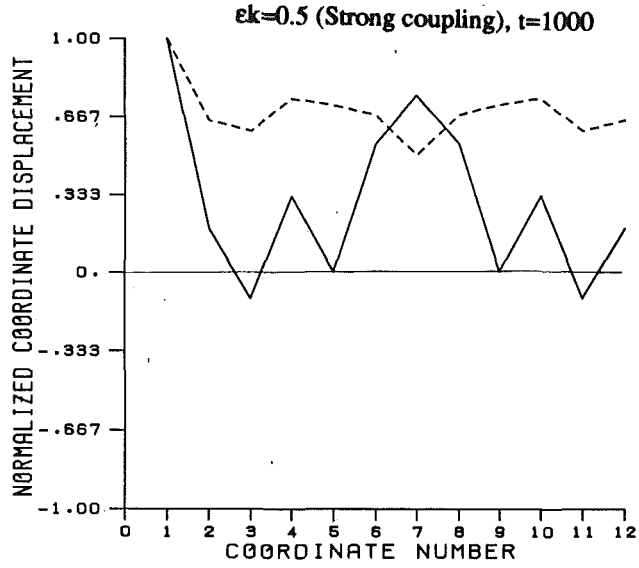


Fig. 7(*b*)

Fig. 7 Motion confinement in an impulsively loaded system with 12 DOF (impulse applied at subsystem 1), for (*a*) weak coupling ($kl/\mu = 0.166$), (*b*) medium ($kl/\mu = 0.666$) and strong coupling ($kl/\mu = 1.666$): ——— nonlinear system - - - - - linear systems.

Qualitatively different solution branches exist for the 5-DOF cyclic system, where the branches of solutions giving rise to mode localization do not bifurcate from any other branch of solutions; the localized modes become nonlocalized as (k/μ) increases, their modal ratios reaching the asymptotic values $a_2/a_1 = a_5/a_1 = 0.8$ and $a_3/a_1 = a_4/ = 0.3$ as $(k/\mu) \to \infty$. Again, for sufficiently low values of (k/μ) (≤ 0.1), the numerical solutions are approximately equal to the perturbation results (20). As a final remark it must be noted that, in addition to the solutions presented in Figs. 5 and 6, some other normal mode solutions exist; however, these additional solution branches are either orbitally unstable, or do not give rise to mode localization.

3 Motion Confinement in the Cyclic Structure

In order to demonstrate the effect of the localized modes on the dynamics of the nonlinear cyclic structure, we computed the response of cyclic systems with 12 and 50 DOF excited by an impulsive load on one of their subsystems. Such computations have been previously performed for weakly perturbed linear discrete and distributed cyclic structures using finite-element techniques (Bendiksen, 1987; Cornwell, and Bendiksen 1989). In these studies it was shown that linear mode locali-

Downloaded 03 May 2010 to 171.66.16.245. Redistribution subject to ASME license or copyright; see http://www.asme.org/terms/Terms_Use.cfm

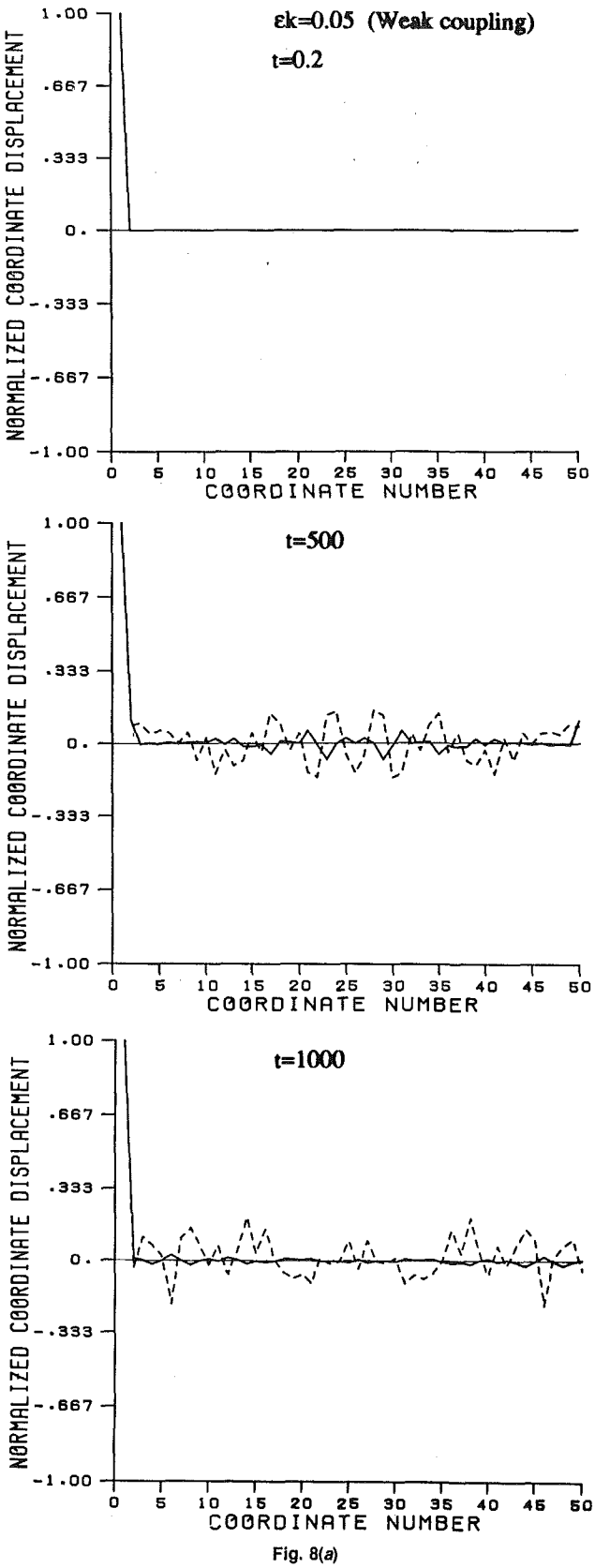


Fig. 8(*a*)

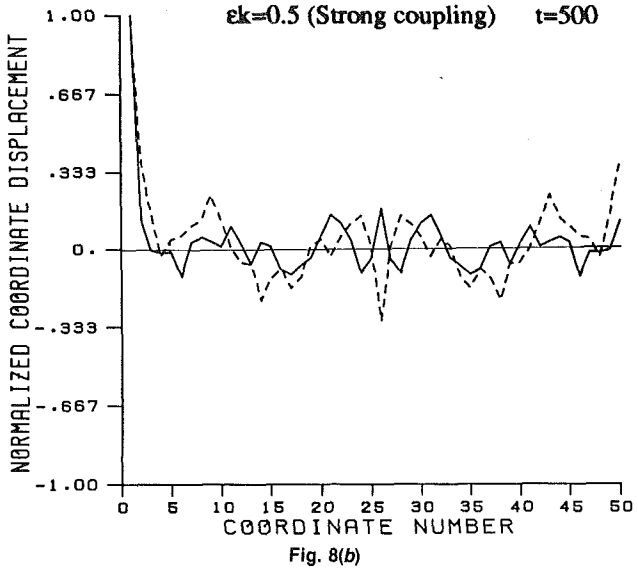


Fig. 8(*b*)

Fig. 8 Motion confinement in an impulsively loaded system with 50 DOF (impulse applied at subsystem 1), for (*a*) weak coupling ($k/\mu = 0.166$), (*b*) strong coupling ($k/\mu = 1.666$): ——— nonlinear system - - - - - linear system

zation gives rise to motion confinement of the impulsive response, a fact that can be potentially useful for developing robust control algorithms for the active vibration isolation of cyclic structures.

In this work the impulsive responses were computed by finite element computations. The global equations of motion were first assembled and were subsequently integrated using the Newmark numerical algorithm (Bathe, 1982). A force of magnitude 1 was applied for a duration of $\Delta t = 0.2$ seconds on subsystem 1 and the resulting displacements of the system were evaluated by numerical time integrations. In Fig. 7(*a*) the impulsive responses of a 12-DOF cyclic system with parameters $\epsilon\mu = 0.3$ and $\epsilon k = 0.05$ (corresponding to $k/\mu = 0.166$, i.e., to a weakly coupled system), are shown at times $t = 0.2$, 500, and 1000 sec. For comparison purposes, the respective responses of the linear system (corresponding to $\epsilon\mu = 0$) are also shown in these graphs. In the nonlinear system the energy of the impulse is confined to the point of its application, in contrast to the linear system where the energy propagates to the other components of the system; the motion confinement in the nonlinear system is clearly attributed to the nonlinear localized modes, which do not exist in the corresponding linear structure.

To test the theoretical prediction that the localized modes become non-localized as the ratio (k/μ) increases, we increased the coupling strength initially to $\epsilon k = 0.2$ $(k/\mu = 0.666)$, and then to $\epsilon k = 0.5$ $(k/\mu = 1.666)$, and computed the responses of the corresponding strongly coupled systems under the same loading conditions with the one used in the weakly coupled case. The impulsive responses of the strongly coupled systems are presented in Fig. 7(*b*) at time $t = 1000$ sec. We see that the energy of the impulse is no longer confined in the first subsystem, but instead "spreads" through the structure. This result demonstrates that nonlinear mode localization becomes less effective as the ratio (k/μ) increases, a result which is in full agreement with theoretical predictions.

Finally, in Fig. 8 the impulsive responses of systems with 50 DOF are presented. The dynamic response of a weakly coupled structure is shown in Fig. 8(*a*) (with $\epsilon\mu = 0.3$, $\epsilon k = 0.05$, $k/\mu = 0.166$) at $t = 0.2$, 500 and 1000 sec. Again, motion confinement is detected due to the presence of the nonlinear localized modes. When ϵk is increased ($\epsilon k = 0.5$, $k/\mu = 1.666$), it is found that the effects of mode localization are eliminated (Fig. 8*b*)).

The results reported in this section show that the phenomenon of nonlinear mode localization can have potential use for the vibration isolation of periodic systems. This is because a structure whose inherent dynamics lead to motion confinement of external disturbances is much more amenable to con-

Downloaded 03 May 2010 to 171.66.16.245. Redistribution subject to ASME license or copyright; see http://www.asme.org/terms/Terms_Use.cfm

trol or passive isolation than is a structure possessing extended dynamic responses.

4 Discussion

In this work mode localization in a nonlinear cyclic structure was analyzed by the averaging method of multiple scales. A prerequisite for the application of any averaging method is that the system under consideration "neighbors" a linear one, and thus, the analytic results reported in the present work only hold for systems with weak nonlinearities. In this regard the presented averaging analysis is less general than the asymptotic methodology of (Vakakis and Cetinkaya, 1991) in which no restriction on the nonlinearities was posed. However, in that previous work the assumption of "weak" coupling was imposed, a restriction which is relaxed in the present study.

Using the multiple-scales method we were able to study the transition from mode localization to mode nonlocalization as the structural parameters of the system varied. The essential variable which controls the mode localization in the system under investigation was found to be the ratio (k/μ) of the linear coupling stiffness to the nonlinear grounding nonlinearity. For sufficiently small values of this ratio nonlinear mode localization always existed, irrespective of the number of DOF of the system. Moreover, an interesting analytical result was that for sufficiently small coupling and/or large nonlinearity, the ratio of the amplitude of the $O(1)$ coordinate to the amplitudes of its adjacent coordinates is a constant not depending on the actual number of DOF of the system. As (k/μ) increases the branches of localized modes became nonlocalized in two distinct warp. For systems with odd DOF, the branches of solutions existed for arbitrary large values of (k/μ) with the modal ratios reaching specific asymptotic values as $(k/\mu)\to\infty$. However, for systems with even DOF the branches of localized modes were found to bifurcate from the antisymmetric mode of the system in degenerate "multiple" inverse pitchfork hamiltonian bifurcations.

In order to physically understand the phenomenon of nonlinear mode localization, we examined the uncoupled degenerate system. It was shown that the uncoupled n-DOF system is approximately equivalent to a system of n-linear oscillators whose frequencies vary due to certain "frequency mistunings"; it was established that the degenerate localized modes of the uncoupled system occur at extremum values of these "frequency mistunings." Based on the results presented in this work it is concluded that the origin of nonlinear mode localization in periodic system with nonlinear components is the dependence of the frequency of oscillation of the nonlinear components on their amplitude; thus, nonlinear mode localization takes place even in the absence of mistuning between substructures (which is a prerequisite for linear mode localization), and as a result, *perfectly periodic systems with nonlinearities are more susceptible to mode localization than linear ones*. As two (unknown) reviewers point out, it would be of great interest to investigate how the effects of parameters mistuning and nonlinearities interact in nearly periodic nonlinear structures. This is the topic of future planned research by the authors.

The generation of the localized modes in the 2-DOF was studied by means of Poincare′ maps and it was shown that at the limit of no coupling two homoclinic branches of an unstable antisymmetric mode coalesce into a closed line of equilibrium positions. Finally, the impulsive responses of systems with 12 and 50 DOF were computed in order to demonstrate the effects on the dynamics of the localized modes. The numerical simulations showed that the existence of localized modes in a structure can have a dramatic effect on its dynamic response; in particular, motion confinement of external impulses in the weakly coupled nonlinear cyclic systems was detected, a phenomenon with interesting implications as far as the passive and active vibration isolation of such systems is concerned.

Acknowledgments

Thanks are due to Prof. Daniel Tortorelli of the University of Illinois at Urbana-Champaign and to Mr. Samuel Rea for help with the finite element computations presented in Section 3 of this work. Part of this work is supported by the NSF Graduate Fellowships Program.

This work was supported by NSF Grant No. MSS 92-07318. Dr. D. Garg is the grant monitor.

References

Bathe, K. J., 1982, *Finite Element Procedures in Engineering Analysis*, Prentice-Hall, Englewood Cliffs, NJ.

Bendiksen, O. O., 1987, "Mode Localization Phenomena in Large Space Structures," *AIAA Journal*, Vol. 25, No. 9, pp. 1241–1248.

Caughey, T., Vakakis, A., and Sivo, J., 1990, "Analytical Study of Similar Normal Modes and Their Bifurcations in a Class of Strongly Nonlinear Systems," *International Journal of Nonlinear Mechanics*, Vol. 25, No. 5, pp. 521–533.

Caughey, T. K., and Vakakis, A. F., 1991, "A Method for Examining Steady State Solutions of Forced Discrete Systems with Strong Non-linearities," *International Journal of Nonlinear Mechanics*, Vol. 26, pp. 89–103.

Cornwell, P. J., and Bendiksen, O. O., 1989, "Localization of Vibrations in Large Space Reflectors," *AIAA Journal*, Vol. 27, No. 2, pp. 29–226.

Hodges, C. H., 1982, "Confinement of Vibration by Structural Irregularity," *Journal of Sound and Vibration*, Vol. 82, No. 3, pp. 411–424.

Kissel, G. J., 1987, "Localization in Disordered Periodic Structures," Ph.D. Thesis, Massachusetts Institute of Technology, Cambridge, MA.

Manevich, L., and Mikhlin, I., 1972, "On Periodic Solutions Close to Rectilinear Normal Vibration Modes," *PPM*, Vol. 36, No. 6, pp. 1051–1058.

Month, L., 1979, "On Approximate First Integrals of Hamiltonian Systems with an Application to Nonlinear Normal Modes in a two DOF Oscillator," PhD. Thesis, Cornell University, Ithaca, NY.

Month, L., and Rand, R., 1980, "An Application of the Poincare Map to the Stability of Nonlinear Normal Modes," ASME JOURNAL OF APPLIED MECHANICS, Vol. 47, pp. 645–651.

Nayfeh, A. H., and Mook, D., 1979, *Nonlinear Oscillations*, John Wiley and Sons, New York, NY

Pierre, C., and Cha, P., 1989, "Strong Mode Localization in Nearly Periodic Disordered Structures," *AIAA Journal*, Vol. 27, No. 2, pp. 227–241.

Pierre, C., and Shaw, S., 1991, "Mode Localization due to Symmetry-Breaking Nonlinearities," *International Journal of Bifurcation and Chaos*, Vol. 1, No. 2, pp. 471–575.

Rand, R., 1971, "A Higher Order Approximation for Nonlinear Normal Modes in Two-DOF Systems," *International Journal of Non-Linear Mechanics*, Vol. 6, pp. 545–547.

Rand, R., 1974, "A Direct Method for Nonlinear Normal Modes," *International Journal of Nonlinear Mechanics*, Vol. 9, pp. 363–368.

Rand, R., and Armbruster, D., 1987, *Perturbation Methods, Bifurcation Theory and Computer Algebra*, Springer-Verlag, New York.

Rosenberg, R. M., 1966 "On Nonlinear Vibrations of Systems with Many Degrees of Freedom," *Advances in Applied Mechanics*, Vol. 9, pp. 155–242.

Shaw, S., and Pierre, C., 1991, "Normal Modes for Nonlinear Vibratory Systems," *Journal of Sound and Vibration*, (in press).

Vakakis, A., 1991, "Nonsimilar Normal Oscillations in a Strongly Nonlinear Discrete System," *Journal of Sound and Vibration*, Vol. 158, No. 2, pp. 341–361.

Vakakis, A. F., and Caughey, T. K., 1991, "A Theorem on the Exact Nonsimilar Steady-States of a Nonsimilar Oscillator," ASME JOURNAL OF APPLIED MECHANICS, Vol. 59, No. 2, pp. 418–424.

Vakakis, A., and Cetinkaya, C., 1991, "Mode Localization in a Class of Multi-Degree-of-Freedom Nonlinear Systems with Cyclic Symmetry," *SIAM Journal on Applied Mathematics*, Vol. 53, pp. 265–292.

Vakakis, A., and Rand, R., 1991, "Normal Modes and Global Dynamics of a Two Degree of Freedom Nonlinear System I: Low Energies & II: High Energies," *International Journal of Non-Linear Mechanics*, Vol. 27, No. 5, pp. 861–888.

Vedenova, E. G., Manevich, L. I., and Pilipchuk, V. N., 1985, "Normal Oscillations of a String with Concentrated Masses on Non-Linearly Elastic Supports," *PMM*, Vol. 49, No. 2, pp. 203–211.

Wei, S.-T., and Pierre, C., 1988, "Localization Phenomena in Mistuned Assemblies with Cyclic Symmetry Part I: Free Vibrations," ASME *Journal of Vibration, Acoustics and Reliability in Design*, Vol. 110, pp. 429–438.

Wei, S.-T., and Pierre, C., 1988, "Localization Phenomena in Mistuned Assemblies with Cyclic Symmetry Part II: Forced Vibrations," ASME *Journal of Vibration, Acoustics and Reliability in Design*, Vol. 110, pp. 439–448.

APPENDIX

Determination of Nonlinear Localized Modes for n = 4 and 5

For the cyclic system with $n=4$, we seek normal mode solutions satisfying the relations (see expressions 18*b*)):

Downloaded 03 May 2010 to 171.66.16.245. Redistribution subject to ASME license or copyright; see http://www.asme.org/terms/Terms_Use.cfm

$$a_2 = a_4,\ \phi_1 = \phi_2 = \phi_4 = \pi,\ \phi_3 = -3\pi. \quad \text{(A1)}$$

The amplitudes of the motion are then determined from Eqs. (19*b*) by setting $n = 4$:

$$(3\mu/8k)(a_1^2 - a_2^2) - (1/2)(a_1^2 - a_2^2)/a_1a_2 + (1/2)[(a_2/a_1) - (a_3/a_2)] = 0$$

$$(3\mu/8k)(a_2^2 - a_3^2) - (1/2)(a_2^2 - a_3^2)/a_2a_3 + (1/2)[(a_1/a_2) - (a_2/a_3)] = 0. \quad \text{(A2)}$$

These equations are complemented by a relation analogous to Eq. (11):

$$a_1^2 + 2a_2^2 + a_3^2 = \rho^2 \quad \text{(A3)}$$

The numerical solutions of the set of nonlinear algebraic equations (A2,3) are graphically presented in Fig. 5.

For the system with $n = 5$, we impose the conditions (see expressions (18*a*)):

$$a_2 = a_5,\ a_3 = a_4,\ \phi_1 = \phi_2 = \phi_3 = \phi_5 = \pi,\ \phi_4 = -4\pi \quad \text{(A4)}$$

which lead to the following set of algebraic equations for the unknown amplitudes (see also Eqs. (19*a*)):

$$(3\mu/8\mathrm{k})(a_1^2 - a_2^2) - (1/2)(a_1^2 - a_2^2)/a_1a_2 + (1/2)[(a_2/a_1) - (a_3/a_2)] = 0$$

$$(3\mu/8\mathrm{k})(a_2^2 - a_3^2) - (1/2)(a_2^2 - a_3^2)/a_2a_3 + (1/2)[1 + (a_2/a_1)] = 0 \quad \text{(A5)}$$

with the additional equation:

$$a_1^2 + 2a_2^2 + 2a_3^2 = \rho^2 \quad \text{(A6)}$$

The solutions of Eqs. (A5, 6) are presented in Fig. 6.

Downloaded 03 May 2010 to 171.66.16.245. Redistribution subject to ASME license or copyright; see http://www.asme.org/terms/Terms_Use.cfm

F. P. J. Rimrott
Professor of Mechanical Engineering,
Fellow ASME

W. M. Szczygielski
University of Toronto,
Toronto, ON M5S 1A4, Canada

B. Tabarrok
University of Victoria,
Victoria, BC, Canada

Kinetic Energy and Complementary Kinetic Energy in Gyrodynamics

The concepts of kinetic energy and complementary kinetic energy permit to distinguish between two different formulations of what happens to be the same quantity in Newtonian mechanics. These formulations turn out to play a significant role in gyrodynamics in that they can be used very effectively to establish fundamental equations. It is relatively straightforward to establish a complementary kinetic energy expression. The establishment of the kinetic energy expression is, in spite of its unambiguous definition, more complicated, and a way is presented how to obtain it without too much difficulty. Equations are presented for the more common angle systems, i.e., for Euler angles of the first kind, Cardan angles of the first kind, both because of their fundamental importance, and Cardan angles of the fifth kind because of its prevalence in aeronautics.

Fundamental Concepts

Following Crandall (1957) and Tabarrok (1981), we adopt the concepts of kinetic energy T, and complementary kinetic energy T^*, as analogies to potential energy V and complementary potential energy V^*. Using generalized coordinates q_i and generalized momenta p_i of analytical mechanics, the kinetic energy of a scleronomic (i.e., where the time t does not appear explicitly) system with n-degrees-of-freedom is defined by

$$T = \int \dot{q}_i(q,p)\,dp_i \tag{1}$$

while its complementary kinetic energy is

$$T^* = \int p_i(q,\dot{q})\,d\dot{q}_i \tag{2}$$

with $i = 1, 2, 3, \ldots, n$.

For a point mass m on a straight path q, as an example,

$$T = \frac{1}{2}\frac{p^2}{m} \quad T^* = \frac{1}{2}m\dot{q}^2. \tag{3a,b}$$

Generalized velocities and generalized momenta are obtained by partial differentiation and defined by

$$\dot{q}_i = \frac{\partial}{\partial p_i}T(q,p) \tag{4}$$

$$p_i = \frac{\partial}{\partial \dot{q}_i}T^*(q,\dot{q}) \tag{5}$$

For a point mass m on a straight path q, as an example,

$$\dot{q} = \frac{\partial}{\partial p}\left(\frac{1}{2}\frac{p^2}{m}\right) = \frac{p}{m} \quad p = \frac{\partial}{\partial \dot{q}}\left(\frac{1}{2}m\dot{q}^2\right) = m\dot{q}. \tag{6a,b}$$

In Newtonian mechanics it so happens that kinetic energy T and complementary kinetic energy T^* have the same magnitude (Fig. 1). This circumstance can often be exploited to great advantage. But in order to be able to apply formulas (4) and (5), the kinetic energy T *must* be expressed in terms of q and p, while the complementary kinetic energy T^* *must* be expressed in terms of q and $\dot{q}$. Thus it is possible to establish $T^* = T^*(q, \dot{q})$ which, in the case of gyrodynamics of rigid bodies, is usually readily done. Partial differentiation with respect to the generalized velocities $\dot{q}_i$ then results in the generalized momenta p_i. With the generalized momenta p_i known, it becomes then possible to form $T = T(q, p)$, which can subsequently be differentiated partially with respect to the

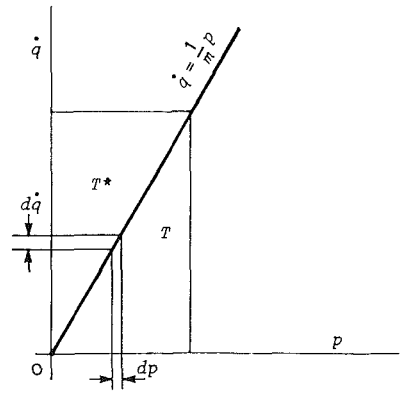


Fig. 1 Kinetic energy T and complementary kinetic energy T^* for a single point mass in Newtonian mechanics

Contributed by the Applied Mechanics Division of THE AMERICAN SOCIETY OF MECHANICAL ENGINEERS for presentation at the First Joint ASCE-EMD, ASME-AMD, SES Meeting, Charlottesville, VA, June 6–9, 1993.

Discussion on this paper should be addressed to the Technical Editor, Professor Lewis T. Wheeler, Department of Mechanical Engineering, University of Houston, Houston, TX 77204-4792, and will be accepted until four months after final publication of the paper itself in the ASME JOURNAL OF APPLIED MECHANICS.

Manuscript received by the ASME Applied Mechanics Division, July 5, 1991; final revision, Mar. 18, 1992. Associate Technical Editor: R. L. Huston.

Paper No. 93-APM-8.

Copyright © 1993 by ASME
Downloaded 03 May 2010 to 171.66.16.245. Redistribution subject to ASME license or copyright; see http://www.asme.org/terms/Terms_Use.cfm

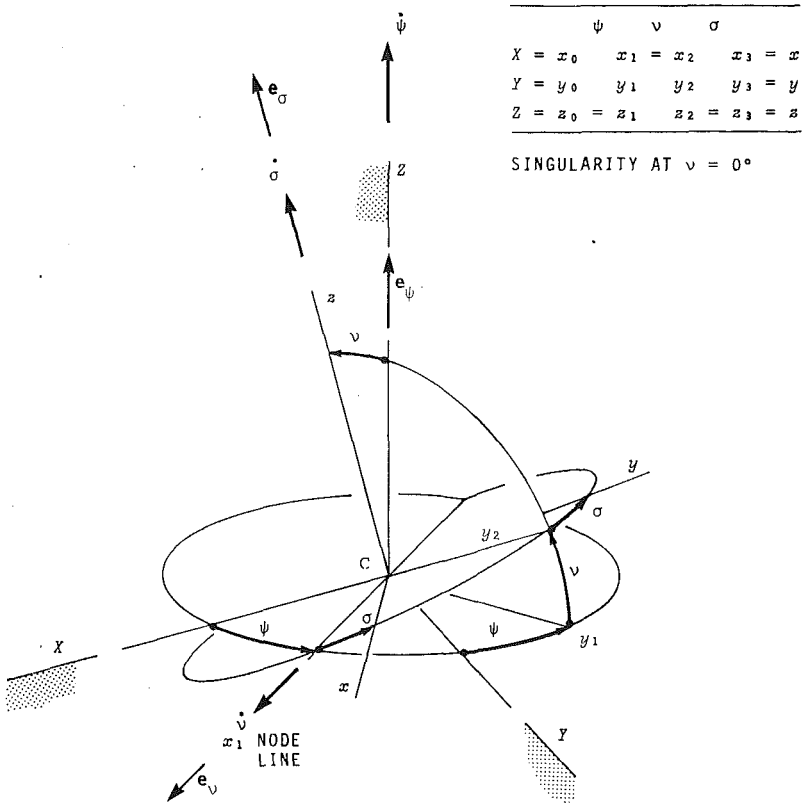


Fig. 2 Euler angles of the first kind

generalized momenta p_i, to obtain the generalized velocities $\dot{q}_i$. This process is used in the present paper to establish the fundamental relationships for a single rigid gyro, first with Euler angles as generalized coordinates, and then with Cardan angles as generalized coordinates.

Kinetic Energy of Rotation. A suitable ansatz for the complementary kinetic energy of rotation of a single rigid gyro is

$$T^* = \frac{1}{2}\,(A\omega_x^2 + B\omega_y^2 + C\omega_z^2) \tag{7}$$

where the angular velocity is

$$\omega = [\mathbf{e}_x \quad \mathbf{e}_y \quad \mathbf{e}_x] \begin{bmatrix} \omega_x \\ \omega_y \\ \omega_z \end{bmatrix} \tag{8}$$

and the inertia tensor is

$$[I] = \begin{bmatrix} A & 0 & 0 \\ 0 & B & 0 \\ 0 & 0 & C \end{bmatrix}. \tag{9}$$

The *Cxyz* coordinate system is body fixed, coincides with the gyro's principal axes, and originates at the gyro's mass center *C*.

Since angular momentum components and angular velocity components are related by

$$\begin{aligned} H_x &= A\omega_x \\ H_y &= B\omega_y \\ H_z &= C\omega_z, \end{aligned} \tag{10}$$

Eq. (7) can then be rearranged to supply an ansatz for the kinetic energy

$$T = \frac{1}{2}\left(\frac{H_x^2}{A} + \frac{H_y^2}{B} + \frac{H_z^2}{C}\right). \tag{11}$$

Expressions (7) and (11) are, however, neither specifically a kinetic energy T, nor specifically a complementary kinetic energy T^*, in the sense of Eqs. (1) and (2). In order to express them properly, we need generalized coordinates, for which Euler angles are suitable, as well as Cardan angles.

It is well known (Magnus, 1971) that Cartesian coordinates of the angular velocity are nonholonomic quantities (nonintegrable with respect to time) and therefore cannot be used as generalized velocities. However, as long as the kinetic energies as defined in Eqs. (1) and (2) are not explicitly dependent on generalized coordinates themselves, they can be adopted for nonholomic velocities as well. This is specifically the case in Eq. (7), and by analogy in Eq. (11). Distinguishing between the terms complementary kinetic (7) and kinetic energy (11) is justified here solely by the role the expression can play in further application in the present paper.

Euler Angles of the First Kind

In order to establish the angular position, often called the *attitude* of a gyro, three angular coordinates, the so-called *Euler angles* may be used. In Fig. 2 a *Cxyz* coordinate system is shown at angles ψ, ν, σ with respect to a *CXYZ* coordinate system. The *CXYZ* coordinate system is fixed in space, while the *Cxyz* coordinate system is body fixed (i.e., fixed to the gyro). The x_1-line, representing the intersection of the *xy*-plane with the *XY*-plane, is called the *node line*. The time derivatives of the Euler angles are the *Euler frequencies* (or *Euler rates*), viz. precession $\dot{\psi}$, nutation $\dot{\nu}$, and spin $\dot{\sigma}$. The Euler frequencies can readily be integrated to yield the Euler angles

$$\begin{aligned} \psi &= \psi_0 + \int \dot{\psi}\,dt \\ \nu &= \nu_0 + \int \dot{\nu}\,dt \\ \sigma &= \sigma_0 + \int \dot{\sigma}\,dt \end{aligned} \tag{12}$$

Downloaded 03 May 2010 to 171.66.16.245. Redistribution subject to ASME license or copyright; see http://www.asme.org/terms/Terms_Use.cfm

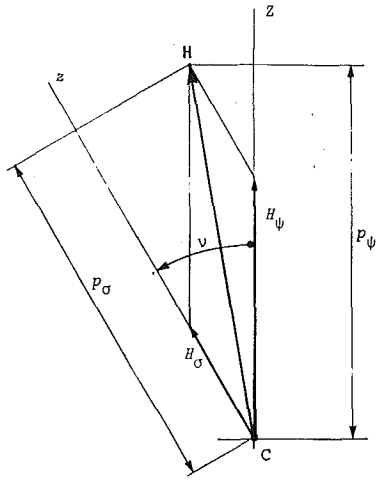


Fig. 3 Angular momentum components and generalized momenta for Euler angles of the first kind (when $H_\nu = 0$)

and thus give the attitude of the gyro as a function of time. This property makes Euler angles suitable as generalized coordinates.

The angular velocity ω of the gyro can be written (Rimrott, 1988)

$$\omega = [\mathbf{e}_x \quad \mathbf{e}_y \quad \mathbf{e}_z]\begin{bmatrix}\omega_x\\ \omega_y\\ \omega_z\end{bmatrix} = [\mathbf{e}_\psi \quad \mathbf{e}_\nu \quad \mathbf{e}_\sigma]\begin{bmatrix}\dot\psi\\ \dot\nu\\ \dot\sigma\end{bmatrix} \tag{13}$$

where $Cxyz$ are gyro-fixed Cartesian coordinate axes, and $q_1 = \psi$, $q_2 = \nu$, $q_3 = \sigma$ are the generalized position coordinates of analytical mechanics.

The transition is given by

$$\begin{bmatrix}\omega_x\\ \omega_y\\ \omega_z\end{bmatrix} = \begin{bmatrix}\sin\nu\sin\sigma & \cos\sigma & 0\\ \sin\nu\cos\sigma & -\sin\sigma & 0\\ \cos\nu & 0 & 1\end{bmatrix}\begin{bmatrix}\dot\psi\\ \dot\nu\\ \dot\sigma\end{bmatrix}. \tag{14}$$

The angular momentum components follow the same transition (14), i.e.,

$$\begin{bmatrix}H_x\\ H_y\\ H_z\end{bmatrix} = \begin{bmatrix}\sin\nu\sin\sigma & \cos\sigma & 0\\ \sin\nu\cos\sigma & -\sin\sigma & 0\\ \cos\nu & 0 & 1\end{bmatrix}\begin{bmatrix}H_\psi\\ H_\nu\\ H_\sigma\end{bmatrix}. \tag{15}$$

Complementary Kinetic Energy. Combining Eqs. (2), (7), and (14) gives us now the complementary kinetic energy, properly expressed in terms of generalized coordinates and generalized velocities,

$$T^* = \frac{1}{2}[A(\dot\psi\sin\nu\sin\sigma + \dot\nu\cos\sigma)^2 + B(\dot\psi\sin\nu\cos\sigma - \dot\nu\sin\sigma)^2 + C(\dot\psi\cos\nu + \dot\sigma)^2], \tag{16}$$

where the Euler angles ψ, ν, σ are the generalized coordinates q_i of analytical mechanics.

Generalized Momenta. According to Eq. (5), the generalized momenta p_i are obtained by partial differentiation of the complementary kinetic energy T^* with respect to the generalized velocities $\dot q_i$, with $\dot q_1 = \dot\psi$, $\dot q_2 = \dot\nu$, and $\dot q_3 = \dot\sigma$. Thus (Greenwood, 1988),

$$p_\psi = \frac{\partial T^*}{\partial\dot\psi} = A(\dot\psi\sin\nu\sin\sigma + \dot\nu\cos\sigma)\sin\nu\sin\sigma + B(\dot\psi\sin\nu\cos\sigma - \dot\nu\sin\sigma)\sin\nu\cos\sigma + C(\dot\psi\cos\nu + \dot\sigma)\cos\nu \tag{17a}$$

$$p_\nu = \frac{\partial T^*}{\partial\dot\nu} = A(\dot\psi\sin\nu\sin\sigma + \dot\nu\cos\sigma)\cos\sigma - B(\dot\psi\sin\nu\cos\sigma - \dot\nu\sin\sigma)\sin\sigma \tag{17b}$$

$$p_\sigma = \frac{\partial T^*}{\partial\dot\sigma} = C(\dot\psi\cos\nu + \dot\sigma). \tag{17c}$$

Note that the generalized momenta p_i are angular and represent the *projections* (covariant components) of the angular momentum vector **H** onto the $\dot\psi$, $\dot\nu$, and $\dot\sigma$ directions. They do not represent the (contravariant) components H_ψ, H_ν, and H_σ of the angular momentum vector, to which they are related by (Fig. 3)

$$\begin{bmatrix}p_\psi\\ p_\nu\\ p_\sigma\end{bmatrix} = \begin{bmatrix}1 & 0 & \cos\nu\\ 0 & 1 & 0\\ \cos\nu & 0 & 1\end{bmatrix}\begin{bmatrix}H_\psi\\ H_\nu\\ H_\sigma\end{bmatrix}. \tag{18}$$

The inverse relationship is

$$\begin{bmatrix}H_\psi\\ H_\nu\\ H_\sigma\end{bmatrix} = \begin{bmatrix}\dfrac{1}{\sin^2\nu} & 0 & \dfrac{-\cos\nu}{\sin^2\nu}\\ 0 & 1 & 0\\ \dfrac{-\cos\nu}{\sin^2\nu} & 0 & \dfrac{1}{\sin^2\nu}\end{bmatrix}\begin{bmatrix}p_\psi\\ p_\nu\\ p_\sigma\end{bmatrix} \tag{19}$$

Equations (17) can be written in matrix form

$$\begin{bmatrix}p_\psi\\ p_\nu\\ p_\sigma\end{bmatrix} = \begin{bmatrix}(A\sin^2\sigma + B\cos^2\sigma)\sin^2\nu + C\cos^2\nu & (A-B)\sin\nu\sin\sigma\cos\sigma & C\cos\nu\\ (A-B)\sin\nu\sin\sigma\cos\sigma & A\cos^2\sigma + B\sin^2\sigma & 0\\ C\cos\nu & 0 & C\end{bmatrix}\begin{bmatrix}\dot\psi\\ \dot\nu\\ \dot\sigma\end{bmatrix} \tag{20}$$

or, in shorthand notation,

$$\{p\} = [A]\{\dot q\}. \tag{21}$$

It is seen that the inertia coefficient matrix $[A]$ is a symmetric transformation matrix which maps the generalized velocities into the generalized momenta.

The transformation matrix contains partial derivatives as elements.

$$[A] = \begin{bmatrix}\dfrac{\partial p_\psi}{\partial\dot\psi} & \dfrac{\partial p_\psi}{\partial\dot\nu} & \dfrac{\partial p_\psi}{\partial\dot\sigma}\\ \dfrac{\partial p_\nu}{\partial\dot\psi} & \dfrac{\partial p_\nu}{\partial\dot\nu} & \dfrac{\partial p_\nu}{\partial\dot\sigma}\\ \dfrac{\partial p_\sigma}{\partial\dot\psi} & \dfrac{\partial p_\sigma}{\partial\dot\nu} & \dfrac{\partial p_\sigma}{\partial\dot\sigma}\end{bmatrix} = \left[\frac{\partial p_i}{\partial\dot q_j}\right] \tag{22}$$

Symmetry means that, e.g.,

$$\frac{\partial p_\psi}{\partial\dot\nu} = \frac{\partial p_\nu}{\partial\dot\psi}, \tag{23}$$

etc., or in general we have that

$$\frac{\partial p_i}{\partial\dot q_j} = \frac{\partial p_j}{\partial\dot q_i} \quad i,j = \psi,\nu,\sigma. \tag{24}$$

With the help of Eq. (21) the complementary kinetic energy (16) can now be expressed as

$$T^* = \frac{1}{2}\{\dot q\}^T[A]\{\dot q\}. \tag{25}$$

Lagrange Equation. All loading cases for a single rigid gyro are covered by Lagrange's equation in its fundamental form

Downloaded 03 May 2010 to 171.66.16.245. Redistribution subject to ASME license or copyright; see http://www.asme.org/terms/Terms_Use.cfm

$$\frac{d}{dt}\frac{\partial T^*}{\partial \dot{q}_i}-\frac{\partial T^*}{\partial q_i}=Q_i \tag{26}$$

With the generalized momenta (17) and the complementary kinetic energy (16), the three Lagrange equations become

$$\frac{d}{dt}p_\psi-\frac{\partial T^*}{\partial \psi}=Q_\psi \tag{27a}$$

$$\frac{d}{dt}p_\nu-\frac{\partial T^*}{\partial \nu}=Q_\nu \tag{27b}$$

$$\frac{d}{dt}p_\sigma-\frac{\partial T^*}{\partial \sigma}=Q_\sigma. \tag{27c}$$

An inspection of Eq. (16) shows that the complementary kinetic energy T^* does not contain the generalized coordinate ψ explicitly, thus $\partial T^*/\partial\psi = 0$ in Eq. (27a). Note that the Q_i are covariant torque components, which are related to the contravariant torque components M_i by the same transformation as in Eq. (19), i.e.,

$$\begin{bmatrix} M_\psi \\ M_\nu \\ M_\sigma \end{bmatrix}=\begin{bmatrix} \frac{1}{\sin^2\nu} & 0 & \frac{-\cos\nu}{\sin^2\nu} \\ 0 & 1 & 0 \\ \frac{-\cos\nu}{\sin^2\nu} & 0 & \frac{1}{\sin^2\nu} \end{bmatrix}\begin{bmatrix} Q_\psi \\ Q_\nu \\ Q_\sigma \end{bmatrix} \tag{28}$$

The square of the magnitude of the torque applied can be shown to be

$$M^2=M_x^2+M_y^2+M_z^2 \tag{29a}$$

$$M^2=M_\psi^2+M_\nu^2+M_\sigma^2+2M_\psi M_\sigma\cos\nu \tag{29b}$$

$$M^2=\frac{1}{\sin^2\nu}\,(Q_\psi^2+Q_\nu^2\sin^2\nu+Q_\sigma^2)-\frac{2\cos\nu}{\sin^2\nu}\,Q_\psi Q_\sigma \tag{29c}$$

D'Alembert's Principle. D'Alembert's principle, involving the vanishing of the virtual work of applied torques and inertial torques, reads

$$\delta W=(\mathbf{M}-\dot{\mathbf{H}})\cdot\delta\theta=0. \tag{30}$$

Using Eulerian angles as generalized coordinates, D'Alembert's principle can now be written as

$$\delta W=\left(Q_\psi-\left(\dot{p}_\psi-\frac{\partial T^*}{\partial\psi}\right)\right)\delta\psi+\left(Q_\nu-\left(\dot{p}_\nu-\frac{\partial T^*}{\partial\nu}\right)\right)\delta\nu+\left(Q_\sigma-\left(\dot{p}_\sigma-\frac{\partial T^*}{\partial\sigma}\right)\right)\delta\sigma=0. \tag{31}$$

Since the three variations $\delta\psi$, $\delta\nu$, and $\delta\sigma$ do not vanish and are independent, their coefficients must vanish, i.e., they must satisfy the Lagrange Eqs. (27).

Kinetic Energy. Inverting Eq. (21) results in

$$\{\dot{q}\}=[A]^{-1}\{p\} \tag{32}$$

and the kinetic energy (1) can then be obtained as

$$T=\frac{1}{2}\,\{p\}^T[A]^{-1}\{p\}. \tag{33}$$

The inversion of the matrix $[A]$ is, however, cumbersome, and a more tractable approach for obtaining the kinetic energy is the following: beginning with Eqs. (11) and (15) we obtain, as an intermediate expression,

$$T=\frac{1}{2}\left(\frac{1}{A}\,(H_\psi\sin\nu\sin\sigma+H_\nu\cos\sigma)^2+\frac{1}{B}\,(H_\psi\sin\nu\cos\sigma-H_\nu\sin\sigma)^2+\frac{1}{C}\,(H_\psi\cos\nu+H_\sigma)^2\right). \tag{34}$$

The reader is asked to compare Eqs. (34) and (16) and to note the similarity of the terms in round brackets.

Properly expressed in terms of the generalized momenta p_ψ, p_ν, p_σ, the kinetic energy (1) is, from Eqs. (19) and (34),

$$T=\frac{1}{2}\left[\frac{1}{\sin^2\nu}\left(\frac{\sin^2\sigma}{A}+\frac{\cos^2\sigma}{B}\right)p_\psi^2+\left(\frac{\cos^2\sigma}{A}+\frac{\sin^2\sigma}{B}\right)p_\nu^2+\left(\frac{1}{C}+\frac{1}{\tan^2\nu}\left(\frac{\sin^2\sigma}{A}+\frac{\cos^2\sigma}{B}\right)\right)p_\sigma^2+\frac{2\sin\sigma\cos\sigma}{\sin\nu}\left(\frac{1}{A}-\frac{1}{B}\right)p_\psi p_\nu-\frac{2\sin\sigma\cos\sigma}{\tan\nu}\left(\frac{1}{A}-\frac{1}{B}\right)p_\nu p_\sigma-\frac{2}{\sin\nu\tan\nu}\left(\frac{\sin^2\sigma}{A}+\frac{\cos^2\sigma}{B}\right)p_\psi p_\sigma\right]. \tag{35}$$

Generalized Velocities. According to definition (4), the generalized velocities are obtained by partial differentiation of the kinetic energy (35) with respect to the generalized momenta.

$$\dot{\psi}=\frac{\partial T}{\partial p_\psi}=\frac{1}{\sin^2\nu}\left(\frac{\sin^2\sigma}{A}+\frac{\cos^2\sigma}{B}\right)p_\psi+\frac{\sin\sigma\cos\sigma}{\sin\nu}\left(\frac{1}{A}-\frac{1}{B}\right)p_\nu-\frac{1}{\sin\nu\tan\nu}\left(\frac{\sin^2\sigma}{A}+\frac{\cos^2\sigma}{B}\right)p_\sigma \tag{36a}$$

$$\dot{\nu}=\frac{\partial T}{\partial p_\nu}=\frac{\sin\sigma\cos\sigma}{\sin\nu}\left(\frac{1}{A}-\frac{1}{B}\right)p_\psi+\left(\frac{\cos^2\sigma}{A}+\frac{\sin^2\sigma}{B}\right)p_\nu-\frac{\sin\sigma\cos\sigma}{\tan\nu}\left(\frac{1}{A}-\frac{1}{B}\right)p_\sigma \tag{36b}$$

$$\dot{\sigma}=\frac{\partial T}{\partial p_\sigma}=-\frac{1}{\sin\nu\tan\nu}\left(\frac{\sin^2\sigma}{A}+\frac{\cos^2\sigma}{B}\right)p_\psi-\frac{\sin\sigma\cos\sigma}{\tan\nu}\left(\frac{1}{A}-\frac{1}{B}\right)p_\nu+\left(\frac{1}{C}+\frac{1}{\tan^2\nu}\left(\frac{\sin^2\sigma}{A}+\frac{\cos^2\sigma}{B}\right)\right)p_\sigma \tag{36c}$$

Writing Eqs. (36) in matrix form gives

$$\begin{bmatrix} \dot{\psi} \\ \dot{\nu} \\ \dot{\sigma} \end{bmatrix}=\begin{bmatrix} \left(\frac{\sin^2\sigma}{A}+\frac{\cos^2\sigma}{B}\right)\frac{1}{\sin^2\nu} & \left(\frac{1}{A}-\frac{1}{B}\right)\frac{\sin\sigma\cos\sigma}{\sin\nu} & -\left(\frac{\sin^2\sigma}{A}+\frac{\cos^2\sigma}{B}\right)\frac{1}{\sin\nu\tan\nu} \\ \left(\frac{1}{A}-\frac{1}{B}\right)\frac{\sin\sigma\cos\sigma}{\sin\nu} & \frac{\cos^2\sigma}{A}+\frac{\sin^2\sigma}{B} & -\left(\frac{1}{A}-\frac{1}{B}\right)\frac{\sin\sigma\cos\sigma}{\tan\nu} \\ -\left(\frac{\sin^2\sigma}{A}+\frac{\cos^2\sigma}{B}\right)\frac{1}{\sin\nu\tan\nu} & -\left(\frac{1}{A}-\frac{1}{B}\right)\frac{\sin\sigma\cos\sigma}{\tan\nu} & \frac{1}{C}+\left(\frac{\sin^2\sigma}{A}+\frac{\cos^2\sigma}{B}\right)\frac{1}{\tan^2\nu} \end{bmatrix}\begin{bmatrix} p_\psi \\ p_\nu \\ p_\sigma \end{bmatrix} \tag{37}$$

or, in shorthand notation,

$$\{\dot{q}\}=[A]^{-1}\{p\}, \tag{38}$$

i.e., the same as Eq. (32). The (symmetric) matrix $[A]^{-1}$ is the inverse of the transformation matrix of Eq. (20) and maps the generalized momenta into the generalized velocities.

Cardan Angles of the First Kind

Just as was the case with Euler angles, Cardan frequencies can be integrated to yield the Cardan angles

Downloaded 03 May 2010 to 171.66.16.245. Redistribution subject to ASME license or copyright; see http://www.asme.org/terms/Terms_Use.cfm

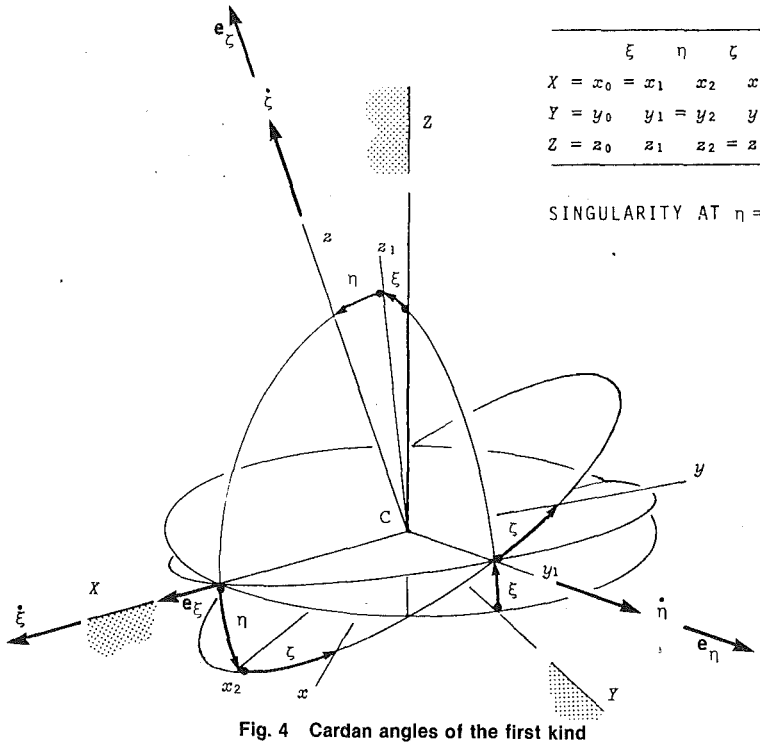


Fig. 4 Cardan angles of the first kind

$$\xi = \xi_0 + \int \dot{\xi}\, dt$$
$$\eta = \eta_0 + \int \dot{\eta}\, dt$$
$$\zeta = \zeta_0 + \int \dot{\zeta}\, dt, \tag{39}$$

and thus give the attitude of the gyro as function of time. This property makes Cardan angles suitable as generalized coordinates.

When terms such as *yaw* (or *heading*) angle, *pitch* (or *flight path*) angle, and *roll* (or *bank*) angle are used, then Cardan angles are involved. Depending on the choice of axes, altogether six kinds of Cardan angle systems can be employed (Rimrott, 1988). The subsequent equations are for Cardan angles of the first kind (Fig. 4), consisting of ξ (about the space-fixed X-axis), η (about the once carried y_1-axis), and ζ (about the twice-carried z-axis).

The angular velocity ω of the gyro can either be expressed in terms of components along the body-fixed $Cxyz$ coordinate system, or in terms of the *Cardan frequencies* along the pertinent (nonorthogonal) carried coordinates:

$$\boldsymbol{\omega} = [\mathbf{e}_x \quad \mathbf{e}_y \quad \mathbf{e}_z] \begin{bmatrix} \omega_x \\ \omega_y \\ \omega_z \end{bmatrix} = [\mathbf{e}_\xi \quad \mathbf{e}_\eta \quad \mathbf{e}_\zeta] \begin{bmatrix} \dot{\xi} \\ \dot{\eta} \\ \dot{\zeta} \end{bmatrix}. \tag{40}$$

The transition between the two coordinate system can be effected by

$$\begin{bmatrix} \omega_x \\ \omega_y \\ \omega_z \end{bmatrix} = \begin{bmatrix} \cos\eta\cos\zeta & \sin\zeta & 0 \\ -\cos\eta\sin\zeta & \cos\zeta & 0 \\ \sin\eta & 0 & 1 \end{bmatrix} \begin{bmatrix} \dot{\xi} \\ \dot{\eta} \\ \dot{\zeta} \end{bmatrix}. \tag{41}$$

Transition (41) is also valid for the angular momentum components, i.e.,

$$\begin{bmatrix} H_x \\ H_y \\ H_z \end{bmatrix} = \begin{bmatrix} \cos\eta\cos\zeta & \sin\zeta & 0 \\ -\cos\eta\sin\zeta & \cos\zeta & 0 \\ \sin\eta & 0 & 1 \end{bmatrix} \begin{bmatrix} H_\xi \\ H_\eta \\ H_\zeta \end{bmatrix}. \tag{42}$$

Complementary Kinetic Energy. Combining Eqs. (2), (7), and (41) gives us now, for the complementary kinetic energy,

$$T^* = \frac{1}{2}[A(\dot{\xi}\cos\eta\cos\zeta + \dot{\eta}\sin\zeta)^2 + B(-\dot{\xi}\cos\eta\sin\zeta + \dot{\eta}\cos\zeta)^2 + C(\dot{\xi}\sin\eta + \dot{\zeta})^2], \tag{43}$$

where the Cardan angles ξ, η, and ζ are the generalized coordinates q_i of analytical mechanics.

Generalized Momenta. The generalized momenta p_i are obtained by partial differentiation of the complementary kinetic energy T^* with respect to the generalized velocities q_i, with $\dot{q}_1 = \dot{\xi}$, $\dot{q}_2 = \dot{\eta}$, $\dot{q}_3 = \dot{\zeta}$. Thus,

$$p_\xi = \frac{\partial T^*}{\partial \dot{\xi}} = A(\dot{\xi}\cos\eta\cos\zeta + \dot{\eta}\sin\zeta)\cos\eta\cos\zeta + B(\dot{\xi}\cos\eta\sin\zeta - \dot{\eta}\cos\zeta)\cos\eta\sin\zeta + C(\dot{\xi}\sin\eta + \dot{\zeta})\sin\eta \tag{44a}$$

$$p_\eta = \frac{\partial T^*}{\partial \dot{\eta}} = A(\dot{\xi}\cos\eta\cos\zeta + \dot{\eta}\sin\zeta)\sin\zeta + B(-\dot{\xi}\cos\eta\sin\zeta + \dot{\eta}\cos\zeta)\cos\zeta \tag{44b}$$

$$p_\zeta = \frac{\partial T^*}{\partial \dot{\zeta}} = C(\dot{\xi}\sin\eta + \dot{\zeta}). \tag{44c}$$

The generalized momenta p_i are related to the components H_ξ, H_η, and H_ζ of the angular momentum vector (Fig. 5),

$$\begin{bmatrix} p_\xi \\ p_\eta \\ p_\zeta \end{bmatrix} = \begin{bmatrix} 1 & 0 & \sin\eta \\ 0 & 1 & 0 \\ \sin\eta & 0 & 1 \end{bmatrix} \begin{bmatrix} H_\xi \\ H_\eta \\ H_\zeta \end{bmatrix}. \tag{45}$$

The inverse relationship is

$$\begin{bmatrix} H_\xi \\ H_\eta \\ H_\zeta \end{bmatrix} = \begin{bmatrix} \dfrac{1}{\cos^2\eta} & 0 & \dfrac{-\sin\eta}{\cos^2\eta} \\ 0 & 1 & 0 \\ \dfrac{-\sin\eta}{\cos^2\eta} & 0 & \dfrac{1}{\cos^2\eta} \end{bmatrix} \begin{bmatrix} p_\xi \\ p_\eta \\ p_\zeta \end{bmatrix}. \tag{46}$$

Lagrange Equation. With the generalized momenta (44) and the complementary kinetic energy (43), the three Lagrange equations become

Downloaded 03 May 2010 to 171.66.16.245. Redistribution subject to ASME license or copyright; see http://www.asme.org/terms/Terms_Use.cfm

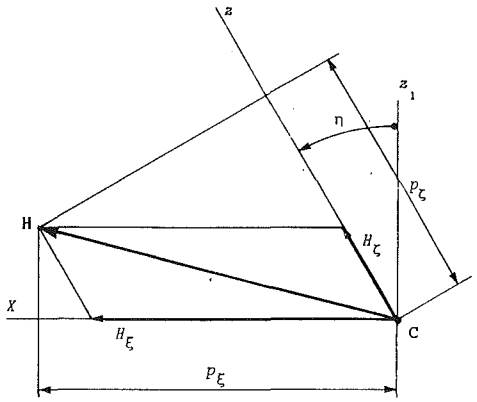


Fig. 5 Angular momentum components and generalized momenta for Cardan angles of the first kind (when $H_\eta = 0$)

$$\frac{d}{dt}p_\xi - \frac{\partial T^*}{\partial \xi} = Q_\xi \tag{47a}$$

$$\frac{d}{dt}p_\eta - \frac{\partial T^*}{\partial \eta} = Q_\eta \tag{47b}$$

$$\frac{d}{dt}p_\zeta - \frac{\partial T^*}{\partial \zeta} = Q_\zeta. \tag{47c}$$

For Cardan angles of the first kind, the angle ξ is taken about a space-fixed axis, thus $\partial T^*/\partial \xi = 0$ in Eq. (47*a*). D'Alembert's principle (30) can be expressed in terms of Cardan angles of the first kind by using the Lagrange Eqs. (47).

Note that the generalized forces Q_i are covariant components of the applied torque similar to Eqs. (29) and the square of the magnitude of the torque applied can be shown to be

$$M^2 = M_x^2 + M_y^2 + M_z^2 \tag{48a}$$

$$M^2 = M_\xi^2 + M_\eta^2 + M_\zeta^2 + 2M_\xi M_\zeta \sin\eta \tag{48b}$$

$$M^2 = \frac{1}{\cos^2\eta}\,(Q_\xi^2 + Q_\eta^2\cos^2\eta + Q_\zeta^2) - \frac{2\sin\eta}{\cos^2\eta}\,Q_\xi Q_\zeta, \tag{48c}$$

where M_x, M_y, M_z are the torque components along gyro-fixed Cartesian axes, and M_ξ, M_η, M_ζ are the contravariant torque components.

Kinetic Energy. Using Eqs. (11) and (42) an intermediate expression is obtained:

$$T = \frac{1}{2}\left(\frac{1}{A}\,(H_\xi\cos\eta\cos\zeta + H_\eta\sin\zeta)^2 + \frac{1}{B}\,(-H_\xi\cos\eta\sin\zeta + H_\eta\cos\zeta)^2 + \frac{1}{C}\,(H_\xi\sin\eta + H_\zeta)^2\right). \tag{49}$$

Note again the similarities, of the terms in round brackets, between Eqs. (49) and (43).

The kinetic energy (1) in terms of Cardan angles and Cardan momenta is obtained by combining Eqs. (49) and (46), and is

$$T = \frac{1}{2}\left[\frac{1}{\cos^2\eta}\left(\frac{\cos^2\zeta}{A} + \frac{\sin^2\zeta}{B}\right)p_\xi^2 + \left(\frac{\sin^2\zeta}{A} + \frac{\cos^2\zeta}{B}\right)p_\eta^2 + \left(\frac{1}{C} + \tan^2\eta\left(\frac{\cos^2\zeta}{A} + \frac{\sin^2\zeta}{B}\right)\right)p_\zeta^2 + \frac{2\sin\zeta\cos\zeta}{\cos\eta}\left(\frac{1}{A} - \frac{1}{B}\right)p_\xi p_\eta - 2\tan\eta\sin\zeta\cos\zeta\left(\frac{1}{A} - \frac{1}{B}\right)p_\eta p_\zeta - \frac{2\tan\eta}{\cos\eta}\left(\frac{\cos^2\zeta}{A} + \frac{\sin^2\zeta}{B}\right)p_\xi p_\zeta\right]. \tag{50}$$

Generalized Velocities. The generalized velocities are obtained by forming the appropriate partial derivatives

$$\dot\xi = \frac{\partial T}{\partial p_\xi} = \frac{1}{\cos^2\eta}\left(\frac{\cos^2\zeta}{A} + \frac{\sin^2\zeta}{B}\right)p_\xi + \frac{\sin\zeta\cos\zeta}{\cos\eta}\left(\frac{1}{A} - \frac{1}{B}\right)p_\eta - \frac{\tan\eta}{\cos\eta}\left(\frac{\cos^2\zeta}{A} + \frac{\sin^2\zeta}{B}\right)p_\zeta \tag{51a}$$

$$\dot\eta = \frac{\partial T}{\partial p_\eta} = \frac{\sin\zeta\cos\zeta}{\cos\eta}\left(\frac{1}{A} - \frac{1}{B}\right)p_\xi + \left(\frac{\sin^2\zeta}{A} + \frac{\cos^2\zeta}{B}\right)p_\eta - \tan\eta\sin\zeta\cos\zeta\left(\frac{1}{A} - \frac{1}{B}\right)p_\zeta \tag{51b}$$

$$\dot\zeta = \frac{\partial T}{\partial p_\zeta} = -\frac{\tan\eta}{\cos\eta}\left(\frac{\cos^2\zeta}{A} + \frac{\sin^2\zeta}{B}\right)p_\xi - \tan\eta\sin\zeta\cos\zeta\left(\frac{1}{A} - \frac{1}{B}\right)p_\eta + \left(\frac{1}{C} + \tan^2\eta\left(\frac{\cos^2\zeta}{A} + \frac{\sin^2\zeta}{B}\right)\right)p_\zeta \tag{51c}$$

Equations for Cardan angles of the second and third kinds (Rimrott, 1988) can be obtained by appropriate cyclic interchanges.

Cardan Angles of the Fifth Kind

Of importance in airplane flight dynamics, Euler angles of the fifth kind (Rimrott, 1988) consist of a *yaw* (heading) angle ζ about a space-fixed line to the zenith, a *pitch* angle η about a once-carried (through ζ) line to the horizon, and a *roll* (bank) angle ξ about a twice-carried (through ζ and η) gyro-fixed line (Fig. 6).

The angular velocity can be expressed in two ways:

$$\omega = [\mathbf{e}_x \quad \mathbf{e}_y \quad \mathbf{e}_z]\begin{bmatrix}\omega_x\\ \omega_y\\ \omega_z\end{bmatrix} = [\mathbf{e}_\xi \quad \mathbf{e}_\eta \quad \mathbf{e}_\zeta]\begin{bmatrix}\dot\xi\\ \dot\eta\\ \dot\zeta\end{bmatrix}. \tag{52}$$

The transition relation is

$$\begin{bmatrix}\omega_x\\ \omega_y\\ \omega_z\end{bmatrix} = \begin{bmatrix}1 & 0 & -\sin\eta\\ 0 & \cos\xi & \sin\xi\cos\eta\\ 0 & -\sin\xi & \cos\xi\cos\eta\end{bmatrix}\begin{bmatrix}\dot\xi\\ \dot\eta\\ \dot\zeta\end{bmatrix}. \tag{53}$$

Similarly, for the angular momentum components,

$$\begin{bmatrix}H_x\\ H_y\\ H_z\end{bmatrix} = \begin{bmatrix}1 & 0 & -\sin\eta\\ 0 & \cos\xi & \sin\xi\cos\eta\\ 0 & -\sin\xi & \cos\xi\cos\eta\end{bmatrix}\begin{bmatrix}H_\xi\\ H_\eta\\ H_\zeta\end{bmatrix}. \tag{54}$$

Complementary Kinetic Energy. Combining Eqs. (1) and (53) gives the complementary kinetic energy

$$T^* = \frac{1}{2}\,(A(\dot\xi - \dot\zeta\sin\eta)^2 + B(\dot\eta\cos\xi + \dot\zeta\sin\xi\cos\eta)^2 + C(-\dot\eta\sin\xi + \dot\zeta\cos\xi\cos\eta)^2). \tag{55}$$

Generalized Momenta. Forming partial derivatives leads to the generalized momenta (5)

$$p_\xi = \frac{\partial T^*}{\partial \dot\xi} = A(\dot\xi - \dot\zeta\sin\eta) \tag{56a}$$

$$p_\eta = \frac{\partial T^*}{\partial \dot\eta} = B(\dot\eta\cos\xi + \dot\zeta\sin\xi\cos\eta)\cos\xi + C(\dot\eta\sin\xi - \dot\zeta\cos\xi\cos\eta)\sin\xi \tag{56b}$$

$$p_\zeta = \frac{\partial T^*}{\partial \dot\zeta} = -A(\dot\xi - \dot\zeta\sin\eta)\sin\eta + B(\dot\eta\cos\xi + \dot\zeta\sin\xi\cos\eta)\sin\xi\cos\eta + C(-\dot\eta\sin\xi + \dot\zeta\cos\xi\cos\eta)\cos\xi\cos\eta. \tag{56c}$$

Downloaded 03 May 2010 to 171.66.16.245. Redistribution subject to ASME license or copyright; see http://www.asme.org/terms/Terms_Use.cfm

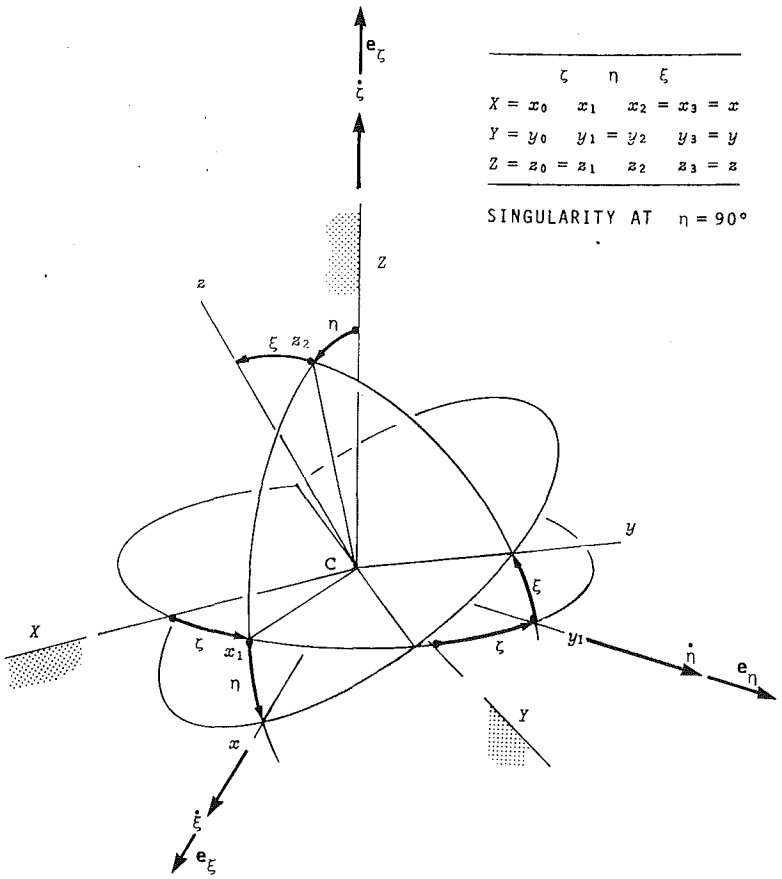


Fig. 6 Cardan angles of the fifth kind

The generalized momenta p_j are related to the angular momentum components H_i (Fig. 7) by

$$\begin{bmatrix} p_\xi \\ p_\eta \\ p_\zeta \end{bmatrix} = \begin{bmatrix} 1 & 0 & -\sin\eta \\ 0 & 1 & 0 \\ -\sin\eta & 0 & 1 \end{bmatrix} \begin{bmatrix} H_\xi \\ H_\eta \\ H_\zeta \end{bmatrix}. \tag{57}$$

The inverse relationship is

$$\begin{bmatrix} H_\xi \\ H_\eta \\ H_\zeta \end{bmatrix} = \begin{bmatrix} \dfrac{1}{\cos^2\eta} & 0 & \dfrac{\sin\eta}{\cos^2\eta} \\ 0 & 1 & 0 \\ \dfrac{\sin\eta}{\cos^2\eta} & 0 & \dfrac{1}{\cos^2\eta} \end{bmatrix} \begin{bmatrix} p_\xi \\ p_\eta \\ p_\zeta \end{bmatrix}. \tag{58}$$

Kinetic Energy. The kinetic energy can be obtained by first using the angular momentum components (54) and Eq. (11), resulting in

$$T = \frac{1}{2}\left(\frac{1}{A}\,(H_\xi - H_\zeta \sin\eta)^2 + \frac{1}{B}\,(H_\eta \cos\xi + H_\zeta \sin\xi \cos\eta)^2 + \frac{1}{C}\,(-H_\eta \sin\xi + H_\zeta \cos\xi \cos\eta)^2\right). \tag{59}$$

Note again the similarity of the terms in round brackets of Eqs. (59) and (55). But Eq. (59) is not yet in terms of generalized momenta. To achieve this we call upon Eq. (59), with the help of which we eventually obtain

$$T = \frac{1}{2}\left[\left(\frac{1}{A} + \left(\frac{\sin^2\xi}{B} + \frac{\cos^2\xi}{C}\right)\tan^2\eta\right)p_\xi^2 + \left(\frac{\cos^2\xi}{B} + \frac{\sin^2\xi}{C}\right)p_\eta^2 + \frac{1}{\cos^2\eta}\left(\frac{\sin^2\xi}{B} + \frac{\cos^2\xi}{C}\right)p_\zeta^2 + 2\sin\xi\cos\xi\tan\eta\left(\frac{1}{B} - \frac{1}{C}\right)p_\xi p_\eta + \frac{2\sin\xi\cos\xi}{\cos\eta} + \left(\frac{1}{B} - \frac{1}{C}\right)p_\eta p_\zeta + 2\frac{\tan\eta}{\cos\eta}\left(\frac{\sin^2\xi}{B} + \frac{\cos^2\xi}{C}\right)p_\xi p_\zeta\right]. \tag{60}$$

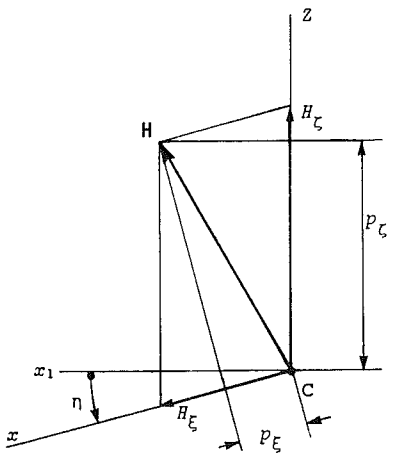


Fig. 7 Angular momentum components and generalized momenta for Cardan angles of the fifth kind (when $H_\eta = 0$)

Generalized Velocities. By partial differentiation we obtain the generalized velocities (4).

Downloaded 03 May 2010 to 171.66.16.245. Redistribution subject to ASME license or copyright; see http://www.asme.org/terms/Terms_Use.cfm

$$\dot{\xi} = \frac{\partial T}{\partial p_\xi} = \left[\frac{1}{A} + \left(\frac{\sin^2\xi}{B} + \frac{\cos^2\xi}{C}\right)\tan^2\eta\right] p_\xi$$

$$+ \left(\frac{1}{B} - \frac{1}{C}\right)\sin\xi\,\cos\xi\,\tan\eta\, p_\eta + \left(\frac{\sin^2\xi}{B} + \frac{\cos^2\xi}{C}\right)\frac{\tan\eta}{\cos\eta}\, p_\zeta \quad (61a)$$

$$\dot{\eta} = \frac{\partial T}{\partial p_\eta} = \left(\frac{1}{B} - \frac{1}{C}\right)\sin\xi\,\cos\xi\,\tan\eta\, p_\xi + \left(\frac{\cos^2\xi}{B} + \frac{\sin^2\xi}{C}\right) p_\eta$$

$$+ \left(\frac{1}{B} - \frac{1}{C}\right)\frac{\sin\xi\,\cos\xi}{\cos\eta}\, p_\zeta \quad (61b)$$

$$\dot{\zeta} = \frac{\partial T}{\partial p_\zeta} = \left(\frac{\sin^2\xi}{B} + \frac{\cos^2\xi}{C}\right)\frac{\tan\eta}{\cos\eta}\, p_\xi + \left(\frac{1}{B} - \frac{1}{C}\right)\frac{\sin\xi\,\cos\xi}{\cos\eta}\, p_\eta$$

$$+ \left(\frac{\sin^2\xi}{B} + \frac{\cos^2\xi}{C}\right)\frac{1}{\cos^2\eta}\, p_\zeta \quad (61c)$$

The Lagrange equations are valid in the form given by Eqs. (47), and D'Alembert's principle (30) can also readily be expressed in terms of Cardan angles of the fifth kind. Equations for Cardan angles of the fourth and sixth kinds (Rimrott, 1988) can be obtained by appropriate cyclic interchanges.

Conclusions

For a proper analytical mechanics treatment of gyrodynamic problems, generalized coordinates are essential. Depending on circumstances, either Euler angles or Cardan angles are suitable. In the present paper the fundamental equations for generalized momenta and generalized velocities are given. For their derivation, the concepts of kinetic energy and complementary kinetic energy have been employed.

References

Crandall, S., 1957, "Complementary Extremum Principles for Dynamics," *Proceedings, Ninth International Congress of Applied Mechanics*, Vol. 5, pp. 80–87.

Greenwood, Donald T., 1988, *Principles of Dynamics*, 2nd ed., Prentice-Hall, Englewood Cliffs, N.J.

Magnus, K., 1971, *Kreisel*, Springer-Verlag, Berlin.

Rimrott, F. P. J., 1988, *Introductory Attitude Dynamics*, Springer-Verlag, New York.

Tabarrok, B., 1981, "On the Principle of Least Action and its Complementary Form," *Solid Mechanics Archives*, Vol. 7, pp.309–329.

Downloaded 03 May 2010 to 171.66.16.245. Redistribution subject to ASME license or copyright; see http://www.asme.org/terms/Terms_Use.cfm

M. Ozturk

F. Erdogan
Fellow ASME.

Department of Mechanical Engineering
and Mechanics,
Lehigh University,
Bethlehem, PA 18015

The Axisymmetric Crack Problem in a Nonhomogeneous Medium

In this paper, the axisymmetric crack problem for a nonhomogeneous medium is considered. It is assumed that the shear modulus is a function of z approximated by $\mu = \mu_0 e^{\alpha z}$. This is a simple simulation of materials and interfacial zones with intentionally or naturally graded properties. The problem is a mixed-mode problem and is formualated in terms of a pair of singular integral equations. With fracture mechanics applications in mind, the main results given are the stress intensity factors as a function of the nonhomogeneity parameter α for various loading conditions. Also given are some sample results showing the crack opening displacements.

Introduction

In solid mechanics many of the engineering materials, such as composites and large variety of bonded materials and structural components, are generally modeled as nonhomogeneous continua. The thermomechanical parameters of these materials are usually assumed to be discontinuous functions, very often piece-wise constants, in space variables. However, there are some important applications in which the spatial variation in material properties is continuous. As examples for such materials we may mention the following: (a) geophysical materials with naturally graded compositions such as shale-sandstone. In studying, for example, hydraulic fracturing of such a medium it would be necessary to take into account the mechanical property gradient of the material; (b) interfacial regions with graded properties in diffusion bonded materials, in plasma spray coating, and in ion plating (Batakis and Vogan, 1985, Houck, 1987); (c) material nonhomogeneity resulting from temperature gradients in the solid in which thermomechanical constants of the medium are significantly dependent on temperature; and finally, (d) the tailored materials with predetermined continuously varying volume fractions.

Some of the important applications in the last category of materials may be found in ceramic coating of metal substrates and in metal-ceramic composites with graded properties. It is known that certain strength-related properties of ceramic coatings can be improved by layering the interfacial zone going from metal-rich to ceramic-rich compositions. For example, in joining tungsten to zirconia by introducing four intermediate layers that contain 80/20, 60/40, 40/60, and 20/80 percent W/ZrO_2, respectively, it has been shown that the peak value of the residual stress is reduced by approximately sixfold compared to that resulting from direct tungsten/zirconia bonding (Hirano et al., 1988; Hirano and Yamada, 1988).

The fatigue and fracture characterization of materials and the related analysis require the solution of certain standard crack problems. With the exception of the problem of "torsion" of an infinite medium containing a penny-shaped crack (Kassir, 1972), the existing solutions of the crack problems in nonhomogeneous materials with continuously varying properties have been obtained under the assumption of plane strain, generalized plane stress, or antiplane shear loading (see, for example, Dhalival and Sing, 1978; Gerasoulis and Srivastav, 1980; Delale and Erdogan, 1983, 1988a, 1988b; Erdogan, 1985; Konda and Erdogan, 1989). One of the practical problems in this area is that of an internal circular crack in a nonhomogeneous solid subjected to "tension." The problem is always a mixed-mode problem. In this paper we consider the simplest of these problems, namely that of an axisymmetric crack in an infinite solid with elastic properties varying in the axial direction only (Fig. 1). The corresponding plane-strain mixed-

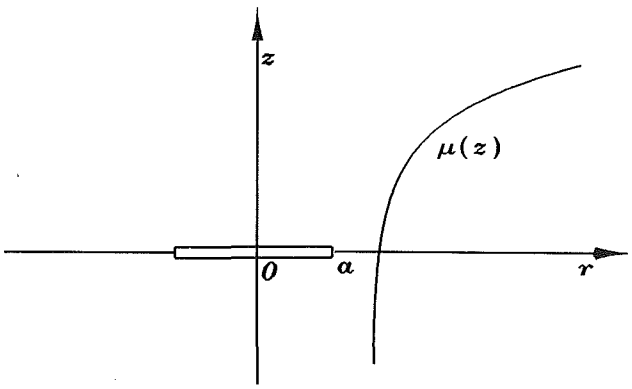


Fig. 1 Crack geometry and notation

Contributed by the Applied Mechanics Division of THE AMERICAN SOCIETY OF MECHANICAL ENGINEERS for presentation at the First Joint ASCE-EMD, ASME-AMD, SES Meeting, Charlottesville, VA, June 6–9, 1993.

Discussion on this paper should be addressed to the Technical Editor, Professor Lewis T. Wheeler, Department of Mechanical Engineering, University of Houston, Houston, TX 77204-4792, and will be accepted until four months after final publication of the paper itself in the ASME JOURNAL OF APPLIED MECHANICS.

Manuscript received by the ASME Applied Mechanics Division, Jan. 23, 1990; final revision, Mar. 19, 1992. Associate Technical Editor: L. T. Wheeler.

Paper No. 93-APM-4.

Copyright © 1993 by ASME
Downloaded 03 May 2010 to 171.66.16.245. Redistribution subject to ASME license or copyright; see http://www.asme.org/terms/Terms_Use.cfm

mode problem was recently considered by Konda and Erdogan (1992).

Formulation of the Problem

In the crack problem shown in Fig. 1, for a large elastic solid it is assumed that the external loads as well as the geometry are axisymmetric. Therefore, one may easily separate the torsion component of the problem in which $u_\theta = v(r, z)$, $\sigma_{\theta r}$, and $\sigma_{\theta z}$ are the only nonzero displacement and stress components. Similarly, by solving the remaining problem under the given external loads in the absence of a crack and by using superposition, the problem may be reduced to that of a nonhomogeneous solid containing a penny-shaped crack in which

$$\sigma_{zz}(r, 0)=p_1(r),\ \sigma_{rz}(r, 0)=p_2(r),\ 0\le r<a \quad (1a, b)$$

are the only external loads. Furthermore, if the crack radius a is small in comparison with the nearest distance from the crack to the boundary of the solid, then in the perturbation problem the medium can be assumed to be infinite. Needless to say, from the viewpoint of fracture mechanics, the perturbation problem would contain all the relevant information such as the stress intensity factors and the crack-opening displacements. If we now assume that locally the elastic properties of the medium may be approximated by

$$\mu(y)=\mu_0 e^{\alpha z},\ \nu=\text{constant}, \quad (2)$$

for the axisymmetric problem under consideration by using the kinematic relations

$$\epsilon_{rr}=\frac{\partial u}{\partial r},\ \epsilon_{\theta\theta}=\frac{u}{r},\ \epsilon_{zz}=\frac{\partial w}{\partial z},\ 2\epsilon_{rz}=\frac{\partial u}{\partial z}+\frac{\partial w}{\partial r}, \quad (3)$$

and the Hooke's law

$$\sigma_{ij}=2\mu\epsilon_{ij}+\lambda\epsilon_{kk}\delta_{ij},\ (i, j=r, \theta, z), \quad (4)$$

the equilibrium equations

$$\frac{\partial\sigma_{rr}}{\partial r}+\frac{\partial\sigma_{rz}}{\partial z}+\frac{1}{r}(\sigma_{rr}-\sigma_{\theta\theta})=0$$

$$\frac{\partial\sigma_{rz}}{\partial r}+\frac{\partial\sigma_{zz}}{\partial z}+\frac{1}{r}\sigma_{rz}=0 \quad (5a, 5b)$$

may be expressed as follows:

$$(\kappa+1)\left\{\frac{\partial^2 u}{\partial r^2}+\frac{\partial u}{r\partial r}-\frac{1}{r^2}u+\frac{\partial^2 w}{\partial r\partial z}\right\}+(\kappa-1)\alpha\left(\frac{\partial u}{\partial z}+\frac{\partial w}{\partial r}\right)+(\kappa-1)\left\{\frac{\partial^2 u}{\partial z^2}-\frac{\partial^2 w}{\partial r\partial z}\right\}=0,$$

$$(\kappa+1)\left\{\frac{\partial^2 u}{\partial r\partial z}+\frac{\partial u}{r\partial r}-\frac{\partial^2 w}{\partial z^2}\right\}-(\kappa-1)\left\{\frac{\partial^2 u}{\partial r\partial z}-\frac{\partial^2 w}{\partial r^2}\right\}-\frac{(\kappa-1)}{r}\left(\frac{\partial u}{\partial z}-\frac{\partial w}{\partial r}\right)+(3-\kappa)\alpha\left(\frac{\partial u}{\partial r}+\frac{u}{r}\right)+(\kappa+1)\alpha\frac{\partial w}{\partial z}=0 \quad (6a, 6b)$$

where u and w are, respectively, the r and z components of the displacement vector, μ is the shear modulus, ν the Poisson's ratio, $\lambda/\mu = 2\nu/(1-2\nu)$, and $\kappa = 3-4\nu$. In addition to the boundary conditions given by (1) and the regularity conditions at infinity (requiring that u and w must vanish as $r^2+z^2\to\infty$), the crack problem must be solved under the following conditions:

$$\sigma_{zz}(r, +0)=\sigma_{zz}(r, -0),\ \sigma_{rz}(r, +0)=\sigma_{rz}(r, -0),\ 0\le r<\infty, \quad (7a, 7b)$$

$$u(r, +0)=u(r, -0),\ w(r, +0)=w(r, -0),\ a<r<\infty. \quad (8a, 8b)$$

We now assume the solution of (6) in the form

$$u(r,z)=\int_0^\infty F(z,\rho)\rho J_1(r\rho)d\rho,$$

$$w(r,z)=\int_0^\infty G(z,\rho)\rho J_0(r\rho)d\rho, \quad (9a, 9b)$$

where J_0 and J_1 are the Bessel functions of the first kind. Substituting from (9) into (6), defining $D = d/dz$, and inverting the related Hankel transforms we find

$$\{(\kappa-1)D^2+\alpha(\kappa-1)D-(\kappa+1)\rho^2\}F-\{2\rho D+\alpha(\kappa-1)\}G=0,$$

$$\{2\rho D+\alpha(3-\kappa)\rho\}F+\{(\kappa+1)D^2+\alpha(\kappa+1)D-(\kappa-1)\rho^2\}G=0, \quad (10a, 10b)$$

where the following relationships have been used:

$$\left(\frac{d^2}{dr^2}+\frac{1}{r}\frac{d}{dr}-\frac{1}{r^2}\right)J_1(r\rho)=-\rho^2 J_1(r\rho),$$

$$\left(\frac{d}{dr}+\frac{1}{r}\right)J_1(r\rho)=\rho J_0(r\rho),$$

$$\frac{d^2}{dr^2}J_0(r\rho)=\frac{\rho}{r}J_1(r\rho)-\rho^2 J_0(r\rho). \quad (11a\text{-}c)$$

The solution of the system of the differential Eqs. (10) is found to be

$$F(z,\rho)=\sum_{k=1}^{4}A_k(\rho)e^{m_k z},$$

$$G(z,\rho)=\sum_{k=1}^{4}a_k(\rho)A_k(\rho)e^{m_k z}, \quad (12a, b)$$

where the functions A_k, $(k = 1, \ldots, 4)$ are arbitrary unknowns, $m_1, \ldots, m_4$ are the roots of the following characteristic equation:

$$m^4+2\alpha m^3+(\alpha^2-2\rho^2)m^2-2\rho^2\alpha m+\frac{3-\kappa}{\kappa+1}\alpha^2\rho^2+\rho^4=0, \quad (13)$$

and the coefficients $a_1, \ldots, a_4$ are given by

$$a_k=-\frac{2\rho m_k+\rho\alpha(3-\kappa)}{(\kappa+1)m_k^2+\alpha(\kappa+1)m_k-(\kappa-1)\rho},\ (k=1, \ldots, 4). \quad (14)$$

The characteristic Eq. (13) may easily be expressed as

$$(m^2+\alpha m-\rho^2)^2+\frac{3-\kappa}{\kappa+1}\alpha^2\rho^2=0 \quad (15)$$

from which it follows that

$$m_1=\overline{m}_3=-\frac{\alpha}{2}+\frac{1}{2}\left\{\alpha^2+\rho^2+i4\sqrt{\frac{3-\kappa}{\kappa+1}}\alpha\rho\right\}^{1/2},$$

$$m_2=\overline{m}_4=-\frac{\alpha}{2}-\frac{1}{2}\left\{\alpha^2+\rho^2+i4\sqrt{\frac{3-\kappa}{\kappa+1}}\alpha\rho\right\}^{1/2}. \quad (16a, b)$$

After solving for $m_1, \ldots, m_4$, the expressions for coefficients a_k given by (14) may be simplified as follows:

$$a_k=-\frac{2m_k\alpha(3-\kappa)}{2\rho+i\alpha\sqrt{(3-\kappa)(1+\kappa)}},\ (k=1,2)$$

$$a_3=\overline{a}_1,\ a_4=\overline{a}_2. \quad (17a\text{-}c)$$

By observing that $\Re(m_1, m_3) > 0$ and $\Re(m_2, m_4) < 0$, to satisfy the regularity conditions at $z = \pm\infty$ in the solution given by (12), we must delete the terms involving A_1 and A_3 for $z > 0$ and A_2 and A_4 for $z < 0$. Thus, the problem may be considered as that of two half-spaces involving two un-

Downloaded 03 May 2010 to 171.66.16.245. Redistribution subject to ASME license or copyright; see http://www.asme.org/terms/Terms_Use.cfm

knowns, A_2 and A_4, for the upper half-space and two, A_1 and A_3, for the lower half. Of these four unknowns, two may be eliminated by using the stress continuity conditions (7). Thus, by eliminating A_1 and A_3, from (12) and (7) it can be shown that

$$F(r,\rho)=\begin{cases}A_2e^{m_2z}+A_4e^{m_4z}, & z>0,\\ (\lambda_1A_2+\lambda_2A_4)e^{m_1z}+(\lambda_3A_2+\lambda_4A_4)e^{m_3z}, & z<0\end{cases} \tag{18}$$

$$G(r,\rho)=\begin{cases}a_2A_2e^{m_2z}+a_4A_4e^{m_4z}, & z>0,\\ a_1(\lambda_1A_2+\lambda_2A_4)e^{m_1z}+a_3(\lambda_3A_2+\lambda_4A_4)e^{m_3z}, & z<0\end{cases} \tag{19}$$

where the expressions for the coefficients $\lambda_1, \ldots, \lambda_4$ are given in the Appendix. The unknowns A_2 and A_4 may now be determined from the mixed boundary conditions (1) and (8).

The Integral Equations

To reduce the mixed boundary conditions (1) and (8) to a system of integral equations we first define the following new unknown functions:

$$g_1(r)=\frac{\partial}{\partial r}\{w(r,+0)-w(r,-0)\},$$

$$g_2(r)=\frac{1}{r}\frac{\partial}{\partial r}\{ru(r,+0)-ru(r,-0)\}. \tag{20a, b}$$

From (9), (18), (19), and (20) it then follows that

$$g_1(r)=\int_0^\infty(-\rho(a_2+G_2)A_2-\rho(a_4+G_4)A_4)\rho J_1(r\rho)d\rho,$$

$$g_2(r)=\int_0^\infty(\rho(1-E_2)A_2+\rho(1-E_4)A_4)\rho J_0(r\rho)d\rho, \tag{21a, b}$$

where the functions E_2, E_4, G_2, and G_4 are defined in the Appendix. Equations (21) determine A_2 and A_4 in terms of g_1 and g_2.

By substituting now from (18) and (19) into (9) and by using (3) and (4), the boundary conditions (1) may be expressed as

$$\int_0^\infty F_1(\rho)\rho J_0(r\rho)d\rho=\frac{\kappa-1}{\mu_0}p_1(r),\ 0\le r<a,$$

$$\int_0^\infty F_2(\rho)\rho J_1(r\rho)d\rho=\frac{1}{\mu_0}p_2(r),\ 0\le r<a, \tag{22a, b}$$

$$F_1(\rho)=n_2A_2+n_4A_4,$$

$$F_2(\rho)=v_2A_2+v_4A_4, \tag{23a, b}$$

where the functions n_2, n_4, v_2, and v_4 are again defined in the Appendix. Inverting the transforms given by (21) and from (8) and (20) observing that $g_k(r) = 0$ for $r > a$, $(k = 1, 2)$, the functions F_1 and F_2 are found to be

$$F_1(\rho)=\int_0^a(-d_{11}J_1(\rho s)g_1(s)+d_{12}J_0(\rho s)g_2(s))sds,$$

$$F_2(\rho)=\int_0^a(-d_{21}J_1(\rho s)g_1(s)+d_{22}J_0(\rho s)g_2(s))sds, \tag{24a, b}$$

where the functions $d_{ij}(\rho)$, $(i, j = 1, 2)$ are also defined in the Appendix.

In order to avoid working with divergent kernels and to simplify the analysis regarding the asymptotic behavior of the kernels, first both sides of (22) are integrated in r. By using (24) it may then be shown that

$$\int_0^\infty J_1(r\rho)d\rho\int_0^a(-d_{11}J_1(\rho s)g_1(s)+d_{12}J_0(\rho s)g_2(s))sds=\frac{\kappa-1}{\mu_0 r}\left(\int^r sp_1(s)ds+C_1\right)$$

$$-\int_0^\infty J_0(r\rho)d\rho\int_0^a(-d_{21}J_1(\rho s)g_1(s)+d_{22}J_0(\rho s)g_2(s))sds=\frac{1}{\mu_0}\left(\int^r p_2(s)ds+C_2\right), \tag{25a, b}$$

where C_1 and C_2 are arbitrary constants. Equations (25) are essentially the integral equations that determine g_1 and g_2. For $\rho \to \infty$ it can be shown that the functions $d_{ij}(\rho)$ have the following asymptotic behavior:

$$d_{11}(\rho)=-2\frac{\kappa-1}{\kappa+1}+O(\rho^{-2}),\ d_{12}(\rho)=\frac{\kappa-1}{\kappa+1}\frac{\alpha}{\rho}+O(\rho^{-3}),$$

$$d_{21}(\rho)=\frac{1}{\kappa+1}\frac{\alpha}{\rho}+O(\rho^{-3}),\ d_{22}(\rho)=-\frac{2}{\kappa+1}+O(\rho^{-2}). \tag{26a–d}$$

Thus, from (25) and (26) we find

$$\int_0^a\{(H_{11}(r,s)+h_{11}(r,s))g_1(s)+h_{12}(r,s)g_2(s)\}sds=\frac{\kappa+1}{2\mu_0 r}\left(\int^r sp_1(s)ds+C_1\right),$$

$$\int_0^a\{h_{21}(r,s)g_1(s)+(H_{22}(r,s)+h_{22}(r,s))g_2(s)\}sds=\frac{\kappa+1}{2\mu_0}\left(\int^r p_2(s)ds+C_2\right), \tag{27a, b}$$

where

$$H_{11}(r,s)=\int_0^\infty J_1(r\rho)J_1(s\rho)d\rho=\frac{2}{\pi}\begin{cases}\frac{1}{s}[K(s/r)-E(s/r)], & s<r,\\ \frac{1}{r}[K(r/s)-E(r/s)], & s>r,\end{cases} \tag{28}$$

$$H_{22}(r,s)=\int_0^\infty J_0(r\rho)J_0(s\rho)d\rho=\frac{2}{\pi}\begin{cases}\frac{1}{r}K(s/r), & s<r,\\ \frac{1}{s}K(r/s), & s>r,\end{cases} \tag{29}$$

$$h_{11}(r,s)=\int_0^\infty D_{11}(\rho)J_1(r\rho)J_1(s\rho)d\rho,$$

$$h_{12}(r,s)=-\int_0^\infty D_{12}(\rho)J_0(r\rho)J_1(s\rho)d\rho,$$

$$h_{21}(r,s)=-\int_0^\infty D_{21}(\rho)J_1(r\rho)J_0(s\rho)d\rho,$$

$$h_{22}(r,s)=\int_0^\infty D_{22}(\rho)J_0(r\rho)J_0(s\rho)d\rho, \tag{30a–d}$$

$$D_{11}(\rho)=\left(\frac{d_{11}(\rho)}{d_{11}(\infty)}-1\right),$$

$$D_{12}(\rho)=\frac{d_{12}(\rho)}{d_{11}(\infty)},$$

Downloaded 03 May 2010 to 171.66.16.245. Redistribution subject to ASME license or copyright; see http://www.asme.org/terms/Terms_Use.cfm

$$D_{21}(\rho)=\frac{d_{21}(\rho)}{d_{22}(\infty)},$$

$$D_{22}(\rho)=\left(\frac{d_{22}(\rho)}{d_{22}(\infty)}-1\right),$$

$$d_{11}(\infty)=-2\,\frac{\kappa-1}{\kappa+1},\ d_{22}(\infty)=-\frac{2}{\kappa+1}, \qquad (31a\text{-}f)$$

where K and E are the complete elliptic integrals of the first and second kind, respectively. By differentiating, (27) can further be reduced to the following standard form:

$$\frac{1}{\pi}\int_0^a\left(\frac{1}{s-r}+\frac{1}{s+r}\right)g_1(s)ds+\frac{1}{\pi}\int_0^a\sum_{j=1}^{2}k_{1j}(r,s)g_j(s)ds=\frac{\kappa+1}{2\mu_0}p_1(r),$$

$$\frac{1}{\pi}\int_0^a\left(\frac{1}{s-r}-\frac{1}{s+r}\right)g_2(s)ds+\frac{1}{\pi}\int_0^a\sum_{j=1}^{2}k_{2j}(r,s)g_j(s)ds=\frac{\kappa+1}{2\mu_0}p_2(r), \qquad (32a,\ b)$$

where the Fredholm kernels k_{ij} are given by

$$k_{11}(r,s)=\frac{M_1(r,s)-1}{s-r}+\frac{M_1(r,s)-1}{s+r}+\pi s\int_0^\infty D_{11}(\rho)\rho J_0(r\rho)J_1(s\rho)d\rho,$$

$$k_{12}(r,s)=-\pi s\int_0^\infty D_{12}(\rho)\rho J_0(r\rho)J_0(s\rho)d\rho,$$

$$k_{21}(r,s)=\pi s\int_0^\infty D_{21}(\rho)\rho J_1(r\rho)J_1(s\rho)d\rho,$$

$$k_{22}(r,s)=\frac{M_2(r,s)-1}{s-r}-\frac{M_2(r,s)-1}{s+r}-\pi s\int_0^\infty D_{22}(\rho)\rho J_1(r\rho)J_0(s\rho)d\rho, \qquad (33a\text{-}d)$$

$$M_1(r,s)=\begin{cases}\dfrac{r}{s}E\left(\dfrac{s}{r}\right)+\dfrac{s^2-r^2}{rs}K\left(\dfrac{s}{r}\right), & s<r,\\[2ex] E\left(\dfrac{r}{s}\right), & s>r,\end{cases} \qquad (34)$$

$$M_2(r,s)=\begin{cases}\dfrac{s}{r}E\left(\dfrac{s}{r}\right), & s<r,\\[2ex] \dfrac{s^2}{r^2}E\left(\dfrac{r}{s}\right)-\dfrac{s^2-r^2}{r^2}K\left(\dfrac{r}{s}\right), & s>r.\end{cases} \qquad (35)$$

Note that the dominant kernels of the system of integral Eqs. (32) are of the generalized Cauchy type (Erdogan, 1978). Thus, expressing the solution by

$$g_k(s)=\frac{h_k(s)}{(a-s)^{\gamma_k}s^{\beta_k}},\ k=1,2, \qquad (36)$$

and using the function-theoretic method described, for example, by Erdogan (1978), the characteristic equations giving γ_k and β_k may be obtained as follows:

$$\cot\pi\gamma_k=0,\ k=1,2, \qquad (37)$$

$$\cos\pi\beta_1=-1,\ \cos\pi\beta_2=1. \qquad (38a,\ b)$$

In (36), h_1 and h_2 are unknown bounded functions which are nonzero at the end points $s = a$ and $s = 0$. Equation (37) gives the expected results $\gamma_1 = 1/2$, $\gamma_2 = 1/2$. On the other hand, considering the physical constraints $g_1(0) = 0$ and $u(0, +0) = u(0, -0) = 0$, it may be seen that the admissible roots of (38) are $\beta_1 = -1$, $\beta_2 = 0$ giving

$$g_1(s)=\frac{s}{(a-s)^{1/2}}h_1(s),\quad g_2(s)=\frac{1}{(a-s)^{1/2}}h_2(s). \qquad (39)$$

From (20) and (39) it can be shown that for small values of r/a the crack surface displacements would have the following asymptotic form:

$$w^+-w^-\simeq w_0+\frac{h_1(0)}{2\sqrt{a}}r^2,\ u^+-u^-\simeq\frac{h_2(0)}{2\sqrt{a}}r,\ r\ll a. \qquad (40)$$

Also, from the physical conditions $ru^+ - ru^- = 0$ for $r = 0$ and $r = a$, it is clear that the unknown function g_2 must satisfy

$$\int_0^a rg_2(r)dr=0. \qquad (41)$$

In solving equations such as (32), the accuracy is very highly dependent on the correct evaluation of the kernels k_{ij}, $(i, j = 1, 2)$. For this it is necessary that the asymptotic behavior of k_{ij} for $s \to r$ be examined and the weak singularities, if any, be separated. From (26b, c), (31e, f), and

$$K(\lambda)\to\log(4/\sqrt{1-\lambda^2})\ \text{for}\ \lambda\to 1, \qquad (42)$$

it can indeed be shown that for $s \to r$ the kernels k_{ij} have logarithmic singularities that may be extracted as

$$\frac{M_1(r,s)-1}{s-r}=-\frac{1}{2r}\log|s-r|-\frac{1}{r}(1-\log\sqrt{8r})+m_{11}(r,s),$$

$$\frac{M_2(r,s)-1}{s-r}=\frac{1}{2r}\log|s-r|+\frac{1}{r}(2-\log\sqrt{8r})+m_{22}(r,s),$$

$$k_{12}(r,s)=-\frac{\pi}{2}\alpha sH_{22}(r,s)-\pi s\int_0^\infty\left(D_{12}(\rho)\rho+\frac{\alpha}{2}\right)J_0(r\rho)J_0(s\rho)d\rho,$$

$$k_{21}(r,s)=\frac{\pi}{2}\alpha sH_{11}(r,s)+\pi s\int_0^\infty\left(D_{21}(\rho)\rho+\frac{\alpha}{2}\right)J_1(r\rho)J_1(s\rho)d\rho, \qquad (43a\text{-}d)$$

where H_{11} and H_{22} are given by (28) and (29) and, by virtue of (42), are also seen to have logarithmic singularities and m_{11} and m_{22} are known functions which are bounded in the closed interval $0 \le (r, s) \le a$.

The Solution

The integral equations may be solved by extending the interval and the definition of the unknown functions and the kernels into $(-a, 0)$ and by using the properties of the Chebyshev polynomials T_n and U_n (Erdogan, 1978). These equations may also be solved by observing from (39) that the orthogonal polynomials corresponding to the weight functions $w_1(y) = (1 + y)/\sqrt{1-y}$ and $w_2(y) = 1/\sqrt{1-y}$, $y = 2s/a - 1$, are $P_n^{(-1/2,1)}(y)$ and $P_n^{(-1/2,0)}(y)$, respectively, and by expressing the unknown functions g_1 and g_2 as follows:

$$g_1(s)=\phi_1(y)=\frac{1+y}{\sqrt{1-y}}\sum_0^\infty A_{1n}P_n^{(-1/2,1)}(y)$$

$$g_2(s)=\phi_2(y)=\frac{1}{\sqrt{1-y}}\sum_0^\infty A_{2n}P_n^{(-1/2,0)}(y). \qquad (44a,\ b)$$

Downloaded 03 May 2010 to 171.66.16.245. Redistribution subject to ASME license or copyright; see http://www.asme.org/terms/Terms_Use.cfm

The integral equations may then be regularized by using the properties of Jacobi polynomials and may be solved by truncating the series in (44) and using an appropriate collocation technique (Mahajan, 1992). However, a somewhat more efficient technique may also be developed by defining

$$g_1(as')=f_1(s')\left(\frac{s'}{1-s'}\right)^{1/2},\quad g_2(as')=\frac{f_2(s')}{\sqrt{s'(1-s')}},$$

$$s'=s/a,\quad (45a,\ b)$$

and by requiring that $f_1(0)=0$, $f_2(0)=0$. The orthogonal polynomials related to the weight functions in (45) are

$$P_n^{(-1/2,1/2)}(t)=\frac{\Gamma\left(n+\frac{1}{2}\right)}{n!\sqrt{\pi}}\frac{\cos\left(n+\frac{1}{2}\right)\theta}{\cos\frac{\theta}{2}}=\frac{\Gamma\left(n+\frac{1}{2}\right)}{n!\sqrt{\pi}}t_n(t),$$

$$P_n^{(-1/2,-1/2)}(t)=\frac{\Gamma\left(n+\frac{1}{2}\right)}{n!\sqrt{\pi}}\cos n\theta$$

$$=\frac{\Gamma\left(n+\frac{1}{2}\right)}{n!\sqrt{\pi}}T_n(t),\quad (46a,\ b)$$

$$t=2s'-1=\cos\theta,\ (1+t)t_n(t)=T_n(t)+T_{n+1}(t),\ -1<t<1. \quad (47)$$

We then express g_1 and g_2 in terms of the following infinite series:

$$\frac{2\mu_0}{\kappa+1}g_1(as')=\sqrt{\frac{s'}{1-s'}}\sum_0^\infty B_{1n}t_n(2s'-1),$$

$$\frac{2\mu_0}{\kappa+1}g_2(as')=\frac{1}{\sqrt{s'(1-s')}}\sum_0^\infty B_{2n}T_n(2s'-1).\quad (48a,\ b)$$

By substituting from (48) into (32) and by observing that

$$\frac{1}{\pi}\int_0^1\sqrt{\frac{s'}{1-s'}}\frac{t_n(2s'-1)ds'}{s'-r'}=\frac{1}{\pi}\int_{-1}^1\frac{T_n(t)+T_{n+1}(t)}{(t-x)\sqrt{1-t^2}}dt$$

$$\frac{1}{\pi}\int_0^1\sqrt{\frac{s'}{1-s'}}\frac{t_n(2s'-1)ds'}{s'-r'}=\begin{cases}U_{n-1}(x)+U_n(x),\ |x|<1,\\ G_n(x)+G_{n+1}(x),\ x>1,\end{cases}\quad (49)$$

$$r'=r/a,\ x=2r'-1,\ U_n(x)=\frac{\sin(n+1)\theta}{\sin\theta},$$

$$|x|<1,\ \cos\theta=x,\ n=0,1,\ldots,\quad (50)$$

$$G_n(x)=-\frac{(x-\sqrt{x^2-1})^n}{\sqrt{x^2-1}},\ (x>1),\ n=0,1,\ldots,\quad (51)$$

the integral Eqs. (32) may be reduced to the following system of equations:

$$\sum_0^\infty\{B_{1n}[U_{n-1}(x)+U_n(x)+K_{11}(x)]+B_{2n}K_{12n}(x)\}=P_1(x),$$

$$\sum_0^\infty\{B_{1n}K_{21n}(x)+B_{2n}[2U_{n-1}(x)+K_{22n}(x)]\}=P_2(x),$$

$$(-1<x<1)\quad (52a,\ b)$$

where

$$P_j(x)=p_j(r),\ j=1,2,\ x=\frac{2r}{a}-1=2r'-1,$$

$$K_{i1n}(x)=\frac{1}{\pi}\int_0^\infty k_{i1}(ar',\ as')\sqrt{\frac{s'}{1-s'}}\,t_n(2s'-1)ds',\ (i=1,2),$$

$$K_{i2n}(x)=\frac{1}{\pi}\int_0^\infty k_{i2}(ar',\ as')\frac{T_n(2s'-1)}{\sqrt{s'(1-s')}}ds',\ (i=1,2),$$

$$(53a\text{–}c)$$

Also, by substituting from (48b) into (41) and by using the orthogonality conditions

$$\frac{1}{\pi}\int_{-1}^1\frac{T_i(t)T_j(t)}{\sqrt{1-t^2}}dt=\begin{cases}1,\ i=j=0,\\ 1/2,\ i=j>0,\\ 0,\ i\neq j,\end{cases}\quad (54)$$

it may easily be shown that

$$B_{20}+\frac{1}{2}B_{21}=0.\quad (55)$$

Equations (52) and (55) are solved by truncating the series and by using a simple collocation technique. Very fast converging results are obtained if the collocation points x_j are selected as follows:

$$T_N(x_j)=0,\ x_j=\cos\theta_j,\ \theta_j=\frac{\pi}{2N}(2j-1).\quad (56)$$

From the derivation of the integral Eqs. (32) we observe that the right-hand side of (32) represents σ_{zz} $(r, 0)$ and $\sigma_{rz}(r, 0)$ for $a<r<\infty$ as well as for $0\le r<a$. Thus, defining the modes I and II stress intensity factors by

$$k_1=\lim_{r\to a}\sqrt{2(r-a)}\ \sigma_{zz}(r,0),$$

$$k_2=\lim_{r\to a}\sqrt{2(r-a)}\ \sigma_{rz}(r,0),\quad (57a,\ b)$$

and by using (51), from (47), (48) and (32) it can be shown that

$$k_1=-\sqrt{2a}\sum_0^\infty B_{1n},\ k_2=-\sqrt{2a}\sum_0^\infty B_{2n}.\quad (58)$$

For a homogeneous medium (i.e., for $\alpha=0$ in (2)) modes I and II crack problems are uncoupled and the stress intensity factors are given by

$$k_1=-\frac{2}{\pi\sqrt{a}}\int_0^a\frac{rp_1(r)}{\sqrt{a^2-r^2}}dr,\quad k_2=-\frac{2}{\pi a^{3/2}}\int_0^a\frac{r^2p_2(r)}{\sqrt{a^2-r^2}}dr.$$

$$(59)$$

The Results

The main results of this study are the stress intensity factors calculated for various loading conditions as functions of the nonhomogeneity constant α by defining the shear modulus in $\mu(z)=\mu_0\exp(\alpha z)$. Table 1 shows the six different loading conditions used in the calculations. The table also shows the corresponding modes I and II stress intensity factors in a homogeneous medium containing a penny-shaped crack of radius a obtained from (59). For the nonhomogeneous medium, the normalized stress intensity factors calculated for $\nu=0.3$ are shown in Table 2. As in the plane-strain problem, for all loading conditions both k_1 and k_2 increase with increasing $a\alpha$, the dimensionless nonhomogeneity constant. Comparing the results given in Table 2 with the corresponding plane-strain results obtained by Konda and Erdogan (1992), it may be seen

Downloaded 03 May 2010 to 171.66.16.245. Redistribution subject to ASME license or copyright; see http://www.asme.org/terms/Terms_Use.cfm

Table 1 Loading conditions used and the corresponding stress intensity factors for $\alpha = 0$

$p_1(r)$	$-p_0$	$-p_1\frac{r}{a}$	$-p_2(\frac{r}{a})^2$	0	0	0
$p_2(r)$	0	0	0	$-q_0$	$-q_1(\frac{r}{a})$	$-q_2(\frac{r}{a})^2$
k_1	$\frac{2}{\pi}p_0\sqrt{a}$	$\frac{1}{2}p_1\sqrt{a}$	$\frac{4}{3\pi}p_2\sqrt{a}$	0	0	0
k_2	0	0	0	$\frac{1}{2}q_0\sqrt{a}$	$\frac{4}{3\pi}q_1\sqrt{a}$	$\frac{3}{8}q_2\sqrt{a}$

Table 2 The variation of stress intensity factors with α for various loading conditions shown in Table 1, $\nu = 0.3$

$\sigma_{zz}(r,0) = p_1(r),\ \sigma_{rz}(r,0) = 0$						
$a\alpha$	$\frac{k_1}{p_0\sqrt{a}}$	$\frac{k_2}{p_0\sqrt{a}}$	$\frac{k_1}{p_1\sqrt{a}}$	$\frac{k_2}{p_1\sqrt{a}}$	$\frac{k_1}{p_2\sqrt{a}}$	$\frac{k_2}{p_2\sqrt{a}}$
0.0	0.6366	0.0	0.5	0.0	0.4244	0.0
0.1	0.6378	0.0106	0.5008	0.0063	0.4249	0.0042
0.2	0.6413	0.0212	0.5028	0.0125	0.4263	0.0085
0.3	0.6465	0.0319	0.5058	0.0188	0.4284	0.0128
0.4	0.6580	0.0425	0.5097	0.0250	0.4309	0.0169
0.5	0.6608	0.0532	0.5143	0.0313	0.4341	0.0213
0.6	0.6695	0.0639	0.5193	0.0376	0.4376	0.0255
0.75	0.6841	0.0801	0.5279	0.0471	0.4434	0.0319
1.0	0.7115	0.1073	0.5441	0.0631	0.4544	0.0428
1.5	0.7741	0.1628	0.5811	0.0955	0.4795	0.0647
2.0	0.8435	0.2202	0.6219	0.1289	0.5073	0.0872
3.0	0.9943	0.3413	0.7108	0.1988	0.5676	0.1339
4.0	1.1558	0.4714	0.8057	0.2732	0.6319	0.1833
5.0	1.3256	0.6105	0.9053	0.3521	0.6994	0.2355
$\sigma_{zz}(r,0) = 0,\ \sigma_{rz}(r,0) = p_2(r)$						
$a\alpha$	$\frac{k_1}{q_0\sqrt{a}}$	$\frac{k_2}{q_0\sqrt{a}}$	$\frac{k_1}{q_1\sqrt{a}}$	$\frac{k_2}{q_1\sqrt{a}}$	$\frac{k_1}{q_2\sqrt{a}}$	$\frac{k_2}{q_2\sqrt{a}}$
0.0	0.0	0.5	0.0	0.4244	0.0	0.3750
0.1	0.000	0.5001	0.000	0.4244	0.000	0.3750
0.2	0.000	0.5003	0.000	0.4246	0.000	0.3751
0.3	0.000	0.5006	0.000	0.4248	0.000	0.3753
0.4	0.000	0.5012	0.000	0.4252	0.000	0.3756
0.5	0.000	0.5018	0.000	0.4256	0.000	0.3759
0.6	0.000	0.5026	0.000	0.4262	0.000	0.3763
0.75	0.000	0.5039	0.000	0.4271	0.000	0.3770
1.0	0.000	0.5068	0.000	0.4290	0.000	0.3784
1.5	0.000	0.5142	0.000	0.4341	0.000	0.3821
2.0	0.000	0.5233	0.000	0.4403	0.000	0.3867
3.0	0.000	0.5447	0.000	0.4550	0.000	0.3976
4.0	−0.0001	0.5682	0.000	0.4713	0.000	0.4097
5.0	−0.0004	0.5926	0.0002	0.4882	−0.0001	0.4224

that, aside from the factor $2/\pi$ characterizing the difference between penny-shaped and plane-strain cracks, the increase in the stress intensity factors k_1 and k_2 with increasing $a\alpha$ in the axisymmetric case is not as severe as in the plane-strain crack. For the case of pressurized cracks (i.e., for $\sigma_{zz}(r, 0) = -p_0$, $\sigma_{rz}(r, 0) = 0$ and $\sigma_{yy}(x, 0) = -p_0$, $\sigma_{xy}(x, 0) = 0$) the comparison of the two sets of results is shown in Table 3.

Note that the results given in Table 2 may be used to obtain the stress intensity factors for arbitrary crack surface tractions by superposition to the extent that the tractions may be approximated by a second-degree polynomials in r.

After determining g_1 and g_2 or the coefficients B_{1n} and B_{2n} shown in (48), the crack-opening displacements may be obtained from (20) as follows:

Table 3 Comparison of the stress intensity factors for pressurized plane-strain and penny-shaped cracks in a nonhomogeneous medium ($\nu = 0.3$)

αa	0	0.1	0.25	0.5	1.0	2.5	5.0
	Plane strain crack						
$\frac{k_1}{p_0\sqrt{a}}$	1	1.008	1.036	1.101	1.258	1.808	2.869
$\frac{k_2}{p_0\sqrt{a}}$	0.0	0.026	0.065	0.129	0.263	0.697	1.567
	Penny-shaped crack						
$\frac{k_1}{p_0\sqrt{a}}$	0.637	0.638	0.644	0.661	0.712	0.918	1.326
$\frac{k_2}{p_0\sqrt{a}}$	0.0	0.011	0.026	0.053	0.107	0.280	0.611

$$w(r,+0)-w(r,-0) = -\int_r^a g_1(s)ds$$
$$= -\frac{a(\kappa+1)}{4\mu_0}\left\{B_{10}\left(\theta' + \frac{1}{2}\sin 2\theta'\right) + \sum_1^\infty B_{1n}\left(\frac{1}{2(n+1)}\sin(2n+2)\theta' + \frac{1}{2n}\sin 2n\theta'\right)\right\}, \quad (60)$$

$$r[u(r,+0)-u(r,-0)] = -\int_r^a sg_2(s)ds$$
$$= -\frac{a^2(\kappa+1)}{2\mu_0}\left\{B_{21}\left(\frac{1}{4}\sin 2\theta' + \frac{1}{8}\sin 4\theta'\right) + \sum_2^\infty B_{2n}\left(\frac{1}{2n}\sin 2n\theta' + \frac{1}{4n+4}\sin(2n+2)\theta' + \frac{1}{4n-4}\sin(2n-2)\theta'\right)\right\}, \quad (61)$$

where

$$\cos^2\theta' = \frac{r}{a}.$$

It should be observed that $u^+ - u^-$ vanishes for $r \to 0$. This may be seen from (40) and also from (61) and (45) by using the condition (41) as follows:

$$\lim_{r\to 0}[u(r,+0)-u(r,-0)] = -\lim_{r\to 0}\frac{1}{r}\int_r^a sg_2(s)ds$$
$$= -\lim_{r\to 0}\frac{d}{dr}\int_r^a sg_2(s)ds$$
$$= \lim_{r\to 0} r\frac{f_2(r)}{\sqrt{r(a-r)}} = 0. \quad (62)$$

Figures 2 and 3 show some sample results for the crack-opening displacements. In Fig. 2 the external loads are $\sigma_{zz}(r, 0) = -p_0$, $\sigma_{rz}(r, 0) = 0$ and the dimensionless displacement shown is defined by

$$W(r) = \frac{w(r,+0)-w(r,-0)}{w_0},\ w_0 = \frac{(1+\kappa)}{2\mu_0}p_0 a. \quad (63)$$

In Fig. 3 it is assumed that $\sigma_{zz}(r, 0) = 0$, $\sigma_{rz}(r, 0) = -q_0$ and the displacement is normalized as follows:

$$U(r) = \frac{u(r,+0)-u(r,-0)}{u_0},\ u_0 = \frac{(1+\kappa)}{2\mu_0}q_0 a. \quad (64)$$

From Figs. 2 and 3 it may be seen that the influence of the nonhomogeneity constant α is much more significant on the axial displacement than on the radial displacement. For ref-

Downloaded 03 May 2010 to 171.66.16.245. Redistribution subject to ASME license or copyright; see http://www.asme.org/terms/Terms_Use.cfm

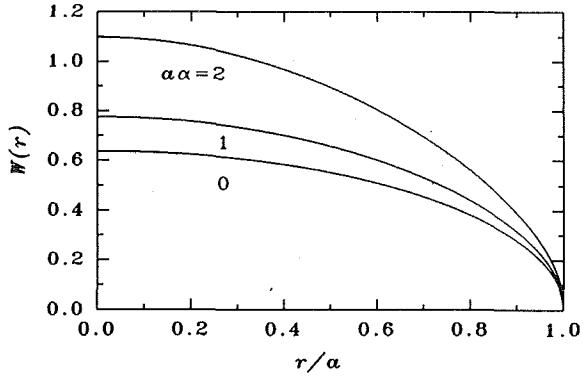


Fig. 2 z-component of the normalized crack opening displacement, $W = (w^+ - w^-)/w_0$, $w_0 = (1 + \kappa)p_0a/2\mu_0$ for the external loading $\sigma_{zz}(r, 0) = -p_0$, $\sigma_{rz}(r, 0) = 0$

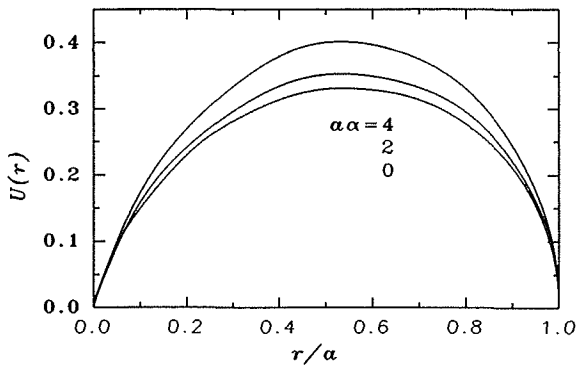


Fig. 3 r-component of the normalized crack opening displacement, $U = (u^+ - u^-)/u_0$, $u_0 = (1 + \kappa)q_0a/2\mu_0$ for the external loading $\sigma_{zz}(r, 0) = 0$, $\sigma_{rz}(r, 0) = -q_0$

erence we note that for $\alpha = 0$ in pressurized plane-strain and penny-shaped cracks the crack-opening displacements are, respectively, given by

$$u_y(x, +0) - u_y(x, -0)] = w_0\sqrt{1 - x^2/a^2},$$

$$w(r, +0) - w(r, -0)] = \frac{2}{\pi} w_0\sqrt{1 - r^2/a^2}, \quad w_0 = \frac{(1+\kappa)}{2\mu_0} p_0 a. \tag{65a-c}$$

In this study, largely to simplify the analysis, the Poisson's ratio ν is assumed to be constant. In an actual nonhomogeneous medium this, of course, is not possible. The assumption can only be justified if the fracture mechanics parameters of interest, in this case the stress intensity factors, prove to be relatively insensitive to variations in the Poisson's ratio. To give some idea about the influence of the variations in ν on the stress intensity factors, some additional results are given in Table 4. The table shows the normalized stress intensity factors for various values of ν and for a small and a large value of the dimensionless nonhomogeneity constant αa. In these examples the external loads are assumed to be $\sigma_{zz}(r, 0) = p_1(r) = (-p_0, -p_1(r/a), -p_2(r/a)^2)$, $0 \le r < a$, $\sigma_{rz}(r, 0) = p_2(r) = 0$. Particularly considering the fact that the Poisson's ratio of the constituent materials and consequently that of the composite nonhomogeneous medium is likely to vary within a much narrower range than shown in the table, the influence of ν on the stress intensity factors does not seem to be very significant.

Table 4 The influence of the Poisson's ratio on the stress intensity factors, loading: $\sigma_{rz}(r, 0) = 0$, $\sigma_{zz}(r, 0) = (-p_0, -p_1(r/a), -p_2(r/a)^2)$, $0 \le r < a$

ν	$\frac{k_1}{p_0\sqrt{a}}$	$\frac{k_2}{p_0\sqrt{a}}$	$\frac{k_1}{p_1\sqrt{a}}$	$\frac{k_2}{p_1\sqrt{a}}$	$\frac{k_1}{p_2\sqrt{a}}$	$\frac{k_2}{p_2\sqrt{a}}$
$\alpha a = 0.3$						
0.01	0.6428	0.0318	0.5037	0.0188	0.4269	0.0127
0.1	0.6437	0.0318	0.5042	0.0188	0.4273	0.0127
0.2	0.6449	0.0319	0.5049	0.0188	0.4277	0.0127
0.3	0.6465	0.0319	0.5058	0.0188	0.4284	0.0127
0.4	0.6484	0.0319	0.5069	0.0188	0.4291	0.0127
0.45	0.6496	0.0319	0.5077	0.0188	0.4296	0.0127
$\alpha a = 3.0$						
0.01	0.9193	0.3370	0.6659	0.1967	0.5367	0.1327
0.1	0.9389	0.3381	0.6776	0.1973	0.5448	0.1330
0.2	0.9642	0.3395	0.6928	0.1979	0.5552	0.1334
0.3	0.9943	0.3413	0.7108	0.1988	0.5676	0.1339
0.4	1.031	0.3434	0.7328	0.1999	0.5827	0.1346
0.45	1.053	0.3447	0.7458	0.2006	0.5917	0.1349

Acknowledgments

This work was supported by ONR under the Contract N00014-89-J-3188 and by NSF under the Grant MSM-8613611.

References

Batakis, A. P., and Vogan, J. M., 1985, "Rocket Thrust Chamber Thermal Barrier Coating," NASA CR-1750222.

Delale, F., and Erdogan, F., 1983, "The Crack Problem for a Nonhomogeneous Plane," ASME JOURNAL OF APPLIED MECHANICS, Vol. 50, pp. 609–614.

Delale, F., and Erdogan, F., 1988a, "Interface Crack in a Nonhomogeneous Medium," *Int. J. Engng. Sci.*, Vol. 26, pp. 559–568.

Delale, F., and Erdogan, F., 1988b, "On the Mechanical Modeling of the Interfacial Region in Bonded Materials," ASME JOURNAL OF APPLIED MECHANICS, Vol. 55, pp. 317–324.

Dhalival, R. S., and Sing, B. M., 1978, "On the Theory of Elasticity of a Nonhomogeneous Medium," *J. Elasticity*, Vol. 8, pp. 211–219.

Erdogan, F., 1978, "Mixed Boundary Value Problems in Mechanics," *Mechanics Today*, S. Nemat-Nasser, ed., Vol. 4, pp. 1–86.

Erdogan, F., 1985, "The Crack Problem for Bonded Nonhomogeneous Materials under Antiplane Shear Loading," ASME JOURNAL OF APPLIED MECHANICS, Vol. 52, pp. 823–828.

Gerasoulis, A., and Srivastav, R. P., 1980, "A Griffith Crack Problem for a Nonhomogeneous Medium," *Int. J. Engng. Sci.*, Vol. 18, pp. 239–247.

Hirano, T., and Yamada, T., 1988, "Multi-Paradigm Expert System Architecture Based upon the Inverse Design Concept," Int. Workshop On Artificial Intelligence For Industrial Applications, Hitachi, Japan.

Hirano, T., Yamada, T., Teraki, J., Niino, M., and Kumakawa, A., 1988, "A Study on a Functionally Gradient Material Design System for a Thrust Chamber," *Proc. 16th Int. Symposium On Space Technology And Science*, Sapporo, Japan.

Houck, D. L., ed., 1987, "Thermal Spray: Advances in Coating Technology," *Proc. Of The National Thermal Spray Conference*, Orlando, FL, ASM International.

Kassir, M. K., 1972, "A Note on the Twisting Deformation of a Nonhomogeneous Shaft Containing a Circular Crack," *Int. J. Fracture Mech.*, Vol. 8, pp. 325–334.

Konda, N., and Erdogan, F., 1989, "The Mixed-Mode Crack Problem in a Nonhomogeneous Medium," ONR Report, Contract N00014-89-J-3188, *Trans. Japan Soc. Mech. Engineers* to appear.

Mahajan, R., 1992, "Crack Problems for an Elastic Film Bonded to an Orthotropic Substrate," Ph.D. Dissertation, Lehigh University, Bethlehem, PA.

APPENDIX

Expressions for various functions that appear in analysis.

$$\lambda_1(\rho) = (n_2v_3 - n_3v_2)/\Delta_1,\ \lambda_2(\rho) = (n_4v_3 - n_3v_4)/\Delta_1,$$

$$\lambda_3(\rho) = (n_1v_2 - n_2v_1)/\Delta_1,\ \lambda_4(\rho) = (n_1v_4 - n_4v_1)/\Delta_1. \tag{A1-4}$$

$$n_j(\rho) = (3 - \kappa)\rho - (1 + \kappa)m_ja_j,\ v_j(\rho) = m_j + \rho a_j,\ j = 1, \ldots, 4,$$

$$\Delta_1(\rho) = n_1v_3 - n_3v_1. \tag{A5-7}$$

Downloaded 03 May 2010 to 171.66.16.245. Redistribution subject to ASME license or copyright; see http://www.asme.org/terms/Terms_Use.cfm

$$E_j(\rho)=\frac{1}{\Delta_1}\{n_j[m_3-m_1+\rho(a_3-a_1)]+(1+\kappa)v_j(a_3m_3-a_1m_1)\},$$

$$G_j(\rho)=\frac{1}{\Delta_1}\{n_j(a_1m_3-a_3m_1)+v_{2j}[(3-\kappa)(a_3-a_1)\rho + (1+\kappa)(m_3-m_1)a_1a_3]\},\ (j=2,4). \quad \text{(A8, 9)}$$

$$d_{11}(\rho)=\frac{n_2}{\Delta_2}(1-E_4)-\frac{n_4}{\Delta_2}(1-E_2),$$

$$d_{12}(\rho)=\frac{n_2}{\Delta_2}(a_4-G_4)-\frac{n_4}{\Delta_2}(a_2-G_2),$$

$$d_{21}(\rho)=\frac{v_2}{\Delta_2}(1-E_4)-\frac{v_4}{\Delta_2}(1-E_2),$$

$$d_{22}(\rho)=\frac{v_2}{\Delta_2}(a_4-G_4)-\frac{v_4}{\Delta_2}(a_2-G_2), \quad \text{(A10–13)}$$

$$\Delta_2(\rho)=\rho((1-E_2)(a_4-G_4)-(1-E_4)(a_2-G_2)). \quad \text{(A14)}$$

Downloaded 03 May 2010 to 171.66.16.245. Redistribution subject to ASME license or copyright; see http://www.asme.org/terms/Terms_Use.cfm

Vibration of Elastic Structures With Cracks

I. Y. Shen
Department of Engineering Mechanics,
University of Nebraska-Lincoln,
Lincoln, NE 68588-0347
Assoc. Mem. ASME

An analytical algorithm is proposed to represent eigensolutions $[\lambda_m^2, \psi_m(\mathbf{r})]_{m=1}^{\infty}$ *of an imperfect structure* C *containing cracks in terms of crack configuration* σ_c *and eigensolutions* $[\omega_n^2, \phi_n(\mathbf{r})]_{n=1}^{\infty}$ *of a perfect structure* P *without the cracks. To illustrate this algorithm on mechanical systems governed by the two-dimensional Helmholtz operator, the Green's identity and Green's function of* P *are used to represent* $\psi_m(\mathbf{r})$ *in terms of an infinite series of* $\phi_n(\mathbf{r})$. *Substitution of the* $\psi_n(\mathbf{r})$ *representation into the Kamke quotient of* C *and stationarity of the quotient result in a matrix Fredholm integral equation. The eigensolutions of the Fredholm integral equation then predict* λ_m^2 *and* $\psi_m(\mathbf{r})$ *of* C. *Finally, eigensolutions of two rectangular elastic solids under antiplane strain vibration, one with a boundary crack and the other with an oblique internal crack, are calculated numerically.*

1 Introduction

Elastic mechanical systems have wide applications in aircraft, automobiles, turbo-engines, robots, and machine tools. In some applications, slots and holes are introduced purposely to perform specific functions. In other applications, cracks emerge as a result of fatigue loadings and will subsequently cause catastrophic damage to the systems.

As an example, circular saws often possess radial rim slots to release thermal stresses induced during the cutting process (Yu and Mote, 1987). By doing so, circular saws will remain flat under severe cutting conditions. In addition, circular saws have to meet specific vibration requirements. For instance, circular saws must not present large vibration at specific cutting speeds used by sawmills (Yu and Mote, 1987). Because slot location and slot geometry will substantially affect the vibration response of a circular saw, it is critical to design the slots so that the saw will not present large vibration at those cutting speeds.

The current design procedure for machine parts containing slots in a process of trial and error. Engineers often propose an initial slot design based on their best "engineering judgement." Then they determine vibration response of the machine parts primarily through experimental methods (Tang and Huang, 1983; Yu and Mote, 1987) and numerical methods (Mote, 1972; Tang and Huang, 1983; Chen and Chen 1988; Parker and Mote, 1991). Analytical methods are also available for structures with simple geometry (Stahl and Keer, 1972) or with small cracks (Gudmundson, 1982). If the resulting design may cause large vibration, then the initial slot design is modified and the whole process is repeated.

In contrast, fatigue cracks are deleterious because they cause sudden and complete fracture of machines when the cracks are "big" enough. Statistics shows that at least 28 rotor failures, which can be attributed to shaft fatigue cracks, have occurred for the past 15 years in the North American utility industry alone (Muszyńska, 1982; Nelson and Nataraj, 1986). In order to detect possible cracks in a machine, engineers usually monitor vibration response of the machine. For instance, an undamaged rotating shaft in a turbine engine will present a regular vibration response caused by engine loads. When a crack emerges somewhere in the shaft, the vibration will deviate from the normal one (Grabowski, 1980; Mayes and Davies, 1984; Nelson and Nataraj, 1986; Wauer, 1990). The deviation depends on the size and the location of the crack. Therefore, comparison of vibration response of normal and damaged shafts can help engineers identify the location and size of the crack (Ju and Minovich, 1988; Shen and Pierre, 1990; Wauer, 1990).

In vibration monitoring, the current approach to predict vibration response of a machine component containing cracks greatly depends on the geometry of the component. For one-dimensional structures with cracks, there are various avenues to obtain approximate vibration response. A complete review on this subject is by Wauer (1990). For two or three-dimensional machine structures, engineers heavily rely on numerical methods and trial-and-error procedures (Cawley and Adams, 1979; Nezu and Kidoguchi, 1980; Petroski and Glazik, 1980; Chen and Chen, 1980).

In both vibration monitoring and design of slotted machine parts, engineers encounter a fundamental problem—vibration of elastic structures with cracks. Understanding the physics of and obtaining a solution to this fundamental problem, of course, will lead to major progress in both areas. Nevertheless, how the location and geometry of cracks will affect eigensolutions of a structure remains open for structures with large cracks (Gudmundson, 1982), for structures with arbitrary ge-

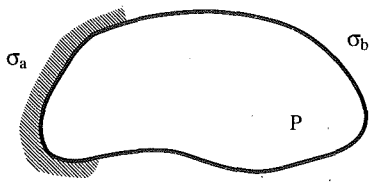
Contributed by the Applied Mechanics Division of THE AMERICAN SOCIETY OF MECHANICAL ENGINEERS for presentation at the First Joint ASCE-EMD, ASME-AMD, SES Meeting, Chralottesville, VA, June 6-9, 1993.

Discussion on this paper should be addressed to the Technical Editor, Professor Lewis T. Wheeler, Department of Mechanical Engineering, University of Houston, Houston, TX 77204-4792, and will be accepted until four months after final publication of the paper itself in the ASME JOURNAL OF APPLIED MECHANICS.

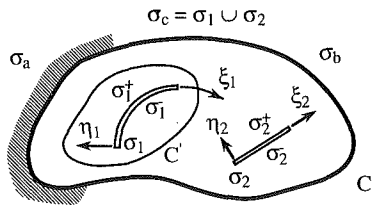
Manuscript received by the ASME Applied Mechanics Division, Jan. 9, 1992; final revision, June 8, 1992. Associate Technical Editor: D. J. Inman.

Paper No. 93-APM-15.

Copyright © 1993 by ASME
Downloaded 03 May 2010 to 171.66.16.245. Redistribution subject to ASME license or copyright; see http://www.asme.org/terms/Terms_Use.cfm



(a) A Perfect Structure P



(b) A Structure C with Cracks

Fig. 1 (*a*)A perfect structure *P* containing no cracks with eigenvalues ω_n^2 and eigenfunctions $\phi_n(\mathbf{r})$; (*b*) a cracked structure *C* with crack geometry σ_c, eigenvalues λ_m^2, and eigenfunctions $\psi_m(\mathbf{r})$

ometry (Stahl and Keer, 1972), and for structures that are not one-dimensional (Shen and Pierre, 1990).

This paper is to study the dependence of eigensolutions on the location and geometry of emerging cracks. Consider a perfect structure P with eigenvalues ω_n^2 and eigenfunctions $\phi_n(\mathbf{r})$ as shown in Fig. 1(a). When cracks $\sigma_c(\equiv \sigma_1 \cup \sigma_2)$ emerge in P, the eigensolutions shift to λ_m^2 and $\psi_m(\mathbf{r})$. See the structure C in Fig. 1(b). The purpose of this paper is to determine $f_m(\cdot)$ and $g_m(\cdot)$ analytically such that

$$\begin{cases} \lambda_m^2 = f_m(\omega_n^2, \phi_n(\mathbf{r}); \sigma_c), \\ \qquad\qquad m,n = 1,2,3, \ldots \\ \psi_m(\mathbf{r}) = g_m(\omega_n^2, \psi_n(\mathbf{r}); \sigma_c), \end{cases} \tag{1}$$

where the crack configuration σ_c refers to the location and geometry of the emerging cracks.

The contribution of this analytical approach is threefold. First, this approach is not limited to one-dimensional structures (Shen and Pierre, 1990). Instead, this approach will predict vibration response of two and three-dimensional structures with cracks, which have direct industrial applications such as design of slotted circular saws (Yu and Mote, 1987) and crack detection of rolling element bearings (Collacott 1979; White 1991). Second, this approach is not limited to structures with small cracks (Gudmundson, 1982) or structures with simple geometry (Stahl and Keer, 1972). Instead, it is valid for any structure provided that $[\omega_n^2, \phi_n(\mathbf{r})]_{n=1}^{\infty}$ and σ_c are known. Third, this approach will predict λ_m^2 and $\psi_m(\mathbf{r})$ in any frequency range. In contrast, typical numerical methods require very fine discretization and long calculations to predict high-frequency response.

This analytical algorithm might have applications to inverse problems as well. For example, it might be possible to invert (1) to represent σ_c in terms of ω_n^2, $\psi_n(\mathbf{r})$, λ_m^2, and $\psi_m(\mathbf{r})$, i.e.,

$$\sigma_c = \sigma_c(\omega_n^2, \phi_n(\mathbf{r}), \lambda_m^2, \psi_m(\mathbf{r})). \tag{2}$$

If so, the location and geometry of cracks in a structure may be identified through (2) by monitoring the vibration responses of the structure.

In general, inverse problems contain three major elements: existence of σ_c, uniqueness of σ_c, and reconstruction of σ_c (Gladwell, 1986). Like any inverse function, σ_c in (2) may not be defined for all $[\omega_n^2, \psi_n(\mathbf{r})]_{n=1}^{\infty}$ and $[\lambda_m^2, \psi_m(\mathbf{r})]_{m=1}^{\infty}$. This corresponds to the existence of σ_c in inverse problems. Like any inverse function, σ_c in (2) may not be single valued for some $[\omega_n^2, \psi_n(\mathbf{r})]_{n=1}^{\infty}$ and $[\lambda_m^2, \psi_m(\mathbf{r})]_{n=1}^{\infty}$. This corresponds to the uniqueness of σ_c in inverse problems. Like any inverse function, the only way to obtain σ_c is to invert (1) by definition. This corresponds to the reconstruction of σ_c in inverse problems. Although the main concern of this paper is not inverse problems, the algorithm proposed here, hopefully, could provide a different perspective on this research area.

In this paper, the analytical algorithm is illustrated on mechanical systems whose response is governed by the two-dimensional Helmholtz equation. This includes antiplane strain vibration of elastic solids under Mode III fracture and diffraction and scattering of acoustic standing waves in two-dimensional acoustic cavities containing rigid obstacles. Use of the Green's identity and the Green's function of P represents $\psi_m(\mathbf{r})$ in terms of an infinite eigenfunction series of $\phi_n(\mathbf{r})$. The coefficients of the eigenfunction series depend on the crack configuration σ_c, the opening shape $\Delta\psi_m$ of the cracks, and both λ_m^2 and ω_n^2. Substitution of the eigenfunction series into the Kamket quotient of C and the stationarity of the quotient result in a matrix Fredholm integral equation whose eigensolutions predict λ_m^2 and the opening shape $\Delta\psi_m$. Finally, eigensolutions of two rectangular elastic solids under antiplane strain vibration, one with a boundary crack and the other with an oblique internal crack, are calculated numerically.

2 Formulation

Consider a two-dimensional, elastic solid P with shear modulus T and density ρ occupying a finite domain τ with fixed boundary σ_a and zero traction boundary σ_b. See Fig. 1(a). When P is under antiplane strain vibration, eigenfunctions $\phi_n(\mathbf{r})$ and eigenvalues ω_n^2 of P then satisfy

$$-T\nabla^2\phi_n(\mathbf{r}) = \rho\omega_n^2\phi_n(\mathbf{r}), \mathbf{r}\in\tau \tag{3}$$

with boundary conditions

$$\phi_n(\mathbf{r}) = 0, \ \mathbf{r}\in\sigma_a \tag{4}$$

$$T\frac{\partial\phi_n(\mathbf{r})}{\partial n} = 0, \ \mathbf{r}\in\sigma_b. \tag{5}$$

In addition, the eigensolutions also satisfy orthonormality conditions

$$\int_\tau \rho\phi_m(\mathbf{r})\phi_n(\mathbf{r})\,d\tau = \delta_{mn} \tag{6}$$

$$-\int_\tau T\phi_m(\mathbf{r})\nabla^2\phi_n(\mathbf{r})\,d\tau = \omega_n^2\delta_{mn} \tag{7}$$

$$\int_\tau T\nabla\phi_m(\mathbf{r})\cdot\nabla\phi_n(\mathbf{r})\,d\tau = \omega_n^2\delta_{mn}. \tag{8}$$

Consider an elastic solid C occupying the same domain τ with n_c cracks that posses zero traction. In addition, the crack width is infinitesimal. See Fig. 1(b). When C is under antiplane strain vibration, eigenfunction $\psi(\mathbf{r})$ and eigenvalue λ^2 of C satisfy

$$-T\nabla^2\psi(\mathbf{r}) = \rho\lambda^2\psi(\mathbf{r}), \mathbf{r}\in\tau' \tag{9}$$

with boundary conditions

$$\psi(\mathbf{r}) = 0, \ \mathbf{r}\in\sigma_a \tag{10}$$

$$T\frac{\partial\psi(\mathbf{r})}{\partial n} = 0, \ \mathbf{r}\in\sigma_b\cup\sigma_c. \tag{11}$$

Here, $\sigma_c \equiv \cup_{i=1}^{n_c}\sigma_i$, where σ_i is the boundary of the ith cracks, and $\tau' \equiv \tau - \sigma_c$.

Equations (3) to (11) will also describe diffraction and scattering of standing acoustic waves in a closed acoustic cavity containing rigid obstacles, if $c = \sqrt{T/\rho}$ is the acoustic wave speed and σ_c represents the location and geometry of the rigid obstacles.

Downloaded 03 May 2010 to 171.66.16.245. Redistribution subject to ASME license or copyright; see http://www.asme.org/terms/Terms_Use.cfm

3 Eigenfunctions of C

Consider the Green's identity over the crack domain τ'

$$-\int_{\tau'} Tw_1\nabla^2 w_2 d\tau+\oint_{\sigma_b\cup\sigma_c} Tw_1\frac{\partial w_2}{\partial n}d\sigma= -\int_{\tau'} Tw_2\nabla^2 w_1 d\tau+\oint_{\sigma_b\cup\sigma_c} Tw_2\frac{\partial w_1}{\partial n}d\sigma \quad (12)$$

where $w_1(\mathbf{r})$ and $w_2(\mathbf{r})$ are two admissible functions satisfying $w_1(\mathbf{r}) = 0$ and $w_2(\mathbf{r}) = 0$ on σ_a. Let $w_1(\mathbf{r})$ be the eigenfunction $\psi(\mathbf{r})$ of C satisfying (9), (10), and (11). Let $w_2(\mathbf{r})$ be the Green's function $G(\mathbf{r}|\mathbf{r}_0)$ of P under a concentrated harmonic load $\delta(\mathbf{r}-\mathbf{r}_0)e^{i\lambda t}$ acting at $\mathbf{r}_0$. Therefore, $G(\mathbf{r}|\mathbf{r}_0)$ satisfies

$$-T\nabla^2 G(\mathbf{r}|\mathbf{r}_0)=\rho\lambda^2 G(\mathbf{r}|\mathbf{r}_0)+\delta(\mathbf{r}-\mathbf{r}_0),\ \mathbf{r},\ \mathbf{r}_0\in\tau \quad (13)$$

with boundary conditions

$$G(\mathbf{r}|\mathbf{r}_0)=0,\ \mathbf{r}\in\sigma_a,\ \mathbf{r}_0\in\tau \quad (14)$$

$$T\frac{\partial G(\mathbf{r}|\mathbf{r}_0)}{\partial n}=0,\ \mathbf{r}\in\sigma_b,\ \mathbf{r}_0\in\tau. \quad (15)$$

In addition, $G(\mathbf{r}|\mathbf{r}_0)$ allows an eigenfunction expansion

$$G(\mathbf{r}|\mathbf{r}_0)=-\sum_{n=1}^{\infty}\frac{\phi_n(\mathbf{r})}{\lambda^2-\omega_n^2}\phi_n(\mathbf{r}_0). \quad (16)$$

Substitute (9)–(11) and (13)–(16) into (12) to obtain

$$\psi(\mathbf{r})=\sum_{n=1}^{\infty}\frac{A_n}{\lambda^2-\omega_n^2}\phi_n(\mathbf{r}),\ \mathbf{r}\in\tau' \quad (17)$$

where

$$A_n=\oint_{\sigma_c} T\psi(\mathbf{r})\frac{\partial\phi_n(\mathbf{r})}{\partial n}d\sigma=\sum_{i=1}^{n_c}\int_{\sigma_i^+} T\Delta\psi(\xi_i)\frac{\partial\phi_n(\xi_i)}{\partial n}d\sigma_i. \quad (18)$$

Here, ξ_i is a curvilinear coordinate alone the ith crack, $d\sigma_i$ is the arc length of $d\xi_i$, and $\Delta\psi(\xi_i)\equiv\psi(\sigma_i^+)-\psi(\sigma_i^-)$ is the opening shape of the ith crack in Fig. 1(b). Equations (17) and (18) represent an eigenfunction $\psi(\mathbf{r})$ in terms of $\psi_n(\mathbf{r})$ and ω_n^2 provided that the opening shape $\Delta\psi$ and the eigenvalue λ^2 corresponds to mode $\psi(\mathbf{r})$ are known. In addition, if σ_c coincides with antinodes of $\phi_N(\mathbf{r})$, then $\partial\phi_N/\partial n = 0$ and $A_N = 0$. Therefore, the Nth term in (17) vanishes, and the Nth eigenvalue of P remains unchanged when the cracks σ_c are introduced.

4 Kamke Quotient of C

Consider the Kamke quotient of C

$$\lambda^2[\psi]=\frac{I_s[\psi]}{I_k[\psi]}, \quad (19)$$

where

$$I_k[\psi]=\int_{\tau'}\rho\psi^2(\mathbf{r})d\tau \quad (20)$$

and

$$I_s[\psi]=\int_{\tau'} T\Delta\psi(\mathbf{r})\cdot\nabla\psi(\mathbf{r})d\tau. \quad (21)$$

For $I_k[\psi]$, (17) implies that

$$I_k[\psi]=\sum_{n=1}^{\infty}\frac{A_n^2}{(\lambda^2-\omega_n^2)^2} \quad (22)$$

where the orthonormality (6) has been used. For $I_s[\psi]$, however, direct substitution of (17) into (21) does not result in an L_2 convergent series because of the discontinuity $\Delta\psi$ across σ_c. Decompose $\nabla\psi(\mathbf{r})$ into

$$\nabla\psi(\mathbf{r})=\sum_{n=1}^{\infty}C_n\nabla\phi_n(\mathbf{r})+\Phi(\mathbf{r}),\ \mathbf{r}\in\tau', \quad (23)$$

where the vector $\Phi(\mathbf{r})$ is orthogonal to $\nabla\phi_n(\mathbf{r})$, $n = 1, 2, \ldots$, i.e.,

$$\int_{\tau'} T\nabla\phi_n(\mathbf{r})\cdot\Phi(\mathbf{r})d\tau=0,\ n=1, 2, \ldots \quad (24)$$

In addition, C_n is determined by

$$C_n=\frac{1}{\omega_n^2}\int_{\tau'} T\nabla\psi(\mathbf{r})\cdot\nabla\phi_n(\mathbf{r})d\tau. \quad (25)$$

Notice that the circulations of $\nabla\psi(\mathbf{r})$ and $\Sigma_{n=1}^{\infty}C_n\nabla\phi_n(\mathbf{r})$, along any curve C' in τ' not crossing the cracks σ_c (cf. Fig. 1(b)), are zero because $\Sigma_{n=1}^{\infty}C_n\nabla\phi_n(\mathbf{r})$ and $\nabla\psi(\mathbf{r})$ are single-valued functions in τ'. Therefore, (23) results in $\oint_{C'}\Phi(\mathbf{r})\cdot ds = 0$ implying that there exists a single-valued displacement field $\chi(\mathbf{r})$, $\mathbf{r}\in\tau'$, such that

$$\Phi(\mathbf{r})=\nabla\chi(\mathbf{r}),\ \mathbf{r}\in\tau'.$$

Hence,

$$\psi(\mathbf{r})=\sum_{n=1}^{\infty}C_n\phi_n(\mathbf{r})+\chi(\mathbf{r}),\ \mathbf{r}\in\tau'. \quad (26)$$

To determine C_n and $\chi(\mathbf{r})$ explicitly, $\psi(\mathbf{r})$ is expanded as an eigenfunction series

$$\psi(\mathbf{r})=\sum_{n=1}^{\infty}\left[\int_{\tau'}\rho\psi(\mathbf{r})\phi_n(\mathbf{r})d\tau\right]\phi_n(\mathbf{r}) =-\sum_{n=1}^{\infty}\left[\frac{1}{\omega_n^2}\int_{\tau'}T\psi(\mathbf{r})\nabla^2\phi_n(\mathbf{r})d\tau\right]\phi_n(\mathbf{r}) =\sum_{n=1}^{\infty}\left[\frac{1}{\omega_n^2}\int_{\tau'}T\nabla\psi(\mathbf{r})\cdot\nabla\phi_n(\mathbf{r})d\tau -\frac{1}{\omega_n^2}\oint_{\sigma_c}T\psi(\mathbf{r})\frac{\partial\phi_n(\mathbf{r})}{\partial n}d\sigma\right]\phi_n(\mathbf{r})=\sum_{n=1}^{\infty}\left[C_n-\frac{A_n}{\omega_n^2}\right]\phi_n(\mathbf{r}). \quad (27)$$

Compare (17) and (27) to obtain

$$C_n=\frac{A_n}{\lambda^2-\omega_n^2}+\frac{A_n}{\omega_n^2}=\frac{\lambda^2 A_n}{\omega_n^2(\lambda^2-\omega_n^2)}. \quad (28)$$

Compare (27) with (26) to obtain

$$\chi(\mathbf{r})=-\sum_{n=1}^{\infty}\frac{A_n}{\omega_n^2}\phi_n(\mathbf{r}),\ \mathbf{r}\in\tau'. \quad (29)$$

In addition, $\Sigma_{n=1}^{\infty}C_n\phi_n(\mathbf{r})$ is continuous across σ_c because $\Sigma_{n=1}^{\infty}C_n\nabla\phi_n(\mathbf{r})$ converges in the L_2 sense for all $\mathbf{r}\in\tau$. Therefore, (26) implies that $\chi(\mathbf{r})$ undergoes a discontinuity

$$\Delta\chi(\mathbf{r})\equiv\chi(\sigma_c^+)-\chi(\sigma_c^-)=\Delta\psi(\mathbf{r}),\ \mathbf{r}\in\sigma_c. \quad (30)$$

Substitute (23) into (21) and recall the orthonormality condition (8) to obtain

$$I_s[\psi]=\sum_{n=1}^{\infty}\frac{\lambda^4 A_n^2}{\omega_n^2(\lambda^2-\omega_n^2)^2}+\|\nabla\chi\|^2, \quad (31)$$

where

$$\|\nabla\chi\|^2=\int_{\tau'}T\nabla\chi(\mathbf{r})\cdot\nabla\chi(\mathbf{r})d\tau. \quad (32)$$

Notice that $\|\nabla\chi\|^2$ is independent of λ^2. In addition, $\nabla\chi(\mathbf{r})$ cannot be determined by direct differentiation of (29) because $\chi(\mathbf{r})$ possesses the discontinuity (30) across σ_c. An analytic representation of $\|\nabla\chi\|^2$ in terms of $\Delta\psi(\mathbf{r})$ is derived in Appendix A.

Downloaded 03 May 2010 to 171.66.16.245. Redistribution subject to ASME license or copyright; see http://www.asme.org/terms/Terms_Use.cfm

5 Eigenvalues of C

Eigenvalues λ^2 of C must satisfy stationarity of the Kamke quotient (19), i.e.,

$$\delta J[\Delta\chi] = \delta I_s[\psi] - \lambda^2 \delta I_k[\psi] = \sum_{n=1}^{\infty} \frac{\lambda^2 \delta A_n^2}{\omega_n^2(\lambda^2 - \omega_n^2)} + \delta \| \nabla \chi \|^2 = 0. \quad (33)$$

Substitute (18) into (33) and recall that $\delta\Delta\psi(\xi_i)$ is arbitrary on σ_i to obtain the following matrix Fredholm integral equation:

$$\mathbf{A}(\lambda^2)\Delta\boldsymbol{\Psi} \equiv T^2 \sum_{n=1}^{\infty} \frac{\lambda^2 \mathbf{g}_n \langle \mathbf{g}_n | \Delta\boldsymbol{\Psi} \rangle}{\omega_n^2(\lambda^2 - \omega_n^2)} + \mathbf{R}\Delta\boldsymbol{\Psi} = \mathbf{0}. \quad (34)$$

Here $\Delta\boldsymbol{\Psi}$ and $\mathbf{g}_n$ are column vectors

$$\Delta\boldsymbol{\Psi} = [\Delta\psi(\xi_1), \Delta\psi(\xi_2), \ldots, \Delta\psi(\xi_{n_c})]^T, \quad (35)$$

$$\mathbf{g}_n = \left[\frac{\partial\phi_n(\xi_1)}{\partial n}, \frac{\partial\phi_n(\xi_2)}{\partial n}, \ldots, \frac{\partial\phi_n(\xi_{n_c})}{\partial n} \right]^T. \quad (36)$$

$\langle \mathbf{g}_n | \Delta\boldsymbol{\Psi} \rangle$ is an inner product operator defined as

$$\langle \mathbf{g}_n | \Delta\boldsymbol{\Psi} \rangle \equiv \sum_{i=1}^{n_c} \int_{\sigma_i^+} \frac{\partial\phi_n(\xi_i)}{\partial n} \Delta\psi(\xi_i) d\sigma_i \quad (37)$$

with its natural norm

$$\| \mathbf{g}_n \| = \sqrt{\langle \mathbf{g}_n | \mathbf{g}_n \rangle}. \quad (38)$$

In addition, $\mathbf{R}$ is a symmetric, positive definite operator satisfying

$$\langle \Delta\boldsymbol{\Psi} | \mathbf{R}\Delta\boldsymbol{\Psi} \rangle = \| \nabla\chi \|^2. \quad (39)$$

The explicit expression of $\mathbf{R}$ is derived in Appendix B. Also notice that $\mathbf{A}(\lambda^2)$ is self-adjoint under the inner product defined in (37), i.e.,

$$\langle \mathbf{u} | \mathbf{A}\mathbf{v} \rangle = \langle \mathbf{v} | \mathbf{A}\mathbf{u} \rangle \quad (40)$$

for arbitrary $\mathbf{u}$ and $\mathbf{v}$.

Obtaining nontrivial λ^2 and $\Delta\boldsymbol{\Psi}$ from (34) is generally unwiedly, because (34) is nonlinear in λ^2. For example, (34) may or may not have nontrivial λ^2 in a given interval $[a, b]$. If it does, (34) may have multiple nontrivial λ^2 sparsely spaced in $[a, b]$ or clustered in a small subinterval of $[a, b]$. Therefore, searching nontrivial λ^2 of (34) in $[a, b]$ can be unwieldly, because an optimal step size is difficult to determine.

To overcome problems as such, an algorithm that will predict nontrivial λ^2 and $\Delta\Psi$ systematically is proposed as follows. Let $\mu(\lambda^2)$ and $\mathbf{v}(\lambda^2)$ be eigenvalues and eigenfunctions of the Fredholm operator $\mathbf{A}(\lambda^2)$ in (34), i.e.,

$$\mathbf{A}(\lambda^2)\mathbf{v}(\lambda^2) = \mu(\lambda^2)\mathbf{v}(\lambda^2). \quad (41)$$

Comparison of (34) with (41) shows that the mth eigenvalue λ_m^2 of C is a zero of $\mu(\lambda^2)$, i.e.,

$$\mu(\lambda_m^2) = 0. \quad (42)$$

In addition, the mth opening shape is $\Delta\boldsymbol{\Psi}_m = \mathbf{v}(\lambda_m^2)$.

6 A Ritz Solution

Exact nontrivial solutions of (34) can be approximated through the method of eigenfunction expansion, for example. Let $\mathbf{e}_1, \mathbf{e}_2, \ldots,$ be an orthonormal basis satisfying orthonormality $\langle \mathbf{e}_i | \mathbf{e}_j \rangle = \delta_{ij}$. Then

$$\Delta\boldsymbol{\Psi} = \sum_{n=1}^{\infty} c_n \mathbf{e}_n = \mathbf{E}\mathbf{c}, \quad (43)$$

where

$$\mathbf{E} = [\mathbf{e}_1, \mathbf{e}_2, \ldots], \quad (44)$$

and

$$\mathbf{c} = [c_1, c_2, \ldots]^T. \quad (45)$$

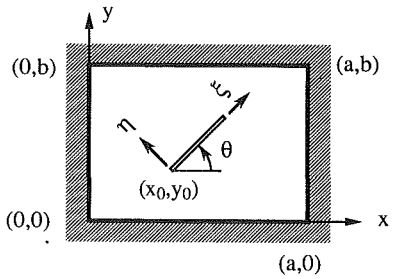


Fig. 2 A fixed rectangular elastic solid under antiplane strain vibration with an oblique internal crack

Substitute (43) into (34), take inner product with $\mathbf{E}^T$, and apply the orthonormality to obtain

$$\mathbf{A}^*(\lambda^2)\mathbf{c} \equiv \sum_{n=1}^{\infty} \frac{\lambda^2 \mathbf{B}_n}{\omega_n^2(\lambda^2 - \omega_n^2)} \mathbf{c} + \mathbf{Q}\mathbf{c} = \mathbf{0}, \quad (46)$$

where

$$\mathbf{B}_n = T^2 \langle \mathbf{E}^T | \mathbf{g}_n \rangle \langle \mathbf{g}_n | \mathbf{E} \rangle, \quad (47)$$

and

$$\mathbf{Q} = \langle \mathbf{E}^T | \mathbf{R}\mathbf{E} \rangle. \quad (48)$$

Similar to (42), nontrivial λ^2 and $\mathbf{c}$ of (46) can be determined as follows. Let $\mu^*(\lambda^2)$ and $\mathbf{v}^*(\lambda^2)$ be eigenvalues and eigenfunctions of $\mathbf{A}^*(\lambda^2)$. $\mu^*(\lambda^2)$ can be calculated numerically as a function of λ^2 if finite terms are retained in (46). Therefore, zeros of $\mu^*(\lambda^2)$ will approximate λ_m^2 of C, and $\Delta\boldsymbol{\Psi} \approx \mathbf{E}\mathbf{v}^*(\lambda_m^2)$. In the sequel, this approximate solution will be called a Ritz solution.

7 A Numerical Example

Consider a rectangular elastic solid under antiplane strain vibration fixed at all boundaries with dimensions a and b. An oblique internal crack is introduced at (x_0, y_0) with length l. The angle between the crack and the x-axis is θ. See Fig. 2. The crack coordinates (ξ, η) are

$$x = x_0 + \xi \cos\theta - \eta \sin\theta$$

$$y = y_0 + \xi \sin\theta + \eta \cos\theta.$$

In addition, eigensolutions of the uncracked solid are

$$\omega_{mn}^2 = c^2 \left[\left(\frac{m\pi}{a} \right)^2 + \left(\frac{n\pi}{b} \right)^2 \right]; \quad c^2 = \frac{T}{\rho} \quad (49)$$

$$\phi_{mn}(\mathbf{r}) = \frac{2}{\sqrt{\rho ab}} \sin\left(\frac{m\pi x}{a} \right) \sin\left(\frac{n\pi y}{b} \right)$$

$$= \frac{1}{\sqrt{\rho ab}} [\cos(A_1\xi + B_1\eta + C_1) - \cos(A_2\xi + B_2\eta + C_2)], \quad (50)$$

where

$$A_1 = \frac{m\pi}{a}\cos\theta - \frac{n\pi}{b}\sin\theta, \quad A_2 = \frac{m\pi}{a}\cos\theta + \frac{n\pi}{b}\sin\theta,$$

$$B_1 = -\frac{m\pi}{a}\sin\theta - \frac{n\pi}{b}\cos\theta, \quad B_2 = -\frac{m\pi}{a}\sin\theta + \frac{n\pi}{b}\cos\theta,$$

$$C_1 = \frac{m\pi x_0}{a} - \frac{n\pi y_0}{b}, \quad C_2 = \frac{m\pi x_0}{a} + \frac{n\pi y_0}{b}.$$

A Ritz solution to approximate λ_m^2 and $\psi_m(\mathbf{r})$ of C is illustrated as follows. $\mathbf{g}_{mn} \equiv [\ldots, \partial\phi_{mn}/\partial n, \ldots]^T$ is determined with

$$\frac{\partial\phi_{mn}}{\partial n} = -\frac{1}{\sqrt{\rho ab}} [B_1 \sin(A_1\xi + C_1) - B_2 \sin(A_2\xi + C_2)]. \quad (51)$$

In addition, $\mathbf{b}_{mn} \equiv [\ldots, \beta_{mn}, \ldots]^T$ is determined with

Downloaded 03 May 2010 to 171.66.16.245. Redistribution subject to ASME license or copyright; see http://www.asme.org/terms/Terms_Use.cfm

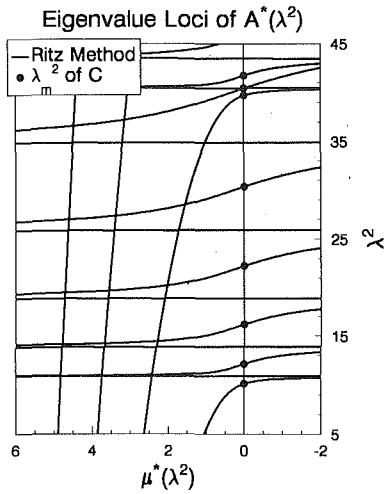


Fig. 3 Eigenvalue loci $\mu^*(\lambda^2)$ of the solid with $(x_0, y_0) = (0, 0)$ and $\theta = 90$ deg

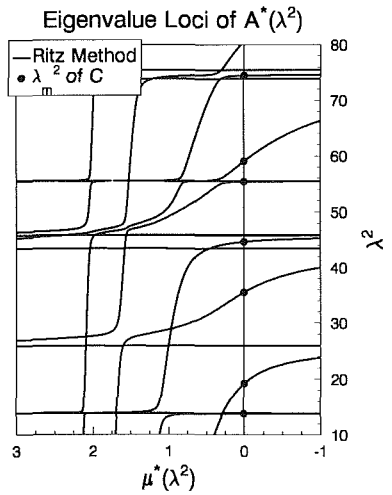


Fig. 4 Eigenvalue loci $\mu^*(\lambda^2)$ of the solid with $(x_0, y_0) = (06, 0.3)$ and $\theta = 45$ deg

$$\beta_{mn}(\xi) = -\frac{T}{\sqrt{\rho ab}}\left[\frac{A_1^2}{B_1}\sin(A_1\xi + C_1) - \frac{A_2^2}{B_2}\sin(A_2\xi + C_2)\right] + \frac{2\rho\omega_{mn}^2}{\sqrt{\rho ab}}\left\{\frac{\sin\frac{B_1\Delta\eta}{2}}{B_1^2\Delta\eta}\sin\left[A_1\xi + C_1 + \frac{B_1}{2}(\eta^+ - \eta^-)\right] - \frac{\sin\frac{B_2\Delta\eta}{2}}{B_2^2\Delta\eta}\sin\left[A_2\xi + C_2 + \frac{B_2}{2}(\eta^+ - \eta^-)\right]\right\} \quad (52)$$

according to (70), (74), and (76) in Appendix A. The operator $\mathbf{R}$ can be formulated through (78) in Appendix B with $\mathbf{g}_{mn}$ and $\mathbf{b}_{mn}$ shown in (51) and (52).

Based on the $\mathbf{g}_{mn}$, $\mathbf{b}_{mn}$, and $\mathbf{R}$ derived above, $\mathbf{B}_{mn}$ and $\mathbf{Q}$ can be calculated through (47) and (48) with $\mathbf{E} = [\mathbf{e}_1, \ldots, \mathbf{e}_5]$, where

$$\mathbf{e}_i(\xi) = \sqrt{\frac{2}{l}}\sin\frac{i\pi\xi}{l},\ i = 1, 2, \ldots, 5. \quad (53)$$

In addition, 324 terms are retained in (46) when calculating eigenvalue loci $\mu^*(\lambda^2)$ of $\mathbf{A}^*(\lambda^2)$.

Figure 3 illustrates eigenvalue loci $\mu^*(\lambda^2)$ of a rectangular solid with $T = \rho = 1$, $a = \pi$, $b = 1$, $(x_0, y_0) = (0, 0)$, $\theta = 90$ deg, $l = 1$, $\eta^+ = 0$, and $\eta^- = \pi$. This corresponds to a rectangular solid with a free end at $x = 0$ whose exact eigensolutions are known. Horizontal lines represent eigenvalues ω_n^2 of P. The zeros of $\mu^*(\lambda^2)$ are circled in Fig. 3 and tabulated in Table 1. Exact eigenvalues are also listed in Table 1 for comparison. They agree very well and the maximum difference is less than one percent. In fact, it can be shown that the exact eigensolutions of the cracked solid satisfy (34).

Table 1 Eigenvalues λ_m^2 of the solid with $(x_0, y_0) = (0, 0)$ and $\theta = 90$ deg

Eigenvalues λ_m^2		Difference
Exact	Ritz Method	in %
10.120	10.122	0.02%
12.120	12.145	0.21%
16.120	16.190	0.44%
22.120	22.257	0.62%
30.120	30.347	0.76%
39.728	39.731	0.02%
40.120	40.460	0.85%
41.728	41.754	0.06%
45.728	45.798	0.15%

Table 2 Eigenvalues λ_m^2 of the solid with $(x_0, y_0) = (0.6, 0.3)$ and $\theta = 45$ deg

ω_n^2	λ_n^2	$\frac{\omega_n^2 - \lambda_n^2}{\omega_n^2}$
13.870	13.811	0.425 %
25.870	19.217	25.717 %
43.478	35.524	18.294 %
45.869	44.688	2.632 %
55.478	55.386	0.166 %
73.869	59.024	20.096 %
75.478	74.497	1.300 %

Figure 4 illustrates eigenvalue loci $\mu^*(\lambda^2)$ of a rectangular solid with $T = \rho = 1$, $a = \pi/2$, $b = 1$, $(x_0, y_0) = (0.6, 0.3)$, $\theta = 45$ deg, $l = 2\sqrt{2}/5$, and $\eta^+ = \eta^- = 0.4$. Horizontal lines represent eigenvalues ω_n^2 of P. The zeros of $\mu^*(\lambda^2)$ are circled in Fig. 3 and tabulated in Table 2. ω_m^2 and change of eigenvalues are both listed in Table 2 for comparison. The change of eigenvalues resulting from the crack can be as large as 25 percent. Figure 5 illustrates eigenfunction $\psi_3(\mathbf{r})$ for $\lambda_3^2 = 35.524$. The thick line in the three-dimensional mode shape highlights

Downloaded 03 May 2010 to 171.66.16.245. Redistribution subject to ASME license or copyright; see http://www.asme.org/terms/Terms_Use.cfm

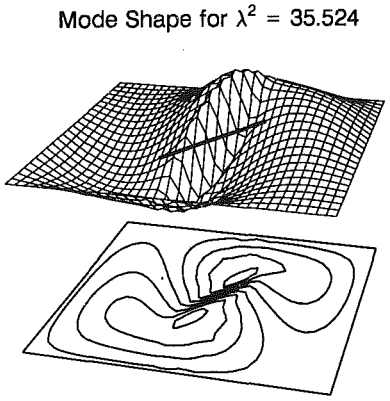


Fig. 5 Eigenfunction $\psi_3(\mathbf{r})$ for $\lambda_3^2 = 35.524$

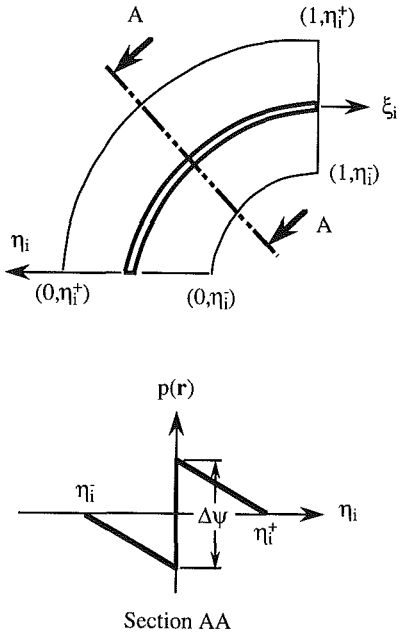


Fig. 6 Curvilinear coordinates on the *i*th crack

the location of the crack. Because eigenfunctions $\phi_n(\mathbf{r})$ are continuous across the crack, the opening shape $\Delta\psi$ of the crack is interpreted in an L_2 sense by the shape gradient of the displacement field across the crack.

8 Conclusions

1 This paper illustrates an analytical algorithm to predict eigensolutions $[\lambda_m^2, \psi_m(\mathbf{r})]_{m=1}^{\infty}$ of a cracked structure C whose response is governed by the two-dimensional Helmholtz equation. $[\lambda_m^2, \psi_m(\mathbf{r})]_{m=1}^{\infty}$ are presented in terms of eigensolutions $[\omega_n^2, \phi_n(\mathbf{r})]_{n=1}^{\infty}$ of a perfect structure P and the crack configuration σ_c. This algorithm is valid for structures of arbitrary shapes and arbitrary cracks, provided that $[\omega_n^2, \phi_n(\mathbf{r})]_{n=1}^{\infty}$ and σ_c are known.

2 Eigenvalues λ_m^2 of C are the zeros of eigenvalue loci $\mu(\lambda^2)$ of the Fredholm integral operator $\mathbf{A}(\lambda^2)$ defined in (34). Eigenfunctions of $\mathbf{A}(\lambda^2)$, evaluated at $\lambda = \lambda_m$, predict the opening shape $\Delta\psi_m$ of C. $\Delta\psi_m$, together with λ_m, will determine eigenfunction $\psi_m(\mathbf{r})$ of C through (17).

3 Eigensolutions of two rectangular elastic solids under antiplane strain vibration, one with a boundary crack and the other with an oblique internal crack, are illustrated through a Ritz solution. Eigensolutions of the solid with the boundary crack agree very well with the exact solutions. The opening shape $\Delta\psi$ of the crack is described in the L_2 sense by the steep gradient of the displacement field across the crack.

Acknowledgments

The author thanks Prof. M. F. Beatty and S. I. Chou for making comments on the manuscript to the author.

References

Cawley, P., and Adams, R. D., 1979, "The Location of Defects in Structures from Measurements of Natural Frequencies," *Journal of Strain Analysis*, Vol. 14, pp. 49–57.

Chen, L.-W., and Chen, C.-L., 1988, "Vibration and Stability of Cracked Thick Rotating Blades," *Computers & Structures*, Vol. 28, pp. 67–74.

Collacott, R. A., 1979, *Vibration Monitoring and Diagnosis*, John Wiley and Sons, New York.

Gladwell, G. M. L., 1986, *Inverse Problems in Vibration*, Dordrecht, Boston.

Grabowski, B., 1980, "The Vibrational Behavior of a Turbine Rotor Containing a Transverse Crack," ASME *Journal of Mechanical Design*, Vol. 102, pp. 140–146.

Gudmundson, P., 1982, "Eigenfrequency Changes of Structures Due to Cracks, Notches or Other Geometrical Changes," *Journal of the Mechanical and Physics of Solids*, Vol. 30, pp. 339–353.

Ju, F. D., and Mimovich, M. E., 1988, "Experimental Diagnosis of Fracture Damage in Structures by the Modal Frequency Method," ASME *Journal of Vibration, Acoustics, Stress, and Reliability in Design*, Vol. 110, pp. 456–463.

Mayes, I. W., and Davies, W. G. R., 1984, "Analysis of the Response of a Multi-Rotor-Bearing System Containing a Transverse Crack in a Rotor," ASME *Journal of Vibration Acoustics, Stress, and Reliability in Design*, Vol. 106, pp. 139–145.

Mote, C. D., Jr., 1972, "Stability Control Analysis of Rotating Plates by Finite Element: Emphasis on Slots and Holes," ASME *Journal of Dynamic Systems, Measurement, and Control*, Vol. 94, pp. 64–70.

Muszyńska, A., 1982, "Shaft Crack Detection," *Seventh Machinery Dynamic Seminar*, Canada.

Nelson, H. D., and Nataraj, C., 1986, "The Dynamics of a Rotor System with a Cracked Shaft," ASME *Journal of Vibration, Acoustics, Stress, and Reliability in Design*, Vol. 108, pp. 189–196.

Nezu, K., and Kidoguchi, H., 1980, "A New Damage Detecting Method by Mechanical Impedance Measurements," *Bulletin of the JSME*, Vol. 23, pp. 2125–2131.

Parker, R. G., and Mote, C. D., Jr., 1991, "Tuning of the Natural Frequency Spectrum of a Circular Plate by In-Plane Stresses," *Journal of Sound and Vibration*, Vol. 145, pp. 95–110.

Petroski, H. J., and Glazik, J. L., Jr., 1980, "The Response of Cracked Cylindrical Shells," ASME JOURNAL OF APPLIED MECHANICS, Vol. 47, pp. 444–446.

Shen, M.-H. H., and Pierre, C., 1990, "Natural Modes of Bernoulli-Euler Beams With Symmetric Cracks," *Journal of Sound and Vibration*, Vol. 138, pp. 115–134.

Stahl, B., and Keer, L. M., 1972, "Vibration and Stability of Cracked Rectangular Plates," *International Journal of Solids and Structures*, Vol. 8, pp. 69–91.

Tang, Z. Q., and Huang, T. C., 1983, "Modal Analysis of a Cylindrical Shell with a Longitudinal Crack," *Modal Testing and Model Refinement*, ASME, AMD-Vol. 59, pp. 77–84.

Wauer, Jörg, 1990, "On the Dynamics of Cracked Rotors: A Literature Survey," ASME *Applied Mechanics Review*, Vol. 43, pp. 13–17.

White, G., 1991, "Amplitude Demodulation—A New Tool for Predictive Maintenance," *Sound and Vibration*, Vol. 25, No. 9, pp. 14–19.

Yu, R. C., and Mote, C. D., Jr., 1987, "Vibration and Parametric Excitation in Asymmetric Circular Plates Under Moving Loads," *Journal of Sound and Vibration*, Vol. 119, pp. 409–427.

APPENDIX A

Evaluation of $\|\nabla\chi\|^2$

The purpose of this appendix is to derive an explicit formula to represent $\|\nabla\chi\|^2$ in terms of $\Delta\psi(\mathbf{r})$. Consider any piecewide continuous function $p(\mathbf{r})$, $\mathbf{r}\in\tau'$, satisfying

Downloaded 03 May 2010 to 171.66.16.245. Redistribution subject to ASME license or copyright; see http://www.asme.org/terms/Terms_Use.cfm

$$\Delta p(\mathbf{r}) = \Delta\psi(\mathbf{r}),\ \mathbf{r}\in\sigma_c, \tag{54}$$

$$\frac{\partial p(\mathbf{r})}{\partial n}\bigg|_{\sigma_c^+} + \frac{\partial p(\mathbf{r})}{\partial n}\bigg|_{\sigma_c^-} = 0,\ \mathbf{r}\in\sigma_c, \tag{55}$$

and boundary conditions

$$p(\mathbf{r}) = 0,\ \mathbf{r}\in\sigma_a, \tag{56}$$

$$\frac{\partial p(\mathbf{r})}{\partial n} = 0,\ \mathbf{r}\in\sigma_b. \tag{57}$$

Expand $p(\mathbf{r})$, through a derivation similar to (27), to obtain

$$p(\mathbf{r}) = \sum_{n=1}^{\infty}\left[\int_{\tau'}\rho p(\mathbf{r})\phi_n(\mathbf{r})d\tau\right]\phi_n(\mathbf{r}) = \chi(\mathbf{r}) + \sum_{n=1}^{\infty}\frac{B_n}{\omega_n^2}\phi_n(\mathbf{r}), \tag{58}$$

where

$$B_n = \int_{\tau'} T\nabla p(\mathbf{r})\cdot\nabla\phi_n(\mathbf{r})d\tau = A_n + \omega_n^2\int_{\tau'}\rho p(\mathbf{r})\phi_n(\mathbf{r})d\tau. \tag{59}$$

Substitute (58) into (32) and recall (8) and (24) to obtain

$$\|\nabla\chi\|^2 = \int_{\tau'} T\nabla p(\mathbf{r})\cdot\nabla p(\mathbf{r})d\tau - \sum_{n=1}^{\infty}\frac{B_n^2}{\omega_n^2}$$

$$= \oint_{\sigma_c} Tp(\mathbf{r})\frac{\partial p(\mathbf{r})}{\partial n}d\sigma - \int_{\tau'} Tp(\mathbf{r})\nabla^2 p(\mathbf{r})d\tau - \sum_{n=1}^{\infty}\frac{B_n^2}{\omega_n^2}. \tag{60}$$

Expand $\nabla^2 p(\mathbf{r})$ in (60) to obtain

$$\nabla^2 p(\mathbf{r}) = \sum_{n=1}^{\infty}\left[\int_{\tau'}\rho\phi_n(\mathbf{r})\nabla^2 p(\mathbf{r})d\tau\right]\phi_n(\mathbf{r}) = -\sum_{n=1}^{\infty}\frac{\rho}{T}B_n\phi_n(\mathbf{r}), \tag{61}$$

where the divergence theorem and (55) to (57) have been used. Substitute (61) into (60) and recall (29) to obtain

$$\|\nabla\chi\|^2 = \sum_{i=1}^{n_c}\int_{\sigma_i^+} T\Delta\psi(\mathbf{r})\frac{\partial p(\mathbf{r})}{\partial n}d\sigma_i - \sum_{n=1}^{\infty}\frac{A_nB_n}{\omega_n^2} \tag{62}$$

where (54) and (55) have been used.

Equation (62) determines $\|\nabla\chi\|^2$ explicitly if the crack geometry is described explicitly. Let ξ_i and η_i be two orthogonal curvilinear coordinates. Let the ith crack be located at $\eta_i(x, y) = 0$ extending from $\xi_i(x, y) = 0$ to $\xi_i(x, y) = l_i$. See Fig. 6. Decompose $p(\mathbf{r})$ as

$$p(\mathbf{r}) = \sum_{i=1}^{n_c} P_i(\mathbf{r}), \tag{63}$$

where $P_i(\mathbf{r})$ is chosen as

$$P_i(\mathbf{r}) = \begin{cases} -\dfrac{\Delta\psi(\xi_i)}{\Delta\eta_i}(\eta_i+\eta_i^-), & -\eta_i^- < \eta_i < 0, \quad 0 < \xi_i < l_i \\ -\dfrac{\Delta\psi(\xi_i)}{\Delta\eta_i}(\eta_i-\eta_i^+), & 0 < \eta_i < \eta_i^+, \quad 0 < \xi_i < l_i \\ 0, & \text{Otherwise,} \end{cases} \tag{64}$$

Here η_i^- and η_i^+ are arbitrary constants such that $\tau_i \equiv \{(\xi_i, \eta_i) | 0 < \xi_i < l_i,\ -\eta_i^- < \eta_i < \eta_i^+\}$, $i = 1, 2, \ldots, n_c$, are disconnected. In addition, $\tau_i \subset \tau$ and $\Delta\eta_i \equiv \eta_i^- + \eta_i^+$, $i = 1, 2, \ldots, n_c$. Notice that $P_i(\mathbf{r})$ satisfies conditions (54) to (57).

Let h_{ξ_i} and h_{η_i} be metric coefficients associated with the curvilinear coordinates ξ_i and η_i, i.e.,

$$h_{\xi_i}(\xi_i, \eta_i) = \sqrt{\left(\frac{\partial x}{\partial\xi_i}\right)^2 + \left(\frac{\partial y}{\partial\xi_i}\right)^2},$$

$$h_{\eta_i}(\xi_i, \eta_i) = \sqrt{\left(\frac{\partial x}{\partial\eta_i}\right)^2 + \left(\frac{\partial y}{\partial\eta_i}\right)^2}. \tag{65}$$

For the ith crack, tensor calculus shows that a length element along the crack is $d\sigma_i = h_{\xi_i}(\xi_i, 0)d\xi_i$ and

$$\frac{\partial P_i(\mathbf{r})}{\partial n} = -\frac{1}{h_{\eta_i}(\xi_i, 0)}\frac{\partial P_i(\mathbf{r})}{\partial\eta_i} = \frac{1}{h_{\eta_i}(\xi_i, 0)}\frac{\Delta\psi(\xi_i)}{\Delta\eta_i}, \tag{66}$$

where (64) is used. Therefore,

$$\sum_{i=1}^{n_c}\int_{\sigma_i^+} T\Delta\psi(\mathbf{r})\frac{\partial p(\mathbf{r})}{\partial n}d\sigma_i = \sum_{i=1}^{n_c}\int_0^{l_i} T\frac{h_{\xi_i}(\xi_i, 0)}{h_{\eta_i}(\xi_i, 0)}\frac{\Delta[\psi(\xi_i)]^2}{\Delta\eta_i}d\xi_i. \tag{67}$$

Similarly,

$$\int_{\tau'}\rho p(\mathbf{r})\phi_n(\mathbf{r})d\tau = \sum_{i=1}^{n_c}\int_0^{l_i}\int_{-\eta_i^-}^{\eta_i^+}\rho P_i(\mathbf{r})\phi_n(\xi_i, \eta_i)h_{\xi_i}h_{\eta_i}d\eta_i d\xi_i. \tag{68}$$

Substitute (64) into (68) to obtain

$$\int_{\tau'}\rho p(\mathbf{r})\phi_n(\mathbf{r})d\tau = -\sum_{i=1}^{n_c}\int_0^{l_i}\rho\frac{\Delta\psi(\xi_i)}{\Delta\eta_i}d\xi_i \times\left\{\int_{-\eta_i^-}^{0}(\eta_i+\eta_i^-)\phi_n(\xi_i, \eta_i)h_{\xi_i}h_{\eta_i}d\eta_i + \int_0^{\eta_i^+}(\eta_i-\eta_i^+)\phi_n(\xi_i, \eta_i)h_{\xi_i}h_{\eta_i}d\eta_i\right\}. \tag{69}$$

In order to simplify (69), define

$$\theta_n(\xi_i, \eta_i) = \int_0^{\eta_i}\phi_n(\xi_i, \zeta_i)h_{\xi_i}(\xi_i, \zeta_i)h_{\eta_i}(\xi_i, \zeta_i)d\zeta_i. \tag{70}$$

Notice that

$$\frac{\partial\theta_n}{\partial\eta_i} = \phi_n(\xi_i, \eta_i)h_{\xi_i}(\xi_i, \eta_i)h_{\eta_i}(\xi_i, \eta_i), \tag{71}$$

and

$$\theta(\xi_i, 0) = 0. \tag{72}$$

Substitute (70) into (69), integrate (69) by parts, and apply the condition (72) to obtain

$$\int_{\tau'}\rho p(\mathbf{r})\phi_n(\mathbf{r})d\tau = \sum_{i=1}^{n_c}\int_0^{l_i}\rho\Delta\psi(\xi_i)\alpha_n(\xi_i)d\xi_i, \tag{73}$$

where

$$\alpha_n(\xi_i) = \frac{1}{\Delta\eta_i}\int_{-\eta_i^-}^{\eta_i^+}\theta_n(\xi_i, \eta_i)d\eta_i. \tag{74}$$

Substitute (67) and (73) into (62) and recall $d\sigma_i = h_{\xi_i}(\xi_i, 0)d\xi_i$ to obtain

$$\|\nabla\chi\|^2 = \sum_{i=1}^{n_c}\int_{\sigma_i^+}\frac{T[\Delta\psi(\xi_i)]^2}{h_{\eta_i}(\xi_i, 0)\Delta\eta_i}d\sigma_i - \sum_{n=1}^{\infty}\frac{A_n}{\omega_n^2}\left[\sum_{i=1}^{n_c}\int_{\sigma_i^+}\Delta\psi(\xi_i)\beta_n(\xi_i)d\sigma_i\right], \tag{75}$$

where

Downloaded 03 May 2010 to 171.66.16.245. Redistribution subject to ASME license or copyright; see http://www.asme.org/terms/Terms_Use.cfm

$$\beta_n(\xi_i)=\frac{\rho\omega_n^2\alpha_n(\xi_i)}{h_{\xi_i}(\xi_i,0)}-\frac{T}{h_{\eta_i}(\xi_i,\,0)}\frac{\partial\phi_n(\xi_i,\,0)}{\partial\eta_i}. \tag{76}$$

APPENDIX B

Explicit Expression of R

The variation of (39) implies that

$$\delta\|\nabla\chi\|^2=2\langle\delta\Delta\Psi\,|\,\mathbf{R}\Psi\rangle. \tag{77}$$

Comparing (77) with the variation of (75) results in

$$\mathbf{R}\Delta\Psi\equiv\mathbf{K}\Delta\Psi-\sum_{n=1}^{\infty}\frac{T}{2\omega_n^2}\,[\mathbf{g}_n\langle\mathbf{b}_n\,|\,\Delta\Psi\rangle+\mathbf{b}_n\langle\mathbf{g}_n\,|\,\Delta\Psi\rangle], \tag{78}$$

where $\mathbf{K}$ is a diagonal matrix

$$\mathbf{K}=\mathrm{diag}[k_1,\,k_2,\,\ldots,\,k_{n_c}];\;k_i=\frac{T}{\Delta\eta_i h_{\eta_i}(\xi_i,\,0)}, \tag{79}$$

and $\mathbf{b}_n$ is a column vector

$$\mathbf{b}_n=[\beta_n(\xi_1),\,\beta_n(\xi_2),\,\ldots,\,\beta_n(\xi_{\eta_c})]^T. \tag{80}$$

Downloaded 03 May 2010 to 171.66.16.245. Redistribution subject to ASME license or copyright; see http://www.asme.org/terms/Terms_Use.cfm

J. Qu
School of Mechanical Engineering,
Georgia Institute of Technology,
Atlanta, GA
Assoc. Mem. ASME

J. L. Bassani
Department of Mechanical Engineering
and Applied Mechanics,
University of Pennsylvania,
Philadelphia, PA 19104-6315
Mem. ASME

Interfacial Fracture Mechanics for Anisotropic Bimaterials

This paper focuses on aspects of fracture mechanics of interface cracks in anisotropic bimaterials. In this case there is a coupling of all three crack-tip fracture modes in the natural interface-crack coordinate system, whereas in the isotropic case, mode 3 is decoupled from modes 1 and 2. This paper intends to shed light on how to interpret the crack-tip fields which are given explicitly along the interface in terms of two (real 3 × 3) bimaterial matrices **W** *and* **D**. *A matric function* **Y** *is defined in terms of* **W** *and* **D** *which determines the coupling and oscillations in the crack-tip fields. Explicit expressions for the crack-tip fields and the associated stress intensity factors are given as well as for the energy release rate. The finite (Griffith) interface crack is considered in detail.*

1 Introduction

This paper focuses on fracture mechanics aspects of interface cracks in anisotropic bimaterials which involves an algebraic complexity that is absent in the isotropic case. As a result, complete analyses of the stress fields have not been carried out in the most general cases of bimaterial anisotropy. This work intends to shed light on how to interpret the near-tip displacement and stress fields, which are shown to have a remarkably simple structure with similarities to the isotropic case. The problem of a finite (Griffith) crack along the interface between two semi-infinite solids is completely solved as an illustrative example. It is found that two (real 3 × 3) bimaterial matrices, **W** and **D**, play a fundamental role in the solution and completely incorporate the influence of material properties on the interface stresses. Explicit expressions are given for the crack-opening displacements and the tractions along the interface, where the components of each are represented in the natural interface-crack coordinate system. Definitions of stress intensity factors as well as the energy release rate also are given explicitly in terms of the loading and the bimaterial constants.

Two-dimensional problems, i.e., $u_i(x_1, x_2)$, $i = 1, 2, 3$, for cracks along an interface between two different isotropic elastic solids have been studied by many investigators (see, e.g., Hutchinson, et al., 1987; Rice, 1988; Suo and Hutchinson, 1988). The elasticity solutions that require both displacement and traction continuity across the bonded interface but neglect contact of the crack faces display (as they do in the anisotropic case) singular crack-tip stresses that oscillate and crack faces that overlap. In the isotropic case, there is a coupling between mode 1 and 2 deformations while mode 3 is decoupled. Three stress intensity factors provide proper characterizing parameters for the near-tip state when the crack-tip contact zone is much smaller than the crack length. In this case the energy release rate is a valid parameter to predict the stability of the crack in the sense of the Griffith-Irwin fracture criterion.

Finite cracks along the interface between anisotropic plates appear first to have been studied by Gotoh (1967). The generalized plane-strain problem of a crack on the interface between two generally anisotropic solids has been considered by Clements (1971), Willis (1971), Ting (1986), Qu and Bassani (1989), Suo (19909), Li and Qu (1990a), and Ni and Nemat-Nasser (1990). A special case of the Griffith problem is solved explicitly by Bassani and Qu (1989), while Suo (1990) and Li and Qu (1990a) have obtained the solution to the general problem.

In Section 2 of this paper, general integral representations for displacement and stress fields in anisotropic elasticity derived by Qu and Bassani (1989) are used to formulate the Griffith crack problem in terms of a Cauchy singular integral equation for the unknown dislocation density. One of the advantages of this formulation is that once the dislocation density is determined, the complete displacement and stress fields can be represented in terms of the dislocation density. Another advantage of this formulation is that it can be easily extended to finite geometries, for example, to an interface crack in a bimaterial strip. The solution to the Cauchy singular integral equation that governs the dislocation density is given in Section 3. Then, the fields along the interface are given explicitly in Section 4 where it is seen that a matrix function **Y**, whose dependence is given explicitly in terms of $\mathbf{D}^{-}\mathbf{W}$, completely specifies the interface tractions while **Y** and **DY** completely specify the crack-opening displacement. Stress intensity factors and energy release rate are defined in Section 5. A general discussion of the oscillatory nature of the crack-tip fields and crack-face contact, specimen size effects, interfacial toughness, and the dependence on material properties

Contributed by the Applied Mechanics Division of THE AMERICAN SOCIETY OF MECHANICAL ENGINEERS for publication in the ASME JOURNAL OF APPLIED MECHANICS.

Discussion on this paper should be addressed to the Technical Editor, Professor Lewis T. Wheeler, Department of Mechanical Engineering, University of Houston, Houston, TX 77204-4792, and will be accepted until four months after final publication of the paper itself in the ASME JOURNAL OF APPLIED MECHANICS.

Manuscript received by the ASME Applied Mechanics Division, Aug. 23, 1990; final revision, July 23, 1991. Associate Technical Editor: M. E. Fourney.

Copyright © 1993 by ASME
Downloaded 03 May 2010 to 171.66.16.245. Redistribution subject to ASME license or copyright; see http://www.asme.org/terms/Terms_Use.cfm

is presented in the last section. Finally, issues concerning superposition giving rise to equivalent crack-tip fields for loading at infinity and loading along the crack surface are discussed in Appendix A.

2 Formulation

The Material Eigenvalue Problem. Consider a generalized two-dimensional deformation of an anisotropic solid in which the three components of displacement depend only on in-plane coordinates, i.e., $u_i = u_i(x_1, x_2)$, $i = 1, 2, 3$, and $\epsilon_{33} = 0$. With the stress-strain relations expressed as $\sigma_{ij} = C_{ijkl}\,\epsilon_{kl}$, the general representations of the displacement and stress fields are given by Qu and Bassani (1989, Eqs. ((2.22)–(2.23)). They show that these two-dimensional anisotropic solutions to the Navier equations depend on the elastic constants C_{ijkl} through three complex 3×3 matrices $\mathbf{P}$, $\mathbf{A}$, and $\mathbf{B}$, where

$$\mathbf{P} = \mathrm{diag}[p_1, p_2, p_3],\ \mathbf{A} = [\mathbf{a}_1, \mathbf{a}_2, \mathbf{a}_3], \tag{1a,b}$$

$$\mathbf{B} = \mathbf{R}^T\mathbf{A} + \mathbf{T}\mathbf{A}\mathbf{P} = -(\mathbf{Q}\mathbf{A} + \mathbf{R}\mathbf{A}\mathbf{P})\mathbf{P}^{-1}, \tag{2a,b}$$

$$\mathbf{Q} = (Q_{ik}) = (C_{i1k1}),$$

$$\mathbf{R} = (R_{ik}) = (C_{i1k2}),$$

$$\mathbf{T} = (T_{ik}) = (C_{i2k2}), \tag{3a,b,c}$$

where in (1a, b), p_n and $\mathbf{a}_n$ are the eigenvalues and the eigenvectors of the following nonlinear eigenvalue problem

$$[\mathbf{Q} + p_n(\mathbf{R} + \mathbf{R}^T) + p_n^2\mathbf{T}]\mathbf{a}_n = \mathbf{0},\ n = 1,3 \tag{4}$$

with the restriction that $\mathrm{Im}\{p_n\} > 0$. Given that C_{ijkl} is positive definite with the usual symmetries, $\mathbf{Q}$ and $\mathbf{T}$ are symmetric and positive definite while $\mathbf{R}$ is not; these three matrices have been introduced by Ting (1986).

Integral Relations for Infinite Bimaterials. Consider an elastic bimaterial of infinite extent. Let x_i, $i = 1, 3$ be the Cartesian interfacial coordinates where the interface lies in the $x_2 = 0$ plane. The elastic constants of the inhomogeneous composite solid are represented as

$$C_{ijkl} = \begin{cases} C^{(1)}_{ijkl}, & x_2 > 0, \\ C^{(2)}_{ijkl}, & x_2 < 0. \end{cases} \tag{5}$$

General integral representations for the displacements and stresses in the infinite bimaterial that vanish at infinity follow from the formal solutions for two-dimensional anisotropic elasticity derived by Bassani and Qu (1989, Eqs. (2.7)–(2.8))

$$\mathbf{u}_1(x_1,x_2) = \overline{\mathbf{A}}_1 \int_0^\infty \mathbf{G}_1(\xi,x_2)\mathbf{g}_1(\xi)\exp(-i\xi x_1)d\xi + \mathbf{A}_1 \int_0^\infty \mathbf{G}_1(-\xi,x_2)\mathbf{g}_1(-\xi)\exp(i\xi x_1)d\xi, \tag{6a}$$

$$\mathbf{u}_2(x_1,x_2) = \mathbf{A}_2 \int_0^\infty \mathbf{F}_2(\xi,x_2)\mathbf{f}_2(\xi)\exp(-i\xi x_1)d\xi + \overline{\mathbf{A}}_2 \int_0^\infty \mathbf{F}_2(-\xi,x_2)\mathbf{f}_2(-\xi)\exp(i\xi x_1)d\xi, \tag{6b}$$

$$\tau_1(x_1,x_2) = -i\overline{\mathbf{B}}_1 \int_0^\infty \xi\mathbf{G}_1(\xi,x_2)\mathbf{g}_1(\xi)\exp(-i\xi x_1)d\xi + i\mathbf{B}_1 \int_0^\infty \xi\mathbf{G}_1(-\xi,x_2)\mathbf{g}_1(-\xi)\exp(i\xi x_1)d\xi, \tag{7a}$$

$$\tau_2(x_1,x_2) = -i\mathbf{B}_2 \int_0^\infty \xi\mathbf{F}_2(\xi,x_2)\mathbf{f}_2(\xi)\exp(-i\xi x_1)d\xi + i\overline{\mathbf{B}}_2 \int_0^\infty \xi\mathbf{F}_2(-\xi,x_2)\mathbf{f}_2(-\xi)\exp(i\xi x_1)d\xi, \tag{7b}$$

where

$$\tau_\alpha(x_1,x_2) = \{\sigma_{21}^{(\alpha)}, \sigma_{22}^{(\alpha)}, \sigma_{23}^{(\alpha)}\}^T,\ \alpha = 1,2, \tag{8}$$

and

$$\mathbf{F}_1(\xi,x_2) = \mathrm{diag}\{\exp(-i\eta_1^{(2)}x_2),\ \exp(-i\eta_2^{(2)}x_2),\ \exp(-i\eta_3^{(2)}x_2)\},$$

$$\mathbf{G}_1(\xi,x_2) = \mathrm{diag}\{\exp(-i\overline{\eta}_1^{(1)}x_2),\ \exp(-i\overline{\eta}_2^{(1)}x_2),\ \exp(-i\overline{\eta}_3^{(1)}x_2)\}, \tag{9a,b}$$

with

$$\eta_n^{(\alpha)} = \begin{cases} p_n^{(\alpha)}\xi, & \xi > 0 \\ \overline{p}_n^{(\alpha)}\xi, & \xi < 0 \end{cases},\ n = 1,2,3;\ \alpha = 1,2. \tag{9c}$$

In (9c), the p_n's are the eigenvalues of (4), and in (6) and (7), $\mathbf{f}_2(\xi)$ and $\mathbf{g}_1(\xi)$ are unknown vectors to be determined by the boundary conditions of a given problem. In Eqs. (6)–(9), the tensor quantities with subscript 1 and 2 correspond to material 1 (upper half-space) and material 2 (lower half-space), respectively, while for components, the materials are distinguished by superscripts in parentheses.

For the problems considered in this paper, tractions must be continuous everywhere along the interface $x_2 = 0$ (including identical traction distributions along the two crack faces). Note that along the interface ($x_2 = 0$), $\mathbf{F}_2 = \mathbf{G}_1 = \mathbf{I}$ in (9a, b), where $\mathbf{I}$ is the 3×3 identity matrix. Thus, continuity of traction across the interface, with (7a, b), implies

$$\overline{\mathbf{B}}_1 \int_0^\infty \xi\mathbf{g}_1(\xi)\exp(-i\xi x_1)d\xi - \mathbf{B}_1 \int_0^\infty \xi\mathbf{g}_1(-\xi)\exp(i\xi x_1)d\xi = \mathbf{B}_2 \int_0^\infty \xi\mathbf{f}_2(\xi)\exp(-i\xi x_1)dx - \overline{\mathbf{B}}_2 \int_0^\infty \xi\mathbf{f}_2(-\xi)\exp(i\xi x_1)d\xi. \tag{10}$$

It is easily seen that (10) is satisfied if

$$\overline{\mathbf{B}}_1\mathbf{g}_1(\xi) = \mathbf{B}_2\mathbf{f}_2(\xi), \tag{11}$$

with

$$\mathbf{f}_2(\xi) = \overline{\mathbf{f}}_2(-\xi),\ \mathbf{g}_1(\xi) = \overline{\mathbf{g}}_1(-\xi). \tag{12a,b}$$

Finally, the jump in displacement along $x_2 = 0$ is defined as

$$\boldsymbol{\Delta}(x_1) = \mathbf{u}_1(x_1,0) - \mathbf{u}_2(x_1,0). \tag{13}$$

From (6) and the traction continuity conditions (11) and (12) it follows that

$$\boldsymbol{\Delta}(x_1) = -(\mathbf{W} - i\mathbf{D})\mathbf{B}_2 \int_0^\infty \mathbf{f}_2(\xi)\exp(-i\xi x_1)d\xi - (\mathbf{W} + i\mathbf{D})\overline{\mathbf{B}}_2 \int_0^\infty \overline{\mathbf{f}}_2(\xi)\exp(i\xi x_1)]d\xi, \tag{14}$$

where

$$\mathbf{W} = -\mathrm{Re}(\mathbf{A}_1\mathbf{B}_1^{-1} - \overline{\mathbf{A}}_2\overline{\mathbf{B}}_2^{-1}),\ \mathbf{D} = -\mathrm{Im}(\mathbf{A}_1\mathbf{B}_1^{-1} - \overline{\mathbf{A}}_2\overline{\mathbf{B}}_2^{-1}) \tag{15a,b}$$

are referred to as interfacial matrices. As noted by Qu and Bassani (1989), $\mathbf{W}$ is real and antisymmetric, $\mathbf{D}$ is real, symmetric and positive definite, while $\mathbf{W} + i\mathbf{D}$ is nonsingular. They are related to the complex interfacial matrix $\mathbf{H} = \mathbf{D} - i\mathbf{W}$ introduced by Suo (1990). Explicit expressions for $\mathbf{W}$ and $\mathbf{D}$ are given at the end of Section 4 for bimaterials composed of orthotropic constituents.

Griffith Interface Crack. Now, consider a Griffith crack of length $2a$ along the interface with the crack fronts parallel

Downloaded 03 May 2010 to 171.66.16.245. Redistribution subject to ASME license or copyright; see http://www.asme.org/terms/Terms_Use.cfm

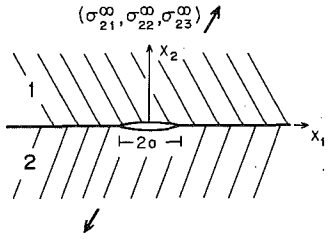


Fig. 1 Two-dimensional configuration for interface crack

to the x_3-axis as depicted in Fig. 1. Through linear superposition, the solution to the Griffith traction-free crack problem corresponding to loading at infinity can be obtained from solutions to two problems, one for an uncracked body and the other for loading along the crack faces by self-equilibrated tractions. However, even in the case of uniform tractions at infinity, e.g., σ_{21}^{∞}, σ_{22}^{∞}, σ_{23}^{∞}, this superposition is simple (in the sense that these same tractions are applied along the crack faces in the latter problem) only if certain combinations of σ_{11}^{∞}, σ_{22}^{∞}, and σ_{12}^{∞} are also applied (Bassani and Qu, 1990). These latter stress components are discontinuous across the interface. Formulas for the combinations of tractions that must be applied for the superposition to be simple are given in Appendix A. In the remainder of this paper, explicit results (e.g., stress intensity factors) given for the Griffith problem correspond to tractions applied along the crack surfaces.

Let the load vector on the upper surface of the crack be $\mathbf{t}(x_1)$ and that on the lower surface of the crack be $-\mathbf{t}(x_1)$. The boundary conditions for the Griffith crack of length $2a$ are

$$\mathbf{u}_1(x_1,0^-)=\mathbf{u}_2(x_1,0^+),\ |x_1|>a, \tag{16}$$

$$\tau_1(x_1,0^-)=\tau_2(x_1,0^+)=-\mathbf{t}(x_1),\ |x_1|<a. \tag{17}$$

Dual Integral Equations. With the tractions $\mathbf{t}(x_1)$ applied along the crack faces according to (17), substitution of (7*b*) or (7*a*) with (11), (12) into (17) gives

$$i\mathbf{B}_2\int_0^{\infty}\xi\mathbf{f}_2(\xi)\exp(-i\xi x_1)d\xi - i\overline{\mathbf{B}}_2\int_0^{\infty}\xi\overline{\mathbf{f}}_2(\xi)\exp(i\xi x_1)d\xi=\mathbf{t}(x_1),\ |x_1|<a. \tag{18}$$

Along $-a<x_1<a$, $\Delta(x_1)$ is the nonzero crack-opening displacement. For displacement continuity along the bonded interface, $|x_1|>a$, $\Delta(x_1)=\mathbf{0}$, so that from (14)

$$(\mathbf{W}-i\mathbf{D})\mathbf{B}_2\int_0^{\infty}\mathbf{f}_2(\xi)\exp(-i\xi x_1)d\xi + (\mathbf{W}+i\mathbf{D})\overline{\mathbf{B}}_2\int_0^{\infty}\overline{\mathbf{f}}_2(\xi)\exp(i\xi x_1)d\xi=\mathbf{0},\ |x_1|>a. \tag{19}$$

Cauchy Integral Equation. Equations (18) and (19) are a pair of vector dual integral equations for the unknown vector $\mathbf{f}_2(\xi)$ which can be transformed into the following single Cauchy singular integral equation (see Appendix B)

$$\mathbf{UWD}^{-1}\mathbf{f}(x_1)-\frac{1}{\pi}\int_{-a}^{a}\frac{\mathbf{U}f(\xi)}{\xi-x_1}d\xi=\mathbf{t}(x_1),\ |x_1|<a, \tag{20}$$

with the auxiliary condition

$$\int_{-a}^{a}\mathbf{f}(\xi)d\xi=\mathbf{0}, \tag{21}$$

which ensures the single-valued displacements. In (20)

$$\mathbf{U}=(\mathbf{D}+\mathbf{WD}^{-1}\mathbf{W})^{-1}, \tag{22}$$

and the unknown dislocation density vector $\mathbf{f}(\xi)$ is given by

$$\mathbf{f}(x_1)=-\frac{d}{dx_1}\Delta(x_1)=-\frac{d}{dx_1}[\mathbf{u}_1(x_1,0^+)-\mathbf{u}_2(x_1,0^-)], \tag{23}$$

which is related to $\mathbf{f}_2$ through

$$\mathbf{f}_2(\xi)=-(2\pi\xi)^{-1}\mathbf{B}_2^{-1}\mathbf{U}(\mathbf{I}-i\mathbf{WD}^{-1})\int_{-a}^{a}\mathbf{f}(t)\exp(i\xi t)dt. \tag{24a}$$

where $\mathbf{I}$ is the identity matrix. It then follows from (11) that

$$\mathbf{g}_2(\xi)=-(2\pi\xi)^{-1}\overline{\mathbf{B}}_1^{-1}\mathbf{U}(\mathbf{I}-i\mathbf{WD}^{-1})\int_{-a}^{a}\mathbf{f}(t)\exp(i\xi t)dt. \tag{24b}$$

The dislocation density $\mathbf{f}(\xi)$ is determined from the solution to the integral equation (20), and then the unknown functions $\mathbf{f}_2$ and $\mathbf{g}_1$ in the general integral representations (6)–(7) are calculated from (24*a*, *b*). The crack opening displacement Δ is calculated from (23), and the full stress field is obtained by substituting (24*a*, *b*) into the general expressions (7*a*, *b*)

$$\tau_1(x_1,x_2)=\frac{1}{\pi}\,\mathrm{Re}\left\{\int_{-a}^{a}\overline{\mathbf{B}}_1\langle(\xi-x_1-\overline{p}_n^{(1)}x_2)^{-1}\rangle\overline{\mathbf{B}}_1^{-1}(i\mathbf{D}^{-1}\mathbf{W}-\mathbf{I})\mathbf{U}\mathbf{f}(\xi)d\xi\right\},$$

$$\tau_2(x_1,x_2)=\frac{1}{\pi}\,\mathrm{Re}\left\{\int_{-a}^{a}\mathbf{B}_2\langle(\xi-x_1-p_n^{(2)}x_2)^{-1}\rangle\mathbf{B}_2^{-1}(i\mathbf{D}^{-1}\mathbf{W}-\mathbf{I})\mathbf{U}\mathbf{f}(\xi)d\xi\right\}. \tag{25a,b}$$

Here and in the sequel, angle brackets denote a 3×3 diagonal matrix, e.g.,

$$\langle h(z_n)\rangle=\mathrm{diag}[h(z_1),\ h(z_2),\ h(z_3)].$$

Note that $\mathbf{f}$ is real so that the traction vector on the interface is obtained from (25)

$$\tau(x_1)=\tau_1(x_1,0)=\tau_2(x_1,0)=-\frac{1}{\pi}\int_{-a}^{a}\frac{\mathbf{U}\mathbf{f}(\xi)}{\xi-x_1}d\xi \tag{26}$$

Equation (20) is for a Griffith interface crack in an infinite bimaterial. For interface crack(s) in a finite bimaterial, the governing Cauchy singular integral equation will have a Fredholm term. Therefore, the dominate part of the solution which governs the crack-tip fields will remain the same.

3 Solutions to the Cauchy Integral Equation

The Cauchy integral Eq. (20) has been solved by Li and Qu (1990a). Below we only give a brief derivation of the solution. The integral Eq. (20) is cast as a Hilbert problem by introducing a sectionally analytical function

$$\Phi(z)=\frac{1}{2\pi i}\int_{-a}^{a}\frac{\mathbf{f}(\xi)}{\xi-z}d\xi,$$

where $z=x_1+ix_2$. It then follows from the Plemelj formulas that

$$\Phi_+(x_1)+\Phi_-(x_1)=\frac{1}{\pi i}\int_{-a}^{a}\frac{\mathbf{f}(\xi)}{\xi-x_1}d\xi,$$

$$\Phi_+(x_1)-\Phi_-(x_1)=\mathbf{f}(x_1), \tag{28a,b}$$

where the conventional notations of Muskhelishvili (1953) have been employed for the boundary values of Φ. The Hilbert problem associated with the Cauchy singular integral equation is obtained by substituting (28) into (20)

$$\mathbf{E}\Phi_+(x_1)+\overline{\mathbf{E}}\Phi_-(x_1)=i\mathbf{t}(x_1),\ -a<x<a, \tag{29}$$

where

Downloaded 03 May 2010 to 171.66.16.245. Redistribution subject to ASME license or copyright; see http://www.asme.org/terms/Terms_Use.cfm

$$\mathbf{E}=\mathbf{U}+i\mathbf{U}\mathbf{W}\mathbf{D}^{-1}=(\mathbf{D}+\mathbf{W}\mathbf{D}^{-1}\mathbf{W})^{-1}(\mathbf{I}+i\mathbf{W}\mathbf{D}^{-1}). \quad (30)$$

It can be shown (Li and Qu, 1990a) that $\mathbf{E}$ is a positive definite Hermitian matrix and $\mathbf{E}^{-1} = \mathbf{D} - i\mathbf{W} = \mathbf{H}$, where $\mathbf{H}$ is the complex interfacial matrix used by Suo (1990).

The solution to the inhomogeneous Hilbert problem (29) is given by Li and Qu (1990a)

$$\mathbf{\Phi}(z)=\frac{1}{2\pi}\mathbf{X}(z)\int_{-a}^{a}\{[\mathbf{X}_{+}^{-1}(\xi)\mathbf{E}^{-1}\mathbf{t}(\xi)]/(\xi-z)\}d\xi, \quad (31)$$

where

$$\mathbf{X}(z)=\mathbf{V}\mathbf{\Lambda}(z)(z^2-a^2)^{-1/2}, \quad (32)$$

$$\mathbf{\Lambda}(z)=\text{diag}\left[\left(\frac{z-a}{z+a}\right)^{i\epsilon},\left(\frac{z-a}{z+a}\right)^{-i\epsilon},1\right], \quad (33)$$

$$\epsilon=(1/2\pi)\ln\left(\frac{1+\beta}{1-\beta}\right),\ \beta=[-(1/2)\text{tr}(\mathbf{W}\mathbf{D}^{-1})^2]^{1/2}. \quad (34a,b)$$

From (34a), $\beta = \tanh(\pi\epsilon)$. In (32), $\mathbf{V} = (\mathbf{v}_1, \mathbf{v}_2, \mathbf{v}_3)$ where $\mathbf{v}_n$ are the eigenvectors of the following eigenvalue problem:

$$[\mathbf{E}\exp(2i\pi\delta_n)+\bar{\mathbf{E}}]\mathbf{v}_n=\mathbf{0},\ n=1,2,3, \quad (35a)$$

where

$$\delta_1=1/2+i\epsilon,\ \delta_2=1/2-i\epsilon,\ \delta_3=1/2. \quad (35b)$$

It is easy to see from (35a,b) that $\mathbf{v}_1 = \bar{\mathbf{v}}_2$ and $\mathbf{v}_3$ is real. Since $\mathbf{E}$ is positive definite, the eigenvectors $\mathbf{v}_n$ in (35) can be normalized such that

$$\bar{\mathbf{V}}^T\mathbf{E}\mathbf{V}=\mathbf{I}+\beta\mathbf{I}_1, \quad (36)$$

where $\mathbf{I}$ is the 3×3 identity matrix and $\mathbf{I}_1 = \text{diag}\,[1, -1, 0]$.

It is seen that the solution (31)–(34) is oscillatory unless $\epsilon = 0$, which corresponds to $\beta = 0$. It has been shown by Qu and Bassani (1989) that $\beta = 0$ if and only if $\mathbf{W} = \mathbf{0}$.

Finally, the dislocation density $\mathbf{f}(x_1)$, which is nonzero in $|x_1| \le a$, is obtained by substituting (31) into (28b)

$$\mathbf{f}(x_1)=\frac{1}{\pi}\mathbf{D}\mathbf{E}\mathbf{X}_{+}(x_1)\int_{-a}^{a}\{[\mathbf{X}_{+}^{-1}(\xi)\mathbf{E}^{-1}\mathbf{t}(\xi)]/(\xi-x_1)\}d\xi+\mathbf{W}\mathbf{t}(x_1). \quad (37)$$

It can be shown by direct integration that the dislocation density $\mathbf{f}(x_1)$ given by (37) indeed satisfies the auxiliary condition (21). From (24a, b), respectively, the functions $\mathbf{f}_2$ and $\mathbf{g}_1$ are calculated in terms of $\mathbf{f}$ and then the displacement and stresses are calculated throughout the body from (6) and (7), respectively.

4 Fields Along the Interface

Tractions. The traction $\tau(x_1)$ on the interface is now readily obtained from (26) and (27),

$$\tau(x_1)=-2i\mathbf{U}\mathbf{\Phi}(x_1),\ |x_1|>a. \quad (38)$$

Substituting of (30), (32)–(34) into (31) and the result into (38) yields the traction on the interface for $x_1 > a$

$$\tau(x_1)=a(x_1^2-a^2)^{-1/2}\mathbf{Y}\left[(1+2i\epsilon)\left(\frac{x_1-a}{x_1+a}\right)^{i\epsilon}\right]\mathbf{q}(x_1), \quad (39)$$

where the generalized load vector is

$$\mathbf{q}(x_1)=\frac{1}{\pi a}\int_{-a}^{a}(a^2-\xi^2)^{1/2}\mathbf{Y}\left[\left(\frac{a+\xi}{a-\xi}\right)^{i\epsilon}\left(\frac{\cosh\pi\epsilon}{1+2i\epsilon}\right)\right]\mathbf{t}(\xi)\frac{d\xi}{1^{x-\xi}}. \quad (40)$$

In (39)–(40) $\mathbf{Y}[\ ]$ is a (real) 3×3 matrix function defined by

$$\mathbf{Y}(\eta)=(\bar{\mathbf{V}}^T)^{-1}\text{diag}[\eta,\bar{\eta},1]\bar{\mathbf{V}}^T \quad (41)$$

where $\mathbf{V}$ is the matrix whose columns are the eigenvectors $\mathbf{v}_n$ in (35a) that are normalized in (36). Obviously, from (41)

$$\mathbf{Y}[\eta_1]\mathbf{Y}[\eta_2]=\mathbf{Y}[\eta_1\eta_2]=\mathbf{Y}[\eta_2]\mathbf{Y}[\eta_1], \quad (42a)$$

and, since $\mathbf{Y}[1] = \mathbf{I}$,

$$\mathbf{Y}^{-1}[\eta]=\mathbf{Y}[1/\eta]. \quad (42b)$$

It has been shown by Li and Qu (1990a) that $\mathbf{Y}[\eta]$ can be written explicitly in terms of $\mathbf{W}$ and $\mathbf{D}$ as

$$\mathbf{Y}[\eta]=\mathbf{I}-\frac{\text{Im}\{\eta\}}{\beta}\mathbf{D}^{-1}\mathbf{W}+\frac{(1-\text{Re}\{\eta\})}{\beta^2}(\mathbf{D}^{-1}\mathbf{W})^2, \quad (43)$$

where $\mathbf{I}$ is the identity matrix. Properties of the matrix function $\mathbf{Y}[\eta]$ are elaborated on below. Here we note that $\mathbf{Y}[\eta]$ is real and dimensionless if η is dimensionless and that as $\beta \to 0$, $\mathbf{D}^{-1}\mathbf{W}/\beta$ is bounded. Furthermore, from (43) $\mathbf{D}\mathbf{Y}[\eta] = \mathbf{Y}^T[\bar{\eta}]\mathbf{D}$.

Dislocation Density and Crack-Opening Displacement. Substitution of (30), (32)–(34) into (37) with (40) and (41) leads to

$$\mathbf{f}(\xi)=-a(a^2-\xi^2)^{-1/2}\mathbf{D}\mathbf{Y}\left[\left(\frac{1+2i\epsilon}{\cosh\pi\epsilon}\right)\left(\frac{a-\xi}{a+\xi}\right)^{i\epsilon}\right]\mathbf{q}(\xi)+\mathbf{W}t(\xi). \quad (44)$$

The crack-opening displacement is obtained from (23) with (44)

$$\mathbf{\Delta}(x_1)=-\int_{a}^{x_1}\mathbf{f}(\xi)d\xi=\int_{x_1}^{a}\mathbf{f}(\xi)d\xi,\ |x_1|<a. \quad (45)$$

When the applied load is uniform, e.g., $\mathbf{t}(\xi) = \mathbf{t}_o$, the crack-opening displacement can be obtained explicitly from (8) by direct integration

$$\mathbf{\Delta}(x_1)=(a^2-x_1^2)^{1/2}\mathbf{D}\mathbf{Y}\left[\left(\frac{a-x_1}{a+x_1}\right)^{i\epsilon}/\cosh\pi\epsilon\right]\mathbf{t}_o,\ |x_1|<a. \quad (46)$$

From (39) and from (44) and (45) (or more simply from (46) when $\mathbf{t} = \mathbf{t}_o$) it can be seen with the help of (40) and (43) that (i) for a general $\mathbf{D}^{-1}\mathbf{W}$, all three components of τ and $\mathbf{\Delta}$ along the interface are oscillatory and coupled to each component of $\mathbf{t}$, and (ii) whenever the components $(\mathbf{D}^{-1}\mathbf{W})_{3i}$ and $(\mathbf{D}^{-1}\mathbf{W})_{i3}$, $i = 1, 3$, vanish then the components σ_{32} and Δ_3 are nonoscillatory and are decoupled from t_1 and t_2. In any case, the oscillations die out for $|x_1| \gg a$. For isotropic bimaterials, the antiplane components are not oscillatory.

The Matrix Function Y. The matrix $\mathbf{Y}$ defined in (41) is fundamental in representing the fields along the interface induced by the traction $\mathbf{t}$ on the crack surfaces. This function is uniquely represented in terms of the real bimaterial matrices $\mathbf{W}$ and $\mathbf{D}$ by (43). Through this representation we are able to write down the crack fields along the interface in the natural interface-crack coordinate system. Recall that the components of τ are σ_{3i} and the components of $\mathbf{\Delta}$ are jumps in u_i, $i = 1, 3$. This is in contrast to the solution of Suo (1990) which is given in a coordinate system whose base vectors are the eigenvectors of the eigenvalue problem (35a). In general, to determine these base vectors the eigenvalue problem (35a) must be solved numerically. Furthermore, explicit expressions for the stress intensity factors, energy release rate and crack-opening displacement can be given in terms of $\mathbf{Y}$ as noted below.

Note from (43) that $\mathbf{Y}[\eta] = \mathbf{I}$ if the crack-tip fields are nonoscillatory ($\mathbf{W} = \mathbf{0}$). When $\mathbf{W} \neq \mathbf{0}$, the arguments for $\mathbf{Y}$ are in the form $\eta = c(1 \pm 2i\epsilon)\xi^{i\epsilon}$ (in the expressions for interface tractions (39), load vector (43), crack-opening displacement (46)–(47), and stress intensity factors given below), where c and ξ are real and depend on material properties only through ϵ. In this case it is straightforward to show that

Downloaded 03 May 2010 to 171.66.16.245. Redistribution subject to ASME license or copyright; see http://www.asme.org/terms/Terms_Use.cfm

$$\mathbf{Y}[c(1\pm 2i\epsilon)\xi^{i\epsilon}]=\mathbf{I}-\frac{c}{\beta}\,[\sin(\epsilon\ln\xi)\pm 2\epsilon\cos(\epsilon\ln\xi)]\mathbf{D}^{-1}\mathbf{W}$$

$$+\frac{c}{\beta^2}\,[1-\cos(\epsilon\ln\xi)\pm 2\epsilon\sin(\epsilon\ln\xi)](\mathbf{D}^{-1}\mathbf{W})^2. \quad (47)$$

Clearly, the matrix product $\mathbf{D}^{-1}\mathbf{W}$ is crucial in representing $\mathbf{Y}$. It can be shown that $\mathbf{D}^{-1}\mathbf{W}$ is nondimensional.

For an orthotropic bimaterial aligned with the interface-crack coordinate system (e.g., a 0/90 deg laminate where the fibers are parallel to the crack front in one material and perpendicular in the other), the eigenvector $\mathbf{v}_3$ in (35) is in the x_3 direction and $\mathbf{W}$ and $\mathbf{D}$ can be given explicitly (Li and Qu, 1990b) as

$$\mathbf{W}=(s_1-s_2)\begin{bmatrix}0 & -1 & 0\\ 1 & 0 & 0\\ 0 & 0 & 0\end{bmatrix}, \quad (48a)$$

$$\mathbf{D}=\begin{bmatrix}D_{11} & 0 & 0\\ 0 & D_{22} & 0\\ 0 & 0 & D_{33}\end{bmatrix}, \quad (48b)$$

where

$$D_{11}=s_1/\eta_1+s_2/\eta_2,$$

$$D_{22}=s_1\rho_1/\eta_1+s_2\rho_2/\eta_2,$$

$$D_{33}=[C_{44}^{(1)}C_{55}^{(1)}]^{1/2}+[C_{44}^{(2)}C_{55}^{(2)}]^{1/2}. \quad (48c)$$

In (48a, b) the constants s_α, η_α and ρ_α (α = 1, 2) are positive and related to the elastic constants of the bimaterial by

$$s_\alpha=[C_{12}^{(\alpha)}+(C_{11}^{(\alpha)}C_{22}^{(\alpha)})^{1/2}]^{-1}, \quad (49a)$$

$$\eta_\alpha=\left[\frac{C_{66}^{(\alpha)}[(C_{11}^{(\alpha)}C_{22}^{(\alpha)})^{1/2}-C_{12}^{(\alpha)}]}{C_{22}^{(\alpha)}[2C_{66}^{(\alpha)}+C_{12}^{(\alpha)}+(C_{11}^{(\alpha)}C_{22}^{(\alpha)})^{1/2}]}\right]^{1/2}, \quad (49b)$$

$$\rho_\alpha=[C_{11}^{(\alpha)}/C_{22}^{(\alpha)}]^{1/2}, \quad (49c)$$

where $C_{ij}^{(\alpha)}$ are the components of the 6 × 6 matrix representation of the elastic moduli for material α = 1, 2. With $\mathbf{W}$ and $\mathbf{D}$ given by (48a, b), it is easy to compute $\mathbf{D}^{-1}\mathbf{W}$ for orthotropic bimaterials

$$\mathbf{D}^{-1}\mathbf{W}=\begin{bmatrix}0 & -\beta'' & 0\\ \beta' & 0 & 0\\ 0 & 0 & 0\end{bmatrix}, \quad (50)$$

where

$$\beta'=(s_1-s_2)/[s_1\rho_1/\eta_1+s_2\rho_2/\eta_2], \quad (51a)$$

$$\beta''=(s_1-s_2)/[s_1/\eta_1+s_2/\eta_2]. \quad (51b)$$

In this case of orthotropy, τ_3 and Δ_3 are nonoscillatory and are zero if g_3 is zero, while in general τ_1, τ_2, Δ_1, and Δ_2 are oscillatory, where the oscillation parameter ϵ in (34) is determined from $\beta=(\beta'\,\beta'')^{1/2}$. From (48) there is oscillation (i.e., $\mathbf{W}=\mathbf{0}$ and $\beta=\epsilon=0$) if $s_1=s_2$.

Special cases, such as cubic and transversely isotropic bimaterials, can be easily obtained from (48)–(51) by specifying a particular relationship among the elastic constants. For example, $\rho_\alpha=1$ for cubic materials, in which case $\beta'=\beta''$. For isotropic bimaterials, $\beta'=\beta''=\beta$, the Dundurs constant and $\mathbf{Y}$ is orthogonal. In general, $\mathbf{Y}$ is not an orthogonal matrix.

5 Fracture Parameters

The singular stress distribution along the interface near $x_1=a$ is readily obtained by letting $x_1\to a^+$ in (39)

$$\tau(x)=(a/2x)^{1/2}\mathbf{Y}[(1+2i\epsilon)(x/2a)^{i\epsilon}]\mathbf{q}_a, \quad (52)$$

where $x=x_1-a>0$ is the distance from the tip along the interface and, from (40), the generalized load vector

$$\mathbf{q}_a\equiv\mathbf{q}(a)=\frac{1}{\pi a}\int_{-a}^{a}\left(\frac{a+\xi}{a-\xi}\right)^{1/2}\mathbf{Y}\left[\left(\frac{\cosh\pi\epsilon}{1+2i\epsilon}\right)\left(\frac{a+\xi}{a-\xi}\right)^{i\epsilon}\right]\mathbf{t}(\xi)\,d\xi. \quad (53a)$$

When $\mathbf{t}(\xi)=\mathbf{t}_o$, which corresponds to constant tractions along the crack faces, the integral in (53a) can be evaluated to give

$$\mathbf{q}_a=\mathbf{q}(a)=\mathbf{t}_o. \quad (53b)$$

The structure of the near-tip stresses (interface tractions) is now clear and, in terms of these stresses, the three fracture modes can be explicitly identified. Form (52) with (43), the three modes are coupled unless $\mathbf{D}^{-1}\mathbf{W}$ is diagonal which is the case iff $\mathbf{W}=\mathbf{0}$ (Qu and Bassani, 1989). In the orthotropic case (50) or the isotropic case with $\beta\neq 0$, modes 1 and 2 are coupled while mode 3 is decoupled from the other two. The coupling of modes can also be seen in terms of the crack-tip opening displacement as noted below.

For general loading, the integration in (45) can be carried out explicitly for $0\le a-x_1\ll a$ to give the crack-tip opening displacement (CTOD) near $x_1=a$

$$\mathbf{\Delta}(-x)\approx[2a(-x)]^{1/2}\mathbf{D}\mathbf{Y}[(-x/2a)^{i\epsilon}/\cosh(\pi\epsilon)]\mathbf{g}_a, \quad (54)$$

where $-x=a-x_1$. Note that it is possible that even in the absence of coupling of the crack-tip stressing modes, i.e., even when $\mathbf{D}^{-1}\mathbf{W}$ is diagonal ($\mathbf{W}=\mathbf{0}$), that the opening modes can be coupled if $\mathbf{D}$ is not diagonal (Bassani and Qu, 1989). The existence of such a case is not known to the authors.

Stress Intensity Factors. From (52) with (42), the crack-tip stress intensity factors are defined as the amplitude of the interface tractions, according to

$$\mathbf{k}=(K_2,K_1,K_3)^T=\sqrt{2\pi}\lim_{x\to 0}\{\sqrt{x}\mathbf{Y}(x^{-i\epsilon})\tau(x)\}$$

$$=\sqrt{\pi a}\;\mathbf{Y}[(1+2i\epsilon)(2a)^{-i\epsilon}]\mathbf{q}_a, \quad (55a)$$

where K_1, K_2, and K_3 are the stress intensity factors corresponding to crack-tip interface stresses σ_{22}, σ_{21}, and σ_{23}, respectively. With (43), (55a) can be expressed as

$$\mathbf{k}=\sqrt{\pi a}\{\mathbf{I}-\beta^{-1}[2\epsilon\cos(\epsilon\ln 2a)-\sin(\epsilon\ln 2a)\mathbf{D}^{-1}\mathbf{W}]$$

$$+\beta^{-2}[1-\cos(\epsilon\ln 2a)-2\epsilon\sin(\epsilon\ln 2a)](\mathbf{D}^{-1}\mathbf{W})^2]\}\mathbf{g}_a. \quad (55b)$$

As noted above, in general, only in the case of isotropic bimaterials is the $\mathbf{Y}$-matrix orthogonal in which case $\mathbf{k}$ is simply a rotation of $\sqrt{\pi a}\mathbf{q}_a$.

In terms of $\mathbf{k}$, the singular part of the interface stress (traction) given in (52) can be expressed as

$$\tau(x)=\mathbf{Y}(x^{i\epsilon})\frac{\mathbf{k}}{\sqrt{2\pi x}}, \quad (56a)$$

or, with (47),

$$\tau(x)=\left[\mathbf{I}-\frac{\sin(\epsilon\ln x)}{\beta}\mathbf{D}^{-1}\mathbf{W}+\frac{1-\cos(\epsilon\ln x)}{\beta^2}(\mathbf{D}^{-1}\mathbf{W})^2\right]\frac{\mathbf{k}}{\sqrt{2\pi x}}. \quad (56b)$$

It should be noted that these stress intensity factors, which give the amplitude of the singular crack-tip stress fields, do not give the ratio of traction components at any point along the interface since $\mathbf{Y}$ is not a diagonal matrix when $\epsilon\neq 0$. Nevertheless, these ratios can be directly computed from (56a) with (55) given the applied load $\mathbf{g}_a$. Therefore, when $\mathbf{W}\neq\mathbf{0}$ care must be taken when associating the stress intensity factors with modes 1, 2, or 3 since in this case the local modes do not correspond to either the local stress ratios along the interface (which continuous vary) or the far-field modes of loading.

The crack-tip opening displacement (CTOD) can also be expressed in terms of the stress intensity factors from (54) with (42)

Downloaded 03 May 2010 to 171.66.16.245. Redistribution subject to ASME license or copyright; see http://www.asme.org/terms/Terms_Use.cfm

$$\Delta(-x)=\mathbf{D}\mathbf{Y}\left[\frac{(-x)^{i\epsilon}}{(1+2i\epsilon)\cosh(\pi\epsilon)}\right]\mathbf{k}\sqrt{2x/\pi}. \qquad (56c)$$

In summary, when $\mathbf{W}\neq\mathbf{0}$ so that the crack-tip stressing modes and the CTOD are coupled, oscillations of each of the stress and CTOD components are not in phase. The ratios of traction components within the singular field are not constant along the interface (see (56*b*)) nor are the CTOD components (see (56*c*)) and, therefore, are not simply given in terms of ratios of the stress intensity factors. Nevertheless, the latter uniquely characterize the singular stress field and the CTOD, while their values depends on the units of measure whenever $\beta\neq 0$ ($\epsilon\neq 0$) due to the terms involving $\ln(2a)$ in (55*c*). Only in cases when the material pair degenerates so that $\mathbf{W}=\mathbf{0}$ ($\beta=0$ and $\epsilon=0$) does $\mathbf{k}$ have proper units and reduce to the classical definition of stress intensity factors. Even when $\mathbf{W}\neq\mathbf{0}$, stress intensity factors with proper units can be defined by introducing an arbitrary length scale as Shih and Asaro (1988) suggested.

For orthotropic bimaterials, $\mathbf{D}^{-1}\mathbf{W}$ is given in (50) with (49) and (51). In this case, with uniform tractions along the crack faces, i.e., $\mathbf{q}_a=\mathbf{t}_o=(t_{o1},t_{o2},t_{o3})^T=(\sigma_{21},\sigma_{22},\sigma_{23})^T$, the stress intensity factors are

$$K_1=\sqrt{\pi a}[c't_{o2}+(\beta''/\beta')c''t_{o1}], \qquad (57a)$$

$$K_2=\sqrt{\pi a}[c't_{o1}+(\beta'/\beta'')c''t_{o2}], \qquad (57b)$$

$$K_3=\sqrt{\pi a}t_{o3}, \qquad (57c)$$

where β' and β'' are given in (51) and

$$c'=\cos[\epsilon\ln(2a)]+2\epsilon\sin[\epsilon\ln(2a)], \qquad (57d)$$

$$c''=\sin[\epsilon\ln(2a)]-2\epsilon\cos[\epsilon\ln(2a)], \qquad (57e)$$

and ϵ is given in (34). Once again we note that in this orthotropic case that modes 1 and 2 are coupled while mode 3 is decoupled.

It is straightforward to show from (57) that for the isotroic case

$$K_1+iK_2=\sqrt{\pi}\cosh(\pi\epsilon)(k_1+ik_2)=K \qquad (58)$$

where k_1 and k_2 are the stress intensity factors introduced by Rice and Sih (1965) and K is the complex stress intensity factor introduced by Hutchinson et al. (1987).

Another definition of the stress intensity factors for the case of general bimaterial anisotropy has been introduced by Suo (1990) (also see Willis, 1971) which agree uniquely with those given above when $\mathbf{W}\neq\mathbf{0}$ only if each material is isotropic (they can be chosen to agree in the orthotropic case discussed above or, of course, in the degenerate case when $\mathbf{W}=\mathbf{0}$, in which case $\mathbf{Y}=\mathbf{I}$ and $\beta=0=\epsilon$). The stress intensity factors defined in (55) are based on the physical components of the traction vector, i.e., σ_{21}, σ_{22}, and σ_{23} along the interface which are associated with the in-plane shear, tensile and antiplane shear interface fracture modes. Suo's definition is based on components of the traction vector in a coordinate system whose base vectors are the orthogonal eigenvectors $\mathbf{v}_n$, $n=1,3$ in (35) (which Suo, 1990, labels $\mathbf{w}$, $\bar{\mathbf{w}}$, and $\mathbf{w}_3$). The reason for this choice is mathematical convenience in the sense that the component of the interface traction in the direction of the third vector $\mathbf{v}_3$ (or $\mathbf{w}_3$) is nonoscillatory. Nevertheless, These vectors, which generally do not lie normal to or in the interface (crack) plane, are only known through the solution of the eigen problem (35). (In the isotropic case, $\mathbf{v}_3$ lies along the crack front and the in-plane interface crack fields are decoupled from the nonoscillatory antiplane field.)

In contrast, with the particular choice of the stress intensity factors $\mathbf{k}=(K_2,K_1,K_3)$ given in (55), there is no need to solve the eigenvalue problem (35) to determine the crack-tip interface stresses σ_{21}, σ_{22}, and σ_{23} and the CTOD's Δ_2, Δ_1, and Δ_3. Furthermore, these stress intensity factors are related explicitly to the applied tractions $\mathbf{t}$ through $\mathbf{q}_a$ in (53). Given $\mathbf{t}$ and the bimaterial matrices $\mathbf{W}$ and $\mathbf{D}$ then $\mathbf{k}$, τ, and Δ are given explicitly in (52)–(56). The matrix function $\mathbf{Y}$, which is given explicitly in (43) in terms of $\mathbf{D}^{-1}\mathbf{W}$, plays an important role in determining the solution along the interface.

Stress intensity factors of the classical type, i.e, having dimensions of stress times square root of length, also can be defined, for example as

$$\mathbf{k}_R\equiv\mathbf{Y}[R^{i\epsilon}]\mathbf{k}=\sqrt{\pi a}\mathbf{Y}[(R/2a)^{i\epsilon}(1+2i\epsilon)]\mathbf{q}_a, \qquad (59)$$

where R is a characteristic length parameter. As suggested by Rice (1988) for the isotropic case, $\mathbf{k}_R$ defined by (59) should be referred to as the classical stress intensity factors based on the characteristic length R. One natural choice for R is, of course,the crack length (Li and Qu, 1990a; also see Shih and Asaro (1988) for the isotropic case). For $R=2a$, for the Griffith crack one has from (59) with (43)

$$\mathbf{k}_R=\sqrt{\pi a}\mathbf{Y}[1+2i\epsilon]\mathbf{q}_a=\sqrt{\pi a}\left[\mathbf{I}-\frac{2\epsilon}{\beta}\mathbf{D}^{-1}\mathbf{W}\right]\mathbf{q}_a. \qquad (60)$$

For any R, in terms of $\mathbf{k}_R$, from (56*a*) with (59) the singular stress field is given by

$$\tau(x)=\mathbf{Y}[(x/R)^{i\epsilon}]\frac{\mathbf{k}_R}{\sqrt{2\pi x}}. \qquad (61)$$

From the expression for $\mathbf{Y}$ given in (47), (61) can be written alternatively as

$$\tau(x)=\left\{\mathbf{I}-\frac{\sin[\epsilon\ln(x/R)]}{\beta}\mathbf{D}^{-1}\mathbf{W}+\frac{1-\cos[\epsilon\ln(x/R)]}{\beta^2}(\mathbf{D}^{-1}\mathbf{W})^2\right\}\frac{\mathbf{k}_R}{\sqrt{2\pi x}}. \qquad (62)$$

It is seen from (61)–(62) that the stress intensity vector $\mathbf{k}_R$ defined by (59) does have the dimension of stress times square root of length. The disadvantage of this definition is that $\mathbf{k}_R$ alone can not uniquely specify the singular field, the length parameter R is also required. Again, for isotropic bimaterials, when R is taken to be the crack length,

$$\mathbf{k}_R=\sqrt{\pi a}\begin{bmatrix}1 & -2\epsilon & 0\\ -2\epsilon & 1 & 0\\ 0 & 0 & 1\end{bmatrix}\mathbf{t}_o. \qquad (63)$$

These are the stress intensity factors introduced by Shih and Asaro (1988).

Energy Release Rate. Now assume that under load the crack tip at $x_1=a$ advances along the interface to $x_1=a+\delta a$. The energy release rate per unit thickness (the decrease of the strain energy associated with the vanishes of tractions on the newly formed free surfaces) during this process is defined by

$$G=\frac{1}{2}\operatorname*{Lim}_{\delta a\to 0}\int_a^{a+\delta a}\tau^T(x)\Delta\mathbf{u}(x-\delta a)dx. \qquad (65)$$

Substituting (52) and (54) into (65) and carrying out the integration, we obtain an expression for G that is quadratic in the generalized load $\mathbf{q}_a$ given in (53)

$$G=\frac{\pi a}{4}\mathbf{q}_a^T\mathbf{D}\mathbf{Y}\left[\frac{1+4\epsilon^2}{\cosh^2\pi\epsilon}\right]\mathbf{q}_a, \qquad (66)$$

which can be further simplified using (43) with $\beta=\tanh(\pi\epsilon)$ and the fact that $\mathbf{W}$ is antisymmetric,

$$G=\frac{\pi a}{4}[\mathbf{q}_a^T\mathbf{D}\mathbf{q}_a-g'(\mathbf{W}\mathbf{q}_a)^T\mathbf{D}^{-1}(\mathbf{W}\mathbf{g}_a)], \qquad (67a)$$

where

$$g'=1-4\epsilon^2/\sinh^2(\pi\epsilon). \qquad (67b)$$

Downloaded 03 May 2010 to 171.66.16.245. Redistribution subject to ASME license or copyright; see http://www.asme.org/terms/Terms_Use.cfm

Note that the second quadratic term on the right-hand side of (67*a*) vanishes in the case of no oscillations, i.e., $\mathbf{W} = \mathbf{0}$, or when $\mathbf{W} \neq \mathbf{0}$ and $\mathbf{W}\mathbf{q}_a = \mathbf{0}$, otherwise it is positive, since $\mathbf{D}$ is positive definite and (one can show that) $0 < g' < 1$. This has the following implication. Qu and Bassani (1989) have shown that $\beta = 0$ iff $\mathbf{W} = \mathbf{0}$, i.e., the singular field is non-oscillatory iff $\mathbf{W} = \mathbf{0}$. Thus, if the β effect is neglected, as suggested by Hutchinson et al. (1987), then the energy release rate computed generally will be greater than the actual value given in (67*a*). This holds for both isotropic and anisotropic bimaterials.

Using (55*a*) $\beta = \tanh(\pi\epsilon)$, and the two relations noted in Section 4, namely $\mathbf{Y}^{-1}[\eta] = \mathbf{Y}[1/\eta]$ from (42*b*) and $\mathbf{D}\mathbf{Y}[\eta] = \mathbf{Y}^T[\overline{\eta}]\mathbf{D}$, the energy release rate (66) is expressed in terms of the stress intensity factors as

$$G = \frac{1}{4}\mathbf{k}^T\mathbf{U}^{-1}\mathbf{k} = \frac{1}{4}\mathbf{k}_R^T\mathbf{U}^{-1}\mathbf{k}_R. \tag{68}$$

where $\mathbf{U}^{-1} = \mathbf{D} + \mathbf{W}\mathbf{D}^{-1}\mathbf{W}$ as given in (22). Again, we note that the energy release rate given by Suo (1990) in terms of the stress intensity factors (and essentially that given by Willis, 1971) explicitly involves the eigenvectors $\mathbf{v}_n$ of (35). On the other hand, the definition of the stress intensity factors introduced in (55) or (59) leads to the simple expression of the energy release rate G given in (68). Thus, the eigenvalue problem (35) is circumvented, and the expression for G only involves the stress intensity factors and bimaterial matrices $\mathbf{W}$ and $\mathbf{D}$.

6 Other Issues of Interfacial Fracture Mechanics

Oscillatory Fields and Small-Scale Contact. It is seen clearly from (56*b*) and (56*c*) with (47) that the singular stress and strain fields and the crack-tip opening displacement are oscillatory if $\beta \neq 0$ ($\epsilon \neq 0$). In each case, the $\mathbf{Y}$ matrix modulates the usual $x^{\mp i\epsilon}$ variation of these crack-tip fields. From the expression for the interface traction given in (62) with (43), we note that: (i) the modulation is slow and nearly linear in regions where $|\epsilon \ln(x/R)| < \pi/2$, (ii) the third term in $\mathbf{Y}$ involving $(\mathbf{D}^{-1}\mathbf{W})^2$ is negligible compared to the other two if $|\epsilon \ln(x/R)|$ is sufficiently small, and (iii) $\mathbf{Y} \simeq \mathbf{I}$ if $|\epsilon \ln(x/R)| \ll 1$. Within the crack-tip asymptotic field but outside of the region of oscillations, i.e.,the range of x satisfying (iii), from (56*a*) $\tau(x) \simeq \mathbf{k}/\sqrt{2\pi x}$ and from (56*c*) $\Delta(-x) \simeq \mathbf{D}\mathbf{k}\sqrt{2x/\pi}$. That is, in this range of x the interface tractions are parallel to $\mathbf{k}$ while the CTOD is parallel to $\mathbf{D}\mathbf{k}$. Recall, for the orthotropic bimaterial considered at the end of Section 4, where the principal axes of orthotropy are aligned with the interface-crack coordinate system, that $\mathbf{D}$ is a diagonal matrix (including the isotropic case where $D_{11} = D_{22}$) while in the general anisotropic case $\mathbf{D}$ is not diagonal (but is symmetric and positive definite). This fact has implications regarding mixed-mode interfacial toughness which is discussed as follows.

Oscillations in the crack-tip displacements imply that Δ_2 can be negative, which is physically implausible and leads to the expectation that the crack faces are in contact near the tip (see, e.g., Comninou, 1977; Aravas and Sharma, 1990; Ni and Nemat-Nasser, 1990). The classical boundary value problems with prescribed crack-face tractions (such as those posed in this paper; see, e.g., (17)) do not account for the possibility of crack face contact in the sense that the resulting crack face tractions depend on the solution in the contact region. Following Rice (1988) and Anderson (1989), the size of the contact zone can be estimated from the expressions for the crack-tip opening displacement given above. For example, from the general expressions (45) with (44), or from the expression for uniform applied tractions (46), or from the asymptotic expressions (54) or (56*c*), the contact zone size is estimated as the maximum value of x (the distance from the crack tip) in the range $0 < x < a$ for which $\Delta_2 = 0$. So long as this contact zone size is significantly less than characteristic specimen dimensions, such as crack length, then the solutions derived in this paper are physically relevant in small-scale yielding. This requirement will generally be met if there is a significant tensile component (t_2) of the applied traction; it will not when the loading is dominated by shear.

Recently, based on complete analyses of several specimen geometries for isotropic bimaterials, Hutchinson and his colleagues (see, e.g., Hutchinson, 1989; Suo and Hutchinson, 1988) proposed to systematically take $\beta = 0$ ($\epsilon = 0$), both in the determination of critical toughness data and in the use of this data to predict fracture. This notion of ignoring β grew from the fact that for many bimaterial combinations of interest β is very small (Suga et al., 1988) and that the dependence of the stress intensity factors on β is weak for the geometries that have beeh analyzed. The conditions under which this proposition is valid require further investigation. Recall, from (67), that neglecting β, with everything else the same, tends to overestimate the energy release rate.

In general anisotropic case, both far-field in-plane and antiplane shear lead to nonzero Δ_2 in contrast to the isotropic case or when $\mathbf{v}_3$ in (35) is in the x_3 direction in which cases antiplane shear modes are decoupled from the other two. When $\epsilon = 0$ ($\beta = 0$) in (56) or (61), one eliminates the oscillations and, consequently, the near-tip stress intensity vector is in phase with the interfacial traction, i.e., τ and $\mathbf{k}$ (or $\mathbf{k}_R$) are in the same direction. The mode coupling, nevertheless, still exists through (55) or (59) in the sense that normal loading will induce shear traction on the interface.

Size Effects. To consider the coupled effects of specimen size and load phase, for simplicity, let $\mathbf{t} = \mathbf{t}_o$. Then it follows from (55) that

$$\mathbf{k} = \sqrt{\pi a}\,\mathbf{Y}[(1 + 2i\epsilon)(2a)^{-i\epsilon})]\mathbf{t}_o. \tag{69}$$

Suppose one wishes to duplicate the near-tip state on another test specimen with a crack of length $2a'$ under loading $\mathbf{t}_o'$. To do so, the load $\mathbf{t}_o'$ must be adjusted such that $\mathbf{k}' = \mathbf{k}$, since the near-tip stress field is uniquely specified by $\mathbf{k}$. This implies, by using (42) that $\mathbf{t}_o'$ must be related to $\mathbf{t}_o$ through

$$\mathbf{t}_o' = (a/a')^{1/2}\mathbf{Y}[(a'/a)^{i\epsilon}]\mathbf{t}_o. \tag{70}$$

Obviously, when $\epsilon = 0$, one need only to rescale the magnitude of $\mathbf{t}_o$ to obtain $\mathbf{t}_o'$. No phase change is needed. However, when $\epsilon \neq 0$, not only the magnitude $\mathbf{t}_o$ has to be changed, but also its phase angle, as has been pointed out by Rice (1988) for the isotropic case. For isotropic bimaterials, $\mathbf{Y}$ is an orthogonal matrix. Therefore, the phase change is independent of $\mathbf{t}_o$, i.e., once the crack length ratio a'/a is given, the change in phase angle is a constant. For anisotropic bimaterials, the matter becomes more complicated since $\mathbf{Y}$, in general, is not an orthogonal matrix. Thus, for a given crack length ratio a'/a, the change in phase angle depends on $\mathbf{t}_o$ as well. Furthermore, the change in magnitude in not simply proportional to $(a/a')^{1/2}$.

Interfacial Toughness. For isotropic bimaterials, the in-plane and antiplane deformations are decoupled. Under the in-plane deformation, toughness is defined by the critical value of the energy release rate, G_c, as a function of Ψ (Hutchinson, 1990), where Ψ is the phase angle corresponding to the ratio of the in-plane shear and tensile crack-tip modes. The G_c-Ψ curve gives the in-plane toughness locus. For three simultaneous modes another angle must be introduced. In this case one might choose Ψ and another angle Φ to be the Euler angles in $\mathbf{k}$ space such that

$$\mathbf{k} \equiv (K_2, K_1, K_3) = \|\mathbf{k}\|(\sin\Phi\cos\Psi, \sin\Phi\sin\Psi, \cos\Phi)^T, \tag{71}$$

with $0 \leq \Phi \leq \pi$ and $0 \leq \Psi \leq 2\pi$. (Jensen et al. (1990), in defining Ψ and Φ for isotropic bimaterials, include a factor

Downloaded 03 May 2010 to 171.66.16.245. Redistribution subject to ASME license or copyright; see http://www.asme.org/terms/Terms_Use.cfm

multiplying K_3 in (71), which depends on material properties through the ratio of the coefficient of K_3^2 to the coefficient of $(K_1^2 + K_2^2)$ in the expression for G and is on the order of unity. Analogous factors can be introduced in the anisotropic case but will not be elaborated on here.) Crack-tip mode mixity is uniquely specified once the values of Ψ and Φ are given so that critical values of G can be expressed as a function of Ψ and Φ, i.e.,

$$G_c = G_c(\Psi, \Phi). \tag{72}$$

In general (see Hutchinson, 1990), the interfacial toughness increases as the shear components of the mode mixity increase. For example, for in-plane loading of isotropic bimaterials, G_c tends to increase as $|\Psi|$ increases. Presumably, in most cases this is due to a resistance to relative sliding of the crack surfaces when there is some contact of those surfaces.

For anisotropic bimaterials, all three fracture modes are coupled so that one must expect, in general, that the variation of interfacial toughness with mode mixity is a function of two parameters. The question arises as to how best define mode mixity. One possibility is given above in (71). Alternatively, if the resistance to relative sliding of the crack surfaces is most directly responsible for variations in G_c with mode mixity then it may be best to define the mode mixity angles in terms of the CTOD direction. Of course, near the crack tip where $\boldsymbol{\Delta}$ oscillates the direction also oscillates while, as noted above, for $|\epsilon \ln(x/R)| \ll 1$ where $\mathbf{Y} \simeq \mathbf{I}$, $\boldsymbol{\Delta}(-x) \simeq \mathbf{D}\mathbf{k}\sqrt{2x/\pi}$. Therefore, for the purpose of unifying variations in G_c for different bimaterial systems, mode mixity might best be defined in terms of the direction of $\boldsymbol{\Delta}$ as

$$\mathbf{D}\mathbf{k} = \|\mathbf{D}\mathbf{k}\|(\sin\Phi\cos\Psi, \sin\Phi\sin\Psi, \cos\Phi)^T. \tag{73}$$

Whether classification of mode mixity in terms of these Euler angles or those defined in terms of $\mathbf{k}$ in (71) or some other choice is most appropriate requires experimental investigation and is outside the scope of this paper. Nevertheless, there is intuitive appeal to the choice (73) based upon the effects of relative sliding of the crack surfaces without significant opening on interfacial toughness. Finally, we also note that in the isotropic case (73) is consistent with the definition for Ψ and Φ adopted by Jensen et al. (1990).

Material Dependence. It was shown by Dundurs (1969) that the two-dimensional stress field in an isotropic bimaterial composite depends on the material constants through only two nondimensional parameters, namely α and β, if only traction boundary conditions are given. Recently, Hutchinson and his colleagues demonstrated that for some interface crack problems the effect of β is negligible. The parameter α is more important. Naturally, one would ask if there are counterparts of α and β in anisotropic bimaterial.

By analogy, it is easy to see that the β defined in (34*b*) is the anisotropic version of Dundurs' β since it enters the solution in the same manner with respect to oscillations and it reduces to the same value when the bimaterial is composed of isotropic solids. However, to find the anisotropic counterpart of Dundurs α is not easy because, as observed by Hutchinson, α does not enter the interface traction solution for an interface crack in an infinite isotropic bimaterial.

First of all, one has to realize that the reduction of material dependence for isotropic bimaterial is valid only for plane deformation, i.e., plane strain or plane stress. However, as discussed in the Introduction, plane-strain and plane-stress deformations are well defined if and only if the bimaterial has a plane of symmetry, i.e., monoclinic bimaterial. Therefore, identifying the anisotropic counterpart of α is meaningful if and only if the bimaterial is monoclinic. If the plane of symmetry is taken to be the x_1-x_2 plane, then the in-plane and antiplane deformations are decouple in the crack-interface coordinate system (Qu and Basani, 1989). In this case, again by analogy with the isotropic solutions for displacement and energy release rate, one may define c_1 and c_2 (see Rice, 1988) such that

$$c_1 + c_2 = D_{11} + D_{22} \tag{74}$$

where D_{11} and D_{22} are the diagonal element of $\mathbf{D}$. The anisotropic α is defined by

$$\frac{1+\alpha}{1-\alpha} = \frac{c_1}{c_2}. \tag{75}$$

It can be shown that the anisotropic α defined by (74) reduces to Dundurs' α for isotropic materials.

Acknowledgment

This work was supported by the NSF/MRL program at the University of Pennsylvania under Grant DMR 8519059.

References

Anderson, P. M., 1988, "Small Scale Contact Conditions for the Linear-Elastic Interface Crack," ASME JOURNAL OF APPLIED MECHANICS, Vol. 55, pp. 814–817.

Aravas, N., and Sharma, S. M., 1990, "An Elastoplastic Analysis of the Interface Crack with Contact Zones," *J. Mech. Phys. Solids*, to appear.

Bassani, J. L., and Qu, J., 1989, "Finite Crack on Bimaterial and Bicrystal Interfaces," *J. Mech. Phys. Solids*, Vol. 37, pp. 435–454.

Bassani, J. L., and Qu, J., 1990, "Interfacial Discontinuities and Average Bimaterial Properties," *Acta/Scripta Metallurgica Proceedings Series*, Vol. 4, pp. 401–406.

Clements, D. L., 1971, "A Crack Between Dissimilar Anisotropic Media," *Int. J. Engng. Sci,*, Vol. 9, pp. 257–265.

Comninou, M., 1977, "The Interface Crack," ASME JOURNAL OF APPLIED MECHANICS, Vol. 44, pp. 631–636.

Erdogan, F., 1968,"Simultaneous Dual Integral Equations with Trignometric and Bessel Kernels," *ZAMM*, Vol. 48, pp. 217–225.

Gotoh, M., 1967, "Some Problems of Bonded Anisotropic Plates with Cracks Along the Bond," *Int. J. Fracture Mech.*, Vol. 3, pp. 253–260.

Hill, R., 1972, "An Invariant Treatment of Interfacial Discontinuities in Elastic Composites," *Continuum Mechanics and Related Problems of Analysis*, L. I. Sedov, ed., Academy of Sciences, USSR, pp. 597–604.

Hutchinson, J. W., "Mixed Mode Fracture Mechanics of Interfaces," *Acta/Scripta Metallurgica Proceedings Series*, Vol. 4, pp. 295–306.

Hutchinson, J. W., Mear, M., and Rice, J. R., 1987, "Crack Paralleling an Interface Between Dissimilar Materials," ASME JOURNAL OF APPLIED MECHANICS, Vol. 54, pp. 828–832.

Jensen, H. M., Hutchinson, J. W., and Kim, K.-S., 1990, "Decohesion of a Cut Prestressed Film on a Substrate," *Int. J. Solids Struct.*, Vol. 26, pp. 1099–1114.

Li, Q. Q., and Qu, J., 1990a, "Interfacial Dislocation and Its Applications to Interface Crack in Anisotropic Bimaterials," *J. Elasticity*, to appear.

Li, Q. Q., and Qu, J., 1990b, "Interface Crack in Anisotropic Bimaterials Under Plane-Strain Deformation: I—The Classical Solutions," in progress.

Muskhelishvili, N. I., 1953, *Singular Integral Equations*, P. Noordhoff Ltd., Groningen, Holland.

Ni, L., and Nemat-Nasser, S., "Interface Crack in Anisotropic Dissimilar Materials: An Analytic Solution," Applied Mechanics and Engineering Science, University of California at San Diego, San Diego, CA.

Qu, J., and Bassani, J. L., 1989, "Cracks on Bimaterial and Bicrystal Interfaces," *J. Mech. Phys. Solids*, Vol. 37, pp. 417–433.

Rice, J. R., 1988, "Elastic Fracture Mechanics Concepts for Interfacial Cracks," ASME JOURNAL OF APPLIED MECHANICS, Vol. 55, pp. 98–103.

Rice, J. R., and Sih, G. C., 1965, "Plane Problem of Cracks in Dissimilar Media," ASME JOURNAL OF APPLIED MECHANICS, Vol. 32, pp. 418–423.

Shih, C. F., and Asaro, R. J., 1988, "Elastic-Plastic Analysis of Cracks on Bimaterial Interfaces: Part I—Small Scale Yielding," ASME JOURNAL OF APPLIED MECHANICS, Vol. 55, pp. 229–316.

Suga, T., Elssner, G., and Schmauder, S., 1988, "Composite Parameters and Mechanical Compatibility of Material Joints," *J. Comp. Mat.*, Vol. 22, pp. 917–934.

Suo, Z., 1990, "Singularities, Interfaces and Cracks in Dissimilar Anisotropic Media," *Proc. Royal Soc. London*, Vol. A447, pp. 331–358.

Suo, Z., and Hutchinson, J. W., 1988, "On Sandwich Test Specimens for Measuring Interface Crack Toughness," *Mater. Sci. Engng.*, Vol. A107, pp. 135–143.

Ting, T. C. T., 19 , "Explicit Solutions and Invariance of the Singularities at an Interface Crack in Anisotropic Composites," *Int. J. Solids Struct.*, Vol. 18, pp. 139–152.

Willis, J. R., 1971, "Fracture Mechanics of Interfacial Cracks," *J. Mech. Phys. Solids*, Vol. 19, pp. 353–368.

Downloaded 03 May 2010 to 171.66.16.245. Redistribution subject to ASME license or copyright; see http://www.asme.org/terms/Terms_Use.cfm

APPENDIX A

The problem addressed below relates to superposition of solutions for an uncracked body loaded externally and a cracked body loaded along the crack surface. Superposition of these two solutions to obtain the solution for a cracked body loaded externally is practical when the external loads are simple (e.g., uniform tractions) and the corresponding loads along the crack surface are simple (e.g., the same uniform tractions). To address this problem, consider an uncracked block of bimaterial loaded by piecewise uniform tractions. A Cartesian coordinate is introduced such that the interface is the x_1-x_3 plane as shown in Fig. 2. The loadings on the bimaterial block can be classified into two categories: those which would be tractions if applied along the interface, i.e., t_{21}, t_{22}, and t_{23}, and those which cannot be interface tractions, i.e., $t_{11}^{(\alpha)}$, $t_{33}^{(\alpha)}$, and $t_{13}^{(\alpha)}$, $\alpha = 1, 2$, as shown in Fig. 2. Hill (1972) refers to the former as exterior components of stress (σ_E) and the latter as interior components of stress (σ_I). In fracture mechanics, with a crack aligned parallel to the interface the latter are sometimes (at least in the case of homogeneous bodies) referred to as "T" stresses (Rice, 1988). Below we determine the conditions on the interior components such that the tractions along the interface are identically the uniform exterior parts.

For a piecewise uniform stress (or strain) field throughout the bimaterial (possibly with a discontinuity of the first kind), we look for solutions

$$\boldsymbol{\sigma}_E = \boldsymbol{\sigma}_E^{(1)} = \boldsymbol{\sigma}_E^{(2)} = \begin{bmatrix} 0 & t_{12} & 0 \\ t_{12} & t_{22} & t_{23} \\ 0 & t_{23} & 0 \end{bmatrix}, \quad \boldsymbol{\sigma}_I^{(\alpha)} = \begin{bmatrix} t_{11}^{(\alpha)} & 0 & t_{13}^{(\alpha)} \\ 0 & 0 & 0 \\ t_{13}^{(\alpha)} & 0 & t_{33}^{(\alpha)} \end{bmatrix}. \tag{A1a,b}$$

where $\boldsymbol{\sigma}_E$ and $\boldsymbol{\sigma}_I$ are, respectively, the exterior and interior parts of the stress tensor (see Bassani and Qu, 1990) and $\alpha = 1, 2$ denotes the two materials. Clearly, the piecewise uniform stress field given by (A1) satisfies equilibrium everywhere and traction continuity across the interface. Bassani and Qu (1990) have shown that the continuity of the displacements further requires that the stress fields given by (A1) should also satisfy

$$\mathbf{S}^{(1)} \cdot \mathbf{t}^{(1)} - \mathbf{S}^{(2)} \cdot \mathbf{t}^{(2)} = t_{21}\mathbf{m}_{21} + t_{22}\mathbf{m}_{22} + t_{23}\mathbf{m}_{23}, \tag{A2}$$

where

$$\mathbf{S}^{(\alpha)} = \begin{bmatrix} M_{1111}^{(\alpha)} & M_{1133}^{(\alpha)} & 2M_{1131}^{(\alpha)} \\ M_{3311}^{(\alpha)} & M_{3333}^{(\alpha)} & 2M_{3331}^{(\alpha)} \\ 2M_{3111}^{(\alpha)} & 2M_{3133}^{(\alpha)} & M_{3131}^{(\alpha)} \end{bmatrix}, \tag{A3}$$

$$\mathbf{t}^{(\alpha)} = \begin{bmatrix} t_{11}^{(\alpha)} \\ t_{33}^{(\alpha)} \\ t_{13}^{(\alpha)} \end{bmatrix}, \tag{A4}$$

$$\mathbf{m}_{ij} = \begin{bmatrix} M_{11ij}^{(2)} - M_{11ij}^{(1)} \\ M_{33ij}^{(2)} - M_{33ij}^{(1)} \\ 2M_{13ij}^{(2)} - 2M_{13ij}^{(1)} \end{bmatrix}, \tag{A5}$$

where $\mathbf{M}_{ijkl}$ is the elastic compliance tensor. Since $\mathbf{M}_{ijkl}$ is symmetric and positive definite, $\mathbf{S}^{(n)}$ is also symmetric and positive definite. Thus, in general, when $\mathbf{m}_{ij} \neq \mathbf{0}$, for a given surface loading t_{21}, t_{22}, and t_{23}, a piecewise uniform field in the rectangular bimaterial results only if discontinuous $t_{11}^{(n)}$, $t_{33}^{(n)}$ and $t_{13}^{(n)}$ are also applied. The jump in $\mathbf{t}^{(n)}$ across the interface is determined by (A2). One can always choose either $\mathbf{t}^{(1)}$ or $\mathbf{t}^{(2)}$, e.g., equal to zero, and then determine the other from (A2).

However, for example, if from (A2) and (A5) $\mathbf{m}_{22} = \mathbf{0}$, then, a uniform normal loading t_{22} leads to a piecewise uniform solution with no additional $\mathbf{t}^{(n)}$ needed. We may call bimaterials of this kind consonant in tension (after Dundurs (1969) in the two-dimensional isotropic case). Similarly, bimaterials that satisfy $\mathbf{m}_{12} = \mathbf{0}$ or $\mathbf{m}_{32} = \mathbf{0}$ may be called consonant in in-plane and antiplane shear, respectively.

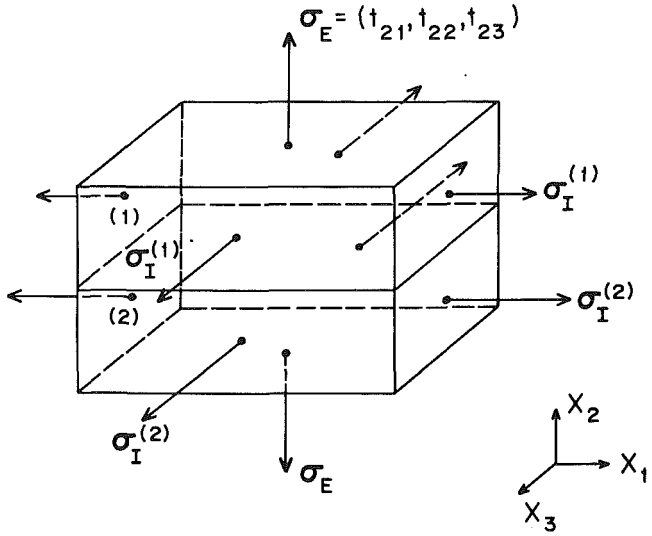


Fig. 2 Exterior (σ_E) and interior (σ_I) parts of the load on a bimaterial block defined with respect to the interface

Equation (A2) is simplified in the two-dimensional deformation considered in this paper, i.e., the displacements are functions of x_1 and x_2 only. In this case, $\epsilon_{33} = 0$ and (A2) reduces to

$$\hat{\mathbf{S}}^{(1)} \cdot \hat{\mathbf{t}}^{(1)} - \hat{\mathbf{S}}^{(2)} \cdot \hat{\mathbf{t}}^{(2)} = t_{21}\hat{\mathbf{m}}_{21} + t_{22}\hat{\mathbf{m}}_{22} + t_{23}\hat{\mathbf{m}}_{23}, \tag{A6}$$

where

$$\hat{\mathbf{S}}^{(n)} = \begin{bmatrix} \hat{M}_{1111}^{(n)} & 2\hat{M}_{1131}^{(n)} \\ 2\hat{M}_{3111}^{(n)} & \hat{M}_{3131}^{(n)} \end{bmatrix}, \quad \hat{\mathbf{m}}_{ij} = \begin{bmatrix} \hat{M}_{11ij}^{(2)} - 2\hat{M}_{11ij}^{(1)} \\ 2\hat{M}_{31ij}^{(2)} - 2\hat{M}_{31ij}^{(1)} \end{bmatrix},$$

$$\hat{\mathbf{t}}^{(n)} = \begin{bmatrix} \hat{F}t_{11}^{(n)} \\ \hat{t}_{13}^{(n)} \end{bmatrix},$$

$$\hat{M}_{ijkl}^{(n)} = M_{ijkl}^{(n)} - M_{ij33}^{(n)} M_{33kl}^{(n)} / M_{3333}^{(n)}.$$

In the case of isotropic materials,

$$\hat{M}_{1111}^{(n)} = \frac{1-\nu_n^2}{E_n}; \quad \hat{M}_{1122}^{(n)} = -\frac{\nu_n(1+\nu_n)}{E_n}; \quad \hat{M}_{3131}^{(n)} = \frac{1}{G_n};$$

$$\hat{M}_{1121}^{(n)} = \hat{M}_{1131}^{(n)} = \hat{M}_{1132}^{(n)} = \hat{M}_{3121}^{(n)} = \hat{M}_{3122}^{(n)} = \hat{M}_{3132}^{(n)} = 0.$$

For normal loading t_{22} only, (A6) then reduces to

$$t_{11}^{(1)} = \frac{E_1}{E_2}\left(\frac{1-\nu_2^2}{1-\nu_1^2}\right) t_{11}^{(2)} + \left[\frac{\nu_1}{1-\nu_1} - \frac{E_1}{E_2}\frac{\nu_1(1+\nu_2)}{1-\nu_1^2}\right] t_{22},$$

which agrees with Rice and Sih (1965).

APPENDIX B

We first list some of the integrals involved in the derivation (Erdogan, 1968)

$$\int_0^\infty \xi^{-1}\cos(\xi t)\cos(\xi x)\,d\xi = -\frac{1}{2}\ln|(x+t)(x-t)| + C, \tag{B1}$$

$$\int_0^\infty \xi^{-1}\sin(\xi t)\sin(\xi x)\,d\xi = \frac{1}{2}\ln|(x+t)(x-t)|, \tag{B2}$$

$$\int_0^\infty \xi^{-1}\cos(\xi t)\sin(\xi x)\,d\xi = \frac{\pi}{2}H(x-t), \tag{B3}$$

Downloaded 03 May 2010 to 171.66.16.245. Redistribution subject to ASME license or copyright; see http://www.asme.org/terms/Terms_Use.cfm

$$\int_0^\infty \xi^{-1}\sin(\xi t)\cos(\xi x)d\xi = \frac{\pi}{2} H(x-t), \tag{B4}$$

where $H(t)$ is the Heaviside unit step function.

Now, let

$$\mathbf{f}_2(\xi) = -(2\pi\xi)^{-1}\mathbf{B}_2^{-1}\mathbf{U}(\mathbf{D}-i\mathbf{W})\mathbf{D}^{-1}\int_{-a}^{a}\mathbf{f}(t)\exp(i\xi t)dt. \tag{B5}$$

Note that (Li and Qu, 1981a)

$$(\mathbf{D}+i\mathbf{W})(\mathbf{U}-i\mathbf{U}\mathbf{W}\mathbf{D}^{-1}) = \mathbf{I}. \tag{B6}$$

Therefore, substitute (B5) into (17) and make use of (B3)–(B4), we have

$$\Delta(x) = \int_0^a \mathbf{f}_s(t)H(x-t)dt - \int_0^a \mathbf{f}_a(t)H(t-x)dt, \tag{B7}$$

where

$$\mathbf{f}_s(x) = \frac{1}{2}[\mathbf{f}(x)+\mathbf{f}(-x)],\ \mathbf{f}_a(x) = \frac{1}{2}[\mathbf{f}(x)-\mathbf{f}(-x)]. \tag{B8}$$

Thus, for $|x| < a$, (B7) gives

$$\Delta(x) = \int_{-a}^{x}\mathbf{f}(t)dt, \tag{B9}$$

which proves (23), whereas, for $|x| > a$, (B7) becomes

$$\Delta(s) = \mathbf{0}, \tag{B10}$$

which implies that the displacement continuity condition (16) is automatically satisfied by (B5). In deriving (B7)–(B10), the auxiliary condition (21) has been used.

Next, substitute (B5) into the traction expression (19). Again, by splitting $\mathbf{f}$ into its symmetric and antisymmetric parts and making use of the integral (B1)–(B3), we arrive at, for $|x| < a$, the Cauchy integral Eq. (20).

Downloaded 03 May 2010 to 171.66.16.245. Redistribution subject to ASME license or copyright; see http://www.asme.org/terms/Terms_Use.cfm

The $r^{-1/2}$ (ln r) Singularities at Interface Cracks in Monoclinic and Isotropic Bimaterials due to Heat Flow

G. Yan
Assoc. Mem. ASME

T. C. T. Ting
Fellow ASME

Department of Civil Engineering, Mechanics, and Metallurgy, University of Illinois at Chicago, Chicago, IL 60680

It is known that the stress singularities at an interface crack tip of bimaterials with the effects of heat flow may have the form $r^{-1/2}$ (ln r). *The existence conditions of the higher order singularitiy* $r^{-1/2}$ (ln r) *are studied for monoclinic bimaterials whose plane of symmetry is at* $x_3 = 0$. *It is shown that the higher order singularity does not exist if the bimaterial is mismatched. If the bimaterial is non-mismatched, the higher order singularity does not exist when a certain condition is satisfied. This condition is given explicitly for monoclinic bimaterials with the plane of symmetry of* $x_3 = 0$ *and in a simple form for isotropic bimaterials.*

1 Introduction

The stress singularities at the tip of an interface crack in an anisotropic bimaterial subject to heat flow have been studied by Ting and Yan (1992). It was shown that there are four stress singularities at the interface crack tip. One of them depends on the heat conduction coefficients κ_{ij}, and the other three depend on the elasticity constants C_{ijks}. When the heat conduction coefficients in the two materials are identical or when the Onsager reciprocal relations are invoked so that κ_{ij} is symmetric, one of the $r^{-1/2}$ singularities, where r is the radial distance from the crack tip, may convert into a $r^{-1/2}$ (ln r) singularity. The conditions for the possible existence of this higher order singularity has been given. The nature of the stress singularity, $k^* r^{-1/2}$ (ln r), at the interface crack tip does not depend on the complete boundary conditions, though the proportional factor k^* in the singular solution does. The knowledge of the existence conditions of the higher order singularity can serve two purposes. One is to determine when to include the term $k^* r^{-1/2}$ (ln r) in the series solution, when the eigenfunction expansion technique is used to determine the whole field solution. The other is to design a composite to avoid this kind of higher order singularity.

The necessary conditions for the existence of the higher order singularity as given in (Ting and Yan, 1992) involve quantities which are not available explicitly for general anisotropic materials. In this paper we consider monoclinic materials whose plane of symmetry is at $x_3 = 0$. For this case of materials all quantities relevant to the existence conditions can be obtained explicitly. After briefly presenting the extension of the Stroh formalism (Stroh, 1958, 1962) to include heat flow (Hwu, 1990) in Section 2, the order of stress singularity δ and the conditions for the existence of the higher order singularity $r^{-1/2}$ (ln r) (Ting and Yan, 1992) are given in Section 3. The crucial constant vector γ_2, which was given in an integral form in (Ting and Yan, 1992), has an explicit expression with an alterntive algebraic derivation presented in Section 4. The algebraic representation of γ_2 is applicable to general anisotropic materials. In Section 5 we apply the results obtained for monoclinic materials with the symmetry plane at $x_3 = 0$. An unexpected result is that the higher order singularity does not exist if the bimaterial is mismatched. It does not exist in non-mismatched bimaterials provided a condition which is derived here is satisfied. In Section 6, this condition is presented in a simple form for isotropic bimaterials.

2 The Stroh Formalism

The general solution to the class of problems in anisotropic materials in which the displacement and hence the stress is independent of the x_3-coordinate in a fixed rectangular coordinate system x_i, $i = 1, 2, 3$, was first obtained by Eshelby et al. (1953). They applied their results to the determination of the displacement and stress fields due to a straight line dislocation. Extensions to a line singularity were made by Stroh (1958) who subsequently developed a powerful six-dimensional theory of dislocations and surface waves in anisotropic solids (Stroh, 1962). The Stroh formalism can be extended to thermo-anisotropic elasticity (Clements, 1973; Wu, 1984; Hwu, 1990).

Let u_i, σ_{ij}, h_i, and T be the displacement, the stress, the heat

Contributed by the Applied Mechanics Division of The American Society of Mechanical Engineers for presentation at the First Joint ASCE-EMD, ASME-AMD, SES Meeting, Charlottesville, VA, June 6-9, 1993.

Discussion on this paper should be addressed to the Technical Editor, Professor Lewis T. Wheeler, Department of Mechanical Engineering, University of Houston, Houston, TX 77204-4792, and will be accepted until four months after final publication of the paper itself in the ASME Journal of Applied Mechanics.

Manuscript received by the ASME Applied Mechanics Division, Apr. 24, 1992; final revision, Dec. 10, 1992. Associate Technical Editor: X. Markenscoff.

Paper No. 93-APM-39.

Copyright © 1993 by ASME
Downloaded 03 May 2010 to 171.66.16.245. Redistribution subject to ASME license or copyright; see http://www.asme.org/terms/Terms_Use.cfm

flux, and the temperature of a homogeneous anisotropic elastic body. The equations governing the stress-strain laws, the equilibrium, the heat conduction, and the balance of energy can be written as (Boley and Weiner, 1960; Nowacki, 1962)

$$\left.\begin{aligned}&\sigma_{ij}=C_{ijks}u_{k,s}-\beta_{ij}T,\\&\sigma_{ij,j}=0,\\&h_i=-\kappa_{ij}T_{,j},\\&h_{i,i}=0,\end{aligned}\right\}\tag{2.1}$$

In the above, a comma stands for differentiation, repeated indices imply summation, and β_{ij}, κ_{ij} are the thermal moduli and the heat conduction coefficients, respectively. C_{ijks} are the elasticity constants which are assumed to be fully symmetric and positive definite so that the strain energy is positive. For two-dimensional deformations for which u_i and T depend on x_1 and x_2 only, a general solution to (2.1) has the expression

$$\left.\begin{aligned}&T=\dot{g}(z_\tau),\\&\mathbf{u}=\mathbf{a}f(z)+\mathbf{c}g(z_\tau),\end{aligned}\right\}\tag{2.2}$$

$$z=x_1+px_2,$$

$$z_\tau=x_1+\tau x_2,$$

where $\mathbf{u}$ is a 3×1 matrix whose elements are (u_1, u_2, u_3), f, g are, respectively, arbitrary functions of z, z_τ and the dot denotes differentiation with the arguments. The p, τ, $\mathbf{a}$, and $\mathbf{c}$ are constants which, upon substituting (2.2) into (2.1), satisfy the following equations

$$\kappa_{22}\tau^2+(\kappa_{12}+\kappa_{21})\tau+\kappa_{11}=0,\tag{2.3}$$

$$\left.\begin{aligned}&\{\mathbf{Q}+p(\mathbf{R}+\mathbf{R}^T)+p^2\mathbf{T}\}\mathbf{a}=\mathbf{0},\\&\{\mathbf{Q}+\tau(\mathbf{R}+\mathbf{R}^T)+\tau^2\mathbf{T}\}\mathbf{c}=\beta_1+\tau\beta_2.\end{aligned}\right\}\tag{2.4}$$

In (2.4) the superscript T denotes the transpose and the components of the 3×1 matrices β_1, β_2, and the 3×3 matrices $\mathbf{Q}$, $\mathbf{R}$, $\mathbf{T}$ are

$$(\beta_1)_i=\beta_{i1},\quad (\beta_2)_i=\beta_{i2},\tag{2.5}$$

$$Q_{ik}=C_{i1k1},\quad R_{ik}=C_{i1k2},\quad T_{ik}=C_{i2k2}.\tag{2.6}$$

We see that $\mathbf{Q}$ and $\mathbf{T}$ are symmetric and positive definite.

The heat flux $\mathbf{h}$ and the stresses σ_{ij} obtained from $(2.1)_{3,1}$ can be written as

$$\mathbf{h}=-(\kappa_1+\tau\kappa_2)\ddot{g}(z_\tau),\tag{2.7}$$

$$\sigma_{i1}=-\phi_{i,2},\quad \sigma_{i2}=\phi_{i,1},\tag{2.8}$$

where ϕ is the stress function given by

$$\phi=\mathbf{b}f(z)+\mathbf{d}g(z_\tau)\tag{2.9}$$

and

$$(\kappa_1)_i=\kappa_{i1},\quad (\kappa_2)_i=\kappa_{i2},\tag{2.10}$$

$$\left.\begin{aligned}&\mathbf{b}=(\mathbf{R}^T+p\mathbf{T})\mathbf{a}=-\frac{1}{p}(\mathbf{Q}+p\mathbf{R})\mathbf{a},\\&\mathbf{d}=(\mathbf{R}^T+\tau\mathbf{T})\mathbf{c}-\beta_2=-\frac{1}{\tau}[(\mathbf{Q}+\tau\mathbf{R})\mathbf{c}-\beta_1].\end{aligned}\right\}\tag{2.11}$$

The second equalities for $\mathbf{b}$ and $\mathbf{d}$ follow from (2.4).

Equation $(2.4)_1$ is an eigenrelation with p being the eigenvalue and $\mathbf{a}$ the eigenvector. It can be shown (Eshelby et al., 1953) that p cannot be real if the strain energy is positive. Therefore $(2.4)_1$ provides three pairs of complex conjugates for p. If p_α, $\mathbf{a}_\alpha$ ($\alpha = 1,2, \ldots 6$) are the eigenvalues and the eigenvectors we let

$$\mathrm{Im}(p_\alpha)>0,\quad p_{\alpha+3}=\bar{p}_\alpha,\quad \mathbf{a}_{\alpha+3}=\bar{\alpha}_\alpha,\quad \alpha=1,2,3,$$

where Im denotes the imaginary part and the overbar stands for the complex conjugate.

The fact that heat flows from higher temperature to lower temperature means that

$$h_iT_{,i}<0.$$

It follows from $(2.1)_3$ that

$$\kappa_{ij}y_iy_j>0\tag{2.12}$$

for any real vector y_i. Therefore (2.3) rewritten as

$$\kappa_{ij}(\delta_{i1}+\tau\delta_{i2})(\delta_{j1}+\tau\delta_{j2})=0$$

where δ_{ij} is the Kronecker delta tells us that τ cannot be real. If τ and $\bar{\tau}$ are the roots of (2.3) we let

$$\tau=-\left(\frac{\kappa_{12}+\kappa_{21}}{2\kappa_{22}}\right)+i\left[\frac{\kappa_{11}}{\kappa_{22}}-\left(\frac{\kappa_{12}+\kappa_{21}}{2\kappa_{22}}\right)^2\right]^{1/2}.\tag{2.13}$$

We assume in this paper that either τ is not equal to anyone of the p or, if $\tau = p$, $\mathbf{c}$ of $(2.4)_2$ has a solution. Modifications required when $\tau = p$ and $\mathbf{c}$ of $(2.4)_2$ has no solutions can be found in (Wu, 1984).

The general solutions for T and $\mathbf{u}$ obtained from (2.2) by superimposing six solutions associated with p and two solutions associated with τ can be written as

$$T=\dot{g}_1(z_\tau)+\dot{g}_2(\bar{z}_\tau),\tag{2.14}$$

$$\mathbf{u}=\sum_{\alpha=1}^{3}\{\mathbf{a}_\alpha f_\alpha(z_\alpha)+\bar{\mathbf{a}}_\alpha f_{\alpha+3}(\bar{z}_\alpha)\}+\mathbf{c}g_1(z_\tau)+\bar{\mathbf{c}}g_2(\bar{z}_\tau).\tag{2.15}$$

The functions g_1, g_2, f_1, f_2, . . . , f_6 are arbitrary and

$$z_\alpha=x_1+p_\alpha x_2.$$

The general solutions for $\mathbf{h}$ and ϕ from (2.7) and (2.9) are

$$\mathbf{h}=-(\kappa_1+\tau\kappa_2)\ddot{g}_1(z_\tau)-(\kappa_1+\bar{\tau}\kappa_2)\ddot{g}_2(\bar{z}_\tau),\tag{2.16}$$

$$\phi=\sum_{\alpha=1}^{3}\{\mathbf{b}_\alpha f_\alpha(z_\alpha)+\bar{\mathbf{b}}_\alpha f_{\alpha+3}(\bar{z}_\alpha)\}+\mathbf{d}g_1(z_\tau)+\bar{\mathbf{d}}g_2(\bar{z}_\tau).\tag{2.17}$$

The two equations for $\mathbf{c}$ and $\mathbf{d}$ in (2.11) can be rewritten as (Hwu, 1990)

$$\begin{bmatrix}\mathbf{N}_1 & \mathbf{N}_2\\ \mathbf{N}_3 & \mathbf{N}_1^T\end{bmatrix}\begin{bmatrix}\mathbf{c}\\ \mathbf{d}\end{bmatrix}=\tau\begin{bmatrix}\mathbf{c}\\ \mathbf{d}\end{bmatrix}-\begin{bmatrix}\mathbf{0} & \mathbf{N}_2\\ \mathbf{I} & \mathbf{N}_1^T\end{bmatrix}\begin{bmatrix}\beta_1\\ \beta_2\end{bmatrix}\tag{2.18}$$

in which

$$\mathbf{N}_1=-\mathbf{T}^{-1}\mathbf{R}^T,\quad \mathbf{N}_2=\mathbf{T}^{-1},\quad \mathbf{N}_3=\mathbf{R}\mathbf{T}^{-1}\mathbf{R}^T-\mathbf{Q}.\tag{2.19}$$

If we rotate the coordinate system about the x_3-axis an angle θ, (2.18) takes the form,

$$\begin{bmatrix}\mathbf{N}_1(\theta) & \mathbf{N}_2(\theta)\\ \mathbf{N}_3(\theta) & \mathbf{N}_1^T(\theta)\end{bmatrix}\begin{bmatrix}\mathbf{c}\\ \mathbf{d}\end{bmatrix}=\tau(\theta)\begin{bmatrix}\mathbf{c}\\ \mathbf{d}\end{bmatrix}-\lambda^{-1}(\theta)\begin{bmatrix}\mathbf{0} & \mathbf{N}_2(\theta)\\ \mathbf{I} & \mathbf{N}_1^T(\theta)\end{bmatrix}\begin{bmatrix}\beta_1(\theta)\\ \beta_2(\theta)\end{bmatrix}\tag{2.20}$$

where

$$\mathbf{N}_1(\theta)=-\mathbf{T}^{-1}(\theta)\mathbf{R}^T(\theta),\quad \mathbf{N}_2(\theta)=\mathbf{T}^{-1}(\theta),$$

$$\mathbf{N}_3(\theta)=\mathbf{R}(\theta)\mathbf{T}^{-1}(\theta)\mathbf{R}^T(\theta)-\mathbf{Q}(\theta),\tag{2.21}$$

$$\tau(\theta)=\frac{\tau\cos\theta-\sin\theta}{\tau\sin\theta+\cos\theta},\quad \lambda(\theta)=\cos\theta+\tau\sin\theta,\tag{2.22}$$

$$[\beta_1(\theta)]_i=\beta_{ij}n_j,\quad [\beta_2(\theta)]_i=\beta_{ij}m_j.\tag{2.23}$$

In the above,

$$n_j=(\cos\theta,\ \sin\theta,\ 0),\quad m_j=(-\sin\theta,\ \cos\theta,\ 0),\tag{2.24}$$

and the components of $\mathbf{Q}(\theta)$, $\mathbf{R}(\theta)$, $\mathbf{T}(\theta)$ are

$$Q_{ik}(\theta)=C_{ijks}n_jn_s,\quad R_{ik}(\theta)=C_{ijks}n_jm_s,\quad T_{ik}(\theta)=C_{ijks}m_jm_s.\tag{2.25}$$

They reduce to Q_{ik}, R_{ik}, T_{ik} in (2.6) when $\theta = 0$. Introducing the three real matrices $\mathbf{S}$, $\mathbf{H}$, $\mathbf{L}$ (Barnett and Lothe, 1973) by

$$\mathbf{S}=\frac{1}{\pi}\int_0^\pi\mathbf{N}_1(\theta)d\theta,\quad \mathbf{H}=\frac{1}{\pi}\int_0^\pi\mathbf{N}_2(\theta)d\theta,\quad \mathbf{L}=-\frac{1}{\pi}\int_0^\pi\mathbf{N}_3(\theta)d\theta,\tag{2.26}$$

Downloaded 03 May 2010 to 171.66.16.245. Redistribution subject to ASME license or copyright; see http://www.asme.org/terms/Terms_Use.cfm

integration of (2.20) leads to

$$\begin{bmatrix} \mathbf{S} & \mathbf{H} \\ -\mathbf{L} & \mathbf{S}^T \end{bmatrix} \begin{bmatrix} \mathbf{c} \\ \mathbf{d} \end{bmatrix} = i \begin{bmatrix} \mathbf{c} \\ \mathbf{d} \end{bmatrix} - \begin{bmatrix} \boldsymbol{\gamma}_1 \\ \boldsymbol{\gamma}_2 \end{bmatrix} \tag{2.27}$$

where

$$\boldsymbol{\gamma}_1 = \frac{1}{\pi} \int_0^{\pi} \lambda^{-1}(\theta) \mathbf{N}_2(\theta) \boldsymbol{\beta}_2(\theta) d\theta,$$

$$\boldsymbol{\gamma}_2 = \frac{1}{\pi} \int_0^{\pi} \lambda^{-1}(\theta) [\boldsymbol{\beta}_1(\theta) + \mathbf{N}_1^T(\theta) \boldsymbol{\beta}_2(\theta)] d\theta. \tag{2.28}$$

The constant vectors $\boldsymbol{\gamma}_1$ and $\boldsymbol{\gamma}_2$ play key roles in thermo-anisotropic elasticity problems. Equations (2.28) provide an integral formula for $\boldsymbol{\gamma}_1$ and $\boldsymbol{\gamma}_2$, by which a numerical solution can be obtained for $\boldsymbol{\gamma}_1$ and $\boldsymbol{\gamma}_2$.

3 Stress Singularities at an Interface Crack

To study the stress singularities at the tip of an interface crack, we take the origin of the coordinate system at the crack tip and choose the functions $f_\alpha(z_\alpha)$, $g(z_\tau)$ to be proportional to $z_\alpha^{\delta+1}$, $z_\tau^{\delta+1}$, respectively (Williams, 1952). Introducing the 3 × 3 matrices $\mathbf{A}$ and $\mathbf{B}$ by

$$\mathbf{A} = [\mathbf{a}_1, \mathbf{a}_2, \mathbf{a}_3], \quad \mathbf{B} = [\mathbf{b}_1, \mathbf{b}_2, \mathbf{b}_3]$$

and the diagonal matrix $\mathbf{Z}$ by

$$\mathbf{Z} = \text{diag}[z_1, z_2, z_3],$$

the solutions (2.14)–(2.17) can be written as

$$\left.\begin{aligned} T &= (\delta+1)[\xi z_\tau^\delta + \eta \bar{z}_\tau^\delta], \\ \mathbf{h} &= -\delta(\delta+1)[(\kappa_1 + \tau\kappa_2)\xi z_\tau^{\delta-1} + (\kappa_1 + \bar{\tau}\kappa_2)\eta \bar{z}_\tau^{\delta-1}], \\ \mathbf{u} &= \mathbf{A}\mathbf{Z}^{\delta+1}\mathbf{q} + \bar{\mathbf{A}}\,\bar{\mathbf{Z}}^{\delta+1}\mathbf{y} + \xi z_\tau^{\delta+1}\mathbf{c} + \eta \bar{z}_\tau^{\delta+1}\bar{\mathbf{c}}, \\ \boldsymbol{\phi} &= \mathbf{B}\mathbf{A}^{\delta+1}\mathbf{q} + \bar{\mathbf{B}}\,\bar{\mathbf{Z}}^{\delta+1}\mathbf{y} + \xi z_\tau^{\delta+1}\mathbf{d} + \eta \bar{z}_\tau^{\delta+1}\bar{\mathbf{d}}, \end{aligned}\right\} \tag{3.1}$$

in which $\mathbf{q}$, $\mathbf{y}$, ξ, and η are the proportionality factors.

Using the polar coordinates

$$x_1 = r\cos\theta, \quad x_2 = r\sin\theta,$$

we have

$$z_\alpha = r(\cos\theta + p_\alpha \sin\theta),$$
$$z_\tau = r(\cos\theta + \tau\sin\theta).$$

The stresses obtained from $(3.1)_4$ and (2.8) are then proportional to r^δ and are singular if the real part of δ is negative. We therefore look for δ in the range

$$-1 < \text{Re}\,\delta < 0 \tag{3.2}$$

where Re stands for the real part. The left inequality assures us that the strain energy at the crack tip is bounded.

For the interface crack in an anisotropic bimaterial, let the space $x_2 > 0$ be occupied by material 1 and the space $x_2 < 0$ be occupied by material 2. The interface crack is located at $x_2 = 0, x_1 < 0$. The solutions presented in (3.1) apply to material 1 in $x_2 > 0$ ($\pi > \theta > 0$). The corresponding solutions which apply to material 2 in $x_2 < 0$ ($-\pi < \theta < 0$) will be denoted by a prime. We assume that the crack surfaces are traction-free and thermally insulated. By substituting (3.1) into the continuity and boundary conditions, a system of sixteen homogeneous equations, $\mathbf{K}\mathbf{x} = \mathbf{0}$, can be obtained. The orders of stress singularities δ are the roots of the determinant of $\mathbf{K}$. One of them, denoted by δ_κ, which falls in the range (3.2) is (Ting and Hwu, 1991)

$$\cot(\delta_\kappa \pi) = \frac{\hat{\kappa}_I' - \hat{\kappa}_I}{\hat{\kappa}_{II}' + \hat{\kappa}_{II}}, \tag{3.3}$$

where

$$\hat{\kappa}_I = \frac{\kappa_I}{(\kappa_I^2 + \kappa_{II}^2)}, \quad \hat{\kappa}_{II} = \frac{\kappa_{II}}{(\kappa_I^2 + \kappa_{II}^2)}. \tag{3.4}$$

In the above,

$$\left.\begin{aligned} \kappa_I &= \frac{1}{2}(\kappa_{21} - \kappa_{12}), \\ \kappa_{II} &= \left[\kappa_{11}\kappa_{22} - \left(\frac{\kappa_{12} + \kappa_{21}}{2}\right)^2\right]^{1/2}. \end{aligned}\right\} \tag{3.5}$$

We see that δ_κ depends exclusively on heat conduction coefficients κ_{ij} and that $\delta_\kappa = -1/2$ when

$$\frac{\kappa_I}{\kappa_I^2 + \kappa_{II}^2} = \frac{\kappa_I'}{\kappa_I'^2 + \kappa_{II}'^2}.$$

This is satisfied, in particular, when the two materials have the same heat conduction coefficients κ_{ij} or when the Onsager reciprocal relations are invoked so that $\kappa_I = \kappa_I' = 0$. The remaining three eigenvalues, denoted by δ_c, depend on the elasticity constants C_{ijks} only. They were given in (Ting, 1986) as

$$\delta_c = -\frac{1}{2}, \text{ and } -\frac{1}{2} \pm i\gamma, \tag{3.6}$$

$$\left.\begin{aligned} \gamma &= \frac{1}{2\pi} \ln\frac{1+\beta}{1-\beta} = \frac{1}{\pi}\tanh^{-1}\beta, \\ \beta &= \left\{-\frac{1}{2}\,\text{tr}(\mathbf{D}^{-1}\mathbf{W})^2\right\}^{1/2}, \end{aligned}\right\} \tag{3.7}$$

In the above, tr stands for the trace of the matrix and

$$\mathbf{D} = \mathbf{L}^{-1} + \mathbf{L}'^{-1}, \quad \mathbf{W} = \mathbf{S}\mathbf{L}^{-1} - \mathbf{S}'\mathbf{L}'^{-1}, \tag{3.8}$$

in which $\mathbf{S}$, $\mathbf{L}$ are 3 × 3 real matrices defined in (2.26). They are also related to $\mathbf{A}$ and $\mathbf{B}$ through the relation (Barnett and Lothe, 1973; Chadwick and Smith, 1977)

$$i\mathbf{A}\mathbf{B}^{-1} = \mathbf{L}^{-1} - i\mathbf{S}\mathbf{L}^{-1}. \tag{3.9}$$

The matrix $\mathbf{L}$, and hence $\mathbf{L}^{-1}$, is symmetric positive definite while $\mathbf{S}\mathbf{L}^{-1}$ is antisymmetric. Moreover, $i\mathbf{A}\mathbf{B}^{-1}$ is a positive definite Hermantian. Noting that $\mathbf{W}$ is antisymmetric, let

$$\mathbf{W} = \mathbf{S}\mathbf{L}^{-1} - \mathbf{S}'\mathbf{L}'^{-1} = \begin{bmatrix} 0 & -w_3 & w_2 \\ w_3 & 0 & -w_1 \\ -w_2 & w_1 & 0 \end{bmatrix}, \text{ say.} \tag{3.10}$$

It is easily seen that, if $\mathbf{W} \neq \mathbf{0}$, the null vector $\mathbf{w}$ is

$$\mathbf{W}\mathbf{w} = \mathbf{0}, \quad \mathbf{w} = \begin{bmatrix} w_1 \\ w_2 \\ w_3 \end{bmatrix}. \tag{3.11}$$

Bimaterials for which $\mathbf{W} \neq \mathbf{0}$, (and hence $\mathbf{w} \neq \mathbf{0}$, $\beta \neq 0$, $\gamma \neq 0$) are called "mismatched" bimaterials for which the displacement and stress at crack tip are oscillatory. It can be shown that $\gamma \neq 0$ (or $\beta \neq 0$) if and only if $\mathbf{W} \neq \mathbf{0}$ (Ting, 1986; Qu and Bassani, 1989). Thus mismatched bimaterials are characterized by nonzero γ, β or $\mathbf{W}$. It can be seen from (3.6) and (3.7) that when $\delta_\kappa = -1/2$ and $\mathbf{W} \neq \mathbf{0}$, $\delta = -1/2$ is a double root of $\mathbf{K}$, and that when $\delta_\kappa = -1/2$ and $\mathbf{W} = \mathbf{0}$, $\delta = -1/2$ is a root of multiplicity four. When $\delta = -1/2$ is a root of multiplicity two (or four), we may not have two (or four) independent eigenfunctions associated with $\delta = -1/2$. When that happens, an independent solution can be obtained from (3.1) by replacing the right-hand side of (3.1) by the derivatives with respect to δ and setting $\delta = -1/2$ (Dempsey and Sinclair, 1979; Ting and Chou, 1981; Zwiers et al., 1982). Thus, for instance,

Downloaded 03 May 2010 to 171.66.16.245. Redistribution subject to ASME license or copyright; see http://www.asme.org/terms/Terms_Use.cfm

$$T=\frac{\partial}{\partial\delta}\{(\delta+1)[\xi z_\tau^{\delta}+\eta\bar{z}_\tau^{\delta}]\}\,|_{\delta=-1/2}$$

$$=[\xi z_\tau^{-1/2}+\eta\bar{z}_\tau^{-1/2}]+\frac{1}{2}[\dot{\xi}z_\tau^{-1/2}+\dot{\eta}\bar{z}_\tau^{-1/2}]$$

$$+\frac{1}{2}[\xi z_\tau^{-1/2}\ln z_\tau+\eta\bar{z}_\tau^{-1/2}\ln\bar{z}_\tau]. \quad (3.12)$$

In carrying out the differentiation, ξ and η are assumed to depend on δ. Hence, the dot denotes differentiation with δ and setting $\delta=-1/2$. Equation (3.12) contains the $r^{-1/2}$ term as well as the $r^{-1/2}(\ln r)$ term. It is shown in (Ting and Yan, 1992) that a necessary and sufficient condition for non-existence of the $r^{-1/2}(\ln r)$ singularity is

$$\mathbf{w}\cdot\mathbf{s}=0, \text{ when } \mathbf{w}\neq\mathbf{0}, \quad (3.13)$$

$$\mathbf{s}=\mathbf{0}, \text{ when } \mathbf{w}=\mathbf{0}, \quad (3.14)$$

where

$$\mathbf{s}=\frac{1}{2}\mathbf{L}^{-1}[\hat{\kappa}_{II}(\gamma_2-\bar{\gamma}_2)+i\hat{\kappa}_I(\gamma_2+\bar{\gamma}_2)]$$

$$-\frac{1}{2}\mathbf{L}'^{-1}[\hat{\kappa}'_{II}(\gamma'_2-\bar{\gamma}'_2)+i\hat{\kappa}'_I(\gamma'_2+\bar{\gamma}'_2)]$$

$$=i\mathbf{L}^{-1}[\hat{\kappa}_{II}\,\mathrm{Im}\,\gamma_2+\hat{\kappa}_I\,\mathrm{Re}\,\gamma_2]$$

$$-i\mathbf{L}'^{-1}[\hat{\kappa}'_{II}\,\mathrm{Im}\,\gamma'_2+\hat{\kappa}'_I\,\mathrm{Re}\,\gamma'_2]. \quad (3.15)$$

If $\kappa_I=\kappa'_I=0$, we have $\hat{\kappa}_I=\hat{\kappa}'_I=0$, $\hat{\kappa}_{II}=\kappa_{II}^{-1}$, $\hat{\kappa}'_{II}=\kappa'^{-1}_{II}$, and (3.15) reduces to

$$\mathbf{s}=i(\kappa_{II}^{-1}\mathbf{L}^{-1}\,\mathrm{Im}\,\gamma_2-\kappa'^{-1}_{II}\mathbf{L}'^{-1}\,\mathrm{Im}\,\gamma'_2). \quad (3.16)$$

4 Explicit Expressions of γ_1, γ_2

The condition for nonexistence of the higher order singularity $r^{-1/2}(\ln r)$ as given by (3.13) and (3.14) requires the quantities $\mathbf{w}$ and $\mathbf{s}$. From (3.10), $(3.11)_2$, and (3.15), this means that we need $\mathbf{S}$, $\mathbf{L}$, and γ_2 for each material in the bimaterial. The γ_2 defined in (2.28) is an integral representation for which a closed form expression may not be possible for general materials and a numerical integration may be necessary.

In this section we derive an algebraic representation for γ_1 and γ_2. This can be achieved by solving $(\mathbf{c}, \mathbf{d})$ from (2.18) and substituting the result in (2.27). We first write (2.18) as

$$(\mathbf{N}-\tau\mathbf{I})\begin{bmatrix}\mathbf{c}\\ \mathbf{d}\end{bmatrix}=-\begin{bmatrix}\mathbf{0} & \mathbf{N}_2\\ \mathbf{I} & \mathbf{N}_1^T\end{bmatrix}\begin{bmatrix}\beta_1\\ \beta_2\end{bmatrix} \quad (4.1)$$

where

$$\mathbf{N}=\begin{bmatrix}\mathbf{N}_1 & \mathbf{N}_2\\ \mathbf{N}_3 & \mathbf{N}_1^T\end{bmatrix}. \quad (4.2)$$

It can be shown that (Kirchner and Loethe, 1986)

$$\mathbf{N}\begin{bmatrix}\mathbf{S} & \mathbf{H}\\ -\mathbf{L} & \mathbf{S}^T\end{bmatrix}=\begin{bmatrix}\mathbf{S} & \mathbf{H}\\ -\mathbf{L} & \mathbf{S}^T\end{bmatrix}\mathbf{N}, \quad (4.3)$$

because the two 6×6 matrices have the same set of eigenvectors. Multiplication of (2.27) by $(\mathbf{N}-\tau\mathbf{I})$ and using (4.1) and (4.3) yields

$$(\mathbf{N}-\tau\mathbf{I})\begin{bmatrix}\gamma_1\\ \gamma_2\end{bmatrix}=\begin{bmatrix}\mathbf{y}_1\\ \mathbf{y}_2\end{bmatrix}, \quad (4.4)$$

where

$$\begin{bmatrix}\mathbf{y}_1\\ \mathbf{y}_2\end{bmatrix}=\left\{\begin{bmatrix}\mathbf{S} & \mathbf{H}\\ -\mathbf{L} & \mathbf{S}^T\end{bmatrix}-i\mathbf{I}\right\}\begin{bmatrix}\mathbf{0} & \mathbf{N}_2\\ \mathbf{I} & \mathbf{N}_1^T\end{bmatrix}\begin{bmatrix}\beta_1\\ \beta_2\end{bmatrix}. \quad (4.5)$$

Equation (4.4) can be solved for γ_1 and γ_2 as follows. With (4.2), (4.4) can be written as

$$\tilde{\mathbf{N}}_1\gamma_1+\mathbf{N}_2\gamma_2=\mathbf{y}_1,$$

$$\mathbf{N}_3\gamma_1+\tilde{\mathbf{N}}_1^T\gamma_2=\mathbf{y}_2, \quad (4.6)$$

where

$$\tilde{\mathbf{N}}_1=\mathbf{N}_1-\tau\mathbf{I}. \quad (4.7)$$

Observing that $\mathbf{N}_2$ is positive definite, $(4.6)_1$ gives

$$\gamma_2=\mathbf{N}_2^{-1}\mathbf{y}_1-\mathbf{N}_2^{-1}\tilde{\mathbf{N}}_1\gamma_1 \quad (4.8)$$

and $(4.6)_2$ leads to

$$\{\mathbf{N}_3-\tilde{\mathbf{N}}_1^T\mathbf{N}_2^{-1}\tilde{\mathbf{N}}_1\}\gamma_1=\mathbf{y}_2-\tilde{\mathbf{N}}_1^T\mathbf{N}_2^{-1}\mathbf{y}_1. \quad (4.9)$$

Since we have assumed that $\tau\neq p$, $(\mathbf{N}-\tau\mathbf{I})$ is not singular (Chadwick and Smith, 1977) and a unique solution for (γ_1, γ_2) from (4.4) exists. This assures us that the coefficient of γ_1 in (4.9) is not singular. Therefore, γ_2 is given by (4.8) in which γ_1 is furnished by (4.9).

If $\tilde{\mathbf{N}}_1$ is nonsingular, a more direct derivation for γ_2 is to multiply $(4.6)_1$ by $\mathbf{N}_3\tilde{\mathbf{N}}_1^{-1}$ and subtract $(4.6)_2$ from the result. We have

$$\gamma_2=\Phi^{-1}\psi \quad (4.10)$$

where

$$\Phi=\mathbf{N}_3\tilde{\mathbf{N}}_1^{-1}\mathbf{N}_2-\tilde{\mathbf{N}}_1^T,$$

$$\psi=\mathbf{N}_3\tilde{\mathbf{N}}_1^{-1}\mathbf{y}_1-\mathbf{y}_2. \quad (4.11)$$

5 The $r^{-1/2}(\ln r)$ Singularity in Monoclinic Bimaterials

The explicit expressions for $\mathbf{S}$ and $\mathbf{L}$ for monoclinic materials with the symmetry plane at $x_3=0$ has been obtained by Ting (1992). With γ_2 given in (4.8) or (4.10), the conditions for existence or nonexistence of the $r^{-1/2}(\ln r)$ singularity can be obtained explicitly. It should be pointed out that, when the material has a plane of symmetry at $x_3=0$, the in-plane displacements and the ex-plane displacements are uncoupled. The matrices β_{ij}, κ_{ij}, $\mathbf{Q}$, $\mathbf{R}$, $\mathbf{T}$ which appeared in Section 2 all have the structure

$$\begin{bmatrix}* & * & 0\\ * & * & 0\\ 0 & 0 & *\end{bmatrix} \quad (5.1)$$

where the asterisk * denotes a possibly nonzero element. Likewise $\mathbf{N}_i$ of (2.19), $\mathbf{N}_i(\theta)$ of (2.21), and $\mathbf{S}$, $\mathbf{H}$, $\mathbf{L}$ of (2.26) also have the structure (5.1). It is clear from (2.28) that the third element of γ_2 vanishes identically. Hence γ_2 has the structure

$$\gamma_2^T=(*, *, 0) \quad (5.2)$$

and $\mathbf{s}$ of (3.15) has the same structure. It was shown in (Ting, 1992) that the only nonzero element in (3.10) is w_3 and $(3.11)_2$ reduces to

$$\mathbf{w}^T=(0, 0, w_3). \quad (5.3)$$

Therefore, when $\mathbf{w}\neq\mathbf{0}$, (i.e., $w_3\neq 0$), (3.13) is automatically satisfied. We thus have the result that there is no $r^{-1/2}(\ln r)$ singularity for mismatched monoclinic bimaterials with the symmetry plane at $x_3=0$.

For nonmismatched bimaterials, $\mathbf{w}=\mathbf{0}$, (i.e., $w_3=0$), the condition (3.14) requires that $\mathbf{s}$ vanishes identically, i.e.,

$$\mathbf{s}=\mathbf{0}. \quad (5.4)$$

Since all relevant 3×3 matrices have the structure (5.1), it suffices to consider 2×2 reduced matrices which are obtained from the original matrices by deleting the third row and the third column. As to the vectors γ_2 and $\mathbf{s}$, we need to consider only the first two components of the 3×1 matrices.

Let p_1 and p_2 be the two roots with positive imaginary parts of the quartic equation

$$\hat{s}_{11}p^4-2\hat{s}_{16}p^3+(\hat{s}_{66}+2\hat{s}_{12})p^2-2\hat{s}_{26}p+\hat{s}_{22}=0$$

where

$$\hat{s}_{ij}=s_{ij}-(s_{i3}s_{3j})s_{33}^{-1}, \quad (5.5)$$

Downloaded 03 May 2010 to 171.66.16.245. Redistribution subject to ASME license or copyright; see http://www.asme.org/terms/Terms_Use.cfm

and s_{ij} are the elastic compliances. The reduced 2×2 matrices for **S**, **H**, **L** are (Ting, 1992)

$$\mathbf{S} = gh\begin{bmatrix} d & -b \\ e & -d \end{bmatrix},$$

$$\mathbf{L} = \frac{h}{\hat{s}_{11}}\begin{bmatrix} e & -d \\ -d & b \end{bmatrix},$$

$$\mathbf{H} = \hat{s}_{11}(1 - g^2 h)\begin{bmatrix} b & d \\ d & e \end{bmatrix}. \tag{5.6}$$

Therefore,

$$\mathbf{L}^{-1} = \hat{s}_{11}\begin{bmatrix} b & d \\ d & e \end{bmatrix},$$

$$\mathbf{S}\mathbf{L}^{-1} = \hat{s}_{11} g\begin{bmatrix} 0 & -1 \\ 1 & 0 \end{bmatrix}. \tag{5.7}$$

In the above,

$$p_1 + p_2 = a + bi, \quad p_1 p_2 = c + di,$$
$$e = ad - bc, \quad g = \hat{s}_{12}/\hat{s}_{11} - c, \quad h = (be - d^2)^{-1}. \tag{5.8}$$

With (3.10) and (5.7), the w_3 of (5.3) is

$$w_3 = \hat{s}_{11} g - \hat{s}'_{11} g'. \tag{5.9}$$

The matrices $\mathbf{N}_1$ and $\mathbf{N}_3$ have simple expressions in terms of $\hat{s}_{ij}$ (Ting, 1988). The matrix $\mathbf{N}_2$ is the inverse of **T**. The reduced 2×2 matrices have the expressions

$$\mathbf{N}_1 = \begin{bmatrix} \lambda_1 & -1 \\ \lambda_2 & 0 \end{bmatrix},$$

$$\mathbf{N}_2 = \begin{bmatrix} \lambda_3 & \lambda_5 \\ \lambda_5 & \lambda_4 \end{bmatrix},$$

$$\mathbf{N}_3 = \begin{bmatrix} \lambda_6 & 0 \\ 0 & 0 \end{bmatrix}, \tag{5.10}$$

where

$$\lambda_1 = \hat{s}_{16}/\hat{s}_{11}, \quad \lambda_2 = \hat{s}_{12}/\hat{s}_{11},$$
$$\lambda_3 = c_{22}/(c_{22}c_{66} - c_{26}^2) = (\hat{s}_{11}\hat{s}_{66} - \hat{s}_{16}^2)/\hat{s}_{11},$$
$$\lambda_4 = c_{66}/(c_{22}c_{66} - c_{26}^2) = (\hat{s}_{11}\hat{s}_{22} - \hat{s}_{12}^2)/\hat{s}_{11},$$
$$\lambda_5 = -c_{26}/(c_{22}c_{66} - c_{26}^2) = (\hat{s}_{11}\hat{s}_{26} - \hat{s}_{12}\hat{s}_{16})/\hat{s}_{11},$$
$$\lambda_6 = -1/\hat{s}_{11}. \tag{5.11}$$

The second equalities for λ_3, λ_4, λ_5 are obtained by applying Eqs. (A12) and (A13) in (Ting, 1992). Finally, (4.7) and $(4.11)_1$ gives

$$\tilde{\mathbf{N}}_1^{-1} = \frac{-1}{\tilde{\omega}}\begin{bmatrix} \tau & -1 \\ \lambda_2 & \tau - \lambda_1 \end{bmatrix} \tag{5.12}$$

and

$$\mathbf{\Phi}^{-1} = \frac{1}{\tau\rho_1 + \rho_2}\begin{bmatrix} \tau & \rho_2 \\ -1 & \rho_1 \end{bmatrix} \tag{5.13}$$

where

$$\rho_1 = \tau - \lambda_1 - \tilde{\omega}^{-1}\lambda_6(\tau\lambda_3 - \lambda_5),$$
$$\rho_2 = \lambda_2 + \tilde{\omega}^{-1}\lambda_6(\tau\lambda_5 - \lambda_4),$$
$$\tilde{\omega} = \tau(\tau - \lambda_1) + \lambda_2. \tag{5.14}$$

We have thus obtained explicit expressions for all quantities necessary for verifying if (5.4) is satisfied. In the next section we will specialize the results for isotropic bimaterials.

6 Isotropic Bimaterials

If the bimaterials are made of isotropic materials, the nonzero elastic compliances s_{ij} are

$$s_{11} = s_{22} = s_{33} = \frac{1}{E} = \frac{1}{2\mu(1+\nu)},$$
$$s_{44} = s_{55} = s_{66} = \frac{1}{\mu},$$
$$s_{12} = s_{21} = s_{13} = s_{31} = s_{23} = s_{32} = -\frac{\nu}{E} = -\frac{\nu}{2\mu(1+2\nu)},$$

where μ, ν and E are the shear modulus, Poisson's ratio and Young's modulus, respectively. From (5.5), the nonzero $\hat{s}_{ij}$ are

$$\hat{s}_{11} = \hat{s}_{22} = \hat{s}_{33} = \frac{1-\nu^2}{E} = \frac{1-\nu}{2\mu},$$
$$\hat{s}_{44} = \hat{s}_{55} = \hat{s}_{66} = \frac{1}{\mu},$$
$$\hat{s}_{12} = \hat{s}_{21} = -\frac{\nu(1+\nu)}{E} = -\frac{\nu}{2\mu}. \tag{6.1}$$

For isotropic materials, $p_1 = p_2 = p_3 = i$ and by (5.8) and (5.9),

$$a = d = 0, \quad b = 2, \quad c = -1,$$
$$e = 2, \quad g = \hat{s}_{12}/\hat{s}_{11} + 1, \quad h = 1/4, \tag{6.2}$$
$$w_3 = \frac{1-2\nu}{2\mu} - \frac{1-2\nu'}{2\mu'}. \tag{6.3}$$

The heat conduction coefficients κ_{ij} and the thermal moduli β_{ii} for isotropic materials are

$$\kappa_{ij} = \kappa\delta_{ij}, \quad \beta_{ij} = \frac{E\alpha}{1-2\nu}\delta_{ij}, \tag{6.4}$$

where α and κ are the thermal expansion coefficient and the heat conductivity, respectively. Equations (3.5) reduce to

$$\kappa_I = 0, \quad \kappa_{II} = \kappa.$$

For isotropic materials $\tau = i$, which is identical to the elasticity eigenvalues p. It can be shown that **c** of $(2.4)_2$ has a solution for $\tau = i$ and hence the analyses remain valid. However, the matrix Φ of $(4.11)_1$ is singular at $\tau = i$ and each component of $\Phi^{-1}\psi$ in (4.10) has the form of zero divided by zero. The solution for γ_2 can be obtained by using the L'hospital's rule. The result is

$$\gamma_2 = \frac{E\alpha}{2(1-\nu)}\begin{bmatrix} 1 \\ -i \\ 0 \end{bmatrix}. \tag{6.5}$$

We have also calculated γ_2 using the integral representation $(2.28)_2$ and obtained the same result shown in (6.5). Finally, (3.16) gives

$$\mathbf{s} = \left[\frac{\alpha'(1+\nu')}{\kappa'} - \frac{\alpha(1+\nu)}{\kappa}\right]\begin{bmatrix} 0 \\ i \\ 0 \end{bmatrix}. \tag{6.6}$$

For the non-mismatched isotropic bimaterials for which $\omega_3 = 0$, i.e., by (6.3),

$$\frac{1-2\nu}{\mu} = \frac{1-2\nu'}{\mu'}, \tag{6.7}$$

the condition of nonexistence of higher order singularity $r^{-1/2}(\ln r)$, (5.4), leads to

$$\frac{\alpha(1+\nu)}{\kappa} = \frac{\alpha'(1+\nu')}{\kappa'}. \tag{6.8}$$

We therefore have the result that, for mismatched materials for which (6.7) is violated, there is no higher order singularity $r^{-1/2}(\ln r)$ at the interface crack tip. For nonmismatched bimaterials for which (6.7) holds, the $r^{-1/2}(\ln r)$ singularity does not exist if (6.8) is satisfied. When the two materials are incompressible, i.e., $\nu = \nu' = 1/2$, (6.7) is automatically

Downloaded 03 May 2010 to 171.66.16.245. Redistribution subject to ASME license or copyright; see http://www.asme.org/terms/Terms_Use.cfm

satisfied. The condition of nonexistence of higher order singularity $r^{-1/2}$ (ln r) becomes

$$\kappa\alpha' = \kappa'\alpha,$$

which is independent of the elasticity constants of the two materials.

Concluding Remarks

The singularity analysis presented here is an asymptotic analysis for points near a crack tip. For an interfacial crack of finite length subject to an external loading the solutions presented here apply to the two tips of the crack. It remains to be studied the effects of the existence of the higher order stress singularity on the probability of an interfacial failure. Another point that should be looked at in a finite crack is whether the higher order singularity presents the interpenetration problem (Comninou, 1977; Comninou and Schmueser, 1979; Gautesen and Dundurs, 1988; Wu and Hwang, 1990; Wu, 1992). Even though the displacement for the higher order singularity $r^{-1/2}$ (ln r) is not oscillatory, the displacement at the surfaces of the crack should be checked to see if an interpenetration occurs.

Acknowledgments

The work presented here is supported by the U.S. Air Force Office of Scientific Research through grant F49620-92-J-0087.

References

Barnett, D. M., and Lothe, J., 1973, "Synthesis of the Sextic and the Integral Formalism for Dislocations, Greens Function and Surface Waves in Anisotropic Elastic Solids," *Phys. Nor.*, Vol. 7, pp. 13–19.

Boley, B. A., and Weiner, J. H., 1960, *Theory of Thermal Stresses*, John Wiley and Sons, New York.

Chadwick, P., and Smith, G. D., 1977, "Foundations of the Theory of Surface Waves in Anisotropic Elastic Materials," *Adv. Appl. Mech.*, Vol. 17, pp. 303–376.

Clements, D. L., 1973, "Thermal Stress in an Anisotropic Elastic Half-Space," *SIAM J. Appl. Math.*, Vol. 24, pp. 332–337.

Comninou, M., 1977, "The Interface Crack," ASME JOURNAL OF APPLIED MECHANICS, Vol. 44, pp. 631–636.

Comninou, M., and Schmueser, D., 1979, "The Interface Crack in a Combined Tension-Compression and Shear Field," ASME JOURNAL OF APPLIED MECHANICS, Vol. 46, pp. 345–358.

Dempsey, J. P., and Sinclair, G. B., 1979, "On the Stress Singularities in the Plane Elasticity of the Composite Wedge," *J. Elasticity*, Vol. 9, pp. 373–391.

Eshelby, J. D., Read, W. T., and Shockley, W, 1953, "Anisotropic Elasticity with Applications to Dislocation Theory," *Acta Metallurgica*, Vol. 1, pp. 251–259.

Gautesen, A. K., and Dundurs, J., 1988, "The Interface Crack Under Combined Loading," ASME JOURNAL OF APPLIED MECHANICS, Vol. 55, pp. 580–586.

Hwu, C., 1990, "Thermal Stresses in an Anisotropic Plate Disturbed by an Insulated Elliptic Hole or Crack," ASME JOURNAL OF APPLIED MECHANICS, Vol. 57, pp. 916–922.

Kirchner, H. O. K., and Lothe, J., 1986, "On the Redundancy of the N Matrix of Anisotropic Elasticity," *Phil. Mag., A.*, Vol. 53, L7-L10.

Nowacki, W., 1962, *Thermoelasticity*, Addison-Wesley, Reading, MA.

Qu, J., and Bassani, J. L., 1989, "Cracks on Bimaterial and Bicrystal Interfaces," *J. Mech. Phys. Solids*, Vol. 37, pp. 417–433.

Stroh, A. N., 1958, "Dislocations and Cracks in Anisotropic Elasticity," *Phil. Mag.* Vol. 3, pp. 625–646.

Stroh, A. N., 1962, "Steady State Problems in Anisotropic Elasticity," *J. Math. Phys.*, Vol. 41, pp. 77–103.

Ting, T. C. T., 1986, "Explicit Solution and Invariance of the Singularities at an Interface Crack in Anisotropic Composites," *Int. J. Solids Structures*, Vol. 22, pp. 965–983.

Ting, T. C. T., 1988, "Some Identities and the Structure of N_i in the Stroh Formalism of Anisotropic Elasticity," *Q. Appl. Math.*, Vol. 46, pp. 109–120.

Ting, T. C. T., 1992, "Barnett-Lothe Tensors and Their Associated Tensors for Monoclinic Materials with the Symmetry Plane at $x_3 = 0$," *J. Elasticity*, Vol. 27, pp. 143–165.

Ting, T. C. T., and Chou, S. C., 1981, "Edge Singularities in Anisotropic Composites," *Int. J. Solids Structures*, Vol. 17, pp. 1057–1068.

Ting, T. C. T., and Hwu, C., 1991, "Effects of Heat Flow on Stress Singularities at the Interface Crack," *Mechanics of Composites at Elevated and Cryogenic Temperatures*, S. N. Singhal, W. F. Jones, and C. T. Herakovich, eds., ASME AMD-Vol. 118, G00618, pp. 231–238.

Ting, T. C. T., and Yan, G., 1992, "The $r^{-1/2}$ (ln r) Singularity at Interface Cracks in Anisotropic Bimaterials Due to Heat Flow," *J. Thermal Stresses*, Vol. 15, pp. 85–99.

Williams, M. L., 1952, "Stress Singularities Resulting from Various Boundary Conditions in Angular Corners of Planes in Extension," ASME JOURNAL OF APPLIED MECHANICS, Vol. 19, pp. 526–528.

Wu, C. H., 1984, "Plane Anisotropic Thermoelasticity," ASME JOURNAL OF APPLIED MECHANICS, Vol. 51, pp. 724–726.

Wu, K. C., and Shyh-Jye Hwang, 1990, "Correspondence Relations for the Interface Crack in Monoclinic Composites under Mixed Loading," ASME JOURNAL OF APPLIED MECHANICS, Vol. 57, pp. 894–900.

Wu, K. C., 1992, "The Contact Zone Model for Interface Cracks," ASME JOURNAL OF APPLIED MECHANICS, Vol. 59, pp. 92–94.

Zwiers, R. I., Ting, T. C. T., and Spilker, R. L., 1982, "On the Logarithmic Singularity of Free-Edge Stress in Laminated Composites Under Uniform Extension," ASME JOURNAL OF APPLIED MECHANICS, Vol. 49, pp. 561–569.

Downloaded 03 May 2010 to 171.66.16.245. Redistribution subject to ASME license or copyright; see http://www.asme.org/terms/Terms_Use.cfm

Perturbation Eigensolutions of Elastic Structures With Cracks

I. Y. Shen
Assistant Professor,
Department of Engineering Mechanics,
University of Nebraska-Lincoln,
Lincoln, NE 68588-0347
Assoc. Mem. ASME

The purpose of this paper is to determine approximate eigensolutions of a class of cracked mechanical systems governed by the two-dimensional Helmholtz equation through a perturbation approach. Shen (1993) shows that exact eigenvalues λ_m^2 and their corresponding crack-opening shapes $\Delta\Psi_m$ of such mechanical systems satisfy a Fredholm integral equation $\mathbf{A}(\lambda_m^2)\Delta\Psi_m = 0$. Following the integral equation approach, the approximation in this paper consists of formulating the Rayleigh quotient of the Fredholm operator $\mathbf{A}(\lambda^2)$ and estimating eigenvalues $\mu(\lambda^2)$ of the operator $\mathbf{A}(\lambda^2)$ through perturbation and stationarity of the Rayleigh quotient. The zeros of $\mu(\lambda^2)$ then approximate eigenvalues λ_m^2 of the cracked systems. Finally, approximate λ_m^2 are calculated for two-dimensional elastic solids under antiplane-strain vibration with an oblique internal crack and a boundary crack.

1 Introduction

Vibration of elastic mechanical systems containing cracks or slots has wide applications in industry. For example, design of slotted circular saws requires knowledge of natural frequencies and mode shapes of circular plates with radial rim slots (Yu and Mote, 1987). On-line detection of emerging cracks in a spinning rotor through vibration monitoring requires knowledge of vibration characteristics of a damaged (cracked) rotor (Wauer, 1990). Estimation of the flutter speed of a damaged aircraft substructure requires knowledge of vibration behaviors of the damaged aircraft substructure. For those areas described above, engineers encounter a common but fundamental problem—vibration of elastic mechanical systems with cracks or slots. Understanding the physics of and obtaining a solution of this fundamental problem will lead to major progress in those areas.

For one-dimensional machine structures with cracks such as beams and rotors, there are various avenues to obtain approximate vibration response. A complete review on this subject is by Wauer (1990). For two or three-dimensional structures containing cracks, vibration response is predicted through experimental methods (Tang and Huang, 1983; Yu and Mote, 1987) and numerical methods (Mote, 1972; Cawley and Adams, 1979; Tang and Huang, 1983; Chen and Chen, 1988; Gounaris and Dimarogonas, 1988; Parker and Mote, 1991). Analytical methods are also available for structures with simple geometry (Stahl and Keer, 1972) or with small cracks (Gudmundson, 1982).

This paper has two objectives. The first objective is to obtain perturbative eigensolutions of a class of cracked mechanical systems governed by the two-dimensional Helmholtz equation, which include antiplane-strain vibration of elastic solids under mode III fracture and scattering and diffraction of standing acoustic waves in a closed acoustic cavity with rigid obstacles. Solutions of simple systems as such will help understanding the physics of more complicated systems such as vibration of slotted plates (Stahl and Keer, 1972; Yu and Mote, 1987; Parker and Mote; 1991).

The second objective of this paper is to develop an approximate analytical relation relating eigensolutions $[\omega_n^2, \phi_n(\mathbf{r})]_{n=1}^{\infty}$ of a perfect system, eigensolutions $[\lambda_m^2, \psi_m(\mathbf{r})]_{m=1}^{\infty}$ of a cracked system, and crack configuration σ_c, i.e.,

$$f([\omega_n^2, \phi_n(\mathbf{r})]_{n=1}^{\infty}, \ [\lambda_m^2, \psi_m(\mathbf{r})]_{m=1}^{\infty}, \sigma_c) = 0. \tag{1}$$

Equation (1) has many engineering applications. For example, if eigensolutions of a mechanical system are monitored before and after cracks emerge, then the crack configuration σ_c may be detected by solving σ_c in terms of $[\omega_n^2, \phi_n(\mathbf{r})]_{n=1}^{\infty}$ and $[\lambda_m^2, \psi_m(\mathbf{r})]_{m=1}^{\infty}$ from (1). Another application of (1) is design of slotted machine components. In case of slot design of circular saws, eigensolutions $[\lambda_m^2, \psi_m(\mathbf{r})]_{m=1}^{\infty}$ of a slotted circular saws and eigensolutions $[\omega_n^2, \phi_n(\mathbf{r})]_{n=1}^{\infty}$ of an axisymmetric saw are both known, then (1) may be inverted to give the optimal slot configuration σ_c.

In this paper, both objectives are achieved for systems governed by the two-dimensional Helmholtz equation. According to Shen (1993), exact eigenvalues λ_m^2 and their corresponding crack-opening shapes $\Delta\Psi_m$ satisfy a Fredholm integral equation $\mathbf{A}(\lambda_m^2)\Delta\Psi_m = 0$. Following the integral equation approach, the approximation in this paper consists of formulating the Rayleigh quotient of the Fredholm operator $\mathbf{A}(\lambda^2)$ and estimating eigenvalues $\mu(\lambda^2)$ of the operator $\mathbf{A}(\lambda^2)$ through perturbation and stationarity of the Rayleigh quotient. The zeros of $\mu(\lambda^2)$ then approximate eigenvalues λ_m^2 of the cracked systems. Finally, approximate λ_m^2 are calculated for two-dimensional elas-

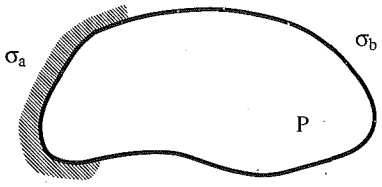
Contributed by the Applied Mechanics Division of THE AMERICAN SOCIETY OF MECHANICAL ENGINEERS for presentation at the First Joint ASCE-EMD, ASME-AMD, SES Meeting, Charlottesville, VA, June 6-9, 1993.

Discussion on this paper should be addressed to the Technical Editor, Professor Lewis T. Wheeler, Department of Mechanical Engineering, University of Houston, Houston, TX 77204-4792, and will be accepted until four months after final publication of the paper itself in the ASME JOURNAL OF APPLIED MECHANICS.

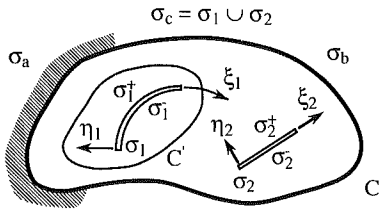
Manuscript received by the ASME Applied Mechanics Division, Jan. 24, 1992; final revision, Apr. 21, 1992. Associate Technical Editor: A. K. Noor.

Paper No. 93-APM-36.

Copyright © 1993 by ASME
Downloaded 03 May 2010 to 171.66.16.245. Redistribution subject to ASME license or copyright; see http://www.asme.org/terms/Terms_Use.cfm



(a) A Perfect Structure P



(b) A Structure C with Cracks

Fig. 1(*a*) A perfect structure *P* containing no cracks with eigenvalues ω_n^2 and eigenfunctions $\phi_n(\mathbf{r})$; (*b*) a cracked structure *C* with crack geometry σ_c, eigenvalues λ_m^2, and eigenfunctions $\psi_m(\mathbf{r})$

tic solids under antiplane-strain vibration with an oblique internal crack and a boundary crack.

2 Formulation

Consider a two-dimensional, linear, elastic solid P with shear modulus G and density ρ occupying a finite domain τ with a fixed boundary σ_a and a free boundary σ_b; see Fig. 1(*a*). When the solid P is under antiplane-strain vibration, eigenfunctions $\phi_n(\mathbf{r})$ and eigenvalues ω_n^2 of P satisfy

$$-G\nabla^2\phi_n(\mathbf{r}) = \rho\omega_n^2\phi_n(\mathbf{r}), \quad \mathbf{r}\in\tau \tag{2}$$

with boundary conditions

$$\phi_n(\mathbf{r}) = 0, \quad \mathbf{r}\in\sigma_a \tag{3}$$

$$G\frac{\partial\phi_n(\mathbf{r})}{\partial n} = 0, \quad \mathbf{r}\in\sigma_b \tag{4}$$

and orthonormality condition

$$\int_\tau \rho\phi_m(\mathbf{r})\phi_n(\mathbf{r})d\tau = \delta_{mn}. \tag{5}$$

Consider a linear, elastic solid C occupying the same domain τ with n_c cracks of zero traction. In addition, the crack width is infinitesimal; see Fig. 1(*b*). When the solid C is also under antiplane-strain vibration, eigenfunctions $\psi(\mathbf{r})$ and eigenvalues λ^2 of C satisfy

$$-G\nabla^2\psi(\mathbf{r}) = \rho\lambda^2\psi(\mathbf{r}), \quad \mathbf{r}\in\tau' \tag{6}$$

with boundary conditions

$$\psi(\mathbf{r}) = 0, \quad \mathbf{r}\in\sigma_a \tag{7}$$

$$G\frac{\partial\psi(\mathbf{r})}{\partial n} = 0, \quad \mathbf{r}\in\sigma_b\cup\sigma_c \tag{8}$$

Here $\sigma_c \equiv \cup_{i=1}^{n_c}\sigma_i$, where σ_i is the boundary of the ith cracks, and $\tau' \equiv \tau - \sigma_c$. (Equations (2) to (8) also describe scattering and diffraction of standing acoustic waves in a closed acoustic cavity, if $c \equiv \sqrt{G/\rho}$ is the acoustic wave speed and σ_c represents rigid obstacles in the cavity.)

According to Shen (1993), $\psi(\mathbf{r})$ can be represented as

$$\psi(\mathbf{r}) = \sum_{n=1}^{\infty}\frac{A_n}{\lambda^2-\omega_n^2}\phi_n(\mathbf{r}), \quad \mathbf{r}\in\tau' \tag{9}$$

where

$$A_n = G\langle\mathbf{g}_n|\Delta\boldsymbol{\Psi}\rangle \tag{10}$$

Here $\Delta\boldsymbol{\Psi}$ and $\mathbf{g}_n$ are column vectors

$$\Delta\boldsymbol{\Psi} = [\Delta\psi(\xi_1), \Delta\psi(\xi_2), \ldots, \Delta\psi(\xi_{n_c})]^T \tag{11}$$

$$\mathbf{g}_n = \left[\frac{\partial\phi_n(\xi_1)}{\partial n}, \frac{\partial\phi_n(\xi_2)}{\partial n}, \ldots, \frac{\partial\phi_n(\xi_{n_c})}{\partial n}\right]^T \tag{12}$$

and $\langle\mathbf{g}_n|\Delta\boldsymbol{\Psi}\rangle$ is an inner product defined as

$$\langle\mathbf{g}_n|\Delta\boldsymbol{\Psi}\rangle \equiv \sum_{i=1}^{n_c}\int_{\sigma_i^+}\frac{\partial\phi_n(\xi_i)}{\partial n}\Delta\psi(\xi_i)d\sigma_i \tag{13}$$

where ξ_i is a curvilinear coordinate along the ith crack, $d\sigma_i$ is the arc length of $d\xi_i$, and $\Delta\psi(\xi_i) \equiv \psi(\sigma_i^+) - \psi(\sigma_i^-)$ is the opening shape across the ith crack in Fig. 1(*b*). If σ_c coincides with antinodes of $\phi\sigma_N(\mathbf{r})$, then $\mathbf{g}_N = \mathbf{0}$ and $A_N = 0$. Therefore, the Nth term in (9) vanishes, and the Nth eigenvalue of P remains unchanged when the cracks are introduced (i.e., $\lambda_N = \omega_N$).

According to Shen (1993), eigensolutions λ^2 and $\Delta\psi$ satisfy the following Fredholm integral equation:

$$\mathbf{A}(\lambda^2)\Delta\boldsymbol{\Psi} \equiv G^2\sum_{n=1}^{\infty}\frac{\lambda^2\mathbf{g}_n\langle\mathbf{g}_n|\Delta\boldsymbol{\Psi}\rangle}{\omega_n^2(\lambda^2-\omega_n^2)} + \mathbf{R}\Delta\boldsymbol{\Psi} = \mathbf{0}. \tag{14}$$

Here $\mathbf{R}$ is a symmetric, positive definite operator satisfying

$$\langle\Delta\boldsymbol{\Psi}|\mathbf{R}\Delta\boldsymbol{\Psi}\rangle = \|\nabla\chi\|^2 \tag{15}$$

where

$$\|\nabla\chi\|^2 = \int_{\tau'} G\nabla\chi(\mathbf{r})\cdot\nabla\chi(\mathbf{r})d\tau \tag{16}$$

and

$$\chi(\mathbf{r}) = -\sum_{n=1}^{\infty}\frac{A_n}{\omega_n^2}\phi_n(\mathbf{r}), \quad \mathbf{r}\in\tau'. \tag{17}$$

It can be shown that $\chi(\mathbf{r})$ is the antiplane-strain displacement field of C subjected to a pair of equal and opposite tractions tearing the cracks with an opening shape $\Delta\boldsymbol{\Psi}$. In addition, $\|\nabla\chi\|^2$ is twice the strain energy of C under the antiplane-strain deformation. Moreover, explicit expression of $\mathbf{R}$ has been determined by Shen (1993).

Obtaining nontrivial λ^2 and $\Delta\boldsymbol{\Psi}$ from (14) is generally unwieldy, because (14) is nonlinear in λ^2. For example, (14) may or may not have nontrivial λ^2 in a given interval $[\omega_a^2, \omega_b^2]$. If it does, (14) may have multiple nontrivial λ^2 sparsely spaced in $[\omega_a^2, \omega_b^2]$ or clustered in a small subinterval of $[\omega_a^2, \omega_b^2]$. Therefore, searching nontrivial λ^2 of (14) in $[\omega_a^2, \omega_b^2]$ can be unwieldy, because an optimal step size is difficult to determine.

To overcome problems as such, an algorithm that will predict nontrivial λ^2 and $\Delta\boldsymbol{\Psi}$ systematically is proposed as follows. Let $\mu(\lambda^2)$ and $\mathbf{v}(\lambda^2)$ be eigenvalues and eigenfunctions of the Fredholm operator $\mathbf{A}(\lambda^2)$ in (14), i.e.,

$$\mathbf{A}(\lambda^2)\mathbf{v}(\lambda^2) = \mu(\lambda^2)\mathbf{v}(\lambda^2). \tag{18}$$

Comparison of (14) with (18) shows that the mth eigenvalue λ_m^2 of C is the mth zero of $\mu(\lambda^2)$ satisfying $\mu(\lambda_m^2) = 0$. In addition, $\Delta\boldsymbol{\Psi}_m = \mathbf{v}(\lambda_m^2)$. Figure 2 shows typical $\mu(\lambda^2)$.

The solid lines in Fig. 2 illustrate eigenvalue loci $\mu(\lambda^2)$ of a rectangular elastic solid shown in Fig. 3. The solid is under antiplane-strain vibration with $G = \rho = 1$, $a = \pi/2$, $b = 1$, $(x_0, y_0) = (0.6, 0.3)$, $\theta = 45$ deg. The crack length is $l = 2\sqrt{2}/5$. The eigenvalue loci are obtained by discretizing the Fredholm operator $\mathbf{A}(\lambda^2)$ through a Ritz method (Shen, 1993). Vertical lines in Fig. 2 represent eigenvalues ω_n^2 of P. In addition, a unique eigenvalue locus $\mu(\lambda^2)$ becomes singular as $\lambda \to \omega_n$. Furthermore, each singular locus has a unique zero corresponding to an eigenvalue λ_m^2 of C. The zeros are denoted by arrows in Fig. 2. Therefore, λ_m^2 of C can be determined systematically

Downloaded 03 May 2010 to 171.66.16.245. Redistribution subject to ASME license or copyright; see http://www.asme.org/terms/Terms_Use.cfm

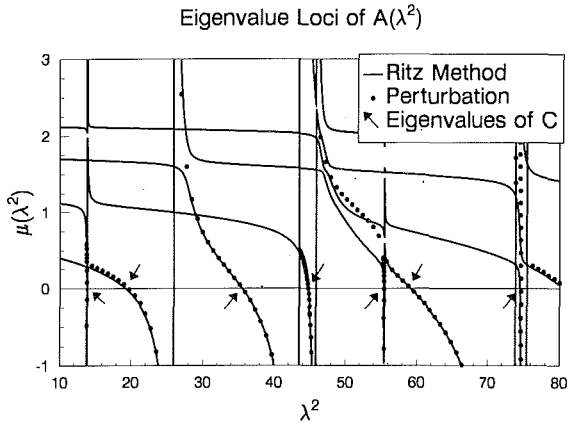


Fig. 2 Eigenvalue loci $\mu(\lambda^2)$ of an elastic solid under antiplane-strain vibration with $G=\rho=1$, $a=\pi/2$, $b=1$ $(x_0, y_0)=(0.6, 0.3)$, $l=2\sqrt{2}/5$, and $\theta=45$ deg

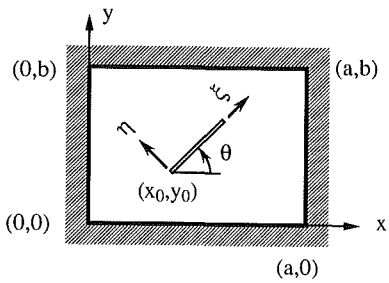


Fig. 3 A two-dimensional elastic solid under antiplane-strain vibration with an oblique crack

by searching the unique zero of each singular locus $\mu(\lambda^2)$ from the singularity with decreasing λ^2.

To implement this algorithm, the rest of the paper describes a perturbation method to approximate each singular locus of $\mathbf{A}(\lambda^2)$.

3 Singular Eigenvalue Loci of $\mathbf{A}(\lambda^2)$

Consider the eigenvalue locus $\mu(\lambda^2)$ that is singular as $\lambda \to \omega_N^-$. This locus is also the lowest eigenvalue locus of $\mathbf{A}(\lambda^2)$ for $\omega_{N-1}^2 < \lambda^2 < \lambda_N^2$. Assume that $\mathbf{g}_N$ and $\mathbf{g}_{N-1}$ are linearly independent and span a two dimensional space S_N. It will be shown as follows that $\mathbf{\Delta\Psi}$ corresponding to the lowest eigenvalue locus of $\mathbf{A}(\lambda^2)$ is dominated by a linear combination of $\mathbf{g}_N$ and $\mathbf{g}_{N-1}$ when $\omega_{N-1}^2 < \lambda^2 < \omega_N^2$.

When

$$\lambda^2 - \omega_N^2 \sim \epsilon\omega_N^2 \tag{19}$$

where ϵ is a small parameter, $\mathbf{A}(\lambda^2)$ is asymptotic to

$$\mathbf{A}(\lambda^2) \sim \frac{G^2 \mathbf{g}_N \langle \mathbf{g}_N | \bullet \rangle}{\epsilon\omega_N^2} \tag{20}$$

The lowest eigenvalue locus, which is singular as $\lambda \to \omega_N^-$ in Fig. 2, is

$$\mu(\lambda^2) \sim \frac{G^2\langle \mathbf{g}_N | \mathbf{g}_N \rangle}{\epsilon\omega_N^2} \sim \frac{G^2\langle \mathbf{g}_N | \mathbf{g}_N \rangle}{\lambda^2 - \omega_N^2} \tag{21}$$

with the corresponding eigenfunction

$$\mathbf{\Delta\Psi} \sim \mathbf{g}_N. \tag{22}$$

In addition, eigenfunctions corresponding to those eigenvalue loci that are regular at $\lambda^2 = \omega_N^2$ in Fig. 2 satisfy

$$\langle \mathbf{\Delta\Psi} | \mathbf{g}_N \rangle = 0. \tag{23}$$

For $\omega_{N-1}^2 < \lambda^2 < \omega_N^2$, $\mathbf{A}(\lambda^2)$ can be decomposed as

$$\mathbf{A}\mathbf{\Delta\Psi} = \mathbf{A}^{(N)}\mathbf{\Delta\Psi} + \overline{\mathbf{A}}^{(N)}\mathbf{\Delta\Psi} \tag{24}$$

where

$$\mathbf{A}^{(N)}\mathbf{\Delta\Psi} \equiv \frac{G^2\lambda^2 \mathbf{g}_{N-1}\langle \mathbf{g}_{N-1} | \mathbf{\Delta\Psi} \rangle}{\omega_{N-1}^2(\lambda^2 - \omega_{N-1}^2)} + \frac{G^2\lambda^2 \mathbf{g}_N \langle \mathbf{g}_N | \mathbf{\Delta\Psi} \rangle}{\omega_N^2(\lambda^2 - \omega_N^2)} \tag{25}$$

and

$$\overline{\mathbf{A}}^{(N)}\mathbf{\Delta\Psi} \equiv G^2 \sum_{n \neq N-1}^{N} \frac{\lambda^2 \mathbf{g}_n \langle \mathbf{g}_n | \mathbf{\Delta\Psi} \rangle}{\omega_n^2(\lambda^2 - \omega_n^2)} + \mathbf{R}\mathbf{\Delta\Psi} \tag{26}$$

Here $\Sigma_{n\neq N-1}^{N} \equiv \Sigma_{n=1}^{\infty}$ with $n \neq N-1, N$. Notice that $\mathbf{A}^{(N)}$ is dominant because of its denominators $(\lambda^2 - \omega_{N-1}^2)$ and $(\lambda^2 - \omega_N^2)$. Let $\mu^{(N)}(\lambda^2)$ and $\mathbf{\Delta\Psi}^{(N)}(\lambda^2)$ be the lowest eigenvalue and the corresponding eigenfunction of $\mathbf{A}^{(N)}(\lambda^2)$. Then $\mathbf{\Delta\Psi}^{(N)}$ is a linear combination of $\mathbf{g}_{N-1}$ and $\mathbf{g}_N$

$$\mathbf{\Delta\Psi}^{(N)} = \mathbf{g}_N + y(\lambda^2)\mathbf{g}_{N-1} \in S_N \tag{27}$$

because $\mathbf{\Delta\Psi}^{(N)}$ satisfies the asymptotic property (22) with

$$\lim_{\lambda \to \omega_N^-} y(\lambda^2) = 0 \tag{28}$$

Consider $\mathbf{A}^{(N)}$ as an unperturbed operator and $\overline{\mathbf{A}}^{(N)}$ as a perturbation to $\mathbf{A}^{(N)}$ for $\omega_{N-1}^2 < \lambda^2 < \omega_N^2$. According to operator perturbation theories (Courant and Hilbert, 1953), the eigenfunction $\mathbf{\Delta\Psi}(\lambda^2)$ of $\mathbf{A}(\lambda^2)$ is

$$\mathbf{\Delta\Psi} = \mathbf{\Delta\Psi}^{(N)} + \delta_1 \tag{29}$$

where $\delta_1 \perp \mathbf{\Delta\Psi}^{(N)}$ and $\|\delta_1\| \ll \|\mathbf{\Delta\Psi}^{(N)}\|$. Equations (27) and (29) imply that the opening shape of the cracks primarily consists of $\mathbf{g}_N$ and $\mathbf{g}_{N-1}$ if the cracked system is in resonance at $\omega_{N-1} < \lambda < \omega_N$.

The radius of convergence of the perturbation solutions (29) may be zero at particular λ_0, where the lowest eigenvalue locus and another eigenvalue locus of $\mathbf{A}(\lambda^2)$ are approximately equal. In this case, $\mathbf{\Delta\Psi}(\lambda^2)$ will deviate away from (29) abruptly when λ^2 passes λ_0^2. This is known as curve veering (Perkins and Mote, 1986). The derivation thereafter will hold only when curve veering does not occur.

The lowest eigenvalue locus of $\mathbf{A}(\lambda^2)$ can be determined through the Rayleigh quotient

$$\mu(\lambda^2) = \frac{\langle \mathbf{\Delta\Psi} | \mathbf{A}\mathbf{\Delta\Psi} \rangle}{\langle \mathbf{\Delta\Psi} | \mathbf{\Delta\Psi} \rangle}. \tag{30}$$

Substitute (29) and (27) into (30) and recall $\|\delta_1\| \ll \|\mathbf{\Delta\Psi}^{(N)}\|$ to obtain

$$\mu(\lambda^2) \approx \frac{\langle \mathbf{\Delta\Psi}^{(N)} | \mathbf{A}\mathbf{\Delta\Psi}^{(N)} \rangle}{\langle \mathbf{\Delta\Psi}^{(N)} | \mathbf{\Delta\Psi}^{(N)} \rangle} \equiv \frac{I_1}{I_2} \tag{31}$$

where

$$I_1 = \langle \mathbf{g}_{N-1} | \mathbf{A}\mathbf{g}_{N-1} \rangle y^2 + 2\langle \mathbf{g}_{N-1} | \mathbf{A}\mathbf{g}_N \rangle y + \langle \mathbf{g}_N | \mathbf{A}\mathbf{g}_N \rangle \tag{32}$$

and

$$I_2 = \langle \mathbf{g}_{N-1} | \mathbf{g}_{N-1} \rangle y^2 + 2\langle \mathbf{g}_{N-1} | \mathbf{g}_N \rangle y + \langle \mathbf{g}_N | \mathbf{g}_N \rangle. \tag{33}$$

In addition, the Rayleigh quotient (30) is stationary at an eigenfunction $\mathbf{\Delta\Psi}$. This is approximated by

$$\frac{d\mu}{dy} = \frac{1}{I_2^2}\left[I_2 \frac{dI_1}{dy} - I_1 \frac{dI_2}{dy} \right] = 0. \tag{34}$$

Substitute (32) and (33) into (34) to obtain

$$\alpha y^2 + \beta y + \gamma = 0 \tag{35}$$

where

$$\alpha = \langle \mathbf{g}_{N-1} | \mathbf{g}_N \rangle \langle \mathbf{g}_{N-1} | \mathbf{A}\mathbf{g}_{N-1} \rangle - \langle \mathbf{g}_{N-1} | \mathbf{g}_{N-1} \rangle \langle \mathbf{g}_{N-1} | \mathbf{A}\mathbf{g}_N \rangle \tag{36}$$

$$\beta = \langle \mathbf{g}_N | \mathbf{g}_N \rangle \langle \mathbf{g}_{N-1} | \mathbf{A}\mathbf{g}_{N-1} \rangle - \langle \mathbf{g}_{N-1} | \mathbf{g}_{N-1} \rangle \langle \mathbf{g}_N | \mathbf{A}\mathbf{g}_N \rangle \tag{37}$$

$$\gamma = \langle \mathbf{g}_N | \mathbf{g}_N \rangle \langle \mathbf{g}_{N-1} | \mathbf{A}\mathbf{g}_N \rangle - \langle \mathbf{g}_{N-1} | \mathbf{g}_N \rangle \langle \mathbf{g}_N | \mathbf{A}\mathbf{g}_N \rangle \tag{38}$$

Downloaded 03 May 2010 to 171.66.16.245. Redistribution subject to ASME license or copyright; see http://www.asme.org/terms/Terms_Use.cfm

Solve (35) for y to obtain

$$y = y_{1,2} = \frac{-\beta \pm \sqrt{\beta^2 - 4\alpha\gamma}}{2\alpha}. \tag{39}$$

y_1 and y_2 in (39) describe two eigenvalue loci whose eigenfunctions are dominated by (29). Nevertheless, only the one that satisfies (28) corresponds to the lowest eigenvalue locus. It is determined as follows.

Equations (21) and (22) imply that

$$\lim_{\lambda \to \omega_N^-} \gamma = 0. \tag{40}$$

Also, rewrite $\mathbf{g}_{N-1}$ as

$$\mathbf{g}_{N-1} = \frac{\langle \mathbf{g}_{N-1} | \mathbf{g}_N \rangle}{\langle \mathbf{g}_N | \mathbf{g}_N \rangle} \mathbf{g}_N + \left[\mathbf{g}_{N-1} - \frac{\langle \mathbf{g}_{N-1} | \mathbf{g}_N \rangle}{\langle \mathbf{g}_N | \mathbf{g}_N \rangle} \mathbf{g}_N \right]. \tag{41}$$

When $\lambda \to \omega_N^-$,

$$\langle \mathbf{g}_{N-1} | \mathbf{A} \mathbf{g}_{N-1} \rangle \sim \mu(\omega_N^2) \frac{\langle \mathbf{g}_{N-1} | \mathbf{g}_N \rangle^2}{\langle \mathbf{g}_N | \mathbf{g}_N \rangle}. \tag{42}$$

Hence,

$$\beta \sim \mu(\omega_N^2)[\langle \mathbf{g}_{N-1} | \mathbf{g}_N \rangle^2 - \langle \mathbf{g}_{N-1} | \mathbf{g}_{N-1} \rangle \langle \mathbf{g}_N | \mathbf{g}_N \rangle] > 0, \tag{43}$$

by Schwartz inequality when $\lambda \to \omega_N^-$. Therefore, the lowest eigenvalues $\mu(\lambda^2)$ and its eigenfunctions $\Delta\Psi$ are approximated by (27) and (30) with

$$y = y_1 = \frac{-\beta + \sqrt{\beta^2 - 4\alpha\gamma}}{2\alpha} \tag{44}$$

because $\lim_{\lambda \to \omega_N^-} y_1 = 0$ according to (40) and (43).

In summary, eigenvalues λ_m^2 of a cracked system C can be predicted systematically by searching the unique zero of every singular eigenvalue locus of $\mathbf{A}(\lambda^2)$ from the singularity with decreasing λ^2. For the locus $\mu(\lambda^2)$ that is singular at $\lambda \to \omega_N^-$, the crack-opening shape $\Delta\Psi$ is dominated by a linear combination of $\mathbf{g}_N$ and $\mathbf{g}_{N-1}$ when $\omega_{N-1} < \lambda < \omega_N$. The relative contribution of $\mathbf{g}_N$ and $\mathbf{g}_{N-1}$, represented by $y_1(\lambda^2)$, is determined by the stationarity of the Rayleigh quotient of $\mathbf{A}(\lambda^2)$. Because λ_m^2 of C are zeros of $\mu(\lambda^2)$, (30) implies that λ_m^2 satisfy an algebraic equation

$$\langle \Delta\Psi(\lambda^2) | \mathbf{A}(\lambda^2) \Delta\Psi(\lambda^2) \rangle = 0. \tag{45}$$

Furthermore, (45) has one and only one zero for each singular locus of $\mathbf{A}(\lambda^2)$.

4 Extending the Singular Loci of $\mathbf{A}(\lambda^2)$

For the eigenvalue locus $\mu(\lambda^2)$ that is singular at $\lambda \to \omega_N^-$, the zero of (45), sometimes, may not be in the interval $[\omega_{N-1}^2, \omega_N^2]$. In this case, the zero may be determined by extending the locus to $\omega_{N-2}^2 < \lambda^2 < \omega_{N-1}^2$. For example, the solid lines in Fig. 4 show eigenvalue loci $\mu(\lambda^2)$ of the system in Fig. 3 with $65 < \lambda^2 < 100$, $G = \rho = 1$, $a = \pi$, $b = 1$, $(x_0, y_0) = (0, 0)$ and $\theta = 90$ deg. The crack length is $l = 1$. In addition, the zero of the locus that is singular at $\lambda^2 \approx 75.478$ does not lie in $[\omega_{13}^2, \omega_{14}^2] = [73.869, 75.478]$. Nevertheless, the zero can be obtained by extending the locus to $[\omega_{12}^2, \omega_{13}^2] = [64.478, 73.869]$. Such zeros are denoted by arrows in Fig. 4.

To extend the singular locus to $\omega_{N-2}^2 < \lambda^2 < \omega_{N-1}^2$, asymptotic behaviors of the y_1 locus as $\lambda \to \omega_{N-1}^+$ are needed. Similar to (40) and (43), it can be shown that $\alpha \sim 0$ and

$$y_1 \sim -\frac{\gamma}{\beta} = -\frac{\langle \mathbf{g}_N | \mathbf{g}_{N-1} \rangle}{\langle \mathbf{g}_{N-1} | \mathbf{g}_{N-1} \rangle} \tag{46}$$

when $\lambda \to \omega_{N-1}^+$. Therefore, (27) and (46) imply that

$$\Delta\Psi = \mathbf{H}_{N-1} \mathbf{g}_N \tag{47}$$

when $\lambda \to \omega_{N-1}^+$, where

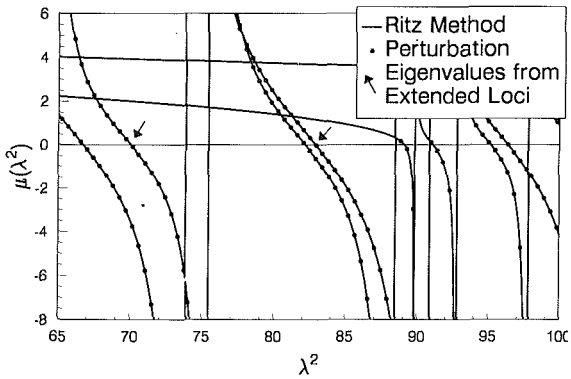


Fig. 4 Eigenvalue loci $\mu(\lambda^2)$ of an elastic solid under antiplane-strain vibration with $G = \rho = 1$, $a = \pi$, $b = 1$, $(x_0, y_0) = (0, 0)$, $l = 1$, and $\theta = 90$ deg

$$\mathbf{H}_{N-1} \equiv \mathbf{I} - \frac{\mathbf{g}_{N-1} \langle \mathbf{g}_{N-1} | \bullet \rangle}{\langle \mathbf{g}_{N-1} | \mathbf{g}_{N-1} \rangle} \tag{48}$$

Notice that $\langle \mathbf{g}_{N-1} | \mathbf{H}_{N-1} \mathbf{g}_N \rangle = 0$, and the lowest eigenvalue locus is regular when $\lambda \to \omega_{N-1}^+$.

Motivated by the asymptotic behavior (47) and the structure of $\Delta\Psi$ given in (27), a two-term approximation

$$\Delta\Psi^{(N-1)} = \mathbf{H}_{N-1} \mathbf{g}_N + y(\lambda^2) \mathbf{g}_{N-2} \tag{49}$$

is assumed for the extension of the singular locus to $\omega_{N-2}^2 < \lambda^2 < \omega_{N-1}^2$. Therefore, all the formulas derived for the singular locus in $\omega_{N-1}^2 < \lambda^2 < \omega_N^2$ can be applied to the extended locus in $\omega_{N-2}^2 < \lambda^2 < \omega_{N-1}^2$, provided that $\mathbf{g}_N$ and $\mathbf{g}_{N-1}$ are replaced by $\mathbf{H}_{N-1} \mathbf{g}_N$ and $\mathbf{g}_{N-2}$, respectively. Similarly, the singular locus extended to $\omega_{N-i-1}^2 < \lambda^2 < \omega_{N-i}^2$ can be predicted through those formulas with $\mathbf{g}_N$ and $\mathbf{g}_{N-1}$ replaced by $(\Pi_{k=0}^{i-1} \mathbf{H}_{N+k-i}) \mathbf{g}_N$ and $\mathbf{g}_{N-i-1}$.

5 Special Cases

Two special cases can occur: $\mathbf{g}_{N-1} \| \mathbf{g}_N$ and $N = 1$. If $\mathbf{g}_{N-1} \| \mathbf{g}_N$, then $\Delta\Psi^{(N)} = \mathbf{g}_N$. Therefore, (31) implies that

$$\mu(\lambda^2) \approx \frac{\langle \mathbf{g}_N | \mathbf{A} \mathbf{g}_N \rangle}{\langle \mathbf{g}_N | \mathbf{g}_N \rangle} \tag{50}$$

For $N = 1$, $\Delta\Psi \approx \mathbf{g}_1$. Therefore, μ is given by (50) with $N = 1$.

6 Numerical Examples

Eigenvalues λ_m^2 of the two systems illustrated earlier in the paper are calculated here using the perturbation solutions. Figure 2 shows $\mu(\lambda^2)$ of the system with an oblique internal crack. The circular points are approximations to the lowest eigenvalue through y_1 in (27), (30), and (44). They predict the lowest eigenvalue very well until the lowest eigenvalue locus intersects with another eigenvalue locus (e.g., $26 < \lambda^2 < 42$) or curve veering occurs (e.g., $74 < \lambda^2 < 76$). At these specific occasions, $\Delta\Psi$ changes abruptly away from (29) causing the $\mu(\lambda^2)$ predicted by (30) to deviate away from the lowest locus. Table 1 shows the zeros obtained from the Ritz method and the perturbation method. The zeros show very good agreement and the maximum difference is about 2.2 percent.

Figure 4 shows the eigenvalue loci of the system with a boundary crack. The circular points are approximations from (27), (30), and (44) for the lowest eigenvalue locus, and from (49) for the extension of the lowest eigenvalue locus. Table 2 shows the zeros obtained from the Ritz method and the perturbation method. These zeros agree very well and the maximum difference is less than 0.1 percent.

As mentioned earlier in the paper, this perturbation scheme will break down when curve veering occurs; see $\lambda^2 \approx 174$ and

Downloaded 03 May 2010 to 171.66.16.245. Redistribution subject to ASME license or copyright; see http://www.asme.org/terms/Terms_Use.cfm

Table 1 Eigenvalues λ_m^2 of the elastic solid with $(x_0, y_0) = (0.6, 0.3)$ and $\theta = 45$ deg

Eigenvalues λ_m^2		
Ritz Method	Perturbation	Difference
13.811	13.814	0.02%
19.217	19.638	2.19%
35.524	35.525	0.00%
44.688	44.737	0.11%
55.386	55.418	0.06%
59.024	59.051	0.05%
74.497	74.545	0.06%

Table 2 Eigenvalues λ_m^2 of the elastic solid with $(x_0, y_0) = (0, 0)$ and $\theta = 90$ deg

Eigenvalues λ_m^2		
Ritz Method	Perturbation	Difference
66.755	66.753	0.00%
70.069	70.067	0.00%
82.204	82.203	0.00%
82.938	82.936	0.00%
89.097	89.078	0.02%
91.102	91.100	0.00%
95.146	95.145	0.00%
96.363	96.362	0.00%

$\lambda^2 \approx 183$ in Fig. 5. Figure 5 shows eigenvalue loci of the system in Fig., 3 with $165 < \lambda^2 < 190$, $G = \rho = 1$, $a = \pi$, $b = 1$, $(x_0, y_0) = (0, 0)$, $\theta = 90$ deg, $l = 0.5$. The perturbation solutions (circular points) start to deviate from the Ritz solutions (solid lines) when curve veering (arrows) occurs. Because the curve veering occurs at $\mu(\lambda^2) < 0$, the perturbation solutions fail to predict the zeros of the loci.

7 Conclusions

1 This paper proposes an algorithm to approximate eigensolutions $[\lambda_m^2, \psi_m(\mathbf{r})]_{m=1}^{\infty}$ of a cracked system governed by the two-dimensional Helmholtz equation. Through a perturbation method, this algorithm searches the unique zero of each singular eigenvalue locus of $\mathbf{A}(\lambda^2)$ from the singularity with decreasing λ^2. The zero then predicts an eigenvalue λ_m^2 of the cracked system.

2 For an eigenvalue locus $\mu(\lambda^2)$ that is singular as $\lambda \to \omega_N^-$, the opening shape $\Delta\Psi$ of the cracks is governed by $\Delta\Psi = \mathbf{g}_N + y_1(\lambda^2)\mathbf{g}_{N-1}$ for $\omega_{N-1}^2 < \lambda^2 < \omega_N^2$ and $\Delta\Psi = (\Pi_{k=0}^{i-1}\mathbf{H}_{N-i+k})\mathbf{g}_N + y_1(\lambda^2)\mathbf{g}_{N-i-1}$ for $\omega_{N-i-1}^2 < \lambda^2 < \omega_{N-i}^2$, $i = 1, 2, \ldots, N-2$. The relative contribution between $\mathbf{g}_N$ and $\mathbf{g}_{N-1}$, represented by $y_1(\lambda^2)$, is determined by (44).

3 For an eigenvalue locus $\mu(\lambda^2)$ that is singular as $\lambda \to \omega_N^-$,

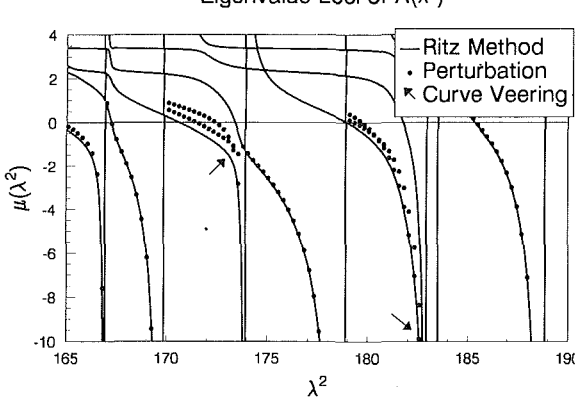


Fig. 5 Eigenvalue loci $\mu(\lambda^2)$ of an elastic solid under antiplane-strain vibration with $G = \rho = 1$, $a = \pi$, $b = 1$, $(x_0, y_0) = (0, 0)$, $l = 0.5$, and $\theta = 90$ deg

its unique zero satisfying the algebraic Eq. (45) will approximate an eigenvalue λ_m^2 of C. Moreover, (45) is analytical expression relating eigenvalues λ_m^2 of C, eigensolutions $[\omega_n^2, \phi_n(\mathbf{r})]_{n=1}^{\infty}$ of P, and the crack configuration σ_c. Therefore, the crack configuration σ_c may be detected by solving σ_c in (45) in terms λ_m^2 and $[\omega_n^2, \phi_n(\mathbf{r})]_{n=1}^{\infty}$.

4 Numerical examples show that the above perturbation solutions agree very well with existing numerical solutions, provided that curve veering does not occur.

Acknowledgments

The author thanks Prof. Millard F. Beatty and S. I. Chou for making comments on the manuscript to the author.

References

Cawley, P., and Adams, R. D., 1979, "The Location of Defects in Structures from Measurements of Natural Frequencies," *Journal of Strain Analysis*, Vol. 14, pp. 49–57.

Chen, L.-W., and Chen, C.-L., 1988, "Vibration and Stability of Cracked Thick Rotating Blades," *Computers & Structures*, Vol. 28, pp. 67–74.

Courant, B., and Hilbert, D., 1953, *Method of Mathematical Physics*, Vol. I, Interscience Publishers, New York.

Gounaris, G., and Dimarogonas, A., 1988, "A Finite Element of a Cracked Prismatic Beam for Structural Analysis," *Computers & Structures*, Vol. 28, pp. 309–313.

Gudmundson, P., 1982, "Eigenfrequency Changes of Structures Due to Cracks, Notches or Other Geometrical Changes," *Journal of the Mechanics and Physics of Solids*, Vol. 30, pp. 339–353.

Mote, C. D., Jr., 1972, "Stability Control Analysis of Rotating Plates by Finite Element: Emphasis on Slots and Holes," ASME *Journal of Dynamic Systems, Measurement, and Control*, Vol. 94, pp. 64–70.

Parker, R. G., and Mote, C. D., Jr., 1991, "Tuning of the Natural Frequency Spectrum of a Circular Plate by In-plane Stresses," *Journal of Sound and Vibration*, Vol. *145*, pp. *95–110*.

Perkins, N. C., and Mote, C. D., Jr., 1986, "Comments on Curve Veering in Eigenvalue Problems," *Journal of Sound and Vibration*, Vol. 106, pp. 451–463.

Shen, I. Y., 1993, "Vibration of Elastic Structures with Cracks," ASME JOURNAL OF APPLIED MECHANICS, in press.

Stahl, B., and Keer, L. M., 1972, "Vibration and Stability of Cracked Rectangular Plates," *International Journal of Solids and Structures*, Vol. 8, pp. 69–91.

Tang, Z. Q., and Huang, T. C., 1983, "Modal Analysis of a Cylindrical Shell with a Longitudinal Crack," *Modal Testing and Model Refinement*, ASME, AMD-Vol. 59, pp. 77–84.

Wauer, Jörg, 1990, "On the Dynamics of Cracked Rotors: A Literature Survey," ASME *Applied Mechanics Review*, Vol. 43, pp. 13–17.

Yu, R. C., and Mote, C. D., Jr., 1987, "Vibration and Parametric Excitation in Asymmetric Circular Plates Under Moving Loads," *Journal of Sound and Vibration*, Vol. 119, pp. 409–427.

Downloaded 03 May 2010 to 171.66.16.245. Redistribution subject to ASME license or copyright; see http://www.asme.org/terms/Terms_Use.cfm

Separation of Strain Components in Composite Materials From Thermoelastic Temperature Measurements

S. A. Dunn[1]
Department of Mechanical and Manufacturing Engineering, University of Melbourne, Parkville, Victoria, Australia

In this paper experimental data is used to demonstrate how point-to-point strain components can be determined from thermoelastic temperature data. This is done by making use of the very obvious effects of thermal conduction on the cyclic surface temperature changes which can occur as a composite material undergoes an oscillating stress. By observing the cyclic surface temperature changes for different loading frequencies, the adiabatic heat generated in the different plies may be determined. With this knowledge, the strain components experienced by a composite laminate may be found.

1 Introduction

The significance of thermal conduction effects on thermoelastic temperature measurements was first reported in Dunn et al. (1989). It was shown how the different thermoelastic heats generated in piles of different fiber orientations can give rise to significant thermal conduction. This work was extended in Wong (1990) and Dunn (1991). Wong (1990) showed how this effect can be used to determine the strain components by observing the surface temperature changes resulting from different loading frequencies (provided the laminate was made of plies of at least three different orientations. In Dunn (1991), an analytical solution of the heat equation, as it applies to thermoelastic heats generated in composite materials, was presented. The present paper solves the inverse problem to that presented in Dunn (1991). In this way, the heats generated in each ply of the composite material are determined from experimental data. Use is then made of the ideas presented in Wong (1991) to use these data to determine the strain components experienced by the composite laminates.

The basis of the technique used in this paper relies upon using the classical thermoelastic equation which is typically used to determine the change in temperature of a body as it undergoes a change in stress under adiabatic conditions. This equation can be used to determine the thermoelastic heats generated given a change in stress. These heats are then used as source terms for equations encompassing heat transfer by which the interaction of the thermal waves from the different sources (different plies in a composite material) may then be analyzed.

2 Specimens and Equipment

The specimens used here were made of AS4/3501-6 graphite/epoxy. Two-ply configurations were used: a $[(0°, \pm 45°)_4]_s$ laminate and a $[(90°, \mp 45°)_4]_s$ laminate (the first number in the stacking sequence gives the direction of the fibers in the surface plies with subsequent numbers giving the fiber direction in the subsequent plies, the numerical subscript gives the number of times this sequence is repeated in the half-thickness, the s subscript denotes that the laminate is symmetric about the midplane). The specimens were rectangular with one specimen 145 mm long by 30 mm wide from each of the laminate configurations and a specimen 180 mm long by 42 mm wide from the $[(0°, \pm 45°)_4]_s$ laminate with a 10-mm diameter hole through the center. Each of the specimens had bonded aluminum end tabs. Loading was applied via bolts which passed through holes in the end tabs and composite material. These bolts were tightened, clamping bushes on either side of the end tabs such that the stress concentration effects of these holes were minimized.

The specimens were loaded in a 50kN MTS servo-hydraulic testing machine. The cyclic temperature changes on the surface were monitored using the infrared detector of a SPATE 8000 system. The scanning by the infrared detector was digitally driven, and the data from the infrared detector and load transducer were analyzed, using a 386 personal computer with a Data Translation DT2827 A/D, D/A card. The digital analysis of the data makes use of the fact that the frequency of loading is well known; this is used to carry out a least-squares analysis of the data to determine both orthogonal components in the cyclic variations. Effectively, this means that simultaneous measurement of both the amplitude and phase of the load transducer and infrared detector response is carried out.

[1] Permanent address: Aircraft Structures Division, Aeronautical Research Laboratory, Fishermen's Bend, Victoria 3207, Australia.

Contributed by the Applied Mechanics Division of THE AMERICAN SOCIETY OF MECHANICAL ENGINEERS for publication in the ASME JOURNAL OF APPLIED MECHANICS.

Discussion on this paper should be addressed to the Technical Editor, Professor Lewis T. Wheeler, Department of Mechanical Engineering, University of Houston, Houston, TX 77204-4792, and will be accepted until four months after final publication of the paper itself in the ASME JOURNAL OF APPLIED MECHANICS.

Manuscript received by the ASME Applied Mechanics Division, Oct. 7, 1991; final revision, Feb. 26, 1992. Associate Technical Editor: A. K. Noor.

Copyright © 1993 by ASME
Downloaded 03 May 2010 to 171.66.16.245. Redistribution subject to ASME license or copyright; see http://www.asme.org/terms/Terms_Use.cfm

3 Thermoelastic Heats Generated in a Composite Material

A method for determining thermoelastic heats generated in a composite material was presented in Dunn (1991).

The adiabatic thermoelastic equation describing the reversible change in temperature generated in a two-dimensional orthotropic material due to applied stresses in the elastic regime can be written as (Biot, 1956)

$$-\rho c\frac{\Delta T}{T}=\alpha_1\Delta\sigma_1+\alpha_2\Delta\sigma_2 \tag{1}$$

in which ρ is the density, c is the specific heat, ΔT is the change in temperature, T is the absolute temperature, α is the coefficient of linear thermal expansion, $\Delta\sigma$ is the change in stress, and the subscripts 1 and 2 denote the longitudinal and transverse to fiber directions, respectively. Equation (1) describes the heat generated in an orthotropic two-dimensional body subjected to stresses in the elastic regime. The mechanics of composite materials show that the stresses in different plies may vary greatly depending on the fiber orientations. As a consequence, the temperatures generated in each ply, as described by Eq. (1), will be very different.

To evaluate the adiabatic heat generated in a ply in a composite material, the material properties, and therefore stresses and heats, of the matrix material and fibers, can be considered independently. These heats may then be summed, based on the volume ratios and specific heats of each material, to give the adiabatic heat generated in the ply.

Given an orthotropic material, the relationship between the stresses and strains with respect to the laminate orthotropic (x, y) axes, may be written as

$$\begin{Bmatrix}\epsilon_x\\ \epsilon_y\\ \gamma_{xy}\end{Bmatrix}=\begin{bmatrix}1/E_x & -\nu_{yx}/E_y & 0\\ -\nu_{xy}/E_x & 1/E_y & 0\\ 0 & 0 & 1/G_{xy}\end{bmatrix}\begin{Bmatrix}\sigma_x\\ \sigma_y\\ \tau_{xy}\end{Bmatrix}. \tag{2}$$

In order to determine the average stresses in the fibers, the strains with respect to the ply orthotropic (1, 2) axes must be determined. The relationship between the strains in the two axis systems is given as

$$\begin{Bmatrix}\epsilon_1\\ \epsilon_2\\ \gamma_{12}\end{Bmatrix}=\begin{bmatrix}m^2 & n^2 & mn\\ n^2 & m^2 & -mn\\ -2mn & 2mn & m^2-n^2\end{bmatrix}\begin{Bmatrix}\epsilon_x\\ \epsilon_y\\ \gamma_{xy}\end{Bmatrix} \tag{3}$$

where $m=\cos\theta$ and $n=\sin\theta$ (θ is the angle between the 1, 2 axes and the x, y axes). Given that the adiabatic heat generation (Eq. (1)) is dependent only upon the principal stresses, an average of these stresses in the fibers may be determined using

$$\begin{Bmatrix}\sigma_1\\ \sigma_2\end{Bmatrix}=\frac{1}{1-\nu_{12}\nu_{21}}\begin{bmatrix}E_1 & \nu_{12}E_2\\ \nu_{21}E_1 & E_2\end{bmatrix}\begin{Bmatrix}\epsilon_1\\ \epsilon_2\end{Bmatrix} \tag{4}$$

and substituting the fiber material properties. Equation (1), which is used to calculate the heat generated in the materials, is a linear equation, and the heat diffusion between fiber and matrix is very rapid (Wong, 1990); given this, such average stresses, rather than a micromechanical stress distribution, are all that is required here.

Substituting Eq. (3) into (4) gives the stresses in the fibers in the ply orthotropic axis with respect to the strains in the laminate orthotropic axes as

$$\begin{Bmatrix}\sigma_1\\ \sigma_2\end{Bmatrix}\Bigg|_{0^\circ\text{ fibers}}=\frac{1}{1-\nu_{12f}\nu_{21f}}\begin{bmatrix}E_{1f} & \nu_{12f}E_{2f}\\ \nu_{21f}E_{1f} & E_{2f}\end{bmatrix}\begin{Bmatrix}\epsilon_x\\ \epsilon_y\end{Bmatrix}, \tag{5}$$

$$\begin{Bmatrix}\sigma_1\\ \sigma_2\end{Bmatrix}\Bigg|_{45^\circ\text{ fibers}}=\frac{1}{2(1-\nu_{12f}\nu_{21f})}\times\begin{bmatrix}E_{1f}+\nu_{12f}E_{2f} & E_{1f}-\nu_{12f}E_{2f}\\ \nu_{21f}E_{1f}+E_{2f} & \nu_{21f}E_{1f}-E_{2f}\end{bmatrix}\begin{Bmatrix}\epsilon_x+\epsilon_y\\ \gamma_{xy}\end{Bmatrix} \tag{6}$$

and

$$\begin{Bmatrix}\sigma_1\\ \sigma_2\end{Bmatrix}\Bigg|_{-45^\circ\text{ fibers}}=\frac{1}{2(1-\nu_{12f}\nu_{21f})}\times\begin{bmatrix}E_{1f}+\nu_{12f}E_{2f} & \nu_{12f}E_{2f}-E_{1f}\\ \nu_{21f}E_{1f}+E_{2f} & E_{2f}-\nu_{21f}E_{1f}\end{bmatrix}\begin{Bmatrix}\epsilon_x+\epsilon_y\\ \gamma_{xy}\end{Bmatrix}. \tag{7}$$

Given that the epoxy is an isotropic material, the stresses in terms of the laminate orthotropic axes may be written as

$$\begin{Bmatrix}\sigma_x\\ \sigma_y\end{Bmatrix}\Bigg|_{\text{matrix}}=\frac{E_m}{1-\nu_m^2}\begin{bmatrix}1 & \nu_m\\ \nu_m & 1\end{bmatrix}\begin{Bmatrix}\epsilon_x\\ \epsilon_y\end{Bmatrix}. \tag{8}$$

Substituting these stresses into Eq. (1) to determine the relative adiabatic temperature change, which is directly proportional to the heat generated, gives

$$\frac{\Delta T}{T}\Bigg|_{0^\circ\text{ fibers}}=\frac{1}{\rho_f c_f}\left[\frac{1}{1-\nu_{12f}\nu_{21f}}((\alpha_{1f}E_{1f}+\alpha_{2f}\nu_{21f}E_{1f})\epsilon_x+(\alpha_{1f}\nu_{12f}E_{2f}+\alpha_{2f}E_{2f})\epsilon_y)\right]$$

$$\frac{\Delta T}{T}\Bigg|_{45^\circ\text{ fibers}}=\frac{1}{\rho_f c_f}\left[\frac{1}{2(1-\nu_{12f}\nu_{21f})}\times((\alpha_{1f}(E_{1f}+\nu_{12f}E_{2f})+\alpha_{2f}(\nu_{21f}E_{1f}+E_{2f}))(\epsilon_x+\epsilon_y)+(\alpha_{1f}(E_{1f}-\nu_{12f}E_{2f})+\alpha_{2f}(\nu_{21f}E_{1f}-E_{2f})))\gamma_{xy}\right]$$

$$\frac{\Delta T}{T}\Bigg|_{-45^\circ\text{ fibers}}=\frac{1}{\rho_f c_f}\left[\frac{1}{2(1-\nu_{12f}\nu_{21f})}\times((\alpha_{1f}(E_{1f}+\nu_{12f}E_{2f})+\alpha_{2f}(\nu_{21f}E_{1f}+E_{2f}))(\epsilon_x+\epsilon_y)-(\alpha_{1f}(E_{1f}-\nu_{12f}E_{2f})+\alpha_{2f}(\nu_{21f}E_{1f}-E_{2f})))\gamma_{xy}\right]$$

$$\frac{\Delta T}{T}\Bigg|_{\text{matrix}}=\frac{1}{\rho_m c_m}\left[\frac{\alpha_m E_m}{1-\nu_m^2}(1+\nu_m)(\epsilon_x+\epsilon_y)\right]. \tag{9}$$

The heats of the respective constituents may be summed by

$$\Delta T_{\text{ply}}=\frac{V_f\rho_f c_f\Delta T_f+V_m\rho_m c_m\Delta T_m}{V_f\rho_f c_f+V_m\rho_m c_m} \tag{10}$$

in which V_f and V_m are the proportionate volumes of the fiber and matrix materials, respectively. The material properties from Table 1 can be substituted into Eq. (9), the results of which may then be substituted into Eq. (10) to give the adiabatic temperatures generated in each ply with respect to the strains in the laminate orthotropic directions. Given that the denominator of Eq. (10) is the same for each ply and as only the relative heats (i.e., the heat generated in one ply relative to the other plies, not the absolute values of heat) generated in each ply will be dealt with here, the normalized adiabatic temperature changes, a, in each ply can be written as

Table 1 Material properties for AS graphite fibers and high modulus matrix material (Chamis, 1984)

fiber longitudinal modulus	E_{f1}	214 GPa
fiber transverse modulus	E_{f2}	13.8 GPa
fiber longitudinal Poisson's ratio	ν_{f12}	0.20
fiber transverse Poisson's ratio	ν_{f21}	0.013
fiber longitudinal thermal exponential coefficient	α_{f1}	-1.0×10^{-6}/K
fiber transverse thermal exponential coefficient	α_{f2}	10×10^{-6}/K
matrix modulus	E_m	5.2 GPa
matrix Poisson's ratio	ν_m	0.35
matrix thermal exponential coefficient	α_m	72×10^{-6}/K

Downloaded 03 May 2010 to 171.66.16.245. Redistribution subject to ASME license or copyright; see http://www.asme.org/terms/Terms_Use.cfm

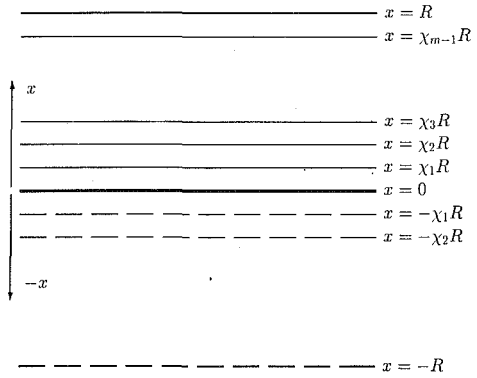


Fig. 1 Diagram of geometry used in the mathematical model

$$\begin{Bmatrix} a|_{0\,\text{deg ply}} \\ a|_{45\,\text{deg ply}} \\ a|_{-45\,\text{deg ply}} \end{Bmatrix} = \begin{bmatrix} 119 & 312 & 0 \\ 215 & 215 & -97 \\ 215 & 215 & 97 \end{bmatrix} \begin{Bmatrix} \epsilon_x \\ \epsilon_y \\ \gamma_{xy} \end{Bmatrix}. \tag{11}$$

4 Inverse Problem

In Dunn (1991), the steady-state temperature oscillation on the surface of a symmetric composite laminate of $2m$ plies and total thickness $2R$ with surfaces at $\pm R$, subjected to sinusoidal loading frequency of ω was shown to be

$$T(R, t)|_{t\to\infty} = \frac{1}{2}\sin\omega t\left[\left\{\sum_{j=1}^{m-1}\chi_j(a_j - a_{j+1})\right\} + a_m\right] + \frac{1}{\pi}\left[\sum_{n=1}^{\infty}\frac{(-1)^n}{n}\frac{\sin\omega t + \eta\cos\omega t}{(1+\eta^2)}\left\{\sum_{j=1}^{m-1}(a_j - a_{j+1})\sin\chi_j n\pi\right\}\right] \tag{12}$$

in which $\eta = \kappa n^2\pi^2/R^2\omega$, κ is the thermal diffusivity, a_j is the peak-to-peak adiabatic temperatures generated in each ply such that

$$a_j = \begin{cases} a_1 & \text{for } 0 < x < \chi_1 R; \\ a_2 & \text{for } \chi_1 R < x < \chi_2 R; \\ \vdots & \vdots \\ a_m & \text{for } \chi_{m-1}R < x < R \end{cases} \tag{13}$$

and χ_j can be described as the proportionate position of the ply interfaces in the laminate such that the thickness of the jth ply is $\chi_j R - \chi_{j-1}R$ (Fig. 1). Equation (12) can be rewritten as

$$T(t) = A\sin\omega t + B\cos\omega t \tag{14}$$

in which A can be written as

$$A = \sum_{j=1}^{m} a_j\left\{\frac{1}{2}(\chi_j - \chi_{j-1}) + \frac{1}{\pi}\sum_{n=1}^{\infty}\frac{(-1)^n}{n}\frac{1}{1+\eta^2} \times (\sin\chi_j n\pi - \sin\chi_{j-1}n\pi)\right\} = \sum_{j=1}^{m} a_j X_j \tag{15}$$

and B as

$$B = \sum_{j=1}^{m} a_j\left\{\frac{1}{\pi}\sum_{n=1}^{\infty}\frac{(-1)^n}{n}\frac{\eta}{1+\eta^2}(\sin\chi_j n\pi - \sin\chi_{j-1}n\pi)\right\} = \sum_{j=1}^{m} a_j Y_j. \tag{16}$$

The aim of the problem is to find the adiabatic heats generated in each ply by observing the surface temperature changes at different frequencies. This can be achieved by determining the adiabatic temperature changes, a_j, for each ply in a least-squares manner.

The objective function to minimize is

$$f = \frac{1}{2}\sum_{k=1}^{N}\left(A_k - \left[\sum_{j=1}^{m} a_j X_j\right]_k\right)^2 + \frac{1}{2}\sum_{k=1}^{N}\left(B_k - \left[\sum_{j=1}^{m} a_j Y_j\right]_k\right)^2 \tag{17}$$

for N measurements of A_k and B_k. Differentiating Eq. (17) with respect to a_j gives the following least-squares equation:

$$\begin{bmatrix} \sum^N (X_1^2 + Y_1^2) & \sum^N (X_1X_2 + Y_1Y_2) & \cdots & \sum^N (X_1X_m + Y_1Y_m) \\ & \sum^N (X_2^2 + Y_2^2) & & \vdots \\ & & \ddots & \vdots \\ & & & \sum^N (X_m^2 + Y_m^2) \end{bmatrix} \times \begin{Bmatrix} \hat{a}_1 \\ \hat{a}_2 \\ \vdots \\ \hat{a}_m \end{Bmatrix} = \begin{Bmatrix} \sum_{k=1}^{N}(X_1A_k + Y_1B_k) \\ \sum_{k=1}^{N}(X_2A_k + Y_2B_k) \\ \vdots \\ \sum_{k=1}^{N}(X_mA_k + Y_mB_k) \end{Bmatrix} \tag{18}$$

in which $\hat{a}_j$ is an estimate for the adiabatic temperatures generated in each ply. To obtain $\hat{a}_j$ for m plies, it is necessary to gather N sets of data encompassing at least m different loading frequencies. It should be noted that the least-squares matrix in Eq. (18) tends to be very ill-conditioned. This is not surprising considering that all measurements are taken on the surface; to determine the adiabatic heating in, for example, the jth ply, it is required that the effect of heating in the jth ply be observable in the surface temperature changes. It is obvious that the deeper the ply the less effect the heating in this ply will have on the surface temperature changes; therefore, the more difficult it will be to determine the heating in this ply. Given this, all information available should be used in formulating the least-squares equation. One useful piece of information is that plies of the same orientation will generate the same amount of heat. As an example, in the $[(0°, \pm 45°)_4]_s$ laminate used here, every third ply in the half-thickness, generates the same amount of heat; so, instead of determining 12 parameters for the half-thickness of the laminate only three parameters need be found.

Given the adiabatic heat generated in each ply, Eq. (11) can be solved to give the strain components.

5 Experiments and Analysis

5.1 Uniform $(0°, \pm 45°)_4]_s$ and $[(90°, \mp 45°)_4]_s$ Specimens. The first experiment involved observing a single point on a uniform $[(0°, \pm 45°)_4]_s$ graphite/epoxy specimen loaded uniaxially. The aim of this was to confirm the expected adiabatic temperatures calculated in Eq. (11) under known strain conditions. An additional aim was to determine the thermal diffusivity in the through-thickness direction for the laminate and to investigate the sensitivity of the problem to thermal diffusivity.

Three sets of data were collected from different points about the center of the specimen with cyclic load amplitudes of 5 kN for 11 frequencies ranging from 2 to 12 Hz. These data were corrected for instrumentation biases as described in Wong (1990). Given that the loading was uniaxial with no shear stress applied, as can be seen from Eq. (11), the heat generated in

Downloaded 03 May 2010 to 171.66.16.245. Redistribution subject to ASME license or copyright; see http://www.asme.org/terms/Terms_Use.cfm

Table 2 Laminate properties for $[(0°, \pm 45°)_4]_s$ and $[(90°, \mp 45°)_4]_s$ laminate

$[(0°, \pm 45°)_4]_s$		
longitudinal modulus	E_x	57.4 GPa
transverse modulus	E_y	24.2 GPa
longitudinal Poisson's ratio	ν_{xy}	0.68
transverse Poisson's ratio	ν_{yx}	0.29
fiber/matrix volume ratio	V_f/V_m	0.6/0.4
$[(90°, \mp 45°)_4]_s$		
longitudinal modulus	E_x	24.2 GPa
transverse modulus	E_y	57.4 GPa
longitudinal Poisson's ratio	ν_{xy}	0.29
transverse Poisson's ratio	ν_{yx}	0.68
fiber/matrix volume ratio	V_f/V_m	0.6/0.4

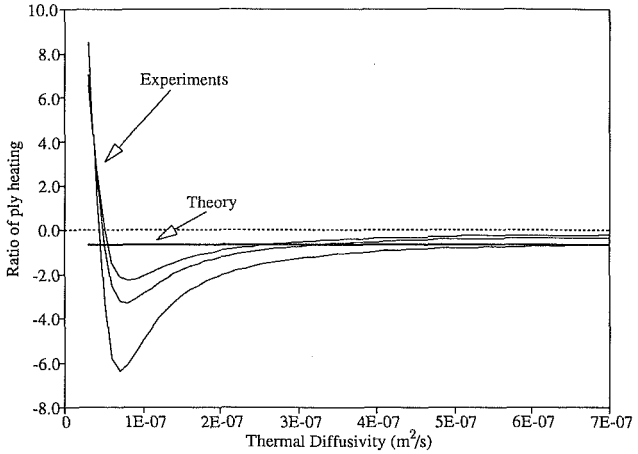


Fig. 2 Ratio of heating for the ±45 deg plies to the 0 deg ply for a uniform $[(0°, \pm 45°)_4]_s$ specimen as found from Eq. (19) for a range of thermal diffusivities (κ's) at three different locations compared with the expected values as determined from Eq. (11). (Note: for small values of κ, $<1<10^{-7}$ m²/s the mathematical model tends to become rigid.)

the ±45 deg plies was equal; this means that in the least-squares equation given in the previous section, only two parameters were to be found. Equation (18) can therefore be reduced to

$$\left[\begin{array}{cc} \sum^{N}\left(\sum_{i=1,2,4,5,..}^{m-1}\sum_{j=1,2,4,5..}^{m-1} XY_{ij}\right) & \sum^{N}\left(\sum_{i=1,2,4,5,..}^{m-1}\sum_{j=3,6..}^{m} XY_{ij}\right) \\ & \sum^{N}\left(\sum_{i=3,6..}^{m}\sum_{j=3,6..}^{m} XY_{ij}\right) \end{array}\right] \times \left\{\begin{array}{c} \hat{a}_{m-1} \\ \hat{a}_m \end{array}\right\} = \left\{\begin{array}{c} \sum^{N}\left(\sum_{i=1,2,4,5,..}^{m-1}(X_iA + Y_iB)\right) \\ \sum^{N}\left(\sum_{i=3,6..}^{m}(X_iA + Y_iB)\right) \end{array}\right\} \quad (19)$$

in which m, in this case, is 12 and XY_{ij} is defined as

$$XY_{ij} = (X_iX_j + Y_iY_j). \quad (20)$$

The experimental data were substituted into Eq. (19) and solved for a range of thermal diffusivities; the results for $\hat{a}|_{\pm 45\ \mathrm{deg}}/\hat{a}|_{0\ \mathrm{deg}}$ are shown in Fig. 2. Substituting the laminate properties for the $[(0°, \pm 45°)_4]_s$ laminate given in Table 2 into Eq. (11) gives the ratio of $a|_{\pm 45\ \mathrm{deg}}/a|_{0\ \mathrm{deg}}$ to be -0.73; this is compared with that found from the experimental data in Fig. 2. As can be seen in Fig. 2, the determination of the ratio of heats generated in the plies is relatively independent on the value of κ for a significant range of thermal diffusivities shown here.

The previously described experiments were repeated for a $[(90°, \mp 45°)_4]_s$ graphite/epoxy specimen at two different points. Once again the data were substituted into Eq. (19) and solved for the adiabatic temperatures generated in each ply for a range of thermal diffusivities; the results for $\hat{a}|_{\pm 45\ \mathrm{deg}}/\hat{a}|_{90\ \mathrm{deg}}$ are shown in Fig. 3. Substituting the laminate properties for the $[(90°, \mp 45°)_4]_s$ laminate given in Table 2 into Eq. (11) (interchanging the 1,1 with the 1,2 term in the matrix given in Eq. (11) to account for the 90 deg ply rather than a 0 deg ply) gives the ratio of $\hat{a}|_{\pm 45\ \mathrm{deg}}/\hat{a}|_{90\ \mathrm{deg}}$ to be 0.55; this is compared with that found from the experimental data in Fig. 3. Once again, the ratio of heating in the plies is relatively independent of κ for a significant range of thermal diffusivities shown here.

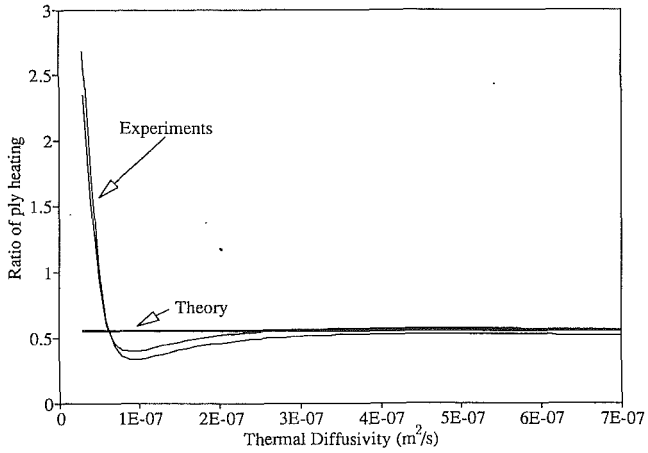


Fig. 3 Ratio of heating for the ±45 deg plies to the 90 deg ply for a uniform $[(90°, \mp 45°)_4]_s$ specimen as found from Eq. (19) for a range of thermal diffusivities (κ's) at two different locations compared with the expected values as determined from Eq. (11). (Note: for small values of κ, $<1 \times 10^{-7}$ m²/s the mathematical model tends to become rigid.)

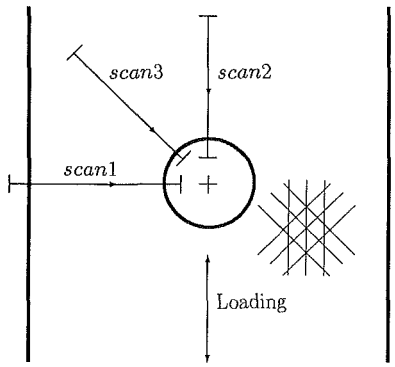


Fig. 4 Diagram showing the lines over which the scans were carried out for the $[(0°, \pm 45°)_4]_s$ hole specimen

These results suggests that the method of calculating the adiabatic heating in each ply is acceptable and show that the final solutions will not be strongly dependent upon the choice of κ. The κ at which the standard deviation of the least-squares fit was a minimum was determined for each set of data. The average of these κ's was found to be 4.7×10^{-7} m²/s and was the thermal diffusivity used for the subsequent analysis.

5.2 $[(0°, \pm 45°)_4]_s$ Graphite/Epoxy Specimen with a Hole. The next experiment involved investigating a more interesting case; one with spatially varying strains. For this, a graphite/epoxy specimen with a hole through its center was used. The aim was to determine how the heats generated through the thickness of the laminate vary spatially and therefore how the strains vary.

For this problem, every third ply for the half-thickness of the laminate can be assumed to give the same heating. The least-squares equation, Eq. (18), can therefore be modified to give

Downloaded 03 May 2010 to 171.66.16.245. Redistribution subject to ASME license or copyright; see http://www.asme.org/terms/Terms_Use.cfm

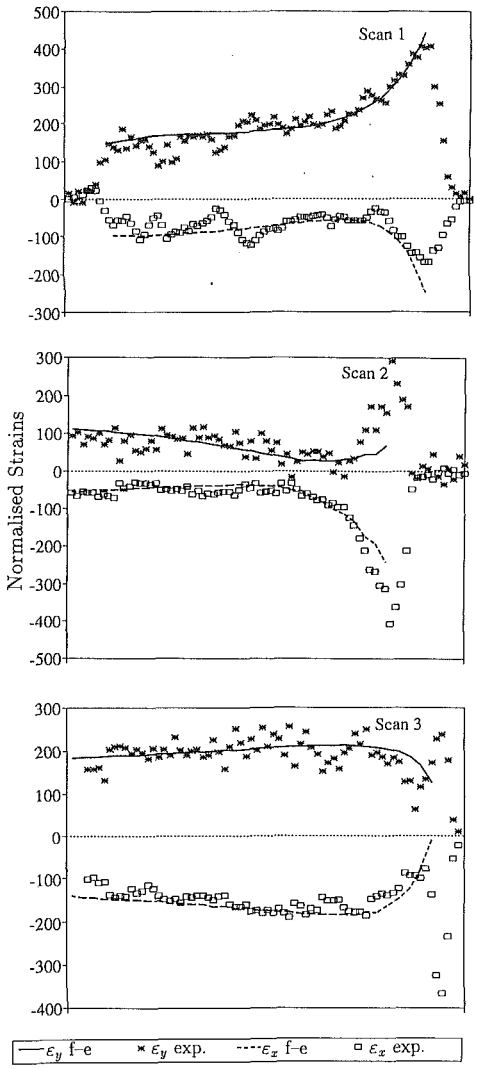


Fig. 5 Normal strains found from the thermoelastic data for the three line scans shown in Fig. 4. These are compared with results from finite element analysis.

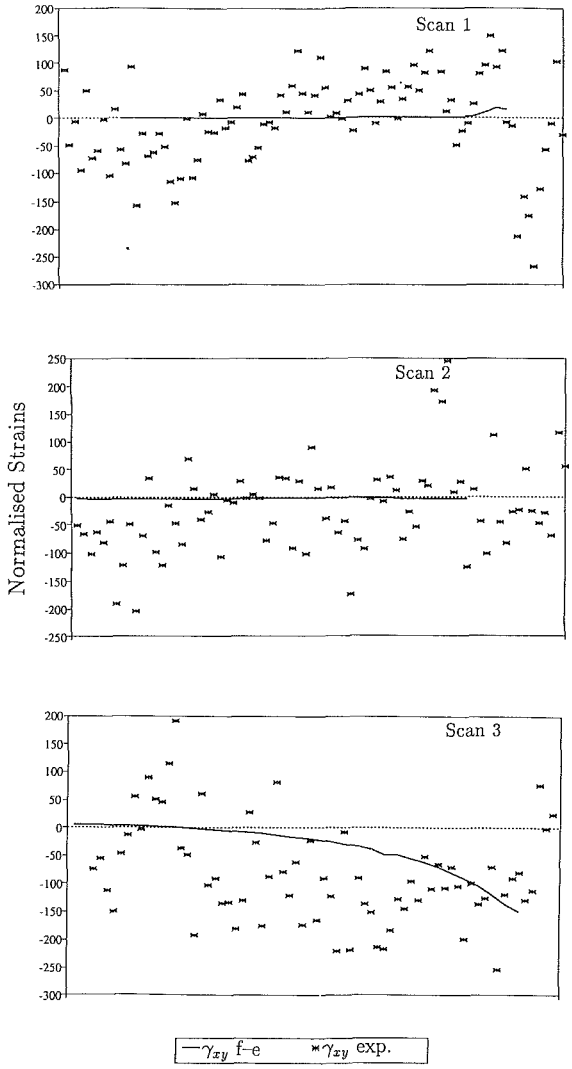


Fig. 6 Shear strains found from the thermoelastic data for the three line scans shown in Fig. 4. These are compared with results from finite element analysis.

$$\begin{bmatrix} \sum^{N}\left(\sum_{i=1,4,..}^{m-2}\sum_{j=1,4,..}^{m-2} XY_{ij}\right) & \sum^{N}\left(\sum_{i=1,4..}^{m-2}\sum_{j=2,5..}^{m-1} XY_{ij}\right) & \sum^{N}\left(\sum_{i=1,4..}^{m-2}\sum_{j=3,6..}^{m-1} XY_{ij}\right) \\ \sum^{N}\left(\sum_{i=2,5..}^{m-1}\sum_{j=2,5..}^{m-1} XY_{ij}\right) & \sum^{N}\left(\sum_{i=2,5..}^{m-1}\sum_{j=3,6..}^{m-1} XY_{ij}\right) & \\ & \sum^{N}\left(\sum_{i=3,6..}^{m}\sum_{j=3,6..}^{m} XY_{ij}\right) & \end{bmatrix} \begin{Bmatrix} \hat{a}_{m-2} \\ \hat{a}_{m-1} \\ \hat{a}_m \end{Bmatrix} = \begin{Bmatrix} \sum^{N}\left(\sum_{i=1,4..}^{m-2}(X_iA + Y_iB)\right) \\ \sum^{N}\left(\sum_{i=2,5..}^{m-1}(X_iA + Y_iB)\right) \\ \sum^{N}\left(\sum_{i=3,6..}^{m}(X_iA + Y_iB)\right) \end{Bmatrix}. \quad (21)$$

The specimen was loaded with a load amplitude of 8 kN at 13 frequencies ranging from 3 to 15 Hz. At each frequency, three line scans were collected over each of the lines shown in Fig. 4. These data were then substituted into Eq. (21), point by point, to determine the adiabatic temperature generated in each ply. These results were then substituted into Eq. (11) to give the strains in terms of the laminate orthotropic axes. These strains are compared with those determined from a finite element model in Figs. 5 and 6. It should be noted that these are relative, not absolute, values of strain and that the data have been scaled by a common scaling factor.

6 Discussion

As can be seen in Fig. 5 there is a good agreement between the normal strains determined from experimental temperature data and that determined from the finite element model. The comparison, however, becomes poor near free edges, particularly for the vertical line scan. This is to be expected, as thermoelastic temperature measurements typically deteriorate near an edge because the detector "sees" both specimen and free space. This effect is greatly accentuated for a free edge perpendicular to the direction of loading, as for the edge effect evident in the vertical line scan; the reason for this is that, during a loading cycle, the detector "sees" alternately more or less of the specimen. This variation in the amount of specimen being observed can give rise to significantly corrupted temperature readings. An additional cause of corruption in the data of the vertical line scan near the hole is that the thermoelastic temperature changes vary greatly over a very short distance in the direction of motion. The effect of such

Downloaded 03 May 2010 to 171.66.16.245. Redistribution subject to ASME license or copyright; see http://www.asme.org/terms/Terms_Use.cfm

rapid spatial variation has been shown in Van Hemelrijck et al. (1991) for composite materials with irreversible heating caused by damage. Such effects are not as great for an undamaged specimen, but it is easily shown that for a spatially nonlinear variation in thermoelastic heating, the temperature data may be significantly biased.

The shear strains shown in Fig. 6 are quite poorly determined. From Eq. (11), it can be seen that for the surface 0 deg ply there will be no adiabatic heat generated by shear strains and that the subsurface plies generate considerably less heat per unit shear strain than that for normal strains. It is obvious that the heating in the surface ply will be the best determined heating, while those of the subsurface plies will be progressively less well determined. With only the subsurface plies contributing to the measurement of shear strains, these strains will be more poorly determined than direct strains.

7 Conclusion

In this paper, a least-square model is formulated which allows the heats generated in individual plies to be determined from surface temperature data collected at different loading frequencies. Given these heats, it is shown how individual strain components can be found. It has been demonstrated that normal strain components can successfully be determined from experimental data using this technique.

Acknowledgments

The author gratefully acknowledges the advice and assistance given by Drs. J. G. Sparrow, A. K. Wong, and T. G. Ryall of Aircraft Structures Division, Aeronautical Research Laboratory.

References

Biot, M. A., 1956, "Thermoelasticity and Irreversible Thermodynamics," *J. Appl. Phys.*, Vol. 27, pp. 240–253.

Chamis, C. C., 1984, "Simplified Composite Micromechanics Equations for Strength, Fracture Toughness and Environmental Effects," *39th Annual Conference, Reinforced Plastic/Composites Institute*, The Society of the Plastics Industry, Inc., Session II-D, pp. 1–16.

Dunn, S. A., Lombardo, D., and Sparrow, J. G., 1989, "The Mean Stress Effect in Metallic Alloys and Composites," *Stress and Vibration: Recent Developments in Industrial Measurement and Analysis*, Peter Stanley, ed., SPIE Vol. 1084, pp. 129–142.

Dunn, S. A., 1993, "Analysis of Thermal Conduction Effects on Thermoelastic Temperature Measurements for Composite Materials," ASME JOURNAL OF APPLIED MECHANICS, in press.

Van Hemelrijk, D., Schillemans, L., Cardon, A. H., and Wong, A. K., 1991, "The Effects of Motion on Thermoelastic Stress Analysis," *Composite Structures*, Vol. 18, pp. 221–238.

Wong, A. K., 1990, "A Non-Adiabatic Thermoelastic Theory and the Use of SPATE on Composite Laminates," *Proceedings of the 9th International Conference on Experimental Mechanics*, Copenhagen, Vol. 2, pp. 793–802.

Downloaded 03 May 2010 to 171.66.16.245. Redistribution subject to ASME license or copyright; see http://www.asme.org/terms/Terms_Use.cfm

C. W. Bert
Perkinson Chair Professor
and Director,
Fellow ASME.

S. Huang
Visiting Assistant Professor,
Assoc. Mem. ASME.

School of Aerospace and
Mechanical Engineering,
The University of Oklahoma,
Norman, OK 73019-0601

On the Thermal Expansion Coefficient and Specific Heat at Constant Strain for Finite Plastic Deformation

General expressions for thermal expansion coefficient and specific heat at constant strain in the case of finite plastic deformation are derived from a general analysis of thermodynamics and finite plasticity theory. The present results show that these two thermal parameters are dependent, in a very complicated way, on the mechanical behavior of the material, such as the plastic yielding and flow, work-hardening and stress-strain relation. They are not constants but vary with the stress state, deformation state, and deformation history. It is shown that previously published experimental observations on thermal expansion coefficient can be described by the theory presented in this paper.

1 Introduction

In modern technological applications and manufacturing processes, there are cases in which the structures or materials are subjected to severe thermal as well as mechanical loadings. Examples of these structures are airframes and propulsion systems for hypersonic aircraft such as the X-30 NASP, spacecraft such as the Shuttle and Space Station, advanced nuclear reactors, and miniature solid-state electronic devices. Examples in manufacturing processes include hot-working metal forming and the curing process of advanced composite materials. Under severe thermal and mechanical loadings, structures or materials will sometimes undergo larger plastic deformation, especially in metal forming processes. Therefore, in addition to the mechanical behavior of materials under large plastic deformation, it is necessary to know the thermal properties of materials, such as thermal expansion coefficient and specific heat at large plastic deformation, in order to properly design and analyze these structures and processes.

The research on thermomechanical coupling was initiated 185 years ago by Gough (1805). Since then, it has been well known that mechanical properties of materials, such as elastic moduli, yield stress, and ultimate strength change with temperature. Similarly, the thermal behavior of materials, such as thermal expansion coefficient, has been found to be dependent on mechanical responses, such as stress, elastic moduli, and plastic deformation. This interesting phenomenon was first measured by Rosenfield and Averbach (1956) for five different materials.

The theoretical treatment of thermomechanical coupling was pioneered by Clausius (1850) and Lord Kelvin (Thomson, 1857), who formulated the first and second laws of thermodynamics. For about 140 years, great progress has been made in the area of thermodynamics by many researchers, and the reader is referred to Truesdell and Noll (1965) for a summary of later developments. The classical treatments of thermomechanical coupling are based on the first and second laws of thermodynamics and conservation laws of mass and momentum and are limited to the infinitesimal elastic deformation region. In an early work Hilton (1952) considered the temperature dependence of elastic moduli. Recently, in connection with research on the thermoelastic parameter, Wong et al. (1987a, 1987b, 1988) developed some thermoelastic theory with stress-dependent thermal expansion coefficient. In a recent work, Bert and Fu (1990) emphasized the important thermodynamic consequence that the temperature dependency of the elastic stiffness requires that the thermal expansion coefficient must be stress dependent. They did a thermosolid mechanics analysis based on sound thermodynamic and mechanical principles and derived the dependency of thermal expansion coefficient on the stress. The theory was then applied to the case of slender elastic members with full axial constraint and subjected to a uniform increase in temperature.

The purpose of the present paper is to extend the theoretical analysis of Bert and Fu (1990) to the case of large elastic-plastic deformation and to present a theory for the effects of stress state and large plastic deformation on the thermal expansion coefficient and specific heat at constant strain state. For this purpose, the thermodynamic theory formulated by Green and Naghdi (1977, 1978a, 1978b) is used as the theoretical basis. At the end of this paper, the results derived in this paper are

Contributed by the Applied Mechanics Division of THE AMERICAN SOCIETY OF MECHANICAL ENGINEERS for presentation at the First Joint ASCE-EMD, ASME-AMD, SES Meeting, Charlottesville, VA, June 6-9, 1993.

Discussion on this paper should be addressed to the Technical Editor, Professor Lewis T. Wheeler, Department of Mechanical Engineering, University of Houston, Houston, TX 77204-4792, and will be accepted until four months after final publication of the paper itself in the ASME JOURNAL OF APPLIED MECHANICS.

Manuscript received by the ASME Applied Mechanics Division, Nov. 7, 1991; final revision, May 1, 1992. Associate Technical Editor: R. M. Bowen.

Paper No. 93-APM-17.

Copyright © 1993 by ASME
Downloaded 03 May 2010 to 171.66.16.245. Redistribution subject to ASME license or copyright; see http://www.asme.org/terms/Terms_Use.cfm

discussed and compared with experimental results obtained by Rosenfield and Averbach (1956). It is shown that the present theory can predict the experimental results provided that an appropriate constitutive equation is assumed for the Helmholtz potential ψ.

Before closing this section, we make some remarks concerning notation. A superposed dot denotes material time differentiation. The symbol $\otimes$ represents the tensor product. An inner product of two second-order tensors $\mathbf{A}$ and $\mathbf{B}$, is defined by $(\mathbf{A}\cdot\mathbf{B})_{ij}=A_{ik}B_{kj}$; an inner product of a fourth-order tensor $\mathbf{C}$ with a second-order tensor $\mathbf{B}$ is defined by $(\mathbf{C}\cdot\mathbf{B})_{ij}=C_{ijkl}B_{kl}$. Similarly, for two second-order tensors, $(\mathbf{A}\cdot\mathbf{B})=A_{ij}B_{ij}$.

2 Formulation

All the equations in this paper are expressed in a Lagrangian formulation. Finite plastic deformation is considered and the constitutive equations are formulated in strain space (Naghdi (1990) and the cited referenes).

There are various formulations for the laws of thermodynamics, especially the second law. Since the constitutive equations for large plastic deformation used in this paper are consistent with those developed by Green and Naghdi (1965 and 1991), Naghdi and Trapp (1975), and Naghdi (1990), the formulation of thermodynamics developed by Green and Naghdi (1977, 1987a, 1987b) is used in this paper. A brief summary of this formulation of thermodynamics and the constitutive equations of thermoplasticity for finite deformation are presented in the appendices of the paper.

Note that from Eq. (B4)

$$\dot{\eta}=\frac{\partial\eta}{\partial\mathbf{E}}\colon\dot{\mathbf{E}}+\frac{\partial\eta}{\partial\theta}\dot{\theta}+\frac{\partial\eta}{\partial\mathbf{E}^p}\colon\dot{\mathbf{E}}^p+\frac{\partial\eta}{\partial k}\dot{k}. \tag{1}$$

Substituting this into Eq. (A4) results in

$$\mathrm{Div}\,\mathbf{q}_R=-\rho_0\theta\left[\frac{\partial\eta}{\partial\mathbf{E}}\colon\dot{\mathbf{E}}+\frac{\partial\eta}{\partial\theta}\dot{\theta}+\frac{\partial\eta}{\partial\mathbf{E}^p}\colon\dot{\mathbf{E}}^p+\frac{\partial\eta}{\partial k}\dot{k}\right]+\rho_0\theta\xi \tag{2}$$

However, using Eqs. (B8), the above equation can be rewritten as

$$\mathrm{Div}\,\mathbf{q}_R=\rho_0\theta\left[\frac{\partial^2\hat{\psi}}{\partial\theta\partial\mathbf{E}}\colon\dot{\mathbf{E}}+\frac{\partial^2\hat{\psi}}{\partial\theta^2}\dot{\theta}+\frac{\partial^2\hat{\psi}}{\partial\theta\partial\mathbf{E}^p}\colon\dot{\mathbf{E}}^p+\frac{\partial^2\hat{\psi}}{\partial\theta\partial k}\dot{k}\right]+\rho_0\theta\xi. \tag{3}$$

This, after using Eq. (B7), can be further simplified to

$$\mathrm{Div}\,\mathbf{q}_R=\theta\left[\frac{\partial\mathbf{S}}{\partial\theta}\colon\dot{\mathbf{E}}+\rho_0\frac{\partial^2\hat{\psi}}{\partial\theta^2}\dot{\theta}+\frac{\partial^2\hat{\psi}}{\partial\theta\partial\mathbf{E}^p}\colon\dot{\mathbf{E}}^p+\rho_0\frac{\partial^2\hat{\psi}}{\partial\theta\partial k}\dot{k}\right]+\rho_0\theta\xi. \tag{4}$$

In the case of elastic deformation $\dot{\mathbf{E}}^p=\mathbf{0}$, $\dot{k}=0$, and $\xi=0$; thus, Eq. (4) reduces to

$$\mathrm{Div}\,\mathbf{q}_R=\theta\left[\frac{\partial\mathbf{S}}{\partial\theta}\colon\dot{\mathbf{E}}+\rho_0\frac{\partial^2\hat{\psi}}{\partial\theta^2}\dot{\theta}\right]. \tag{5}$$

This is in agreement with the result of Bert and Fu (1990) in the case of infinitesimal elastic deformation.

The specific heat $C_{\mathbf{E}}$ at constant strain ($\dot{\mathbf{E}}=\mathbf{0}$) is defined as the quantity of heat required to produce a unit temperature increase in a unit mass of material. Therefore, neglecting internal heat sources, one can write

$$\mathrm{Div}\,\mathbf{q}_R=-\rho_0 C_{\mathbf{E}}\dot{\theta}. \tag{6}$$

On the other hand, Eq. (5), in the situation of constant strain ($\dot{\mathbf{E}}=\mathbf{0}$), becomes

$$\mathrm{Div}\,\mathbf{q}_R=\rho_0\theta\frac{\partial^2\hat{\psi}}{\partial\theta^2}\dot{\theta}. \tag{7}$$

By comparing Eq. (6) with Eq.(7) the following relation is obtained:

$$C_{\mathbf{E}}=-\theta\frac{\partial^2\hat{\psi}}{\partial\theta^2} \tag{8}$$

This equation, valid for finite deformation, is established based on the consideration of elastic deformation. However, since the right-hand side of Eq. (8) is a state function, $C_{\mathbf{E}}$ defined in this way must not depend on any specific process or path. Therefore, by using this result, Eqs. (4) and (5), respectively, can be rewritten as

$$\mathrm{Div}\,\mathbf{q}_R=\theta\frac{\partial\mathbf{S}}{\partial\theta}\colon\dot{\mathbf{E}}-\rho_0 C_{\mathbf{E}}\dot{\theta}-\rho_0\left[\frac{\partial\hat{\psi}}{\partial\mathbf{E}^p}-\theta\frac{\partial^2\hat{\psi}}{\partial\theta\partial\mathbf{E}^p}\right]\colon\dot{\mathbf{E}}^p-\rho_0\left[\frac{\partial\hat{\psi}}{\partial k}-\theta\frac{\partial^2\hat{\psi}}{\partial\theta\partial k}\right]\dot{k} \tag{9}$$

for finite elastic-plastic deformation, and

$$\mathrm{Div}\,\mathbf{q}_R=\theta\frac{\partial\mathbf{S}}{\partial\theta}\colon\dot{\mathbf{E}}-\rho_0 C_{\mathbf{E}}\dot{\theta} \tag{10}$$

for finite elastic deformation. In writing Eq. (9), Eq. (B9) has been used.

In the following, only adiabatic processes are considered. Then

$$\mathrm{Div}\,\mathbf{q}_R=0 \tag{11}$$

and Eqs. (9) and (10) become

$$\rho_0 C_{\mathbf{E}}\dot{\theta}=\theta\frac{\partial\mathbf{S}}{\partial\theta}\colon\dot{\mathbf{E}}-\rho_0\left[\frac{\partial\hat{\psi}}{\partial\mathbf{E}^p}-\theta\frac{\partial^2\hat{\psi}}{\partial\theta\partial\mathbf{E}^p}\right)\colon\dot{\mathbf{E}}^p-\rho_0\left(\frac{\partial\hat{\psi}}{\partial k}-\theta\frac{\partial^2\hat{\psi}}{\partial\theta\partial k}\right)\dot{k} \tag{12}$$

and

$$\rho_0 C_{\mathbf{E}}\dot{\theta}=\theta\frac{\partial\mathbf{S}}{\partial\theta}\colon\dot{\mathbf{E}}. \tag{13}$$

For linear elastic materials, $\mathbf{S}$ is given by

$$\mathbf{S}=\mathbf{C}(\theta)\colon(\mathbf{E}-\boldsymbol{\alpha}\Delta\theta) \tag{14}$$

where $\mathbf{C}$ is the fourth-order elastic stiffness tensor which is assumed to be temperature dependent, $\boldsymbol{\alpha}$ is a second-order, symmetric tensor with thermal expansion coefficients as its components in a given coordinate system, and $\Delta\theta=\theta-\theta_0$, where θ_0 is a reference temperature. It should be noted that anisotropy can be accommodated by (14). Substitution of (14) into (13) leads to the following:

$$\rho_0 C_{\mathbf{E}}\dot{\theta}=-\theta\left[\boldsymbol{\alpha}-\mathbf{C}^{-1}\colon\frac{d\mathbf{C}}{d\theta}\colon\mathbf{C}^{-1}\colon\mathbf{S}\right]\colon\mathbf{C}\colon\dot{\mathbf{E}} \tag{15}$$

where $\mathbf{C}^{-1}$ is inverse of $\mathbf{C}$.

If $\mathbf{C}$ is not temperature dependent, the above equation becomes

$$\rho_0 C_{\mathbf{E}}\dot{\theta}=-\theta\boldsymbol{\alpha}\colon\mathbf{C}\colon\dot{\mathbf{E}} \tag{16}$$

By direct comparisons of Eqs. (15) and (16), it is obvious that one can introduce the effective thermal expansion coefficient $\boldsymbol{\alpha}_{\mathrm{eff}}$ for linear elastic material with temperature-dependent $\mathbf{C}$ and rewrite (15) as follows:

$$\rho_0 C_{\mathbf{E}}\dot{\theta}=-\theta\boldsymbol{\alpha}_{\mathrm{eff}}\colon\mathbf{C}\colon\dot{\mathbf{E}} \tag{17}$$

with $\boldsymbol{\alpha}_{\mathrm{eff}}$ given by

$$\boldsymbol{\alpha}_{\mathrm{eff}}=\boldsymbol{\alpha}_0-\mathbf{C}^{-1}\colon\frac{d\mathbf{C}}{d\theta}\colon\mathbf{C}^{-1}\colon\mathbf{S} \tag{18}$$

where $\boldsymbol{\alpha}_0$ stands for thermal expansion coefficient at zero stress. This equation has been derived by Bert and Fu (1990) for the case of uniaxial stress and infinitesimal deformation and for the general case by Wong (1991).

The quantity $\boldsymbol{\alpha}_{\mathrm{eff}}$ given by (18) represents the effective thermal expansion coefficient at any constant stress and can actually be derived directly from (14) without the consideration

Downloaded 03 May 2010 to 171.66.16.245. Redistribution subject to ASME license or copyright; see http://www.asme.org/terms/Terms_Use.cfm

of thermodynamics. In fact, taking the time derivative of both sides of Eq. (14) leads to the following:

$$\dot{\mathbf{S}} = \frac{d\mathbf{C}}{d\theta} : (\mathbf{E} - \boldsymbol{\alpha}\Delta\theta)\dot{\theta} + \mathbf{C} : (\dot{\mathbf{E}} - \boldsymbol{\alpha}\dot{\theta}), \tag{19}$$

which can be rewritten as

$$\dot{\mathbf{E}}/\dot{\theta} = \mathbf{C}^{-1} : \dot{\mathbf{S}}/\dot{\theta} + \left(\boldsymbol{\alpha} - \mathbf{C}^{-1}\frac{d\mathbf{C}}{d\theta} : \mathbf{C}^{-1} : \mathbf{S}\right). \tag{20}$$

The effective thermal expansion coefficient at constant stress is then defined as

$$\boldsymbol{\alpha}_{\text{eff}} = \left.\frac{\dot{\mathbf{E}}}{\dot{\theta}}\right|_{\dot{\mathbf{S}}=\mathbf{0}}. \tag{21}$$

Obviously, Eqs. (20) and (21) result in the same expression as Eq. (18), which has been derived from thermodynamics, if one notes that $\boldsymbol{\alpha}$ in Eq. (20) is actually $\boldsymbol{\alpha}_0$, the thermal expansion coefficient at zero stress.

Although the effective thermal expansion coefficient can be studied without consulting thermodynamics as demonstrated above, the definition of specific heat at constant strain has to be based on the laws of thermodynamics. Since the interest of this paper is in both thermal expansion coefficient and specific heat, and since it has been shown that the thermodynamics approach provides the same expression for $\boldsymbol{\alpha}_{\text{eff}}$ as the approach based on definition (21), the systematic thermodynamics consideration is retained in the following discussions.

For nonlinear elastic materials, Eq. (13) can be rewritten as

$$\rho_0 C_{\mathbf{E}}\dot{\theta} = -\theta\left[-\frac{\partial\mathbf{S}}{\partial\theta} : \mathbf{C}_t^{-1}\right] : \mathbf{C}_t : \dot{\mathbf{E}} \tag{22}$$

where $\mathbf{C}_t$ is the tangential stiffness tensor defined by

$$\mathbf{C}_t = \frac{\partial\dot{\mathbf{S}}}{\partial\dot{\mathbf{E}}}. \tag{23}$$

By direct comparison of Eqs. (22) and (16), it is observed that the thermal expansion coefficient for nonlinear elastic material with temperature dependence is

$$\boldsymbol{\alpha}_{\text{eff}} = -\frac{\partial\mathbf{S}}{\partial\theta} : \mathbf{C}_t^{-1} = -\rho_0\frac{\partial^2\hat{\psi}}{\partial\theta\partial\mathbf{E}} : \mathbf{C}_t^{-1} \tag{24}$$

It is easy to verify that (18) can be derived from (24) if $\mathbf{S}$ is given by (14). Indeed, in this case, $\mathbf{C}_t = \mathbf{C}$, and

$$\begin{aligned}\frac{\partial\mathbf{S}}{\partial\theta} &= \frac{d\mathbf{C}}{d\theta} : (\mathbf{E} - \boldsymbol{\alpha}\Delta\theta) - \mathbf{C} : \boldsymbol{\alpha} \\ &= \frac{d\mathbf{C}}{d\theta} : \mathbf{C}^{-1} : \mathbf{S} - \mathbf{C} : \boldsymbol{\alpha}.\end{aligned} \tag{25}$$

Substituting this into (24) and noting the symmetry of $\mathbf{C}$ result in (18). It is interesting to note that the effective thermal expansion coefficient $\boldsymbol{\alpha}_{\text{eff}}$ is not an independent material property and it depends upon the Helmholtz potential $\hat{\psi}$.

For a general elastic-plastic material subjected to finite deformation, (12) has to be used. After substitution of (B11)–(B15) into (12) and rearrangement of the result, the following expression can be obtained:

$$\begin{aligned}\rho_0\left\{C_{\mathbf{E}} + \left[\frac{\partial\hat{\psi}}{\partial\mathbf{E}^p} - \theta\frac{\partial^2\hat{\psi}}{\partial\theta\partial\mathbf{E}^p}\right] : \boldsymbol{\beta}\frac{\partial g}{\partial\theta} + \lambda\left[\frac{\partial\hat{\psi}}{\partial k} - \theta\frac{\partial^2\hat{\psi}}{\partial\theta\partial k}\right]\frac{\partial g}{\partial\theta}\right\}\dot{\theta} = \\ = -\theta\left\{\frac{\partial\mathbf{S}}{\partial\theta} : \mathbf{C}_t^{-1} + \left[\rho_0\left(\frac{1}{\theta}\frac{\partial\hat{\psi}}{\partial\mathbf{E}^p} - \frac{\partial^2\hat{\psi}}{\partial\theta\partial\mathbf{E}^p}\right) : \left(\boldsymbol{\beta}\otimes\frac{\partial g}{\partial\mathbf{E}}\right)\right.\right. \\ \left.\left. + \rho_0\left(\frac{1}{\theta}\frac{\partial\hat{\psi}}{\partial k} - \frac{\partial^2\hat{\psi}}{\partial\theta\partial k}\right)\lambda\frac{\partial g}{\partial\mathbf{E}}\right] : \mathbf{C}_t^{-1}\right\} : \mathbf{C}_t : \dot{\mathbf{E}}.\end{aligned} \tag{26}$$

By direct comparison of (26) and (16), it can be seen that the effective thermal expansion coefficient $\boldsymbol{\alpha}_{\text{eff}}$ and the effective specific heat at constant strain $C_{\mathbf{E}_{\text{eff}}}$, for a material subjected to finite elastic-plastic deformation, are

$$\begin{aligned}\boldsymbol{\alpha}_{\text{eff}} = -\frac{\partial\mathbf{S}}{\partial\theta} : \mathbf{C}_t^{-1} + \left[\rho_0\left(\frac{1}{\theta}\frac{\partial\hat{\psi}}{\partial\mathbf{E}^p} - \frac{\partial^2\hat{\psi}}{\partial\theta\partial\mathbf{E}^p}\right) : \right. \\ \left.\left(\boldsymbol{\beta}\otimes\frac{\partial g}{\partial\mathbf{E}}\right) + \rho_0\left(\frac{1}{\theta}\frac{\partial\hat{\psi}}{\partial k} - \frac{\partial^2\hat{\psi}}{\partial\theta\partial k}\right)\lambda\frac{\partial g}{\partial\mathbf{E}}\right] : \mathbf{C}_t^{-1}\end{aligned} \tag{27}$$

$$C_{\mathbf{E}_{\text{eff}}} = C_{\mathbf{E}}^0 + \left(\frac{\partial\hat{\psi}}{\partial\mathbf{E}^p} - \theta\frac{\partial^2\hat{\psi}}{\partial\theta\partial\mathbf{E}^p}\right) : \boldsymbol{\beta}\frac{\partial g}{\partial\theta} + \lambda\left(\frac{\partial\hat{\psi}}{\partial k} - \theta\frac{\partial^2\hat{\psi}}{\partial\theta\partial k}\right)\frac{\partial g}{\partial\theta}, \tag{28}$$

where $C_{\mathbf{E}}^0$ is given by (8) and stands for the original specific heat at constant strain.

Equations (27) and (28) are new results derived in this paper. It can be seen that during large elastic-plastic deformation, the thermal coefficients, i.e., $\boldsymbol{\alpha}_{\text{eff}}$ and $C_{\mathbf{E}_{\text{eff}}}$, will change with the stress state and deformation. This change depends on the thermomechanical properties of the material, that is, the Helmholtz potential $\hat{\psi}$, yield function g, and the constitutive behavior of plastic deformation and hardening, $\boldsymbol{\beta}$ and λ. These constitutive functions are material dependent and have to be determined by well-designed experiments.

It is obvious that (24) is only a special case of (27) when the plastic deformation is zero during the process. Equations (27) and (28) are the general expressions for effective thermal expansion coefficients and specific heat at constant strain.

3 Special Cases

In this section, a special type of material is considered for which the Helmholtz potential can be written as

$$\psi = \hat{\psi}(\mathbf{E}, \theta, \mathbf{E}^p, k) = \bar{\psi}(\mathbf{E} - \mathbf{E}^p, \theta, k). \tag{29}$$

As was pointed out by Naghdi (1990), this special form (29) includes as a special case the generalized Hooke's law and it has been used in the development of the well-known Prandtl-Reuss constitutive relations for the elastic-work hardening materials at small deformations. It is easy to calculate that

$$\rho_0\frac{\partial\hat{\psi}}{\partial\mathbf{E}} = \rho_0\frac{\partial\bar{\psi}}{\partial(\mathbf{E} - \mathbf{E}^p)} = \mathbf{S} \tag{30}$$

$$\frac{\partial\hat{\psi}}{\partial\theta} = \frac{\partial\bar{\psi}}{\partial\theta} = -\eta \tag{31}$$

$$\rho_0\frac{\partial\hat{\psi}}{\partial\mathbf{E}^p} = -\rho_0\frac{\partial\bar{\psi}}{\partial(\mathbf{E} - \mathbf{E}^p)} = -\mathbf{S} \tag{32}$$

$$\frac{\partial\hat{\psi}}{\partial k} = \frac{\partial\bar{\psi}}{\partial k};\quad \frac{\partial^2\hat{\psi}}{\partial\theta\partial k} = \frac{\partial^2\bar{\psi}}{\partial\theta\partial k}. \tag{33}$$

Substituting these relations into (27) gives

$$\begin{aligned}\boldsymbol{\alpha}_{\text{eff}} = -\frac{\partial\mathbf{S}}{\partial\theta} : \mathbf{C}_t^{-1} : \left(\boldsymbol{\Psi} - \boldsymbol{\beta}\otimes\frac{\partial g}{\partial\mathbf{E}}\right) - \frac{1}{\theta}\mathbf{S} : \\ \left(\boldsymbol{\beta}\otimes\frac{\partial g}{\partial\mathbf{E}}\right) : \mathbf{C}_t^{-1} + \rho_0\left(\frac{1}{\theta}\frac{\partial\bar{\psi}}{\partial k} - \frac{\partial^2\bar{\psi}}{\partial\theta\partial k}\right)\lambda\frac{\partial g}{\partial\mathbf{E}} : \mathbf{C}_t^{-1}\end{aligned} \tag{34}$$

where $\boldsymbol{\Psi}$ is a fourth-order identity tensor and its component form is

$$\mathcal{I}_{ijkl} = \frac{1}{2}(\delta_{ik}\delta_{jl} + \delta_{il}\delta_{jk}) \tag{35}$$

Similarly, for this case (28) can be rewritten as

$$C_{\mathbf{E}_{\text{eff}}} = C_{\mathbf{E}}^0 + \left(\theta\frac{\partial\mathbf{S}}{\partial\theta} - \mathbf{S}\right) : \boldsymbol{\beta}\frac{1}{\rho_0}\frac{\partial g}{\partial\theta} + \lambda\left(\frac{\partial\bar{\psi}}{\partial k} - \theta\frac{\partial^2\bar{\psi}}{\partial\theta\partial k}\right)\frac{\partial g}{\partial\theta}. \tag{36}$$

The temperature, stress, and plastic deformation dependence of $\boldsymbol{\alpha}_{\text{eff}}$ and $C_{\mathbf{E}_{\text{eff}}}$ can be clearly seen from (34) and (36).

If it is further assumed that the material can be characterized by the following stress response:

$$\mathbf{S} = \mathbf{C}(\theta) : (\mathbf{E} - \mathbf{E}^p - \boldsymbol{\alpha}\Delta\theta), \tag{37}$$

Downloaded 03 May 2010 to 171.66.16.245. Redistribution subject to ASME license or copyright; see http://www.asme.org/terms/Terms_Use.cfm

and therefore the Helmholtz potential of the form (according to (30))

$$\overline{\psi}=\frac{1}{\rho_0}\frac{1}{2}(\mathbf{E}-\mathbf{E}^p-\alpha\Delta\theta)\colon \mathbf{C}(\theta)\colon (\mathbf{E}-\mathbf{E}^p-\alpha\Delta\theta)+\overline{\psi}_1(\theta,\ k), \quad (38)$$

where $\overline{\psi}_1$ is a function of θ and k. Then (34) and (36) can be further simplified to be

$$\alpha_{\text{eff}}=\left(\alpha_0-\mathbf{C}^{-1}\colon\frac{d\mathbf{C}}{d\theta}\colon\mathbf{C}^{-1}\colon\mathbf{S}\right)\colon\mathbf{C}\colon\mathbf{C}_t^{-1}\colon\left(\mathbf{\Psi}-\beta\otimes\frac{\partial g}{\partial\mathbf{E}}\right)-\frac{1}{\theta}\mathbf{S}\colon\left(\beta\otimes\frac{\partial g}{\partial\mathbf{E}}\right)\colon\mathbf{C}_t^{-1}+\rho_0\left(\frac{1}{\theta}\frac{\partial\overline{\psi}_1}{\partial k}-\frac{\partial^2\overline{\psi}_1}{\partial\theta\partial k}\right)\lambda\frac{\partial g}{\partial\mathbf{E}}\colon\mathbf{C}_t^{-1} \quad (39)$$

$$C_{\mathbf{E}_{\text{eff}}}=C^0_{\mathbf{E}_{\text{eff}}}-\left[\theta\left(\mathbf{C}\colon\alpha-\frac{d\mathbf{C}}{d\theta}\colon\mathbf{C}^{-1}\colon\mathbf{S}\right)+\mathbf{S}\right]\colon\beta\frac{1}{\rho_0}\frac{\partial g}{\partial\theta}+\lambda\left(\frac{\partial\overline{\psi}_1}{\partial k}-\theta\frac{\partial^2\overline{\psi}_1}{\partial\theta\partial k}\right)\frac{\partial g}{\partial\theta}. \quad (40)$$

In cases where $\mathbf{C}\colon\mathbf{C}_t^{-1}=\mathbf{C}_t^{-1}\colon\mathbf{C}$ (for example, proportional loading), it can be shown (see Appendix C) that

$$\mathbf{C}\colon\mathbf{C}_t^{-1}\colon\left(\mathbf{\Psi}-\beta\otimes\frac{\partial g}{\partial\mathbf{E}}\right)=\mathbf{\Psi}. \quad (41)$$

Therefore, (39) reduces to

$$\alpha_{\text{eff}}=\left(\alpha_0-\mathbf{C}^{-1}\colon\frac{d\mathbf{C}}{d\theta}\colon\overline{C}^{-1}\colon\mathbf{S}\right)-\frac{1}{\theta}\mathbf{S}\colon\left(\beta\otimes\frac{\partial g}{\partial\mathbf{E}}\right)\colon\mathbf{C}_t^{-1}+\rho_0\left(\frac{1}{\theta}\frac{\partial\overline{\psi}_1}{\partial k}-\frac{\partial^2\overline{\psi}_1}{\partial\theta\partial k}\right)\lambda\frac{\partial g}{\partial\mathbf{E}}\colon\mathbf{C}_t^{-1}. \quad (42)$$

It is interesting to compare this equation with (18), which is the result for linear elastic materials with temperature-dependent $\mathbf{C}$. It is obvious that (18) is a special case of (42): the latter leads to the former when the process involves only elastic deformation.

In order to clearly see the implication of each term in (34) and (36), the one-dimensional case (uniaxial stress) will be discussed in detail in the rest of this paper. The comparison of the theory derived in this paper with the experimental data obtained by Rosenfield and Averbach (1956) is also briefly considered.

4 One-Dimensional Case: Uniaxial Stress

In this case, (12) can be written as

$$\rho_0 C_{E_{11}}\dot{\theta}=\theta\frac{\partial S_{11}}{\partial\theta}\dot{E}_{11}-\rho_0\left(\frac{\partial\overline{\psi}}{\partial E^p_{11}}-\theta\frac{\partial^2\hat{\psi}}{\partial\theta\partial E^p_{11}}\right)\dot{E}^p_{11}-\rho_0\left(\frac{\partial\hat{\psi}}{\partial k}-\theta\frac{\partial^2\hat{\psi}}{\partial\theta\partial k}\right)\dot{k} \quad (43)$$

where S_{11}, E_{11}, and E^p_{11} are the stress, strain, and plastic strain, respectively.

Assuming that

$$S_{11}=E(\theta)\,(E_{11}-E^p_{11}-\alpha\Delta\theta) \quad (44)$$

where E is the Young's modulus and is assumed to be temperature dependent. The Helmholtz potential can then be deduced from (44) to be

$$\psi=\hat{\psi}(E_{11},\ \theta,\ E^p_{11},\ k)=\overline{\psi}(E_{11}-E^p_{11},\ \theta,\ E^p_{11},\ k)=\frac{1}{\rho_0}\frac{1}{2}E(E_{11}-E^p_{11}-\alpha\Delta\theta)^2+\overline{\psi}(E^p_{11},\ \theta,\ k). \quad (45)$$

From (44) and (45), it can be determined that

$$\frac{\partial S_{11}}{\partial\theta}=\frac{S_{11}}{E}\frac{dE}{d\theta}-E\alpha \quad (46)$$

$$\rho_0\frac{\partial\hat{\psi}}{\partial E^p_{11}}=-S_{11}+\rho_0\frac{\partial\overline{\psi}_1}{\partial E^p_{11}};\quad\frac{\partial^2\hat{\psi}}{\partial\theta\partial E^p_{11}}=\frac{\partial^2\overline{\psi}_1}{\partial\theta\partial E^p_{11}}-\frac{\partial S_{11}}{\partial\theta} \quad (47)$$

$$\frac{\partial\hat{\psi}}{\partial k}=\frac{\partial\overline{\psi}_1}{\partial k};\quad\frac{\partial^2\hat{\psi}}{\partial\theta\partial k}=\frac{\partial^2\overline{\psi}_1}{\partial\theta\partial k}. \quad (48)$$

Substituting (46)–(48) into (43) results in

$$\rho_0 C_{\mathbf{E}}\dot{\theta}=-\theta\left(E\alpha-\frac{S_{11}}{E}\frac{dE}{d\theta}\right)(\dot{E}_{11}-\dot{E}^p_{11})+\left(S_{11}-\rho_0\frac{\partial\overline{\psi}_1}{\partial E^p_{11}}-\rho_0\theta\frac{\partial^2\overline{\psi}_1}{\partial\theta\partial E^p_{11}}\right)\dot{E}^p_{11}-\rho_0\left(\frac{\partial\overline{\psi}_1}{\partial k}-\theta\frac{\partial^2\overline{\psi}_1}{\partial\theta\partial k}\right)\dot{k}. \quad (49)$$

In the one-dimensional case, E^p_{11} can be expressed as

$$\dot{E}^p_{11}=a\,\dot{E}_{11}+b\,\dot{\theta} \quad (50)$$

where a and b are material properties.

The evolution of k can be given by

$$\dot{k}=\frac{\partial k}{\partial E_{11}}\dot{E}_{11}+\frac{\partial k}{\partial\theta}\dot{\theta} \quad (51)$$

where k can be identified with the current yield stress and is equal to the current stress S_{11} in case of plastic loading.

For a given constant temperature, one can perform a uniaxial stress experiment to obtain the $S_{11}-E_{11}$ curve. This curve can be converted to the $S_{11}-E^p_{11}$ curve if the constitutive Eq. (44) is used to subtract the strain $E_{11}-E^p_{11}$ (elastic strain if the deformation is small) from E_{11}. Therefore, one can determine

$$E_p=\frac{\partial\dot{S}_{11}}{\partial\dot{E}^p_{11}};\quad E_t=\frac{\partial\dot{S}_{11}}{\partial\dot{E}_{11}} \quad (52)$$

where E_p and E_t are, respectively, the tangential slope of $S_{11}-E^p_{11}$ and $S_{11}-E_{11}$ curves. Note that

$$E=\frac{\partial\dot{S}_{11}}{\partial(\dot{E}_{11}-\dot{E}^p_{11})};\quad\frac{1}{E_t}=\frac{1}{E_p}+\frac{1}{E}. \quad (53)$$

It is easy to obtain that

$$a=\frac{\partial\dot{E}^p_{11}}{\partial\dot{E}_{11}}=\frac{E_t}{E_p}=\frac{E}{E+E_p}\le 1 \quad (54)$$

As mentioned previously, hardening parameter k is the yield stress in uniaxial loading. Therefore,

$$\frac{\partial\dot{k}}{\partial\dot{E}_{11}}=E_t \quad (55)$$

in case of plastic loading. Similarly, b and $\partial k/\partial\theta$ can be determined from experiments where the plastic deformation is caused by temperature change.

Substitution of (50) and (51) into (49) and rearrangement of the result give the following:

$$\rho_0\dot{\theta}\left\{C_{E_{11}}-\left[\frac{\theta}{\rho_0}\left(E\alpha-\frac{S_{11}}{E}\frac{dE}{d\theta}\right)+\frac{S_{11}}{\rho_0}-\left(\frac{\partial\overline{\psi}_1}{\partial E^p_{11}}+\theta\frac{\partial^2\overline{\psi}_1}{\partial\theta\partial E^p_{11}}\right)\right]b+\left(\frac{\partial\overline{\psi}_1}{\partial k}-\theta\frac{\partial^2\overline{\psi}_1}{\partial\theta\partial k}\right)\frac{\partial k}{\partial\theta}\right\}=-E_t\theta\dot{E}_{11}\left\{\left(\alpha-\frac{S_{11}}{E^2}\frac{dE}{d\theta}\right)-\frac{S_{11}}{E_p\theta}+\frac{\rho_0}{\mathrm{E}_p\theta}\left(\frac{\partial\overline{\psi}_1}{\partial\mathrm{E}^p_{11}}+\theta\frac{\partial^2\overline{\psi}_1}{\partial\theta\partial E^p_{11}}\right)+\frac{\rho_0}{\theta}\left(\frac{\partial\overline{\psi}_1}{\partial k}-\theta\frac{\partial^2\overline{\psi}_1}{\partial\theta\partial k}\right)\right\} \quad (56)$$

where relations (54) and (55) have been used to simplify the result.

From (56), it is observed that in case of uniaxial stress, the effective specific heat at constant strain and the effective thermal expansion coefficient are

Downloaded 03 May 2010 to 171.66.16.245. Redistribution subject to ASME license or copyright; see http://www.asme.org/terms/Terms_Use.cfm

$$C_{E_{11}\text{eff}} = C^0_{E_{11}} - \left[\frac{\theta}{\rho_0}\left(E\alpha_0 - \frac{S_{11}}{E}\frac{dE}{d\theta}\right) + \frac{S_{11}}{\rho_0} - \left(\frac{\partial\bar{\psi}_1}{\partial E^p_{11}} + \theta\frac{\partial^2\bar{\psi}_1}{\partial\theta\partial E^p_{11}}\right)\right] b + \left(\frac{\partial\bar{\psi}_1}{\partial k} - \theta\frac{\partial^2\bar{\psi}_1}{\partial\theta\partial k}\right)\frac{\partial k}{\partial\theta} \quad (57)$$

$$\alpha_{\text{eff}} = \left(\alpha_0 - \frac{S_{11}}{E^2}\frac{dE}{d\theta}\right) - \frac{S_{11}}{E_p\theta} + \frac{\rho_0}{E_p\theta}\left(\frac{\partial\bar{\psi}_1}{\partial E^p_{11}} + \theta\frac{\partial^2\bar{\psi}_1}{\partial\theta\partial E^p_{11}}\right) + \frac{\rho_0}{\theta}\left(\frac{\partial\bar{\psi}_1}{\partial k} - \theta\frac{\partial^2\bar{\psi}_1}{\partial\theta\partial k}\right) \quad (58)$$

where $C^0_{E_{11}}$ is the specific heat at constant strain in case of no plastic deformation, α_0 is the thermal expansion coefficient at zero stress and no plastic deformation.

It is important to note at this stage that $C_{E_{11}\text{eff}}$ and α_{eff} depend on the constitutive behavior of the material. The accurate evaluation of them requires the accurate determination of the Helmholtz potential ψ, the yield function g, the hardening parameter k, and the plastic strain $\mathbf{E}^p$.

In early work by Rosenfield and Averbach (1956), the thermal expansion coefficients for five different materials were determined from zero stress up to the stress level close to ultimate stress (the thermal expansion coefficients were reported as a function of stress but the strain levels were not given). The major conclusions, which can be drawn from their experiments for materials with $dE/d\theta > 0$, are the following:

(*i*) α_{eff} increases linearly in the elastic deformation range;

(*ii*) In the plastic deformation range, α_{eff} increases faster initially, then reaches a maximum, followed by a rapid decrease; and

(*iii*) After removal of the stress, α_{eff} restores its original value α_0 if the loading was in the elastic region; α_{eff} differs from α_0 if the loading was in the plastic region: initially, α_{eff} α_0, then α_{eff} reaches a maximum value, followed by a rapid decrease.

As discussed before, α_{eff} and $C_{E_{11}\text{eff}}$ are not independent constitutive quantities but derived from the fundamental constitutive quantities ψ, g, k, and E^p_{11}. Since the experimental data to completely determine these quantities (especially ψ) for materials tested by Rosenfield and Averbach in the case of finite elastic—plastic deformation are not available at the present time, it is difficult to compare quantitatively the theory developed in this paper with the experimental observation mentioned here. However, a qualitative comparison can be made and is presented as follows. Only uniaxial tension ($S_{11} > 0$) is considered.

(*i*) Loading and unloading within the elastic deformation range:

Since $\dot{E}^p_{11} = E^p_{11} = \dot{k} = 0$, α_{eff} is given by

$$\alpha_{\text{eff}} = \alpha_0 - \frac{S_{11}}{E^2}\frac{dE}{d\theta} \quad (59)$$

For materials with $dE/d\theta < 0$, α_{eff} increases linearly with stress S_{11}, which is in accord with experimental observations. After unloading $S_{11} = 0$,

$$\alpha_{\text{eff}} = \alpha_0. \quad (60)$$

Again, this is in agreement with the aforementioned experimental observation.

(*ii*) Loading and unloading within the plastic deformation range:

The effective thermal expansion coefficient α_{eff} is given by (58). It is seen that α_{eff} consists of four terms: the first term represents a linear increase of α_{eff} with S_{11} and the slope of this linear increase is $-1/E^2\, dE/d\theta$; the second term represents a linear decrease with S_{11} and the slope is given by $1/E_p\theta$. Since $E_p < E$ and generally $|dE/d\theta|$ is two orders less than E (Rosenfield and Averbach, 1956), the quantity $|1/E^2\, dE/d\theta|$ is more than two orders smaller than $1/E_p\theta$, therefore, the second term causes α_{eff} to decrease rapidly in the plastic deformation range. This is in agreement with the aforementioned experimental results. Finally, the last two terms on the right-hand side of (58) denote the change of α_{eff} due to the plastic deformation and their specific forms depend on the specific dependence of ψ on θ, k, and E^p_{11}. Here, one has the flexibility to choose the appropriate form to fit the experimental data, such as those obtained by Rosenfield and Averbach (1956).

After unloading to $S_{11} = 0$ within the plastic deformation range, α_{eff} becomes

$$\alpha_{\text{eff}} = \alpha_0 + \frac{\rho_0}{E_p\theta}\left(\frac{\partial\bar{\psi}_1}{\partial E^p_{11}} + \theta\frac{\partial^2\bar{\psi}_1}{\partial\theta\partial E^p_{11}}\right) + \frac{\rho_0}{\theta}\left(\frac{\partial\bar{\psi}_1}{\partial k} - \theta\frac{\partial^2\bar{\psi}_1}{\partial\theta\partial k}\right) \quad (61)$$

Hence, after unloading from plastic deformation, α_{eff} is equal to α_0 plus the permanent change caused by plastic deformation. Once again, if the dependence of ψ on θ, k, and E^p_{11} is chosen properly (or α and C_E directly), any experimental observation can be modeled by the theory presented here. The curve fitting process for α_{eff} by appropriately choosing $\bar{\psi}_1$ is not pursued in this paper because, as mentioned before, ψ is a fundamental constitutive quantity and its determination needs the consideration of all the fundamental constitutive behavior, such as the stress response and entropy production at finite elastic-plastic deformation. A systematic research investigation on all these aspects, including the effective thermal expansion coefficient and specific heat at constant strain, is required for this purpose. This is a topic for further study. However, the general results obtained in this paper, (27) and (28), are valid no matter how ψ is determined, since they are derived from the general thermodynamics considerations and the general finite elastic-plastic theory.

It should be noted that (57) and (58) are derived based on the one-dimensional stress-strain-temperature relation (44). In the general case, S_{11} is expressed by

$$S_{11} = \hat{S}_{11}(E_{11}, \theta, E^p_{11}, k). \quad (62)$$

Substitution of this equation and (50) and (51) into (43) results in the following general expressions for effective thermal expansion coefficient and specific heat at constant strain in case of one-dimensional stress:

$$\alpha_{\text{eff}} = -\frac{1}{E_t}\frac{\partial S_{11}}{\partial\theta} + \frac{\rho_0}{E_p\theta}\left(\frac{\partial\hat{\psi}}{\partial E^p_{11}} - \theta\frac{\partial^2\hat{\psi}}{\partial\theta\partial E^p_{11}}\right) + \frac{\rho_0}{\theta}\left(\frac{\partial\hat{\psi}}{\partial k} - \theta\frac{\partial^2\hat{\psi}}{\partial\theta\partial k}\right) \quad (63)$$

$$C_{E_{11}\text{eff}} = C^0_{E_{11}} + \left(\frac{\partial\hat{\psi}}{\partial E^p_{11}} - \theta\frac{\partial^2\hat{\psi}}{\partial\theta\partial E^p_{11}}\right) b + \left(\frac{\partial\hat{\psi}}{\partial k} - \theta\frac{\partial^2\hat{\psi}}{\partial\theta\partial k}\right)\frac{\partial k}{\partial\theta}. \quad (64)$$

5 Conclusions

In this paper, a mathematical theory has been developed for the effective thermal expansion coefficient and specific heat at constant strain in the case of finite elastic-plastic deformation based on general thermodynamics analysis and finite plasticity theory formulated in strain space. The theory developed here includes previously published results as special cases. It has been shown that the above two thermal behavior parameters are not independent constitutive quantities but can be derived from the fundamental constitutive quantities, the Helmholtz potential ψ, yield function g, and evolution functions of the hardening parameter k and plastic strain $\mathbf{E}^p$. Therefore, the thermal expansion coefficient and specific heat depend on the stress and deformation state and its history in a very complicated way. It has been discussed in this paper that the previously published experimental results of effective thermal expansion coefficient can be described by the present theory. However, further experimental and theoretical studies are necessary to establish systematically all of the constitutive func-

Downloaded 03 May 2010 to 171.66.16.245. Redistribution subject to ASME license or copyright; see http://www.asme.org/terms/Terms_Use.cfm

tions and qualitatively predict the thermomechanical behavior of a solid at finite deformation.

The present research does not consider the plasticity model with back stress as an internal variable. However, extension to this model of the present theory is straight forward without any difficulty and hence is omitted here.

References

Bert, C. W., and Fu, C., 1990, "Implications of Stress Dependency of the Thermal Expansion Coefficient on Thermal Buckling," *Thermal Effects on Structures and Materials*, V. Birman and D. Hui, eds., PVP-Vol. 203/AMD-Vol. 110, ASME, New York, pp. 1-5; ASME *Journal of Pressure Vessel Technology*, Vol. 114, pp. 189-192.

Clausius, R., 1850, "On the Moving Force of Heat and the Laws Which May Be Deduced Therefrom," *Poggendorff's Annalen*, Vol. 79, pp. 368-500.

Gough, J., 1805, "A Description of a Property of Caoutchouc or Indian-Rubber," *Manchester Philosophical Memoirs*, 2nd Series, Vol. 1, pp. 288-295.

Green, A. E. and Naghdi, P. M., 1977, "On Thermodynamics of and the Nature of the Second Law," *Proceedings, Royal Society of London*, Vol. 357, pp. 253-270.

Green, A. E. and Naghdi, P. M., 1978a, "The Second Law of Thermodynamics and Cyclic Processes," ASME JOURNAL OF APPLIED MECHANICS, Vol. 45, pp. 487-482.

Green, A. E., and Naghdi, P. M., 1978b, "On the Thermodynamic Restrictions in the Theory of Elastic-Plastic Materials," *Acta Mechanica*, Vol. 30, pp. 157-162.

Green, A. E., and Naghdi, P. M., 1965, "A General Theory of an Elastic-Plastic Continuum," *Archive of Rational Mechanics and Analysis*, Vol. 18, pp. 251-281.

Hill, R., 1978, "Aspects of Invariance in Solid Mechanics," *Advances in Applied Mechanics*, Vol. 18, pp. 1-75.

Hilton, H. H., 1952, "Thermal Stresses in Bodies Exhibiting Temperature-Dependent Elastic Properties," ASME JOURNAL OF APPLIED MECHANICS, Vol. 19, pp. 350-354.

Naghdi, P. M., 1990, "A Critical Review of the State of Finite Plasticity," *Journal of Applied Mathematics and Physics (ZAMP)*, Vol. 41, pp. 315-394.

Naghdi, P. M., and Trapp, J. A., 1975, "The Significance of Formulating Plasticity Theory with Reference to Loading Surface in Strain Space," *International Journal of Engineering Science*, Vol. 13, pp. 785-797.

Rosenfield, A. R., and Averbach, B. L., 1956, "Effects of Stress on the Expansion Coefficient," *Journal of Applied Physics*, Vol. 27, pp. 154-156.

Thomson, W., 1857, "On the Thermo-elastic and Thermo-magnetic Properties of Matter," *Quarterly Journal of Mathematics*, Vol. 1, pp. 57-77.

Truesdell, C., and Noll, W., 1965, "The Nonlinear Field Theories of Mechanics," *Encyclopedia of Physics*, Vol. III/3, S. Flügge, ed., Springer-Verlag, Berlin.

Wong, A. K., 1991, "The Thermoelastic Effect—A Higher-Order Consideration," *Thermoelastic Stress Analysis*, Adam Hilger, England, pp. 167-182.

Wong, A. K., Jones, R., and Sparrow, J. G, 1987a, "Thermoelastic Constant or Thermoelastic Parameter?" *Journal of the Physics and Chemistry of Solids*, Vol. 48, pp. 749-753.

Wong, A. K., Sparrow, J. G., and Dunn, S. A., 1987b, "Recent Work on the Stress Dependence of the Thermoelastic Parameter," *Optomechanical Systems Engineering*, Society of Photo-Optical Instrumentation Engineers, Vol. 817, pp. 147-151.

Wong, A. K., Sparrow, J. G., and Dunn, S. A., 1988, "On the Revised Theory of the Thermoelastic Effect," *Journal of the Physics and Chemistry of Solids*, Vol. 49, pp. 395-400.

APPENDIX A

First and Second Laws of Thermodynamics

Using the formulation developed by Green and Naghdi (1977, 1987a, 1987b), one can express the conservation of energy (the first law of thermodynamics) and the entropy balance (the second law of thermodynamics) as follows, respectively,

$$-\rho_0(\dot{\psi}+\eta\dot{\theta})+P-\rho_0\theta\xi-\frac{1}{\theta}\mathbf{q}_R\cdot\mathbf{g}_R=0 \tag{A1}$$

$$\rho_0\gamma-\text{Div}\,\mathbf{q}_R+\frac{1}{\theta}\mathbf{q}_R\cdot\mathbf{g}_R+\rho_0\theta\xi=\rho_0\theta\dot{\eta} \tag{A2}$$

where

- ρ_0 = density in the reference configuration k_0
- θ = temperature
- ψ = Helmholtz (Gibbs free energy) potential per unit mass in k_0
- η = entropy per unit mass in k_0
- ξ = internal rate of production of entropy per unit mass in k_0
- γ = internal heat supply rate per unit mass in k_0
- $\mathbf{q}_R$ = heat flux vector per unit area in k_0
- $\mathbf{g}_R$ = temperature gradient relative to k_0
- P = mechanical power.

Equations (A1) and (A2) are the general forms of the first and second laws of thermodynamics valid for reversible as well as irreversible processes involving finite elastic-plastic deformation.

In this paper, the internal heat supply rate is neglected and the attention is focused on homogeneous temperature fields so that $\mathbf{g}_R=\mathbf{0}$. Therefore, (A1) and (A2) reduce to the following:

$$-\rho_0(\dot{\psi}+\eta\dot{\theta})+P-\rho_0\theta\xi=0 \tag{A3}$$

$$-\text{Div}\,\mathbf{q}_R+\rho_0\theta\xi=\rho_0\theta\dot{\eta}. \tag{A4}$$

According to the second law of thermodynamics, the internal rate of production of entropy ξ must satisfy

$$\xi\geq 0. \tag{A5}$$

APPENDIX B

Constitutive Equations

It is assumed that the state of the continuum is completely determined by the strain tensor $\mathbf{E}$, temperature θ, and a set of internal or hidden variables α_I, $I=1, 2, 3, \ldots, N$. The α_I can be scalar, vector, or tensor of any order, depending on the need for describing the specific behavior of the inelastic material. The purpose of these internal variables is to describe the deformation history of the plastic deformation. The accuracy of this description can be improved by the appropriate identification of the internal variables with the physical processes of plastic deformation or by increasing the total number N of these variables. Therefore, formally, the variables are taken to be the following set:

$$\{\mathbf{E},\ \theta,\ \alpha_I,\ I=1, 2, 3, \ldots N\}. \tag{B1}$$

In order to simplify the discussion, only two internal variables, the plastic strain tensor $\mathbf{E}^p$, which is assumed to be a symmetric, second-order tensor (Green and Naghdi, 1965; Naghdi, 1990), and a strain-hardening parameter k, which is a scalar, are used in the rest of the paper. The discussion based on this simplification can easily be generalized to the more general case in which more internal variables, such as the back stress for anisotropic hardening materials, are involved. Therefore, in this paper, the variable set (B1) reduces to

$$\{\mathbf{E},\ \theta,\ \mathbf{E}^p,\ k\} \tag{B2}$$

The constitutive equations for ψ, η, $\mathbf{S}$ and $\mathbf{q}_R$ are assumed to be in the following general forms:

$$\psi=\hat{\psi}(\mathbf{E},\ \theta,\ \mathbf{E}^p,\ k) \tag{B3}$$

$$\eta=\hat{\eta}(\mathbf{E},\ \theta,\ \mathbf{E}^p,\ k) \tag{B4}$$

$$\mathbf{S}=\hat{\mathbf{S}}(\mathbf{E},\ \theta,\ \mathbf{E}^p,\ k) \tag{B5}$$

$$\mathbf{q}_R=\hat{\mathbf{q}}_R(\mathbf{E},\ \theta,\ \mathbf{E}^p,\ k) \tag{B6}$$

Substituting these equations into (A1) readily leads to the following restrictions (Green and Naghdi, 1978b; Naghdi, 1990):

$$\mathbf{S}=\rho_0\frac{\partial\hat{\psi}}{\partial\mathbf{E}} \tag{B7}$$

$$\eta=-\frac{\partial\hat{\psi}}{\partial\theta} \tag{B8}$$

Downloaded 03 May 2010 to 171.66.16.245. Redistribution subject to ASME license or copyright; see http://www.asme.org/terms/Terms_Use.cfm

$$\rho_0 \frac{\partial \hat{\psi}}{\partial \mathbf{E}^p} : \dot{\mathbf{E}}^p + \frac{\partial \hat{\psi}}{\partial k} \dot{k} + \rho_0 \theta \xi = 0. \tag{B9}$$

Therefore, among the four constitutive Eqs. (B3)–(B6), two of them ($\hat{\mathbf{S}}$ and $\hat{\eta}$) can be derived from $\hat{\psi}$ and do not need to be established independently.

In order to characterize plastic deformation, it is assumed that there exists a yield surface in strain and temperature space described by the following functional form (Naghdi, 1990):

$$g(\mathbf{E}, \theta, \mathbf{E}^p, k) = 0, \tag{B10}$$

where $\mathbf{E}^p$ and k play the role of parameters. In general, the evolution of $\mathbf{E}^p$ and k can be expressed by

$$\dot{\mathbf{E}}^p = \beta \hat{g} \tag{B11}$$

$$\dot{k} = \lambda \hat{g} \tag{B12}$$

where

$$\beta = \hat{\beta}(\mathbf{E}, \theta, \dot{\mathbf{E}}^p, k) \tag{B13}$$

$$\lambda = \hat{\lambda}(\mathbf{E}, \theta, \dot{\mathbf{E}}^p, k) \tag{B14}$$

are two constitutive functions and $\hat{g}$ is given by

$$\hat{g} = \frac{\partial g}{\partial \mathbf{E}} : \dot{\mathbf{E}} + \frac{\partial g}{\partial \theta} \dot{\theta}. \tag{B15}$$

Equations (19)–(24) are the general constitutive equations for finite plastic deformation developed in detail by Naghdi (1990). In addition to these equations, there are well-established loading-unloading criteria which were also described in detail by Naghdi (1990).

In summary, a thermoplasticity theory for large (finite) deformation needs the following five constitutive quantities: $\hat{\psi}$, $\mathbf{q}_R$, $\mathbf{g}$, β, and $\hat{\lambda}$.

APPENDIX C

Proof of Eq. (41)

From Eq. (37), it is easy to calculate that

$$\mathbf{C} = \frac{\partial \dot{\mathbf{S}}}{\partial (\dot{\mathbf{E}} - \dot{\mathbf{E}}^p)}, \tag{C1}$$

and by definition,

$$\mathbf{C}_t = \frac{\partial \dot{\mathbf{S}}}{\partial \dot{\mathbf{E}}}. \tag{C2}$$

One can further introduce the following notations:

$$\frac{\partial \dot{\mathbf{E}}^p}{\partial \dot{\mathbf{E}}} = \beta \otimes \frac{\partial g}{\partial \mathbf{E}} = \mathbf{A} \tag{C3}$$

and

$$\frac{\partial \dot{\mathbf{S}}}{\partial \dot{\mathbf{E}}^p} = \frac{\partial \dot{\mathbf{S}}}{\partial \dot{\mathbf{E}}} : \frac{\partial \dot{\mathbf{E}}}{\partial \dot{\mathbf{E}}^p} = \mathbf{C}_p \tag{C4}$$

Hence, from (C2)–(C4), it can be shown that

$$\mathbf{C}_p = \mathbf{C}_t : \mathbf{A}^{-1}. \tag{C5}$$

On the other hand,

$$\frac{\partial \dot{\mathbf{E}}}{\partial \dot{\mathbf{S}}} = \frac{\partial (\dot{\mathbf{E}} - \dot{\mathbf{E}}^p) + \partial \dot{\mathbf{E}}^p}{\partial \dot{\mathbf{S}}}.$$

That is,

$$\mathbf{C}_t^{-1} = \mathbf{C}^{-1} + \mathbf{C}_p^{-1},$$

which leads to

$$\mathbf{C}_p = (\mathbf{C}_t^{-1} - \mathbf{C}^{-1})^{-1} \tag{C6}$$

From (C5) and (C6),

$$\mathbf{A} = (\mathbf{C}_t^{-1} - \mathbf{C}^{-1}) : \mathbf{C}_t = \mathbf{\Psi} - \mathbf{C}^{-1} : \mathbf{C}_t \tag{C7}$$

Therefore,

$$\mathbf{C} : \mathbf{C}_t^{-1} \left(\mathbf{\Psi} - \beta \otimes \frac{\partial g}{\partial \mathbf{E}} \right) = \mathbf{C}_t^{-1} : \mathbf{C} : (\mathbf{\Psi} - \mathbf{A})$$

$$= \mathbf{C}_t^{-1} : \mathbf{C} : \mathbf{C}^{-1} : \mathbf{C}_t^{-1} = \mathbf{\Psi}, \tag{C8}$$

which is (41).

However, in general, $\mathbf{C} : \mathbf{C}_t^{-1} = \mathbf{C}_t^{-1} : \mathbf{C}$; thus, (41) does not hold for the general case.

Downloaded 03 May 2010 to 171.66.16.245. Redistribution subject to ASME license or copyright; see http://www.asme.org/terms/Terms_Use.cfm

On Uncoupling and Solving the Equations of Motion of Vibrating Linear Discrete Systems

S. F. Felszeghy
Department of Mechanical Engineering,
California State University, Los Angeles,
Los Angeles, CA 90032-8153
Mem. ASME

The equations of motion governing the vibrations of a linear, viscously damped, discrete system are generally mutually coupled. This article examines the problem, when the viscous damping is nonclassical, of how best to uncouple and solve by approximation the governing second-order differential equations of motion. It is shown that when the equations of motion are expressed in normal coordinates, the equations can then be transformed by an orthogonal coordinate transformation to a new generalized coordinate system in which a bound on the relative error introduced in the response by discarding all the coupling terms is a minimum. This approach extends the applicability of undamped modal analysis to certain types of nonclassically damped systems. The analytical results and the effectiveness of the proposed method are illustrated with four examples taken from other previously published approaches to the stated problem.

1 Introduction

The motion of a linear viscously damped discrete system is governed by a system of ordinary, second-order, linear differential equations which are generally coupled through the acceleration, velocity and displacement terms appearing in the equations. When large numbers of equations are involved, it is desirable for computational economy to transform the governing equations to an uncoupled form, or at least to a form that exhibits the smallest number of coupling terms possible, before a solution is developed. The conditions under which the governing equations can be transformed to the stated forms are well known (Newland, 1989).

The governing equations of a linear discrete system can, in principle, always be solved exactly in state space if the forcing function is deterministic. However, when large numbers of equations are involved, then those methods of solution are preferred, be they exact or approximate, which uncouple the governing equations without increasing, as required by state-space methods, the total number of original equations. Such a preferred method is the normal coordinate transformation method wherein the equations are transformed to the normal coordinates associated with the modal vectors of the undamped system. The normal coordinate transformation produces equations of motion with uncoupled acceleration and displacement terms, but the transformation generally leaves behind coupled velocity terms in the equations. One common approach to further uncoupled the normal coordinate equations of motion is to simply discard in each equation all those velocity terms that are derivatives of coordinates different from the coordinate appearing in each single acceleration term. In matrix terminology, this approach discards the off-diagonal entries in the generalized damping matrix. The error that is introduced in the approximate solution by this simplification has been widely studied and quantified for a variety of system parameters and excitations. See, for example, the works of Cronin (1976), Prater and Singh (1986), Yae and Inman (1987), Shahruz and Ma (1988), Shahruz (1990), Bellos and Inman (1990), Udwadia and Esfandiari (1990), and Hwang and Ma (1992a,b). In general, the approximation methods that discard the off-diagonal entries in the generalized damping matrix, leave the generalized mass and generalized stiffness matrices intact. In this article, a related but different approach is developed. Here, the normal coordinate equations of motion are transformed with an orthogonal coordinate transformation to a new generalized coordinate system which is so chosen that elimination of the off-diagonal entries in *both* the generalized damping and generalized stiffness matrices gives the smallest possible bound for the relative error of the approximate solution.

2 Problem Statement

Let M be the mass matrix, C be the viscous damping matrix, K be the stiffness matrix, $\mathbf{x}$ be the displacement vector, and $\mathbf{f}$ be the applied force vector of an n-degree-of-freedom discrete system. Assume that M, C, and K are all real symmetric positive definite matrices. The displacement vector $\mathbf{x}$ and force vector $\mathbf{f}$ are functions of time t. The motion of this system is governed by the equation of motion

$$M\ddot{\mathbf{x}} + C\dot{\mathbf{x}} + K\mathbf{x} = \mathbf{f}, \tag{1}$$

and the initial conditions

Contributed by the Applied Mechanics Division of THE AMERICAN SOCIETY OF MECHANICAL ENGINEERS for presentation at the First Joint ASCE-EMD, ASME-AMD, SES Meeting, Charlottesville, VA, June 6-9, 1993.
Discussion on this paper should be addressed to the Technical Editor, Professor Lewis T. Wheeler, Department of Mechanical Engineering, University of Houston, Houston, TX 77204-4792, and will be accepted until four months after final publication of the paper itself in the ASME JOURNAL OF APPLIED MECHANICS.
Manuscript received by the ASME Applied Mechanics Division, Sept. 5, 1991; final revision, June 8, 1992. Associate Technical Editor: D. J. Inman.
Paper No. 93-APM-13.

Copyright © 1993 by ASME
Downloaded 03 May 2010 to 171.66.16.245. Redistribution subject to ASME license or copyright; see http://www.asme.org/terms/Terms_Use.cfm

$$\mathbf{x}(0)=\mathbf{x}_o,\ \dot{\mathbf{x}}(0)=\dot{\mathbf{x}}_o. \tag{2}$$

We seek the response $\mathbf{x}(t)$ of this system for $t > 0$.

As indicated in Section 1, the governing equations are transformed first to normal coordinates. Hence, let the $n \times n$ matrix Φ be the undamped modal matrix orthonormalized to give $\Phi^T M\Phi = I$, where Φ^T denotes the transpose of Φ, and I is the $n \times n$ identity matrix. Substitution of the transformation $\mathbf{x} = \Phi\mathbf{q}$ in (1) and (2), and premultiplication of the resulting equation of motion by Φ^T, gives

$$\ddot{\mathbf{q}}+C^*\dot{\mathbf{q}}+K^*\mathbf{q}=\mathbf{g},\ \mathbf{q}_o=\Phi^T M\mathbf{x}_o,\ \dot{\mathbf{q}}_o=\Phi^T M\dot{\mathbf{x}}_o, \tag{3}$$

where $\mathbf{q}$ is the normal coordinate vector, $C^* = \Phi^T C\Phi$, $K^* = \Phi^T K\Phi$ and $\mathbf{g} = \Phi^T\mathbf{f}$. The matrix K^* is a diagonal matrix whose diagonal entries are the undamped natural frequencies squared.

It is well known that matrices $M^{-1}K$ and $M^{-1}C$ commute if and only if a normal coordinate transformation exists which uncouples Eq. (1) (Felszeghy, 1989a). Consequently, we will focus here mainly on the case when matrices $M^{-1}K$ and $M^{-1}C$ do not commute. In such a case, the viscous damping is said to be *nonclassical*.

As the next step towards solving (3), we will search for an $n \times n$ *orthogonal* coordinate transformation matrix P such that in the new coordinate system defined by the transformation $\mathbf{q} = P\mathbf{r}$, where $\mathbf{r}$ is a new generalized coordinate vector, the n equations of motion in $\mathbf{r}$ have negligible coupling terms. The property sought for the new equations is that when the off-diagonal entries appearing in the transformed matrix equation of motion are discarded, and the resulting uncoupled system of equations is solved, then a bound on the relative error of the approximate solution is as small as it can possibly be. In other words, we seek a new, uncoupled, approximate, transformed representation of (3), which is the best uncoupled representation possible in the sense that a bound on the relative error of the approximate solution has a minimum value. An expression for the bound on the relative error, and the sense in which the bound is minimal are yet to be developed.

3 Development of Coordinate Transformation

Substitute the transformation $\mathbf{q} = P\mathbf{r}$ in (3), and premultiply the resulting equation of motion by the transpose of P, or P^T, to obtain

$$\ddot{\mathbf{r}}+\tilde{C}\dot{\mathbf{r}}+\tilde{K}\mathbf{r}=\mathbf{p},\ \mathbf{r}_o=P^T\mathbf{q}_o,\ \dot{\mathbf{r}}_o=P^T\dot{\mathbf{q}}_o, \tag{4}$$

where $\tilde{C} = P^T C^* P$ is the generalized damping matrix, $\tilde{K} = P^T K^* P$ is the generalized stiffness matrix, and $\mathbf{p} = P^T\mathbf{g}$ is the generalized force vector. Let C_d be a diagonal matrix whose diagonal entries are identical to the diagonal entries of $\tilde{C}$, and let K_d be a diagonal matrix whose diagonal entries are identical to the diagonal entries of $\tilde{K}$. Define the uncoupled system of equations approximating (4) as

$$\ddot{\mathbf{r}}_a+C_d\dot{\mathbf{r}}_a+K_d\mathbf{r}_a=\mathbf{p},\ \mathbf{r}_{ao}=P^T\mathbf{q}_o,\ \dot{\mathbf{r}}_{ao}=P^T\dot{\mathbf{q}}_o, \tag{5}$$

where $\mathbf{r}_a$ is the approximate solution to (4) when the off-diagonal entries in both $\tilde{C}$ and $\tilde{K}$ in (4) are discarded. Let the error in vector $\mathbf{r}_a$ be the error vector $\mathbf{r}_e$,

$$\mathbf{r}_e=\mathbf{r}-\mathbf{r}_a. \tag{6}$$

Substitution of (6) for $\mathbf{r}$ in (4), and simplification gives

$$\ddot{\mathbf{r}}_e+C_d\dot{\mathbf{r}}_e+K_d\mathbf{r}_e=-C_r\dot{\mathbf{r}}-K_r\mathbf{r},\ \mathbf{r}_{eo}=\mathbf{0},\ \dot{\mathbf{r}}_{eo}=\mathbf{0}, \tag{7}$$

where $C_r = \tilde{C} - C_d$ and $K_r = \tilde{K} - K_d$ are remainder damping and stiffness matrices, respectively, whose diagonal elements are all zero.

Let $H(t)$ be the matrix impulse response of (7) when the forcing function on the right-hand side of the equation of motion is $I\delta(t)$, where $\delta(t)$ is the Dirac delta function. Since the left-hand side of the equation of motion in (7) is uncoupled, $H(t)$ is a diagonal matrix. Note also that $H(0) = 0$. The solution to (7) as a convolution integral is

$$\mathbf{r}_e(t)=\int_0^t\left[\frac{dH(t-\tau)}{d\tau}C_r-H(t-\tau)K_r\right]\mathbf{r}(\tau)d\tau+H(t)C_r\mathbf{r}_o. \tag{8}$$

The first term on the right-hand side of (8) defines an $n \times n$ matrix of linear integral operators, say A, whose kernels are defined by the $n \times n$ matrix function inside the brackets. Then,

$$\mathbf{r}_e=A\mathbf{r}+HC_r\mathbf{r}_o. \tag{9}$$

To associate with the error vector $\mathbf{r}_e$ a number which represents the error vector's size, we introduce the L_n^∞-norm of the $n \times 1$ vector function, $\mathbf{r}(t)$:

$$\|\mathbf{r}\|_\infty=\max_{1\le i\le n}\ \operatorname{ess\,sup}_{t\ge 0}\ |r_i(t)|. \tag{10}$$

Then, the induced norm of A, or $\|A\|_\infty$, is given by

$$\|A\|_\infty=\max_{1\le i\le n}\sum_{j=1}^{n}\int_0^\infty |a_{ij}(t)|\,dt, \tag{11}$$

where $a_{ij}(t)$ is given by

$$a_{ij}(t)=\left[\frac{dH(t)}{dt}C_r-H(t)K_r\right]_{ij}=\frac{dh_i(t)}{dt}c_{ij}-h_i(t)k_{ij}, \tag{12}$$

and, where $h_i(t)$ is the ith diagonal element of $H(t)$, and c_{ij} and k_{ij} are the (i, j)th elements of C_r and K_r, respectively. Note that $a_{ij}(t) = 0$ when $i = j$. From (9), and the triangle inequality, it follows that

$$\|\mathbf{r}_e\|=\|A\mathbf{r}+HC_r\mathbf{r}_o\|\le\|A\|\ \|\mathbf{r}\|+\|HC_r\mathbf{r}_o\|, \tag{13}$$

where the subscript ∞ has been left off. The extreme right-hand side of (13) defines a bound for $\|\mathbf{r}_e\|$. Clearly, this bound is dependent on the initial condition $\mathbf{r}_o$. To simplify the problem to follow, it will be assumed hereafter, without serious loss of generality, that $\mathbf{r}_o = \mathbf{0}$. Thus,

$$\mathbf{r}_e=A\mathbf{r}, \tag{14}$$

and

$$\frac{\|\mathbf{r}_e\|}{\|\mathbf{r}\|}\le\|A\|. \tag{15}$$

We now define the best uncoupled approximation to the equation of motion in (4) to be the equation that has the form in (5) and for which the bound on the relative error, $\|\mathbf{r}_e\|/\|\mathbf{r}\|$, in (15) is a minimum. To find this best approximation equation, we note first that the elements of matrices C_d, C_r, K_d and K_r appearing in (7) are all quadratic functions of the elements of P. Thus, norm $\|A\|$ is a function of the elements of P. The problem of finding the best approximation equation reduces, therefore, to finding a matrix P which minimizes $\|A\|$. This is a problem in optimization. From Eq. (11) it is seen that the value of $\|A\|$ is unchanged if P is a coordinate reflection. Hence, the search for P can be limited to proper orthogonal matrices.

The fundamental problem of finding an orthogonal matrix P which minimizes $\|A\|$ is computationally no less challenging than solving the original coupled system of equations. Therefore, for the sake of computational simplicity and economy, a relatively easy method patterned after the cyclic Jacobi method (Parlett, 1980), normally used to diagonalize to within preassigned limits of accuracy a symmetric matrix, is chosen here for constructing the P matrix. To this end, let index i take on the values of $1, \ldots, (n-1)$, and, for each i, let index j take on the values of $(i+1), \ldots, n$. We associate next with each (i, j) pair two axes defining a plane in n-space that is rotated through an angle, say θ, by a plane rotation matrix, say R. The entries along the diagonal of R are all 1's except

Downloaded 03 May 2010 to 171.66.16.245. Redistribution subject to ASME license or copyright; see http://www.asme.org/terms/Terms_Use.cfm

that $(R)_{ii} = \cos\theta$, $(R)_{ij} = -\sin\theta$, $(R)_{ji} = \sin\theta$, and $(R)_{jj} = \cos\theta$. Similar to the cyclic Jacobi method, the P matrix is developed in a sequential, step-by-step fashion, by letting (i, j) take on the values $(1, 2), (1, 3), \ldots, (n-1, n)$. At each step, the damping and stiffness matrices from the previous step are preliminarily transformed by pre and postmultiplying them by R^T and R, respectively. The norm $\|A\|$ for the current step becomes thereby a continuous function in θ. Note that if $\theta = \pi/2$, the R matrix first interchanges the ith and jth axes and then reverses the direction of the new ith axis. This transformation leaves $\|A\|$ unchanged, and hence $\|A\|$ is periodic in θ with a period of $\pi/2$. We search in the half-open interval $[-\pi/4, \pi/4)$ for the angle θ that minimizes $\|A\|$. By limiting θ to this interval, a potential reordering of the equations of motion from one step to the next is prevented. If an angle $\theta \neq 0$ minimizing $\|A\|$ has been found, the step is concluded by permanently transforming the damping and stiffness matrices with the minimizing R matrix. Otherwise, the step is concluded with the matrices unchanged. The calculations are repeated in the next step for the next (i, j) pair of values. The entire process begins, of course, with the first R matrix being applied to the original damping and stiffness matrices. Similar to the cyclic Jacobi method, the sweeps through the domains of indices i and j are repeated until the reduction in the value of $\|A\|$, from one sweep to the next, becomes insignificant, or until the value of $\|A\|$ is less than some preassigned value. At the end, the orthogonal matrix P equals the product of the sequence of all the minimizing plane rotation matrices R. The formulas for evaluating the integrals in (11) appear in Appendix A.

Application of the proposed technique to Eq. (3) is tantamount to searching for an optimal uncoupled system of equations in the neighborhood of the normal coordinate equation of motion. The above scheme for finding P does not, however, guarantee that the resulting P matrix produces a global minimum for $\|A\|$. Nevertheless, any reduction in the value of $\|A\|$, even if it represents only a local minimum and not a global minimum, is still an improvement over the common approximation method of discarding the off-diagonal entries of C^* in (3). The proposed approach has the added benefit that for nonclassically damped systems which possess a mixture of classical and nonclassical natural modes of free vibration, some equations in (3) can be uncoupled at the very start (Felszeghy, 1989a, 1989b, 1991, 1992). These uncoupled equations can then be removed from further consideration, and, consequently, it will be assumed hereafter that the n equations in (3) represent a reduced set of equations that are all coupled through C^*. Thus, the positive definite property assumed for C and K is actually needed only for C^* and K^* in order to guarantee the existence of the integrals in (11).

4 Bounds on Norms of Errors

Once the best uncoupled approximation to the equation of motion in (4) has been found, the bounds on the norms of the individual elements of error vector $\mathbf{r}_e$ can be determined. We introduce the L^∞-norm of the scalar function, $r_i(t)$; then

$$\|r_i\|_\infty = \operatorname*{ess\,sup}_{t\geq 0} |r_i(t)|. \tag{16}$$

From applying (16) to the elements of (14), we get

$$\begin{Bmatrix} \|r_{e1}\| \\ \cdots \\ \|r_{en}\| \end{Bmatrix} \leq \begin{bmatrix} 0 & \cdots & \int_0^\infty |a_{1n}(t)|\,dt \\ \cdots & & \cdots \\ \int_0^\infty |a_{n1}(t)|\,dt & \cdots & 0 \end{bmatrix} \begin{Bmatrix} \|r_1\| \\ \cdots \\ \|r_n\| \end{Bmatrix}, \tag{17}$$

or

$$\begin{Bmatrix} \|r_{e1}\| \\ \cdots \\ \|r_{en}\| \end{Bmatrix} \leq D \begin{Bmatrix} \|r_1\| \\ \cdots \\ \|r_n\| \end{Bmatrix}, \tag{18}$$

where the subscript ∞ has been left off, and where D on the right-hand side of (18) is the $n \times n$ non-negative matrix of induced norms of the $n \times n$ matrix of linear integral operators defined by the error integral operator A.

If $\|A\| < 1$, then application of the triangle inequality to $\mathbf{r} = \mathbf{r}_a + \mathbf{r}_e$, and substitution of (15) for $\|\mathbf{r}\|$ gives

$$\|\mathbf{r}_e\| \leq [\|A\|/(1-\|A\|)]\|\mathbf{r}_a\|. \tag{19}$$

The right-hand side of (19) is the bound on the norm of the error vector expressed in terms of the norm of the approximate solution. Correspondingly, from (18) and the triangle inequality, we get the bounds on the norms of the individual elements of $\mathbf{r}_e$:

$$\begin{Bmatrix} \|r_{e1}\| \\ \cdots \\ \|r_{en}\| \end{Bmatrix} \leq (I-D)^{-1} D \begin{Bmatrix} \|r_{a1}\| \\ \cdots \\ \|r_{an}\| \end{Bmatrix}. \tag{20}$$

Note that the coefficient of $\|\mathbf{r}_a\|$ in (19) and the coefficient matrix of $[\|r_{a1}\| \ \ldots \ \|r_{an}\|]^T$ in (20) are independent of the excitation.

In terms of the normal coordinate vector $\mathbf{q}$, the approximation solution is given by $\mathbf{q}_a = \mathbf{P}\mathbf{r}_a$, and the error vector is given by $\mathbf{q}_e = \mathbf{q} - \mathbf{q}_a$. The bounds on the norms of the errors are

$$\|\mathbf{q}_e\| \leq \|P\|\ \|\mathbf{r}_e\|, \tag{21}$$

and

$$\begin{Bmatrix} \|q_{e1}\| \\ \cdots \\ \|q_{en}\| \end{Bmatrix} \leq \begin{bmatrix} |p_{11}| & \cdots & |p_{1n}| \\ \cdots & & \cdots \\ |p_{n1}| & \cdots & |p_{nn}| \end{bmatrix} \begin{Bmatrix} \|r_{e1}\| \\ \cdots \\ \|r_{en}\| \end{Bmatrix}, \tag{22}$$

where $\|P\| = \|P\|_\infty$, and the p_{ij} are the elements of P.

In terms of the physical coordinate vector $\mathbf{x}$, the approximate solution is given by $\mathbf{x}_a = \Phi\mathbf{q}_a$, and the error vector is given by $\mathbf{x}_e = \mathbf{x} - \mathbf{x}_a$. The bounds on the norms of the errors are

$$\|\mathbf{x}_e\| \leq \|\Phi\|\ \|\mathbf{q}_e\|, \tag{23}$$

and

$$\begin{Bmatrix} \|x_{e1}\| \\ \cdots \\ \|x_{en}\| \end{Bmatrix} \leq \begin{bmatrix} |\phi_{11}| & \cdots & |\phi_{1n}| \\ \cdots & & \cdots \\ |\phi_{n1}| & \cdots & |\phi_{nn}| \end{bmatrix} \begin{Bmatrix} \|q_{e1}\| \\ \cdots \\ \|q_{en}\| \end{Bmatrix}, \tag{24}$$

where $\|\Phi\| = \|\Phi\|_\infty$, and the ϕ_{ij} are the elements of Φ.

5 Examples

As stated in Section 1, the errors that are introduced by discarding the off-diagonal entries in the generalized damping matrix of the normal coordinate matrix equation of motion have been studied before. Therefore, to illustrate the effectiveness of the technique developed here, four problems that appeared in the literature before will be discussed.

Example 1. The following problem is taken from the works of Shahruz and Ma (1988) and Hwang and Ma (1992a). A two-degree-of-freedom system subject to a sinusoidal forcing function is governed by the normal coordinate equations:

$$\begin{Bmatrix} \ddot{q}_1 \\ \ddot{q}_2 \end{Bmatrix} + \begin{bmatrix} 1.559 & -0.2 \\ -0.2 & 1.6 \end{bmatrix} \begin{Bmatrix} \dot{q}_1 \\ \dot{q}_2 \end{Bmatrix} + \begin{bmatrix} 3.8 & 0 \\ 0 & 4 \end{bmatrix} \begin{Bmatrix} q_1 \\ q_2 \end{Bmatrix} = \begin{Bmatrix} 1 \\ 1 \end{Bmatrix} \sin 2t, \tag{25}$$

Downloaded 03 May 2010 to 171.66.16.245. Redistribution subject to ASME license or copyright; see http://www.asme.org/terms/Terms_Use.cfm

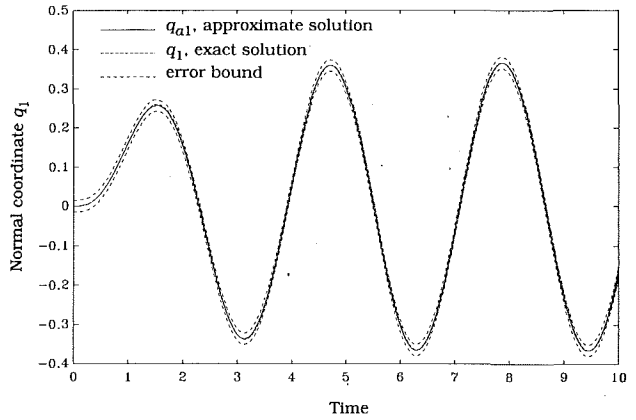


Fig. 1 Solutions for normal coordinate q_1 from Example 1

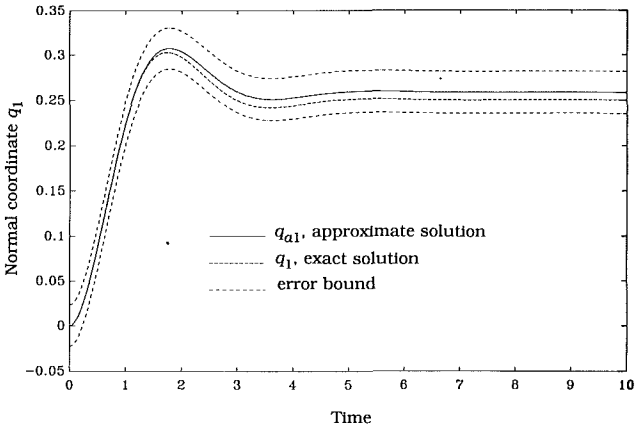


Fig. 2 Solutions for normal coordinate q_1 from Example 2

$$q_{1o}=q_{2o}=0, \quad \dot{q}_{1o}=\dot{q}_{2o}=0. \tag{26}$$

Both Shahruz and Ma (1988) and Hwang and Ma (1992a) computed bounds on $\|\mathbf{q}_e\|$ when the off-diagonal elements $(C^*)_{12} = (C^*)_{21} = -0.2$ above are discarded. The bound of Shahruz and Ma (1988) is expressed in the form of a coefficient multiplying $\|\mathbf{q}_a\|$ similar to Eq. (19) except that $\mathbf{q}$ replaces $\mathbf{r}$ and $\|A\|$ is computed with the assumption that $P = I$, where I is the 2×2 identity matrix. The coefficient is necessarily independent of the excitation. The bound is $\|\mathbf{q}_e\| \leq 0.199\ \|\mathbf{q}_a\| = 0.0637$. The bound of Hwang and Ma (1992a) in turn is based on an exact Laplace transformed expression for $\mathbf{q}_e$ incorporating the excitation, and it is tighter than the bound of Shahruz and Ma (1988). The bound is $\|\mathbf{q}_e\| \leq 0.046$. For reference purposes, these two types of bounds will be referred to hereafter as type 1 and type 2 bounds, respectively.

We now solve the above problem using the technique developed in this article. The orthogonal transformation

$$P=\begin{bmatrix} 0.7436 & -0.6686 \\ 0.6686 & 0.7436 \end{bmatrix} \tag{27}$$

obtained after performing two cyclic sweeps produces a global minimum value of $\|A\|$ of 0.0485. The sweeps consumed 100 seconds of computer time when executed on an IBM PS/2 Model 70 386 computer using the PC-MATLAB software package (Moler et al., 1987). The corresponding governing equations in $\mathbf{r}$ are

$$\begin{Bmatrix} \ddot{r}_1 \\ \ddot{r}_2 \end{Bmatrix} + \begin{bmatrix} 1.3785 & -0.0008 \\ -0.0008 & 1.7805 \end{bmatrix} \begin{Bmatrix} \dot{r}_1 \\ \dot{r}_2 \end{Bmatrix} + \begin{bmatrix} 3.8894 & 0.0994 \\ 0.0994 & 3.9106 \end{bmatrix} \begin{Bmatrix} r_1 \\ r_2 \end{Bmatrix} = \begin{Bmatrix} 1.4122 \\ 0.0749 \end{Bmatrix} \sin 2t, \tag{28}$$

$$r_{1o}=r_{2o}=0, \quad \dot{r}_{1o}=\dot{r}_{2o}=0. \tag{29}$$

After discarding all the off-diagonal entries in (28) and solving for $\mathbf{r}_a$, we obtain

$$r_{a1}=1.4122\ G(t,\ 1.9722,\ 0.3495,\ 2),$$
$$r_{a2}=0.0749\ G(t,\ 1.9775,\ 0.4502,\ 2), \tag{30}$$

where the function $G(t, \omega_n, \zeta, \omega)$ and its arguments are defined in Appendix B. Substitution of (30) in $\mathbf{q}_a = P\mathbf{r}_a$ gives the results for q_{a1} shown in Fig. 1. The norm of approximate response $\mathbf{r}_a$ is $\|\mathbf{r}_a\| = 0.5120$. From (19) and (21), the bound on the norm of the error vector $\mathbf{q}_e$ is $\|\mathbf{q}_e\| \leq 0.0369$. This error bound is 42 percent smaller than the type 1 bound of Shahruz and Ma (1988), and 20 percent smaller than the type 2 bound of Hwang and Ma (1992a).

The norms of the individual approximate response elements are: $\|r_{a1}\| = 0.5120$, $\|r_{a2}\| = 0.0211$. The matrix D is

$$D=\begin{bmatrix} 0 & 0.0485 \\ 0.0386 & 0 \end{bmatrix}. \tag{31}$$

From (20) and (22), $\|q_{e1}\| \leq 0.0147$ and $\|q_{e2}\| \leq 0.0161$. The bound for $\|q_{e1}\|$ is interpreted and plotted in Fig. 1 as a band that encloses the approximate solution q_{a1} and the exact solution q_1. Comparison of these results with those plotted by Hwang and Ma (1992a) shows that the new band is at least 68 percent narrower.

Example 2. The following problem is taken from Shahruz (1990). A three-degree-of-freedom system with a step forcing function is governed by the normal coordinate equations

$$\begin{Bmatrix} \ddot{q}_1 \\ \ddot{q}_2 \\ \ddot{q}_3 \end{Bmatrix} + \begin{bmatrix} 2 & -0.15 & -0.15 \\ -0.15 & 4.2 & -0.2 \\ -0.15 & -0.2 & 6.6 \end{bmatrix} \begin{Bmatrix} \dot{q}_1 \\ \dot{q}_2 \\ \dot{q}_3 \end{Bmatrix} + \begin{bmatrix} 4.0 & 0 & 0 \\ 0 & 4.41 & 0 \\ 0 & 0 & 9 \end{bmatrix} \begin{Bmatrix} q_1 \\ q_2 \\ q_3 \end{Bmatrix} = \begin{Bmatrix} 1 \\ 1.2 \\ 2.5 \end{Bmatrix} u(t), \tag{32}$$

$$q_{1o}=q_{2o}=q_{3o}=0, \quad \dot{q}_{1o}=\dot{q}_{2o}=\dot{q}_{3o}=0, \tag{33}$$

where $u(t)$ is a unit step function. Shahruz (1990) computed the type 1 bound to be $\|\mathbf{q}_e\| \leq 0.07$.

Solution of the above problem by the technique presented here gives, after two cyclic sweeps consuming 570 seconds of computer time, the local minimum value of $\|A\|$ of 0.0726 when the orthogonal transformation P is

$$P=\begin{bmatrix} 0.997424 & -0.068796 & -0.020318 \\ -0.068781 & 0.997631 & -0.001405 \\ 0.020367 & 0.000004 & 0.999793 \end{bmatrix}. \tag{34}$$

The governing equations in $\mathbf{r}$ and their approximate solutions are omitted, and only the norms of the approximate responses will be given: $\|\mathbf{r}_a\| = 0.3294$; $\|r_{a1}\| = 0.3294$, $\|r_{a2}\| = 0.2560$, $\|r_{a3}\| = 0.2753$. These results give the following bounds on the norms of the errors: $\|\mathbf{q}_e\| \leq 0.0280$; $\|q_{e1}\| \leq 0.0231$, $\|q_{e2}\| \leq 0.0232$, $\|q_{e3}\| \leq 0.0206$.

The bound on the norm of q_{e1} is plotted in Fig. 2 as a band that encloses the approximate solution q_{a1} and the exact solution q_1. Comparison of these results with those plotted by Shahruz (1990) shows that the new band is 67 percent narrower.

Example 3. The following problem is taken from Hwang and Ma (1992b). A three-degree-of-freedom system subject to a sinusoidal forcing function is governed by the normal coordinate equations:

Downloaded 03 May 2010 to 171.66.16.245. Redistribution subject to ASME license or copyright; see http://www.asme.org/terms/Terms_Use.cfm

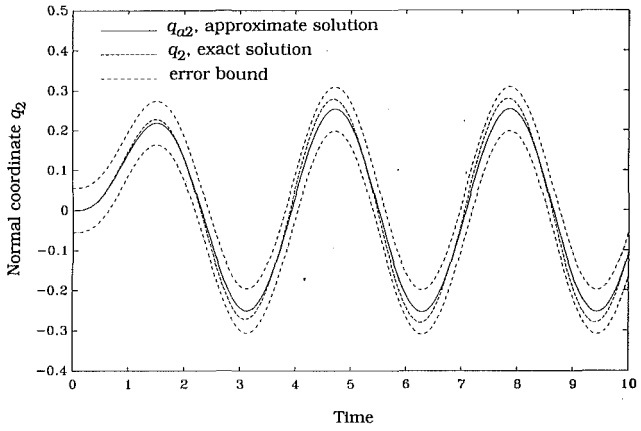


Fig. 3 Solutions for normal coordinate q_2 from Example 3

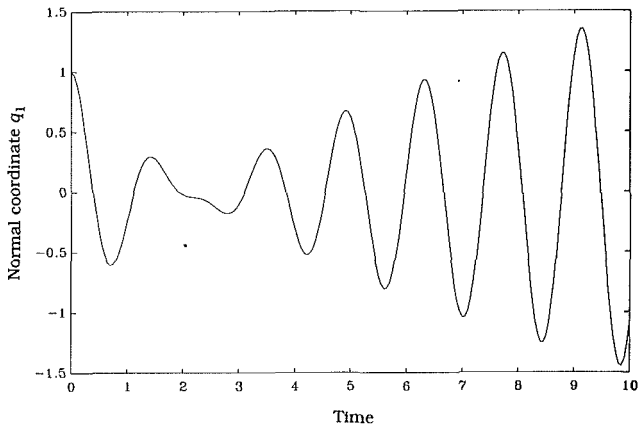


Fig. 4 Exact solution for normal coordinate q_1 from Example 4

$$\begin{Bmatrix} \ddot{q}_1 \\ \ddot{q}_2 \\ \ddot{q}_3 \end{Bmatrix} + \begin{bmatrix} 2.04 & -0.2 & -0.19 \\ -0.2 & 2.2 & -0.3 \\ -0.19 & -0.3 & 2.8 \end{bmatrix} \begin{Bmatrix} \dot{q}_1 \\ \dot{q}_2 \\ \dot{q}_3 \end{Bmatrix} + \begin{bmatrix} 3.8 & 0 & 0 \\ 0 & 4.0 & 0 \\ 0 & 0 & 6.5 \end{bmatrix} \begin{Bmatrix} q_1 \\ q_2 \\ q_3 \end{Bmatrix} = \begin{Bmatrix} 1 \\ 1 \\ 1 \end{Bmatrix} \sin 2t, \quad (35)$$

$$q_{1o} = q_{2o} = q_{3o} = 0, \quad \dot{q}_{1o} = \dot{q}_{2o} = \dot{q}_{3o} = 0 \quad (36)$$

Hwang and Ma (1992b) computed the type 1 bound to be $\|\mathbf{q}_e\| \leq 0.1042$. In the same article, Hwang and Ma developed another bound which is excitation dependent, but is limited to a periodic forcing function. This bound is tighter than the type 1 bound and is easier to compute. For the above problem, this second bound is $\|\mathbf{q}_e\| \leq 0.072$.

Solution of the above problem by the technique presented here gives, after two cyclic sweeps consuming 626 seconds of computer time, the local minimum value of $\|A\|$ of 0.227 when the orthogonal transformation P is:

$$P = \begin{bmatrix} 0.8437 & -0.5163 & -0.1471 \\ 0.5266 & 0.8492 & 0.0398 \\ 0.1044 & -0.1110 & 0.9883 \end{bmatrix}. \quad (37)$$

The governing equations in $\mathbf{r}$ and their approximate solutions are omitted, and only the norms of the approximate responses will be given: $\|\mathbf{r}_a\| = 0.3973$; $\|r_{a1}\| = 0.3973$, $\|r_{a2}\| = 0.0472$, $\|r_{a3}\| = 0.1438$. These results give the following bounds on the norms of the errors: $\|\mathbf{q}_e\| \leq 0.176$; $\|q_{e1}\| \leq 0.0647$, $\|q_{e2}\| \leq 0.0551$, $\|q_{e3}\| \leq 0.0724$.

The bound on the norm of q_{e2} is plotted in Fig. 3 as a band that encloses the approximate solution q_{a2} and the exact solution q_2. Comparison of these results with those plotted by Hwang and Ma (1992b) shows that the new band is 23 percent narrower.

Example 4. The following example is taken from the work of Udwadia and Esfandiari (1990). A three-degree-of-freedom system subject to a sinusoidal forcing function is governed by the normal coordinate equations:

$$\begin{Bmatrix} \ddot{q}_1 \\ \ddot{q}_2 \\ \ddot{q}_3 \end{Bmatrix} + \begin{bmatrix} 0.4 & 0.3 & 0.1 \\ 0.3 & 0.6 & 0.34 \\ 0.1 & 0.34 & 0.5 \end{bmatrix} \begin{Bmatrix} \dot{q}_1 \\ \dot{q}_2 \\ \dot{q}_3 \end{Bmatrix} + \begin{bmatrix} 20 & 0 & 0 \\ 0 & 20 & 0 \\ 0 & 0 & 20 \end{bmatrix} \begin{Bmatrix} q_1 \\ q_2 \\ q_3 \end{Bmatrix} = \begin{Bmatrix} 2 \\ -2 \\ 2 \end{Bmatrix} \sin\sqrt{(20)}t, \quad (38)$$

$$q_{1o} = q_{2o} = q_{3o} = 1, \quad \dot{q}_{1o} = \dot{q}_{2o} = \dot{q}_{3o} = 0. \quad (39)$$

For this problem, it is clear that $C^*K^* = K^*C^*$. Hence, the damping is classical, and there exists a matrix P that totally uncouples the equations of motion. The matrix P can be found as described by Felszeghy (1989a). Accordingly, we first solve the unsprung eigenvalue problem

$$C^*\mathbf{b} = \gamma\mathbf{b}, \quad (40)$$

where $\mathbf{b}$ is an $n \times 1$ amplitude vector, and γ is a parameter. This gives the eigenvalues $\gamma_1 = 1.0327$, $\gamma_2 = 0.3468$, $\gamma_3 = 0.1205$. The corresponding normalized unsprung modal matrix is the desired P matrix:

$$P = \begin{bmatrix} 0.4285 & 0.7035 & -0.5670 \\ 0.7230 & 0.1094 & 0.6821 \\ 0.5419 & -0.7022 & -0.4617 \end{bmatrix}. \quad (41)$$

The resulting governing equations in $\mathbf{r}$ are:

$$\ddot{r}_1 + 1.0327\ \dot{r}_1 + 20\ r_1 = -3.4217 \sin\sqrt{(20)}t,$$
$$\ddot{r}_2 + 0.3468\ \dot{r}_2 + 20\ r_2 = -0.2162 \sin\sqrt{(20)}t,$$
$$\ddot{r}_3 + 0.1205\ \dot{r}_3 + 20\ r_3 = 0.4949 \sin\sqrt{(20)}t, \quad (42)$$
$$r_{1o} = 1.6934,\ r_{2o} = 0.1107,\ r_{3o} = -0.3466,$$
$$\dot{r}_{1o} = \dot{r}_{2o} = \dot{r}_{3o} = 0. \quad (43)$$

The formulas for the exact solutions to (42) are omitted. Instead, the exact solution for normal coordinate q_1 is plotted in Fig. 4. Notice the initial decaying free vibrations and the subsequent build up of forced vibrations.

Udwadia and Esfandiari (1990) offered the above problem as an example of a coupled system of equations of motion requiring numerical integration in time for its solution. The solution technique presented here makes apparent the possibility of obtaining an exact closed form solution. Comparison of the plot in Fig. 4 with a similar plot by Udwadia and Esfandiari (1990) shows that the exact results in Fig. 4 agree with the numerically integrated results.

6 Conclusions

A method has been presented for obtaining approximate solutions from uncoupled second-order differential equations of motion for vibrating discrete systems when the viscous damping is nonclassical. The method in effect searches for another coordinate system in the neighborhood of the normal coordinate system so that in the new coordinate system removal of the coupling terms in the equations of motion produces a minimum bound on the relative error introduced in the ap-

Downloaded 03 May 2010 to 171.66.16.245. Redistribution subject to ASME license or copyright; see http://www.asme.org/terms/Terms_Use.cfm

proximate solution. Formulas were derived which give the bounds on the norms of the errors. The error bounds were expressed as coefficients independent of the excitation multiplying the norms of the approximate solutions. The advantage of having available errors bounds independent of the excitation is that once the computational investment of finding the best uncoupled approximation equations has been made, the equations can then be solved repeatedly for a variety of excitations without further modifications, and without any changes to the error bound formulas. The formulas for the error bounds are applicable as long as the norm of the error integral operator is less than one. The proposed method extends the applicability of undamped modal analysis to those systems with nonclassical damping for which the approximations presented here produce error bounds of a size acceptable to the analyst. The effectiveness of the method was demonstrated by the examples. In the first three examples, the error bounds on the norms of the errors obtained by the proposed method were smaller, sometimes significantly smaller, than those obtained previously by other approaches. In the last example, an error-free exact solution was found.

Acknowledgments

The author wishes to thank former CSULA graduate student, Mr. Min-Chan Hwang, for working out some preliminary details of the analysis presented here. The author also wishes to thank CSULA for awarding him a creative leave for one academic quarter which permitted him in part to write this article. Finally, the author wishes to thank the reviewers for their helpful comments.

References

Bellos, J., and Inman, D. J., 1990, "Frequency Response of Nonproportionally Damped, Lumped Parameter, Linear Dynamic Systems," ASME *Journal of Vibration, Acoustics, Stress, and Reliability in Design*, Vol. 112, No. 2, pp. 194–201.

Cronin, D. L., 1976, "Approximation for Determining Harmonically Excited Response of Nonclassically Damped Systems," ASME *Journal of Engineering and Industry*, Vol. 98, No. 1, pp. 43–47.

Felszeghy, S. F., 1989a, "The Development of Natural Modes of Free Vibration for Linear Discrete Systems from the Synchronous Motion Assumption," ASME *Journal of Vibration, Acoustics, Stress, and Reliability in Design*, Vol. 111, No. 1, pp. 77–81.

Felszeghy, S. F., 1989b, Discussion on "Approximate Decoupling of the Equations of Motion of Linear Underdamped Systems," ASME JOURNAL OF APPLIED MECHANICS, Vol. 56, No. 3, p. 731.

Felszeghy, S. F., 1991, Errata on "The Development of Natural Modes of Free Vibration for Linear Discrete Systems from the Synchronous Motion Assumption," ASME *Journal of Vibration, Acoustics, Stress, and Reliability in Design*, Vol. 113, No. 4, p. 468.

Felszeghy, S. F., 1992, "Development of Biorthonormal Eigenvectors for Modal Analysis of Linear Nonclassically Damped Systems," *Journal of Sound and Vibration*, in press.

Hwang, J. H., and Ma, F., 1992a, "On the Approximate Solution of Nonclassically Damped Linear Systems," ASME JOURNAL OF APPLIED MECHANICS, in press.

Hwang, J. H., and Ma, F., 1992b, "On the Approximate Solution of Nonproportionality Damped Linear Systems," ASME JOURNAL OF APPLIED MECHANICS, under revision for publication.

Moler, C., Little, J., and Bangert, S., 1987, *PC-MATLAB User's Guide*, The MathWorks, Inc., South Natick, MA.

Newland, D. E., 1989, *Mechanical Vibration Analysis and Computation*, Longman Scientific and Technical, Essex, U.K.

Parlett, B. N., 1980, *The Symmetric Eigenvalue Problem*, Prentice-Hall, Englewood Cliffs, New Jersey.

Prater, G., Jr., and Singh, R., 1986, "Quantification of the Extent of Non-Proportional Viscous Damping in Discrete Vibratory Systems," *Journal of Sound and Vibration*, Vol. 104, No. 1, pp. 109–125.

Shahruz, S. M., 1990, "Approximate Decoupling of the Equations of Motion of Damped Linear Systems," *Journal of Sound and Vibration*, Vol. 136, No. 1, pp. 51–64.

Shahruz, S. M., and Ma, F., 1988, "Approximate Decoupling of the Equations of Motion of Linear Underdamped Systems," ASME JOURNAL OF APPLIED MECHANICS, Vol. 55, No. 3, pp. 716–720.

Udwadia, F. E., and Esfandiari, R. S., 1990, "Nonclassically Damped Dynamic Systems: An Iterative Approach," ASME JOURNAL OF APPLIED MECHANICS, Vol. 57, No. 2, pp. 423–433.

Yae, K. H., and Inman, D. J., 1987, "Response Bounds for Linear Underdamped Systems," ASME JOURNAL OF APPLIED MECHANICS, Vol. 54, No. 2, pp. 419–423.

APPENDIX A

The impulse response $h_i(t)$ appearing in (12) is the solution to

$$\ddot{h}_i + (C_d)_{ii}\dot{h}_i + (K_d)_{ii}h_i = 0, \quad h_{io} = 0, \quad \dot{h}_{io} = 1. \tag{A1}$$

Let $\Omega_i = \sqrt{(K_d)_{ii}}$ and $\zeta_i = 0.5\,(C_d)_{ii}/\Omega_i$, where Ω_i is an apparent natural frequency and ζ_i is an apparent damping ratio. We will evaluate the integral $\int_0^\infty |a_{ij}(t)|dt$ in (11) for (*a*) the underdamped case: $0 < \zeta_i < 1$, (*b*) the critically damped case: $\zeta_i = 1$, and (*c*) the overdamped case: $\zeta_i > 1$.

Case (*a*): $0 < \zeta_i < 1$.
In this case,

$$a_{ij}(t) = -\alpha e^{-\zeta_i\Omega_i t}\sin(\Omega_{di}t + \phi), \tag{A2}$$

where $\alpha = \sqrt{\{[(k_{ij} - \zeta_i\Omega_i c_{ij})/\Omega_{di}]^2 + c_{ij}^2\}}$, $\Omega_{di} = \Omega_i/(1-\zeta_i^2)$, $\phi = \tan^{-1}\{c_{ij}/[(k_{ij} - \zeta_i\Omega_i c_{ij})/\Omega_{di}]\}$, $0 \le \phi < 2\pi$, and the quadrant of ϕ is determined by the signs of the numerator and denominator of the argument of $\tan^{-1}$. Let time t_o be the time when $a_{ij}(t)$ crosses the t-axis for the first time after $t = 0$. Then, $t_o = 0$ when $\phi = 0$, $t_o = (\pi - \phi)/\Omega_{di}$ when $0 < \phi \le \pi$, and $t_o = (2\pi - \phi)/\Omega_{di}$ when $\pi < \phi < 2\pi$. Let $\rho = -\zeta_i\pi/\sqrt{(1-\zeta_i^2)}$ and $\epsilon = e^{-\zeta_i\Omega_i t_o}$; then

$$\int_0^\infty |a_{ij}(t)|dt = \alpha\epsilon(1+e^\rho)\sqrt{(1-\zeta_i^2)}/[\Omega_i(1-e^\rho)] + \alpha|F(t_o, \zeta_i, \Omega_i, \Omega_{di}, \phi) - F(0, \zeta_i, \Omega_i, \Omega_{di}, \phi)|, \tag{A3}$$

where

$$F(t, \zeta_i, \Omega_i, \Omega_{di}, \phi) = \zeta_i e^{-\zeta_i\Omega_i t}[\sin(\Omega_{di}t + \phi) + \Omega_{di}\cos(\Omega_{di}t + \phi)/\zeta_i\Omega_i]/\Omega_i. \tag{A4}$$

Case (*b*): $\zeta_i = 1$.
In this case,

$$a_{ij}(t) = -(c_{ij}s_o + k_{ij})te^{s_o t} - c_{ij}e^{s_o t}, \tag{A5}$$

where $s_o = -\Omega_i$. Let time t_o be the time when $a_{ij}(t)$ crosses the t-axis. Then, $t_o = -c_{ij}/(c_{ij}s_o + k_{ij})$. If $t_o \le 0$, then

$$\int_0^\infty |a_{ij}(t)|dt = |(c_{ij}s_o + k_{ij})/s_o^2 - c_{ij}/s_o|. \tag{A6}$$

If $t_o > 0$, then

$$\int_0^\infty |a_{ij}(t)|dt = |(c_{ij}s_o + k_{ij})(t_o - 1/s_o)e^{s_o t_o}/s_o + c_{ij}e^{s_o t_o}/s_o + (c_{ij}s_o + k_{ij})/s_o^2 - c_{ij}/s_o| + |(c_{ij}s_o + k_{ij})(t_o - 1/s_o)e^{s_o t_o}/s_o + c_{ij}e^{s_o t_o}/s_o|. \tag{A7}$$

Case (*c*): $\zeta_i > 1$.
In this case,

$$a_{ij}(t) = -[e^{s_1 t}(s_1c_{ij} + k_{ij}) - e^{s_2 t}(s_2c_{ij} + k_{ij})]/(s_1 - s_2), \tag{A8}$$

where $s_1 = -\zeta_i\Omega_i + \Omega_i\sqrt{(\zeta_i^2 - 1)}$ and $s_2 = -\zeta_i\Omega_i - \Omega_i\sqrt{(\zeta_i^2 - 1)}$. Let $d = (s_2c_{ij} + k_{ij})/(s_1c_{ij} + k_{ij})$. If $d > 0$, then the time t_o when $a_{ij}(t)$ crosses the t-axis is $t_o = \ln(d)/(s_1 - s_2)$. If $d \le 0$, or if $d > 0$ and $t_o \le 0$, then

Downloaded 03 May 2010 to 171.66.16.245. Redistribution subject to ASME license or copyright; see http://www.asme.org/terms/Terms_Use.cfm

$$\int_0^\infty |a_{ij}(t)|\,dt = |-(s_1c_{ij}+k_{ij})/s_1 + (s_2c_{ij}+k_{ij})/s_2|/(s_1-s_2). \quad \text{(A9)}$$

If $d > 0$ and $t_o > 0$, then

$$\int_0^\infty |a_{ij}(t)|\,dt = |(s_1c_{ij}+k_{ij})(e^{s_1t_o}-1)/s_1 - (s_2c_{ij}+k_{ij})(e^{s_2t_o}-1)/s_2|/(s_1-s_2) + |(s_1c_{ij}+k_{ij})e^{s_1t_o}/s_1 - (s_2c_{ij}+k_{ij})e^{s_2t_o}/s_2|/(s_1-s_2). \quad \text{(A10)}$$

APPENDIX B

The solution to

$$\ddot{y}+2\zeta\omega_n\dot{y}+\omega_n^2y=\sin\omega t, \quad y(0)=\dot{y}(0)=0, \quad \text{(B1)}$$

is

$$y(t) = \frac{1}{[(\omega_n^2-\omega^2)^2+4\zeta^2\omega_n^2\omega^2]}[(\omega/\omega_d)(2\zeta^2\omega_n^2-\omega_n^2+\omega^2)e^{-\zeta\omega_nt}\sin\omega_dt + 2\zeta\omega_n\omega(e^{-\zeta\omega_nt}\cos\omega_dt-\cos\omega t)+(\omega_n^2-\omega^2)\sin\omega t] \quad \text{(B2)}$$

where $\omega_d = \omega_n\sqrt{(1-\zeta^2)}$, and $0 < \zeta < 1$. Finally, we let $G(t, \omega_n, \zeta, \omega) = y(t)$.

Downloaded 03 May 2010 to 171.66.16.245. Redistribution subject to ASME license or copyright; see http://www.asme.org/terms/Terms_Use.cfm

Thickness Expansions for Higher-Order Effects in Vibrating Cylindrical Shells

J. G. McDaniel
Scientist,
BBN Systems and Technology,
Cambridge, MA 02138
Mem. ASME

J. H. Ginsberg
George W. Woodruff Chair,
Fellow ASME

School of Mechanical Engineering,
Georgia Institute of Technology,
Atlanta, GA 30332

In the spirit of Mindlin and others who have used series expansions to express transverse dependences in thin bodies, the present work uses Ritz expansions in a variational formulation for cylindrical shell vibrations. By expanding displacements in spatial coordinates, integral expressions for strain and kinetic energy are converted to quadratic sums involving time-dependent generalized coordinates. Hamilton's principle provides ordinary differential equations for these coordinates. This viewpoint yields physical insight into the mechanisms of energy storage and avoids the geometrically thin assumption inherent to many formulations. A set of Legendre polynomials multiplied by a radial factor represent the radial dependences of displacement components, while circumferential variations are represented by sinusoidal functions. Excellent agreement in natural frequencies is found between this approach and analytical solutions over the entire range of shell thicknesses, including the limiting case of a solid cylinder. Comparisons to several thin shell theories are given, leading to conclusions about the range of validity of these theories.

1 Historical Introduction

Many researchers have applied an idea originating in the works of Poisson and Cauchy to the static and dynamic analysis of bars, plates, and shells. This idea involves expanding various elastic variables relative to a reference surface or line, followed by integration over the thin dimension. Approaches differ depending on which variables are expanded, the method of integrating elasticity equations, and the types of basis functions used in the expansions.

Perhaps the first to use the idea for shells after its introduction by Poisson and Cauchy was Basset (1890). Shortly after Love's landmark paper on shell vibrations (1888), Basset expanded stresses about the midsurface in Taylor series. These expansions were used to derive equations of motion through the virtual work method of Kirchhoff. Basset used the results to discuss the effect of thickness on the natural frequencies of cylindrical and spherical shells. As a referee of the Royal Society, Lord Kelvin noted the importance of Basset's work by referring to it as ". . . one of the most important contributions to one of the most difficult subjects in dynamics." (Calladine, 1988).

The idea saw widespread application in the 1950's, largely through the efforts of Mindlin. To analyze vibrations of elastic plates Mindlin (1955) expanded displacements in power series, and then used Kirchhoff's method to deduce the approximate differential equations of motion in the remaining dimensions. From these, he derived dispersion relations for wave propagation in the remaining dimensions. On a suggestion from Prager, Mindlin (1959) later used Legendre polynomials for displacement expansions in extensional vibrations of elastic plates, which had the effect of uncoupling to some degree the resulting differential equations. Mindlin also applied the idea to axially symmetric wave propagation in circular rods (1960) by using Jacobi polynomials, and to St. Venant's problem of torsion in bars (1975) by using power series. Legendre polynomial expansions also appeared in Cicalo's controlled approximations for static analysis of shells (1961) as expansion functions for all elastic variables.

Vlasov (1957) applied the idea to the static analysis of thick plates and shells by using Taylor series expansions of stresses and displacements in the static elasticity equations. His formalism, referred to in the literature as the "method of initial functions," was applied to the static analysis of thick cylindrical shells by Iyengar et al. (1975) and Faraji and Archer (1985). Later, Faraji and Archer (1988) presented a variational derivation to produce the differential equations and boundary conditions, again for the static case. For finite cylindrical shells, Fellers (1968), and Fellers and Soler (1970) used a set of related Legendre polynomials for displacements and Legendre polynomials for stresses. These expansions were used directly in the static elasticity equations. Additionally, Soler (1969) presented a new beam theory using the approach just described. The Ritz expansion method was recently used for the free vibrations of anisotropic elastic cylinders and spheres by Hey-

Contributed by the Applied Mechanics Division of THE AMERICAN SOCIETY OF MECHANICAL ENGINEERS for presentation at the First Joint ASCE-EMD, ASME-AMD, SES Meeting, Charlottesville, VA, June 6-9, 1993.

Discussion on this paper should be addressed to the Technical Editor, Professor Lewis T. Wheeler, Department of Mechanical Engineering, University of Houston, Houston, TX 77204-4792, and will be accepted until four months after final publication of the paper itself in the ASME JOURNAL OF APPLIED MECHANICS.

Manuscript received by the ASME Applied Mechanics Division, Mar. 17, 1992; final revision, July 28, 1992. Associate Technical Editor: F. Y. M. Wan.

Paper No. 93-APM-22.

Copyright © 1993 by ASME
Downloaded 03 May 2010 to 171.66.16.245. Redistribution subject to ASME license or copyright; see http://www.asme.org/terms/Terms_Use.cfm

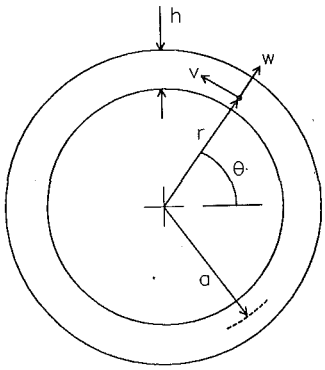


Fig. 1 Definition of geometric parameters and displacements for an infinite cylindrical shell in plane strain

liger and Jilani (1991). For the cylinder, powers of the radial coordinate were used as expansion functions in conjunction with Fourier series expansions about the circumference.

The above list is incomplete, but it suggests that researchers have historically sought simplified differential equations through the adoption of various series expansions. Relatively few researchers have used displacement-based approximations, preferring instead to expand stresses and strains in the elasticity equations. However, expansions of displacements provide a physically clear picture of the approximations introduced by series truncations. Much physical insight is gained by viewing displacement expansions as basis functions for a variational solution using the Ritz method and Hamilton's principle. In our approach, the challenge is to choose basis functions for the series expansions that display as many features of the model as possible. This challenge is accompanied by the desire to choose functions that allow analytic integration of strain and kinetic energy. As we shall show, these are not entirely different aims, because basis functions that work well mathematically also lead to physical insight.

The infinite cylindrical shell is a well-documented model that will be used to illustrate our approach. Many theories have been proposed to analyze geometrically thin shells, that is, shells whose thickness is much smaller than the principle radii of curvature of their surface. (For a comprehensive discussion of these, see Markus, 1988). Comparisons of some popular higher-order shell theories to analytic solutions were carried out by Greenspon (1960). These theories are typically restricted by initial assumptions regarding variations through the thickness of certain elastic variables. However, the recent use of materials with low bulk dilatational and shear phase speeds as coatings and constrained layer dampers has prompted us to narrow our definition of a "thin" shell to mean one whose thickness is also much smaller than characteristic elastic wavelengths. We will refer to these shells as being acoustically thin.

When the bulk wave speeds are very low, it is likely that a low-frequency excitation will excite higher order modes whose variation in the radial direction is drastically different from the linear and quadratic dependences contained in the various shell theories. The present theory is intended to develop versatile approximations that are suitable for shells that are not acoustically thin. The result fills the gap between the elastic potential solutions, which may be difficult to formulate and solve, and the thin shell theories, in which assumptions regarding the nature of the deformation are inherent.

Analysis by elastic potentials of the free vibrations of infinite cylindrical shells has been carried out by Armenàkas et al. (1969), with the special case of axial plane-strain vibrations analyzed specifically by Gazis (1958). Even for free vibrations, the analysis becomes complicated by an eigenvalue problem in which eigenvalues appear as arguments of Bessel functions. Although we will validate the present theory by comparison to results tabulated by Armenàkas et al., the method will also be formulated for forced vibration analysis. Additionally, we shall compare the predictions for natural frequencies to several thin shell theories, and explore the effect of shell thickness and circumferential harmonic number on natural frequencies by considering various contributions to the strain energies.

2 Analysis

Figure 1 shows displacements and geometric parameters for the infinite cylindrical shell. Displacements are nondimensionalized by the midsurface radius a, so that av and aw are the circumferential and radial displacements, respectively, at an arbitrary point inside the shell. The following nondimensional radial coordinate was introduced by Fellers (1968) and will be used in the present work:

$$\eta=\frac{1}{\epsilon}\left(\frac{r}{a}-1\right),\ \epsilon=\frac{h}{2a}. \tag{1}$$

This coordinate ranges from -1 at the inner surface to 1 at the outer surface. Because the midsurface radius of a solid cylinder is half its thickness h, $\epsilon = 1$ represents a solid cylinder. Further nondimensionalizations employ the frequency of the lowest thickness shear mode in an infinite plate, given by

$$\omega_s=\frac{\pi}{h}\left(\frac{\mu}{\rho}\right)^{1/2}, \tag{2}$$

where μ is the Lamé constant and ρ is the material density. Nondimensional time t is defined such that t/ω_s is the dimensional quantity, while any nondimensional frequency Ω is defined such that $\Omega\omega_s$ is the dimensional quantity.

Linear elasticity equations for a Hookean material in plane-strain axially can be found in many elementary texts. Consistent with the Ritz expansion approach, we choose displacements as independent variables, and write expressions for strain and kinetic energy, which are nondimensionalized by the factor $\pi\epsilon\rho a^4\omega_s^2$. To isolate the effects of the various strains on natural frequencies, we write strain energy as a sum of terms relating to distinct types of strains

$$U_{\text{tot}}=(U_{\text{rad}}+U_{\text{cir}}+U_{\text{coup}}+U_{\text{shear}}), \tag{3}$$

where the respective terms refer to energies resulting from radial, circumferential, coupled radial-circumferential, and shear strains, respectively,

$$U_{\text{rad}}=\frac{8\epsilon^2}{\pi^2}\frac{1}{2\pi}\int_0^{2\pi}\int_{-1}^{1}\frac{1-\nu}{1-2\nu}\frac{1+\epsilon\eta}{\epsilon^2}w,_{\eta}^{2}d\eta d\theta, \tag{4a}$$

$$U_{\text{cir}}=\frac{8\epsilon^2}{\pi^2}\frac{1}{2\pi}\int_0^{2\pi}\int_{-1}^{1}\frac{1-\nu}{1-2\nu}(v,_{\theta}+w)^2(1+\epsilon\eta)d\eta d\theta \tag{4b}$$

$$U_{\text{coup}}=\frac{8\epsilon^2}{\pi^2}\frac{1}{2\pi}\int_0^{2\pi}\int_{-1}^{1}\frac{2\nu}{1-2\nu}\frac{1}{\epsilon}w,_{\eta}(v,_{\theta}+w)d\eta d\theta, \tag{4c}$$

$$U_{\text{shear}}=\frac{8\epsilon^2}{\pi^2}\frac{1}{2\pi}\int_0^{2\pi}\int_{-1}^{1}\frac{1}{2}\frac{1}{1+\epsilon\eta}\left(w,_{\theta}-v+\frac{1+\epsilon\eta}{\epsilon}v,_{\eta}\right)^2 d\eta d\theta. \tag{4d}$$

Nondimensional kinetic energy is given by

$$T=\frac{1}{2\pi}\int_0^{2\pi}\int_{-1}^{1}(\dot{v}^2+\dot{w}^2)(1+\epsilon\eta)d\eta d\theta, \tag{5}$$

where the overdot indicates differentiation with respect to nondimensional time.

We will formulate forced response based on two tractions, Γ_r and Γ_θ, acting on the outer surface of the shell in the radial and tangential directions, respectively. The Ritz method requires formulation of the virtual work done by each traction for a virtual displacement in the direction of that traction. The expression for the virtual work per unit length, also nondimensionalized by the factor $\pi\epsilon\rho a^4\omega_s^2$, is

Downloaded 03 May 2010 to 171.66.16.245. Redistribution subject to ASME license or copyright; see http://www.asme.org/terms/Terms_Use.cfm

$$\delta W = \frac{1+\epsilon}{\pi\epsilon\rho a^2\omega_s^2}\int_0^{2\pi}(\Gamma_\theta \delta v|_{\eta=1} + \Gamma_r \delta w|_{\eta=1})\,d\theta. \tag{6}$$

In accord with the Ritz method, we expand the radial dependence of the displacement components in series of admissible functions of the spatial coordinates, that is, functions that satisfy geometric boundary conditions, but need not satisfy natural ones. Natural boundary conditions are satisfied through the principle of virtual work, in which any such condition that is not satisfied identically results in a contribution to the generalized forces. We desire two mathematical properties for the radial expansion functions. First, the functions must allow analytic integration over η in Eqs. (4) and (5). This task is complicated by the presence of uncancelled factors of $(1 + \epsilon\eta)$ in the denominator of the integrand in Eqs. (4*d*). Second, we wish to limit the amount of coupling between basis functions by choosing functions that are orthogonal in some sense. Clearly, only the exact eigenfunctions are uncoupled. However, it is possible to choose functions that result in a finite coupling bandwidth.

Expansions satisfying these criteria are

$$v(\eta,\theta,t) = (1+\epsilon\eta)^{1/2}\sum_{m=0}^{M} V_m(\theta,t)R_m(\eta), \tag{7a}$$

$$w(\eta,\theta,t) = (1+\epsilon\eta)^{1/2}\sum_{m=0}^{M} W_m(\theta,t)R_m(\eta), \tag{7b}$$

where the functions $R_m(\eta)$, which were apparently first used by Fellers (1968), shall be referred to here as related Legendre polynomials (distinct from associated Legendre polynomials). They are defined in terms of the Legendre polynomials by

$$R_m(\eta) = P_m(\eta) - P_{m-2}(\eta), \text{ where } P_m(\eta) \equiv 0 \text{ for } m<0. \tag{8}$$

Fellers derived many properties of these polynomials. The following one will be useful in evaluating the displacement variations in Eq. (6):

$$R_m(-1) = R_m(1) = 0 \text{ if } m>1, \tag{9}$$

which implies that, according to Eqs. (7), each displacement component on the inner and outer surfaces of the shell is determined by its first two basis functions, and higher functions only affect displacements in the interior of the shell. For example, we have

$$\delta v|_{\eta=1} = (1+\epsilon)^{1/2}(\delta V_0 + \delta V_1). \tag{10}$$

Alternatives to the related Legendre polynomials are simple powers of the thickness coordinate. These are attractive because they are easy to integrate analytically; however, the related Legendre polynomials possess orthogonalities that reduce substantially the amount of modal coupling. In addition, because of the property in Eq. (9), geometric boundary conditions are easily met. Although these boundary conditions will not arise in the present work, future work involving elastic shells with compliant coatings will benefit greatly from the ability to simplify the displacement compatibility conditions between the layers.

The $(1 + \epsilon\eta)^{1/2}$ factor, which is recognized as the square root of r/a, was considered by Fellers (1968), but not used. Its inclusion here, which we believe marks its first published implementation, is crucial. Mathematically, it leads to cancellation of the reciprocal of $(1 + \epsilon\eta)$ in the denominator of Eqs. (4*d*), thereby simplifying the coupling between different orders of thickness variation after analytic integration over η. Also, the inclusion of the $(1 + \epsilon\eta)^{1/2}$ factor has a physical basis because it leads to identical satisfaction of the continuity condition that the displacement of a solid cylinder ($h/a = 2$) should vanish at the center (except for a rigid-body mode). Note that, for a geometrically thin shell, this radial factor has a negligible effect.

Determination of the series coefficients begins with substitution of Eqs. (7) into Eqs. (4) and (5). Because the integrands in these equations are quadratic in displacements and their spatial derivatives, we obtain double summations over the thickness orders, which are moved outside the integrals. Analytic integration over η is performed by using identities derived by Fellers to convert series involving functionals of the related Legendre polynomials to series involving Legendre polynomials. These expressions are listed below for the v expansion, but they are also valid for w, and for θ and t derivatives of v and w,

$$\sum_{m=0}^{M} V_m R_m(\eta) = \sum_{m=0}^{M}(V_m - V_{m+2})P_m(\eta) \tag{11a}$$

$$\sum_{m=0}^{M}(1+\epsilon\eta)V_m R_m(\eta) = \sum_{m=0}^{M}\left(\frac{m\epsilon}{(2m-1)}V_{m-1} + V_m - \frac{(2m+1)\epsilon}{(2m-1)(2m+3)}V_{m+1} - V_{m+2} - \frac{(m+1)\epsilon}{(2m+3)}V_{m+3}\right)P_m(\eta) \tag{11b}$$

$$\sum_{m=0}^{M}(1+\epsilon\eta)V_m R_m'(\eta) = \sum_{m=0}^{M}[m\epsilon V_m + (2m+1)V_{m+1} + (m+1)\epsilon V_{m+2}]P_m(\eta), \tag{11c}$$

where we have implicitly defined $V_{-1} = 0$. Integration through the thickness is expedited by the orthogonality of the Legendre polynomials,

$$\int_{-1}^{1} P_i(\eta)P_j(\eta)\,d\eta = \begin{cases} 0 & i \neq j \\ \dfrac{2}{2i+1} & i = j \end{cases}. \tag{12}$$

The results of these operations are given in Appendix A.

At this point, we could derive $2M + 2$ coupled partial differential equations and boundary conditions for V_m and W_m as functions of θ and t by using Hamilton's principle,

$$\int_{t_1}^{t_2}(\delta T - \delta U + \delta W)\,dt = 0. \tag{13}$$

This would be appropriate for an open shell. However, for the closed cylindrical shell the 2π periodicity of displacement leads directly to a Fourier series expansion of displacements,

$$V_m(\theta,t) = \frac{V_{m0}}{2} + \sum_{n=1}^{N} V_{mn}(t)\,\sin(n\theta), \tag{14a}$$

$$W_m(\theta,t) = \frac{W_{m0}}{2} + \sum_{n=1}^{N} W_{mn}(t)\,\cos(n\theta). \tag{14b}$$

The constant term in tangential displacement is included to allow calculation of the simple $n = 0$ torsional modes. Ignoring this term, the above series expansions represents a displacement field that is symmetric about $\theta = 0$. For the tangential and radial surface tractions, we consider functions that are time-harmonic and consistent with the displacement symmetries,

$$\Gamma_\theta = \mathrm{Re}\left\{\left[\frac{\hat{F}_0}{2} + \sum_{n=1}^{N}\hat{F}_n\,\sin(n\theta)\right]e^{-i\Omega t}\right\}, \tag{15a}$$

$$\Gamma_r = \mathrm{Re}\left\{\left[\frac{\hat{G}_0}{2} + \sum_{n=1}^{N}\hat{G}_n\,\cos(n\theta)\right]e^{-i\Omega t}\right\}, \tag{15b}$$

where the overcarat denotes a complex-valued amplitude.

Substitution of these expansions into equations for T, U, and δW results in analytic integration over θ due to the orthogonality of the trigonometric functions. Because these modes uncouple, we remove the n subscript on V_{mn} and W_{mn},

Downloaded 03 May 2010 to 171.66.16.245. Redistribution subject to ASME license or copyright; see http://www.asme.org/terms/Terms_Use.cfm

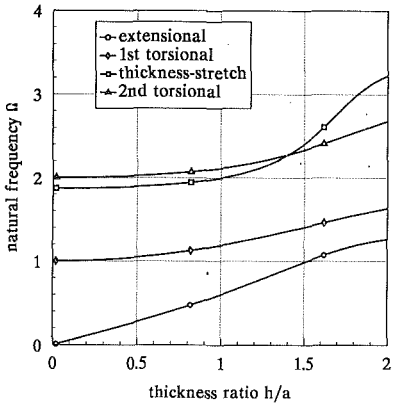


Fig. 2 Thickness dependences of lowest four natural frequencies for $n = 0$

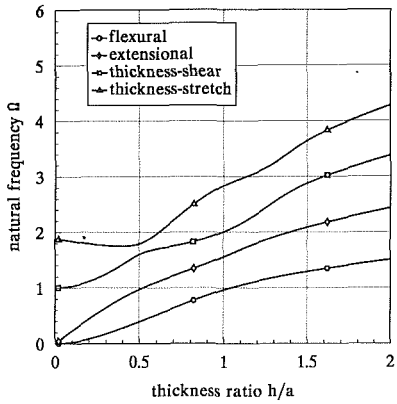


Fig. 3 Thickness dependences of lowest four natural frequencies for $n = 4$

so that V_m and W_m shall henceforth refer to the mth thickness order of the nth circumferential harmonic. The integrations over θ result in the following expressions for the strain and kinetic energies of the nth harmonic:

$$U_n = \frac{1}{2}\sum_{m=0}^{M}\sum_{p=-2}^{2}\left[(\kappa_{vv})_{m,m+p}V_mV_{m+p} + (\kappa_{vw})_{m,m+p}V_mW_{m+p} + (\kappa_{ww})_{m,m+p}W_mW_{m+p}\right] \quad (16a)$$

and

$$T_n = \frac{1}{2}\sum_{m=0}^{M}\sum_{p=-3}^{3}\left[(\mu_{vv})_{m,m+p}\dot{V}_m\dot{V}_{m+p} + (\mu_{ww})_{m,m+p}\dot{W}_m\dot{W}_{m+p}\right]. \quad (16b)$$

Note that strain energy couples modes over a bandwidth of five thickness orders, while kinetic energy has a bandwidth of seven. Because the modes are coupled, errors are introduced in a truncation at the Mth thickness order. The quantitative results we present are based on the convergence of a set of eigenvalues and eigenvectors to a desired accuracy.

The generalized forces for the nth harmonic are the coefficients of the virtual increments δV_m and δW_m in Eq. (6). Because of the simplification illustrated in Eq. (10), the only nonzero generalized forces are those associated with the $m = 0$ and $m = 1$ thickness orders, given by

$$(Q_v)_0 = (Q_v)_1 = \frac{(1+\epsilon)^{3/2}}{\pi\epsilon\rho a^2\omega_s^2}\,\mathrm{Re}\{\hat{F}_n e^{-i\Omega t}\}, \quad (17a)$$

$$(Q_w)_0 = (Q_w)_1 = \frac{(1+\epsilon)^{3/2}}{\pi\epsilon\rho a^2\omega_s^2}\,\mathrm{Re}\{\hat{G}_n e^{-i\Omega t}\}. \quad (17b)$$

It follows that the higher thickness orders are not driven directly by surface excitation.

Hamilton's principle leads to nondimensional Lagrange's equations of motion governing the generalized coordinates,

$$\frac{d}{dt}\left(\frac{\partial T_n}{\partial \dot{V}_m}\right) + \frac{\partial U_n}{\partial V_m} = (Q_v)_m \text{ and } \frac{d}{dt}\left(\frac{\partial T_n}{\partial \dot{W}_m}\right) + \frac{\partial U_n}{\partial W_m} = (Q_w)_m. \quad (18)$$

After taking the derivatives in the above equations, we recognize that the displacement coefficients V_m and W_m must also be harmonic in time, for example $V_m = \hat{V}_m e^{-i\Omega t}$. To band the mass and stiffness matrices that follow, we define the following vectors of generalized coordinate and force amplitudes:

$$\{\hat{q}\} = \{\hat{V}_0\hat{W}_0\hat{V}_1\hat{W}_1 \cdots \hat{V}_M\hat{W}_M\}^T, \quad (19a)$$

$$\{\hat{Q}\} = \frac{(1+\epsilon)^{3/2}}{\pi\epsilon\rho a^2\omega_s^2}\{\hat{F}_n\hat{G}_n\hat{F}_n\hat{G}_n\{0\}^T\}^T. \quad (19b)$$

Cancellation of the harmonic time dependence in Lagrange's equations yields a set of complex linear equations that can be solved for the generalized coordinate amplitudes,

$$[[\kappa] - \Omega^2[\mu]]\{\hat{q}\} = \{\hat{Q}\}, \quad (20)$$

where $[\kappa]$ and $[\mu]$ are the nondimensionalized stiffness and mass matrices, respectively, defined by Eqs. (18) and renumbered in accord with Eqs. (19) and (20). Analytic expressions for the elements of these matrices are given by McDaniel (1992). They are real, symmetric matrices whose elements are functions of ν and the circumferential harmonic number n. Their derivation in algebraic form for truncation at an arbitrary order M is achieved with the aid of a symbolic manipulation computer language.

For free vibration, the right-hand side of Eq. (20) is the null vector, which leads to a generalized eigenvalue problem for the natural frequencies and mode shapes:

$$[[\kappa] - \Omega_i^2[\mu]]\{\hat{q}_i\} = \{0\},\ i = 1,2,\ \ldots,\ 2M+2, \quad (21)$$

where the eigenvalues and eigenfunctions are real. Efficient computer codes exist that numerically solve this equation. The eigenmodes are normalized so that the modal kinetic energy is unity, i.e.

$$\frac{1}{2}\{\hat{q}_i\}^T[\mu]\{\hat{q}_j\} = \delta_{ij}. \quad (22)$$

3 Numerical Results

The free vibration problem in Eq. (21) was solved for a range of thickness ratios and circumferential harmonics, with $\nu = 0.3$. Successively higher truncations (larger M) were evaluated until each of the first ten nonzero eigenvalues changed less than 1 percent. For all of the results discussed below, this accuracy was achieved with a truncation of $22 \le M \le 25$. The convergence of rigid-body modes, which correspond to $\Omega = 0$, was not examined because the radial expansions exclude these modes for the special case of a solid cylinder. For example, rigid-body translation is excluded because the displacement expansions in Eqs. (7) vanish at the center. We monitored convergence of the mode shapes as the truncation number M was increased. Let $\{\hat{q}_i^M\}$ denote the ith mode shape corresponding to a specified M. We found that when M was sufficient to attain the convergence of the first ten eigenvalues, the norm of $\{\hat{q}_i^M\} - \{\hat{q}_i^{M-1}\}$ was less than 1 percent of the norm of $\{\hat{q}_i^{M-1}\}$ for each of the first ten eigenvectors.

Figures 2 and 3 show the transition from a thin shell ($h/a \to 0$) to a solid cylinder ($h/a = 2$) for $n = 0$ and $n = 4$, respectively. Tables 1 and 2 present some numerical values from these figures. These results have been checked against tables given by Armenàkas et al., with which they agree to within 1 percent. The thickness-stretch mode in Fig. 2 was not

Downloaded 03 May 2010 to 171.66.16.245. Redistribution subject to ASME license or copyright; see http://www.asme.org/terms/Terms_Use.cfm

Table 1 Lowest four natural frequencies for $n = 0$

h/a	extensional	1st torsional	thickness-stretch	2nd torsional
0.1	0.0539	1.00	1.87	2.00
0.5	0.277	1.05	1.89	2.02
1.0	0.601	1.19	2.00	2.12
1.5	0.988	1.41	2.33	2.40
2.0	1.27	1.63	2.68	3.22

Table 2 Lowest four natural frequencies for $n = 4$

h/a	flexural	extensional	thickness-shear	thickness-stretch
0.1	0.0220	0.221	1.03	1.84
0.5	0.388	0.968	1.66	1.79
1.0	0.959	1.56	2.00	2.83
1.5	1.29	2.08	2.88	3.64
2.0	1.50	2.43	3.38	4.28

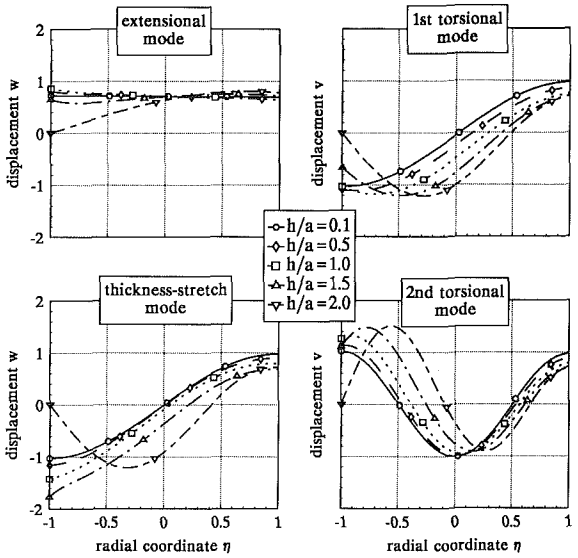


Fig. 4 Radial variations of modal displacements for $n = 0$

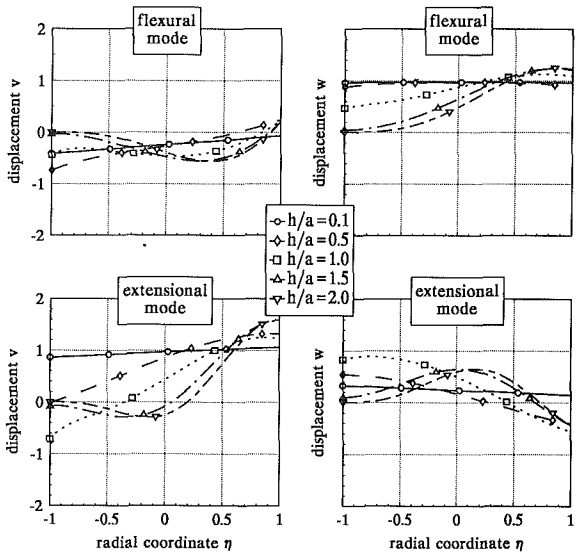


Fig. 5 Radial variations of modal displacements for $n = 4$, flexural and extensional modes

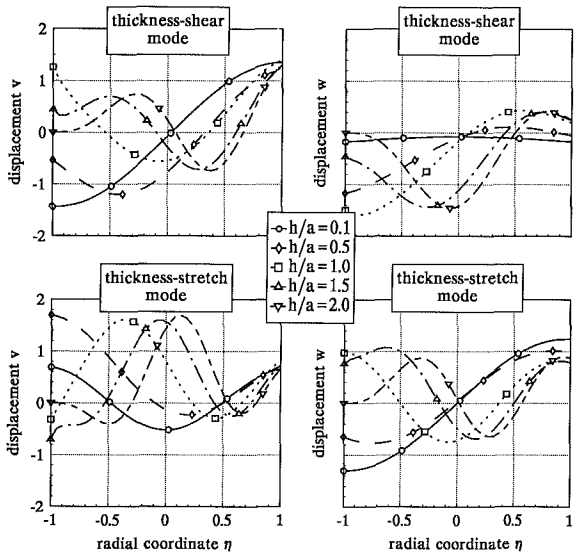


Fig. 6 Radial variations of modal displacements for $n = 4$, thickness-shear and thickness-stretch modes

verified for $h/a > 0.4$ because data was not available. The types of modes are labelled using terminology from Armenàkas et al., where a torsional mode describes an axisymmetric motion with only shear strains. Thickness-shear modes are easily identifiable because Ω approaches integral values as $h/a \to 0$ and the shell behaves like a thin plate. Figures 4–6 show mode shapes corresponding to the eigenvalues in Figs. 2 and 3 for five thickness ratios.

A thorough visual assessment of the effect of h/a on the variation of the displacement components through the thickness would require an inordinate number of graphs. Useful conclusions can be obtained by considering the dependence of "eigen-energies," that is, the partitioning of strain energies associated with eigenvectors that have been normalized to have unit kinetic energy. For each mode in Figs. 2 and 3, the various strain energies and their sum, U_{tot}, are plotted as functions of h/a in Figs. 7 and 8. Exceptions are the two torsional modes in Fig. 2, for which only U_{shear} is nonzero. Note that, because of the manner in which the modes are normalized, U_{tot} is equal to the square of the natural frequency of that mode.

Knowledge of the partitioning of the modal strain energy enables one to identify the importance of various strain energies to the natural frequency of that mode. For $n = 0$, Fig. 7 shows that circumferential strain energy is dominant in the extensional mode up to $h/a = 1.4$, after which radial and coupled circumferential-radial strain energy also become important. Similarly, Fig. 7 shows that radial strain dominates the frequency of the thickness-stretch mode up to $h/a = 1$, after which circumferential strains play an increasing role. When $n = 4$, Fig. 8 shows similar results. In general, we conclude from Fig. 8 that, for $h/a > 1$, all modes except for the extensional one involve all types of strain energies.

For a very thin shell with $h/a = 0.01$, we further explored the effect of circumferential harmonic number n. Figure 9 shows the lowest four natural frequencies as functions of n. Also plotted, for the lower two branches, are results from various thin-shell theories summarized by Markus (1988). Al-

Downloaded 03 May 2010 to 171.66.16.245. Redistribution subject to ASME license or copyright; see http://www.asme.org/terms/Terms_Use.cfm

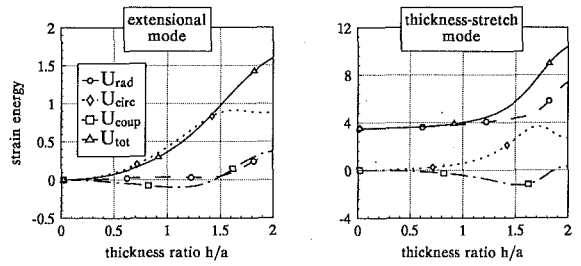


Fig. 7 Thickness dependences of eigen-energies for $n = 0$

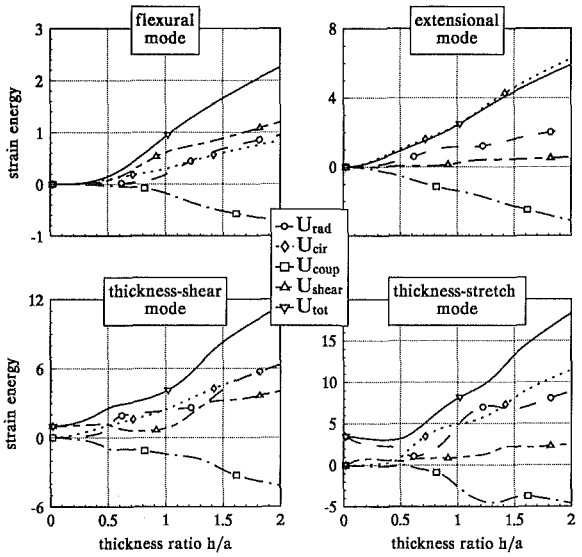


Fig. 8 Thickness dependences of eigen-energies for $n = 4$

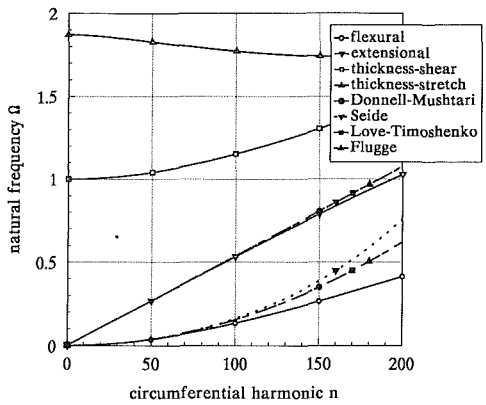


Fig. 9 Circumferential harmonic dependences of lowest four natural frequencies for $h/a = 0.01$, with the first two compared to thin-shell theories

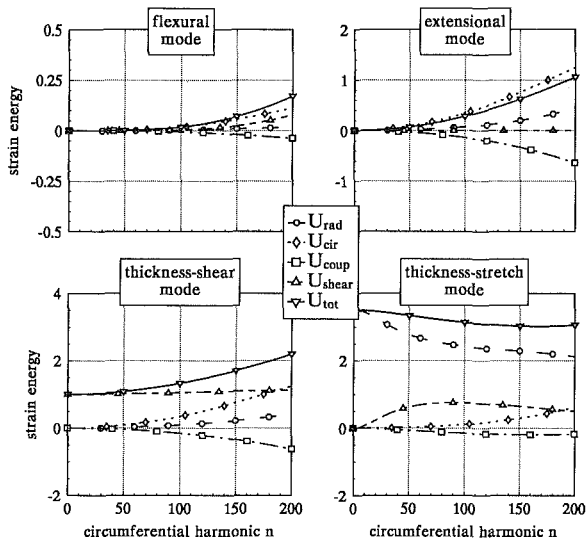


Fig. 10 Circumferential harmonic dependences of eigen-energies for $h/a = 0.01$

though a complete comparison of these theories is beyond our scope, we note that they are distinguished by certain approximations regarding variations through the shell thickness. Markus states that Seide's theory ". . . has been very successful in dynamic problems because it includes the effect of rotatory inertia of the cross-section." However, Fig. 9 indicates that Seide's theory fails at the same circumferential harmonic as the other thin-shell theories. Specifically, errors in the flexural natural frequency become significant at $n = 100$, while errors in the extensional natural frequency become noticeable at $n = 150$.

In comparison to Fig. 3, a surprising result is that the quantitative effect of increasing n from 0 to 200 for $h/a = 0.01$ is comparable to increasing h/a from 0 to 0.5 for $n = 4$. Comparison of Fig. 8 to Fig. 10 shows that this similarity extends to the partitioning of energy. Consideration of the energy expressions in Eqs. (4) in the limit of small ϵ helps to explain this similarity. In this limit, squares of derivatives with respect to θ dominate for even moderately low n because these terms are proportional to n^2. We observe that U_{cir} and U_{shear} are proportional to $(\epsilon n)^2$, U_{coup} is proportional to ϵn, and U_{rad} does not depend on either ϵ or n. Clearly, in this limit the behavior is primarily dependent on the product ϵn.

With this fact, we are able to understand the similarities described above, because in Figs. 3 and 9, ϵn ranges from 0 to 2. The quantity $\epsilon n/\pi$ is the ratio of the shell thickness to the circumferential standing wavelength corresponding to the nth harmonic. Based on this, we suggest ϵn as a parameter for narrowing the definition of "thin," such that a thin shell is understood to mean one for which $\epsilon n \ll 1$. Note that the thin shell theories in Fig. 9 begin to fail for the flexural frequency at $\epsilon n \approx 1$. We conclude that thin shell theories tend to fail when the scale of standing wavelengths is on the scale of the shell thickness.

4 Conclusions

A shell theory has been proposed that has its roots in the works of Poisson, Cauchy, and Basset, but is cast in the form of a variationally based Ritz expansion. Previous research by Fellers (1968) provided clues about optimal normalization and expansions in the radial coordinate. Several advantages are gained by viewing series expansions in the radial and circumferential coordinates as Ritz expansions. Integrands of kinetic and potential energies are expressed as functions of displacements only, which provides for physically clear approximations when truncating series expansions. The inclusion of an irrational radial factor to meet displacement compatibility conditions at the center of a solid cylinder also facilitates the exact integrations of potential and kinetic energies. For this reason, the geometrically thin assumption, which accompanies thin-shell theories, does not appear in the present formulation. As a result, the theory is valid for arbitrary thickness, provided that enough terms are included for a convergent answer. Partitioning of strain energy provides insight into energy storage mechanisms for various thickness and circumferential harmonic numbers. The formulation suggests extending the thinness criteria for shell theory to a requirement that the thickness should be much smaller than any standing wavelengths. Finally, the exposition discussed the formulation for problems involving harmonic excitation, but no results were obtained for such problems. The Ritz expansion approach is not limited

Downloaded 03 May 2010 to 171.66.16.245. Redistribution subject to ASME license or copyright; see http://www.asme.org/terms/Terms_Use.cfm

to the two-dimensional problem described above. The general case of axial dependences and displacements is tractable, but would complicate the exposition of the theory. The formulation could also be applied to the development of higher order shell elements.

5 References

Armenàkas, A. E., Gazis, D. C., and Herrmann, G., 1969, *Free Vibrations of Circular Cylindrical Shells*, Pergamon Press, New York.

Basset, A. B., 1890, "On the Extension and Flexure of Cylindrical and Spherical Thin Elastic Shells," *Philosophical Transactions of the Royal Society of London*, Vol. 181, pp. 433–480.

Calladine, C. R., 1988, "The Theory of Thin Shell Structures 1888–1988," *Proceedings of the Institution of Mechanical Engineers*, Vol. 202, No. A3, pp. 141–149.

Cicalo, P., 1961, *Controlled Approximation Theory for Thin Elastic Shells, Part 1—The Differential System*, Torino, Italy.

Faraji, S., Archer, R. R., 1985, "Method of Initial Functions for Thick Shells," *International Journal of Solids and Structures*, Vol. 21, pp. 851–863.

Faraji, S., Archer, R. R., 1988, "Higher Order Theories for Thick Cylindrical Shells," *Acta Mechanica*, Vol. 74, pp. 9–24.

Fellers, J. I., 1968, "A Thick Cylindrical Shell Theory," Ph.D. Dissertation, University of Pennsylvania, Engineering Mechanics.

Fellers, J. I., and Soler, A. I., 1970, "Approximate Solution of the Finite Cylinder Problem Using Legendre Polynomials," *AIAA Journal*, Vol. 8, pp. 2037–2042.

Gazis, D. C., 1958, "Exact Analysis of the Plane-Strain Vibrations of Thick-Walled Hollow Cylinders," *Journal of the Acoustical Society of America*, Vol. 30, pp. 786–794.

Greenspon, J. E., 1960, "Vibrations of a Thick-Walled Cylindrical Shell—Comparison of the Exact Theory with Approximate Theories," *Journal of the Acoustical Society of America*, Vol. 32, pp. 571–578.

Heyliger, P. R., and Jilani, A., 1991, "The Free Vibrations of Elastic Anisotropic Cylinders and Spheres," *American Institute of Aeronautics and Astronautics*, Vol. AIAA-91-1245-CP, pp. 3039–3046.

Iyengar, K. T. S. R., Chandrashekhara, K., Sebastian, V. K., 1975, "Thick Circular Cylindrical Shells Under Axisymmetric Loading," *Acta Mechnica*, Vol. 23, pp. 137–144.

Love, A. E. H., 1888, "The Small Free Vibrations and Deformation of a Thin Elastic Shell," *Philosophical Transactions of the Royal Society of London*, Vol. 179A, pp. 491–546.

Markus, S., 1988, *The Mechanics of Vibrations of Cylindrical Shells*, (Studies in Applied Mechanics 17), Elsevier, New York, pp. 36–100.

McDaniel, J. G., 1992, "A New Higher-Order Shell Theory for Vibration and Acoustic Scattering from Bare and Viscoelastically-Coated Circular Cylindrical Shells," Ph.D. Dissertation, Georgia Institute of Technology, Department of Mechanical Engineering, Atlanta, GA.

Mindlin, R. D., 1955, *An Introduction to the Mathematical Theory of Elastic Plates*, Monograph prepared for U.S. Army Signal Corps Engineering Laboratories, Fort Monmouth, NJ.

Mindlin, R. D., 1959, "Extensional Vibrations of Elastic Plates," ASME JOURNAL OF APPLIED MECHANICS, Vol. 26, pp. 561–569.

Mindlin, R. D., 1960, "Axially Symmetric Waves in Elastic Rods," ASME JOURNAL OF APPLIED MECHANICS, Vol. 27, pp. 145–151.

Soler, A. I., 1969, "Higher-Order Theories for Structural Analysis Using Legendre Polynomial Expansions," ASME JOURNAL OF APPLIED MECHANICS, Vol. 36, pp. 757–762.

Vlasov, V. Z., 1957, "The Method of Initial Functions in Problems of the Theory of Thick Plates and Shells," *9th International Congress of Applied Mechanics* (Brussels), pp. 321–330.

APPENDIX A

Expressions for Strain and Kinetic Energies

$$U_{\text{rad}}=\frac{8}{\pi^2}\frac{1}{2\pi}\frac{1-\nu}{1-2\nu}\sum_{m=0}^{M}\frac{2}{2m+1}\int_0^{2\pi}[\epsilon(m+0.5)W_m + (2m+1)W_{m+1}+\epsilon(m+0.5)W_{m+2}]^2 d\theta \quad \text{(A1)}$$

$$U_{\text{cir}}=\frac{8\epsilon^2}{\pi^2}\frac{1}{2\pi}\frac{1-\nu}{1-2\nu}\sum_{m=0}^{M}\frac{2}{2m+1} \times \int_0^{2\pi}(V_m'-V_{m+2}'+W_m-W_{m+2})^2 d\theta \quad \text{(A2)}$$

$$U_{\text{coup}}=\frac{8\epsilon}{\pi^2}\frac{1}{2\pi}\frac{2\nu}{1-2\nu}\sum_{m=0}^{M}\frac{2}{2m+1} \times \int_0^{2\pi}[\epsilon(m+0.5)W_m+(2m+1)W_{m+1} + \epsilon(m+0.5)W_{m+2}][V_m'-V_{m+2}'+W_m-W_{m+2}]d\theta \quad \text{(A3)}$$

$$U_{\text{shear}}=\frac{8}{\pi^2}\frac{1}{2\pi}\sum_{m=0}^{M}\frac{1}{2m+1}\int_0^{2\pi}[\epsilon W_m'-\epsilon W_{m+2}'+\epsilon(m-0.5)V_m + (2m+1)V_{m+1}+\epsilon(m+1.5)W_{m+2}]^2 d\theta, \quad \text{(A4)}$$

where a prime ($'$) denotes differentiation with respect to θ.

$$T=\frac{2}{2\pi}\sum_{m=0}^{M}\frac{2}{2m+1} \times \int_0^{2\pi}\left[\left(\frac{m\epsilon}{(2m-1)}\dot{V}_{m-1}+\dot{V}_m-\frac{(2m+1)\epsilon}{(2m-1)(2m+3)}\dot{V}_{m+1} - \dot{V}_{m+2}-\frac{(m+1)\epsilon}{(2m+3)}\dot{V}_{m+3}\right)^2+\left(\frac{m\epsilon}{(2m-1)}\dot{W}_{m-1}+\dot{W}_m - \frac{(2m+1)\epsilon}{(2m-1)(2m+3)}\dot{W}_{m+1}-\dot{W}_{m+2}-\frac{(m+1)}{(2m+3)}\dot{W}_{m+3}\right)^2\right]d\theta. \quad \text{(A5)}$$

Downloaded 03 May 2010 to 171.66.16.245. Redistribution subject to ASME license or copyright; see http://www.asme.org/terms/Terms_Use.cfm

Natural Frequencies and Stability of a Flexible Spinning Disk-Stationary Load System With Rigid-Body Tilting

Jen-San Chen
Department of Mechanical Engineering,
National Taiwan University,
Taipei, Taiwan 107

D. B. Bogy
Computer Mechanics Laboratory,
Department of Mechanical Engineering,
University of California,
Berkeley, CA 94720

The effects of rigid-body tilting on the natural frequencies and stability of the head-disk interface of a flexible spinning disk are studied both by analysis and numerical computation. Another problem of a stationary flexible disk with rigid body tilting subject to a rotating load system is also studied. In the conventional case without rigid-body tilting, these two problems are mathematically identical except for the additional membrane stress terms arising from the centrifugal force. When the rigid-body tilting is included, however, these two problems differ not only by the centrifugal effect, but also by additional terms which arise from the gyrodynamic effect. After properly defining the inner product between two state vectors, the set of equations of motion is proven to fall into the category of gyrosopic systems. Then the derivatives of the eigenvalues of the coupled system are obtained to provide a better understanding of the numerical results.

Introduction

Interest in the dynamics of a spinning disk in contact with a stationary load system arises from its applications in such fields as computer disk drives and circular saws. Conventionally, the circular disk is free at the outer radius and clamped at the inner radius by a central clamp, usually assumed to be rigid. The stationary load system, which may contain mass, damping, and stiffness elements, both linear and rotary, represents the head suspension in the computer disk drive, or the saw guide in the circular saw, respectively. Various techniques have been used to predict the natural frequencies and the stability properties of such a coupled system, for example, the classical eigenfunction expansion (Iwan and Moeller, 1976; Shen and Mote, 1991) and the finite element method (Ono et al., 1991). In all these analyses the disk, together with the rigid central clamp, rotate about a fixed axis of symmetry of the disk.

In a recent experiment with hard disk drives, Jeong and Bogy (1991) reported that the disk may undergo a small rigid-body displacement as well as deformation when the read-write system is loaded onto the spinning disk. It has also been known in the wood cutting industry that allowing the central clamping collar to slide transversely along the axis of rotation can improve the stability of the cutting process. In order to understand the effects of the rigid-body motion on the natural frequencies and stability of the spinning flexible disk, it is necessary to generalize the conventional model to include the rigid-body motion of the clamp or collar.

The dynamic response of the head-disk interface of a spinning flexible disk with axial spindle translation has been thoroughly studied (Mote, 1977; Price, 1987; Chen and Bogy, 1992c). However, the effects of rigid-body tilting on the natural frequencies and stability of the system are still not well understood. Arnold and Maunder (1961) derived the equations of motion and described the gyrodynamic behavior of an elastically supported spinning rigid disk. Stahl and Iwan (1973a) investigated the dynamic response of an elastically supported stationary rigid disk subject to a rotating load system. It was shown that the response behavior of the rigid disk is directly analogous to that of a stationary elastic disk without rigid-body tilting and subject to a circumferentially moving load system. Yang (1988) formulated the equations of motion for a general system with coupled rigid and flexible body motion, and applied it to the stability analysis of a spinning flexible disk with rigid body translation and tilting. However, his numerical results showed the combined effects of rigid-body translation and tilting, from which it is difficult to obtain physical insight into the gyrodynamic effects of rigid-body tilting alone.

In the present paper we consider a spinning flexible disk clamped at the inner radius and subject to a stationary load system. The clamp is considered as rigid and allowed to tilt about a fixed point in space, but resisted by a torsional spring

Contributed by the Applied Mechanics Division of THE AMERICAN SOCIETY OF MECHANICAL ENGINEERS for presentation at the First Joint ASCE-EMD, ASME-AMD, SES Meeting, Charlottesville, VA, June 6–9, 1993.

Discussion on this paper should be addressed to the Technical Editor, Professor Lewis T. Wheeler, Department of Mechanical Engineering, University of Houston, Houston, TX 77204-4792, and will be accepted until four months after final publication of the paper itself in the ASME JOURNAL OF APPLIED MECHANICS.

Manuscript received by the ASME Applied Mechanics Division, Jan. 16, 1992; final revision, June 22, 1992. Associate Technical Editor: D. J. Inman.

Paper No. 93-APM-32.

Copyright © 1993 by ASME
Downloaded 03 May 2010 to 171.66.16.245. Redistribution subject to ASME license or copyright; see http://www.asme.org/terms/Terms_Use.cfm

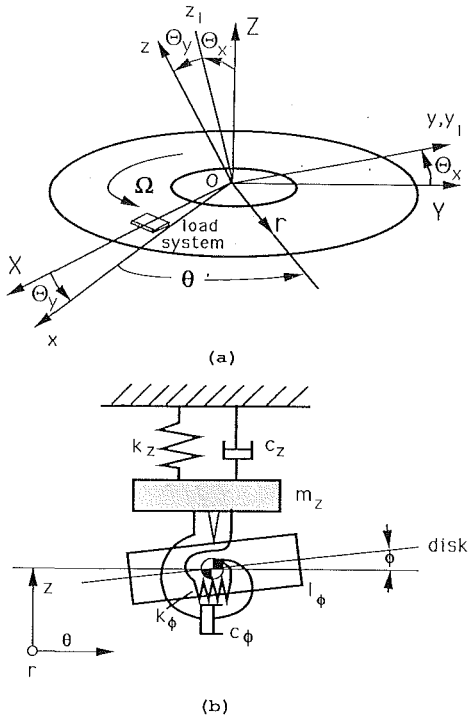


Fig. 1 *(a)* **Global picture of a spinning disk with rigid-body tilting and the stationary load system; *(b)* parameters in the load system**

and a torsional damper. In the special case when the stiffness of the clamp spring and the value of the clamp damping are zero, we show by numerical simulation, as well as by an analytical method, that the natural frequencies of all the one-nodal diameter modes (as seen by an observer moving with the tilting clamp) increase, as could be expected due to the inertial effect. Another problem of a stationary flexible disk with rigid-body tilting and subject to a rotating load system is also studied. It is found that these two types of problems differ not only by the stress terms arising from the centrifugal force, but also by additional terms arising from the gyrodynamic effects. After properly defining the inner product between two state vectors, we show that the set of equations fall into the category of gyroscopic systems. Then the derivatives of the eigenvalues of the system with respect to various load parameters in the load system are derived to explain several phenomena discovered in the numerical simulation when the load parameters are introduced.

Equations of Motion and Numerical Results

Figure 1 shows a flexible spinning disk with rigid body tilting. The spinning disk is clamped at the inner radius $r = a$ by a rigid clamp, and is free at the outer radius $r = b$. The rigid clamp is allowed to tilt, but it is supported by a torsional spring k_Θ and a torsional damper c_Θ. The center of the clamp is fixed at a point O in space. The motion of a spinning flexible disk can be described in two coordinate frames, as shown in Fig. 1. The frame *o-xyz*, together with the rigid clamp, tilts relative to the inertial frame *O-XYZ*. The orientation of *O-xyz* with respect to *O-XYZ* is obtained by rotation Θ_x about *OX* to *O-*$x_1y_1z_1$ and then rotation Θ_y about Oy_1 to *O-xyz*. The elastic transverse displacement w of the disk is measured with respect to the local noninertial *O-xyz* frame. The disk rotates about the *Oz*-axis and is in contact with a stationary load system containing transverse inertia m_z, spring k_z, dashpot c_z, and the analogous pitching elements I_ϕ, k_ϕ, and c_ϕ. By using D'Alembert's principle and by assuming that tilting angles Θ_x and Θ_y are infinitesimal, the equation of motion of the disk in terms of w and with respect to the local coordinate system (r, θ) can be written as

$$\rho h(w_{,tt}+2\Omega w_{,t\theta}+\Omega^2 w_{,\theta\theta})+D\nabla^4 w-\frac{h}{r}(\sigma_r r w_{,r})_{,r}$$
$$-\frac{h\sigma_\theta}{r^2}w_{,\theta\theta}+r\rho h(\ddot{\Theta}_x\sin\theta-\ddot{\Theta}_y\cos\theta)$$
$$+2\Omega r\rho h(\dot{\Theta}_x\cos\theta+\dot{\Theta}_y\sin\theta)=\frac{1}{r}\delta(r-\xi)\delta(\theta)F_z$$
$$-\frac{1}{r^2}\delta(r-\xi)[M_\phi\delta(\theta)]_{,\theta} \quad (1)$$

where

$$F_z=-m_z(w_{,tt}-\xi\ddot{\Theta}_y)-c_z(w_{,t}-\xi\dot{\Theta}_y)-k_z(w-\xi\Theta_y)$$
$$M_\phi=-\frac{1}{r}[I_\phi(w_{,tt\theta}+\xi\ddot{\Theta}_x)+c_\phi(w_{,t\theta}+\xi\dot{\Theta}_x)+k_\phi(w+\xi\Theta_x)]$$

and

$$D=\frac{Eh^3}{12(1-\nu^2)}$$

The standard subscript notation for partial derivatives is used here, and the superposed dot means material time derivative. The parameters Ω, ρ, h, E, ν, and D are the rotation speed, density, thickness, Young's modulus, Poisson's ratio, and flexural rigidity of the disk. $\delta(:)$ is the Dirac delta function. The coupling position between the load system and disk is assumed to be $r = \xi$ and $\theta = 0$. The generalized plane stress components σ_r and σ_θ are due to the centrifugal effect.

We next consider a particle on the flexible spinning disk with coordinates ($r\cos\theta$, $r\sin\theta$, w) with respect to the local *O-xyz* frame. The coordinates of the position vector $\mathbf{p}$ with respect to the inertial frame *O-XYZ* can be calculated by the following transformation

$$\mathbf{p}=\begin{Bmatrix}\mathbf{X}\\ \mathbf{Y}\\ \mathbf{Z}\end{Bmatrix}=\begin{bmatrix}\cos\Theta_y & 0 & \sin\Theta_y\\ 0 & 1 & 0\\ -\sin\Theta_y & 0 & \cos\Theta_y\end{bmatrix}\begin{bmatrix}1 & 0 & 0\\ 0 & \cos\Theta_x & -\sin\Theta_x\\ 0 & \sin\Theta_x & \cos\Theta_x\end{bmatrix}$$
$$\times\begin{Bmatrix}r\cos\theta\\ r\sin\theta\\ w\end{Bmatrix}=\mathbf{Q}\begin{Bmatrix}r\cos\theta\\ r\sin\theta\\ w\end{Bmatrix}$$

where $\mathbf{Q}$ is the product matrix of the two rotation matrices. The absolute velocity of this particle is

$$\dot{\mathbf{p}}=\dot{\mathbf{Q}}\begin{Bmatrix}r\cos\theta\\ r\sin\theta\\ w\end{Bmatrix}+\mathbf{Q}\begin{Bmatrix}-r\Omega\sin\theta\\ r\Omega\cos\theta\\ \dot{w}\end{Bmatrix}.$$

The total angular momentum $\mathbf{H}$ of the disk, with respect to the origin O, is

$$\mathbf{H}=\rho h\int_0^{2\pi}\int_a^b \mathbf{p}\times\dot{\mathbf{p}}\,r\,dr\,d\theta.$$

The material derivative of $\mathbf{H}$ is

$$\dot{\mathbf{H}}=\rho h\int_0^{2\pi}\int_a^b \mathbf{p}\times\ddot{\mathbf{p}}\,r\,dr\,d\theta.$$

By considering the balance between $\dot{\mathbf{H}}$ and the resultant moment of the forces exerted by the stationary load system, the clamp spring k_Θ, and the clamp damper c_Θ, and by linearizing the equations in Θ_x, Θ_y, and w, one can obtain two additional equations of motion,

$$(I+I_c)(\ddot{\Theta}_x+2\Omega\dot{\Theta}_y)+\int_0^{2\pi}\int_a^b\rho h\sin\theta(w_{,tt}+2\Omega w_{,t\theta})r^2\,dr\,d\theta$$
$$=M_\phi\delta(r-\xi)\delta(\theta)-k_\Theta\Theta_x-c_\Theta\dot{\Theta}_x \quad (2)$$

Downloaded 03 May 2010 to 171.66.16.245. Redistribution subject to ASME license or copyright; see http://www.asme.org/terms/Terms_Use.cfm

$$(I+I_c)(\ddot{\Theta}_y - 2\Omega\dot{\Theta}_x) - \int_0^{2\pi}\int_a^b \rho h \cos\theta(w_{,tt}+2\Omega w_{,t\theta})r^2 dr d\theta$$
$$= \xi F_z \delta(r-\xi)\delta(\theta) - k_\Theta \Theta_y - c_\Theta \dot{\Theta}_y, \quad (3)$$

where $I = \pi\rho h(b^2-a^4)/4$ is the moment of inertia of the circular plate and I_c is the moment of inertia of the rigid clamp. These additional equations of motion account for the fact that there are two additional degrees-of-freedom, i.e., Θ_x and Θ_y, of the present system. For the conventional freely spinning disk with $k_\Theta = \infty$, $c_\Theta = 0$, $F_z = 0$, and $M_\phi = 0$, the eigenvalues $\lambda_{mn} = \lambda^0_{mn}$ are all purely imaginary, i.e., $\lambda^0_{mn} = i\omega^0_{mn}$, where ω^0_{mn} is real. The corresponding eigenfunctions are, in general, complex and assume the form

$$w^0_{mn} = R^0_{mn}(r)e^{\pm i n\theta}, \quad n = 1,2,3, \ldots \quad (4)$$

in which R^0_{mn} is a real-valued function of r. The eigenfunction corresponding to $\bar{\lambda}^0_{mn}$ is $\bar{w}^0_{mn}$, where the overbar means complex conjugate. If we consider only the positive ω^0_{mn}, then w^0_{mn} in Eq. (4) with $+in\theta$ is a backward travelling wave with n nodal diameters and m nodal circles, which is also denoted by $(m, n)_b$. Similarly, w^0_{mn} with $-in\theta$ is a forward travelling wave $(m, n)_f$. The critical speed Ω_c for the mode (m, n) is defined as the rotation speed at which ω^0_{mn} of the backward travelling wave $(m, n)_b$ is zero. For Ω greater than Ω_c, this mode is a forward travelling wave, and is called a "reflected wave," denoted by $(m, n)_r$.

In the case of a freely spinning disk with the clamp allowed to tilt freely, i.e., $k_\Theta = 0$ and $c_\Theta = 0$, one can multiply Eqs. (2) and (3) by $\sin\theta$ and $\cos\theta$, respectively, and substitute the results into Eq. (1) to obtain

$$\rho h(w_{,tt}+2\Omega w_{,t\theta}+\Omega^2 w_{,\theta\theta}) + D\nabla^4 w - \frac{h}{r}(\sigma_r r w_{,r})_{,r} - \frac{h\sigma_\theta}{r^2} w_{,\theta\theta}$$
$$- \frac{r\rho^2 h^2}{(I+I_c)}\left[\cos\theta\int_0^{2\pi}\int_a^b r^2\cos\theta(w_{,tt}+2\Omega w_{,t\theta})dr d\theta\right.$$
$$\left. + \sin\theta\int_0^{2\pi}\int_a^b r^2\sin\theta(w_{,tt}+2\Omega w_{,t\theta})dr d\theta\right] = 0. \quad (5)$$

The only difference between Eq. (5) and that of a conventional freely spinning disk with a nontilting clamp is the additional integral terms at the end of Eq. (5), which account for the inertial coupling between the elastic modes and the rigid-body tilting. It has been shown by Chen and Bogy (1992a,b) that the eigenfunctions w^0_{mn} are orthogonal and form a complete system of functions in r and θ in the domain $0 \le \theta \le 2\pi$, $a \le r \le b$. We therefore can express the solution w of Eq. (5) as the following infinite series:

$$w = \sum_{m=0}^{\infty}\sum_{n=-\infty}^{\infty} c_{mn} w^0_{mn}(r, \theta). \quad (6)$$

From Eqs. (5) and (6) it is obvious that due to the integration only the one-nodal diameter modes will be affected by the inertial force associated with the rigid-body tilting. Using a technique presented in Chen and Bogy (1992a), the natural frequency change for mode $(m, 1)$ due to the rigid-body tilting can be estimated as

$$\Delta\lambda_{m1} = \frac{i\pi\rho^2 h^2 \omega^0_{m1}(\omega^0_{m1} \pm 2\Omega)\left[\int_a^b R^0_{m1}(r)r dr\right]^2}{2(I+I_c)(\omega^0_{m1} \pm \Omega)\int_a^b [R^0_{m1}(r)]^2 r dr} \begin{cases} + & \text{for backward wave} \\ - & \text{for forward wave.} \end{cases} \quad (7)$$

It is emphasized here that the displacement w in Eqs. (1)–(6) is measured relative to the noninertial tilting frame. So, the $(m, 1)$ mode of a spinning disk with a tilting clamp in Eq. (7) is a mode with m nodal circles and one nodal diameter as seen by an observer moving with the tilting frame. To an observer in the inertial frame, however, this mode appears to be an $(m+1, 1)$ mode. Therefore, $\Delta\lambda_{m1}$ in Eq. (7) can be reinterpretated by using the mode label system with respect to the inertial frame as the change of natural frequency from an $(m, 1)$ mode of the spinning disk without rigid body tilting to an $(m+1, 1)$ mode of the spinning disk with rigid-body tilting. The advantage of using the model label with respect to the inertial frame is that as the clamp torsional spring k_Θ varies from zero to infinity, the natural frequency of the $(m, 1)$ mode with rigid-body tilting converges to that of the $(m, 1)$ mode without rigid-body tilting. Although the mode label with respect to the tilting frame is more convenient for analysis and understanding in the context of our system of equations, the mode label with respect to the inertial frame gives a more standard notation. Therefore we will adopt the latter mode label with respect to the inertial frame in the following discussions and all the figures, unless stated otherwise explicitly. However, the switch between these two slightly different notations can be easily made.

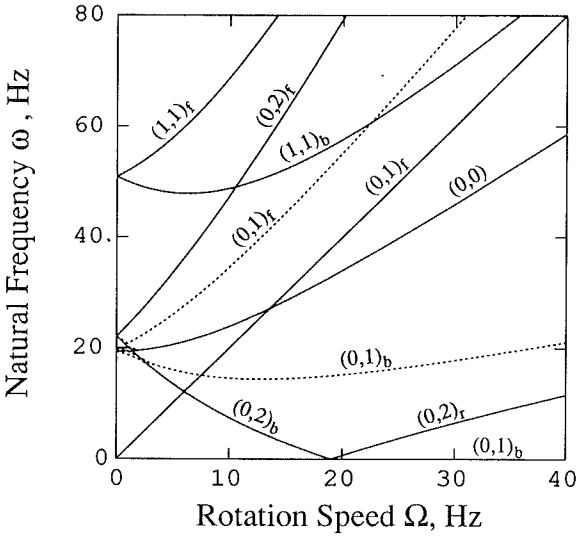


Fig. 2 Natural frequency versus rotation speed for a freely spinning flexible disk

It is obvious that $\Delta\lambda_{m1}$ in Eq. (7) is nonnegative for a backward travelling wave. However, for a forward travelling wave the term $\omega^0_{m1} - 2\Omega$ casts some uncertainties on whether $\Delta\lambda_{m1}$ is positive or negative. Figure 2 shows the relation between the natural frequencies of the spinning disk and the rotation speed. This result is obtained by a finite element computation which is similar to the one presented in Ono et al. (1991). The material properties of the disk used in the calculation are $\rho = 1.3 \times 10^3 \text{kg/m}^3$, $I_c = 0$, $E = 4.9 \times 10^9 \text{N/m}^2$, $\nu = 0.3$, $h = 0.078$ mm, $a = 30.0$ mm, $b = 65.0$ mm, and $\xi/b = 0.9$. For simplicity, only the first few modes with less than three nodal diameters are presented here. The dashed lines and the solid lines are the results for the spinning disk without and with rigid-body tilting, respectively. It is noted that for the system with rigid-body tilting, the mode label system with respect to the inertial frame has been adopted. The $(0, 1)_f$ mode (the diagonal line) and the $(0, 1)_b$ mode (the horizontal line with zero natural frequency) for the system with rigid-body tilting are the rigid displacement modes, i.e., $w = 0$. This can be easily checked by showing that the mode shapes $w = 0$, $\Theta_x = 1$, and $\Theta_y = \pm i$ with natural frequencies $\omega = 2\Omega$ and 0 satisfy

Downloaded 03 May 2010 to 171.66.16.245. Redistribution subject to ASME license or copyright; see http://www.asme.org/terms/Terms_Use.cfm

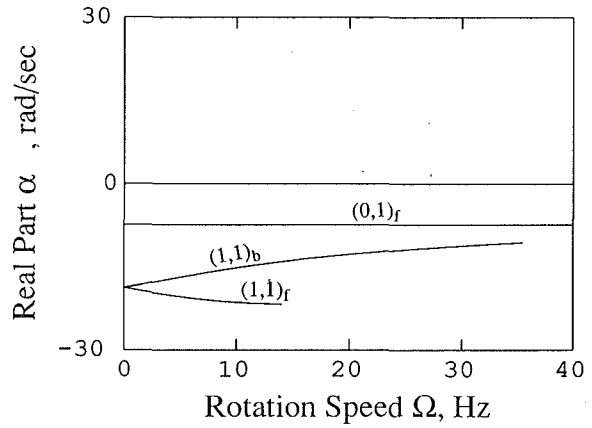


Fig. 3 Effects of clamp damping $c_\Theta = 10^{-5}$ Nms/rad

Eqs. (1)–(3). Because the ratio of the vertical and horizontal scales in Fig. 2 is 2, the slope of the diagonal line is actually 2. Now, in order for the term $\omega_{m1}^0 - 2\Omega$ in Eq. (7) to be negative, the dashed curve corresponding to the forward travelling wave would have to intersect the diagonal line. As we can see from Fig. 2, the dashed curve starts with unit slope at $\Omega = 0$, and increases its slope to more than 2 due to the effect of the centrifugal force. Consequently, the dashed line does not meet the diagonal line and the term $\omega_{m1}^0 - 2\Omega$ is always positive. This explains why the natural frequencies of both the forward and backward travelling waves (as seen by an observer moving with the tilting frame) increase for fixed Ω when the clamp is allowed to tilt freely. The modeshape of each one-nodal diameter mode (except for the rigid displacement modes $(0, 1)_f$ and $(0, 1)_b$) involves rigid body tiltings Θ_x and Θ_y with amplitudes

$$\Theta_{ym1} = \frac{\pi\rho h}{I}\int_a^b R_{m1}(r)r^2dr = \pm i\Theta_{xm1}\begin{cases}+\text{for backward wave}\\ -\text{for forward wave}\end{cases}$$

where $R_{m1}(r)$ corresponds to the new modeshape of the disk with rigid-body tilting.

We now consider the effects of changing the value of clamp damping c_Θ from 0 to 10^{-5} Nms/rad on the eigenvalues of the freely spinning disk with rigid-body tilting. It is found that the natural frequency-rotation speed diagram is not affected by the change of c_Θ and remains the same as the solid lines in Fig. 2. However, the real parts corresponding to the one-nodal diameter modes become negative for all the rotation speeds, as shown in Fig. 3. The real parts of all other modes are not affected by the change of c_Θ.

It is interesting to investigate the role that the centrifugal force plays in the dynamic behavior of this system. Figure 4 is the calculation result similar to that plotted in Fig. 2, except that the membrane stresses σ_r and σ_θ in Eq. (1) are set to zero. Now the slope of the dashed frequency locus corresponding to the forward travelling wave with one nodal diameter is exactly one and it meets the diagonal line at rotation speed Ω_A, at which $\omega_{m1}^0 - 2\Omega_A$ is equal to zero. To an observer moving with the tilting frame, as can be predicted by Eq. (7), the natural frequency of the forward travelling wave increases (from dashed line $(0, 1)_f$ to solid line $(1, 1)_f$ in Fig. 4) due to rigid body tilting when $\Omega < \Omega_A$, and decreases when $\Omega > \Omega_A$. The natural frequency of the backward travelling wave increases for all Ω except at the critical speed, at which the natural frequency remains zero. As Ω exceeds Ω_A, the forward travelling wave decreases and eventually merges with the reflected wave at point B, and instability is induced. Of course no physical phenomenon corresponding to Fig. 4 will occur because the centrifugal force always exists when the disk is spinning. However, this discussion shows that the centrifugal force plays a very important role in stabilizing the present system with rigid body

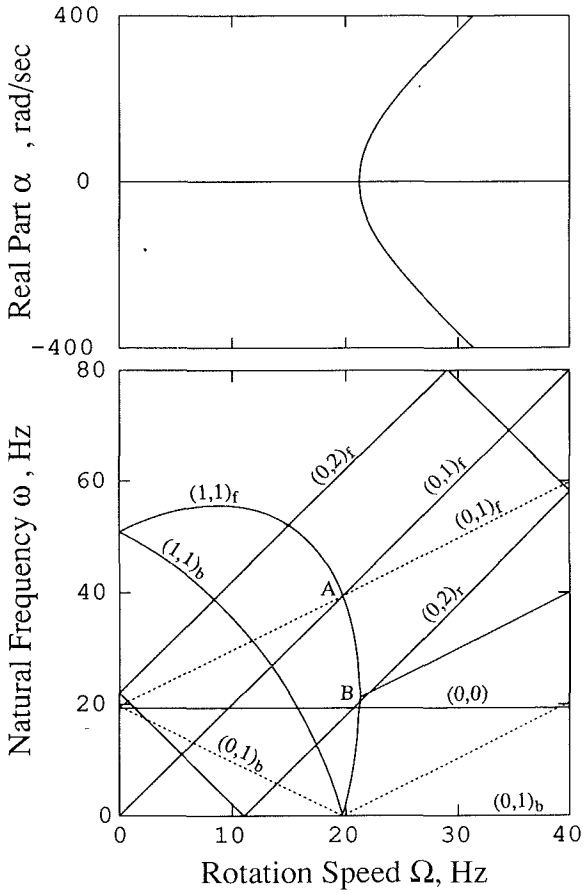


Fig. 4 The same as in Fig. 2 except that the membrane stresses are *neglected in the calculation*

tilting. In the conventional case without rigid-body tilting, on the other hand, neglecting the centrifugal force in the calculation will not induce any instability (Chen and Bogy, 1992a).

Stationary Disk With Rotating Load System

It is interesting to compare the results obtained in the previous section to the case of a stationary flexible disk with rigid-body tilting and subject to a rotating load system. To derive the equations of motion for this system, we first neglect F_z and M_ϕ and set Ω to zero in Eqs. (1), (2), and (3) to get the equations of motion of a stationary disk with respect to the *O-XYZ* frame. Suppose the *O-xyz* frame is rotating with the load system about the *OZ*-axis with rotation speed $-\Omega$. The terms $(\ddot{w})_{XYZ}$, $(\ddot{\Theta}_x)_{XYZ}$, and $(\ddot{\Theta}_y)_{XYZ}$ observed in the *O-XYZ* frame are related to the corresponding terms observed in the *O-xyz* frame through the equations

$$(\ddot{w})_{XYZ} = (w_{,tt})_{xyz} + 2\Omega(w_{,t\theta})_{xyz} + \Omega^2(w_{,\theta\theta})_{xyz} \tag{8}$$

$$(\ddot{\Theta}_x)_{XYZ} = (\ddot{\Theta}_x)_{xyz} + 2\Omega(\dot{\Theta}_y)_{xyz} - \Omega^2(\Theta_x)_{xyz} \tag{9}$$

$$(\ddot{\Theta}_y)_{XYZ} = (\ddot{\Theta}_y)_{xyz} - 2\Omega(\dot{\Theta}_x)_{xyz} - \Omega^2(\Theta_y)_{xyz}. \tag{10}$$

Equation (8) shows the relation between the Lagrangian and Eulerian descriptions of the function w. Equations (9) and (10) are the component forms of the well-known transformation equation of a single vector observed in two different frames (Meriam, 1980),

$$(\ddot{\boldsymbol{\Theta}})_{XYZ} = (\ddot{\boldsymbol{\Theta}})_{xyz} + 2\boldsymbol{\Omega}\times(\dot{\boldsymbol{\Theta}})_{xyz} + \boldsymbol{\Omega}\times\boldsymbol{\Omega}\times\boldsymbol{\Theta}$$

where vector $\boldsymbol{\Theta}$ is in the *XY*-plane with components $(\Theta_x, \Theta_y, 0)$, and vector $\boldsymbol{\Omega}$ is in the *OZ*-direction with amplitude Ω. As a consequence, the equations of motion for a stationary flexible disk with a rotating load system are, (relative to the rotating coordinate system)

Downloaded 03 May 2010 to 171.66.16.245. Redistribution subject to ASME license or copyright; see http://www.asme.org/terms/Terms_Use.cfm

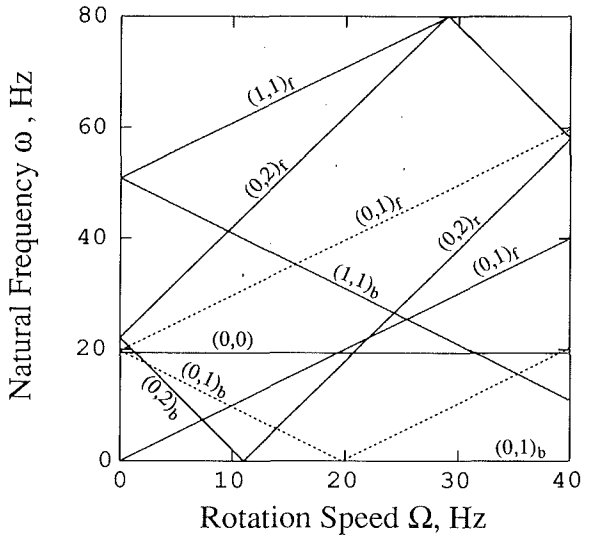


Fig. 5 Natural frequency versus rotation speed for a stationary flexible disk with rotating observer

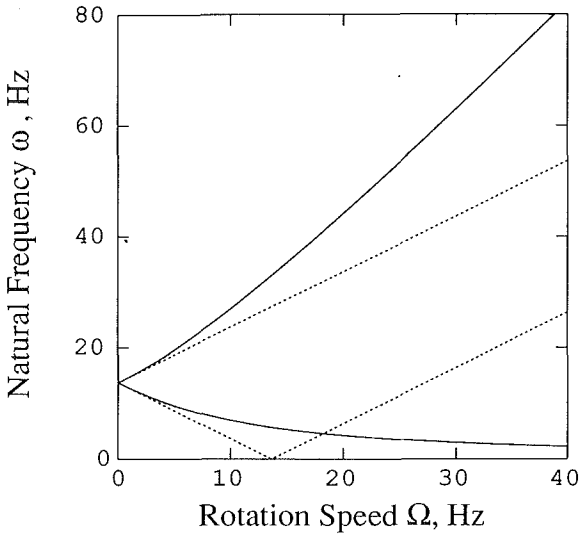


Fig. 6 Natural frequency versus rotation speed for an elastically supported rigid disk; k_Θ = 0.01 Nms/rad

$$\rho h(w_{,tt}+2\Omega w_{,t\theta}+\Omega^2 w_{,\theta\theta})+D\nabla^4 w+\rho hr[\ddot{\Theta}_x+2\Omega\dot{\Theta}_y-\Omega^2\Theta_x)\sin\theta - (\ddot{\Theta}_y-2\Omega\dot{\Theta}_x-\Omega^2\Theta_y)\cos\theta]=\frac{1}{r}\delta(r-\xi)\delta(\theta)F_z - \frac{1}{r^2}\delta(r-\xi)[M_\phi\delta(\theta)]_{,\theta} \quad (11)$$

$$(I+I_c)(\ddot{\Theta}_x+2\Omega\dot{\Theta}_y-\Omega^2\Theta_x)+\int_0^{2\pi}\int_a^b \rho h\sin\theta(w_{,tt}+2\Omega w_{,t\theta} + \Omega^2 w_{,\theta\theta})r^2 dr d\theta = M_\phi\delta(r-\xi)\delta(\theta)-k_\Theta\Theta_x-c_\Theta\dot{\Theta}_x \quad (12)$$

$$(I+I_c)(\ddot{\Theta}_y-2\Omega\dot{\Theta}_x-\Omega^2\Theta_y)-\int_0^{2\pi}\int_a^b \rho h\cos\theta(w_{,tt}+2\Omega w_{,t\theta} + \Omega^2 w_{,\theta\theta})r^2 dr d\theta = \xi F_z\delta(r-\xi)\delta(\theta)-k_\Theta\Theta_y-c_\Theta\dot{\Theta}_y. \quad (13)$$

After setting $k_\Theta = 0$, $c_\Theta = 0$, $F_z = 0$, $M_\phi = 0$, and substituting Eqs. (12) and (13) into Eq. (11), we obtain for the freely tilting disk in the absence of the load system

$$\rho h(w_{,tt}+2\Omega w_{,t\theta}+\Omega^2 w_{,\theta\theta})+D\nabla^4 w - \frac{r\rho^2 h^2}{(I+I_c)}\left[\cos\theta\int_0^{2\pi}\int_a^b r^2\cos\theta(w_{,tt}+2\Omega w_{,t\theta}+\Omega^2 w_{,\theta\theta})dr d\theta + \sin\theta\int_0^{2\pi}\int_a^b r^2\sin\theta(w_{,tt}+2\Omega w_{,t\theta}+\Omega^2 w_{,\theta\theta})dr d\theta\right]=0 \quad (14)$$

It is important to note that neglecting the membrane stresses σ_r and σ_θ in Eq. (5) does not result in Eq. (14) exactly, which contains the additional $w_{,\theta\theta}$ terms in the integrals. The natural frequency change for mode $(m, 1)$ (with respect to the tilting frame) due to rigid-body tilting can now be estimated as

$$\Delta\lambda_{m1}=\frac{i\pi\rho^2h^2(\omega_{m1}^0\pm\Omega)\left[\int_a^b R_{m1}^0(r)r dr\right]^2}{2(I+I_c)\int_a^b [R_{m1}^0(r)]^2 r dr}\begin{cases}+ \text{ for backward wave}\\ - \text{ for forward and reflected waves.}\end{cases} \quad (15)$$

It is noted that $R_{m1}^0(r)$ in Eq. (15) is independent of rotation speed Ω because no centrifugal force is involved. Furthermore, the term $\omega_{m1}^0 \pm \Omega$ is a constant and is equal to the natural frequency when $\Omega = 0$ (Chen and Bogy, 1992a). Consequently, $\Delta\lambda_{m1}$ is a constant and independent of the rotation speed. Figure 5 shows the relation between the natural frequency of the stationary flexible disk as observed from a rotating frame and the rotation speed of the frame. The dashed lines and the solid lines are the results for the cases without and with rigid-body tilting, respectively. The dashed lines in Fig. 5 are the same as those in Fig. 4, as explained in (Chen and Bogy, 1992a). The solid lines for the (1, 1) modes are parallel to the dashed lines for the (0, 1) modes with a constant shifting upward. No instability is induced due to the addition of the rigid-body tilting.

A Special Case: Elastically Supported Rigid Disk

The equations of motion in the inertial frame of a spinning rigid disk with tilting supported by a torsional spring k_Θ are obtained from Eqs. (2) and (3) by setting $w = 0$,

$$I(\ddot{\Theta}_x+2\Omega\dot{\Theta}_y)+k_\Theta\Theta_x+c_\Theta\dot{\Theta}_x=M_\phi\delta(r-\xi)\delta(\theta) \quad (16)$$

$$I(\ddot{\Theta}_y-2\Omega\dot{\Theta}_x)+k_\Theta\Theta_y+c_\Theta\dot{\Theta}_y=\xi F_z\delta(r-\xi)\delta(\theta). \quad (17)$$

On the other hand, the equations of motion in the rotating frame for a stationary rigid-disk subjected to a rotating load system are derived from Eqs. (12) and (13),

$$I(\ddot{\Theta}_x+2\Omega\dot{\Theta}_y-\Omega^2)+k_\Theta\Theta_x+c_\Theta\dot{\Theta}_x=M_\phi\delta(r-\xi)\delta(\theta) \quad (18)$$

$$I(\ddot{\Theta}_y-2\Omega\dot{\Theta}_x-\Omega^2)+k_\Theta\Theta_y+c_\Theta\dot{\Theta}_y=\xi F_z\delta(r-\xi)\delta(\theta). \quad (19)$$

It is noted that Stahl and Iwan (1973a,b) used different Euler angles in writing the equations of motion for a stationary disk with rotating load system. As a result their equations are more complicated than Eqs. (18) and (19), although they are essentially the same. We find here that the problem of a spinning rigid disk with a stationary load system is not exactly equivalent to the problem of a stationary rigid disk with rotating load system when rigid-body tilting is included. The differences between Eqs. (16), (17) and Eqs. (18), (19) are the terms containing Ω^2. In the case without rigid-body tilting, the equations of these two problems are exactly the same. The dashed straight lines in Fig. 6 are the natural frequencies of the stationary rigid disk with rotating observer. The stiffness of the clamp spring k_Θ is 0.01 Nm/rad and the value of the clamp damping c_Θ is 0. The slopes of the forward and backward waves are 1 and -1, respectively. There is a critical speed, beyond which the backward wave becomes a reflected wave. The solid lines are the natural frequencies of a spinning rigid disk observed

Downloaded 03 May 2010 to 171.66.16.245. Redistribution subject to ASME license or copyright; see http://www.asme.org/terms/Terms_Use.cfm

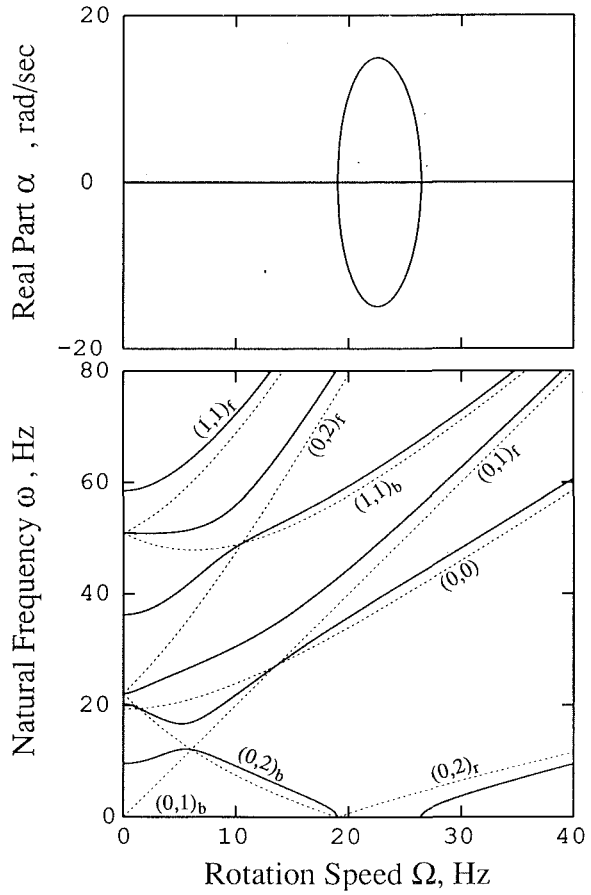


Fig. 7 Effects of transverse stiffness k_z = 5 N/m on the natural frequencies and stability of a flexible disk

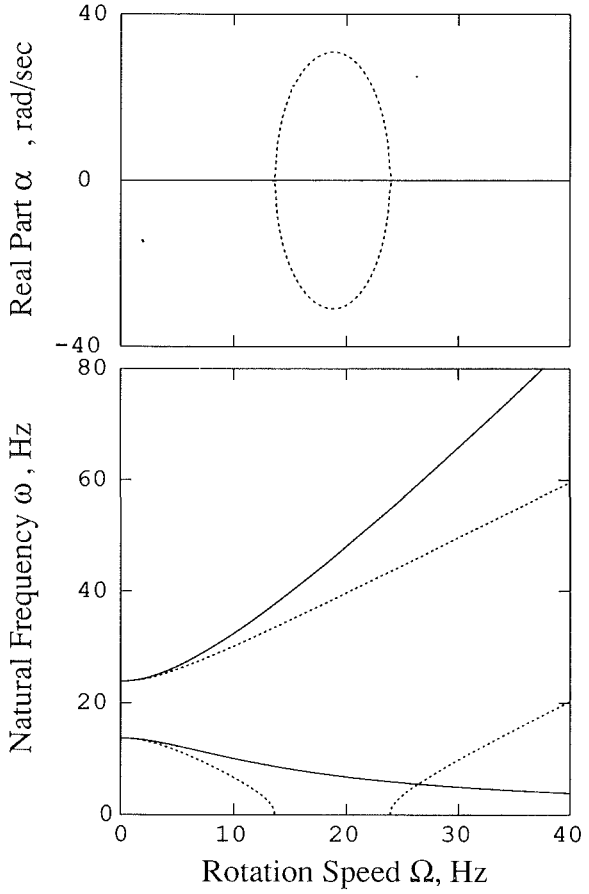


Fig. 8 Effects of transverse stiffness k_z = 5 N/m on the natural frequencies and stability of a rigid disk

by a stationary observer. The forward and backward frequency loci start with slope 1 and -1, respectively, at $\Omega = 0$. However, the slope of the forward wave approaches 2 as Ω increases. On the other hand, the natural frequency of the backward wave approaches zero asymptotically so there is no critical speed, and the backward wave will never become a reflected wave. These behaviors of the solid lines have been explained analytically by Arnold and Maunder (1961). The importance of this comparison between these two types of problems lies in the fact that instability will be induced when the rotating load system is loaded onto the stationary disk, as discussed by Stahl and Iwan (1973a,b). However, no instability will be induced when the stationary load system is loaded onto the spinning disk. An example will be given in the next section.

Effects of Load Parameters

We next consider the effects of the stationary load system spring with constant k_z on the natural frequencies and stability of the spinning flexible disk with rigid-body tilting. The clamp spring k_Θ and clamp damper c_Θ are set to 0. The dashed and the solid lines in Fig. 7 are the results for $k_z = 0$ and $k_z = 5$ N/m, respectively. By comparing the dashed lines and the solid lines, we can see that veering occurs whenever a forward or backward wave meets either another zero-nodal diameter mode, a forward or a backward wave. At the intersection point of any two curves for $k_z = 0$ at least one eigenvalue remains unchanged when k_z is introduced. When the eigenvalue of interest is well separated from the others the addition of k_z increases the natural frequency of a zero-nodal diameter mode, a forward or backward wave, but it decreases the natural frequency of a reflected wave. Furthermore, k_z causes a stationary-type instability (Ono et al., 1991) in a finite rotational speed range just beyond the critical speed. These properties are qualitatively the same as the effects of k_z in a conventional disk without rigid-body tilting (Chen and Bogy, 1992a,b). Unlike the case of a spinning flexible disk with axial translation (Chen and Bogy, 1992c), the additional rigid-body tilting mode does not eliminate the stationary-type instability induced by a load system transverse spring k_z.

Figure 8 shows the effects of $k_z = 5$ N/m on the elastically supported rigid disk, with the clamp spring $k_\Theta = 0.01$ Nm/rad. Similar to those in Fig. 6, the dashed lines are the results for a stationary disk with rotating load system, and the solid lines are the results for a spinning disk with stationary load system. By comparing with Fig. 6 we can see that for a stationary rigid disk k_z induces a stationary-type instability, as reported by Stahl and Iwan (1973a,b). On the other hand, for a spinning rigid disk k_z simply increases the natural frequencies of both the forward and backward waves, and induces no instability.

Figure 9 shows the effects of the load system mass m_z on the eigenvalues of a disk with rigid-body tilting. The dashed lines are the results for a freely spinning disk, and the solid lines are the results for $m_z = 1$ g. By comparing these results with those presented in Chen and Bogy (1992a,b) for the conventional case, we observe that the effects of m_z are qualitatively the same for both the cases, with and without rigid-body tilting. Additional calculations for the parameters c_z, k_ϕ, c_ϕ, and I_ϕ also show that the effects of these parameters are qualitatively the same for both the cases, with and without tilting. In particular, none of the pitching parameters have an effect on the zero nodal diameter modes. The dashed lines in Fig. 10 are for the freely spinning disk with rigid-body tilting and

Downloaded 03 May 2010 to 171.66.16.245. Redistribution subject to ASME license or copyright; see http://www.asme.org/terms/Terms_Use.cfm

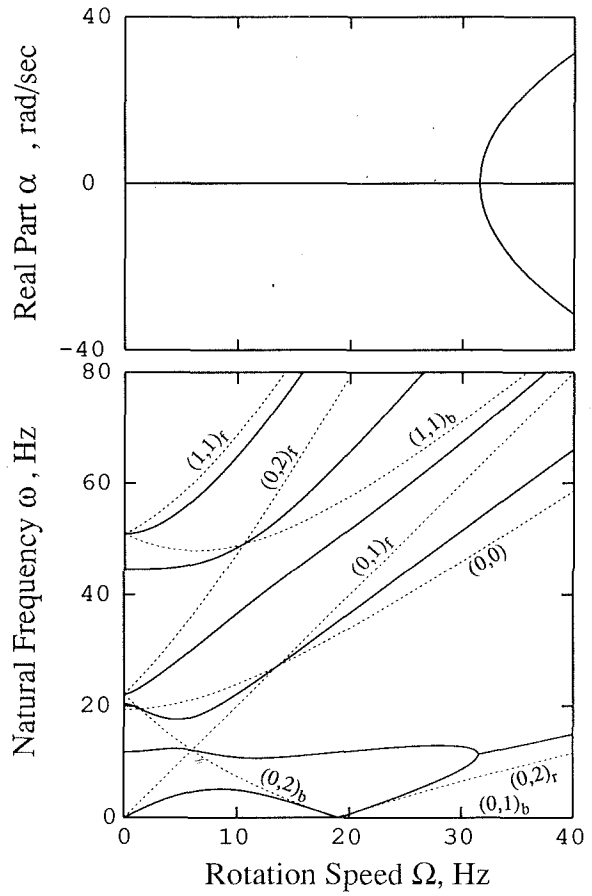


Fig. 9 Effects of transverse inertia m_z = 1 g

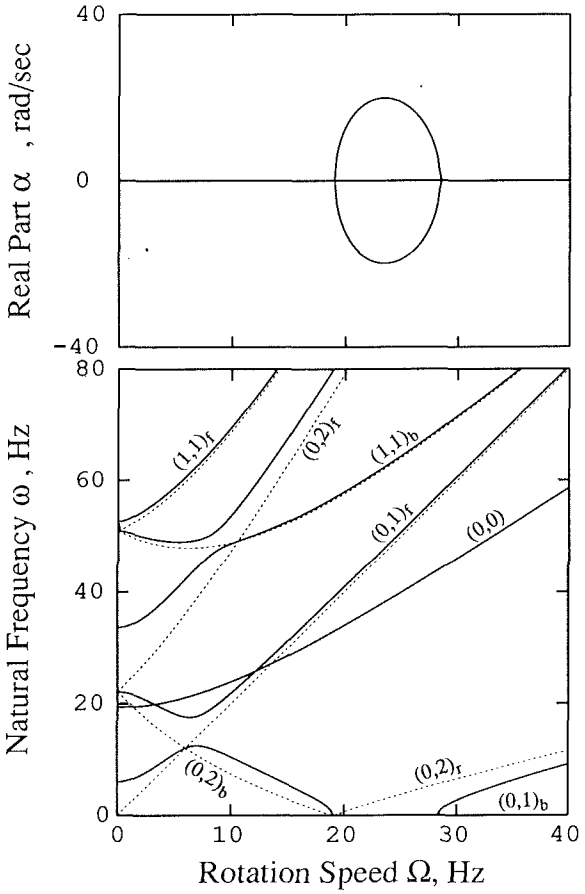


Fig. 10 Effects of pitching stiffness k_ϕ = 0.005 Nm/rad

the solid lines are for k_ϕ = 0.005 Nm/rad. It is noted that rigid-body tilting does not eliminate the stationary-type instability induced by the pitching stiffness k_ϕ.

Derivatives of the Eigenvalues

In Chen and Bogy (1992a), we showed that for a freely spinning disk without rigid-body tilting, the eigenfunctions are orthogonal to each other. Also it was shown that expressions for the derivatives of the eigenvalues with respect to the various parameters in the stationary load system can be derived and used to predict the change of eigenvalues for small values of the parameters. In Chen and Bogy (1992c), we extended this analysis to the case when the axial translation is included, and showed that the equations of motion fall into the category of gyroscopic systems. In this section we further extend the analysis to the case when the rigid-body tilting is included.

By following the same procedure as in Chen and Bogy (1992c), we can rewrite Eqs. (1), (2), and (3) in the matrix form

$$(\mathbf{M}+\hat{\mathbf{M}})\mathbf{u}_{,tt}+(\mathbf{G}+\hat{\mathbf{G}})\mathbf{u}_{,t}+(\mathbf{K}+\hat{\mathbf{K}})\mathbf{u}=0 \tag{20}$$

where the vector $\mathbf{u}$ is defined as

$$\mathbf{u}=\begin{Bmatrix} w \\ \Theta_x \\ \Theta_y \end{Bmatrix}$$

The matrix operators $\mathbf{M}$, $\mathbf{G}$, and $\mathbf{K}$ are associated with the freely spinning disk, while $\hat{\mathbf{M}}$, $\hat{\mathbf{G}}$, and $\hat{\mathbf{K}}$ are associated with the stationary load system. It is noted that Θ_x and Θ_y are functions of time only while w is also a function of r and θ. The inner product between two vectors $\mathbf{u}_1$ and $\mathbf{u}_2$ is defined as

$$\langle \mathbf{u}_1, \mathbf{u}_2\rangle = \int_0^{2\pi}\int_a^b \overline{w}_1 w_2 r dr d\theta + \overline{\Theta}_{x1}\Theta_{x2} + \overline{\Theta}_{y1}\Theta_{y2}.$$

In the case of a freely spinning disk, Eq. (20) reduces to

$$\mathbf{M}\mathbf{u}_{,tt}+\mathbf{G}\mathbf{u}_{,t}+\mathbf{K}\mathbf{u}=0. \tag{21}$$

It can be shown that the matrix operators $\mathbf{M}$ and $\mathbf{K}$ are symmetric and $\mathbf{G}$ is skew, i.e.,

$$\langle \mathbf{M}\mathbf{u}_1, \mathbf{u}_2\rangle = \langle \mathbf{u}_1, \mathbf{M}\mathbf{u}_2\rangle$$

$$\langle \mathbf{K}\mathbf{u}_1, \mathbf{u}_2\rangle = \langle \mathbf{u}_1, \mathbf{K}\mathbf{u}_2\rangle$$

$$\langle \mathbf{G}\mathbf{u}_1, \mathbf{u}_2\rangle = -\langle \mathbf{u}_1, \mathbf{G}\mathbf{u}_2\rangle$$

Equation (20) can also be written in the first order form

$$(\mathbf{A}+\hat{\mathbf{A}})\mathbf{x}_{,t}-(\mathbf{B}+\hat{\mathbf{B}})\mathbf{x}=\mathbf{0} \tag{22}$$

by defining the state vector

$$\mathbf{x}\equiv\begin{Bmatrix}\mathbf{u}_{,t}\\ \mathbf{u}\end{Bmatrix}$$

and the matrix operators

$$\mathbf{A}\equiv\begin{bmatrix}\mathbf{M} & \mathbf{0}\\ \mathbf{0} & \mathbf{K}\end{bmatrix},\quad \mathbf{B}\equiv\begin{bmatrix}-\mathbf{G} & -\mathbf{K}\\ \mathbf{K} & \mathbf{0}\end{bmatrix},$$

$$\hat{\mathbf{A}}\equiv\begin{bmatrix}\hat{\mathbf{M}} & \mathbf{0}\\ \mathbf{0} & \hat{\mathbf{K}}\end{bmatrix},\quad \hat{\mathbf{B}}\equiv\begin{bmatrix}-\hat{\mathbf{G}} & -\hat{\mathbf{K}}\\ \hat{\mathbf{K}} & \mathbf{0}\end{bmatrix}.$$

Now, the inner product between vectors $\mathbf{x}_1$ and $\mathbf{x}_2$ is defined as

$$\langle \mathbf{x}_1, \mathbf{x}_2\rangle = \int_0^{2\pi}\int_a^b (\overline{w}_{1,t}w_{2,t}+\overline{w}_1 w_2) r dr d\theta$$

$$+\dot{\overline{\Theta}}_{x1}\dot{\Theta}_{x2}+\overline{\Theta}_{x1}\Theta_{x2}+\dot{\overline{\Theta}}_{y1}\dot{\Theta}_{y2}+\overline{\Theta}_{y1}\Theta_{y2}$$

Again, it can be shown that $\mathbf{A}$ is symmetric and $\mathbf{B}$ is skew.

After establishing the above definitions and following the same procedure as that presented in Chen and Bogy (1992a),

Downloaded 03 May 2010 to 171.66.16.245. Redistribution subject to ASME license or copyright; see http://www.asme.org/terms/Terms_Use.cfm

we can readily show that the eigenfunctions $\mathbf{x}_{mn}$ and $\mathbf{x}_{pq}$ of a freely spinning disk with rigid-body tilting are orthogonal with respect to the operator $\mathbf{A}$, and that the derivative of eigenvalues with respect to a load parameter ρ_k is

$$\lambda_{mn,k} = -\frac{\langle \mathbf{x}_{mn}, (\lambda_{mn}\hat{\mathbf{A}}_{,k} - \hat{\mathbf{B}}_{,k})\mathbf{x}_{mn}\rangle}{\langle \mathbf{x}_{mn}, \mathbf{A}\mathbf{x}_{mn}\rangle} \tag{23}$$

where

$$\mathbf{x}_{mn} \equiv \begin{Bmatrix} i\omega_{mn} w_{mn} \\ i\omega_{mn}\Theta_{xmn} \\ i\omega_{mn}\Theta_{ymn} \\ w_{mn} \\ \Theta_{xmn} \\ \Theta_{ymn} \end{Bmatrix}.$$

By taking into account the fact that Θ_{xmn} and Θ_{ymn} are zero unless $n = 1$, a simple calculation (Chen and Bogy, 1992a) leads to

$$\langle \mathbf{x}_{mn}, \mathbf{A}\mathbf{x}_{mn}\rangle = \begin{cases} 4\pi\omega_{mn}(\omega_{mn} \pm n\Omega)\displaystyle\int_a^b R_{mn}^2(r) r dr & n \neq \pm 1 \\ 4\pi\omega_{mn}(\omega_{mn} + n\Omega)\left[\displaystyle\int_a^b R_{mn}^2(r) r dr - \frac{4\left(\displaystyle\int_a^b R_{mn}(r) r^2 dr\right)^2}{b^4 - a^4}\right] & n = \pm 1 \end{cases}. \tag{24}$$

For $n \neq \pm 1$, the term $\langle \mathbf{x}_{mn}, \mathbf{A}\mathbf{x}_{mn}\rangle$ is positive for both forward and backward travelling waves, and is negative for the reflected wave, as explained in Chen and Bogy (1992a). At the critical speed, however, the term $\langle \mathbf{x}_{mn}, \mathbf{A}\mathbf{x}_{mn}\rangle$ vanishes because ω_{mn} becomes zero. For $n = \pm 1$ the term $\langle \mathbf{x}_{mn}, \mathbf{A}\mathbf{x}_{mn}\rangle$ can be shown to be non-negative by using the Schwartz inequality

$$\left(\int_0^{2\pi}\int_a^b \overline{w}_1 w_2 r dr d\theta\right)^2 \leq \int_0^{2\pi}\int_a^b \overline{w}_1 w_1 r dr d\theta \quad \int_0^{2\pi}\int_a^b \overline{w}_2 w_2 r dr d\theta$$

where we choose $w_1 = R_{m1}(r)e^{i\theta}$ and $w_2 = re^{i\theta}$.

With Eq. (23) we now can calculate the derivative of the eigenvalue with respect to the transverse stiffness parameter k_z. We first derive $\partial\hat{\mathbf{A}}/\partial k_z$ and $\partial\hat{\mathbf{B}}/\partial k_z$, and substitute the results into Eq. (23) to obtain

$$\frac{\partial\lambda_{mn}}{\partial k_z} = \frac{i\omega_{mn}[R_{mn}(\xi) - \xi\Theta_{ymn}]^2}{\rho h\langle \mathbf{x}_{mn}, \mathbf{A}\mathbf{x}_{mn}\rangle} \tag{25}$$

Since $\Theta_{xmn} = 0$, $\Theta_{ymn} = 0$, and $R_{mn}(r) = R_{mn}^0(r)$ for $n \neq 1$, this expression is the same as that for the conventional disk without rigid-body tilting presented in Chen and Bogy (1992a) for the modes with other than one nodal diameter. This means that for $n \neq 1$ the effects of k_z on the eigenvalues are the same for both cases, with and without rigid-body tilting. For the one-nodal diameter modes, on the other hand, k_z increases the natural frequencies but by different amounts for the cases with and without rigid-body tilting.

By following similar procedures, we obtain the derivatives of the eigenvalues with respect to c_z and m_z by replacing $i\omega_{mn}$ in Eq. (25) by $-\omega_{mn}^2$ and $-i\omega_{mn}^3$, respectively, and similar conclusions follow accordingly. The derivatives with respect to the pitching parameters are the same as those of their transverse counterparts, except that there is a multiplicative factor n^2/ξ^2 in the numerators. This confirms the numerical results, which showed that pitching parameters have no effect on the zero-nodal diameter modes because $n = 0$.

Conclusions

The effects of rigid-body tilting on the dynamics of a flexible spinning disk in contact with a stationary load system are examined both numerically and analytically. The results of these analyses can be summarized as follows:

(1) To an observer moving with the tilting frame, the natural frequencies of one-nodal diameter modes increase due to the inertial coupling between the rigid-body tilting and the elastic deformation, while the natural frequencies of the modes with other than one-nodal diameter are not affected.

(2) In the conventional case without rigid-body tilting, neglecting the centrifugal force in the calculation will not affect the stability property of the freely spinning disk. However, in the present case with rigid-body tilting, the centrifugal force is very important in stabilizing the system.

(3) Another type of problem in which a stationary flexible disk is subject to a rotating load system is also considered. In the conventional case without rigid-body tilting, these two types of problems are mathematically identical except for the additional stress terms arising from the centrifugal force. In the case with rigid-body tilting, however, these two types of problem differ not only by the centrifugal effect, but also by the terms arising from the gyrodynamic effect.

(4) The rigid-body tilting does not eliminate any instability induced by any parameter in the stationary load system. It may be futile trying to improve the stability property of a spinning disk by allowing it to tilt.

(5) The system of equations of motion is again proven to be gyroscopic in the presence of rigid-body tilting. As a result, the techniques developed in previous papers (Chen and Bogy, 1992a,b,c) are extended to the current case to obtain the derivatives of eigenvalues with respect to various load system parameters. These derivatives provide a theoretical understanding for the numerical results obtained.

Acknowledgment

This work was supported by the Computer Mechanics Laboratory at the University of California at Berkeley.

References

Arnold, R. N., and Maunder, L., 1961, *Gyrodynamics and Its Engineering Applications*, Academic Press, New York.

Chen, J.-S., and Bogy, D. B., 1992a, "Effects of Load Parameters on the Natural Frequencies and Stability of a Flexible Spinning Disk With a Stationary Load System," ASME JOURNAL OF APPLIED MECHANICS, Vol. 59, pp. S230–S235.

Chen, J.-S., and Bogy, D. B., 1992b, "Mathematical Structure of Modal Interactions in a Spinning Disk-Stationary Load System," ASME JOURNAL OF APPLIED MECHANICS, Vol. 59, pp. 390–397.

Chen, J.-S., and Bogy, D. B., 1992c, "Natural Frequencies and Stability of a Flexible Spinning Disk-Stationary Load System With Axial Spindle Displacement," submitted to ASME JOURNAL OF APPLIED MECHANICS.

Iwan, W. D. and Moeller, T. L., 1976, "The Stability of a Spinning Elastic Disk With a Transverse Load System," ASME JOURNAL OF APPLIED MECHANICS, Vol. 43, pp. 485–490.

Jeong, T. G., and Bogy, D. B., 1991, "Slider-Disk Contacts During Dynamic Load-Unload," *IEEE Transactions on Magnetics*, Vol. 27, pp. 5073–5075.

Meriam, J. L., 1980, *Dynamics*, John Wiley and Sons, New York.

Mote, C. D., Jr., 1977, "Moving Load Stability of a Circular Plate on a Floating Central Collar," *Journal of Acoustical Society of America*, Vol. 61, No. 2, pp. 445–451.

Ono, K., Chen, J.-S., and Bogy, D. B., 1991, "Stability Analysis of the Head-Disk Interface in a Flexible Disk Drive," ASME JOURNAL OF APPLIED MECHANICS, Vol. 58, No. 4, pp. 1005–1014.

Price, K. B., 1987, "Analysis of the Dynamics of Guided Rotating Free Center Plates," Ph.D. Dissertation, University of California, Berkeley.

Shen, I.-Y., and Mote, C. D., Jr., 1991, "On the Mechanisms of Instability of a Circular Plate Under a Rotating Spring-Mass-Dashpot System," *Journal of Sound and Vibration*, Vol. 148, No. 2, pp. 307–318.

Stahl, K. J., and Iwan, W. D., 1973a, "On the Response of an Elastically Supported Rigid Disk With a Moving Massive Load," *International Journal of Mechanical Science*, Vol. 15, pp. 535–546.

Stahl, K. J., and Iwan, W. D., 1973b, "On the Response of a Two-Degree-of-Freedom Rigid Disk With a Moving Massive Load," ASME JOURNAL OF APPLIED MECHANICS, pp. 114–120.

Yang, S.-M., 1988, "Vibration and Stability of Rotating and Translating Plates," Ph.D. Dissertation, University of California, Berkeley.

Downloaded 03 May 2010 to 171.66.16.245. Redistribution subject to ASME license or copyright; see http://www.asme.org/terms/Terms_Use.cfm

Exact Analytical Solutions for the Vibrations of Sectorial Plates With Simply-Supported Radial Edges

C. S. Huang
Department of Civil Engineering.

A. W. Leissa
Department of Engineering Mechanics, Fellow ASME.

O. G. McGee
Department of Civil Engineering.

Ohio State University, Columbus, OH 43210

The first known exact analytical solutions are derived for the free vibrations of sectorial thin plates having their radial edges simply supported, with arbitrary conditions along their circular edges. This requires satisfying: (1) the differential equation of motion, (2) boundary conditions along the radial and circular edges, and (3) proper regularity conditions at the vertex of the radial edges. The solution to the differential equation involves ordinary and modified Bessel functions of the first and second kinds, of non-integer order, and four constants of integration. Utilizing a careful limiting process, the regularity conditions are invoked to develop two equations of constraint among the four constants for sector angles exceeding 180 deg (re-entrant corners). Moment singularities for re-entrant corners are shown to be the same as the ones determined by Williams (1952) for statically loaded sectorial plates. Frequency determinants and equations are generated for circular boundaries which are clamped, simply-supported, or free. Nondimensional frequency parameters are presented for all three types of configurations for sector angles of 195, 210, 270, 330, and 360 deg (i.e., re-entrant corners).

Introduction

At least 200 published references can be found in the literature dealing with the free vibrations of complete circular plates (i.e., no radial boundaries). However, relatively little has been done for the sectorial plate; that is, a plate bounded by a circle arc and two radial lines (see Fig. 1). Approximate theoretical results were obtained by Ben-Amoz (1959), Westmann (1962), Rubin (1975), and Bhattacharya and Bhowmic (1975) for cases when the radial boundaries are clamped. Experimental results were reported by Maruyama and Ichinomiya (1981) for the case when all three edges are clamped.

It was shown by Leissa (1969) that the exact, analytical solutions for free vibrations of complete circular plates with arbitrary (but continuous) conditions along the boundaries (e.g., clamped, simply-supported, or free) may also be applied to sectorial plates with the radial edges simply-supported. These solutions utilize the Bessel functions of the first kind, $J_\mu(kr)$ and $I_\mu(kr)$, where μ is typically not an integer. An equivalent procedure was later used by Rubin (1975); however, solutions to the equation of motion were developed by the Frobenius method, instead of using Bessel functions.

A recent investigation by the present authors (1992a) demonstrated that the Bessel function solution of complete circular plates may not be used for sectorial plates with simply-supported radial edges when the sector angle, α (see Fig. 1), exceeds 180 deg. This is because the singularity in the vibratory bending moment is incorrectly represented by this solution. It was shown, rather, that such configurations could be represented by an *annular* sectorial plate (i.e., one having a simply-supported inner radius, b, as well as an outer radius, a), and taking the limit by a numerical procedure as $b/a \rightarrow 0$. This solution was verified by an approximate, but accurate, procedure utilizing the Ritz method along with two sets of admissible transverse displacement functions, simultaneously employed—one set consisting of algebraic-trigonometric polynomials, and the other one of corner functions which yield the proper corner singularities.

In the present paper the first known *exact* analytical solutions

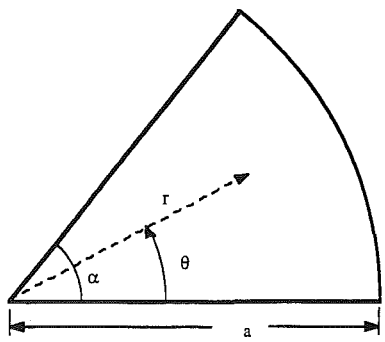


Fig. 1 Sectorial plate

Contributed by the Applied Mechanics Division of THE AMERICAN SOCIETY OF MECHANICAL ENGINEERS for presentation at the First Joint ASCE-EMD, ASME-AMD, SES Meeting, Charlottesville, VA, June 6-9, 1993.

Discussion on this paper should be addressed to the Technical Editor, Professor Lewis T. Wheeler, Department of Mechanical Engineering, University of Houston, Houston, TX 77204-4792, and will be accepted until four months after final publication of the paper itself in the ASME JOURNAL OF APPLIED MECHANICS.

Manuscript received by the ASME Applied Mechanics Division, Oct. 21, 1991; final revision, Aug. 7, 1992. Associate Technical Editor: F. Y. M. Wan.

Paper No. 93-APM-31.

Copyright © 1993 by ASME
Downloaded 03 May 2010 to 171.66.16.245. Redistribution subject to ASME license or copyright; see http://www.asme.org/terms/Terms_Use.cfm

are developed for the free vibrations of sectorial plates having simply-supported radial edges forming re-entrant corners ($\alpha > 180$ deg). With these solutions, the intricate computational procedures required of the two methods described above are not required.

Exact Solution

The equation of motion for the free vibration of a thin, homogeneous, isotropic plate is (cf. Leissa, 1969)

$$D\nabla^4 w + \rho \frac{\partial^2 w}{\partial t^2} = 0 \tag{1}$$

where $w = w(r, \theta, t)$ is the transverse displacement, ∇^4 is the biharmonic differential operator, $D = Eh^3/12(1-\nu^2)$ is the flexural rigidity, E is the modulus of elasticity, h is the thickness, ν is Poisson's ratio, and ρ is the mass density per unit plate area. Assuming first a sinusoidal motion in time,

$$w(r,\theta,t) = W(r,\theta)\cos \omega t, \tag{2}$$

then Eq. (1) becomes

$$(\nabla^4 - k^4) W = 0 \tag{3}$$

where $k^4 = \rho\omega^2/D$.

Equation (3) may be factored into

$$(\nabla^2 + k^2)(\nabla^2 - k^2) W = 0 \tag{4}$$

and the solution of Eq. (4) is then the sum of the two solutions W_1 and W_2 arising from

$$(\nabla^2 + k^2) W_1 = 0 \tag{5a}$$

$$(\nabla^2 - k^2) W_2 = 0. \tag{5b}$$

Utilizing the polar coordinates of Fig. 1, it is further assumed that

$$W_i(r,\theta) = R_{ni}(r)\sin \frac{n\pi\theta}{\alpha} \quad (i = 1, 2;\ n = 1, 2, \ldots). \tag{6}$$

This satisfies the simply-supported boundary conditions along $\theta = 0$ and $\theta = \alpha$ exactly. That is,

$$w(r,0,t) = w(r,\alpha,t) = 0 \tag{7a}$$

$$M_\theta(r,0,t) = M_\theta(r,\alpha,t) = 0 \tag{7b}$$

where M_θ is the circumferential bending moment

$$M_\theta = -D\left[\left(\frac{1}{r}\frac{\partial w}{\partial r} + \frac{1}{r^2}\frac{\partial^2 w}{\partial \theta^2}\right) + \nu \frac{\partial^2 w}{\partial r^2}\right]. \tag{8}$$

Substituting Eq. (6), and considering the orthogonality of $\sin n\pi/\theta$ over the interval $0 \le \theta \le \alpha$, Eqs. (5) become

$$r^2 R_{n1}'' + r R_{n1}' + (k^2 r^2 - \mu^2) R_{n1} = 0 \tag{9a}$$

$$r^2 R_{n2}'' + r R_{n2}' - (k^2 r^2 - \mu^2) R_{n2} = 0 \tag{9b}$$

where the primes indicate derivatives, and $\mu = n\pi/\alpha$ is positive and is typically *not* an integer (although it can be). Equations (9) have solutions

$$R_{n1} = A_n J_\mu(kr) + B_n Y_\mu(kr) \tag{10a}$$

$$R_{n2} = C_n I_\mu(kr) + D_n K_\mu(kr) \tag{10b}$$

where J_μ, Y_μ, I_μ, and K_μ are ordinary and modified Bessel functions of the first and second kinds, and A_n, B_n, C_n, and D_n are arbitrary constants of integration.

Thus, the solution to the equation of motion (1) for each mode of free vibration is

$$w(r,\theta,t) = [A_n J_\mu(kr) + B_n Y_\mu(kr) + C_n I_\mu(kr) + D_n K_\mu(kr)]\sin \mu\theta \cos \omega t \quad (\mu > 0). \tag{11}$$

Equation (11) is the same as the classical solution employed for complete circular plates, except that:

(1) μ is not, in general, and integer, and

(2) B_n and D_n are not necessarily set equal to zero.

That is, for the complete circular plate, the Bessel functions of the second kinds Y_μ and K_μ are dropped from the solution to eliminate all singularities at the plate center ($r = 0$). For the sectorial plate with a re-entrant corner ($\alpha > \pi$), certain singularities are acceptable at the corner (e.g., bending moments and transverse shearing forces). However, two regularity conditions must be enforced at $r = 0$:

$$(1) \quad w(0,\theta,t) = 0 \tag{12a}$$

$$(2) \quad \frac{\partial w}{\partial r}(0,\theta,t) = \text{finite}. \tag{12b}$$

Considering first the displacement condition given by Eq. (12a), since

$$J_\mu(0) = I_\mu(0) = 0 \quad (\text{for } \mu > 0), \tag{13}$$

then Eq. (12a) becomes

$$\lim_{r\to 0}[B_n Y_\mu(kr) + D_n K_\mu(kr)] = 0. \tag{14}$$

The Bessel functions of the second kind may be expressed as (cf. Tranter, 1968)

$$Y_\mu(kr) = \frac{\cos \mu\pi \cdot J_\mu(kr) - J_{-\mu}(kr)}{\sin \mu\pi} \tag{15a}$$

$$K_\mu(kr) = \frac{\pi}{2}\frac{I_{-\mu}(kr) - I_\mu(kr)}{\sin \mu\pi}. \tag{15b}$$

Utilizing Eq. (13) in (15), and substituting this in Eq. (14), the latter becomes

$$\lim_{r\to 0}\left[-B_n J_{-\mu}(kr) + \frac{\pi}{2} D_n I_{-\mu}(kr)\right] = 0. \tag{16}$$

The Bessel functions may be expressed in terms of their power series

$$J_{-\mu}(kr) = \sum_{j=0,1}^{\infty} \frac{(-1)^j (kr/2)^{-\mu+2j}}{j!\Gamma(-\mu+j+1)} \tag{17a}$$

$$I_{-\mu}(kr) = \sum_{j=0,1}^{\infty} \frac{(kr/2)^{-\mu+2j}}{j!\Gamma(-\mu+j+1)} \tag{17b}$$

where Γ is the gamma function. Substituting Eqs. (17) into (16), and considering that B_n and D_n are finite, to satisfy Eq. (16) the coefficients of r with degree $(-\mu + 2j)$ less than or equal to zero must vanish. That is,

$$-(-1)^j B_n + \frac{\pi}{2} D_n = 0 \quad (-\mu + 2j \le 0;\ \ j = 0, 1, 2 \ldots). \tag{18}$$

Taking up next the slope condition given by Eq. (12b), it may be written as

$$\lim_{r\to 0}[A_n J_\mu'(kr) + B_n Y_\mu'(kr) + C_n I_\mu'(kr) + D_n K_\mu'(kr)] = \text{finite}. \tag{19}$$

The derivatives of the Bessel functions may be expressed as (cf. Tranter, 1968):

$$\begin{aligned} 2J_\mu'(kr) &= J_{\mu-1}(kr) - J_{\mu+1}(kr) \\ 2Y_\mu'(kr) &= Y_{\mu-1}(kr) - Y_{\mu+1}(kr) \\ 2I_\mu'(kr) &= I_{\mu-1}(kr) + I_{\mu+1}(kr) \\ 2K_\mu'(kr) &= -K_{\mu-1}(kr) - K_{\mu+1}(kr). \end{aligned} \tag{20}$$

Substituting Eqs. (15) and (20), and using (13), Eq. (19) becomes

Downloaded 03 May 2010 to 171.66.16.245. Redistribution subject to ASME license or copyright; see http://www.asme.org/terms/Terms_Use.cfm

$$\lim_{r\to 0}\left\{A_n J_{\mu-1}(kr)+B_n\left[\frac{\cos(\mu-1)\pi\cdot J_{\mu-1}(kr)-J_{-\mu+1}(kr)}{\sin(\mu-1)\pi}+\frac{J_{-\mu-1}(kr)}{\sin(\mu+1)\pi}\right]+C_n I_{\mu-1}(kr)-D_n\frac{\pi}{2}\times\left[\frac{I_{-\mu+1}(kr)-I_{\mu-1}(kr)}{\sin(\mu-1)\pi}+\frac{I_{-\mu-1}(kr)}{\sin(\mu+1)\pi}\right]\right\}=\text{finite}. \quad (21)$$

This yields, upon substituting Eqs. (17),

$$\lim_{r\to 0}\sum_{j=0,1}^{\infty}\left\{A_n\frac{(-1)^j(kr/2)^{\mu+2j-1}}{j!\Gamma(\mu+j)}+B_n\left[\frac{\cos(\mu-1)\pi}{\sin(\mu-1)\pi}\cdot\frac{(-1)^j(kr/2)^{\mu+2j-1}}{j!\Gamma(\mu+j)}-\frac{1}{\sin(\mu-1)\pi}\cdot\frac{(-1)^j(kr/2)^{-\mu+2j+1}}{j!\Gamma(-\mu+j+2)}+\frac{1}{\sin(\mu+1)\pi}\cdot\frac{(-1)^j(kr/2)^{-\mu+2j-1}}{j!\Gamma(-\mu+j)}\right]+C_n\frac{(kr/2)^{\mu+2j-1}}{j!\Gamma(\mu+j)}-D_n\left[\frac{\pi}{2\sin(\mu-1)\pi}\cdot\frac{(kr/2)^{-\mu+2j+1}}{j!\Gamma(-\mu+j+2)}-\frac{\pi}{2\sin(\mu-1)\pi}\frac{(kr/2)^{\mu+2j-1}}{j!\Gamma(\mu+j)}+\frac{\pi}{2\sin(\mu+1)\pi}\times\frac{(kr/2)^{-\mu+2j-1}}{j!\Gamma(-\mu+j)}\right]\right\}=\text{finite} \quad (22)$$

Because $A_n, \ldots, D_n$ are finite, satisfaction of Eq. (22) requires that the coefficients of r with power less than zero vanish. To simplify the analysis without loss of generality, the range of μ will first be taken up in detail in the subintervals $0 < \mu < 1$ and $1 < \mu < 2$.

Case 1: $0 < \mu < 1$. In this case all terms vanish in the limit except those of $j = 0$. The remaining terms contain $r^{\mu-1}$ and $r^{-\mu-1}$. From the coefficients of $r^{-\mu-1}$,

$$\frac{1}{\sin(\mu-1)\pi}\cdot\frac{B_n}{\Gamma(-\mu)}-\frac{\pi}{2\sin(\mu+1)\pi}\cdot\frac{D_n}{\Gamma(-\mu)}=0. \quad (23)$$

From the coefficients of $r^{\mu-1}$,

$$\frac{A_n}{\Gamma(\mu)}+\frac{\cos(\mu-1)\pi}{\sin(\mu-1)\pi}\frac{B_n}{\Gamma(\mu)}+\frac{C_n}{\Gamma(\mu)}+\frac{\pi}{2\sin(\mu-1)\pi}\cdot\frac{D_n}{\Gamma(\mu)}=0. \quad (24)$$

Equation (23) reduces to

$$B_n=\frac{\pi}{2}D_n \quad (25)$$

which is consistent with Eq. (18). Using this in Eq. (24), and simplifying the latter, gives

$$A_n+\frac{1+\cos(\mu-1)\pi}{\sin(\mu-1)\pi}B_n+C_n=0. \quad (26)$$

Case 2: $1 < \mu < 2$. In this case all terms vanish in the limit except those containing $r^{-\mu+2j+1}$ for $j = 0$ and $r^{-\mu+2j-1}$ for $j = 0$ and 1. The remaining terms contain $r^{-\mu+1}$ and $r^{-\mu-1}$. The coefficients of $r^{-\mu-1}$ yield Eq. (25). From the coefficients of $r^{-\mu+1}$,

$$B_n\left[-\frac{1}{\sin(\mu-1)\pi}\cdot\frac{1}{\Gamma(-\mu+2)}+\frac{1}{\sin(\mu+1)\pi}\cdot\frac{1}{\Gamma(-\mu+1)}\right]-D_n\left[\frac{\pi}{2\sin(\mu-1)\pi}\cdot\frac{1}{\Gamma(-\mu+2)}+\frac{\pi}{2\sin(\mu+1)\pi}\cdot\frac{1}{\Gamma(-\mu+1)}\right]=0. \quad (27)$$

Equations (25) and (27) together yield $B_n = D_n = 0$.

For $\mu > 2$, one finds that Eq. (22) generates more than two linearly independent, homogeneous equations in B_n and D_n. Therefore, again $B_n = D_n = 0$.

For *integer* values of μ, in a manner similar to that above, one can also prove that $B_n = D_n = 0$. This can be easily done using equations similar to (15) and (17), but for Bessel functions of integer order.

Moment Singularities

It has been shown (Huang, 1991; Leissa, McGee, and Huang, 1992a) that the bending moment singularities in the sectorial plate vibration solutions for $\mu \geq 1$ (i.e., $\alpha \leq \pi$ in Fig. 1) are exactly the same as those found in the static, biharmonic functions derived by Williams (1952). That is, as shown in the preceding section, for such sector angles, $B_n = D_n = 0$. Furthermore, whereas the moment singularity occurs for $\mu < 2$ (i.e., $\alpha > \pi/2$), the sectorial plate vibration solutions using $B_n = D_n = 0$ were found to yield the correct singularities in the range $1 \leq \mu < 2$; that is, $\pi/2 < \alpha \leq \pi$.

It remains to be shown that the solutions using Eqs. (25) and (26) represent the singularities correctly in the range $0 < \mu < 1$ ($\alpha > \pi$).

The radial bending moment is given by

$$M_r=-D\left[\frac{\partial^2 W}{\partial r^2}+\nu\left(\frac{1}{r}\frac{\partial W}{\partial r}+\frac{1}{r^2}\frac{\partial^2 W}{\partial\theta^2}\right)\right]. \quad (28)$$

Let $\overline{M}_r$ be the quantity in the brackets of Eq. (28), evaluated at a typical time (t) and along a typical radial line (θ = constant). Then, using Eq. (11) and derivative formulas similar to Eqs. (20), $\overline{M}_r$ may be expressed as

$$\overline{M}_r=A_n\left\{J_\mu(kr)-(1-\nu)\left[\frac{\mu(\mu-1)}{(kr)^2}J_\mu(kr)+\frac{1}{kr}J_{\mu+1}(kr)\right]\right\}+B_n\left\{Y_\mu(kr)-(1-\nu)\left[\frac{\mu(\mu-1)}{(kr)^2}Y_\mu(kr)+\frac{1}{kr}Y_{\mu+1}(kr)\right]\right\}-C_n\left\{I_\mu(kr)+(1-\nu)\left[\frac{\mu(\mu-1)}{(kr)^2}I_\mu(kr)-\frac{1}{kr}I_{\mu+1}(kr)\right]\right\}-D_n\left\{K_\mu(kr)+(1-\nu)\left[\frac{\mu(\mu-1)}{(kr)^2}K_\mu(kr)+\frac{1}{kr}K_{\mu+1}(kr)\right]\right\}. \quad (29)$$

Substituting Eqs. (15), (17), (25), and (26) into (29) one finds that

$$\overline{M}_r|_{r=0}=\lim_{r\to 0}\left[-2B_n\left\{\frac{1}{\sin\mu\pi\cdot\Gamma(-\mu+1)}+\left[(1-\nu)\frac{\mu(\mu-1)}{4\sin\mu\pi\cdot\Gamma(-\mu+2)}+\frac{1}{2\sin(\mu+1)\pi\cdot\Gamma(\mu+1)}\right]\right\}\left(\frac{kr}{2}\right)^{-\mu}\right]. \quad (30)$$

Equation (30) shows that the order of the singularity for M_r at $r = 0$ is $-\mu$, which is the same as for Williams' (1952) static biharmonic functions. Similarly, as expected, the order of the singularities in the circumferential bending moment (M_θ) and the twisting moment ($M_{r\theta}$) at $r = 0$ is also $-\mu$.

Frequency Determinants and Equations

In the work above, the solution to the differential equation of motion (1), which also satisfies the radial edge simple support boundary conditions (7), is given in Eq. (11). Imposing regularity conditions at $r = 0$ yields two constraint equations among the constants $A_n, \ldots, D_n$, either Eqs. (25) and (26)

Downloaded 03 May 2010 to 171.66.16.245. Redistribution subject to ASME license or copyright; see http://www.asme.org/terms/Terms_Use.cfm

(for $0 < \mu < 1$) or $B_n = D_n = 0$ (for $\mu \geq 1$). Two additional equations may be obtained by applying the boundary conditions along the circular edge ($r = a$). Doing so yields four homogeneous, algebraic equations in $A_n, \ldots, D_n$. Setting the determinant of the fourth-order coefficient matrix equal to zero results in the frequency determinant, from which the eigenvalues

$$\lambda = ka = (\omega a^2 \sqrt{\rho/D})^{1/2} \tag{31}$$

may be determined. The two cases, $0 < \mu < 1$ and $\mu \geq 1$, must be considered separately.

Case 1: $0 < \mu < 1$. In this case the sector angle exceeds a semicircle ($\alpha > 180$ deg), and there are no radial node lines. Free vibration modes with radial node lines for 180 deg $< \alpha \leq$ 360 deg fall into Case 2, because radial node lines duplicate simply-supported boundary conditions.

Three types of boundary conditions are considered along the circular edge:

clamped: $$w(a,\theta,t) = \frac{\partial w}{\partial r}(a,\theta,t) = 0 \tag{32a}$$

simply-supported: $$w(a,\theta,t) = M_r(a,\theta,t) = 0 \tag{32b}$$

free: $$M_r(a,\theta,t) = V_r(a,\theta,t) = 0 \tag{32c}$$

where M_r is the radial bending moment, given by Eq. (28) and V_r is the radial (Kelvin-Kirchhoff) edge reaction, given by

$$V_r = -D\frac{\partial}{\partial r}\left[(\nabla^2 w) + \frac{1-\nu}{r}\frac{\partial}{\partial\theta}\left(\frac{1}{r}\frac{\partial w}{\partial\theta}\right)\right]. \tag{33}$$

The fourth-order frequency determinant described above which arises for each type of boundary conditions is easily reduced to third order because of the simplicity of Eq. (25). Frequency determinants for each type are displayed below:

(i) clamped:
$$\begin{vmatrix} f_1(\lambda) & f_2(\lambda) & f_3(\lambda) \\ J_\mu(\lambda) & Y_\mu(\lambda) + \frac{2}{\pi}K_\mu(\lambda) & I_\mu(\lambda) \\ 1 & \frac{1+\cos(\mu-1)\pi}{\sin(\mu-1)\pi} & 1 \end{vmatrix} = 0 \tag{34}$$

where

$$f_1(\lambda) = \frac{\mu}{\lambda}J_\mu(\lambda) - J_{\mu+1}(\lambda)$$

$$f_2(\lambda) = \frac{\mu}{\lambda}Y_\mu(\lambda) - Y_{\mu+1}(\lambda) + \frac{2}{\pi}\left[\frac{\mu}{\lambda}K_\mu(\lambda) - K_{\mu+1}(\lambda)\right]$$

$$f_3(\lambda) = \frac{\mu}{\lambda}I_\mu(\lambda) + I_{\mu+1}(\lambda) \tag{35}$$

(ii) simply supported:
$$\begin{vmatrix} g_1(\lambda) & g_2(\lambda) & g_3(\lambda) \\ J_\mu(\lambda) & Y_\mu(\lambda) + \frac{2}{\pi}K_\mu(\lambda) & I_\mu(\lambda) \\ 1 & \frac{1+\cos(\mu-1)\pi}{\sin(\mu-1)\pi} & 1 \end{vmatrix} = 0 \tag{36}$$

where

$$g_1(\lambda) = J_\mu(\lambda) - (1-\nu)\left[\frac{\mu(\mu-1)}{\lambda^2}J_\mu(\lambda) + \frac{1}{\lambda}J_{\mu+1}(\lambda)\right]$$

$$g_2(\lambda) = Y_\mu(\lambda) - (1-\nu)\left[\frac{\mu(\mu-1)}{\lambda^2}Y_\mu(\lambda) + \frac{1}{\lambda}Y_{\mu+1}(\lambda)\right] - \frac{2}{\pi}\left\{K_\mu(\lambda) + (1-\nu)\left[\frac{\mu(\mu-1)}{\lambda^2}K_\mu(\lambda) + \frac{1}{\lambda}K_{\mu+1}(\lambda)\right]\right\}$$

$$g_3(\lambda) = -\left\{I_\mu(\lambda) + (1-\nu)\left[\frac{\mu(\mu-1)}{\lambda^2}I_\mu(\lambda) - \frac{1}{\lambda}I_{\mu+1}(\lambda)\right]\right\} \tag{37}$$

(iii) free:
$$\begin{vmatrix} g_1(\lambda) & g_2(\lambda) & g_3(\lambda) \\ h_1(\lambda) & h_2(\lambda) & h_3(\lambda) \\ 1 & \frac{1+\cos(\mu-1)\pi}{\sin(\mu-1)\pi} & 1 \end{vmatrix} = 0 \tag{38}$$

where g_1, g_2, and g_3 are as in Eqs. (37), and where

$$h_1(\lambda) = \mu J_\mu(\lambda) - \lambda J_{\mu+1}(\lambda) + \frac{\mu^2(1-\nu)}{\lambda^2}[(\mu-1)J_\mu(\lambda) - \lambda J_{\mu+1}(\lambda)]$$

$$h_2(\lambda) = \mu Y_\mu(\lambda) - \lambda Y_{\mu+1}(\lambda) + \frac{\mu^2(1-\nu)}{\lambda^2}[(\mu-1)Y_\mu(\lambda) - \lambda Y_{\mu+1}(\lambda)] - \frac{2}{\pi}\left\{\mu K_\mu(\lambda) - \lambda K_{\mu+1}(\lambda) - \frac{\mu^2(1-\nu)}{\lambda^2}[(\mu-1)K_\mu(\lambda) - \lambda K_{\mu+1}(\lambda)]\right\}$$

$$h_3(\lambda) = -\left\{\mu I_\mu(\lambda) + \lambda I_{\mu+1}(\lambda) - \frac{\mu^2(1-\nu)}{\lambda^2}[(\mu-1)I_\mu(\lambda) + \lambda I_{\mu+1}(\lambda)]\right\}. \tag{39}$$

Case 2: $\mu \geq 1$. As previously described, this case applies to all free vibration modes when $\alpha \leq 180$ deg, and for the higher modes (having one or more radial node lines) when 180 deg $< \alpha \leq$ 360 deg. In this case $B_n = D_n = 0$, and the fourth-order determinants described above reduce to second order. Expanding the second-order determinants results in the following frequency equations, corresponding to the various circular edge boundary conditions.

(i) clamped: $$J_\mu(\lambda)I_{\mu+1}(\lambda) + I_\mu(\lambda)J_{\mu+1}(\lambda) = 0 \tag{40}$$

(ii) simply supported: $$\frac{J_{\mu+1}(\lambda)}{J_\mu(\lambda)} + \frac{I_{\mu+1}(\lambda)}{I_\mu(\lambda)} - \frac{2\lambda}{1-\nu} = 0 \tag{41}$$

(iii) free: $$g_1(\lambda)h_3(\lambda) - g_3(\lambda)h_1(\lambda) = 0 \tag{42}$$

where the g_i and h_i are as given in Eqs. (37) and (39).

Numerical Results

Accurate numerical results for the nondimensional free vibration frequencies $\omega a^2\sqrt{\rho/D}$ are presented in Table 1 for sectorial plates with re-entrant corners (180 deg $< \alpha \leq$ 360 deg). That is, all frequencies correspond to mode shapes having no radial nodal lines. Given are the lowest five (nonzero) values

Downloaded 03 May 2010 to 171.66.16.245. Redistribution subject to ASME license or copyright; see http://www.asme.org/terms/Terms_Use.cfm

Table 1 Nondimensional frequencies $\omega a^2\sqrt{\rho/D}$ for sectorial plates having their radial edges simply-supported, with various edge conditions on the circular edges; mode shapes having no radial node lines

α (degrees)	μ	Nodal circles	$\omega a^2\sqrt{\rho/D}$		
			Clamped (Arbitrary ν)	S.S. (ν = 0.3)	Free (ν = 0.3)
195	0.9231	0	21.4829	14.0366	1.40452
		1	60.9960	48.6272	20.5428
		2	120.242	102.921	59.9349
		3	199.213	176.949	119.084
		4	297.917	270.714	198.003
210	0.8571	0	21.6581	14.1458	1.88840
		1	61.1285	48.7447	20.5959
		2	120.371	103.038	60.0327
		3	199.339	177.066	119.185
		4	298.042	270.831	198.107
270	0.6667	0	22.0881	14.4129	2.75864
		1	61.4550	49.0344	20.7233
		2	120.690	103.328	60.2745
		3	199.651	177.356	119.434
		4	298.349	271.121	198.364
330	0.5455	0	22.3038	14.5467	3.11642
		1	61.6196	49.1807	20.7858
		2	120.851	103.474	60.3959
		3	199.808	177.503	119.560
		4	298.505	271.268	198.495
360	0.5000	0	22.3733	14.5897	3.22484
		1	61.6729	49.2279	20.8057
		2	120.903	103.522	60.4364
		3	199.860	177.550	119.600
		4	298.555	271.315	198.537

of the frequency determinant Eqs. (34), (36), and (38). A Poisson's ratio of $\nu = 0.3$ was used in the calculations for the simply-supported and free circular edges. ($\omega a^2\sqrt{\rho/D}$ is independent of ν for the clamped circular edge.)

With one inconsequential exception, the data presented in Table 1 for the simply-supported circular edge agrees to six significant figures with the accurate (but approximate) results obtained by the present authors (1992a) using the Ritz method with admissible functions which are sums of algebraic-trigonometric and corner functions. In that exception, the nondimensional frequency of the first mode for $\alpha = 195$ deg (14.0366) differs negligibly from the previously reported upper bound value of 14.0367.

The frequency data displayed in Table 1 for clamped or free circular edges are the first known results obtained for such plate problems.

Examining Table 1, it is observed that, with the exception of the lowest frequency for the plate with a free circular edge, the frequencies change only slightly as α is varied between being nearly semicircular (195 deg) to being circular (360 deg). The most rapid changes with α occur for the smaller α. Data are presented for $\alpha = 330$ deg to verify that no drastic changes in frequency occur due to the "notch effect" as α approaches 360 deg.

The large reduction in the lowest frequency in the case of the free circular boundary as α approaches 180 deg is due to the fact that it must be zero for $\alpha = 180$ deg (a semicircular plate). This zero frequency corresponds to rigid-body rotation about the simply-supported (e.g., hinged) diameter.

As α approaches 360 deg, the radial boundaries form a hinged crack. At $\alpha = 360$ deg, the two edges become coincident, but no circumferential moment (M_θ) is transferred across the boundaries—both radial edges may be regarded as being attached to a single hinge. These frequencies may be compared with the corresponding ones (i.e., no radial node lines) for complete circular plates (see Table 2). The hinge support for the 360 deg sectorial plate clearly increases the stiffness more than is lost due to the vanishing circumferential moment. This may be seen from the frequencies for $\alpha = 360$ deg in Table 1 all being greater than those in Table 2.

Concluding Remarks

The first known exact analytical solutions have been derived herein for the free vibration frequencies of sectorial plates having the radial edges simply supported, with re-entrant corners ($\alpha > 180$ deg). To do so required using careful limiting processes to enforce the proper regularity conditions at the sharp corner.

Although infinite bending moments at sharp (re-entrant) corners cannot exist in real materials, it is expected that highly localized yielding occurring during the vibratory motion should make the present analysis appropriate for plates composed of ductile materials. Moreover, machining processes typically result in corners which are at least slightly rounded. For small amplitude vibrations, the bending moments generated at the corner may then be large, but not infinite.

The numerical values of frequency listed in Table 1 are the first known data obtained for sectorial plates with simply-supported radial edges and clamped or free circular edges. The data for simply-supported circular edges were found to agree accurately with previous values obtained by the present authors (1992a) using approximate methods.

Downloaded 03 May 2010 to 171.66.16.245. Redistribution subject to ASME license or copyright; see http://www.asme.org/terms/Terms_Use.cfm

Table 2 Nondimensional frequencies $\omega a^2\sqrt{\rho/D}$ for complete circular plates (ν = 0.3); axisymmetric modes (no radial node lines)

Nodal circles	$\omega a^2\sqrt{\rho/D}$		
	Clamped* (Arbitrary ν)	S.S.** (ν = 0.3)	Free+ (ν = 0.3)
0	10.2158	4.93515	0++
1	39.771	29.7200	9.0031
2	89.104	74.1560	38.443
3	158.183	138.318	87.750
4	247.005	222.215	156.82

* from Leissa (1969)
** from Leissa and Narita (1980)
\+ from equation (42), which is also applicable to complete circular plates (cf, Leissa (1969) page 10)
++ rigid body translation

No frequency data were presented for sectorial plates having salient angles ($\alpha \leq 180$ deg). These may be easily found from the frequency Eqs. (40)-(42). For $\alpha = 180$ deg/n, where $n = 1, 2, 3, \ldots$, frequencies for sectorial plates are available in the published data for complete circular plates (see references in footnotes to Table 2), because the nodal diameters of complete circular plates duplicate the simply-supported radial edge boundary conditions of sectorial plates.

It should also be noted that although the solution yielding Table 1 is valid for $0 < \mu < 1$, data presented there were limited to the range $0.5 \leq \mu < 1$. This is because $\mu < 0.5$ corresponds to plates having overlapping radial boundaries ($\alpha > 360$ deg). Physical limitations, particularly at the sharp corner, make the practical validity of the solution for $0 < \mu < 0.5$ highly questionable.

For sectorial plates having their radial edges both simply-supported, nodal patterns (if any) consist solely of nodal radii and circles. This is a consequence of the variables separable form of solution in Eq. (6). For other boundary conditions along the radial edges, nodal patterns do not consist of nodal radii or circles, as was found by the present authors (1992b) in analyzing sectorial plates having V-notches (with both radial edges free).

Frequency determinants and equations were derived for the relatively simple circular boundary conditions (clamped, simply-supported, free). They can also be straightforwardly derived for circular boundaries which are elastically restrained, or have an attached distributed mass, or both (e.g., an attached elastic stiffening ring). The proper mathematical boundary conditions for such situations are given in the monograph by Leissa (1969).

Acknowledgments

This research was supported by the National Science Foundation, Award No. MSM-8821143.

References

Ben-Amoz, M., 1959, "Note on Deflections and Flexural Vibrations of Clamped Sectorial Plates," ASME JOURNAL OF APPLIED MECHANICS, Vol. 26, No. 1, pp. 136-137.

Bhattacharya, A. P., and Bhowmic, K. N., 1975, "Free Vibration of a Sectorial Plate," *Journal of Sound and Vibration*, Vol. 41, No. 4, pp. 503-505.

Huang, C. S., 1991, "Singularities in Plate Vibration Problems," Ph.D. Dissertation, The Ohio State University, Columbus, OH.

Leissa, A. W., 1969, "Vibration of Plates," NASA SP-160, U.S. Government Printing Office.

Leissa, A. W., McGee, O. G., and Huang, C. S., 1992a, "Vibrations of Sectorial Plates Having Corner Stress Singularities," submitted for publication.

Leissa, A. W., McGee, O. G., and Huang, C. S., 1992b, "Vibrations of Circular Plates with V-Notches," submitted for publication.

Leissa, A. W., and Narita, Y., 1980, "Natural Frequencies of Simply Supported Circular Plates," *Journal of Sound and Vibration*, Vol. 70, No. 2, pp. 221-229.

Maruyama, K., and Ichinomiya, O., 1981, "Experimental Investigation of Free Vibrations of Clamped Sector Plates," *Journal of Sound and Vibration*, Vol. 74, No. 4, pp. 563-573.

Rubin, C., 1975, "Nodal Circles and Natural Frequencies for the Isotropic Wedge," *Journal of Sound and Vibration*, Vol. 39, No. 4, pp. 523-526.

Tranter, C. J., 1968, *Bessel Functions With Some Physical Applications*, The English Universities Press Ltd.

Westmann, R. A., 1962, "A Note on Free Vibrations of Triangular and Sector Plates," *Journal of the Aerospace Sciences*, Vol. 29, No. 9, pp. 1139-1140.

Williams, M. L., 1952, "Surface Stress Singularities Resulting from Various Boundary Conditions in Angular Plates under Bending," *Proceedings of the First U.S. National Congress of Applied Mechanics*, pp. 325-329.

Downloaded 03 May 2010 to 171.66.16.245. Redistribution subject to ASME license or copyright; see http://www.asme.org/terms/Terms_Use.cfm

On the Dynamic Response of Continuous Systems Including Model Uncertainty

W. D. Iwan
Professor,
Division of Engineering and Applied Science,
California Institute of Technology,
Pasadena, CA 91125
Fellow ASME

H. Jensen
Assistant Professor,
Universidad Tecnica Federico
Santa Maria,
Valparaiso, Chile
Mem. ASME

This paper presents a technique for obtaining the response of linear continuous systems with parameter uncertainties subjected to deterministic excitation. The parameter uncertainties are modeled as random fields and are assumed to be time independent. The general formulation of the method is developed for a particular class of partial differential equations with random coefficients. Random shape functions are introduced to approximate the solution in the spatial domain and in the random space. A system of linear ordinary differential equations for the unknowns of the problem is derived using the weighted residual method. The system of equations is integrated in time and the response variability is computed. Application of the new method is made to a continuum described by the one-dimensional wave equation in which the stiffness properties exhibit a spatial random variation. Validation calculations show that the results from the method agree well with those obtained by direct numerical integration.

Introduction

Uncertainty must be accounted for in many engineering problems. One common source of uncertainty is in the specification of external loads. Many structural excitations encountered in practice are stochastic in nature and are considered as such in analysis. Examples of excitations which possess random-like qualities are seismic excitation, blast loading, wind loading, water wave excitation, and aerodynamic turbulence. Another source of uncertainty yet usually ignored arises from characterization of the structure. This includes uncertainty in material properties, structural dimensions, and boundary conditions.

Uncertainty in structural characteristics has a direct relationship to the reliability of many engineering structures. For example, the response of secondary structures attached to primary structures such as nuclear containment structures, space structures, and offshore structures is quite sensitive to parameter uncertainties (Igusa and Der Kiureghian, 1988). In such cases, it is necessary to employ an analysis that takes into account all the features of the structure and its excitation, including uncertainties. If these uncertainties are not accounted for, the computed response represents only one result in a spectrum of possible results.

A number of papers have been published demonstrating the application of probability theory and random field theory to the study of physical systems with uncertain parameters. Early applications used simulation methods to investigate the effects of uncertainty in structural properties on the response of structures to static loading (Shinozuka and Jan, 1972). Later, first and second-order perturbation methods were used to compute second-moment statistics of response quantities in structural and geotechnical applications (Hisada and Nakagiri, 1981; Liu et al., 1987). Shinozuka (1972; 1987) and Yamazaki et al. (1988) have used simulation methods and the Neuman expansion method to obtain the statistical properties of the response, when static loads of a deterministic nature are considered.

The effects of uncertainty in structural properties, when dynamic loads are considered, have been investigated mainly by simulation and perturbation methods (Branstetter and Paez, 1986; Liu et al., 1988). Simulation methods are very powerful, but in general provide limited insight into the behavior and sensitivity of the system under different parameter uncertainties. Perturbation methods are quite general and they are easily integrable into any deterministic solution technique. However, they usually suffer from questions of accuracy and convergence. These questions become more crucial as the degree of uncertainty becomes more pronounced, and when dynamic, particularly transient and wave propagation problems must be considered (Benaroya and Rehak, 1988; Liu et al., 1988). Recently, a Fourier series approach has been used to compute the mean and variance of the response of a single-degree-of-freedom system with uncertain natural frequency (Beck and Katafygiotis, 1989). This approach, however, becomes cumbersome if the number of uncertain parameters is more than one.

It is the objective of this paper to present an alternative

Contributed by the Applied Mechanics Division of THE AMERICAN SOCIETY OF MECHANICAL ENGINEERS for presentation at the First Joint ASCE-EMD, ASME-AMD, SES Meeting, Charlottesville, VA, June 6-9, 1993.

Discussion on this paper should be addressed to the Technical Editor, Professor Lewis T. Wheeler, Department of Mechanical Engineering, University of Houston, Houston, TX 77204-4792, and will be accepted until four months after final publication of the paper itself in the ASME JOURNAL OF APPLIED MECHANICS.

Manuscript received by the ASME Applied Mechanics Division, June 26, 1991; final revision, Apr. 7, 1992. Associate Technical Editor: P. D. Spanos.

Paper No. 93-APM-25.

Copyright © 1993 by ASME
Downloaded 03 May 2010 to 171.66.16.245. Redistribution subject to ASME license or copyright; see http://www.asme.org/terms/Terms_Use.cfm

method for the dynamic analysis of linear continuous systems with parameter uncertainties when these systems are subjected to deterministic excitation. The parameter uncertainties are described as random fields and are assumed to be time independent. In what follows, the general linear continuous system to be examined is described.

Problem Definition

Consider the continuous linear system described by the partial differential equation

$$\nabla \cdot \tau(\mathbf{k}(\mathbf{x}),\mathbf{u}) - \mathbf{Q}(\mathbf{c}(\mathbf{x}),\dot{\mathbf{u}}) - \mathbf{m}(\mathbf{x})\ddot{\mathbf{u}} + \mathbf{f}(\mathbf{x},t) = \mathbf{0} \quad \text{on } \Omega \times]0,T_0[, \quad (1)$$

where $\mathbf{u} = \mathbf{u}(\mathbf{x}, t)$ is the dependent variable representing the displacement field on the spatial domain Ω and the time interval $]0, T_0[$; $\mathbf{m}(\mathbf{x})$, $\mathbf{k}(\mathbf{x})$, and $\mathbf{c}(\mathbf{x})$ are the mass, stiffness, and damping parameter fields, respectively; τ is a linear stress operator of first order; $\mathbf{Q}$ is a linear damping operator; and $\mathbf{f}(\mathbf{x}, t)$ is an externally applied load. On the boundary $\partial\Omega$, homogeneous geometric and natural boundary conditions are assumed to hold. Appropriate initial conditions are also assumed to be given.

The terms, such as τ, $\mathbf{u}$, and $\mathbf{x}$ in Eq. (1) represent indexed sets. These may be scalars, vectors, or tensors, depending on the number of indices required to describe the particular physical quantity under consideration. The class of systems modeled by Eq. (1) is one of significant engineering importance since it contains many common physical problems, such as the axial vibration of a rod, the propagation of plane waves in a continuum, vibration of a shear beam, etc. Physically speaking, $\mathbf{k}(\mathbf{x})$ and $\mathbf{c}(\mathbf{x})$ represent the material properties of the system under consideration. These material properties as well as the external load $\mathbf{f}(\mathbf{x}, t)$ are permitted to have spatially random properties, so the stiffness, damping, and the external load are modeled as random fields.

Random Field Representation

In a second-order representation, a random process $G(\mathbf{x})$ can be defined in terms of its mean value plus its deviatoric component as

$$G(\mathbf{x}) = \overline{G}(\mathbf{x}) + Z(\mathbf{x}), \quad (2)$$

where $\overline{G}(\mathbf{x})$ is the expected value of $G(\mathbf{x})$ over all possible realizations of the process, and $Z(\mathbf{x})$ is a process with zero mean and autocorrelation function $R_{GG}(\mathbf{x}, \mathbf{y})$. This function, which by definition is symmetric and positive semi-definite, describes the spatial dependence between the values of $G(\mathbf{x})$ at different points in space. In practice, the correlation data is defined at a finite set of discrete points in Ω. Then, the discretized version of Eq. (2) can be written as

$$\mathbf{g} = \overline{\mathbf{g}} + \mathbf{z}, \quad (3)$$

where $\mathbf{g}$ is a random vector that represents the spatial variation of $G(\mathbf{x})$ at the finite set of discrete points, $\overline{\mathbf{g}}$ is the mean value vector of the process, and $\mathbf{z}$ is a vector of random variables with zero mean and covariance matrix C.

By means of the spectral decomposition of the covariance matrix, the random field can be described in terms of a vector of uncorrelated random variables, and Eq. (3) becomes

$$\mathbf{g} = \overline{\mathbf{g}} + \Phi\mathbf{b}, \quad (4)$$

where Φ is the matrix of eigenvectors of the covariance matrix C, and $\mathbf{b}$ is a vector of uncorrelated random variables with zero mean and covariance matrix Λ given by

$$\Lambda = \Phi^T C \Phi. \quad (5)$$

Equation (4) corresponds to the Karhunen-Loeve expansion for discrete random processes (Naylor, 1982), and it gives the discretized representation of the random field $G(\mathbf{x})$. This characterization of random fields has previously been used by a number of authors (e.g., Dias and Nagtegaal, 1985; Yamazaki and Shinozuka, 1988; Spanos and Ghanem, 1989). It is noted that if $G(\mathbf{x})$ is a Gaussian process, then the new set of random variables are jointly Gaussian and since they are uncorrelated, they are also independent. The process $G(\mathbf{x})$ will subsequently be assumed to be Gaussian.

In the formulation that follows, the continuous representation of the random process will be needed. In order to define its representation in the entire domain Ω, the following functions of $\mathbf{x}$ are defined:

$$\hat{G}(\mathbf{x}) = \sum_{i=1}^{NR} g_i \Psi_i(\mathbf{x}), \quad G_0(\mathbf{x}) = \sum_{i=1}^{NR} \overline{g}_i \Psi_i(\mathbf{x}),$$

$$G_n(\mathbf{x}) = \sum_{i=1}^{NR} \Phi_{in} \Psi_i(\mathbf{x}), \quad (6)$$

where NR is the dimension of the vector of random variables $\mathbf{z}$ and it is equal to the number of points in Ω where the correlation data is known, g_i is the ith component of the random vector $\mathbf{g}$, $\overline{g}_i$ is the ith component of the mean value vector $\overline{\mathbf{g}}$, Φ_{in} is the ith component of the nth eigenvector of the covariance matrix, and $\Psi_i(\mathbf{x})$, $i = 1, \ldots, NR$, are linearly independent known interpolation functions of $\mathbf{x}$, satisfying

$$\Psi_i(\mathbf{x}_j) = \delta_{ij}, \quad (7)$$

where $\mathbf{x}_j$ represents the points in Ω where the random field is defined, that is, where the correlation data is known, and δ_{ij} is the Kronecker delta.

Relations (6) together with Eq. (4) give the following representation for the random process:

$$\hat{G}(\mathbf{x}) = G_0(\mathbf{x}) + \sum_{n=1}^{NR} G_n(\mathbf{x}) b_n, \quad (8)$$

where b_n is the nth component of the random vector $\mathbf{b}$. The function $G_0(\mathbf{x})$ represents an approximation of the expected value of the random process $G(\mathbf{x})$, while the functions $G_n(\mathbf{x})$, $n = 1, \ldots, NR$, denote a continuous representation in Ω of the eigenvectors of the covariance matrix, that is, $G_n(\mathbf{x}_i) = \Phi_{in}$, $i = 1, \ldots, NR$. Equation (8) is the characterization for random fields which will be used in the present formulation. Finally, it is noted that a similar representation for random fields has been implemented by Lawrence (1987) to compute first and second-order moments of the response of structural systems with uncertain properties subjected to static loads.

Strong Form of the Problem

Making use of the characterization given by Eq. (8) for random fields, and considering the linearity of operators τ and $\mathbf{Q}$, Eq. (1) can be written as

$$\nabla \cdot \tau(\mathbf{k}_0(\mathbf{x}),\mathbf{u}) - \mathbf{Q}(\mathbf{c}_0(\mathbf{x}),\dot{\mathbf{u}}) + \sum_{n=1}^{r} (\nabla \cdot \tau(\mathbf{k}_n(\mathbf{x}),\mathbf{u}) - \mathbf{Q}(\mathbf{c}_n(\mathbf{x}),\dot{\mathbf{u}}))b_n$$

$$- \mathbf{m}(\mathbf{x})\ddot{\mathbf{u}} + \mathbf{f}_0(\mathbf{x},t) + \sum_{n=1}^{r} \mathbf{f}_n(\mathbf{x},t) b_n = 0, \quad (9)$$

where r is the total number of random variables used for the representation of the random fields; $\mathbf{k}_0(\mathbf{x})$, $\mathbf{c}_0(\mathbf{x})$, and $\mathbf{f}_0(\mathbf{x}, t)$ denote the expected value of the stiffness, damping and external load fields, respectively; and $\mathbf{k}_n(\mathbf{x})$, $\mathbf{c}_n(\mathbf{x})$ and $\mathbf{f}_n(\mathbf{x}, t)$ represent the continuous representation in Ω of the eigenvectors of the corresponding covariance matrices.

Equation (9), together with its initial and boundary conditions, represents the strong or classical form of the initial boundary value problem. To simplify the notation, it will subsequently be assumed that the dependent variable $\mathbf{u}(\mathbf{x}, t)$ is a scalar, $u(\mathbf{x}, t)$. Formulations similar to that which follows are easily developed for cases where u is a vector. It is noted that

Downloaded 03 May 2010 to 171.66.16.245. Redistribution subject to ASME license or copyright; see http://www.asme.org/terms/Terms_Use.cfm

the dependent variable $u(\mathbf{x}, t)$ is now an explicit function of the random vector $\mathbf{b}$, that is, $u(\mathbf{x}, \mathbf{b}, t)$.

Approximate Solution

In order to obtain an approximate solution of Eq. (9), let the domain Ω be subdivided into *NEL* elements Ω^e. Further, let $u^e(\mathbf{x}, \mathbf{b}, t)$, $\mathbf{x} \in \Omega^e$ denote the restriction of $u(\mathbf{x}, \mathbf{b}, t)$ to Ω^e, so that

$$u^e(\mathbf{x},\mathbf{b},t) = \begin{cases} u(\mathbf{x},\mathbf{b},t) & \forall \mathbf{x} \in \Omega^e \\ 0 & \forall \mathbf{x} \notin \Omega^e. \end{cases} \tag{10}$$

Then, the solution field is represented as the summation of all these restrictions,

$$u(\mathbf{x},\mathbf{b},t) = \sum_{e=1}^{NEL} u^e(\mathbf{x},\mathbf{b},t). \tag{11}$$

In the present formulation, the dependent variable $u^e(\mathbf{x}, \mathbf{b}, t)$ is expanded as a double series over $\mathbf{x}$ and $\mathbf{b}$. The approximation of the solution in the spatial domain is assumed to be given by the finite element shape functions, while an orthogonal set of polynomials is used to approximate the solution in the random space. Then, the solution takes the form of a double series of space dependent interpolation functions and orthogonal polynomials weighted by time-dependent functions. Thus, the dependent variable $u^e(\mathbf{x}, \mathbf{b}, t)$ is expressed as

$$u^e(\mathbf{x},\mathbf{b},t) = \sum_{j=1}^{NEN} \phi_j^e(\mathbf{x}) \sum_{0 \le |\mathbf{l}| \le NP} u^e_{jl_1 \ldots l_r}(t) \prod_{s=1}^{r} H_{l_s}^{b_s}(b_s), \tag{12}$$

where *NP* is the order of approximation in the random space, *NEN* is the number of nodes per element, $\phi_j^e(\mathbf{x})$ is the finite element shape function for node j of element e, $u^e_{jl_1 \ldots l_r}(t)$ is an unknown deterministic function of time, $\mathbf{l}$ is a vector with components l_s, $s = 1, \ldots, r$, $|\mathbf{l}|$ stand for the norm of $\mathbf{l}$ defined by

$$|\mathbf{l}| = \sum_{s=1}^{r} l_s, \tag{13}$$

$H_{l_s}^{b_s}(b_s)$ is a polynomial in the variable b_s of degree l_s, $l_s = 0, 1, \ldots$, and the set of polynomials $\{H_l^{b_s}(b_s)\}_{l=0}^{\infty}$ is orthogonal in the inner product space defined by the mean operation. That is,

$$E[H_l^{b_s}(b_s) H_p^{b_s}(b_s)] = \delta_{lp}; \quad H_0^{b_s}(b_s) = 1, \tag{14}$$

where $E[*]$ is the expectation operation. It is noted that the second summation in Eq. (12) corresponds to a polynomial expansion of degree *NP* in r variables.

The selection for the set of polynomials depends on the probability density function of the random variable b_s. For example, the Hermite polynomials satisfy Eq. (14) for Gaussian random variables, the Legendre polynomials do likewise for uniform random variables, the Laguerre polynomials are appropriate for exponential random variables, the ultraspherical polynomials are used for random variables with probability density function of a parabolic shape, etc. (Jensen, 1989). As previously mentioned, Gaussian random variables are used in this study. An expansion similar to Eq. (12) was implemented by Sun (1979) to study a particular class of ordinary differential equations with one random parameter and has been extended by the authors to study the dynamic response of structures with uncertain parameters (Jensen, 1989). An orthogonal expansion has also been implemented, independently, by Ghanem and Spanos (1990) to study the static response of systems with uncertain parameters.

The orthogonality condition of the set of polynomials, given by Eq. (14), is used in the next section to simplify the derivation of the set of equations for the unknowns of the problem. If the orthogonality relationship is not satisfy, the procedure is still valid but the resulting set of equations is more complex and the numerical implementation of the method is computationally more intense (Jensen, 1989). Therefore, the present technique could handle cases in which the choice of suitable orthogonal polynomials is not available for a given probabilistic distribution. In what follows, a system of linear ordinary differential equations for the unknowns of the problem, $u^e_{jl_1 \ldots l_r}(t)$, is derived using the weighted residual method.

Matrix Equations

In order to obtain a set of differential equations for the coefficients $u^e_{jl_1 \ldots l_r}(t)$, the following recurrence relation for the orthogonal set of polynomials $\{H_l^{b_s}(b_s)\}_{l=0}^{\infty}$ is employed (Abramowitz and Stegun, 1964)

$$b_n H_{l_n}^{b_n}(b_n) = a_{l_n-1}^{b_n} H_{l_n-1}^{b_n}(b_n) + a_{l_n}^{b_n} H_{l_n}^{b_n}(b_n) + a_{l_n+1}^{b_n} H_{l_n+1}^{b_n}(b_n),$$
$$n = 1, \ldots, r$$
$$l_n = 0, 1, \ldots \tag{15}$$

where $a_{l_n}^{b_n}$, $l_n = 0, 1, \ldots$, are constant coefficients.

The desired set of differential equations is derived using the weighted residual method with weighting functions defined as

$$\left\{ \phi_j(\mathbf{x}) \prod_{s=1}^{r} H_{l_s}^{b_s}(b_s) P_{b_s}(b_s) \right\}_{\substack{j=1,\ldots,NTOT \\ l_s=0,1,\ldots}}, \tag{16}$$

where $\phi_j(\mathbf{x})$ is the global shape function for node j, $P_{b_s}(b_s)$ is the Gaussian probability density function, *NTOT* is the total number of nodes in the finite element discretization, and all other terms are as previously defined.

Using the characterization of the dependent variable $u(\mathbf{x}, \mathbf{b}, t)$ in the governing Eq. (9), multiplying the differential equation by a weighting function, integrating by parts over the domain Ω, taking the expectation, and finally considering the orthogonality of the set of polynomials defined in Eq. (14) and the recurrence relation (15) yields the following set of equations for the element e of the finite element mesh

$$\sum_{j=1}^{NEN} \Bigg\{ m_{ij}^e \ddot{u}^e_{jl_1 \ldots l_r}(t) + c_{0ij}^e \dot{u}^e_{jl_1 \ldots l_r}(t) + k_{0ij}^e u^e_{jl_1 \ldots l_r}(t)$$
$$+ \sum_{n=1}^{r} \Big[c_{nij}^e (a_{l_n-1}^{b_n} \dot{u}^e_{jl_1 \ldots l_{n-1} \ldots l_r}(t) + a_{l_n}^{b_n} \dot{u}^e_{jl_1 \ldots l_n \ldots l_r}(t)$$
$$+ a_{l_n+1}^{b_n} \dot{u}^e_{jl_1 \ldots l_{n+1} \ldots l_r}(t)) + k_{nij}^e (a_{l_n-1}^{b_n} u^e_{jl_1 \ldots l_{n-1} \ldots l_r}(t)$$
$$+ a_{l_n}^{b_n} u^e_{jl_1 \ldots l_n \ldots l_r}(t) + a_{l_n+1}^{b_n} u^e_{jl_1 \ldots l_{n+1} \ldots l_r}(t)) \Big] \Bigg\}$$
$$= f_{0i}^e \prod_{s=1}^{r} \delta_{l_s 0} + \sum_{n=1}^{r} f_{ni}^e \left(a_0^{b_n} \prod_{s=1}^{r} \delta_{l_s 0} + a_1^{b_n} \prod_{\substack{s=1 \\ s \neq n}}^{r} \delta_{l_s 0} \delta_{l_n 1} \right),$$
$$i = 1, \ldots, NEN,$$
$$l_s = 0, 1, \ldots$$
$$s = 1, \ldots, r \tag{17}$$

plus initial condition equations, where $m_{ij}^e = \int_{\Omega^e} m(\mathbf{x}) \phi_i^e(\mathbf{x}) \phi_j^e(\mathbf{x}) d\Omega$ defines the element mass matrix, $c_{nij}^e = \int_{\Omega^e} \mathbf{Q}(\mathbf{c}_n(\mathbf{x}), \phi_j^e(\mathbf{x})) \phi_i^e(\mathbf{x}) d\Omega$, $n = 0, \ldots, r$ defines the element damping matrix, $k_{nij}^e = \int_{\Omega^e} \tau(\mathbf{k}_n(\mathbf{x}), \phi_j^e(\mathbf{x})) \nabla \phi_i^e(\mathbf{x}) d\Omega$, $n = 0, \ldots, r$ defines the element stiffness matrix, and $f_{ni}^e = \int_{\Omega^e} f_n(\mathbf{x}, t) \phi_i^e(\mathbf{x}) d\Omega$, $n = 0, \ldots, r$ defines the element force vector.

The coupled system of linear ordinary differential equations for the unknowns is found by assembling Eq. (17) for all elements, into a set of global equations. This leads to an equation of the form

$$\mathbf{M}\ddot{\mathbf{d}}(t) + \mathbf{C}\dot{\mathbf{d}}(t) + \mathbf{K}\mathbf{d}(t) = \mathbf{p}(t), \tag{18}$$

where $\mathbf{d}(t)$ is the global vector of unknowns with components

Downloaded 03 May 2010 to 171.66.16.245. Redistribution subject to ASME license or copyright; see http://www.asme.org/terms/Terms_Use.cfm

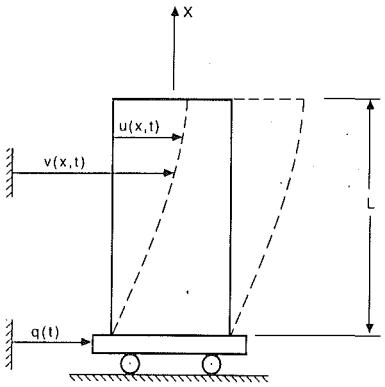


Fig. 1 Shear beam under base excitation

$u_{jl_1\ldots l_r}(t)$, $\mathbf{p}(t)$ is the generalized total effective load vector, and $\mathbf{M}$, $\mathbf{C}$, and $\mathbf{K}$ are the generalized mass, damping and stiffness matrices for the system, respectively.

It can be shown that the number of unknowns per node, NT, as a function of the number of random variables and the order of approximation in the random space is given by $NT = 1 + \Sigma_{l=1}^{NP}(1/l!)\,\Pi_{k=0}^{l-1}(k + r)$, where the same order of approximation has been considered for each one of the random variables. In general, however, the approximation of the response in terms of a random variable with a small variance requires lower order of approximation than for a random variable with a large variance. Thus, the number of unknowns per node can be reduced significantly. It can be shown that the dimension of the matrices $\mathbf{M}$, $\mathbf{C}$, and $\mathbf{K}$ increase very rapidly with both the number of random variables b_n, and the order of approximation of the finite element solution in the random space (Eq. (12)). Nevertheless, these matrices are sparse, that is, there are relatively few nonzero terms.

Discrete Time Solution

Equation (18) can be integrated in time to find the global vector of unknowns $\mathbf{d}(t)$ for all times. Most time integration schemes fall into one of two classes: implicit or explicit. An implicit algorithm requires the solution of a matrix equation at every time step to advance the solution. In contrast, explicit algorithms do not demand a simultaneous equation solution, but do require smaller time step to maintain stability and accuracy. As previously pointed out, the size of the matrices $\mathbf{M}$, $\mathbf{C}$, and $\mathbf{K}$ may become very large, so the time integration algorithm should be chosen such that computer high-speed memory requirements are minimized. Low-order explicit algorithms are very memory efficient, thus allowing solution of large problems in a given memory size. Since no matrix decompositions are involved, only the nonzero terms of $\mathbf{M}$, $\mathbf{C}$, and $\mathbf{K}$ need to be stored for computer implementation to produce a more efficient scheme.

The algorithm considered for the numerical examples presented in this paper is the modified Euler scheme. This is an explicit, second-order accurate integration procedure which is well suited to solve the first-order state space equation corresponding to Eq. (18) (Jensen, 1989). This algorithm is conditionally stable, with stability guaranteed for a sufficiently small time step Δt (Hughes, 1987).

Response Uncertainty and Statistics

Once the unknowns $u^e_{jl_1\ldots l_r}(t)$ have been determined, an analytical approximation to the solution in the spatial and random space is completely defined by Eq. (12). The response, which is random, will be described by its probability density or cumulative probability function, or by its statistical moments. Of particular importance is the second moment representation defined by the mean or expected response of all possible outcomes, and by the variance and covariance of the response.

Using Eq. (12) together with the orthogonality of the set of polynomials as defined in Eq. (14), the second moment representation for the element response is given by

$$E[u^e(\mathbf{x},\mathbf{b},t)] = \sum_{j=1}^{NEN} u^e_{j_{0\ldots0}}(t)\phi^e_j(\mathbf{x}), \quad e = 1, \ldots, NEL \tag{19}$$

$$V_{ar}[u^e(\mathbf{x},\mathbf{b},t)] = \sum_{i=1}^{NEN}\sum_{j=1}^{NEN}\sum_{1\le|l|\le NP} \times u^e_{il_1\ldots l_r}(t)u^e_{jl_1\ldots l_r}(t)\phi^e_i(\mathbf{x})\phi^e_j(\mathbf{x}), \quad e = 1, \ldots, NEL \tag{20}$$

and

$$C_{ov}[u^{e_1}(\mathbf{x},\mathbf{b},t_1),\ u^{e_2}(\mathbf{y},\mathbf{b},t_2)] = \sum_{i=1}^{NEN}\sum_{j=1}^{NEN}\sum_{1\le|l|\le NP} \times u^{e_1}_{il_1\ldots l_r}(t_1)u^{e_2}_{jl_1\ldots l_r}(t_2)\phi^{e_1}_i(\mathbf{x})\phi^{e_2}_j(\mathbf{y}), \quad e_1, e_2 = 1, \ldots, NEL \tag{21}$$

where Eqs. (19), (20), and (21) represent the mean value, variance and covariance response, respectively.

This characterization of the response is completely defined by the nodal unknowns $u^e_{jl_1\ldots l_r}(t)$, and does not require the solution of a multiple integral in the random space. A similar characterization can also be defined for the velocity, acceleration, strain and stress response fields. Finally, it is noted that using the analytical approximation for the response, given by Eq. (12), higher statistical moments can be computed. They can be obtained using higher-order recurrence relations for the orthogonal set of polynomials (Jensen, 1989).

Application to a One-Dimensional Continuum

To illustrate the application of the proposed method, a one-dimensional continuum described by the wave equation in which the physical properties exhibit a one-dimensional spatial random variation is considered. As a physical conceptualization of this equation, a base-excited shear beam whose rigidity varies randomly along its length is chosen for study. As shown in Fig. 1, the beam lies along the x-axis. The transverse displacement in an inertial coordinate frame is denoted by $v(x, t)$, while the displacement relative to the base of any point x at time t is denoted by $u(x, t)$. The beam is assumed to have constant mass, m, per unit of length. Finally, L is the length of the shear beam and $\ddot{q}(t)$ represents the base acceleration.

The equation of motion for this system is easily shown to be

$$\frac{\partial}{\partial x}\left(k(x)\,\frac{\partial u}{\partial x}\right) = m\ddot{u} + m\ddot{q}, \tag{22}$$

where $k(x)$ is the shear stiffness and all other terms are as defined above. This system is cast into the general form, previously described, by letting the stiffness parameter $k(x)$ represent the shear stiffness, the divergence operator ∇ represent the derivative with respect to the variable x, and the external load f represent the load due to the base excitation, with the operator $\tau(\bullet)$ defined as

$$\tau(k(x),u) = k(x)\,\frac{\partial u}{\partial x}. \tag{23}$$

To complete the formulation of the system, some amount of damping is added to the mathematical model. One form of damping widely used in structural calculations is Rayleigh damping, where the damping matrix is constructed as a linear combination of the stiffness and mass matrices. This form of damping is achieved in the model by defining the operators $\tau(\bullet)$ and $\mathbf{Q}(\bullet)$, which are described in Eq. (1), as

Downloaded 03 May 2010 to 171.66.16.245. Redistribution subject to ASME license or copyright; see http://www.asme.org/terms/Terms_Use.cfm

$$\tau(k(x),u) = k(x)\left(\frac{\partial u}{\partial x} + c_1 \frac{\partial^2 u}{\partial x \partial t}\right) \tag{24}$$

$$\mathbf{Q}(c(x),\dot{u}) = c(x)\dot{u}, \tag{25}$$

where

$$c(x) = c_2 m, \tag{26}$$

and c_1 and c_2 are constant parameters reflecting the participation of damping proportional to stiffness and mass, respectively. It is emphasized that the new method of analysis is not restricted to Rayleigh damping in any way, and that many other techniques could equally well be used to incorporate damping into the model.

In order to consider the uncertainty in the beam rigidity along its axis, the spatial variation of the shear stiffness $k(x)$, is assumed to be a one-dimensional homogeneous Gaussian random field. It is defined, as in Eq. (2), in terms of a mean value plus a deviatoric component, that is

$$k(x) = \bar{k}(x) + Z(x), \tag{27}$$

where $\bar{k}(x)$ is the shear stiffness mean value, and $Z(x)$ represents its fluctuating or deviatoric component, which is a process with zero mean and autocorrelation function $R_{kk}(x, y)$. Since the random field is assumed to be homogeneous, the autocorrelation function of the spatial variation is a function only of the distance between the two points. While the new method of analysis is not restricted to any particular form of the autocorrelation function, the following exponential function is considered in this example:

$$R_{kk}(\zeta) = \sigma^2 e^{-(\zeta/\delta L)^2}, \tag{28}$$

where σ is the standard deviation of the random process, ζ is the distance between two points along the x-axis, L is the length of the shear beam, and δ is a dimensionless parameter. The parameter δ is a measure of the correlation length and the product δL is usually defined as the scale or strength of correlation (Der Kiureghian and Ke, 1988). The assumption of a normal distribution implies the possibility of generating negative values of shear stiffness. To avoid this possibility, a probability density function with a finite range is used in this study to approximate the normal distribution (Jensen, 1989).

An important issue related with the finite element analysis and the discretization of the random field is the selection of the mesh size. When the material properties exhibit spatial variability two separate factors should be considered for this selection. One is the expected gradient of the stress field and the other is the expected rate of fluctuation of the random field, as measured, for example, by the corresponding strength of correlation (Der Kiureghian and Ke, 1988). The two requirements, do not necessarily coincide in each region of the structure and, hence, it is usually necessary to consider two or more separate meshes. In the present application, the finite element mesh is selected such that both sets of requirements in each region of the beam are satisfied.

The random field can now be discretized in accordance with a suitable finite element mesh, which should satisfy the requirements pointed out above. This discretization can be written in terms of a vector of independent random variables as in Eq. (4), and takes the form

$$\mathbf{k} = \bar{\mathbf{k}} + \sum_{n=1}^{NR} \phi_n b_n, \tag{29}$$

where $\mathbf{k}$ is the random vector that represents the spatial variation of the shear stiffness at the midpoint of the elements of the finite element discretization, $\bar{\mathbf{k}}$ is the mean value vector of the process, b_n is the nth component of the random vector $\mathbf{b}$, NR is the dimension of the vector of random variables, and ϕ_n is the eigenvector corresponding to the nth eigenvalue of the covariance matrix of the random field. The components of this covariance matrix are obtained directly in terms of the autocorrelation function, defined in Eq. (28). In the representation given by Eq. (29), it is assumed that the eigenvalues are ordered in decreasing order.

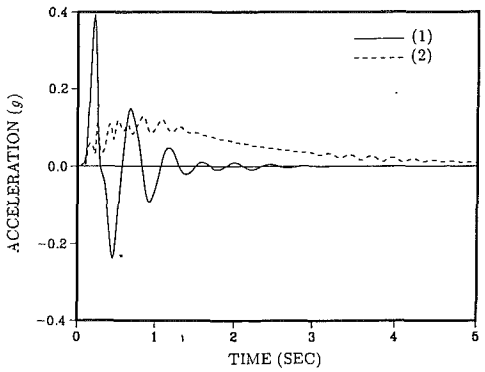


Fig. 2 (1) Mean value of the absolute acceleration response at the free end of the shear beam; (2) standard deviation of the absolute acceleration response at the free end of the shear beam

The contribution of each successive eigenvalue-eigenvector pair to the representation of the random field is observed to decrease steadily for many problem of interest (Liu et al., 1987). Consequently, there is the possibility of truncating the series in (Eq. (29)) at some value $n < NR$ without significant loss of accuracy. This reduction of variables is particularly important in the representation of strongly correlated random fields, allowing their description by a proper set of uncorrelated random variables. The actual number of random variables that are retained in the analysis depends on the correlation length parameter of the random field. Of course, such a truncation will not be possible if the random field is totally uncorrelated.

Special Case of Impulsive Loading. In order to illustrate the influence of uncertain stiffness on the response of the shear beam, an impulsive base excitation is first considered in this example. The continuous system is taken to have uniform mean value properties throughout its length, with a fundamental frequency of 2 Hz, and a Rayleigh damping corresponding to five percent of critical in the first two modes. The random field that describes the spatial variation of the shear stiffness is assumed to have a 20 percent coefficient of variation, and a correlation length parameter, δ, equal to 0.5. The response process to be considered in this application is the absolute acceleration at the top of the beam.

As discussed previously, one of the factors that should be considered in the selection of the mesh size for the finite element analysis is the expected rate of fluctuation of the random field. Therefore, in order to assure that the mesh used for this example problem adequately represents the physical behavior of the system, a parametric study of mesh size is conducted. For a uniform mesh of 20 elements, it is found that the statistical fluctuations of the random field is very small within each element. That is, the random field is almost fully correlated within each element. At the same time, it is found that the response is nearly invariant to a finer mesh. Based on these results, a uniform 20 element mesh is judged adequate for the current problem.

The response variability of the absolute acceleration at the free end of the shear beam is presented in Fig. 2. The dispersion about the mean value response, as measured by the standard deviation, is substantial. In fact, for all times greater than 0.8 second, the standard deviation response is greater than the mean value response. This level of response uncertainty shows that the presence of uncertainty in a structures physical properties can markedly alter its response characteristics. At the same time, these results suggest that for lightly damped systems, great caution must be exercised when interpreting calculated response if the physical properties are not precisely known.

Downloaded 03 May 2010 to 171.66.16.245. Redistribution subject to ASME license or copyright; see http://www.asme.org/terms/Terms_Use.cfm

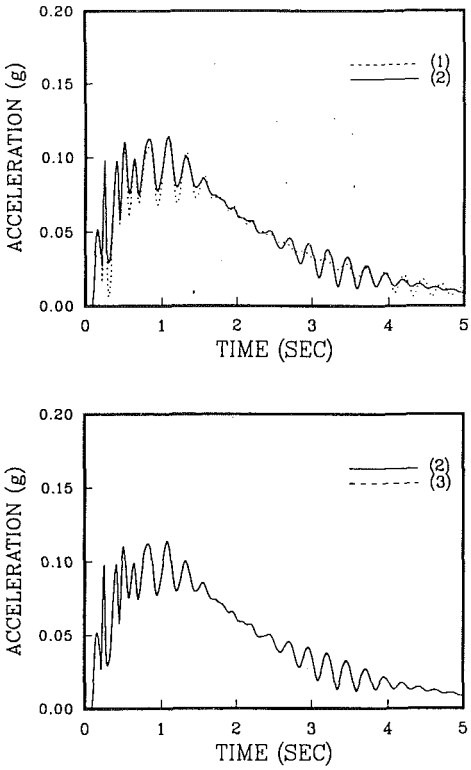


Fig. 3 Standard deviation of the response considering the three most significant pairs of eigenvectors-eigenvalues of the random field covariance matrix; (1) first random variable only; (2) first two random variables only; (3) first three random variables

The finite element mesh used in this example implies that the discretized random field is represented by 20 independent random variables (Eq. (29)). However, the correlation length parameter that is considered in this example allow truncation of the eigenvectors-eigenvalues of the random field covariance matrix. Thus, the number of eigenvectors, and hence the number of random variables in Eq. (29) can be reduced. In fact, the number of random variables that are retained in this analysis is two. Figure 3 shows the uncertainty in the response due to the three most significant pairs of eigenvectors-eigenvalues of the random field covariance matrix. In the graph at the top of Fig. 3, curve (1) represents the solution using only the first random variable and curve (2) is the solution using the first two random variables. In the graph at the bottom of Fig. 3, curve (2) is the solution using the first two terms and curve (3) is the solution using the first three terms (identical to (2)). It is clear that the contribution of each successive eigenvector-eigenvalue pair to the response variability decreases steadily. The first two random variables capture the major characteristics of the random field, and the contribution of lower eigenvector-eigenvalue pairs of the covariance matrix to the response variability is negligible.

It is noted that the following orders of approximation of the response in the random space are used for the two random variables that are retained in the analysis: a sixth-order approximation is used for the first random variable, and a fourth-order approximation is used for the second random variable. The influence of higher order approximation is found to have negligible effect on the response.

Verification of Accuracy of Proposed Method. In order to evaluate the performance of the newly developed method, validation calculations have been conducted and the results of the proposed method have been compared to those obtained by an *exact* solution. In the *exact* solution, the mean value response and the standard deviation response, which by definition are multiple integrals in the random space, are computed by numerical integration over the range of shear stiffness values. The agreement between the proposed method and the *exact* solution is found to be excellent. In fact, the two solutions are coincident for all time and therefore cannot be distinguished in Figs. 2 and 3 (Jensen, 1989).

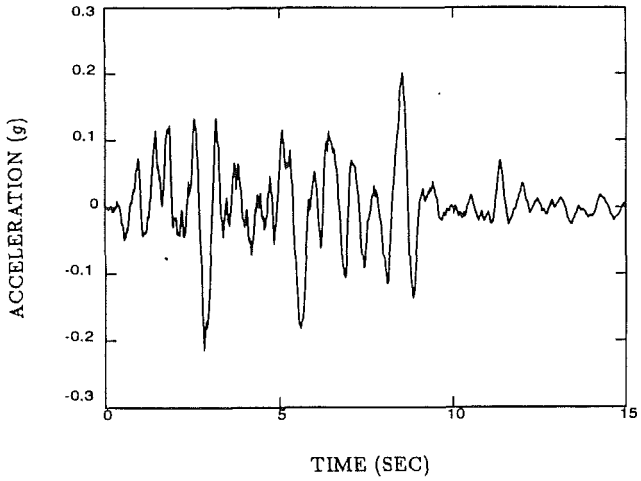


Fig. 4 Earthquake-like base excitation

Special Case of Earthquake-like Excitation. The uncertainty of the response at the top of the shear beam to an impulsive base excitation has been presented in Fig. 2. When a more complex deterministic base excitation is considered, a similar or greater deviation of the response from its mean value may result. In order to illustrate this point, an earthquake-like excitation is considered as a base acceleration. The base excitation is generated using the procedure described by Ruiz and Penzien (1969), and its time history is shown in Fig. 4.

In Fig. 5, the mean value and the standard deviation of the absolute acceleration responses are illustrated. In addition, a variability parameter is also presented. This parameter is defined as the ratio between the standard deviation and the maximum value of the mean value response, in this example, 0.53 g. The maximum value of the variability parameter is about 0.50, that is, 50 percent of the maximum mean value. This value clearly indicates that the variability of physical properties of a system can have a strong effect on its response characteristics. Therefore, these uncertainties must be properly accounted for in the analysis of such systems.

As in the case of the impulsive base excitation, the number of random variables that are retained in the analysis is two. It is found that the contribution of each successive eigenvector-eigenvalue pair to the response variability decreases steadily, and the major characteristics of the random field are captured by the first two random variables. The same orders of approximation of the response in the random space that were used before are used in this case. The influence of higher order approximation is found to have negligible effect on the response.

Conclusions

The newly developed solution method represents an extension of the deterministic finite element method to problems involving parameter uncertainties. It is believed to be a potentially powerful tool for obtaining the random response of linear continuous systems in which the system parameters are permitted to have random properties. Although the numerical solution of problems involving parameter uncertainties is computationally quite intensive when compared with deterministic analysis, this method can handle complex engineering problems using present computers hardware.

Downloaded 03 May 2010 to 171.66.16.245. Redistribution subject to ASME license or copyright; see http://www.asme.org/terms/Terms_Use.cfm

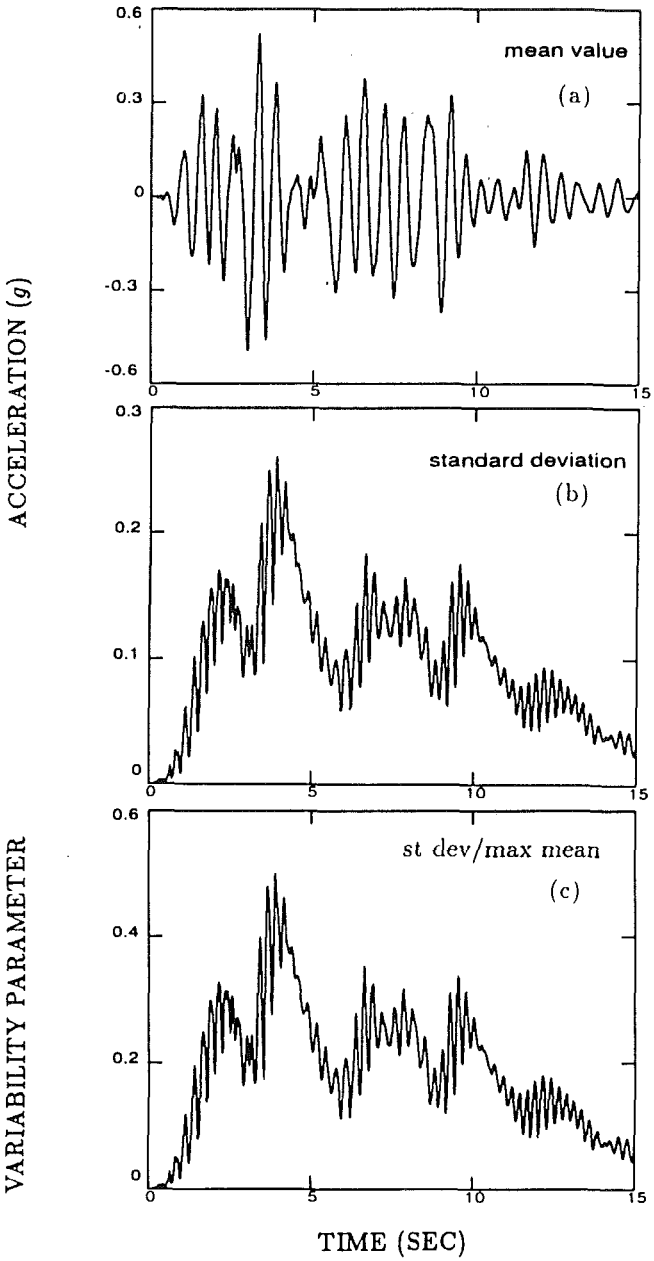


Fig. 5 Second-moment characterization of the absolute acceleration response; (*a*) mean value response; (*b*) standard deviation response; (*c*) variability parameter

Finally, it is noted that the new formulation can easily be extended to consider partial differential equations of order higher than two. This class of equations allows the modeling of many structures of interest in mechanical and civil engineering. Among these are structures modeled with beam elements, plate elements, and shell elements. Therefore, the new method could be extended to the area of structural finite elements. This extension would allow random response solutions for a broad range of complex engineering problems. In addition, modifications in the formulation of the method to permit randomness in the mass of the system and randomness in boundary conditions can also be considered.

References

Abramowitz, M., and Stegun, I. A., 1964, *Handbook of Mathematical Functions*, Dover Publications, New York, pp. 773–802.

Beck, J. L., and Katafygiotis, L., 1989, "Treating Model Uncertainties in Structural Dynamics," *Proceedings of Ninth World Conference on Earthquake Engineering*, Vol. 5, Tokyo-Kyoto, Japan, P3D-03.

Benaroya, H., and Rehak, M., 1988, "Finite Element Methods in Probabilistic Structural Analysis: A Selective Review," ASME *Applied Mechanics Reviews*, Vol. 41, pp. 201–213.

Branstetter, L., and Paez, T., 1986, "Dynamic Response of Random Parametered Structures with Random Excitation," Sandia National Laboratories, Report SAND85-1175, Albuquerque, NM.

Der Kiureghian, A., and Ke, J., 1988, "The Stochastic Finite Element Method in Structural Reliability," *Probabilistic Engineering Mechanics*, Vol. 3, pp. 83–91.

Dias, J. B., and Nagtegaal, J. C., 1985, "Efficient Algorithms for Use in Probabilistic Finite Element Analysis," *Symposium on Probabilistic Structural Analysis and Design*, ASME, Winter Annual Meeting, Miami, pp. 37–50.

Ghanem, R., and Spanos, P., 1990, "Polynomial Chaos in Stochastic Finite Element," ASME JOURNAL OF APPLIED MECHANICS, Vol. 57, pp. 197–202.

Hisada, T., and Nakagiri, S., 1981, "Stochastic Finite Element Method Developed for Structural Safety and Reliability," *3rd International Conference on Structural Safety and Reliability*, Trondheim, Norway.

Hughes, T. J. R., 1987, *The Finite Element Method: Linear Static and Dynamic Finite Element Analysis*, Prentice-Hall, Englewood Cliffs, NJ, pp. 459–488.

Igusa, T., and Der Kiureghian, A., 1988, "Response of Uncertain Systems to Stochastic Excitation," *Journal of Engineering Mechanics*, Vol. 114, pp. 812–832.

Jensen, H., 1989, "Dynamic Response of Structures with Uncertain Parameters," Earthquake Engineering Research Laboratory, California Institute of Technology, Report EERL 89-2, Pasadena, CA.

Lawrence, M. A., 1987, "Basis Random Variable in Finite Element Analysis," *International Journal of Numerical Methods in Engineering*, Vol. 24, pp. 1849–1863.

Liu, W. K., Mani, and Belytschko, T., 1987, "Finite Element Methods in Probabilistic Mechanics," *Probabilistic Engineering Mechanics*, Vol. 2, pp. 201–213.

Liu, W. K., Besterfield, G. H., and Belytschko, T., 1988, "Variational Approach to Probabilistic Finite Elements," *Journal of Engineering Mechanics*, Vol. 114, pp. 2115–2133.

Naylor, A., 1982, *Linear Operator Theory in Engineering and Science*, Springer-Verlag, New York, pp. 473–476.

Ruiz, P., and Penzien, J., 1969, "Probabilistic Study of the Behavior of Structures During Earthquakes," College of Engineering, University of California, Report No. EERC 69-3, Berkeley, CA.

Shinozuka, M., and Jan, C. M., 1972, "Digital Simulation of Random Processes and Its Applications," *Journal of Sound and Vibration*, Vol. 25, pp. 111–128.

Shinozuka, M., 1972, "Probabilistic Modeling of Concrete Structures," *Journal of the Engineering Mechanics Division*, ASCE, Vol. 98, pp. 1433–1451.

Shinozuka, M., 1987, "Structural Response Variability," *Journal of Engineering Mechanics*, Vol. 113, pp. 825–842.

Spanos, P., and Ghanem, R., 1989, "Stochastic Finite Element Expansion for Random Media," *Journal of the Engineering Mechanics Division*, ASCE, Vol. 115, pp. 1035–1053.

Sun, T. C., 1997, "A Finite Element Method for Random Differential Equations with Random Coefficients," *International Journal of Numerical Analysis*, Vol. 16, pp. 1019–1035.

Yamazaki, F., Shinozuka, M., and Dasgupta, G., 1988, "Neumann Expansion for Stochastic Finite Element Analysis," *Journal of Engineering Mechanics*, Vol. 114, pp. 1335–1354.

Downloaded 03 May 2010 to 171.66.16.245. Redistribution subject to ASME license or copyright; see http://www.asme.org/terms/Terms_Use.cfm

Stability of Conventional Controller Design for Flexible Manipulators[1]

L. Tang
Research Engineer,
Mechanical Dynamics, Inc.,
Ann Arbor, MI 48187
Assoc. Mem. ASME

S. B. Skaar
Associate Professor,
Department of Aerospace and
Mechanical Engineering,
University of Notre Dame,
Notre Dame, IN 46556

The paper investigates the independent joint control of flexible manipulators which are acted upon by gravity. Both finite-dimensional coordinates, and infinite-dimensional, spatially varying, distributed coordinates are used to describe the deformation of the flexible links. The effects of the flexibility on the closed-loop system behavior in the presence of both derivative and integral feedback control are studied both in the Laplace transform domain using the linearized model of the original nonlinear system and in the time domain using the original nonlinear model. The use of infinite-dimensional coordinates is shown to be especially effective in obtaining the frequency domain characteristics of the linearized model because the exact frequency content of the linearized system may be extracted without involving the difficult order reduction problem. The problem of convergence onto an incorrect solution which is associated with using the eigenvectors of a clamped-free beam as the comparison functions in approximating the motion of the flexible arm is demonstrated and various factors affecting the performance of the flexible manipulator, such as control gains and material damping, are studied.

1 Introduction

Two major issues arise in controlling robot arms. The first is the determination of the joint-angle positions with which the manipulator would satisfy the prescribed control objectives. Secondly, given the desired sequence of angular positions, the robot arm is actuated and travels from its latest position to the desired location in a manner that satisfies some selected criteria. The primary difficulties in controlling nonrigid robot arms are due to the dynamic coupling of the links and the deformation due to gravity. As the coupling of flexible links leads to greater difficulty in controlling the robot in the transient state, the static deformation of the links causes the end-effector of the robot arm to be placed away from its intended objective. The deformation of a robot arm is commonly minimized by constructing the robot with heavy, rigid members. A very large portion of the control effort therefore is expended just to lift the arm itself. The desirability of a lightweight manipulator is therefore obvious. However, the use of flexible links further complicates the already complicated robot dynamics and control design (Book et al., 1975; Hanagud and Sarkar, 1989; Cetinkunt and Book, 1990). The interaction between rigid robot links is demonstrated (Asada and Takeyama, 1982). As the feedforward control scheme is shown to be suitable in suppressing the excessive oscillatory motion due to the coupling of rigid links (Luh, 1983), it is also clear that the feedforward control for the flexible arms is computationally very intensive and may be unrealistic. Hence, we regard as two of the primary requirements for controlling flexible manipulators first the establishment of a robust estimation method for the proper joint angular coordinates for end-effector positioning, and second a reliable and stable feedback control scheme.

We will focus here on the modeling and dynamic control of the flexible arm. Therefore, the required final joint angular positions are assumed given in this study. (Among other approaches, there has been developed a robust vision sensing and estimation algorithm (Skaar et al., 1990) that has been shown to estimate accurately the required terminal angular positions for end-tip positioning of a nonrigid arm.) A two-link flexible arm is examined herein using infinite- and finite-dimensional coordinates for motion of the deformable body. The flexible links for the two-link arm are modeled as Euler-Bernoulli beams. No stretching or shortening of the flexible link is considered. For the infinite-dimensional coordinates approach, a spatially varying deflection is chosen to model the motion of each flexible link. For the finite-dimensional coordinates approach, the elastic deflection is approximated using various sets of shape functions.

Among the factors affecting the behavior of a robot, the following are studied: link flexibility, gravitation, selection of the approximation functions, damping, and control. The effects of the link flexibility on the stability characteristics and the performance of a robot are studied in the Laplace transform domain using the linearized system of the nonlinear model, and in the time domain by examining the results obtained from integrating the full set of nonlinear equations of motion. In particular, comparison functions from both complete and in-

[1]This work is supported partially by the U.S. Office of Naval Research under Contract N00014-89-1533.

Contributed by the Applied Mechanics Division of THE AMERICAN SOCIETY OF MECHANICAL ENGINEERS for publication in the ASME JOURNAL OF APPLIED MECHANICS.

Discussion on this paper should be addressed to the Technical Editor, Professor Lewis T. Wheeler, Department of Mechanical Engineering, University of Houston, Houston, TX 77204-4792, and will be accepted until four months after final publication of the paper itself in the ASME JOURNAL OF APPLIED MECHANICS.

Manuscript received by the ASME Applied Mechanics Division, Mar. 14, 1991; final revision, Jan. 16, 1992. Associate Technical Editor: D. J. Inman.

Copyright © 1993 by ASME
Downloaded 03 May 2010 to 171.66.16.245. Redistribution subject to ASME license or copyright; see http://www.asme.org/terms/Terms_Use.cfm

complete sets are employed to demonstrate the importance of choosing the appropriate approximation functions. It is shown that the approximation functions chosen from certain sets of eigenvectors which are derived using the flexible links with clamped-free boundary conditions lead to inaccurate dynamic solutions, but fairly reliable results in the Laplace transform domain.

The consideration of gravity requires the use of integral control to prevent terminal joint-positioning error of the flexible manipulator. This is very significant since, even for collocated sensor/actuator pairs, proportional, derivative and integral (PID) control, unlike proportional and derivative (PD) control, is known to be the cause of system instability. Finally, a closed-loop PID control system is analyzed using the linearized model, and also a dynamic simulation is performed with the full, nonlinear model to validate the analytical conclusions based on the linearized system.

2 Flexible Arm Model

A robot can be considered as the assembly of many flexible or rigid links. Our model of a basic flexible link is shown in Fig. 1. Generally, it is composed of a flexible member, a rigid hub at one end, and a mass attached at the opposite end of the member. The adjacent links, if any, are connected to the flexible link at their ends. The flexible member is assumed to be slender such that the Euler-Bernoulli beam assumption is valid. We further assume that the link is maneuvered in the vertical plane and that the out-of-plane deflection is negligible. The constants m_b and I_b are the mass and the mass moment of inertia of the rigid hub, respectively. The constant I is the area moment of inertia of the cross-section about the neutral axis. The constant ρ is the uniform mass per unit length of the flexible member. The end-tip mass is denoted as m_e and the mass moment of inertia of this portion of the arm is assumed to be negligible, i.e., $I_e = 0$. The vectors $\mathbf{r}_b$ and $\mathbf{v}_b$ are the position and velocity of the hub referred to the ground reference frame. If we assume that the deformation in the axial direction of the link is negligible, and neglect the thickness of the member itself, then the position of any point along the member can be written as

$$\mathbf{r}_i = \mathbf{r}_b + \mathbf{z} + \mathbf{y} \tag{1}$$

where

$$\mathbf{z} = z\mathbf{e}_z \tag{2}$$

$$\mathbf{y} = y(z, t)\mathbf{e}_y \tag{3}$$

and where $y(x, t)$ is the deflection of the elastic member measured from its undeformed configuration. The $\mathbf{e}_y$ and $\mathbf{e}_z$ are unit vectors in the y and z directions, respectively, as shown in Fig. 1. Differentiating the expression for the position vector with respect to time, we obtain the velocity of any point along the member.

$$\mathbf{v}_i = \mathbf{v}_b + \omega \times \mathbf{z} + \dot{\mathbf{y}} \tag{4}$$

where ω is the angular velocity of the rigid hub measured with respect to the inertial frame. The symbol, $\times$, denotes the vector cross product and $(\dot{})$ denotes the derivative with respect to time. Using the velocity expression, we write the kinetic energy of a flexible link as

$$T_e = \frac{1}{2} I_o \omega^2 + \frac{1}{2} \int_0^L \rho^* \mathbf{v}_i \cdot \mathbf{v}_i dz \tag{5}$$

where the symbol, $\cdot$, is the dot product or inner product and $\rho^* = \rho(z) + m_b\delta(z) + m_e\delta(z - L)$, and δ is the dirac delta function. Using the position vector, we write the potential energy of a cross-sectional element as

$$V_e = V_s + V_g = \frac{1}{2} \int_0^L EI(y'')^2 dz + \mathbf{g} \cdot \int_0^L \rho \mathbf{r}_i dz \tag{6}$$

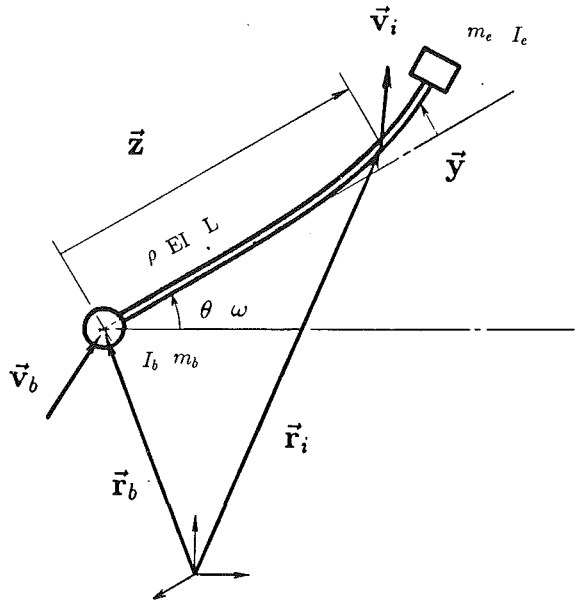


Fig. 1 Flexible arm element

where V_s is the elastic strain energy and V_g is the gravitational potential energy. The $(\,)''$ denotes the second derivative with respect to the variable z. Using the kinetic and potential energy, we may obtain the Lagrangian of the entire flexible system by summing the Lagrangian of all the links of the flexible robot together and invoke the extended Hamilton's Principle (Meirovitch, 1970) to derive the governing differential equations. Depending on the selected modeling method for the flexible components, we may obtain either PDE's or ODE's as the equations of motion for the flexible system.

When the distributed coordinate $y(z, t)$ is used to describe the elastic deflection of the flexible link, the extended Hamilton's Principle is applicable for deriving the system governing partial differential equations.

$$\delta \int_{t_1}^{t_2} L dt + \int_{t_1}^{t_2} \delta W_{nc} dt = 0 \tag{7}$$

where L denotes the Lagrangian of the entire flexible system. Since the torque at the base of an individual link is supplied by the member or ground that the rigid hub is fixed upon, the work done by the nonconservative control torque is found by multiplying the applied torque at the rigid hub with the variation of the angular rotation of the hub relative to the previous link or ground.

$$\delta W_{nc} = \sum_{i=1}^{m} T_{qi} \delta\theta_i \tag{8}$$

where m is the number of the links.

Alternatively, we may approximate the continuous deflection of a flexible link by a set of assumed shape functions and their time-dependent generalized coordinates. The reduced-order model of a flexible member is commonly expressed as

$$y(z, t) = \sum_{i=1}^{n} \phi_i(z) q_i(t) = \{\phi\}^T \{q\} \tag{9}$$

where $\{\phi(z)\}$ are a set of basis functions, $\{q(t)\}$ are the time functions corresponding to the basis functions, and n is the number of these functions. By using the Extended Hamilton's Principle in the form of Lagrange's equations (Meirovitch, 1970), a set of nonlinear ODE's results.

2.1 Two-Link Flexible Arm. The notations employed to describe the two-link arm are shown in Fig. 2. In general, a subscript is added to all the variables and link properties to denote where these quantities reside. For example, the dis-

Downloaded 03 May 2010 to 171.66.16.245. Redistribution subject to ASME license or copyright; see http://www.asme.org/terms/Terms_Use.cfm

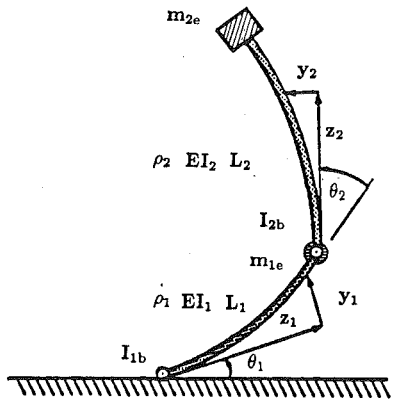


Fig. 2 Two-link flexible arm model

tributed deflections, y_1 and y_2, are the deflections of the first link and second link. These deflections are measured from their undeformed configurations. The angle θ_1 is measured from the x-axis of the ground reference frame. The angle θ_2 is the joint rotation of the rigid base on the second link measured from the tangent line at the end-tip of the first link. Later, we assume the control applied at the intermediate joint of the links is generated by an actuator located at the end of the first link which acts upon the rigid base of the second link. Let $\mathbf{r}_1$ and $\mathbf{r}_2$ denote the position vectors of a point on link one and link two, respectively.

$$\mathbf{r}_1 = z_1\mathbf{e}_{z1} + y_1\mathbf{e}_{y1} \tag{10}$$

$$\mathbf{r}_2 = L_1\mathbf{e}_{z1} + y_1(L_1)\mathbf{e}_{y1} + z_2\mathbf{e}_{z2} + y_2\mathbf{e}_{y2} \tag{11}$$

$$\mathbf{v}_1 \cong (z_1\dot{\theta}_1 + \dot{y}_1)\mathbf{e}_{y1} \tag{12}$$

$$\mathbf{v}_2 \cong [L_1\dot{\theta}_1 + \dot{y}_1(L_1)]\mathbf{e}_{y1} + (z_2(\dot{\theta}_1 + \dot{\theta}_2 + \dot{y}_1'(L_1)) + \dot{y}_2)\mathbf{e}_{y2} \tag{13}$$

where the z-axis is along the length of the arm and the in-plane y-axis is perpendicular to the z-axis and measured from the undeformed configuration of the arm. As one notices, terms such as $y_1\dot{\theta}_1\mathbf{e}_{z1}$ in the velocity expression have been dropped. These terms, which are small for small deformations and low angular velocities, are eliminated to avoid a so called "softening effect" (Kane et al., 1987). The behavior of a flexible system may become unrealistic when these terms are considered, as for instance in the case of a spinning satellite. Unless a dynamic stiffening effect is introduced (Baruh and Tadikonda, 1989), the solutions from solving the system equations without the terms that cause the softening effect are believed to correspond more closely with physical reality than those obtained by retaining the those terms. With the position and velocity vectors, we write the potential and kinetic energy of links one and two as

$$V_1 = \frac{1}{2}\int_0^{L_1} EI_1(y_1'')^2 dz + \int_0^{L_1} \rho_1^* g[z\sin\theta_1 + y_1\cos\theta_1]dz \tag{14}$$

$$V_2 = \frac{1}{2}\int_0^{L_2} EI_2(y_2'')^2 dz + \int_0^{L_2} \rho_2^* g[L_1\sin\theta_1 + y_1(L_1)\cos\theta_1 + z\sin(\theta_1 + y_1'(L_1) + \theta_2) + y_2\sin(\theta_1 + y_1'(L_1) + \theta_2)]dz \tag{15}$$

$$T_1 = \frac{1}{2}I_{b1}\dot{\theta}_1^2 + \frac{1}{2}\int_0^{L_1} \rho_1^*[z\dot{\theta}_1 + \dot{y}_1]^2 dz \tag{16}$$

$$T_2 = \frac{1}{2}I_{b2}(\dot{\theta}_1 + \dot{y}_1'(L_1) + \dot{\theta}_2)^2 + \frac{1}{2}\int_0^{L_2} \rho_2^*(L_1\dot{\theta}_1 + \dot{y}_1(L_1))^2 dz + \frac{1}{2}\int_0^{L_2} \rho_2^*[z(\dot{\theta}_1 + \dot{y}_1'(L_1) + \dot{\theta}_2) + \dot{y}_2]^2 dz + \int_0^{L_2} \rho_2^*(L_1\dot{\theta}_1 + \dot{y}_1'(L_1))[z(\dot{\theta}_1 + \dot{y}_1'(L_1) + \dot{\theta}_2) + \dot{y}_2]dz \times \cos(\theta_1 + y_1'(L_1) + \theta_2). \tag{17}$$

The work done by the nonconservative torque at the joints is

$$\delta W_{nc} = T_{q1}\delta\theta_1 + T_{q2}\delta\theta_2. \tag{18}$$

The variational principle is utilized to produce four nonlinear governing differential equations. Two of the four differential equations are in integral form and involve the control torques, while the remaining two equations have both partial derivatives with respect to time and partial derivatives with respect to z. There are four boundary conditions associated with each of the mixed ordinary and partial differential equations. Among the boundary conditions, the two natural boundary conditions at the tip of link one are extremely complicated, and involve the instantaneous state of the whole of link two.

For the stability analysis of the linearized system, we perturb the joint angles, deflections and applied torques about an arbitrarily selected static equilibrium configuration. The joint angles, deflections, and torques, are first written as the sum of their static equilibrium values plus variable perturbations. These expressions are then substituted into the nonlinear PDE's and boundary conditions to obtain a set of linearized PDE's and boundary conditions. These linear differential equations are transformed into the Laplace transform domain and used to solve for the four open-loop transfer functions relating the joint angular responses to the control torques. Using the open-loop transfer functions and the control gains, one can derive the PID-control closed-loop transfer functions describing the perturbed joint angular responses and perturbed reference inputs. Both the expressions for the open-loop and closed-loop transfer functions are very lengthy, and they are derived partially using Macsyma (Symbolics Inc., 1985). Due to the complexity of these expressions, we will not write them explicitly here.

2.2 The Ritz Approximation of the Two-Link Flexible Arm. The distributed deflections of the two-link flexible arm are approximated by $\{\phi_1\}$, $\{q_1\}$, $\{\phi_2\}$, and $\{q_2\}$ according to Eq. (9). The $\{\phi_1\}$ and $\{\phi_2\}$ are two sets of admissible functions. We define the collection of all the variables of the system as

$$\{\psi\}^T = \{\theta_1, \theta_2, \{q_1\}^T, \{q_2\}^T\}. \tag{19}$$

Using Lagrange's equations, we arrive at the general form of the system ODE's:

$$[M]\{\ddot{\psi}\} + [\dot{M}]\{\dot{\psi}\} - \frac{1}{2}\frac{\partial(\{\dot{\psi}\}^T[M]\{\dot{\psi}\})}{\partial\{\psi\}} + [K]\{\psi\} + \frac{\partial V_q}{\partial\{\psi\}} = \{T_q\}. \tag{20}$$

Noting that

$$\frac{\partial(\{\dot{\psi}\}^T[M]\{\dot{\psi}\})}{\partial\{\psi\}} = [\dot{M}]\{\dot{\psi}\} \tag{21}$$

the equations of motion can finally be written as

$$[M]\{\ddot{\psi}\} + \frac{1}{2}[\dot{M}]\{\dot{\psi}\} + [K]\{\psi\} + \frac{\partial V_g}{\partial\{\psi\}} = \{T_q\} \tag{22}$$

where V_g is the gravitational potential energy, and the elements of $[M]$ and $[K]$ can be extracted directly from the kinetic and potential energy expressions. For instance, the $[K]$ matrix for the two-link arm has the form shown as follows:

$$[K] = \begin{bmatrix} [0]_{2\times 2} & [0]_{2\times n1} & [0]_{2\times n2} \\ [0]_{n1\times 2} & [K^1]_{n1\times n1} & [0]_{n1\times n2} \\ [0]_{n2\times 2} & [0]_{n2\times n1} & [K^2]_{n2\times n2} \end{bmatrix} \tag{23}$$

Downloaded 03 May 2010 to 171.66.16.245. Redistribution subject to ASME license or copyright; see http://www.asme.org/terms/Terms_Use.cfm

where

$$K_{ij}^{1}=\int_0^{L_1} EI_1\phi_{1i}''\phi_{1j}''dz \tag{24}$$

$$K_{ij}^{2}=\int_0^{L_2} EI_2\phi_{2i}''\phi_{2j}''dz \tag{25}$$

If closed-loop PID control is considered, an additional state variable in Eq. (26) is defined for each link.

$$\psi_e=\int^t (\theta_d(\tau)-\theta(\tau))d\tau+\psi_{eo} \tag{26}$$

In order to perform local linear stability analysis, the nonlinear system differential equations are linearized to form an expanded eigenvalue problem (Hurty and Rubinstein, 1964).

3 Viscoelastic Damping: Kelvin Material

For the Kelvin material, the non-conservative moment acting in the flexible link has a special form and is derived using the following stress-strain relationship:

$$\sigma_z=E\left(\epsilon_z+a\frac{d\epsilon_z}{dt}\right)=E(\epsilon_z+a\dot{\epsilon}_z). \tag{27}$$

This expression is used in conjunction with the element beam theory and variational principle to give to the work done by the nonconservative damping force in Eq. (7).

$$\delta W_{nc}=\int_0^L EIa\dot{y}''\delta y''dz \tag{28}$$

For the purpose of this study, the regeneration of system PDE's is not necessary due to the following: (1) Damping does not change the static configuration. (2) The exact transfer functions can be re-evaluated using the Correspondence Principle (Christensen, 1982). The use of the Correspondence Principle requires only the following substitutions in the transfer functions:

$$EI_i=EI_i(1+a_is) \quad i=1,\ 2, \tag{29}$$

where a_1 and a_2 are the coefficients as defined in Eq. (27). The procedure for obtaining the poles of the open- or closed-loop transfer functions are identical with that for the undamped systems. For the discrete coordinate approach, the Kelvin damping contributes to the damping matrix $[C]$. For instant, the matrix $[C]$ for the two-link flexible arm becomes

$$[C]=\begin{bmatrix} [0]_{2\times 2} & [0]_{2\times n1} & [0]_{2\times n2} \\ [0]_{n1\times 2} & [C^1]_{n1\times n1} & [0]_{n1\times n2} \\ [0]_{n2\times 2} & [0]_{n2\times n1} & [C^2]_{n2\times n2} \end{bmatrix} \tag{30}$$

where the components of the $[C^1]$ and $[C^2]$ are

$$C_{ij}^m=a_mK_{ij}^m \quad m=1,\ 2. \tag{31}$$

4 Comparison Functions

Four sets of comparison functions of two different types are used in approximating the deformation of the flexible links, including polynomials and free vibrational mode shapes of cantilever beams. Since the Ritz method requires that all basis functions satisfy the essential boundary conditions of the flexible member, we choose the polynomial comparison functions as follows:

$$\phi_i(z)=\left(\frac{z}{L}\right)^{i+1} \quad i=1,\ n. \tag{32}$$

Clearly, the geometric boundary conditions of the flexible links are satisfied since the polynomials in Eq. (32) always lead to $\phi_i(0)=\phi_i'(0)=0$. Additionally, three different sets of shape functions associated with five cantilever beams are generated. The cantilever beams used to generate the first set of shape functions have the properties as listed in Table 1 except that the end-tip masses are zero, i.e., the eigenfunctions of a cantilever beam with $\rho=0.3$ and $m_e=0$ are used for link one and those of a cantilever beam with $\rho=0.1$ and $m_e=0$ are used for link two. The second set of functions is obtained using the beams with properties of Table 1. The final set of comparison functions is obtained using a cantilever beam with $\rho=0.3$ and an end mass equal to 0.25 Kg. This set of eigenfunctions is used to approximate both link one and link two. In the order that they are defined, the three sets of functions are identified as Set A, Set B, and Set C. These shape functions are determined by using the roots in k of the following characteristic equation along with Eq. (35):

Table 1 Two-link arm properties

Properties	L	ρ	EI	m_b	m_e	I_b	I_e
Link 1	1 m	0.3 Kg/m	45 N/m^2	0.00	0.15 Kg	0.2 Kgm^2	0
Link 2	1 m	0.1 Kg/m	5 N/m^2	0.00	0.10 Kg	0.067 Kgm^2	0

$$\begin{aligned}1+\cos(kL)\cosh(kL)+(kL)^4\alpha\beta[\cos(kL)\cosh(kL)-1]\\ +(kL)^3\beta[\sin(kL)\cosh(kL)+\cos(kL)\sinh(kL)]\\ +kL\alpha[\sin(kL)\cosh(kL)-\cos(kL)\sinh(kL)]=0\end{aligned} \tag{33}$$

where

$$\alpha=\frac{m_e}{\rho L} \quad \beta=\frac{I_e}{\rho L^3} \quad \omega=k^2\left(\frac{EI}{\rho}\right)^{1/2} \tag{34}$$

$$\phi_i=\cosh(k_ix)-\cos(k_ix)-\frac{\cosh(k_iL)+\cos(k_iL)}{\sinh(k_iL)+\sin(k_iL)}[\sinh(k_ix)-\sin(k_ix)]. \tag{35}$$

Once these eigenfunctions are obtained, they are substituted into Eq. (9) to approximate the deflections which in turn are used to derive the ODE's for the dynamic and frequency domain analyses. Since the end-tip position of a robot arm is a common maneuvering objective, it will be used as the measurement of the accuracy of the dynamic solutions that individual sets of functions can achieve. For all the analyses we performed, no exact solution is available. However, the solution obtained using the polynomials, in theory, will converge to the exact solution. Therefore, it is used as the basis for monitoring the error due to the use of eigenfunctions as the shape functions. For this case, the percent error is defined as

$$\text{Percent Error}=100\left|\frac{\Delta_{\text{Cantilever mode}}}{\Delta_{\text{polynomial}}}\right| \tag{36}$$

For this study, the two-link flexible arm with the properties listed in Table 1 is utilized as the physical model and magnitude of gravitational constant is 9.81 m/sec^2. The end-tip deflection of link two, Δ, is measured from the end-tip position of a two-link rigid arm with identical inertial properties and joint angular coordinates.

5 Frequency Domain Analysis

When motion of a deformable body is approximated with discretizing functions, the frequency content of the approximation can be used as a criterion to test the accuracy of the approximation. One fact to bear in mind with the choice of frequency content as the measurement of a successful approximation is that the approximate mode shapes of a system are less accurate than the approximated frequency values. In other words, if a frequency of the approximated system has significant error compared with the exact value, the mode shape corresponding to that frequency is also inaccurate. This implies that when a set of comparison functions fails to estimate the frequency components of a flexible system accurately above a particular freuency value, for instance, ω_n, then the response of the flexible system is likely incorrect if any eigenvector

Downloaded 03 May 2010 to 171.66.16.245. Redistribution subject to ASME license or copyright; see http://www.asme.org/terms/Terms_Use.cfm

corresponding to the frequencies which are higher than ω_n participates significantly during the motion. We notice that, during the development of the eigenfunctions, a zero-moment condition at one end of the flexible link is assumed. However, when this zero-moment end is connected to the base of another link to construct the two-link robot arm, none of the eigenfunctions is capable of developing the torque which is required to hold both links together and the control exerted between the links. Mathematically, this difficulty arises because the eigenfunctions can never satisfy the natural boundary condition of the flexible links. Hence, they do not form a complete set. Theoretically, when the functions chosen from incomplete set are used for approximation, convergence of the approximate solution to the exact solution is not assured. However, the magnitude of the error in the approximate solution due to this modeling deficiency have to be determined case by case.

5.1 Convergence in Frequency Domain. The arm is at rest with joint angles $\theta_1 = 0$ and $\theta_2 = 0$. Three comparison functions are used for each link and gravity is omitted for this case. Both exact frequencies, which are obtained from the transfer function approach, and approximate solutions, which are obtained from eigenvalue analysis, are shown in Table 2. The selected cantilever modes are the Sets A and B.

It is obvious that, at the high frequencies, the cantilever modes give the best results despite the fact that they are taken from an incomplete set of functions. The polynomial solutions are improved by raising the order of the approximation. If we increase the number of polynomials to six, the original ill-predicted higher frequencies approach the exact values very closely. Similar results are observed for both one- and two-link, open- and closed-loop systems, regardless of the set points for θ_1 and θ_2.

5.2 Linear Stability. Two root locus plots are given to demonstrate the effects of flexibility and control on the two-link flexible-arm PID control systems. The root locus plot in Fig. 3 is generated using the following control gains: $K_{1d} = 3$, $K_{1i} = 1$, $K_{2p} = 5$, $K_{2d} = 1$ and $K_{2i} = 1$; and varying K_{1p}, the proportional gain for link one, from 0 to infinity at three angular positions of (θ_1, θ_2): $(-90$ deg, 30 deg), (0 deg, 30 deg) and (90 deg, 30 deg). Parallel to the analysis of the flexible arm, the same procedures are performed on the rigid arm using the same inertial properties. Examining Fig. 4, the influences of angular position about which linearization occurs on the system characteristics are clearly important for the rigid case as well. A stable control system at $(-90$ deg, 30 deg) may become unstable at (90 deg, 30 deg). Comparing the results from the flexible and rigid models, the importance of flexibility is evident. The marginal instability, for example, which occurs in a certain region corresponding to a high position gain is missing for the rigid model. For the models we tested, all the higher poles remain to the left of the imaginary axis once the lowest poles associated with the rigid-body motion are stabilized. If the PID controllers are replaced by PD controllers, the sufficient condition for a stable PD control design can be proved using Liapunov's direct method. A positive-definite stiffness matrix of the linearized system ensures stable PD control.

6 Nonlinear Dynamic Simulation

Two nonlinear dynamic simulations are given. In the first test case, the two-link arm is released from an equilibrium position and undergoes free falling motion. The motion of the arm together with the energy are monitored to demonstrate the chaotic behavior of the conservative system. In the second test, control at the joints is activated to drive the links to follow the reference inputs. The predicted linear system responses are compared to the results obtained by numerically integrating the full set of nonlinear ODE's to show that the behavior of the flexible arm near equilibrium may be predictable by the linearized system.

Table 2 Poles of open-loop Two-link flexible arm

Mode	Exact (rad/sec)	Set B (rad/sec)	Polynomial (rad/sec)	Set A (rad/sec)
1,2	(0 , 0.00)	(0 , 0.00)	(0 , 0.00)	(0 , 0.00)
3	(0 , 19.15)	(0 , 19.15)	(0 , 19.15)	(0 , 19.15)
4	(0 , 33.47)	(0 , 33.47)	(0 , 33.47)	(0 , 33.45)
5	(0 ,121.79)	(0 ,121.79)	(0 , 121.79)	(0 ,122.08)
6	(0 ,207.36)	(0 ,207.39)	(0 , 208.08)	(0 ,208.31)
7	(0 ,367.62)	(0 ,367.67)	(0 , 556.56)	(0 ,376.76)
8	(0 ,631.57)	(0 ,632.62)	(0 , 973.63)	(0 ,645.64)

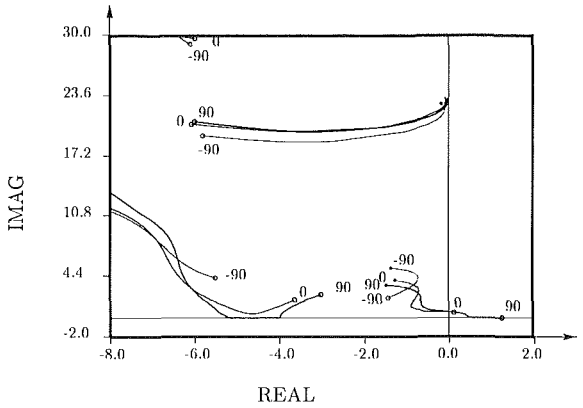


Fig. 3 Two-link flexible arm PID control root locus

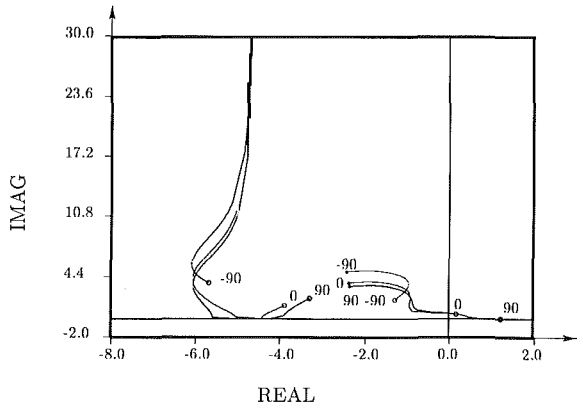


Fig. 4 Two-link rigid arm PID control root locus

6.1 Two-Link Flexible Arm Subjected to No Control Torques. The motion is generated by releasing the two-link arm from the static equilibrium position at $(\theta_1, \theta_2) = (30$ deg, 30 deg). Since there is no nonconservative force/torque applied to the system, the total system energy is conserved, i.e., the sum of the kinetic and potential energy remains constant. The simulation results, with five polynomial basis functions, at selected time steps, are shown in Fig. 5. The trace of the end-tip position of link two is also plotted for the first five seconds. The deformation of the arm is noticeable particularly after 0.6 sec. The total energy, potential energy, elastic energy, and kinetic energy are plotted in Fig. 6. We observe in this figure that the total energy is conserved and the elastic energy is not

Downloaded 03 May 2010 to 171.66.16.245. Redistribution subject to ASME license or copyright; see http://www.asme.org/terms/Terms_Use.cfm

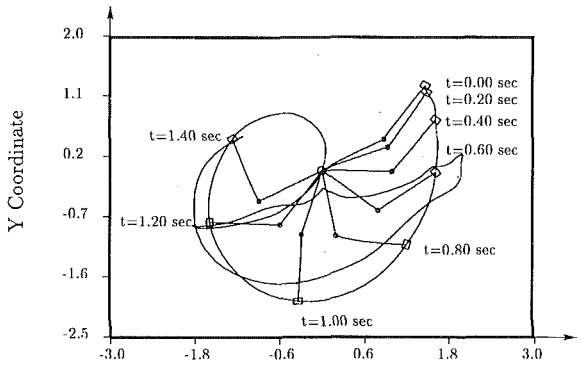


Fig. 5 Free-falling two-link flexible arm

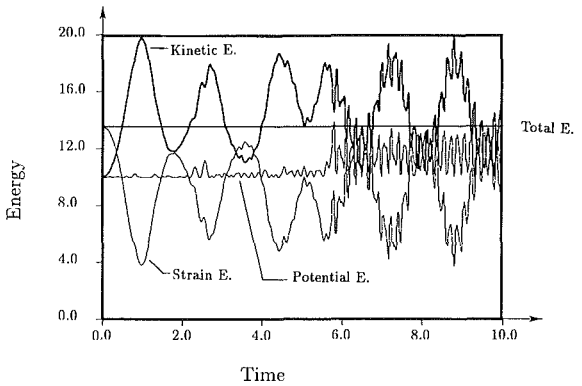


Fig. 6 Energy plot of free-falling undamped two-link flexible arm

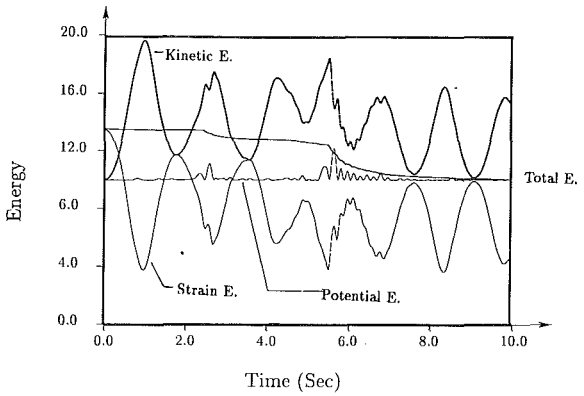


Fig. 7 Energy plot of free-falling two-link flexible arm with Kelvin material

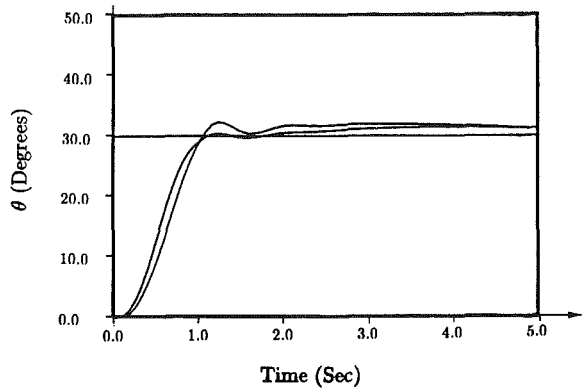


Fig. 8 Joint angular position of two-link flexible arm subjected to PID control

negligible. The noticeable elastic vibration of the flexible links may be reduced if material damping is introduced to the arm. By setting the damping coefficients as defined in Eq. (29) to $a_1 = a_2 = 0.005$, we obtain the energy plot shown in Fig. 7 in which the elastic energy of the undamped system is shown to dissipate very quickly.

6.2 Two-Link Flexible Arm With PID Controller. Prediction from the linear analysis is evaluated using a numerically integrated approximation to a large-scale, nonlinear motion. The flexible arm is driven by a PID controller at the base of each link. The reference inputs to the joints are in the form of

$$\theta_d = \begin{cases} (\theta_f - \theta_i)\left[10\left(\frac{t}{t_f}\right)^3 - 15\left(\frac{t}{t_f}\right)^4 + 6\left(\frac{t}{t_f}\right)^5\right] + \theta_i & t \le t_f \\ \theta_f & t > t_f \end{cases} \quad (37)$$

where θ_i and θ_f are the initial and final angular positions of the respective link. For link one, t_{1f} and θ_{1f} are used for t_f and θ_f in Eq. (37). The time t_{1f} represents the instant at which the reference input of link one reaches θ_{1f}. The same convention applies to link two. The control gains, $K_{1p} = 10$, $K_{1d} = 15$, $K_{1i} = 5$, $K_{2p} = 10$, $K_{2d} = 15$ and $K_{2i} = 5$ are used for the closed-loop PID control system. The angular positions about which the differential equations are linearized are $\theta_1 = 30$ deg and $\theta_2 = 30$ deg. For this linearized PID control system, the first pair of the resulting poles which have lowest value of nonzero imaginary parts is $(-0.968, \pm 0.752)$. If the linearized solution is valid, the flexible arm driven by the specified control would suffer from the relatively long response time due to the large time constant associated with the lowest frequency of the closed-loop system. In other words, if the control excites the motion which contains the lowest frequencies, the joint angular responses of this control system are likely oscillatory and the elapsed time for the flexible arm to approach the desired position will be fairly large. A dynamic simulation is performed to validate this. For this analysis, both t_{1f} and t_{2f} are set to one second. The arm is initially at rest with the angular positions $\theta_1 = 0$ and $\theta_2 = 0$. The desired final angular positions are identical with the values used for the linear analysis, i.e., $\theta_{1f} = 30$ deg and $\theta_{2f} = 30$ deg. The plot of angular responses are shown in Fig. 8. It is clear that the control system approaches the final reference position very slowly as is predicted by the Laplace domain analysis of the linearized system.

If, in lieu of the polynomials, the cantilever modes are used as the approximation functions in the simulation, the five-term approximation results have the error as defined in Eq. (36) in the range of 2 to 10 percent more. Depending on the type of cantilever mode shapes used, the magnitude of the error differs. In general, Sets B and C result in solutions closer to those of the polynomials than does Set A. By increasing the number of the approximation functions, the errors of all the results obtained using the cantilever modes decrease. However, the decreasing rate of the error is also different depending on the type of the comparison function chosen. The end-tip displacements obtained using the four-term and five-term polynomial functions have relative error in the order of 10^{-3} percent, while the results obtained using four-term and five-term cantilever beam shape functions still differ by ten percent or higher.

7 Conclusions

In this paper, both partial and ordinary differential equations of a two-link flexible arm are derived and used to obtain static solutions and Laplace transform domain characteristics. Also, the time-domain behavior of a two-link arm is obtained by integrating a set of nonlinear ordinary differential equations based on a consistent approximation of the distributed motion. It is shown that, when functions selected from a set of eigenvectors which are derived from cantilever beams with clamped-free boundary conditions are used for approximating the de-

Downloaded 03 May 2010 to 171.66.16.245. Redistribution subject to ASME license or copyright; see http://www.asme.org/terms/Terms_Use.cfm

flection of the flexible arm, the Laplace domain information may be fairly accurate. However, the time domain results converge to inaccurate solutions. It is revealed that the use of an incomplete set of discretizing comparison functions for the innermost of the two members leads to this problem.

It is also shown that the degree of flexibility, the set point of joint angles, the consideration of gravitation, the choice of closed-loop PID control gains, and material damping all have a large influence on the stability characteristics and performance of the flexible arm.

Finally, a PID control system which is selected based on the linear analysis is tested by large-angle, nonlinear dynamic simulation. The time-domain response of the flexible arm at the terminal angular position of the large angle maneuver is very well predicted by the linearized frequency domain analysis when the reference inputs to the control are chosen properly. This observation suggests the possibility of improving the control system by adjusting the control gains using the pole placement technique.

References

Asada, H. T., and Takeyama, I., 1982, "Control of a Direct-drive Arm," Robotics Inst., Carnegie-Mellon University, Pittsburgh, PA, Report CMU-RI-TR-82-4.

Baruh, H., and Tadikonda, S. S. K., 1989, "Issues in the Dynamics and Control of Flexible Robot Manipulators," *Journal of Guidance, Control and Dynamics*, Vol. 12, No. 5, Sept.-Oct., pp. 659-671.

Book, W. J., Maizza-Neto, O., and Whitney, D. E., 1975, "Feedback Control of Two Beam, Two Joint Systems with Distributed Flexibility," ASME *Journal of Dynamics Systems, Measurement, and Control*, Vol. 101, pp. 178-192.

Cetinkunt, S., and Book, W. J., 1990, "Flexibility Effects on the Control System Performance of Large Scale Robotic Manipulators," *Journal of Astronautical Sciences*, Vol. 38, No. 4, Oct.-Dec., pp. 531-556.

Christensen, R. M., 1982, *Theory of Viscoelasticity: An Introduction*, 2nd ed., Academic Press, New York.

Hanagud, S., and Sarkar, S., 1989, "Problem of the Dynamics of a Cantilever Beam Attached to a Moving Base," *Journal of Guidance, Control and Dynamics*, Vol. 12, No. 3, May-June, pp. 438-441.

Hurty, W. C., and Rubinstein, M. F., 1964, *Dynamics of Structures*, Prentice-Hall, Englewood Cliffs, New Jersey.

Luh, J. Y. S., 1983, "Conventional Controller Design for Industrial Robots—A Tutorial," *IEEE Transactions on System, Man, and Cybrnetics*, Vol. SMC-13, No. 3, May-June, pp. 298-316.

Meirovitch, L., 1970, *Analytical Methods in Analytical Dynamics*, McGraw-Hill, New York.

Kane, T. R., Ryan, R. R., and Banerjee, A. K., 1987, "Dynamics of a Cantilever Beam Attached to a Moving Base," *Journal of Guidance, Control and Dynamics*, Vol. 10, No. 2, Mar.-Apr., pp. 139-151.

Skaar, Steven B., Brockman, William H., and Jang, W. S., 1990, "Three-Dimensional Manipulation," *The International Journal of Robotics Research*, Vol. 9, No. 4, Aug., pp. 22-39.

Symbolics, Inc., 1985, *VAX UNIX MACSYMA Reference Manual*, Version 11.

Downloaded 03 May 2010 to 171.66.16.245. Redistribution subject to ASME license or copyright; see http://www.asme.org/terms/Terms_Use.cfm

Z. Tan

J. A. Witz

Department of Mechanical Engineering,
University College London,
London, WC1E 7JE, U.K.

On the Flexural-Torsional Behavior of a Straight Elastic Beam Subject to Terminal Moments

This paper discusses the large-displacement flexural-torsional behavior of a straight elastic beam with uniform circular cross-section subject to arbitrary terminal bending and twisting moments. The beam is assumed to be free from any kinematic constraints at both ends. The equilibrium equation is solved analytically with the full expression for curvature to obtain the deformed configuration in a three-dimensional Cartesian coordinate system. The results show the influence of the terminal moments on the beam's deflected configuration.

1 Introduction

It is well known that a slender beam will form a tortuous configuration under the action of combined bending and twisting moments. An early discussion on this phenomenon can be found in Timoshenko's book (1964) where it was associated with the problem of buckling. A comprehensive description of the three-dimensional deformation of an elastic beam is also provided by Love (1944), which was developed on the basis of equilibrium of a curved beam. Owing to the complicated mathematical expressions, analytical solution is only available for the helical configuration which occurs when the beam is subjected to terminal moments and forces acting in the longitudinal direction of the helix. A numerical approach with the aid of a computer was suggested by Konopasek (1972) for seeking a general deflected configuration of a fiber experiencing simultaneous flexural and torsional moments. In last few decades, however, the theory of the three-dimensional deflection of an elastic beam with nonlinear geometric and material properties have been established by several researchers with the aid of the variational methods. For instance, Antmen and Kenney (1981) considered the large buckled states of nonlinearity elastic rods under torsion, thrust, and gravity. The variational method finally results in a boundary value problem with integral forms. Numerical solutions are usually required to obtain the deflected configuration. An alternative approach is to utilize the potential energy method introduced by van Erp et al. (1988). The advantage of this method is that it is mathematically possible to consider various nonuniform properties of the beam. However, certain simplifications are needed for final solution. Consequently, the results are usually applicable for small deformation cases. A similar approach based upon the principle of virtual work has been introduced by Iura and Atluri (1989). Unfortunately, the same limitations exist.

The discussion of the large nonlinear elastic deformation of a slender elastic beam is encountered in Timoshenko's book (1964) in relation to buckling, where the beam is subjected to a compressive axial force. Timoshenko showed that the deformed configuration is two-dimensional and could be described analytically in terms of elliptic functions. Recently, Wang (1990) investigated the large elastic deformation of a beam lifted at two points. The deformed configurations remained planar. For small beam flexibility, the configuration can be expressed by polynomials of the arc length. However, for large-beam flexibility, only numerical results are available for giving the deformed configurations.

The number of analytical solutions available in literature for the three-dimensional configuration of an elastic beam is relatively small. This is not surprising when one considers the relatively complex nonlinear mathematical formulae describing the equilibrium of the beams. Here, it is worthwhile to mention Reissner's paper (1957), where the finite twisting and bending of thin rectangular elastic plates was investigated. The corresponding von Karman equations for the plate without the presence of surface loads were solved analytically. For a large aspect ratio, the plate is reduced to a straight beam with rectangular cross-section, consequently the problem is an analogue of the topic of this paper. This paper presents an analytical solution for the comparatively simple case of a slender elastic beam with uniform circular cross-section subject to the combined action of arbitrary terminal bending and twisting moments without the presence of any terminal forces. The terminal bending moments are applied antisymmetrically, while the twisting moments are applied symmetrically. The beam is idealized as a perfect elastica; i.e., the elastic limit of the material is sufficiently high. The moment equilibrium equation is given with respect to a three-dimensional curved beam. The mathematical expression describing the deformed configuration is derived using the full expression for curvatures. As a result,

Contributed by the Applied Mechanics Division of THE AMERICAN SOCIETY OF MECHANICAL ENGINEERS for presentation at the First Joint ASCE-EMD, ASME-AMD, SES Meeting, Charlottesville, VA, June 6-9, 1993.

Discussion on this paper should be addressed to the Technical Editor, Professor Lewis T. Wheeler, Department of Mechanical Engineering, University of Houston, Houston, TX 77204-4792, and will be accepted until four months after final publication of the paper itself in the ASME JOURNAL OF APPLIED MECHANICS.

Manuscript received by the ASME Applied Mechanics Division, Aug. 26, 1991; final revision, Jan. 16, 1992. Associate Technical Editor: F. M. Wan.

Paper No. 93-APM-3.

Copyright © 1993 by ASME

Downloaded 03 May 2010 to 171.66.16.245. Redistribution subject to ASME license or copyright; see http://www.asme.org/terms/Terms_Use.cfm

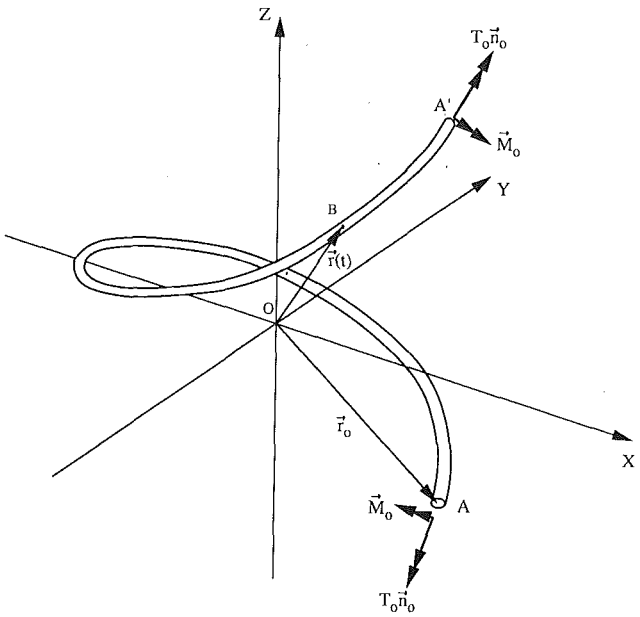


Fig. 1 Distortion of a straight elastic beam under combined bending and twisting moments

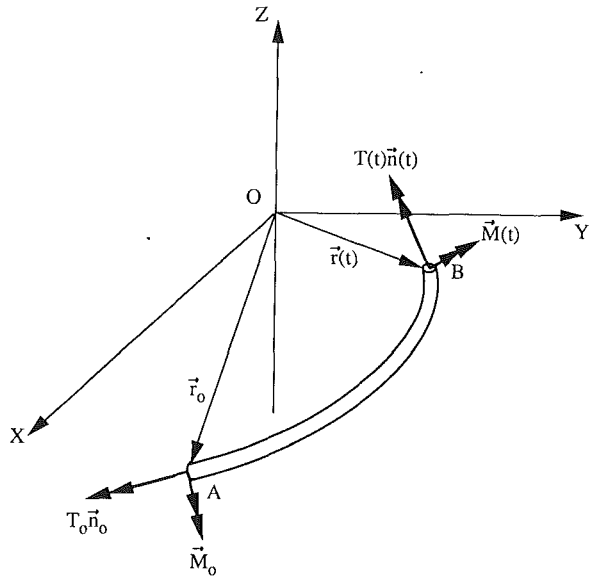


Fig. 2 Equilibrium of a beam segment

the corresponding solution is applicable for large nonlinear elastic deformations.

2 Theoretical Analysis

A typical deformed configuration of an initially straight beam with uniform circular cross-section is presented schematically in Fig. 1. It is subject to the combined action of twisting moment, $T_o\mathbf{n}_o$, and bending moment, $\mathbf{M}_o$, at both of its ends, A and A'. The twisting moments are applied symmetrically and the bending moments are applied antisymmetrically. The tortuous configuration can be parametrically described by a position vector $\mathbf{r}(t)$:

$$\mathbf{r}(t) = X(t)\mathbf{i} + Y(t)\mathbf{j} + Z(t)\mathbf{k} \tag{1}$$

where $\mathbf{i}$, $\mathbf{j}$, and $\mathbf{k}$ are the components of a unit direction vector and t is a permissible variable for the curve. The corresponding moment equilibrium of a beam segment AB, shown in Fig. 2, can be written out directly according to Euler-Bernoulli bending theory:

$$EI\boldsymbol{\kappa}(t) + T(t)\mathbf{n}(t) + T_o\mathbf{n}_o + \mathbf{M}_o = 0, \tag{2}$$

where T_o is the magnitude of the acting twisting moment at end A, whose direction coincides with the direction of the beam. $\mathbf{M}_o$ is an acting bending moment vector and is orthogonal to the twisting moment vector, $T_o\mathbf{n}_o$. $\mathbf{n}(t)$ and $\mathbf{n}_o$ are unit direction vectors at an arbitrary point B and end A, respectively. The subscript "o" refers to the position of end A. $T(t)$ is the magnitude of the internal twisting moment at point B resulted from deformation which acts at the beam's direction. $EI\boldsymbol{\kappa}(t)$ is the internal bending moment at point B due to deflection, EI is the flexural stiffness of the beam. $\boldsymbol{\kappa}(t)$ is the curvature vector of the distorted beam. It should be emphasized here that the beam is assumed to be an elastica. $EI\boldsymbol{\kappa}(t)$ is valid for large elastic deformations as soon as the curvature $\boldsymbol{\kappa}(t)$ is given by its full expression (see Timoshenko (1964) and C. Y. Wang (1990)). This large deformation is usually referred to as nonlinear elastic deformation in the literature. It should be pointed out that the large deformation discussed in this paper should be understood as the large nonlinear elastic deformation where the Young's modulus is constant and the curvature is given by its full expression. In many practical cases, $EI\boldsymbol{\kappa}(t)$ is applicable until the deformation exceeds the elastic limit of the structure's material. As a result, the following derived results are applicable as long as the beam's material remains elastic. The curvature and the direction vectors are given, respectively, by

$$\mathbf{n}(t) = \frac{\dfrac{d}{dt}\mathbf{r}(t)}{\left|\dfrac{d}{dt}\mathbf{r}(t)\right|} = n_x(t)\mathbf{i} + n_y(t)\mathbf{j} + n_z(t)\mathbf{k}$$

$$\boldsymbol{\kappa}(t) = \frac{\dfrac{d}{dt}\mathbf{r}(t) \times \dfrac{d^2}{dt^2}\mathbf{r}(t)}{\left|\dfrac{d}{dt}\mathbf{r}(t)\right|^3} = \kappa_x(t)\mathbf{i} + \kappa_y(t)\mathbf{j} + \kappa_z(t)\mathbf{k}. \tag{3}$$

Without loss of generality, the coordinate z is set to variable t, i.e., $z(t) = t$. This will simplify the following mathematical expressions. It is noted here that an appropriate choice of the origin and orientation of the Cartesian coordinate system simplifies the following mathematical derivation significantly. Here, the coordinate system is chosen to ensure that the principal plane xz is parallel with the resultant acting bending and twisting moments. As a result, the projection of the resultant moments on the y-axis vanishes.

For explicit illustration, the following nondimensional variables are now introduced:

$$x = \frac{X}{L_o} \qquad \tau_o = \frac{T_o L_o}{EI} \qquad \tau(t) = \frac{T(t)L_o}{EI}$$

$$\mu_x = \frac{M_{ox}L_o}{EI} \qquad m_x = \tau_o n_{ox} + \mu_x$$

$$y = \frac{Y}{L_o} \qquad \mu_y = \frac{M_{oy}L_o}{EI} \qquad m_y = \tau_o n_{oy} + \mu_y$$

$$z = \frac{Z}{L_o} \qquad \mu_z = \frac{M_{oz}L_o}{EI} \qquad m_z = \tau_o n_{oz} + \mu_z$$

where the subscripts x, y, and z denote the x, y, and z components of the corresponding vectors. L_o is the length of the beam. m_x and m_z ($m_y = 0$) are the components of the resultant acting bending and twisting moments, which are treaded as vectors. Thus, with full expressions for the direction and curvature vectors, equilibrium Eq. (2) can be decomposed into the following equations:

Downloaded 03 May 2010 to 171.66.16.245. Redistribution subject to ASME license or copyright; see http://www.asme.org/terms/Terms_Use.cfm

$$\begin{cases} \dfrac{-\ddot{y}}{(\dot{x}^2+\dot{y}^2+1)^{3/2}}+\tau(z)\ \dfrac{\dot{x}}{(\dot{x}^2+\dot{y}^2+1)^{1/2}}+m_x=0 \\ \dfrac{\ddot{x}}{(\dot{x}^2+\dot{y}^2+1)^{3/2}}+\tau(z)\ \dfrac{\dot{y}}{(\dot{x}^2+\dot{y}^2+1)^{1/2}}=0 \\ \dfrac{\dot{x}\ddot{y}-\ddot{x}\dot{y}}{(\dot{x}^2+\dot{y}^2+1)^{3/2}}+\tau(z)\ \dfrac{1}{(\dot{x}^2+\dot{y}^2+1)^{1/2}}+m_z=0 \end{cases} \tag{4a,b,c}$$

where x, y, and z are nondimensional coordinate variables. It should be noted that x and y are functions of z, and a dot superscript here refers to differentiation with respect to variable z. The component of the resultant acting moments pointing in the y-direction disappears under the chosen coordinate system.

From Eqs. (4a) and 4(b), the relationship between function $x(z)$ and $y(z)$ can be deduced as

$$\dot{y}\left(\frac{-\ddot{y}}{|\dot{r}|^3}+m_x\right)=\dot{x}\ \frac{\ddot{x}}{|\dot{r}|^3}, \tag{5}$$

where

$$|\dot{r}|=(\dot{x}^2+\dot{y}^2+1)^{1/2}.$$

From Eq. (5), it is found that functions $x(z)$ and $y(z)$ could be odd and even functions, respectively; i.e., $x(-z) = -x(z)$ and $y(-z) = y(z)$. Integrating Eq. (5) with respect to variable z gives the relationship between the two unknown functions, $x(z)$ and $y(z)$,

$$\frac{1}{(1+\dot{x}^2+\dot{y}^2)^{1/2}}+m_x y=C_1, \tag{6}$$

where C_1 is the unknown constant of integration.

Substituting Eq. (4c) into (4a) and (4b) to eliminate the internal twisting moment, $\tau(z)$, gives the following equations:

$$\begin{cases} \dfrac{\dot{x}\ddot{y}-\dot{y}^2\ddot{x}-\ddot{x}}{(\dot{x}^2+\dot{y}^2+1)^{3/2}}+m_z\dot{y}=0 \\ \dfrac{\dot{x}^2\ddot{y}-\dot{x}\dot{y}\ddot{x}+\ddot{y}}{(\dot{x}^2+\dot{y}^2+1)^{3/2}}+m_z\dot{x}-m_x=0. \end{cases} \tag{7a,b}$$

By integrating Eqs. (7a) and 7(b) with respect to z, the following equations are obtained:

$$\begin{cases} -\dfrac{\dot{x}}{(1+\dot{y}^2+\dot{x}^2)^{1/2}}+m_z y=C_2 \\ \dfrac{\dot{y}}{(1+\dot{y}^2+\dot{x}^2)^{1/2}}+m_z x-m_x z=C_3 \end{cases} \tag{8a,b}$$

where C_2 and C_3 are the unknown constants of integration. C_3 is zero since $x(z)$ and $y(z)$ are odd and even functions, respectively.

By further substituting Eq. (6) into Eq. (8a), it is found that the first-order derivative of function $y(z)$ can be expressed as a function of $y(z)$:

$$\dot{y}^2=\omega^2\frac{p^2-(y-q)^2}{(C_1-m_x y)^2} \tag{9}$$

where

$$\omega^2=m_x^2+m_z^2$$

$$p^2=\frac{(C_1m_x+C_2m_z)^2+\omega^2(1-C_1^2-C_2^2)}{\omega^4}$$

$$q=\frac{C_1m_x+C_2m_z}{\omega^2}. \tag{10a,b,c}$$

Finally, the analytical form of function $y(z)$ is obtained by integrating Eq. (9) with respect to z, giving

$$\frac{m_x}{\omega}[p^2-(y-q)^2]^{1/2}+\frac{C_1-m_xq}{\omega}\times\left[(-1)^k\arcsin\left(\frac{y-q}{p}\right)+k\pi\right]=\pm z+C_4$$
$$k=1,2,3,\ \ldots\ldots \qquad z\in[-z_o,z_o] \tag{11}$$

where C_4 is the unknown constant of integration. The positive and negative sign of z on the right-hand side of the equation indicates two branches. Without loss of generality, the positive sign is taken for $z > 0$ and the negative sign for $z < 0$. k is an integer constant resulting from the periodic property of the sinusoidal function and refers to the number of complete cycles occurring in the projection on to the plane yz. z_o is half the projected length on the z-axis of the deformed configuration.

Function $x(z)$ is obtained directly from Eq. (8b) where all first-order derivatives are replaced by Eqs. (6) and (9). This gives

$$\frac{-m_z}{\omega}[p^2-(y-q)^2]^{1/2}+\frac{m_x(C_1-m_xq)}{m_z\omega}\times\left[(-1)^k\arcsin\left(\frac{y-q}{p}\right)+k\pi\right]=\pm x+C_4\frac{m_x}{m_z}$$
$$k=1,2,3,\ \ldots\ldots \qquad z\in[-z_o,z_o]. \tag{12}$$

The positive sign of $x(z)$ refers to $z > 0$ and the negative sign for $z < 0$, which indicates two branches located above and below the xy-plane ($z = 0$), respectively. The final configuration of a distorted beam under arbitrary combined bending and twisting moments can be described parametrically by Eqs. (11) and (12). Since $x(z)$ and $y(z)$ are odd and even functions, respectively, only a half of the deflected configuration needs to be studied. By translating the coordinate system along the y-axis by a distance q, the parametric equations for the deflected configuration can be simplified to

$$\begin{cases} \dfrac{C_1}{\omega}\left[(-1)^k\arcsin\left(\dfrac{y}{p}\right)+k\pi\right]+\dfrac{m_x}{\omega}(p^2-y^2)^{1/2}=z+C_4 \\ \dfrac{m_xC_1}{m_z\omega}\left[(-1)^k\arcsin\left(\dfrac{y}{p}\right)+k\pi\right] \\ \qquad -\dfrac{m_z}{\omega}(p^2-y^2)^{1/2}=x+C_4\dfrac{m_x}{m_z} \\ k=1,2,3,\ \ldots \qquad z\in[0,z_o] \end{cases} \tag{13a,b}$$

where the translation leads to the following conditions between the parameters:

$$q=C_1m_x+C_2m_z=0 \tag{14a}$$

$$p^2=\frac{1-C_1^2-C_2^2}{\omega^2}. \tag{14b}$$

It is noted in Eq. (13) that p is the displacement amplitude of the function $y(z)$. By defining the position of the configuration as $y(0) = p$ and $x(0) = 0$, then the constant C_4 becomes

$$C_4=\frac{\pi C_1}{2\omega}. \tag{15}$$

The deformed configuration can be now determined from Eq. (13) if the parameters m_x, m_z, C_1, and C_2 are known. It is interesting to note that if the component of the acting mo-

Downloaded 03 May 2010 to 171.66.16.245. Redistribution subject to ASME license or copyright; see http://www.asme.org/terms/Terms_Use.cfm

ment in the x-direction is set to zero, i.e., $m_x = 0$, which can be achieved by rotation of the Cartesian coordinate system, then Eq. (13) represents a helix in three-dimensional space. This is consistent with Love's results for zero longitudinal force (1944, Art. 270 p. 414–415).

3 Boundary Conditions

The deflected configuration of the beam depends on the boundary conditions imposed upon the ends of the beam. Our interest here is to determine the deformed configuration of the beam when it undergoes arbitrary acting bending and twisting moments at both of its ends. The ends are free from any kinematic constraints. This boundary condition is given by

$$\begin{cases} m_x + \lim\limits_{z\to z_o}[\kappa_x(z) + \tau(z)n_x(z)] = 0 \\ \lim\limits_{z\to z_o}[\kappa_y(z) + \tau(z)n_y(z)] = 0 \\ m_z + \lim\limits_{z\to z_o}[\kappa_z(z) + \tau(z)n_z(z)] = 0. \end{cases} \quad (16a,b,c)$$

Note that the following discussion is restricted to half of the configuration ($z > 0$) according to the symmetric and antisymmetric properties of the functions $x(z)$ and $y(z)$. It is noted that Eq. (16) is automatically satisfied as long as the equilibrium equation are true.

Owing to the fact that the beam is free from terminal acting forces, no internal axial and shear forces are expected along the beam and, therefore, the beam does not elongate. Consequently, the beam maintains the same length before and after deformation. Thus,

$$1 = \int_{-z_o}^{z_o} \sqrt{\dot{x}^2 + \dot{y}^2 + 1}\, dz, \quad (17a)$$

i.e.,

$$y_o = p\cos\left(\frac{\omega}{2}\right) \quad (17b)$$

where the subscript "o" refers to the position of end $z = z_o$.

The components of the direction vector at the end $z = z_o$ are derived from Eq. (13) with the aid of Eq. (17b):

$$\begin{cases} n_{ox} = m_z p\cos\left(\frac{\omega}{2}\right) - C_2 \\ n_{oy} = \omega p \sin\left(\frac{\omega}{2}\right) \\ n_{oz} = -m_x p\cos\left(\frac{\omega}{2}\right) + C_1. \end{cases} \quad (18a,b,c)$$

As previously defined, the component of the resultant acting moments in the y-direction m_y is zero, and the acting bending and twisting moments are orthogonal to each other. The mathematical expressions for these conditions are given by

$$\begin{cases} m_y = 0 \\ m_x n_{ox} + m_z n_{oz} = \tau_o. \end{cases} \quad (19a,b)$$

By substituting Eq. (18a) and (18c) into Eq. (19b), the following equation is obtained:

$$C_1 m_z - C_2 m_x = \tau_o. \quad (20)$$

The constants C_1 and C_2 can be expressed in term of the acting bending and twisting moments by combining Eq. (20) and (14a):

$$\begin{cases} C_1 = \dfrac{\tau_o m_z}{\omega^2} \\ C_2 = -\dfrac{\tau_o m_x}{\omega^2} \end{cases} \quad (21a,b)$$

Finally, Eq. (18) can be rewritten as

$$\begin{cases} n_{ox} = m_z p\cos\left(\frac{\omega}{2}\right) + \dfrac{\tau_o m_x}{\omega^2} \\ n_{oy} = \omega p \sin\left(\frac{\omega}{2}\right) \\ n_{oz} = -m_x p\cos\left(\frac{\omega}{2}\right) + \dfrac{\tau_o m_z}{\omega^2}. \end{cases} \quad (22a,b,c)$$

By substituting Eqs. (21a) and (21b) into Eq. (14b), the deflection amplitude p is given by

$$p^2 = \frac{\omega^2 - \tau_o^2}{\omega^4}. \quad (23)$$

The deformed configuration can now be easily determined if the magnitude of the acting twisting moment, τ_o, and the components of the resultant acting bending and twisting moments m_x and m_z are known. This is because the constants C_1 and C_2 can be obtained from Eqs. (21a) and (21b), respectively. The deflection amplitude p and the constant C_4 are given by Eqs. (14b) and (15), respectively, where parameter p is taken as positive. Since all the parameters appearing in Eq. (13) are given uniquely in this case, the deflected configuration can be determined. The components of the direction vector at the end are given by Eq. (22), which is obtained by differentiating Eq. (13). Thus, the corresponding components of the terminal bending moment (μ_x, μ_y and μ_z) can be evaluated directly from the previously introduced definitions:

$$\begin{cases} m_x = \tau_o n_{ox} + \mu_x \\ m_y = \tau_o n_{oy} + \mu_y \\ m_z = \tau_o n_{oz} + \mu_z \end{cases}$$

where $m_y = 0$. According to the above equations, the components of the bending moment are given uniquely. In this sense, it is concluded that the configuration of the deflected beam is uniquely determined with respect to the knowledge of the magnitude of the twisting moment τ_o and two components of the resultant acting moment m_x and m_z.

If only the acting bending and twisting moments are known, then the determination of the deformed configuration becomes more difficult. The reason is that the components of the resultant acting moments, which appear in Eq. (13), are uncertain since these components are dependent upon the direction vector at the beam's end. For the purposes of illustration, one comparatively simple case is discussed here where both the magnitudes of the acting bending and twisting moments (μ_o, τ_o) are taken as known variables and, additionally, one component of the bending moment, say μ_x, is also taken as known (the same conclusion can be achieved if μ_z is taken as known). It is readily shown that in this case the remaining components of the acting moments can be determined uniquely. It is now convenient to express the parameter ω in terms of the magnitudes of the acting bending and twisting moments. With the aid of Eq. (19a), ω can be rewritten as

$$\omega^2 = \mu_o^2 + \tau_o^2, \quad (24)$$

where

$$\mu_o^2 = \mu_x^2 + \mu_y^2 + \mu_z^2.$$

Since both magnitudes are taken as known variables, then the component of the direction vector n_{oy} is determined. By substituting Eq. (23) into Eq. (22b), the component is written as

$$n_{oy} = \frac{\mu_o}{\omega}\sin\left(\frac{\omega}{2}\right), \quad (25)$$

Downloaded 03 May 2010 to 171.66.16.245. Redistribution subject to ASME license or copyright; see http://www.asme.org/terms/Terms_Use.cfm

where ω is given by Eq. (24). Consequently, the component of the acting bending moment μ_y is given by Eq. (19a):

$$\mu_y = -\frac{\mu_o \tau_o}{\omega} \sin\left(\frac{\omega}{2}\right) \tag{26}$$

From Eqs. (22a) and (22c), the components of the direction vector n_{ox} and n_{oy} are given by

$$n_{ox} = \frac{\mu_z \omega^2 \cos\left(\frac{\omega}{2}\right) + \tau_o \mu_o \mu_x \sin^2\left(\frac{\omega}{2}\right)}{\mu_o\left(\mu_o^2 + \tau_o^2 \cos^2\left(\frac{\omega}{2}\right)\right)}$$

$$n_{oz} = \frac{-\mu_x \omega^2 \cos\left(\frac{\omega}{2}\right) + \tau_o \mu_o \mu_z \sin^2\left(\frac{\omega}{2}\right)}{\mu_o\left(\mu_o^2 + \tau_o^2 \cos^2\left(\frac{\omega}{2}\right)\right)} \tag{27a,b}$$

where

$$\mu_x^2 + \mu_z^2 = \mu_o^2 - \mu_y^2 = \frac{\mu_o^2}{\omega^2}\left[\mu_o^2 + \tau_o^2 \cos^2\left(\frac{\omega}{2}\right)\right]. \tag{28}$$

Since one of two components of the acting bending moment (either μ_x or μ_z) is known, the other can be evaluated directly from Eq. (28), where the magnitudes of both acting bending and twisting moments are taken as known parameters. Without loss of generality, the component of the bending moment evaluated from Eq. (28) is always taken as positive. Then, the components of the direction vector, n_{ox} and n_{oz}, can be determined uniquely by Eqs. (27a) and (27b), respectively, as a result, the components of the resultant acting moments can be obtained according to the definitions. Thus, the corresponding constants C_1 and C_2 can be obtained by Eqs. (21a) and (21b), respectively, the deflection amplitude p and the constant C_4 can be given by Eqs. (14b) and (15), respectively. Once all the parameters occurring in Eq. (13) are found, the deformed configuration is finally determined by substituting these parameters into Eq. (13). Since these parameters are determined uniquely according to the knowledge of the magnitudes of both acting bending and twisting moments, τ_o and μ_o, and one component of the bending moment, either μ_x or μ_z, the deformed configuration is unique.

4 Results

The results of two extreme deflection configurations first merit discussion. The first extreme case is when the magnitude of the acting bending moment is zero and the magnitude of the acting twisting moment is nonzero. In this case, the amplitude of the deflection p reduces to zero. As a result, the component of the direction vector n_{oy} is zero owing to $\mu_y = 0$ (see Eq. (19a)). Therefore, it is deduced that the first derivative of the function $y(z)$ is zero, which implies $y(z)$ is a constant. Substituting this conclusion into Eq. (9) gives $y(z) = 0$ ($q = 0$). As a result, function $x(z)$ must be proportional to z (see Eq. (8b)) and the configuration of the beam becomes

$$\begin{cases} n_{oz}x - n_{ox}z = 0 \\ y = 0. \end{cases} \tag{29}$$

This expression represents a straight line in the plane xz which passes the origin of the coordinate system. It is concluded that pure twist does not deflect an initially straight beam which is free from any terminal bending.

The second extreme case is when the terminal acting twisting moment is zero. In this case, the deflection amplitude becomes $1/\mu_o$. From Eq. (19a) the component of the bending moment μ_y must be zero, and the constants C_1, C_2, and C_4 reduce to zero owing to the zero twisting moment. In this extreme case Eq. (13) becomes

$$\begin{cases} \frac{\mu_x}{\mu_o}\left(\frac{1}{\mu_o^2} - y^2\right)^{1/2} = z \\ \frac{\mu_z}{\mu_o}\left(\frac{1}{\mu_o^2} - y^2\right)^{1/2} = x \end{cases} \tag{30}$$

where

$$\mu_o^2 = \mu_x^2 + \mu_z^2.$$

It can be seen that the projections on both planes xy and yz are ellipses or partial ellipses. If the component of the bending moment μ_x is zero, which can be achieved by rotating the coordinate system, then the ellipse on the plane xy becomes a circle of radius $1/\mu_o$, and the ellipse on the plane yz reduces to a line. This result is in agreement with Euler-Bernoulli bending theory. Consequently, it is concluded that if there is not twisting, then the terminal bending moment deforms the beam into an arc of constant radius in a plane.

In general, both the acting bending and twisting moments are nonzero. Figures 3 to 4 show representative results of the analysis. Figures 3(a), 3(b), and 3(c) show the projected configuration on the three principal planes for applied moments $\tau_o = 2$, $\mu_x = 0$ and $0.5 \le \mu_o \le 8.0$. It is seen that the deflection curvature along the beam increases with increasing bending moment μ_o. Meanwhile, both ends of the beam approach to each other longitudinally (along the z-axis) and the deflected beam forms more than one cycle. As the projected length on the z-axis reduces, the deflected configuration tends to be two-dimensional. However, owing to the nonzero twisting moment, the beam can not form a two-dimensional configuration. Figures 4(a), 4(b), and 4(c) show the projected configurations for applied moments $\mu_o = 3$, $\mu_x = 0$ and $0.5 \le \tau_o \le 8.0$. It is observed that the beam forms more cycles with increasing the twisting moment τ_o, but the difference in this case is that both ends of the beam tend to move away from each other. If the acting twisting moment is further increased, the beam tends towards a straight line with many cycles. However, it can never reduce to its original straight-line configuration due to the nonzero bending moment.

5 Conclusions

The deformed configuration of a straight elastic beam with constant circular cross-section is investigated analytically when it is subjected to the combined action of terminal bending and twisting moments at both of its ends which are free from kinematic restraints. In the presence of twisting, the beam will form a three-dimensional configuration. This paper shows that the deflected configuration of the beam can be uniquely determined with respect to a Cartesian coordinate system if the magnitude of the acting twisting moment τ_o and two components of the resultant acting moment (m_x and m_z) are known, or if the magnitudes of both acting bending and twisting moments (τ_o and μ_o) and one of two components of the acting bending moment (either μ_x or μ_z) are known. It is demonstrated that the analysis is consistent with the theory presented by Love (1944).

Acknowledgment

The first author would like to gratefully acknowledge the support of the Sino-British Friendship Scholarship.

Downloaded 03 May 2010 to 171.66.16.245. Redistribution subject to ASME license or copyright; see http://www.asme.org/terms/Terms_Use.cfm

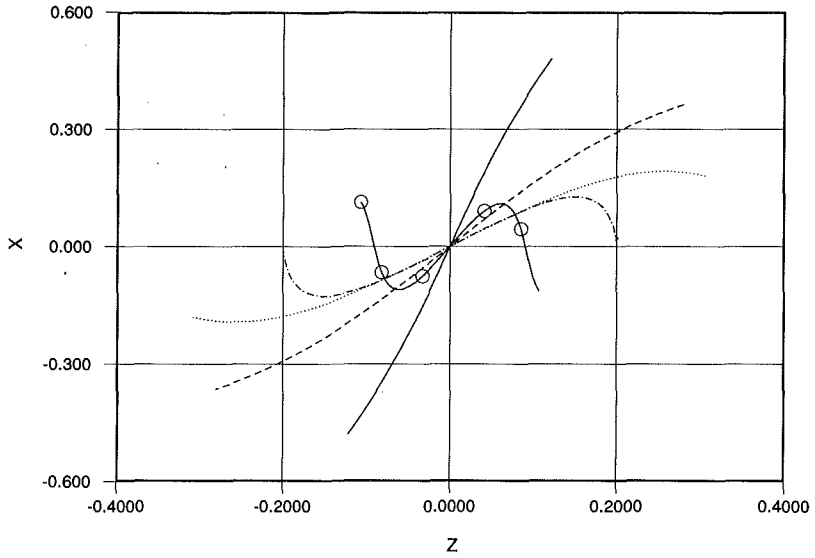


Fig. 3(*a*) Projected configurations on the *xz*-plane

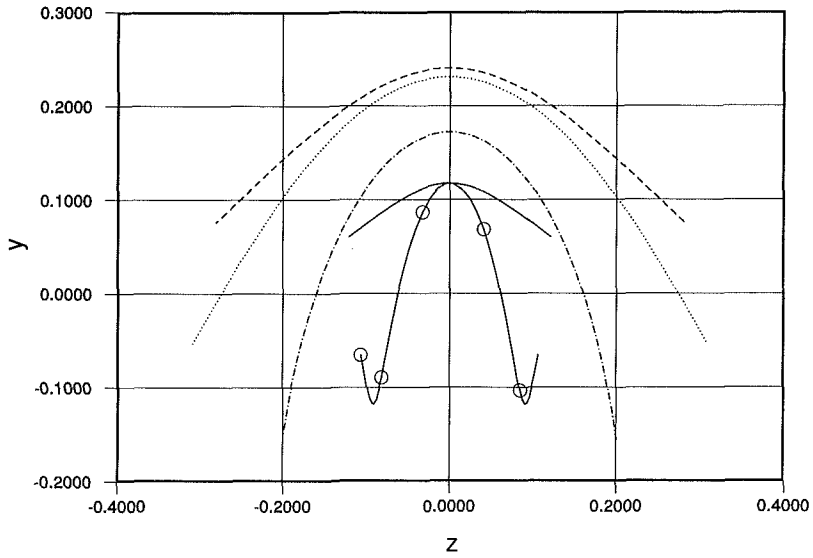


Fig. 3(*b*) Projected configurations on the *yz* plane

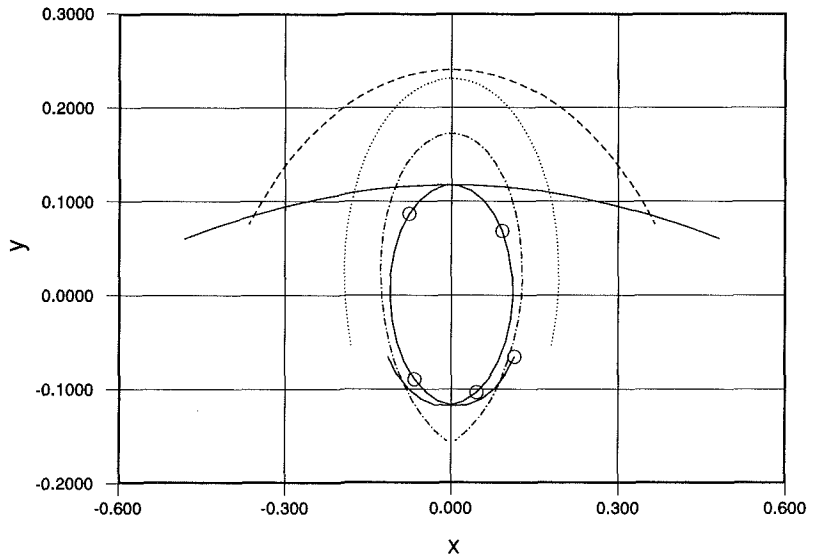


Fig. 3(*c*) Projected configurations on the *xy* plane

Fig. 3 Deflected configurations of the beam under different terminal bending moments with $\tau_o = 2$ and $\mu_x = 0$; ——— $\mu_o = 0.5$, — — — — $\mu_o = 1.5$, - - - - $\mu_o = 3.0$, —•—•—• $\mu_o = 5.0$, —o— $\mu_o = 8.0$

Downloaded 03 May 2010 to 171.66.16.245. Redistribution subject to ASME license or copyright; see http://www.asme.org/terms/Terms_Use.cfm

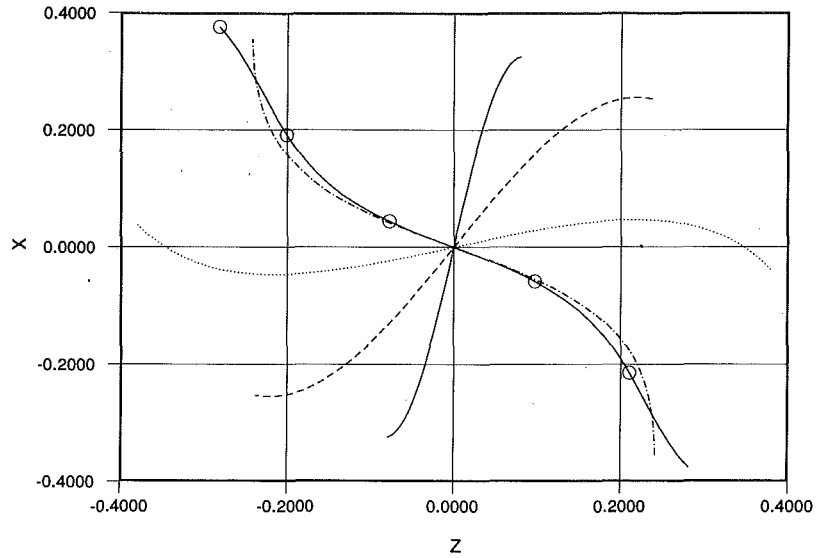


Fig. 4(*a*) Projected configurations on the *xz* plane

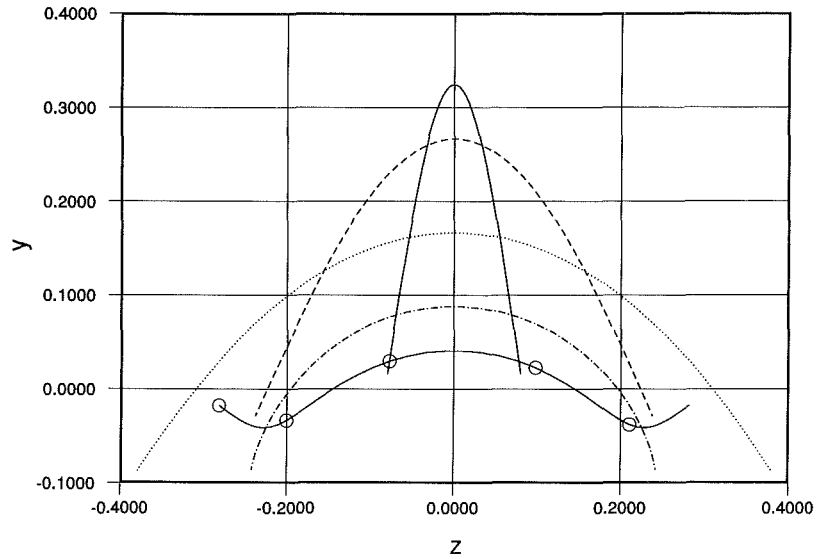


Fig. 4(*b*) Projected configurations on the *yz* plane

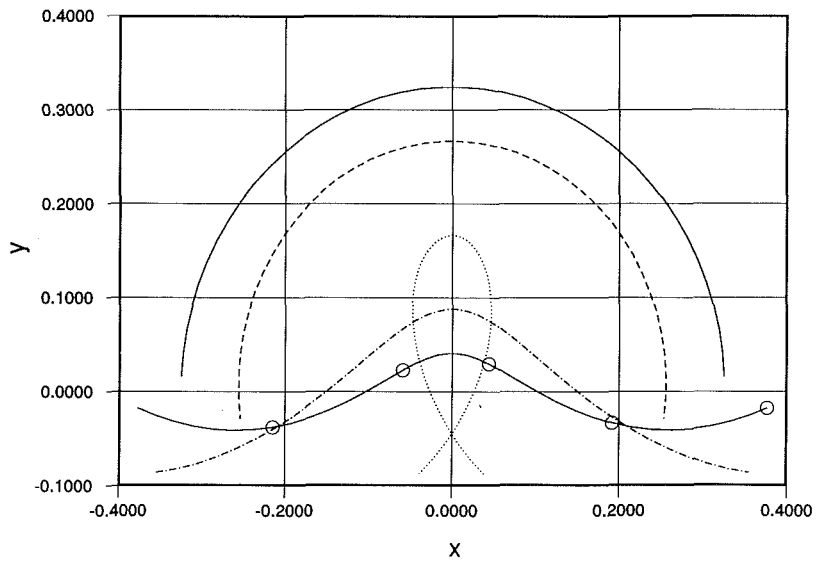


Fig. 4(*c*) Projected configurations on the *xy* plane

Fig. 4 Deflected configurations of the beam under different terminal twisting moments with $\mu_o = 2$ and $\mu_x = 0$; ——— $\tau_o = 0.5$, — — — — $\tau_o = 1.5$, - - - - $\tau_o = 3.0$, —•—•—• $\tau_o = 5.0$, —o— $\tau_o = 8.0$

Downloaded 03 May 2010 to 171.66.16.245. Redistribution subject to ASME license or copyright; see http://www.asme.org/terms/Terms_Use.cfm

References

Antman, S. S., and Kenney, C. S., 1981, "Large Buckled States of Nonlinearly Elastic Rods Under Torsional, Thrust, and Gravity," *Archive for Rational Mechanics and Analysis*, Vol. 76, pp. 289–338.

Iura, M., and Atluri, S. N., 1989, "On a Consistent Theory, and Variational Formulation of Finitely Stretched and Rotated 3D Space-Curved Beams," *Computational Mechanics*, No. 4, pp. 73–88.

Konopasek, M., 1972, "On Large Bending and Torsional Deformation of Fibers in Space," *Textile Research Journal*, Vol. 42, pp. 586–590.

Love, A. E. H., 1944, "A Treatise on the Mathematical Theory of Elasticity," 4th ed., Dover, New York.

van Erp, G. M., Menken, C. M., and Veldpaus, F. E., 1988, "Non-linear Flexural-Torsional Behaviour of Straight Slender Elastic Beams With Arbitrary Cross Section," *Thin-Walled Structures*, Vol. 6, No. 5, pp. 385–404.

Reissner, E., 1957, "Finite Twisting and Bending of Thin Rectangular Elastic Plates," ASME JOURNAL OF APPLIED MECHANICS, Vol. 24, pp. 391–396.

Timoshenko, S., 1964, "Theory of Elastic Stability," 4th Ed., McGraw-Hill, New York.

Wang, C. Y., 1990, "Lifting Horizontal Elastic Beam at Two Points," *Journal of Engineering Mechanics*, Vol. 116, No. 1, Jan., pp. 141–151.

Downloaded 03 May 2010 to 171.66.16.245. Redistribution subject to ASME license or copyright; see http://www.asme.org/terms/Terms_Use.cfm

Stability Loss in Thick Transversely Isotropic Cylindrical Shells Under Axial Compression

G. A. Kardomateas
Associate Professor,
School of Aerospace Engineering,
Georgia Institute of Technology,
Atlanta, GA 30332-0150
Mem. ASME

The stability of equilibrium of a transversely isotropic thick cylindrical shell under axial compression is investigated. The problem is treated by making appropriate use of the three-dimensional theory of elasticity. The results are compared with the critical loads furnished by classical shell theories. For the isotropic material cases considered, the elasticity approach predicts a lower critical load than the shell theories, the percentage reduction being larger with increasing thickness. However, both the Flügge and Danielson and Simmonds theories predict critical loads much closer to the elasticity value than the Donnell theory. Moreover, the values of n, m (number of circumferential waves and number of axial half-waves, respectively, at the critical point) for both the elasticity, and the Flügge and the Danielson and Simmonds theories, show perfect agreement, unlike the Donnell shell theory.

Introduction

Loss of stability is of primary concern in composite structural applications because of the large strength-to-weight ratio of these materials. Shell-like components of modest thickness are considered for possible applications in the marine industry, as well as the automobile and space industries. The accurate prediction of buckling under axial compression is an important consideration because of the uniaxial or, more generally, biaxial compressive fields that can be encountered in such applications.

Buckling of shells has been almost exclusively researched to date through the application of the cylindrical shell theory (e.g., Simitses, Shaw, and Sheinman, 1985). The classical solution, derived through the Donnell formulation, yields for an isotropic shell of radius R_0 and thickness h (Fig. 1), a critical stress directly proportional to h/R_0 and independent of the length, l, of the shell.

It has already been pointed out that this solution can yield incorrect results for very long cylinders, which can buckle as columns with undeformed cross-sections (Timoshenko and Gere, 1961). For very short cylinders the classical formula is also inadequate and a trial-and-error procedure through different combinations of the number of circumferential waves, n, and the number of axial half-waves, m, is needed (Brush and Almroth, 1970).

In this respect, Danielson and Simmonds (1969) obtained a set of accurate shell theory buckling equations for arbitrary cylindrical elastic shells of finite length. Their critical loads for shell of finite length were as simple as those predicted by the simplified Donnell equations, yet as accurate as those predicted by the more elaborate Flügge equations (Flügge, 1960). Simmonds and Danielson (1970) used their set of accurate buckling equations to compute the critical loads of axially compressed circular cylindrical shells subjected to "relaxed" boundary conditions. Their results showed that as $l/R_0 \to 0$ or as $l/R_0 \to \infty$, the buckling load approaches zero, in contrast to the behavior predicted by the Donnell equations. All the previously mentioned studies considered thin shells.

It seems natural that a comprehensive investigation of the performance of the simple classical solution and the various shell theories with respect to the shell thickness would be of interest in view of possible structural applications of modest thickness. An accurate solution for the stability characteristics of moderately thick shells is also needed in order to compare the accuracy of the predictions from various improved shell theories (e.g., Whitney and Sun, 1974; Librescu, 1975; Reddy and Liu, 1985; see also Noor and Burton, 1990, for a review of shear deformation theories).

Kardomateas (1993) presented a three-dimensional elasticity formulation and solution for the buckling of cylindrical orthotropic shells subjected to external pressure. It was shown that the critical load predicted by shell theory can be nonconservative (in particular, for the example case of glass/epoxy material considered, it was 34 percent higher than the elasticity solution for ratio of outside/inside radius $R_2/R_1 = 1.3$). This work was based on a simplified problem definition in that the prebuckling stress and displacement field was axisymmetric, and the buckling modes were assumed two-dimensional, i.e., no z-component of the displacement field, and no z-dependence of the r and θ displacement components.

Contributed by the Applied Mechanics Division of THE AMERICAN SOCIETY OF MECHANICAL ENGINEERS for presentation at the First Joint ASCE-EMD, ASME-AMD, SES Meeting, Charlottesville, VA, June 6-9, 1993.

Discussion on this paper should be addressed to the Technical Editor, Professor Lewis T. Wheeler, Department of Mechanical Engineering, University of Houston, Houston, TX 77204-4792, and will be accepted until four months after final publication of the paper itself in the ASME JOURNAL OF APPLIED MECHANICS.

Manuscript received by the ASME Applied Mechanics Division, Feb. 24, 1992; final revision, Sept. 10, 1992. Associate Technical Editor: F. Y. M. Wan.

Paper No. 93-APM-33.

Copyright © 1993 by ASME
Downloaded 03 May 2010 to 171.66.16.245. Redistribution subject to ASME license or copyright; see http://www.asme.org/terms/Terms_Use.cfm

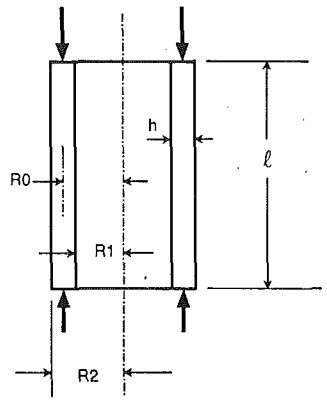


Fig. 1 Cylindrical shell under axial compression

To further assess the thickness effects on the stability of shells, the problem of buckling of a traversely isotropic thick cylindrical shell under axial compression is investigated. No restrictive assumptions are made concerning the thickness. Again, the nonlinear three-dimensional theory of elasticity is appropriately formulated, and closed-form analytical solutions are produced. The formulation is different from the previous work by Kardomateas (1993) because a finite length and a full dependence on r, θ, and z of the buckling modes is now assumed, which increases the complexity of the problem. Specific results will be presented for the critical load and the buckling modes. The results will be compared with the simplified Donnell formula, the critical load from the nonsimplified Donnell shell theory, the Flügge (1960) shell theory, and the Danielson and Simmonds (1969) formulation.

It should be noted that although composite shells may exhibit general anisotropy, we shall restrict ourselves to transverse isotropy, because more general anisotropy would not allow a direct solution of the corresponding three-dimensional elasticity problem. Actually, Elliott (1948) was the first to address the problem of obtaining closed-form solutions for transverse isotropy.

Formulation

The equations of equilibrium are taken in terms of the second Piola-Kirchhoff stress tensor $\boldsymbol{\Sigma}$ in the form

$$\text{div}\,(\boldsymbol{\Sigma}.\mathbf{F}^T)=0, \tag{1a}$$

where $\mathbf{F}$ is the deformation gradient defined by

$$\mathbf{F}=\mathbf{I}+\text{grad}\,V, \tag{1b}$$

where V is the displacement vector and $\mathbf{I}$ is the identity tensor.

Notice that the strain tensor is defined by

$$\mathbf{E}=\frac{1}{2}\,(\mathbf{F}^T.\mathbf{F}-\mathbf{I}) \tag{1c}$$

More specifically, in terms of the linear strains:

$$e_{rr}=\frac{\partial u}{\partial r},\quad e_{\theta\theta}=\frac{1}{r}\frac{\partial v}{\partial \theta}+\frac{u}{r},\quad e_{zz}=\frac{\partial w}{\partial z}, \tag{2a}$$

$$e_{r\theta}=\frac{1}{r}\frac{\partial u}{\partial \theta}+\frac{\partial v}{\partial r}-\frac{v}{r},\quad e_{rz}=\frac{\partial u}{\partial z}+\frac{\partial w}{\partial r},e_{\theta z}=\frac{\partial v}{\partial z}+\frac{1}{r}\frac{\partial w}{\partial \theta}, \tag{2b}$$

and the linear rotations:

$$2\omega_r=\frac{1}{r}\frac{\partial w}{\partial \theta}-\frac{\partial v}{\partial z},\quad 2\omega_\theta=\frac{\partial u}{\partial z}-\frac{\partial w}{\partial r},2\omega_z=\frac{\partial v}{\partial r}+\frac{v}{r}-\frac{1}{r}\frac{\partial u}{\partial \theta}, \tag{2c}$$

the deformation gradient $\mathbf{F}$ is

$$\mathbf{F}=\begin{bmatrix} 1+e_{rr} & \frac{1}{2}e_{r\theta}-\omega_z & \frac{1}{2}e_{rz}+\omega_\theta \\ \frac{1}{2}e_{r\theta}+\omega_z & 1+e_{\theta\theta} & \frac{1}{2}e_{\theta z}-\omega_r \\ \frac{1}{2}e_{rz}-\omega_\theta & \frac{1}{2}e_{\theta z}+\omega_r & 1+e_{zz} \end{bmatrix}. \tag{3}$$

At the critical load there are two possible infinitely close positions of equilibrium. Denote by u_0, v_0, w_0 the r, θ, and z components of the displacement corresponding to the primary position. A perturbed position is denoted by

$$u=u_0+\alpha u_1;\quad v=v_0+\alpha v_1;\quad w=w_0+\alpha w_1, \tag{4}$$

where α is an infinitesimally small quantity. Here, $\alpha u_1(r, \theta, z)$, $\alpha v_1(r, \theta, z)$, $\alpha w_1(r, \theta, z)$ are the displacements to which the points of the body must be subjected to shift them from the initial position of equilibrium to the new equilibrium position. The functions $u_1(r, \theta, z)$, $v_1(r, \theta, z)$, $w_1(r, \theta, z)$ are assumed finite and α is an infinitesimally small quantity independent of r, θ, z.

Following Kardomateas (1993), we obtain the following buckling equations:

$$\frac{\partial}{\partial r}\,(\sigma_{rr}'-\tau_{r\theta}^0\omega_z'+\tau_{rz}^0\omega_\theta')+\frac{1}{r}\frac{\partial}{\partial \theta}\,(\tau_{r\theta}'-\sigma_{\theta\theta}^0\omega_z'+\tau_{\theta z}^0\omega_\theta')$$
$$+\frac{\partial}{\partial z}\,(\tau_{rz}'-\tau_{\theta z}^0\omega_z'+\sigma_{zz}^0\omega_\theta')$$
$$+\frac{1}{r}\,(\sigma_{rr}'-\sigma_{\theta\theta}'+\tau_{rz}^0\omega_\theta'+\tau_{\theta z}^0\omega_r'-2\tau_{r\theta}^0\omega_z')=0, \tag{5a}$$

$$\frac{\partial}{\partial r}\,(\tau_{r\theta}'+\sigma_{rr}^0\omega_z'-\tau_{rz}^0\omega_r')+\frac{1}{r}\frac{\partial}{\partial \theta}\,(\sigma_{\theta\theta}'+\tau_{r\theta}^0\omega_z'-\tau_{\theta z}^0\omega_r')$$
$$+\frac{\partial}{\partial z}\,(\tau_{\theta z}'+\tau_{rz}^0\omega_z'-\sigma_{zz}^0\omega_r')$$
$$+\frac{1}{r}\,(2\tau_{r\theta}'+\sigma_{rr}^0\omega_z'-\sigma_{\theta\theta}^0\omega_z'+\tau_{\theta z}^0\omega_\theta'-\tau_{rz}^0\omega_r')=0, \tag{5b}$$

$$\frac{\partial}{\partial r}\,(\tau_{rz}'-\sigma_{rr}^0\omega_\theta'+\tau_{r\theta}^0\omega_r')+\frac{1}{r}\frac{\partial}{\partial \theta}\,(\tau_{\theta z}'-\tau_{r\theta}^0\omega_\theta'+\sigma_{\theta\theta}^0\omega_r')$$
$$+\frac{\partial}{\partial z}\,(\sigma_{zz}'-\tau_{rz}^0\omega_\theta'+\tau_{\theta z}^0\omega_r')+\frac{1}{r}\,(\tau_{rz}'-\sigma_{rr}^0\omega_\theta'+\tau_{r\theta}^0\omega_r')=0. \tag{5c}$$

In the previous equations, σ_{ij}^0 and ω_j^0 are the values of σ_{ij} and ω_j at the initial equilibrium position, i.e., for $u = u_0$, $v = v_0$ and $w = w_0$, and σ_{ij}' and ω_j' are the values at the perturbed position, i.e., for $u = u_1$, $v = v_1$ and $w = w_1$.

The boundary conditions associated with (1a) can be expressed as:

$$(\mathbf{F}.\boldsymbol{\Sigma}^T).\hat{n}=t(V), \tag{6}$$

where t is the traction vector on the surface which has outward unit normal $\hat{n} = (l, m, n)$ before any deformation. The traction vector t depends on the displacement field $V = (u, v, w)$. Again, following Kardomateas (1992), we obtain for the lateral and end surfaces:

$$(\sigma_{rr}'-\tau_{r\theta}^0\omega_z'+\tau_{rz}^0\omega_\theta')l+(\tau_{r\theta}'-\sigma_{\theta\theta}^0\omega_z'+\tau_{\theta z}^0\omega_\theta')m$$
$$+(\tau_{rz}'-\tau_{\theta z}^0\omega_z'+\sigma_{zz}^0\omega_\theta')n=0, \tag{7a}$$

$$(\tau_{r\theta}'+\sigma_{rr}^0\omega_z'-\tau_{rz}^0\omega_r')l+(\sigma_{\theta\theta}'+\tau_{r\theta}^0\omega_z'-\tau_{\theta z}^0\omega_r')m$$
$$+(\tau_{\theta z}'+\tau_{rz}^0\omega_z'-\sigma_{zz}^0\omega_r')n=0, \tag{7b}$$

$$(\tau_{rz}'+\tau_{r\theta}^0\omega_r'-\sigma_{rr}^0\omega_\theta')l+(\tau_{\theta z}'+\sigma_{\theta\theta}^0\omega_r'-\tau_{r\theta}^0\omega_\theta')m$$
$$+(\sigma_{zz}'+\tau_{\theta z}^0\omega_r'-\tau_{rz}^0\omega_\theta')n=0. \tag{7c}$$

Prebuckling State. The problem under consideration is that

Downloaded 03 May 2010 to 171.66.16.245. Redistribution subject to ASME license or copyright; see http://www.asme.org/terms/Terms_Use.cfm

of a transversely isotropic cylindrical shell compressed by an axial force applied at the ends. The stress-strain relations for the transversely isotropic material are as follows:

$$\begin{bmatrix}\sigma_{rr}\\ \sigma_{\theta\theta}\\ \sigma_{zz}\\ \tau_{\theta z}\\ \tau_{rz}\\ \tau_{r\theta}\end{bmatrix}=\begin{bmatrix}c_{11} & c_{12} & c_{13} & 0 & 0 & 0\\ c_{12} & c_{11} & c_{13} & 0 & 0 & 0\\ c_{13} & c_{13} & c_{33} & 0 & 0 & 0\\ 0 & 0 & 0 & c_{55} & 0 & 0\\ 0 & 0 & 0 & 0 & c_{55} & 0\\ 0 & 0 & 0 & 0 & 0 & (c_{11}-c_{12})/2\end{bmatrix}\begin{bmatrix}\epsilon_{rr}\\ \epsilon_{\theta\theta}\\ \epsilon_{zz}\\ \gamma_{\theta z}\\ \gamma_{rz}\\ \gamma_{r\theta}\end{bmatrix}, \quad (8)$$

where c_{ij} are the elastic constants (we have used the notation $1 \equiv r$, $2 \equiv \theta$, $3 \equiv z$).

Denote the length of the shell by l and the area of the transverse section by A. If we assume that the stresses along the loaded upper end ($z = l$) and the reaction along the lower end ($z = 0$) of the shell are distributed uniformly, and are normal to the bounding planes, then the components of stress tensor that satisfy the equations of equilibrium and the traction conditions on the surfaces are simply

$$\sigma_{zz}=-\frac{P}{A}=-\sigma_0; \quad \sigma^0_{rr}=\sigma^0_{\theta\theta}=\tau^0_{r\theta}=\tau^0_{rz}=\tau^0_{\theta z}=0. \quad (9a)$$

For a transversely isotropic body, the corresponding displacement field can be found by using (8) and (2):

$$u_0=\frac{c_{13}}{c_{33}(c_{11}+c_{12})-2c_{13}^2}\sigma_0 r; \quad v_0=0;$$

$$w_0=-\frac{c_{11}+c_{12}}{c_{33}(c_{11}+c_{12})-2c_{13}^2}\sigma_0 z. \quad (9b)$$

Perturbed State. Using (5) and (9), the three-dimensional elasticity equilibrium equations for the perturbed position can be written as follows:

$$\frac{\partial \sigma_{rr}'}{\partial r}+\frac{1}{r}\frac{\partial \tau_{r\theta}'}{\partial \theta}+\frac{\partial}{\partial z}(\tau_{rz}'-\sigma_0\omega_\theta')+\frac{1}{r}(\sigma_{rr}'-\sigma_{\theta\theta}')=0, \quad (10a)$$

$$\frac{\partial \tau_{r\theta}'}{\partial r}+\frac{1}{r}\frac{\partial \sigma_{\theta\theta}'}{\partial \theta}+\frac{\partial}{\partial z}(\tau_{\theta z}'+\sigma_0\omega_r')+\frac{2\tau_{r\theta}'}{r}=0, \quad (10b)$$

$$\frac{\partial \tau_{rz}'}{\partial r}+\frac{1}{r}\frac{\partial \tau_{\theta z}'}{\partial \theta}+\frac{\partial \sigma_{zz}'}{\partial z}+\frac{\tau_{rz}'}{r}=0. \quad (10c)$$

In the above equations, σ^0_{ij}, σ_{ij}' are expressed in terms of ϵ^0_{ij}, ϵ_{ij}', respectively, in the same manner as Eqs. (8) for σ_{ij} in terms of ϵ_{ij}. The strains ϵ_{ij}', are in turn expressed in terms of the displacements, u_1, v_1, w_1, in the same manner as the linear strain displacement relations (2). Substituting, we obtain the equations of equilibrium in terms of the displacements at the perturbed state, u_1, v_1, w_1 as follows:

$$c_{11}\left(\frac{\partial^2 u_1}{\partial r^2}+\frac{1}{r}\frac{\partial u_1}{\partial r}-\frac{u_1}{r^2}\right)+\frac{1}{2}(c_{11}-c_{12})\frac{1}{r^2}\frac{\partial^2 u_1}{\partial \theta^2}+\left(c_{55}-\frac{\sigma_0}{2}\right)\frac{\partial^2 u_1}{\partial z^2}+\frac{1}{2}(c_{11}+c_{12})\frac{\partial}{\partial r}\left(\frac{1}{r}\frac{\partial v_1}{\partial \theta}\right)-(c_{11}-c_{12})\frac{1}{r^2}\frac{\partial v_1}{\partial \theta}+\left[(c_{13}+c_{55})+\frac{\sigma_0}{2}\right]\frac{\partial^2 w_1}{\partial r\partial z}=0, \quad (11a)$$

$$\frac{1}{2}(c_{11}-c_{12})\left(\frac{\partial^2 v_1}{\partial r^2}+\frac{1}{r}\frac{\partial v_1}{\partial r}-\frac{v_1}{r^2}\right)+c_{11}\frac{1}{r^2}\frac{\partial^2 v_1}{\partial \theta^2}+\left(c_{55}-\frac{\sigma_0}{2}\right)\frac{\partial^2 v_1}{\partial z^2}+\frac{1}{r}\frac{\partial}{\partial \theta}\left\{\frac{1}{2}(c_{11}+c_{12})\left(\frac{\partial u_1}{\partial r}+\frac{u_1}{r}\right)+(c_{11}-c_{12})\frac{u_1}{r}+\left[(c_{13}+c_{55})+\frac{\sigma_0}{2}\right]\frac{\partial w_1}{\partial z}\right\}=0, \quad (11b)$$

$$c_{55}\left(\frac{\partial^2 w_1}{\partial r^2}+\frac{1}{r}\frac{\partial w_1}{\partial r}+\frac{1}{r^2}\frac{\partial^2 w_1}{\partial \theta^2}\right)+c_{33}\frac{\partial^2 w_1}{\partial z^2}+(c_{13}+c_{55})\frac{\partial}{\partial z}\left(\frac{\partial u_1}{\partial r}+\frac{u_1}{r}+\frac{1}{r}\frac{\partial v_1}{\partial \theta}\right)=0, \quad (11c)$$

(a) We seek a first group of solutions in terms of a function ϕ in the form

$$u_1=\frac{\partial \phi}{\partial r}; \quad v_1=\frac{1}{r}\frac{\partial \phi}{\partial \theta}; \quad w_1=k\frac{\partial \phi}{\partial z}. \quad (12)$$

A similar form had been used by Elliott (1948) for Cartesian coordinates. Then equations (11a) and (11b) are satisfied if

$$c_{11}\left(\frac{\partial^2 \phi}{\partial r^2}+\frac{1}{r}\frac{\partial \phi}{\partial r}+\frac{1}{r^2}\frac{\partial^2 \phi}{\partial \theta^2}\right)+\left[c_{55}+k(c_{13}+c_{55})+\frac{\sigma_0}{2}(k-1)\right]\frac{\partial^2 \phi}{\partial z^2}=0, \quad (13a)$$

and (11c) is satisfied if

$$[(c_{13}+c_{55})+kc_{55}]\left(\frac{\partial^2 \phi}{\partial r^2}+\frac{1}{r}\frac{\partial \phi}{\partial r}+\frac{1}{r^2}\frac{\partial^2 \phi}{\partial \theta^2}\right)+kc_{33}\frac{\partial^2 \phi}{\partial z^2}=0. \quad (13b)$$

A nonzero solution of these Eqs. (13a) and (13b) can be found only if they are identical; this occurs if

$$\frac{c_{55}+k(c_{13}+c_{55})+(k-1)(\sigma_0/2)}{c_{11}}=\frac{kc_{33}}{(c_{13}+c_{55})+kc_{55}}=s^2. \quad (14a)$$

This gives a quadratic equation for s^2 or k. The equation for $x = s^2$, with roots s_1^2 and s_2^2, depending on the compressive stress σ_0, is

$$c_{11}c_{55}x^2+\left[(c_{13}+c_{55})\left(c_{13}+c_{55}+\frac{\sigma_0}{2}\right)-c_{55}\left(c_{55}-\frac{\sigma_0}{2}\right)-c_{11}c_{33}\right]x+c_{33}\left(c_{55}-\frac{\sigma_0}{2}\right)=0, \quad (14b)$$

and the corresponding k_i:

$$k_i=\frac{s_i^2c_{11}-c_{55}+(\sigma_0/2)}{c_{13}+c_{55}+(\sigma_0/2)} \quad i=1,2. \quad (14c)$$

(b) A second group of solutions is sought in terms of the function ψ in the form:

$$u_1=\frac{1}{r}\frac{\partial \psi}{\partial \theta}; \quad v_1=-\frac{\partial \psi}{\partial r}; \quad w_1=0. \quad (15)$$

Then Eqs. (11a) and (11b) are satisfied if

$$\frac{1}{2}(c_{11}-c_{12})\left(\frac{\partial^2 \psi}{\partial r^2}+\frac{1}{r}\frac{\partial \psi}{\partial r}+\frac{1}{r^2}\frac{\partial^2 \psi}{\partial \theta^2}\right)+\left(c_{55}-\frac{\sigma_0}{2}\right)\frac{\partial^2 \psi}{\partial z^2}=0, \quad (16)$$

and Eq. (11c) is identically satisfied.

(c) Finally, an obvious third group of solutions is the rigid-body displacement field with components V_x, V_y, and V_z along the Cartesian x, y, z coordinate system:

$$u_1=V_x\cos\theta+V_y\sin\theta; \quad v_1=-V_x\sin\theta+V_y\cos\theta; \quad w_1=V_z. \quad (17)$$

The displacement is a superposition of the fields (a), (b), and (c).

Now the functions ϕ and ψ are sought in a separable form:

Downloaded 03 May 2010 to 171.66.16.245. Redistribution subject to ASME license or copyright; see http://www.asme.org/terms/Terms_Use.cfm

$\phi_i(r, \theta, z) = Z(z)A_i(\lambda r) \cos n\theta;$

$$i = 1,2 \text{ corresponding to } s_1, s_2, \tag{18a}$$

$$\psi(r, \theta, z) = Z(z)B(\lambda r) \sin n\theta. \tag{18b}$$

Notice that the decomposition in terms of the three functions ϕ_1, ϕ_2, and ψ may be considered complete in the sense that it results in the number of constants needed for the formulation of the eigenvalue problem as will be seen in the following.

Now set

$$\rho = \lambda r. \tag{18c}$$

Substituting in (13a), we obtain the ordinary differential equations:

$$A_i''(\rho) + \frac{1}{\rho} A_i'(\rho) - \left(s_i^2 + \frac{n}{\rho^2}\right) A_i(\rho) = 0, \tag{19a}$$

where s_i^2 are given in (14a). In a similar fashion, substituting in (16), we obtain the ordinary differential equation:

$$B''(\rho) + \frac{1}{\rho} B'(\rho) - \left(q^2 + \frac{n}{\rho^2}\right) B(\rho) = 0 \quad \text{where } q^2 = \frac{2c_{55} - \sigma_0}{c_{11} - c_{12}}, \tag{19b}$$

Moreover, $Z(z)$ is found to satisfy

$$Z''(z) + \lambda^2 Z(z) = 0. \tag{19c}$$

The assumption

$$Z(z) = \sin \lambda z \tag{19d}$$

satisfies the third differential Eq. (19c).

For a hollow cylinder, since we do not have a restriction of finite values at $r = 0$, the solution to the two Eqs. (19a) and (19b) involves the modified Bessel functions of both the first and the second kind.

$$A_i(\rho) = C_i I_n(s_i\rho) + D_i K_n(s_i\rho); \quad B(\rho) = C_0 I_n(q\rho) + D_0 K_n(q\rho), \tag{20}$$

where the constants $\{C_1, C_2\}$ and $\{D_1, D_2\}$ are in general complex conjugate pairs and C_0 and D_0 are real.

Before satisfying the boundary conditions at the lateral surfaces, we shall discuss the boundary conditions at the ends. From (7), the boundary conditions on the ends are

$$\tau_{rz}' + \sigma_{zz}^0 \omega_\theta' = 0; \quad \tau_{\theta z}' - \sigma_{zz}^0 \omega_r' = 0; \quad \sigma_{zz}' = 0, \quad \text{at } z = 0, l \tag{21}$$

Since, σ_{zz}' varies as $\sin \lambda z$, the condition $\sigma_{zz}' = 0$ on both the lower end $z = 0$, and the upper end $z = l$, is satisfied if

$$\lambda = \frac{m\pi}{l}. \tag{22}$$

In a cartesian coordinate system (x, y, z), the first two of the conditions in (21) can be written as follows:

$$\tau_{xz}' + \sigma_{zz}^0 \omega_y' = 0; \quad \tau_{yz}' - \sigma_{zz}^0 \omega_x' = 0. \tag{23}$$

It will be proved now that these remaining two conditions are satisfied on the average.

The lateral surface boundary conditions in the cartesian coordinate system (analogous to (7)), with $\hat{n}$ the normal to the circular cross are (notice that from the prebuckling state $\sigma_{xx}^0 = \sigma_{yy}^0 = \tau_{xy}^0 = 0$):

$$\sigma_{xx}' \cos(\hat{n}, x) + \tau_{xy}' \cos(\hat{n}, y) = 0, \tag{24a}$$

$$\tau_{xy}' \cos(\hat{n}, x) + \sigma_{yy}' \cos(\hat{n}, y) = 0. \tag{24b}$$

Using the equilibrium equation in cartesian coordinates (analogous to (5)), gives

$$\frac{\partial}{\partial z} \int\int_A (\tau_{xz}' + \sigma_{zz}^0 \omega_y') dA = -\int\int_A \left(\frac{\partial \sigma_{xx}'}{\partial x} + \frac{\partial \tau_{xy}'}{\partial y}\right) dA. \tag{25a}$$

Using now the divergence theorem for transformation of an area integral into a contour integral, and the condition (24a) on the contour, gives the previous integral as

$$-\int_\gamma [\sigma_{xx}' \cos(\hat{n}, x) + \tau_{xy}' \cos(\hat{n}, y)] ds = 0,$$

where A denotes the area of the annular cross section and γ the corresponding contour. Therefore,

$$\int\int_A (\tau_{xz}' + \sigma_{zz}^0 \omega_y') dA = \text{const.} \tag{25b}$$

Since based on the buckling modes, τ_{rz}', ω_θ', $\tau_{\theta z}'$ and ω_r' and hence τ_{xz}', ω_y', τ_{yz}', and ω_x', all have a $\cos(m\pi z/l)$ variation, they become zero at $z = l/(2m)$. Therefore, it is concluded that the constant in (25b) is zero. Similar arguments hold for τ_{yz}'.

Moreover, it can also be proved that the system of resultant stresses (23) would produce no torsional moment. Indeed,

$$\frac{\partial}{\partial z} \int\int_A [x(\tau_{yz}' - \sigma_{zz}^0 \omega_x') - y(\tau_{xz}' + \sigma_{zz}^0 \omega_y')] dA$$

$$= -\int\int_A \left\{ x\left(\frac{\partial \tau_{xy}'}{\partial x} + \frac{\partial \sigma_{yy}'}{\partial y}\right) - y\left(\frac{\partial \sigma_{xx}'}{\partial x} + \frac{\partial \tau_{xy}'}{\partial y}\right) \right\} dA.$$

Again, using the divergence theorem, the previous integral becomes

$$-\int_\gamma \{x[\tau_{xy}' \cos(\hat{n}, x) + \sigma_{yy}' \cos(\hat{n}, y)] - y[\sigma_{xx}' \cos(\hat{n}, x) + \tau_{xy}' \cos(\hat{n}, y)]\} ds = 0. \tag{26a}$$

Hence,

$$\int\int_A [x(\tau_{yz}' - \sigma_{zz}^0 \omega_x') - y(\tau_{xz}' + \sigma_{zz}^0 \omega_y')] dA = \text{const}, \tag{26b}$$

and this constant is again zero since $\tau_{xz}' = \tau_{yz}' = \omega_x' = \omega_y' = 0$ at $z = l/(2m)$.

Finally, it should be noted that since u_1 varies as $\sin \lambda z$,

$$u_1 = \frac{d^2 u_1}{dz^2} = 0 \text{ at } z = 0, l, \tag{26c}$$

which is the condition of simply-supported ends; furthermore, w_1 and v_1 can be made equal to zero at some point at the end $z = 0$ by the choice of the constants V_i in (17).

Notice that based on the previous analysis, we have found that

$$\phi_i(r, \theta, z) = [C_i I_n(s_i\lambda r) + D_i K_n(s_i\lambda r)] \cos n\theta \sin \lambda z; \quad i = 1,2 \tag{26d}$$

and

$$\psi(r, \theta, z) = [C_0 I_n(q\lambda r) + D_0 K_n(q\lambda r)] \sin n\theta \sin \lambda z. \tag{26e}$$

Now we proceed to the boundary conditions on the lateral surfaces $r = R_j$, $j = 1, 2$, which will ultimately give the characteristic equation for the critical load.

From (7), we obtain

$$\sigma_{rr}' = 0; \quad \tau_{r\theta}' = 0; \quad \tau_{rz}' = 0, \quad \text{at } r = R_1, R_2. \tag{27}$$

Substituting in (27), (15), (12), (2), and (8), and using the identities for the derivatives of Bessel functions, we obtain a system of six linear homogeneous equations in C_i, D_i, $i = 1$, 2, and C_0, D_0. In particular, the boundary condition $\sigma_{rr}' = 0$ at $r = R_j$, $j = 1, 2$ gives

$$(c_{11} - c_{12}) \left\{ C_0 \left[n(n-1) \frac{I_n}{R_j^2} + n\lambda q \frac{I_{n+1}}{R_j} \right] + D_0 \left[n(n-1) \frac{K_n}{R_j^2} - n\lambda q \frac{K_{n+1}}{R_j} \right] \right\}$$

Downloaded 03 May 2010 to 171.66.16.245. Redistribution subject to ASME license or copyright; see http://www.asme.org/terms/Terms_Use.cfm

$$+\sum_{i=1,2} C_i\Bigg\{c_{11}\left[\lambda^2 s_i^2 I_n + n(n-1)\frac{I_n}{R_j^2} - \lambda s_i \frac{I_{n+1}}{R_j}\right]$$

$$+c_{12}\left[-n(n-1)\frac{I_n}{R_j^2}+\lambda s_i\frac{I_{n+1}}{R_j}\right]$$

$$-c_{13}k_i\lambda^2 I_n\Bigg\}+\sum_{i=1,2} D_i\Bigg\{c_{11}\left[\lambda^2 s_i^2 K_n + n(n-1)\frac{K_n}{R_j^2}+\lambda s_i\frac{K_{n+1}}{R_j}\right]$$

$$-c_{12}\left[n(n-1)\frac{K_n}{R_j^2}+\lambda s_i\frac{K_{n+1}}{R_j}\right]$$

$$-c_{13}k_i\lambda^2 K_n\Bigg\}=0,\quad j=1,2. \qquad (28a)$$

The boundary condition $\tau'_{r\theta} = 0$ at $r = R_j$, $j = 1, 2$ gives

$$C_0\left[2\lambda q\frac{I_{n+1}}{R_j}-2n(n-1)\frac{I_n}{R_j^2}-\lambda^2 q^2 I_n\right]$$

$$-D_0\left[2\lambda q\frac{K_{n+1}}{R_j}+2n(n-1)\frac{K_n}{R_j^2}+\lambda^2 q^2 K_n\right]$$

$$-\sum_{i=1,2} C_i\left[2n(n-1)\frac{I_n}{R_j^2}+2n\lambda s_i\frac{I_{n+1}}{R_j}\right]$$

$$+\sum_{i=1,2} D_i\left[-2n(n-1)\frac{K_n}{R_j^2}+2n\lambda s_i\frac{K_{n+1}}{R_j}\right]=0,\ j=1,2. \qquad (28b)$$

In a similar fashion, the condition $\tau'_{rz} = 0$ at $r = R_j$, $j = 1, 2$ gives

$$C_0\frac{nI_n}{R_j}+D_0\frac{nK_n}{R_j}+\sum_{i=1,2} C_i(k_i+1)\left[\frac{nI_n}{R_j}+\lambda s_i I_{n+1}\right]$$

$$+\sum_{i=1,2} D_i(k_i+1)\left[\frac{nK_n}{R_j}-\lambda s_i K_{n+1}\right],\quad j=1,2. \qquad (28c)$$

The Bessel functions $I_{\{n,n+1\}}$ and $K_{\{n,n+1\}}$ are assumed to be evaluated at $\lambda s_i R_j$ if they are inside the sum, Σ, and hence belong to the coefficients of C_i and D_i, i.e., $I_{\{n,n+1\}} \equiv I_{\{n,n+1\}}(\lambda s_i R_j)$; they are evaluated at $\lambda q R_j$ if they are outside, and hence belong to the coefficients of C_0 and D_0, i.e., $I_{\{n,n+1\}} \equiv I_{\{n,n+1\}}(\lambda q R_j)$.

By equating the determinant of the above system (28) to zero, we obtain an equation for σ_0 (characteristic equation) which can be solved to obtain the critical load. In general, the roots s_1 and s_2 are either both real or complex conjugates, whereas q, defined in (19b), is normally a real variable. In the case of real s_1, s_2, the determinant of the linear system (28) is real.

In the case of a complex conjugate pair $\{s_1, s_2\}$, the Bessel functions have complex arguments and the constants C_1, C_2 and D_1, D_2 are complex conjugates, whereas C_0 and D_0 are real variables. Furthermore, $\{I_n(\lambda s_1 R_j),\ I_n(\lambda s_2 R_j)\}$ and $\{I_{n+1}(\lambda s_1 R_j),\ I_{n+1}(\lambda s_2 R_j)\}$ are also complex conjugate pairs and the same holds true for $\{K_n(\lambda s_1 R_j),\ K_n(\lambda_{s2} R_j\}$ and $\{K_{n+1}(\lambda s_1 R_j),\ K_{n+1}(\lambda s_2 R_j)$. The 6 × 6 matrix of coefficients of the linear system (28) has two real columns (corresponding to C_0 and D_0 and the remaining four are two pairs of complex conjugates. Therefore, it turns out that in this case the determinant of (28) is also real. In either case, equating to zero the determinant results in a nonlinear real equation for σ_0.

The modified Bessel functions of zero and first order are evaluated from polynomial coefficients given by Abramowitz and Stegun (1964) and those of the higher order from the associated recurrence relations. It should be noted that due to these polynomial approximations for the Bessel functions, the equation for zero determinant turns out to have a large number of very closely spaced roots, for R_2/R_1 less than about 1.15, which renders this procedure unsuitable for finding the bifurcation load for thin shell construction; for moderate thickness, however, a single, well-defined root is found.

Discussion of Results

In a cylindrical shell subjected to axial compression, a large number of instability modes correspond to a single bifurcation point. By setting

$$\tilde{m} = \frac{m\pi R_0}{l}, \qquad (29)$$

we obtain the simple formula for the eigenvalues of isotropic shells from the Donnell theory as follows (Timoshenko and Gere, 1961):

$$\sigma_{0,S-\text{Donnell}} = \frac{E}{(1-\nu^2)}\frac{h^2}{12R_0^2}\frac{(\tilde{m}^2+n^2)^2}{\tilde{m}^2}+E\frac{\tilde{m}^2}{(\tilde{m}^2+n^2)^2}, \qquad (30)$$

where E is the modulus of elasticity and ν is the Poisson's ratio. A distinct eigenvalue corresponds to each pair of the positive integers m and n. The pair corresponding to the smallest eigenvalue can be determined by trial. Analytical minimization of σ_0 from (30) with respect to the quantity $[(\tilde{m}^2 + n^2)/\tilde{m}]^2$ gives the well-known classical result:

$$\sigma_{0cr,\ C-\text{Donnell}} = \frac{Eh}{R_0\sqrt{3(1-\nu^2)}}. \qquad (31)$$

As discussed in the Introduction, this formula holds true for shells of intermediate length; for short shells the trial-and-error procedure is necessarily used (Batdorf, 1947). In the classical shell theory solution, the radial displacement is constant through the thickness and the axial and circumferential ones have a linear variation, i.e., the displacements are in the form:

$$u_1(r,\theta,z) = U_0\cos n\theta\sin\lambda z,$$

$$v_1(r,\theta,z) = \left[V_0+\frac{r-R}{R}(V_0+nU_0)\right]\sin n\theta\sin\lambda z. \qquad (32a)$$

$$w_1(r,\theta,z) = [W_0-(r-R)\lambda U_0]\cos n\theta\cos\lambda z. \qquad (32b)$$

where U_0, V_0, W_0 are constants (these displacement field variations would satisfy the classical assumptions of $e_{rr} = e_{r\theta} = e_{rz} = 0$).

Two other shell theories, namely the Flügge (1960) and the Danielson and Simmonds (1969), have produced results for the critical loads in shells and should therefore be compared with the present elasticity solution. The expression for the eigenvalues derived from the Flügge equations (Flügge, 1960), $\sigma_{0,F}$ and the more simplified but just as accurate one by Danielson and Simmonds (1969), $\sigma_{0,DS}$ are

$$\sigma_{0,\{F,DS\}} = E\frac{Q_{F,DS}}{\tilde{m}^2[(\tilde{m}^2+n^2)^2+n^2]}, \qquad (33a)$$

where the numerator for the Flügge theory is

$$Q_F = \frac{h^2}{12R_0^2(1-\nu^2)}\{(\tilde{m}^2+n^2)^4-2[\nu\tilde{m}^2+3\tilde{m}^4n^2$$

$$+(4-\nu)\tilde{m}^2n^4+n^6]+2(2-\nu)\tilde{m}^2n^2+n^4\}+\tilde{m}^4; \qquad (33b)$$

and for the Danielson and Simmonds equations,

$$Q_{DS} = \frac{h^2}{12R_0^2(1-\nu^2)}(\tilde{m}^2+n^2)^2(\tilde{m}^2+n^2-1)^2+\tilde{m}^4. \qquad (33c)$$

Again, a distinct eigenvalue corresponds to each pair of the positive integers m and n, the critical load being for the pair that renders the lowest eigenvalue.

Concerning the present elasticity formulation, the critical load is obtained by finding the solution σ_0 of the determinant

Downloaded 03 May 2010 to 171.66.16.245. Redistribution subject to ASME license or copyright; see http://www.asme.org/terms/Terms_Use.cfm

of (28) for a range of n and m, and keeping the minimum value. Table 1 shows the critical load and the corresponding n, m, as predicted by the present three-dimensional elasticity formulation, and the critical load and the corresponding n, m, as predicted by the simple Donnell shell formula, Eq. (30). A length ratio $l/R_2 = 5$, and isotropic material with $E = 14$ GPa and Poisson's ratio $\nu = 0.3$ have been assumed. In all cases, a value of $R_2 = 1$ m is taken, and a range of outside versus inside radius ratios, R_2/R_1, which would probably constitute moderately thick shells is examined. In general, the number of axial half-waves, m, is less for the elasticity solution than that of the shell theory, although the number of circumferential waves, n, is mostly the same. The shell theory predicts a higher load than the elasticity approach, the nonconservatism increasing with thicker shells. For a ratio of outside/inside radius $R_2/R_1 = 1.20$, the simple Donnell shell formula prediction is higher than the elasticity one by more than 50 percent. The last column in Table 1 gives the predictions of the elasticity formulation for the same n, m as in the shell theory solution; again the elasticity results are lower than the corresponding shell theory ones, even for the same n, m values.

One other point should also be mentioned. In order to produce a closed-form expression, the simple Donnell shell formula is based on approximations regarding several terms in the final system of the Donnell shell equations, for example it neglects $h^2/(12R_0^2)$. If these approximations are not enforced, which would result in a more involved formula, we obtain expressions which are referred here as the eigenvalues from the "nonsimplified Donnell shell theory," and these are given in the Appendix. The minimum values (critical loads) from this procedure are compared in Table 2. In general, the difference between the elasticity and the Donnell shell theory becomes smaller for the non-simplified formulas.

Table 2 gives the predictions of the different shell theories for $l/R_2 = 5$ and isotropic material in comparison with the elasticity one. It is clearly seen that:

(1) the values of n, m (number of circumferential waves and number of axial half-waves, respectively, at the critical point) for both the elasticity, and the Flügge, and the Danielson and Simmonds theories agree, unlike the Donnell shell theory.

(2) all shell theories predict higher critical values than the elasticity solution, the percentage increase being larger with thicker shells. However, both the Flügge and Danielson and Simmonds theories predict critical loads much closer to the elasticity value than the Donnell theory. For instance, at $R_2/R_1 = 1.20$, the Flügge theory predicts a 5.7 percent higher value and the Danielson and Simmonds theory a 7.7 percent higher value than the elasticity solution, whereas the Donnell theory gives a 51.1 percent and a 20.7 percent higher value for the simple and the nonsimplified formulas, respectively. Especially noteworthy is the good performance of the Danielson and Simmonds theory despite its simplicity relative to the Flügge theory.

To further examine the eigenvalues for different n, m, Figs. 2(a, b) show the solution σ_0 of the determinant of (28) for values of m (number of axial half-waves) ranging from 1 to 20 and for n (number of circumferential waves) equal to 1, 2, 3. These curves are for $R_2/R_1 = 1.20$, $l/R_2 = 5$ and isotropic material. For this case, the minimum σ_0 (critical stress) is obtained for $n = 2$ and $m = 2$.

If the displacements of the elasticity solution are set in a form analogous to (32), where instead of the constants U_0, V_0, W_0, we have functions of r, we can write these r-dependences as follows:

$$U(r) = C_0 n \frac{I_n}{r} + D_0 n \frac{K_n}{r} \sum_{i=1,2} C_i \left[n \frac{I_n}{r} + \lambda s_i I_{n+1} \right] + D_i \left[n \frac{K_n}{r} - \lambda s_i K_{n+1} \right], \quad (34a)$$

$$V(r) = -\left\{ C_0 \left[n \frac{I_n}{r} + \lambda q I_{n+1} \right] + D_0 \left[n \frac{K_n}{r} - \lambda q K_{n+1} \right] + \sum_{i=1,2} C_i n \frac{I_n}{r} + D_i n \frac{K_n}{r} \right\}, \quad (34b)$$

$$W(r) = \lambda \sum_{i=1,2} k_i (C_i I_n + D_i K_n), \quad (34c)$$

where again the Bessel functions are assumed to be evaluated at $\lambda s_i r$ if they are inside the sum, and hence belong to the coefficients of C_i and D_i; they are evaluated at $\lambda q r$ if they are outside and hence belong to the coefficients of C_0 and D_0. As an illustration, for the critical load of the previous example of $R_2/R_1 = 1.20$, Fig. 3 shows the eigenfunction $U_1(r)$, which seems to be nearly constant (shell theory would have a constant value $U_1 = 1$)

Concerning the effect of material data, it can be proved that for an isotropic material which is characterized by the two

Table 1 Comparison With Classical Donnell Shell Theory
Critical Loads, $\sigma_0 R_2/(E_3 h)$
Isotropic, $E = E_3$, $\nu = 0.3$
$l/R_2 = 5$

R_2/R_1	Elasticity (n, m)	Classical Shell[1] (Simplified Donnell) (n, m)	Percent Increase	[Elasticity, at same (n, m) as Shell]
1.15	0.454 (2,1)	0.648 (1,8)	42.7%	(0.627)
1.20	0.437 (2,2)	0.660 (2,5)	51.0%	(0.580)
1.25	0.443 (2,2)	0.675 (2,4)	52.3%	(0.545)
1.30	0.449 (1,1)	0.685 (1,6)	52.6%	(0.635)

[1]From Eq. (30)

Table 2 Comparison With Various Shell Theories
Critical Loads, $\sigma_0 R_2/(E_3 h)$
Isotropic, $E = E_3$, $\nu = 0.3$
$l/R_2 = 5$

R_2/R_1	Elasticity (n, m)	Classical[1] (Simplified Donnell) (n, m) Percent Increase	Non-Simplified[2] Donnell (n, m) Percent Increase	Flügge[3] (n, m) Percent Increase	Danielson[3] and Simmonds (n, m) Percent Increase
1.15	0.454 (2,1)	0.648 (1,8) 42.7%	0.549 (2,2) 20.9%	0.471 (2,1) 3.7%	0.481 (2,1) 5.9%
1.20	0.437 (2,2)	0.660 (2,5) 51.0%	0.527 (2,2) 20.6%	0.462 (2,2) 5.7%	0.470 (2,2) 7.6%
1.25	0.443 (2,2)	0.675 (2,4) 52.3%	0.540 (2,2) 21.9%	0.473 (2,2) 6.8%	0.484 (2,2) 9.3%
1.30	0.449 (1,1)	0.685 (1,6) 52.6%	0.571 (2,2) 27.2%	0.492 (1,1) 9.6%	0.499 (1,1) 11.1%

[1]From Eq. (30)
[2]From Eq. (A1)
[3]From Eqs. (33)

Downloaded 03 May 2010 to 171.66.16.245. Redistribution subject to ASME license or copyright; see http://www.asme.org/terms/Terms_Use.cfm

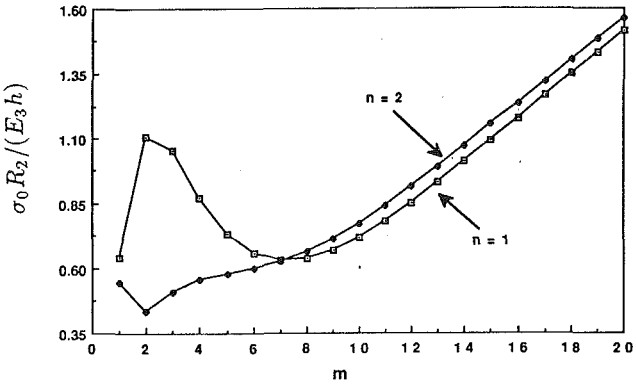


Fig. 2(*a*) Eigenvalues $\sigma_0 R_2/(E_3 h)$ for $n = 1, 2$ (number of circumferential waves) and for m (number of axial half-waves) ranging from 1 to 20. The curves are for $R_2/R_1 = 1.20$, $l/R_2 = 5$ and isotropic material (minimum σ_0, i.e., critical stress, is for $n = 2$ and $m = 2$).

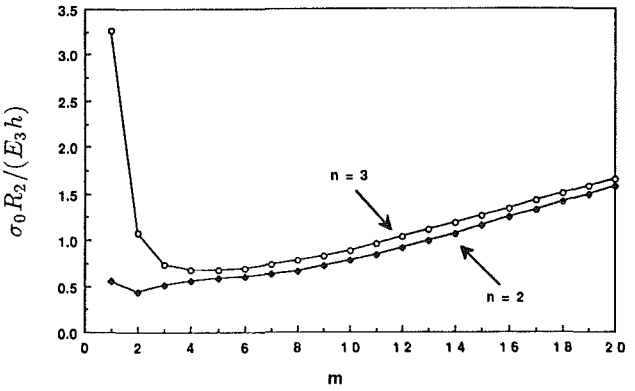


Fig. 2(*b*) Eigenvalues $\sigma_0 R_2/(E_3 h)$ for $n = 2, 3$ and for m ranging from 1 to 20. The curves are for $R_2/R_1 = 1.20$, $l/R_2 = 5$ and isotropic material (minimum σ_0, i.e., critical stress, is for $n = 2$ and $m = 2$).

stiffness constants $c_{11} = c_{33}$ and c_{55}, ($c_{12} = c_{13} = c_{11} - 2c_{55}$), the roots of (14*b*) are

$$s_1 = 1 \text{ and } s_2 = q = \left(1 - \frac{\sigma_0}{2c_{55}}\right)^{1/2}. \tag{35}$$

For a transversely isotropic material the roots are in general complex conjugates. We take as an example case the same geometrical dimensions as before, i.e., $l/R_2 = 5.0$, and a transversely isotropic material and with moduli (in GPa): $E_3 = 57$, $E_2 = E_1 = 14$, $G_{31} = G_{23} = 5.7$, and Poisson's ratios: $\nu_{23} = \nu_{13} = 0.068$, $\nu_{12} = 0.400$ (these data can approximate glass/epoxy material with reinforcement along the z-axis). Notice that we have used the notation $1 \equiv r$, $2 \equiv \theta$, $3 \equiv z$. Table 3 gives the critical load and the corresponding n, m, as predicted by the present three-dimensional elasticity formulation, and the critical load and the corresponding n, m, as predicted by the nonsimplified transversely isotropic Donnell shell theory (Appendix). Again, the shell theory predicts a higher load than the elasticity approach. Notice that the critical load for the transversely isotropic material (with a reinforced axial direction) has been normalized with a higher value of E_3 with regard to the one for the isotropic case (Table 1); the non-normalized value is actually higher.

Acknowledgment

The financial support of the Office of Naval Research, Mechanics Division, Grant N00014-91-J-1892, and the interest and encouragement of the Project Monitor, Dr. Y. Rajapakse, are both gratefully acknowledged.

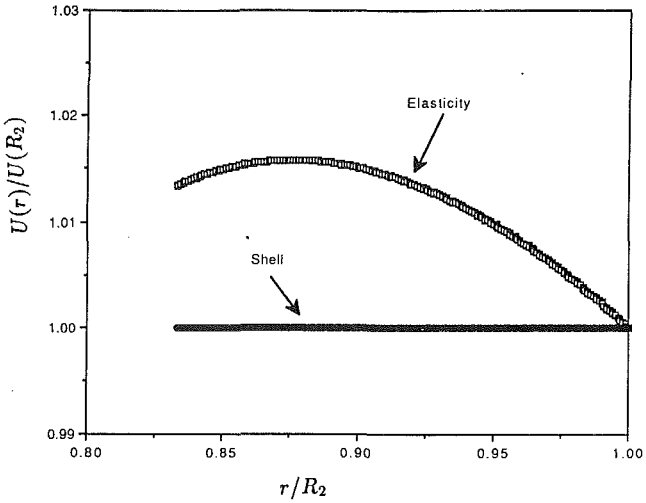


Fig. 3 "Eigenfunction" $U(r)/U(R_2)$ versus normalized radial distance r/R_2, $R_2/R_1 = 1.20$, $l/R_2 = 5$ and isotropic material (shell theory would have a constant value throughout, $U(r)/U(R_2) = 1$)

Table 3 Transversely Isotropic Material Critical Loads, $\sigma_0 R_2/(E_3 h)$
Moduli: (in GPa) $E_3 = 57$, $E_2 = E_1 = 14$, $G_{31} = G_{23} = 5.7$
Poisson's ratios: $\nu_{12} = 0.400$, $\nu_{23} = \nu_{13} = 0.068$
$l/R_2 = 5$

R_2/R_1	Elasticity (n, m)	Nonsimplified[1] Donnell (n, m)	Percent Increase
1.10	0.167 (2,1)	0.193 (3,3)	15.6%
1.15	0.162 (2,1)	0.194 (2,1)	19.7%
1.20	0.164 (2,2)	0.185 (2,2)	12.8%
1.25	0.163 (2,2)	0.186 (2,2)	14.1%
1.30	0.167 (2,2)	0.192 (2,2)	15.0%

[1]From Eq. (A1)

References

Abramowitz, M., and Stegun, I. A., 1964, *Handbook of Mathematical Functions*, (Applied Mathematics Series, Vol. 55), Washington National Bureau of Standards (reprinted 1968 by Dover Publications, New York) Sect. 9.8.

Batdorf, S. B., 1947, "A Simplified Method of Elastic Stability Analysis for Thin Cylindrical Shells," NACA Rep. 874.

Brush, D. O., and Almroth, B. O., 1975, *Buckling of Bars, Plates, and Shells*, McGraw-Hill, New York.

Danielson, D. A., and Simmonds, J. G., 1969, "Accurate Buckling Equations for Arbitrary and Cylindrical Elastic Shells," *Int. J. Eng. Sci.*, Vol. 7, pp. 459–468.

Elliott, H. A., 1948, "Three-Dimensional Stress Distribution in Hexagonal Aeolotropic Crystals," *Proceedings of the Cambridge Philosophical Society*, Vol. 44, pp. 522–533.

Flügge, W., 1960, *Stresses in Shells*, Springer Verlag, New York, pp. 426–432.

Kardomateas, G. A., 1993, "Buckling of Thick Orthotropic Cylindrical Shells Under External Pressure," ASME JOURNAL OF APPLIED MECHANICS, Vol. 60, pp. 195–202.

Librescu, L., 1975, *Elastostatics and Kinetics of Anisotropic and Heterogeneous Shell-Type Structures*, Nordhoff International, Leyden.

Noor, A. K., and Burton, W. S., 1990, "Assessment of Computational Models for Multi-layered Composite Shells," *Appl. Mech. Rev.*, Vol. 43, No. 4, pp. 67–97.

Reddy, J. N., and Liu, C. F., 1985, "A Higher-Order Shear Deformation Theory of Laminated Elastic Shells," *Int. J. Eng. Sci.*, Vol. 23, No. 3, pp. 319–330.

Simitses, G. J., Shaw, D., and Sheinman, I., 1985, "Stability of Cylindrical Shells by Various Nonlinear Shell Theories," *ZAMM, Z. Angew. Math. u. Mech.*, Vol. 65, No. 3, pp. 159–166.

Simmonds, J. G., and Danielson, D. A., 1970, "New Results for the Buckling Loads of Axially Compressed Cylindrical Shells Subject to Relaxed Boundary Conditions," ASME JOURNAL OF APPLIED MECHANICS, Vol. 37, pp. 93–100.

Timoshenko, S. P., and Gere, J. M., 1961, *Theory of Elastic Stability*, McGraw-Hill, New York.

Whitney, J. M., and Sun, C. T., 1974, "A Refined Theory for Laminated Anisotropic Cylindrical Shells," ASME JOURNAL OF APPLIED MECHANICS, Vol. 41, No. 2, pp. 471–476.

Downloaded 03 May 2010 to 171.66.16.245. Redistribution subject to ASME license or copyright; see http://www.asme.org/terms/Terms_Use.cfm

APPENDIX

Eigenvalues From Nonsimplified Donnell Shell Equations

In terms of

$$\alpha = \frac{h^2}{12R_0^2}; \quad \tilde{\lambda} = R_0\lambda; \quad \tilde{E}_3 = \frac{E_3}{1-\nu_{23}\nu_{32}}; \quad \tilde{E}_2 = \frac{E_2}{1-\nu_{23}\nu_{32}},$$

define the following constants that depend on α, the material properties, and the values of n, m:

$$a_{11} = \tilde{E}_3\nu_{23}\tilde{\lambda}, \quad a_{12} = (\tilde{E}_3\nu_{23} + G_{23})n\tilde{\lambda}; \quad a_{13} = -(\tilde{E}_3\tilde{\lambda}^2 + G_{23}n^2)$$

$$a_{21} = -(\tilde{E}_2 + \tilde{E}_2\alpha n^2 + \tilde{E}_2\nu_{32}\alpha\tilde{\lambda}^2 + 2G_{23}\alpha\tilde{\lambda}^2)n$$

$$a_{22} = -(\tilde{E}_2 n^2 + \tilde{E}_2\alpha n^2 + G_{23}\tilde{\lambda}^2 + 2G_{23}\alpha\tilde{\lambda}^2);$$

$$a_{23} = (\tilde{E}_3\nu_{23} + G_{23})n\tilde{\lambda}$$

$$a_{31} = (\tilde{E}_2 + \tilde{E}_3\alpha\tilde{\lambda}^4 + 2\tilde{E}_2\nu_{32}\alpha\tilde{\lambda}^2 n^2 + \tilde{E}_2\alpha n^4 + 4G_{23}\alpha\tilde{\lambda}^2 n^2)$$

$$a_{32} = (\tilde{E}_2 + \hat{E}_2\nu_{32}\alpha\tilde{\lambda}^2 + \tilde{E}_2\alpha n^2 + 4G_{23}\alpha\tilde{\lambda}^2)n; \quad a_{33} = -\tilde{E}_3\nu_{23}\tilde{\lambda}.$$

The eigenvalues for a transversely isotropic material are then given by

$$\sigma_{NS-\text{Donnell}} = -\frac{DET}{(a_{22}a_{13} - a_{12}a_{23})\tilde{\lambda}^2}, \tag{A1}$$

where

$$DET = \begin{vmatrix} a_{11} & a_{12} & a_{13} \\ a_{21} & a_{22} & a_{23} \\ a_{31} & a_{32} & a_{33} \end{vmatrix}.$$

Downloaded 03 May 2010 to 171.66.16.245. Redistribution subject to ASME license or copyright; see http://www.asme.org/terms/Terms_Use.cfm

V. Birman
Engineering Education Center,
University of Missouri-Rolla,
St Louis, MO 63121
Mem. ASME

C. W. Bert
School of Aerospace and Mechanical Engineering,
University of Oklahoma,
Norman, OK 73019
Fellow ASME

Buckling and Post-buckling of Composite Plates and Shells Subjected to Elevated Temperature

Effects of temperature on buckling and post-buckling behavior of reinforced and unstiffened composite plates or cylindrical shells are considered. First, equilibrium equations are formulated for a shell subjected to the simultaneous action of a thermal field and an axial loading. These equations are used to predict a general form of the algebraic equations describing the post-buckling response of a shell. Conditions for the snap-through of a shell subjected to thermomechanical loading are formulated. As an example, the theory is applied to prediction of post-buckling response of flat large-aspect-ratio panels reinforced in the direction of their short edges.

Introduction

The paper considers post-buckling response of composite cylindrical shells subjected to compressive axial loads and elevated temperature. It is shown that a quasi-static increase of temperature at a constant compressive load can result in a snap-through of the shell to a new equilibrium position. A shell can also exhibit a snap-through if it is subjected to an increasing compression and a steady-state thermal field. In the latter case, temperature reduces the upper and lower critical loads. Therefore, a concept of temperature sensitivity associated with a snap-through of a heated shell can be introduced by analogy to the well-known imperfection sensitivity concept in mechanically loaded structures.

The research on imperfection sensitivity of shells was initiated in Koiter's thesis (1945) and in his subsequent studies (1967). This theory was later extended and applied to both static and dynamic buckling problems by Budiansky and Hutchinson (1964), Budiansky (1967), and Elishakoff (1980). Imperfection sensitivity of composite material shells was studied by Simitses, et al. (1985), Hui and Du (1987), and others. The problem of post-buckling behavior of composite cylindrical shells reinforced in the axial and circumferential directions was considered by Birman (1990a).

Effects of temperature on behavior of composite cylindrical shells have been investigated by Ambartsumyan (1974), Kalam and Tauchert (1978), Hyer and Rousseau (1987), and Hyer and Cooper (1986) among others. The recent papers dealt with transient thermal stresses in an orthotropic cylinder (Kardomateas, 1989) and interfacial stresses in bi-annular assemblies subjected to a uniform temperature (Suhir and Sullivan, 1989).

Thermoelastic problems of reinforced composite cylindrical shells received relatively little attention. Birman (1991) considered axisymmetric thermal bending of shear deformable shells reinforced by ring stiffeners. The problems of thermal shock of reinforced cylindrical shells were also studied (Birman, 1990). Dynamic stability of reinforced composite cylinders was analyzed by Birman and Bert (1991).

An important difference between the studies of imperfection sensitivity and temperature sensitivity is the nature of imperfections versus that of temperature. Initial imperfections which are usually inherited from a technological process are probabilistic in the sense that neither their shapes nor their magnitude can be predicted a priori with certainty. This leads to a probabilistic approach to shell buckling reflected in the works of Roorda and Hansen (1976), Elishakoff and Arbocz (1981), and others. In contrast to imperfections, temperature is usually due to working equipment, solar or aerodynamic heating. Therefore, the distribution of a thermal field is usually more predictable and thus the problem is more deterministic.

Analysis: Governing Equations

Consider a thin circular cylindrical shell or panel reinforced by axial and ring stiffeners and subjected to the simultaneous action of axial compressive loads of intensity N_1 and thermal field $T(x,y,z)$ where x and y are the coordinates in the axial and circumferential directions, respectively, and z is the radial coordinate. A nonlinear thermoelastic version of Love's first approximation theory is used in the analysis.

Nonlinear strain-displacement relationships for an arbitrary layer of such a shell are

$$\epsilon_x^0 = u_{,x} + (1/2)w_{,x}^2 + \alpha_x T$$

$$\epsilon_y^0 = v_{,y} - \frac{w}{R} + (1/2)w_{,y}^2 + \alpha_y T$$

Contributed by the Applied Mechanics Division of THE AMERICAN SOCIETY OF MECHANICAL ENGINEERS for publication in the ASME JOURNAL OF APPLIED MECHANICS.

Discussion on this paper should be addressed to the Technical Editor, Professor Lewis T. Wheeler, Department of Mechanical Engineering, University of Houston, Houston, TX 77204-4792, and will be accepted until four months after final publication of the paper itself in the ASME JOURNAL OF APPLIED MECHANICS.

Manuscript received by the ASME Applied Mechanics Division, Apr. 3, 1991; final revision, Nov. 11, 1991. Associate Technical Editor: J. G. Simmonds.

Copyright © 1993 by ASME
Downloaded 03 May 2010 to 171.66.16.245. Redistribution subject to ASME license or copyright; see http://www.asme.org/terms/Terms_Use.cfm

$$\gamma_{xy}^0 = u_{,y} + v_{,x} + w_{,x}w_{,y} + \alpha_{xy}T$$

$$\kappa_x = -w_{,xx}$$

$$\kappa_y = -w_{,yy} + \frac{v_{,y}}{R}$$

$$\kappa_{xy} = -2w_{,xy} + \frac{v_{,x}}{R}. \tag{1}$$

All notations in (1) are standard in the theory of shells. The superscript "0" refers to the strains in the middle surface. The positive directions of the radial coordinate and the radial deflection w are inward on the shell.

The constitutive relations for the shell are written here by assuming that the material is symmetrically laminated about the middle surface and the torsional stiffness of reinforcements is negligible:

$$N_x = A_{11}\epsilon_x^0 + A_{12}\epsilon_y^0 + \sum_s \delta(y-y_s)E_sA_s(\epsilon_x^0 + z_s\kappa_x) - N_x^T$$

$$N_y = A_{12}\epsilon_x^0 + A_{22}\epsilon_y^0 + \sum_r \delta(x-x_r)E_rA_r(\epsilon_y^0 + z_r\kappa_y) - N_y^T$$

$$N_{xy} = A_{66}\gamma_{xy}^0 - N_{xy}^T$$

$$M_x = D_{11}\kappa_x + D_{12}\kappa_y + \sum_s \delta(y-y_s)E_x(A_sz_s\epsilon_x^0 + I_{0s}\kappa_x) - M_x^T$$

$$M_y = D_{12}\kappa_x + D_{22}\kappa_y + \sum_r \delta(x-x_r)E_r(A_rz_r\epsilon_y^0 + I_{0r}\kappa_y) - M_y^T$$

$$M_{xy} = D_{66}\kappa_{xy} - M_{xy}^T. \tag{2}$$

In (2), I_{ro} and I_{so} are moments of inertia of circumferential and axial stiffeners with respect to the middle surface, E_r and E_s are moduli of elasticity of circumferential and axial stiffeners, and A_r and A_s are cross-sectional areas of the respective stiffeners. The distances from centroids of cross-sections of circumferential and axial stiffeners to shell middle surface are denoted by z_r and z_s respectively. The coordinates of the stiffeners are x_r and y_s. Thermal terms in (2) are given by

$$\{N_x^T,\ M_x^T\} = \int_{-h/2}^{h/2} A_{11}\alpha_x\{1,z\}Tdz + \int_{-h/2}^{h/2} A_{12}\alpha_y\{1,z\}Tdz + \sum_s \delta(y-y_s)E_sA_s\alpha_x^s\{1,z\}T(z_s)$$

$$\{N_y^T,\ M_y^T\} = \int_{-h/2}^{h/2} A_{12}\alpha_y\{1,z\}Tdz + \int_{-h/2}^{h/2} A_{22}\alpha_y\{1,z\}Tdz + \sum_r \delta(x-x_r)E_rA_r\alpha_y^r\{1,z\}T(z_r)$$

$$\{N_{xy}^T,\ M_{xy}^T\} = \int_{-h/2}^{h/2} A_{66}\alpha_{xy}\{1,z\}Tdz \tag{3}$$

where α_y^r and α_x^s are the coefficients of thermal expansion of the ring and stringer materials. Equations of equilibrium of a shell written within the framework of Love's first approximation theory are

$$N_{x,x} + N_{xy,y} = 0$$

$$N_{xy,x} + N_{y,y} + (M_{xy,x} + M_{y,y})/R = 0$$

$$M_{x,xx} + 2M_{xy,xy} + M_{y,yy} - N_y/R + (N_xw_{,x} + N_{xy}w_{,y})_{,x} + (N_{xy}w_{,x} + N_yw_{,y})_{,y} - N_1w_{,xx} = 0 \tag{4}$$

where $N_1 > 0$ implies compression. The substitution of (2) into (4) yields equations of equilibrium in terms of displacements:

$$\left[A_{11} + \sum_s \delta(y-y_s)E_sA_s\right]u_{,xx} + A_{66}u_{,yy} + (A_{12}+A_{66})v_{,xy} - A_{12}w_{,x}/R - \sum_s \delta(y-y_s)E_sA_sz_sw_{,xxx} + \left[A_{11} + \sum_s \delta(y-y_s)E_sA_s\right](w_{,x}w_{,xx}) + (A_{12}+A_{66})w_{,y}w_{,xy} + A_{66}w_{,x}w_{,yy} = N_{x,x}^T + N_{xy,y}^T$$

$$(A_{12}+A_{66})u_{,xy} + \left(A_{66} + \frac{D_{66}}{R^2}\right)v_{,xx} + \left\{A_{22} + \sum_r \delta(x-x_r)E_rA_r\left(1+\frac{2z_r}{R}\right) + \frac{1}{R^2}\left[D_{22} + \sum_r \delta(x-x_r)E_rI_{or}\right]\right\}v_{,yy} - \left[A_{22} + \sum_r \delta(x-x_r)E_rA_r\left(1+\frac{z_r}{R}\right)\right]\frac{w_{,y}}{R} - \left\{\sum_r \delta(x-x_r)E_rA_rz_r + \frac{1}{R}\left[D_{22} + \sum_r \delta(x-x_r)E_rI_{or}\right]\right\}w_{,yyy} - \frac{1}{R}(D_{12}+2D_{66})w_{,xxy} + \left[A_{22} + \sum_r \delta(x-x_r)E_rA_r \times \left(1+\frac{z_r}{R}\right)\right]w_{,y}w_{,yy} + (A_{12}+A_{66})w_{,x}w_{,xy} + A_{66}w_{,xx}w_{,y} = N_{xy,x}^T + N_{y,y}^T + \frac{1}{R}(M_{xy,x}^T + M_{y,y}^T) - \left[D_{11} + \sum_s \delta(y-y_s)E_sI_{os}\right]w_{,xxxx} - 2(D_{12}+2D_{66})w_{,xxyy} - \left[D_{22} + \sum_r \delta(x-x_r)E_rI_{or}\right]w_{,yyyy} - \frac{2}{R}\sum_r \delta(x-x_r)E_rA_rz_rw_{,yy} - N_1w_{,xx} - \frac{1}{R^2}\left[A_{22} + \sum_r \delta(x-x_r)E_rA_r\right]w + (D_{12}+2D_{66})\frac{v_{,xxy}}{R} + \left[\frac{D_{22}}{R} + \sum_r \delta(x-x_r)E_r\left(\frac{I_{or}}{R} + A_rz_r\right)\right]v_{,yyy} + \frac{1}{R}\left[A_{22} + \sum_r \delta(x-x_r)E_rA_r\left(1+\frac{z_r}{R}\right)\right]v_{,y} + \sum_s \delta(y-y_s)E_sA_sz_su_{,xxx} + \frac{A_{12}}{R}u_{,x} + \sum_s \delta(y-y_s)E_sA_sz_s\left(w_{,x}w_{,xxx} + w_{,xx}^2\right) + \sum_r \delta(x-x_r)E_rA_rz_r(w_{,y}w_{,yyy} + w_{,yy}^2) + \frac{1}{2R}\left[A_{22} + \sum_r \delta(x-x_r)E_rA_r\right]w_{,y}^2 + \left\{\left\{\left[A_{11} + \sum_s \delta(y-y_s)E_sA_s\right]\left(u_{,x} + \frac{1}{2}w_{,x}^2\right)\right.\right.$$

Downloaded 03 May 2010 to 171.66.16.245. Redistribution subject to ASME license or copyright; see http://www.asme.org/terms/Terms_Use.cfm

$$+A_{12}\left(v_{,y}-\frac{w}{R}+\frac{1}{2}w_{,y}^2\right)-\sum_s \delta(y-y_s)E_sA_sz_sw_{,xx}\Bigg\}w_{,x}$$

$$+A_{66}(u_{,y}+v_{,x}+w_{,x}w_{,y})w_{,y}\Bigg]\Bigg\}_{,x}$$

$$+\left\{A_{66}(u_{,y}+v_{,x}+w_{,x}w_{,y})w_{,x}+\left\{A_{12}\left(u_{,x}+\frac{1}{2}w_{,x}^2\right)\right.\right.$$

$$+\left[A_{22}+\delta(x-x_r)E_rA_r\right]\left(v_{,y}-\frac{w}{R}+\frac{1}{2}w_{,y}^2\right)$$

$$+\sum_r \delta(x-x_r)E_rA_rz_r\left(-w_{,yy}+\frac{v_{,y}}{R}\right)\Bigg\}w_{,y}\Bigg\}_{,y}=M_{x,xx}^T+2M_{xy,xy}^T$$

$$+M_{y,yy}^T+\frac{N_y^T}{R}+(N_x^Tw_{,x}+N_{xy}^Tw_{,y})_{,x}$$

$$+(N_{xy}^Tw_{,x}+N_y^Tw_{,y})_{,y}. \quad (5)$$

It is important to consider the form of equilibrium equations obtained if each of the shell displacements is modeled by a single assumed function of each coordinate, i.e.,

$$u=Uf_1(x)\phi_1(y)$$

$$v=Vf_2(x)\phi_2(y)$$

$$w=Wf_3(x)\phi_3(y) \quad (6)$$

where $f_i(x)$ and $\phi_j(y)$ are shape functions that satisfy boundary and periodicity conditions. The Galerkin procedure applied to (5) yields

$$U=k_1W+n_1W^2+t_1$$

$$V=k_2W+n_2W^2+t_2 \quad (7)$$

$$a_3W^3+a_2W^2+(a_1+b_1T)W+b_0N_1W+a_0T=0. \quad (8)$$

Here Eqs. (7) are obtained from the first two Eqs. (5) that are solved for U and V. Then these expressions are substituted into the third Eq. (5) yielding (8).

In (7) and (8), k_i, n_j, t_l, a_p, and b_r are constant coefficients and T is a parameter that characterizes a steady thermal field. An example of these coefficients for the case of a simply supported, flat, large-aspect-ratio panel reinforced along the short edges is shown later in the paper.

Response of Flat Composite Panels to a Uniform Thermal Field (Constant Compression)

If a panel is flat and the temperature is uniform, the analysis of the coefficients of equation (8) indicates that $a_0 = 0$. Accordingly,

$$T=-(a_3W^2+a_2W+a_1+b_0N_1)/b_1 \quad (9)$$

where $W \neq 0$. The curve $T(W)$ has an extremum at $dT/dW = 0$, i.e., at $W_0 = -a_2/2a_3$ as shown in Fig. 1. As follows from this figure, the plate subjected to elevated temperature can exhibit a snap-through to a new equilibrium position ("immedite snap-through:" cases a, c). Note that the curves corresponding to Figs. 1(*a*) and 1(*c*) are similar to those describing a behavior of imperfection-sensitive shells. Therefore, buckling is possible at $T < T_1$ if initial imperfections are present.

On the other hand, a behavior corresponding to the cases *b* and *d* could be called a "delayed snap-through." In these cases plate deformations increase with an increase of temperature beyond $T = T_1$. However, at $W = W_0$ the response becomes unstable and a snap-through occurs. Obviously, if a_2 and a_3 have different signs, W_0 is positive while, if the signs of a_2 and a_3 coincide, the root of $dT/dW = 0$ is negative. The character of the response, i.e., the temperature of a snap-through can be examined by an analysis of the sign of dT/dW at $W = 0$, $T_1 = -(a_1 + b_0N_1)/b_1$. A snap-through occurs at $T = T_1$, if $dT/dW < 0$ and $a_2a_3 < 0$ (Fig. 1(*a*)) and if $dT/dW > 0$ and $a_2a_3 > 0$ (Fig. 1(*c*)).

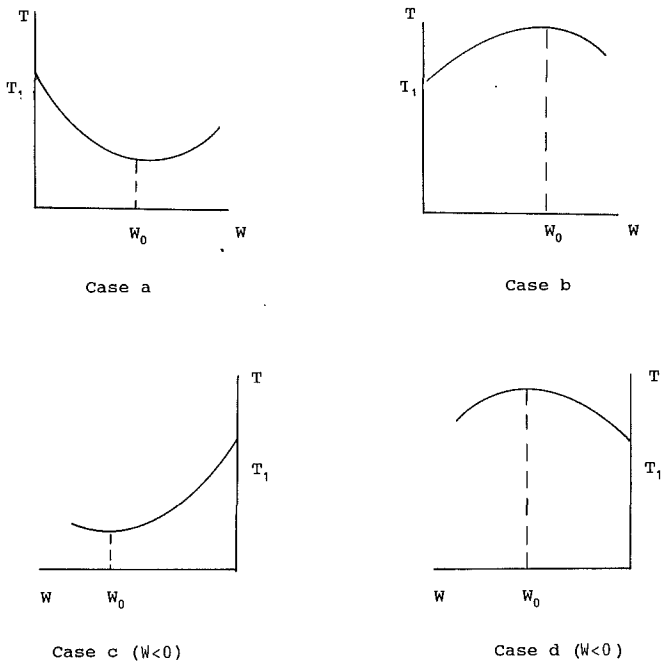


Fig. 1 Response of flat stiffened plates to a uniform temperature. Cases (*a*)-(*d*) correspond to coefficient signs in Table 1.

In the cases shown in Figs. 1(*b*) and 1(*d*), a snap-through occurs at a higher temperature calculated by (9) where $W = W_0$. Note here that although the structure exhibits a snap-through in all four cases shown in Fig. 1, it has higher stability resources and prebuckling deformations in the cases corresponding to Figs. 1(*b*), 1(*d*).

An immediate snap-through occurs, if

$$a_2b_1>0, \quad a_2a_3<0$$

or

$$a_2b_1<0, \quad a_2a_3>0 \quad (10)$$

which correspond to Figs. 1(*a*) and 1(*c*), respectively. Delayed snap-through conditions are

$$a_2b_1<0, \quad a_2a_3<0 \quad \text{(Fig. 1(}b\text{))}$$

and

$$a_2b_1>0, \quad a_2a_3>0 \quad \text{(Fig. 1(}d\text{))}. \quad (11)$$

Similar conclusions are obtained by examining the sign of $d^2T/W^2 = -2a_3/b_1$. The relationships between the coefficients of Eq. (8) correspond to a behavior reflected in Figs. 1(*a*) – 1(*d*) and shown in Table 1. In a particular case of an unstiffened panel, the coefficient $a_2 = 0$. In this case

$$\frac{dT}{dW}=-\frac{2a_3}{b_1}W, \quad (12)$$

i.e., an extremum of the curve $T(W)$ corresponds to $W = 0$ (Fig. 2). By examining the sign d^2T/dW^2 one obtains the conclusion that a panel does not exhibit a snap-through, i.e., it behaves similarly to an imperfection-insensitive structure, if $a_3b_1<0$ (Fig. 2(*a*)). On the other hand, if $a_3b_1>0$, any increase of temperature beyond T_1 will result in a snap-through (Fig. 2(*b*)).

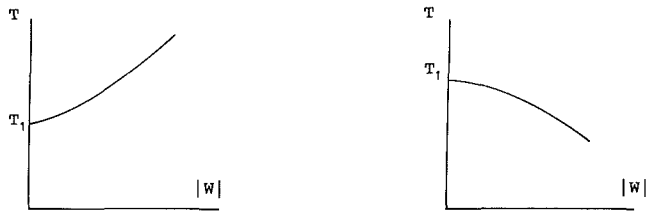
It can be noted here that all unstiffened panels known to the authors satisfy the condition $a_3b_1<0$. However, an addition of stiffeners results in either immediate or delayed snap-through

Downloaded 03 May 2010 to 171.66.16.245. Redistribution subject to ASME license or copyright; see http://www.asme.org/terms/Terms_Use.cfm

Table 1 Interrelationships among coefficients corresponding to responses shown in Figs. 1 and 3

Case		Relationship among coefficients of (8)
Figs. 1(*a*), 3(*a*)		$\{a_3<0 \quad a_2>0 \quad b_i>0\}$
	or	
		$\{a_3>0 \quad a_2<0 \quad b_i<0\}$
Figs. 1(*b*), 3(*b*)		$\{a_3>0 \quad a_2<0 \quad b_i>0\}$
	or	
		$\{a_3<0 \quad a_2>0 \quad b_i<0\}$
Figs. 1(*c*), 3(*c*)		$\{a_3<0 \quad a_2<0 \quad b_i>0\}$
	or	
		$\{a_3>0 \quad a_2>0 \quad b_i<0\}$
Figs. 1(*d*), 3(*d*)		$\{a_3>0 \quad a_2>0 \quad b_i>0\}$
	or	
		$\{a_3<0 \quad a_2<0 \quad b_i<0\}$

Note: subscript $i = 1$ and 0 for Figs 1 and 3, respectively.



Case a Case b

Fig. 2 Response of flat unstiffened plates to a uniform temperature; Case a: $b_3b_1<0$; Case b: $a_3b_1>0$

of a panel in a uniform thermal field. Physically this can be associated with structure asymmetry due to stiffeners.

Response of Flat Composite Panels to Increasing Compression in the Presence of a Constant Uniform Temperature

In this problem, $a_0 = 0$ as in the previous case and the load-deflection curve is given by

$$N_1 = -[a_3W^2 + a_2W + (a_1 + b_1T)]/b_0 \tag{13}$$

where $W \neq 0$. Obviously, temperature changes can only shift $N_1(W)$ curves along the N_1 − axis by an amount

$$\Delta N_1 = -b_1T/b_0.$$

Possible responses of the structure are shown in Fig. 3. To establish the kind of response for a particular structure, three conditions must be examined (similar to those used to obtain relationships between the coefficients for Fig. 1).

(*a*) Extremum, i.e., $dN_1/dW = 0$, occurs at $W_0 = -a_2/2a_3$. Obviously, $a_2a_3<0$ corresponds to Figs. 3(*a*) and 3(*b*).

(*b*) Maximum or minimum, i.e., sign (d^2N_1/dW^2) = sign $(-a_3/b_0)$. Maximum occurs if $a_3b_0>0$, minimum corresponds to $a_3b_0<0$.

(*c*) The slope of the curve at $W = 0$ is $dN_1/dW = -a_2/b_0$.

(14)

Hence, Figs. (3*a*) and 3(*d*) correspond to $a_2b_0>0$ and Figs. 3(*b*) and 3(*c*) require that $a_2b_0<0$. The analysis of these three conditions yields the criteria of panel behavior summarized in Table 1.

Note that coefficients a_1b_1 do not affect the character of the response. However, they determine the value of upper and lower critical loads. Obviously, Figs. 3(*a*) and 3(*c*) correspond to a snap-through behavior (temperature-sensitive panel) while

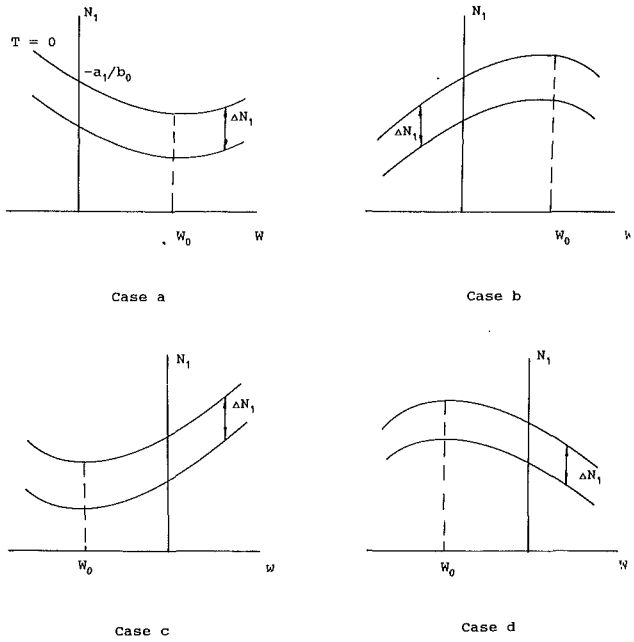


Fig. 3 Response of flat stiffened panels to compression. Cases (*a*)-(*d*) correspond to coefficient signs in Table 1.

in Figs. 3(*b*) and 3(*d*) deflections increase gradually with load (temperature-insensitive panel).

If the panel is unstiffened, its behavior can be characterized by Fig. 2 where T and T_1 are replaced by N_1 and N_{cr} respectively, the latter being the buckling load in the presence of temperature. It is easy to show that Fig. 2(*a*) corresponds to $a_3b_0<0$ while Fig. 2(*b*) represents the case $a_3b_0>0$.

Snap-Through of a Shell Subjected to a Constant Compression and Increasing Temperature

In a general case, none of the coefficients of (8) is equal to zero. The condition $dT/dW = 0$ yields

$$2a_3b_1W^3 + (3a_0a_3 + a_2b_1)W^2 + 2a_0a_2W + a_0(a_1 + b_0N_1) = 0. \tag{15}$$

The situation shown in Figs. 4(*a*) and 4(*b*) occurs if $dT/dW>0$ at $W = 0$. This condition implies

$$a_0(a_1 + b_0N_1)<0. \tag{16}$$

The condition (16) can be satisfied, i.e., the shell bends in the inward ($W>0$) direction, if

$$\begin{cases} a_0>0 \\ N_1<-a_1/b_0 \end{cases} \quad \text{or} \quad \begin{cases} a_0<0 \\ N_1>-a_1/b_0. \end{cases} \tag{17}$$

As follows from the Descartes rule of signs, the shell exhibits a snap-through if the condition (17) is satisfied and there is at least one change of sign of the coefficients of (15). Then Eq. (15) has at least one positive root and the behavior of the shell reflects that shown in Fig. 4(*a*). Since the last term in (15) is negative, this requirement yields

$$a_3b_1>0 \quad \text{or} \quad 3a_0a_3 + a_2b_1>0 \quad \text{or} \quad a_0a_2>0. \tag{18}$$

If none of the conditions (18) is satisfied, the behavior of the shell corresponds to Fig. 4(*b*). The situation shown in Figs. 4(*c*) and 4(*d*) occurs if

$$a_0(a_1 + b_0N_1)>0. \tag{19}$$

Then the condition of a snap-through reduces to that of Eq. (15) having at least one negative real root. This occurs if there is at least one change of sign of the coefficients of the equation obtained from (15) by replacement of W with $(-W)$. The

Downloaded 03 May 2010 to 171.66.16.245. Redistribution subject to ASME license or copyright; see http://www.asme.org/terms/Terms_Use.cfm

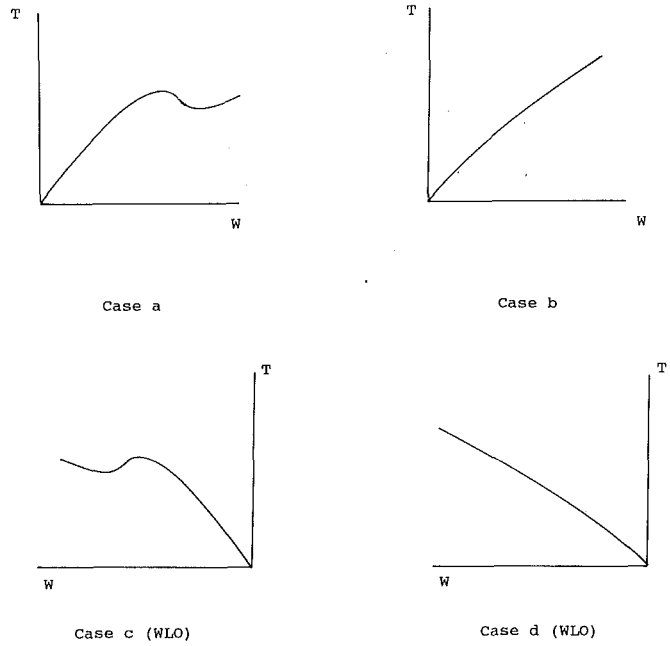


Fig. 4 Response of stiffened cylindrical shells to a uniform temperature. Conditions corresponding to cases (*a*)-(*d*) are discussed in the text

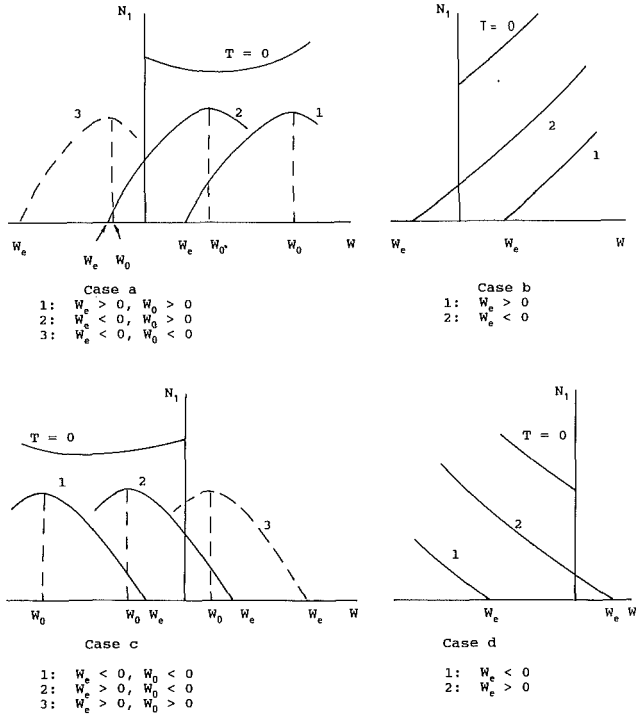


Fig. 5 Response of stiffened cylindrical shells to compression. Curves 1-3 correspond to various signs of W_e and W_0

corresponding mathematical formulation can be obtained easily.

Snap-Through of a Shell Subjected to a Constant Temperature and Increasing Compression

The equilibrium of a shell subjected to an action of a steady-state thermal field can be obtained from (8). If $N_1 = 0$ and temperature is relatively low so that deflections remain small, a linear counterpart of (8) yields

$$W_e = -a_0 T/(a_1 + b_1 T). \tag{20}$$

An extremum of the curve $N_1(W)$ corresponds to $dN_1/dW = 0$, i.e.,

$$f(W) = 2a_3 W^3 + a_2 W^2 - a_0 T = 0. \tag{21}$$

The direction of the curve $N_1(W)$ at $W = W_e$, i.e., the sign of its slope is determined as sign $[F(W_e)]$ where

$$F(W_e) = -f(W_e) b_0. \tag{22}$$

If $F(W_e) > 0$ and Eq. (21) has a positive root, the shell has a snap-through (Fig. 5(*a*)). Note that a possibility of a maximum corresponding to a negative value of W (curve 3) is not discussed here. The case where $F(W_e) > 0$ but none of the roots of (21) is positive is shown in Fig. 5(*b*): the shell does not a snap-through as temperature increases. Accordingly, it can be characterized as temperature insensitive. The conditions of temperature insensitivity follow from the Routh-Hurwitz criterion:

$$a_2/a_3 > 0 \quad a_0/a_3 > 0 \tag{23}$$

These conditions yield

$$a_3 > 0 \quad a_2 > 0 \quad a_0 > 0$$

or

$$a_3 < 0 \quad a_2 < 0 \quad a_0 < 0 \tag{24}$$

which must be satisfied together with $F(W_e) > 0$.

If $F(W_e) < 0$ and one of the roots of equation (21) is negative, the shell behavior is of the type shown in Fig. 5(*c*) (the case shown by curve 3 is not considered here). The number of negative roots is equal to the number of sign changes of coefficients of the equation

$$f(-W) = 0, \text{ i.e.,}$$
$$2a_3 W^3 - a_2 W^2 + a_0 T = 0. \tag{25}$$

On the other hand, if all roots of Eq. (25) are positive, i.e.,

$$a_2/a_3 < 0 \quad a_0/a_3 < 0 \tag{26}$$

the shell behaves according to Fig. 4(*d*). Conditions (26) can also be written as

$$a_3 > 0 \quad a_2 < 0 \quad a_0 < 0$$

or

$$a_3 < 0 \quad a_2 > 0 \quad a_0 > 0 \tag{27}$$

which must be satisfied together with $F(W_e) < 0$. Obviously, if $T = 0$, the extremum of the curve $N_1(W)$ corresponds to $W_0 = -a_2/2a_3$. The case $W_0 > 0$ is obtained if $a_2 a_3 < 0$. This condition contradicts conditions of temperature insensitivity given by (24). If $W_0 < 0$ and $a_2 a_3 > 0$, conditions of temperature insensitivity (27) cannot be satisfied either. Notably, the extremum of $N_1(W)$ in the absence of temperature does not have to be a minimum as shown in Figs. 5(*a*) and 5(*c*). Even if this extremum corresponds to a maximum (not shown in Fig. 5), the conclusions related to temperature sensitivity remain valid.

Example: Cylindrical Thermal Buckling of Reinforced Flat Panels. Consider a flat, large-aspect-ratio panel reinforced by equally spaced stiffeners in the x-direction, i.e., along the short edges (Fig. 6). Such a panel subjected to a uniform temperature can buckle forming a cylindrical surface. Equilibrium Eq. (5) are uncoupled so that the displacement V does not affect the solution in the planes y = constant. If the long edges cannot move in the x-direction, displacements of the panel can be represented by

$$u = U \sin 2\alpha x$$
$$w = W \sin \alpha x \tag{28}$$

where $\alpha = m\pi/L$.

The substitution of (28) into (5) and use of the Galerkin procedure yield Eq. (8) where

Downloaded 03 May 2010 to 171.66.16.245. Redistribution subject to ASME license or copyright; see http://www.asme.org/terms/Terms_Use.cfm

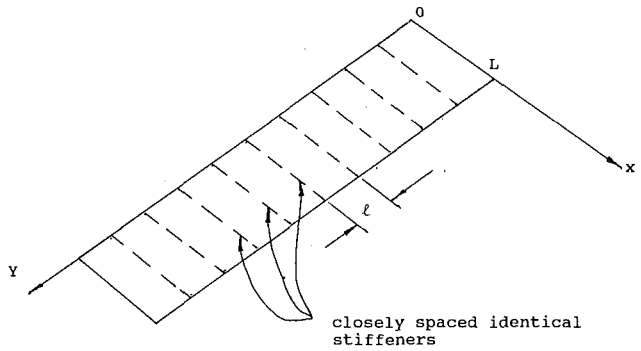


Fig. 6 Large-aspect-ratio panel reinforced along its short edges

$$a_3 = 3\alpha^2\overline{A}_{11}/32 \quad a_2 = 2\alpha\overline{E}\delta_m/3l$$
$$a_1 = \alpha^2\overline{D}_{11}/2 \quad b_1 = -n/2$$
$$a_0 = b_0 = 0. \tag{29}$$

In (29),

$$\delta_m = \begin{cases} 2, \text{ if } m = \text{odd} \\ 0, \text{ if } m = \text{even} \end{cases}$$

$$\overline{E} = E_s A_s z_s/l, \quad \overline{A}_{11} = A_{11} + \frac{E_s A_s}{l}$$

$$\overline{D}_{11} = D_{11} + \frac{E_s I_{os}}{l}, \quad N_x^T = nT \tag{30}$$

where l is the spacing of stiffeners (the smeared stiffeners technique is used, since if the number of stiffeners is small, neither this technique nor the assumption that the buckling mode shape is cylindrical are applicable).

Obviously, $a_3 > 0$, $a_1 > 0$ and $b_1 < 0$. If $a_2 > 0$, $a_2 b_1 < 0$ and $a_2 a_3 > 0$, according to (10) the panel exhibits an immediate snap-through as soon as the temperature T_1 is reached (Fig. 1(*c*)). If $a_2 < 0$, $a_2 b_1 > 0$ and $a_2 a_3 < 0$, the panel behaves similarly (Fig. 1(*a*)).

On the other hand, if one considers buckling with formation of an even number of half-waves in the x-direction, i.e., $\delta_m = 0$, then $a_2 = 0$. Now, since $a_3 b_1 < 0$, the behavior of the panel resembles that shown in Fig. 2(*a*). In conclusion, one can expect snap-through buckling with formation of one half-wave along the x-axis since min (T_1) corresponds to $m = 1$.

In a particular case of an unstiffened panel

$$a_3 = 3\alpha^2 A_{11}/16 > 0 \quad a_2 = 0$$
$$a_1 = \alpha^2 D_{11} > 0 \quad b_1 = -n < 0 \tag{31}$$

Since $a_3 b_1 < 0$, the postbuckling behavior corresponds to Fig. 2(*a*). This is not surprising since symmetrically laminated panels are also imperfection insensitive.

Conclusions

Temperature sensitivity of reinforced and unstiffened composite cylindrical shells and plates has been discussed. Equilibrium equations for symmetrically laminated or geometrically nonlinear shells are formulated based on Love's first approximation shell theory. Post-buckling response is analyzed in the case where shell displacements are modeled by a single function of each in-surface coordinate.

Two loading scenarios are considered. In the first scenario, mechanical compressive loading is kept at a constant prebuckling level while the uniform temperature is increased steadily. In the second case, a uniform prebuckling thermal field is complemented by quasi-statically increasing mechanical compressive loading. In both cases, conditions of shell snap-through are analyzed for stiffened plates as well as for reinforced cylindrical shells and criteria for various types of behavior are established.

Cylindrical thermal buckling of a large-aspect-ratio symmetrically laminated flat panel reinforced in the direction of its short edges by closely spaced identical stiffeners is considered as an example. It is shown that such plates always exhibit snap-through as soon as a buckling temperature is reached. On the other hand, if reinforcements are absent, the plate deformations increase gradually when temperature exceeds the buckling value and no snap-through occurs.

References

Ambartsumyan, S. A., 1974, *General Theory of Anisotropic Shells*. Nauka Publishers, Moscow (in Russian).

Birman, V., 1990a, "On the Post-Buckling Behavior of Reinforced Composite Shells," *Journal of Ship Research*, Vol. 34, pp. 207–211.

Birman, V., 1990b, "Thermal Dynamic Problem of Reinforced Composite Cylinders," ASME JOURNAL OF APPLIED MECHANICS, Vol. 57, pp. 941–947.

Birman, V., 1991, "Thermal Bending of Shear Deformable Orthotropic Cylindrical Shells Reinforced by Cylindrically Orthotropic Rings," *International Journal of Solids and Structures*, Vol. 28, pp. 819–830.

Birman, V., and Bert, C. W., 1990, "Dynamic Stability of Reinforced Composite Cylindrical Shells in Thermal Fields," *Journal of Sound and Vibration*, Vol. 142, pp. 183–190.

Budiansky, B., and Hutchinson, J. W., 1964, "Dynamic Buckling of Imperfection-Sensitive Structures," *Proceedings, Eleventh International Congress of Applied Mechanics*, H. Goertler, ed., Munich, Springer-Verlag, Berlin, pp. 636–651.

Budiansky, B., 1967, "Dynamic Buckling of Elastic Structures: Criteria and Estimates," *Dynamic Stability of Structures*, G. Herrmann, ed., Pergamon Press, Oxford, pp. 83–106.

Elishakoff, I., 1980, "Remarks on the Static and Dynamic Imperfection-Sensitivity of Nonsymmetric Structures," ASME JOURNAL OF APPLIED MECHANICS, Vol. 47, pp. 111–115.

Elishakoff, I., and Arbocz, J., 1981, "Buckling of Shells with General Random Imperfections," *Stability in the Mechanics of Continua*, F. H. Schroeder, ed., Springer-Verlag, Berlin, pp. 306–317.

Hui, D., and Du, I. H. Y., 1987, "Imperfection-Sensitivity of Long Antisymmetric Cross-Ply Cylindrical Panels Under Shear Loads," ASME JOURNAL OF APPLIED MECHANICS, Vol. 54, pp. 292–298.

Hyer, M. W., and Cooper, D. E., 1986, "Stresses and Deformations in Composite Tubes Due to a Circumferential Temperature Gradient," ASME JOURNAL OF APPLIED MECHANICS, Vol. 53, pp. 757–764.

Hyer, M. W., and Rousseau, C. Q., 1987, "Thermally Induced Stresses and Deformations in Angle-Ply Composite Tubes," *Journal of Composite Materials*, Vol. 21, pp. 454–480.

Kalam, M. A., and Tauchert, T. R., 1978, "Stresses in an Orthotropic Elastic Cylinder Due to a Plane Temperature Distribution $T(r,\theta)$," *Journal of Thermal Stresses*, Vol. 1, pp. 13–24.

Kardomateas, G. A., 1989, "Transient Thermal Stresses in Cylindrically Orthotropic Composite Tubes," ASME JOURNAL OF APPLIED MECHANICS, Vol. 56, pp. 411–417.

Koiter, W. T., 1945, "On the Stability of Elastic Equilibrium," Thesis, Delft University (Dutch); English translation: NASA TT-F-10,833 (1967). NTIS Document No. N67-25033. Also: Air Force Flight Dynamics Laboratory Rept. AFFDL-TR-70-25, NTIS Document No. AD704124, Feb. 1970.

Koiter, W. T., 1967, "General Equations of Elastic Stability for Thin Shells," *Proceedings, Symposium on the Theory of Shells to Honor Lloyd Hamilton Donnell*, D. Muster, ed., University of Houston, Houston, Texas, pp. 187–227.

Roorda, J., and Hansen, J. C., 1972, "Random Buckling Behavior in Axially Loaded Cylindrical Shells with Axisymmetric Imperfection," *Journal of Spacecraft and Rockets*, Vol. 9, pp. 88–91.

Simitses, G. J., Shaw, D., and Sheinman, I., 1985, "Imperfection Sensitivity of Laminated Cylindrical Shells in Torsion and Axial Compression," *Composite Structures*, Vol. 4, pp. 335–360.

Suhir, E., and Sullivan, T. M., 1990, "Analysis of Interfacial Thermal Stresses and Adhesive Strength of Bi-Annular Cylinders," *International Journal of Solids and Structures*, Vol. 26, pp. 581–600.

Downloaded 03 May 2010 to 171.66.16.245. Redistribution subject to ASME license or copyright; see http://www.asme.org/terms/Terms_Use.cfm

Elastic Wrinkling of a Tensioned Circular Plate Using von Kármán Plate Theory

G. G. Adams
Professor,
Department of Mechanical Engineering,
Northeastern University,
Boston, MA 02115
Mem. ASME

A circular elastic plate, with a uniform tension field applied at its outer edge, is acted upon by a centrally applied transverse force. As the force is increased, the tension state as determined from von Kármán plate theory, changes. In particular for sufficiently large values of the transverse force or displacement, the plate can develop a compressive circumferential membrane stress. When this compressive stress becomes sufficiently large, wrinkling can result. The corresponding value of the transverse displacement is determined by investigating an eigenvalue problem in which wrinkling is indicated by the vanishing of the lowest eigenvalue. The results are the values of the central transverse deflection which induces wrinkling for a range of in-plane tensions and are sensitive to the in-plane boundary support conditions at the outer edge.

1 Introduction

When a very thin elastic plate is acted upon by a set of loads, the resulting stress and deformation fields are, depending on the type of loads and support conditions, often determined using membrane theory. Such calculations may show the presence of a region of negative principal stress which, for a pure membrane (i.e., no bending stiffness), is unacceptable (Steigmann, 1986). *Tension field theory* (Wagner, 1929; Reissner, 1938; Kondo, Moriguti, Muraski, 1955) is a modification of membrane theory in which the stress field is not allowed to be compressive and wrinkling is assumed to occur in the direction perpendicular to the lines of uniaxial tension. Unfortunately, the use of tension field theory is complicated by the necessity of knowing, *a priori*, which region is wrinkled and which is not. Furthermore, the solution does not indicate anything about the wrinkles themselves. The latter deficiency is due to the fact that wrinkling is controlled by bending stiffness which is completely neglected in membrane theory. Croll (1985) investigates the wrinkling of a circular elastic plate, with a compliant in-plane edge restraint, which is subjected to a uniform pressure. The plate is divided into an inner region of tensile circumferential stress and an outer annulus in which tension field theory is used. In the interior region, the von Kármám plate equations are solved using a Galerkin approximation, and is matched to the tension field of the annulus. Wrinkling of membranes using finite plane stress theory (Wu, 1981) has also been investigated. The deformation tensor was modified by introducing an extra parameter whose value is determined from the condition that the stress in the wrinkled direction is zero.

It was recently shown (Pipkin, 1986) that a *relaxed* energy density can be defined and used to replace the strain energy function in tension field theory. The solution yields the average deformation without any details of the wrinkling. Tension field theory, with the relaxed energy density, was used to determine the wrinkling of membranes (Steigmann and Pipkin, 1989a) and of pressurized membranes (Steigmann and Pipkin, 1989b).

Applications of wrinkling problems exist in a wide variety of areas including modeling in biomechanics, web rolling, drawing of sheet metal, and honeycomb, sandwich, and fabric structures. In biomechanics the tissues which connect muscles to bone are thin membrane-like structures which can wrinkle and influence the transmission of force (Roddeman et al., 1987a, b). With respect to circular geometries, the axisymmetric deep-drawing and forming processes have attracted considerable attention over the years. It is important that the flange of the workpiece yield without the onset of elastic wrinkling. Geckeler (1929) presented a simplified one-dimensional model which attempted to predict the circumferential stress and the number of wrinkle waves. Extensions to two-dimensions were made (Yu and Johnson, 1982) using the energy method and a combination of the Kantorovich and Galerkin methods (Yu and Zhang, 1986). In these analyses the applied tension field is determined from the plane stress solution and hence assumed unaffected by the transverse loading. A two-term approximation to the transverse deflection of a shallow spherical shell was used by Panov and Freodossiev (1948) in order to estimate the onset of wrinkling due to a uniform pressure.

In the current investigation, von Kármán plate theory is used in order to predict the wrinkling of a transversely loaded circular plate. The plate is subjected to an applied tension field

Contributed by the Applied Mechanics Division of THE AMERICAN SOCIETY OF MECHANICAL ENGINEERS for presentation at the First Joint ASCE-EMD, ASME-AMD, SES Meeting, Charlottesville, VA, June 6-9, 1993.

Discussion on this paper should be addressed to the Technical Editor, Professor Lewis T. Wheeler, Department of Mechanical Engineering, University of Houston, Houston, TX 77204-4792, and will be accepted until four months after final publication of the paper itself in the ASME JOURNAL OF APPLIED MECHANICS.

Manuscript received by the ASME Applied Mechanics Division, Oct. 15, 1991; final revision, June 23, 1992. Associate Technical Editor: A. K. Noor.

Paper No. 93-APM-21.

Copyright © 1993 by ASME
Downloaded 03 May 2010 to 171.66.16.245. Redistribution subject to ASME license or copyright; see http://www.asme.org/terms/Terms_Use.cfm

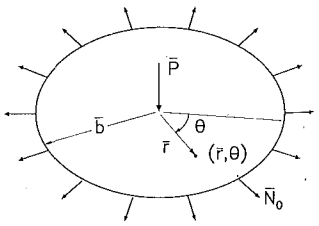


Fig. 1 A circular elastic plate under tension and acted upon by a centrally applied transverse load

and loaded by a concentrated force at its center. Thus, as the transverse load is increased, the transverse deflection causes a differential annular ring of the plate to be pulled radially inward, tending to cause compression in the circumferential direction. Depending upon the support conditions at the outer radius, a sufficiently large load can produce compressive circumferential membrane stresses which eventually give rise to wrinkling. This problem is solved by a linearization of the nonaxisymmetric equations of motion about the axisymmetric configuration. The vanishing of an eigenvalue, representing the square of the lowest natural frequency of vibration, indicates the onset of wrinkling. Results are given for a range of applied tensions and are sensitive to the in-plane boundary conditions.

2 Mathematical Model of the Membrane Plate

Consider the circular elastic plate of radius $\bar{b}$ and constant thickness $\bar{h}$ as shown in Fig. 1. The von Kármán equations of motion for the *dimensionless* radial, circumferential, and transverse components of deflection (u, v, w) are given as (Soedel, 1981)

$$\frac{\partial N_{rr}}{\partial r}+\frac{1}{r}\frac{\partial N_{r\theta}}{\partial \theta}+\frac{N_{rr}-N_{\theta\theta}}{r}=\left(\frac{\bar{h}}{\bar{b}}\right)^2\frac{\partial^2 u}{\partial t^2}, \tag{1}$$

$$\frac{\partial N_{r\theta}}{\partial r}+\frac{1}{r}\frac{\partial N_{\theta\theta}}{\partial \theta}+2\frac{N_{r\theta}}{r}=\left(\frac{\bar{h}}{\bar{b}}\right)^2\frac{\partial^2 v}{\partial t^2}, \tag{2}$$

$$q(r,\theta)+\frac{1}{r}\frac{\partial}{\partial r}\left(rN_{rr}\frac{\partial w}{\partial r}\right)+\frac{1}{r^2}\frac{\partial}{\partial \theta}\left(N_{\theta\theta}\frac{\partial w}{\partial \theta}\right)+\frac{1}{r}\frac{\partial}{\partial \theta}\left(N_{r\theta}\frac{\partial w}{\partial r}\right)+\frac{1}{r}\frac{\partial}{\partial r}\left(N_{r\theta}\frac{\partial w}{\partial \theta}\right)-\frac{1}{12}\nabla^4 w=\frac{\partial^2 w}{\partial t^2}, \tag{3}$$

where

$$r=\bar{r}/\bar{b},\ u=\bar{b}\,\bar{u}/\bar{h}^2,\ v=\bar{b}\,\bar{v}/\bar{h}^2,\ w=\bar{w}/\bar{h},$$
$$q=\bar{b}^4\bar{q}/12D\bar{h},\ D=E\bar{h}^3/12(1-\nu^2),$$
$$N_{rr}=\frac{\bar{b}^2}{12D}\bar{N}_{rr},\ N_{r\theta}=\frac{\bar{b}^2}{12D}\bar{N}_{r\theta},$$
$$N_{\theta\theta}=\frac{\bar{b}^2}{12D}\bar{N}_{\theta\theta},\ t=\frac{\bar{h}}{\bar{b}^2}\sqrt{\frac{E}{\rho(1-\nu^2)}}\,\bar{t}.$$

In (1)–(3), N_{rr}, $N_{\theta\theta}$, $N_{r\theta}$ are the dimensionless in-plane membrane forces per unit length, and $q(r,\theta)$ is the externally applied dimensionless transverse force per unit area. The corresponding dimensioned terms are indicated with the overbar symbol ($\bar{}$). The plate has an elastic Young's modulus E, Poisson's ratio ν, flexural rigidity D, and mass density ρ. Due to the $(\bar{h}/\bar{b})^2$ factors on the right-hand side of (1)–(2), the inertia effects corresponding to in-plane motion will be neglected. Also, the external loading $q(r,\theta)$ will vanish everywhere except at the center. It is then possible to rewrite (1)–(3) in a more conventional form (Mansfied, 1989).

The membrane terms are related to the displacements through

$$N_{rr}=\frac{\partial u}{\partial r}+\frac{1}{2}\left(\frac{\partial w}{\partial r}\right)^2+\nu\frac{u}{r}+\frac{\nu}{r}\frac{\partial v}{\partial \theta}+\frac{\nu}{2}\left(\frac{1}{r}\frac{\partial w}{\partial \theta}\right)^2, \tag{4}$$

$$N_{\theta\theta}=\nu\frac{\partial u}{\partial r}+\frac{\nu}{2}\left(\frac{\partial w}{\partial r}\right)^2+\frac{u}{r}+\frac{1}{r}\frac{\partial v}{\partial \theta}+\frac{1}{2}\left(\frac{1}{r}\frac{\partial w}{\partial \theta}\right)^2, \tag{5}$$

$$N_{r\theta}=\frac{(1-\nu)}{2}\left[\frac{1}{r}\frac{\partial u}{\partial \theta}+\frac{1}{r}\frac{\partial w}{\partial r}\frac{\partial w}{\partial \theta}-\frac{v}{r}+\frac{\partial v}{\partial r}\right], \tag{6}$$

and the dimensional effective transverse shear stress resultant is given by

$$V_r=-\frac{1}{12}\left[\frac{\partial^3 w}{\partial r^3}+\frac{1}{r}\frac{\partial^2 w}{\partial r^2}-\frac{1}{r^2}\frac{\partial w}{\partial r}+\frac{(2-\nu)}{r^2}\frac{\partial^3 w}{\partial r\partial\theta^2}-\frac{(3-\nu)}{r^3}\frac{\partial^2 w}{\partial\theta^2}\right]. \tag{7}$$

At the outer edge ($r=1$), the plate has an appropriate combination of boundary conditions corresponding to the requirement of two in-plane and two transverse conditions. In the transverse direction the plate may be either simply supported:

$$w(1,\theta,t)=0,$$
$$M_{rr}(1,\theta,t)=-\frac{1}{12}\left[\frac{\partial^2 w}{\partial r^2}+\frac{\nu}{r}\left(\frac{\partial w}{\partial r}+\frac{1}{r}\frac{\partial^2 w}{\partial\theta^2}\right)\right]_{r=1}=0, \tag{8}$$

or clamped:

$$w(1,\theta,t)=0,\ \frac{\partial w}{\partial r}(1,\theta,t)=0. \tag{9}$$

For the in-plane directions, either the stress resultants are prescribed:

$$N_{rr}(1,\theta,t)=N_0,\ N_{r\theta}(1,\theta,t)=0, \tag{10}$$

where N_0 is the applied uniform tension, or the displacements are known:

$$u(1,\theta,t)=N_0/(1-\nu^2),\ v(1,\theta,t)=0. \tag{11}$$

In the foregoing equation, the in-plane conditions are applied after the sheet is stretched by the applied tension N_0. It is noted that the combination of (8) and (10) is commonly known as a roller support, whereas (8) and (11) together form a pin connection. Furthermore (9) and (10) form a partial clamp, while (9) and (11) constitute a complete clamp.

3 Method of Solution

First, consider the axisymmetric form of (1)–(6) under static conditions which is valid for the *pre*wrinkled state. Setting

$$u=u(r),\ v=0,\ w=w(r), \tag{12}$$

results in considerable simplification. In particular, (2) is automatically satisfied whereas (1) and (3) yield

$$\frac{d^2u}{dr^2}+\frac{1}{r}\frac{du}{dr}-\frac{u}{r^2}=-\left[\frac{d^2w}{dr^2}+\frac{(1-\nu)}{2r}\frac{dw}{dr}\right]\frac{dw}{dr}, \tag{13}$$

and

$$\frac{d^4w}{dr^4}+f_1(r)\frac{d^3w}{dr^3}+f_2(r)\frac{d^2w}{dr^2}+f_3(r)\frac{dw}{dr}=0, \tag{14}$$

respectively, in which

$$f_1(r)=\frac{2}{r},\quad f_2(r)=-\frac{1}{r^2}-12\left[\frac{du}{dr}+\nu\frac{u}{r}+\frac{1}{2}\left(\frac{dw}{dr}\right)^2\right],$$
$$f_3(r)=-12\left[\frac{d^2u}{dr^2}+\frac{(1+\nu)}{r}\frac{du}{dr}+\frac{1}{2r}\left(\frac{dw}{dr}\right)^2+\frac{dw}{dr}\frac{d^2w}{dr^2}\right]+\frac{1}{r^3}. \tag{15}$$

The axisymmetric governing equations will eventually be cast in finite difference form. However, due to the nonlinearities, (13) was written with the nonlinear terms appearing on the right-hand side as if they were known quantities. Furthermore, the fourth-order equation (14) can be reduced to second order by introducing an auxiliary function ψ defined by

Downloaded 03 May 2010 to 171.66.16.245. Redistribution subject to ASME license or copyright; see http://www.asme.org/terms/Terms_Use.cfm

$$\psi = r\frac{dw}{dr} - 3Pr^2(1+2\ln r)/2\pi, \tag{16}$$

where P is the dimensionless concentrated force applied at the origin. In terms of ψ, (13) becomes

$$\frac{d^2\psi}{dr^2} - \frac{1}{r}\frac{d\psi}{dr} - 12N_{rr}\psi = \frac{18P}{\pi}N_{rr}r^2(1+2\ln r). \tag{17}$$

At the origin, the radial displacement vanishes, and the dimensionless effective shear stress resultant (V_r) is known in terms of the applied load P, i.e.,

$$u(0)=0,\ V_r(0) = -\frac{1}{12}\lim_{r\to 0}\left[\frac{d^3w}{dr^3}+\frac{1}{r}\frac{d^2w}{dr^2}-\frac{1}{r^2}\frac{dw}{dr}\right] = -\lim_{r\to 0}\frac{P}{2\pi r}. \tag{18}$$

It is noted that, whereas the shear and hence the third derivative of w are infinite at the origin, ψ has the singular nature of the shear built directly into (16) and (17). Hence, the transverse boundary condition at the center of the plate becomes

$$\psi(0) = 0. \tag{19}$$

At the outer radius of a clamped plate

$$\psi(1) = -3P/2\pi, \tag{20}$$

and for a simply-supported plate,

$$\left[\frac{d\psi}{dr} - (1-\nu)\psi\right]_{r=1} = -(3+\nu)\frac{3P}{2\pi}. \tag{21}$$

The second-order differential Eq. (17) requires only one condition at each end. Once ψ is determined, the transverse plate deflection can then be determined by integration of (16).

Each of the differential Eqs., (13) and (17), is replaced by a set of N algebraic equations using a three-point central finite difference scheme (Fox, 1957). This procedure yields $2N$ algebraic equations, one pair at each evenly spaced radial grid point ($r_i = i/N$, $i = 1, 2, \ldots N$), and $2N+4$ unknowns (u_i, ψ_i, $i = 0, 1, \ldots N+1$). Thus, (13) is supplemented by $(18)_1$ and either $(10)_1$ or $(11)_1$, while (17) is complemented by (19) and either (20) or (21). The resulting banded algebraic equations are nonlinear and can be solved by iteration. An initial guess is made for u_i, and the predicted value of ψ_i ($\tilde{\psi}_i$) is solved for from the solution of (17). Then $\tilde{\psi}_i$ is used in (13) in order to find the predicted value of u_i ($\tilde{u}_i$). Iteration proceeds from step k to step $k+1$ according to

$$\psi_i^{k+1} = \psi_i^k + R_\psi(\tilde{\psi}_i^{k+1} - \psi_i^k),\ u_i^{k+1} = u_i^k + R_u(\tilde{u}_i^{k+1} - u_i^k), \tag{22}$$

where R_ψ and R_u are relaxation factors. Convergence is obtained when the differences between the calculated values $\tilde{u}_i^{k+1}$, $\tilde{\psi}_i^{k+1}$ and the previous values u_i^k, ψ_i^k are sufficiently small.

Attention is now focussed on the investigation of the nonaxisymmetric problem given by (1)–(11). It is noted that, for known w, (1) and (2) are linear in u and v. Similarly, if the membrane terms N_{rr}, $N_{\theta\theta}$, $N_{r\theta}$ were prescribed, then (3) would be a linear equation for w. A solution (u, v, w) will be obtained for a small dynamic deflection *away* from the axisymmetric reference configuration using perturbation theory (Cole, 1968). First, the dimensionless displacements are replaced by perturbation expansions in ϵ as given by

$$\begin{aligned} u &= u^{(0)} + \epsilon u^{(1)} + \epsilon^2 u^{(2)} + \ldots, \\ v &= v^{(0)} + \epsilon v^{(1)} + \epsilon^2 v^{(2)} + \ldots, \\ w &= w^{(0)} + \epsilon w^{(1)} + \epsilon^2 w^{(2)} + \ldots. \end{aligned} \tag{23}$$

Substitution of (23) into (1)–(6) and the collection of terms of the same power of ϵ results in the axisymmetric configuration (12)–(14) for the zeroth order solution, while the first-order terms in ϵ yield

$$\frac{\partial N_{rr}^{(1)}}{\partial r} + \frac{1}{r}\frac{\partial N_{r\theta}^{(1)}}{\partial \theta} + \frac{N_{rr}^{(1)} - N_{\theta\theta}^{(1)}}{r} = 0, \tag{24}$$

$$\frac{\partial N_{r\theta}^{(1)}}{\partial r} + \frac{1}{r}\frac{\partial N_{\theta\theta}^{(1)}}{\partial \theta} + 2\frac{N_{r\theta}^{(1)}}{r} = 0, \tag{25}$$

$$\frac{1}{r}\frac{\partial}{\partial r}\left(rN_{rr}^{(0)}\frac{\partial w^{(1)}}{\partial r}\right) + \frac{N_{\theta\theta}^{(0)}}{r^2}\frac{\partial^2 w^{(1)}}{\partial \theta^2} + \frac{1}{r}\frac{\partial}{\partial r}\left(rN_{rr}^{(1)}\frac{dw^{(0)}}{dr}\right) + \frac{1}{r}\frac{dw^{(0)}}{dr}\frac{\partial N_{r\theta}^{(1)}}{\partial \theta} - D\nabla^4 w^{(1)} = \frac{\partial^2 w^{(1)}}{\partial t^2}. \tag{26}$$

Equations (24)–(26) are linear but coupled. The first-order changes in the in-plane tensions are related to the changes in the transverse deflections through

$$N_{rr}^{(1)} = \frac{\partial u^{(1)}}{\partial r} + \frac{dw^{(0)}}{dr}\frac{\partial w^{(1)}}{\partial r} + \nu\frac{u^{(1)}}{r} + \frac{\nu}{r}\frac{\partial v^{(1)}}{\partial \theta}, \tag{27}$$

$$N_{\theta\theta}^{(1)} = \nu\frac{\partial u^{(1)}}{\partial r} + \nu\frac{dw^{(0)}}{dr}\frac{\partial w^{(1)}}{\partial r} + \frac{u^{(1)}}{r} + \frac{1}{r}\frac{\partial v^{(1)}}{\partial \theta}, \tag{28}$$

$$N_{r\theta}^{(1)} = \frac{(1-\nu)}{2}\left[\frac{1}{r}\frac{\partial u^{(1)}}{\partial \theta} + \frac{1}{r}\frac{dw^{(0)}}{dr}\frac{\partial w^{(1)}}{\partial \theta} - \frac{v^{(1)}}{r} + \frac{\partial v^{(1)}}{\partial r}\right]. \tag{29}$$

In order to solve (24)–(29), each of $u^{(1)}$, $v^{(1)}$, $w^{(1)}$ is taken to be a harmonic function of time given by

$$u^{(1)}(r,\theta,t) = u^*(r,\theta)e^{i\omega t},\ v^{(1)}(r,\theta,t) = v^*(r,\theta)e^{i\omega t},\ w^{(1)}(r,\theta,t) = w^*(r,\theta)e^{i\omega t}, \tag{30}$$

where ω is the dimensionless natural frequency of vibration (not yet determined). The functions $u^*(r,\theta)$, $v^*(r,\theta)$, $w^*(r,\theta)$ are then represented by exponential Fourier series expansions in the circumferential direction according to

$$u^*(r,\theta) = \sum_{m=-\infty}^{\infty} U_m(r)e^{im\theta},\ v^*(r,\theta) = \sum_{m=-\infty}^{\infty} V_m(r)e^{im\theta},\ w^*(r,\theta) = \sum_{m=-\infty}^{\infty} W_m(r)e^{im\theta}, \tag{31}$$

where

$$U_m(r) = \frac{1}{2\pi}\int_0^{2\pi} u^*(r,\theta)e^{-im\theta}d\theta,\ V_m(r) = \frac{1}{2\pi}\int_0^{2\pi} v^*(r,\theta)e^{-im\theta}d\theta,$$

$$W_m(r) = \frac{1}{2\pi}\int_0^{2\pi} w^*(r,\theta)e^{-im\theta}d\theta,$$

$$m = -\infty, \ldots, -1, 0, 1, \ldots, \infty.$$

Each of the partial differential Eqs. (24)–(26), thus yields an infinite set of ordinary differential equations for the Fourier components ($U_m(r)$, $V_m(r)$, $W_m(r)$) of the displacements given by

$$A_1U_m'' + A_2U_m' + A_3U_m + A_4V_m' + A_5V_m + A_6W_m'' + A_7W_m' + A_8W_m = 0, \tag{32}$$

$$B_1U_m' + B_2U_m + B_3V_m'' + B_4V_m' + B_5V_m + B_6W_m' + B_7W_m = 0, \tag{33}$$

$$C_1U_m'' + C_2U_m' + C_3U_m + C_4V_m' + C_5V_m + C_6W_m'''' + C_7W_m''' + C_8W_m'' + C_9W_m' + C_{10}W_m = -\omega^2 W_m, \quad m = -\infty, \ldots, -1, 0, 1, \ldots, \infty. \tag{34}$$

In (32)–(34), prime ($'$) denotes differentiation with respect to r, and the coefficients are given by

$$A_1 = 1,\ A_2 = 1/r,\ A_3 = -\frac{1}{r^2}\left[1 + \frac{(1-\nu)}{2}m^2\right],$$

$$A_4 = im(1+\nu)/2r,\ A_5 = -im(3-\nu)/2r^2,\ A_6 = \frac{dw^{(0)}}{dr},$$

Downloaded 03 May 2010 to 171.66.16.245. Redistribution subject to ASME license or copyright; see http://www.asme.org/terms/Terms_Use.cfm

$$A_7=\frac{d^2w^{(0)}}{dr^2}+\frac{(1-\nu)}{r}\frac{dw^{(0)}}{dr},\ A_8=-m^2\frac{(1-\nu)}{2r^2}\frac{dw^{(0)}}{dr},\quad (35)$$

$$B_1=im\frac{(1+\nu)}{2r},\ B_2=im\frac{(3-\nu)}{2r^2},\ B_3=\frac{(1-\nu)}{2},\ B_4=\frac{(1-\nu)}{2r},$$

$$B_5=-\left[\frac{(1-\nu)}{2}+m^2\right]/r^2,\ B_6=im\frac{(1+\nu)}{2r}\frac{dw^{(0)}}{dr},$$

$$B_7=im\frac{(1-\nu)}{2r}\left[\frac{d^2w^{(0)}}{dr^2}+\frac{1}{r}\frac{dw^{(0)}}{dr}\right],\quad (36)$$

$$C_1=\frac{dw^{(0)}}{dr},\ C_2=\frac{(1+\nu)}{r}\frac{dw^{(0)}}{dr}+\frac{d^2w^{(0)}}{dr^2},\ C_4=\frac{im(1+\nu)}{2r}\frac{dw^{(0)}}{dr},$$

$$C_3=\frac{\nu}{r}\frac{d^2w^{(0)}}{dr^2}-m^2\frac{(1-\nu)}{2r^2}\frac{dw^{(0)}}{dr},$$

$$C_8=N_{rr}^{(0)}+\left(\frac{dw^{(0)}}{dr}\right)^2+\frac{(1+2m^2)}{12r^2},$$

$$C_5=im\left[\frac{\nu}{r}\frac{d^2w^{(0)}}{dr^2}-\frac{(1-\nu)}{2r}\frac{dw^{(0)}}{dr}\right],$$

$$C_6=-1/12,\ C_7=-1/6r,$$

$$C_9=\frac{N_{rr}^{(0)}}{r}+\frac{dN_{rr}^{(0)}}{dr}+2\frac{dw^{(0)}}{dr}\frac{d^2w^{(0)}}{dr^2}+\frac{1}{r}\left(\frac{dw^{(0)}}{dr}\right)^2-\frac{(1+2m^2)}{12r^3},$$

$$C_{10}=-\frac{m^2}{r^2}\left[N_{\theta\theta}^{(0)}+\frac{1(-\nu)}{2}\left(\frac{dw^{(0)}}{dr}\right)^2+\frac{(m^2-4)}{12r^2}\right].\quad (37)$$

It is emphasized that three different equations exist for each Fourier mode. Furthermore, some of the coefficients (A_i, B_i, C_i) are complex as are the Fourier coefficients. However, it can be easily shown that if the equations are written in terms of U_m, iV_m, W_m then all of the coefficients become real. This would be the equivalent of a *cosine* Fourier series for the radial and transverse deflections along with a *sine* Fourier series of the circumferential displacement. Only the nonnegative values of m need now be considered. Furthermore, it can be shown that the eigenvalue problem (32)–(34), is, with appropriate boundary conditions, self-adjoint. The procedure for demonstrating the self-adjoint property is to multiply (32)–(34) by $r\hat{U}_m(r)$, $r\hat{V}_m$, $r\hat{W}_m$, respectively, and to integrate from $r=0$ to $r=1$. The procedure is long and tedious, involving integration by parts several times (Meirovitch, 1967), and will not be shown here.

The boundary conditions for this perturbation problem are the corresponding modal finite differenced *homogeneous* versions of (8)–(11). For a transverse simple support,

$$W_m(1)=0,\ W_m''(1)+\nu W_m'(1)=0,\ m=0,\ 1,2,\ldots\infty,\quad (38)$$

while at a transverse clamp,

$$W_m(1)=0,\ W_m'(1)=0,\quad m=0,1,2,\ldots\infty,\quad (39)$$

For constrained in-plane displacements,

$$U_m(1)=0,\ V_m(1)=0,\ m=0,\ 1,2,\ldots\infty,\quad (40)$$

and for unrestrained in-plane motion,

$$U_m'(1)+\nu U_m(1)+w'(1)W_m'(1)+im\nu V_m(1)=0,$$
$$mU_m(1)+mw'(1)\ W_m(1)+iV_m(1)-iV_m'(1)=0,$$
$$m=0,1,2,\ldots\infty\quad (41)$$

The plate must be continuous at its center; hence,

$$U_m(0)=0,\ V_m(0)=0,\ W_m(0)=0,\ W_m'(0)=0,$$
$$m=2,3,4,\ldots\infty.\quad (42)$$

Note that $W_0(0)\neq 0$ and $W_1'(0)\neq 0$; these conditions are replaced by corresponding conditions on the effective shear and moment at the origin when investigating the $m=0$ and $m=1$ modes. However, $m=0$, 1 do not correspond to wrinkled solutions and so the conditions for those modes will not be recorded here.

For a given Fourier mode m, each of the ordinary differential Eq. (32)–(34), along with the appropriate boundary conditions, is converted into a set of N linear algebraic equations using a three-point approximation for $U_m(r)$ and $V_m(r)$ and a five-point finite difference approximation (Fox, 1957) for $W_m(r)$. The resulting linear algebraic equations are combined with the finite difference form of the appropriate boundary conditions. A system of $3N$ banded linear algebraic equations result, which constitute a generalized matrix eigenvalue problem for each Fourier mode, of the form

$$\mathbf{EX}=\lambda\mathbf{FX}.\quad (43)$$

In (43), $\mathbf{E}$ contains the finite difference coefficients, and

$$F_{i,j}=0,\ i\neq j\ i=1,2,\ldots 3N,\ j=1,2,\ldots 3N,$$
$$F_{3i-2,\,3i-2}=0,\ F_{3i-1,\,3i-1}=0,\ i=1,2,\ldots,N,$$
$$F_{3i,\,3i}=-1,\ i=1,2,\ldots N-1,$$
$$F_{3N,\,3N}=0,\ X_{3i-2}=U_m(r_i),\ X_{3i-1}=V_m(r_i),\ X_{3i}=W_m(r_i),$$
$$i=1,2,\ldots N.\quad (44)$$

The eigenvalue problem defined by (43) and (44) can be solved by standard methods (IMSL, 1989) for the eigenvalues (λ), which are equal to the squares of the natural frequencies of vibration (ω^2), and for the eigenvectors representing the corresponding displacement mode shapes. Although it would be possible to reduce (43) to a system of N equations by solving for $U_m(r_i)$ and $V_m(r_i)$ in terms of $W_m(r_i)$, the resulting equations would no longer be banded. Wrinkling under static conditions is manifested by the vanishing of the lowest eigenvalue in a particular Fourier mode.

4 Results and Discussion

Numerical results were obtained using the methods of the previous section. The in-plane tension was held constant while the transversely applied force was varied from zero to a large value. For each value of N_0 and P, the axisymmetric solution of (13) and (17) was determined using finite differences along with iteration as described in the previous section. It was found necessary to use at least 100 uniformly spaced radial grid points for sufficient accuracy and low values of the two relaxation factors (0.01) in order to achieve convergence. Convergence was deemed to occur when, during an iteration step k, the residuals were sufficiently small, i.e., when

$$\sum_{i=1}^{N}(\tilde{u}_i^{k+1}-u_i^k)^2<1\times 10^{-10},$$
$$\sum_{i=1}^{N}(\tilde{\psi}_i^{k+1}-\psi_i^k)^2<1\times 10^{-10}.\quad (45)$$

Computations were performed on a workstation. The initial guesses for u_i and ψ_i were chosen as the solutions to the corresponding linear problem. Convergence to the accuracy given in (45) was consistently without difficulty.

The center deflection ($w(0)$) was then determined by integration of (16) using Simpson's rule subject to the condition of vanishing displacement on the boundary, i.e., $w(1)=0$. Also calculated was the minimum membrane hoop stress ($N_{\theta\theta}$). These graphs are shown in Figs. 2 and 3, respectively, for various values of applied tension and with $\nu=0.3$. The two combinations of plate supports which lead to wrinkling were considered. First, the plate was taken to be clamped transversely and free radially, i.e., a partial clamp. Secondly, the case of a roller support (transversely simply supported but free radially) was treated. As expected, the response in Fig. 2 shows a nonlinear stiffening effect for both sets of conditions. As the applied load increases, an imaginary circumferential annulus

Downloaded 03 May 2010 to 171.66.16.245. Redistribution subject to ASME license or copyright; see http://www.asme.org/terms/Terms_Use.cfm

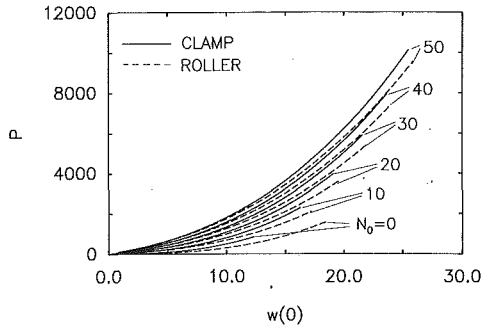


Fig. 2 Transverse load (P) versus center displacement ($w(0)$) for various values of tension (N_0) and with $\nu = 0.3$

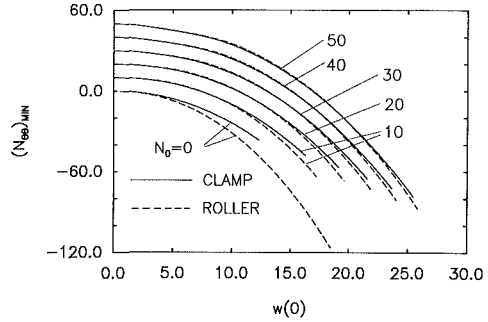


Fig. 3 Minimum circumferential membrane stress resultant ($N_{\theta\theta}$) versus center displacement ($w(0)$) for various values of tension (N_0) and with $\nu = 0.3$

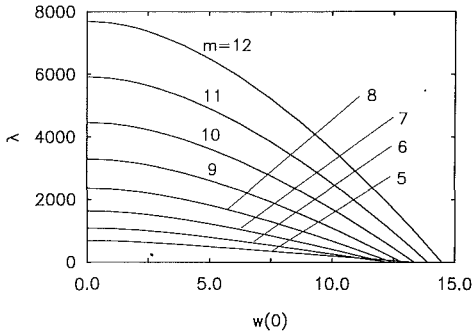


Fig. 4 Minimum eigenvalue (λ) versus center displacement ($w(0)$) for various Fourier modes m, with $N_0 = 0$, $\nu = 0.3$, and for a partial clamp

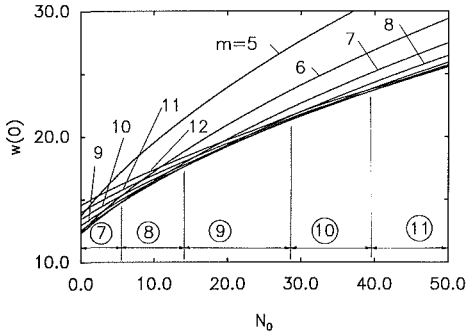


Fig. 5 Center displacement ($w(0)$) versus applied in-plane tension (N_0), corresponding to wrinkling for various Fourier modes (m), with $\nu = 0.3$, and for a partial clamp

of the plate is pulled radially inward due to the transverse displacement. This induces an increased radial stress (N_{rr}) which stiffens the plate. However, the transverse displacement also causes the annulus to undergo a negative circumferential strain. Depending on the relationship between the positive radial strain and the negative circumferential strain, the membrane hoop stress can become negative and, in fact, sufficiently compressive to induce wrinkling (buckling). The effect of the negative $N_{\theta\theta}$ depends strongly on the Fourier mode number m, whereas the effect of the positive N_{rr} does not. Figure 3 shows this phenomena which occurs for the boundary conditions of a partial clamp and for a roller. Other conditions, which involved a fixed edge, did not lead to compressive membrane hoop stresses; this was not unexpected. For large forces, the minimum membrane hoop stress occurs near the outer radius. The curves shown in Figs. 2 and 3 terminate at values of $w(0)$ for which wrinkling occurs as is discussed later. As is expected, the axisymmetric deflection shape for the partial clamp is stiffer than for the roller.

The validity of von Kármán plate theory is limited by the condition that the magnitude of the square of the slope be small compared to unity (Mansfield, 1989). Due to the nondimensional quantities used here, the moderate slope condition is satisfied if $(dw/dr)^2 \ll (\bar{b}/\bar{h})^2$. The maximum dimensionless slope for all cases shown in Fig. 2 was 49.5, which occurred just prior to wrinkling with a partial clamp and $N_0 = 50$. Thus, the von Kármán assumptions are valid provided $(\bar{b}/\bar{h})^2 \gg 2500$. The finite difference solution of (13) and (17) was checked against existing two-term approximate solutions for moderately large deflections of a circular plate with various boundary conditions (Timoshenko and Woinowsky-Krieger, 1959). The agreement between Fig. 2 and the approximate solutions was very good (within 2.5 percent) in the range for which those approximation solutions are expected to be considered valid ($\bar{w}/\bar{h} < 2$). For large values of the membrane stiffness (i.e., large N_0 or a transverse load which induces a large value of N_{rr}), the results of Fig. 2 approach the analytical solution of the pure nonlinear membrane problem (Jahsman, Field, and Holmes, 1962). In particular, for $N_0 = 50$, the partial clamp and roller solutions for the wrinkling-inducing deflections in Fig. 2 were less than those predicted by the nonlinear membrane for the same transverse force by 8.5 percent and 3.6 percent, respectively.

For each axisymmetric solution, the generalized eigenvalue problem (43) was solved for the eigenvalues and eigenvectors using standard numerical methods (IMSL, 1989). The eigenvalues and eigenvectors depend additionally on the Fourier mode number, i.e., each mode has a different result due to the appearance of the mode number m in (35)–(37). A plot of the lowest eigenvalue λ versus $w(0)$ for various mode numbers is shown in Fig. 4 for a partial clamp with $N_0 = 0$. Wah (1962) gives a closed-form solution for the natural frequencies of vibration of tensioned circular plates with clamped and pinned edges. For $w(0) \to 0$, the natural frequencies obtained here agree to within 0.07 percent of those of Wah for both the clamped and pinned cases. Although von Kármán theory has a stiffening effect on the axisymmetric deflection (Fig. 2), it is seen to have the reverse effect on the natural frequencies of the higher modes (Fig. 4). This is a consequence of the interplay between the stiffening N_{rr} and the decreased $N_{\theta\theta}$ discussed previously. Notice that it is the $m = 7$ Fourier mode for which the eigenvalue first vanishes. Since $\lambda = \omega^2$, a vanishing eigenvalue corresponds to a natural frequency of zero; this may also be viewed as a bifurcation buckling. Only the onset of wrinkling is investigated here; the post-wrinkled behavior is beyond the scope of this work.

Wrinkled solutions are shown in Fig. 5 as a plot of $w(0)$ versus N_0 for various Fourier modes, all with a partial clamp and $\nu = 0.3$. These solutions can be obtained by iterating on the eigenvalue problem until a zero eigenvalue is obtained. This is equivalent to the vanishing of the determinant of the matrix $\mathbf{E}$ in (43). Hence, from a computational point of view, it is far more efficient to calculate the determinant of $\mathbf{E}$ and iterate on the applied transverse force until the determinant is equal to zero. For a given value of N_0, many wrinkled solutions

Downloaded 03 May 2010 to 171.66.16.245. Redistribution subject to ASME license or copyright; see http://www.asme.org/terms/Terms_Use.cfm

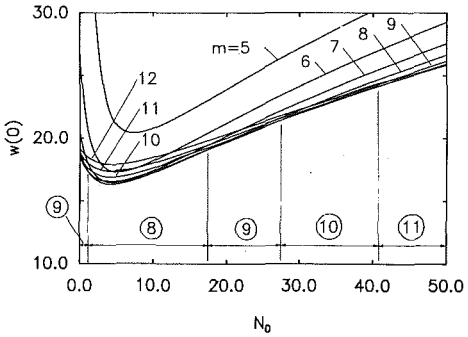


Fig. 6 Center displacement ($w(0)$) versus applied in-plane tension (N_0), corresponding to wrinkling for various Fourier modes (m), with $\nu = 0.3$, and for a roller support

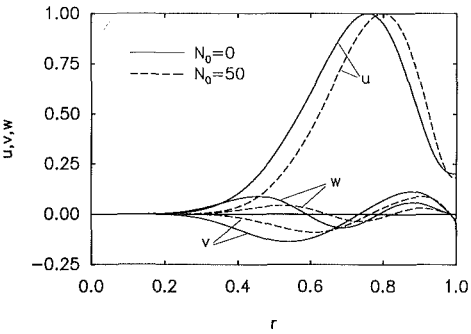


Fig. 7 Radial, circumferential, and transverse displacement eigenfunctions for two values of N_0 that correspond to the onset of wrinkling for a partial clamp support condition.

exist. It is the solution of lowest $w(0)$ which is expected to be physically attained. Hence, for $N_0 = 0$, wrinkling occurs for $m = 7$; higher values of N_0 correspond to wrinkling occurring with greater values of m. The encircled numbers in Fig. 5 correspond to the mode number which results in the minimum $w(0)$ for wrinkling in a certain range of N_0. Results for a roller support were also obtained and are shown in Fig. 6. The results were similar to those of Fig. 5 with wrinkling occurring at somewhat higher values of $w(0)$, but lower values of force P (Fig. 2). Glancing back to Fig. 3, it is noted that wrinkling with a roller support occurs at greater compressive values of $N_{\theta\theta}$. This latter effect is a result of the ability of the roller support to allow a plate rotation at the outer radius where the compressive stress is greatest. Hence the compressive $N_{\theta\theta}$ is more localized and has less of an effect on the overall plate behavior than does the partial clamp. The difference between the two support conditions becomes less significant for greater values of applied tension since at higher levels of N_0 the effect of bending stiffness is dwarfed by the membrane stiffness. In both cases the initiation of wrinkling (Fig. 3) occurred at *negative* values of the minimum value of $N_{\theta\theta}$. The load and transverse deflection which caused wrinkling were each significantly greater than their corresponding values which first produced a negative value of $N_{\theta\theta}$ (Fig. 3). This effect is accounted for here by the use von Kármán theory; it cannot be predicted using membrane theory, in which wrinkling occurs when $N_{\theta\theta} = 0$.

Figure 7 shows the eigenfunctions corresponding to the radial, circumferential, and transverse deflections for two values of N_0 which caused wrinkling (Fig. 5). It is observed that the deflections are very small near the center of the plate. Furthermore, the transverse deflection goes from positive to negative and back to positive along a given radial line. Higher values of N_0 have a tendency to shift the deflection patterns further toward the outer edge of the plate. The deflected shape in the circumferential direction, which gives the wrinkled wavelength, is governed by the Fourier mode number m.

5 Conclusions

The problem of wrinkling of a tensioned circular elastic plate has been investigated. The effect of the coupling between the transverse loading and the in-plane stress state (i.e., von Kármán plate theory) has been included. Depending upon the in-plane support conditions, the axisymmetric transverse displacements can give rise to compressive circumferential membrane stresses which become large enough to induce wrinkling of the plate. This effect cannot be predicted by linear plate theory. Furthermore, the use of a nonlinear membrane theory would give wrinkling when the circumferential stress becomes zero. The results presented in this paper demonstrate that the plate can be deflected well beyond the point of zero membrane stress before the initiation of wrinkling.

References

Cole, J. D., 1968, *Perturbation Methods in Applied Mathematics*, Blaisdell Publishing Company, Waltham, MA.

Croll, J. G. A., 1985, "A Tension Field Solution for Non-Linear Circular Plates," *Aspects of the Analysis of Plate Structures: A Volume in Honor of W. H. Wittrick*, edited by D. J. Dawe et al., eds., Oxford University Press, Oxford, pp. 309–323.

Fox, L., 1957, *Two-Point Boundary Problems in Ordinary Differential Equations*, Oxford University Press, London.

IMSL Math Library, 1989, Softcover edition 1.1, *International Mathematics and Statistical Library*, Houston, Texas.

Jahsman, W. E., Field, F. A., and Holmes, A. M. C., 1962, "Finite Deformations in a Prestressed, Centrally Loaded, Circular Elastic Membrane," *Proceedings of the Fourth U.S. National Congress of Applied Mechanics*, Vol. 1, pp. 585–594.

Kondo, K., Iai, T., Moriguti, S., and Muraski, T., 1955, "Tension Field Theory," *Memoirs of the Unifying Study of the Basic Problems in Engineering Sciences by Means of Geometry*, Vol. 1, C-V, *Gakujutsu Bunken Fukyu-Kai*, Tokyo, pp. 61–85.

Mansfield, E. H., 1989, *The Bending and Stretching of Plates*, 2nd ed., Cambridge University Press, Cambridge, U.K.

Meirovitch, L., 1967, *Analytical Methods in Vibrations*, Macmillan, London.

Panov, D. Y., and Feodossiev, V. I., 1948, "About Equilibrium and Losing Stability of Shallow Shells in the Case of Large Displacements," (in Russian), *Prikladnaia Matematikai Mekhanika*, Vol. 12, pp. 389–406.

Pipkin, A. C., 1986, "The Relaxed Energy Density for Isotropic Elastic Membranes," *IMA Journal of Applied Mathematics*, Vol. 36, pp. 85–89.

Reissner, E., 1938, "On Tension Field Theory," *Proceedings of the 5th International Congress of Applied Mechanics*, pp. 88–92.

Roddeman, D. G., Drukker, J., Oomens, C. W. J., and Janssen, J. D., 1987, "The Wrinkling of Thin Membranes: Part I—Theory," ASME JOURNAL OF APPLIED MECHANICS, Vol. 54, pp. 884–887.

Roddeman, D. G., Drukker, J., Oomens, C. W. J., and Janssen, J. D., 1987, "The Wrinkling of Thin Membranes: Part II—Numerical Analysis," ASME JOURNAL OF APPLIED MECHANICS, Vol. 54, pp. 888–892.

Soedel, W., 1981, *Vibrations of Shells and Plates*, Marcel Dekker, New York.

Steigmann, D. J., 1986, "Proof of a Conjecture in Elastic Membrane Theory," ASME JOURNAL OF APPLIED MECHANICS, Vol. 53, pp. 955–956.

Steigmann, D. J., and Pipkin, A. C., 1989, "Wrinkling of Pressurized Membranes," ASME JOURNAL OF APPLIED MECHANICS, Vol. 56, pp. 624–628.

Steigmann, D. J., and Pipkin, A. C., 1989, "Finite Deformation of Wrinkled Membranes," *Quarterly Journal of Mechanics and Applied Mathematics*, Vol. 42, pp. 427–440.

Timoshenko, S., and Woinowsky-Krieger, S., 1959, *Theory of Plates and Shells*, 2nd ed., McGraw-Hill, New York.

Wagner, H., 1929, "Flat Sheet Metal Girders With Very Thin Metal Webs," *Zeitschrift Flugtechnik u. Motorluftschiffahrt*, Vol. 20, pp. 200–314.

Wah, T., 1962, "Vibration of Circular Plates," *Journal of the Acoustical Society of America*, Vol. 34, pp. 275–281.

Yu, T. X., and Zhang, L. C., 1986, "The Elastic Wrinkling of an Annular Plate Under Uniform Tension on its Inner Edge," *International Journal of Mechanical Sciences*, Vol. 28, pp. 729–737.

Zhang, L. C., and Yu, T. X., 1988, "The Plastic Wrinkling of an Annular Plate Under Uniform Tension on its Inner Edge," *International Journal of Solids and Structures*, Vol. 24, pp. 497–503.

Zhang, L. C., and Yu, T. X., 1989, "Modified Adaptive Dynamic Relaxation Method and its Application to Elastic-Plastic Bending and Wrinkling of Circular Plates," *Computers and Structures*, Vol. 33, pp. 609–614.

Zhang, L. C., and Yu, T. X., 1989, "Investigation of Sheet Metal Forming by Bending—Part IV: Bending and Wrinkling of Circular Sheets Pressed by a Hemispherical Punch," *International Journal of Mechanical Sciences*, Vol. 31, pp. 335–348.

Downloaded 03 May 2010 to 171.66.16.245. Redistribution subject to ASME license or copyright; see http://www.asme.org/terms/Terms_Use.cfm

Post-buckling of Geometrically Imperfect Shear-Deformable Flat Panels Under Combined Thermal and Compressive Edge Loadings[1]

L. Librescu
Professor of Engineering Science and Mechanics,
Virginia Polytechnic Institute and State University,
Blacksburg, VA 24061-0219

M. A. Souza
Professor of Civil Engineering,
Pontificia Universidade Catholica do Rio de Janeiro,
Rio de Janeiro, Brazil

The static post-buckling of simply-supported flat panels exposed to a stationary nonuniform temperature field and subjected to a system of subcritical in-plane compressive edge loads is investigated. The study is performed within a refined theory of composite laminated plates incorporating the effect of transverse shear and the geometric nonlinearities. The influence played by a number of effects, among them transverse shear deformation, initial geometric imperfections, the character of the in-plane boundary conditions and thickness ratio are studied and a series of conclusions are outlined. The influence played by the complete temperature field (i.e., the uniform through thickness and thickness-wise gradient) as compared to the one induced by only the uniform one, is discussed and the peculiarities of the resulting post-buckling behaviors are enlightened.

Introduction

A great deal of interest for the analysis of laminated composite structures is being manifested in the specialized literature. This interest is mainly due to the advent of the new composite material systems exhibiting exotic properties as compared to the traditional, metallic ones. Due to their very attractive thermomechanical properties these new materials are going to play a great role in the construction of the future generations of aeronautical and aerospace vehicles as well as of turbojet engines, large space structures, nuclear reactor components, etc.

A major part of these structures are going to operate in hostile thermomechanical environments which could result in significant detrimental modifications of their response characteristics. Their design poses severe challenges to structural designers. This is especially valid for supersonic space vehicles where, as a result of aerodynamic heating, their structure is exposed to a nonuniform temperature field. Being of an equal importance to the external in-plane loads, their combined effect on the structural response has always to be incorporated. Having in view that a rational design of flight structures required an exhaustive use of their post-buckling strength, the study of this problem when considering the simultaneous action of thermal and mechanical loading becomes of an evident importance. The investigation of this problem constitutes the major goal of this paper.

In contrast to their metallic counterparts, the advanced composite material structures exhibit high flexibilities in transverse shear. This feature, considered in conjunction with the fact that the structures of flight vehicles composed of advanced composite materials are thicker than the standard metallic ones, rises some questions about the suitability of application of Kirchhoff plate model to structures exhibiting such characteristics. For these reasons, in this study a refined plate model discarding Kirchhoff's hypothesis and incorporating transverse shear effects will be used. Moreover, these new composite structures may exhibit, like the classic ones, some unavoidable initial geometric imperfections. Their presence could result in significant differences and sometimes even in drastic changes of their behavior as compared to their perfect counterparts.

Within this paper, the static post-buckling behavior of simply-supported flat panels exposed to a stationary nonuniform temperature field and subjected to a system of in-plane subcritical compressive edge loads is investigated. Particular attention is given to the effects played by transverse shear, as well as by the character of in-plane boundary conditions on the capacity of flat panels to carry compressive edge loads and resist a temperature rise. In addition, the influence played by small initial deviations from flatness on the post-buckling behavior is analyzed. It should be underlined that, in spite of its enormous practical importance, the research in this field appears to be extremely scarce, a conclusion which could be

[1]This paper represents an amended and updated version of the ones presented at "The 111th ASME Winter Annual Meeting," Dallas, TX, Nov. 1990 and "The ASME Applied Mechanics Conference," Columbus, OH, June 1991.

Contributed by the Applied Mechanics Division of THE AMERICAN SOCIETY OF MECHANICAL ENGINEERS for presentation at the First Joint ASCE-EMD, ASME-AMD, SES Meeting, Charlottesville, VA, June 6–9, 1993.

Discussion on this paper should be addressed to the Technical Editor, Professor Lewis T. Wheeler, Department of Mechanical Engineering, University of Houston, Houston, TX 77204-4792, and will be accepted until four months after final publication of the paper itself in the ASME JOURNAL OF APPLIED MECHANICS.

Manuscript received by the ASME Applied Mechanics Division, May 1, 1992; final revision, Oct. 21, 1992. Associate Technical Editor: A. K. Noor.

Paper No. 93-APM-23.

Copyright © 1993 by ASME
Downloaded 03 May 2010 to 171.66.16.245. Redistribution subject to ASME license or copyright; see http://www.asme.org/terms/Terms_Use.cfm

drawn from the monograph by Leissa (1985), the recent survey paper by Tauchert (1991) and the most comprehensive review paper by Noor and Burton (1992a).

With the exception of the papers by Noor and Burton (1991) and Noor et al. (1992b), to the best of our knowledge, this problem was approached only within the classical Kirchhoff constraints (see, e.g., Prabhu and Durvasula (1976), Huang and Tauchert (1988a,b), Chen and Chen (1989), Myers and Hyer (1991, 1992)).

Although the numerical results displayed here concern the case of single-layered plates, for the sake of generality, the equations are derived for a symmetrically laminated composite.

General Considerations

The case of a flat plate of uniform thickness H, symmetrically laminated of $2m+1$ ($m=1,2,\ldots$) elastic transversely isotropic layers is considered. It is assumed that the planes of isotropy of each material layer are parallel at each point to the reference plane of the composite panel (selected to coincide with the midplane of the midlayer). One of the materials exhibiting transverse isotropy properties both in elastic constants and thermal (expansion and conductivity) coefficients is the pyrolitic graphite. Due to its special properties (see, e.g., Terner (1962), Garber (1963), and Vinson and Chou (1974)), this material is specifically suited for the thermal protection of aerospace vehicles and is used in the design of missile and reentry vehicle structures. This material (as well as the new products of alloys of pyrolitic graphite) is characterized by a negative in-plane Poisson's ratio, ν, and a large flexibility in transverse shear (manifested by large ratios of E/G' where E and G' denote the in-plane Young's modulus and transverse shear modulus, respectively). Moreover, the ratio $15 \leq \alpha'/\alpha \leq 60$ is also characteristic to the material where α, (α') denote the thermal expansion coefficients in the plane of isotropy (and in the plane normal to the isotropy plane), respectively (see Terner, 1962). It is also supposed that the layers are in perfect bond, implying that no slip between two contiguous layers may occur.

The points of the three-dimensional space of the plate are referred to a set of rectangular Cartesian normal system of coordinates x_i, where x_α, ($\alpha=1,2$) and x_3 denote the in-plane coordinates, and the normal one to the plane $x_3=0$ (defining the reference plane), respectively. For this case, the following relations for the components of the metric tensor hold valid

$$g_{\alpha\beta}=a_{\alpha\beta}\equiv\delta_{\alpha\beta};\quad g_{\alpha 3}=0;\quad g_{33}=1, \tag{1}$$

where g_{ij}, $a_{\alpha\beta}$, and $\delta_{\alpha\beta}$ denote the components of the spatial and surface metric tensors, and of the Kronecker delta, respectively. Partial differentiation (coinciding in this system of coordinates with the covariant one) will be denoted by a comma $(\ )_{,i}\equiv\partial(\ )/\partial x_i$. Throughout the paper, unless otherwise stated, Einstein's summation convention associated with any repeated index will be used with Latin indices ranging from 1 to 3 and Greek indices ranging from 1 to 2. An index in the brackets "$\langle\ \rangle$" associated with a field quantity identifies its affiliation to the layer of the laminate indicated by that index.

Displacement Representation and Strain Measures

The results obtained, e.g., by Librescu and Stein (1991) and Noor and Burton (1989, 1991) reveal that, especially in problems involving global responses, the first-order transverse shear deformation (FSDT) provides results in excellent agreement to the ones obtained via higher order theories. This is the reason why in the forthcoming development, the geometrically nonlinear theory of imperfect flat composite panels is modeled within the framework of the FSDT. As a result, the three-dimensional displacement field will be represented as

$$V_\alpha(x_\omega, x_3)=v_\alpha+x_3\psi_\alpha,$$
$$V_3(x_\omega, x_3)=v_3, \tag{2}$$

where $v_\alpha\equiv v_\alpha(x_\omega)$, $v_3\equiv v_3(x_\omega)$ and $\psi_\alpha(x_\omega)$ denote the in-plane, transversal, and the angles of rotation of the normal to the midplane, respectively. It is also assumed that the midplane of the unloaded and unheated panel exhibits an initial, out-of-plane stress-free geometrical deviation $\overset{\circ}{v}_3\equiv\overset{\circ}{v}_3(x_\omega)$ from the x_1x_2 plane. By convention, the transverse deflection $v_3(x_\omega)$ is measured from the imperfect surface.

Within the framework of the Lagrangian formulation and in spirit of the von Kármán's concept (implying the small strains and moderately small rotations approximation), the strain tensor e_{ij} assumes the form

$$2e_{ij}=V_{i,j}+V_{j,i}+V_{3,i}V_{3,j}. \tag{3}$$

Consideration of (2) into (3) and incorporation of the stress-free geometric imperfection $\overset{\circ}{v}_3$ results in the expressions for the three-dimensional strain components,

$$e_{\alpha\beta}=\epsilon_{\alpha\beta}+x_3\kappa_{\alpha\beta},\quad e_{\alpha 3}=\epsilon_{\alpha 3},\quad e_{33}=0. \tag{4}$$

In Eqs. (4) the two-dimensional strain measures assume the form

$$2\epsilon_{\alpha\beta}=v_{\alpha,\beta}+v_{\beta,\alpha}+v_{3,\alpha}\overset{\circ}{v}_{3,\beta}+\overset{\circ}{v}_{3,\alpha}v_{3,\beta}+v_{3,\alpha}v_{3,\beta}, \tag{5a}$$
$$2\kappa_{\alpha\beta}=\psi_{\alpha,\beta}+\psi_{\beta,\alpha},\quad 2\epsilon_{\alpha 3}=\psi_\alpha+v_{3,\alpha}. \tag{5b,c}$$

Within the classical Kirchhoff plate model, $\psi_\alpha=-v_{3,\alpha}$.

The Equations of Equilibrium

The two-dimensional equations of equilibrium of flat composite panels are obtained by taking the nth moments ($n=0,1$) of the equations of equilibrium of the three-dimensional geometrically nonlinear elasticity theory in Lagrangian description (see Librescu, 1975)

$$[s_{ij}(\delta_{jr}+V_{j,r})]_{,i}=0, \tag{6}$$

where s_{ij} denotes the second Piola-Kirchhoff stress tensor. Incorporation in (6) of the effect of geometric imperfection and consistent with von Kármán's concept, the following equations of two-dimensional equilibrium of a plate element are obtained:

$$L_{\alpha\beta,\beta}=0, \tag{7a}$$
$$L_{\alpha\beta}(v_{3,\beta}+\overset{\circ}{v}_{3,\beta})_{,\alpha}+Q_{\alpha,\alpha}+p_3=0, \tag{7b}$$
$$M_{\alpha\beta,\beta}-Q_\alpha=0. \tag{7c}$$

Here, $L_{\alpha\beta}$, $M_{\alpha\beta}$, and Q_α denote the stress-resultant, stress couple and transverse-shear stress resultants, respectively.

Constitutive Equations

In the absence of stresses in the undeformed body, the stress-strain-temperature relationship for an elastic anisotropy three-dimensional medium can be expressed as

$$s_{\alpha\beta}=\tilde{E}_{\alpha\beta\omega\rho}e_{\omega\rho}+\tilde{\lambda}_{\alpha\beta}T, \tag{8}$$
$$s_{\alpha 3}=2E_{\alpha 3\omega 3}e_{\omega 3}. \tag{9}$$

In the case of a transversely isotropic body (the planes of isotropy being parallel to the midplane $x_3=0$) (see Librescu, 1975):

$$\tilde{E}_{\alpha\beta\omega\zeta}=\frac{E}{1+\nu}\left[\frac{1}{2}\,(a_{\alpha\omega}a_{\beta\zeta}+a_{\alpha\zeta}\,a_{\beta\omega})+\frac{\nu}{1-\nu}\,a_{\omega\zeta}a_{\alpha\beta}\right], \tag{10a}$$
$$E_{\alpha 3\omega 3}=G'a_{\alpha\omega}, \tag{10b}$$
$$\tilde{\lambda}_{\alpha\beta}=\tilde{\lambda}a_{\alpha\beta}, \tag{10c}$$

while

$$\tilde{\lambda}=A\lambda,\ \text{where}\ A=1-\frac{E\nu'}{E'(1-\nu)}\,\frac{\lambda'}{\lambda}. \tag{10d,e}$$

Downloaded 03 May 2010 to 171.66.16.245. Redistribution subject to ASME license or copyright; see http://www.asme.org/terms/Terms_Use.cfm

Here E, ν, $G(\equiv E/2(1+\nu))$, λ and E', ν', G', λ' denote Young's modulus, Poisson's ratio, shear modulus, and the thermal expansion coefficient in the plane of isotropy and perpendicular to the isotropy plane, respectively. $T(\equiv T(x_\omega,x_3))$ denotes the temperature rise above the one associated to the unstrained state. In this analysis a linear variation of T across the plate thickness is postulated:

$$T(x_\omega,x_3)=\overset{\circ}{T}(x_\omega)+x_3\overset{1}{T}(x_\omega) \tag{11a}$$

where

$$\overset{\circ}{T}(\equiv(T_u+T_b)/2) \text{ and } \overset{1}{T}(\equiv(T_u-T_b)/H) \tag{11b}$$

denote the uniform through thickness (the membrane) and thickness-wise temperature gradient, respectively, while

$$T_u(\equiv T|_{x_3=H/2}) \text{ and } T_b(\equiv T|_{x_3=-H/2}) \tag{11c}$$

denote the temperatures at the upper and bottom bounding planes of the panel, respectively. At this point, it should be remarked that specific of fiber-reinforced materials, in general, and to pyrolitic-graphite ones, in particular, the coefficient A (Eq. (10e)) could be a positive (close to zero) or a negative valued quantity, while for the standard metallic materials the coefficient $A(\equiv(1-2\nu)/1-\nu)$ could be only a positive valued quantity smaller than unity. This trend has strong implications for the thermal post-buckling behavior of flat structures. Another remark concerns the fact that in the thermoelastic constitutive equations, the transverse normal Young's modulus E' enters into play even within the FSDT considered herein. Since $E/E'>1$, this ratio will exert a notable influence on thermal post-buckling.

Postulating the independence of the material properties upon the temperature field, and using the expressions of stress resultants and stress couples in conjunction with Eqs. (8), (9), (10), (4), and (5), the following two-dimensional constitutive equations are obtained:

$$L_{\alpha\beta}=\frac{1}{2}\mathfrak{C}_{\alpha\beta\omega\zeta}(v_{\omega,\zeta}+v_{\zeta,\omega}+v_{3,\omega}v_{3,\zeta}+\overset{\circ}{v}_{3,\omega}v_{3,\zeta}+v_{3,\omega}\overset{\circ}{v}_{3,\zeta})+\Lambda_{\alpha\beta}\overset{\circ}{T}, \tag{12a}$$

$$M_{\alpha\beta}=\frac{1}{2}\mathfrak{D}_{\alpha\beta\omega\zeta}(\psi_{\omega,\zeta}+\psi_{\zeta,\omega})+\Pi_{\alpha\beta}\overset{1}{T}, \tag{12b}$$

$$Q_\alpha=\mathfrak{R}_{\alpha3\omega3}(\psi_\omega+v_{3,\omega}). \tag{12c}$$

In Eqs. (12), $\mathfrak{C}_{\alpha\beta\omega\zeta}$, $\mathfrak{D}_{\alpha\beta\omega\zeta}$, and $\mathfrak{R}_{\alpha3\omega3}$ denote the stretching, bending, and transverse shear mechanical stiffness tensors, respectively, while $\Lambda_{\alpha\beta}$ and $\Pi_{\alpha\beta}$ denote the thermal stretching and bending stiffness tensors, respectively. Here, only the expressions of $\Lambda_{\alpha\beta}$ and $\Pi_{\alpha\beta}$ will be displayed. These are:

$$\Lambda_{\alpha\beta}=2\left[{}_{\langle m+1\rangle}\tilde{\lambda}_{\alpha\beta}h_{\langle m+1\rangle}+\sum_{r=1}^{m}{}_{\langle r\rangle}\tilde{\lambda}_{\alpha\beta}(h_{\langle r\rangle}-h_{\langle r+1\rangle})\right], \tag{13a}$$

$$\Pi_{\alpha\beta}=\frac{2}{3}\left[{}_{\langle m+1\rangle}\tilde{\lambda}_{\alpha\beta}h^3_{\langle m+1\rangle}+\sum_{r=1}^{m}{}_{\langle r\rangle}\tilde{\lambda}_{\alpha\beta}(h^3_{\langle r\rangle}-h^3_{\langle r-1\rangle})\right]. \tag{13b}$$

The remaining ones could be found in Librescu and Souza (1991), p. 309.

For a single-layered plate $\sum_{r=1}^{m}(\bullet)\to 0$ and $h_{\langle m+1\rangle}\to h/2$.

It should be mentioned that the constitutive Eqs. (12) are general, in the sense that they are valid for monoclinic, orthotropic, and transversely isotropic-type materials.

The Governing System

A mixed formulation of the governing equations of geometrically nonlinear imperfect composite flat panels will be given. This formulation represents a generalization to the thermoelastic shear-deformable imperfect composite plates of von Kármán's classical equations. The necessary steps are as follows:

(1) Expression of stress-resultant $L_{\alpha\beta}$ in terms of in-plane strains $\epsilon_{\alpha\beta}$ and the temperature $\overset{\circ}{T}$. For transversely isotropic materials, the relationship is

$$L_{\alpha\beta}=b\epsilon_{\alpha\beta}+c\delta_{\alpha\beta}\epsilon_{\omega\omega}+\Lambda\delta_{\alpha\beta}\overset{\circ}{T}, \tag{14a}$$

while its inverted counterpart is

$$\epsilon_{\alpha\beta}=\tilde{b}L_{\alpha\beta}+\tilde{c}\delta_{\alpha\beta}L_{\omega\omega}+\tilde{\Lambda}\delta_{\alpha\beta}\overset{\circ}{T}. \tag{14b}$$

The coefficients b, c, Λ and their tilded counterparts could be found in the Appendix of the paper by Librescu and Souza (1991).

(2) Representation of the stress resultants $L_{\alpha\beta}$ in terms of the Airy stress function $F(\equiv F(x_\omega))$. This representation allowing ones to satisfy identically Eq. (7a) is

$$L_{\alpha\beta}=c_{\alpha\lambda}c_{\beta\omega}F_{,\lambda\omega}, \tag{15}$$

where $c_{\alpha\beta}$ denotes the permutation symbol.

(3) Deduction of the compatibility equation (CE). To this end elimination of v_α in the Eq. (5a) yields the CE:

$$c_{\alpha\pi}c_{\beta\lambda}\left[\epsilon_{\alpha\beta,\pi\lambda}+\frac{1}{2}v_{3,\alpha\beta}v_{3,\pi\lambda}+\frac{1}{2}\overset{\circ}{v}_{3,\pi\lambda}v_{3,\alpha\beta}+\frac{1}{2}v_{3,\pi\lambda}\overset{\circ}{v}_{3,\alpha\beta}\right]=0. \tag{16}$$

(4) Substitution of Eqs. (12) (specialized for transversely isotropic materials) in Eqs. (7b,c) and (16) considered in conjunction with Eqs. (13)–(15). This yields the following system of partial differential equations in terms of the unknown functions F, v_3, and ψ_α:

$$c_{\alpha\beta}c_{\beta\mu}F_{,\lambda\mu}(v_{3,\alpha\beta}+\overset{\circ}{v}_{3,\alpha\beta})+S(\psi_{\omega,\omega}+v_{3,\omega\omega})+p_3=0, \tag{17a}$$

$$B\psi_{\omega,\omega\alpha}+C\psi_{\alpha,\omega\omega}-S(\psi_\alpha+v_{3,\alpha})+\Pi\overset{1}{T}_{,\alpha}=0, \tag{17b}$$

$$(\tilde{b}+\tilde{c})F_{,\lambda\lambda\omega\omega}+\frac{1}{2}(v_{3,\lambda\lambda}v_{3,\zeta\zeta}-v_{3,\lambda\zeta}v_{3,\lambda\zeta})+(\overset{\circ}{v}_{3,\lambda\lambda}v_{3,\zeta\zeta}-\overset{\circ}{v}_{3,\lambda\zeta}v_{3,\lambda\zeta})+\tilde{\Lambda}\overset{\circ}{T}_{,\lambda\lambda}=0. \tag{17c}$$

In these equations the operators $(\bullet)_{,\lambda\lambda}(\equiv\nabla^2(\bullet)=\Delta(\bullet))$ and $(\bullet)_{,\lambda\lambda\omega\omega}(\equiv\nabla^2\nabla^2(\bullet))$ denote Laplace and biharmonic operators, respectively, the rigidity quantities, B, C, S are defined in the paper by Librescu and Souza (1991), while Π can be obtained by comparing Eqs. (13b) with (10c).

(5) The final step enabling one to recast the problem to a form which can be viewed as a generalization of von Kármán classical large deflection plate theory consists of expressing ψ_α in Eq. (17a,b) in terms of a potential function $\phi(\equiv\phi(x_\omega))$, as

$$\psi_\alpha=-\frac{B+C}{S}v_{3,\omega\omega\alpha}+\frac{1}{S}c_{\alpha\mu}\phi_{,\mu}-v_{3,\alpha}-\frac{B+C}{S^2}p_{3,\alpha}-\frac{B+C}{S^2}[L_{\omega\rho}(v_{3,\omega\rho}+\overset{\circ}{v}_{3,\omega\rho})]_{,\alpha}+\frac{\Pi}{S}\overset{1}{T}_{,\alpha}. \tag{18}$$

Substitution of (18) into Eqs (17a, b) yields

$$D\nabla^4v_3-c_{\alpha\lambda}c_{\beta\omega}F_{,\lambda\omega}(v_{3,\alpha\beta}+\overset{\circ}{v}_{3,\alpha\beta})+\frac{B+C}{S}c_{\alpha\lambda}c_{\beta\omega}\nabla^2[F_{,\lambda\omega}(v_{3,\alpha\beta}+\overset{\circ}{v}_{3,\alpha\beta})]-p_3+\frac{B+C}{S}\nabla^2p_3-\Pi\nabla^2\overset{1}{T}=0, \tag{19}$$

and

$$\phi-\frac{C}{S}\Delta\phi=0. \tag{20}$$

As concerns Eq. (17c), it is part of the governing system. Under a more condensed form it is written as

Downloaded 03 May 2010 to 171.66.16.245. Redistribution subject to ASME license or copyright; see http://www.asme.org/terms/Terms_Use.cfm

$$(\tilde{b}+\tilde{c})\nabla^4 F+(v_{3,11}v_{3,22}-(v_{3,12})^2 + v_{3,11}\overset{\circ}{v}_{3,22}+v_{3,22}\overset{\circ}{v}_{3,11}-2\overset{\circ}{v}_{3,12}v_{3,12})+\tilde{\Lambda}\nabla^2\overset{\circ}{T}=0. \quad (21)$$

In Eq. (20), D stands for the bending rigidity of the plate.

Equations (19)–(21) constitute the thermoelastic shear deformable counterpart of the classical von Kármán, large deflection plate theory. Special forms of these equations can be found in Librescu (1975), Librescu and Stein (1991), and Reissner (1985, 1986). It may easily be seen that for $G_{\langle k\rangle}\to\infty$ (yielding $S\to\infty$) and for the geometrically perfect case Eqs. (20)–(22) reduce to the familiar von Kármán equations.

It should be remarked that Eq. (20) (of a Helmholtz-type), whose solution has the character of a boundary layer solution), is not coupled with the remaining two governing equations (i.e., Eqs. (19) and (21)). However, as it could easily be inferred, the function ϕ intervenes in a coupled form in the boundary conditions.

Furthermore, for simply-supported boundary conditions, it could be shown (see the results of Pelech (1978) obtained in a special case and the ones by Librescu and Stein (1988, 1991) obtained in a more general framework) that the function ϕ could be decoupled in the boundary condition (BCs) to result as

$$\partial\phi/\partial\nu=0, \quad (22)$$

at a boundary whose outward normal to the contour is $\nu=\nu\mathbf{e}_\nu$. Since the governing equation for ϕ is homogeneous, Eq. (20), in conjunction with BC (22), yields the zero solution ($\phi=0$) throughout the domain of the plate. In such a case, Eq. (20) could exactly be discarded and consequently the governing system reduces to Eqs. (19) and (21). This entails a reduction of the order of governing equations from ten to eight and, as a result, the number of BCs reduces from five to four. For the case of plates (and shells), the BCs have been displayed in Librescu and Stein (1991), and Librescu and Chang (1992), respectively. When the thickness-wise temperature distribution $\overset{1}{T}$ is only considered, in light of Eq. (19), the thermal post-buckling problem can be reduced formally to the case of the purely mechanical one under the equivalent pressure distribution

$$\tilde{p}_3(x_1,x_2)=p_3-\frac{B+C}{S}\nabla^2 p_3+\Pi\nabla^2\overset{1}{T}. \quad (23)$$

Such an approach of the thermal post-buckling was dealt with by Libove and Tong (1963).

Thermal Post-Buckling of Compressed Rectangular Imperfect Shear-Deformable Panels

The previously obtained equations will be used to study the thermal post-buckling of simply-supported (SS) composite rectangular ($l_1\times l_2$) flat panels. The in-plane rectangular axes x_α are selected to coincide with the panel edges. We assume that the panel is subjected to a system of uniform in-plane biaxial compressive edge loads $\tilde{L}_1$ and $\tilde{L}_2$ and that during the post-buckling process no delamination may occur. Within this problem the terms associated with the transversal load p_3, should be discarded. Depending upon the in-plane behavior at the edges, two cases, labeled as the Case FM and the Case IM will be considered:

Case FM: The edges are SS and freely movable (in the in-plane direction). In addition, the panel is subjected to biaxial compressive edge loads $\tilde{L}_1$ and $\tilde{L}_2$.

Case IM: The edges are SS. Uniaxial compressive edge loads are applied in the direction of the x_1-coordinate. The edges $x_1=0,l_1$ are considered freely movable (in the in-plane direction), the remaining two edges being unloaded and restrained against expansion in the x_2-direction (immovable).

For both cases the associated boundary conditions could be found in Librescu and Stein (1992) and Librescu and Chang (1992).

Post-Buckling Approach. Expressing

$$(v_3,\overset{\circ}{v}_3)=(f_{mn},\overset{\circ}{f}_{mn})\sin\lambda_m x_1\sin\mu_n x_2, \quad (\lambda_m\equiv m\pi/l_1;\ \mu_n=n\pi/l_2), \quad (24)$$

(where the shape of geometric imperfection is similar to the one of the buckling mode) and $\overset{1}{T}$ in the form given by Eq. (25), the out-of-plane BCs are identically satisfied. The temperature field will be represented as

$$\begin{Bmatrix}\overset{\circ}{T}(x_1,x_2)\\ \overset{1}{T}(x_1,x_2)\end{Bmatrix}=\sum_{m,n}\begin{Bmatrix}\overset{\circ}{T}_{mn}\\ \overset{1}{T}_{mn}\end{Bmatrix}\sin\lambda_m x_1\sin\mu_n x_2. \quad (25)$$

The in-plane BCs will be satisfied on an average. To this end, function F is represented as

$$F(x_1,x_2)=F_1(x_1,x_2)-\frac{1}{2}\left((x_2)^2\tilde{L}_1+(x_1)^2\tilde{L}_2\right). \quad (26)$$

Here, $F_1(x_1,x_2)$ is a particular solution of Eq. (21), (determined in conjunction with Eq. (24)), while $\tilde{L}_1$ and $\tilde{L}_2$ denote the in-plane normal edge loads (considered positive in compression). Upon imposing the conditions which concern the function F_1 (see Librescu and Stein (1990), $\tilde{L}_1$ and $\tilde{L}_2$ acquire the meaning of *average* in-plane normal edge loads. As concerns Case IM, the condition for the immovable edges $x_2=0$, l_2 may be expressed, on an average sense as (Librescu, 1975)

$$\int_0^{l_1}\int_0^{l_2} v_{2,2}dx_1dx_2=0. \quad (27)$$

By virtue of (5*a*), and (14), the condition (27) assumes the form

$$\int_0^{l_1}\int_0^{l_2}\left[(\tilde{b}+\tilde{c})F_{,11}+\tilde{c}F_{,22}-\frac{1}{2}(v_{3,2})^2-v_{3,2}\overset{\circ}{v}_{3,2}-\frac{\Lambda}{b+2c}\overset{\circ}{T}\right]dx_1dx_2=0. \quad (28)$$

The particular solution $F_1(x_1,x_2)$ is easily determinable in the form

$$F_1(x_1,x_2)=A_1\cos 2\lambda_m x_1+A_2\cos 2\mu_n x_2+\sum_{p,q}D_{pq}\sin\lambda_p x_1\sin\mu_q x_2, \quad (29)$$

where

$$A_1=\frac{f_{mn}^2+2f_{mn}\overset{\circ}{f}_{mn}}{32(\tilde{b}+\tilde{c})}\frac{\mu_n^2}{\lambda_m^2};\quad A_2=A_1\lambda_m^4/\mu_n^4$$
$$D_{pq}=-\frac{\Lambda}{(b+2c)(\tilde{b}+\tilde{c})}\frac{\overset{\circ}{T}_{pq}}{\lambda_p^2+\mu_q^2}\qquad \sum_{m,n} \quad (30)$$

while $\sum_{m,n}$ indicates that in the equations accompanied by this sign there is no summation with respect to the indices m and n. The final step consists of application of Galerkin's method to the Eq. (20). This yields the equation governing the thermal post-buckling of composite shear deformable panels subjected to biaxial compressive in-plane edge loads. The obtained equation which is very long and tedious is not displayed here. It is used to determine the dependence of the in-plane compressive edge loads versus total transverse displacement (for given temperature rise) and conversely, the variation of the temperature rise vs. total transverse displacement (for given compressive edge load).

In the case of the immovable edges $x_2=0,l_2$, employment of Eqs. (24)–(26) in Eq. (28) yields

Downloaded 03 May 2010 to 171.66.16.245. Redistribution subject to ASME license or copyright; see http://www.asme.org/terms/Terms_Use.cfm

$$\tilde{\tilde{L}}_2 = -\frac{\tilde{c}}{\tilde{b}+\tilde{c}}\left[\tilde{\tilde{L}}_1 + \frac{1}{8\tilde{c}}\frac{n^2\phi^2}{D}f_{mn}^2 + \frac{1}{4\tilde{c}}\frac{n^2\phi^2}{D}f_{mn}\overset{\circ}{f}_{mn}\right]$$
$$+\frac{4\Lambda\phi\overset{\circ}{T}_{mn}}{\pi^2 D(\tilde{b}+\tilde{c})(b+2c)(\lambda_m^2+\mu_n^2)}\left[\frac{\lambda_m}{\mu_n}+\frac{\tilde{c}}{\tilde{b}+\tilde{c}}\frac{\mu_n}{\lambda_m}\right]\delta_{n,2r-1}^{m,2p-1},$$
$$+\frac{4\phi}{\pi^2}\frac{\tilde{\Lambda}}{D(\tilde{b}+\tilde{c})}\sum_{m,n}\frac{1}{\mu_n\lambda_m}\overset{\circ}{T}_{mn}\delta_{n,2r-1}^{m,2p-1}. \quad (31)$$

$\tilde{\tilde{L}}_2$ given by Eq. (31) represents the nondimensional fictitious compressive edge load rendering the edges $x_2 = 0, l_2$ immovable. By such a procedure, the Case IM was reduced formally to a biaxially applied edge load case where $\tilde{\tilde{L}}_2$ is prescribed by Eq. (31). Here the newly introduced notations are

$$\{\tilde{\tilde{L}}_1, \tilde{\tilde{L}}_2\} \equiv \{(\tilde{L}_1, \tilde{L}_2)l_1^2/\pi^2 D\};$$
$$\delta_{n,2r-1}^{m,2p-1} = \begin{matrix}1 \text{ when } m=2p-1 \text{ and } n=2r-1\\ 0 \text{ otherwise.}\end{matrix} \quad (32)$$

In order to establish the relationship between the average applied compressive load and the average end-shortening for given temperature rise or the relationship between the temperature rise and the end shortening (for given compressive loads), we define

$$\Delta_1 = -\frac{1}{l_1 l_2}\int_0^{l_1}\int_0^{l_2} u_{1,1}dx_1 dx_2, \quad (33)$$

as the nondimensional average end-shortening in the x_1-direction. Adequate employment in Eq. (33) of Eqs. (14), (15), (26), and (29), yields

$$\Delta_1 = (\tilde{b}+\tilde{c})\tilde{L}_1 + c\tilde{L}_2 + \frac{4D_{mn}}{l_1 l_2}\left[(\tilde{b}+\tilde{c})\frac{\mu_n}{\lambda_m}+\tilde{c}\frac{\lambda_m}{\mu_n}\right]\delta_{n,2r-1}^{m,2p-1}$$
$$+\frac{1}{8}f_{mn}^2\lambda_m^2 + \frac{1}{4}f_{mn}\overset{\circ}{f}_{mn}\lambda_m^2 - \frac{4}{l_1 l_2}\tilde{\Lambda}\sum_{m,n}\frac{\overset{\circ}{T}_{mn}}{\lambda_m\mu_n}\delta_{n,2p-1}^{m,2r-1}. \quad (34)$$

In order to be able to use Eq. (34) for compressive load (or temperature rise) versus end-shortening representation, further information from the previously obtained equation, expressing the dependence load (or temperature) versus total transverse displacement should be implemented.

Numerical Illustrations

Keeping in mind that one-term approximation in the representation of v_3 yields the most critical conditions (see, e.g., Huang and Tauchert, 1988b), this case will be considered here. As a result, the numerical illustrations concern the case of single-layered square ($l_1/l_2 = 1$) flat plates and are related to the mode (1,1) of the plate bending. The initial imperfection and the temperatures $\overset{\circ}{T}$ and $\overset{1}{T}$, (i.e., the uniform through the thickness and the thickness-wise temperature gradient) are considered in the shape of mode (1,1).

In the following, for the sake of simplification, δ_{11}, $\overset{\circ}{\delta}_{11}$, $\overset{1}{T}_{11}$, and $\overset{\circ}{T}_{11}$ will be denoted as δ, $\overset{\circ}{\delta}$, $\overset{\circ}{T}$, and $\overset{1}{T}$, respectively.

For further use we record also the equation

$$\overset{1}{HT} = 2(\overset{\circ}{T} - T_b) \quad (35)$$

obtained from Eq. (11b), which reveals that $\overset{1}{HT} \geq 0$ for $\overset{\circ}{T} \geq T_b$.

Figures (1a,b) display in the plane $(\overset{\circ}{T},\delta)$ in the absence of compressive edge loads, the thermal post-buckling behavior of geometrically perfect square panels of different thickness ratios. The cases where the temperature rise is due to $\overset{\circ}{T}$ only, and to both $\overset{\circ}{T}$ and $\overset{1}{HT}$, are considered on the same graphs and identified as Case Z and N, respectively. Within these two graphs the results correspond to Case FM and IM, respectively.

Figures 2(a) and 2(b) depict in the plane $(\overset{\circ}{T}, \delta+\overset{\circ}{\delta})$ the post-buckling response of geometrically perfect and imperfect panels for the cases labelled above as Z and N. Since the ratio E/E' intervenes in the expression of $\tilde{\Lambda}$, (Eqs. (10d,e)), in Fig. 3(b) its influence in conjunction with the effect of the compressive edge load $\tilde{\tilde{L}}_1$, was considered.

In Fig. 4, the post-buckling response of square panels exhibiting movable and immovable in-plane edge conditions (according to the cases FM and IM), subjected to the edge load $\tilde{\tilde{L}}_1 = 1$ and to the temperature rises associated with Cases Z and N, is displayed.

In Figs. 5(a) and 5(b), the post-buckling behavior in the plane $(\tilde{\tilde{L}}_1,\delta)$ and $(\tilde{\tilde{L}}_1,\delta+\overset{\circ}{\delta})$ for the cases FM and IM of the square panel under the temperatures $T_u = 3000°\text{F}$ and $T_b = 70°\text{F}$ was depicted.

As it results from Figs. 4 and 5(a), the character of in-plane boundary conditions (i.e., movable and immovable) exerts an opposite influence on $\overset{\circ}{T}_{cr}$ and $(\tilde{\tilde{L}}_1)_{cr}$.

Figure 6 presents the interrelation $(\overset{\circ}{T}_{cr}, \tilde{\tilde{L}}_1)$ for movable and

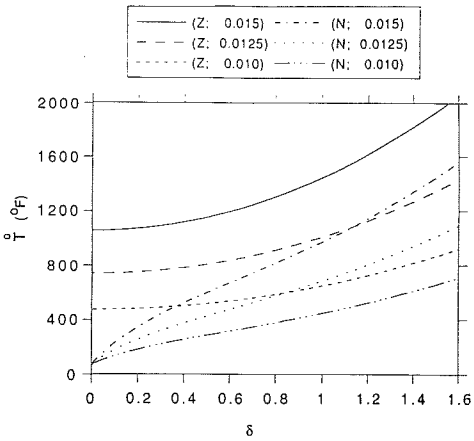


Fig. 1(a) Case FM

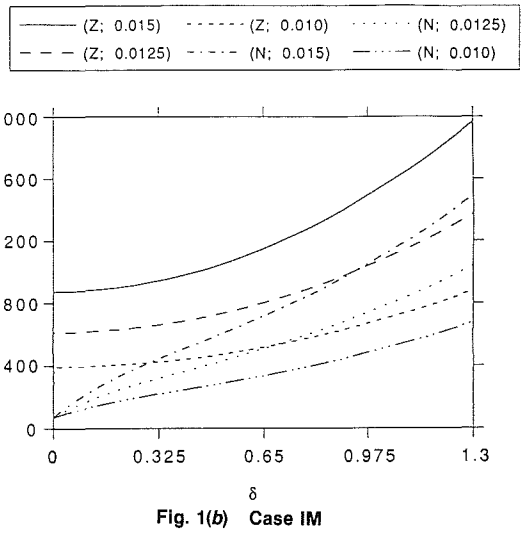


Fig. 1(b) Case IM

Fig. 1 Thermal post-buckling of geometrically perfect square panels for six combinations of the temperature rises and thickness ratios. These combinations are generally expressed as $(Z,H/l_1)$ or $(N,H/l_1)$, where Z implies $\overset{\circ}{T} \neq 0$, $\overset{1}{T} \neq 0$. Here $E/E' = 3$, $E/G' = 20$, $\nu' = 0.33$, $\nu = -0.15$, $\lambda/E = -1.43 \times 10^{-5}$; $\lambda'/\lambda = 1.0694$, $\tilde{\tilde{L}}_1 = 0$.

Downloaded 03 May 2010 to 171.66.16.245. Redistribution subject to ASME license or copyright; see http://www.asme.org/terms/Terms_Use.cfm

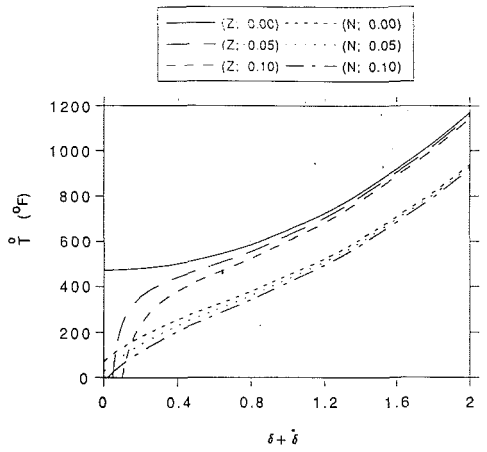


Fig. 2(*a*) Case FM

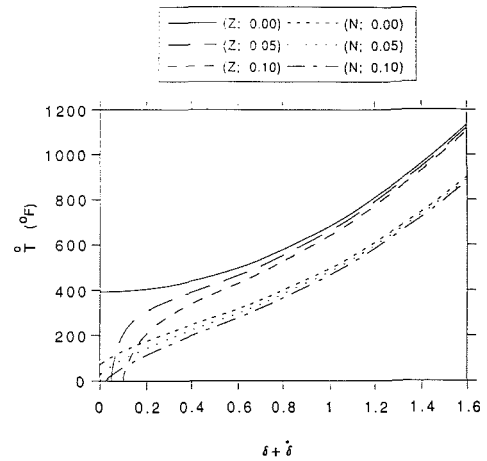
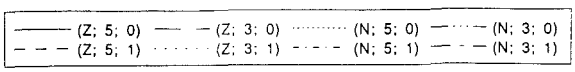


Fig. 2(*b*) Case IM

Fig. 2 Thermal post-buckling of geometrically perfect and imperfect square panels for six combinations of the temperature rise and imperfection amplitude. These combinations are generically expressed at $(Z,\overset{\circ}{\delta})$ or $(N,\overset{\circ}{\delta})$. Excepting $H/l_1 = 0.01$, the remaining data are the same as in Figs. 1



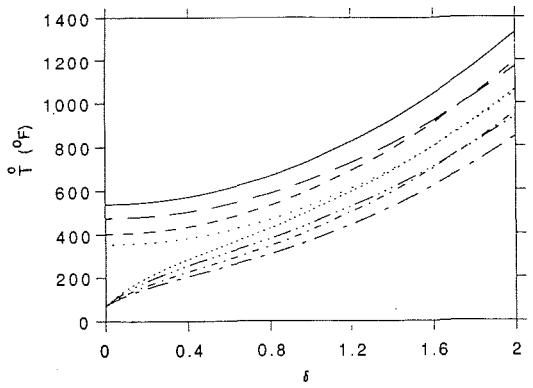
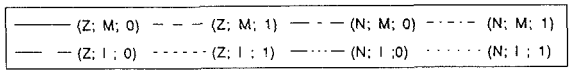


Fig. 3 Thermal post-buckling of geometrically perfect square panels for 12 combinations of the temperature rise, E/E' ratio and the uniaxial compressive load $\tilde{L}_1$. These combinations are generically expressed as $(Z, E/E', \tilde{L}_1)$. Here $E/G' = 20$, $\nu = -0.15$, $H/l_1 = 0.10$ and following Terner (1962), when $E/E' = 3$, and $\nu' = 0.33$, then $\lambda/E = -1.43 \times 10^{-5}$, and $\lambda'/\lambda = 1.0694$ while when $E/E' - 5$, and $\nu' = 0.20$, then $\lambda/E = 10^{-6}$, and $\lambda'/\lambda = 0.9625$. Case FM.



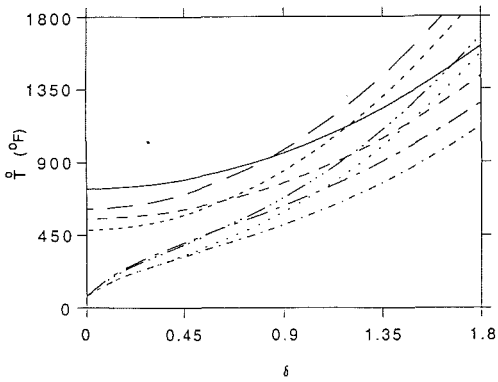


Fig. 4 Thermal post-buckling of geometrically perfect square panels for eight combinations of the temperature rise, the character of in-plane boundary conditions and the intensity of uniaxial compressive load. These combination are generically expressed as $(Z/N, M/I, \tilde{L}_1)$ where M and I means Case FM and IM, respectively. Here $H/l_1 = 0.0125$. In the remaining the same data as in Figs. 1 were used.

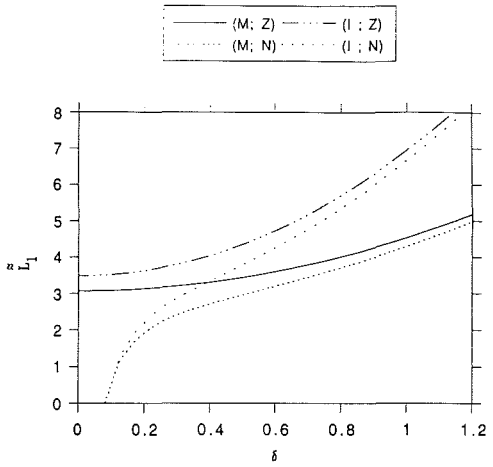


Fig. 5(*a*) Variation of $\tilde{L}_1$ versus δ for four combinations $(M/I, Z/N)$, where the meaning of M, I, Z, and N was explained previously. Here the temperature rise is given in terms of $T_u = 3000°F$ and $T_b = 70°F$. Here $H/l_1 = 0.05$, $\overset{\circ}{\delta} = 0$. In the remaining the data is the same as in Figs. 1.

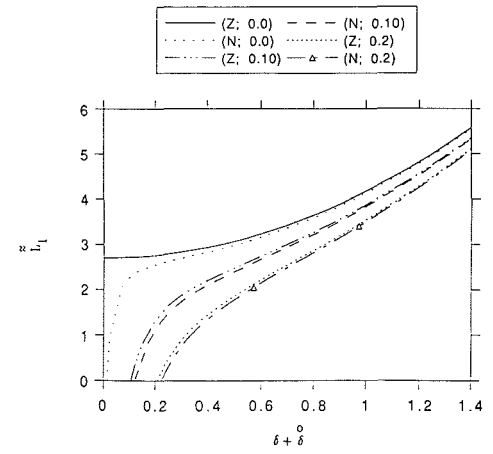


Fig. 5(*b*) Variation of $\tilde{L}_1$ versus $\delta + \overset{\circ}{\delta}$ for six combinations $(Z/N, \overset{\circ}{\delta})$. Here the temperature rise is similar as in Fig. 5(*a*). $H/l_1 = 0.10$, $E/G' = 20$, $E/E' = 5$, $\nu' = 0.20$, $\nu = -0.15$, the remaining the data being as in Figs. 3.

Downloaded 03 May 2010 to 171.66.16.245. Redistribution subject to ASME license or copyright; see http://www.asme.org/terms/Terms_Use.cfm

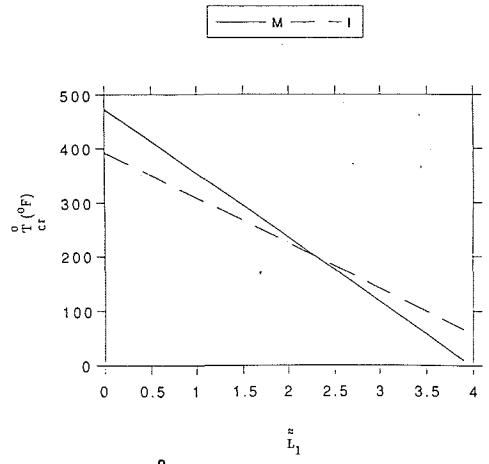


Fig. 6 The interaction $(\overset{\circ}{T}_{cr}, \tilde{\tilde{L}}_1)$ for IM and FM edge conditions. Here $H/l_1 = 0.010$, the remaining parameters being the same as in Figs. 1.

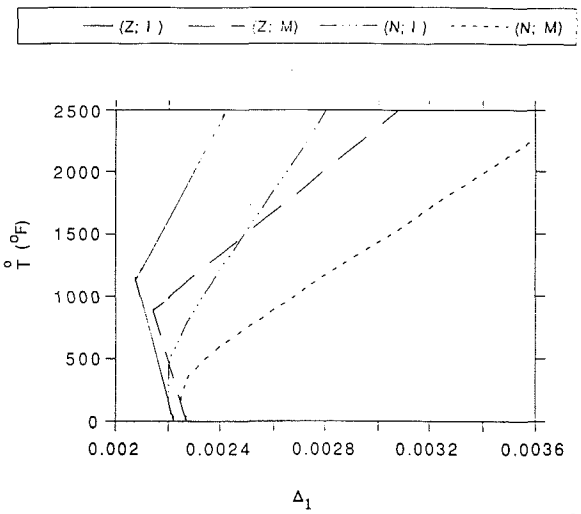


Fig. 7 Thermal post-buckling of perfect flat panels expressed as $(\overset{\circ}{T}, \Delta_1)$ for four combinations (*Z/N*, *I/M*). Here $H/l_1 = 0.03$, $\tilde{\tilde{L}}_1 = 3$, $\overset{\circ}{\delta} = 0$. In the remaining, the same parameters as in Fig. 1 were used.

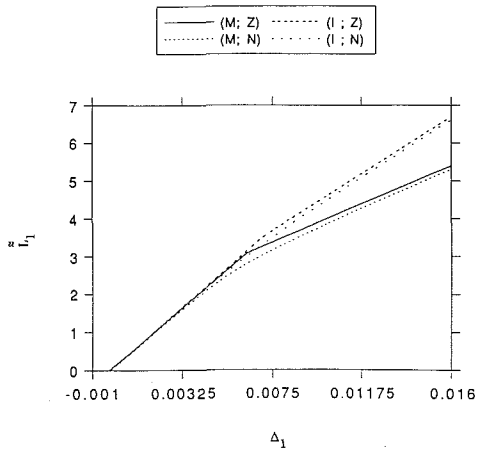


Fig. 8 The influence of the given temperature rise on the post-buckling of uniaxially compressed square panels. Here $H/l_1 = 0.05$. In the remaining the same parameters as in Figs. 1 were used.

immovable in-plane edge conditions and for a given set of parameters.

Finally, Figs. 7 and 8 display, in the space $(\overset{\circ}{T}, \Delta_1)$ and $(\tilde{\tilde{L}}_1, \Delta_1)$, the post-buckling for a plate exhibiting movable and immovable in-plane edge conditions, under a fixed $\tilde{\tilde{L}}_1 (= 3)$ and a given temperature field ($T_u = 3000°\text{F}$ and $T_b = 70°\text{F}$), respectively. Throughout these numerical illustrations the transverse shear correction factor was considered $K^2 = 5/6$ which, even for composite laminated panels, was found by Noor and Burton (1991) to result in accurate results.

Conclusions

The results displayed in Figs. 1–8 allow one to outline the following conclusions:

(1) The geometrically perfect and imperfect panels subjected to a given compressive edge loads are capable to resist temperature rises of $\overset{\circ}{T}$ beyond the critical buckling temperature (identified by the points on the axis of ordinates and corresponding to perfect panels and the absence of $\overset{\circ}{T}_I$).

(2) The carrying capacity of the panel is larger in the case of the existence of a temperature temperature field uniform through thickness only (i.e., in the case labeled as Case *Z*) than in its Case *N* counterpart.

(3) Big differences between the post-buckling responses of flat panels experiencing initial geometric imperfections and subjected, on one hand, to a uniform through thickness temperature rise and, on the other hand, to a full temperature field (identified as Case *N*), are remarked.

In the former case, the geometric imperfections play the usual role (see Librescu and Stein, 1991)), in the sense that the plate starts to deflect from the beginning of heating, without exhibiting thermal buckling bifurcation followed, in the vicinity of the buckling bifurcation of the perfect plate counterpart, by a marked increase of the bending. Moreover, in the deep post-buckling range, the curves of the initially imperfect plate approach the ones of their perfect counterparts. However, in the Case *N*, although the curves associated with the perfect and imperfect panels are close to each other from the initial start of the panel deflection (occurring, for perfect panels, at $\overset{\circ}{T} = T_b$), the results reveal that the overall thermal carrying capacity is much lower than in the former case.

(4) As expected, the increase of thickness ratio and the decrease of compressive edge loads yield an increase of the temperature carrying capacity of the panel. In addition, the ratio E/E' plays a not negligible role in the increase or decrease of this capacity. It should be remarked that in the present case this ratio appears only in conjunction with the thermomechanical transverse anisotropy properties of the panel (see Eqs. (10*d*,*e*)).

(5) The character of in-plane boundary conditions (i.e., movable and immovable) has a significant effect on the post-buckling behavior. As it could be remarked, the benefits of using the panel in the post-buckling range are much greater for the panel having the unloaded edges prevented to expand in the normal direction (Case IM) than in its FM counterpart.

However, at this point it should be remarked that in the case of the panel characterized by $\nu < 0$, the buckling bifurcation load is higher than in case characterized by $\nu > 0$. Moreover, in the case $\nu < 0$, depending on the magnitude of the applied compressive uniaxial load $\tilde{\tilde{L}}_1$, $(\overset{\circ}{T})_{cr}$ in the case of movable edges could be higher or lower than the one associated to its immovable counterpart (see Fig. 6).

(6) The curves $(\overset{\circ}{T}, \Delta_1)$ (for given compressive load) and $(\tilde{\tilde{L}}_1, \Delta_1)$ (for given temperature rise), exhibit peculiar trends not encountered within the usual post-buckling problems.

As Fig. 7 reveals, under a temperature rise $\overset{\circ}{T}$, the initially compressed panel exhibits an extension (i.e., negative end-shortening) followed, from the point associated with the critical buckling temperature, by an increase of the end-shortening. In the case where both the uniform and the thickness-wise

Downloaded 03 May 2010 to 171.66.16.245. Redistribution subject to ASME license or copyright; see http://www.asme.org/terms/Terms_Use.cfm

temperature gradient are involved, these two phase have a continuous character, reminding the behavior of the imperfect panel. However, this graph reveals again that under the rise of both $\overset{\circ}{T}$ and $\overset{1}{T}$, lower temperature carrying capacities of the panel are obtained as compared to the case when the rise of only $\overset{\circ}{T}$ is involved.

(7) Compared to the case of the panel subjected to the rise of the uniaxial compressive edge load $\tilde{\tilde{L}}_1$ and exposed to a given $\overset{\circ}{T}$, its post-buckling response counterpart arising in the case of the existence of a full temperature field (i.e., of both $\overset{\circ}{T}$ and $\overset{1}{T}$) reveals a similar trend to the one manifested in the case of imperfect panels subjected only to compressive loads (see Fig. 8). It is also worth noting that corresponding to $\tilde{\tilde{L}}_1 = 0$, Δ_1 is a negative valued quantity becoming more negative as T_u and T_b become larger and larger.

(8) Larger end-shortening displacements are exhibited under the rise of both $\overset{\circ}{T}$ and $\overset{1}{T}$ than under its membrane counterpart, $\overset{\circ}{T}$, only. The same trend is featured in the case of movable edges (Case FM), as compared to its IM counterpart (Fig. 7).

As Fig. 7 reveals, under a temperature rise T, the initially compressed panel exhibits an extension (i.e., negative end-shortening) followed, from the point associated with the critical buckling temperature, by an increase of the end-shortening. In the case where both the uniform and the thickness-wise temperature gradient are involved, these two phases have a continuous character, reminding the behavior of the imperfect panel. However, this graph reveals again that under the rise of both $\overset{\circ}{T}$ and $\overset{1}{T}$, lower temperature carrying capacities of the panel are obtained as compared to the case when the rise of only $\overset{\circ}{T}$ is involved.

(7) Compared to the case of the panel subjected to the rise of the uniaxial compressive edge load $\tilde{\tilde{L}}_1$ and exposed to a given $\overset{\circ}{T}$, its post-buckling response counterpart arising in the case of the existence of a full temperature field (i.e., of both $\overset{\circ}{T}$ and $\overset{1}{T}$) reveals a similar trend to the one manifested in the case of imperfect panels subjected only to compressive loads (see Fig. 8). It is also worth noting that corresponding to $\tilde{\tilde{L}}_1 = 0$, Δ_1 is a negative valued quantity becoming more negative as T_u and T_b become larger and larger.

(8) Larger end-shortening displacements are exhibited under the rise of both $\overset{\circ}{T}$ and $\overset{1}{T}$ than under its membrane counterpart, $\overset{\circ}{T}$, only. The same trend is featured in the case of movable edges (Case FM), as compared to its IM counterpart (Fig. 7).

(9) The obtained results reveal that, from the post-buckling behavior point of view, the flat panels are imperfection insensitive both when the rises of the membrane and of the complete temperature fields are involved.

It is hoped that the results reported here will be useful towards a better understanding of the thermal postbuckling of shear deformable panels subjected to compressive edge loads.

Acknowledgment

L. Librescu gratefully acknowledges the partial support of this work by NASA Langley Research Center through Grant NAG-1-1300.

References

Chen, L.-W., and Chen, L.-Y., 1989, "Thermal Postbuckling Analysis of Laminated Composite Plates by the Finite Element Method," *Composite Structures*, Vol. 12, No. 4, pp. 257–270.

Garber, A. M., 1963, "Pyrolitic Materials for Thermal Protection Systems," *Aerospace Engineering*, Jan., pp. 126–137.

Huang, N. N., and Tauchert, T. R., 1988a, "Postbuckling Response of Antisymmetric Single-Ply Laminates to Uniform Temperature Loading," *Acta Mechanica*, Vol. 72, pp. 173–183.

Huang, H. H., and Tauchert, T. R., 1988b, "Large Deformation of Antisymmetric Angle-Ply Laminates Resulting From Nonuniform Temperature Loadings," *Journal of Thermal Stresses*, Vol. 11, pp. 287–297.

Leissa, A. W., 1985, "Buckling of Laminated Composite Plates and Shell Panels," AFWAL-TR-85-3069.

Libove, C., and Tong, K. N., 1963, "Influence of Thickness-Wise Temperature Gradients on Large Deflections and Stability of Thin Elastic Shells," *Developments in Theoretical and Applied Mechanics*, Vol. 1, Plenum Press, New York.

Librescu, L., 1975, *Elasto-Statics and Kinetics of Anisotropic and Heterogeneous Shell-Type Structures*, Noordhoff International Publishers, Leyden, Netherlands.

Librescu, L., and Stein, M., 1990, "Postbuckling Analysis of Shear Deformable Composite Panels Taking into Account Geometrical Imperfections," AIAA/ASME/ASCE/AHS/ASC 31st Structures, Structural Dynamics and Materials Conference, Part 2, Structures, pp. 1857–1864 (an amended version of this paper was published in *AIAA Journal*, Vol. 30, No. 5, pp. 1352–1360).

Librescu, L., and Stein, M., 1991, "A Geometrically Nonlinear Theory of Transversely-Isotropic Laminated Composite Plates and Its Use in the Postbuckling Analysis," *Thin Walled Structures*, Special Issue of *Aeronautical Structures*, Vol. 11, pp. 177–201.

Librescu, L., and Souze, M. A., 1991, "Thermal Postbuckling Behavior of Geometrically Imperfect Shear-Deformable Composite Flat Panels," *Mechanics of Composites of Elevated and Cyrogenic Temperatures*, AMD-Vol. 118, ASME, S. N. Singhal, W. I. Jones and C. T. Herakovich, eds., pp. 305–321.

Librescu, L., and Chang, M. Y., 1992, "Imperfection Sensitivity and Postbuckling Behavior of Shear-Deformable Composite Doubly-Curved Shallow Panels," *Internat Journal Solids Structures*, Vol. 29, No. 9, pp. 1065–1083.

Meyers, A. C., and Hyer, M. W., 1991, "Thermal Buckling and Postbuckling of Symmetrically Laminated Composite Plates," *J. Thermal Stresses*, Vol. 14, pp. 519–540.

Meyers, A. C., and Hyer, M. W., 1992, "Thermally-Induced, Geometrically Nonlinear Response of Symmetrically Laminated Composite Plates," *Proceedings of the 33rd AIAA/ASME/ASCE/IHHS/ASC Structures, Structural Dynamics and Materials Conference*, AIAA-92-2539 CP, Apr., Dallas, TX, pp. 1027–1037.

Noor, A. K., and Burton, W. S., 1989, "Assessment of Shear Deformation Theories for Multilayered Composite Plates," *Appl. Mech. Rev.*, Vol. 42, No. 1, pp. 1–12.

Noor, A. K., and Burton, W. S., 1991, "Predictor-Corrector Procedures for Thermal Buckling Analysis of Multilayered Composite Plates," *Computer and Structures*, Vol. 40, No. 5, pp. 1071–1084.

Noor, A. K., and Burton, W. S., 1992a, "Computational Models for High-Temperature Multilayered Composite Plates and Shells," *Appl. Mech. Rev.*, Vol. 45, No. 5.

Noor, A. K., Starnes, Jr., J. H., and Peters, J. M., 1992b, "Thermomechanical Buckling and Postbuckling of Multilayered Composite Panels," Paper AIAA-92-2541CP, *Proceedings of the 33rd AIAA/ASME/ASCE/AHS/ASC Structures, Structural Dynamics and Material Conference*, Apr. 13–15, Dallas, TX.

Pelech, B. L., 1978, *Generalized Theory of Shells*, (in Russian), High School, Lvov.

Prabhu, M. S. S., and Durvasula, S., 1976, "Thermal Postbuckling Characteristics of Clamped Skew Plates," *Computer and Structures*, Vol. 6, pp. 177–185.

Reissner, E., 1986, "On Small Finite Deflections of Shear Deformable Elastic Plates," *Computer Methods in Applied Mechanics and Engr.*, Vol. 59, pp. 227–233.

Reissner, E., 1985, "Reflections on the Theory of Elastic Plates," *Appl. Mech. Rev.*, Vol. 28, Nov., pp. 1453–1464.

Tauchert, T. R., 1991, "Thermally Induced Flexure, Buckling and Vibration of Plates," *Appl. Mech. Rev.*, Vol. 44, No. 8, pp. 347–360.

Terner, E., 1962, "On Thermal Stresses in Certain Transversely Isotropic, Pyrolitic Materials," *Proceedings of the Fourth U.S. National Congress of Applied Mechanics*, Vol. 2, pp. 1147–1152.

Vinson, J. R., and Chou, T. W., 1974, *Composite Materials and their Use in Structures*, John Wiley and Sons, New York.

Downloaded 03 May 2010 to 171.66.16.245. Redistribution subject to ASME license or copyright; see http://www.asme.org/terms/Terms_Use.cfm

Viscoelastic Response of a Strand

T. A. Conway
Assistant Professor,
Department of Mechanical Engineering,
University of Akron,
Akron, OH 44325-3903
Assoc. Mem. ASME

G. A. Costello
Department of Theoretical and
Applied Mechanics,
University of Illinois at Urbana-Champaign,
Urbana, IL 61801
Fellow ASME

A method is presented in which the axial viscoelastic response of a multiple filament strand, constrained by a no-end rotation boundary condition, may be predicted. This method is an initial attempt to describe the time-dependent response of the multilayer strand by incorporating the stress relaxation data for a linearly viscoelastic construction material. Specifically, a strand consisting of a core filament, six filaments in the second layer, and twelve filaments in the outer layer is analyzed. This analysis could, however, include any number of layers of filaments where each layer has a concentric helix radius. The particular material used in this paper is polymethyl methacrylate (PMMA). The stress relaxation for PMMA is modeled analytically using the Schapery collocation method which determines the constant coefficient values for the elements of a Wiechert response model. Since this is a first approximation model, the approach is limited to linear viscoelasticity. The geometric effects of the strand are then combined with the Wiechert response model to develop a system of convolution integrals which satisfy the equilibrium and imposed boundary conditions for the multiple filament strand construction. The solutions for these integrals are approximated numerically using a modified Newton's iterative method combined with a numerical technique which takes into account the material's stress-strain history.

Introduction

Multiple filament cords composed of twisted polymer filaments are utilized in many of today's manufactured goods. They are the main components in most textile products and the reinforcing components in many composite structures (tires, biomedical devices). The advantage of the multiple filament cord over a solid filament with an equivalent radius is the lower bending stiffness while maintaining a high axial stiffness.

Since the simple strand, Fig. 1, is a fundamental building component of many cords with multiple layered cross-sections, Fig. 2, an understanding of the simple strand's mechanical response is necessary. Conway and Costello (1991) analyzed the elastic axial mechanical response of a simple strand. They demonstrated, analytically, that a significant reduction in contact stresses between strand wires could be achieved by a slight modification of the wire's cross-sectional geometry. Conway and Costello (1993b), further, analyzed the viscoelastic response of a simple strand and developed a set of constitutive equations which described the strand's time-dependent response to a static, axial load.

As is evident from the literature, an extensive development of the elastic strand model presently exists (Costello, 1990). Attempts to develop a model for the response of a multiple layer strand which incorporates the time-dependent material behavior for polymer filaments have also been met with some success (Hearle et al., 1969). This paper is an initial attempt to continue in the efforts of Hearle and his colleagues by developing a theory capable of predicting, within limits, the time-dependent mechanical response of a multilayered strand. Since this is an initial attempt to develop a useful theory, the effects of friction and material compliance are ignored. The authors are aware that these first-order effects are quite important in the realistic description of a strand's response to loading and will incorporate them in the subsequent development of the theory for polymer cords. This initial development of the theory is accomplished by using a method similar to that described by Conway and Costello (1993a & b). First, a viscoelastic model that incorporates relatively realistic material properties is generated. The model is then integrated into a set of constitutive equations for a strand. Finally, the mechanical response of the strand is evaluated numerically.

Theory

Most polymer strand applications ideally require that the strand not retain any residual strains after a period of time subsequent to the removal of the applied load. The analytical model chosen to describe the strand material's response to loading must, therefore, represent a viscoelastic solid. It is assumed that the material is slightly compressible and behaves in a linearly viscoelastic manner, a number of analytical models are available to describe the material's mechanical response. This assumption is valid for relatively small strains and will be used throughout this work (Bland, 1960). Further, it is assumed that the material functions in an isothermal environment, thus any changes in the mechanical properties due to a temperature change are not considered.

Contributed by the Applied Mechanics Division of THE AMERICAN SOCIETY OF MECHANICAL ENGINEERS for presentation at the First Joint ASCE-EMD, ASME-AMD, SES Meeting, Charlottesville, VA, June 6-9, 1993.

Discussion on this paper should be addressed to the Technical Editor, Professor Lewis T. Wheeler, Department of Mechanical Engineering, University of Houston, Houston, TX 77204-4792, and will be accepted until four months after final publication of the paper itself in the ASME JOURNAL OF APPLIED MECHANICS.

Manuscript received by the ASME Applied Mechanics Division, Feb. 20, 1992; final revision, Oct. 23, 1992. Associate Technical Editor: D. J. Inman.

Paper No. 93-APM-28.

Copyright © 1993 by ASME
Downloaded 03 May 2010 to 171.66.16.245. Redistribution subject to ASME license or copyright; see http://www.asme.org/terms/Terms_Use.cfm

The authors of this paper have chosen to use a modified generalized Maxwell model, known as a Wiechert model, Fig. 3, because of its relative convenience in modeling the stress relaxation for a given material resulting from an imposed strain. Since linear viscoelasticity is assumed for the material property, the response to loading for each element in the Wiechert model is linear and is described by a constant coefficient. The values for these coefficients are calculated from the experimental stress relaxation data by using the Schapery Collocation method (Lee and Rogers, 1963).

The Schapery Collocation method models each of the material's major transitions as a single relaxation time process, Fig. 4. Thus the values for the stress-strain relationship

$$\sigma(t) = \left\{ E_0 + \sum_{j=1}^{N} E_j \exp\left(\frac{-t}{\tau_j}\right) \right\} \epsilon_0 \tag{1}$$

can be determined where E_0 is the rubbery modulus, E_j is the modulus for each successive transition, τ_j is the relaxation time for the corresponding transition, and ϵ_0 is the imposed constant strain.

Once the strand's material has been mechanically characterized, the geometric constraints for the strand must be determined. The lateral cross-section view of an undeformed three-layered strand is illustrated in Fig. 2. The core filament has an initial radius, R_1, the second layer of six filaments each has a radius, R_2, and the outer layer has 12 filaments each with a radius, R_3. The subscripts refer to the layer of filaments, with the first layer being the core filament.

The initial and time-dependent helix radius of the second layer of filaments are

$$r_2 = R_1 + R_2 \tag{2}$$

and

$$r_2(t) = R_1(t) + R_2(t). \tag{3}$$

The initial helix radius for the third layer of filaments is

$$r_3 = R_1 + 2R_2 + R_3 \tag{4}$$

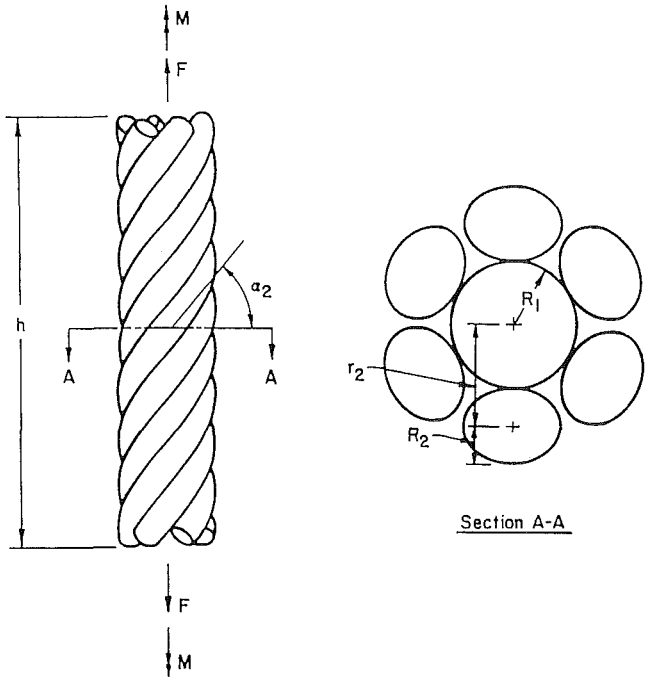


Fig. 1 Side view and cross-section of a simple strand

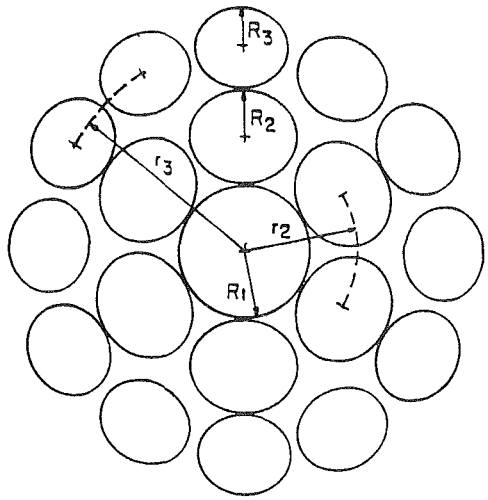


Fig. 2 Cross-section of a three-layer strand

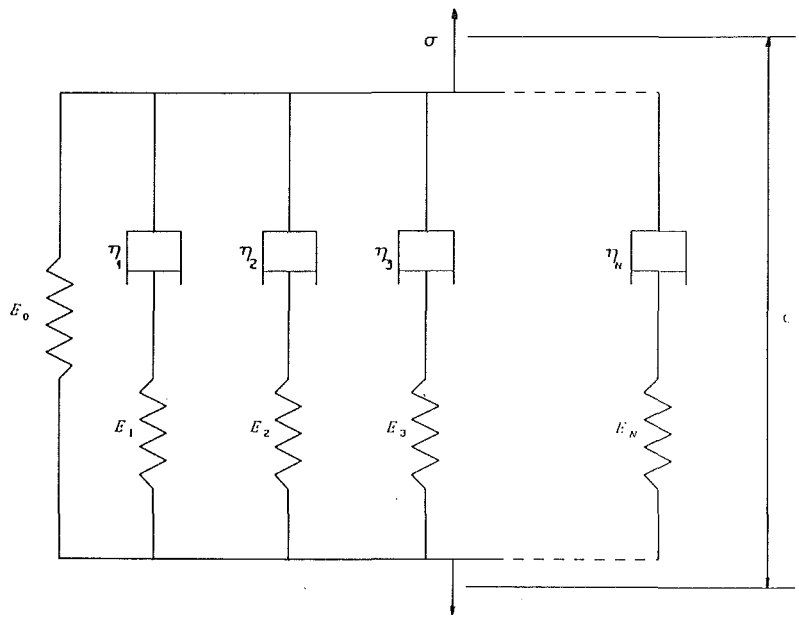


Fig. 3 Wiechert model

Downloaded 03 May 2010 to 171.66.16.245. Redistribution subject to ASME license or copyright; see http://www.asme.org/terms/Terms_Use.cfm

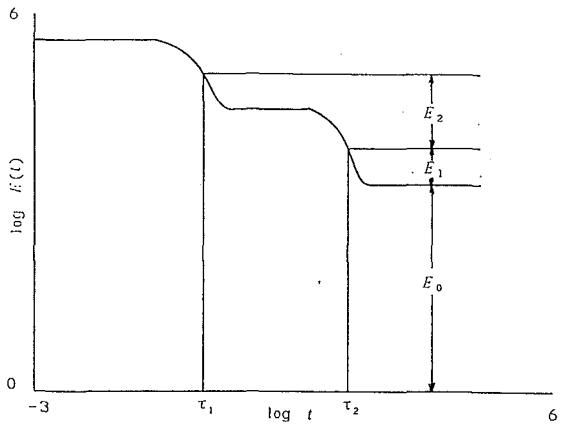


Fig. 4 Theoretical stress relaxation response

and the time-dependent helix radius is

$$r_3(t) = R_1(t) + 2R_2(t) + R_3(t). \tag{5}$$

The initial helix angle of the second, third, etc. layer of filaments, α_i, where $i = 2, 3, \ldots$, is determined from the layer's initial pitch, P_i, of its filaments, or

$$\alpha_i = \tan^{-1}\frac{P_i}{2\pi r_i}. \tag{6}$$

In a purely elastic material, the time necessary for molecular rearrangement is virtually infinite (Tschoegl, 1989). A comparison of an elastic strand's initial configuration and final configuration can, therefore, be used to determine the strand's mechanical response to loading or deformation. If a load is applied to a polymer strand, however, the helix angles, $\alpha_2(t)$ and $\alpha_3(t)$, each filament radius, $R_1(t)$, $R_2(t)$, and $R_3(t)$, and helix radii, $r_2(t)$ and $r_3(t)$, all vary as a function of time. Thus a description of a viscoelastic solid's final configuration is not applicable. Instead, a description of the strand's configuration at some time, $t > 0$, is necessary.

For a given length of strand, the second layer of filaments will have Q_0 turns in the undeformed state and Q turns after deformation at some time $t > 0$. The undeformed length of the strand is

$$L_0 = 2\pi Q_0 r_2 \tan\alpha_2 \tag{7}$$

and the deformed length at $t > 0$ is

$$L(t) = 2\pi Q r_2(t)\tan\alpha_2(t). \tag{8}$$

The corresponding undeformed length of a second layer filament is

$$l_0 = 2\pi Q_0 r_2 \sec\alpha_2 \tag{9}$$

and the corresponding deformed length is

$$l(t) = 2\pi Q r_2(t)\sec\alpha_2(t). \tag{10}$$

The axial strain in the strand is, thus,

$$\epsilon_1(t) = \frac{L(t)}{L_0} - 1 = \frac{Q r_2(t)\tan\alpha_2(t)}{Q_0 r_2 \tan\alpha_2} - 1 \tag{11}$$

and the axial strain in a filament is

$$\xi_2(t) = \frac{l(t)}{l_0} - 1 = \frac{Q r_2(t)\cos\alpha_2}{Q_0 r_2 \cos\alpha_2(t)} - 1. \tag{12}$$

From Poisson's relationship

$$\frac{R_2(t)}{R_2} - 1 = -\nu\xi_2(t), \tag{13}$$

where ν is Poisson's ratio and is considered to be constant for relatively small deformations.

A combination of Eqs. (11)-(13) results in

$$\epsilon_1(t) = \frac{\sin\alpha_2(t)}{\sin\alpha_2}\left[1 + \frac{1}{\nu}\left(1 - \frac{R_2(t)}{R_2}\right)\right] - 1. \tag{14}$$

The angle of twist per unit length for the second layer of the strand is

$$\tau_c(t) = \frac{2\pi(Q - Q_0)}{L_0} = \frac{1}{r_2\tan\alpha_2}\left(\frac{Q}{Q_0} - 1\right). \tag{15}$$

By combining Eqs. (13), (14), and (16), the twist per unit length becomes

$$\tau_c(t) = \frac{1}{r_2\tan\alpha_2}\left\{\frac{r_2\cos\alpha_2(t)}{r_2(t)\cos\alpha_2}\left[1 + \frac{1}{\nu}\left(1 - \frac{R_2(t)}{R_2}\right)\right] - 1\right\}. \tag{16}$$

Equation (16) shows that if the strand ends are allowed to rotate, the strain will be coupled with a twist. If, however, the ends of the strand are not allowed to rotate, such that $\tau_c(t) = 0$, then an additional constrained condition exists. From Eq. (16), this constraint is

$$\frac{\cos\alpha_2}{r_2} = \frac{\cos\alpha_2(t)}{r_2(t)}\left[1 + \frac{1}{\nu}\left(1 - \frac{R_2(t)}{R_2}\right)\right]. \tag{17}$$

By incorporating Eqs. (2) and (17), a relationship between the helix angle, $\alpha_2(t)$, and the second layer filament radius, $R_2(t)$, can be shown to be

$$\cos\alpha_2(t) = \frac{(R_1(t) + R_2(t))\cos\alpha_2}{(R_1 + R_2)\left[1 + \frac{1}{\nu}\left(1 - \frac{R_2(t)}{R_2}\right)\right]}. \tag{18}$$

Similarly, the relationship between $\alpha_3(t)$ and $R_3(t)$ in the third layer of filaments is

$$\cos\alpha_3(t) = \frac{r_3(t)\cos\alpha_3}{r_3\left[1 + \frac{1}{\nu}\left(1 - \frac{R_3(t)}{R_3}\right)\right]}. \tag{19}$$

The general design of a strand minimizes the contact stresses between the filaments by requiring $R_1(t) > R_2(t) > R_3(t)$. This reduction in radius does not have to be very large, usually on the order of 3 percent for a polymer with a Poisson's ratio near 1/2. This now allows a relationship between $R_1(t)$, $R_2(t)$, and $R_3(t)$ to be known.

Once the geometric constraints for the strand are determined, the equilibrium equations can be developed. Before the viscoelastic material properties are incorporated into this configuration, however, a review of the elastic equilibrium equations for a simple strand are necessary.

Costello (1990) has shown that for an axially loaded strand, the filaments in each layer deform from one helical configuration to another. The equations of equilibrium that must be satisfied for each wire are:

$$N_2'\tau_2 - T_2\kappa_2' - X_2 = 0 \tag{20}$$

$$G_2'\tau_2 - H_2\kappa_2' + N_2 = 0 \tag{21}$$

$$N_3'\tau_3 - T_3\kappa_3' - X_3 = 0 \tag{22}$$

and

$$G_3'\tau_3 - H_3\kappa_3' + N_3 = 0 \tag{23}$$

where the subscripts 2 and 3 refer to the second and third layer of wires, N_2' and N_3' are the binormal components of the shear load, τ_2 and τ_3 are the twist per unit length of the wire's centerline, T_2 and T_3 are the wire's axial load, κ_2' and κ_3' are the binormal components of curvature, X_2 and X_3 are the resultant line loads per unit length of the wire's centerline, G_2' and G_3' are the binormal components of the bending moment and H_2 and H_3 are the twisting moments. Further, Costello (1990) showed that for naturally curved thin rods

$$G_2' = \frac{\pi R_2^4}{4} E\left[\frac{\cos^2\bar{\alpha}_2}{\bar{r}_2} - \frac{\cos^2\alpha_2}{r_2}\right] \tag{24}$$

Downloaded 03 May 2010 to 171.66.16.245. Redistribution subject to ASME license or copyright; see http://www.asme.org/terms/Terms_Use.cfm

$$H_2=\frac{\pi R_2^4}{4(1+\nu)}E\left[\frac{\sin\bar{\alpha}_2\cos\bar{\alpha}_2}{\bar{r}_2}-\frac{\sin\alpha_2\cos\alpha_2}{r_2}\right] \quad (25)$$

$$G_3'=\frac{\pi R_3^4}{4}E\left[\frac{\cos^3\bar{\alpha}_3}{\bar{r}_3}-\frac{\cos^3\alpha_3}{r_3}\right] \quad (26)$$

and

$$H_3=\frac{\pi R_3^4}{4(1+\nu)}E\left[\frac{\sin\bar{\alpha}_3\cos\bar{\alpha}_3}{\bar{r}_3}-\frac{\sin\alpha_3\cos\alpha_3}{r_3}\right] \quad (27)$$

where R_2 and R_3 are the wire radii for each layer after loading, E is the wire material's elastic modulus, $\bar{\alpha}_2$ and $\bar{\alpha}_3$ are the helix angles of the loaded wire and $\bar{r}_2$ and $\bar{r}_3$ are the helix radii for each layer of the loaded strand. Also in the elastic case, the axial load in each wire of layers 2 and 3 may be determined from

$$T_2=\frac{\pi R_2^2}{\nu}E\left[1-\frac{R_2}{(R_2)_0}\right] \quad (28)$$

and

$$T_3=\frac{\pi R_3^2}{\nu}E\left[1-\frac{R_3}{(R_3)_0}\right]. \quad (29)$$

Equations (21), (24), and (25) can be used to determine an expression for N_2' in terms of $\bar{\alpha}_2$ and R_2 given ν, α_2, $(R_2)_0$ and E. Equations (23), (26), and (27) can be used to determine an expression for N_3' in terms of $\bar{\alpha}_3$ and R_3 given ν, α_3, $(R_3)_0$ and E.

The total forces, F_2 and F_3, and twisting moments, M_2 and M_3, for each layer of wires are

$$F_2=6[T_2\sin\alpha_2+N_2'\cos\alpha_2] \quad (30)$$

$$F_3=12[T_3\sin\alpha_3+N_3'\cos\alpha_3] \quad (31)$$

$$M_2=6[H_2\sin\alpha_2+G_2'\cos\alpha_2+T_2r_2\cos\alpha_2-N_2'r_2\sin\alpha_2] \quad (32)$$

and

$$M_3=12[H_3\sin\alpha_3+G_3'\cos\alpha_3+T_3r_3\cos\alpha_3-N_3'r_3\sin\alpha_3]. \quad (33)$$

The total force, F_1, in the core wire can be calculated by

$$F_1=-\frac{\pi R_1^2}{\nu}E\left[1-\frac{R_1}{(R_1)_0}\right]. \quad (34)$$

The total moment, M_1, in the core wire is equal to zero as a result of the no-end-rotation boundary condition imposed on the simple strand.

Finally, the total axial load, F_T, and the total moment, M_T, in the strand are

$$F_T=F_1+F_2+F_3 \quad (35)$$

and

$$M_T=0+M_2+M_3. \quad (36)$$

Returning now to the time dependent behavior of the polymer strand, according to the correspondence principle of viscoelasticity, the tensile relaxation modulus can be treated as an integral operation. The correspondence principle allows Hooke's law to be used in the Laplace transform space and is represented as

$$\bar{\sigma}(p)=p\tilde{E}(p)\bar{\epsilon}(p) \quad (37)$$

where p is the transform variable. Inversion of this transform yields an expression for the Boltzmann superposition integral (Tschoegl, 1989). This general solution to the inverse transform of Eq. (37) is

$$\sigma(t)=\int_0^t E(t-t_1)\frac{d\epsilon(t_1)}{dt_1}dt_1. \quad (38)$$

Now, instead of varying the modulus and the strain, we hold the strain constant, as in stress relaxation, and allow another parameter of the design to vary. The convolution integral would have the general form

$$\int_0^t E(t-t_1)\dot{f}(t_1)dt_1. \quad (39)$$

If the differential term is denoted as

$$df=\dot{f}, \quad (39)$$

then the convolution integral, Eq. (39), can be represented as

$$(E^*df)(t). \quad (41)$$

The time-dependent relationships for the binormal components of the bending moment, $G_2'(t)$ and $G_3'(t)$, and the twisting moment, $H_2(t)$ and $H_3(t)$, for the respective filament can now be determined. These components of the moment become

$$G_2'(t)=\frac{\pi R_2^4(t)}{4}\left(E^*d\left[\frac{\cos^2\alpha_2}{r_2}\right]\right)(t) \quad (42)$$

$$G_3'(t)=\frac{\pi R_3^4(t)}{4}\left(E^*d\left[\frac{\cos^2\alpha_3}{r_3}\right]\right)(t) \quad (43)$$

$$H_2(t)=\frac{\pi R_2^4(t)}{4(1+\nu)}\left(E^*d\left[\frac{\sin\alpha_2\cos\alpha_2}{r_2}\right]\right)(t) \quad (44)$$

and

$$H_3(t)=\frac{\pi R_3^4(t)}{4(1+\nu)}\left(E^*d\left[\frac{\sin\alpha_3\cos\alpha_3}{r_3}\right]\right)(t). \quad (45)$$

By incorporating Eqs. (21), (42), and (44), the binormal component of shear, $N_2'(t)$, is

$$N_2'(t)=\frac{\pi R_2^4(t)\cos\alpha_2(t)}{4r_2(t)}\left\{\left[\frac{\cos\alpha_2(t)}{1+\nu}\right]\left(E^*d\left[\frac{\sin\alpha_2\cos\alpha_2}{r_2}\right]\right)(t)-\sin\alpha_2(t)\left(E^*d\left[\frac{\cos^2\alpha_2}{r_2}\right]\right)(t)\right\} \quad (46)$$

By incorporating Eqs. (23), (43), and (45), the binormal component of shear, $N_3'(t)$, is

$$N_3'(t)=\frac{\pi R_3^4(t)\cos\alpha_3(t)}{4r_3(t)}\left\{\left[\frac{\cos\alpha_3(t)}{1+\nu}\right]\left(E^*d\left[\frac{\sin\alpha_3\cos\alpha_3}{r_3}\right]\right)(t)-\sin\alpha_3(t)\left(E^*d\left[\frac{\cos^2\alpha_3}{r_3}\right]\right)(t)\right\}. \quad (47)$$

The axial load in a second layer filament can be determined from Eq. (28) to be

$$T_2(t)=-\frac{\pi R_2^2(t)}{\nu R_2}(E^*dR_2)(t). \quad (48)$$

The axial load in a third layer filament can be determined from Eq. (29) to be

$$T_3(t)=-\frac{\pi R_3^2(t)}{\nu R_3}(E^*dR_3)(t). \quad (49)$$

The total force, $F_2(t)$, and moment, $M_2(t)$, for the second layer of filaments are

$$F_2(t)=6[T_2(t)\sin\alpha_2(t)+N_2'(t)\cos\alpha_2(t)] \quad (50)$$

and

$$M_2(t)=6[H_2(t)\sin\alpha_2(t)+G_2'(t)\cos\alpha_2(t)+T_2(t)r_2(t)\cos\alpha_2(t)-N_2'(t)r_2(t)\sin\alpha_2(t)]. \quad (51)$$

The total force, $F_3(t)$, and moment, $M_3(t)$, for the third layer of filaments are

$$F_3(t)=12[T_3(t)\sin\alpha_3(t)+N_3'(t)\cos\alpha_3(t)] \quad (52)$$

and

Downloaded 03 May 2010 to 171.66.16.245. Redistribution subject to ASME license or copyright; see http://www.asme.org/terms/Terms_Use.cfm

$$M_3(t) = 12[H_3(t)\sin\alpha_3(t) + G_3'(t)\cos\alpha_3(t) + T_3(t)r_3(t)\cos\alpha_3(t) - N_3'(t)r_3(t)\sin\alpha_3(t)]. \quad (53)$$

The total force, $F_1(t)$, in the core filament is calculated similarly to the axial load in a second or third layer filament where

$$F_1(t) = -\frac{\pi R_1^2(t)}{\nu R_1}\,(E^* dR_1)(t). \quad (54)$$

The total moment, $M_1(t)$, in the core filament is, again, equal to zero as a result of the no end rotation boundary condition imposed on the simple strand.

Finally, the total axial load, $F(t)$, and the total twisting moment, $M(t)$, in the three layer strand are

$$F(t) = F_1(t) + F_2(t) + F_3(t) \quad (55)$$

and

$$M(t) = 0 + M_2(t) + M_3(t). \quad (56)$$

With Eqs. (41)–(56), the mathematical tools are now available for the development of a solution technique for the response of a strand given a specific loading criterion.

General Method of Solution

It is convenient now to nondimensionalize the parameters used to calculate the various aspects of the strand response. In the subsequent analysis, R_2, R_3, $R_2(t)$, and $R_3(t)$ will be evaluated in terms of R_1 and $R_1(t)$. Also, the tensile modulus at time, $t = 0^-$, is $E(0^+)$ and is denoted by E_0. Thus, all of the variables can be nondimensionalized in terms of E_0 and R_1. The bar above each variable indicates a dimensionless quantity.

$$\bar{E} = \frac{E(t)}{E_0}, \quad \bar{R}_1(t) = \frac{R_1(t)}{R_1}, \quad \bar{R}_2(t) = \frac{R_2(t)}{R_1}, \quad \bar{R}_3(t) = \frac{R_3(t)}{R_1}$$

$$\bar{R}_1 = 1, \quad \bar{R}_2 = \frac{R_2}{R_1}, \quad \bar{R}_3 = \frac{R_3}{R_1}, \quad \bar{r}_2(t) = \frac{r_2(t)}{R_1}, \quad \bar{r}_3(t) = \frac{r_3(t)}{R_1}$$

$$\bar{T}_2(t) = \frac{T_2(t)}{E_0\pi R_1^2}, \quad \bar{T}_3(t) = \frac{T_3(t)}{E_0\pi R_1^2}, \quad \bar{N}_2'(t) = \frac{N_2'(t)}{E_0\pi R_1^2}$$

$$\bar{N}_3'(t) = \frac{N_3'(t)}{E_0\pi R_1^2}, \quad \bar{G}_2'(t) = \frac{G_2'(t)}{E_0\pi R_1^3}, \quad \bar{G}_3'(t) = \frac{G_3'(t)}{E_0\pi R_1^3}$$

$$\bar{H}_2(t) = \frac{H_2(t)}{E_0\pi R_1^3}, \quad \bar{H}_3(t) = \frac{H_3(t)}{E_0\pi R_1^3}, \quad \bar{F}_1(t) = \frac{F_1(t)}{E_0\pi R_1^2},$$

$$\bar{F}_2(t) = \frac{F_2(t)}{E_0\pi R_1^2}, \quad \bar{F}_3(t) = \frac{F_3(t)}{E_0\pi R_1^2}, \quad \bar{M}_2(t) = \frac{M_2(t)}{E_0\pi R_1^3},$$

$$\bar{M}_3(t) = \frac{M_3(t)}{E_0\pi R_1^3}, \quad \bar{F}(t) = \frac{F(t)}{E_0\pi R_1^2}, \quad \bar{M}(t) = \frac{M(t)}{E_0\pi R_1^3}. \quad (57)$$

For specific values of ν, $F(t)$, and $E(t)$, the viscoelastic deformation of a three-layer strand is governed by the following equations:

$$\bar{F}_1(t) = -\frac{1}{\nu}\,\bar{R}_1^2(t)\,(\bar{E}^* d\bar{R}_1)(t) \quad (58)$$

$$\bar{T}_2(t) = -\frac{1}{\nu}\,\bar{R}_2^2(t)\,(\bar{E}^* d\bar{R}_2)(t) \quad (59)$$

$$\bar{N}_2'(t) = \frac{\bar{R}_2^4(t)\cos\alpha_2(t)}{4\bar{r}_2(t)}\left\{\left[\frac{\cos\alpha_2(t)}{1+\nu}\right]\left(\bar{E}^* d\left[\frac{\sin\alpha_2\cos\alpha_2}{\bar{r}_2}\right]\right)(t) - \sin\alpha_2(t)\left(\bar{E}^* d\left[\frac{\cos^2\alpha_2}{\bar{r}_2}\right]\right)(t)\right\} \quad (60)$$

$$\bar{G}_2'(t) = \frac{\bar{R}_2^4(t)}{4}\left(\bar{E}^* d\left[\frac{\cos^2\alpha_2}{\bar{r}_2}\right]\right)(t) \quad (61)$$

$$\bar{H}_2(t) = \frac{\bar{R}_2^4(t)}{4(1+\nu)}\left(\bar{E}^* d\left[\frac{\sin\alpha_2\cos\alpha_2}{\bar{r}_2}\right]\right)(t) \quad (62)$$

$$\bar{T}_3(t) = -\frac{1}{\nu}\,\bar{R}_3^2(t)\,(\bar{E}^* d\bar{R}_3)(t) \quad (63)$$

$$\bar{N}_3'(t) = \frac{\bar{R}_3^4(t)\cos\alpha_3(t)}{4\bar{r}_3(t)}\left\{\left[\frac{\cos\alpha_3(t)}{1+\nu}\right]\left(\bar{E}^* d\left[\frac{\sin\alpha_3\cos\alpha_3}{\bar{r}_3}\right]\right)(t) - \sin\alpha_3(t)\left(\bar{E}^* d\left[\frac{\cos^2\alpha_3}{\bar{r}_3}\right]\right)(t)\right\} \quad (64)$$

$$\bar{G}_3'(t) = \frac{\bar{R}_3^4(t)}{4}\left(\bar{E}^* d\left[\frac{\cos^2\alpha_3}{\bar{r}_3}\right]\right)(t) \quad (65)$$

$$\bar{H}_3(t) = \frac{\bar{R}_3^4(t)}{4(1+\nu)}\left(\bar{E}^* d\left[\frac{\sin\alpha_3\cos\alpha_3}{\bar{r}_3}\right]\right)(t) \quad (66)$$

$$\phi = \bar{F}(t) - \{\bar{F}_1(t) + 6[\bar{T}_2(t)\sin\alpha_2(t) + \bar{N}_2'(t)\cos\alpha_2(t)] + 12[\bar{T}_3(t)\sin\alpha_3(t) + \bar{N}_3'(t)\cos\alpha_3(t)]\} \quad (67)$$

$$\bar{M}(t) = 6[\bar{H}_2(t)\sin\alpha_2(t) + \bar{G}_2'(t)\cos\alpha_2(t) + \bar{T}_2(t)\bar{r}_2(t)\cos\alpha_2(t) - \bar{N}_2'(t)\bar{r}_2(t)\sin\alpha_2(t)] + 12[\bar{H}_3(t)\sin\alpha_3(t) + \bar{G}_3'(t)\cos\alpha_3(t) + \bar{T}_3(t)\bar{r}_3(t)\cos\alpha_3(t) - \bar{N}_3'(t)\bar{r}_3(t)\sin\alpha_3(t)]. \quad (68)$$

When the external force, $F(t)$, and a boundary condition such as no end rotation are applied at $t = 0$, the instantaneous response at $t = 0^+$ is elastic.

In order to find the correct value for $\bar{R}(0^+)$ in Eqs. (58)–(66) and (68), an iterative method must be used to satisfy Eq. (67). A modified Newton's iterative method is employed. This method uses three values of $\bar{R}(0^+)$. These are $\bar{R}_i(0^+)$, $\bar{R}_i(0^+) - \Delta$ and $\bar{R}_i(0^+) + \Delta$, where Δ is a small number. From these values the corresponding terms ϕ_1, ϕ_2, and ϕ_3 can be calculated. The derivative $d\phi/d\bar{R}$ at $\bar{R}(0^+) = \bar{R}_i(0^+)$ can be approximated by using a central difference equation

$$\phi' = \left.\frac{d\phi}{d\bar{R}}\right|_{\bar{R}=\bar{R}_i} = \frac{1}{2\Delta}\,(\phi_3 - \phi_2). \quad (69)$$

Newton's iterative formula can be used to determine a new value for $\bar{R}(0^+)$ which is

$$\bar{R}_{i+1} = \bar{R}_i - \frac{\phi_1(0^+)}{\phi'} = \frac{2\Delta\phi_1(0^+)}{\phi_3(0^+) - \phi_2(0^+)} \quad (70)$$

This technique is used until $\phi_1(0^+) \approx 0$. When this value is arrived at, the corresponding value for $\bar{R}(0^+)$ is used to determine the loads and moments at $t = 0^+$.

Once the filaments in a strand are deformed into a new helical configuration by this elastic response, they continue to vary with respect to loading and deformation over time, depending on the viscoelastic properties of the strand's construction material. This time-dependent behavior can be closely approximated by using a numerical integration technique developed by Lee and Rogers (1963) which evaluates the hereditary integral introduced in Eq. (38). This technique uses the equation

$$\int_0^t \bar{E}(t-t_1)\dot{f}(t_1)dt_1 = S_N + \frac{1}{2}\,[1 + \bar{E}(t_N - t_{N-1})]f(t_N) \quad (71)$$

where

$$S_N = \bar{E}(t_N)[f(0^+) - f_0] - \frac{1}{2}\,[1 + \bar{E}(t_N - t_{N-1})]f(t_{N-1}) \times \frac{1}{2}\sum_{i=0}^{N-2}\{[\bar{E}(t_N - t_{i+1}) + \bar{E}(t_N - t_i)][f(t_{i+1}) - f(t_i)]\}. \quad (72)$$

In this numerical scheme the time, t, is divided into N intervals where t_0 is the time of the initial elastic response and t_N is the time when the viscoelastic response is to be evaluated. Also, f is the function that is differentiated with respect to time in Eqs. (42)–(49). At each step in the time interval, a value for the convolution integral is determined from this

Downloaded 03 May 2010 to 171.66.16.245. Redistribution subject to ASME license or copyright; see http://www.asme.org/terms/Terms_Use.cfm

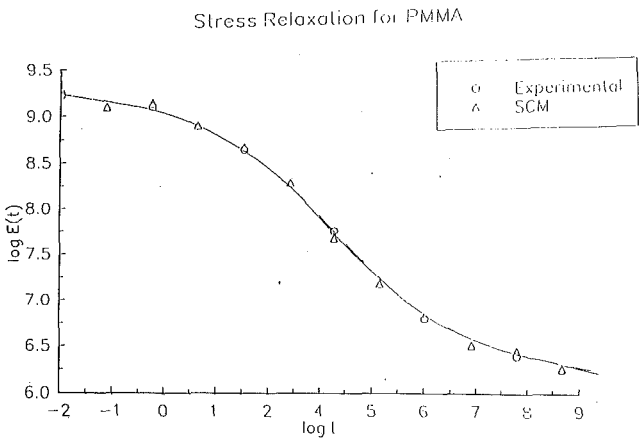


Fig. 5 Stress relaxation for polymethyl methacrylate (Lee and Rogers, 1963)

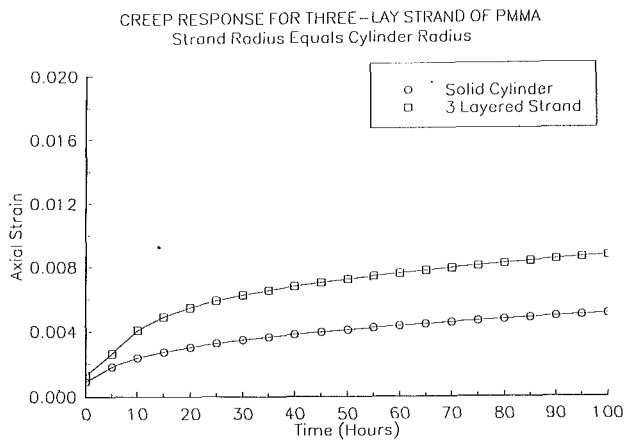


Fig. 6 Creep response for three-layer strand of PMMA

method. This value is used to determine values for $\overline{N}_2'(t)$, $\overline{N}_3'(t)$, $\overline{T}_2(t)$, and $\overline{T}_3(t)$ from Eqs. (46)–(49). $\overline{N}_2'(t)$, $\overline{N}_3'(t)$, $\overline{T}_2(t)$, and $\overline{T}_3(t)$ are then placed in Eq. (67). If ϕ is not less than some prescribed value, the modified Newton's iterative method is used to evaluate a $\overline{R}_i(t)$ which will satisfy the conditions for ϕ. Once a value for $\overline{R}_i(t)$ is determined, $\alpha_2(t)$ and $\alpha_3(t)$ can be calculated from Eqs. (18) and (19). These can then be used to determine $\overline{F}_1(t)$, $\overline{T}_2(t)$, $\overline{T}_3(t)$, $\overline{N}_2'(t)$, $\overline{N}_3'(t)$, $\overline{G}_2'(t)$, $\overline{G}_3'(t)$, $\overline{H}_2(t)$, $\overline{H}_3(t)$, $\overline{M}_2(t)$, $\overline{M}_3(t)$, and $\epsilon_1(t)$ from Eqs. (58)–(66) and (68), for the specific time interval from which $\overline{R}_i(t)$ was evaluated. This iterative technique must then be used at each time interval in order to describe, satisfactorily, the viscoelastic response for the strand.

Strand Response for a Particular Viscoelastic Material

In order to determine the time-dependent response of a polymer strand, a viscoelastic material must be chosen. This material must have a linear stress-strain relationship in the Laplace transform space since the correspondence principle in viscoelasticity is used in the subsequent analysis. A material which meets this criterion is polymethyl methacrylate (PMMA). The modulus relaxation is shown in Fig. 5. Also in this figure is the corresponding theoretical curve determined from the Schapery collocation method. As discussed previously, the Wierchert model is used in the prediction of this theoretical curve. For good correlation between the experimental data for PMMA and the theoretical results, ten Maxwell elements are required along with a spring in parallel. The relaxation modulus equation is thus

$$E(t) = 2.24\times10^6 + 1.60\times10^9 e^{(-t/0.01)} - 7.01\times10^8 e^{(-t/0.1)} + 9.65\times10^8 e^{(-t)} + 4.36\times10^8 e^{(-t/10)} + 4.12\times10^8 e^{(-t/100)} + 2.47\times10^8 e^{(-t/1000)} + 4.98\times10^7 e^{(-t/10000)} + 1.27\times10^7 e^{(-t/100000)} + 5.85\times10^6 e^{(-t/1000000)} + 1.94\times10^6 e^{(-t/100000000)} \quad (73)$$

where at $t > 10^9$ hours, $E(t) \sim 10^{6.35}$ Newtons/m^2.

Once the relaxation modulus is closely approximated numerically, the creep response for a solid cylindrical rod and a three-layer strand with equal diameters can be computed. Figure 6 shows a comparison of axial strain versus time for both the rod and the strand, where each have an overall initial diameter of 9.6463 cm, a Poisson's ratio of 0.45, and a total axial load of 2×10^4 Newtons. The second and third layers of filaments for the strand have helix angles of 75 deg and 100 deg, respectively. Also, the second and third-layer filament diameters are 1.94 cm and 1.8818 cm, respectively. This difference in diameters ensures that during deformation the resultant contact loads are not influenced by a filament significantly touching another in the same layer. The instantaneous jump in strain at $t = 0^+$ is, again, caused by the initial elastic response of the material. Both strains asymptotically approach an equilibrium value corresponding to the delayed time modulus for PMMA of $10^{6.35}$ Newtons/m^2, shown in Fig. 5.

Other time-dependent geometric relationships including helix angles and helix radii in the three layer strand also show the asymptotic approach equilibrium values. The helix angle of the second layer of filaments increases while the helix angle of the third layer decreases. The helix radii for each layer of filaments decreases with respect to time. The results are consistent with those expected for the creep response of the strand.

The shear loads for each filament decrease over time, while the axial loads remain relatively constant. This is due to the large helix angles for each layer resulting in relatively small shear load components for the filaments in those layers. As the filaments straighten out during the creep response, the shear load components are transferred to the axial load components. The shear loads are, however, three to four orders of magnitude less than the axial loads and produce no significant addition to the axial load components with respect to time. This time-dependent behavior is also observed with respect to the bending and twisting components of the imposed moments for the filaments in each layer of the strand.

Summary and Conclusions

An analytical method is presented for determining various mechanical properties of a multilayer strand. Specifically, a three-layer strand is analyzed; however, the technique developed can be used for any strand with concentric layers of filaments with circular cross-sections. The mechanical properties that are determined include the overall axial, time-dependent strain of the strand as well as the internal time-dependent, geometric and loading variations. The internal construction parameters of the strand are also incorporated in this model.

The mechanical stress-strain relationship for a linear viscoelastic solid is modeled by combining linear springs and dashpots into what is known as the Wiechert model. The parameters for this time-dependent model are determined for a specific linear viscoelastic material, polymethyl methacrylate (PMMA), by using the Schapery collocation method. A numerical integration technique is then introduced to solve a convolution integral which developed, as a result of the correspondence principle of linear viscoelasticity, from the inverse Laplace transform of the elastic solution for a multilayer strand. This integration technique is combined with a modified Newton's iterative technique to solve the time-dependent, geometric, and loading relationships in the strand.

Downloaded 03 May 2010 to 171.66.16.245. Redistribution subject to ASME license or copyright; see http://www.asme.org/terms/Terms_Use.cfm

This modeling and analysis approach is useful in that it incorporates the strand's actual geometry as opposed to an idealized geometric model. Further, this approach utilizes the construction material's mechanical properties as described by linear viscoelastic theory. The authors' efforts represent an initial attempt to develop a theory which predicts, within limits, the time-dependent mechanical response of a helically twisted polymer cord. Since this is an initial attempt to develop an useful theory, the effects of friction and material compliance are ignored. The authors are aware that these first-order effects are quite important in the realistic description of a cord's response to loading and will incorporate them in the subsequent development of the theory for polymer cords.

Acknowledgments

TAC acknowledges, with thanks, the State of Ohio: Board of Regents (Grant FRG #1208) for its support.

References

Bland, D. R., 1960, *The Theory Of Linear Viscoelasticity*, Pergamon Press, New York, Chapter 1.

Conway, T. A., and Costello, G. A., 1991, "Response Of A Strand With Elliptical Outer Wires," *International Journal Of Solids and Structures*, Vol. 28, No. 1, pp. 33–42.

Conway, T. A., and Costello, G. A., 1993a, "Time-Dependent Response Of A Three Filament Cord," *Journal of Engineering Mechanics*, ASCE, Vol. 119, No. 4, pp. 833–849.

Conway, T. A., and Costello, G. A., 1993b, "Viscoelastic Response Of A Simple Strand," *International Journal of Solids and Structures*, Vol. 30, No. 4, pp. 553–567.

Costello, G. A., 1990, *Theory of Wire Rope*, Springer-Verlag, New York, Chapters 1–4.

Hearle, J. W. S., Grosberg, P., and Backer, S., 1969, *Structural Mechanics of Fibers, Yarns, and Fabrics*, John Wiley and Sons, New York, Chapter 4.

Lee, E. H., and Rogers, T. G., 1963, "Solution Of Viscoelastic Stress Analysis Problems Using Measured Creep Or Relaxation Functions," ASME JOURNAL OF APPLIED MECHANICS, Vol. 33, pp. 127–133.

Tschoegl, N. W., 1989, *The Phenomenological Theory Of Linear Viscoelastic Behavior*, Springer-Verlag, New York, Sections 2.0, 3.6 and 11.4.

Downloaded 03 May 2010 to 171.66.16.245. Redistribution subject to ASME license or copyright; see http://www.asme.org/terms/Terms_Use.cfm

Multiply Loaded Timoshenko Beam on a Stressed Orthotropic Half-Plane via a Thin Elastic Layer

H. Bjarnehed
Research Associate,
Division of Solid Mechanics,
Chalmers University of Technology,
S-412 96 Göteborg, Sweden

The problem of bonded contact between a uniform finite Timoshenko beam and an orthotropic half-plane via a thin elastic layer is considered in this paper. The beam is loaded by distributions of normal and tangential forces, and a uniaxial stress load is applied to the half-plane. The Timoshenko beam theory is extended in such a way that the tangential load is included when the shear contribution to the beam central line deflection is calculated. The layer is formulated as a generalized Winkler cushion including also shear stresses and strains. Governing singular integral equations are stated and numerically solved for the unknown interface stresses. A comparison with a corresponding FE-model is also performed.

1 Introduction

The background of the title problem is a steel clamping joint attached in the middle of a composite truck leaf spring, which consists of a glass fiber-reinforced polymer. The clamping joint transmits a number of loads to the leaf spring. First, the joint is preloaded by a clamping force. Second, a vertical force, a horizontal force, and a tilting moment from the wheel axle are transmitted to the leaf spring. Cracks and delaminations have been observed in the clamped region, and wear has been detected in the contact area of such springs used under running conditions.

The steel clamps and the composite beam form sharp corners at the ends of the interfaces of contact. It is a well-known theoretical result that the stresses reach infinite values at interface corners between elastic bodies in contact (Bogy and Wang, 1971). It is of main interest, therefore, to reduce the effect of these very high local interface stresses. In order to protect the composite beam from wear, thin polymer layers have been glued on to the composite at the area of contact. However, these thin layers will also affect the distribution of the interface stresses in a favorable way.

In this study the contact is modeled as a generalized finite Timoshenko beam (steel clamp) pressed onto an orthotropic half-plane (composite leaf spring) via a thin generalized Winkler cushion (polymer layer) as shown in Fig. 1. The Timoshenko beam theory used here includes not only bending and shear deformations (where effects of both normal and tangential load are considered) but also axial deformation due to the significant tangential load. The elastic cushion, which is made up of non interacting springs, can transmit both normal and shear stresses. In addition to the loads mentioned above there is a load of uniform stress applied to the half-plane (representing bending stress at the surface of the leaf spring). In a paper by Bjarnehed (1992) the above model was studied for the case of a rigid beam. Among other results was shown the levelling effect of a soft cushion on the interface stress distribution. The generalized Winkler model of the thin layer was verified through a corresponding FEM comparison.

Problems concerning the contact between a beam and an elastic foundation are well represented in the literature. The frictionless receding contact between a transversely loaded finite Timoshenko beam and an elastic layer, including half-plane formulation, was studied by Li and Dempsey (1988). Some of their conclusions are that the influence of shear deformations is significant when concentrated loads are dominant and/or the beam is very flexible. Large values of the shear

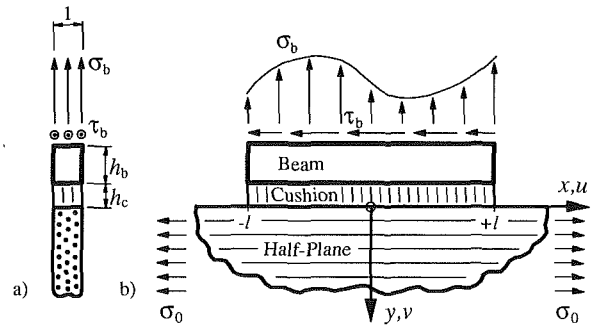


Fig. 1 Timoshenko beam on orthotropic half-plane via thin elastic cushion; (*a*) side view; (*b*) front view. The beam shown here has a rectangular cross-section with thickness $b \equiv 1$.

Contributed by the Applied Mechanics Division of THE AMERICAN SOCIETY OF MECHANICAL ENGINEERS for presentation at the First Joint ASCE-EMD, ASME-AMD, SES Meeting, Charlottesville, VA, June 6–9, 1993.

Discussion on this paper should be addressed to the Technical Editor, Professor Lewis T. Wheeler, Department of Mechanical Engineering, University of Houston, Houston, TX 77204-4792, and will be accepted until four months after final publication of the paper itself in the ASME JOURNAL OF APPLIED MECHANICS.

Manuscript received by the ASME Applied Mechanics Division, Nov. 11, 1991; final revision, June 8, 1992. Associate Technical Editor: G. J. Dvorak.
Paper No. 93-APM-14.

Copyright © 1993 by ASME
Downloaded 03 May 2010 to 171.66.16.245. Redistribution subject to ASME license or copyright; see http://www.asme.org/terms/Terms_Use.cfm

coefficient (Section 3) increase the displacement and contact pressure under a concentrated load but they reduce the maximum bending moment there. Mourelatos and Parsons (1987) made a finite element analysis of transversely and axially loaded beams on elastic foundations including shear and axial effects. The axial load considered is either a constant tensile or compressive force. The importance of shear effects was concluded from an agreement with the results of the above paper by Li and Dempsey (1988). The axial effect was found to be of great importance when the compressive axial load is of the same order of magnitude as the critical (buckling) load. Naturally, the above effects are decreasing with increasing the elastic foundation stiffness.

2 Problem Statement

Consider the orthotropic homogeneous elastic half-plane in Fig. 1. The principal directions of elasticity are parallel and perpendicular to the horizontal edge. The half-plane edge is in contact with a generalized uniform finite Timoshenko beam, with doubly symmetric cross-section, via a thin elastic cushion. The beam is loaded normally (σ_b) and tangentially (τ_b) on its upper face. In addition there is a load of uniform stress (σ_0) in the half-plane, applied in the x-direction. The length of the beam and the cusion is $2l$ and their heights are h_b and h_c, respectively, as specified in Fig. 1. The cushion and the half-plane have unit thickness while the beam is assumed to have a doubly symmetric cross-section with the dimensionless thickness b (related to the unit thickness). Further, it is assumed that the cushion is bonded to the beam as well as to the half-plane. The problem consists in finding the interface stresses and the beam deflection for different combinations of material parameters, geometry, and loads. Naturally the beam cross-sectional stresses, internal half-plane stresses, and half-plane surface displacements are also of interest.

3 Governing Equations

3.1 Basic Equations. Coupled singular integral equations relating the surface stresses (σ_h, τ_h) to the surface displacements (u_h, v_h), see Figs. 2a and 2b, respectively, in the half-plane region $|x| \le l$ can be derived either by means of Fourier transforms (Bjarnehed, 1991) or by using complex analysis (Muskhelishvili, 1949). They read (with $\int$ denoting the principal value of the integral)

$$\int_{-l}^{l} \frac{\tau_h(t)}{x-t}\,dt = -\nu'\sigma_h(x) + E'\frac{du_h}{dx} - \nu_0\sigma_0,$$

$$\int_{-l}^{l} \frac{\sigma_h(t)}{x-t}\,dt = \nu''\tau_h(x) + E''\frac{dv_h}{dx}. \qquad (1a,b)$$

The orthotropic material parameters ν', E', ν'', E'', and ν_0 are defined in Appendix A.

The thin cushion is modeled as a system of an infinite number of linearly elastic springs. It can be considered as an elastic continuum with both normal (E_c) and shear (G_c) stiffness but without any interaction between individual springs (Bjarnehed, 1992). Therefore, the following strain-stress relations are ascribed to the cushion ($|x| \le l$)

$$\gamma_c = \frac{u_h(x) - u_b(x) - \delta_x}{h_c} = \frac{\tau_h(x)}{G_c},$$

$$\epsilon_c = \frac{v_h(x) - v_b(x) - \delta_y}{h_c} = \frac{\sigma_h(x)}{E_c}, \qquad (2a,b)$$

where δ_x and δ_y denote the rigid body displacements of the beam in the directions of x and y, respectively. The displacements u_b and v_b are defined in Fig. 2(b) and specify the displacements of the lower beam face (and the upper cushion face).

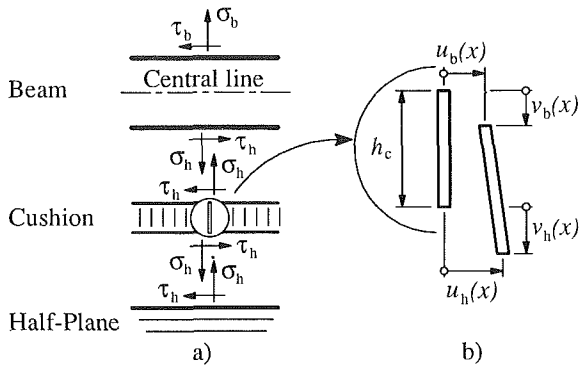


Fig. 2 Definition of beam/cushion and cushion/half-plane interface (*a*) stresses and (*b*) displacements

The governing differential equations, used in this study, of a Timoshenko beam are

$$\frac{du_b}{dx} = \frac{M(x)}{E_bS} + \frac{N(x)}{E_bA}, \quad \frac{d^2v_b}{dx^2} = -\frac{M(x)}{E_bI} + \frac{f_1}{G_bA}\frac{dT}{dx}, \qquad (3a,b)$$

where M, T, and N are the beam cross-sectional bending moment, shear force, and axial force, respectively. The quantities I, $S = I/(h_b/2)$, and A denote the moment of inertia, the section modulus, and the area of the beam cross-section, respectively. The elastic and shear modulus of the beam are specified by E_b and G_b, respectively, and f_1 is a numerical factor for shear due to normal loading (see Appendix B). In (3a), both bending and stretching effects are included when the tangential displacement of the lower beam face is calculated. It should be noted that all material points on a beam cross-section are assumed to have the same vertical deflection v_b, i.e., the central line and the lower face of the beam will have the same deflection v_b. On the other hand, to obtain the curvature of the central line in regions with high gradients of tangential loading τ_b a term of correction will be added. Thus, during such conditions the curvature of the central line is assumed to be

$$\frac{d^2v_b^{\text{cent}}}{dx^2} = \frac{d^2v_b}{dx^2} - \frac{f_2}{G_b}\frac{d}{dx}\frac{(\tau_h+\tau_b)}{2}, \qquad (3c)$$

where f_2 is a numerical factor for shear due to tangential loading (see Appendix B). The shear contributions to the beam curvature in (3b, c) are derived in Appendix B. Equilibrium of the beam give the following three equations valid for $|x| \le l$

$$M(x) = -\int_x^l (t-x)[\sigma_h(t) - \sigma_b(t)]dt + \frac{h_b}{2}\int_x^l [\tau_h(t) + \tau_b(t)]dt, \qquad (4a)$$

$$T(x) = \int_x^l [\sigma_h(t) - \sigma_b(t)]dt, \quad N(x) = \int_x^l [\tau_h(t) - \tau_b(t)]dt. \qquad (4b,c)$$

Notice the shear stress contribution to the beam cross-sectional moment.

3.2 Singular Integral Equations. First, substitute u_h, v_h in Eqs. (2) into Eqs. (1). Second, put M, T, N in Eqs. (4) into Eqs. (3a, b), thus obtaining

$$\int_{-l}^{l} \frac{\tau_h(t)}{x-t}\,dt = -\nu'\sigma_h(x) + \frac{h_c}{G_c/E'}\frac{d\tau_h}{dx} + E'\frac{du_b}{dx} - \nu_0\sigma_0, \qquad (5a)$$

$$\int_{-l}^{l} \frac{\sigma_h(t)}{x-t}\,dt = \nu''\tau_h(x) + \frac{h_c}{E_c/E''}\frac{d\sigma_h}{dx} + E''\frac{dv_b}{dx}, \qquad (5b)$$

Downloaded 03 May 2010 to 171.66.16.245. Redistribution subject to ASME license or copyright; see http://www.asme.org/terms/Terms_Use.cfm

$$\frac{du_b}{dx} = -\int_x^l (t-x)\,\frac{\sigma_h(t)-\sigma_b(t)}{E_bS}\,dt + \int_x^l \frac{\tau_h(t)+\tau_b(t)}{E_bW}\,dt + \int_x^l \frac{\tau_h(t)-\tau_b(t)}{E_bA}\,dt, \quad (5c)$$

$$\frac{d^2v_b}{dx^2} = \int_x^l (t-x)\,\frac{\sigma_h(t)-\sigma_b(t)}{E_bI}\,dt - \int_x^l \frac{\tau_h(t)+\tau_b(t)}{E_bS}\,dt - f_1\,\frac{\sigma_h(x)-\sigma_b(x)}{G_bA}, \quad (5d)$$

where $W = S/(h_b/2)$. The stated problem is reduced to finding the solution of (5), i.e., the distributions of σ_h, τ_h, du_b/dx, and dv_b/dx.

3.3 Nonsingular Integral Equations. It is convenient here to divide the problem into one symmetrical and one antisymmetrical case of loading with respect to the y-axis. We can then formulate and solve the stated problem separately for the two cases of loading and hence it is only necessary to define the Eqs. (5) in the region $0 \le x \le l$. The symmetrical case of loading is represented by the load pair σ_b^s, τ_b^a and the antisymmetrical by σ_b^a, τ_b^s. The superscripts s and a specify the *s*ymmetry and the *a*ntisymmetry, respectively, of the quantity with respect to the y-axis.

To get equations suitable for numerical solution we transform (5*a*, *b*) into coupled nonsingular integrals equations of the Volterra type (Mikhlin, 1957). Therefore, write z for x and apply the operators

$$\bar{f}_1(x) = \int_0^x \sqrt{x^2-z^2}\,f(z)dz \text{ and } \bar{f}_2(x) = \int_0^x z\sqrt{x^2-z^2}\,f(z)dz$$

first, to (5*a*, *b*), respectively. We then obtain (6*a*, *c*) which are valid for the symmetrical case of loading. Second, apply the operators to (5*b*, *a*), respectively, and we get (6*b*, *d*) for the antisymmetrical case of loading. In the derivation of (6*a*–*d*) the symmetrical or the antisymmetrical property of a quantity is used; e.g., $\sigma^s(x) = \sigma(x) = \sigma(-x)$ and $\tau^a(x) = \tau(x) = -\tau(-x)$, thus

$$-\frac{\nu'}{\pi}\int_0^X \begin{Bmatrix}\Phi p^s\\ \Psi p^a\end{Bmatrix} dT - \frac{H_c}{\pi g_c'}\int_0^X \begin{Bmatrix}q^a\\ q^s\end{Bmatrix}\frac{\partial}{\partial T}\begin{Bmatrix}\Phi\\ \Psi\end{Bmatrix} dT + \int_0^1 \begin{Bmatrix}\Gamma q^a\\ \Lambda q^s\end{Bmatrix} dT + \int_0^X \begin{Bmatrix}\Phi U^s\\ \Psi U^a\end{Bmatrix} dT = \frac{X^2}{2}\begin{Bmatrix}\nu_0 p_0/2\\ 1\end{Bmatrix}, \quad \begin{matrix}(6a)\\(6b)\end{matrix}$$

$$\frac{\nu''}{\pi}\int_0^X \begin{Bmatrix}\Psi q^a\\ \Phi q^s\end{Bmatrix} dT - \frac{H_c}{\pi e_c''}\int_0^X \begin{Bmatrix}p^s\\ p^a\end{Bmatrix}\frac{\partial}{\partial T}\begin{Bmatrix}\Psi\\ \Phi\end{Bmatrix} dT + \int_0^1 \begin{Bmatrix}\Lambda p^s\\ \Gamma p^a\end{Bmatrix} dT + \int_0^X \begin{Bmatrix}\Psi V^a\\ \Phi V^s\end{Bmatrix} dT = \frac{X^2}{2}\begin{Bmatrix}1\\ 0\end{Bmatrix}. \quad \begin{matrix}(6c)\\(6d)\end{matrix}$$

The equations (5*c*,*d*) are already nonsingular integral equations of the Volterra type and consequently not in need to be transformed. However, (5*d*) must be integrated with respect to x and, as in (6*a*–*d*), we will introduce dimensionless quantities in (5*c*,*d*). Thus

$$\pi U = -\int_X^1 (T-X)\,\frac{p-\hat{p}}{e_b' s}\,dT + \int_X^1 \frac{q+\hat{q}}{e_b' w}\,dT + \int_X^1 \frac{q-\hat{q}}{e_b' a}\,dT, \quad (6e)$$

$$\pi V^a = -\pi\,\frac{e_b' s}{e_b'' i}\int_0^X U^s dT + \frac{s}{a}\int_0^1 \Theta\,\frac{q^a-\hat{q}^a}{e_b'' i}\,dT - f_1\int_0^X \frac{p^s-\hat{p}^s}{g_b'' a}\,dT, \quad (6f)$$

$$\pi V^s = -\int_0^1 \Omega\,\frac{p^a-\hat{p}^a}{e_b'' i}\,dT + \int_0^X (X-T)\,\frac{q^s+\hat{q}^s}{e_b'' s}\,dT - f_1\int_0^X \frac{p^a-\hat{p}^a}{g_b'' a}\,dT + C_0. \quad (6g)$$

Here the following relations hold:

$$\begin{Bmatrix}\Phi\\ \Psi\end{Bmatrix} = \begin{Bmatrix}1\\ T\end{Bmatrix}\sqrt{X^2-T^2}, \qquad \begin{Bmatrix}\Gamma\\ \Lambda\end{Bmatrix} = \begin{Bmatrix}1\\ T\end{Bmatrix}\left[T - H(T-X)\sqrt{T^2-X^2}\right], \quad \begin{matrix}(7a,b)\\(7c,d)\end{matrix}$$

$$\begin{Bmatrix}\Theta\\ \Omega\end{Bmatrix} = X\begin{Bmatrix}1\\ X/2\end{Bmatrix}H(T-X) + T\begin{Bmatrix}1\\ X-T/2\end{Bmatrix}H(X-T), \qquad C_0 = \pi V^s(0), \quad \begin{matrix}(7e,f)\\(7g)\end{matrix}$$

where H is the Heaviside unit step function. The unknown quantities p, q, U, and V are functions of T and read

$$\begin{Bmatrix}p^s, \hat{p}^s\\ q^a, \hat{q}^a\end{Bmatrix} = \begin{Bmatrix}\sigma_h^s, \sigma_b^s\\ \tau_h^a, \tau_b^a\end{Bmatrix}\frac{1}{(-P/2l)}, \qquad \begin{Bmatrix}U^s\\ V^a\end{Bmatrix} = \frac{d}{dt}\begin{Bmatrix}E' u_b^a\\ E'' \nu_b^s\end{Bmatrix}\frac{1/(\pi l)}{(-P/2l)}, \quad \begin{matrix}(8a,b)\\(8c,d)\end{matrix}$$

$$\begin{Bmatrix}p^a, \hat{p}^a\\ q^s, \hat{q}^s\end{Bmatrix} = \begin{Bmatrix}\sigma_h^a, \sigma_b^a\\ \tau_h^s, \tau_b^s\end{Bmatrix}\frac{1}{(-F/2l)}, \qquad \begin{Bmatrix}U^a\\ V^s\end{Bmatrix} = \frac{d}{dt}\begin{Bmatrix}E' u_b^s\\ E'' \nu_b^a\end{Bmatrix}\frac{1/(\pi l)}{(-F/2l)}, \quad \begin{matrix}(9a,b)\\(9c,d)\end{matrix}$$

Furthermore,

$$P = -2\int_0^l \sigma_b^s(t)dt, \quad F = -2\int_0^l \tau_b^s(t)dt, \quad p_0 = \frac{\sigma_0}{(-P/2l)}, \quad (10a\text{–}c)$$

$$i = I/l^3, \quad s = S/l^2, \quad w = W/l, \quad a = A/l, \quad H_c = h_c/l, \quad X = x/l, \quad T = t/l, \quad (11a\text{–}g)$$

$$g_c' = G_c/E', \quad e_c'' = E_c/E'', \quad e_b' = E_b/E', \quad e_b'' = E_b/E'', \quad g_b'' = G_b/E''. \quad (12a\text{–}e)$$

Finally, we have two sets of equations valid in the region $0 \le X \le 1$, i.e., (6*a*,*c*,*e*,*f*) and (6*b*,*d*,*e*,*g*) for the symmetrical and antisymmetrical case of loading, respectively. As it appears these two sets of equations have (6*e*) in common. This is due to the fact that (6*e*) includes the end boundary conditions of the beam $M(1) = T(1) = N(1) = 0$ which is in common for these two solutions. The solution of the antisymmetrical case of loading contains a contribution from a bending point moment at the middle of the beam central line. The value of this point moment is controlled by the parameter C_0 in (6*g*). These two sets of equations include the following (boundary) conditions:

	Symmetrical loading	Antisymmetrical loading
$X=0$:	$q=0,\ V=0,\ T=0,$	$p=0,\ U=0,\ N=0,$
$X=1$:	$M=0,\ T=0,\ N=0.$	$M=0,\ T=0,\ N=0.$

Equations (6) are solved numerically for the unknowns p, q, U, and V by the method described in Appendix C.

4 Numerical Results

The numerical solutions of the symmetric case of loading (6*a*,*c*,*e*,*f*) and of the antisymmetric case of loading (6*b*,*d*,*e*,*g*) are here presented together with some results from corresponding FE-solutions. The numerical solutions of (6) give the in-

Downloaded 03 May 2010 to 171.66.16.245. Redistribution subject to ASME license or copyright; see http://www.asme.org/terms/Terms_Use.cfm

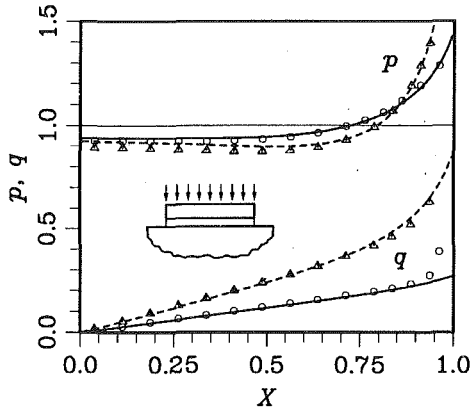


Fig. 3(*a*) Interface stress distributions in the interval $0 \le X \le 1$ for the symmetrical loading of a uniform pressure load $\hat{p}(|X| \le 1) \equiv$ constant. Solid and dotted lines represent $e_c = 2$ and $e_c = 10$, respectively. The markers indicate the FE-solution.

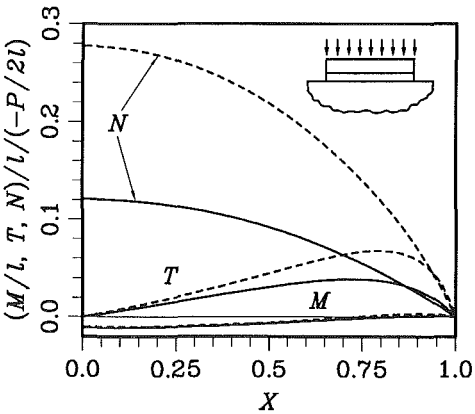


Fig. 3(*b*) Beam cross-sectional force distributions in the interval $0 \le X \le 1$ for the symmetrical loading of a uniform pressure load $\hat{p}(|X| \le 1) \equiv$ constant. Solid and dotted lines represent $e_c = 2$ and $e_c = 10$, respectively.

terface stresses and the deformation of the beam. As secondary results of (6), we obtain the beam cross-sectional forces calculated from (4*a*,*b*,*c*). The FE-code SOLVIA is used to compare the beam and cushion models of this paper with an FE-model where the beam and cushion are modelled as two-dimensional linear elastic continua. Only half of the beam, cushion, and half-plane is modeled due to either symmetry or antisymmetry with respect to the y-axis. The size of the half-plane model is chosen as $6l \times 6l$ where $2l$ is the extent of the beam and cushion. The half-plane boundary conditions used are consistent nodal forces corresponding to (a) symmetrical cases of loading: a uniform interface pressure distribution with resulting double unit vertical force; (*b*) antisymmetrical cases of loading: a uniform interface shear stress distribution with resulting double unit horizontal force and in addition a force couple with the resulting moment of $2 \times (H_b + H_c)$. These nodal forces are calculated on basis of the half-plane stresses presented in Appendix D.

All numerical calculations are performed with the assumption of plane stress. The half-plane parameters are kept constant during all calculations and have the following relations (using standard notation): $E_x/E_y = 5$, $E_y/G_{xy} = 2$, and $\nu_{xy} = 0.3$. The assumed relation between the cushion stiffnesses is $G_c = E_c/2(1 + \nu_c)$ where $\nu_c = 0.3$ is used throughout all calculations. The Winkler formulation of the cushion makes it convenient to introduce the following stiffness parameter: $e_c = (E_c/E_y)/H_c$.

The results from four different kinds of loading on the beam

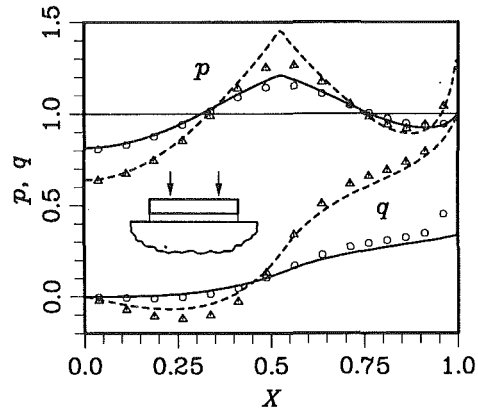


Fig. 4(*a*) Interface stress distributions in the interval $0 \le X \le 1$ for the symmetrical loading of normal point forces P at $|X| = 0.525$. Solid and dotted lines represent $e_c = 2$ and $e_c = 10$, respectively. The markers indicate the FE-solution.

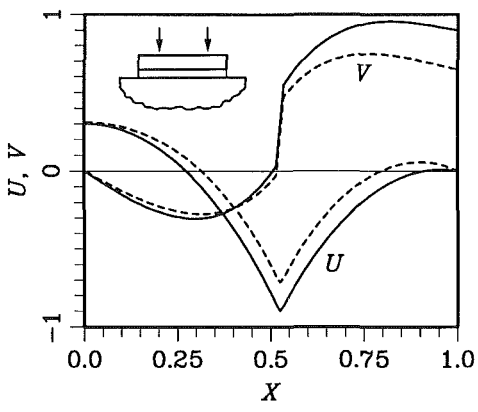


Fig. 4(*b*) Beam deformation distributions in the interval $0 \le X \le 1$ for the symmetrical loading of normal point forces P at $|X| = 0.525$. Solid and dotted lines represent $e_c = 2$ and $e_c = 10$, respectively.

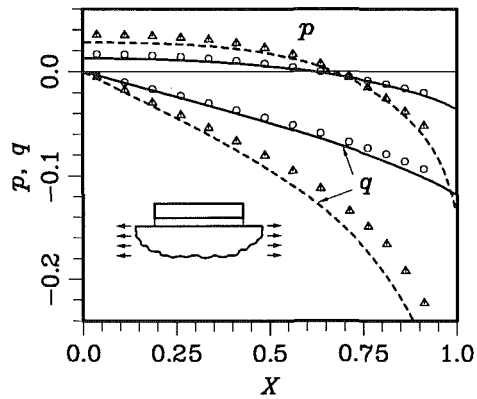


Fig. 5 Interface stress distributions in the interval $0 \le X \le 1$ for the symmetrical loading of a uniform half-plane stress load σ_0. Here p and q are normalized with respect to $-\sigma_0$. Solid and dotted lines represent $e_c = 2$ and $e_c = 10$, respectively. The markers indicate the FE-solution.

and half-plane are presented in Figs. 3–6. In these examples a beam with rectangular cross-section is used with $E_b/E_y = 21$, $\nu_b = 0.3$, $H_b = 0.2$, $b = 1$, and $f_1 = 6/5$ (calculated from (B5)). Furthermore, each quantity is calculated and plotted for two different values of e_c, viz. $e_c = 2$ (solid lines) and 10 (dotted lines). The FE-calculations are performed with the cushion thickness $H_c = 0.05$. The corresponding FE-solutions are indicated with markers.

In Fig. 7 is shown an example of a high gradient tangentially

Downloaded 03 May 2010 to 171.66.16.245. Redistribution subject to ASME license or copyright; see http://www.asme.org/terms/Terms_Use.cfm

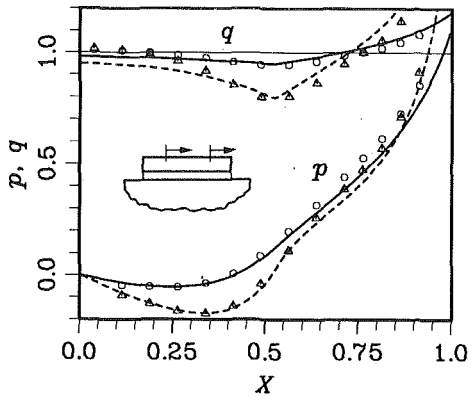


Fig. 6 Interface stress distributions in the interval $0 \le X \le 1$ for the antisymmetrical loading of shear point forces F at $|X| = 0.525$. Solid and dotted lines represent $e_c = 2$ and $e_c = 10$, respectively. The markers indicate the FE-solution.

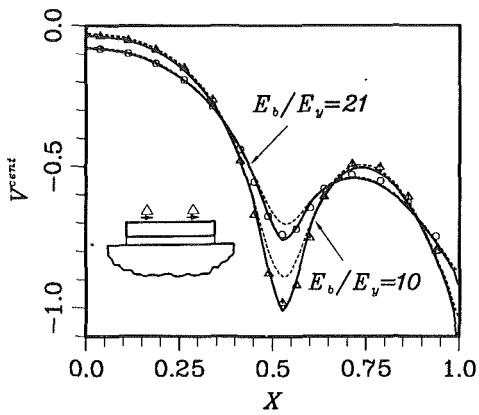


Fig. 7 The slope distribution of the beam central line in the interval $0 \le X \le 1$ for the antisymmetrical loading of a triangular shaped shear stress load in the region $0.45 \le |X| \le 0.6$. The solid and dotted lines are calculated with $f_2 = 0.125$ and $f_2 = 0$, respectively. The markers indicate the FE-solution.

loaded beam where the slope of the beam central line is calculated and plotted with (solid lines) and without (dotted lines) the term of correction in (3*c*). The slopes are plotted for two values of the beam stiffness, viz. $E_b/E_y = 21$ and 10. The beam has a rectangular cross-section with $H_b = 0.15$, $b = 1$, and the factors for shear used are $f_1 = 6/5$ and $f_2 = 0.125$.

5 Discussion

Consider the results for the normally loaded beam shown in Figs. 3–4. The interface shear stress distributions are relatively more sensitive to a change in the cushion stiffness e_c than the interface pressure distributions as shown in Figs. 3(*a*) and 4(*a*). This explains why a change in the cushion stiffness has a much stronger effect on the cross-sectional axial force distributions N than on the cross-sectional moment and shear force distributions, i.e., M and T, respectively (Fig. 3(*b*)).

The contributions from the cross-sectional moment and normal force to the lower beam face strain U are of the same order of magnitude for the case of uniform pressure load as shown in Fig. 3(*b*), especially for the stiffer cushion. Figure 4(*a*) shows that the presence of shear deformation due to normal loading (the f_1 term of (3*b*)) overestimates the pressure in regions close to the normal point force. The term of shear deformation also gives a step-like behavior of the beam slope distribution (V) under the normal point force (Fig. 4(*b*)).

The results from the pure loading of a uniform half-plane stress load σ_0 show that the interface shear stress is the dominating of the two interface stresses for this kind of loading (Fig. 5). This fact gives the axial force an exceptional position among the beam cross-sectional forces.

Then consider the tangential loading of the beam shown in Fig. 6. Both the interface shear and pressure distributions show a relatively low sensitivity to a change in cushion stiffness. This fact is reflected in a relatively small deviations of the cross-sectional forces due to a change in cushion stiffness.

Figure 7 shows that the presence of shear deformation due to tangential loading (the f_2 term in (3*c*)) gives a significant contribution to the slope of the beam central line in the region of high gradient tangential loading ($0.45 \le |X| \le 0.6$). The value $f_2 = 0.125$ is chosen in order to fit the FE-solution.

Due to the Winkler formulation of the cushion the interface stress distribution calculated from the theoretical model of this paper does not show the characteristic singular behavior at $X = 1$. On the other hand, in the corresponding FE-model, where the cushion is formulated as a two-dimensional elastic body, this singular behavior is present as indicated for example in Fig. 3(*a*). Other explanations to the deviations between the FE-solution and the solution of (6) can be the approximative values of the boundary forces used in the FE-model (see Section 4), and thus the fact that the interface shear stress distributions are very sensitive to small changes in boundary conditions as was found by Bjarnehed (1992).

Acknowledgments

I want to thank my supervisor Prof. J. Hult for helpful comments and discussions. This work was partially supported by the Product Development Division at Volvo Truck Corporation at Göteborg (Sweden), and by the Swedish National Board for Technical Development (STU) through the Project No. 722-88-02297.

References

Bjarnehed, H. L., 1991, "Rigid Punch on Stressed Orthotropic Half-Plane with Partial Slip," ASME JOURNAL OF APPLIED MECHANICS, Vol. 58, pp. 128–133; Erratum, ibid., Vol. 58, p. 565.

Bjarnehed, H. L., 1992, "Multiply Loaded Rigid Punch on a Stressed Orthotropic Half-Plane via a Thin Elastic Layer," ASME JOURNAL OF APPLIED MECHANICS, Vol. 59, pp. S115–S122.

Bogy, D. B., and Wang, K. C., 1971, "Stress Singularities at Interface Corners in Bounded Dissimilar Isotropic Elastic Materials," *International Journal of Solids and Structures*, Vol. 7, No. 8, pp. 993–1005.

Cowper, G. R., 1966, "The Shear Coefficient in Timoshenko's Beam Theory," ASME JOURNAL OF APPLIED MECHANICS, Vol. 33, pp. 335–340.

Gere, J. M., and Timoshenko, S. P., 1987, *Mechanics of Materials*, 2nd SI ed., Van Nostrand Reinhold Co. Ltd., London.

Lekhnitski, S. G., 1963, *Theory of Elasticity of an Anisotropic Elastic Body*, Moscow and Leningrad (English translation by P. Fern, Holden-Day).

Lekhnitski, S. G., 1968, *Anisotropic Plates* (English translation by S. W. Tsai and T. Cheron, Gordon and Breach).

Li, H., and Dempsey, J.P., 1988, "Unbounded Contact of Finite Timoshenko Beam on Elastic Layer," *Journal of Engineering Mechanics*, Vol. 114, No. 8, pp. 1265–1284.

Mikhlin, S. G., 1957, *Integral Equations*, 2nd ed., Leningrad (English translation by A. H. Armstrong, Pergamon Press).

Mourelatos, Z. P., and Parsons, M. G., 1987, "A Finite Element Analysis of Beams on Elastic Foundation including Shear and Axial Effects," *Computers & Structures*, Vol. 27, No. 3, pp. 323–331.

Muskhelishvili, N. I., 1949, *Some Basic Problems of the Mathematical Theory of Elasticity*, 3rd ed., Moscow (English translation by J. R. M. Radok, Nordhoff).

APPENDIX A

Material Parameters

The material parameters ν', E', ν'', E'', and ν_0, in the governing equations of the half-plane (1*a*, *b*), all depend on the orthotropic properties of the half-plane. However, Eqs. (1*a*, *b*) are applicable also for an isotropic half-plane. It is only a matter of difference in the material parameters. These parameters can, through their definition, be degenerated to material parameters valid for an isotropic half-plane. A derivation

Downloaded 03 May 2010 to 171.66.16.245. Redistribution subject to ASME license or copyright; see http://www.asme.org/terms/Terms_Use.cfm

of these orthotropic material parameters was made by Bjarnehed (1991) and discussed in more general terms in the paper by Bjarnehed (1992). They read

$$\nu' = \pi \frac{\alpha\beta c_{11} + c_{12}}{(\alpha+\beta)c_{11}}, \quad E' = \frac{\pi}{(\alpha+\beta)c_{11}},$$

$$\nu_0 = \frac{\pi}{\alpha+\beta}, \quad \frac{\nu'}{\nu''} = \frac{E'}{E''} = \alpha\beta, \qquad \text{(A1}a\text{–}e\text{)}$$

where

$$\alpha,\ \beta = \sqrt{\frac{c_{66}+2c_{12}}{2c_{11}} \pm \sqrt{\left(\frac{c_{66}+2c_{12}}{2c_{11}}\right)^2 - \frac{c_{22}}{c_{11}}}}, \qquad \text{(A2}a,b\text{)}$$

and c_{11}, c_{12}, c_{22}, and c_{66}, are the elastic constants in the generalized Hooke's law for an orthotropic medium, i.e.,

$$\epsilon_x = c_{11}\sigma_x + c_{12}\sigma_y, \quad \epsilon_y = c_{12}\sigma_x + c_{22}\sigma_y, \quad \gamma_{xy} = c_{66}\tau_{xy}. \qquad \text{(A3}a\text{–}c\text{)}$$

APPENDIX B

Shear Deformation of a Beam

Here we derive the shear contribution to the beam curvature in (3*b*, *c*) on basis of classical beam theory. The shear deformation of the beam considered in this paper is depending partly on the cross-sectional shear force and partly on the shear stress distributions on the upper and lower beam surfaces.

Longitudinal equilibrium of a segment of a beam lamella gives

$$\tau_{xy}(x, y) = \frac{1}{b(y)} \int_{A^*} \frac{\partial \sigma_a}{\partial x}\, dA + \frac{\tau_h(x)}{b(y)}, \qquad \text{(B1)}$$

where $A^*(y) = \int_y^{h_b/2} dA$, $b(y)$ is the dimensionless beam thickness related to unity thickness, and σ_a is the beam axial stress which for a transversely and longitudinally loaded uniform beam read

$$\sigma_a(x, y) = \frac{M(x)}{I} \cdot y + \frac{N(x)}{A}. \qquad \text{(B2)}$$

By substituting the differentiated Eq. (B2), with respect to x, into (B1) and then eliminating M and N with aid of Eqs. (4), we get the total shear stress distribution for the beam cross-section of a beam lamella, thus

$$\tau_{xy}(x, y) = \frac{T(x)Q(y)}{Ib(y)} + \left(1 - 2\frac{Q(y)}{S}\right) \cdot \frac{\tau_h(x) + \tau_b(x)}{2b(y)} + \left(1 - 2\frac{A^*(y)}{A}\right) \cdot \frac{\tau_h(x) - \tau_b(x)}{2b(y)}, \qquad \text{(B3)}$$

where $Q(y) = \int_{A^*} y dA$ is the first moment of the area A^* about the z-axis. The first two terms in (B3) are symmetrical and the third term is antisymmetrical with respect to the central line of the beam as shown in Fig. 8.

Finally, assume that the slope of the beam central line due to shear alone is proportional to the shear strain at the beam central line, thus

$$\frac{dv_b^{\text{cent,shear}}}{dx} = f_1 \frac{T(x)}{G_b A} - f_2 \frac{\tau_h(x) + \tau_b(x)}{2G_b}, \qquad \text{(B4)}$$

where f_1 and f_2 are beam property dependent factors for shear due to normal and tangential loading of the beam, respectively. One well-known method of proceeding to derive f_1 is to use the definition of strain energy of shear (Gere and Timoshenko, 1989) and it reads as follows:

$$f_1 = \frac{A}{I^2} \int_A \frac{Q^2}{b^2}\, dA. \qquad \text{(B5)}$$

This factor is often called the form factor of shear. Another way is to assume that the slope of the deflection curve due to shear is equal to the shear strain at the neutral axis and the factor obtained is often called the shear coefficient. The application of the shear coefficient gives a rough estimate of the contribution to the slope of deflection curve due to shear. In a paper by Cowper (1966), three-dimensional elasticity theory was used to derive more accurate values of f_1. He found that this factor is not only depending on the geometry of the beam cross-section but also on Poisson's ratio ν. The form factor f_1 in (B5) has values that are very close to corresponding values found by Cowper. No effort to derive accurate values for the factor f_2 has been made in this paper.

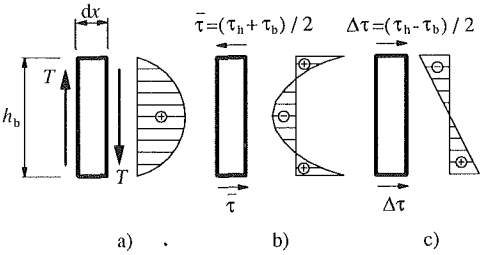


Fig. 8 Shear stress distribution in a beam lamella due to (*a*) the first term, (*b*) the second term, and (*c*) the third term, of the shear stress distribution expressed in Eq. (B3).

APPENDIX C

Numerical Method

Consider the Eqs. (6). The interval of integration ($0 \le T \le 1$) is divided into N subintervals L_j, thus $j = (1, N)$. Let X_j denote the midpoint of subinterval j. The continuous distributions of pressure, shear stress and displacement gradient are approximated by piecewise, i.e., within the subintervals, constant functions, thus

$$L_j = \{T: T_{j-1} < T < T_j\}, \quad 0 = T_0 < T_1 < \ldots < T_N = 1,$$

$$X_j = \frac{1}{2}(T_j + T_{j-1}), \qquad \text{(C1}a\text{–}c\text{)}$$

$$\begin{Bmatrix} p_j, \hat{p}_j \\ q_j, \hat{q}_j \end{Bmatrix} = \begin{Bmatrix} p(X_j), \hat{p}(X_j) \\ q(X_j), \hat{q}(X_j) \end{Bmatrix}, \quad \begin{Bmatrix} U_j \\ V_j \end{Bmatrix} = \begin{Bmatrix} U \\ V \end{Bmatrix}_{T=X_j}, \qquad \begin{matrix} \text{(C2}a,b\text{)} \\ \text{(C2}c,d\text{)} \end{matrix}$$

where the superscripts a and s are omitted in (C2) for considerations of space. However, Eqs. (C2) are used in both the symmetrical and the antisymmetrical case of loading. With the foregoing assumptions we rewrite (6*a*,*c*,*e*,*f*) and (6*b*,*d*,*e*,*g*) as $4N$ linear equations in the $4N$ unknown contact quantities p_j, q_j, U_j, and V_j.

Up to $N = 100$ subintervals have been used. The linear equations are solved by using the numerical routine F04ATF (Mark 14) from the Fortran library NAG (Numerical Algorithms Group). These computations have been performed on a VAX-station.

APPENDIX D

Half-Plane Stress Fields

Here we present the orthotropic half-plane stress fields corresponding to a uniform normal and tangential contact stresses over the surface region $|X| \le 1$, and to a point moment at $X = 0$. These stress fields are used with purpose to calculate the consistent nodal forces for the FE-model in Section 4. Lekhnitski (1963) and (1968) presents expressions in closed form for anisotropic half-space stress fields in some special cases of edge loading. The stress components in an orthotropic half-plane under arbitrary surface load are given by Bjarnehed (1991). By letting the normal and tangential surface tractions

Downloaded 03 May 2010 to 171.66.16.245. Redistribution subject to ASME license or copyright; see http://www.asme.org/terms/Terms_Use.cfm

be constant inside, and identical to zero outside, the region $|X| \leq 1$ we find (using standard notation) (D1) and (D2), respectively. By loading the half-plane edge normally at $X = 1$ with a couple, i.e., two equal and opposite forces with distance Δ apart, we can derive the corresponding half-plane stresses (D3) through a limiting process where $\Delta \to 0$.

$$\frac{\pi(\alpha-\beta)}{\sigma^*}\begin{Bmatrix}\sigma_x\\ \sigma_y\\ \tau_{xy}\end{Bmatrix}_{\sigma^*} = \alpha\begin{Bmatrix}\alpha\beta\\ 1\\ \beta\end{Bmatrix}\begin{Bmatrix}g(X,\,Y,\,\alpha)\\ g(X,\,Y,\,\beta)\\ f(X,\,Y,\,\beta)\end{Bmatrix} - \beta\begin{Bmatrix}\alpha\beta\\ 1\\ \alpha\end{Bmatrix}\begin{Bmatrix}g(X,\,Y,\,\beta)\\ g(X,\,Y,\,\alpha)\\ f(X,\,Y,\,\alpha)\end{Bmatrix}, \quad \begin{Bmatrix}\text{D1}a\\ \text{D1}b\\ \text{D1}c\end{Bmatrix}$$

$$\frac{\pi(\alpha-\beta)}{\tau^*}\begin{Bmatrix}\sigma_x\\ \sigma_y\\ \tau_{xy}\end{Bmatrix}_{\tau^*} = \begin{Bmatrix}\alpha^2\\ 1\\ \alpha\end{Bmatrix}\begin{Bmatrix}f(X,\,Y,\,\alpha)\\ f(X,\,Y,\,\beta)\\ g(X,\,Y,\,\alpha)\end{Bmatrix} - \begin{Bmatrix}\beta^2\\ 1\\ \beta\end{Bmatrix}\begin{Bmatrix}f(X,\,Y,\,\beta)\\ f(X,\,Y,\,\alpha)\\ g(X,\,Y,\,\beta)\end{Bmatrix}, \quad \begin{Bmatrix}\text{D2}a\\ \text{D2}b\\ \text{D2}c\end{Bmatrix}$$

$$\frac{\pi}{M^*}\begin{Bmatrix}\sigma_x\\ \sigma_y\\ \tau_{xy}\end{Bmatrix}_{M^*} = \frac{Y\alpha\beta(\alpha+\beta)}{h(X,\,Y,\,\alpha,\,\beta)}\begin{Bmatrix}2X[(\alpha Y)^2(\beta Y)^2 - X^4]\\ -2XY^2[(\alpha Y)^2 + (\beta Y)^2 + 2X^2]\\ Y[(\alpha Y)^2(\beta Y)^2 - \{(\alpha Y)^2 + (\beta Y)^2\}X^2 - 3X^4]\end{Bmatrix}, \quad \begin{Bmatrix}\text{D3}a\\ \text{D3}b\\ \text{D3}c\end{Bmatrix}$$

where σ^*, τ^*, and M^* are the constant normal and tangential surface tractions, and the point moment, respectively, and

$$f(X,\,Y,\,\alpha) = \ln\sqrt{\frac{(\alpha Y)^2 + (1+X)^2}{(\alpha Y)^2 + (1-X)^2}}, \tag{D3a}$$

$$g(X,\,Y,\,\alpha) = \arctan\left(\frac{1+X}{\alpha Y}\right) + \arctan\left(\frac{1-X}{\alpha Y}\right), \tag{D3b}$$

$$h(X,\,Y,\,\alpha,\,\beta) = \{[(\alpha Y)^2 + X^2][(\beta Y)^2 + X^2]\}^2. \tag{D3c}$$

The material parameters α and β are defined in Appendix A. As it appears the Eqs. (D1) and (D2) are useless for $\alpha = \beta$. For an isotropic half-plane, $\alpha = \beta = 1$, and hence it is not possible to degenerate these orthotropic equations to be valid for an isotropic half-plane. However, isotropic half-plane stress fields corresponding to uniform contact stresses can be derived by putting $\alpha = \beta = 1$ before evaluating the orthotropic half-plane stress components given by Bjarnehed (1991).

Downloaded 03 May 2010 to 171.66.16.245. Redistribution subject to ASME license or copyright; see http://www.asme.org/terms/Terms_Use.cfm

C. H. Chou
Assoc. Mem. ASME

J. Pan
Mem. ASME

Mechanical Engineering and Applied Mechanics,
The University of Michigan,
Ann Arbor, MI 48109

S. C. Tang

Ford Motor Company,
Dearborn, MI 48121
Mem. ASME

A Hardening Rule Between Stress Resultants and Generalized Plastic Strains for Thin Plates of Power-Law Hardening Materials

For power-law hardening materials, a stress resultant constitutive law of incremental plasticity nature for thin plates is constructed. The yield function in the stress resultant space is approximated in quadratic form and an equivalent stress resultant is defined. One of two parameters in the yield function is analytically determined based on the concept of complementary potential surface. The other is determined by the least square method to fit the complementary potential surface of Chou et al., (1991). In analogy to the work of Hill (1979), the equivalent work-conjugate generalized plastic strain rate is derived. Finally, the hardening rule between the equivalent stress resultant and generalized plastic strain is obtained based on the results of Chou et al. (1991) for power-law materials under proportional straining conditions.

1 Introduction

Based on the concept of stress resultant, many constitutive laws were developed to analyze the inelastic behavior of plates and shells. Early in the development, perfectly plastic material behavior was considered for simplicity (Ilyushin, 1948). However, even a plate element or shell element of elastic perfectly plastic materials exhibits hardening phenomena in the stress resultant space except under pure membrane force conditions. This hardening is due to the gradual spread of yielding through the thickness. To account for the hardening, the evolution rules of the subsequent yield surfaces were proposed (Crisfield, 1974; Bieniek and Funaro, 1976; Eggers and Kröplin, 1978; Eidsheim and Larsen, 1981). In these works, interpolation functions between the initial and limit yield surfaces are assumed to define the size and translation of the yield surfaces. An internal variable which represents a measure of plastic deformation (Papadopoulos and Taylor, 1990) was also proposed to characterize the subsequent yield surfaces.

We have employed the evolution rule of Bieniek and Funaro (1976) to simulate the sheet-metal-forming processes for elastic-perfectly plastic materials. The computational results are compared well with those based on the through-the-thickness integration method. However, when we employed the interpolation function of Eidsheim and Larsen (1981) to account for material hardening to simulate sheet-metal-forming processes, the computational results were not satisfactory when compared with those based on the through-the-thickness integration method. This motivates us to find an alternative hardening rule between the stress resultants and the generalized plastic strains due to material plastic hardening without the assumption of the limit yield surface for perfectly plastic materials. In our previous work (Chou et al., 1991), we have derived a stress resultant constitutive law and constructed the complementary potential surface for power-law hardening materials under proportional straining conditions. Based on these results, we here derive a hardening rule between the equivalent stress resultant and generalized plastic strain.

In this paper, we approximate the yield function in quadratic form with two parameters. One parameter α can be analytically determined by the concept of complementary potential surface. The other β is determined by the least square method to fit the complementary potential surfaces for each power hardening exponent n (Chou et al., 1991). We also find that the value of β can be well fitted as a function of n by the rational function interpolation method. The equivalent stress resultant is defined based on this yield function.

In the sense of Naghdi's work (1975), an alternative form of yield surface (loading surface) exists in the strain space. Hill (1979) mentioned there exists a work-equivalent function of plastic strain rate tensor over any yield surface. Referring to Hill's procedures, a similar work-equivalent function of generalized plastic strain rate for a plate element of power-law hardening materials is presented. We combine these equivalent stress resultant and generalized plastic strain rate with the constitutive law derived under proportional loading conditions of Chou et al. (1991) and then set up the hardening rule between the equivalent stress resultant and generalized plastic strain.

Contributed by the Applied Mechanics Division of THE AMERICAN SOCIETY OF MECHANICAL ENGINEERS for presentation at the First Joint ASCE-EMD, ASME-AMD, SES Meeting, Charlottesville, VA, June 6-9, 1993.

Discussion on this paper should be addressed to the Technical Editor Professor Lewis T. Wheeler, Department of Mechanical Engineering, University of Houston, Houston, TX 77204-4792, and will be accepted until four months after final publication of the paper itself in the JOURNAL OF APPLIED MECHANICS.

Manuscript received by the ASME Applied Mechanics Division, Aug. 15, 1990; final revision, Aug. 1, 1992. Associate Technical Editor: R. M. McMeeking.

Paper No. 93-APM-34.

Copyright © 1993 by ASME
Downloaded 03 May 2010 to 171.66.16.245. Redistribution subject to ASME license or copyright; see http://www.asme.org/terms/Terms_Use.cfm

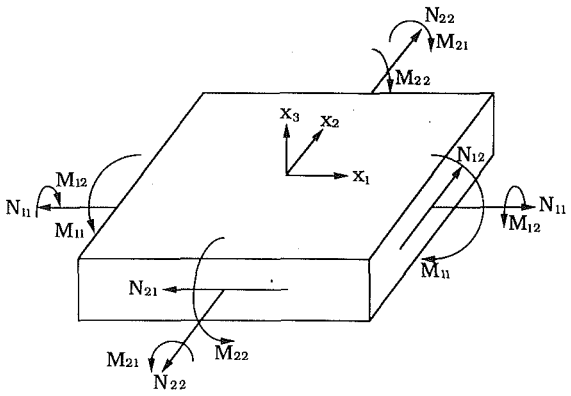


Fig. 1 The conventions of a plate element

2 Yield Function and Equivalent Stress Resultant

The stress resultant **S** and the generalized strain **E** for the plate element as shown in Fig. 1 are defined as

$$\mathbf{S}=\{N_{11},\ N_{22},\ N_{12},\ M_{11},\ M_{22},\ M_{12}\} \tag{1}$$

and

$$\mathbf{E}=\{e_{11},\ e_{22},\ 2e_{12},\ \kappa_{11},\ \kappa_{22},\ 2\kappa_{12}\}, \tag{2}$$

where $N_{\alpha\beta}$ are the membrane forces, $M_{\alpha\beta}$ are the moments, $e_{\alpha\beta}$ are the midplane strains, and $\kappa_{\alpha\beta}$ are the curvatures. Here, Greek subscripts α and β have the range from 1 to 2. First, we will construct a function of yield surface in the stress resultant space for a plate element of power-law hardening materials well into the plastic range. Although the yield functions based on the Tresca yield condition were proposed (Calladine, 1972; Hodge, 1954; Onat, 1955), the yield function of Ilyushin (1948) in the stress resultant space based on the Von Mises yield condition is considered here. Specifically, the yield function including transverse shear effect can be expressed as

$$F=(I_N+\alpha I_M+\beta|I_{MN}|+\gamma I_Q)^{1/2}, \tag{3}$$

where I_N, I_M, I_{MN}, and I_Q are the normalized invariants of the stress resultants. Here, I_Q represents the term due to transverse shear. In this paper, however, we shall neglect the transverse shear effect and assume the yield function for power-law hardening materials as

$$F=(I_N+\alpha I_M+\beta|I_{MN}|)^{1/2}=\bar{\Sigma}, \tag{4}$$

where

$$I_N=\bar{N}_{11}^2+\bar{N}_{22}^2-\bar{N}_{11}\bar{N}_{22}+3\bar{N}_{12}^2,$$
$$I_M=\bar{M}_{11}^2+\bar{M}_{22}^2-\bar{M}_{11}\bar{M}_{22}+3\bar{M}_{12}^2,$$

and

$$I_{MN}=\bar{N}_{11}\bar{M}_{11}+\bar{N}_{22}\bar{M}_{22}-\frac{1}{2}\bar{N}_{11}\bar{M}_{22}$$
$$-\frac{1}{2}\bar{N}_{22}\bar{M}_{11}+3\bar{N}_{12}\bar{M}_{12}.$$

In Eq. (4), α and β are 1 and $1/\sqrt{3}$, respectively, for the limit yield surface of perfectly plastic materials (Ilyushin, 1948). However, α and β are now functions of n which is the hardening exponent of the J_2-deformation plasticity for power-law hardening materials:

$$\epsilon_{ij}=\frac{3}{2}K\left(\frac{\sigma_e}{\sigma_0}\right)^{n-1}\frac{S_{ij}}{\sigma_0}\ i,\ j,\ k=1,\ 2,\ 3, \tag{5}$$

where ϵ_{ij} are the plastic strains, K is a material constant, σ_0 is the reference stress, and s_{ij} are the deviatoric stresses. In this paper, we consider the deformation states where the plastic strains are much larger than the elastic counterparts. Therefore, the elastic stains are neglected and the plastic strains in Eq. (5) are regarded as the total strains. In other words, the materials are modelled as rigid power-law hardening materials for the convenience of the development of constitutive law. The normalized resultants $\bar{N}_{\alpha\beta}$ and $\bar{M}_{\alpha\beta}$ are defined by $\bar{N}_{\alpha\beta}=N_{\alpha\beta}/\sigma_0 n$ and $\bar{M}_{\alpha\beta}=M_{\alpha\beta}/4\ \sigma_0 h^2$, where h is the thickness of plate. $\bar{\Sigma}$ in Eq. (4) represents the normalized equivalent stress resultant and it represents the size of the current yield surface in the normalized stress resultant space. It is taken as a function of the plastic work or the prior plastic deformation history.

To determine the value of α, we consider a plate element subject to uniaxial combined bending and membrane force. Equation (4) becomes

$$\bar{N}_{11}^2+\alpha\bar{M}_{11}^2+\beta|\bar{N}_{11}\bar{M}_{11}|=\bar{\Sigma}^2. \tag{6}$$

We assume the deformation of the plate follows the Kirchhoff assumption such that $\epsilon_{\alpha\beta}=e_{\alpha\beta}+\kappa_{\alpha\beta}x_3$. From Eq. (5), the stress as a function of x_3, which represents the through-the-thickness coordinate as shown in Fig. 1, for power-law materials under uniaxial combined loading conditions is

$$\sigma_{11}=A|\epsilon|^{1/n}\text{sign}(\epsilon), \tag{7}$$

where A is a constant, and $\epsilon=e+\kappa x_3$. Here, $e=e_{11}$ and $\kappa=\kappa_{11}$.

Now, we consider the constitutive behavior in the domain of $\bar{N}_{11}\geq 0$ and $\bar{M}_{11}\geq 0$. For $\bar{N}_{11}=0$ (pure bending), the stress is

$$\sigma_{11}=A(\kappa_p|x_3|)^{1/n}\ \text{sign}\ (x_3), \tag{8}$$

where κ_p represents the curvature under pure bending. The moment can be expressed as

$$M_{11}=A\frac{2n}{2n+1}\kappa_p^{1/n}\left(\frac{h}{2}\right)^{(2n+1)/n}. \tag{9}$$

The complementary potential is

$$\psi_1=\frac{2nA}{(n+1)(2n+1)}\kappa_p^{(1+n)/n}\left(\frac{h}{2}\right)^{(2n+1)/n}. \tag{10}$$

For $\bar{M}_{11}=0$ (pure membrane force), the stress is

$$\sigma_{11}=Ae_p^{1/n}, \tag{11}$$

where e_p represents the midplane strain under pure membrane force. The membrane force is

$$N_{11}=Ae_p^{1/n}\ h. \tag{12}$$

The complementary potential is

$$\Psi_2=\frac{A}{n+1}e_p^{(1+n)/n}\ h. \tag{13}$$

As indicated in the work of Chou et al. (1991), for power-law hardening materials well into the plastic range under proportional straining conditions, the complementary potential surface can be regarded as the yield surface. If both the stress resultant states under pure membrane force and pure bending have the same complementary potential ($\Psi_1=\Psi_2$), then they can be said to be on the same yield surface. From Eqs. (10) and (13), we conclude that

$$\kappa_p=\left(\frac{2n+1}{n}\right)^{n/(1+n)}\frac{2\ e_p}{h}. \tag{14}$$

From Eqs. (9) and (14), the moment at $\bar{N}_{11}=0$ is

$$M_{11}=\frac{Ah^2}{2}\left(\frac{n}{2n+1}\right)^{n/(1+n)}e_p^{1/n}. \tag{15}$$

Combining Eq. (12) with $N_{11}=N_0=\sigma_0 h$ (or $\bar{N}_{11}=1$) and Eq. (15) gives the normalized moment as

$$\bar{M}_{11}=\frac{M_{11}}{1/4\ \sigma_1 h^2}=2\left(\frac{n}{2n+1}\right)^{n/(n+1)}. \tag{16}$$

The values of $\bar{M}_{11}$ of the complementary potential surface for $\bar{N}_{11}=1$ (Chou et al., 1991) and those based on Eq. (16) are listed in Table 1. It shows that the error of the previous numerical results are less than 0.1 percent for each n. On the

Downloaded 03 May 2010 to 171.66.16.245. Redistribution subject to ASME license or copyright; see http://www.asme.org/terms/Terms_Use.cfm

Table 1

n	$\bar{M}$ Numerical Results	$\bar{M}$ Equation (16)	n	$\bar{M}$ Numerical Results	$\bar{M}$ Equation (16)
1	1.15499	1.15470	15	1.01313	1.01266
2	1.08609	1.08577	20	1.01003	1.00954
3	1.05971	1.05937	30	1.00692	1.00638
4	1.04577	1.04540	50	1.00442	1.00384
7	1.02703	1.02662	10000	1.00083	1.00002
10	1.01927	1.01883	∞	1.00000	1.00000

yield surface, if $\overline{N}_{11}=1$ and $\overline{M}_{11}=0$, then $\overline{\Sigma}=1$. Combining $\overline{N}_{11}=0$ and Eqs. (6) and (16) gives the value of α as

$$\alpha=\frac{1}{4[n/(2n+1)]^{2n/(n+1)}}. \tag{17}$$

Chou et al. (1991) have constructed the yield surfaces, i.e., the complementary potential surfaces, under uniaxial combined bending and membrane force by numerical integration. Here, we use these numerical results to determine the value of β by the least square method. From Eq. (6), the square of error is

$$\delta=\sum_{i=1}^{N}(1-\overline{N}_{11i}^2-\alpha\overline{M}_{11i}^2-\beta|\overline{N}_{11i}\,\overline{M}_{11i}|)^2. \tag{18}$$

The value of β is determined by $\partial\delta/\partial\beta=0$ as follows:

$$\beta=\frac{\Sigma_{i=1}^{N}(1-\overline{N}_{11i}^2-\alpha\overline{M}_{11i}^2)|\overline{N}_{11i}\,\overline{M}_{11i}|}{\Sigma_{i=1}^{N}\overline{N}_{11i}^2\,\overline{M}_{11i}^2}. \tag{19}$$

The values of β for several n's are listed in Table 2. Figure 2 shows the yield surfaces based on the quadratic yield function and the exact numerical results of Chou et al. (1991) for $n=1$, 3, 10, and 30. In general, the quadratic yield surfaces fit the exact results very well. However, the error in terms of the direction of the outward normal to the yield surface increases as n increases. This results in some errors in plastic strain rates for low-hardening materials (with large n) when the associated flow rule is employed.

We have used the polynomial interpolation method which is simple to fit the value of β as a function of n from those in Table 2. However, it leads to an oscillational behavior. We therefore take the rational function interpolation method (Press et al., 1986) to fit those values in Table 2. The results appear to be excellent as shown in Fig. 3 where β is plotted as a function of n from 1 to 50 using the rational function. For future application, we reiterate the definition of the normalized equivalent stress resultant $\overline{\Sigma}$ as

$$\overline{\Sigma}=(I_N+\alpha\, I_M+\beta|I_{MN}|)^{1/2}. \tag{20}$$

3 Work Equivalent Function of Generalized Plastic Strain Rate

Hill (1979) has shown the existence of a work-equivalent function of plastic strain rate tensor over any yield surface. Here, we derive this work-equivalent function of generalized plastic strain rate for the plate element as shown in Fig. 1. For convenience, we define the normalized stress resultant $\overline{\mathbf{S}}$ as

$$\overline{\mathbf{S}}=\{\overline{N}_{11},\,\overline{N}_{22},\,\overline{N}_{12},\,\overline{M}_{11},\,\overline{M}_{22},\,\overline{M}_{12}\} \tag{21}$$

Table 2

n	β	n	β	n	β	n	β
1	0.0000	4	0.2793	15	0.4744	50	0.5598
2	0.1458	7	0.3745	20	0.5021	10000	0.6044
3	0.2255	10	0.4260	30	0.5328	∞	0.6064

and the normalized generalized strain $\overline{\mathbf{E}}$ as

$$\overline{\mathbf{E}}=\{\bar{e}_{11},\,\bar{e}_{22},\,2\bar{e}_{12},\,\frac{3}{4}\bar{\kappa}_{11},\,\frac{3}{4}\bar{\kappa}_{22},\,\frac{3}{2}\bar{\kappa}_{12}\}, \tag{22}$$

where $\bar{e}_{\alpha\beta}=e_{\alpha\beta}E/\sigma_0$ and $\bar{\kappa}_{\alpha\beta}=\kappa_{\alpha\beta}Eh/3\sigma_0$. Here, E is Young's modulus. The associate flow rule for a plate element under plastic loading conditions can be expressed as

$$\dot{\mathbf{E}}^p=\dot{\Lambda}\frac{\partial F}{\partial\mathbf{S}}, \tag{23}$$

where $\dot{\mathbf{E}}^p$ is the generalized plastic strain rate, and $\dot{\Lambda}$ is a proportionality and can be determined by the equivalence of plastic work. The normalized form of Eq. (23) is

$$\dot{\bar{E}}^{\,p}=\dot{\bar{\Lambda}}^{*}\frac{\partial F}{\partial\overline{\mathbf{S}}}, \tag{24}$$

where $\dot{\bar{E}}^{\,p}$ is the normalized generalized plastic strain rate, and $\dot{\bar{\Lambda}}^{*}=\dot{\Lambda}E/\sigma_0^2h$. We can rewrite $F\,(=\overline{\Sigma})$ of Eq. (4) as

$$F=\left(\frac{1}{2}\mu_{ij}\,\overline{S}_i\,\overline{S}_j\right)^{1/2}=\overline{\Sigma}.$$

Then, Eq. (24) becomes

$$\dot{\bar{E}}_i^{\,p}=\frac{\dot{\bar{\Lambda}}^{*}}{2\overline{\Sigma}}\mu_{ij}\,\overline{S}_j. \tag{25}$$

Here, $\mu_{ij}\,(=\partial^2F^2/\partial\overline{S}_i\partial\overline{S}_j)$ are expressed as

$$[\mu]=\begin{bmatrix} 2 & -1 & 0 & \beta\lambda & -\frac{\beta\lambda}{2} & 0 \\ -1 & 2 & 0 & -\frac{\beta\lambda}{2} & \beta\lambda & 0 \\ 0 & 0 & 6 & 0 & 0 & 3\beta\lambda \\ \beta\lambda & -\frac{\beta\lambda}{2} & 0 & 2\alpha & -\alpha & 0 \\ -\frac{\beta\lambda}{2} & \beta\lambda & 0 & -\alpha & 2\alpha & 0 \\ 0 & 0 & 3\beta\lambda & 0 & 0 & 6\alpha \end{bmatrix},$$

Downloaded 03 May 2010 to 171.66.16.245. Redistribution subject to ASME license or copyright; see http://www.asme.org/terms/Terms_Use.cfm

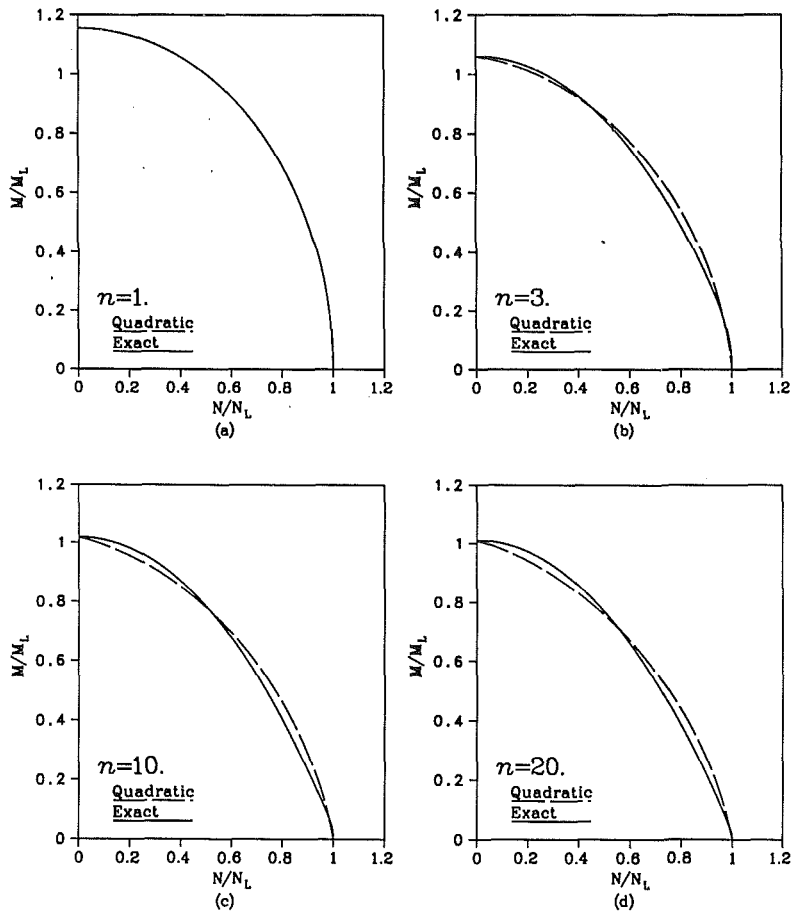


Fig. 2 Comparisons of the yield surfaces based on the quadratic yield function and the exact results of Chou et al. (1991)

where $\lambda = 1$ if $I_{MN} \geq 0$, otherwise $\lambda = -1$. Multiplying equation (25) by $\bar{S}_i$ gives

$$\bar{S}_i \dot{\bar{E}}_i^p = \bar{\Sigma}\, \dot{\bar{\Lambda}}^* \tag{26}$$

Here, it is apparent that $\dot{\bar{\Lambda}}^*$ represents the normalized equivalent plastic strain rate. Equation (25) can be rearranged into

$$\bar{S}_i = \frac{2\bar{\Sigma}}{3(\alpha - \beta^2/4)\, \dot{\bar{\Lambda}}^*}\, \nu_{ij}\, \dot{\bar{E}}_j^p, \tag{27}$$

where ν_{ij} are expressed as

$$[\nu] = \begin{bmatrix} 2\alpha & \alpha & 0 & -\beta\lambda & -\frac{\beta\lambda}{2} & 0 \\ \alpha & 2\alpha & 0 & -\frac{\beta\lambda}{2} & -\beta\lambda & 0 \\ 0 & 0 & \frac{\alpha}{2} & 0 & 0 & -\frac{\beta\lambda}{4} \\ -\beta\lambda & -\frac{\beta\lambda}{2} & 0 & 2 & 1 & 0 \\ -\frac{\beta\lambda}{2} & -\beta\lambda & 0 & 1 & 2 & 0 \\ 0 & 0 & -\frac{\beta\lambda}{4} & 0 & 0 & \frac{1}{2} \end{bmatrix}.$$

We multiply Eq. (27) by $\dot{\bar{E}}_i^p$ and substitute the results into Eq. (26). The work-equivalent function of generalized plastic strain rate is generated as follows:

$$\dot{\bar{\Lambda}}^* = \left[\frac{4\alpha}{3(\alpha - \beta^2/4)} \left(I_{\dot{e}} + \frac{9}{16\alpha} I_{\dot{\kappa}} - \frac{3\beta\lambda}{8\alpha} I_{\dot{e}\kappa} \right) \right]^{1/2}, \tag{28}$$

where

$$I_{\dot{e}} = \dot{\bar{e}}_{11}^{p2} + \dot{\bar{e}}_{22}^{p2} + \dot{\bar{e}}_{11}^{p}\, \dot{\bar{e}}_{22}^{p} + \dot{\bar{e}}_{12}^{p2},$$
$$I_{\dot{\kappa}} = \dot{\bar{\kappa}}_{11}^{p2} + \dot{\bar{\kappa}}_{22}^{p2} + \dot{\bar{\kappa}}_{11}^{p}\, \dot{\bar{\kappa}}_{22}^{p} + \dot{\bar{\kappa}}_{12}^{p2},$$

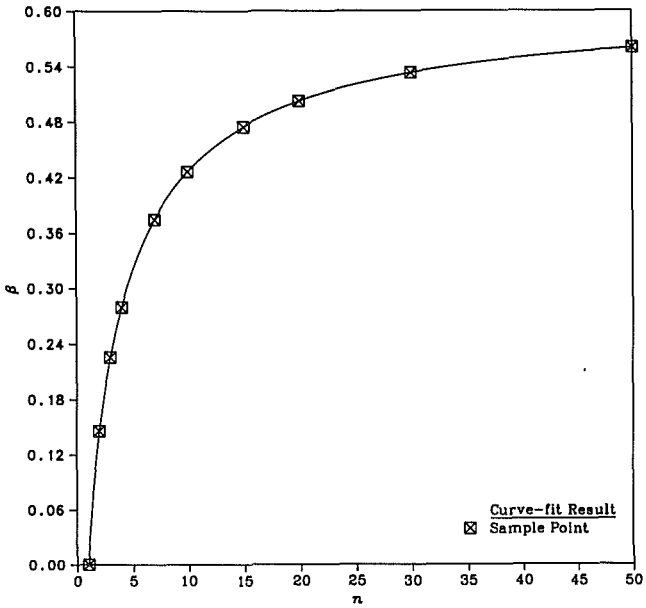


Fig. 3 The value of β as a function of the strain-hardening exponent n

and

$$I_{\dot{e}\kappa} = 2\dot{\bar{e}}_{11}^{p}\, \dot{\bar{\kappa}}_{11}^{p} + 2\dot{\bar{e}}_{22}^{p}\, \dot{\bar{\kappa}}_{22}^{p} + \dot{\bar{e}}_{22}^{p}\, \dot{\bar{\kappa}}_{11}^{p} + \dot{\bar{e}}_{11}^{p}\, \dot{\bar{\kappa}}_{22}^{p} + 2\dot{\bar{e}}_{12}^{p}\, \dot{\bar{\kappa}}_{12}^{p}.$$

For the convenience of the following formulation of a hard-

Downloaded 03 May 2010 to 171.66.16.245. Redistribution subject to ASME license or copyright; see http://www.asme.org/terms/Terms_Use.cfm

ening rule, we define a new normalized equivalent plastic strain rate $\dot{\bar{\Lambda}}$ as

$$\dot{\bar{\Lambda}}=\left[\frac{4}{3}\left(I_{\dot{e}}+\frac{9}{16\alpha}I_{\dot{\kappa}}-\frac{3\beta\lambda}{8\alpha}I_{\dot{e}\kappa}\right)\right]^{1/2}. \tag{29}$$

Note that $\dot{\bar{\Lambda}}^* = \xi\dot{\bar{\Lambda}}$, where $\xi = \sqrt{\alpha/(\alpha-\beta^2/4)}$. The value of ξ monotonically increases from 1 for $n = 1$ to 1.05 for $n = \infty$ as n increases. For some representative materials with the hardening exponent from $n = 3$ to $n = 10$, the value of ξ ranges from 1.01 to 1.02. Under pure membrane force and pure moment conditions, the plastic response based on the flow rule of Eq. (24) differs from that for the corresponding Mises materials by the constant ξ for each n larger than 1 due to the term with β in the yield function of Eq. (4). This term represents the coupling between the membrane forces and moments and it generates corners (or vertices) on the yield surface in the stress resultant space. One remedy to obtain the correct plastic response under pure membrane forces and pure moments is to set $\beta=0$ to get rid of this coupling effect. The $\xi = 1$ and the plastic response for Mises materials under such loading conditions will be recovered from our flow rule.

4 A Hardening Rule Between Equivalent Stress Resultant and Generalized Plastic Strain

Now Eqs. (20) and (29) give the equivalent stress resultant and the equivalent generalized plastic strain in normalized forms. To specify the elastic-plastic constitutive behavior, we need an evolution rule (or a hardening rule) to specify the evolution (or hardening) of the subsequent yield surfaces in the stress resultant space. Here, we assume the equivalent stress resultant $\bar{\Sigma}$ is a function of the accumulated equivalent plastic strain $\bar{\Lambda}$ ($=\int\dot{\bar{\Lambda}}dt$ where dt is the differential time). We will construct this relation based on the constitutive behavior for power-law hardening materials under proportional loading conditions. In other words, the general constitutive behavior based on the hardening rule coincides with the exact result for power-law materials under proportional loading conditions. For power-law materials under proportional straining (loading) conditions, we have the normalized relations (Chou et al., 1991).

$$\bar{\kappa}_{11}=\frac{2}{3}C\bar{e}_{11},\ \bar{e}_{22}=C_1\,\bar{e}_{11},\ \bar{e}_{12}=C_2\bar{e}_{11},$$

$$\bar{\kappa}_{22}=\frac{2}{3}CC_1\bar{e}_{11},\ \text{and}\ \bar{\kappa}_{12}=\frac{2}{3}CC_2\bar{e}_{11},\ ,$$

where C, C_1, and C_2 are constants. Also, these relations are valid for these corresponding strain rates. When the elastic strain is small and neglected, these relations are substituted into Eq. (29) and the equivalent generalized plastic strain rate is

$$\dot{\bar{\Lambda}}=|\dot{\bar{e}}_{11}|B^{1/2}, \tag{30}$$

where

$$B=\left[\frac{4(1+C_1+C_1^2+C_2^2)\,(1+\frac{C^2}{4\alpha}-\frac{\beta C\lambda}{2\alpha})}{3}\right]\geq 0.$$

We can rewrite Eq. (30) as

$$|\bar{e}_{11}|^{1/n}=\bar{\Lambda}^{1/n}\left[\frac{3}{4(1+C_1+C_1^2+C_2^2)\left(1+\frac{C^2}{4\alpha}-\frac{\beta C\lambda}{2\alpha}\right)}\right]^{1/2n} \tag{31}$$

From Eqs. (11) and (12) of Chou et al. (1991), the constitutive law for a plate element of power-law material can be rewritten as

$$\bar{N}_{\alpha\beta}=\frac{A_{\alpha\beta}}{e_{11}}PQ\ |\bar{e}_{11}|^{1/n}\text{sign}(\bar{e}_{11}) \tag{32}$$

and

$$\bar{M}_{\alpha\beta}=\frac{A_{\alpha\beta}}{e_{11}}\left(R-\frac{2}{C}P\right)Q|\bar{e}_{11}|^{1/n}\ \text{sign}(\bar{e}_{11}), \tag{33}$$

where

$$P=\frac{1}{2C}\frac{n}{n+1}\left[|1+C|^{(n+1)/n}-|1-C|^{(n+1)/n}\right],$$

$$Q=\frac{2^{1/n}}{3^{(n+1)/2n}}(1+C_1+C_1^2+C_2^2)^{(1-n)/2n},$$

$$R=\frac{1}{C^2}\frac{n}{2n+1}\left[|1+C|^{(2n+1)/n}\ \text{sign}(1+C)-|1+C|^{2(n+1/n)}\ \text{sign}(1-C)\right],$$

and

$$A_{\alpha\beta}=e_{\gamma\gamma}\,\delta_{\alpha\beta}+e_{\alpha\beta}\ \alpha,\beta,\gamma=1,2.$$

Then, from Eq. (20), the equivalent stress resultant is

$$\bar{\Sigma}=|\bar{e}_{11}|^{1/n}\,Q\left\{3(1+C_1+C_1^2+C_2^2)\left[\left(1+\frac{4\alpha}{C^2}\right)P^2+\alpha R^2-\frac{4\alpha}{C}PR+\beta\,|PR-\frac{2}{C}P^2|\right]\right\}^{1/2}. \tag{34}$$

Substituting Eq. (31) into Eq. (34) gives the relation of the equivalent stress resultant and generalized plastic strain under proportional straining (loading) conditions as

$$\bar{\Sigma}=\eta\bar{\Lambda}^{1/n}, \tag{35}$$

where η is a function of n and C as

$$\eta=\left(\frac{1}{1+\frac{C^2}{4\alpha}-\frac{\beta C\lambda}{2\alpha}}\right)^{1/2n}\left[\left(1+\frac{4\alpha}{C^2}\right)P^2+\alpha R^2-\frac{4\alpha}{C}PR+\beta\,|PR-\frac{2}{C}P^2|\right]^{1/2} \tag{36}$$

and $\lambda = \text{sign}\,[(1 + C_1 + C_1^2 + C_2^2)\,Q^2\,(PR - 2/C\,P^2)] = \text{sign}\,(PR-2P^2/C)$ because $(1 + C_1 + C_1^2 + C_2^2) > 0$. Note that η is a function of one constant C only for each n. When $n \to \infty$, the stress resultants in the Eqs. (16) and (17) of Chou et al. (1991) are

$$\bar{N}_{\alpha\beta}=\text{sign}(\bar{e}_{11})\,\frac{A_{\alpha\beta}}{e_{11}}\,\frac{|1+C|-|1-C|}{2\sqrt{3}C(1+C_1+C_1^2+C_2^2)^{1/2}} \tag{37}$$

and

$$\bar{M}_{\alpha\beta}=\text{sign}\ (\bar{e}_{11})\,\frac{A_{\alpha\beta}}{e_{11}}\,\frac{(1+C)|1+C|-(1-C)|1-C|}{2\sqrt{3}C^2(1+C_1+C_1^2+C_2^2)^{1/2}.} \tag{38}$$

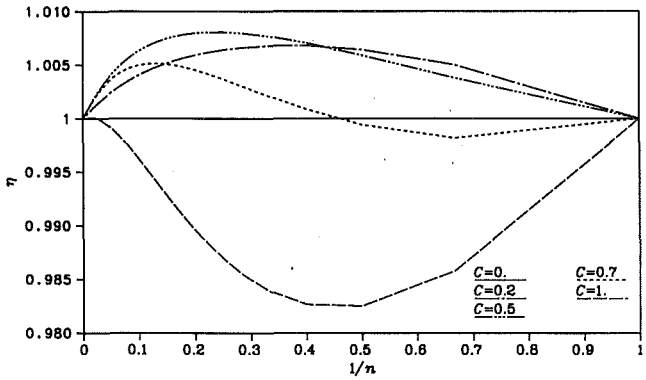
So, the equivalent stress is

$$\bar{\Sigma}=\frac{(1-C^2+C^4+\beta|C^3-C|)^{1/2}}{C^2}\ \text{if}\ |C|\geq 1$$

$$\bar{\Sigma}=1\ \text{if}\ |C|\leq 1. \tag{39}$$

Now, we examine the values of η for the special cases where $C=0$ (pure membrane forces) and $C=\infty$ (pure moments). First, we examine the case of $C=0$. We go back to eq. (3) in the work of Chou et al. (1991) and the stresses under pure membrane forces are

Downloaded 03 May 2010 to 171.66.16.245. Redistribution subject to ASME license or copyright; see http://www.asme.org/terms/Terms_Use.cfm



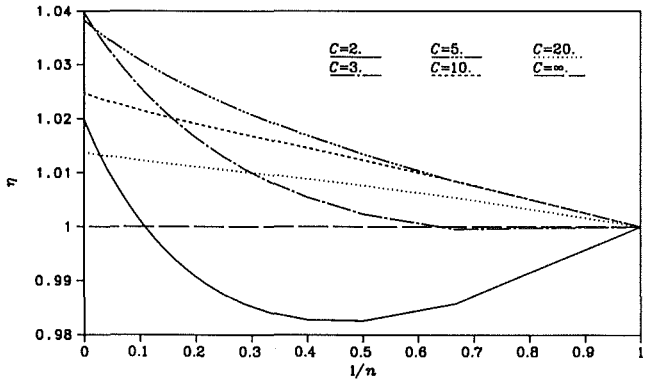
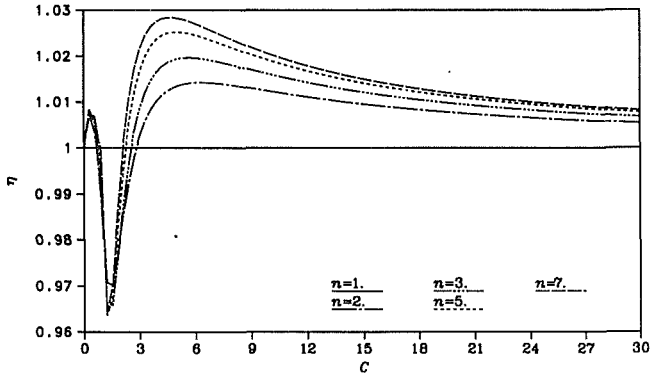


Fig. 4 The value of η as a function of $1/n$ for different strain ratios C's



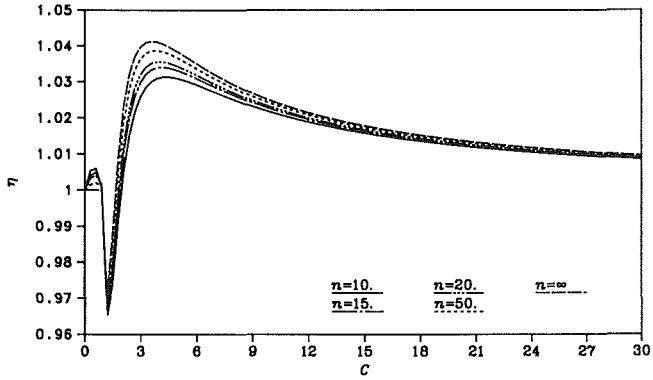


Fig. 5 The value of η as a function of the strain ratio C for different n's

$$\sigma_{\alpha\beta}=A_{\alpha\beta}\frac{2^{1/n}\sigma_0}{3^{(n+1)/2n}(\sigma_0/E)^{1/n}}\,|e_{11}|^{(1-n)/n}\times(1+C_1+C_1^2+C_2^2)^{(1-n)/2n}. \quad (40)$$

Here, we take $K=\sigma_0/E$. The normalized membrane forces are

$$\overline{N}_{\alpha\beta}=\text{sign}(\overline{e}_{11})\frac{A_{\alpha\beta}}{e_{11}}\frac{2^{1/n}}{3^{(n+1)/2n}}\,|\overline{e}_{11}|^{1/n}\times(1+C_1+C_1^2+C_2^2)^{(1-n)/2n}. \quad (41)$$

From Eq. (20), the equivalent stress resultant is

$$\overline{\Sigma}=\left[\frac{4}{3}(1+C_1+C_1^2+C_2^2)\right]^{1/2n}|\overline{e}_{11}|^{1/n}. \quad (42)$$

We go back to Eq. (29), the equivalent generalized plastic strain is

$$\overline{\Lambda}=\left[\frac{4(1+C_1+C_1^2+C_2^2)}{3}\right]^{1/2}|\overline{e}_{11}|. \quad (43)$$

Combining Eqs. (35), (42), and (43) gives

$$\eta=1. \quad (44)$$

When $C=\infty$, referring to Eq. (15) in Chou et al. (1991), the normalized moments are

$$\overline{M}_{\alpha\beta}=\text{sign}\,(\overline{\kappa}_{11})\frac{B_{\alpha\beta}}{\kappa_{11}}\frac{4n}{3^{(n-1)/2n}(4n+2)}\,|\overline{\kappa}_{11}|^{1/n}\times(1+C_1+C_1^2+C_2^2)^{(1-n)/2n}, \quad (45)$$

where

$$B_{\alpha\beta}=\kappa_{\gamma\gamma}\delta_{\alpha\beta}+\kappa_{\alpha\beta},\ C_1=\frac{\kappa_{22}}{\kappa_{11}},\ \text{and}\ C_2=\frac{\kappa_{12}}{\kappa_{11}}.$$

Then the equivalent stress resultant is

$$\overline{\Sigma}=[3(1+C_1+C_1^2+C_2^2)]^{1/2n}\frac{4n}{4n+2}\,|\overline{\kappa}_{11}|^{1/n}\alpha^{1/2} \quad (46)$$

The equivalent generalized plastic strain is

$$\overline{\Lambda}=\left[\frac{3(1+C_1+C_1^2+C_2^2)}{4\alpha}\right]^{1/2}|\overline{\kappa}_{11}|. \quad (47)$$

Combining equations (17), (35), (46), and (47) gives

$$\eta=1. \quad (48)$$

The values of η for the two special cases of $C=0$ and $C=\infty$ are equal to 1 for all n's as indicated in Eqs. (44) and (48). In Fig. 4, the values of η as functions of $1/n$ are shown for several C's. Also, the values of η as functions of C are shown for several n's in Fig. 5. In these figures, in general, η is very close to 1 for all n's and C's. The maximum deviation of η from 1 is about 4 percent at $C\approx 3.6$ for $n=\infty$. For the materials with the hardening exponent from $n=3$ to $n=10$, the maximum deviation of η from 1 is about 3 percents. Therefore, the hardening rule of the yield surfaces in the stress resultant space can be approximately expressed as

$$\overline{\Sigma}=\overline{\Lambda}^{1/n}. \quad (49)$$

5 Conclusion

Although the assumed quadratic yield surfaces are different from those of Chou et al. (1991) except $n=1$, the errors are small for high hardening materials (with small n) as shown in Fig. 2. Under this assumption, the work-equivalent function of generalized plastic strain rate for a plate element is obtained. Furthermore, the hardening rule between the equivalent stress resultant and generalized plastic strain is established by Eqs. (20), (29), and (49) to describe the evolution of subsequent yield surfaces in the stress resultant space. The hardening rule reduces to those for power-law hardening Mises materials un-

Downloaded 03 May 2010 to 171.66.16.245. Redistribution subject to ASME license or copyright; see http://www.asme.org/terms/Terms_Use.cfm

der pure moments and pure membrane forces. The associate flow rule under plastic loading is specified by Eq. (24).

The hardening rule of Eqs. (20), (29), and (49) together with the associate flow rule of Eq. (24) has been examined extensively under proportional and nonproportional loading conditions within the context of both the small-strain and the finite deformation approaches by Chou et al. (1992a). In Chou et al. (1992a), a rate form of stress resultant constitutive law is presented, where an appropriate co-rotational rate of stress resultants and the thickness thinning effect due to finite deformation of plates are considered. The results of the investigation in Chou et al. (1992a) suggest that within the context of finite deformation approach the simple power-law hardening rule for stress resultants can be used to approximate the elastic-plastic behavior of plates for an equivalent membrane strain less than $1/n$. When the equivalent membrane strain becomes larger than $1/n$, the simple power-law hardening rule must be modified to take account for the thinning effect due to finite deformation.

In Chou et al. (1992b), a modified hardening rule has been used to simulate a hemispherical punch stretching to a maximum equivalent membrane strain larger than $1/n$; the results are compared well with those based on the through-the-thickness integration method. Also, in Chou et al. (1992b), the hardening rule has been used to simulate a plane-strain draw operation, where some material elements are subject to substantially nonproportional loading. The results of the computations can catch the essential characteristics of the deformation patterns and are compared extremely well with those based on the through-the-thickness integration method. These investigations of Chou et al. (1992a, b) indicate that the stress resultant constitutive law for power-law hardening materials in Eqs. (20), (24), (29), and (49) with a slight modification due to finite deformation can be used to simulate sheet-metal-forming processes with very good accuracy and significant saving of computational time.

Acknowledgment

The authors acknowledge the support of this work by the University Research Program of Ford Motor Company.

References

Bieniek, M. P., and Funaro, J. R., 1976, "Elasto-Plastic Behavior of Plates and Shells," Report No. DNA-3954T, Weidlinger Associates, New York.

Calladine, C. R., 1972, "On the Derivative of Yield Conditions for Shells," ASME JOURNAL OF APPLIED MECHANICS, pp. 852–853.

Chou, C. H., Pan, J., and Tang, S.C., 1991, "Constitutive Laws for Thin Plates of Power-Law Materials," *Int. J. Solids Struct.*, Vol. 27, pp. 1387–1400.

Chou, C. H., Pan, J., and Tang, S. C., 1992a, "Nonproportional Loading Effects on Elastic-Plastic Behavior Based on Stress Resultants for Thin Plates of Strain Hardening Materials," in Preparation for publication.

Chou, C. H., Pan, J., and Tang, S. C. 1992b, "Applications of a Stress Resultant Constitutive Law to Sheet Metal Forming," in preparation for publication.

Crisfield, M. A., 1974, "On An Approximate Yield Criterion for Thin Steel Shells," TRRL Report LR658, Transport and Road Research Laboratory, Crowthorne, Berkshire, U. K.

Eggers, H., and Kröplin, B., 1978, "Yielding of Plates with Hardening and Large Deformations," *Int. J. Num. Meth. Eng.*, Vol. 12, pp. 739–750.

Eidsheim, O. M., and Larsen, P. K., 1981, "A Study of Some Generalized Constitutive Methods for Elasto-Plastic Shells," *Nonlinear Finite Element Analysis in Structural Mechanics*, W. Underlich, K. J. Bathe, and E. Stein, eds., Springer, Berlin New York, pp. 364–384.

Hill, R., 1979, "Theoretical Plasticity of Textured Aggregates," *Math. Proc. Comb. Phil. Soc.*, Vol. 85, pp. 179–191.

Hodge, P. G., 1954, "The Rigid-Plastic Analysis of Symmetrically Loaded Cylindrical Shells," ASME JOURNAL OF APPLIED MECHANICS, Vol. 21, pp. 336–342.

Ilyushin, A. A., 1948, *Plasticity*, Gostekhizdat, Moscow, (French translation: *Plasticité*, Eyrolles, Paris, 1956).

Naghdi, P. M., and Trapp, J. A., 1975, "The Significance of Formulating Plasticity Theory With Reference to Loading Surfaces in Strain Space," *Int. J. Engng. Sci.*, Vol. 13, pp. 785–797.

Onat, E. T., 1955, "The Plastic Collapse of Cylindical Shells Under Axially Symmetric Loading," *Quarterly of Applied Mathematics*, Vol. 13, pp. 63–72.

Papadopoulos, P., and Taylor, R. L., 1990, "Elasto-Plastic Analysis of Reissner-Mindlin Plates," *Appl. Mech. Rev.*, Vol. 43, No. 5, Part 2, pp. S40–S50.

Press, W. H., Flannery, B. P., Teukolsky, S. A., and Vetterling, W. T., 1986, *Numerical Recipes: The Art of Scientific Computing*, Cambridge University Press, New York.

Downloaded 03 May 2010 to 171.66.16.245. Redistribution subject to ASME license or copyright; see http://www.asme.org/terms/Terms_Use.cfm

Journal of Applied Mechanics

Brief Notes

A Brief Note is a short paper that presents a specific solution of technical interest in mechanics but which does not necessarily contain new general methods or results. A Brief Note should not exceed 1500 words *or equivalent* (a typical one-column figure or table is equivalent to 250 words; a one line equation to 30 words). Brief Notes will be subject to the usual review procedures prior to publication. After approval such Notes will be published as soon as possible. The Notes should be submitted to the Technical Editor of the JOURNAL OF APPLIED MECHANICS. Discussions on the Brief Notes should be addressed to the Editorial Department, ASME, United Engineering Center, 345 East 47th Street, New York, N. Y. 10017, or to the Technical Editor of the JOURNAL OF APPLIED MECHANICS. Discussions on Brief Notes appearing in this issue will be accepted until two months after publication. Readers who need more time to prepare a Discussion should request an extension of the deadline from the Editorial Department.

Analytic Study of Linear and Nonlinear Mode Localization

A. F. Vakakis[1]

The localization of the normal modes of weakly coupled vibrating systems is examined with a new exact, analytical method. Both linear and nonlinear systems are considered and the mode localization is examined by means of "balancing diagrams." This study complements previous studies of the author and co-workers on investigating mode localization in systems with nonlinear stiffness elements.

1 Introduction

The existence of localized modes in linear structures or in structures with weak dry friction is well documented in the literature (Wei and Pierre, 1989; Bendiksen, 1987; Pierre and Dowell, 1987; Hodges, 1982). These modes appear in "mistuned" periodic or cyclic structures, and their main characteristic is that they correspond to free motions whose energy is mainly confined to only a limited number of substructures of the general system. A variety of perturbation and numerical techniques was applied to the localization problem, and it was found that necessary conditions for the existence of localized modes were a "mistuning" of the substructures of the periodic system (i.e., an introduction of random imperfections in the substructures), as well as a weak substructure coupling. All of the aforementioned studies dealt with linear periodic elements, with the exception of (Wei and Pierre, 1989) where dry friction was considered.

In this work, the mode localization of systems with stiffness nonlinearities will be examined. This will be achieved by using the notion of "nonlinear normal mode" (Rosenberg, 1966; Rand, 1974; Caughey et al., 1990; Vakakis, 1990) and by constructing linear and nonlinear "modal balancing diagrams." A "nonlinear normal mode" is defined as a free nonlinear oscillation during which the coordinates of the system oscillate periodically, reaching their extremum amplitudes at the same instant of time. If the motion in the configuration line is a straight line, the mode is termed "similar," whereas if it is a curve, "nonsimilar." A two-degree-of-freedom oscillator is examined, and it is shown that localized similar nonlinear modes exist even *in the absence of "mistuning."* Moreover, by using a linear "modal balancing diagram" it will be shown why the conditions of "mistuning," and of weak coupling are necessary for mode localization in linear systems. The results reported in this work are complementary to those reported in two recent works, (Vakakis, 1992; Vakakis and Cetinkaya, 1992), where nonsimilar mode localization in nonlinear periodic systems was examined.

2 Similar Mode Localization

Consider a two-degree-of-freedom oscillator consisting of two one-degree-of-freedom subsystems, connected by means of a coupling stiffness. All stiffnesses are assumed to be proportional to the sth power of the displacement, where s is an odd number, reflecting on certain symmetries of the potential function (Vakakis, 1990). Moreover, it is assumed that the system is "tuned," i.e., that its individual subsystems are identical. The assumption of "tuning" is common in the existing works on mode linearization. The two equations of motion are given by

$$\ddot{x}_1 + f_{1s}x_1^s + f_{2s}(x_1 - x_2)^s = 0$$
$$\ddot{x}_2 + f_{1s}x_2^s + f_{2s}(x_2 - x_1)^s = 0 \tag{1}$$

where $f_{js} > 0$, $j = 1, 2$. The similar normal modes of this system can be obtained by requiring that (Caughey et al., 1990):

$$x_2 = cx_1. \tag{2}$$

Substituting (2) into (1), and equating the respective coefficients of x_1^s and x_2^s in the two equations, the following "modal balancing equation" for c results:

$$c(1 - c^{s-1})f_{1s} = (c-1)^s(c+1)f_{2s}. \tag{3}$$

The values $c = \pm 1$ are always solutions of (3). However, additional roots for c are possible. For $s = 1$ (linear system), the additional solution ($f_{21} = 0$, c = arbitrary) exists; as shown later, the perturbation of this solution by small linear imperfections gives rise to linear mode localization, i.e., to free

[1]Department of Mechanical and Industrial Engineering, University of Illinois at Urbana-Champaign, Urbana, IL 61801. Assoc. Mem. ASME.

Contributed by the Applied Mechanics Division of THE AMERICAN SOCIETY OF MECHANICAL ENGINEERS for publication in the ASME JOURNAL OF APPLIED MECHANICS.

Manuscript received by the ASME Applied Mechanics Division, Nov. 10, 1990; final revision, May 17, 1992. Associate Technical Editor: P. D. Spanos.

Copyright © 1993 by ASME
Downloaded 03 May 2010 to 171.66.16.245. Redistribution subject to ASME license or copyright; see http://www.asme.org/terms/Terms_Use.cfm

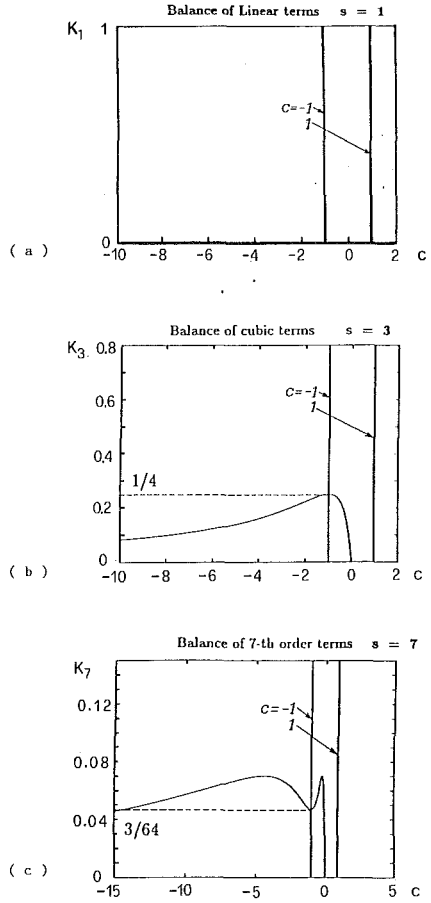


Fig. 1 Modal balancing diagrams: (*a*) linear, (*b*) cubic, (*c*) seventh order

motions confined in only one of the two masses of the system. For $s = 3, 5, \ldots$ the additional roots for c are given by

$$\sum_{p=1}^{(s-1)/2} c^{2p-1} + (f_{2s}/f_{1s})(1-c)^{s-1} = 0. \quad (4)$$

These additional modes bifurcate from the antisymmetric nonlinear normal mode $c = -1$ when the ratio $K_s = f_{2s}/f_{1s}$ is (Vakakis, 1990)

$$K_s = (K_s)_{\text{bif}} = (f_{2s}/f_{1s})_{\text{bif}} = \left[\sum_{p=1}^{(s-1)/2} (-1)^{2p-1}\right] / 2^{s-1} = (s-1)/2^s. \quad (5)$$

The solutions of Eqs. (3) are graphically presented in Fig. 1, for $s = 1$, 3 and 7, and the associated plots are termed "modal balancing diagrams." Note that, the bifurcating modes can only occur for *weak* coupling between subsystems, i.e., only for $K_s \ll 1$. For the linear system, no mode localization is possible. This is concluded from Fig. 1 (*a*), where both modes of the system are "global" (the magnitudes of x_1 and x_2 are of the same order), for all values of substructure coupling. *However, this is not the case for the nonlinear systems.*

Indeed, for $s = 3$, 7 and for weak coupling, the bifurcating modes are localized: the corresponding bifurcating values of c are either close to zero, or are very large quantities (actually, as shown in Vakakis (1990), both bifurcating modes represent the same motion due to the symmetry of the system). Thus, for weak nonlinear coupling, both bifurcating modes are localized about the first or the second coordinate. In addition to these localized nonlinear modes, there exist two nonlocalized ones, corresponding to $c = \pm 1$. A linearized stability analysis indicates that, for weak coupling, the bifurcating modes and

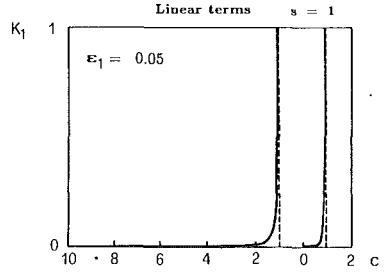


Fig. 2 Linear balancing diagram for the "mistuned" system

the $c = +1$ mode are orbitally stable, whereas the $c = -1$ mode is orbitally unstable. Thus, nonlinear mode localization is a physically observable phenomenon, and it occurs for the "tuned" system, and for low values of nonlinear stiffness coupling. Hence, in contrast to linear systems, no "mistuning" is needed for the occurrence of localized nonlinear modes.

Mode localization can be also observed in the linear system. However, to achieve this, one must perturb the linear balancing diagram of Fig. 1 (*a*), by "mistuning" the system, i.e., by making the two linear subsystems slightly different. Assuming that a structural mistuning ϵ_1 is introduced into one of the stiffnesses f_{1s} of Eqs. (1), the linear balancing equation becomes

$$f_{1s} + f_{2s}(1-c)^s = f_{1s}(1+\epsilon_s)c^{s-1} - f_{2s}(1-c)^s/c, \quad s = 1 \quad (6)$$

and is graphically presented in Fig. 2. Note that, for weak mistuning and large coupling ratios K_1, no mode localization occurs; on the contrary, for weak coupling, mode localization does occur, since the values of c are either close to zero, or are very large quantities. These conclusions are in full agreement with the results reported in the existing works on linear mode localization. The outlined methodology can be easily applied to periodic systems consisting of more than two subsystems, however the associated expressions become more complicated and numerical techniques must be implemented.

3 Discussion

In this work, a simple oscillator was analyzed to demonstrate linear and nonlinear mode localization of systems with identical, weakly coupled, nonlinear subsystems. An exact analysis of mode localization was performed, and mode localization of orbitally stable nonlinear modes was found to exist in the "tuned" nonlinear system, for weak substructure coupling. In addition to localized modes, a pair of nonlocalized modes was found to exist in the nonlinear case. Localization of these later modes is not possible, even in the presence of "mistuning" in the system. Indeed, "modal balancing diagrams" of such "mistuned" nonlinear systems were computed in (Vakakis, 1990), and no localization of the $c = \pm 1$ modes was observed.

For the linear system, mode localization can only exist in the "mistuned" system and for weak substructure coupling. This result is a consequence of the fact that the line ($K_1 = 0$, c = arbitrary) is a solution in the linear "modal balancing diagram." Mode localization can only occur when this solution is perturbed, and this can only be achieved with the introduction of "mistuning." On the contrary, ($K_s = 0$, c = arbitrary) is not a solution in the nonlinear balancing diagrams and as a result, mistuning of the nonlinear system does not introduce any qualitatively different results. In fact, "mistuning" of the nonlinear system results in a mere perturbation of the existing localized and nonlocalized modes: the resulting modes are of the same global shape with that of the unperturbed ones.

Finally, we note that *the occurrence of nonlinear mode localization is not an artifact of the symmetry of the system.* Indeed, in recent works (Vakakis, 1992; Vakakis and Cetinkaya, 1992) it was shown that the nonlinear mode localization is caused by the fact that the nonlinear system has frequencies

Downloaded 03 May 2010 to 171.66.16.245. Redistribution subject to ASME license or copyright; see http://www.asme.org/terms/Terms_Use.cfm

of free oscillation which are amplitude dependent. Therefore, *nonsymmetric initial conditions lead to frequency differences and thus, to effective frequency mistuning between substructures*. In linear cyclic systems such mistunings are only generated when the cyclic symmetry is perturbed by parameter irregularities.

Acknowledgments

The author would like to thank a reviewer who indicated the simplification of Eq. (5).

References

Bendiksen, O., 1987, "Mode Localization in Large Space Structures," *AIAA Journal*, Vol. 25, No. 9, pp. 1241–1248.

Caughey, T. K., Vakakis, A., and Sivo, J. M., 1990, "Analytic Study of Similar Normal Modes and Their Bifurcations in a Class of Strongly Non-Linear Systems," *International Journal of Non-Linear Mechanics*, Vol. 25, No. 5, pp. 521–533.

Hodges, C., 1982, "Confinement of Vibration by Structural Irregularity," *Journal of Sound and Vibration*, Vol. 82, No. 3 pp. 411–424.

Pierre, C., and Dowell, E. H., 1987, "Localization of Vibrations by Structural Irregularity," *Journal of Sound and Vibration*, Vol. 114, No. 3, pp. 549–564.

Rand, R., 1974, "A Direct Method for Nonlinear Normal Modes," *International Journal of Nonlinear Mechanics*, Vol. 9, pp. 363–368.

Rosenberg, R., 1966, "On Nonlinear Vibrations of Systems with Many Degrees of Freedom," *Advances of Applied Mechanics*, Vol. 9, pp. 155–242.

Vakakis, A. F., 1990, "Analysis and Identification of Linear and Nonlinear Normal Modes in Vibrating Systems," PhD Thesis, California Institute of Technology, Pasadena, CA.

Vakakis, A. F., 1992, "Nonsimilar Normal Oscillations in a Strongly Nonlinear Discrete System," *Journal of Sound and Vibration*, Vol. 158, No. 2, pp. 341–361.

Vakakis, A. F., and Cetinkaya, C., 1992, "Mode Localization in a Class of Multi-Degree-of-Freedom Nonlinear Systems with Cyclic Symmetry," *SIAM Journal of Applied Mathematics*, in press.

Wei, S.-T., and Pierre, C., 1989, "Effects of Dry Friction Damping on the Occurrence of Localized Forced Vibrations in Nearly Cyclic Structures," *Journal of Sound and Vibration*, Vol. 129, No. 3, pp. 397–416.

The Elastic Field for a Sliding Conical Punch on an Isotropic Half-Space

M. T. Hanson[2]

1 Introduction

In a recent paper Hanson (1992) has derived closed-form expressions for the elastic field resulting from conical indentation of a transversely isotropic half space. This analysis considered frictionless indentation and indentation with sliding using a Coulomb friction law. Thus, the shear stress for sliding was obtained by multiplying the contact pressure by a friction coefficient. The interested reader is referred to this previous paper which discusses the motivation for the analysis and a review of earlier research on this problem.

One previous solution obtained by Sneddon (1948) evaluated the closed-form expressions for the elastic field resulting from frictionless conical indentation of an isotropic half space. Hanson (1992) showed that by taking a limiting form of his expressions for transverse isotropy he was able to obtain the isotropic solution and it agreed with Sneddon's results. The forms of the expressions are quite different, however, and it seems that the form recently derived by Hanson (1992) is simpler since only two distorted length parameters are needed and the elastic field is given in simple forms of them. The solution given by Sneddon (1948) contains four parameters, two of which are parametric angles, and thus the form of the solution is not quite so convenient.

The previous solution given in Hanson (1992) evaluates the isotropic limit for frictionless indentation only. Here the expressions for shear loading are derived for isotropy. They have not been given previously in the literature.

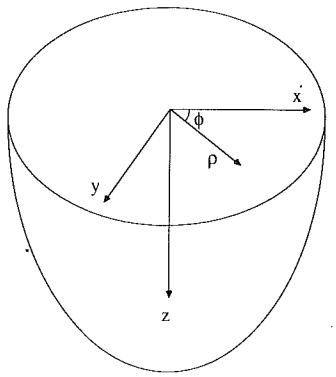


Fig. 1 Geometry and coordinate system

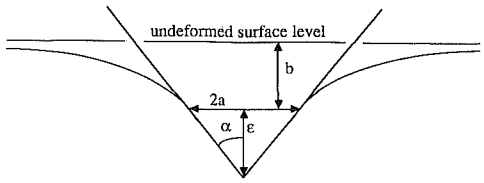


Fig. 2 Geometry of conical indentation

2 Elastic Field for Sliding of a Conical Punch on an Isotropic Half-Space

Consider the half-space $z > 0$ shown in Fig. 1. A cylindrical coordinate system (ρ, ϕ, z) is adopted to locate points inside the half-space. The displacement components u, v, and w in the x, y, and z directions are used along with the stress components σ_{xx}, σ_{yy}, σ_{zz}, τ_{xy}, τ_{xz}, τ_{yz}. The elastic field is given in complex notation by introducing the quantities $u^c = u + iv$, $\sigma_1 = \sigma_{xx} + \sigma_{yy}$, $\sigma_2 = \sigma_{xx} - \sigma_{yy} + 2i\tau_{xy}$ and $\tau_z = \tau_{xz} + i\tau_{yz}$ where i is the complex number $i = \sqrt{-1}$.

Figure 2 shows the problem under consideration which is indentation by a cone shaped punch with vertex angle α. The elastic field for frictionless indentation when the half-space is transversely isotropic or isotropic is given in Hanson (1992) and the relationships between the contact parameters are obtained. This previous analysis also considered sliding by taking the shear traction in the contact region equal to the contact pressure multiplied by a friction coefficient. The elastic field for sliding was given only for the case of transverse isotropy.

To obtain the isotropic solution a limiting form of the transversely isotropic solution is taken. The solution for transverse isotropy is given in terms of the material parameters γ_1, γ_2, γ_3, m_1, m_2, H, A_{44}, and A_{66} which are defined in Hanson (1992), or see Fabrikant (1989). For isotropy γ_1, γ_2, γ_3, m_1, $m_2 \to 1$ (Fabrikant, 1989), while $H = (1 - \nu^2)/\pi E$ and $A_{44} = A_{66} = E/[2(1 + \nu)]$ where E is Young's modulus and ν is Poisson's ratio. To extract the isotropic field from the transversely isotropic results given by Hanson (1992), one needs the relations for the isotropic limit

$$\sum_{k=1}^{2} \frac{1}{m_k - 1} f(z_k) = -f(z) - \frac{z}{2(1-\nu)} f'(z), \qquad (1)$$

[2]Department of Engineering Mechanics, University of Kentucky, Lexington, KY 40506-0046. Mem. ASME.

Contributed by the Applied Mechanics Division of The American Society of Mechanical Engineers for publication in the ASME Journal of Applied Mechanics. Manuscript received by the ASME Applied Mechanics Division, July 5, 1991; final revision, Apr. 23, 1992. Associate Technical Editor: X. Markenscoff.

Downloaded 03 May 2010 to 171.66.16.245. Redistribution subject to ASME license or copyright; see http://www.asme.org/terms/Terms_Use.cfm

of free oscillation which are amplitude dependent. Therefore, *nonsymmetric initial conditions lead to frequency differences and thus, to effective frequency mistuning between substructures*. In linear cyclic systems such mistunings are only generated when the cyclic symmetry is perturbed by parameter irregularities.

Acknowledgments

The author would like to thank a reviewer who indicated the simplification of Eq. (5).

References

Bendiksen, O., 1987, "Mode Localization in Large Space Structures," *AIAA Journal*, Vol. 25, No. 9, pp. 1241–1248.

Caughey, T. K., Vakakis, A., and Sivo, J. M., 1990, "Analytic Study of Similar Normal Modes and Their Bifurcations in a Class of Strongly Non-Linear Systems," *International Journal of Non-Linear Mechanics*, Vol. 25, No. 5, pp. 521–533.

Hodges, C., 1982, "Confinement of Vibration by Structural Irregularity," *Journal of Sound and Vibration*, Vol. 82, No. 3 pp. 411–424.

Pierre, C., and Dowell, E. H., 1987, "Localization of Vibrations by Structural Irregularity," *Journal of Sound and Vibration*, Vol. 114, No. 3, pp. 549–564.

Rand, R., 1974, "A Direct Method for Nonlinear Normal Modes," *International Journal of Nonlinear Mechanics*, Vol. 9, pp. 363–368.

Rosenberg, R., 1966, "On Nonlinear Vibrations of Systems with Many Degrees of Freedom," *Advances of Applied Mechanics*, Vol. 9, pp. 155–242.

Vakakis, A. F., 1990, "Analysis and Identification of Linear and Nonlinear Normal Modes in Vibrating Systems," PhD Thesis, California Institute of Technology, Pasadena, CA.

Vakakis, A. F., 1992, "Nonsimilar Normal Oscillations in a Strongly Nonlinear Discrete System," *Journal of Sound and Vibration*, Vol. 158, No. 2, pp. 341–361.

Vakakis, A. F., and Cetinkaya, C., 1992, "Mode Localization in a Class of Multi-Degree-of-Freedom Nonlinear Systems with Cyclic Symmetry," *SIAM Journal of Applied Mathematics*, in press.

Wei, S.-T., and Pierre, C., 1989, "Effects of Dry Friction Damping on the Occurrence of Localized Forced Vibrations in Nearly Cyclic Structures," *Journal of Sound and Vibration*, Vol. 129, No. 3, pp. 397–416.

The Elastic Field for a Sliding Conical Punch on an Isotropic Half-Space

M. T. Hanson[2]

1 Introduction

In a recent paper Hanson (1992) has derived closed-form expressions for the elastic field resulting from conical indentation of a transversely isotropic half space. This analysis considered frictionless indentation and indentation with sliding using a Coulomb friction law. Thus, the shear stress for sliding was obtained by multiplying the contact pressure by a friction coefficient. The interested reader is referred to this previous paper which discusses the motivation for the analysis and a review of earlier research on this problem.

One previous solution obtained by Sneddon (1948) evaluated the closed-form expressions for the elastic field resulting from frictionless conical indentation of an isotropic half space. Hanson (1992) showed that by taking a limiting form of his expressions for transverse isotropy he was able to obtain the isotropic solution and it agreed with Sneddon's results. The forms of the expressions are quite different, however, and it seems that the form recently derived by Hanson (1992) is simpler since only two distorted length parameters are needed and the elastic field is given in simple forms of them. The solution given by Sneddon (1948) contains four parameters, two of which are parametric angles, and thus the form of the solution is not quite so convenient.

The previous solution given in Hanson (1992) evaluates the isotropic limit for frictionless indentation only. Here the expressions for shear loading are derived for isotropy. They have not been given previously in the literature.

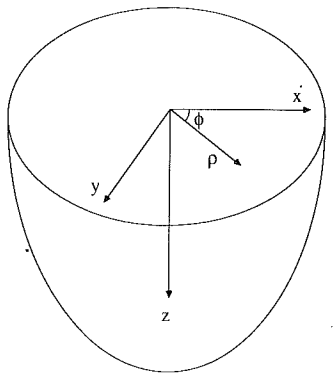


Fig. 1 Geometry and coordinate system

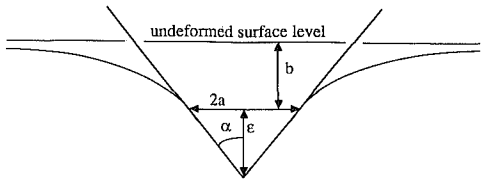


Fig. 2 Geometry of conical indentation

2 Elastic Field for Sliding of a Conical Punch on an Isotropic Half-Space

Consider the half-space $z > 0$ shown in Fig. 1. A cylindrical coordinate system (ρ, ϕ, z) is adopted to locate points inside the half-space. The displacement components u, v, and w in the x, y, and z directions are used along with the stress components σ_{xx}, σ_{yy}, σ_{zz}, τ_{xy}, τ_{xz}, τ_{yz}. The elastic field is given in complex notation by introducing the quantities $u^c = u + iv$, $\sigma_1 = \sigma_{xx} + \sigma_{yy}$, $\sigma_2 = \sigma_{xx} - \sigma_{yy} + 2i\tau_{xy}$ and $\tau_z = \tau_{xz} + i\tau_{yz}$ where i is the complex number $i = \sqrt{-1}$.

Figure 2 shows the problem under consideration which is indentation by a cone shaped punch with vertex angle α. The elastic field for frictionless indentation when the half-space is transversely isotropic or isotropic is given in Hanson (1992) and the relationships between the contact parameters are obtained. This previous analysis also considered sliding by taking the shear traction in the contact region equal to the contact pressure multiplied by a friction coefficient. The elastic field for sliding was given only for the case of transverse isotropy.

To obtain the isotropic solution a limiting form of the transversely isotropic solution is taken. The solution for transverse isotropy is given in terms of the material parameters γ_1, γ_2, γ_3, m_1, m_2, H, A_{44}, and A_{66} which are defined in Hanson (1992), or see Fabrikant (1989). For isotropy γ_1, γ_2, γ_3, m_1, $m_2 \to 1$ (Fabrikant, 1989), while $H = (1 - \nu^2)/\pi E$ and $A_{44} = A_{66} = E/[2(1 + \nu)]$ where E is Young's modulus and ν is Poisson's ratio. To extract the isotropic field from the transversely isotropic results given by Hanson (1992), one needs the relations for the isotropic limit

$$\sum_{k=1}^{2} \frac{1}{m_k - 1} f(z_k) = -f(z) - \frac{z}{2(1-\nu)} f'(z), \qquad (1)$$

[2]Department of Engineering Mechanics, University of Kentucky, Lexington, KY 40506-0046. Mem. ASME.

Contributed by the Applied Mechanics Division of The American Society of Mechanical Engineers for publication in the ASME Journal of Applied Mechanics. Manuscript received by the ASME Applied Mechanics Division, July 5, 1991; final revision, Apr. 23, 1992. Associate Technical Editor: X. Markenscoff.

Copyright © 1993 by ASME
Downloaded 03 May 2010 to 171.66.16.245. Redistribution subject to ASME license or copyright; see http://www.asme.org/terms/Terms_Use.cfm

$$\sum_{k=1}^{2}\frac{m_k}{\gamma_k(m_k-1)}f(z_k)=\frac{(1-2\nu)f(z)-zf'(z)}{2(1-\nu)}, \quad (2)$$

$$\sum_{k=1}^{2}\frac{\gamma_k^2-(1+m_k)\gamma_3^2}{\gamma_k^2(m_k-1)}f(z_k)=\frac{2(1+\nu)f(z)+zf'(z)}{2(1-\nu)}, \quad (3)$$

$$\frac{1}{\gamma_1-\gamma_2}\sum_{k=1}^{2}(-1)^{k+1}f(z_k)=-zf'(z), \quad (4)$$

$$\frac{1}{\gamma_1-\gamma_2}\sum_{k=1}^{2}\frac{(-1)^{k+1}}{\gamma_k}f(z_k)=-f(z)-zf'(z). \quad (5)$$

Applying the above results to the formulas derived by Hanson (1992) for a sliding conical punch on a transversely isotropic half-space, one may verify the following isotropic elastic field:

$$u^c=\frac{(1+\nu)P}{\pi Ea^2}\left\{f\left[(2-\nu)\left((a)\sin^{-1}\frac{l_1(a)}{\rho}+\sqrt{l_2^2(a)-a^2}-\sqrt{\rho^2+z^2}\right)-\frac{(5-2\nu)z}{2}(\ln[l_2(a)+\sqrt{l_2^2(a)-\rho^2}]-\ln[z+\sqrt{\rho^2+z^2}])\right]+\frac{\bar{f}e^{i2\phi}}{6\rho^2}\left[(1-2\nu)3za^2+[2\nu(\rho^2+z^2)-3z^2]\times\sqrt{\rho^2+z^2}+2\nu[4a^2-3l_1^2(a)-l_2^2(a)]\sqrt{l_2^2(a)-a^2}-3z^2\frac{2a^2-l_2^2(a)}{\sqrt{l_2^2(a)-a^2}}\right]\right\}, \quad (6)$$

$$w=\frac{(1+\nu)P}{\pi Ea^2}[f_x\cos\phi+f_y\sin\phi]\left\{(1-2\nu)\left[\frac{\rho}{2}\ln[l_2(a)+\sqrt{l_2^2(a)-\rho^2}]-\frac{\rho}{2}\ln[z+\sqrt{\rho^2+z^2}]+\frac{a^2}{2\rho}-\frac{z\sqrt{\rho^2+z^2}}{2\rho}+\frac{\rho l_2(a)-2al_1(a)}{2\rho^2}\sqrt{l_2^2(a)-\rho^2}\right]-\frac{z}{\rho}(\sqrt{l_2^2(a)-a^2}-\sqrt{\rho^2+z^2})\right\}, \quad (7)$$

$$\sigma_1=\frac{P}{\pi a^2}[f_x\cos\phi+f_y\sin\phi]\left\{\frac{2(1+\nu)}{\rho}(\sqrt{l_2^2(a)-a^2}-\sqrt{\rho^2+z^2})+\frac{z}{\rho}\left(\frac{l_2(a)\sqrt{l_2^2(a)-\rho^2}}{l_2^2(a)-l_1^2(a)}-\frac{z}{\sqrt{\rho^2+z^2}}\right)\right\}, \quad (8)$$

$$\sigma_2=\frac{P}{\pi a^2}\left\{\frac{fe^{i\phi}}{2\rho}\left[2(2-\nu)(\sqrt{l_2^2(a)-a^2}-\sqrt{\rho^2+z^2})+\frac{zl_2(a)\sqrt{l_2^2(a)-\rho^2}}{l_2^2(a)-l_1^2(a)}-\frac{z^2}{\sqrt{\rho^2+z^2}}\right]+\frac{\bar{f}e^{i3\phi}}{6\rho^3}\left[-12(1-2\nu)za^2+\frac{4(3-2\nu)z^4+(9-10\nu)z^2\rho^2-2\nu\rho^4}{\sqrt{\rho^2+z^2}}+2\nu(12l_1^2(a)+4l_2^2(a)-3\rho^2-16a^2)\sqrt{l_2^2(a)-a^2}-\frac{z^2}{\sqrt{l_2^2(a)-a^2}}\left(12l_2^2(a)-24a^2-\frac{3\rho^2l_2^2(a)}{l_2^2(a)-l_1^2(a)}\right)\right]\right\}, \quad (9)$$

$$\sigma_{zz}=-\frac{P}{\pi a^2}[f_x\cos\phi+f_y\sin\phi]\times\frac{z}{\rho}\left(\frac{l_2(a)\sqrt{l_2^2(a)-\rho^2}}{l_2^2(a)-l_1^2(a)}-\frac{z}{\sqrt{\rho^2+z^2}}\right), \quad (10)$$

$$\tau_z=-\frac{P}{2\pi a^2}\left\{f\left[2\ln[l_2(a)+\sqrt{l_2^2(a)-\rho^2}]-2\ln[z+\sqrt{\rho^2+z^2}]+\frac{z\sqrt{l_2^2(a)-a^2}}{l_2^2(a)-l_1^2(a)}-\frac{z}{\sqrt{\rho^2+z^2}}\right]+\bar{f}e^{i2\phi}z\left[\frac{\rho^2+2z^2}{\rho^2\sqrt{\rho^2+z^2}}+\frac{\sqrt{l_2^2(a)-a^2}}{l_2^2(a)-l_1^2(a)}-\frac{2a\sqrt{\rho^2-l_1^2(a)}}{\rho^2l_1(a)}\right]\right\}. \quad (11)$$

In the above formulas, f is the complex friction coefficient $f = f_x + if_y$ (f_x and f_y are the coefficients of sliding friction in the x and y directions) and $l_1(a)$, $l_2(a)$ are defined as

$$l_1(a)=\frac{1}{2}(\sqrt{(\rho+a)^2+z^2}-\sqrt{(\rho-a)^2+z^2})$$

$$l_2(a)=\frac{1}{2}(\sqrt{(\rho+a)^2+z^2}+\sqrt{(\rho-a)^2+z^2}). \quad (12)$$

The elastic field on the surface $z = 0$ can be easily evaluated using the limits

$$\lim_{z\to 0}l_1(a)=\min(a,\rho), \quad \lim_{z\to 0}l_2(a)=\max(a,\rho), \quad (13)$$

where $\min(a, \rho)$ implies the minimum of the two values and $\max(a, \rho)$ the maximum. The traction on the surface $z = 0$ is easily seen to be

$$\sigma_{zz}=0, \qquad 0<\rho<\infty, \quad (14)$$

$$\tau_z=\begin{cases}-\dfrac{fP}{\pi a^2}\cosh^{-1}\left(\dfrac{a}{\rho}\right), & 0<\rho<a,\\ 0, & a<\rho<\infty,\end{cases} \quad (15)$$

where the identity $\cosh^{-1}(a/\rho) = \ln(a + \sqrt{a^2 - \rho^2}/\rho)$ has been used. Thus, the above solution corresponds to a zero normal traction and a shear traction which is equal to a friction coefficient multiplied by the frictionless contact pressure.

It was noted in this previous paper that the solution for sliding was approximate since the surface shear traction will alter the normal displacement on the surface thus altering the contact pressure. This interaction was neglected in deriving the above expressions. It was shown there that this intersection vanishes when the transversely isotropic material parameter $\alpha = 0$. For isotropy $\alpha = (1 - 2\nu)/[2(1 - \nu)]$ and thus $\alpha = 0$ corresponds for isotropy to an incompressible material. From Eq. (7) it is easy to verify that on the surface $z = 0$ the normal displacement $w = 0$ for $\nu = 1/2$.

As a final comment it is important to point out that the above solution is also approximate since it does not satisfy the Coulomb friction law exactly. The shear stress on the surface is not aligned with the tangential displacement. The exact solution satisfying all the necessary conditions of Coulomb friction must be found using a numerical solution procedure. However, the present closed-form expressions should provide a good quantitative estimate which can be simply used when investigating sharp sliding contacts.

References

Fabrikant, V. I., 1989, *Applications of Potential Theory in Mechanics: A Selection of New Results*, Kluwer Academic Publishers, The Netherlands, pp. 71–79.

Downloaded 03 May 2010 to 171.66.16.245. Redistribution subject to ASME license or copyright; see http://www.asme.org/terms/Terms_Use.cfm

Hanson, M. T., 1992, "The Elastic Field for Conical Indentation Including Sliding Friction for Transverse Isotropy," ASME JOURNAL OF APPLIED MECHANICS, Vol. 59, No. 2, Pt. 2, pp. S123–S130.

Sneddon, I. N., 1948, "Boussinesq's Problem for a Rigid Cone," *Proceedings of the Cambridge Philosophical Society*, Vol. 44, pp. 492–507.

On the Peak Shear Stresses in Adhesive Joints With Voids

J. N. Rossettos[3,5] and E. Zang[4,5]

Introduction

Adhesive bonded joints have many advantages in terms of stress distribution, design flexibility, and simplicity of fabrication. It is known, however, that defects in the adhesive can severely reduce the bond strength. The presence of voids or disbond type flaws in the adhesive will increase the peak stress levels which occur at the joint ends and near the flaw itself.

Past work related to the present study was done by Hart-Smith (1981) and Kan and Ratwani (1983). The work deals with voids or disbonds in the adhesive, is a structural mechanics rather than a continuum approach, and uses a shear lag model where the adherends take on only axial load and the adhesive takes only shear. This is appropriate in bonded joints which are designed so that the net load path does not produce bending.

In the present Note, it is shown how the stresses in a single lap joint with a void are completely characterized by two nondimensional parameters. In particular, it is shown, how, for sufficiently large values of a parameter $\bar{\theta}$ (see Eq. 7), peak shear stresses can be essentially unaffected by relatively large central void sizes. Since the parameter $\bar{\theta}$ contains both geometric and material variables, it indicates explicitly how peak stresses can be controlled by selection of geometry and/or material. The influence of the location of the void is also indicated. It is remarked that if transverse shear is also included in a higher order analysis (Renton and Vinson, 1977), the peak shear stress values will occur very near the overlap ends–dropping sharply to zero at the ends (consistent with free adhesive ends). The conclusion of the present Note, however, will change very little if at all.

Analysis

The assumptions in the present model, with the geometry in Fig. 1, are similar to those by Kan and Ratwani (1983), so that the thickness variation of the stresses in the adherends is neglected. Also, in the z direction it is assumed that $\epsilon_{1z} = \epsilon_{2z} = 0$. In what follows, $p_1(x)$ and $p_2(x)$ are resultant forces per unit width in the x-direction in adherends 1 and 2, respectively, and p_o is the resultant force in the adherends away from the joint region. The corresponding displacements are $u_1(x)$ and $u_2(x)$. Since the adhesive is assumed to take on only shear, the shear stress there is

$$\tau(x) = (G/h_o)(u_2 - u_1), \tag{1}$$

where G and h_o are the shear modulus and thickness of the adhesive, respectively. Relations for the forces and stresses in the adherends are written as

$$p_1 + p_2 = p_o; \quad \sigma_{1x} = p_1/h_1; \quad \sigma_{2x} = p_2/h_2. \tag{2}$$

Because of the assumptions ($\sigma_{1y} = \sigma_{2y} = 0$), the stress-strain relations for isotropic adherends are given by

$$\epsilon_{1x} = (1-\nu_1^2)(p_o - p_2)/E_1h_1$$
$$\epsilon_{2x} = (1-\nu_2^2)p_2/E_2h_2 \tag{3}$$

where E_1, E_2 are Young's moduli and ν_1, ν_2 are Poisson's ratios of the adherends. The strain-displacement relations are

$$\epsilon_{1x} = du_1/dx, \quad \epsilon_{2x} = du_2/dx \tag{4}$$

Equilibrium of an element of adherend 2 gives $dp_2/dx - \tau(x) = 0$. The derivative of this equation gives

$$d^2p_2/dx^2 - d\tau/dx = 0 \tag{5}$$

By then using Eqs. (1)–(4), Eq. (5) leads to an equation for p_2. It can be written in nondimensional form as

$$d^2P_2/d\xi^2 - \bar{\theta}^2P_2 = -\bar{\theta}^2/(1+R) \tag{6}$$

where

$$\bar{\theta}^2 = L^2G(1-\nu_1^2)(1+R)/h_oh_1E_1 \tag{7}$$

$$R = (1-\nu_2^2)E_1h_1/(1-\nu_1^2)E_2h_2 \tag{8}$$

and where the nondimensionalization is given by

$$(P_1, P_1) = (p_2, p_1)/p_o; \quad \xi = x/L$$
$$S = L\tau/p_o; \quad (U_2, U_1) = GL(u_2, u_1)/p_oh_o. \tag{9}$$

By observing Eqs. (7) and (8), the parameter, $\bar{\theta}$, involves overlap length and adhesive/adherend geometric and material properties, while R measures the degree to which the adherends are different. Normalized void size is given by $\xi_2 - \xi_1 = a_2/L - a_1/L$. Note that if plate 2 is an orthotropic composite, then without change in the basic Eq. (6), R is given by

$$R = (1-\nu_{2x}\nu_{2z})E_1h_1/(1-\nu_1^2)E_{2x}h_2. \tag{10}$$

In the solution procedure, the adhesive is divided into three regions. Equation (6) applies to the first and the third regions. In the void regions, $\tau = 0$, so Eq. (6) is replaced by $d^2P_2/d\xi^2 = 0$. The solutions to these equations in the three regions lead to six constants of integration which are determined by boundary conditions and appropriate continuity conditions between regions.

In region 1, $(0 \le \xi \le \xi_1)$

$$P_{21}(0) = 0; \quad P_{21}(\xi_1) = P_{22}(\xi_1). \tag{11a, b}$$

In region 2, (void) $(\xi_1 \le \xi \le \xi_2)$

$$P_{22} = \text{constant} \tag{12}$$

$$P'_{23}(\xi_2) = P'_{21}(\xi_1) + (\xi_2 - \xi_1)\bar{\theta}^2(P_{22} - 1/(1+R)), \tag{13}$$

where $(\,)' = d(\,)/d\xi$. Equation (13) represents the change in the shear stress from ξ_1 to ξ_2 because of unequal displacements of the adherends over the void region (Zang, 1990).

In region 3 $(\xi_2 \le \xi \le 1)$,

$$P_{22}(\xi_2) = P_{23}(\xi_2); \quad P_{23}(1) = 1. \tag{14a, b}$$

Note that in the notation, P_{2i}, the subscript, i, denotes the solution for P_2 in region i.

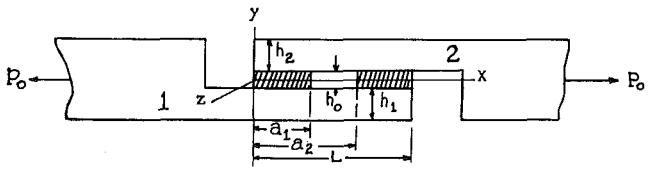


Fig. 1 Step lap joint with a void

[3]Professor. Fellow ASME.

[4]Graduate Student.

[5]Department of Mechanical Engineering, Northeastern University, Boston, MA 02115.

Contributed by the Applied Mechanics Division of THE AMERICAN SOCIETY OF MECHANICAL ENGINEERS for publication in the ASME JOURNAL OF APPLIED MECHANICS. Manuscript received by the ASME Applied Mechanics Division, June 11, 1992; final revision, Mar. 12, 1992. Associate Technical Editor: M. E. Fourney.

Downloaded 03 May 2010 to 171.66.16.245. Redistribution subject to ASME license or copyright; see http://www.asme.org/terms/Terms_Use.cfm

Hanson, M. T., 1992, "The Elastic Field for Conical Indentation Including Sliding Friction for Transverse Isotropy," ASME JOURNAL OF APPLIED MECHANICS, Vol. 59, No. 2, Pt. 2, pp. S123–S130.

Sneddon, I. N., 1948, "Boussinesq's Problem for a Rigid Cone," *Proceedings of the Cambridge Philosophical Society*, Vol. 44, pp. 492–507.

On the Peak Shear Stresses in Adhesive Joints With Voids

J. N. Rossettos[3,5] and E. Zang[4,5]

Introduction

Adhesive bonded joints have many advantages in terms of stress distribution, design flexibility, and simplicity of fabrication. It is known, however, that defects in the adhesive can severely reduce the bond strength. The presence of voids or disbond type flaws in the adhesive will increase the peak stress levels which occur at the joint ends and near the flaw itself.

Past work related to the present study was done by Hart-Smith (1981) and Kan and Ratwani (1983). The work deals with voids or disbonds in the adhesive, is a structural mechanics rather than a continuum approach, and uses a shear lag model where the adherends take on only axial load and the adhesive takes only shear. This is appropriate in bonded joints which are designed so that the net load path does not produce bending.

In the present Note, it is shown how the stresses in a single lap joint with a void are completely characterized by two nondimensional parameters. In particular, it is shown, how, for sufficiently large values of a parameter $\bar{\theta}$ (see Eq. 7), peak shear stresses can be essentially unaffected by relatively large central void sizes. Since the parameter $\bar{\theta}$ contains both geometric and material variables, it indicates explicitly how peak stresses can be controlled by selection of geometry and/or material. The influence of the location of the void is also indicated. It is remarked that if transverse shear is also included in a higher order analysis (Renton and Vinson, 1977), the peak shear stress values will occur very near the overlap ends–dropping sharply to zero at the ends (consistent with free adhesive ends). The conclusion of the present Note, however, will change very little if at all.

Analysis

The assumptions in the present model, with the geometry in Fig. 1, are similar to those by Kan and Ratwani (1983), so that the thickness variation of the stresses in the adherends is neglected. Also, in the z direction it is assumed that $\epsilon_{1z} = \epsilon_{2z} = 0$. In what follows, $p_1(x)$ and $p_2(x)$ are resultant forces per unit width in the x-direction in adherends 1 and 2, respectively, and p_o is the resultant force in the adherends away from the joint region. The corresponding displacements are $u_1(x)$ and $u_2(x)$. Since the adhesive is assumed to take on only shear, the shear stress there is

$$\tau(x) = (G/h_o)(u_2 - u_1), \tag{1}$$

where G and h_o are the shear modulus and thickness of the adhesive, respectively. Relations for the forces and stresses in the adherends are written as

$$p_1 + p_2 = p_o; \quad \sigma_{1x} = p_1/h_1; \quad \sigma_{2x} = p_2/h_2. \tag{2}$$

Because of the assumptions ($\sigma_{1y} = \sigma_{2y} = 0$), the stress-strain relations for isotropic adherends are given by

$$\epsilon_{1x} = (1-\nu_1^2)(p_o - p_2)/E_1h_1$$
$$\epsilon_{2x} = (1-\nu_2^2)p_2/E_2h_2 \tag{3}$$

where E_1, E_2 are Young's moduli and ν_1, ν_2 are Poisson's ratios of the adherends. The strain-displacement relations are

$$\epsilon_{1x} = du_1/dx, \quad \epsilon_{2x} = du_2/dx \tag{4}$$

Equilibrium of an element of adherend 2 gives $dp_2/dx - \tau(x) = 0$. The derivative of this equation gives

$$d^2p_2/dx^2 - d\tau/dx = 0 \tag{5}$$

By then using Eqs. (1)–(4), Eq. (5) leads to an equation for p_2. It can be written in nondimensional form as

$$d^2P_2/d\xi^2 - \bar{\theta}^2P_2 = -\bar{\theta}^2/(1+R) \tag{6}$$

where

$$\bar{\theta}^2 = L^2G(1-\nu_1^2)(1+R)/h_oh_1E_1 \tag{7}$$

$$R = (1-\nu_2^2)E_1h_1/(1-\nu_1^2)E_2h_2 \tag{8}$$

and where the nondimensionalization is given by

$$(P_1, P_1) = (p_2, p_1)/p_o; \quad \xi = x/L$$
$$S = L\tau/p_o; \quad (U_2, U_1) = GL(u_2, u_1)/p_oh_o. \tag{9}$$

By observing Eqs. (7) and (8), the parameter, $\bar{\theta}$, involves overlap length and adhesive/adherend geometric and material properties, while R measures the degree to which the adherends are different. Normalized void size is given by $\xi_2 - \xi_1 = a_2/L - a_1/L$. Note that if plate 2 is an orthotropic composite, then without change in the basic Eq. (6), R is given by

$$R = (1-\nu_{2x}\nu_{2z})E_1h_1/(1-\nu_1^2)E_{2x}h_2. \tag{10}$$

In the solution procedure, the adhesive is divided into three regions. Equation (6) applies to the first and the third regions. In the void regions, $\tau = 0$, so Eq. (6) is replaced by $d^2P_2/d\xi^2 = 0$. The solutions to these equations in the three regions lead to six constants of integration which are determined by boundary conditions and appropriate continuity conditions between regions.

In region 1, $(0 \le \xi \le \xi_1)$

$$P_{21}(0) = 0; \quad P_{21}(\xi_1) = P_{22}(\xi_1). \tag{11a, b}$$

In region 2, (void) $(\xi_1 \le \xi \le \xi_2)$

$$P_{22} = \text{constant} \tag{12}$$

$$P'_{23}(\xi_2) = P'_{21}(\xi_1) + (\xi_2 - \xi_1)\bar{\theta}^2(P_{22} - 1/(1+R)), \tag{13}$$

where $(\,)' = d(\,)/d\xi$. Equation (13) represents the change in the shear stress from ξ_1 to ξ_2 because of unequal displacements of the adherends over the void region (Zang, 1990).

In region 3 $(\xi_2 \le \xi \le 1)$,

$$P_{22}(\xi_2) = P_{23}(\xi_2); \quad P_{23}(1) = 1. \tag{14a, b}$$

Note that in the notation, P_{2i}, the subscript, i, denotes the solution for P_2 in region i.

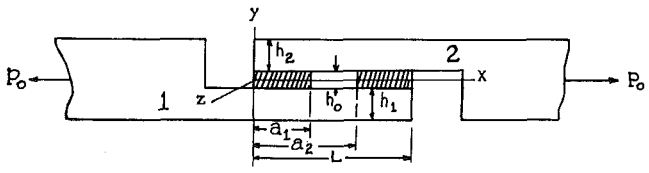


Fig. 1 Step lap joint with a void

[3]Professor. Fellow ASME.

[4]Graduate Student.

[5]Department of Mechanical Engineering, Northeastern University, Boston, MA 02115.

Contributed by the Applied Mechanics Division of THE AMERICAN SOCIETY OF MECHANICAL ENGINEERS for publication in the ASME JOURNAL OF APPLIED MECHANICS. Manuscript received by the ASME Applied Mechanics Division, June 11, 1992; final revision, Mar. 12, 1992. Associate Technical Editor: M. E. Fourney.

Copyright © 1993 by ASME
Downloaded 03 May 2010 to 171.66.16.245. Redistribution subject to ASME license or copyright; see http://www.asme.org/terms/Terms_Use.cfm

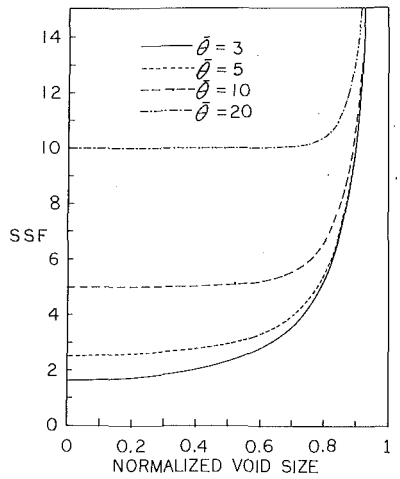


Fig. 2 Shear stress factor (SSF = ratio of peak shear stress to average shear stress) versus normalized void size, $\xi_2 - \xi_1$; symmetric void; $R = 1$

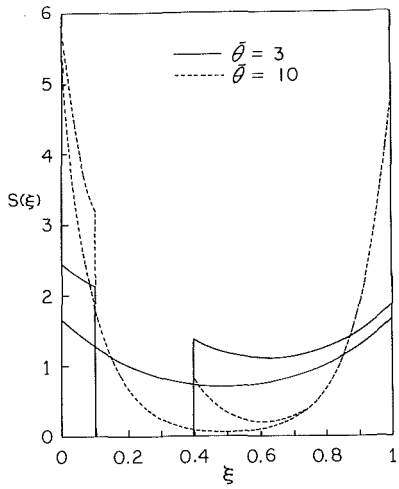


Fig. 3 Nondimensional shear stress, $S(\xi)$, versus ξ for both a void located near the left end of the overlap and no void (continuous curves); $R = 1$

Numerical Results and Discussion

As an example, for identical adherends ($R = 1$), the peak shear stress is shown to depend on both the location and size of the void and the value of $\bar{\theta}$. For the larger values of $\bar{\theta}$, such as $\bar{\theta} = 10$ or greater, a void located at the central portion of the overlap region with void sizes up to 70 percent of the overlap length (Fig. 2), will not affect the peak stress. For the same void located near one end of the overlap (Fig. 3), however, where a high stress gradient already exists, the peak stress can be increased by about 20 percent (for $\bar{\theta} = 10$). Note that even for the relatively large value of $\bar{\theta} = 10$ the stress at the void edge, although not the peak stress, does increase markedly (i.e., by over 35 percent in Fig. 3).

However, for smaller values of $\bar{\theta}$, say $\bar{\theta} = 3$, a void located at the central part of the overlap will also affect the peak stress. For example, when $\bar{\theta} = 3$, for a void one third the size of the overlap, an increase of 18 percent can be obtained for the peak stress, while the same void near one end (Fig. 3) can increase the stress by 39 percent.

By observation of Eq. (6), it is seen that the variation of $\bar{\theta}$ can be either due to changing the adhesive properties G and h_0, or the length of the overlap, L, or adherend properties. Yet, for a given value of $\bar{\theta}$ the non-dimensional shear stress distribution is the same.

Similar trends (Zang, 1990) of the effect of the parameter $\bar{\theta}$, also occur for values of R which differ from unity (i.e., different adherends such as composite/metal). In particular, a higher peak shear stress occurs at $\xi = 1$, when adherend 2 has a smaller stiffness than adherend 1, (i.e., $R > 1$). It turns out that as R increases from 1 to 10, the peak stress almost doubles in value. However, for larger R, the stress rapidly becomes asymptotic to a fixed value, suggesting that adherend 1 is essentially rigid relative to adherend 2.

References

Hart-Smith, L. J., 1981, "Further Developments in the Design and Analysis of Adhesive-Bonded Structural Joints," *Joining of Composite Materials*, ASTM-STP-749, K. T. Kedward, ed., p. 3-31.

Kan, H. P., and Ratwani, M. M., 1983, "Stress Analysis of Stepped-Lap Joints With Bondline Flaws," *Journal of Aircraft*, Vol. 20, No. 10, pp. 848-852.

Renton, W. J., and Vinson, J. R., 1977, "Analysis of Adhesively Bonded Joints Between Panels of Composite Materials," ASME JOURNAL OF APPLIED MECHANICS, Vol. 44, No. 1, pp. 101-106.

Zang, E., 1990, "Analysis of Step Lap Joints With Voids and Thermal Mismatch," M.S. Thesis, Dept. Mechanical Engineering, Northeastern University, Boston, MA.

First-Order Perturbation Analysis of Transient Interlaminar Thermal Stress in Composites

Y. R. Wang[6,8,9] and T.-W. Chou[7,8]

The first-order perturbation analysis of the three-dimensional transient interlaminar thermal stresses of a symmetric composite laminate has been performed in this paper. Numerical results for a four-layer angle-ply laminate have shown that the first-order analysis was necessary for the solution of thick laminate (thickness-to-width ratio $\epsilon \geq 0.02$).

Introduction

This study is a supplement to the work of Wang and Chou (1989), in which the three-dimensional transient interlaminar thermal stresses of a symmetric composite laminate were analyzed by a zeroth-order perturbation technique. Since the higher-order terms were neglected and it seems impossible to make an error analysis due to the mathematical difficulties, the present effort has been made to estimate the accuracy of the result obtained by Wang and Chou (1989) by including the first-order term in the solutions.

[6]Assistant Professor. Assoc. Mem. ASME.

[7]Mem. ASME.

[8]Center for Composite Materials and Department of Mechanical Engineering, University of Delaware, Newark, DE 19716.

[9]Present address: Department of Civil and Mechanical Engineering, McNeese State University, Lake Charles, LA 70609.

Contributed by the Applied Mechanics Division of THE AMERICAN SOCIETY OF MECHANICAL ENGINEERS for publication in the ASME JOURNAL OF APPLIED MECHANICS. Manuscript received by the ASME Applied Mechanics Division, Feb. 5, 1991; final revision, Aug. 14, 1991. Associate Technical Editor: G. J. Dvorak.

Downloaded 03 May 2010 to 171.66.16.245. Redistribution subject to ASME license or copyright; see http://www.asme.org/terms/Terms_Use.cfm

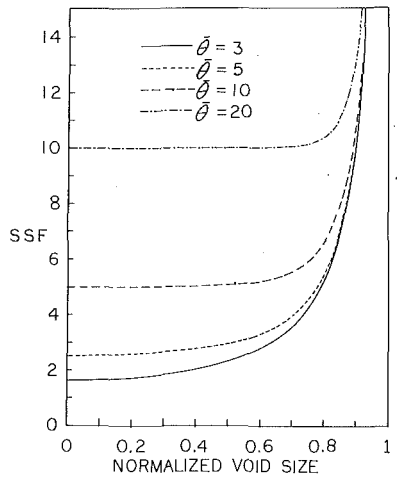


Fig. 2 Shear stress factor (SSF = ratio of peak shear stress to average shear stress) versus normalized void size, $\xi_2 - \xi_1$; symmetric void; $R = 1$

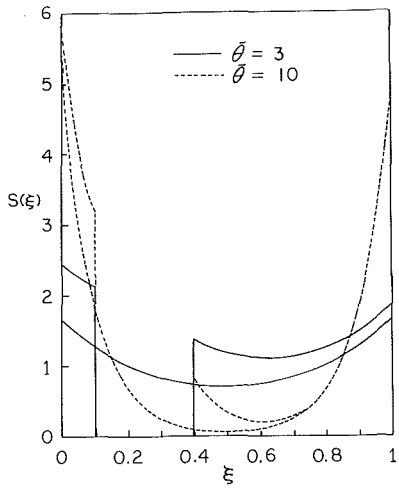


Fig. 3 Nondimensional shear stress, $S(\xi)$, versus ξ for both a void located near the left end of the overlap and no void (continuous curves); $R = 1$

Numerical Results and Discussion

As an example, for identical adherends ($R = 1$), the peak shear stress is shown to depend on both the location and size of the void and the value of $\bar{\theta}$. For the larger values of $\bar{\theta}$, such as $\bar{\theta} = 10$ or greater, a void located at the central portion of the overlap region with void sizes up to 70 percent of the overlap length (Fig. 2), will not affect the peak stress. For the same void located near one end of the overlap (Fig. 3), however, where a high stress gradient already exists, the peak stress can be increased by about 20 percent (for $\bar{\theta} = 10$). Note that even for the relatively large value of $\bar{\theta} = 10$ the stress at the void edge, although not the peak stress, does increase markedly (i.e., by over 35 percent in Fig. 3).

However, for smaller values of $\bar{\theta}$, say $\bar{\theta} = 3$, a void located at the central part of the overlap will also affect the peak stress. For example, when $\bar{\theta} = 3$, for a void one third the size of the overlap, an increase of 18 percent can be obtained for the peak stress, while the same void near one end (Fig. 3) can increase the stress by 39 percent.

By observation of Eq. (6), it is seen that the variation of $\bar{\theta}$ can be either due to changing the adhesive properties G and h_0, or the length of the overlap, L, or adherend properties. Yet, for a given value of $\bar{\theta}$ the non-dimensional shear stress distribution is the same.

Similar trends (Zang, 1990) of the effect of the parameter $\bar{\theta}$, also occur for values of R which differ from unity (i.e., different adherends such as composite/metal). In particular, a higher peak shear stress occurs at $\xi = 1$, when adherend 2 has a smaller stiffness than adherend 1, (i.e., $R > 1$). It turns out that as R increases from 1 to 10, the peak stress almost doubles in value. However, for larger R, the stress rapidly becomes asymptotic to a fixed value, suggesting that adherend 1 is essentially rigid relative to adherend 2.

References

Hart-Smith, L. J., 1981, "Further Developments in the Design and Analysis of Adhesive-Bonded Structural Joints," *Joining of Composite Materials*, ASTM-STP-749, K. T. Kedward, ed., p. 3-31.

Kan, H. P., and Ratwani, M. M., 1983, "Stress Analysis of Stepped-Lap Joints With Bondline Flaws," *Journal of Aircraft*, Vol. 20, No. 10, pp. 848-852.

Renton, W. J., and Vinson, J. R., 1977, "Analysis of Adhesively Bonded Joints Between Panels of Composite Materials," ASME JOURNAL OF APPLIED MECHANICS, Vol. 44, No. 1, pp. 101-106.

Zang, E., 1990, "Analysis of Step Lap Joints With Voids and Thermal Mismatch," M.S. Thesis, Dept. Mechanical Engineering, Northeastern University, Boston, MA.

First-Order Perturbation Analysis of Transient Interlaminar Thermal Stress in Composites

Y. R. Wang[6,8,9] and T.-W. Chou[7,8]

The first-order perturbation analysis of the three-dimensional transient interlaminar thermal stresses of a symmetric composite laminate has been performed in this paper. Numerical results for a four-layer angle-ply laminate have shown that the first-order analysis was necessary for the solution of thick laminate (thickness-to-width ratio $\epsilon \geq 0.02$).

Introduction

This study is a supplement to the work of Wang and Chou (1989), in which the three-dimensional transient interlaminar thermal stresses of a symmetric composite laminate were analyzed by a zeroth-order perturbation technique. Since the higher-order terms were neglected and it seems impossible to make an error analysis due to the mathematical difficulties, the present effort has been made to estimate the accuracy of the result obtained by Wang and Chou (1989) by including the first-order term in the solutions.

[6]Assistant Professor. Assoc. Mem. ASME.

[7]Mem. ASME.

[8]Center for Composite Materials and Department of Mechanical Engineering, University of Delaware, Newark, DE 19716.

[9]Present address: Department of Civil and Mechanical Engineering, McNeese State University, Lake Charles, LA 70609.

Contributed by the Applied Mechanics Division of THE AMERICAN SOCIETY OF MECHANICAL ENGINEERS for publication in the ASME JOURNAL OF APPLIED MECHANICS. Manuscript received by the ASME Applied Mechanics Division, Feb. 5, 1991; final revision, Aug. 14, 1991. Associate Technical Editor: G. J. Dvorak.

Copyright © 1993 by ASME
Downloaded 03 May 2010 to 171.66.16.245. Redistribution subject to ASME license or copyright; see http://www.asme.org/terms/Terms_Use.cfm

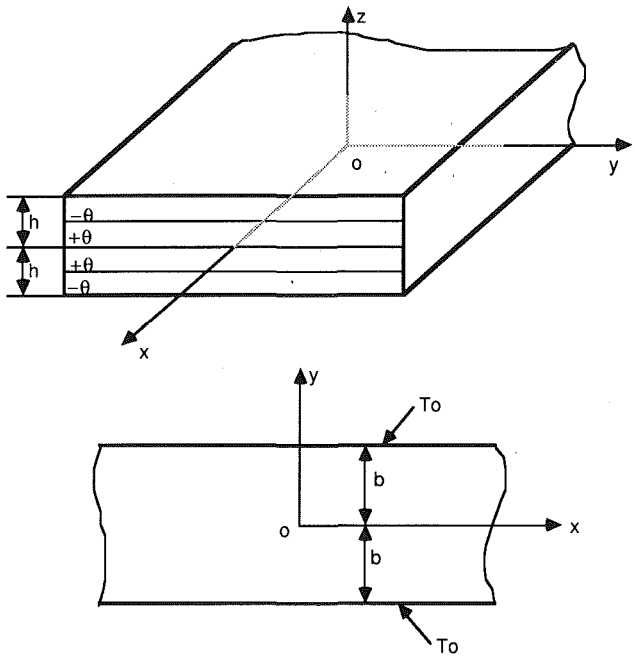


Fig. 1 Geometry and thermal boundary conditions of the laminate for analytical modeling

Problem Formulation

A 4-ply symmetric $(-\theta/\theta)_s$ composite laminate under uniform heating along its two edges ($y = \pm b$) and adiabatic at its top and bottom surfaces ($z = \pm h$) and interfaces ($z = 0, \pm h/2$) is considered in this study. The laminate is of thickness $2h$ and width $2b$; it is infinite in extent along the x-direction (Fig. 1). The nondimensional perturbation parameter (ϵ), displacements (U, V, and W), coordinates (Y and Z), and elastic constants (Q_{ij}) are defined as $\epsilon = h/b$, $U = u/h$, $V = v/h$, $W = w/h$, $Y = y/b$, $Z = z/h$ and $Q_{ij} = C_{ij}/C_{\max}$, where C_{ij} are elastic stiffness constants and $C_{\max}$ is the largest value among all the C_{ij}'s. Then, from Wang and Chou (1989), the nondimensional equilibrium equations are written in the x, y, and z-directions, respectively.

$$Q_{66}\epsilon^2\frac{\partial^2 U}{\partial Y^2}+Q_{55}\frac{\partial^2 U}{\partial Z^2}+Q_{26}\epsilon^2\frac{\partial^2 V}{\partial Y^2}+Q_{36}\epsilon\frac{\partial^2 W}{\partial Y\partial Z}=\epsilon f_1(Y,t)$$

$$Q_{26}\epsilon^2\frac{\partial^2 U}{\partial Y^2}+Q_{22}\epsilon^2\frac{\partial^2 V}{\partial Y^2}+Q_{44}\frac{\partial^2 V}{\partial Z^2}+(Q_{23}+Q_{44})\epsilon\frac{\partial^2 W}{\partial Y\partial Z}=\epsilon f_2(Y,t)$$

$$Q_{36}\epsilon\frac{\partial^2 U}{\partial Y\partial Z}+(Q_{23}+Q_{44})\epsilon\frac{\partial^2 V}{\partial Y\partial Z}+Q_{44}\epsilon^2\frac{\partial^2 W}{\partial Y^2}+Q_{33}\frac{\partial^2 W}{\partial Z^2}=0 \tag{1}$$

where $f_1(Y, t) = \beta_6/C_{\max}\,\partial T/\partial Y$, $f_2(Y, t) = \beta_2/C_{\max}\,\partial T/\partial Y$ and $T(Y, t)$ is the temperature distribution in the laminate. $\beta_2 = \alpha_x C_{12} + \alpha_y C_{22} + \alpha_z C_{23} + \alpha_{xy} C_{26}$ and $\beta_6 = \alpha_x C_{16} + \alpha_y C_{26} + \alpha_z C_{36} + \alpha_{xy} C_{66}$, where α_x, α_y, α_z, and α_{xy} are coefficients of thermal expansion.

Assume the following perturbation solutions including the zeroth-order (ϵ^0) and first-order (ϵ^1) terms:

$$U(Y,Z,t)=\epsilon^0 U_0(Y,Z,t)+\epsilon^1 U_1(Y,Z,t)+\ldots$$

$$V(Y,Z,t)=\epsilon^0 V_0(Y,Z,t)+\epsilon^1 V_1(Y,Z,t)+\ldots$$

$$W(Y,Z,t)=\epsilon^0 W_0(Y,Z,t)+\epsilon^1 W_1(Y,Z,t)+\ldots \tag{2}$$

and substituting Eq. (2) into Eq. (1), the equilibrium equations are written based upon the order of ϵ:

ϵ^0:

$$Q_{55}\frac{\partial^2 U_0}{\partial Z^2}=0$$

$$Q_{44}\frac{\partial^2 V_0}{\partial Z^2}=0$$

$$Q_{33}\frac{\partial^2 W_0}{\partial Z^2}=0 \tag{3}$$

ϵ^1:

$$Q_{55}\frac{\partial^2 U_1}{\partial Z^2}=f_1(Y,t)-Q_{36}\frac{\partial^2 W_0}{\partial Y\partial Z}$$

$$Q_{44}\frac{\partial^2 V_1}{\partial Z^2}=f_2(Y,t)-(Q_{23}+Q_{44})\frac{\partial^2 W_0}{\partial Y\partial Z}$$

$$Q_{33}\frac{\partial^2 W_1}{\partial Z^2}=-Q_{36}\frac{\partial^2 U_0}{\partial Y\partial Z}-(Q_{23}+Q_{44})\frac{\partial^2 V_0}{\partial Y\partial Z} \tag{4}$$

The perturbated equilibrium equations (Eqs. (3) and (4)) do not contain the second-order derivatives in Y as compared to the original equilibrium equations (Eq. (1)). Thus, the boundary conditions on $Y = 0$ and $Y = 1.0$ cannot be satisfied simultaneously. This particular characteristic leads to a singular perturbation problem based upon Van Dyke (1975), for which the straightforward perturbation solution is not uniformly valid throughout the field of interest. In order to obtain the analytical solution, the domain is divided into the interior and boundary layer regions. In the interior region ($0 \le Y < 1$), the boundary conditions at $Y = 0$ are satisfied and the solution is obtained using the classical lamination theory. In the boundary layer region ($0 \ll Y \le 1$), the solution is derived by introducing the stretching parameter and the boundary conditions at $Y = 1.0$ are imposed.

(A) Interior Region: With the classical lamination theory assumption of $\sigma_z = 0$, the following conditions for displacements are obtained.

$$\epsilon^0:\quad C_{33}\frac{\partial W_0}{\partial Z}=\beta_3 T \tag{5a}$$

where $\beta_3 = \alpha_x C_{13} + \alpha_y C_{23} + \alpha_z C_{33} + \alpha_{xy} C_{36}$, and

$$\epsilon^1:\quad C_{23}\frac{\partial V_0}{\partial Y}+C_{33}\frac{\partial W_1}{\partial Z}+C_{36}\frac{\partial U_0}{\partial Y}=0. \tag{5b}$$

Integrating Eqs. (3) and (4), and utilizing the symmetric conditions (7) of Wang and Chou (1989) and Eq. (5a) above, we obtain

$$U_0=B(Y,t)\qquad V_0=D(Y,t)\qquad W_0=\frac{\beta_3}{C_{33}}T(Y,t)Z$$

$$U_1=f_U Z^2+f(Y,t)\quad V_1=f_V Z^2+g(Y,t)\quad W_1=h(Y,t)Z \tag{6}$$

where $f_U = 1/2C_{55}\,(\beta_6 - C_{36}/C_{33}\,\beta_3)\,dT(Y, t)/dY$, $f_V = 1/2C_{44}\,(\beta_2 - (C_{23} + C_{44})/C_{33}\,\beta_3)\,dT(Y, t)/dY$ and $B(Y, t)$, $D(Y, t)$ and $h(Y, t)$ will be determined later. Also, f and g are functions of Y and t only, and have the same characteristics as U_0 and V_0. Therefore, f and g can be omitted without losing generality of the solution.

Considering the equilibrium of forces, we have

$$\sum_{k=1}^{4}\sigma_y^{(k)}(Y,Z,t)h_k=0$$

$$\sum_{k=1}^{4}\tau_{xy}^{(k)}(Y,Z,t)h_k=0 \tag{7}$$

Downloaded 03 May 2010 to 171.66.16.245. Redistribution subject to ASME license or copyright; see http://www.asme.org/terms/Terms_Use.cfm

where k denotes the kth lamina. Integrating Eqs. (7) and (5b) from 0 to Y and utilizing $B(0, t) = D(0, t) = 0$, we obtain

$$\epsilon(q_1 D + q_2 B + q_3 H) + Q_1(Y, t) = 0$$

$$\epsilon(q_2 D + q_4 B + q_5 H) + Q_2(Y, t) = 0$$

$$q_3 D + q_5 B + q_6 H = 0 \tag{8}$$

where

$$Q_1(Y, t) = \sum_{k=1}^{4} \left(\frac{C_{23}}{C_{33}}\beta_3 - \beta_2\right)^{(k)} T^{*(k)}(Y, t) h_k$$

$$Q_2(Y, t) = \sum_{k=1}^{4} \left(\frac{C_{36}}{C_{33}}\beta_3 - \beta_6\right)^{(k)} T^{*(k)}(Y, t) h_k$$

$$q_1 = \sum_{k=1}^{4} C_{22}^{(k)} h_k, \quad q_2 = \sum_{k=1}^{4} C_{26}^{(k)} h_k, \quad q_3 = \sum_{k=1}^{4} C_{23}^{(k)} h_k,$$

$$q_4 = \sum_{k=1}^{4} C_{66}^{(k)} h_k, \quad q_5 = \sum_{k=1}^{4} C_{36}^{(k)} h_k, \quad q_6 = \sum_{k=1}^{4} C_{33}^{(k)} h_k,$$

$$T^*(Y, t) = \int_0^Y T(Y, t)dY \quad H(Y, t) = \int_0^Y h(Y, t)dY.$$

Solving Eqs. (8), we finally obtain the following solutions:

$$B(Y, t) = \frac{f_B(Y, t)}{\epsilon\Delta}$$

$$D(Y, t) = \frac{f_D(Y, t)}{\epsilon\Delta} \quad H(Y, t) = -\frac{f_H(Y, t)}{\epsilon\Delta} \tag{9}$$

where $f_B = (q_3 q_5 - q_2 q_6)Q_1(Y, t) + (q_1 q_6 - q_3^2)Q_2(Y, t)$, $f_D = (q_3 q_5 - q_2 q_6)Q_2(Y, t) + (q_4 q_6 - q_5^2)Q_1(Y, t)$, $f_H = (q_3 q_4 - q_2 q_5)Q_1(Y, t) + (q_1 q_5 - q_2 q_3)Q_2(Y, t)$ and $\Delta = q_1 q_5^2 + q_6 q_2^2 + q_4 q_3^2 - 2q_2 q_3 q_5 - q_1 q_4 q_6$.

(B) Boundary Layer Region: In the boundary layer region, the $O(\epsilon^1)$ and $O(\epsilon^2)$ terms in Eq. (1) are not negligible because the dependent variables undergo sharp changes. A stretching parameter $\eta = (1 - Y)/\epsilon$ is introduced by Wang and Chou (1989). Then, the equilibrium equation (Eq. (1)) becomes

$$Q_{66}\frac{\partial^2 U}{\partial\eta^2} + Q_{55}\frac{\partial^2 U}{\partial Z^2} + Q_{26}\frac{\partial^2 V}{\partial\eta^2} - Q_{36}\frac{\partial^2 W}{\partial\eta\partial Z} = \epsilon f_1(\eta, t)$$

$$Q_{26}\frac{\partial^2 U}{\partial\eta^2} + Q_{22}\frac{\partial^2 V}{\partial\eta^2} + Q_{44}\frac{\partial^2 V}{\partial Z^2} - (Q_{23} + Q_{44})\frac{\partial^2 W}{\partial\eta\partial Z} = \epsilon f_2(\eta, t)$$

$$-Q_{36}\frac{\partial^2 U}{\partial\eta\partial Z} - (Q_{23} + Q_{44})\frac{\partial^2 V}{\partial\eta\partial Z} + Q_{44}\frac{\partial^2 W}{\partial\eta^2} + Q_{33}\frac{\partial^2 W}{\partial Z^2} = 0. \tag{10}$$

To satisfy the matching principle of perturbation and boundary conditions, the following displacement solutions in the boundary layer region are assumed by Hsu and Herakovich (1977):

$$U_b(\eta, Z, t) = \epsilon^0(U_0 + Pe^{\lambda\eta}\cos\alpha Z) + \epsilon^1(U_1 + P'e^{\lambda\eta}\cos\alpha Z)$$

$$V_b(\eta, Z, t) = \epsilon^0(V_0 + Re^{\lambda\eta}\cos\alpha Z) + \epsilon^1(V_1 + R'e^{\lambda\eta}\cos\alpha Z)$$

$$W_b(\eta, Z, t) = \epsilon^0(W_0 + Se^{\lambda\eta}\sin\alpha Z) + \epsilon^1(W_1 + S'e^{\lambda\eta}\sin\alpha Z)$$

where U_0, U_1, V_0, V_1, W_0, and W_1 are interior region solutions obtained in Eq. (6) and P, R, S, P', R', S', λ, and α are undetermined constants. Substituting Eq. (11) into Eq. (10), the equilibrium equations, based upon the order of ϵ, are as follows:

ϵ_0:

$$a_1 P + a_2 R + a_3 S = 0$$
$$a_2 P + a_4 R + a_5 S = 0$$
$$a_3 P + a_5 R + a_6 S = 0 \tag{12}$$

ϵ^1:

$$a_1 P' + a_2 R' + a_3 S' = g_1$$
$$a_2 P' + a_4 R' + a_5 S' = g_2$$
$$a_3 P' + a_5 R' + a_6 S' = 0 \tag{13}$$

where

$$g_1 = \frac{G_1(Y, t)}{e^{\lambda\eta}\cos\alpha Z} \quad g_2 = \frac{G_2(Y, t)}{e^{\lambda\eta}\cos\alpha Z}$$

$$G_1(Y, t) = f_1(Y, t) - 2Q_{55}f_U - \frac{Q_{36}\beta_3}{C_{33}}\frac{\partial T}{\partial Y} - \frac{1}{\Delta}\left(Q_{66}\frac{\partial^2 f_B}{\partial Y^2} + Q_{26}\frac{\partial^2 f_D}{\partial Y^2} + Q_{36}\frac{\partial^2 f_H}{\partial Y^2}\right)$$

$$G_2(Y, t) = f_2(Y, t) - 2Q_{44}f_V - \frac{(Q_{23} + Q_{44})\beta_3}{C_{33}}\frac{\partial T}{\partial Y} - \frac{1}{\Delta}\left(Q_{26}\frac{\partial^2 f_B}{\partial Y^2} + Q_{22}\frac{\partial^2 f_D}{\partial Y^2} + (Q_{23} + Q_{44})\frac{\partial^2 f_H}{\partial Y^2}\right)$$

$$a_1 = Q_{66}\lambda^2 - Q_{55}\alpha^2 \quad a_2 = Q_{26}\lambda^2 \quad a_3 = -Q_{36}\lambda\alpha$$
$$a_4 = Q_{22}\lambda^2 - Q_{44}\alpha^2 \quad a_5 = -(Q_{23} + Q_{44})\lambda\alpha$$
$$a_6 = -(Q_{44}\lambda^2 - Q_{33}\alpha^2).$$

The solutions of Eqs. (13) are

$$P' = \frac{p_1 g_1 + p_2 g_2}{\delta}$$

$$R' = \frac{r_1 g_1 + r_2 g_2}{\delta}$$

$$S' = \frac{s_1 g_1 + s_2 g_2}{\delta} \tag{14}$$

where

$$p_1 = a_4 a_6 - a_5^2 \quad p_2 = a_3 a_5 - a_2 a_6$$
$$r_1 = p_2 \quad r_2 = a_1 a_6 - a_3^2$$
$$s_1 = a_2 a_5 - a_3 a_4 \quad s_2 = a_2 a_3 - a_1 a_5$$
$$\delta = a_1 a_4 a_6 + 2a_2 a_3 a_5 - a_1 a_5^2 - a_6 a_2^2 - a_4 a_3^2.$$

The unknowns P, R, S, λ, and α in the zeroth-order equilibrium equation (Eq. (12)) are given in Wang and Chou (1989).

Numerical Results

A four layer SiC/borosilicate glass $(-\theta/\theta)_s$ laminated plate is taken as a numerical example with $\epsilon = 1/50$. The thermomechanical properties are from Tables 1 and 2 of Wang and Chou (1989).

Figure 2 provides the zeroth ($O(\epsilon^0)$) and first-order ($O(\epsilon^1)$) through-the-thickness displacement solutions. The total displacement is the sum of the zeroth and first-order solutions. The first-order solution gives a negative value contribution to the total displacement result.

The interlaminar normal stress solutions with and without the first-order perturbation term are depicted in Fig. 3. The first-order term ($O(\epsilon^1)$) provides a negative contribution to the stress solution. In the interior region ($Y < 0.8$), the stress solutions with and without the first-order term are the same. This is a direct consequence of the classical lamination theory. In the boundary layer region ($Y > 0.8$), the maximum difference of the two solutions is around 8 percent. The cases for various perturbation parameters ($\epsilon = 0.1, 0.02, 0.01$) have also been studied. The result indicates that the first-order solution becomes more important as ϵ increases. The maximum differences, $(O(\epsilon^1)/(O(\epsilon^0) + O(\epsilon^1)))$, are 3.4 percent, 8 percent, and 20 percent, respectively, for $\epsilon = 0.01, 0.02$, and 0.1. For

Downloaded 03 May 2010 to 171.66.16.245. Redistribution subject to ASME license or copyright; see http://www.asme.org/terms/Terms_Use.cfm

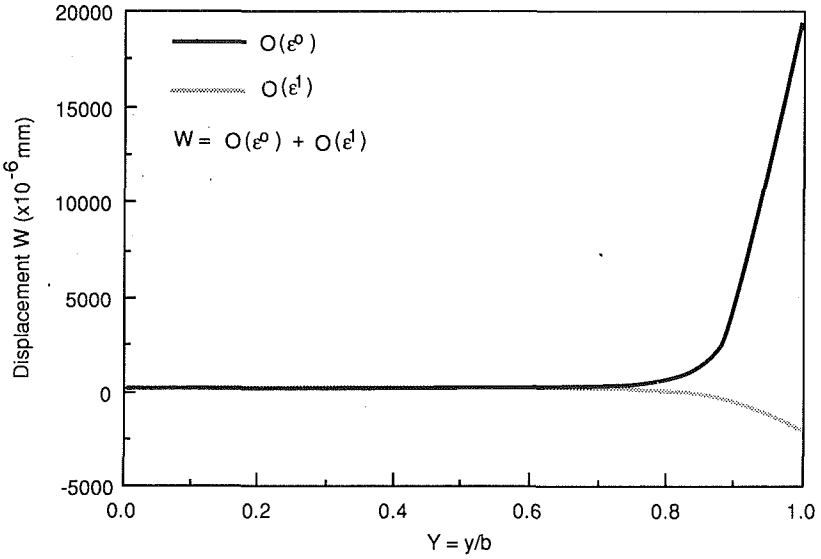


Fig. 2 Displacement profile of zeroth and first-order solution

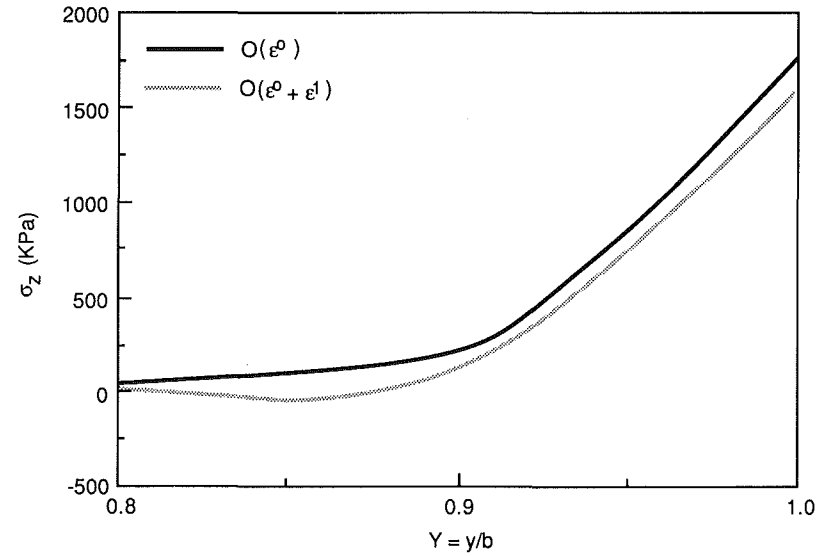


Fig. 3 Stress distribution of zeroth and first-order solution

thick laminate, the zeroth-order solution cannot provide accurate results.

Conclusions and Discussions

(1) The zeroth-order perturbation solution is only accurate for thin laminate ($\epsilon \leq 0.02$). For relatively thick laminate, the higher-order term solution is necessary to obtain a satisfactory result. It can be expected that the higher-order terms, i.e., ϵ^2, ϵ^3, ..., would have less and less influence on the results. In perturbation problems, Van Dyke (1975) pointed out that we often did not know whether the solution series converges or not. It is worth noting that as the perturbation parameter ϵ tends to zero, the present approximate solution becomes increasingly more accurate.

(2) There is still the uncertainty about the existence of the singular behavior of free-edge stresses. No mathematical stress singularity is found based upon the present method of analysis and assumed displacement field.

Acknowledgment

This work is partially supported by the Office of Naval Research.

References

Hsu, P. W., and Herakovich, C. T., 1977, "Edge Effects in Angle-Ply Composite Laminates," *J. of Comp. Mat.*, Vol. 11, pp. 422–428.

Van Dyke, M., 1975, *Perturbation Methods in Fluid Mechanics*, The Parabolic Press, Stanford, CA.

Wang, Y. R., and Chou, T. W., 1989, "Three-Dimensional Transient Interlaminar Thermal Stresses in Angle-Ply Composites," ASME JOURNAL OF APPLIED MECHANICS, Vol. 56, pp. 601–608.

Downloaded 03 May 2010 to 171.66.16.245. Redistribution subject to ASME license or copyright; see http://www.asme.org/terms/Terms_Use.cfm

Journal of Applied Mechanics

Discussion

Equilibrium Configurations of Cantilever Beams Subjected to Inclined End Loads[1]

C. Y. Wang[2]. The authors may not be aware of a paper on the same topic published more than ten years ago (Wang, 1981). The parameters of Wang, (K, α) are exactly the same as those of the present paper (α, β). Both papers showed the number of nonunique solutions for given parameters, e.g., Fig. 2 of Wang (1981) and Tables 1–4 of the present paper, the latter covering a wider range.

Aside from the asymptotic analyses, the numerical method presented by Wang (1981) seems to be much more efficient than the traditional method of using elliptic functions.

References

Wang, C. Y., 1981, "Large Deflections of an Inclined Cantilever with an End Load," *International Journal of Nonlinear Mechanics*, Vol. 16, pp. 155–164.

Author's Closure[3]

I would like to thank Professor Wang for providing the additional reference, Wang (1981). This paper was not seen by the authors during their literature search and was not referenced in their manuscript. The problem investigated by the authors was studied in another form in Wang's paper and was solved using a completely different approach. The results of the two studies also varied, but both showed the existence of the multiple equilibrium solutions for a cantilever beam subjected to a static end load.

In the work of Navaee and Elling (1992), a powerful technique was discussed for the detection and determination of all possible equilibrium configurations of a particular beam subjected to any specific end load. To the best knowledge of the authors, this efficient technique has not been previously shown in any publication. It should be mentioned that the method shown by Wang (1981) can also be employed to obtain the results presented by the authors, but this method is not very efficient mainly because of the following reason.

In the work of Wang, the slope at the free end of the beam for a specific beam and loading condition, is not known at the outset. Therefore, the differential equation of the beam should be numerically solved for a series of guessed values of the free end slope until the correct solution, satisfying the boundary conditions is determined. This requires a lot of computational effort. It should be mentioned that in an earlier work of the author (Navaee, 1989), equilibrium configurations of beams were computed using several different procedures, one of which was similar to the numerical method discussed in Wang's paper. It was determined by Navaee (1989) that the method employing the elliptic integrals was by far the most efficient technique used, because it eliminated a lot of unnecessary computational work.

Aside from the efficiency and usefulness of the technique used in the author's paper, in my view, it is also mathematically interesting to recognize how the well-known solutions expressed in terms of elliptic integrals can be employed to detect and determine the multiple equilibrium configurations of a beam.

References

Navaee, S., 1989, "Alternate Equilibrium Configurations of Flexible Cantilever Beams," Ph.D. Dissertation, Clemson University, Clemson, SC.

Navaee, S., and Elling, R. E., 1992, "Equilibrium Configurations of Cantilever Beams Subjected to Inclined End Loads," ASME JOURNAL OF APPLIED MECHANICS, Vol. 59, pp. 572–579.

Wang, C. Y., 1981, "Large Deflections of an Inclined Cantilever with an End Load," *International Journal of Nonlinear Mechanics*, Vol. 16, pp. 155–164.

Two-Dimensional Rigid-Body Collisions With Friction[4]

W. J. Stronge.[5] The authors analyze two-dimensional or planar collisions between two rough rigid bodies using Routh's graphical method. They attempt to calculate the loss in kinetic energy during collision using a coefficient of restitution defined by either Newton's kinematic law of restitution e or Poisson's hypothesis e_0. In this discussion I prove that the consequences of these definitions are impractical if the collision is eccentric and the direction of sliding changes during contact; e.g., these definitions yield coefficients that depend on orientation of the bodies, friction, and the initial speed of sliding in addition to internal sources of dissipation. Furthermore, elastic collisions are represented by $e = e_0 = 1$ only if the direction of sliding does not change!

In this analysis each rigid body has a velocity for the point of contact. Routh's method gives changes in the difference between these velocities during collision as a function of tangential and normal components of impulse, P_x and P_y, respectively. Changes in relative velocity between two coincident contact points are obtained by implicitly assuming that these points are separated by a deformable particle. The analysis divides the collision process into a period of compression in which the bodies are approaching each other and a period of

[1] By S. Navaee and R. E. Elling and published in the Sept. 1992 issue of the ASME JOURNAL OF APPLIED MECHANICS, Vol. 59, pp. 572–579.

[2] Professor, Michigan State University, East Lansing, MI 48824. Mem. ASME.

[3] S. Navaee, Visiting Assistant Professor, Department of Mechanical Engineering, Clemson University, Clemson, SC 29634-0921.

[4] By Y. Wang and M. T. Mason and published in the Sept. 1992 issue of the ASME JOURNAL OF APPLIED MECHANICS, Vol. 59, pp. 536–642.

[5] Department of Engineering, University of Cambridge, Cambridge, CB2 1PZ, UK.

Copyright © 1993 by ASME
Downloaded 03 May 2010 to 171.66.16.245. Redistribution subject to ASME license or copyright; see http://www.asme.org/terms/Terms_Use.cfm

$$2\hat{W}_y = -(1-e_0^2)[2\mu B_3\tilde{P}_y^2 + (B_2-\mu B_3)\overline{P}_y^2] - 2e_0^2\mu B_3\tilde{P}_y^2. \quad (k)$$

Thus, if e_0 is independent of friction, Poisson's hypothesis exhibits a loss of kinetic energy due to internal irreversible deformation in addition to the energy absorbed by friction. On the other hand, for Newton's kinematic law of restitution, the normal component of impulse does work,

$$2\hat{W}_y = -(1-e^2)[2\mu B_3\tilde{P}_y^2 + (B_2-\mu B_3)\overline{P}_y^2] + 2e^2\mu B_3\tilde{P}_y^2\left[\frac{2\overline{P}_y}{\tilde{P}_y} + \frac{2\mu B_3}{(B_2-\mu B_3)} - 1\right] \quad (l)$$

Here, if e is independent of friction, there is more energy recovered during restitution than was absorbed during compression. Consequently, with friction and slip reversal, $e = e_0 = 1$ do not represent elastic collisions! A similar analysis shows that this conclusion applies also to eccentric collisions which slip stick.

References

Stronge, W. J., 1990, "Rigid Body Collisions With Friction," *Proceedings of the Royal Society, London*, Vol. A431, pp. 169–181.

Stronge, W. J., 1991, "Unravelling Paradoxical Theories for Rigid Body Collisions," ASME JOURNAL OF APPLIED MECHANICS, Vol. 58, pp. 1049–1055.

Stronge, W. J., 1992, "Energy Dissipated in Planar Collision," ASME JOURNAL OF APPLIED MECHANICS, Vol. 59, pp. 681–682.

Authors' Closure[6]

Stronge (1990) develops a new definition of restitution, which is recapitulated in his discussion above. Stronge's definition of restitution is based on an underlying model of the material behavior. This construction provides a means of relating the coefficient of restitution of the elasticity of the materials.

The main issue raised in the discussion is whether Poisson's definition of restitution must be rejected. Stronge takes the position that Poisson's definition violates basic principles, and is untenable. We do not find the argument compelling. If we accept Stronge's modeling assumptions, then Poisson's definition does not work. But might there be another model of the underlying material interactions, departing from Stronge's assumptions, that supports Poisson's definition? The existence of a satisfactory model seems unlikely, but at this time the question remains open. The terms "fallacious" and "defective" should be reserved for ideas that are proven to be inconsistent with generally accepted principles.

A second issue is whether Poisson's coefficient of restitution is a material constant. Stronge suggest that it is actually a function of initial conditions, coefficient of friction, etc. We think the resolution of this issue is quite simple. One should choose the model one prefers, and then stick with it. If one chooses Poisson's definition, then e is a material constant, and an elastic collision is defined to be $e = 1$. If instead one chooses Stronge's definition of an elastic collision, it would be senseless to use Poisson's coefficient of restitution.

The primary issue should be which definition to prefer. Since Stronge's definition of restitution is better founded than Poisson's or Newton's, and in the absence of any apparent drawbacks, the obvious conclusion is that everybody should adopt Stronge's model. We would like to observe that most of our paper is virtually unaffected by this choice. In particular, (1) the use of Routh's method is trivially extended to handle Stronge's restitution; (2) the concept of tangential impact is unaffected; (3) the taxonomy of rigid body impact is unaffected; and (4) the comparison of Poisson's definition to Newton's is unaffected, though less interesting.

[6] Yu Wang, Department of Mechanical Engineering, University of Maryland, 5401 Wilkens Avenue, Baltimore, MD 21228; and Matthew T. Mason, School of Computer Science, Carnegie Mellon University, Pittsburgh, PA 15213.

The Complementary Potentials of Elasticity, Extremal Properties, and Associated Functionals[7]

R. T. Shield[8] and S. J. Lee.[9]

The paper by Wempner (1992) gives several references related to variational principles for finite elastic deformations but omits references to the work of Lee and Shield (1980a, 1980b). In the first paper (1980a) we derive a complementary energy principle which uses trial functions for the actual deformation gradient. This approach avoids difficulties associated with inversion of the constitutive relation which in general involves rotations as well as strains. However, the trial functions used in the complementary energy principle satisfy nonlinear equilibrium equations in general, and this causes varying degrees of difficulty in applying the principle depending on the form of the strain energy function and the particular problem.

In the second paper (1980b), the complementary energy principle and the principle of stationary potential energy were applied to obtain lower and upper bounds on the total strain energy in two problems. For the one-dimensional problem of the all-around extension of a plane sheet with a circular hole, close bounds on the total strain energy were obtained for two forms of the strain energy function, and accurate estimates for the stress resultant at the edge of the sheet were obtained. This problem was treated previously by Rivlin and Thomas (1950) by a numerical approach. The problem of the large extension and torsion of a long elastic cylinder which is bonded at the ends to rigid plates was discussed next, and an approach was described for estimating the resultant end loads from estimates of the total strain energy derived from the variational principles. As an illustration, accurate estimates for the twisting moment and the axial force were obtained for elliptical cylinders with axes in the ratios of 2:1 and 4:1 for a wide range of extension and twist, the neo-Hookean form of the strain energy being assumed for the material of the cylinders.

It may be noted that in Lee and Shield (1980b), the leading term on the right-hand side of Eq. (2.10) should be μ^2.

References

Lee, S. J., and Shield, R. T., 1980a, "Variational Principles in Finite Elastostatics," *Journal of Applied Mathematics and Physics (ZAMP)*, Vol. 31, pp. 437–453.

Lee, S. J., and Shield, R. T., 1980b, "Applications of Variational Principles in Finite Elasticity," *Journal of Applied Mathematics and Physics (ZAMP)*, Vol. 31, pp. 454–472.

Rivlin, R. S., and Thomas, A. G., 1950, "Large Elastic Deformations of Isotropic Materials, Part VIII," *Philosophical Transactions of the Royal Society*, Series A, Vol. 243, pp. 289–298.

[7] By G. Wempner and published in the Sept. 1992 issue of the ASME JOURNAL OF APPLIED MECHANICS, Vol. 59, pp. 568–571.

[8] Oriental, NC 28571-0834.

[9] Loral Vought Systems, Dallas, TX 75265.

Copyright © 1993 by ASME
Downloaded 03 May 2010 to 171.66.16.245. Redistribution subject to ASME license or copyright; see http://www.asme.org/terms/Terms_Use.cfm

Journal of Applied Mechanics

Book Reviews

Biomechanics: Motion, Flow, Stress, and Growth, by Y. C. Fung. Springer-Verlag, New York, 1990. 567 pages. Price: $69.00.

REVIEWED BY S. C. COWIN[1]

This book is the third in a series of volumes by Y. C. Fung on biomechanics. The first two were *Biomechanics: Mechanical Properties of Living Tissues* (1981) and *Biodynamics: Circulation* (1984). In these books the author describes the constitutive behavior of biological tissues, the functional mechanics of the body's organs, and related engineering problems. The present volume, like the previous two, summarizes the application of an enormously wide spectrum of mechanics and thermodynamics to physiology and the engineering of biologically related problems. The mechanics applied includes rigid-body mechanics, mechanical vibration theory, viscous and perfect fluid theory, linear and nonlinear elasticity, wave propagation in fluid and solid media, multiphase mixture theory, chemical thermodynamics, and numerous subtopics of mechanics. The problems addressed cover the spectrum from birds flying and fish swimming to oxygen transport, human impact tolerance, and the engineering of activities at the cellular level.

The introductory chapter describes the principles of mechanics, the modeling of phenomena, and the nature of the practical problems to be dealt with, e.g., basic physiology, prostheses, sports techniques, etc. Chapter 2 discusses the mechanics and modeling of whole bodies or whole body segments. Chapter 3 reviews the mechanics of the fluid dynamic forces that act on bodies moving through the fluid and Chapter 4 applies these results of classical mechanics to the mechanics of flying and swimming. The flight of birds and insects is compared with the flight of aircraft. The mechanics of hovering as well as the swimming of very small flagella are described. The circulatory system is considered in Chapters 5 and 6. Chapter 5 describes blood flow in the heart, lung, arteries, and veins while Chapter 6 addresses the microcirculation, blood rheology and blood flow in the lung. Respiratory gas flow, convection, diffusion, gas exchange, and pulmonary function tests are the topics of Chapter 7. Chapters 8 and 9 concern molecular diffusion and mass transport, fluid movement in interstitial space and across capillary blood vessel walls, filtration and transport across cell membranes. Chapter 10 is a presentation of nonlinear elasticity including the first report I have seen of an additive decomposition of the deformation gradient into a symmetric and an orthogonal matrix of tensor components. This additive decomposition is an analog of the multiplicative polar decomposition theorem used in continuum mechanics to separate the rotational and deformational components of a motion. Chapter 11 concerns residual strains in the arterial walls, stress and strain in the heart and lungs, with some emphasis on the mechanics of the lung. Chapter 12 addresses the topics of strength of biological tissue, injury and repair of organs, trauma due to impact loads, and tolerance of organs to impact and vibratory loads. The final chapter discusses the adaptation of biological tissue and their cells to environmental loading, and the healing of tissue. The discussion of biological adaptation centers on bone adaptation and blood vessel adaptation.

This book is an anthology of modern biomechanics, containing excellent descriptions of most of the topics in the field. It is best read a few topics at a time. The spirit of the book is the wonder of nature and the intellectual excitement of investigating and explaining biological mechanisms, as is easily seen from the problems at the ends of the chapters. For example, Problem 4.13 poses the following question: "An airplane has to rev up the engine to produce the maximum power to take off. How does an eagle take off? One would have to consider the aerodynamic, structural, muscle dynamics, kinematics, metabolic, and energy factors." As another example Problem 8.10 poses a question: "The beautiful flower of water lilies opens up in the sun and closes up when the sun sets. This is a mechanical event of which I know no literature. So let's speculate. Propose a possible explanation, and possible experiments, and quantitative analysis to verify your hypothesis." This volume provides explanations, experiments, and quantitative analysis to explain many of nature's secrets; it also suggests and encourages hypotheses for the investigation of other of nature's secrets.

Stability of Structures: Elastic, Inelastic, Fracture, and Damage Theories, by Z. P. Bazant and L. Cedolin. Oxford University Press, Oxford, U.K., 1991. 1010 pages. Price: $79.00.

REVIEWED BY J. W. HUTCHINSON[2]

Bazant and Cedolin have made a major contribution to mechanics by writing their book on structural ability. The subject is huge and long overdue for a text, and it surely took an act of courage to undertake this effort. As one who was active in the area of structural stability in the 1960s and 1970s, this reviewer saw so much fine work developed during this period which never found its way into any texts or monographs, and it seemed as if no one would rise to the task. Bazant and Cedolin have done so. Their book is truly a major accomplishment. In its nearly one thousand pages the book covers both the elastic and inelastic buckling of columns, frames, plates and shells, and it also has extensive treatment of aspects

[1]Professor, City College, New York, NY 10024.

[2]Division of Engineering and Applied Sciences, Harvard University, Cambridge, MA 02138.

Copyright © 1993 by ASME
Downloaded 03 May 2010 to 171.66.16.245. Redistribution subject to ASME license or copyright; see http://www.asme.org/terms/Terms_Use.cfm

of fracture and localization which are closely tied to stability. The book is well organized. It does a good job of laying out the big picture on each subject as well as giving technical details. The book goes well beyond just an academic treatment of the structural stability. The coverage gives the reader a good sense of how theory and experiment are used in structural applications, although it does not take up design per se. This is particularly true for inelastic buckling. The book contains hundreds of well chosen figures from the literature, problems to be worked by graduate students (or their teachers), and an extensive list of references accompanying each chapter which would be worth the price of the book by itself.

The book is valuable as a reference for anyone in solid mechanics, and it can be used as a graduate text in courses on structural stability. The Preface explains that the book developed out of the authors' graduate courses and gives helpful suggestions for how one might divide the material into semester or quarter long course segments. An instructor using this book as a text will probably want to supplement it with some original papers or possibly, for some topics, with more narrowly focussed texts. The comprehensiveness of the book essentially excludes the possibility of more slowly paced subject development which is desirable for students first making their way in a new subject. For example, this reviewer was delighted to see that Koiter's theory of stability and imperfection-sensitivity for continuum structural systems receives the coverage it so amply deserves, but I was left with the feeling that someone learning the subject for the first time would probably have to go to some of Koiter's papers to actually pick up the various "tricks" and insights needed to carry out analyses on their own.

The book has a total of 13 chapters, seven in the first section under the heading of elastic theories and six in the section on inelastic, damage, and fracture theories. A list of the chapter titles follows:

- Buckling of Elastic Columns by Equilibrium Analysis
- Buckling of Elastic Frames by Equilibrium Analysis
- Dynamic Analysis of Stability
- Energy Methods
- Energy Analysis of Continuous Structures and Approximate Methods
- Thin-Walled Beams
- Plates and Shells
- Elastoplastic Buckling
- Creep Buckling
- Stability of Inelastic Structures, Bifurcation, and Thermodynamic Basis
- Three-Dimensional Continuum Instabilities and Effects of Finite Strain Tensor
- Fracture as a Stability Problem
- Damage and Localization Instabilities

Elasticity: Mathematical Methods and Applications (The Ian N. Sneddon 70th Birthday Volume), by G. Eason and R. W. Ogden. Ellis Horwood Publishers, Chichester, U.K., 1990. 412 pages.

REVIEWED BY R. P. SRIVASTAV[3]

More than 30 years ago, I was visiting Indian Institute of Technology, Kharagpur. One of my friends was a faculty member in the Department of Mathematics. He asked me to accompany him so that he could introduce me to a distinguished visitor from abroad. Being of the irreverent sort—in those days anyway—I asked my friend as to what made this visitor "distinguished." My friend pulled out *Sneddon's Fourier Transforms* (1951) from his bookcase and showed me a citation as a footnote. This incident had a profound effect on me. It made me aware of the importance of Sneddon's work and the high esteem the mathematical community had for him. So, I was ecstatic when I got an opportunity to go to Glasgow in Sept. 1961. My admiration for Ian Sneddon, both the man and the mathematician, has been a monotone-increasing function of time ever since.

The present collection, honoring Ian Sneddon on his 70th birthday, consists of 25 articles contributed by the leading scientists from Canada, Ireland, Italy, Poland, Russia, United Kingdom, and the U.S.A. When I received the book for review, I thought that a comprehensive review was in order. I was disillusioned soon by the broad spectrum of the topics, which in some ways reflects the breadth of Sneddon's influence on the evolution of the mathematical methods for problems in continuum mechanics, especially in the mixed boundary value problems of elasticity. If the review is to be useful, these articles should be reviewed by various experts separately.

In addition to the research articles, George Eason has written a brief biography of Ian Sneddon, which includes the names of Ph.D. students of Professor Sneddon. This is followed by a list of his publications, furnishing a valuable resource for the beginners and experts alike.

The table of contents follows:

1 J. M. Ball and G. Knowles: *Young Measures and Minimization Problems of Mechanics.*

2 L. M. Brock: *Transient Analysis of Edge Dislocation Emission From a Mode I Crack.*

3 Caterina Cassisa and Gaetano Fichera: *A Mechanical Interpretation of the Brothers Riesz Theorem.*

4 S. Davidson, G. Melrose, and J. Tweed: *The Linear Thermoelastic Problem for a Strip With a Line Crack Parallel to Its Edges.*

5 R. S. Dhaliwal, H. S. Saxena, and J. G. Rokne: *Crack at the Interface of an Orthotropic Elastic Layer Bonded to a Dissimilar Orthotropic Elastic Half-Space.*

6 A Cemal Eringen: *On Screw Dislocations and Yield.*

7 J. N. Flavin, R. J. Knops, and L. E. Payne: *Energy Bounds in Dynamical Problems for a Semi-Infinite Elastic Beam.*

8 G. M. L. Gladwell and T. F. Lemczyk: *The Static Reissner-Sagoci Problem for a Finite Cylinder: Another Variation on a Theme of I. N. Sneddon.*

9 A. E. Green, and P. M. Naghdi: *A Direct Theory for Composite Rods.*

10 W. A. Green: *Elastic Waves in Laminated Plates of Inextensible Material.*

11 J. B. Haddow and R. W. Ogden: *Thermoelasticity of Rubber-Like Solids at Small Strains.*

12 M. T. Hanson and L. M. Keer: *Some Aspects of the Quarter-Plane and Quarter-Space Problems.*

13 R. Hill and R. Storåkers: *A Concise Treatment of Axisymmetric Indentation in Elasticity.*

14 V. A. Kondratiev and O. A. Oleinik: *Korn's Type Inequalities for a Class of Bounded Domains and Applications to Boundary Value Problems in Elasticity.*

15 A. I. Murdoch: *A Remark on the Modelling of Thin Three-Dimensional Regions.*

16 Ben Noble: *Boundary Value Problems, Linear Operator Equations, and Variational Methods.*

17 Zbigniew S. Olesiak: *Applications of Weber-Orr Integral Transforms in Problems of Thermoelasticity.*

18 L. E. Payne and R. Straughan: *Improperly Posed and*

[3]Department of Applied Mathematics and Statistics, State University of New York, Stony Brook, NY 11794.

Downloaded 03 May 2010 to 171.66.16.245. Redistribution subject to ASME license or copyright; see http://www.asme.org/terms/Terms_Use.cfm

of fracture and localization which are closely tied to stability. The book is well organized. It does a good job of laying out the big picture on each subject as well as giving technical details. The book goes well beyond just an academic treatment of the structural stability. The coverage gives the reader a good sense of how theory and experiment are used in structural applications, although it does not take up design per se. This is particularly true for inelastic buckling. The book contains hundreds of well chosen figures from the literature, problems to be worked by graduate students (or their teachers), and an extensive list of references accompanying each chapter which would be worth the price of the book by itself.

The book is valuable as a reference for anyone in solid mechanics, and it can be used as a graduate text in courses on structural stability. The Preface explains that the book developed out of the authors' graduate courses and gives helpful suggestions for how one might divide the material into semester or quarter long course segments. An instructor using this book as a text will probably want to supplement it with some original papers or possibly, for some topics, with more narrowly focussed texts. The comprehensiveness of the book essentially excludes the possibility of more slowly paced subject development which is desirable for students first making their way in a new subject. For example, this reviewer was delighted to see that Koiter's theory of stability and imperfection-sensitivity for continuum structural systems receives the coverage it so amply deserves, but I was left with the feeling that someone learning the subject for the first time would probably have to go to some of Koiter's papers to actually pick up the various "tricks" and insights needed to carry out analyses on their own.

The book has a total of 13 chapters, seven in the first section under the heading of elastic theories and six in the section on inelastic, damage, and fracture theories. A list of the chapter titles follows:

- Buckling of Elastic Columns by Equilibrium Analysis
- Buckling of Elastic Frames by Equilibrium Analysis
- Dynamic Analysis of Stability
- Energy Methods
- Energy Analysis of Continuous Structures and Approximate Methods
- Thin-Walled Beams
- Plates and Shells
- Elastoplastic Buckling
- Creep Buckling
- Stability of Inelastic Structures, Bifurcation, and Thermodynamic Basis
- Three-Dimensional Continuum Instabilities and Effects of Finite Strain Tensor
- Fracture as a Stability Problem
- Damage and Localization Instabilities

Elasticity: Mathematical Methods and Applications (The Ian N. Sneddon 70th Birthday Volume), by G. Eason and R. W. Ogden. Ellis Horwood Publishers, Chichester, U.K., 1990. 412 pages.

REVIEWED BY R. P. SRIVASTAV[3]

More than 30 years ago, I was visiting Indian Institute of Technology, Kharagpur. One of my friends was a faculty member in the Department of Mathematics. He asked me to accompany him so that he could introduce me to a distinguished visitor from abroad. Being of the irreverent sort—in those days anyway—I asked my friend as to what made this visitor "distinguished." My friend pulled out *Sneddon's Fourier Transforms* (1951) from his bookcase and showed me a citation as a footnote. This incident had a profound effect on me. It made me aware of the importance of Sneddon's work and the high esteem the mathematical community had for him. So, I was ecstatic when I got an opportunity to go to Glasgow in Sept. 1961. My admiration for Ian Sneddon, both the man and the mathematician, has been a monotone-increasing function of time ever since.

The present collection, honoring Ian Sneddon on his 70th birthday, consists of 25 articles contributed by the leading scientists from Canada, Ireland, Italy, Poland, Russia, United Kingdom, and the U.S.A. When I received the book for review, I thought that a comprehensive review was in order. I was disillusioned soon by the broad spectrum of the topics, which in some ways reflects the breadth of Sneddon's influence on the evolution of the mathematical methods for problems in continuum mechanics, especially in the mixed boundary value problems of elasticity. If the review is to be useful, these articles should be reviewed by various experts separately.

In addition to the research articles, George Eason has written a brief biography of Ian Sneddon, which includes the names of Ph.D. students of Professor Sneddon. This is followed by a list of his publications, furnishing a valuable resource for the beginners and experts alike.

The table of contents follows:

1 J. M. Ball and G. Knowles: *Young Measures and Minimization Problems of Mechanics.*

2 L. M. Brock: *Transient Analysis of Edge Dislocation Emission From a Mode I Crack.*

3 Caterina Cassisa and Gaetano Fichera: *A Mechanical Interpretation of the Brothers Riesz Theorem.*

4 S. Davidson, G. Melrose, and J. Tweed: *The Linear Thermoelastic Problem for a Strip With a Line Crack Parallel to Its Edges.*

5 R. S. Dhaliwal, H. S. Saxena, and J. G. Rokne: *Crack at the Interface of an Orthotropic Elastic Layer Bonded to a Dissimilar Orthotropic Elastic Half-Space.*

6 A Cemal Eringen: *On Screw Dislocations and Yield.*

7 J. N. Flavin, R. J. Knops, and L. E. Payne: *Energy Bounds in Dynamical Problems for a Semi-Infinite Elastic Beam.*

8 G. M. L. Gladwell and T. F. Lemczyk: *The Static Reissner-Sagoci Problem for a Finite Cylinder: Another Variation on a Theme of I. N. Sneddon.*

9 A. E. Green, and P. M. Naghdi: *A Direct Theory for Composite Rods.*

10 W. A. Green: *Elastic Waves in Laminated Plates of Inextensible Material.*

11 J. B. Haddow and R. W. Ogden: *Thermoelasticity of Rubber-Like Solids at Small Strains.*

12 M. T. Hanson and L. M. Keer: *Some Aspects of the Quarter-Plane and Quarter-Space Problems.*

13 R. Hill and R. Storåkers: *A Concise Treatment of Axisymmetric Indentation in Elasticity.*

14 V. A. Kondratiev and O. A. Oleinik: *Korn's Type Inequalities for a Class of Bounded Domains and Applications to Boundary Value Problems in Elasticity.*

15 A. I. Murdoch: *A Remark on the Modelling of Thin Three-Dimensional Regions.*

16 Ben Noble: *Boundary Value Problems, Linear Operator Equations, and Variational Methods.*

17 Zbigniew S. Olesiak: *Applications of Weber-Orr Integral Transforms in Problems of Thermoelasticity.*

18 L. E. Payne and R. Straughan: *Improperly Posed and*

[3]Department of Applied Mathematics and Statistics, State University of New York, Stony Brook, NY 11794.

Copyright © 1993 by ASME
Downloaded 03 May 2010 to 171.66.16.245. Redistribution subject to ASME license or copyright; see http://www.asme.org/terms/Terms_Use.cfm

Nonstandard Problems for Parabolic Partial Differential Equations.

19 T. G. Rogers: *Exact Three-Dimensional Bending Solutions for Inhomogeneous and Laminated Elastic Plates.*

20 M. J. Sewell: *Demonstration of Buckling by Bifurcation and Snapping.*

21 J. M. Spencer: *Three-Dimensional Elasticity Solutions for Stretching of Inhomogeneous and Laminated Plates.*

22 M. P. Stallybrass: *An External Crack Problem—The Ellipse Revisited.*

23 R. J. Tait: *Perturbation Theory and Nonlinear Wave Propagation in Incompressible Elastic Materials.*

24 R. Ursell: *Integrals With a Large Parameter—A Strong Form of Watson's Lemma.*

25 J. R. Willis: *Accelerating Cracks and Related Problems.*

Downloaded 03 May 2010 to 171.66.16.245. Redistribution subject to ASME license or copyright; see http://www.asme.org/terms/Terms_Use.cfm